Thermal Hydraulic Computational Fluid Dynamics Simulations and Experimental Investigation of Deformed Fuel Assemblies

Final Report

Document Submitted to United States Department of Energy, Office of Nuclear Energy

Federal Grant Award Number : DE-NE0008321

Principal Investigator :

Name : Brian Mays
Title : Fluid Mechanics Subject Matter Expert (SME)
Email : brian.mays@areva.com
Phone : 434-832-3849

Name of Submitting Official :

Name : Anthony Chang
Title : Project Manager
Email : anthony.chang@areva.com
Phone : 704-805-2438

Submission Date: March 8, 2017

DUNS Number : 961583429 (previously DUNS Number: 789479578)

Project Period of Performance : February 9, 2015 – March 8, 2017

Report/Product Number : DOE-AFS-0008321-1



Anthony Chang

Submitting AREVA Official

AREVA	AREVA Federal Services LLC
	Engineering Information Record

Document No.:	EIR-3018936	**Rev. No.**	000	**Page 1 of 694**
Project No.:	DE-NE0008321	**Project Name:**	Thermal Hydraulic CFD Simulations and Experimental Investigation of Deformed Fuel Assemblies	
Title:	Toward a Longer-Life Core: Thermal Hydraulic CFD Simulations and Experimental Investigation of Deformed Fuel Assemblies - Final Scientific Technical Report			

Summary:

This Engineering Information Record (EIR) is the final contract deliverable of the Toward a Longer Life Core: Thermal Hydraulic CFD Simulations and Experimental Investigation of Deformed Fuel Assemblies, DOE Project (DE-NE0008321). The EIR consists of a project management and technical summary of all work completed on the project throughout the project performance period.

None of the information presented within is to be considered "Proprietary" by AREVA or any of its sub-recipients.

This material is based upon work supported by the Department of Energy under Award Number DE-NE0008321.

"This report was prepared as an account of work sponsored by an agency of the United States Government. Neither the United States Government nor any agency thereof, nor any of their employees, makes any warranty, express or implied, or assumes any legal liability or responsibility for the accuracy, completeness, or usefulness of any information, apparatus, product, or process disclosed, or represents that its use would not infringe privately owned rights. Reference herein to any specific commercial product, process, or service by trade name, trademark, manufacturer, or otherwise does not necessarily constitute or imply its endorsement, recommendation, or favoring by the United States Government or any agency thereof. The views and opinions of authors expressed herein do not necessarily state or reflect those of the United States Government or any agency thereof."

Contains Unverified Input / Assumptions: Yes: ☐ No: ☒

	Printed Name	Signature	Date
Preparer:	Brian Mays (Principal Investigator)	Brian E. Mays	3/7/2017
Checker:	Anthony Chang (Project Manager)		3/7/2017
Approver:	Ronnie Broughton (AFS Supervisor)		7-MAR-2017
Other:			



AREVA Federal Services LLC

Title: Toward a Longer-Life Core: Thermal Hydraulic CFD Simulations and Experimental Investigation of Deformed Fuel Assemblies - Final Scientific Technical Report

Doc./Rev.: EIR-3018936-000

Project: DE-NE0008321 - Thermal Hydraulic CFD Simulations and Experimental Investigation of Deformed Fuel Assemblies

---

Revision History

Rev.	Changes
000	Initial Release

Table of Contents

Page

REVISION HISTORY 2

LIST OF TABLES 6

LIST OF FIGURES 7

1.0 EXECUTIVE SUMMARY 10
- 1.1 Report and Documentation Description 10

2.0 INTRODUCTION 12

3.0 BACKGROUND 12

4.0 MOTIVATION 13

5.0 PROJECT OBJECTIVES, SCOPE AND STRUCTURE 13
- 5.1 Project Scope 13
- 5.2 Key Objectives 14
- 5.3 Project Team Structure 15
- 5.4 Department of Energy's Stated Goals 16
- 5.5 Comparison of Actual Accomplishments with Goals and Objectives Established 17
- 5.6 Quality Assurance 18

6.0 TECHNICAL ACCOMPLISHMENTS 18
- 6.1 Experiment Description Summary 18
- 6.2 Argonne National Laboratory (ANL) 20
  - 6.2.1 Scope 20
  - 6.2.2 Conjugate Heat Transfer/AREVA Case 22
  - 6.2.3 Isothermal/TAMU Cases 26
- 6.3 AREVA Fuels 36
  - 6.3.1 Scope 36
  - 6.3.2 Design 36
  - 6.3.3 Facility Construction 36
  - 6.3.4 Installation 39
  - 6.3.5 Instrumentation 46
  - 6.3.6 Test Conduct 46
  - 6.3.7 Test Results 47
- 6.4 TerraPower 47
  - 6.4.1 Scope 47

Table of Contents
(continued)

Page

6.4.2 Technical Lead Performance 48
6.4.3 Heated Bundle Descriptions 48
6.4.4 Industry Standard CFD Simulations 50
6.5 Texas A&M University (TAMU) 52
6.5.1 Scope 52
6.5.2 Test Facility Description 52
6.5.3 Facility Construction 57
6.5.4 Procurement and Fabrication 57
6.5.5 Installation 58
6.5.6 Testing 61
6.5.7 Experimental Data 65
6.5.8 Results Analysis 66

7.0 PROJECT TECHNICAL APPROACH 67
7.1 Technical Approach 67
7.1.1 Organizational Collaboration 67
7.1.2 Isothermal Experiment Non-Intrusive Measurement Approach 68
7.1.3 Heated Test Design and Measurement 69
7.1.4 Nek5000 LES Numerical Simulations 69
7.2 Changes in Technical Approach 70

8.0 PROBLEMS OR DELAYS 70
8.1 Rod Degradation – Isothermal Non-Deformed Bundle 70
8.2 Isothermal Deformed Bundle 70
8.3 Duct Leak 71
8.4 Heater Rod Burnout 71
8.5 Heated Rod Fabrication Delay 71
8.6 Computational Resource Limitations 72

9.0 KEY PERSONNEL OR TEAM ARRANGEMENT CHANGES 72

10.0 PRODUCTS PRODUCED OR TECHNOLOGY TRANSFERRED 72

11.0 SCHEDULE MILESTONE PERFORMANCE 72

12.0 FINANCIAL 73
12.1 Cost Share 73

13.0 REFERENCES 74

Table of Contents
(continued)

Page

APPENDIX A : HEATED BUNDLE TEST RESULTS 76

APPENDIX B : TWRP-31-TSPEC-0011, AFAFC AREVA HEATED BUNDLE EXPERIMENT TEST SPECIFICATION 110

APPENDIX C : TWRP-31-RPT-0033, AFAFC HEATED BUNDLE AS-BUILT REPORT 148

APPENDIX D : TWRP-31-RPT-0022, AFAFC RANS PRE-TEST SIMULATION REPORT 202

APPENDIX E : TWRP-31-RPT-0032, AFAFC POST-TEST SIMULATION DETAILS 281

APPENDIX F : TWRP-31-RPT-0036, AFAFC RANS POST-TEST SIMULATION REPORT 298

APPENDIX G : TWRP-31-TSPEC-0010, TAMU FUEL ASSEMBLY FLOW VISUALIZATION TEST SPECIFICATION 349

APPENDIX H : TWRP-31-TREP-0004, AFAFC BENCHMARK SPECIFICATION 377

APPENDIX I : TAMU-WW-QA, TAMU WIRE-WRAPPED QA GUIDELINES 399

APPENDIX J : TAMU-WW-AS, TAMU WIRE-WRAPPED AS-BUILT GEOMETRY (NON-DEFORMED BUNDLE) 405

APPENDIX K : TAMU-WW-TEST-PCM-11-E, TAMU WIRE-WRAPPED TEST SUMMARY OF TEST PCM-11 AT THE EXTERIOR SUBCHANNEL 427

APPENDIX L : TAMU-WW-TEST-PCM-16-C2, TAMU WIRE-WRAPPED TEST SUMMARY OF TEST PCM-16-C2 (CENTER PLANE - 30° OFFSET) 450

APPENDIX M : TAMU-WW-TEST-PCM-14-INT1, TAMU WIRE-WRAPPED TEST SUMMARY OF TEST PCM-14-INT1 AT INTERIOR SUBCHANNEL ONE 472

APPENDIX N : PROJECT CONFERENCE PAPERS AND PRESENTATIONS 492

List of Tables

Page

Table 1: As-Designed Geometric and Operational Conditions of Experiments 19
Table 2: FCTF Loop Equipment and Modifications Made During the Project 37
Table 3: Pressure Hardware Used in the TAMU Non-Deformed, Isothermal Experimental Test 56
Table 4: Shakedown Test Matrix 62
Table 5: Test Matrix for TAMU Non-Deformed, Isothermal Tests 64
Table 6: Project Milestone Baseline Schedule Dates and Submission Dates 73
Table 7: Pressure Drop Cell Information 79
Table 8: Test Boundary Conditions 80
Table 9: Temperature Data Channels Non-Deformed Duct 81
Table 10: Changes to Temperature Data Channels for Deformed Duct 100
Table 11: Pressure Drop Data Comparison Re 20,000[1] 107

List of Figures

Page

Figure 1: Post-Irradiation Fuel Pins [] 13
Figure 2: Toward a Longer Life Core Project Phases and Objectives 14
Figure 3: Toward a Longer Life Core Project Team Structure 16
Figure 4: Visual Comparison between Project Testing/Simulation Goals and Actual Accomplishments 18
Figure 5: Close-up of Nek5000 Mesh (Isothermal) Case that Emphasizes a Fillet around the Wire and Flattening of the Wire between the Pin Cylinders 22
Figure 6: Volume Rendering of Initial Conditions for LES Instantaneous Axial Velocity in 61-Pin Conjugate Heat Transfer AREVA Experiment Geometry at Re=15,000 23
Figure 7: An Axial Slice of Nek5000 SEM Mesh for AREVA/Conjugate-Heat-Transfer Experiment Where the Solid Spectral Elements are Shown in Pink 24
Figure 8: Distribution of Instantaneous Temperature at an Axial Slice at Z=195D (Top) and Upper Part of a Slice at Y=0 (Bottom) 25
Figure 9: A Slice at Z=180.0 of the Time-Averaged Temperature Distribution 26
Figure 10: Nek5000 LES Instantaneous Axial Velocity at Re=10,000 27
Figure 11: Nek5000 LES x-velocity Sensitivity to time Averaging Interval at Re=15,000 28
Figure 12: Nek5000 LES z-velocity and x-velocity Sensitivity to the Reynolds number - Re=10,000 (blue and brown), Re=15,000 (red and green) 29
Figure 13: Velocity - Horizontal (a); Vertical/Axial (b) 30
Figure 14: Horizontal Velocity Plotted in the Domain of Experiment Data Acquisition 31
Figure 15: Horizontal Velocity Plotted in the Domain of Experiment Data Acquisition with Color Map Range Consistent with TerraPower Plots 32
Figure 16: Vertical Velocity Plotted in the Domain of Experiment Data Acquisition 33
Figure 17: Vertical Velocity - (a) in Close Proximity to the Wires, (b) in Close Proximity to the Canister Wall 34
Figure 18: Vertical Component of Velocity Plotted in the Domain that includes the Central Subchannel 35
Figure 19: Horizontal Component of Velocity Plotted in the Domain that includes the Central Subchannel 35
Figure 20: Perpendicular Component of Velocity Plotted in the Domain that includes the Central Subchannel 36
Figure 21: Schematic of the Piping in the FCTF Test Loop 38
Figure 22: Main Vessel Containing the Test Specimen, left; FCTF Overview, right 39
Figure 23: Bundle Assembly, left; Assembled Bundle Showing Upper Tie Plate, right 41
Figure 24: Test Assembly being transferred 42
Figure 25: Instrumented Duct, left; Duct Wrapped in Insulation Blanket being Transferred, right 43
Figure 26: Duct being inserted in the Test Vessel 44
Figure 27: Workers inserting the Bundle into the Duct 45

List of Figures
(continued)

Page

Figure 28: Instrumentation Connection 45
Figure 29: Perspective Diagram of the TAMU Experimental Facility 53
Figure 30: TAMU Isothermal Non-Deformed Test Section, left; Inlet Plenum, bottom right; Outlet Plenum, top right 54
Figure 31: Non-Deformed, Isothermal Experiment Pressure Transducer Locations 55
Figure 32: Face Nomenclature (top-down cross section) 56
Figure 33: Overview of the TAMU Facility Installation 59
Figure 34: TAMU Facility Test Section 60
Figure 35: Typical PIV System Setup 61
Figure 36: Locations of the PIV Planes 63
Figure 37: Experimental Friction Factor and Comparison with CTD [17] 66
Figure 38: Ensemble-Averaged Velocity Field near the Wall (Plane 1) [19] 67
Figure 39: Solid Acrylic Rods and Spacer, left; Solid Rods Immersed in MIR Fluid, right 68
Figure 40: Test Rod Configuration (looking from the bottom up) 77
Figure 41: Pressure Drop Measurement Tap Layout (looking from the bottom up) 78
Figure 42: Internal Duct Thermocouple Radial Locations (viewed from bottom) 84
Figure 43: Pressure Drop Comparison Re 20,000 Non-Deformed Duct vs. Predicted 106
Figure 44: Test05 - Temperature Distribution – Elevation=3074mm, Re=20,000, Power/Pin=24kW 109

Acronym List

Acronym	Definition
2D	Two Dimensional
3D	Three Dimensional
AFS	AREVA Federal Services, LLC.
AMG	Algebraic Multigrid
ANL	Argonne National Laboratory
CAD	Computer-Aided Design
CFD	Computational Fluid Dynamics
CTD	Detailed Cheng-Todreas Correlation
DNS	Direct Numerical Simulation
FCTF	Fuel Cooling Test Facility
GPM	Gallons per Minute
IV	Intellectual Ventures
LES	Large Eddy Simulations
LMFBR	Liquid Metal Fast Breeder Reactor
LOCA	Loss of Coolant Accident
MIR	Mass Index of Refraction
MMS	Method of Manufactured Solutions
NEAMS	Nuclear Energy Modeling Simulation
PIV	Particle Image Velocimetry
PLC	Programmable Logic Controller
PT	Pressure Tap
PTV	Particle Tracking Velocimetry
RANS	Reynolds Average Navier Stokes
RMS	Root-Mean-Square
RTD	Resistance Temperature Detector
SFR	Sodium Fast Reactor
SPIV	Stereoscopic Particle Image Velocimetry
TAMU	Texas A&M University
TC	Thermocouple
U.S. DOE	United States Department of Energy
V&V	Verification and Validation
VFD	Variable Frequency Drive

1.0 EXECUTIVE SUMMARY

This report documents scope, motivation, technical accomplishments and project management of the Department of Energy (DOE) sponsored project, Toward a Longer Life Core: Thermal Hydraulic CFD Simulations and Experimental Investigation of Deformed Fuel Assemblies, DOE project code DE-NE0008321. This was a verification and validation project for flow and heat transfer through wire wrapped simulated liquid metal fuel assemblies that included both experiments and computational fluid dynamics simulations of those experiments. This project was a two-year collaboration between AREVA, TerraPower, Argonne National Laboratory (ANL) and Texas A&M University (TAMU). Experiments were performed by AREVA and TAMU. Numerical simulations of these experiments were performed by TerraPower and ANL. Project management was performed by AREVA Federal Services.

The first of a kind project described herein resulted in the production of both local point temperature measurements and local flow mixing experiment data paired with numerical simulation benchmarking of the experiments. The project experiments included the largest wire-wrapped pin assembly Mass Index of Refraction (MIR) experiment in the world, the first known wire-wrapped assembly experiment with deformed duct geometries and the largest numerical simulations ever produced for wire-wrapped bundles.

This project produced a very large amount of test data from the experiments. Of the large amounts of data, only a portion has been subject to extensive review and used for comparisons to the numerical simulations. While much of the data is of the quality needed for use as Computational Fluid Dynamics (CFD) validation datasets, the following pertinent observations of the test data have been made which may limit its use for this purpose:

1. The heated bundle was instrumented with many thermocouples that measured water fluid temperature as well as embedded internally in the heater rods. Following inspection of the test data, it was determined that the embedded heater thermocouples have limited use for comparison to CFD due to uncertainty in a thermal contact resistance in the heater rod that is necessary to include in the numerical simulation model.
2. The flow visualization bundle pressure drop results showed internal inconsistencies. Pressure drops across uniform lengths corresponding to single wire pitch lengths showed large differences. While some differences are expected due to developing flow effects, the large differences in the test data are unexpected due to the consistent flow area along the bundle length.
3. The flow visualization bundle PIV data in the external wall sub-channel showed an average axial velocity that was slower than the flow area averaged bulk bundle velocity. This is unexpected: due to the packing configuration of the pins in the hexagonal duct, the wall sub-channels are larger in flow area than the internal bundle sub-channels which results in lower flow resistance for flow through the wall sub-channels. Additional review of the velocity measurements at other measurements planes was not performed. A detailed critical review of the Particle Image Velocimetry (PIV) experiment data is recommended before use in CFD validation.

1.1 Report and Documentation Description

This project produced substantial documentation and test data for use for future validation and methods development efforts. Due to the different organizations and project sub-scopes involved, reports were produced throughout the project by the corresponding organizations for the specific project sub-scope. This final project report summarizes the technical and project management aspects of the subject project, Toward a Longer Life Core. This document focuses on the project's technical approaches, experiments and data but also provides project information including personnel and financial reporting data required per the project's contract with the United States Department of Energy (U.S. DOE). Documentation produced by the individual organizations throughout the project and specific to their scope is included as appendices. These reports provide additional

details of the methods used. Additional details of the heated bundle testing performed by AREVA was not released as a separate report, but is contained in Appendix A. Details of the numerical simulation methods employed by ANL are contained in Section 6.2. The following lists the reports that are included in the Appendix:

1. Heated Bundle Experiment Test Specification [Appendix B]
2. Flow Visualization Experiment Test Specification [Appendix G]
3. Benchmark Specification Verification and Validation Plan [Appendix H]
4. Heated Bundle As-Built Report [Appendix C]
5. RANS Pre-Test Simulation Report [Appendix D]
6. Post-Test Simulation Methods Report [Appendix E]
7. RANS Post-Test Simulation Report [Appendix F]
8. TAMU Wire-Wrapped As-Built Geometry (Non-Deformed Bundle) [Appendix J]
9. TAMU Wire-Wrapped Test Summary of Test PCM-11 at Exterior Sub-Channel [Appendix K]
10. TAMU Wire-Wrapped Test Summary of Test PCM-16-C2 (Center Plane – 30° Offset) [Appendix L]
11. TAMU Wire-Wrapped Test Summary of Test PCM-14-INT1 at Interior Sub-channel One [Appendix M]
12. TAMU Wire-Wrapped Quality Assurance Guidelines [Appendix I]

Document 6 in the list above, the Post-Test Simulation Methods Report, was produced to consolidate the information needed by a numerical analyst to model the experiments performed. This document contains geometry details, boundary conditions, and modeling assumptions used to model the experiments.

Conference presentations and associated technical papers from the project are also included as an Appendix. Most of these presentations come from a special session organized at the 2016 ANS Winter Meeting.

1. Verification and Model Sensitivity Analysis for Computational Fluid Dynamics Simulations of Wire-Wrapped Nuclear Fuel Assemblies, *ASME Verification and Validation Symposium*, 2016 [Appendix N]
2. CFD Verification and Validation of Wire-Wrapped Pin Assemblies, *ANS Winter Meeting*, 2016 [Appendix N]
3. Toward a Longer-Life Core: Experimental Data Sets for CFD Calculations of Flow and Heat Transfer in Deformed Fuel Assemblies, *ANS Winter Meeting*, 2016 [Appendix N]
4. Flow Field and Pressure Measurements in a 61-Pin Wire-Wrapped Bundle, *ANS Winter Meeting*, 2016 [Appendix N]
5. Pressure Measurements in a Wire-Wrapped 61-Pin Hexagonal Fuel Bundle, *ANS Winter Meeting*, 2016 [Appendix N]
6. Particle Image Velocimetry Measurements in a Wire-Wrapped 61-Pin Hexagonal Fuel Bundle, *ANS Winter Meeting*, 2016 [Appendix N]
7. Heated Bundle Test in the Fuel Cooling Test Facility (FCTF), *ANS Winter Meeting*, 2016 [Appendix N]
8. Nek5000 Large-Eddy Simulations for Thermal-Hydraulics of Deformed Wire-Wrap Fuel Assemblies, *ANS Winter Meeting*, 2016 [Appendix N]

In addition to the documentation, this project produced a large amount of test data from the heated bundle and flow visualization bundle tests. The following lists the data files for the test data.

Heated Bundle Tests:

Description of the file format is contained in Section A.4.

1. TEST03_re20000_nopower_conversion_08232016.xlsx.
2. TEST05_re20000_power_conversion_08232016.xlsx.
3. TEST19_RE20000_power_10052016_convert.xlsx.
4. TEST24_RE20000_nopower_after_test_10052016_convert.xlsx.

Flow Visualization Bundle Tests:

Each zip file contains a number of .csv and .dat files. Description of the file format is contained in Section 6.5.7 of this report and Sections 3.0 of each Test Summary document.

1. REV2-TAMU-WW-TEST-PCM-11-E-DATA.zip
2. REV1-TAMU-WW-TEST-PCM-16-C2-DATA.zip
3. REV0-TAMU-WW-TEST-PCM-14-INT1-DATA.zip

2.0 INTRODUCTION

The success of this project has proven the ability to fabricate and instrument complex geometries and designs in order to further our understanding of the various phenomena described above. This project successfully provided CFD validation data including as-built geometries and as-tested conditions for use in simulating thermal-fluid mixing in Sodium Fast Reactor (SFR) wire-wrapped fuel assemblies by acquiring CFD grade experiment data characteristic of normal operating conditions. The data acquired in this project improved the validation and application envelope of these CFD methods and furthers our understanding of the flow and heat transfer phenomena to improve reactor safety and design operation limits.

3.0 BACKGROUND

The prediction of the thermal performance in wire wrapped assemblies, which is the typical design in SFR designs, is vital to evaluate the overall performance and safety of the reactor. The current project is the first comprehensive CFD Verification and Validation (V&V) program for wire wrapped assemblies that includes both experiments and numerical simulations.

Liquid Metal Fast Breeder Reactor (LMFBR) designs employ a hexagonal array of pins enclosed in a hexagonally shaped duct for the fuel assemblies. Each fuel pin is helically wrapped by a wire which is used to separate the pins sufficiently to allow sodium coolant to flow through the assembly and promote thermal mixing. Experience with these assemblies has shown that they begin to deform with time during normal operation due to pressure, thermal and irradiation effects which lead to significant changes in core thermal-hydraulics. The effect of pin and duct deformation is increasingly important as reactor designs look toward longer assembly lifetimes. In the EBR-II, local pin overheating was seen due to pin-to-duct and pin-to-pin contact caused by deformations Reference [1]. Overheating of the pins resulted in decreased lifetime of the assemblies.

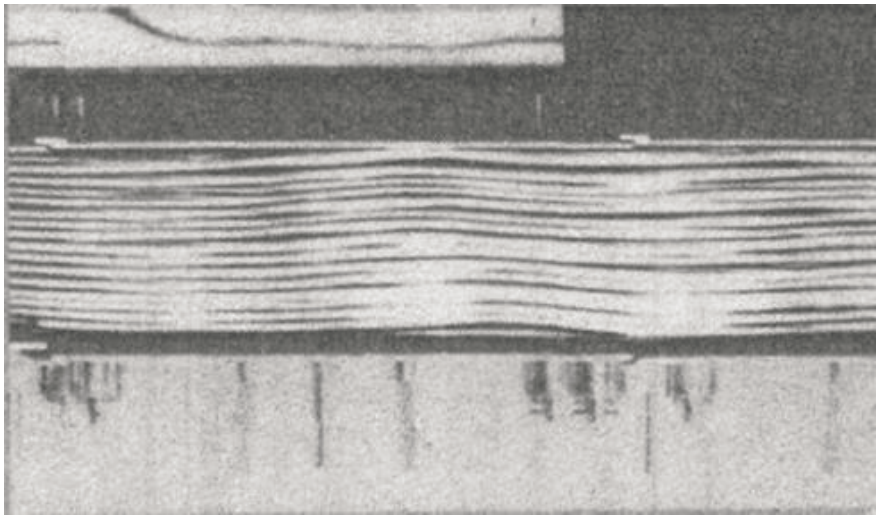


Figure 1: Post-Irradiation Fuel Pins [2]

4.0 MOTIVATION

In SFRs, the high power density and pool reactor design necessitates the use of numerical codes that can capture local heat transfer, 3-Dimensional mixing effects, and natural circulation and transition phenomena which limit the performance and safety for normal operations and accident scenarios. CFD is aptly suited to capture these effects due to its ability to model at a very high spatial and temporal resolution which is not possible with sub-channel and system codes. The motivation for this work is the need to validate CFD codes to accurately model the flow and thermal performance of wire-wrapped fuel assemblies, particularly for deformed end-of-life bundles, as shown in Figure 1. Previous experiments primarily focused on bulk measurements and only for non-deformed geometries for wire-wrapped bundles. These previous experiments lacked the resolution and detail of measurement description and test boundary conditions for use as validation datasets for CFD codes. This project has produced first of a kind, publicly available thermal and flow mixing experimental data with the necessary traceability to be used as CFD validation data for wire wrapped fuel assemblies.

5.0 PROJECT OBJECTIVES, SCOPE AND STRUCTURE

5.1 Project Scope

This project examined the flow phenomena and heat transfer that occur in fluid passing through an LMFBR fuel assembly by providing quality test data to evaluate the ability of numerical simulations to accurately model this flow. The type of fuel assembly considered for this project uses a wire wrap around each fuel pin to provide spacing between the pins. Included in this investigation are the changes to the flow that can result from the deformations of components of the fuel assembly during its operational lifetime in the reactor core. Therefore, the experiments and numerical simulations performed as part of this study consider a geometry with deformations of the kind that have been observed in LMFBR fuel assemblies in addition to the nominal, as-designed fuel assembly geometry.

To accomplish these goals, this project performed two sets of wire wrapped pin bundle experiments. The first measured local velocities while the second set of experiments were heated bundle tests that measured local temperatures. The project also included advanced numerical simulations of these experiments. Thorough documentation of the experiments and simulations is included to aid development of simulation techniques.

5.2 Key Objectives

The project was organized into three phases, which are diagrammed in Figure 2, each with its own set of objectives. The first phase of the project consisted of all of the preparatory work required before the tests begin. In this phase, the test problem was defined and the tests to be performed were designed and documented in formal test specification documents. Existing equipment was refurbished and new equipment was constructed according to these specifications and prepared for the experiments by a series of shakedown tests. While these preparations were being made, pre-test CFD simulations of the tests were performed using the test specifications to define the geometry, operating conditions, and boundary conditions of the simulations. The tests were performed in Phase 2, and the experimental data from the tests were recorded for analysis in the final phase of the project. In Phase 3, the raw test measurements were processed to produce data that is suitable for benchmarking. Additional CFD calculations were performed using the measured, as-built dimensions of the test components and information of the actual operating conditions of the tests. The results of the pre-test and post-test simulations were compared to the test data to evaluate and benchmark the ability of the CFD models to accurately simulate the flow and heat transfer. Following the completion of this work, the results of these efforts were documented in this final report and published with the test data as a validation-quality data set that is available to industry, academia, laboratories, and software development teams for use in benchmarking and improving the methods used to model flow through LMFBR fuel assemblies.

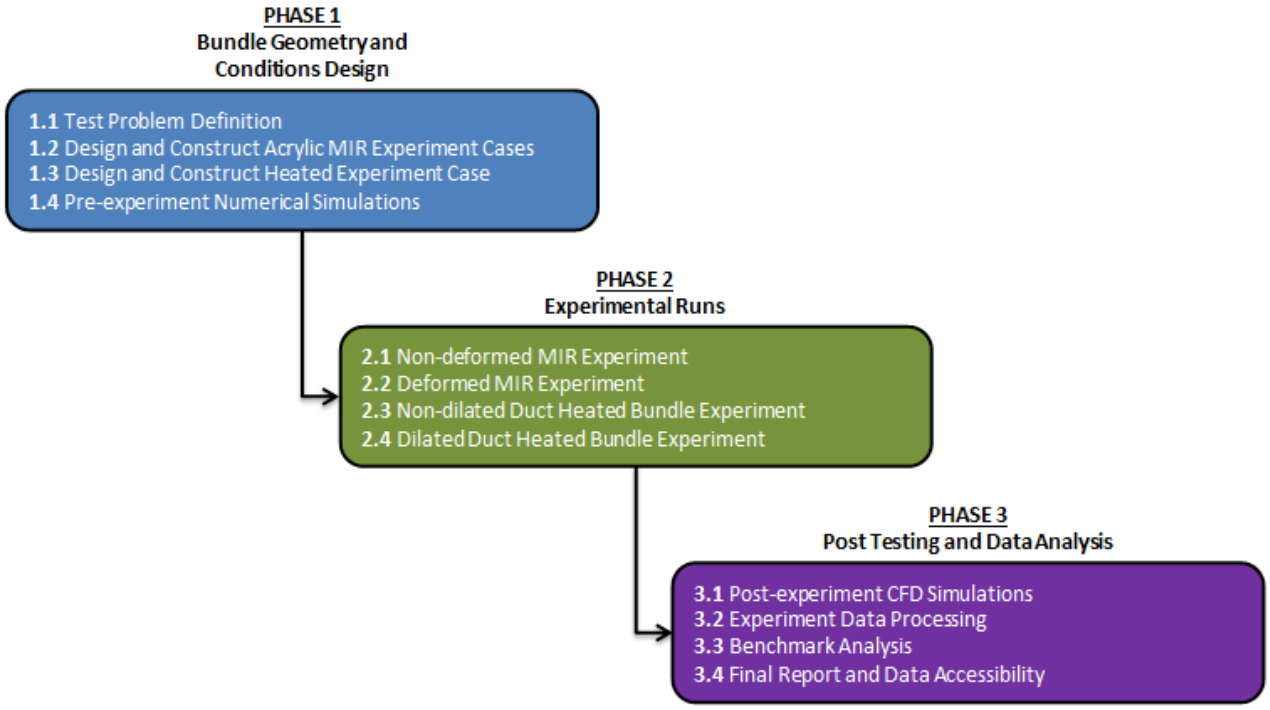


Figure 2: Toward a Longer Life Core Project Phases and Objectives

5.3 Project Team Structure

The project team consisted of leaders in the thermal hydraulics field. The project was a joint effort of these leaders; AREVA, TerraPower, ANL and TAMU. The capabilities and project specific experience is detailed herein. The description of each project team member's contribution is supported by the visual representation shown in Figure 3.

AREVA has extensive experience in boiling water reactor (BWR) and pressurized water reactor (PWR) fuel assembly research and development, design and fabrication. AREVA owns and operates state of the art test facilities capable of investigating mechanical behavior of BWR and PWR fuel bundles. The company has a team of domestic and international design and test engineers that it can use at its discretion to investigate the most challenging fuel bundle design issues. Throughout the company's history, AREVA has performed various thermal hydraulic tests on an array of fuel bundles. AREVA key contribution to this project was the expertise the company's employees held with upgrading the company's existing testing facility to match the needs of this project and expertise with executing the various tests required by the project.

TerraPower has an extensive host of CFD and thermal hydraulics experts. The company's experts are industry leaders with a wide range of technical accomplishments. TerraPower's competence in the design of sodium fuel bundles was one of their key differentiators on this project. Their group brought in-depth technical guidance to the overall team's conversations and decisions. TerraPower was responsible for performing the industry standard Reynolds Averaged Navier Stokes (RANS) CFD comparison simulations of the experiments.

ANL has a wide range of scientists and engineers at their facility that are capable of developing solutions to the industry's most difficult challenges. ANL has extensive experience in simulating wire-wrapped rod bundles with CFD codes. At the time this project was proposed, ANL was developing a highly scalable open-source CFD code capable of producing Large Eddy Simulation (LES) data sets for these wire-wrapped rod bundles at a scale similar to that of this project.

TAMU has personnel with extensive experience in developing both isothermal and non-isothermal flow analysis experiments using PIV and matched index of refraction (MIR) techniques. The university's contribution during this project covered design, construction, and performance of the isothermal MIR flow tests on the fuel bundle to generate high spatial and temporal resolution data of the fluid velocity field using laser-based techniques.

The project was managed by AREVA Federal Services. Management of the project included interfacing with the U.S. DOE, coordinating and executing all project meetings, delivering all project milestone deliverables and development of all project reports.

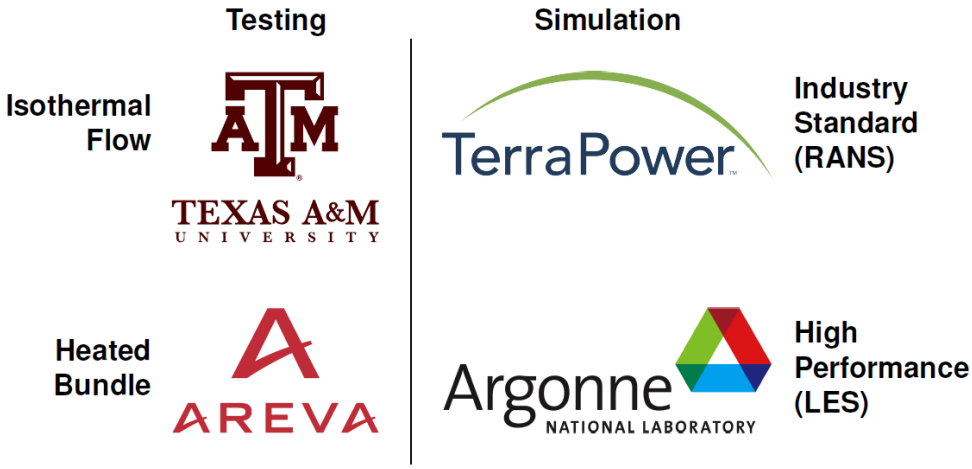


Figure 3: Toward a Longer Life Core Project Team Structure

5.4 Department of Energy's Stated Goals

The purpose of this U.S. DOE funded project is to advance the pedigree of industry practiced CFD techniques through a validation study composed of experimental and numerical components. The particular application of this study is to increase the reliability of predictive methods for modeling flow and thermal performance in distorted LMFBR fuel assemblies, including assemblies with deformations that are characteristic of later-in-reactor life-time, by performing a comprehensive validation study including experiments and corresponding numerical simulations. The availability of an open database of benchmark data suitable for this purpose will promote better modeling approaches in the nuclear industry since this database can be used for high-quality validation efforts by entities wanting to improve their methods.

This purpose was to be accomplished by the following goals:

- Perform four benchmark-quality experiments suitable for the validation of CFD methods;
  - Two isothermal experiments using non-deformed and deformed ducts with 61-pin bundle geometries with an axial length equivalent to 6 wire-wrap pitches using MIR techniques to enable high-speed, laser-based measurements to acquire full-field flow velocities within the bundle.
  - Two heated experiments using non-deformed and deformed ducts with 61-pin bundle geometries with 19 of the pins as heater rods within the bundle, for the purpose of providing thermal mixing components to the validation study.
- Specify assembly geometries of the experimental facilities and computational models using advanced fuels and material modeling approaches for a representative reactor history
- Produce highly resolved CFD simulations for benchmarking lower-fidelity models using techniques that resolve the majority of flow features directly using LES techniques rather than capturing features through the use of time averages of fluctuating quantities combined with empirical models.
- Produce CFD simulations of the project experiments using an industry standard commercial code that employs 2-Equation RANS methods for turbulence modeling.

5.5 Comparison of Actual Accomplishments with Goals and Objectives Established

The objectives of the consortium between AREVA Federal Services, TerraPower, ANL, and TAMU were to further engage industry, the U.S. DOE, and academia while providing well-controlled experimental data and numerical benchmark results for the purpose of validation of CFD modeling techniques for wire-wrapped fuel assemblies with later-in-life deformation as seen in LMFBRs. Additionally, this work was intended to extend synergistic efforts between TerraPower and ANL for wire-wrapped fuel assemblies.

The first phase objectives, as set forth at the onset of the project, included detailed problem definition, test matrix generation, experimental design and construction, and pre-test predictions using CFD. The second phase objective was experimental data acquisition. While the third, and final, phase objectives included post-test blind CFD simulations, experiment data processing, and benchmarking analysis. The project's final goal was the comparison and analysis of the numerical benchmark results in a final project report. The project's end goal was to make the results and report available as a public validation data set for industry, academia, laboratories, and software development teams to use for improvement of modeling methods. The project's goals were set to benefit the industry as a whole with regard to improved reliability, updated best practices, and understanding of uncertainties through verification and validation of methods for predicting thermal performance in advanced liquid metal cooled fast reactors in design spaces not previously explored.

Figure 4 compares the project goals and objectives to accomplishments. All original project goals were achieved with the exception of facility construction and data collection and analysis for the isothermal, deformed duct experiment. The project's inability to construct this duct and execute the associated experimental test is detailed in Section 8.0.

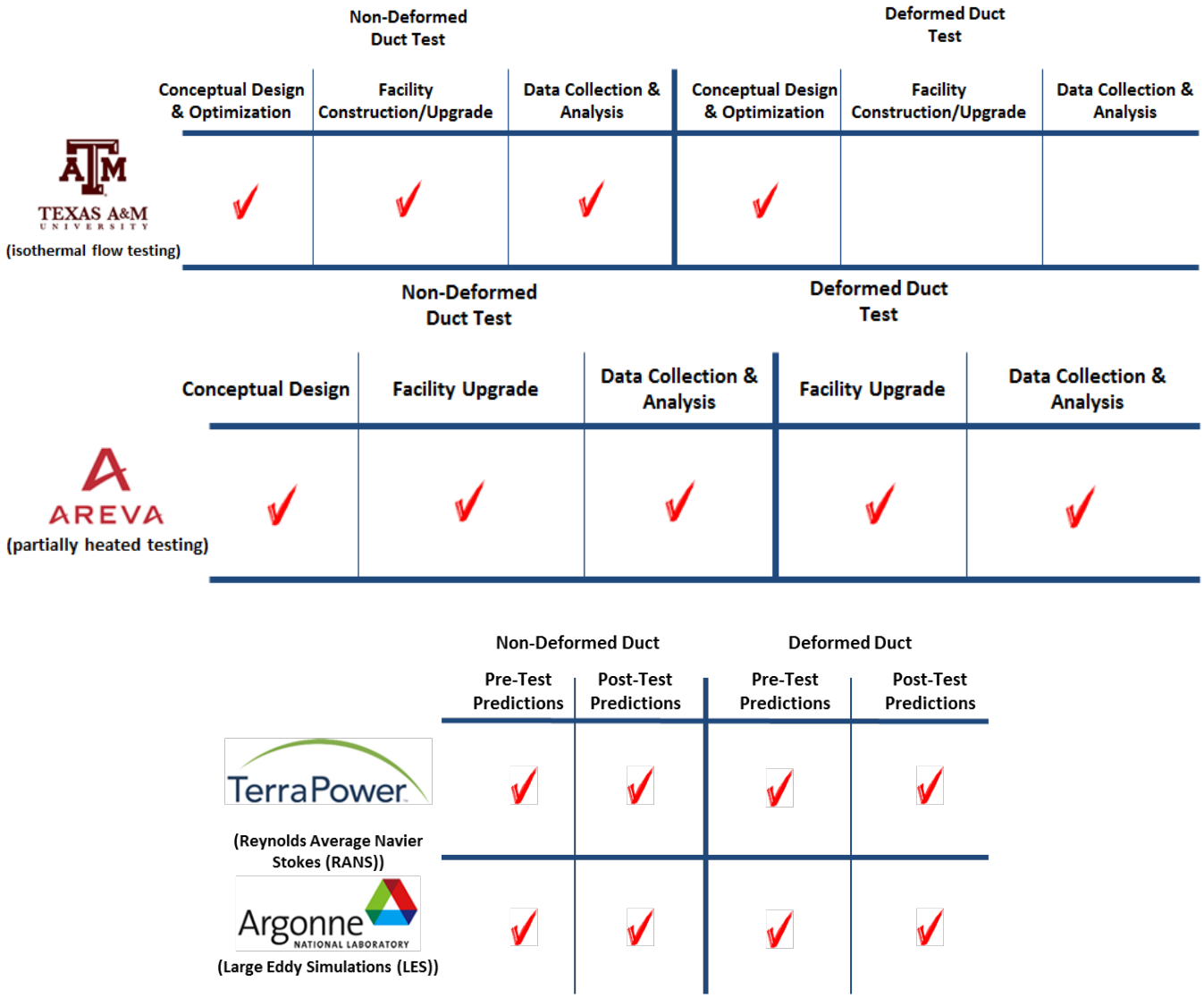


Figure 4: Visual Comparison between Project Testing/Simulation Goals and Actual Accomplishments

5.6 Quality Assurance

Guidelines set forth by AREVA's Quality Assurance Plans used on all of the company's submissions to the U.S. DOE were followed throughout the project. TAMU followed quality assurance guidelines as established by their organization and detailed in Reference [3] [Appendix I].

6.0 TECHNICAL ACCOMPLISHMENTS

6.1 Experiment Description Summary

This project included two experiment test programs as outlined above: isothermal MIR bundle testing performed at TAMU, and heated bundle testing performed at AREVA Fuels. The specific bundle designs are not exact

designs of specific LMFBR fuel assemblies, but are representative in order to acquire data for use in CFD validation. For use as CFD validation datasets, the exact geometry or conditions are not required; however, the experiments must capture the same physics for which the CFD simulations will be used to simulate.

Both experiments were designed to maintain similarity of the critical geometric and operational characteristics. Critical parameters include pin number, pin pitch to pin diameter ratio, wire pitch to pin diameter ratio, wall sub-channel size and Reynolds number. Both experiment bundles used a 61 wire-wrapped pin bundle design. 61 pins was chosen because 61 pins results in a large enough of a bundle, in terms of rows of pins in the hexagonal packing configuration to minimize wall effects, and therefore represent a full size bundle while also limiting the computational resources and experiment costs. Table 1 presents the as-designed geometric and operational conditions of the two experiments.

Table 1: As-Designed Geometric and Operational Conditions of Experiments

Parameter	**Isothermal Experiments**	**Heated Experiments**
Pin Material	Acrylic	Stainless Steel
Working Fluid	p-Cymene	Water
Pin OD (mm)	15.88	9.5
Wire OD (mm)	3.0	1.73
Pin Pitch to Pin Diameter Ratio (P/D)	1.189	1.182
Reynolds Number	20,000	20,000
Wall Gap (percent of tightly packed flat to flat length)	0.77%	0.77%
Wire Pitch to Pin Diameter Ratio	30	30
Bundle Length (in wire pitches)	3.5	14.8

The isothermal bundle uses acrylic for the solid components (pins, wires and duct) and p-Cymene as the working fluid. At the proper temperature, p-Cymene and acrylic have the same index of refraction permitting optical access to the bundle internals enabling use of the MIR to acquire local velocity measurements with laser based diagnostics. The heated bundle tests use 61 wire-wrapped, hexagonally packed pins. Of the 61 pins, 19 are heater rods. Both tests employ a tightly-packed bundle where the wire wrap touches neighboring pins. Pin and wire diameters were chosen to correspond to off-the-shelf part availability while maintaining very close pin pitch to pin diameter ratios between the experiment bundles. Both experiment programs were tested at a Reynolds number of approximately 20,000. One key difference between the two experiments was the total length. Previous studies have shown that it takes approximately 2 wire pitch lengths for the flow to develop due to the

helical wire wrap. The isothermal MIR bundle had a total length of 3.5 wire pitches. This shorter length enabled use of off-the-shelf parts while minimizing flexibility of the acrylic rods. The first 2.25 pitches of the bundle were development length, followed by a single pitch that corresponding to the measurement region. The heated bundle was of a total length of 14.8 pitches. This long length was chosen primarily for compatibility with the existing flow loop at AREVA Fuels. This bundle had approximately 4 wire pitch lengths of development region followed by 8 pitches of measurement region. Of the 8 pitches, 6 were heated. Due to the heating of the fluid, this long length allowed for measurement of the thermal mixing as a function of heat input, and bundle length.

Both bundles measured pressures at specific locations on the duct face to quantify bundle pressure drop. Pressure drops were measured that corresponded to lengths of multiple wire pitch intervals, and lengths of fractional wire pitch intervals to capture the influence of the helical wire wrap on pressure drop. Pressure measurements were also taken on different duct faces to capture the pressure gradient that was expected to develop across the bundle due to the wire wrap.

The isothermal MIR bundle used the PIV method to capture local velocity measurements at locations near the duct wall in addition to internal bundle locations. This is a laser based, non-intrusive method that provides high spatial and temporal resolution of the velocity field.

The heated bundle was instrumented with over 300 thermocouples to measure the thermal field and thermal mixing. Thermocouples were located at surface to fluid interfaces of the duct and pin walls. In addition, heaters were instrumented with internal thermocouples.

6.2 Argonne National Laboratory (ANL)

6.2.1 Scope

ANL has conducted a series of calculations with the open-source high-fidelity code Nek5000 on the MIRA supercomputer simulating the flow in the two experimental campaigns at TAMU and AREVA. Nek5000 is developed under the Nuclear Energy Modeling and Simulation (NEAMS) program as its primary CFD code. Nek5000 is also used within the ART program for the simulation of wire-wrapped assemblies. The present project, presents an invaluable opportunity to foster the validation case for Nek5000.

Nek5000 is based on the spectral element method which is a high-order weighted residual technique that combines the geometric flexibility of finite elements with the rapid convergence and tensor-product efficiencies of global spectral methods. Globally, the SEM is based on a decomposition of the domain into smaller subdomains (elements), which are assumed to be curvilinear hexahedra (bricks) that conform to the domain boundaries. Locally, functions within each element are expanded as *N*th-order polynomials cast in tensor-product form, which allows differential operators to be evaluated at low cost. The principal advantage of the spectral element method is that convergence is exponential in *N*, which implies that significantly fewer gridpoints per wavelength are required to accurately propagate a signal (or turbulent structure) over the extended times associated with high Reynolds number flow simulations. Moreover, Nek5000 has been validated on several types of flows and in particular rod bundle flows.

Temporal discretization is based on a high-order splitting that is 3rd-order accurate in time and reduces the coupled velocity-pressure Stokes problem to four independent solves per timestep: one for each velocity component and one for the pressure. Two formulations are available for the pressure-velocity coupling: P_N-P_N and P_N-P_{N-2}, referring to the polynomial degree of the pressure solution when compared to the velocity solution. The velocity problems are diagonally dominant and thus easily solved by using Jacobi-preconditioned conjugate gradient iteration. The pressure substep requires a Poisson solve at each step, which is effected through multigrid-preconditioned GMRES iteration coupled with temporal projection to find an optimal initial guess. Particularly

important components of Nek5000 are its scalable coarse-grid solvers that are central to parallel multigrid. The code features a fast and fast algebraic multigrid for large processor counts such as those countered here. Counts of 15 GMRES iterations per timestep for billion-gridpoint problems are typical with the current pressure solver. Nek5000 scales extremely well on the BG/P and BG/Q architectures.

In the following sections, two simulation campaigns will be described: one dedicated to the AREVA heated bundle experiment, the other dedicated to the isothermal TAMU bundle experiment. Common features of both simulation campaigns are the methodology and practices used to simulate the experiments are summarized here:

a) Wires are modeled explicitly in both experiments. The contact between wire and pin is modeled through a fillet. A sensitivity study on a reduced set of pins (7) was conducted and it was found that the fillet chosen (0.025*D*, with *D* the pin diameter) produced no significant effect on the quantities of interest for the present experimental comparisons.

b) A gap is assumed between wire and adjacent pin. In order to avoid errors related to an incorrect wire size, the wire is kept to the correct size but is slightly flattened in the proximity of the adjacent pin.

c) Meshing was performed with an in-house code (WireHexMesher) capable to deliver conformal hexahedral meshes of arbitrary pin counts. The code was modernized and modified to handle the present case, in particular a feature was added to model wire flattening and add a mesh layer in the proximity of the canister wall. This layer enables the modeling of the deformation of the canister wall. The mesh resolution was verified independently for all the cases under examination. A sensitivity study to the polynomial order was also conducted for each case. An example of the mesh is provided in Figure 5 emphasizing the flattening of the wire.

d) Turbulence is modeled with a LES approach. The Integral scales of turbulence are simulated directly while the subgrid scales are modeled. The subgrid scale model (SGS model) is based on an explicit filtering technique (with a filter size of 5%) related to the deconvolution model. Given the similar Reynolds number between the two cases, resolution requirements are similar between the two cases.

e) No-slip boundary conditions are assumed for the velocity at the pins surface, wire surface and canister walls.

f) The P_N-P_N formulation for velocity pressure coupling has been used. Pressure and velocity are solved at the same polynomial order. This approach tends to be more accurate.

We also note the following differences between the two simulation campaigns:

a) The solid cladding is modeled only in the AREVA case and a heat flux is imposed at the clad surface interior (but not in the interior of the wire surface). Cladding is modeled in all pins, both heated and unheated. At the top and bottom of the bundle the solid boundary conditions are assumed adiabatic. The canister walls are also considered adiabatic, which may be a source of error since we are not accounting for heat loss. This may be corrected in further post-test simulations.

b) Streamwise boundary conditions vary depending on the case. Boundary conditions are inlet/outlet for the AREVA heat bundle case, comprising the entire test section as well as an entrance and exit length. Inlet/outlet conditions are also used for the TAMU deformed bundle case where multiple pitches (7) are also simulated. Boundary conditions are periodic for the TAMU non-deformed case as the experiment is geometrically invariant and can be considered fully developed in the test section. In this case, a single pitch is simulated.

c) In the cases where inlet/outlet conditions are assumed, a recycling boundary technique is used at the inlet entrance length to ensure that turbulence is fully developed at the test section. With this technique, the flow downstream of the bundle (one pitch) is mapped and rescaled at the inlet.

In the following we will discuss both simulation models and present some select results of such simulations.

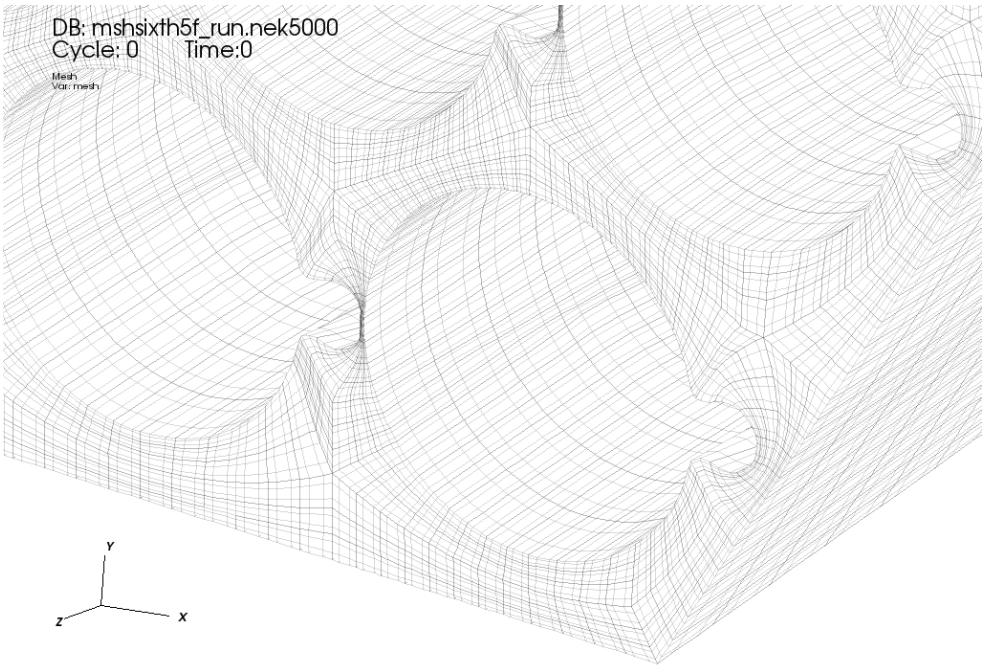


Figure 5: Close-up of Nek5000 Mesh (Isothermal) Case that Emphasizes a Fillet around the Wire and Flattening of the Wire between the Pin Cylinders

6.2.2 Conjugate Heat Transfer/AREVA Case

The AREVA bundle experiment has a larger number of pitches and thus required much larger computational resources that that of the TAMU isothermal non-deformed bundle experiment. Due to limited computational resources, obtained thanks to the ALCC program (and despite two unsuccessful attempts to get computational allocation through the INCITE program which would have allowed for a much larger allocation) ANL progress in the mesh generation, setup, and simulation has been significantly delayed. Nevertheless, ANL has conducted the simulation campaign for the non-deformed geometry in the heated experiment and started the simulation campaign for the deformed geometry. Both activities will be instrumental in furthering the validation case for Nek5000.

Figure 6 illustrates the flow field complexity expected in this experiment geometry. Figure 7 also shows the computational mesh for this case with a layer of elements in pink for solid portion of the pins. Note that for the seven pitches, the spectral element mesh (E) has 15 million elements which makes it the largest mesh attempted with Nek5000 to date in terms of element number. At the polynomial order N=8 for production run resolutions, this simulation will be the largest not only for Nek5000 but for any code in the wire-wrap geometry

(approximately 10 billion degrees of freedom) and scales to the full Mira supercomputer (1,048,576 MPI[1] processes).

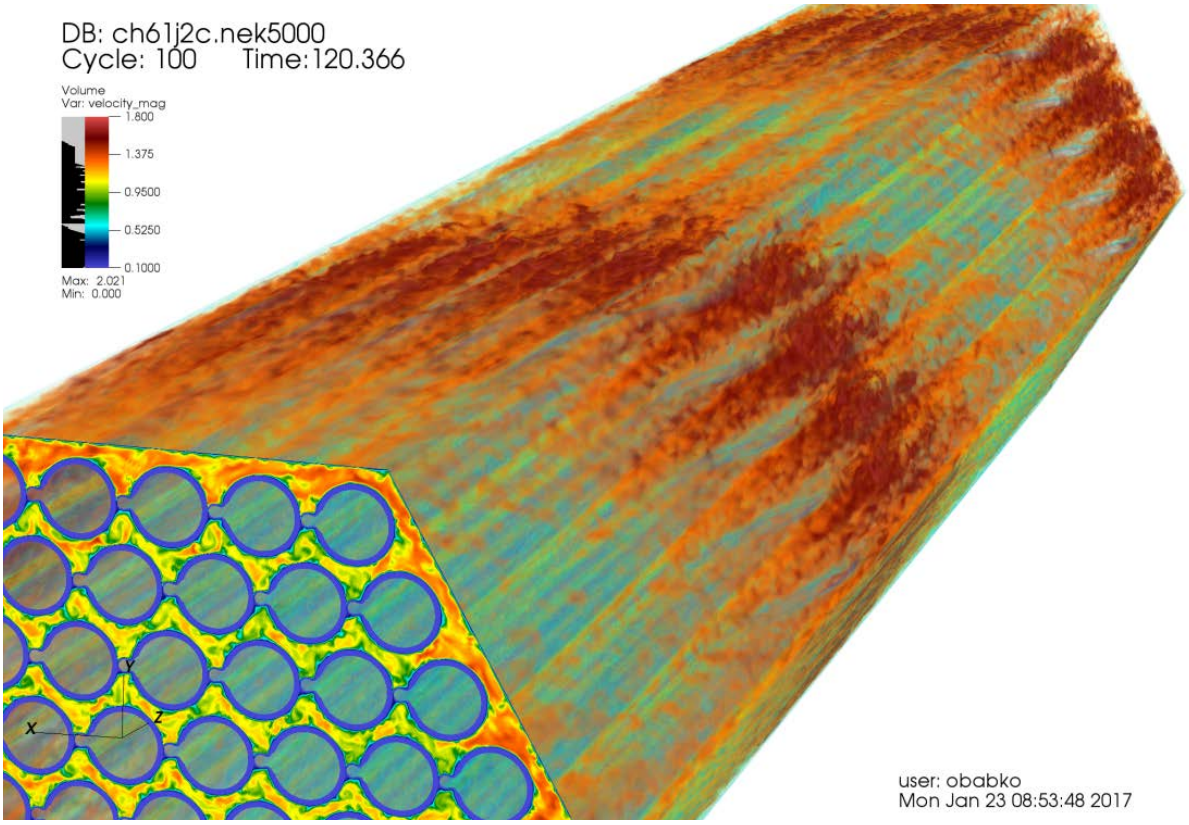


Figure 6: Volume Rendering of Initial Conditions for LES Instantaneous Axial Velocity in 61-Pin Conjugate Heat Transfer AREVA Experiment Geometry at Re=15,000

[1] Message Passing Interface library (for parallel communications)

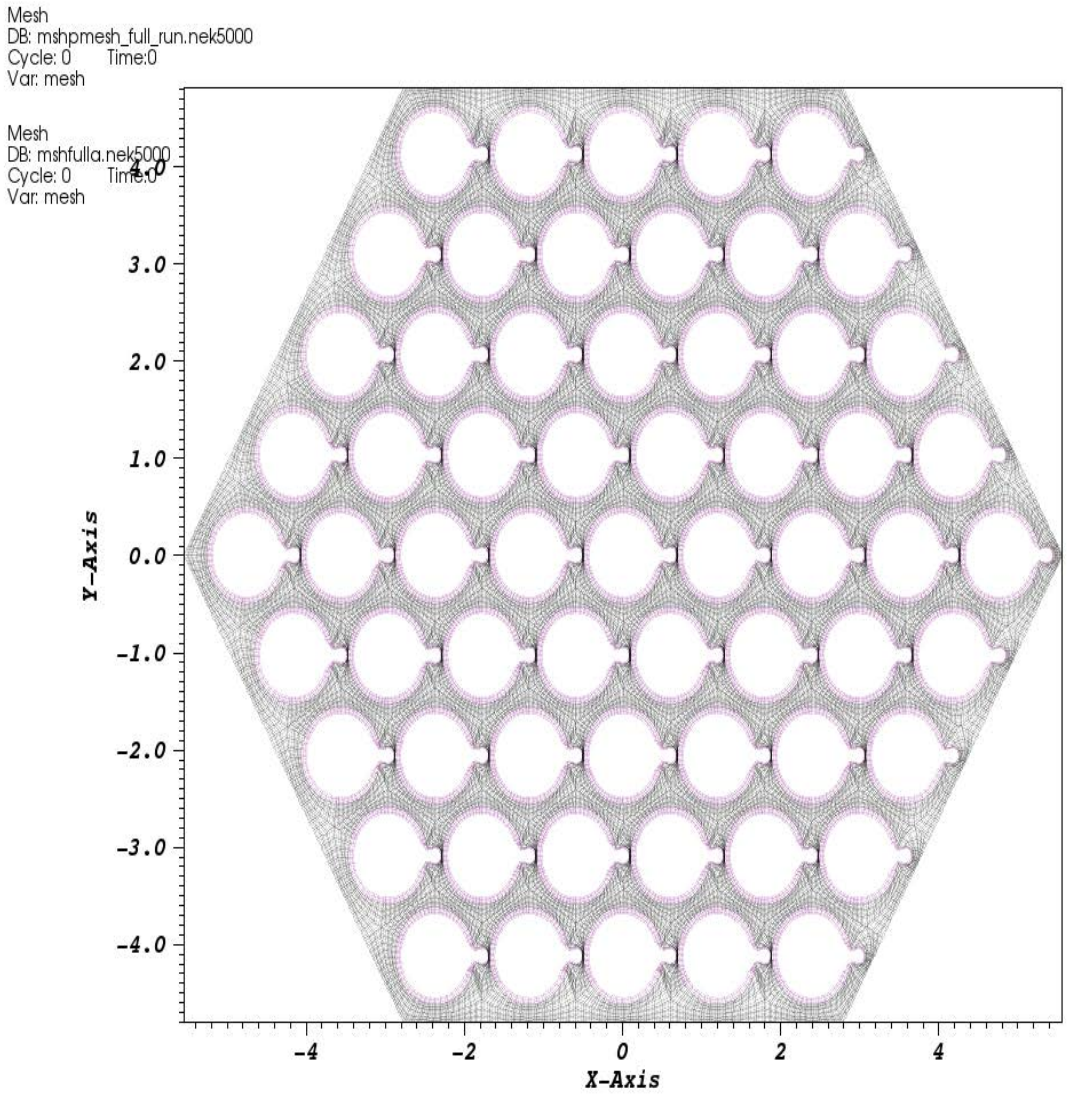


Figure 7: An Axial Slice of Nek5000 SEM Mesh for AREVA/Conjugate-Heat-Transfer Experiment Where the Solid Spectral Elements are Shown in Pink

In Figure 8 and Figure 9 we present some of the snapshots of the flow field obtained in this geometry. We note that the temperature is normalized and in non-dimensional units. Further comparison with the experiment will be reported in the annual NEAMS thermal-hydraulics update report later this year.

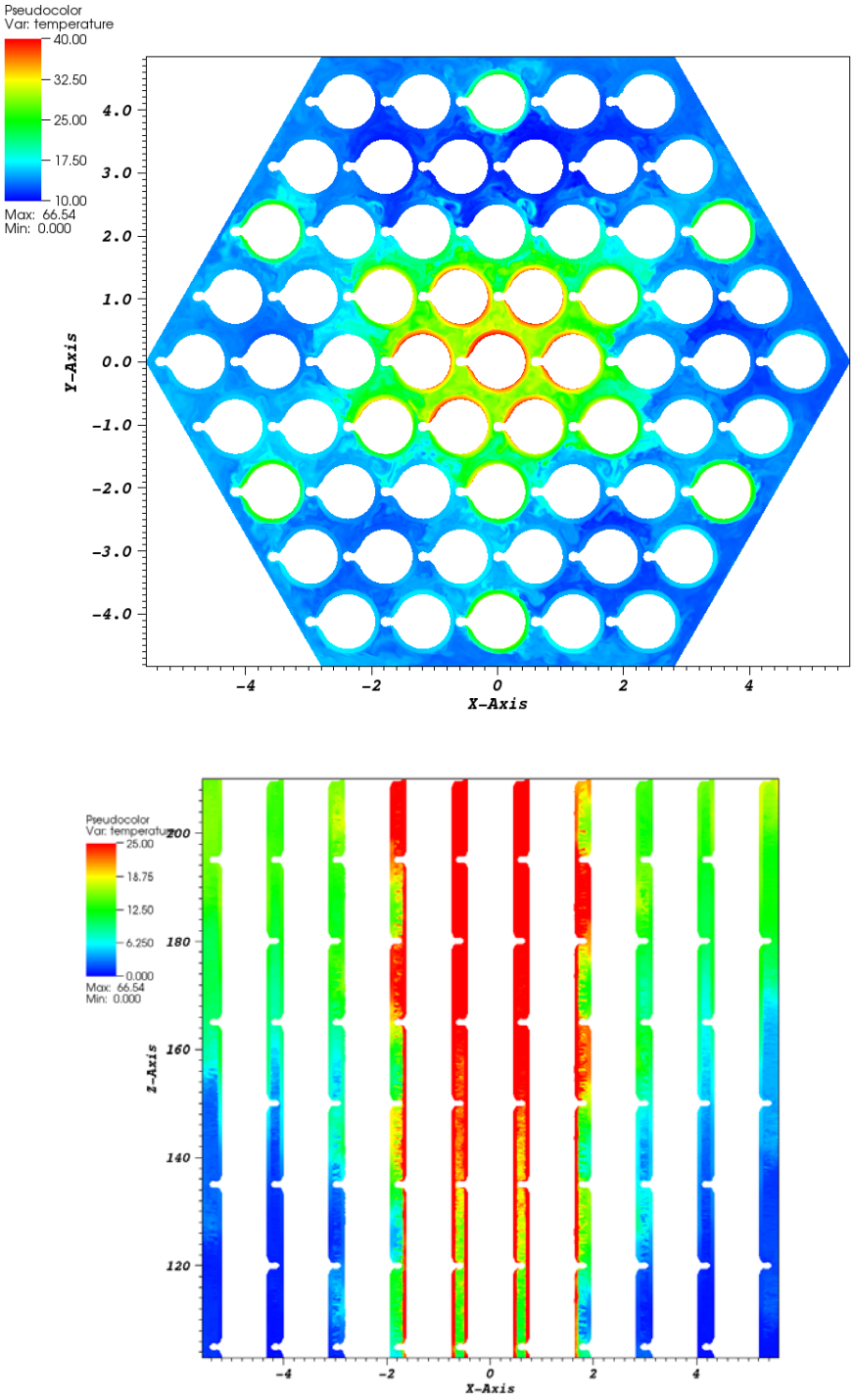


Figure 8: Distribution of Instantaneous Temperature at an Axial Slice at Z=195D (Top) and Upper Part of a Slice at Y=0 (Bottom)

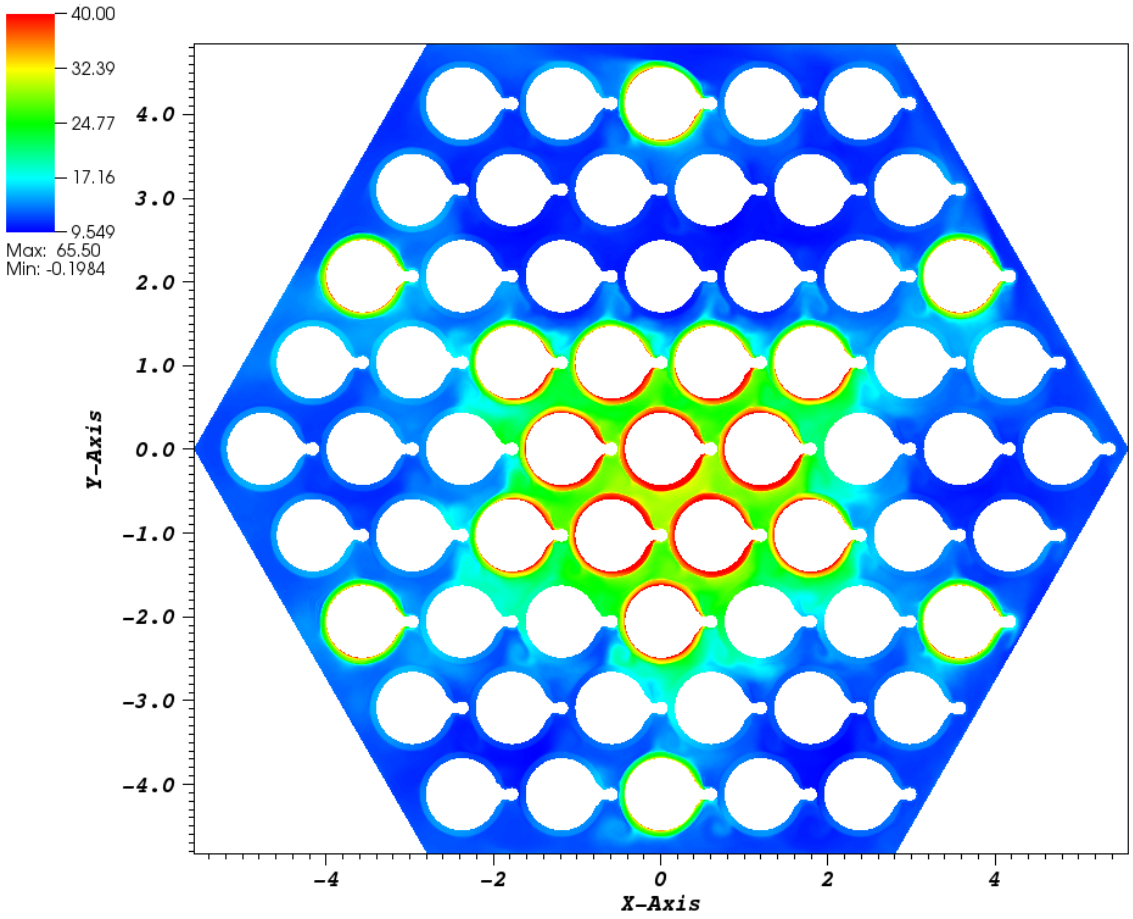


Figure 9: A Slice at Z=180.0 of the Time-Averaged Temperature Distribution

We emphasize that this large calculation produced large amounts of data which will be used to shed additional light on the physics of heat transfer in this geometry and will be instrumental to guide further validation of Nek5000 within the NEAMS and ART programs.

6.2.3 Isothermal/TAMU Cases

ANL has conducted a series of tests and production runs for TAMU isothermal experiment geometry. To accelerate convergence and optimize the use of limited computational resources, ANL began with low resolution and Reynolds number of N=3 and Re=100, respectively, and scaled the runs up to *N*=8 and Re=40,000. Note that the Reynolds number in the present discussion is based on pin diameter, D and is equivalent to the experimental conditions. We note that in the case of the TAMU bundle D/D_h=2.055 where D_h is the hydraulic diameter.

Sensitivity studies on the mesh resolution, time-averaging interval, and sensitivity to flat-to-flat distance were conducted. The mesh settled upon had E=1.6 million spectral elements for a single wire pitch and axially periodic boundary conditions. We note that the choice of periodic boundary conditions was justified by previous experience of observing the quick transition of inlet flow into fully developed flows in wire-wrap geometries. Figure 5 shows the computational mesh for the TAMU cases with *N*=3 with a detail highlighting the flattening of the wire. Production runs have been conducted, for the target Reynolds number at *N*=7.

Figure 10 shows the LES solution at Re=10,000 as flow undergoes transition to fully turbulent flow (see also recording[2]).

Figure 11 illustrates the sensitivity to the time average interval for an unsteady case of production runs and helps establish the necessary time scales and uncertainty for time averaged results. The velocity here is normalized by the bulk velocity and is sampled at *x=0.0* and *z=0.0*. A sensitivity to the polynomial order at Re=15,000 was also conducted demonstrating that a polynomial order N=6 was sufficient. Similar studies were conducted at all Reynolds number. Once acceptable practices have been established for the simulation at low Reynolds number the simulation campaign has been conducted on the Mira supercomputer at the target Reynolds number (Re=40,000). Figure 12 illustrates the Reynolds number dependency. The velocity here is normalized by the bulk velocity and is sampled at *x=0.0* and *z=0.0*.

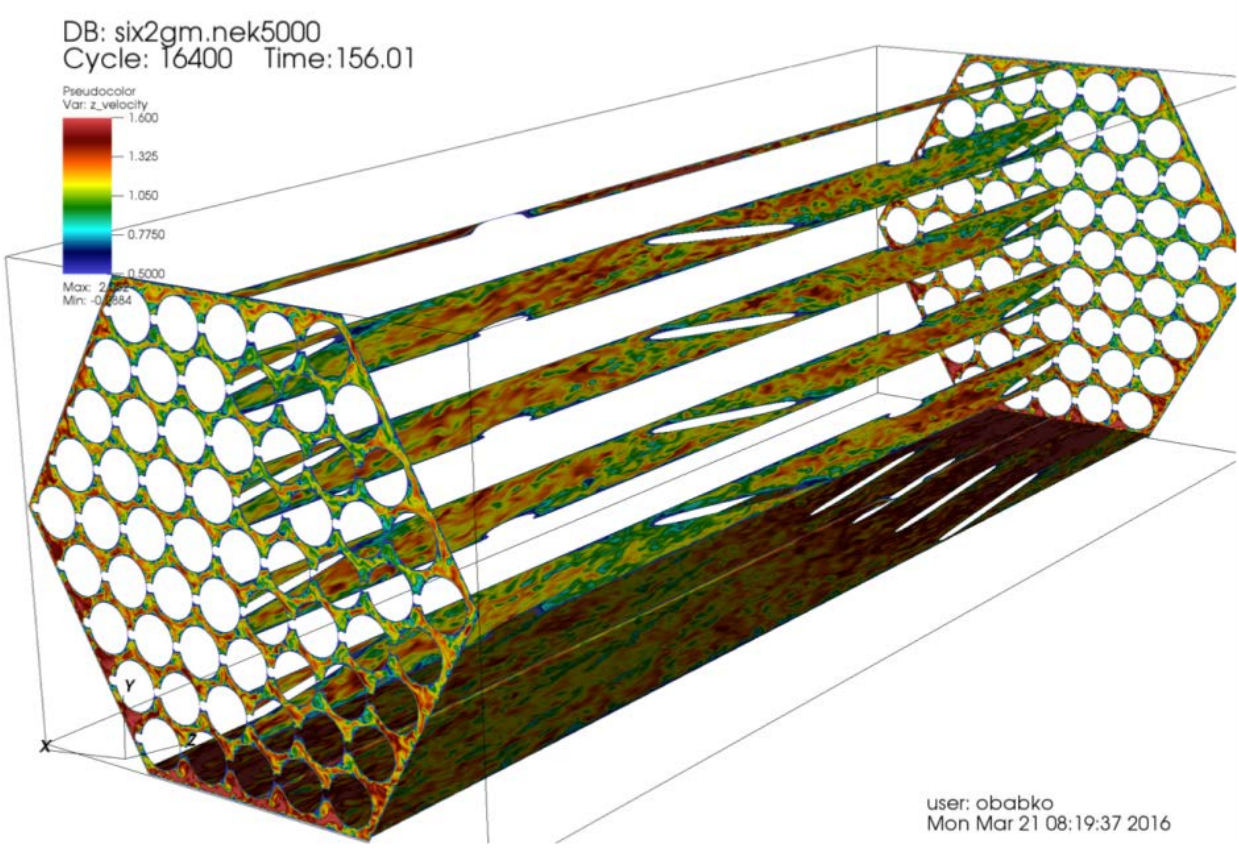


Figure 10: Nek5000 LES Instantaneous Axial Velocity at Re=10,000

[2] http://www.mcs.anl.gov/~obabko/vz_1e4_sls.mpeg

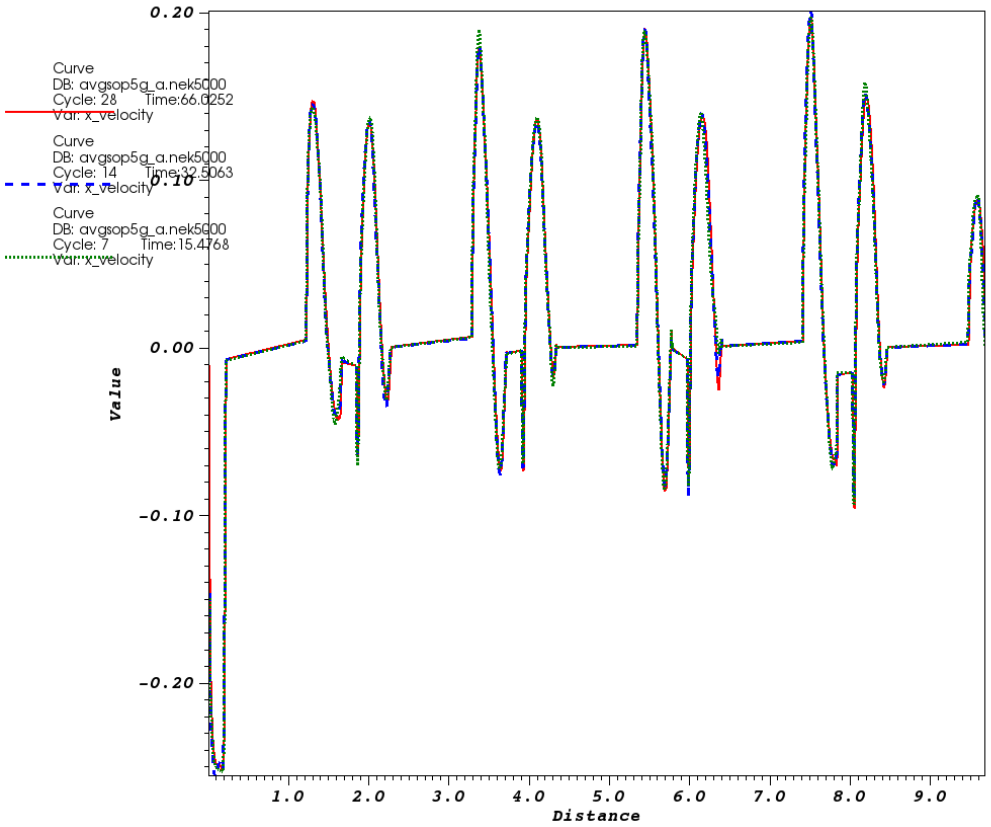


Figure 11: Nek5000 LES x-velocity Sensitivity to time Averaging Interval at Re=15,000

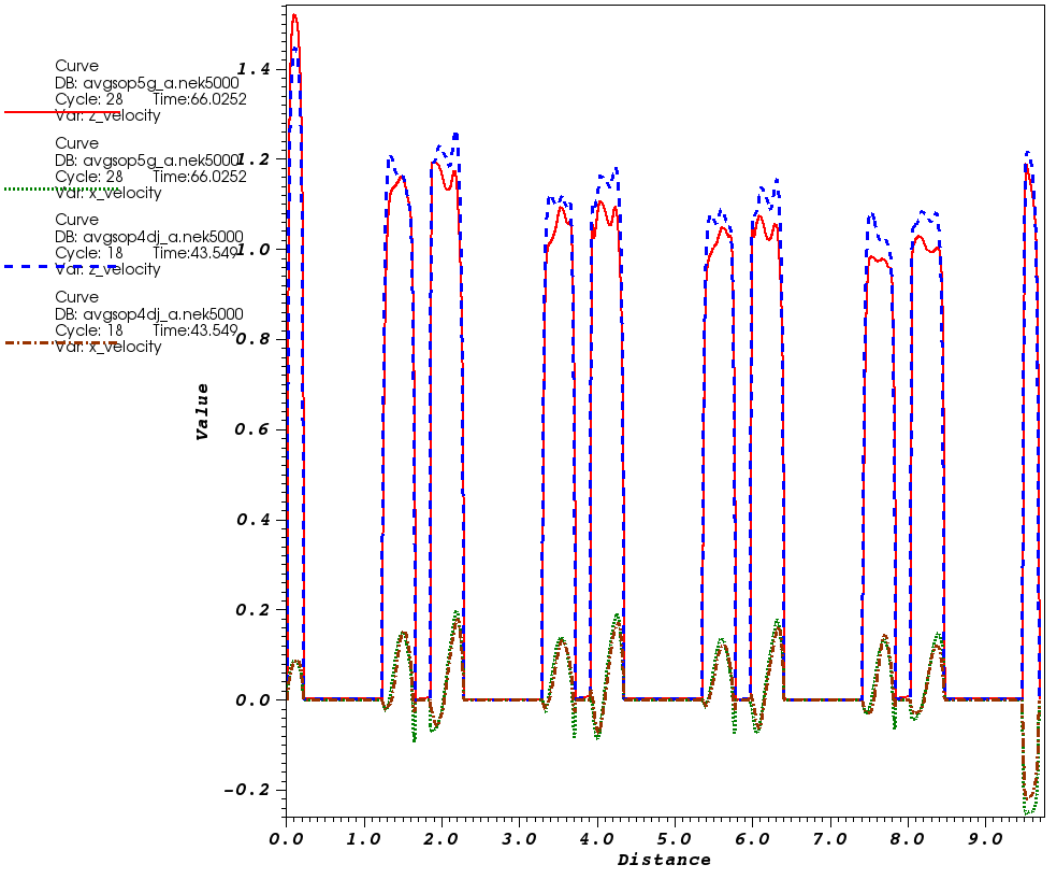


Figure 12: Nek5000 LES z-velocity and x-velocity Sensitivity to the Reynolds number - Re=10,000 (blue and brown), Re=15,000 (red and green).

The following details ANL comparisons with the TAMU bundle experiment. We first address their data at Re=40,000 for an edge sub-channel. As stated, this is a pin diameter Reynolds number and is consistent with the experiment test conditions.

Figure 13 shows a full single wire-pitch slice of horizontal and vertical (i.e. axial) velocity and illustrates its position with respect to the full bundle. Figure 14, Figure 15 and Figure 16 show the zoomed in versions of Figure 13 plotted on the scales consistent with experiment data acquisition window. Note that Figure 15 shows the horizontal velocity with a color map consistent with TerraPower plots to facilitate cross-comparison. Overall, the comparison of the horizontal velocity is in good qualitative agreement with the experiment. The vertical (axial) velocity shows significantly larger values than the experiment which is similar to that of TerraPower calculations.

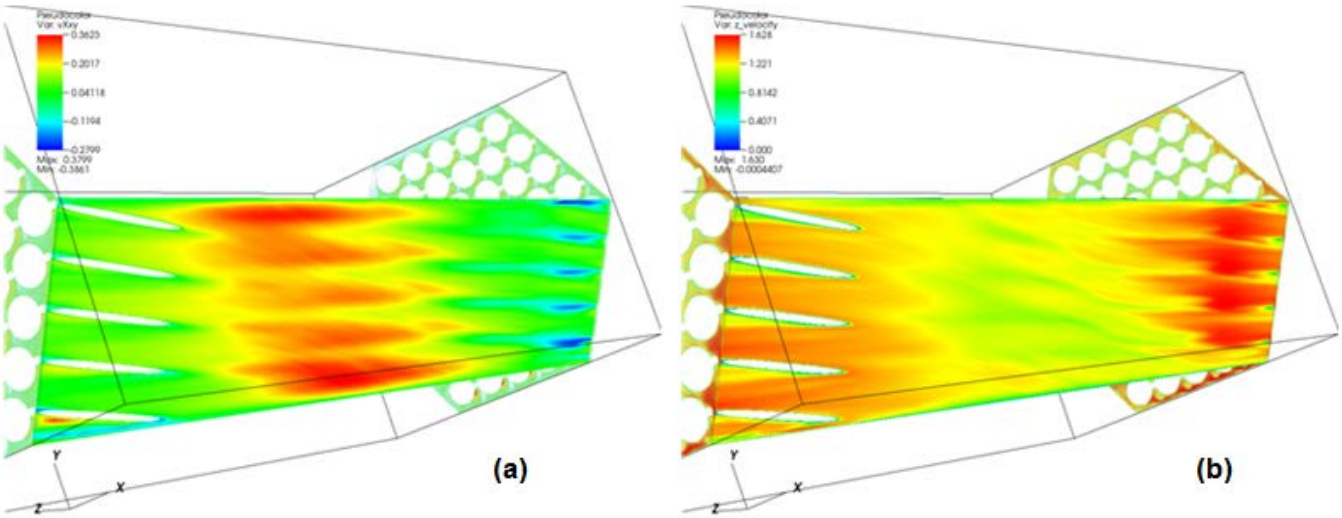


Figure 13: Velocity - Horizontal (a); Vertical/Axial (b)

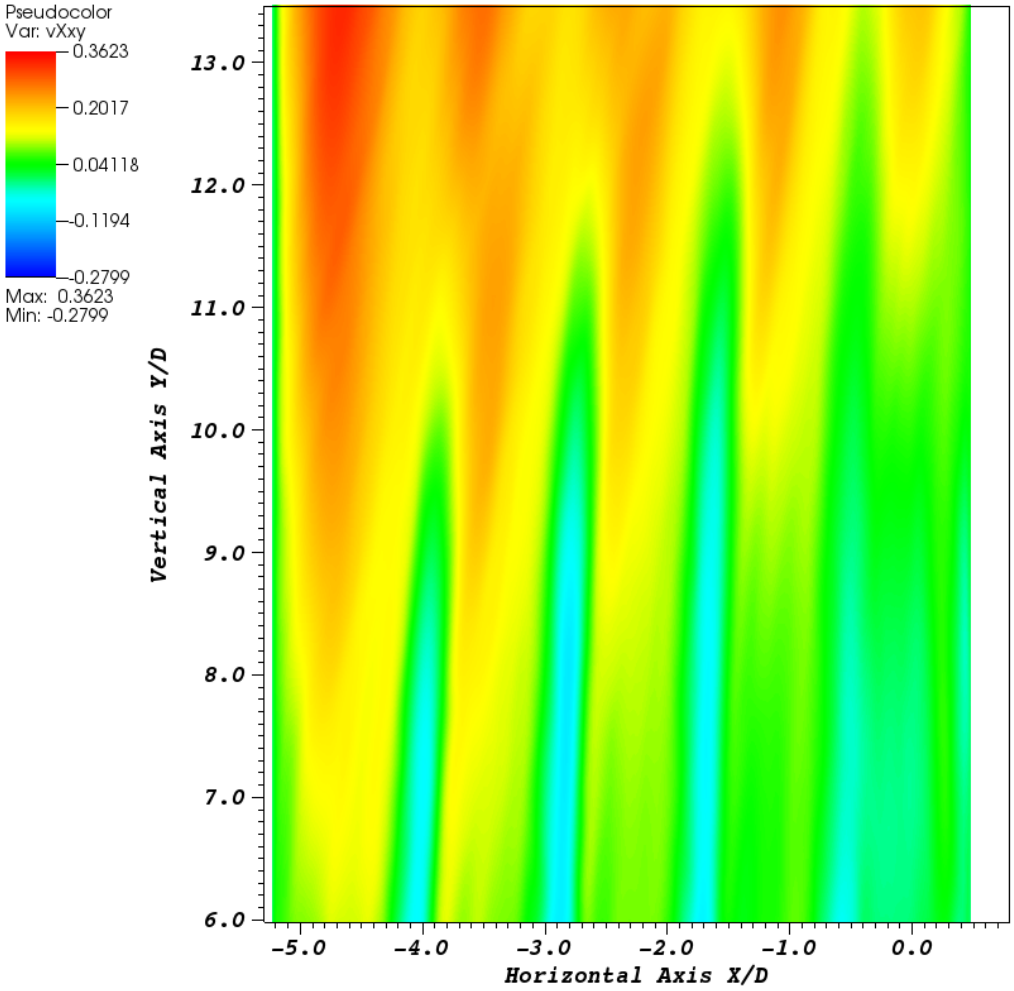


Figure 14: Horizontal Velocity Plotted in the Domain of Experiment Data Acquisition

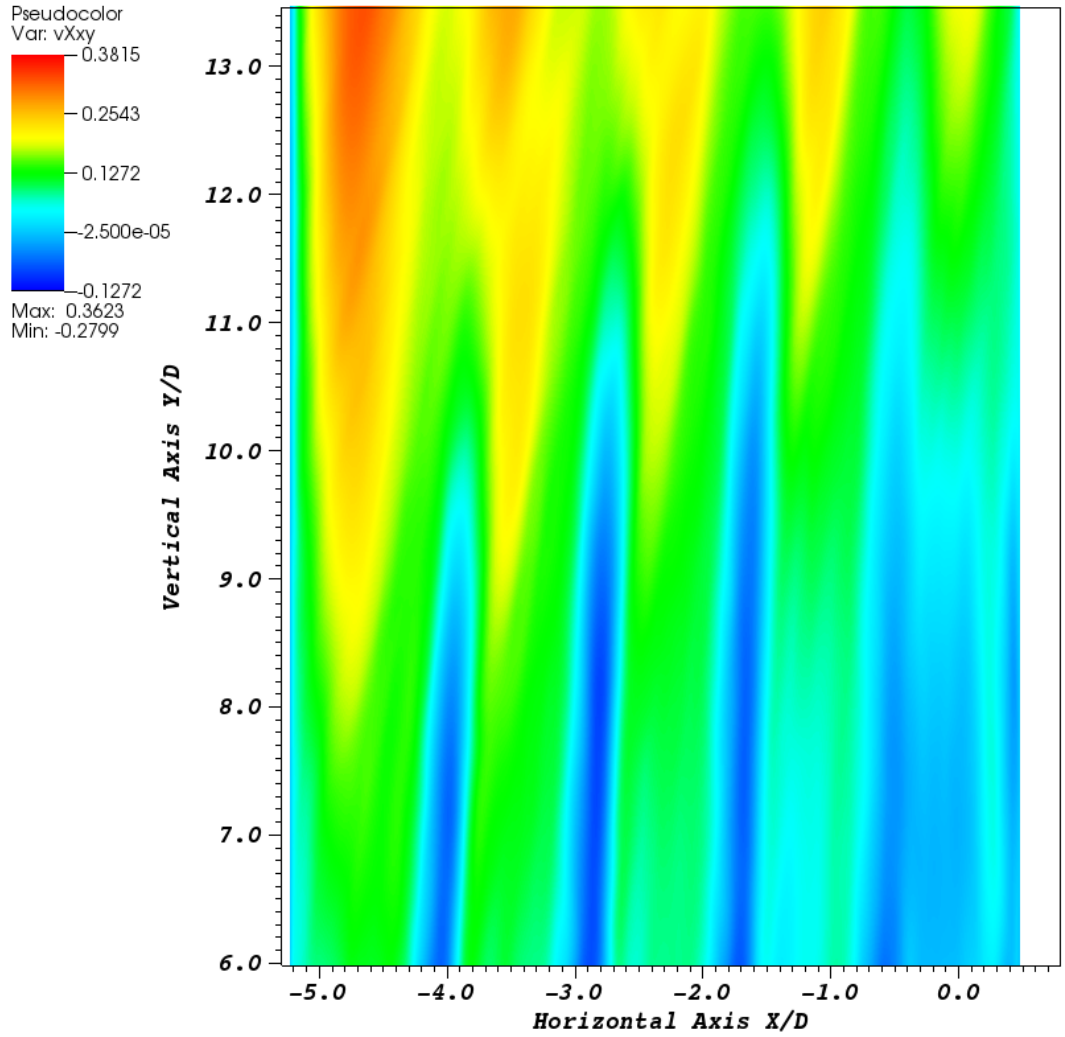


Figure 15: Horizontal Velocity Plotted in the Domain of Experiment Data Acquisition with Color Map Range Consistent with TerraPower Plots

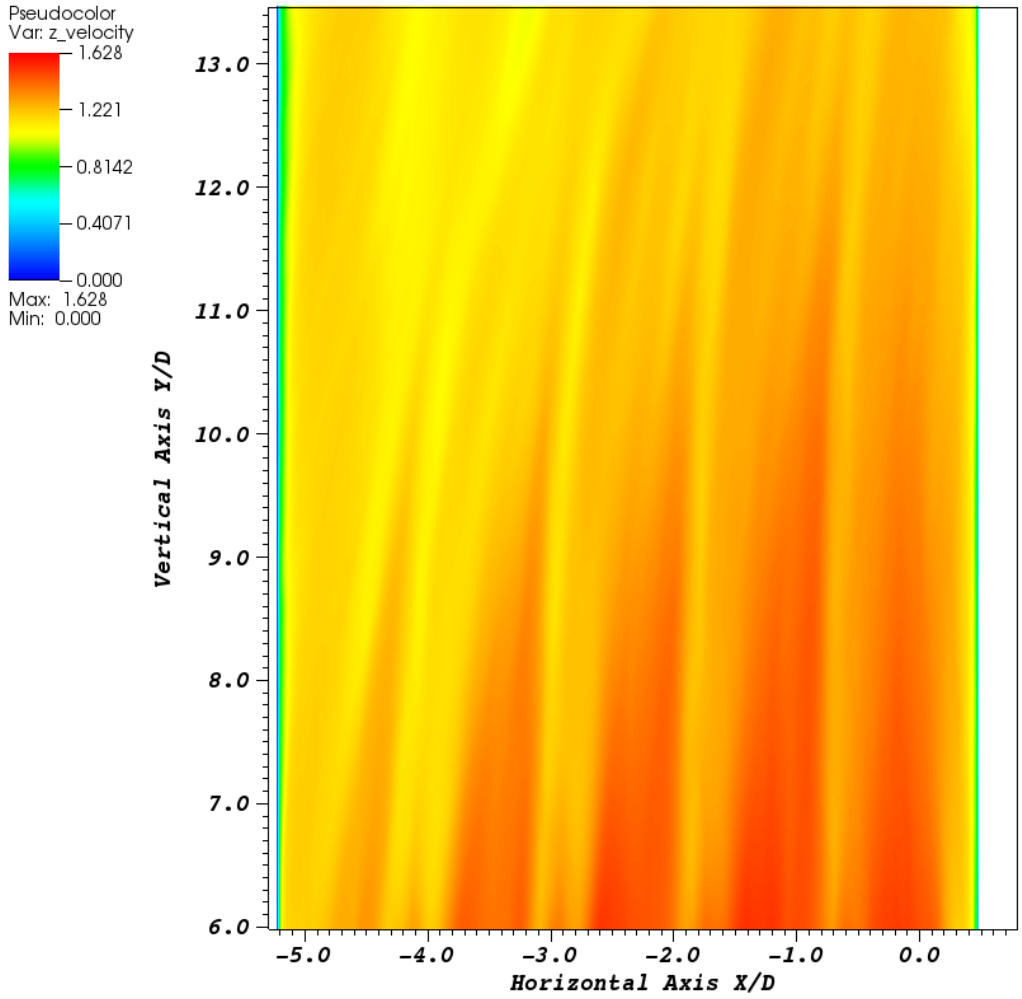


Figure 16: Vertical Velocity Plotted in the Domain of Experiment Data Acquisition

This discrepancy might be explained by significant uncertainty in laser sheet position and thickness. We illustrate this in Figure 17. In fact, we have extracted planes in the immediate vicinity of the canister wall and near the wire pins. These planes present a much lower velocity and confirm the possibility of a lower velocity due to laser sheet position and indicate the need for further investigation. It is possible that the much lower values observed in the experiment are in fact due to a local averaging and/or unknown position of the laser sheet.

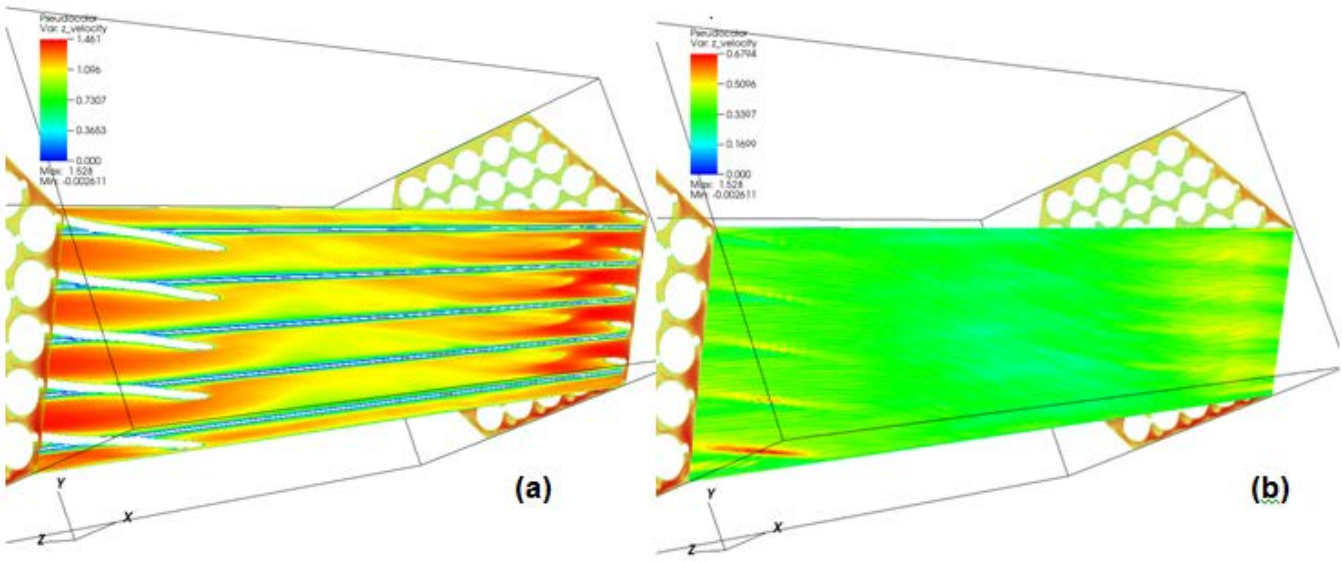


Figure 17: Vertical Velocity - (a) in Close Proximity to the Wires, (b) in Close Proximity to the Canister Wall

As the first step to the central measurement plane with the experimental data we plotted all three components of velocity in Figure 18, Figure 19 and Figure 20. More detailed comparisons will be reported in the annual NEAMS thermal-hydraulics update report later this year.

The calculations performed and the comparisons with experiments help build the case for the validation of Nek5000 and other CFD codes. Comparisons are limited in scope but are consistent. Given the large uncertainty of the experimental results due the complexity of the geometry under examination this work can be considered as a stepping stone of validation exercises in wire-wrapped rod bundles.

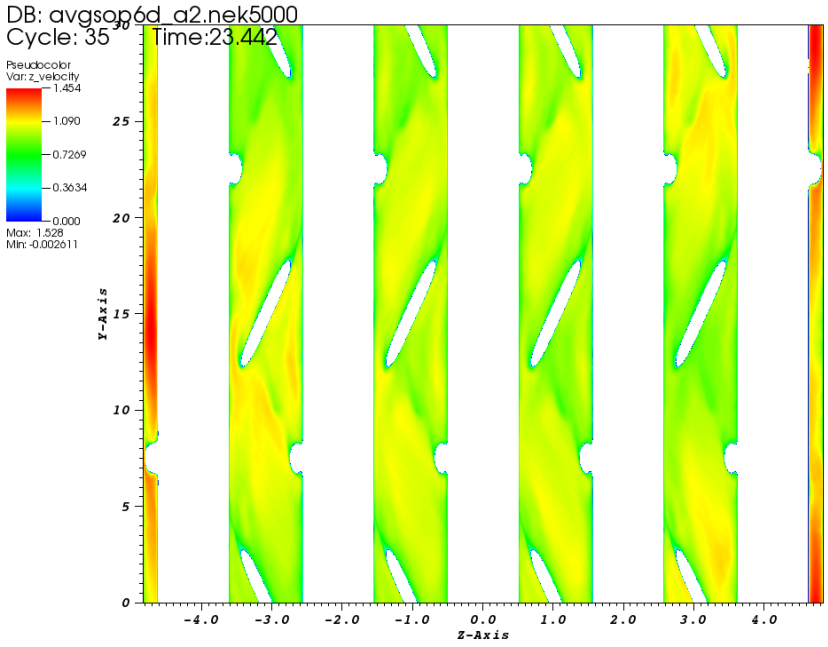


Figure 18: Vertical Component of Velocity Plotted in the Domain that includes the Central Subchannel

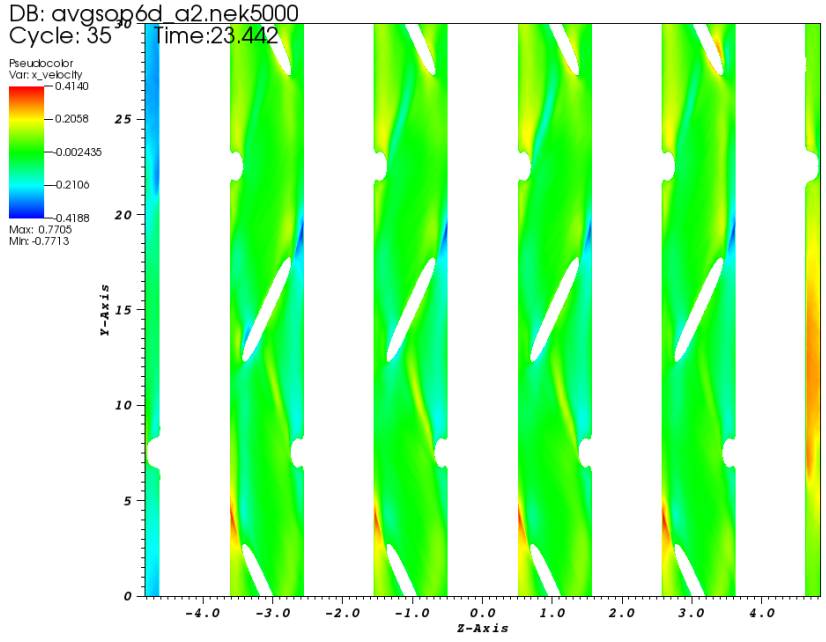


Figure 19: Horizontal Component of Velocity Plotted in the Domain that includes the Central Subchannel

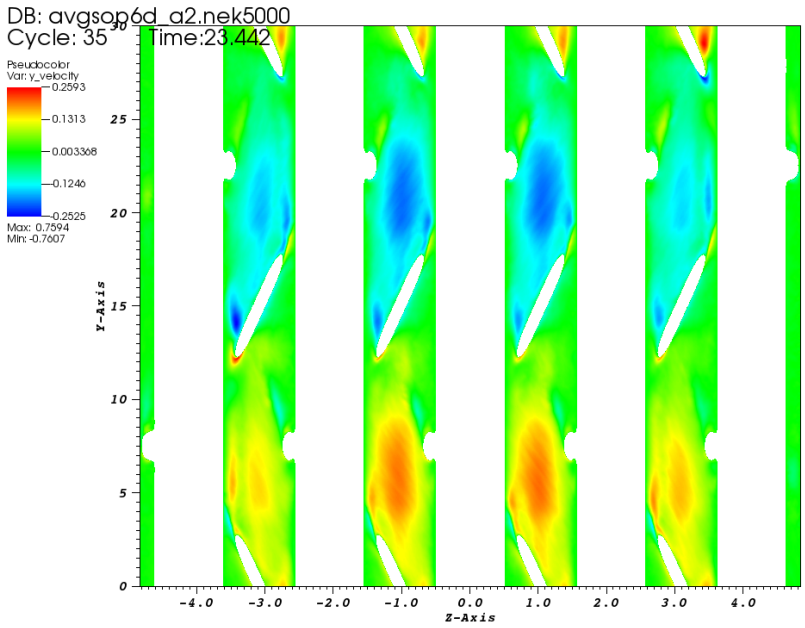


Figure 20: Perpendicular Component of Velocity Plotted in the Domain that includes the Central Subchannel

6.3 AREVA Fuels

6.3.1 Scope

Steady state thermal-hydraulic tests were run with water flowing through a 61 pin hexagonal bundle at Reynolds number 20,000 in the fully turbulent regime as specified in this document. The bundle was partially heated: 19 of the 61 pins were electric heater rods that provided heating. Measurements included thermocouples at the unheated tube wall and fluid interface, embedded inside heaters, and on the internal duct wall. Pressure drop measurements were taken across different lengths of pin bundle to capture entrance effects, planar pressure gradient due to bulk flow swirl, and fully developed conditions.

6.3.2 Design

The experiment bundle design was performed by TerraPower and is detailed in References [4] and [5], Appendix B and Appendix C, respectively. Several parts interfacing between the test section and the test facility were designed by AREVA (upper tie plate, lower seal). These elements have no impact on the test data.

6.3.3 Facility Construction

The Fuel Cooling Test Facility (FCTF) in Richland, Washington, at the AREVA fuel fabrication facility was modified to accommodate this wire wrapped heated pin assembly test. The loop was previously used at atmospheric pressure to test re-flood and spay heat-transfer after a Loss of Coolant Accident (LOCA). Because these previous tests were conducted at atmospheric pressure, the loop was modified to accommodate the requirements of the heated bundle tests, including pressurization to prevent boiling within the test loop.

A schematic of the FCTF loop piping is shown in Figure 21. The main characteristics of the loop are the presence of a powerful power supply (1 MW) and a secondary side that allows the removal of the energy added to the primary circuit. The loop equipment and the modifications that were made to this equipment are itemized in Table 2:

Table 2: FCTF Loop Equipment and Modifications Made During the Project

Equipment	**Modification Made for Testing**
Cooling Tower	Refurbished.
Heat Exchanger	Cleaned and inspected.
Secondary Recirculation Pump	Existing pump need replacing.
Secondary Piping to Cooling Tower	Cleaned, repaired where necessary, inspected.
Power Supply	Power transformer in working order. Silicon-controlled rectifiers (SCR) were replaced.
Data Acquisition System (DAS)	New hardware and software procured and installed.
FCTF Vessel	Used as is.
Test Hardware (Heated Bundle, Duct and Loop Interface Hardware)	New hardware specified, designed, built and installed.
Primary Circulation Pump	New higher capacity pump required for testing. Specified and installed.
Primary Loop Piping	New piping installed to reconfigure loop for test series.
Pressurizer Tank	Inspected and attached to new piping.
Non-Pressurized Tank	Used as is.

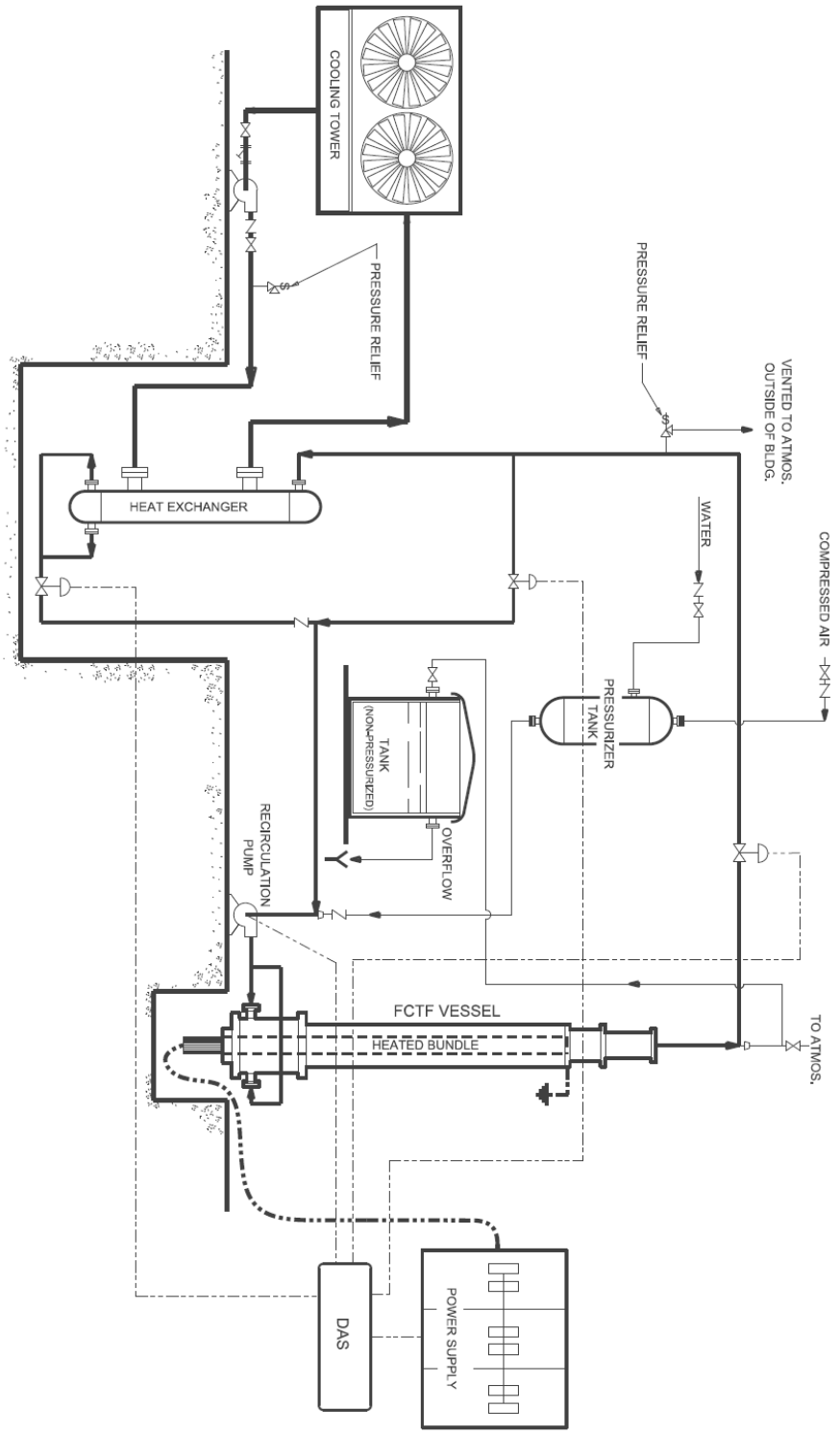


Figure 21: Schematic of the Piping in the FCTF Test Loop

6.3.4 Installation

6.3.4.1 Test Facility

Figure 22 shows the main vessel containing the test section and an overall picture of the facility. The loop is entirely monitored and controlled by computer. In addition to the data collection, a Programmable Logic Controller (PLC) ensures safety of the facility as well as the test section by ensuring that the system shuts down under specific conditions.

The hexagonal duct of the test bundle serves as the pressure boundary. The duct is then contained inside a larger vessel. Lower and upper plena are installed upstream and downstream of the experiment test bundle, respectively. The lower plenum serves as the inlet plenum. The pin bundle penetrates the bottom face of the plenum through a custom seal to allow the rods to thermally grow and the electric leads to be connected. The water inlet is directly connected to the lower plenum using two, 90° elbows that direct the flow downward to avoid direct impingement of the water onto the bundle.

The rods are attached to the upper tie plate that is located at the top of the test bundle and is connected to the vessel and the ground. The upper tie plate is gold plated to allow good electrical contact. The flow passes through flow holes in the upper tie plate and then expands into the upper plenum which is above the experiment test bundle before going into the outlet pipe section. Return piping contains the heat exchanger and pump to complete the loop back to the inlet plenum.



Figure 22: Main Vessel Containing the Test Specimen, left; FCTF Overview, right

6.3.4.2 Bundle

AREVA received the deformed and non-deformed duct from TerraPower along with the 61 wire-wrapped pins. The bundle was assembled at the AREVA test facility. Rods were inserted and placed one by one according to their type and the map shown in Figure 40. All 61 pins are attached to the upper tie plate and rotationally oriented so all the wires are in phase. An upper tie plate and lower seal were designed and manufactured specifically for this test to optimize flow at each end of the test section. Figure 23 illustrates the bundle assembly process. Figure 24 shows the bundle being transported to the test vessel.

The ducts were delivered already assembled. The duct instrumentation (pressure taps and thermocouples) were first connected and tested. A leak test was performed to ensure that no major leaks, through the seals or instrumentation, were present. Then the ducts were wrapped into insulating blankets to minimize the heat losses through the walls during the tests. This is crucial to support the modeling assumption of an adiabatic wall boundary condition in the CFD simulations. Figure 25 shows the duct and the duct wrapped into insulation blankets prior to being inserted into the vessel. Figure 26 shows the duct being inserted into the vessel.

The pins of the bundle pass through the duct attaching to the upper tie plate and the lower seal and therefore do not physically attach to the duct. The duct attaches to the main vessel. Then the pin bundle could be lowered through the duct, as shown in Figure 27. Finally the vessel, containing the duct and the pin bundle test section was attached to the rest of the loop. Figure 28 shows the instrumentation connection to the Data Acquisition System (DAS) (360 thermocouples, 38 pressure tubes). The 19 power leads were then connected to the heater rods. One heater failed during the test series; therefore only 18 heaters are effectively used. Documentation of the location of this heater rod is provided in Appendix A. Shakedown of the different systems was performed along with testing of the embedded safety systems.

Note that the swapping of duct (non-deformed and deformed) required disassembly of the test section. The pin bundle was kept “as-is” and therefore pin location configuration was maintained for both tests. However all the instrumentation had to be disconnected and reconnected, the vessel removed and the bundle unloaded from the duct.

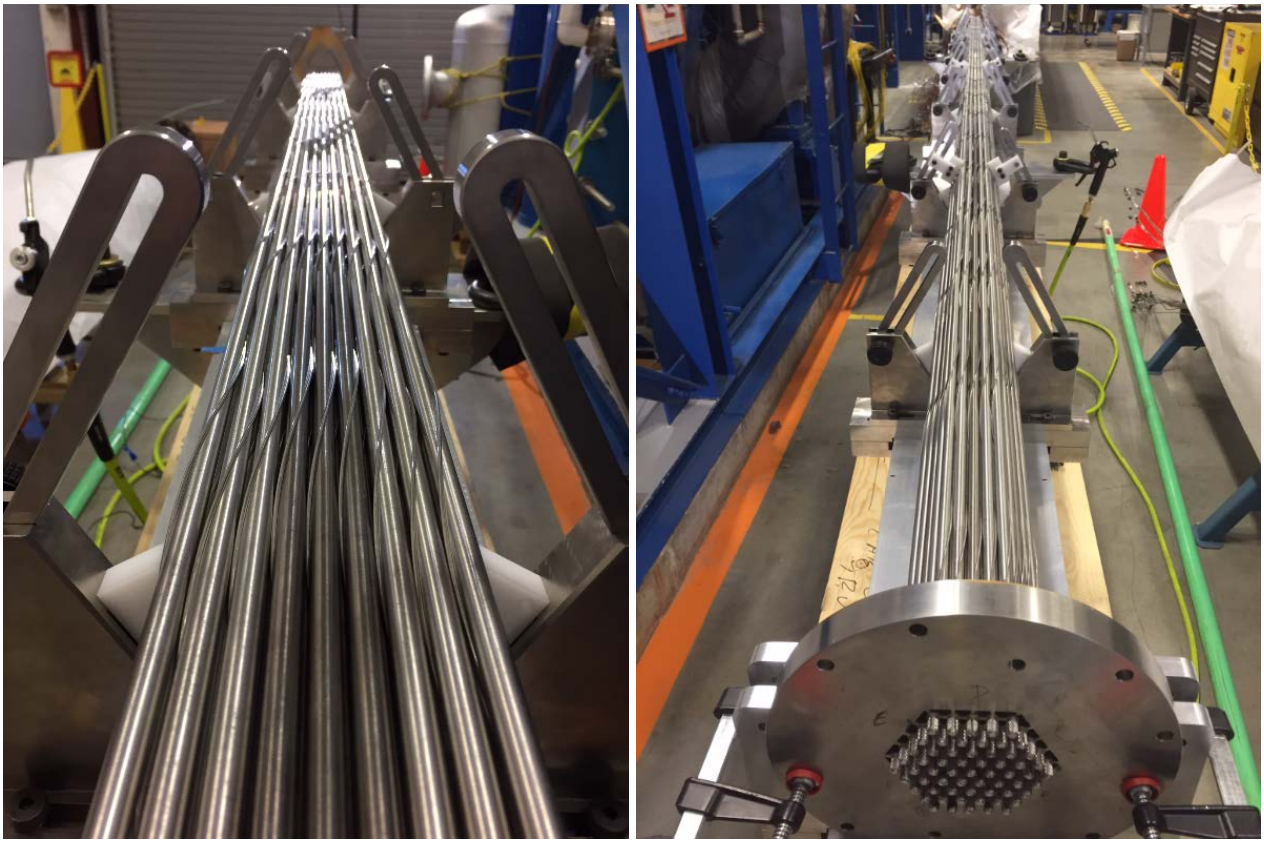


Figure 23: Bundle Assembly, left; Assembled Bundle Showing Upper Tie Plate, right



Figure 24: Test Assembly being transferred



Figure 25: Instrumented Duct, left; Duct Wrapped in Insulation Blanket being Transferred, right



Figure 26: Duct being inserted in the Test Vessel



Figure 27: Workers inserting the Bundle into the Duct



Figure 28: Instrumentation Connection

6.3.5 Instrumentation

A large number of instruments are used to monitor the facility and record test data. An exhaustive list of instruments is provided in Appendix A. Most instruments collecting data directly belong to the test section. A few instruments are specific to facility monitoring. These include two thermocouples that measure the temperature inside the lower plenum. A pressure transducer measures the static pressure upstream of the test section.

Three thermocouples measure the temperature directly inside the upper plenum. However, it was found that due to jetting effects of flow across the upper tie plate, those measurements showed some discrepancies. A more representative well-mixed outlet temperature was taken farther downstream directly inside a return pipe once the flow had a chance to mix. A static pressure transducer also measures the pressure in the upper plenum. 120 psia was prescribed at this location (upper plenum) for these tests.

Two vortex flow meters measure the flow rate. One is located upstream of the test section on the discharge side of the pump and the other is located after the test section, before the heat exchangers.

Power is measured by characterizing the load on each power supply and measuring the current and voltage. A wattmeter combines the two measurements to provide a signal. This setup is calibrated against an alternate reference to provide power for each individual power supply. The resistance each of the heaters is extremely consistent therefore the power of each of the heaters connected to a given power supply is assumed to be the same. Watt meters were characterized before and after the test to ensure that no drift occurred during the test.

Thirty pressure drop transducers were used to measure the pressure drops between specified tap locations. All transducers were appropriately ranged and calibrated based on the pre-test predictions. After the test, all transducers were characterized and compared to the pre-test calibration points to ensure that no drift had occurred.

Over 300 thermocouples were recording the temperature inside the test assembly. An individual system bias was calculated for each thermocouple and applied to the recorded data as explained in Appendix A.

6.3.6 Test Conduct

The tests were conducted first with the non-deformed duct and then with the deformed duct. The following procedure was used for both series of tests:

1) The loop is filled with deionized water.
2) Once the loop is full, a leak path is opened to ensure that no bubbles or gas are trapped.
3) The pressurizer is turned on. A pressure of 120 psi is achieved at the top of the test section (in the upper plenum).
4) The cooling tower fan and pump are turned on to the specified settings for optimum cooling.
5) The primary recirculation pump is then turned on and the flow rate is set to the required value.
6) The pressure is finely adjusted to maintain 120 psia in the exit plenum.
7) The loop is maintained in this condition for a few hours until thermal equilibrium is achieved.
8) All available channels are recorded for 5 minutes to record the first test setpoint corresponding to the non-deformed duct pin assembly geometry, and non-heated configuration.
9) Any leakage from the test section is collected in the annulus region between the duct and the vessel wall. A tube was used to characterize the amount of leakage. The rate of leakage was evaluated by weighting and it was determined to be negligible. No actions were taken. The leakage was periodically monitored to

ensure it remained small. A visual inspection of the loop was performed to ensure proper behavior of the system.

10) The next test corresponds to the non-deformed duct pin assembly geometry at heated conditions. Using the automated control system, the power is slowly ramped up to the target power (~24kW per rod). The internal thermocouples are monitored. Once the power target is reached. The system is held until all instruments show a flat profile. Flow rate and pressure might be adjusted as necessary as heat is added to the system.

11) Once all channels have reached steady state, all channels are recorded for 5 minutes to record the second test setpoint corresponding to the non-deformed duct pin assembly geometry at heated conditions configuration.

12) Power is then ramped down slowly maintaining cooling until all the stored heat in the hardware is removed.

The second test series, using the deformed duct pin assembly geometry follows the exact same steps. Between the first and second test series, the loop is dismantled in order to swap the duct.

6.3.7 Test Results

Test results, data collected for each test and Microsoft Excel tables containing both raw data and post-processed data are provided in Appendix A, which also includes a discussion of the steps used to post-process the raw data. The reader is free to use the raw data or the adjusted values.

6.4 TerraPower

6.4.1 Scope

TerraPower contributions to the project included acting as Technical Lead, design and procurement of the heated bundle hardware for loan to the project, and performing industry standard RANS CFD comparison simulations of the experiments. TerraPower produced reports documenting specifications, technical plans, and scope accomplishments throughout the project. These documents are referenced throughout this report and include the following:

1. Heated Bundle Experiment Test Specification, Reference [4] [Appendix B]
2. Flow Visualization Experiment Test Specification, Reference [11] [Appendix G]
3. Benchmark Specification Verification and Validation Plan, Reference [13] [Appendix H]
4. Heated Bundle As-Built Report, Reference [5] [Appendix C]
5. RANS Pre-Test Simulation Report, Reference [6] [Appendix D]
6. Post-Test Simulation Methods Document, Reference [7] [Appendix E]
7. RANS Post-Test Simulation Report, Reference [8] [Appendix F]

TerraPower also presented scope and accomplishments at two technical conferences. CFD simulation verification methods and experiment simulations results corresponding to the experiments as defined in the Test Specifications were presented at the 2016 ASME Verification and Validation Symposium Reference [9] [Appendix N]. CFD simulations of the experiments corresponding to the as-tested and as-built conditions were presented at the 2016 ANS Winter Meeting Reference [10] [Appendix N].

6.4.2 Technical Lead Performance

As Technical Lead, TerraPower specified geometry, operating conditions, and measurement requirements for the experiments and provided direction for the overall benchmark plan and methods. Experiment requirements were provided in Technical Specification documents, one each for the heated bundle and flow visualization bundle experiments. These documents were produced by TerraPower with input and review of all project organizations. Multiple revisions were made with input from all project organizations as-needed as a result of fabrication and procurement considerations during the initial design and fabrications stages while maintaining the experiment integrity to produce experiment data for use in CFD validation. These documents include the specifications for the physical descriptions of the experiment bundles, test operating conditions, and instrumentation and measurement requirements. While these test specification documents which were used in the design of the experiments are included in this report, the actual as-built geometries, as-tested conditions, and as-measured measurement details are recorded and included in as-built reports and the experiment test reports included in the reference section of this document.

In addition to producing the Test Specification documents, TerraPower provided direction for the project benchmarking. This was done through participation in bi-weekly and monthly conference calls and issuance of appropriate documentation. This included the Benchmark Specification document, Reference [13] [Appendix H], and the Post-Test Simulation Methods document, Reference [7] [Appendix E]. The Benchmark Specification document was issued near the end of Year 1 of the project. The purpose of this document was to provide a description of the verification and validation plan of the project. This document included the project scope, the responsible organizations for performing the work scope, general experiment descriptions, types of measurements to be taken, simulation modeling methodologies, simulation modeling assumptions, and the CFD benchmarking methods.

The Post-Test Simulation document, Reference [8] [Appendix F], was produced following experiment completion, but before the experiment test reports were available. The purpose of this document was to provide the as-built and as-tested experiment conditions to the CFD analysts for use in the Post-Test simulations. While this information is included in the final experiment test reports, this document was needed due to the concurrent schedule of the CFD post-test simulations and experiment documentation phase. This document also contains CFD modeling assumptions used for the post-test simulations including material property temperature dependent correlations, turbulent and flow profile assumptions and other assumptions.

6.4.3 Heated Bundle Descriptions

TerraPower was responsible for the design and procurement of the heated bundle hardware which was lent to the project for use. An overview of the bundle geometry, operating conditions, and measurement types and locations is provided in the Heated Bundle Experiment Test Specification, Reference [4] [Appendix B]. These heated bundle experiments included a 61 pin bundle with a nominal non-deformed duct, and a 61-pin bundle with a deformed duct. The non-deformed duct was a hexagonal duct with the inner duct walls being flat the entire length of the bundle representing a beginning-of-life duct. The deformed duct was a hexagonal duct where the inner duct walls had an axial and lateral (between duct corners for each duct face) profile shape where the hexagonal flow area expanded from the nominal size and then contracted to return to the nominal hexagonal shape along the axial length. This bundle represents a later-in-life duct geometry. Each of the bundles used the same 61 pins for the pin bundle. Of the 61 pins, 19 were instrumented heater rods, 22 were thermocouple instrumented tubes, 8 were pressure tap instrumented tubes, and the remaining 12 were non-instrumented tubes. All heater rods and non-heated tubes were then wire-wrapped for installation. These hardware components were then loaned to the project and supplied to AREVA Fuels where they were installed into the flow loop for the experiments.

TerraPower produced equipment specification documents for the heater rods, non-heated tubes, ducts and wire wrapping that were used with vendors for fabrication specification that provided additional detail beyond the general description given in the Heated Bundle Experiment Test Specification document, Reference [4] [Appendix B]. The final as-built dimensions and installation detail was recorded in the Heated Bundle As-Built Report, Reference [5] [Appendix C]. This document includes inspection measurements of all hardware, and the as-installed configuration in the AREVA Fuels flow loop. Details of the as-installed configuration in the AREVA Fuels flow loop were provided by AREVA Fuels.

6.4.3.1 Heater Rods

Electric heater rods designed for a maximum power output of 30 kW each were produced by STERN Laboratories. These heaters had a specified 9.5 mm outer diameter and a 1.4 peak-to-average cosine shaped axial power profile. These heater rods were then wire wrapped with 1.72 mm specified outer diameter wire with a 285 mm specified axial wire wrap pitch. Each of the heater rods was instrumented with embedded thermocouples as specified in the Heated Bundle Experiment Test Specification document. Geometric measurements were taken of the as-built heater rods and recorded to provide final diameter and length measurements. Functional and location measurements of the thermocouples and heating element resistances were taken and recorded to verify conformance with specification. This information is provided in the Heated Bundle As-Built Report, Reference [5] [Appendix C]. Power levels used in the experiment test runs are provided in the Heated Bundle Test Reports Section 6.3.

6.4.3.2 Non-Heated Pins

The pin bundle consisted of the 19 heater rods, and 42 non-heated tubes. These non-heated tubes were thick walled (0.065” specified inner diameter tube) 304 stainless steel tubes. In order to use off-the-shelf tubing, 3/8” specified OD tubing was used. This is slightly different from the specified diameter sizing of the heater rods. These non-heated tubes were then wire wrapped with 1.72 mm specified outer diameter wire with a 285 mm specified axial wire wrap pitch. As described above, some of these tubes were instrumented with thermocouples, others had pressure taps, and some were non-instrumented as specified in the Heated Bundle Experiment Test Specification document, Reference [4] [Appendix B]. Geometric measurements were taken of the as-built non-heated tubes and recorded to provide final diameter and length measurements. Functional and location measurements of the embedded thermocouples were taken and recorded. This information is provided in the appendix section of the Heated Bundle As-Built Report, Reference [5] [Appendix C].

6.4.3.3 Heated Bundle Duct

Both of the ducts used for the heated bundle tests used the same general design with the difference being in the internal duct wall shape. The non-deformed duct had flat inner duct face surfaces along the length of the bundle. The inner duct face surfaces of the deformed bundle had a shape profile along a section of the duct. The wall thickness of the duct was quite thick and this shape was machined into the duct material. Therefore, the deformed duct did not deform in the experiments, but instead was machined to represent the shape of a deformed duct due to conditions in the reactor. Each duct was fabricated from eight separate pieces. Each piece was a clam-shell section of a half side of the duct. The total length of the duct consisted of four axial sections.

Duct pieces were cast from Silicon Bronze and then machined with a 6-axis mill to the final duct geometry. The final duct geometry was adjusted to correspond to the as-built diameter dimensions of the heater rods and non-heated tubes. The eight duct pieces for each duct were assembled using bolts and gaskets for the pressure boundary.

One issue that arose was that after assembly of the eight pieces that made the non-deformed duct, during pressure testing the duct leaked and was not holding pressure. After investigation of the sealing gaskets that were used between duct pieces, it was discovered that the leaking was occurring through the bronze surfaces. This phenomenon is not uncommon and can occur during the cooling phase of the casting. This material porosity issue was resolved through application of a casting impregnation process. This process vacuum impregnates a low viscosity liquid sealant that fills and seals microscopic voids. Following application of this process to pieces of both the non-deformed and deformed ducts, pressure testing was successful to pressures exceeding experiment test conditions.

Each of the ducts was also instrumented with thermocouples and pressure taps. Pressure taps were installed a different locations of the duct wall and used for pressure drop measurements. Thermocouples were installed from outside the ducts and located at the inner duct face surface to measure fluid temperature at the wall during the experiments.

As-built geometry measurements were taken with a FARO arm that compared discrepancies between the as-built and computer-aided design (CAD) model. These as-built geometry measurements, instrumentation location and functionality measurements, and installation configuration with respect to the pin bundle are reported in the Heated Bundle As-Built Report, Reference [5] [Appendix C].

6.4.3.4 Wire Wrapping

TerraPower contracted with Intellectual Ventures (IV) Laboratory to wire wrap the heater rods and non-heated tubes per the Heated Bundle Experiment Test Specification document. IV Labs constructed a machine that automated the process to ensure wire wrapping was consistent for all pins and heaters and was completed according to the test specification. Following wire wrapping, geometric measurements of the wire wrap diameter, and the wire wrap pitch were taken and recorded. This information for both the heater pins and the non-heated tubes is contained in the Heated Bundle As-Built Report, Reference [5] [Appendix C].

6.4.4 Industry Standard CFD Simulations

TerraPower was responsible for and performed industry standard CFD RANS turbulence model simulations of the experiments and performed benchmarking to the experiment results. These simulations were performed with the commercial code StarCCM+. The bundle geometries were meshed using the commercial code Gridpro. Simulations were performed for both the as-designed experiments, and then a second batch of simulations of each experiment with the as-built and as-tested conditions once the experiments were completed. These were identified as pre-test and post-test simulations, respectively. All of these simulations were done blind: the CFD analyst did not have access to the experiment data.

Included in the pre-test simulation analysis effort was a code and solution verification scope. The code verification used the Method of Manufactured Solutions (MMS) to the extent possible. Access to some aspects of the code was limited due to the commercial nature of the code. Solution verification was performed that included a mesh sensitivity study, quantification of iteration error, round off error and statistical sampling. Description and conclusions from the code and solution verification scope is included in the RANS Pre-Test Simulation Report, Reference [6] [Appendix D].

6.4.4.1 Wire Wrap Modeling

Meshing of a hexagonally packed wire wrapped pin assembly is challenging due to the line contact between the wire wrap and the pin. Two methods were used by TerraPower to model this in the RANS based CFD simulations of the experiments. The primary method was a Momentum Source method. In this method, the

simulation geometry only consists of a hexagonally packed bare pin bundle. The fluid domain in the model corresponds to the locations in the experiment of the fluid and of the wire wrap. Then in the simulation, at the locations that correspond to the wire wrap, a momentum source is included in the momentum equation such that the flow field responds as if the solid wire wrap were present. This momentum source is based on the local velocity field and is based on work from ANL, as detailed in Section 6.2. The use of the momentum source method simplifies the meshing of the bundle geometry, and also provides simulation speedup due to the smaller number of mesh volumes that are required. Description of the Momentum Source method is described in the RANS Pre-Test Simulation Report, Reference [6] [Appendix D].

The second method of wire wrap modeling consists of including the wire wrap in the mesh geometry, but simplifying the line contact between the wire wrap and the pins. Instead of explicitly modeling the geometry of the tangent between the wire wrap and the pin, the wire wrap contains a small flat neck that enlarges the contact between the wire wrap and pin. This allows for meshing at this location. Description of this method is included in the RANS Post-Test Simulation Report, Reference [8] [Appendix F].

6.4.4.2 Pre-Test Analyses

Pre-test simulations correspond to the as-designed experiments as outlined in the test specification documents. These simulations included modeling the experiments as designed for the (1) heated non-deformed bundle, (2) heated deformed bundle, (3) flow visualization non-deformed bundle, and (4) flow visualization deformed bundle tests. In addition to the solution verification that was performed for these pre-test simulations, sensitivity studies were also performed. These included different 2-equation turbulence models and adjustment of momentum source coefficient values. Details, descriptions and conclusions are provided in the RANS Pre-Test Simulation Report Reference [6] [Appendix D].

6.4.4.3 Post-Test Analyses

While fabrication of the test bundles and operating set points of the experiments closely matched those specified in the test specification documents, there were some differences. Therefore RANS CFD simulations were performed of the experiments using the updated as-built geometries and as-tested conditions. These corresponded to three 3 tests: (1) heated non-deformed bundle, (2) heated deformed bundle, and (3) flow visualization non-deformed bundle. Even though the CFD analyst had the as-built and as-tested conditions from the tests, these simulations were performed blind in that the CFD analyst did not have access to the test data. The post-test simulations were performed concurrently as the test reports were being produced. Therefore, to consolidate all test conditions that are needed for the CFD analysts, the Post-Test Simulation Methods Document, Reference [7] [Appendix E], was produced by TerraPower and is included in the appendix. This document summarized as-built geometries, as-tested operating conditions, and CFD modeling assumptions to model the project experiments.

Following the post-test simulations, benchmark comparisons between the simulations and the experiments were performed. A subset of the total experiment data was used for comparisons, due to the very large amount of data that was produced. For the heated bundle tests, this included comparisons of non-dimensional point temperatures representative of the thermocouple measurements, thermal mixing behavior and pressure drop. Most comparisons between thermocouple measurements and the CFD simulation results showed agreement within the measurement uncertainty. Pressure drop comparisons showed good agreement for pressure drop lengths corresponding to multiples of the wire pitch length. However, pressure drops corresponding to lengths of non-integer wire pitch multiple lengths showed some disagreement. It is expected this shortcoming is due to the modeling methodology not fully capturing the pressure gradient that develops across the bundle due to the wire wrap geometry. For the flow visualization bundle, this included velocity field measurements and pressure drops. There were discrepancies for the comparisons between the CFD results and the experiment results for these experiments.

Similar to that which was observed in the Nek5000, ANL, results, a much higher average velocity in the wall sub-channels was calculated for the CFD results in comparison to the experiment.

Description of the CFD post-test simulation methods, results, and comparisons with the experiments are contained in the RANS Post-Test Simulation Report, Reference [8] [Appendix F].

6.5 Texas A&M University (TAMU)

6.5.1 Scope

TAMU designed, constructed, and performed isothermal matched index of refraction flow tests on a 61-pin simulated fuel bundle to generate high spatial and temporal resolution data of the fluid velocity field using laser-based techniques. At multiple axial locations along the test section and at certain azimuthal locations on different duct faces, pressure measurements were taken to complement the velocity measurements. This work was conducted to support benchmark numerical simulations using both industry-standard Reynolds-averaged Navier-Stokes CFD methods and highly resolved large eddy simulation approaches.

TAMU produced reports documenting as-built geometries, test summaries and scope accomplishments throughout the project. These documents are referenced throughout this report and include the following:

1. TAMU Wire-Wrapped As-Built Geometry (Non-Deformed Bundle), Reference [12] [Appendix J]
2. TAMU Wire-Wrapped Test Summary of Test PCM-11 at the Exterior Sub-channel, Reference [14] [Appendix K]
3. TAMU Wire-Wrapped Test Summary of Test PCM-16-C2 (Center plane – 30° offset), Reference [15] [Appendix L]
4. TAMU Wire-Wrapped Test Summary of Test PCM-14-INT1 at Interior Sub-channel One, Reference [16] [Appendix M]
5. Pressure Measurements in a Wire-Wrapped 61-Pin Hexagonal Fuel Bundle, Reference [17] [Appendix N]
6. Particle Image Velocimetry Measurements in a Wire-Wrapped 61-Pin Hexagonal Fuel Bundle, Reference [19] [Appendix N]
7. TAMU Wire-Wrapped Quality Assurance Guidelines, Reference [3] [Appendix I]

6.5.2 Test Facility Description

The experimental facility, shown in Figure 29, consists of two loops, a primary loop and a secondary loop. The primary loop, which provides the flow for the experiments, includes the following components:

- The primary tank, used to store the working fluid between experiments and to serve as an inline surge volume
- The primary pump and associated variable frequency drive (VFD), which controls the flow rate in the test section
- An inline turbine flow meter
- A resistance temperature detector (RTD)
- Nine pressure transducers
- The hexagonal test section containing the 61-pin bundle

The secondary loop performs volume control, temperature control, and filtration. It contains the following components:

- The secondary tank
- The secondary pump and associated VFD
- A heat exchanger supplied with chilled water to control the primary loop temperature
- A filtration system to remove dust, debris, and PIV particle residue from the working fluid between tests

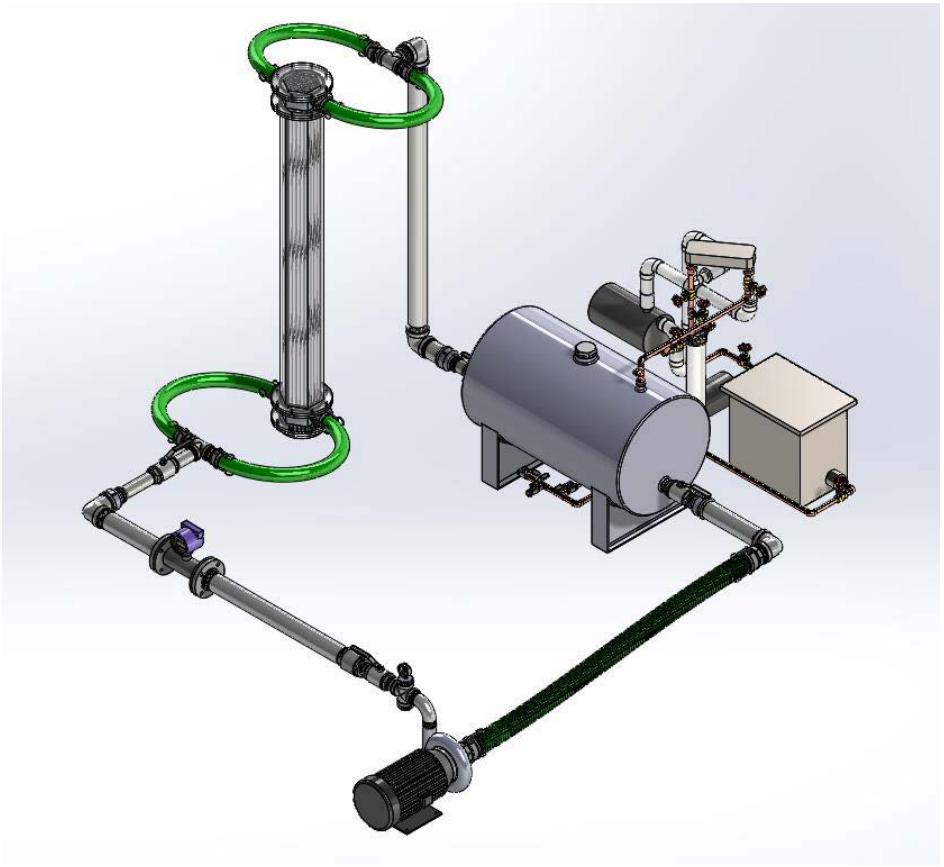


Figure 29: Perspective Diagram of the TAMU Experimental Facility

All pumps, tanks, and piping are made of stainless steel. Chemical-resistant flexible hoses are used to connect the test section inlets and outlets to the primary loop. The hoses are used to minimize vibrations in the test section.

The test section is shown in Figure 30. It can be divided into three distinct sections:

- The lower (inlet) plenum located at the bottom of the bundle
- The central section (test region) where the flow measurements were conducted
- The upper (outlet) plenum located at the top of the bundle.

The test section contains a hexagonally shaped, simulated fuel bundle consisting of 61 helically wrapped pins arranged in a triangular lattice. The pins are attached to a bottom plate that is connected to the lower plenum. The

flow enters the lower plenum and exits the upper plenum symmetrically from two opposite sides of each plenum. The central section containing the bundle is 3.5 wire pitches long to allow for flow development, provide sufficient space for velocity measurements over one full wire pitch, and minimize exit effects. As mentioned previously, the one pitch measurement region was located 2.25 pitches from the bundle entrance.

The design requirements and physical dimensions for the test section were defined in the Test Specification document, Reference [11] [Appendix G]. As-built measurements were taken of the bundle geometry and are provided in the As-Built Geometry report, Reference [12] [Appendix J].

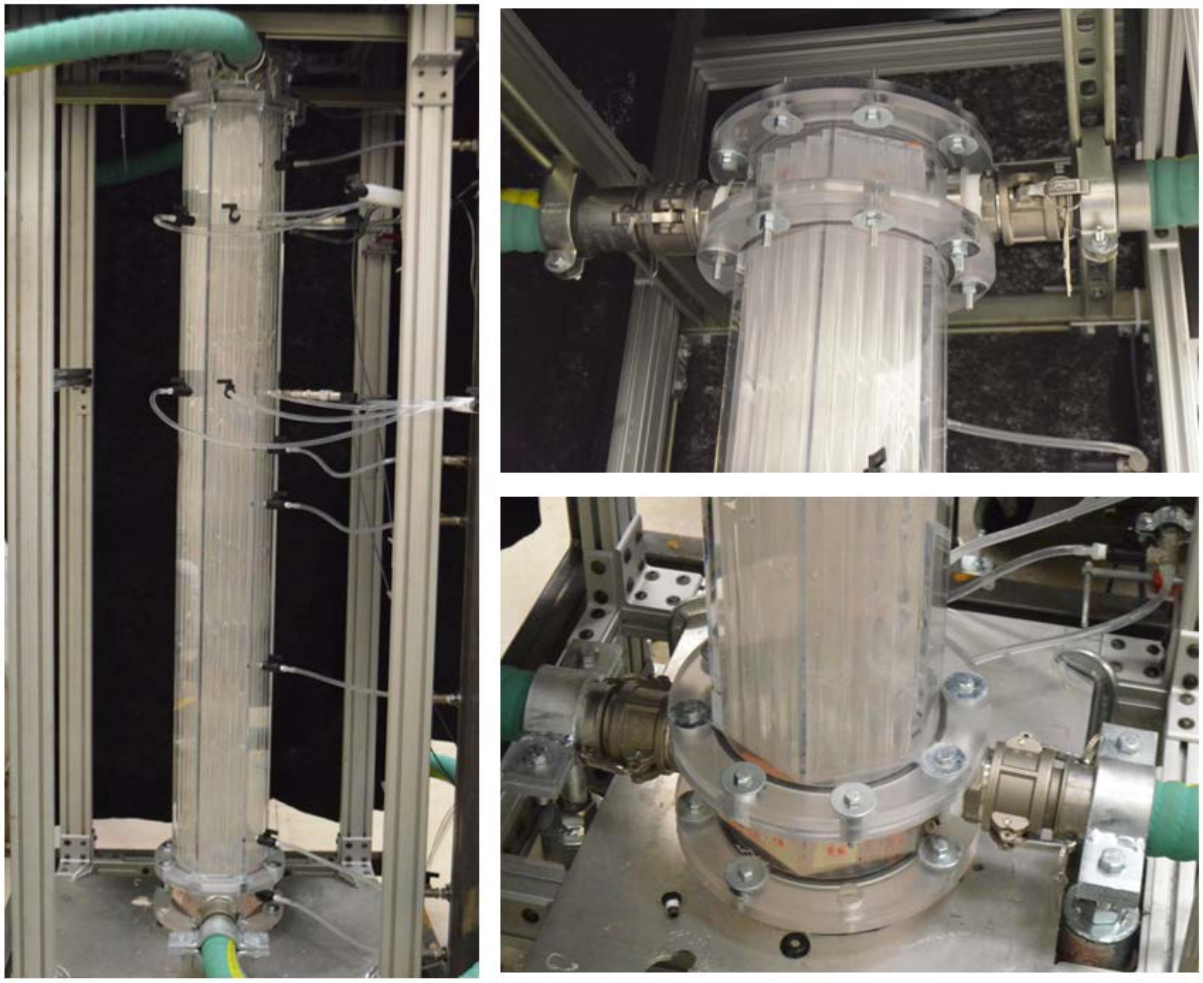


Figure 30: TAMU Isothermal Non-Deformed Test Section, left; Inlet Plenum, bottom right; Outlet Plenum, top right

6.5.2.1 Hardware Overview

6.5.2.1.1 Pressure Instrumentation Hardware

The facility is equipped with pressure transducers to measure the pressure at various axial and azimuthal locations along the duct walls. The locations of the pressure taps (PT) are shown in Figure 31. Each pressure tap is located in the center of one of the six duct faces, which are denoted by letters as diagrammed in Figure 32. Pressure taps are identified by a combination of a number indicating the axial location and a letter identifying the duct face.

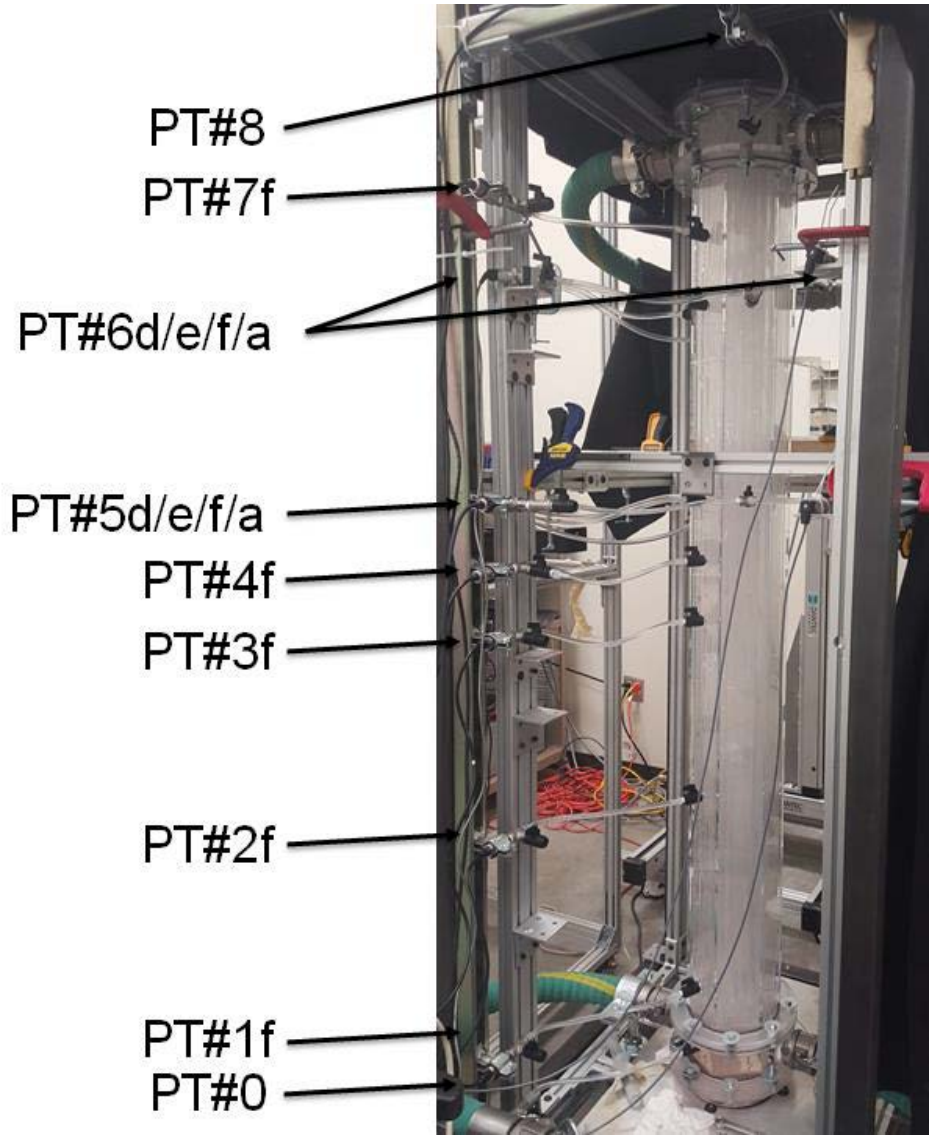


Figure 31: Non-Deformed, Isothermal Experiment Pressure Transducer Locations

Nine of the pressure taps measure the pressure drop along the primary axis of the fuel bundle. PT#0 is located in the lower inlet plenum to monitor the maximum pressure of the test section. The total pressure drop through the entire test section is determined by the difference in pressures measured by PT#0 (inlet tap) and PT#8 (outlet tap). Pressure transducers PT#1-7 are installed on the Face F of the hexagonal duct to record the pressure at seven axial locations along the test section. These taps capture the axially developing flow in the fuel bundle.

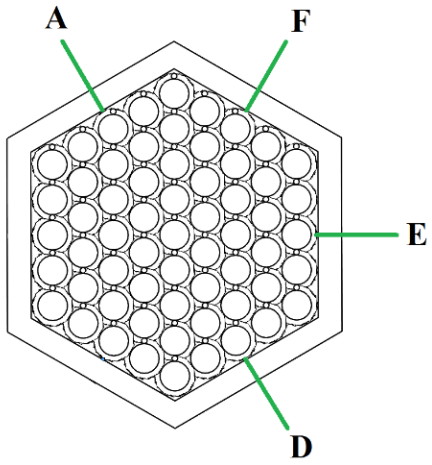


Figure 32: Face Nomenclature (top-down cross section)

At two different axial locations in the fully developed region, pressure taps are installed on four adjacent hexagonal faces of the duct to measure the azimuthal pressure gradient. Each set of these taps captures the flow asymmetry that exists due to the helically wrapped wire spacer. The two sets capture how the flow asymmetry changes as the orientation of the helically wrapped wire spacer changes. Flow enters the lower plenum through Faces B and E. Details of the as-installed locations of the pressure measurements are provided in the As-Built Geometry report, Reference [12] [Appendix J].

Specifications of the pressure transducers are provided in Table 3.

Table 3: Pressure Hardware Used in the TAMU Non-Deformed, Isothermal Experimental Test

Position In Facility	Model Number	Device Description	Accuracy
0F	PX309-030G5V	30 psi Gauge Pressure	< 4% FS
1F	PX309-030G5V	30 psi Gauge Pressure	< 4% FS
2F	PX419-030G5V	30 psi Gauge Pressure	< 0.1% FS
3F	PX419-030G5V	30 psi Gauge Pressure	< 0.1% FS
4F	PX419-030G5V	30 psi Gauge Pressure	< 0.1% FS
5F	MMG015V5P1D0T4A6CEPS	15 psi Gauge Pressure	<0.1% F.S
6F	PX419-030G5V	30 psi Gauge Pressure	< 0.1% FS
7F	MMG015V5P1D0T4A6CEPS	15 psi Gauge Pressure	<0.1% F.S
8A	PX309-015G5V	15 psi Gauge Pressure	< 1% FS
5 D/E/F/A	P55D-4-N-20-S-5-A	5 inch H_2O Differential Pressure	< 4.28% FS
6 D/E/F/A	MMDWB10WBIV5P2D0T2A2CE	10 inch H_2O Differential Pressure	< 0.1% FS

6.5.2.1.2 Data Acquisition Hardware

The data acquisition hardware consisted of equipment manufactured by National Instruments. The chassis used was a 4-slot model SCXI-1000. The input cards were 32-channel analog input modules with model numbers SCXI-1100 and SCXI-1102.

6.5.2.1.3 Temperature Hardware

An RDF Corporation resistance temperature detector (RTD) was utilized to measure the temperature of the p-Cymene during the experiment. The accuracy of the device is ±0.3˚C at 0˚C with an operating range of -196 ˚C to 480˚C.

6.5.2.1.4 Flow Rate Hardware

A Sponsler in-line precision turbine flowmeter (model SP3-MB-PHL-D-4X) was utilized to measure the volumetric flow rate of the working fluid. The uncertainty of the flowmeter analog output is 0.025% of full scale at 20 ºC. The full scale reading is 600 gallons per minute (GPM). A Sponsler IT400 totalizer recorded the analog output from the flowmeter with a digital uncertainty of ±1 GPM.

6.5.2.1.5 Imaging Hardware

The PIV system consisted of a 10 W continuous laser at a wavelength of 527 nm and two digital CMOS Phantom M310 cameras. The laser beam was adjusted by beam combination optics to form a 1.5 mm thick laser sheet for the PIV measurements. The laser position was adjusted with three motorized linear translation stages. The high-speed Phantom M310 cameras have a full resolution of 1280×800 pixels, a pixel size of 20×20 μm^2 and 12 bit-depth image capturing. The seeding particles were silver-coated hollow glass spheres with a mean diameter of 16 µm and a density of 1.6 g cm^{-3}.

6.5.3 Facility Construction

Dimensions and features of the test facility (including the test section) follow the test specifications described in Reference [11] [Appendix G]. Facility construction included:

1. Building a room to control personnel access;
2. Install dedicated ventilation and air conditioning systems;
3. Assembly of the primary and secondary loop components, piping, valves, and supports;
4. Fabrication of structures for mounting of the test section, pressure hardware, and PIV imaging hardware;
5. Installation of pressure and PIV imaging hardware.

6.5.4 Procurement and Fabrication

All the acrylic parts used for the fabrication of the test section were based on commercially available materials.

The acrylic pin and wire were selected based on commercial availability. The diameters are equal to 15.87 mm and 3 mm respectively. Details on pre-testing of single parts and construction of the acrylic pins are described in in the As-Built Geometry document, Reference [12] [Appendix J].

The acrylic duct is constructed from half-inch-thick commercial acrylic panels. The construction of duct, plena, and plates was outsourced to Moore Fabrication. Details on qualification and assembly of the test section are described in in the As-Built Geometry document, Reference [12] [Appendix J].

6.5.5 Installation

The facility is installed inside a controlled room with dedicated ventilation system and air conditioning.

An overview of the experimental installation is shown in Figure 33. Primary and secondary loops, the test section, and the instrumentation installed are visible in the same figure. A close-up view of the test section is shown in Figure 34.

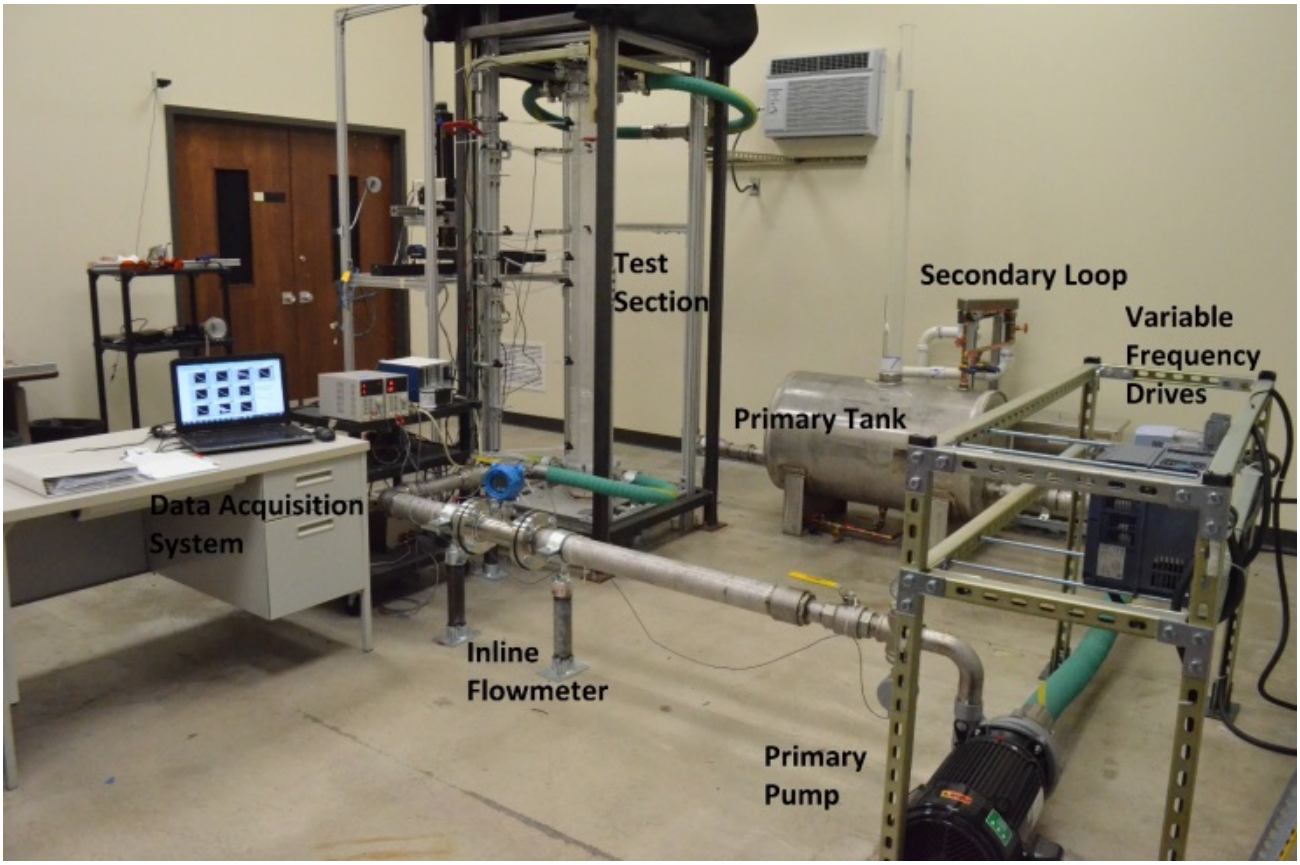


Figure 33: Overview of the TAMU Facility Installation



Figure 34: TAMU Facility Test Section

A typical PIV setup is depicted in Figure 35. Details on the specific setup used during the tests are described in Section 6.5.6.

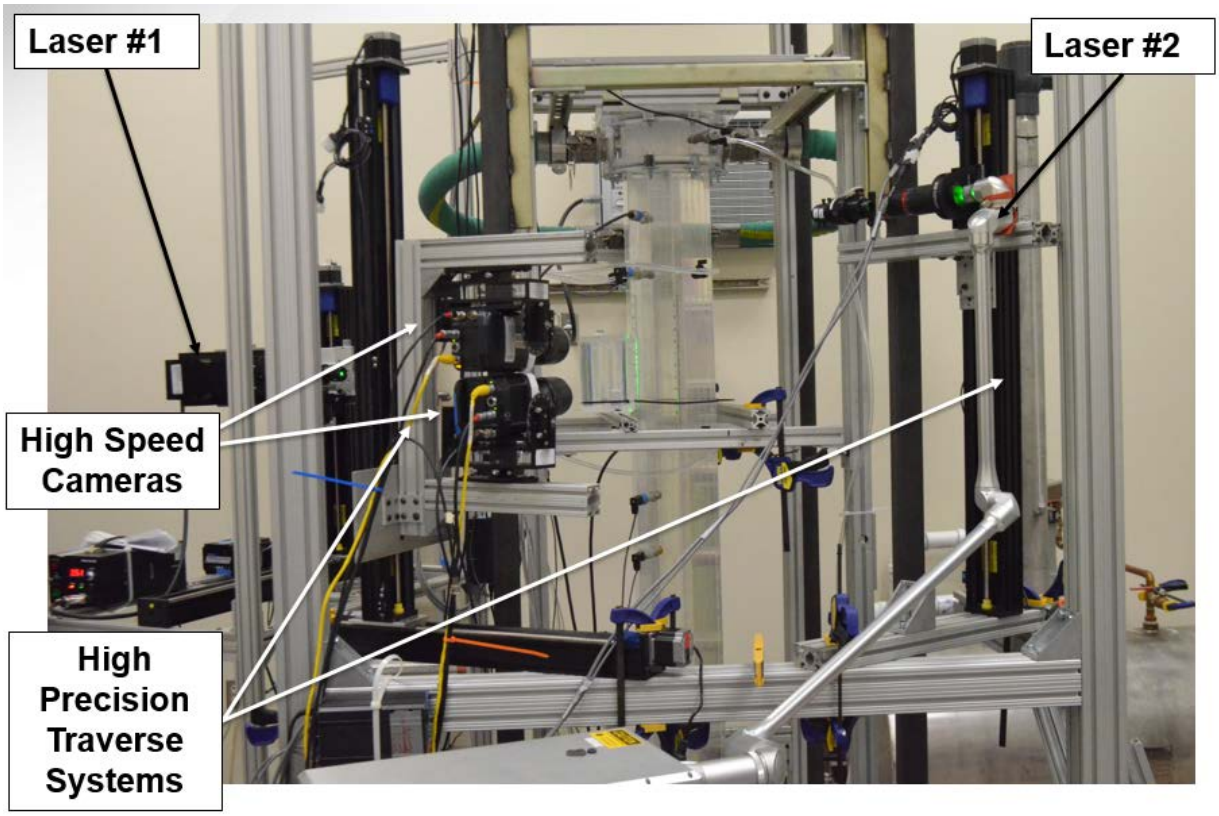


Figure 35: Typical PIV System Setup

6.5.6 Testing

6.5.6.1 Shakedown Testing

Shakedown tests were conducted to achieve the following goals:

- Verify the functionality and operability of the test facility;
- Verify the functionality and operability of the hardware installed;
- Identify any operation limitations;
- Develop the test procedures to be used to conduct the main tests;
- Perform preliminary measurements of near-wall velocity and pressures.

To facilitate the shakedown activity, tests were conducted using de-ionized water at room temperature. Table 4 lists the tests performed during the shakedown activity. Additional shakedown testing was performed with p-Cymene after the completion of the shakedown tests with de-ionized water. The purpose of the p-Cymene shakedown tests was to verify and refine the MIR technique before the final tests were conducted.

Table 4: Shakedown Test Matrix

Test Name	Flowrate (GPM)	Scope	Outcome
H2O-1-E	50, 60, 70, 80, 90	PIV, Face E, Axial Location 1 Axial Pressure on Face F	Adjusted camera framerate to optimize seeding particle shape. Performed preliminary measurements
H2O-2-E	100, 110, 120, 130, 140	PIV, Face E, Axial Location 1 Axial Pressure on Face F	Adjusted camera framerate to optimize seeding particle shape. Performed preliminary measurements Started draft operating procedure
H2O-3-E	50, 60, 70, 150	PIV, Face E, Axial Location 2 Axial Pressure on Face F	Adjusted to new axial location for different PIV visualization region. Performed preliminary measurements
H2O-4-E	70, 80, 90, 100, 110	PIV, Face E, Axial Location 2 Axial Pressure on Face F	Performed preliminary measurements Updated draft operating procedure
H2O-5-E	80, 120, 130, 140, 150	PIV, Face E, Axial Location 2 Axial Pressure on Face F	Performed preliminary measurements
H2O-6-E	0, 50 – 150 (10 GPM steps)	Axial Pressure on Face F Differential Pressure on F-A, F-D, and F-E face combinations	Adjusted azimuthal valves to measure the differential pressure across various faces at two axial locations
H2O-7-E	0, 50 – 150 (10 GPM steps)	Axial Pressure on Face F Differential Pressure on F-A, F-D, and F-E face combinations	Adjusted azimuthal valves to measure the differential pressure across various faces at two axial locations Finalized operating procedure

6.5.6.2 Main Testing

Tests were performed to record high spatial and temporal resolution velocity data using PIV at locations within the fully developed region of the test section. Pressure measurements were also recorded.

All tests were conducted according to the Benchmark Specification, Reference [13] [Appendix H].

6.5.6.2.1 Measurement Locations

Six vertical planes were identified for velocity measurements. The locations of these planes are shown in Figure 36 and consist of the following:

- One near-wall plane (1) to measure the velocity near face F of the duct (also called exterior plane)
- Four planes (2-5) to measure the velocity within interior sub-channel planes parallel to face F of the duct
- One additional plane (6) to measure the velocity within interior sub-channels in a plane offset by 30º from the other planes

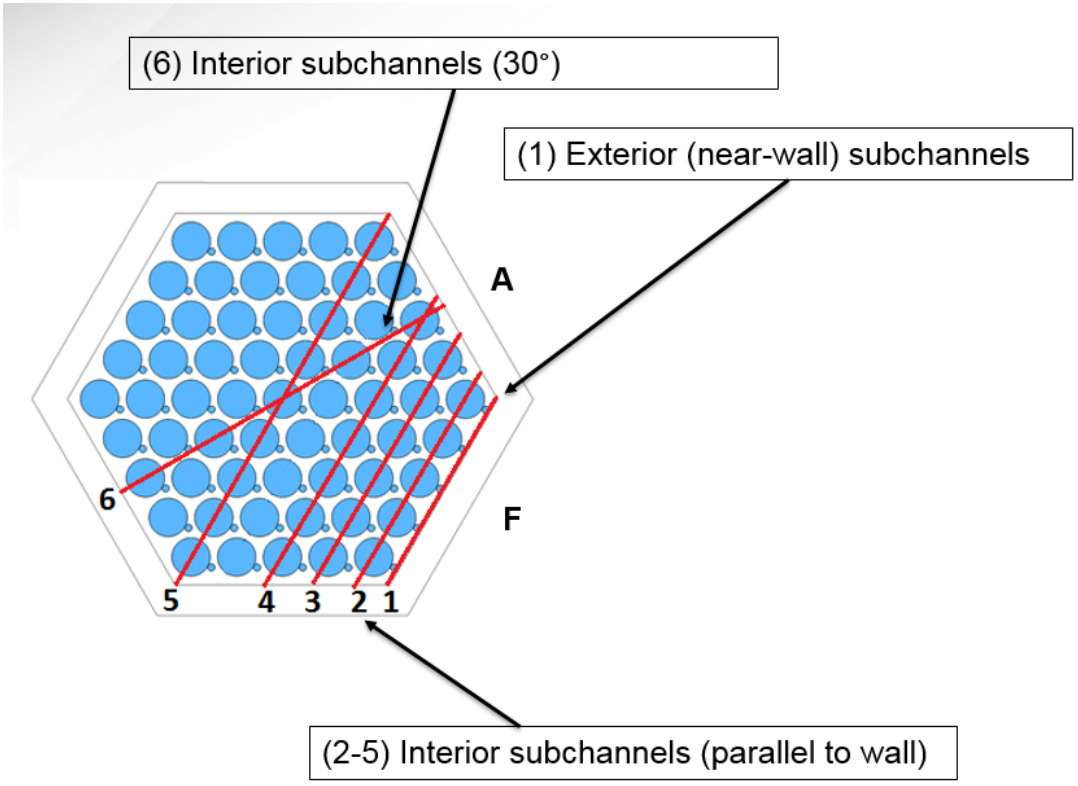


Figure 36: Locations of the PIV Planes

Three of the locations listed above were selected and included in the test matrix. The data recorded during these tests were post-processed, analyzed, and summarized in the test reports.

6.5.6.2.2 Test Matrix

The tests included in the test matrix are listed in Table 5. These tests were executed at a Reynolds number of approximately 19,000. Additional description of the operating conditions is provided in the test reports.

Table 5: Test Matrix for TAMU Non-Deformed, Isothermal Tests

Test Name	Measurement Location[3]	Test Report Reference
TAMU-WW-TEST-PCM-11-E	1	Reference [14] [Appendix K]
TAMU-WW-TEST-PCM-16-C2	6	Reference [15] [Appendix L]
TAMU-WW-TEST-PCM-14-INT1	2	Reference [16] [Appendix M]

Near-wall velocity measurements (plane 1) were complemented with simultaneous measurements of the wall pressure.

6.5.6.2.3 Test Conditions

Test conditions are described in detail in the test reports, References [14,15 and 16] [Appendix K, Appendix L and Appendix M], respectively, and include the following information:

- Velocity measurement location, with reference system
- Fluid temperature
- Pump frequency and flow rate
- Test section Reynolds number
- Sampling frequency (for PIV and pressure measurements)

6.5.6.2.4 Working Fluid

All tests were executed using p-Cymene. The fluid has the same index of refraction of the clear acrylic to apply the MIR technique combined with the PIV measurements.

6.5.6.2.5 Test Repeatability

Tests were executed three times under the same conditions corresponding to three datasets to account for test repeatability in the statistical analysis provided. These datasets were then averaged. Test data contains values corresponding to both the individual datasets and the averaged values.

6.5.6.2.6 Test Procedures

Written test procedures were in place at the time each test was executed. Test procedures included:

[3] Based on Figure 36

- The unique test name and date
- The name of the test operators performing the test
- Test preparation steps, including verification of the instrumentation, calibration, and other settings
- Specific monitoring steps to guarantee the integrity of the test facility and the laboratory safety during tests
- Test termination steps with data saving rules

6.5.6.2.7 Measurement Uncertainty

Uncertainty of the measurements was quantified and described in the test report, References [14, 15 and 16] [Appendix K, Appendix L and Appendix M], respectively. This includes:

- Uncertainty of the temperature measurements
- Uncertainty of the flow rate measurements
- Uncertainty of the pressure measurements
- Uncertainty of the laser sheet dimension and location
- Uncertainty of the PIV velocity measurements

Explanation on how the uncertainty sources were accounted and propagated into the Reynolds number is also described in the test reports. Of particular interest is the uncertainty associated with PIV measurements. This uncertainty was less than 3.0% of the mean axial velocity. Additional detail is provided in Reference [14] [Appendix K].

6.5.7 Experimental Data

Test reports include a description of the experimental data sets produced during each test. The data includes the following information:

- Volumetric Flow Rate Data, recorded for each run, plus a summary containing the arithmetic average, standard deviation, and k-factor conversion for each set.
- Pressure Data (for test TAMU-WW-TEST-PCM-11-E). Pressure from all axial transducers was recorded during each run, together with the azimuthal pressure drop from the differential pressure transducers connected between faces F-E, F-D, and F-A. A summary of the pressure measurements is also provided, containing the arithmetic average and standard deviation for each set.
- Velocity (PIV) Data, including:
    - Instantaneous velocity
    - Time-averaged (mean) velocity
    - Root-Mean-Square (rms) velocity
    - Reynolds Stresses

6.5.8 Results Analysis

6.5.8.1 Pressure Measurements and Friction Factor

An additional activity was conducted to investigate the behavior of the axial pressure drop as a function of the Reynolds number, within laminar, laminar-to-transition, transition-to-turbulent, and turbulent regimes. While this task was not part of the scope of this project, additional tests were conducted to record the pressure within a wide range of Reynolds numbers. The friction factor was calculated based on the pressure drop within selected axial locations and was compared with existing pressure drop correlations for wire wrapped bundles. This analysis was presented at the 2016 American Nuclear Society Winter Meeting in Las Vegas, NV. It is also included in the conference proceedings Reference [17] [Appendix N]. Figure 37 summarizes the experimental data (friction factor) produced and compares it with the Detailed Cheng-Todreas (CTD) correlation, Reference [18]. The experimental data were found to be in good agreement with the correlation.

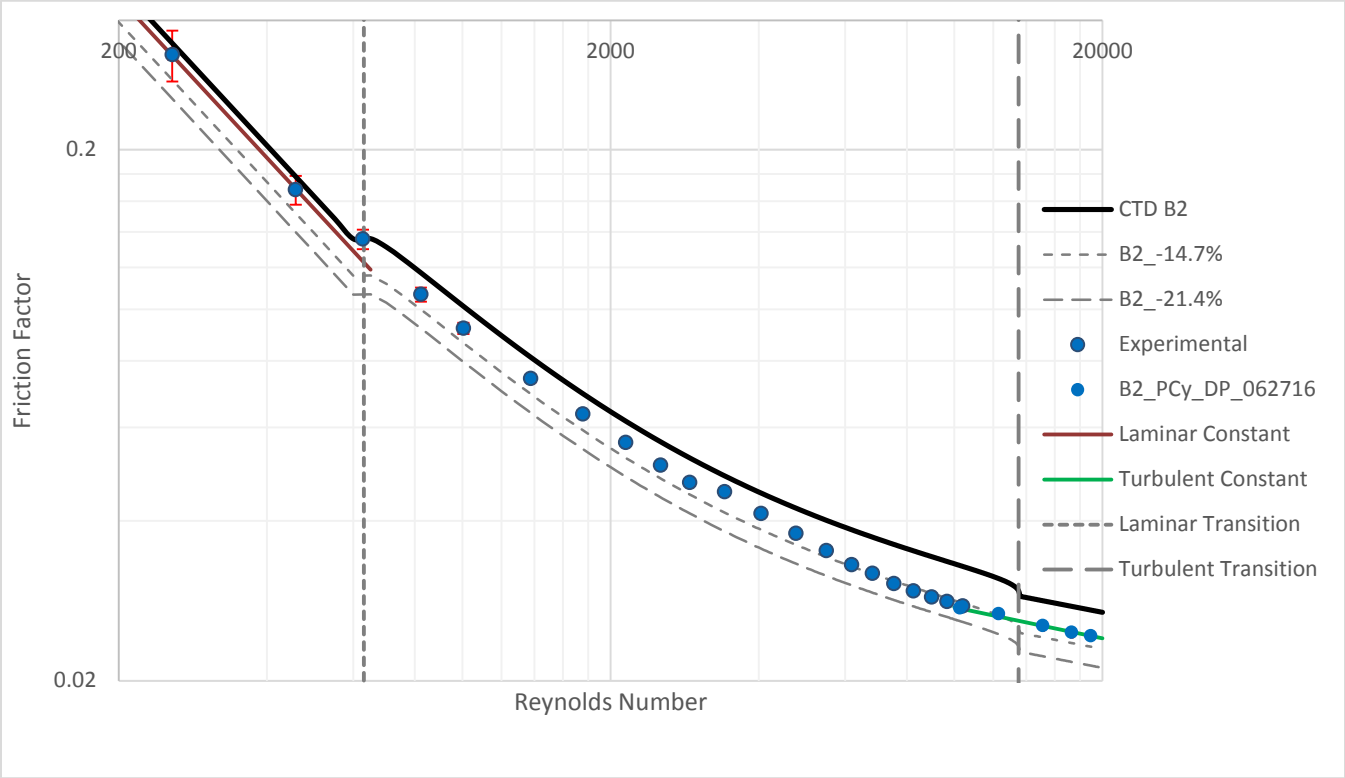


Figure 37: Experimental Friction Factor and Comparison with CTD [17]

6.5.8.2 PIV Data

Analysis of the velocity measurements recorded during the tests was conducted for the three selected planes. The results of this analysis was presented at the 2016 American Nuclear Society Winter Meeting in Las Vegas, NV, and included in the conference proceedings Reference [19] [Appendix N]. An example of the ensemble averaged velocity field in the wall sub-channels is shown below in Figure 38.

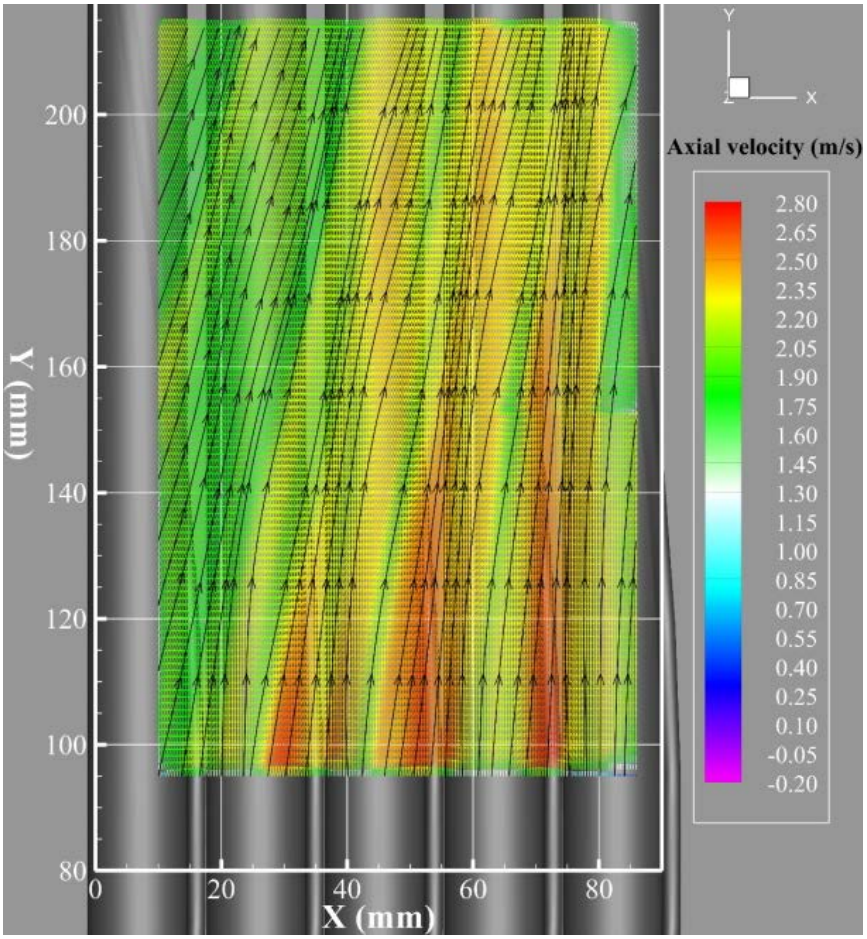


Figure 38: Ensemble-Averaged Velocity Field near the Wall (Plane 1) [19]

7.0 PROJECT TECHNICAL APPROACH

7.1 Technical Approach

The major project objectives were to obtain the local time dependent flow and thermal hydraulic behavior necessary for CFD validation. To achieve these objectives, a variety of approaches were identified as necessary to obtain the validation data while minimizing risk to the project objectives. These approaches include both methods employed for designing, constructing, and performing the experiments and the measurement techniques. The appropriateness and benefits of the methods proposed are described below.

7.1.1 Organizational Collaboration

Integral to the technical approaches of the separate experiment and numerical modeling efforts of the project was a close collaboration that was maintained among the different organization teams throughout the project. In validation projects, challenges often arise due to a discrepancy in the data that is obtained from the experiments, and the data that is needed by the numerical modeling analyst. To overcome this challenge, close collaboration

was maintained between the experiment and the numerical modeling groups. This included initial input to the test specification definition by the numerical analysts of the data needed for validation, initial preliminary CFD analyses of the proposed experiments to inform instrument location details, and a thorough review of all parties of the final test specifications. Throughout the project, collaboration was maintained through monthly conference calls, group updates and review of other groups' progress. This close collaboration enabled the production of data that is directly applicable for the numerical simulation analysts as validation datasets.

7.1.2 Isothermal Experiment Non-Intrusive Measurement Approach

Typical bundle experiments are limited to measurement locations near the duct wall, outlet, or require the use of intrusive measurement probes. The use of the MIR technique allows optical access for obtaining internal sub-channel velocity fields through the use of non-intrusive laser-based measurement techniques. Figure 39 illustrates an example application of the MIR technique.

High-resolution, two-dimensional (2D) velocity measurements were acquired using state-of-the-art 2D Time-Resolved PIV and particle tracking velocimetry (PTV) combined with the MIR technique. PIV is a well-established velocimetry technique able to provide full velocity fields via pictures of the flow equating to transient point measurements corresponding to the PIV interrogation grid resolution. The technique is based on seeding the flow and acquiring consecutive pictures of the particle movement. A laser illuminates the particles crossing the region of interest and the velocity field is calculated from knowledge of the particle movement. The velocity uncertainty associated with the technique for this experiment was 3%. Capturing the 2D form of the velocity field with high temporal resolution will allow the study and quantification of the complex turbulence phenomena found in wire-wrapped fuel assemblies required for CFD code validation.

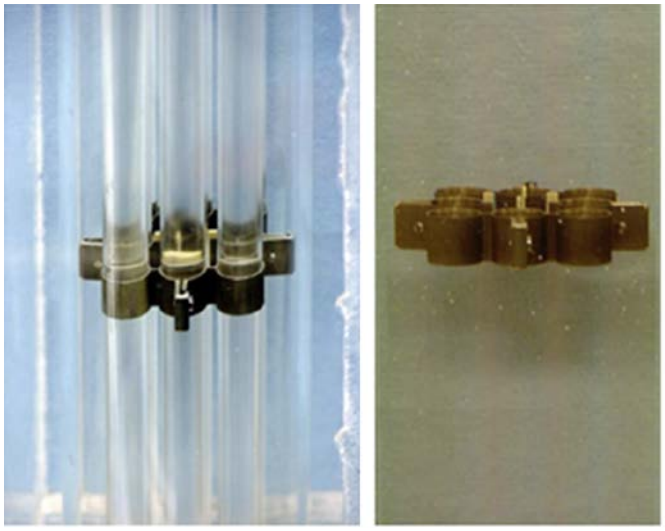


Figure 39: Solid Acrylic Rods and Spacer, left; Solid Rods Immersed in MIR Fluid, right

The cornerstone of TAMU's approach is a state-of-the-art imaging system consisting of a high-energy pulsed twin Nd:YAG laser allowing pulse rates of up to 20 kHz, a three high-speed CMOS camera system capable of frame rates up to 4.8 kHz at full 800 x 600 resolution (and up to over 100 kHz at reduced resolution) with up to 14-bit sensitivity and shutter speeds as fast as 2 μs, thereby enabling the use of advanced ensemble correlations to provide flow field measurements down to the single-pixel level to probe microscale phenomena (i.e., Kolmogorov scales).

7.1.3 Heated Test Design and Measurement

The heated bundle test geometry was designed and constructed by TerraPower and the tests performed by AREVA Federal Services through the AREVA Richland Test Facility as detailed in Section 6.3. For use in CFD validation, it is imperative to provide quality measurement data, as well as as-built and as-tested conditions that are needed in numerical simulations to fully simulate the experiments.

The heated bundle test section was designed by TerraPower with extensive input and review by AREVA Fuels for the non-deformed geometry and deformed duct with straight pins geometry as given in the test specification. An As-Built Report, Reference [5] [Appendix C], corresponding to the as-built and as-installed geometry of the heated bundle test section, including instrumentation location was produced for use in simulation model creation.

The experiments were conducted in the FCTF. The facility is a high-temperature test facility that provides a maximum 750 kW power with distribution control to produce unique radial heater power peaking. Facility instrumentation for temperatures, pressures, and flow rates were used to monitor and set the loop flow conditions, heater powers, and to avoid local boiling in the bundle. Insulation on the test bundle was added by AREVA Fuels to prevent heat loss, and thermocouples were welded to the outside of the test section to monitor and characterize heat loss for use in CFD problem definition. Preliminary scoping CFD simulations showed that from the facility power capabilities, a sufficient temperature radial profile gradient would be developed for location-dependent temperature measurement differentiation for use in CFD validation. Pumping capability corresponding to Reynolds numbers of 15,000-25,000 was met.

The principle CFD validation data from these tests are the many thermocouple temperature measurements with their corresponding locations and uncertainties to provide radial temperature profiles. To ensure the wire wrap did not influence thermocouple measurements, thermocouple locations were characterized in relation to the wire wrap.

The FCTF data acquisition system can record several hundred thermocouple measurements simultaneously. In addition to fluid temperature measurements, heated and unheated pins were instrumented with thermocouples to get wall temperature measurements for use in conjugate heat transfer CFD validation.

7.1.4 Nek5000 LES Numerical Simulations

The use of the Nek5000 LES code on the Mira Supercomputer at ANL provided the ability to compute localized flow detail to support the benchmarking effort. Nek5000 is CFD code designed specifically for DNS and LES simulations of transitional and turbulent flows in complex domains. Nek5000 is based on the spectral element method, which is a high-order weighted residual technique that combines the geometric flexibility of finite elements with the rapid convergence and tensor-product efficiencies of global spectral methods. The principal advantage of the spectral element method is that convergence is exponential in the polynomial order, which implies that significantly fewer grid points per wavelength are required to accurately propagate a signal (or turbulent structure) over the extended times associated with high Reynolds number flow simulations. In addition to its high-order foundation, Nek5000 has several other features that make it ideally suited for the proposed parallel simulations. Temporal discretization is based on a high-order splitting that is 3rd-order accurate in time and reduces the coupled velocity-pressure Stokes problem to four independent elliptic solves per timestep: one for each velocity component and one for the pressure. Particularly important components of Nek5000 are its scalable coarse-grid solvers that are central to parallel multigrid. The code features a fast direct solver that is optimal up to processor counts of P≈100,000, and fast algebraic multigrid for larger processor counts. Nek5000 scales extremely well on the BG/P and BG/Q architectures, where the work is being proposed.

Moreover Nek5000 has a large and growing user base with more than 200 individual users and dozens of institutions worldwide. Nek5000 has been extensively validated on a range of complex flow geometries and ranked first in two recent OECD/NEA benchmarks (Vatenfall T-junction and MATiS rod bundle experiment).

7.2 Changes in Technical Approach

As with any research and development project this size consisting of multiple project groups, changes in technical approach occurred throughout the project. The project had originally proposed the use of deformed pins in combination with the deformed duct for the isothermal MIR bundle testing performed at TAMU. Shortly after project award, this approach was excluded from the project work scope due to the complications associated with the approach. Initially, it was thought that the deformed pins could be fabricated to specification using 3-Dimensional printing technologies. However, after discussions with various suppliers, this approach was deemed to be impractical for the acrylic, isothermal testing due to the requirements for PIV testing.

8.0 PROBLEMS OR DELAYS

Various additional challenges presented themselves as the project team worked towards accomplishing the established project goals. Major project challenges and the actions taken to address these challenges are detailed in the following sections.

8.1 Rod Degradation – Isothermal Non-Deformed Bundle

Following the design and construction of the isothermal, non-deformed duct and pin bundle, the TAMU project group assembled the test components and ran various shakedown tests to address all of the concerns mentioned in Section 6.5.6.1. The acrylic wire pieces were helically wrapped around the acrylic pins and solvent weld connections were made at a few points along the length. All equipment and test components successfully passed shakedown testing and the TAMU project group began experimental testing and data acquisition. Initial tests were performed at flow rates between 50 GPM and 150 GPM (4,000 to 10,000Re). During these initial experimental tests with the p-Cymene fluid, degradation of the wire wrap to pin connection occurred. This inhibited the project group from achieving flow rates of 150 GPM and greater as the group was not confident the simulated fuel bundle was robust enough to withstand such flowrates. Typically, degradation of acrylic from the working fluid is controlled by limiting the exposure time of the acrylic to the fluid. However, the current geometry was additionally challenging due to the wire to pin contacts that were necessary to maintain the wire wrap shape.

To address the bundle degradation issues the TAMU project group constructed a new set of acrylic wire-wrapped pins utilizing a different method of fixing the wire to the pins. This method consisted of using adhesive along the entire interfacing surface between the pins and the wire instead of the previously used point method of adhesion that connected the wire to the pin at single points throughout the length of the pin. The group disassembled the test facility, installed the new pin bundle and re-started the experimental testing, eventually achieving the specified flow rates and Reynolds numbers. This second wire wrapped pin bundle showed successful stability for use in the p-cymene fluid.

8.2 Isothermal Deformed Bundle

As discussed in Section 5.5 above, the TAMU project group was tasked with the objective of running the same experiment tests on both non-deformed and deformed ducts. The degradation of the pin bundle discussed in Section 8.1 required the group to expend time and funding in excess of the non-deformed testing budget. This unforeseen project challenge resulted in the inability to accomplish the isothermal, deformed bundle portion of the

project's scope of work. The TAMU project group was able to develop a conceptual design of the deformed, acrylic duct and arrange a vendor capable of fabricating the duct but the time remaining until the end of the project and project funding were both inadequate to complete the experiment.

8.3 Duct Leak

The hexagonal non-deformed and deformed ducts that were fabricated for use in this project were made from cast bronze. This process consisted of casting bronze in the general shape, and then machining the inside faces of the bronze duct into their final geometry. This machining was necessary to ensure exactitude of the flow geometry. Bronze was selected for the duct material due to the ability to easily machine the interior surfaces. Before installation, pressure testing was performed. During this pressure testing it was observed that ducts were not holding pressure, and the water was actually seeping out through the walls of the bronze duct. It is expected that this problem occurred because the cooling stage of the casting process occurred too quickly, thus creating micro voids acting as flow paths through the bronze duct. This is not uncommon in the casting process. TerraPower, working with Intellectual Ventures Laboratory and the casting manufacturer of the bronze pieces, quickly developed a solution to this issue. The bronze duct pieces were vacuum treated to remove all fluid from the microscopic voids and then were impregnated with a low viscosity resin that fills and seals these voids. Additional pressure testing was performed and it was verified that the duct could meet the system pressure requirements of the test. This solution was implemented before shipment of the duct to AREVA, thereby having minimal impact to the project schedule.

8.4 Heater Rod Burnout

During initial experiment testing at the AREVA facility, one of the heated pins burnt out. The cause of the heater rod failure is currently being investigated by TerraPower and the pin's fabricator but is still unknown. While there were spare rods fabricated and available, due to the time and cost associated with dismantling and disassembling the heated fuel pin bundle, the decision was made to continue testing with the failed pin installed maintaining the per heater rod power as initially planned. Due to the burned out heater, the total heat into the bundle was less than initially specified. While the failed pin results in test conditions different from those outlined in the Test Specification document, it does not compromise the use of these tests and data for use as CFD validation datasets. The associated documentation reports the as-tested and as-built conditions, including the heater rods and heater powers. While numerical simulations of this test followed the Test Specification document (and therefore were not accurate with the actual test conditions), the accurate as-tested and as-built conditions were reported to the CFD analysts and were therefore available for post-test simulations.

8.5 Heated Rod Fabrication Delay

The heater rods used for these experiments are very unique in that they have a very high power output capability as well as are fabricated with installed thermocouples. Due to the requirements of these heater rods, there are not very many available fabricators. STERN Laboratories was contracted to fabricate the heater rods as they have years of experience making heater rods that meet these requirements. However, after initial conversations and design iterations with STERN laboratories, the timeline to produce these heater rods was longer than initially anticipated and planned for in the project schedule. This resulted in a compressed schedule for both heated tests performed at the AREVA facility. This had a potential impact on the schedule due to the time requirements for bundle installation and change-out between the non-deformed duct and deformed duct geometry tests. However, testing at the AREVA facility was able to meet the additional burden of a compressed testing schedule.

8.6 Computational Resource Limitations

ANL also faced project challenges at various stages during the project. ANL's major challenge was the lack of award of computational resources to run the Nek5000 numerical large eddy simulations. The ANL project group members were required to apply for allocation of computational resource hours on the ANL supercomputer. The size of the simulations required an extensive amount of computational resources. Upon completion of the project, the simulations run by ANL will be the largest not only for Nek5000 but for any code in the wire-wrap geometry. The ANL group attempted twice, unsuccessfully, to obtain the computational resources required to perform the CFD studies in the ANL scope of work. The lack of computational resources limited the number of simulations able to be performed by the project group.

9.0 KEY PERSONNEL OR TEAM ARRANGEMENT CHANGES

The AREVA and TerraPower project groups underwent key personnel changes during the project. The AFS project manager was changed from Ashley Spry to Anthony Chang due to task assignment changes internal to the AREVA organization. The AREVA project manager responsible for the heated testing performed at the FCTF facility changed from Ryan Welch to Tom Galioto. Finally, Nate Salpeter, who was initially the TerraPower project manager, left the organization to become a consultant for TerraPower and was replaced by Brian Jackson. Nate Salpeter continued in a reviewer role for the TerraPower CFD simulation scope. All of these personnel changes were brought to the attention of the entire project team as early as possible and had minimal impact, if any at all, to project.

10.0 PRODUCTS PRODUCED OR TECHNOLOGY TRANSFERRED

The project team fabricated an acrylic fuel bundle enclosed in a non-deformed duct for isothermal experiments at TAMU as well as both a non-deformed and deformed duct with 61-pin fuel assembly used in the heated experiments at the AREVA Fuels FCTF facility. The ducts and fuel assembly created for use in the heated experiments were funded privately and fabricated by TerraPower for loan to the project.

Benchmarking data files and associated reports resulting from this project, as detailed throughout this report, will be transferred to the U.S. DOE for public distribution.

11.0 SCHEDULE MILESTONE PERFORMANCE

Milestones established by the U.S. DOE at the outset of the project included quarterly project status reports, a final scientific technical report that covers the project in its entirety and project closeout reports. The quarterly project status reports included two separate reports. One of these reports detailed the project's technical challenges and accomplishments while the other focused on the financial reporting for the project. Table 6 summarizes all of the project's quarterly report submissions inclusive of the baselined schedule date and the actual submission date. The only reporting deadline that was extended past the baselined schedule date was that of the final scientific report. Various project factors required the AFS project manager to request and extension to the period of performance for the project the major factor being the award of additional computational resources to ANL. This report will be submitted to the U.S. DOE on, or before, the updated due date, thereby meeting the project deliverable. The final milestones associated with this project are the project closeout documents that consist of the patent certification document and the final property report. Both of these documents will be submitted along with this final report, successfully meeting the final project requirements and officially closing the project.

Table 6: Project Milestone Baseline Schedule Dates and Submission Dates

Milestone Description	Baseline Finish	Forecast/ Actual
Quarter 1 2015 Reporting to DOE	30-Apr-15	30-Apr-15 A
Quarter 2 2015 Reporting to DOE	30-Jul-15	30-Jul-15 A
Quarter 3 2015 Reporting to DOE	30-Oct-15	30-Oct-15 A
Quarter 4 2015 Reporting to DOE	29-Jan-16	29-Jan-16 A
Quarter 1 2016 Reporting to DOE	29-Apr-16	29-Apr-16 A
Quarter 2 2016 Reporting to DOE	29-Jul-16	29-Jul-16 A
Quarter 3 2016 Reporting to DOE	30-Oct-16	30-Oct-16 A
Quarter 4 2016 Reporting to DOE	31-Jan-17	31-Jan-17 A
Final Scientific Technical Report	08-Feb-17	08-Mar-17

12.0 FINANCIAL

12.1 Cost Share

The U.S. DOE, industry and academia were engaged and invested in the success of this project from before the start of the project. The project's industry participants willingly showed their belief in the need for such a project by contributing $1,129,200 in project funding in the form of cost share, amounting to more than 26% of total project funding. This cost share amount came in the form in-kind contributions of $529,200 and $600,000 from AREVA and TerraPower, respectively. This cost share amount exceeded the required minimum 20% cost share.

13.0 REFERENCES

1. Khan, E.U., "LMFBR In-Core Thermal Hydraulics: The State of the Art and U.S. Research and Development Needs," Battelle Pacific Northwest Laboratory report prepared for Department of Energy. Report PNL-3337 (1980).

2. Bridges, A.E., et al., "A Liquid-Metal Reactor Core Demonstration Experiment Using HT-9," Nuclear Technology, Vol 102, June, pp 353 (1993).

3. TAMU-WW-QA, TAMU Wire-Wrapped QA Guidelines, Rev. 0.0, April 2016.

4. TWRP-31-TSPEC-0011, AFAFC AREVA Heated Bundle Experiment Test Specification, Rev. 2.0, January 4, 2016.

5. TWRP-31-RPT-0033, AFAFC Heated Bundle As-Built Report, Rev.0, January 24, 2017.

6. TWRP-31-RPT-0022, AFAFC RANS Pre-Test Simulation Report, Rev.0, February 6, 2017.

7. TWRP-31-RPT-0032, AFAFC Post-Test Simulation Details, Rev.0, February 6, 2017.

8. TWRP-31-RPT-0036, AFAFC RANS Post-Test Simulation Report, Rev.0, February 27, 2017.

9. Leonard, D.J.; Jackson, R.B.; Steer, K.M., "Verification and Model Sensitivity Analysis for Computational Fluid Dynamics Simulations of Wire-Wrapped Nuclear Fuel Assemblies," *ASME Verification and Validation Symposium*, Las Vegas, NV, May 18-20, 2016.

10. Leonard, D.J.; Jackson, R.B.; Steer, K.M.; Reeves, T.; Salpeter, N., "CFD Verification and Validation of Wire-Wrapped Pin Assemblies," *Transactions American Nuclear Society*, ANS Winter Meeting, 2016.

11. TWRP-31-TSPEC-0010, TAMU Fuel Assembly Flow Visualization Test Specification, Rev.2.0, April 2016.

12. TAMU-WW-AS, TAMU Wire-Wrapped As-Built Geometry (Non-Deformed Bundle), Rev.2.0, November 2016.

13. TWRP-31-TREP-0004, AFAFC Benchmark Specification, Rev. 0, February 2016.

14. TAMU-WW-TEST-PCM-11-E, TAMU Wire-Wrapped Test Summary of Test PCM-11 at the Exterior Subchannel, Rev.2.0, December 2016.

15. TAMU-WW-TEST-PCM-16-C2, TAMU Wire-Wrapped Test Summary of Test PCM-16-C2 (Center plane - 30° offset), Rev.1.0, December 2016.

16. TAMU-WW-TEST-PCM-14-INT1, TAMU Wire-Wrapped Test Summary of Test PCM-14-INT1 at Interior Subchannel One, Rev.0, December 2016.

17. N. Goth, P. Jones, M. Childs, S. Lee, D.T. Nguyen, R. Vaghetto, Y.A. Hassan, “Pressure Measurements in a Wire-Wrapped 61-Pin Hexagonal Fuel Bundle”. American Nuclear Society Winter Meeting, Las Vegas, NV, November 6-10, 2016, Paper #1482.

18. Cheng, S.K.; Todreas, N.E., “Hydrodynamic Models and Correlations for Bare and Wire-Wrapped Hexagonal Rod Bundles – Bundle Friction Factors, Sub-Channel Friction Factors and Mixing Parameters,” *Nuclear Engineering and Design*, vol. 92, pp. 227-251, 1986.

19. N. Goth, P. Jones, M. Childs, S. Lee, D.T. Nguyen, R. Vaghetto, Y.A. Hassan, “Particle Image Velocimetry Measurements in a Wire-Wrapped 61-Pin Hexagonal Fuel Bundle”. American Nuclear Society Winter Meeting, Las Vegas, NV, November 6-10, 2016, Paper #1478.

20. “Cheng, S., and Todreas, N.E., “Evaluation of existing correlations for the prediction of pressure drop in wire-wrapped hexagonal array pin bundles”, Nuclear Engineering and Design 92 (1986) [for turbulent flow], Published by “Nuclear Engineering and Design”, December 2013.

APPENDIX A: HEATED BUNDLE TEST RESULTS

A.1 Introduction

AREVA NP performed a first-of-a-kind heated-bundle test in its Fuel Cooling Test Facility (FCTF) as part of a U.S. DOE funded project: Towards a Longer-Life Core. In partnership with TerraPower, TAMU and ANL, AREVA NP tested a wire-wrapped rod bundle. The bundle consists of electrically heated pins and non-heated pins. This test collected measurements to evaluate thermal hydraulic performance of a wire wrapped bundle, useful for CFD and other software validation.

Four tests were conducted corresponding to two test geometries and both powered and non-powered conditions. Mass flowrates were approximately constant for all four tests and correspond to a Reynolds number (Re) of 20,000 using the hydraulic diameter of the non-deformed duct geometry and fluid properties at the inlet temperature of the heated test conditions. This test series included two different ducts:

1. The non-deformed duct is a straight hexagonal pipe.
2. The deformed hexagonal duct is machined with a cosine shape on the inner duct walls of all six sides over the heated length, with a maximum depth in the center of the heated length of approximately 1mm. Additional detail is provided in the Heated Bundle As-Built Report, Reference [5] [Appendix C].

A.2 Test Setup

Unless otherwise stated, the axial location of the test equipment for this test series uses the bottom of the duct as the datum.

Figure 40 shows the locations, numbering scheme and type of rods. The heater rod at position 17 failed during the test setup. Therefore only a total of 18 heater rods were used during testing.

The pressure taps were setup as shown in Figure 41. Some of the pressure taps were not used and some of the pressure taps in the fuel rod locations did not produce correct results. Pressure tap pairs were used to measure differential pressure: Table 7 presents the final pressure tap combinations.

Table 8 lists the tests recorded for this series.

The non-deformed duct Thermocouple (TC) locations and descriptions are in Table 9.

Figure 42 is a sketch of the azimuthal locations of the duct internal TCs.

Most of the TCs for the deformed duct test were plugged into the same channels as the non-deformed duct test. For TCs that changed channel locations or status, details are listed in Table 10.

Reference [5] [Appendix C] shows the arrangement of the duct and heated bundle in the loop vessel.

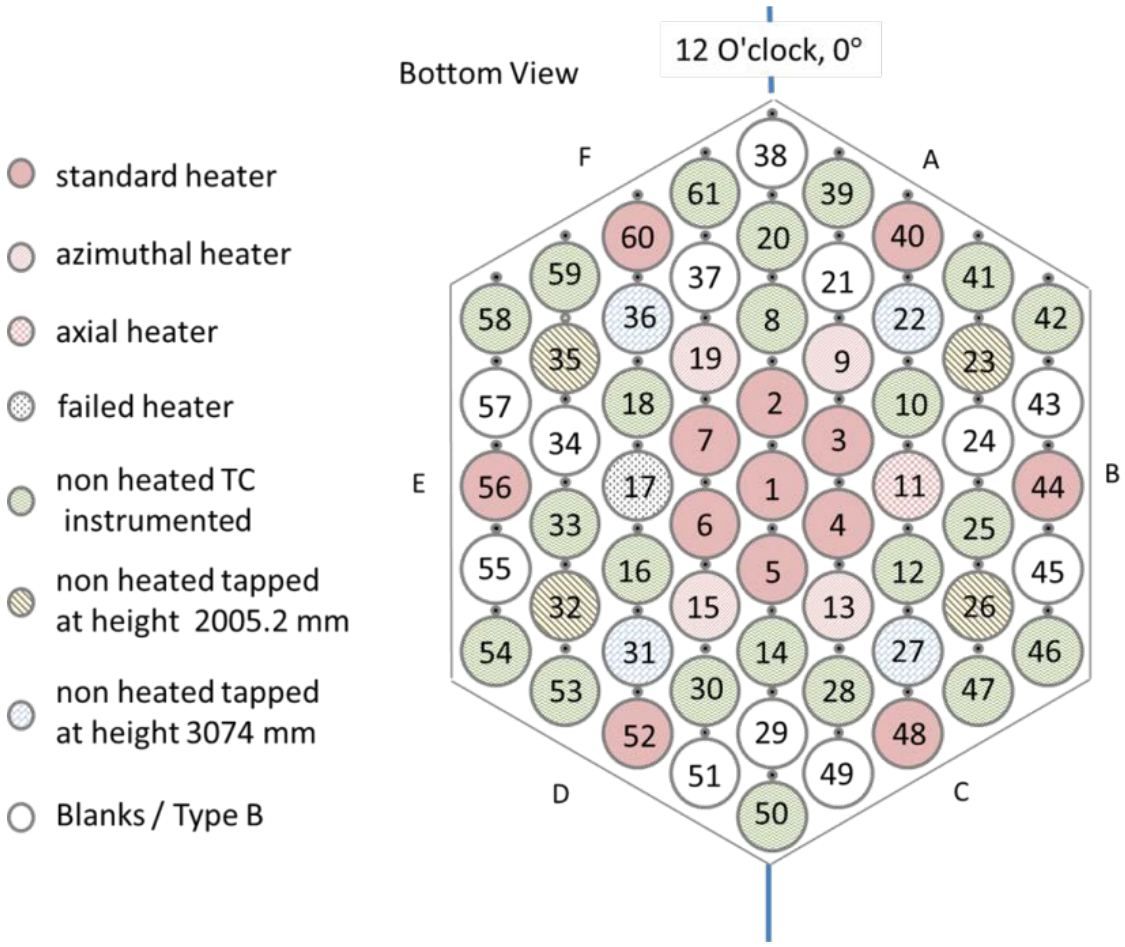


Figure 40: Test Rod Configuration (looking from the bottom up) [4]

[4] The number scheme in this figure is the Rod Positions chosen for this test series.

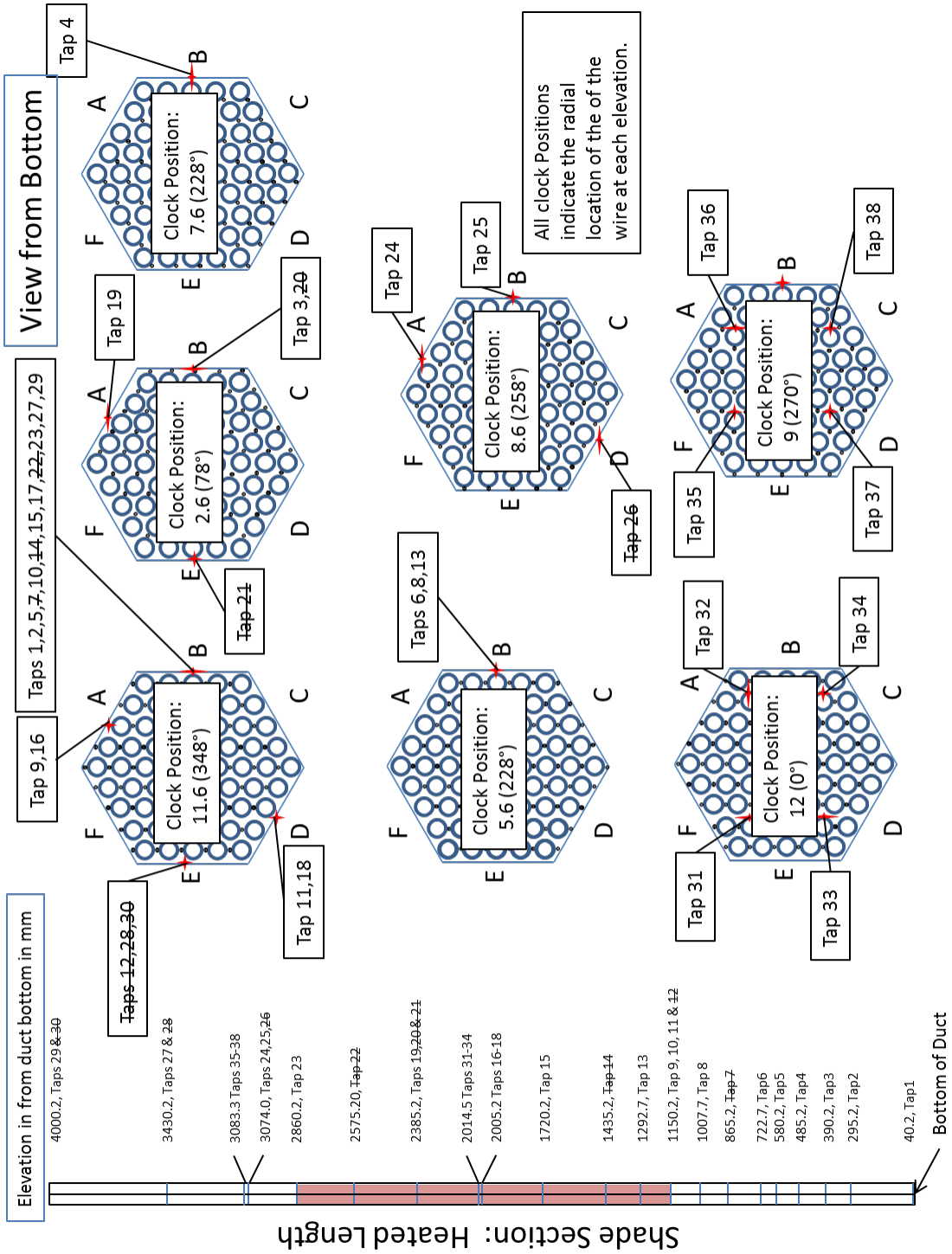


Figure 41: Pressure Drop Measurement Tap Layout (looking from the bottom up)

Table 7: Pressure Drop Cell Information

ID	Tap ID Non-Deformed Duct		Tap ID Deformed Duct Tests		Range (Pa)	Accuracy (Pa)
	Low	High	Low	High		
DP1	2	1	2	1	24884	+/- 78
DP2	5	1	5	1	49768	+/- 156
DP3	6	2	6	2	49768	+/- 156
DP4	9	6	9	6	24884	+/- 78
DP5	4	3	4	3	12442	+/- 39
DP6	6	3	6	3	24884	+/- 78
DP7	6	5	6	5	12442	+/- 249[1]
DP8	8	4	8	4	37326	+/- 117
DP9	13	8	15[2]	8[2]	74652	+/- 233
DP10	15	11	15	11	62210	+/- 194
DP11	15	11	16[2]	11[2]	49768	+/- 156
DP12	17	9	17	9	74652	+/- 233
DP13	17	10	17	10	62210	+/- 194
DP14	25	10	25	10	174188	+/- 544
DP15	18	11	18	11	62210	+/- 194
DP16	35	18	35	18	99536	+/- 311
DP17	36	19	~~36~~[3]	~~19~~[3]	74652	+/- 233
DP18	37	16	37	16	99536	+/- 311
DP19	38	23	38	23	37326	+/- 117
DP20	29	27	29	27	99536	+/- 311
DP21	27	23	27	23	99536	+/- 770[1]
DP22	~~24~~[3]	~~34~~[3]	24[4]	34[4]	74652	+/- 233
DP23	~~24~~[3]	~~31~~[3]	24	31	99536	+/- 311
DP24	25	32	25	32	99536	+/- 311
DP25	38	33	~~38~~[3]	~~33~~[3]	99536	+/- 311
DP26	29	19	29	19	124420	+/- 389
DP27	35	31	35	31	74652	+/- 233
DP28	36	32	~~36~~[3]	~~32~~[3]	74652	+/- 233
DP29	37	33	~~37~~[3]	~~33~~[3]	74652	+/- 233
DP30	~~38~~[3]	~~34~~[3]	38[4]	34[4]	74652	+/- 233

1. Posttest calibration revealed a drift for DP7 and DP21, increasing the accuracy tolerance.
2. Tap Pair changed between Non-Deformed and Deformed,
3. These tap pairs failed to measure. Do not use data.
4. These tap pairs failed to measure for some deformed duct tests. Do not use data from these measurements for Tests 14, 15, 16 and 17.

Table 8: Test Boundary Conditions

REYNOLDS

Test Number[1,2]	Mdot1 [VM1] (kg/s)	Mdot2 [VM62] (kg/s)	Mdot Avg. (kg/s)	Inlet Temp (°C)	Viscocity (kg/m/s)	Reynolds[3]
03	11.955	12.065	12.010	14.91	0.00114	17000
05	9.489	9.576	9.533	32.07	0.000766	20100
24	11.963	12.028	11.996	15.14	0.00114	17000
19	9.568	9.583	9.576	32.31	0.000762	20300

POWER

Test Number[1,2]	SCR1[4] (Watts)	SCR2 [4] (Watts)	SCR3[4] (Watts)	SCR4[4] (Watts)
05	22643	22845	22747	22801
19	22612	22610	22754	22663

NOTES:

1) The Microsoft Excel files associated with each test is identified in Section A.7.
2) Test 03 and 05 used the non-deformed duct. Test 24 and 19 used the deformed duct
3) $Rey = Mdot * Dh/v * FA$; Where Dh = 0.004535 m and FA = 0.002808 m^2.
4) Four Silicon Controlled Rectifiers (SCR) distribute the power as follows: SCR1 powers the heater pins 2, 3, 6 & 7. SCR2 powers the heater pins 4,5,11 & 15. SCR3 powers the heater pins 2, 9, 19, 40 & 60 (See Figure 40). SCR4 powers the heater pins 13, 44, 48, 52 & 56. See Figure 40 for map.

Table 9 provides instrument location and numbering that corresponds to the test data Microsoft Excel files.

Table 9: Temperature Data Channels Non-Deformed Duct

Device Name	TC group	Axial location from duct bottom (mm)	Duct face	Clock position Bottom View	Rod position #	Description	Device Name	Notes
TC 1	**system**					**inlet HX5**	**TC 1**	
TC 2	system					outlet HX5	TC 2	
TC 3	**system**					**outlet HX4**	**TC 3**	
TC 4	system					outlet HX4+5	TC 4	
TC 5	**system**					**outlet pipe**	**TC 5**	
TC 6	system					outlet plenum	TC 6	
TC 7	**system**					**outlet plenum**	**TC 7**	
TC 8	system					outlet plenum	TC 8	
TC 9	**system**					**inlet plenum**	**TC 9**	
TC 10	system					inlet plenum	TC 10	
TC 11							**TC 11**	
TC 12							TC 12	
TC 13							**TC 13**	
TC 14							TC 14	
TC 15							**TC 15**	

Device Name	TC group	Axial location from duct bottom (mm)	Duct face	Clock position	Rod position #	Description	Device Name	Notes
TC 16							TC 16	
TC 17	**outside Duct**	**1767.51**	**E**			**1**	**TC 17**	Centered on Side E
TC 18	outside Duct	1886.35	E			2	TC 18	Centered on Side E
TC 19	**outside Duct**	**2005.2**	**E**			**3**	**TC 19**	Centered on Side E
TC 20	outside Duct	2052.51	E			4	TC 20	Centered on Side E
TC 21	**outside Duct**	**2171.36**	**E**			**5**	**TC 21**	Centered on Side E
TC 22	outside Duct	2337.51	E			6	TC 22	Centered on Side E
TC 23	**outside Duct**	**2409**	**E**			**7**	**TC 23**	Centered on Side E
TC 24	outside Duct	2456.36	E			8	TC 24	Centered on Side E
TC 25	**outside Duct**	**2622.5**	**E**			**9**	**TC 25**	Centered on Side E
TC 26	outside Duct	2741.36	E			10	TC 26	Centered on Side E
TC 27	**outside Duct**	**2907.5**	**E**			**11**	**TC 27**	Centered on Side E
TC 28	outside Duct	3074	E			12	TC 28	Centered on Side E
TC 29							**TC 29**	
TC 30							TC 30	
TC 31							**TC 31**	
TC 32							TC 32	
TC 33	**internal Duct**	**38.1**	**A**			Figure 42	**TC 33**	
TC 34	internal Duct	38.1	E			Figure 42	TC 34	
TC 35	**internal Duct**	2005.2	**E**			Figure 42	**TC 35**	
TC 36	internal Duct	2005.2	E			Figure 42	TC 36	
TC 37	**internal Duct**	2005.2	**E**			Figure 42	**TC 37**	
TC 38	internal Duct	2005.2	E			Figure 42	TC 38	
TC 39	**internal Duct**	2005.2	**E**			Figure 42	**TC 39**	
TC 40	internal Duct	2005.2	E			Figure 42	TC 40	
TC 41	**internal Duct**	2052.7	**E**			Figure 42	**TC 41**	
TC 42	internal Duct	2052.7	E			Figure 42	TC 42	
TC 43	**internal Duct**	2052.7	**E**			Figure 42	**TC 43**	

Device Name	TC group	Axial location from duct bottom (mm)	Duct face	Clock position	Rod position #	Description	Device Name	Notes
TC 44	internal Duct	2052.7	E			Figure 42	TC 44	
TC 45	**internal Duct**	2052.7	**E**			Figure 42	**TC 45**	
TC 46	internal Duct	2052.7	E			Figure 42	TC 46	
TC 47	**internal Duct**	2409	**E**			Figure 42	**TC 47**	
TC 48	internal Duct	2409	E			Figure 42	TC 48	
TC 49	**internal Duct**	2409	**E**			Figure 42	**TC 49**	
TC 50	internal Duct	2409	E			Figure 42	TC 50	
TC 51	**internal Duct**	2409	**E**			Figure 42	**TC 51**	
TC 52	internal Duct	3074	E			Figure 42	TC 52	
TC 53	**internal Duct**	3074	**E**			Figure 42	**TC 53**	
TC 54	internal Duct	3074	E			Figure 42	TC 54	
TC 55	**internal Duct**	3074	**E**			Figure 42	**TC 55**	
TC 56	internal Duct	3074	E			Figure 42	TC 56	

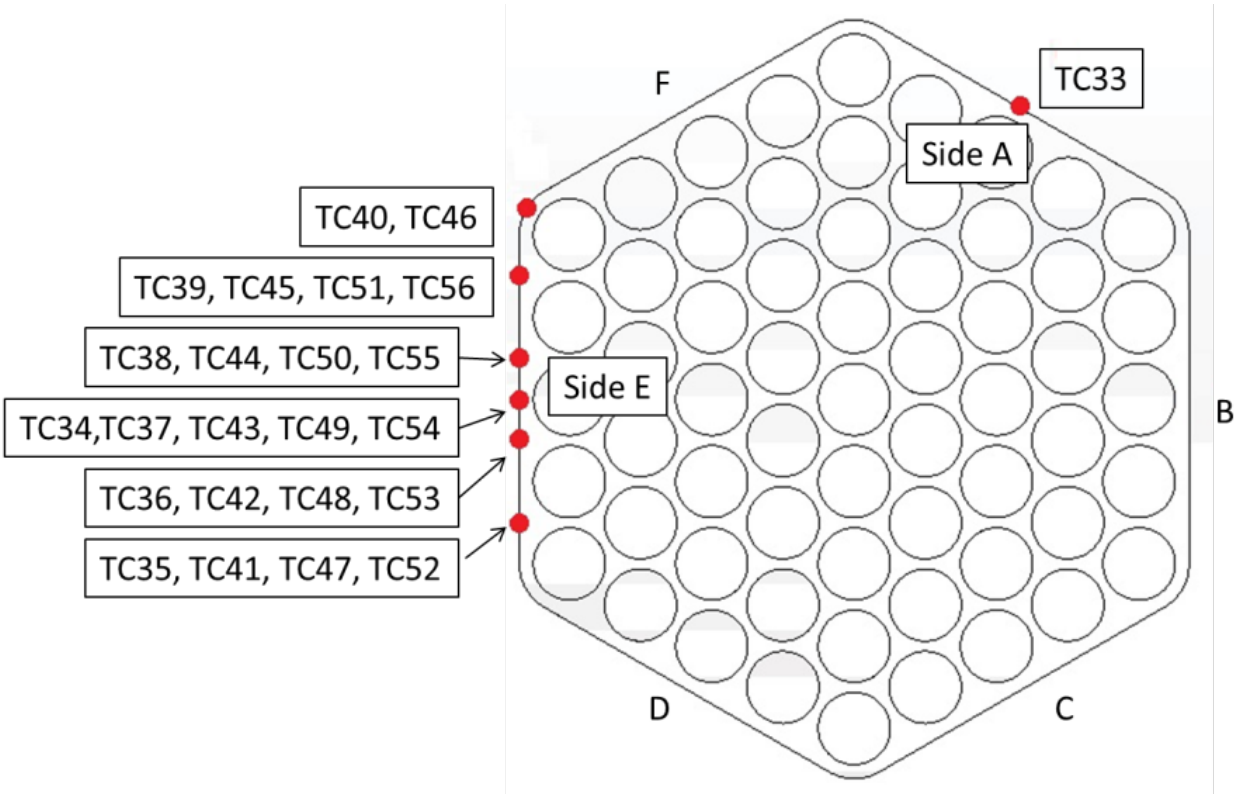


Figure 42: Internal Duct Thermocouple Radial Locations (viewed from bottom)

Table 9: Temperature Data Channels Non-Deformed Duct (continued)

Device Name	TC group	Axial location from duct bottom (mm)	Duct face	Clock position Bottom View	Rod position #	Device Name	Notes
TC 57	**standard heater rods**	**2014.6**		**12 (0)**	**1**	**TC 57**	See Note 1 below
TC 58		2014.6		1 (30)	1	TC 58	See Note 1 below
TC 59		**2418.35**		**4 (120)**	**1**	~~**TC 59**~~	Reading room temperature do not use
TC 60		2418.35		6 (180)	1	TC 60	See Note 1 below
TC 61		**3083.35**		**8 (240)**	**1**	**TC 61**	
TC 62		3083.35		9 (270)	1	TC 62	
TC 63		**3083.35**		**10 (300)**	**1**	**TC 63**	
TC 64		2014.6		11 (330)	1	TC 64	See Note 1 below
TC 65		**2014.6**		**12 (0)**	**2**	**TC 65**	See Note 1 below
TC 66		2014.6		1 (30)	2	TC 66	See Note 1 below
TC 67		**2418.35**		**4 (120)**	**2**	**TC 67**	See Note 1 below
TC 68		2418.35		6 (180)	2	TC 68	See Note 1 below
TC 69		**3083.35**		**8 (240)**	**2**	**TC 69**	
TC 70		3083.35		9 (270)	2	TC 70	
TC 71		**3083.35**		**10 (300)**	**2**	**TC 71**	
TC 72		2014.6		11 (330)	2	TC 72	See Note 1 below
TC 73		**2014.6**		**12 (0)**	**3**	**TC 73**	See Note 1 below
TC 74		2014.6		1 (30)	3	TC 74	See Note 1 below **Table** 9
TC 75		**2418.35**		**4 (120)**	**3**	**TC 75**	See Note 1 below
TC 76		2418.35		6 (180)	3	TC 76	See Note 1 below
TC 77		**3083.35**		**8 (240)**	**3**	**TC 77**	

Device Name	TC group	Axial location from duct bottom (mm)	Duct face	Clock position Bottom View	Rod position #	Device Name	Notes
TC 78		3083.35		9 (270)	3	TC 78	
TC 79		**3083.35**		**10 (300)**	**3**	**TC 79**	
TC 80		2014.6		11 (330)	3	TC 80	See Note 1 below
TC 81		**2014.6**		**12 (0)**	**4**	**TC 81**	See Note 1 below
TC 82		2014.6		1 (30)	4	TC 82	See Note 1 below
TC 83		**2418.35**		**4 (120)**	**4**	**TC 83**	See Note 1 below
TC 84		2418.35		6 (180)	4	TC 84	See Note 1 below
TC 85		**3083.35**		**8 (240)**	**4**	**TC 85**	
TC 86		3083.35		9 (270)	4	TC 86	
TC 87		**3083.35**		**10 (300)**	**4**	**TC 87**	
TC 88		2014.6		11 (330)	4	TC 88	See Note 1 below
TC 89		**2014.6**		**12 (0)**	**5**	**TC 89**	See Note 1 below
TC 90		2014.6		1 (30)	5	TC 90	See Note 1 below
TC 91		**2418.35**		**4 (120)**	**5**	**TC 91**	See Note 1 below
TC 92		2418.35		6 (180)	5	TC 92	See Note 1 below
TC 93		**3083.35**		**8 (240)**	**5**	**TC 93**	
TC 94		3083.35		9 (270)	5	TC 94	
TC 95		**3083.35**		**10 (300)**	**5**	**TC 95**	
TC 96		2014.6		11 (330)	5	TC 96	See Note 1 below
TC 97		**2014.6**		**12 (0)**	**6**	**TC 97**	See Note 1 below
TC 98		2014.6		1 (30)	6	TC 98	See Note 1 below
TC 99		**2418.35**		**4 (120)**	**6**	**TC 99**	See Note 1 below

Device Name	TC group	Axial location from duct bottom (mm)	Duct face	Clock position Bottom View	Rod position #	Device Name	Notes
TC 100		2418.35		6 (180)	6	TC 100	See Note 1 below
TC 101		**3083.35**		**8 (240)**	**6**	**TC 101**	
TC 102		3083.35		9 (270)	6	TC 102	
TC 103		**3083.35**		**10 (300)**	**6**	**TC 103**	
TC 104		2014.6		11 (330)	6	TC 104	See Note 1 below
TC 105		**2014.6**		**12 (0)**	**7**	**TC 105**	See Note 1 below
TC 106		2014.6		1 (30)	7	TC 106	See Note 1 below
TC 107		**2418.35**		**4 (120)**	**7**	**TC 107**	See Note 1 below
TC 108		2418.35		6 (180)	7	TC 108	See Note 1 below
TC 109		**3083.35**		**8 (240)**	**7**	**TC 109**	
TC 110		3083.35		9 (270)	7	TC 110	
TC 111		**3083.35**		**10 (300)**	**7**	**TC 111**	
TC 112		2014.6		11 (330)	7	TC 112	See Note 1 below
~~**TC 113**~~	~~-~~	~~**2014.6**~~	~~-~~	~~**12 (0)**~~	~~**40**~~	~~**TC 113**~~	moved to TC361
~~TC 114~~	~~-~~	~~2014.6~~	~~-~~	~~1 (30)~~	~~40~~	~~TC 114~~	moved to TC362
~~**TC 115**~~	~~-~~	~~**2418.35**~~	~~-~~	~~**4 (120)**~~	~~**40**~~	~~**TC 115**~~	moved to TC363
~~TC 116~~	~~-~~	~~2418.35~~	~~-~~	~~6 (180)~~	~~40~~	~~TC 116~~	moved to TC364
~~**TC 117**~~	~~-~~	~~**3083.35**~~	~~-~~	~~**8 (240)**~~	~~**40**~~	~~**TC 117**~~	moved to TC365
~~TC 118~~	~~-~~	~~3083.35~~	~~-~~	~~9 (270)~~	~~40~~	~~TC 118~~	moved to TC366
~~**TC 119**~~	~~-~~	~~**3083.35**~~	~~-~~	~~**10 (300)**~~	~~**40**~~	~~**TC 119**~~	moved to TC367
~~TC 120~~	~~-~~	~~2014.6~~	~~-~~	~~11 (330)~~	~~40~~	~~TC 120~~	moved to TC368
TC 121		**2014.6**		**12 (0)**	**44**	**TC 121**	See Note 1 below

Device Name	TC group	Axial location from duct bottom (mm)	Duct face	Clock position Bottom View	Rod position #	Device Name	Notes
TC 122		2014.6		1 (30)	44	TC 122	See Note 1 below
TC 123		**2418.35**		**4 (120)**	**44**	**TC 123**	See Note 1 below
TC 124		2418.35		6 (180)	44	TC 124	See Note 1 below
TC 125		**3083.35**		**8 (240)**	**44**	**TC 125**	
TC 126		3083.35		9 (270)	44	TC 126	
TC 127		**3083.35**		**10 (300)**	**44**	**TC 127**	
TC 128		2014.6		11 (330)	44	TC 128	See Note 1 below
~~TC 129~~	-	~~2014.6~~	-	~~12 (0)~~	~~48~~	~~TC 129~~	moved to TC 369
~~TC 130~~	-	~~2014.6~~	-	~~1 (30)~~	~~48~~	~~TC 130~~	moved to TC 370
~~TC 131~~	-	~~2418.35~~	-	~~4 (120)~~	~~48~~	~~TC 131~~	moved to TC 371
~~TC 132~~	-	~~2418.35~~	-	~~6 (180)~~	~~48~~	~~TC 132~~	moved to TC 372
~~TC 133~~	-	~~3083.35~~	-	~~8 (240)~~	~~48~~	~~TC 133~~	moved to TC 373
~~TC 134~~	-	~~3083.35~~	-	~~9 (270)~~	~~48~~	~~TC 134~~	moved to TC 374
~~TC 135~~	-	~~3083.35~~	-	~~10 (300)~~	~~48~~	~~TC 135~~	moved to TC 375
~~TC 136~~	-	~~2014.6~~	-	~~11 (330)~~	~~48~~	~~TC 136~~	moved to TC 376
TC 137		**2014.6**		**12 (0)**	**52**	**TC 137**	See Note 1 below
TC 138		2014.6		1 (30)	52	TC 138	See Note 1 below
TC 139		**2418.35**		**4 (120)**	**52**	**TC 139**	See Note 1 below
TC 140		2418.35		6 (180)	52	TC 140	See Note 1 below
TC 141		**3083.35**		**8 (240)**	**52**	**TC 141**	
TC 142		3083.35		9 (270)	52	TC 142	
TC 143		**3083.35**		**10 (300)**	**52**	**TC 143**	

Device Name	TC group	Axial location from duct bottom (mm)	Duct face	Clock position Bottom View	Rod position #	Device Name	Notes
TC 144		2014.6		11 (330)	52	TC 144	See Note 1 below
TC 145		**2014.6**		**12 (0)**	**56**	**TC 145**	See Note 1 below
TC 146		2014.6		1 (30)	56	TC 146	See Note 1 below
TC 147		**2418.35**		**4 (120)**	**56**	**TC 147**	See Note 1 below
TC 148		2418.35		6 (180)	56	TC 148	See Note 1 below
TC 149		**3083.35**		**8 (240)**	**56**	**TC 149**	
TC 150		3083.35		9 (270)	56	TC 150	
TC 151		**3083.35**		**10 (300)**	**56**	**TC 151**	
TC 152		2014.6		11 (330)	56	TC 152	See Note 1 below
TC 153		**2014.6**		**12 (0)**	**60**	**TC 153**	See Note 1 below
TC 154		2014.6		1 (30)	60	TC 154	See Note 1 below
TC 155		**2418.35**		**4 (120)**	**60**	**TC 155**	See Note 1 below
TC 156		2418.35		6 (180)	60	TC 156	See Note 1 below
TC 157		**3083.35**		**8 (240)**	**60**	**TC 157**	
TC 158		3083.35		9 (270)	60	TC 158	
TC 159		**3083.35**		**10 (300)**	**60**	**TC 159**	
TC 160		2014.6		11 (330)	60	TC 160	See Note 1 below
TC 161	**Axial heater rods**	**2014.6**		**12 (0)**	**11**	**TC 161**	See Note 1 below
TC 162		2062.1		1 (30)	11	TC 162	See Note 1 below
TC 163		**2347.1**		**2 (60)**	**11**	**TC 163**	See Note 1 below
TC 164		2655.9		3 (90)	11	TC 164	See Note 1 below
TC 165		**2964.6**		**4 (120)**	**11**	**TC 165**	
TC 166		3273.4		5 (150)	11	TC 166	

Device Name	TC group	Axial location from duct bottom (mm)	Duct face	Clock position Bottom View	Rod position #	Device Name	Notes
TC 167		**1373.4**		**9 (270)**	**11**	**TC 167**	See Note 1 below
TC 168		1682.1		10 (300)	11	TC 168	See Note 1 below
TC 169		**1967.1**		**11 (330)**	**11**	**TC 169**	See Note 1 below
TC 170		2014.6		12 (0)	17	TC 170	See Note 2 below
TC 171		**2062.1**		**1 (30)**	**17**	**TC 171**	See Note 2 below
TC 172		2347.1		2 (60)	17	TC 172	See Note 2 below
~~**TC 173**~~	-	~~**2655.9**~~	-	~~**3 (90)**~~	~~**17**~~	~~**TC 173**~~	See Note 2 below
TC 174		2964.6		4 (120)	17	TC 174	See Note 2 below
TC 175		**3273.4**		**5 (150)**	**17**	**TC 175**	See Note 2 below
TC 176		1373.4		9 (270)	17	TC 176	See Note 2 below
TC 177		**1682.1**		**10 (300)**	**17**	**TC 177**	See Note 2 below
TC 178		1967.1		11 (330)	17	TC 178	See Note 2 below
TC 179						**TC 179**	
TC 180						TC 180	
TC 181						**TC 181**	
TC 182						TC 182	
TC 183						**TC 183**	
TC 184						TC 184	
TC 185	**azimuthal heater rods**	**2014.6**		**12 (0)**	**9**	**TC 185**	See Note 1 below
TC 186		2418.35		1 (30)	9	TC 186	See Note 1 below
TC 187		**2418.35**		**3 (90)**	**9**	**TC 187**	See Note 1 below
TC 188		2418.35		5 (150)	9	TC 188	See Note 1 below
TC 189		**2014.6**		**6 (180)**	**9**	**TC 189**	See Note 1 below
TC 190		2418.35		7 (210)	9	TC 190	See Note 1 below

Device Name	TC group	Axial location from duct bottom (mm)	Duct face	Clock position Bottom View	Rod position #	Device Name	Notes
~~TC 191~~	-	~~2418.35~~	-	~~9 (270)~~	~~9~~	~~TC 191~~	See Note 1 below
TC 192		2418.35		11 (330)	9	TC 192	See Note 1 below
TC 193		**2014.6**		**12 (0)**	**13**	**TC 193**	See Note 1 below
TC 194		2418.35		1 (30)	13	TC 194	See Note 1 below
TC 195		**2418.35**		**3 (90)**	**13**	**TC 195**	See Note 1 below
TC 196		2418.35		5 (150)	13	TC 196	See Note 1 below
TC 197		**2014.6**		**6 (180)**	**13**	**TC 197**	See Note 1 below
~~TC 198~~	-	~~2418.35~~	-	~~7 (210)~~	~~13~~	~~TC 198~~	Not reading do not use
~~TC 199~~	-	~~2418.35~~	-	~~9 (270)~~	~~13~~	~~TC 199~~	Not reading do not use
TC 200		2418.35		11 (330)	13	TC 200	See Note 1 below
~~TC 201~~	-	~~2014.6~~	-	~~12 (0)~~	~~15~~	~~TC 201~~	moved to TC 378
~~TC 202~~	-	~~2418.35~~	-	~~1 (30)~~	~~15~~	~~TC 202~~	moved to TC 379
~~TC 203~~	-	~~2418.35~~	-	~~3 (90)~~	~~15~~	~~TC 203~~	moved to TC 380
~~TC 204~~	-	~~2418.35~~	-	~~5 (150)~~	~~15~~	~~TC 204~~	moved to TC 381
~~TC 205~~	-	~~2014.6~~	-	~~6 (180)~~	~~15~~	~~TC 205~~	moved to TC 382
~~TC 206~~	-	~~2418.35~~	-	~~7 (210)~~	~~15~~	~~TC 206~~	moved to TC 383
~~TC 207~~	-	~~2418.35~~	-	~~9 (270)~~	~~15~~	~~TC 207~~	moved to TC 384
~~TC 208~~	-	~~2418.35~~	-	~~11 (330)~~	~~15~~	~~TC 208~~	moved to TC 385
TC 209		**2014.6**		**12 (0)**	**19**	**TC 209**	See Note 1 below
TC 210		2418.35		1 (30)	19	TC 210	See Note 1 below
TC 211		**2418.35**		**3 (90)**	**19**	**TC 211**	See Note 1 below
TC 212		2418.35		5 (150)	19	TC 212	See Note 1 below
TC 213		**2014.6**		**6 (180)**	**19**	**TC 213**	See Note 1 below

Device Name	TC group	Axial location from duct bottom (mm)	Duct face	Clock position Bottom View	Rod position #	Device Name	Notes
TC 214		2418.35		7 (210)	19	TC 214	See Note 1 below
TC 215		**2418.35**		**9 (270)**	**19**	**TC 215**	See Note 1 below
TC 216		2418.35		11 (330)	19	TC 216	See Note 1 below
TC 217	**Non HR - type A**	**2014.6**		**1 (30)**	**8**	**TC 217**	
TC 218		2014.6		11 (330)	8	TC 218	
TC 219		**2418.35**		**4 (120)**	**8**	**TC 219**	
TC 220		2418.35		6 (180)	8	TC 220	
TC 221		**3083.35**		**8 (240)**	**8**	**TC 221**	
TC 222		3083.35		10 (300)	8	TC 222	
TC 223		**2014.6**		**1 (30)**	**10**	**TC 223**	
TC 224		2014.6		11 (330)	10	TC 224	
TC 225		**2418.35**		**4 (120)**	**10**	**TC 225**	
TC 226		2418.35		6 (180)	10	TC 226	
TC 227		**3083.35**		**8 (240)**	**10**	**TC 227**	
TC 228		3083.35		10 (300)	10	TC 228	
TC 229		**2014.6**		**1 (30)**	**12**	**TC 229**	
TC 230		2014.6		11 (330)	12	TC 230	
TC 231		**2418.35**		**4 (120)**	**12**	**TC 231**	
TC 232		2418.35		6 (180)	12	TC 232	
~~**TC 233**~~	-	~~**3083.35**~~	-	**8 (240)**	~~**12**~~	~~**TC 233**~~	move to TC 353
~~TC 234~~	-	~~3083.35~~	-	~~10 (300)~~	~~12~~	~~TC 234~~	move to TC 354
~~**TC 235**~~	-	~~**2014.6**~~	-	~~**1(30)**~~	~~**16**~~	~~**TC 235**~~	move to TC 355

Device Name	TC group	Axial location from duct bottom (mm)	Duct face	Clock position Bottom View	Rod position #	Device Name	Notes
~~TC 236~~	-	~~2014.6~~	-	~~11 (330)~~	~~16~~	~~TC 236~~	move to TC 356
~~TC 237~~	-	**~~2418.35~~**	-	**4 (120)**	**~~16~~**	**~~TC 237~~**	move to TC 357
~~TC 238~~	-	~~2418.35~~	-	~~6 (180)~~	~~16~~	~~TC 238~~	move to TC 358
~~TC 239~~	-	**~~3083.35~~**	-	**~~8 (240)~~**	**~~16~~**	**~~TC 239~~**	move to TC 359
~~TC 240~~	-	~~3083.35~~	-	~~10 (300)~~	~~16~~	~~TC 240~~	move to TC 360
TC 241		**2014.6**		**1 (30)**	**18**	**TC 241**	
TC 242		2014.6		11 (330)	18	TC 242	
TC 243		**2418.35**		**4 (120)**	**18**	**TC 243**	
TC 244		2418.35		6 (180)	18	TC 244	
TC 245		**3083.35**		**8 (240)**	**18**	**TC 245**	
TC 246		3083.35		10 (300)	18	TC 246	
TC 247		**2014.6**		**1 (30)**	**20**	**TC 247**	
TC 248		2014.6		11 (330)	20	TC 248	
TC 249		**2418.35**		**4 (120)**	**20**	**TC 249**	
TC 250		2418.35		6 (180)	20	TC 250	
TC 251		**3083.35**		**8 (240)**	**20**	**TC 251**	
TC 252		3083.35		10 (300)	20	TC 252	
TC 253		**2014.6**		**1 (30)**	**25**	**TC 253**	
TC 254		2014.6		11 (330)	25	TC 254	
TC 255		**2418.35**		**4 (120)**	**25**	**TC 255**	
TC 256		2418.35		6 (180)	25	TC 256	
TC 257		**3083.35**		**8**	**25**	**TC 257**	

Device Name	TC group	Axial location from duct bottom (mm)	Duct face	Clock position Bottom View	Rod position #	Device Name	Notes
				(240)			
TC 258		3083.35		10 (300)	25	TC 258	
TC 259		**2014.6**		**1 (30)**	**28**	**TC 259**	
TC 260		2014.6		11 (330)	28	TC 260	
TC 261		**2418.35**		**4 (120)**	**28**	**TC 261**	
TC 262		2418.35		6 (180)	28	TC 262	
TC 263		**3083.35**		**8 (240)**	**28**	**TC 263**	
TC 264		3083.35		10 (300)	28	TC 264	
TC 265		**2014.6**		**1 (30)**	**30**	**TC 265**	
TC 266		2014.6		11 (330)	30	TC 266	
TC 267		**2418.35**		**4 (120)**	**30**	**TC 267**	
TC 268		2418.35		6 (180)	30	TC 268	
TC 269		**3083.35**		**8 (240)**	**30**	**TC 269**	
TC 270		3083.35		10 (300)	30	TC 270	
TC 271		**2014.6**		**1 (30)**	**33**	**TC 271**	
TC 272		2014.6		11 (330)	33	TC 272	
TC 273		**2418.35**		**4 (120)**	**33**	**TC 273**	
TC 274		2418.35		6 (180)	33	TC 274	
TC 275		**3083.35**		**8 (240)**	**33**	**TC 275**	
TC 276		3083.35		10 (300)	33	TC 276	
TC 277		**2014.6**		**1 (30)**	**39**	**TC 277**	
TC 278		2014.6		11 (330)	39	TC 278	

Device Name	TC group	Axial location from duct bottom (mm)	Duct face	Clock position Bottom View	Rod position #	Device Name	Notes
TC 279		**2418.35**		**4 (120)**	**39**	**TC 279**	
TC 280		2418.35		6 (180)	39	TC 280	
TC 281		**3083.35**		**8 (240)**	**39**	**TC 281**	
TC 282		3083.35		10 (300)	39	TC 282	
TC 283		**2014.6**		**1 (30)**	**41**	**TC 283**	
TC 284		2014.6		11 (330)	41	TC 284	
TC 285		**2418.35**		**4 (120)**	**41**	**TC 285**	
TC 286		2418.35		6 (180)	41	TC 286	
TC 287		**3083.35**		**8 (240)**	**41**	**TC 287**	
TC 288		3083.35		10 (300)	41	TC 288	
TC 289		**2014.6**		**1 (30)**	**42**	**TC 289**	
~~TC 290~~	-	~~2014.6~~	-	~~11 (330)~~	~~42~~	~~TC 290~~	move to TC 377
TC 291		**2418.35**		**4 (120)**	**42**	**TC 291**	
TC 292		2418.35		6 (180)	42	TC 292	
TC 293		**3083.35**		**8 (240)**	**42**	**TC 293**	
TC 294		3083.35		10 (300)	42	TC 294	
TC 295		**2014.6**		**1 (30)**	**46**	**TC 295**	
TC 296		2014.6		11 (330)	46	TC 296	
TC 297		**2418.35**		**4 (120)**	**46**	**TC 297**	
TC 298		2418.35		6 (180)	46	TC 298	
TC 299		**3083.35**		**8 (240)**	**46**	**TC 299**	
TC 300		3083.35		10	46	TC 300	

Device Name	TC group	Axial location from duct bottom (mm)	Duct face	Clock position Bottom View	Rod position #	Device Name	Notes
				(300)			
TC 301		**2014.6**		**1 (30)**	**47**	**TC 301**	
TC 302		2014.6		11 (330)	47	TC 302	
TC 303		**2418.35**		**4 (120)**	**47**	**TC 303**	
TC 304		2418.35		6 (180)	47	TC 304	
TC 305		**3083.35**		**8 (240)**	**47**	**TC 305**	
TC 306		3083.35		10 (300)	47	TC 306	
TC 307		**2014.6**		**1 (30)**	**50**	**TC 307**	
TC 308		2014.6		11 (330)	50	TC 308	
TC 309		**2418.35**		**4 (120)**	**50**	**TC 309**	
TC 310		2418.35		6 (180)	50	TC 310	
TC 311		**3083.35**		**8 (240)**	**50**	**TC 311**	
TC 312		3083.35		10 (300)	50	TC 312	
TC 313		**2014.6**		**1 (30)**	**53**	**TC 313**	
TC 314		2014.6		11 (330)	53	TC 314	
TC 315		**2418.35**		**4 (120)**	**53**	**TC 315**	
TC 316		2418.35		6 (180)	53	TC 316	
TC 317		**3083.35**		**8 (240)**	**53**	**TC 317**	
TC 318		3083.35		10 (300)	53	TC 318	
TC 319		**2014.6**		**1 (30)**	**54**	**TC 319**	
TC 320		2014.6		11 (330)	54	TC 320	
TC 321		**2418.35**		**4 (120)**	**54**	**TC 321**	

Device Name	TC group	Axial location from duct bottom (mm)	Duct face	Clock position Bottom View	Rod position #	Device Name	Notes
TC 322		2418.35		6 (180)	54	TC 322	
TC 323		**3083.35**		**8 (240)**	**54**	**TC 323**	
TC 324		3083.35		10 (300)	54	TC 324	
TC 325		**2014.6**		**1 (30)**	**58**	**TC 325**	
TC 326		2014.6		11 (330)	58	TC 326	
TC 327		**2418.35**		**4 (120)**	**58**	**TC 327**	
TC 328		2418.35		6 (180)	58	TC 328	
TC 329		**3083.35**		**8 (240)**	**58**	**TC 329**	
TC 330		3083.35		10 (300)	58	TC 330	
TC 331		**2014.6**		**1 (30)**	**59**	**TC 331**	
TC 332		2014.6		11 (330)	59	TC 332	
TC 333		**2418.35**		**4 (120)**	**59**	**TC 333**	
TC 334		2418.35		6 (180)	59	TC 334	
TC 335		**3083.35**		**8 (240)**	**59**	**TC 335**	
TC 336		3083.35		10 (300)	59	~~TC 336~~	Reading negative do not use
TC 337		**2014.6**		**1 (30)**	**61**	**TC 337**	
TC 338		2014.6		11 (330)	61	TC 338	
TC 339		**2418.35**		**4 (120)**	**61**	**TC 339**	
TC 340		2418.35		6 (180)	61	TC 340	
TC 341		**3083.35**		**8 (240)**	**61**	**TC 341**	
TC 342		3083.35		10 (300)	61	TC 342	
TC 343						**TC 343**	

Device Name	TC group	Axial location from duct bottom (mm)	Duct face	Clock position Bottom View	Rod position #	Device Name	Notes
TC 344						TC 344	
TC 345	**non HR - type E**	**2014.6**			**14**	**TC 345**	
TC 346		2014.6		1 (30)	14	TC 346	
TC 347		**2014.6**		**11 (330)**	**14**	**TC 347**	
TC 348		2418.35		4 (120)	14	TC 348	
TC 349		**2418.35**		**6 (180)**	**14**	**TC 349**	
TC 350		3083.35		8 (240)	14	TC 350	
TC 351		**3083.35**		**10 (300)**	**14**	**TC 351**	
TC 352						TC 352	
TC 353	**Non HR - type A**	**3083.35**		**8 (240)**	**12**	**TC 353**	
TC 354		3083.35		10 (300)	12	TC 354	
TC 355		**2014.6**		**1 (30)**	**16**	**TC 355**	
TC 356		2014.6		11 (330)	16	TC 356	
TC 357		**2418.35**		**4 (120)**	**16**	**TC 357**	
TC 358		2418.35		6 (180)	16	TC 358	
TC 359		**3083.35**		**8 (240)**	**16**	**TC 359**	
TC 360		3083.35		10 (300)	16	TC 360	
TC 361	**standard heater rods**	**2014.6**		**12 (0)**	**40**	**TC 361**	See Note 1 below
TC 362		2014.6		1 (30)	40	TC 362	See Note 1 below
TC 363		**2418.35**		**4 (120)**	**40**	**TC 363**	See Note 1 below
TC 364		2418.35		6 (180)	40	TC 364	See Note 1 below
TC 365		**3083.35**		**8 (240)**	**40**	**TC 365**	

Device Name	TC group	Axial location from duct bottom (mm)	Duct face	Clock position Bottom View	Rod position #	Device Name	Notes
TC 366		3083.35		9 (270)	40	TC 366	
TC 367		**3083.35**		**10 (300)**	**40**	**TC 367**	
TC 368		2014.6		11 (330)	40	TC 368	See Note 1 below
TC 369		**2014.6**		**12 (0)**	**48**	**TC 369**	See Note 1 below
TC 370		2014.6		1 (30)	48	TC 370	See Note 1 below
TC 371		**2418.35**		**4 (120)**	**48**	**TC 371**	See Note 1 below
TC 372		2418.35		6 (180)	48	TC 372	See Note 1 below
TC 373		**3083.35**		**8 (240)**	**48**	**TC 373**	
TC 374		3083.35		9 (270)	48	TC 374	
TC 375		**3083.35**		**10 (300)**	**48**	**TC 375**	
TC 376		2014.6		11 (330)	48	TC 376	See Note 1 below
TC 377	**Non HR - type A**	**2014.6**		**11 (300)**	**42**	**TC 377**	
~~TC 378~~	~~azimuthal heater rods~~	~~2014.6~~	~~-~~	~~12 (0)~~	~~15~~	~~TC 378~~	Data not collected
~~**TC 379**~~	~~-~~	~~**2418.35**~~	~~-~~	~~**1 (30)**~~	~~**15**~~	~~**TC 379**~~	Data not collected
~~TC 380~~	~~-~~	~~2418.35~~	~~-~~	~~3 (90)~~	~~15~~	~~TC 380~~	Data not collected
~~**TC 381**~~	~~-~~	~~**2418.35**~~	~~-~~	~~**5 (150)**~~	~~**15**~~	~~**TC 381**~~	Data not collected
~~TC 382~~	~~-~~	~~2014.6~~	~~-~~	~~6 (180)~~	~~15~~	~~TC 382~~	Data not collected
~~**TC 383**~~	~~-~~	~~**2418.35**~~	~~-~~	~~**7 (210)**~~	~~**15**~~	~~**TC 383**~~	Data not collected
~~TC 384~~	~~-~~	~~2418.35~~	~~-~~	~~9 (270)~~	~~15~~	~~TC 384~~	Data not collected
~~**TC 385**~~	~~-~~	~~**2418.35**~~	~~-~~	~~**11 (330)**~~	~~**15**~~	~~**TC 385**~~	Data not collected

1. The heater rod thermocouples in the heated section of the rods were not reading the water temperature. During the heated tests, these thermocouples read the temperature inside the rod. These values are of

limited use for CFD validation due to uncertainty in a thermal contact resistance of the layers between the heater rod that is necessary for CFD modeling for accurate representation of the experiment.

2. The heater rod (17) was not working during the powered test. Therefore, the thermocouples located on rod 17 read valid water temperature.

Table 10: Changes to Temperature Data Channels for Deformed Duct

Device Name	TC group	Axial location from duct bottom (mm)	Duct face	Clock position	Rod position #	Device Name	Notes
~~TC 17~~	~~outside Duct~~	~~1767.51~~	~~E~~			~~TC 17~~	Not reading
TC 21	**outside Duct**	**2171.36**	**E**			**TC 21**	Reading room Temperature for non-deformed test. Reading normal for deformed test.. OK to use.
TC 59	standard heater rod	2418.35		4 (120)	1	TC 59	See Note 1 below Table 10; Now reading a temperature that is not room temperature
TC 95	**standard heater rod**	**2014.6**		**11 (330)**	**5**	**TC 95**	See Note 1 below Table 10; Was TC96 in non-deformed test
TC 96	standard heater rod	3083.35		10 (300)	5	TC 96	Was TC 95 in non-deformed test
TC 105	**standard heater rod**	**2014.6**		**11 (330)**	**7**	**TC 105**	See Note 1 below Table 10; Was TC112 in non-deformed test
TC 110	standard heater rod	2014.6		12 (0)	7	TC 110	See Note 1 below Table 10; Was TC105 in non-deformed test
TC 112	**standard heater rod**	**3083.35**		**9 (270)**	**7**	**TC 112**	Was TC110 in non-deformed test
~~TC 290~~	~~Non HR Type A~~	~~2014.6~~		~~11 (330)~~	~~42~~	~~TC 290~~	Moved to TC386
~~**TC 309**~~	~~**Non HR Type A**~~	~~**2418.35**~~		~~**4 (120)**~~	~~**50**~~	~~**TC 309**~~	Not reading correctly for Deformed Duct test.
~~TC 336~~	~~Non HR Type A~~	~~3083.35~~		~~10 (300)~~	~~59~~	~~TC 336~~	Not Reading correctly.

Table 10: Changes to Temperature Data Channels for Deformed Duct (continued)

Device Name	TC group	Axial location from duct bottom (mm)	Duct face	Clock position	Rod position #	Device Name	Notes
~~TC 339~~	~~Non HR Type A~~	~~2418.35~~		~~4 (120)~~	~~61~~	~~TC 339~~	Reading too low
TC 363	standard heater rod	2418.35		4 (120)	40	TC 363	See Note 1 below Table 10; Was TC367 in non-deformed test
~~TC 367~~	~~standard heater rod~~	~~3873.75~~		~~10 (300)~~	~~40~~	~~TC 367~~	Was TC363 in non-deformed test. Not Reading
~~TC 377~~	~~Non HR Type A~~	~~2014.6~~		~~11 (330)~~	~~42~~	~~TC 377~~	Not Reading
TC 378	azimuthal heater rod	2014.6		12 (0)	15	TC 378	See Note 1 below Table 10; Included in deformed duct test
~~TC 379~~	~~azimuthal heater rod~~	~~2418.35~~		~~1 (30)~~	~~15~~	~~TC 379~~	Not Reading
~~TC 380~~	~~azimuthal heater rod~~	~~2418.35~~		~~3 (90)~~	~~15~~	~~TC 380~~	Not Reading
~~TC 381~~	~~azimuthal heater rod~~	~~2418.35~~		~~5 (150)~~	~~15~~	~~TC 381~~	Not Reading
TC 382	azimuthal heater rod	2014.6		6 (180)	15	TC 382	See Note 1 below Table 10; Included in deformed duct test
~~TC 383~~	~~azimuthal heater rod~~	~~2418.35~~		~~7 (210)~~	~~15~~	~~TC 383~~	Not Reading
TC 384	~~azimuthal heater rod~~	2418.35		9 (270)	15	TC 384	See Note 1 below Table 10; Included in deformed duct test
~~TC 385~~	~~azimuthal heater rod~~	~~2418.35~~		~~11 (330)~~	~~15~~	~~TC 385~~	Not Reading
TC 386	Non HR Type A	2014.6		11 (330)	42	TC 386	Included in deformed duct test

1. The heater rod thermocouples in the heated section of the rods are not reading the water temperature. During the heated tests, these thermocouples read the temperature inside the rod.

There are additional TC data channels without thermocouples. TC387 through TC400 are not included in this table.

A.3 Measurement Accuracy

The heated tests utilized six types of instruments with the following accuracies and ranges:

1) Differential Pressure (DP) Transmitter of DP Cell:
   - Accuracy: 0.05 mA / (20mA -4mA) * 100 = 0.31 %
   - Range: There are 30 DP cells utilized during testing. The cell range is set appropriate for the planned measurement. The pressure cell ranges typically between 50 in H_20 to 700 in H_20. Some of the cells have reduced accuracy due to out of tolerance calibration.
   - (See Table 7 for more detail)
2) PT Cells
   - Accuracy: 0.05 mA / (20mA -4mA) * 100 = 0.31 %
   - Range: There two pressure cells:
     AI_M_30 is the duct inlet pressure and is ranged up to 200 psi
     AI_M_21 is the duct outlet pressure and is ranged up to 250 psi

3) Two Vortex Flow meters (VM1 and VM62):
   - Accuracy: +/- 1% of full range
   - Range: 30 to 250 gpm.

4) Type K TCs in the system:
   - Accuracy: Type K TC +/- 2 °C
   - Range: 0 to 200 °C

5) Four Silicon-Controlled Rectifiers (SCRs):
   - Accuracy: +/- 1 kW

6) Type K TC in the Rods and the duct:

Accuracy: Type K TC +/- 1.1 °C

A.4 Data Processing

Some of the data obtained from the Data Acquisition System (DAS) is in counts. The DAS produces the values for each channel at each time step. In order to process the data the following steps are taken in each Excel file in:

Some of the data obtained from the Data Acquisition System (DAS) is in counts. The DAS produces the values for each channel at each time step. In order to process the data the following steps are taken in each Excel file:

1) Due to the number of data channels, at random sporadic intervals the DAS wrote incorrect information into the "*csv" file, producing erroneous steps. The erroneous steps produced by the DAS were deleted. This means that some of time steps are larger than the normal 0.75 second step. The purpose of this test

is to produce steady state results at thermal equilibrium. Therefore, deleting a few time steps does not invalidate the data.

2) 200 data steps are copied into the "RAW" worksheet of an Excel file.

3) The average value and standard deviation for each channel is calculated in the Microsoft Excel file.

4) Tests taken without rod power were run with flow for an hour or two before data was taken. This ensures that the loop was at thermal equilibrium. A constant temperature in the test vessel was verified by comparing the TC data in the inlet and exit plenums. Because of the constant temperature a bias for each TC can be calculated as follows:

    a. An average loop temperature is calculated by averaging the two inlet (TC9 and TC10) and the three outlet (TC6, TC7 and TC8) TC channels.

    b. This average is the assumed temperature of all TCs. Each of the TC values is then subtracted from the average value to obtain an individual bias for each thermocouple to be used during the power tests.

5) The TC bias calculated in Step 4b is transferred via copy and paste to the Excel files containing the data taken with power applied to the heater rods. The bias for the power cases was taken from the no power test cases each day.

6) The bias from Step 5 is then added to the average value for each temperature of the power cases.

7) The data is then transferred using formulas in the Microsoft Excel files from the "RAW" worksheet to the "Data" worksheet.

    a. The columns of data are as follows:

Column	Description
A and B	Identify or describe data on the row
C	Average data from the "RAW" file. The TC data includes the temperature bias applied in Step 6)
D	Standard deviation of the data taken.
F before row 43	Calibration Slope
F after row 43	Rod identifier following the convention in Figure 40.
G before row 43	Calibration "y intercept"
G after row 43	Elevation/Location of TC relative to the bottom of the duct.
H before row 43	Raw average data is converted to engineering units
H after row 43	Rod identifier following the convention in Figure 40.
I	Standard deviation in % of raw average value.
J	Identifies engineering units for Column H
K	Average data converted to engineering unit as appropriated based on the calibration slope and intercept.
L	Standard deviation in metric engineering units
M	Identifies the engineering units for columns K and L.

b. The rows of data are as follows:

Identifier	**Rows**	**Description**	**Units for columns C and D**
AI_M_30	4	Upper Plenum Pressure	psia
AI_M_21	5	Lower Plenum Pressure	psia
VM1	6	Volumetric flow from Vortex Meter 1 (before test vessel)	gpm
VM62	7	Volumetric flow from Vortex Meter 2 (after test vessel)	gpm
WM[1-4]_raw	9-11	Power from SCR1 through SCR4	counts
DP[1-30]	13-42	Pressure drop measurements from DP1 through DP30	counts
TC_[1-400]	43-443	TC measurements from TC_1 to TC_400	^{o}C

8) In addition to the above steps each “Data” worksheet contain the following unit conversion values:

Convert gallons to m^3	0.00378541
Convert psia to Pa	6894.76
Convert inH20 to Pa	248.84

9) The volumetric flow rate is converted to mass flow rate in each excel file using the density of water in metric units based on the inlet temperature and assumed at a pressure of 120 psia (based on pressure at the duct inlet).

10) The total electric power value was checked against the total thermal power using a simple heat balance equation:

a. Thermal_power = Mdot * Heat_capacity_water*(Tin-Tout) where:

Mdot:	Mass Flow
Heat_capacity_water:	4170 J/(kg* ^{o}C)
Tin:	The average inlet temperature in the lower plenum (TC_9 and TC_10)
Tout:	the outlet temperature in the pipe connected to the upper plenum (TC_5)

A.5 Pressure Drop Data

Some of the pressure taps in the fuel rod locations did not produce correct results. See Table 7 for the pressure drop data channels that need to be ignored.

Figure 43 compares the non-deformed duct test pressure drop with the simplified Cheng Todreas (Reference [20]) correlation for wire wrapped hexagonal bundle. The turbulent part of the correlation is used because the tested Reynolds numbers are greater than the transition $\mathrm{Re}_T = 10000\left(10^{0.7(P/D-1.0)}\right) = 13395$. The application range of the

correlation is defined in Table 3 of Reference [20] with the uncertainty of the correlation of ±15% for the turbulent region.

Figure 43 compares the predicted values to the non-deformed test. An ideal line with a 10% conservative band was added to the plots.

Some of the data in Figure 43 falls outside of the 10% band, but the figure demonstrates good agreement with the predicted values. The pressure drop data for DP22, DP23 and DP30 are ignored because the data was not accurate (see Table 7).

Table 11 compares the pressure drop data between the non-deformed tests and the deformed duct tests. The following observation can be made:

1) The pressure drop data in the lower non-deformed section of the both duct is only -1.6% to 3.0% different. This difference is within the expected range.
2) The difference in the deformed section is a minimum of -11.4%. This is expected due to increase flow area in the deformed section.

These comparisons show good agreement between the predicted and measured pressure drop for the non-deformed duct. There is also good pressure drop agreement between non-deformed and deform duct tests. Therefore, pressure drop data is acceptable.

The data was further reviewed during the CFD software validation. See Section 6.4.4.3.

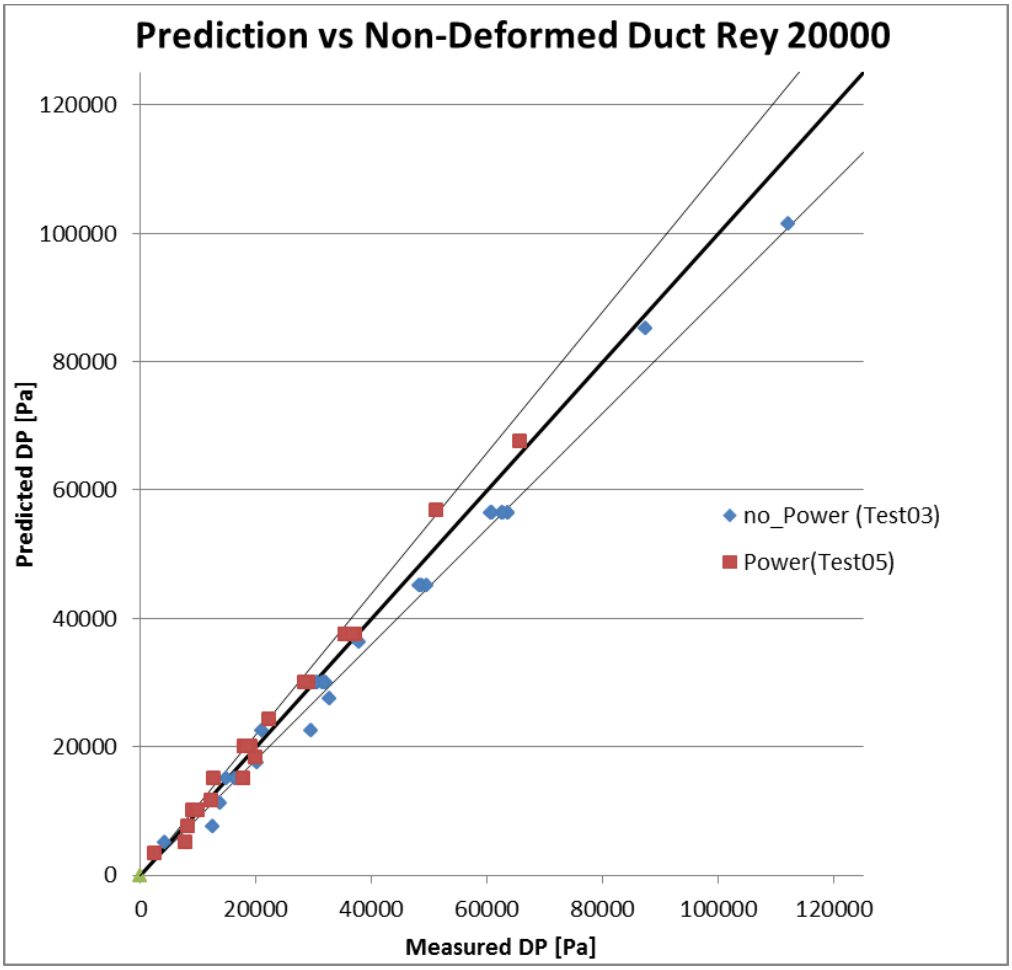


Figure 43: Pressure Drop Comparison Re 20,000 Non-Deformed Duct vs. Predicted

Table 11: Pressure Drop Data Comparison Re 20,000[1]

Cell ID	Tap # High	Tap # Low	Test03 8/23 No Power (Pa)	Test24 10/5 No Power (Pa)	Diff. Test03 to Test24 (%)	Test05 8/23 Power Test (Pa)	Test19 10/5 Power Test (Pa)	Diff. Test05 to Test19 (%)
DP1	1	2	14922	15091	1.1	9103	9382	3.0
DP2	1	5	31490	31709	0.7	19152	19646	2.5
DP3	2	6	29413	29641	0.8	17914	18398	2.6
DP4	6	9	21010	21198	0.9	12775	13124	2.7
DP5	3	4	4083	4018	-1.6	2447	2455	0.3
DP6	3	6	20148	20287	0.7	12248	12568	2.5
DP7	5	6	12410	12410	0.0	7812	7903	1.1
DP8	4	8	32723	32785	0.2	19916	20288	1.8
DP10	11	15	30458	28235	-7.9[2]	17997	16998	-5.9[2]
DP12	9	17	48645	43674	-11.4[2]	28633	26100	-9.7[2]
DP13	10	17	49469	44581	-11.0[2]	29147	26701	-9.2[2]
DP14	10	25	112069	103094	-8.7[2]	65607	61376	-6.9[2]
DP15	11	18	48309	44227	-9.2[2]	28380	26482	-7.2[2]
DP16	18	35	60653	59240	-2.4	35481	35279	-0.6
DP18	16	37	63489	60826	-4.4	37139	36169	-2.7
DP19	23	38	13723	13553	-1.3	8287	8251	-0.4
DP20	27	29	32127	32455	1.0	18959	19497	2.8
DP21	23	27	31954	31867	-0.3	18530	18820	1.5
DP24	32	25	62504	58023	-7.7[2]	36373	34323	-6.0[2]
DP26	19	29	87459	87497	0.0	51314	52287	1.9
DP27	31	35	60715	59743	-1.6	35480	35493	0.0

1. There are several pressure drop measurements not included in the table above for two reasons:
   a. DP9 and DP11 measure different tap pairs for the non-deformed (Test02 and Test 05).
   b. DP17, DP22, DP23, DP25, DP28, DP29 and DP30 did not produce correct values due to issues encountered with the pressure taps located in the test rods.

2. DP10, DP12, DP13, DP14, DP15 and DP24 are measured in the deformed section of the duct causing a difference in pressure drop.

A.6 Temperature Data

The objective of the test was to measure the water temperature for comparison to CFD. The heater rods had internally embedded TCs, and therefore show higher values above the water temperature. Since the purpose of this testing was to measure the water temperature, the TC measurements in the heated section of the rods will be ignored.

As explained in Section A.4, the isothermal tests were run for several hours to ensure a constant loop temperature was achieved. For the powered tests, the heaters were activated and ran for as long as it took to reach thermal equilibrium. Several TCs were monitored until they reached a constant temperature over time. Thermal equilibrium is demonstrated by examining the small standard deviation for the valid TC channels during the test state tests.

Figure 44 is the TC data that measured water temperature above the heated section for the non-deformed duct test with power (Test 05). This TC data demonstrates a temperature gradient from the center of the test section to the duct wall with the peak temperature in the center.

Figure 44 is the important plot or review of the temperature data. Additional reviews of the remaining water temperature data were performed and show reasonable agreement with expected results. The additional reviews were not included in this report. The data files in Section A.7 contain all TC channels for each test.

The data was further reviewed during the CFD software validation. See Section 6.4.4.3

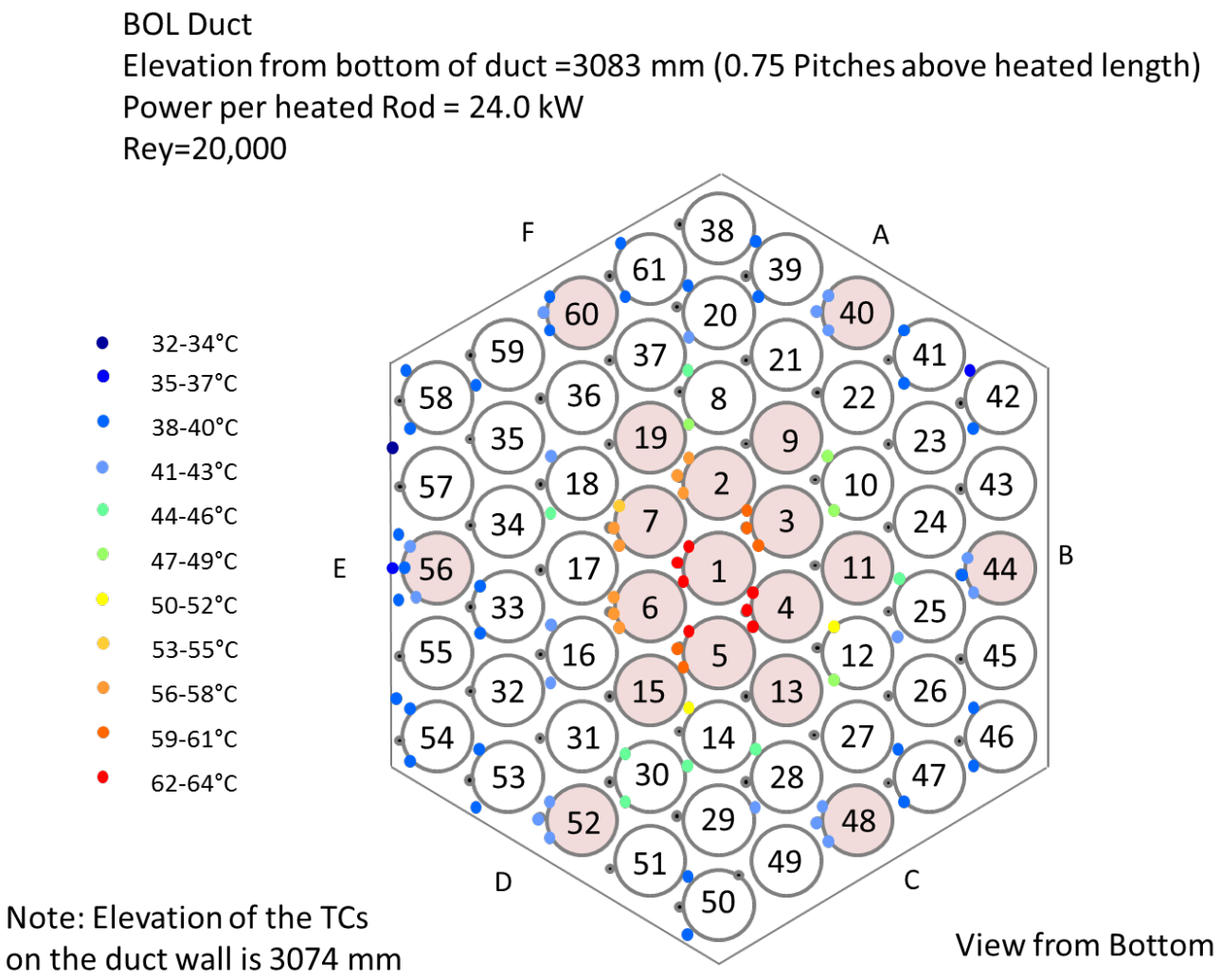


Figure 44: Test05 - Temperature Distribution – Elevation=3074mm, Re=20,000, Power/Pin=24kW

A.7 Data Files

The following files are contained in the "DATA.ZIP" file associated with this report:

Size (Bytes)	Date	Time	Name
468501	Dec 12 2016	16:22:31	Test03_re20000_nopower_conversion_08232016.xlsx
747974	Dec 19 2016	11:47:36	Test05_re20000_power_conversion_08232016.xls
549301	Dec 19 2016	11:51:06	Test19_RE20000_power_10052016_convert.xlsx
540982	Dec 12 2016	16:33:16	Test24_RE20000_nopower_after_test_10052016_convert.xlsx

TERRAPOWER PROJECT DOCUMENTS

APPENDIX B: TWRP-31-TSPEC-0011, AFAFC AREVA HEATED BUNDLE EXPERIMENT TEST SPECIFICATION

Thermal Hydraulic CFD Simulations and Experimental Investigation of Deformed Fuel Assemblies

U.S. Department of Energy
DE-NE0008321
DUNS # 789479578

Document Title:	AFAFC AREVA Heated Bundle Experiment Test Specification
Document Number:	TWRP-31-TSPEC-0011
Prepared By:	TerraPower
Date:	1/4/16
Revision:	2

Name	Title / Company	Signatory Role	Signature	Date
Brian Jackson	Technical Rep. / TerraPower	Preparer		1/7/2016
Tom Galioto	Project Manager / AREVA Fuels	Approver		1.16.16
Ella Merzari	Technical Rep. / Argonne National Lab	Approver		04/21/16
Rodolfo Vaghetto	Technical Rep. / Texas A&M University	Recipient		04/20/16
Anthony Chang	Project Manager/ AFS	Recipient		3/21/16
Brian Mays	Principal Investigator / AFS	Recipient	See Below	–

U.S. Department of Energy
DE-NE0008321
DUNS # 789479578

Document Title:	AFAFC AREVA Heated Bundle Experiment Test Specification
Document Number:	TWRP-31-TSPEC-0011
Prepared By:	TerraPower
Date:	1/4/16
Revision:	2

Name	Title / Company	Signatory Role	Signature	Date
Brian Jackson	Technical Rep. / TerraPower	Preparer		1/4/2016
Tom Galioto	Project Manager / AREVA Fuels	Approver		
Elia Merzari	Technical Rep. / Argonne National Lab	Approver		
Rodolfo Vaghetto	Technical Rep. / Texas A&M University	Recipient		
Anthony Chang	Project Manager/ AFS	Recipient		
Brian Mays	Principal Investigator / AFS	Recipient		1/14/2016

Record of Revisions			Revision: 2
Item #	**Description of Change**	**Effected Pages / Sections**	**Change Initiator**
1	Update inner flat-to-flat dimension for consistency with TAMU bundle	Sec. 3, 4.1, 6	Brian Jackson



Uncontrolled When Printed

TEST SPECIFICATION

Document Number:	TWRP-31-TSPEC-0011	**Revision:**	2
Document Title:	AFAFC AREVA Heated Bundle Experiment Test Specification	**Approval Date** *(Final Signature Date)*:	12/21/2015
Issuing Organization:	Core Design	**Effective Date** *(for Procedures Only)*:	
		Pages:	Page 0 of 34

Approval

Title	Name	Signature	Date
Originator, Thermal Hydraulics Test and Analysis Engineer	Brian Jackson	Electronically approved by Brian Jackson	12/15/2015
Reviewer, Reactor Systems Thermal and Fluids Analyst Consultant	Nate Salpeter	Electronically approved by Nate Salpeter	12/15/2015
Reviewer, Manager, Thermal Hydraulic Test & Analysis	Mike Steer	Electronically approved by Mike Steer	12/17/2015
Approver, Manager, Design Qualification	Rob Corbin	Electronically approved by Rob Corbin	12/21/2015

Document Safety Classification per TWRP-NS-PROC-0002 ('N/A' for Procedures / policies / manuals / guides): Safety-Related ☐ Non-Safety Related ☐ Augmented Quality ☒ N/A ☐

QA Criterion (Select 'N/A' for documents other than procedures/policies/manuals/guides): N/A

Revision History

Revision No.	Effective Date	Affected Section(s)	Description of Change(s)
0	6/12/2015		Initial Release
1	10/9/2015	Sec. 3	Update to geometries and instrumentation following design review meetings.
2	12/21/2015	Sec. 3, 4.1, 6	Update to inner flat to flat dimension to keep consistency with TAMU bundle design.

TABLE OF CONTENTS

1 PURPOSE 4
2 TEST SCOPE 4
2.1 Functional Requirements 4
3 EQUIPMENT HARDWARE 5
3.1 TerraPower Procured Components 5
3.1.1 Heater Rods 5
3.1.2 Non-heated Tubes 6
3.1.3 Nominal Duct 7
3.1.4 Deformed Duct 7
3.2 AREVA Richland Equipment 9
3.2.1 Vessel 9
3.2.2 Tie plate interface detail 9
3.2.3 Electrical System Detail 9
3.2.4 Measurement and Data Acquisition System Detail 9
3.3 Axial Positioning of Heaters in Duct and Vessel 10
4 TEST CONDITIONS 11
4.1 Loop Flow Conditions 11
4.2 Test Measurement Region 12
4.3 Heater Power Conditions 12
5 DATA REQUIRED 13
5.1 Instrumentation Location Coordinate Basis 14
5.2 Loop Characterization Measurements 15
5.3 Pressure Measurements 18
5.3.1 Duct Wall Pressure Measurements 18
5.3.2 Internal Bundle Pressure Measurements 19
5.4 Temperature Measurements 20
5.4.1 Heater Rod Thermocouple Specifications 20
5.4.2 Non-heated Tubes Thermocouple Specification 21
5.4.3 Pressure Tube Axial Thermocouples 21
5.4.4 Duct Wall Subchannel Thermocouples 22
6 TEST PREDICTIONS 22
7 REPORTING 23
8 REFERENCES 23
9 APPENDIX A 24
10 APPENDIX B 25
11 APPENDIX C 30

LIST OF TABLES

Table 1. Heater Rod Specification 5
Table 2. Heater Normalized Axial Heat Flux 6
Table 3. Unheated Rod Specification 7
Table 4. Duct Specification 7
Table 5. Dilated Duct Values 8

Table 6. Tie Plate Detail 9
Table 7. Thermocouple Quantity..... 10
Table 8. Pressure Tap Count..... 10
Table 9. Axial Positioning..... 10
Table 10. Calculated Loop Flowrate Requirements..... 11
Table 11. Heater Power per Rod 12
Table 12. Outer Duct Thermocouple Locations 16
Table 13. Bundle Wall Pressure Tap Locations..... 19
Table 14. Non-heated Tube Tap Hole Position..... 20
Table 15. Standard Heater Instrumentation Configuration..... 20
Table 16. Axial Heater Instrumentation Configuration 20
Table 17. Azimuthal Heater Instrumentation Configuration 21
Table 18. Non-heated Tube Thermocouple configuration..... 21
Table 19. Duct Internal Face E Subchannel Thermocouple Detail 22
Table 20. Predicted Pressure Drop..... 22
Table 21. CFD Maximum Fluid and Heater Wall Temperatures 23

LIST OF FIGURES

Figure 1. Heater Normalized Axial Heat Flux..... 6
Figure 2. Deformed Duct Definition..... 8
Figure 3. Heater Rod Configuration..... 13
Figure 4. Overall Heaters and Tube Instrumentation Configuration..... 14
Figure 5. Duct Position Basis for Instrumentation from Duct Bottom 15
Figure 6. Clocking Direction from Heater Bottom..... 15
Figure 7. Outer Duct Thermocouple Positions..... 17
Figure 8. Duct Entrance Thermocouple Positions..... 18
Figure 9. Duct Internal Wall Subchannel Thermocouples..... 22
Figure 10. (9/12) Pitches into Heated Length 25
Figure 11. (1 + 10/12) Pitches into Heated Length 26
Figure 12. (2 + 10/12) Pitches into Heated Length 26
Figure 13. 3 Pitches into Heated Length..... 27
Figure 14. (3 + 2/12) Pitches into Heated Length 27
Figure 15. (4 + 2/12) Pitches into Heated Length 28
Figure 16. (4+ 5/12) Pitches into Heated Length 28
Figure 17. (5 + 3/12) Pitches into Heated Length 29
Figure 18. (6 + 4/12) Pitches into Heated Length 29
Figure 19. (6 + 9/12) Pitches into Heated Length 30

1 PURPOSE

The purpose of this test is to investigate and measure thermal distribution and pressure drop behavior for two configurations (non-deformed and deformed-duct) of a heated 61-pin, hexagonally packed fast reactor test assembly in the fully turbulent regime for purposes of generating computational fluid dynamics (CFD) validation grade data. To support verification and validation (V&V) of current CFD methods, high quality flow and thermal mixing characterization of flows in the same flow regime as those encountered in wire wrapped fuel assemblies prototypic of liquid metal fast reactors is needed. This test will provide valuable distributed thermocouple temperature and pressure drop measurements for this purpose.

2 TEST SCOPE

Steady state thermal-hydraulic tests will be run with water flowing through a 61 pin hexagonal bundle at Reynolds numbers in the fully turbulent regime as specified in this document. The bundle will be partially heated: only some of the 61 pins will be electric heater rods to provide heating. Flow and heater conditions are described in further detail in the Test Conditions Section. Measurements will include thermocouple measurements at the unheated tube wall and fluid interface, embedded inside heaters, and on the internal duct wall. Pressure drop measurements will be taken across different lengths of pin bundle to capture entrance effects, planar pressure gradient due to bulk flow swirl, and fully developed conditions. Measurement detail is included in the Data Required section. In addition to bundle pressure drop and temperature measurements, as-built geometry and inlet condition measurements will be included for CFD boundary and initial conditions. Final design and fabrication of heaters, non-heated tubes and the duct may necessitate modifications to final instrumentation positions and quantities. Any modifications will be updated as needed, and recorded in the Test Report.

2.1 Functional Requirements

The following functional requirements of the hydraulic flow loop shall apply:

1. Meet flowrate and pressure drop requirements as outlined in the Test Conditions and Test Predictions sections
2. Be flowrate controlled
3. Have temperature control to ensure steady inlet temperature during testing
4. Be a pressurized system
5. Measure flowrate in the test loop
6. Measure pressure and temperature upstream of the test section
7. Measure pressure and temperature downstream of the test section
8. Contain a mechanism to ensure the test section is protected from damage due to over-pressurization (either from internal or annulus pressure)
9. Have interlocks to prevent heater rod damage including protection against depressurization, temperature excursion and loss of flow
10. Contain a data acquisition system with appropriate QA qualification such that reliable and repeatable measurements are ensured and can meet measurements as outlined in this document.
11. Have total heater power capacity of 675 kW.
12. Measure heat input for each power bank.

3 EQUIPMENT HARDWARE

The heated bundle experiments will be conducted at AREVA Richland in the Fuel Cooling Test Facility (FCTF) flow loop. TerraPower will provide the wire wrapped heater rods, unheated wire wrapped tubes (with and without instrumentation), and the hex ducts. AREVA will assemble the bundle, provide the necessary interfacing hardware, and install the test section in the loop. This section details the equipment and interfacing requirements.

3.1 TerraPower Procured Components

TerraPower will procure and provide wire wrapped heater rods, wire wrapped unheated tubes, and the two hex ducts (non-deformed and deformed) for the 61-pin bundle.

3.1.1 Heater Rods

19 heater rods will be assembled in the 61-pin bundle. In addition 3 extra heater rods will be procured to act as replacements as needed. TerraPower will perform or contract to wire wrap the heater rods. The rods will be designed to the following specifications:

Table 1. Heater Rod Specification

Parameter	Value	units	Basis
Heater Rod Quantity	22		19 heater rods with assumed 16% failure rate
Heater Clad OD	9.5	mm	Standard fabrication heater rod size
Total heater length (bottom of cladding to top of threaded endcap)	5080 (200)	mm (in)	Required for installation into loop
Heated Length	1710	mm	6 wire pitch lengths
Flux Profile	Cosine with 1.4 peak/ave		Similar to reactor shapes and typical of heater rods
Wire Wrap OD	0.068 (1.73, 15 ½)	in (mm, gauge)	To maintain similarity with TAMU P/D
Wire Wrap Pitch Height	285	mm	H/D = 30
Wire wrap direction	Clockwise		Clockwise in axial direction of flow
Per heater max power	35.0	kW	Per rod power will be in the range of 15.0 – 35.0 kW and is based on CFD simulations and Reynolds number dependent

The total heater length is 5080 mm including a heated length of 1710 mm. The heater rods will be instrumented with thermocouples. This instrumentation will be performed as part of the heater procurement. These thermocouples measure the internal clad surface temperature. A single ended design will be used for electrical and instrumentation leads coming out of the bottom of the heater rod.

The normalized heater rod axial heat flux profile is shown below and in tabular form. The extended unheated lengths below and above the heated length are cut off in the graph and Table 2. Changes to this curve may be applied by the heater vendor and approved by TerraPower as needed for fabrication purposes. Any changes will be documented.

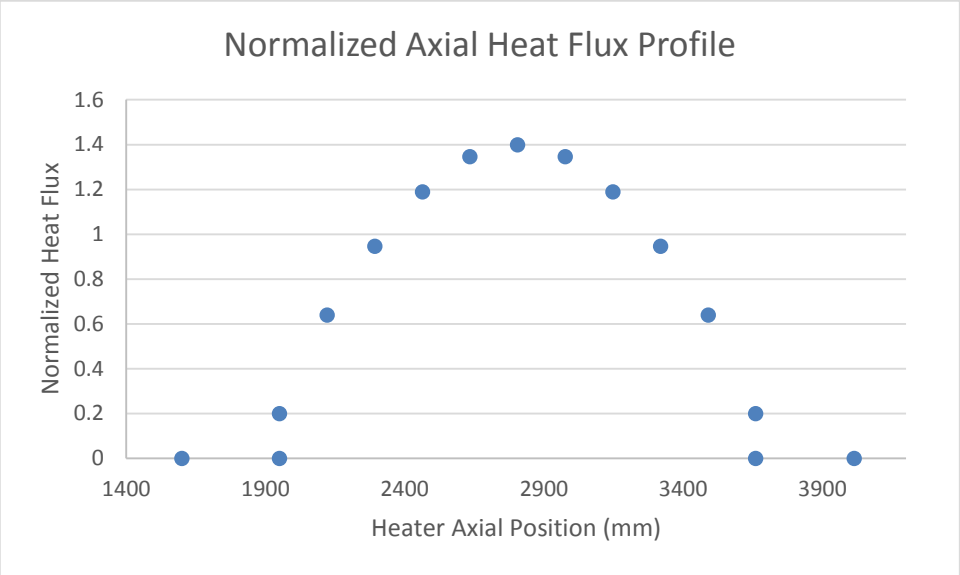


Figure 1. Heater Normalized Axial Heat Flux

Table 2. Heater Normalized Axial Heat Flux

Axial Position (mm)	Normalized Heat Flux
0 – 1950	0
1950	0.2
2121	0.64
2292	0.95
2463	1.19
2634	1.35
2805	1.40
2976	1.35
3147	1.19
3318	0.95
3489	0.64
3660	0.2
3660 - 5080	0

The wire wrap will not pass through the lower and upper tie plates and will be terminated before the end of the rod.

3.1.2 Non-heated Tubes

42 of the 61 pins will be non-heated wire wrapped tubes. The 42 non-heated tubes can be classified into three categories: thermocouple instrumented tubes, pressure measuring tubes and blanks without any instrumentation. These will be provided to AREVA with their wire wrapping complete. Similar to the heated rods, the wire wrapping will terminate inside the vessel. Stock tubing will be used for these non-heated tubes. This is slightly larger than the nominal heater rod OD size, but is within the tolerance of the heater rod OD specification as provided by the vendor.

Table 3. Unheated Rod Specification

Parameter	Value	Units
Unheated, internal clad TC instrumented tubes	22*	
Unheated, external clad TC instrumented Tubes	16*	
Unheated, tapped tubes for pressure measurements	8	
Unheated Clad OD	9.525 (0.375)	mm (in)
Total unheated rod length	5080 (200)	mm (in)
Wire Wrap OD	0.068 (1.73, 15 ½)	in (mm, gauge)
Wire Wrap pitch Height	285	mm

* A total of 4 extras will be fabricated.

3.1.3 Nominal Duct

Heated flow tests will be conducted for two bundle designs. The first is representative of a beginning of life bundle that has straight pins (heated and unheated rods) and a straight hex duct. The second is representative of an early in life condition: straight pins, but with a dilated duct.

The ducts will be a clam-shell design and include flanges to connect to the existing loop. A lower flange will connect to existing bellows, and the upper flange will connect to the vessel. Final design of the interfacing method and design will be approved through release of engineering drawings. However, the following table gives the internal flow area of the duct, which will be the geometry directly used for the pre-test CFD simulations. The duct length corresponds to the distance from upper flange to the lower flange that connects to the bellows. The duct flat to flat corresponds to a tightly packed bundle using the non-heated tube OD (9.525 mm) with an additional 0.77% length for the wall gap. The final flat to flat dimension and wall thickness will be machined to provide flat to flat scaled consistency with the flow visualization bundle to be operated at Texas A&M University. Provided here are the initial design of these parameters.

Table 4. Duct Specification

Parameter	Value	Units
Duct Length	4229.1 (166.5)	mm (in)
Internal Duct Flat to flat	91.64	mm
Duct Corner Radius of Curvature	6.84	mm
Approximate duct wall thickness	18.7 (0.74)	mm (in)
Duct Material	Bronze	
Clam shell design detail	TBD	

3.1.4 Deformed Duct

The second test section to be used for these heated bundle tests will use a deformed duct. Final design of this duct is ongoing, but the dilation will be a smooth bulging of the hex duct in both the axial direction, and azimuthal direction between hex corners. The dilation only occurs for the region corresponding to the heated length. The top and the bottom of the duct, where attachments to the vessel through flanges are located will have the same geometry as the non-

deformed duct. Peak deformation of 1.08 mm occurs at the mid-height of the heated length at the midpoint between duct face corners. This peak deformation value corresponds to the outward translation length of the inner duct face wall at this location. Functional forms of this deformation is given in Table 5 and shown in Figure 2. Final CAD geometry will be provided in the Benchmark Specification.

Table 5. Dilated Duct Values

Parameter	Value	units
Dilation of inner duct surface in functional form *	$y = \left[\frac{D_{max}}{2} * cos\left(\frac{x * \pi}{s/2}\right) + \frac{D_{max}}{2}\right] * sin\left(\frac{(z - 1150.2) * \pi}{z_{tot}}\right)$	
x, y, z coordinate directions (with respect to dilation; unique for each duct face)	See image below	
D_{max}	1.064	mm
s (duct side length)	52.91	mm
Total dilation length (z_{tot})	1710	mm
Beginning of Dilation (Axial Height from duct bottom)	1150.2	mm
End of Dilation (Axial Height from duct bottom)	2860.2	mm

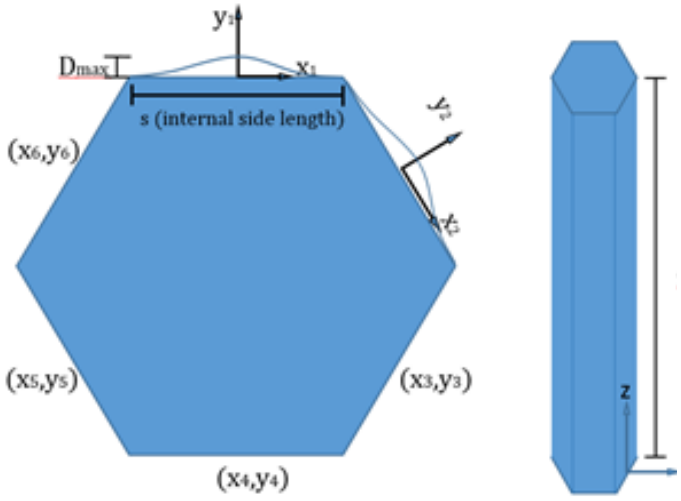


Figure 2. Deformed Duct Definition

3.2 AREVA Richland Equipment

The heated flow experiments will be conducted in the FCTF loop at AREVA Richland. AREVA Fuels will refurbish the facility to meet the test requirements (e.g. flowrates, pressures, powers, DAS), design and fabricate the tie plates for interfacing the test assembly components to the loop, and assemble and install the wire wrapped rods and duct in the flow loop.

3.2.1 Vessel

The duct of the test bundle is installed inside the vessel of the flow loop. A thermal shield and/or insulation will minimize heat loss from the heated duct to the environment. Flanges with appropriate seals will be used to attach the duct to the vessel. In addition, a bellows at the bottom allows for thermal growth in the axial direction.

3.2.2 Tie plate interface detail

The tie plates are the physical interface for the wire wrapped rods. The upper-tie-plate interfaces with the rods and serves as the ground. The rods will be attached and will be hanging. The lower tie plate, or seal gland, allows the heated (and non-heated) rods to exit the vessel maintaining a proper seal. It includes o-rings at each penetration location to guarantee a tight seal and to allow for thermal expansion in the axial direction.

The configuration of the tie plate holes comes from the bundle pitch to diameter ratio (P/D) and rod diameter specifications. It should be noted that the lower end of the heaters and non-heated tubes will be tapered; therefore, the diameter going through the seal gland is smaller than the nominal diameter. The rods will be assembled in a tightly packed configuration where the pitch equals the sum of the tube diameter and wire diameter. The tube diameter corresponds to the non-heated tube diameter (9.525 mm). The additional slop in the bundle is maintained at the wall subchannels. The heater and tube diameter at the upper tie plate is also smaller than the nominal and is threaded. Tie plate interface detail is given below. Further detail of upper and lower connections is provided in Reference 1.

Table 6. Tie Plate Detail

Parameter	Value	Units
Hole configuration	Hexagonal	
Pin packing	Tightly packed	
Pin diameter at seal gland	7.6 (0.30)	mm (in)
Pin diameter at upper tie plate	4.8	mm
Wire diameter	Table 1	mm
P/D	1.18	
Pitch	11.25	mm

3.2.3 Electrical System Detail

The power supply, in its current configuration provides in excess of 675kW of power. The configuration uses 4 SCRs at 650 A each at 277 V max.

3.2.4 Measurement and Data Acquisition System Detail

The measurement and data acquisition system (DAS) will follow the Augmented Quality as described in Appendix C. Measurements will be taken for loop control, test section and component protection, and to acquire CFD validation quality data. Measurements will include

pressure, temperature and flowrate measurements. The following outlines the experiment instrumentation.

Table 7. Thermocouple Quantity

Type	Type Qnty	Per/ Rod	Total
Heater Rod (Standard)	13	8	104
Heater Rod (Axial)	2	9	18
Heater Rod (Azimuthal)	4	8	32
Unheated Tube	22	6	132
Internal Pressure Tube Axial Multipoint Thermocouple	4	6	24
Internal Duct Wall			24
Outer Duct Wall (System TCs)			12
Duct Entrance (System TCs)			3
Plenum (System TCs)			6
Total			355

Pressure taps will be used to measure pressure drop at different axial heights within the pin bundle. These pressure taps will primarily be on the duct wall measuring exterior subchannels. Measurements will be taken to quantify pin pressure drop, thermal-hydraulic flow development and entrance effects, and azimuthal pressure gradients. Further detail of measurement location is presented in the Data Required section (Section 5). The following table provides the pressure tap count. There may be limitations in number of total available pressure transducers, therefore priority of pressure drop measurements are given in a later section.

Table 8. Pressure Tap Count

Type	Type Qnty
Duct Wall Pressure Taps	30
Internal Tube Pressure Taps	8
System Pressure Taps	2
Total	40

Further detail, including data formatting and as needed updates, will be provided in the Benchmark Specification.

3.3 Axial Positioning of Heaters in Duct and Vessel

The heaters and unheated tube axial positioning is interdependent with the duct, vessel, wire wrap and thermocouple locations. The following table gives axial positions of components. Basis for this positioning is from the duct and vessel interface drawings in Appendix A.

Table 9. Axial Positioning

Parameter	Position (in)	Position (mm)
Bottom of Heater Clad	0.0	0.0
Lower Seal Gland Bottom	8.67	220.3

Lower wire wrap connection	20.7	525.0
Bottom Duct (connects to bottom of bellows)	31.49	799.8
Top of Bellows length/ Lower Mt. Flg bottom	37.11	942.6
Top of Mt. Flg.	37.74	958.5
End of Entrance region/ beginning of CFD Study Measurement Region/ Beginning of heated length with wire position at 12 oclock	76.77	1950.0
Top of Heated length	144.09	3660.0
End of Measurement Region	166.54	4230.0
Upper wire wrap connection	197.39	5013.8
Duct Top/ Upper MT Flange Bottom	198.00	5028.9
Upper Mt Flange Top/ Upper Tie plate Bottom	199.00	5054.3
Upper Tie Plate Top	199.80	5074.6
Threaded end top/ Top of Heater Rods	200.0	5080.0

4 TEST CONDITIONS

4.1 Loop Flow Conditions

Reynolds numbers to be tested are 15,000, 20,000 and 25,000 based on cold geometries of the non-deformed bundle and water properties at the inlet temperature. Tests will be run at the corresponding flowrates for both the non-deformed geometry, and the dilated duct geometry. Measurements for flow and temperature shall be examined to provide assurance that data obtained is not influenced by some unknown hydraulic phenomena within the fuel assembly and that steady state conditions are reached before experiment measurements are taken. Additionally, AREVA shall perform replicate tests to ensure repeatability. The following table provides the loop flow requirements for the corresponding Reynolds numbers.

Table 10. Calculated Loop Flowrate Requirements

Parameter	**Value**	**Units**
Water Inlet Temperature	90*	F
System Pressure	150	psia
Heater and Tube Diameter	Table 1	mm
Wire Diameter	Table 1	mm
Duct Flat to flat and corner curvature	Table 4	mm
Re=15,000 loop flowrate	112.1	gpm
Re=20,000 loop flowrate	149.5	gpm
Re=25,000 loop flowrate	186.9	gpm

* Preliminary value: will use lowest controllable temperature setting and update flowrates to maintain desired Reynolds numbers.

4.2 Test Measurement Region

The length of the duct is approximately 15 wire pitch lengths. This long length is useful to ensure fully developed flow before measurements are taken. The wire wrapping starts in the lower plenum approximately 1 wire pitch length below the entrance into the duct. Following entrance into the duct is approximately 4 wire pitch lengths of entrance region to allow the flow to develop. After the entrance region is the measurement region. The beginning of this region coincides with the beginning of the heated length and at this height the wire wrap is at the 12 o'clock position. The measurement region will be the next 8 wire pitch lengths, of which the heated length is the first 6. Following this measurement region will be an additional approximate 2.8 wire pitch lengths to the top of the duct.

4.3 Heater Power Conditions

Each of the 3 Reynolds numbers to be tested will have a corresponding heater power. The heated length section will begin right at the end of the entrance region: approximately 4 wire pitch lengths into the duct. The heated length will be 6 wire pitch lengths. The specific heater powers to be used are flow rate appropriate to cause sufficient fluid thermal gradients for measurement of CFD V&V quality data, while ensuring against boiling and overheating. The Test Plan will describe the methodology to be employed for heater power ramping and flow rate changes to ensure heater rod protection. In addition to a flat radial heat profile, radial peaking is possible with the use of different power banks. If the FCTF is limited on cooling capability at the highest flowrate, this test may be adjusted, either with a lower power or flowrate. Final specification of the heater powers to be tested will be defined in the Benchmark Specification. Current approximate, per-rod powers are presented in the Table 11. These will be adjusted as needed following further CFD calculations.

Table 11. Heater Power per Rod

Parameter	Value	Units
Re=15,000 Run per Rod Power	18.0	kW
Re=20,000 Run per Rod Power	24.0	kW
Re=25,000 Run per Rod power	30.0	kW

The configuration of the 19 heater rods in the 61 pin bundle are shown below. Heaters are shown in red. This configuration was chosen over a center 19 heater configuration because this creates additional thermal gradients near the corner sub-channels. This configuration was chosen over a fully distributed heater rod configuration because larger and unique gradients are created. The numbers in the heaters correspond to power bank. The power banks were for an initial design for the power distribution system. Final heater rod power configuration will be determined as part of the facility shakedown, and be chosen to provide flexibility for different power profiles.

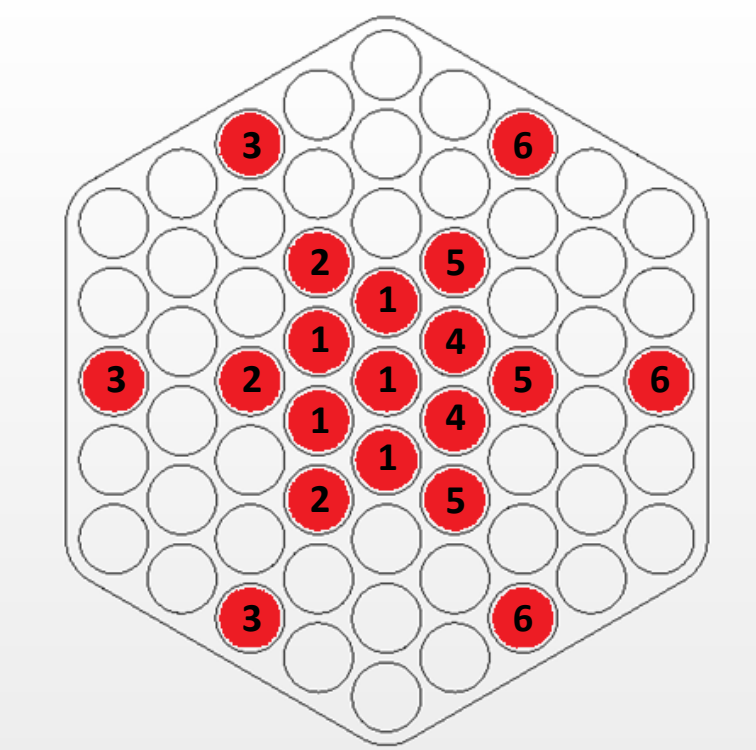
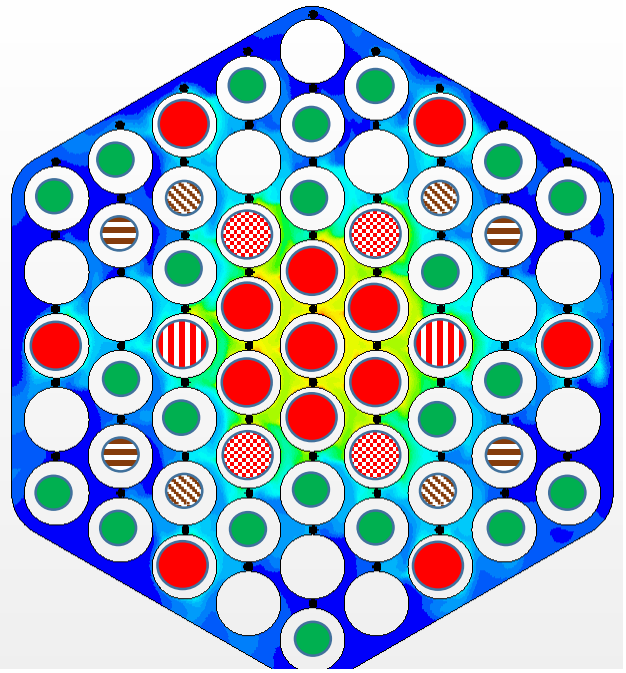


Figure 3. Heater Rod Configuration

5 DATA REQUIRED

For V&V of CFD, both the test section measurements, as well as loop and operational condition setpoint measurements are required. The following sections provide the measurement details in type, quantity and location to be used for these heated bundle tests. The final as-built specifications, due to design and fabrication limitations may necessitate adjustments to these specifications. For validation, point temperatures and pressure drops will be used. As presented in Table 7, heater rods and non-heated tubes will be instrumented with thermocouples, and with pressure taps for temperature and pressure

measurements. The image below shows the overall measurement configuration for the heaters and non-heated tubes. Further detail is provided in sections below.



Key:
Red (Solid): Standard heater config
Red (Checkered): Azimuthal heater config
Red (Striped): Axial heater config
Green: TC instrumented non-heated tube
Brown (Striped): Tapped for P at height A
Brown (Diagonal): Tapped for P at height B

Figure 4. Overall Heaters and Tube Instrumentation Configuration

5.1 Instrumentation Location Coordinate Basis

Each measurement is given in terms of an axial position, and position in the given axial plane. The axial position uses one of two references. The first is the bottom of the clad, and the second is the bottom of the duct. Heater and non-heated tube thermocouples use the clad bottom as the axial basis because these instruments are installed during fabrication of these heaters and non-heated tubes. Duct face pressure taps and thermocouples are given in terms of the bottom of the duct because these are installed in the duct fabrication process. Where useful, axial values from both references are presented. Axial heights are also often referenced with respect to the heated region in terms of wire pitch length.

Position in plane is given both in terms of component position (i.e. pin location, duct face) and azimuthal location in the component. Heater rod and non-heated tube thermocouples are specified in terms of a clocking position (1-12). The clocking direction is from the perspective from the bottom of the heater, looking up, in the direction of axial flow. The duct walls are lettered in a clocking direction as well; also from the bottom of the duct looking upward. Figure 5 and Figure 6 show this. The relationship between axial pin and duct heights is established by the wire wrap. The beginning of the wire wrap is at the 12 clock position.

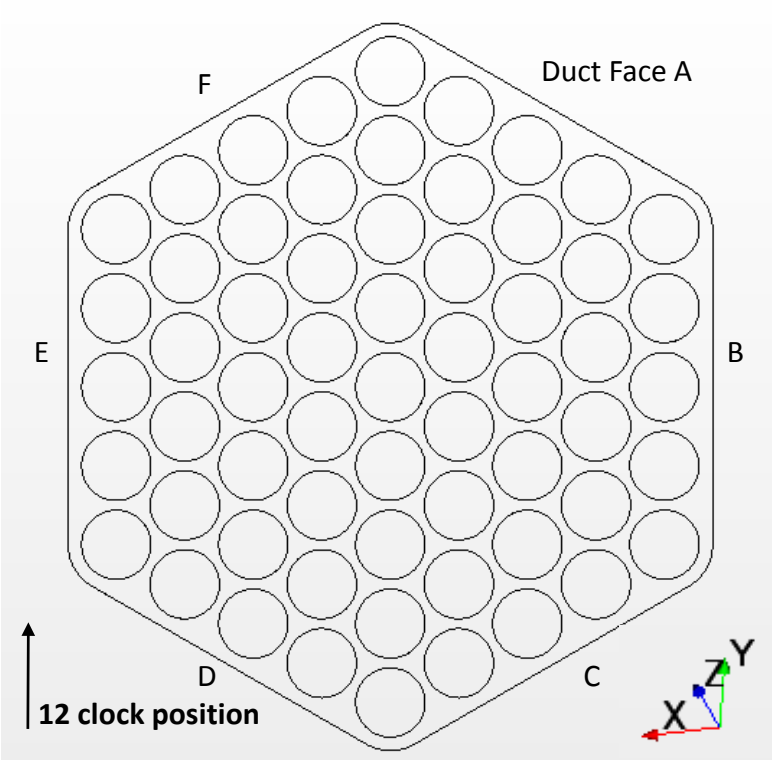


Figure 5. Duct Position Basis for Instrumentation from Duct Bottom

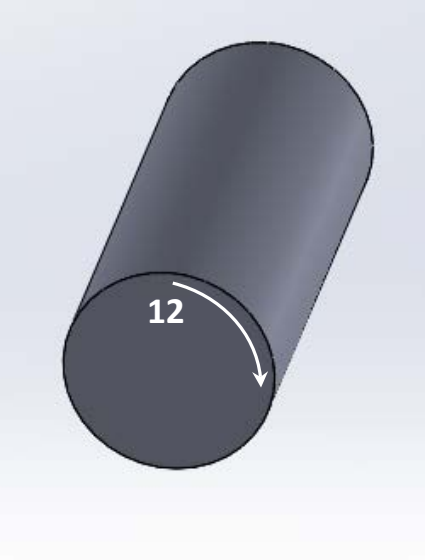


Figure 6. Clocking Direction from Heater Bottom

5.2 Loop Characterization Measurements

Loop and operational conditions are needed to be used as initial and boundary conditions in the CFD simulations. Therefore characterization of the inlet flowrate, the geometry, and test condition measurements must be made.

As built measurements of the test assembly are needed. Due to the complexity of the pin assembly in the duct, these as-built measurements can be taken of the unassembled components with verification

of installation configuration. Measurements should include heater and unheated tube diameter profiles, lengths, concentricity, and straightness; wire wrap diameters, and pitch heights; duct measurements of lengths, flat to flats, and duct face internal straightness; and tie plate rod spacing and configuration (P/D).

21 thermocouples and 2 pressure measurements are allotted for system measurements. The pressure measurements correspond to inlet and outlet pressures with their specific location to be determined. As stated above, due to potential pressure transducer limitations, pressure taps are ranked by priority. For loop control, these system pressure taps are of the highest priority group. The thermocouples will be used for multiple (3) inlet plenum and (3) outlet plenum measurements, (3) fluid measurements near the duct entrance, and 12 thermocouples to be used to measure the outer duct wall temperature to ensure steady state conditions. Figure 7 and Table 12 describe the preliminary positioning of these outer duct wall thermocouples. Current CFD simulations are underway looking at optimal placement for these outer duct thermocouples, as such these positions may be updated in the future, and recorded during the as-built documentation accordingly.

Table 12. Outer Duct Thermocouple Locations

Height: From Duct Entrance (mm)	**Height: From heater rod bottom (mm)**	**Height into heated length by pitch (P)**	**Number of TCs**	**Positions at all heights**
1720.2	2520.0	2P	3	Centers of duct faces A and E. Between faces C and D.
2005.2	2805.0	3P	3	
2409.0	3208.8	(4 + 5/12)P	3	
3074.0	3873.8	(6 + 9/12)P	3	
Total Outer Duct Thermocouples			12	

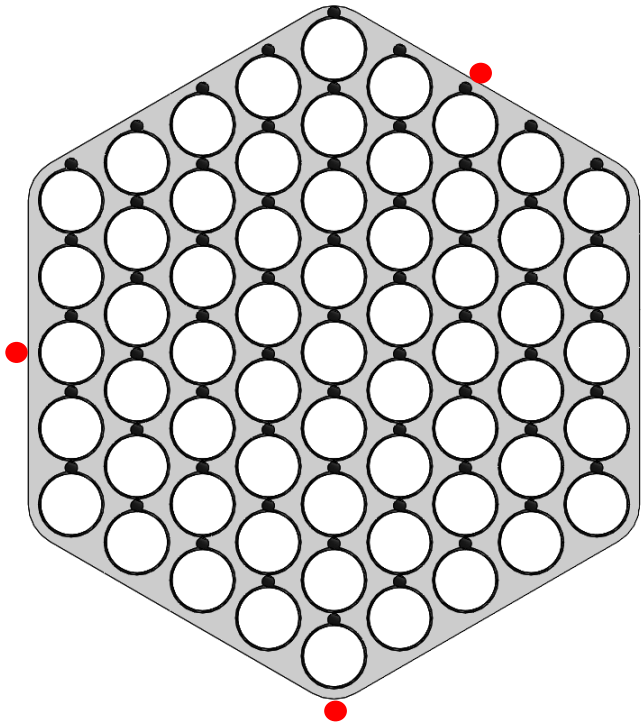


Figure 7. Outer Duct Thermocouple Positions

Specific positioning for the thermocouples to be used in the inlet and outlet plenums is being investigated. Of the three thermocouples to be used at the duct entrance, two will be run through the duct wall and measure the fluid temperature in a wall subchannel. The third will protrude out from a non-heated tube. All of these thermocouples will be at a height 40.2 mm above the duct bottom, so as not to interfere with the lower flange. Figure 8 shows the positioning of these duct entrance thermocouples.

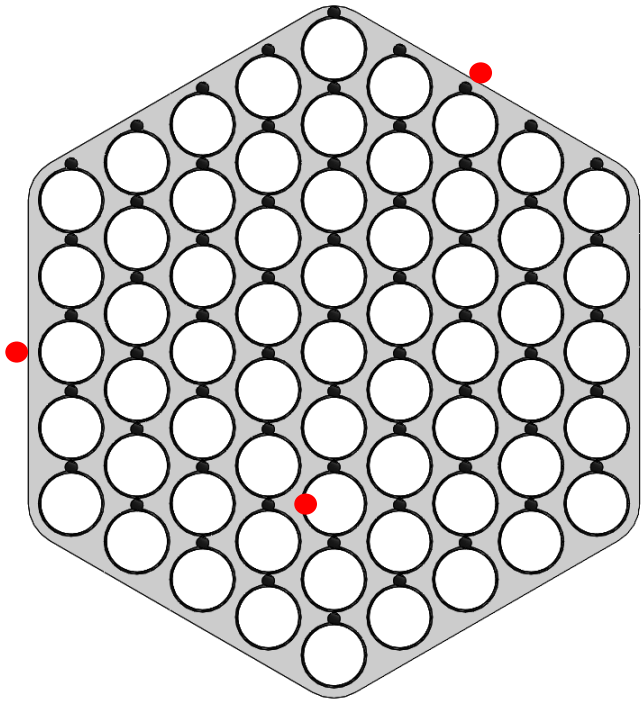


Figure 8. Duct Entrance Thermocouple Positions

Heater rod power inputs shall be measured and recorded to ensure test case target values are met and steady state behavior including power per rod, axial power profile, peaking and total power are recorded.

5.3 Pressure Measurements

Duct wall pressures, internal bundle pressures and inlet and outlet pressures will be measured. Currently 40 pressure measurements are identified. The total available pressure transducers is uncertain at this time. Therefore, the pressure taps are ranked in groups of 10 with respect to their priority with 1 being the critical group measurements. Group 1 includes inlet and outlet plenum pressures.

5.3.1 Duct Wall Pressure Measurements

Pressure taps will be used to measure pressure drop across different bundle lengths and between different azimuthal positions. The following table presents the tap locations. All these taps will be in the azimuthal centerline of the duct face. A single duct face will have the majority of pressure taps. At some heights, pressure taps on other faces will used. As part of the facility refurbishment, a count of number of available pressure transducers is being performed. The following also prioritizes pressure taps in case the facility has less transducers than specified taps.

Table 13. Bundle Wall Pressure Tap Locations

Bundle Region	Pressure Tap Identifiers	Height from duct bottom (mm)	Height from bottom of clad (mm)	H: Axial Height into heated length by Pitch	Group Priority (1-4) 1 is most important*
Entrance Region	PT #1	10.2+	810.0	H = -4P: Face B	1
	PT #2	295.2	1095.0	H = -3P: Face B	1
	PT #3	390.2	1190.0	H = (-2.66)P: Face B	3
	PT #4	485.2	1285.0	H = (-2.33)P: Face B	3
	PT #5	580.2	1380.0	H = -2P: Face B	1
	PT #6	722.7	1522.5	H = (-1.5)P: Face B	2
	PT #7	865.2	1665.0	H = -1P: Face B	1
	PT #8	1007.7	1807.5	H = (-0.5)P: Face B	2
Heated Length	PTs #9 – 12	1150.2	1950.0	H = 0P: Faces A, B, D, E	B-1; A, D – 2; E - 4
	PT #13	1292.7	2092.5	H = (0.5)P: Face B	4
	PT #14	1435.2	2235.0	H = 1P: Face B	4
	PT #15	1720.2	2520.0	H = 2P: Face B	4
	PTs #16 – 18	2005.2	2805.0	H = 3P: Faces A, B, D	B – 1; A, D – 2
	PTs #19 - 21	2385.2	3185.0	H = (4.33)P: Faces A, B, E	4, 4, 4
	PTs #22	2575.2	3375.0	H = 5P: Faces B	4
	PT #23	2860.2	3660.0	H = 6P: Face B	1
Unheated Region	PTs #24 – 26	3074.0	3873.8	H = (6.75)P: Faces A, B, D	3, 3, 3
	PT #27 - 28	3430.2	4230.0	H = 8P: Faces B, E	B – 1; E - 4
	PT # 29 - 30	4000.2	4800.0	H = 10P: Faces B, E	B – 3; E - 4

* 10 Taps per priority group. Other pressure taps include system taps (priority 1) and internal bundle pressure taps (priority group given below)

+ Position at 10.2 mm, or as low as possible to accommodate for lower duct flange

5.3.2 Internal Bundle Pressure Measurements

In addition to duct face pressure measurements, 8 of the unheated tubes will be designed to be used as pressure paths to measure internal pressures. Design of this method is still under development, but it is expected that these non-heated tubes will be tapped at specific heights, with 4 taps at each of the two heights. The bottom of these non-heated tubes will be configured for pressure tubing connections. The position of these pressure tapped non-heated tubes in the bundle is shown in Figure 4. Table 14 presents the height, and azimuthal position of these taps.

Table 14. Non-heated Tube Tap Hole Position

Height: From heater rod bottom (mm)	Height into heated length by pitch (P)	Tap hole clock position	Wire wrap clock position at height	Priority Group
2805.0 (height A)	3P	3	12 (clock position)	2, 2, 2, 2
3873.8 (height B)	(6.75)P	3	9	3, 3, 3, 3

5.4 Temperature Measurements

Heater rods, unheated tubes, and the duct wall will be instrumented with thermocouples to measure temperature. Placement of thermocouples is informed from CFD simulations (Appendix B).

5.4.1 Heater Rod Thermocouple Specifications

Heater rods will be thermocouple instrumented to measure the internal clad temperature. 3 thermocouple configurations will be used that utilize both axial and azimuthal thermocouple arrangements. In addition, all heater rods will have thermocouples at the maximum heat flux height at an azimuthal position behind the wire wrap to measure the expected maximum temperature. 13 heater rods will use the standard configuration, 2 will have the axial configuration, and 4 will have the azimuthal configuration (Table 7).

The tables below present the position detail of the different types of configurations in terms of axial height from the bottom of the heater rod clad and azimuthal position. Azimuthal position is given in terms of clocking position looking up the heater rod. The wire wrap rotates clockwise following the direction of the flow, therefore the majority of the thermocouples in the axial heater rod instrumentation configuration are directly behind the wire wrap at that corresponding axial height. Further detail is provided in Appendix B.

Table 15. Standard Heater Instrumentation Configuration

Standard Heater Rod Instrumentation Configuration			
Height: From heater rod bottom (mm)	**Height into heated length by pitch (P)**	**Number of TCs**	**TC Position (Clock position)**
2805.0	3P	3	11, 12, 1 (clock position)
3208.75	(4.416)P	2	4, 6
3873.75	(6.75)P	3	8, 9, 10
Total Standard heater Rod Thermocouples		104	

Table 16. Axial Heater Instrumentation Configuration

Axial Heater Rod Instrumentation Configuration			
Height: From heater rod bottom (mm)	**Height into heated length by pitch (P)**	**Number of TCs**	**TC locations at given Height (Clock position)**
2163.75	(0.75)P	1	9 (clock position)
2472.5	(1.833)P	1	10
2757.5	(2.833)P	1	11

2805.0	3P	1	12
2852.5	(3.166)P	1	1
3137.5	(4.166)P	1	2
3446.25	(5.25)P	1	3
3755.0	(6.333)P	1	4
4063.75	(7.416)P	1	5
Total Axial Heater Rods Thermocouples		18	

Table 17. Azimuthal Heater Instrumentation Configuration

Azimuthal Heater Rod Instrumentation Configuration			
Height: From heater rod bottom (mm)	**Height into heated length by pitch (P)**	**Number of TCs**	**TC locations at given Height (Clock position)**
2805.0	3P	2	6, 12 (clock position)
3208.75	(4.416)P	6	1, 3, 5, 7, 9, 11
Total Azimuthal Heater Rods Thermocouples		32	

5.4.2 Non-heated Tubes Thermocouple Specification

22 non-heated tubes are being designed to contain 6 thermocouples each. These thermocouples will be at the outer tube surface to measure the wall fluid temperature. The thermocouple leads will run downward through the inside of the non-heated tubes. Placement of these tubes in the bundle is shown in Figure 4. Specification of these non-heated tube thermocouple positions are shown in Table 18. In addition, a single instrumented non-heated tube will have an additional thermocouple at a height 840.0 mm about the clad bottom (40.2 mm into the duct) to measure the fluid temperature at the duct entrance. This is described in section 5.2.

Table 18. Non-heated Tube Thermocouple configuration

Non-Heated Tube Instrumentation Configuration			
Height: From heater rod bottom (mm)	**Height into heated length by pitch (P)**	**Number of TCs**	**TC locations at given Height (Clock position)**
2805.0	3P	2	11, 1 (clock position)
3208.75	(4.416)P	2	4, 6
3873.75	(6.75)P	2	8, 10
Total non-heated tube int. clad TCs		132	

5.4.3 Pressure Tube Axial Thermocouples

As described above, some of the non-heated tubes will be used to measure internal bundle pressure. This pressure reading will be dependent on the static head in the pressure tube, and therefore depend on the density of the water in the tube. Therefore fluid temperature at these points must be measured. It is anticipated that axial thermocouples could be used. Given that the pressure tube method is still under development, currently 24 thermocouples have been allocated for this purpose.

5.4.4 Duct Wall Subchannel Thermocouples

Methods are being investigated for instrumenting the internal duct wall of a single face. 6 thermocouples will be instrumented at 4 axial heights. Figure 9 below shows the thermocouple positions along duct face E. The thermocouple positions will be the azimuthal midpoint between pins, as well as the face center and corner. Table 19 provides detail for axial heights of the thermocouples.

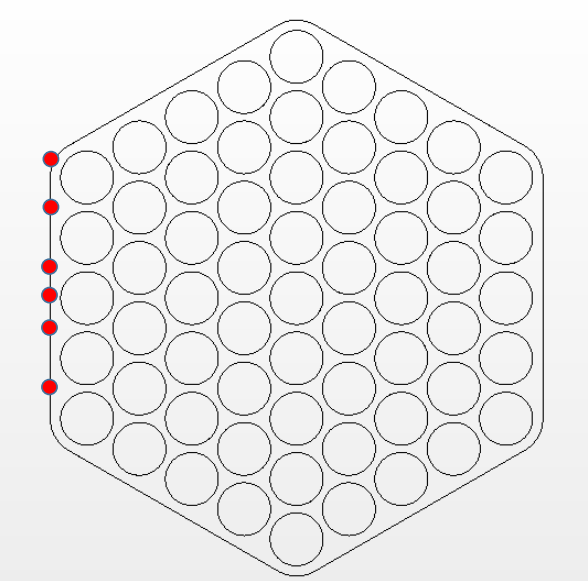


Figure 9. Duct Internal Wall Subchannel Thermocouples

Table 19. Duct Internal Face E Subchannel Thermocouple Detail

Height from duct entrance (mm)	Height: From heater rod bottom (mm)	Height into heated length by pitch (P)	Number of TCs/ height	Wire wrap clock position
2005.2	2805.0	3P	6	12 (clock pos)
2052.7	2852.5	(3.166)P	6	2
2409.0	3208.8	(4.416)P	6	5
3074.0	3873.8	(6.75)P	6	9
Total Internal Duct Wall Thermocouples			24	

6 TEST PREDICTIONS

Hand calculations for pressure drop and preliminary CFD simulations for thermal fields have been conducted to inform the design. For the given Reynolds number cases, the following bundle pressure drops are predicted from the 1D Cheng and Todreas [2] correlation for flow through the duct length. These calculations use inlet Reynolds numbers based on 4.55 mm D_h, a length of 4229.1 mm, and water properties at the inlet temperature. These are conservative because as the flow heats up, the pressure drop is reduced due to the reduction in viscosity.

Table 20. Predicted Pressure Drop

Run	Value	Units
15,000 Run	90,945	Pa

20,000 Run	153,520	Pa
25,000 Run	230,431	Pa

CFD simulations have been performed primarily to inform the maximum heater power that can be used while avoiding the risk of boiling. CFD analyses continue, therefore further detail of the final per rod heater power will be provided in the Benchmark Specification. As stated above, the system will be pressurized to 150 psia, which results in a corresponding boiling temperature of approximately 350 F. The following presents results from preliminary CFD simulations for heater power levels being considered. As described in section 4.3, the design rod power have been updated since these CFD simulations were run.

Table 21. CFD Maximum Fluid and Heater Wall Temperatures

Run	Per Rod Power (kW)	Max Pin Surface Temp (F)	Max Fluid Temp (F)
15,000	17.5	216.5	173.4
20,000	25.0	230.6	179.6
25,000	35.0	251.2	190.2

7 REPORTING

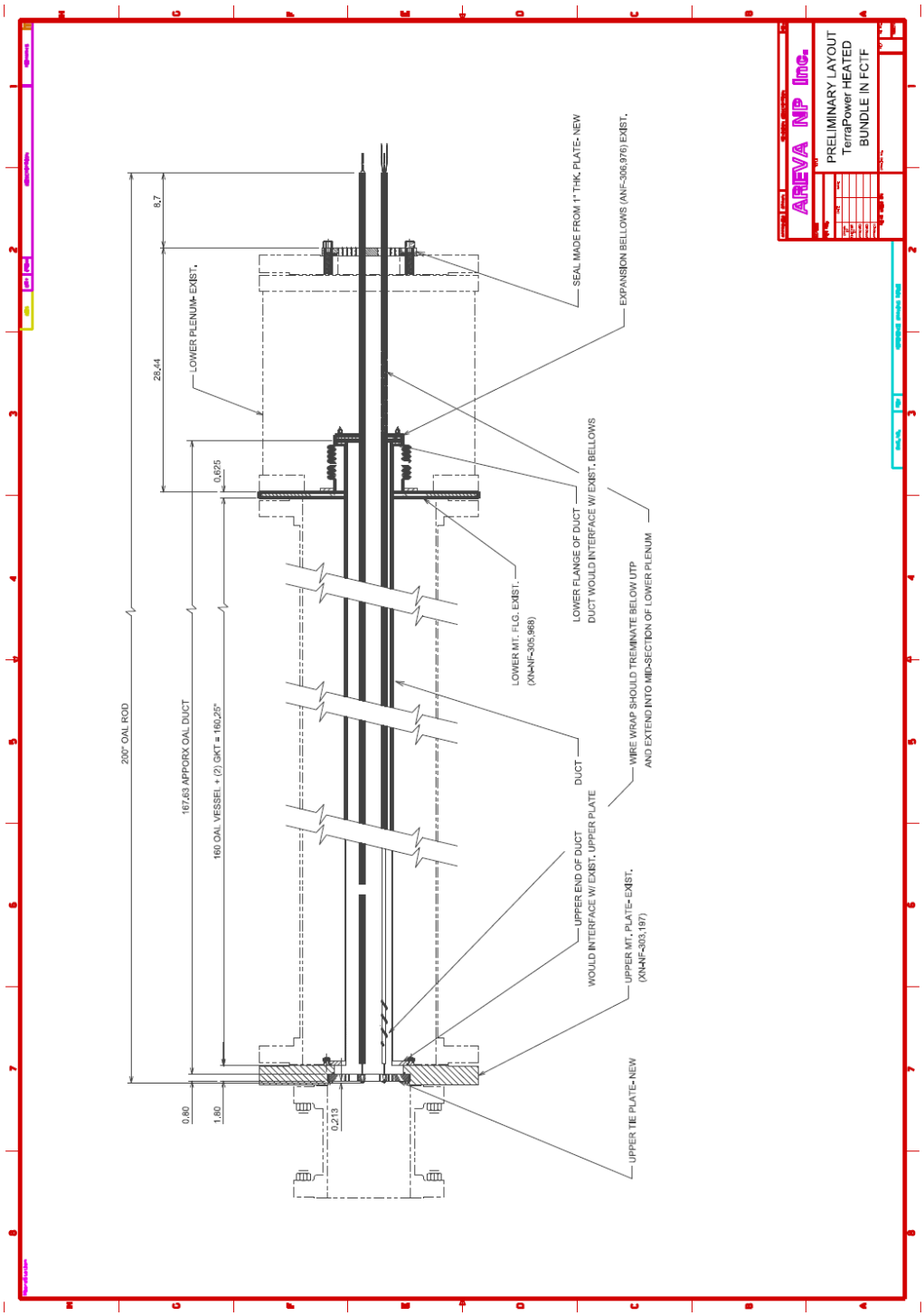
Reporting will include demonstration of stable instrumentation signals (i.e., no data drift) with quantified uncertainties for all ΔP, and temperature measurements. Any duplicate measurements (e.g. flowrate) shall be documented and provided. Data should be provided in metric (MKS) units. Additional documentation and quality assurance requirements for the testing need to comply with requirements given in Appendix C. Final measurement detail will be provided in the Benchmark Specification including formatting of final data package to be established.

8 REFERENCES

1. TWRP-31-FRD-0001-Rev-0, AFAFC Heated Bundle Heater Rod Specification.
2. Cheng, S., and Todreas, N.E., “Hydrodynamic Models and Correlations for Bare and Wire-Wrapped Hexagonal Rod Bundles—Bundle Friction Factors, Subchannel Friction Factors and Mixing Parameters”, Nuclear Engineering and Design 92 (1986).

9 APPENDIX A

Figure showing heater axial positioning in the bundle:



10 APPENDIX B

The following are temperature profiles at different axial heights from CFD simulations similar to the design specification contained herein. The images are from the top down, therefore the clocking direction is opposite. These are for runs at Re = 15,000, and a per rod power of 12.5 kW. This model has a slightly smaller P/D, therefore temperatures are conservative in that the CFD predicts higher than would be expected in the experiment. Instrumentation locations are also shown in these images. The instrumentation locations are as specified in this current document. These images were used to inform thermocouple placement. It should be noted these temperatures are only for the fluid volumes at that height. Heater wall temperatures can be expected to be higher.

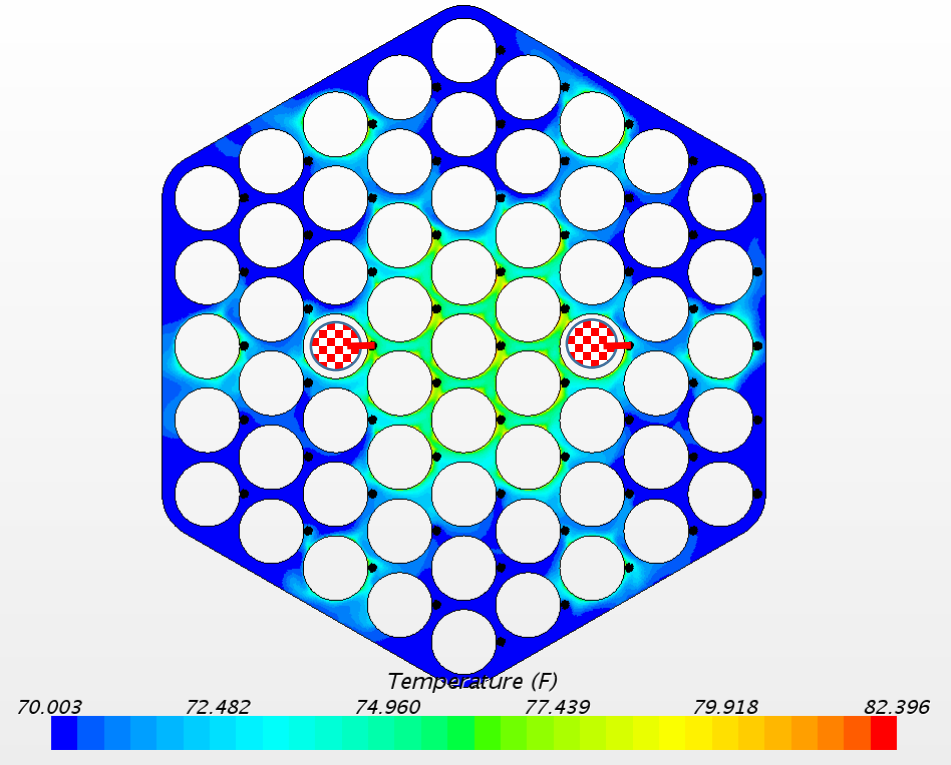


Figure 10. (9/12) Pitches into Heated Length

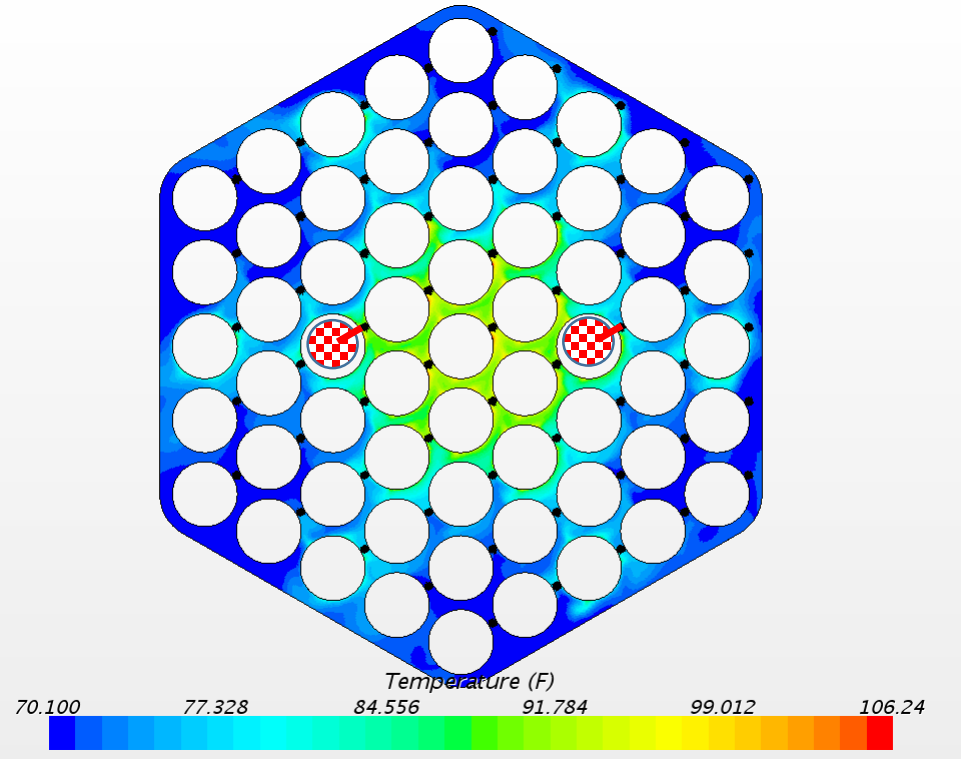


Figure 11. (1 + 10/12) Pitches into Heated Length

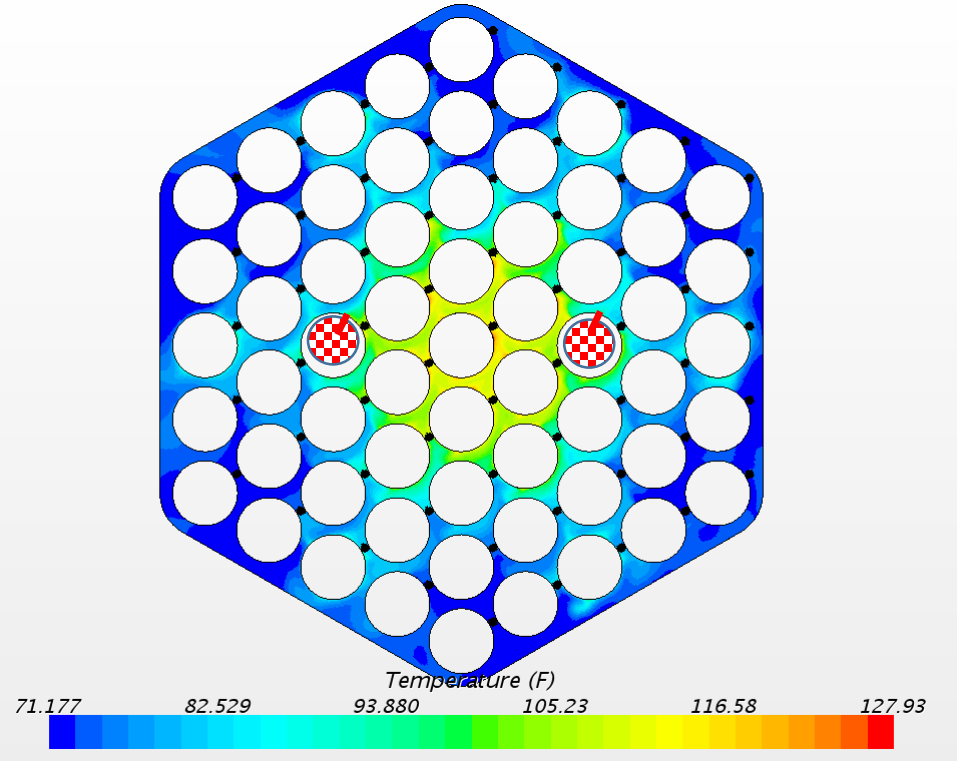


Figure 12. (2 + 10/12) Pitches into Heated Length

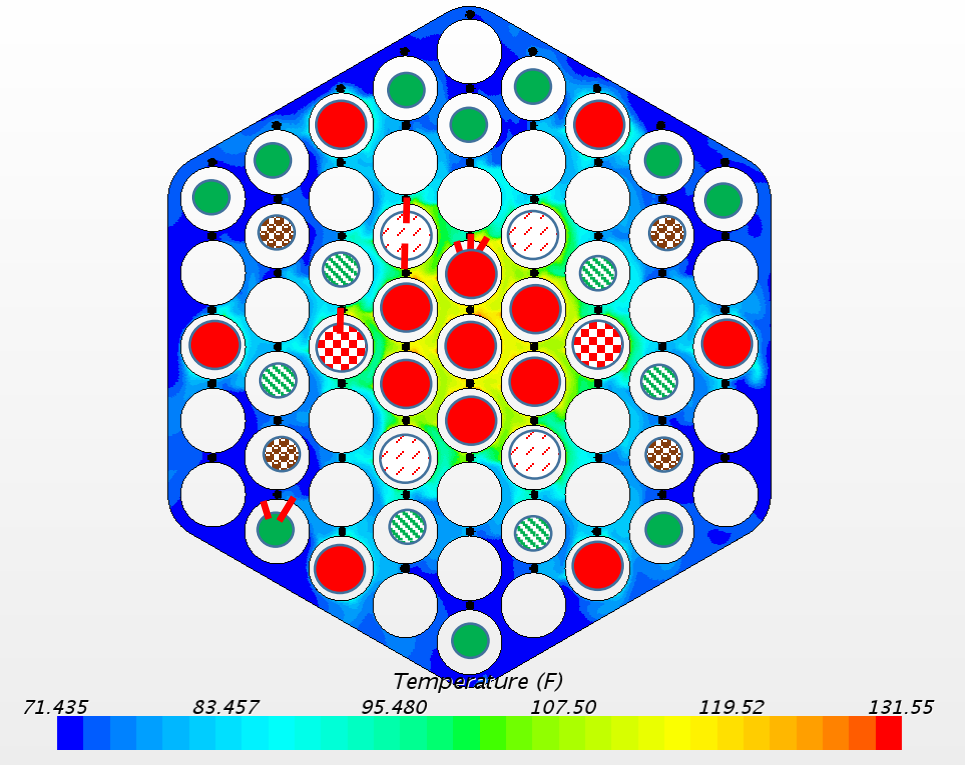


Figure 13. 3 Pitches into Heated Length

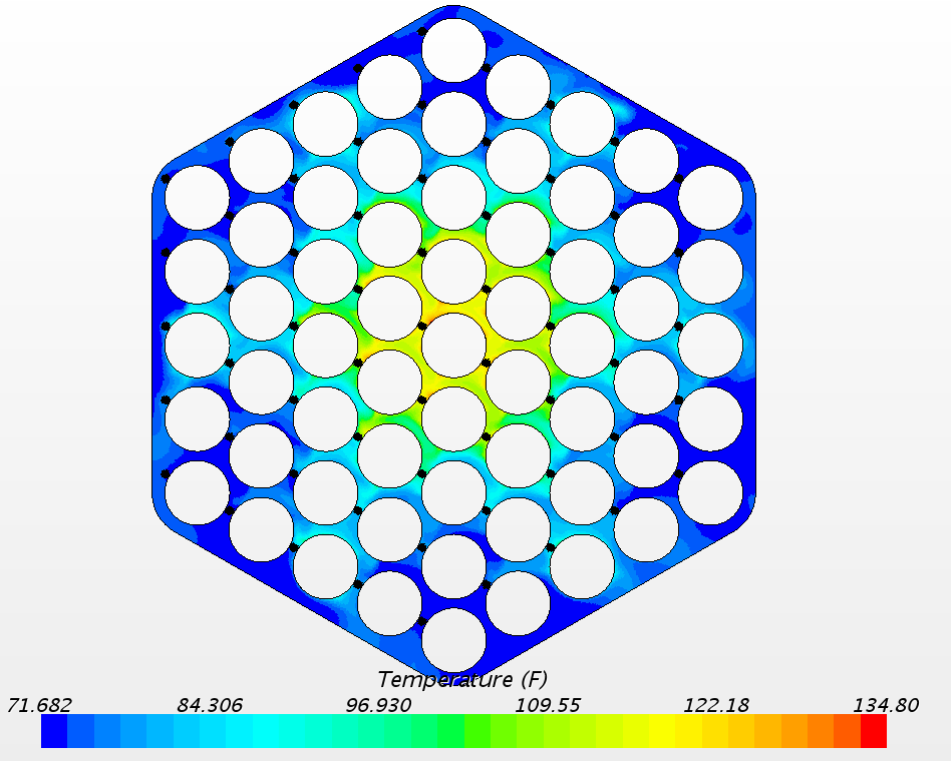


Figure 14. (3 + 2/12) Pitches into Heated Length

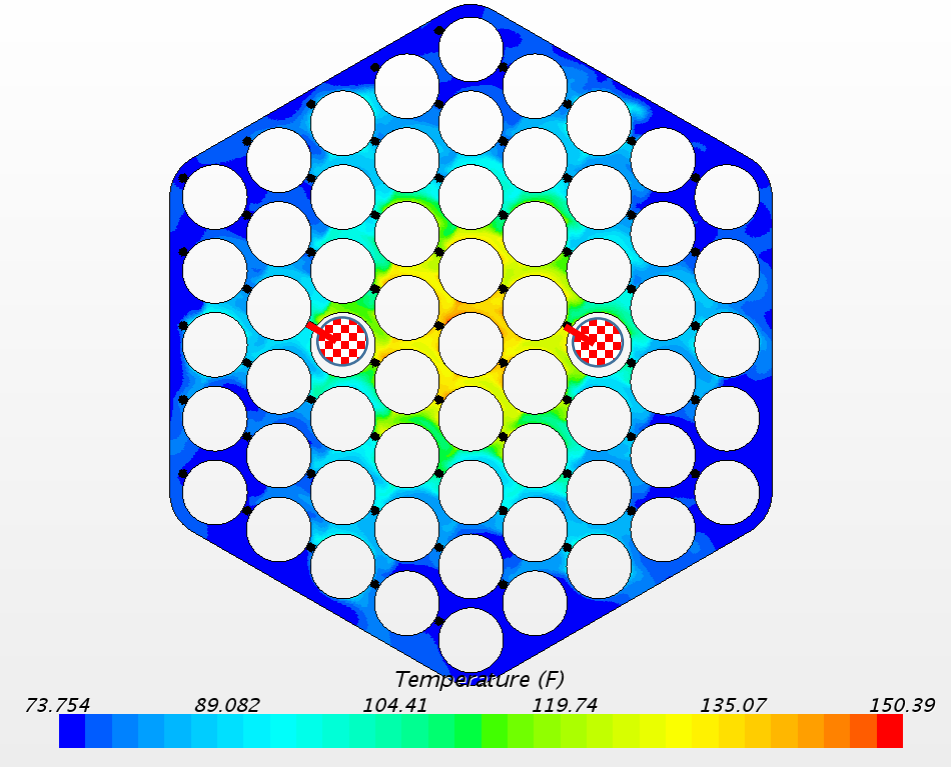


Figure 15. (4 + 2/12) Pitches into Heated Length

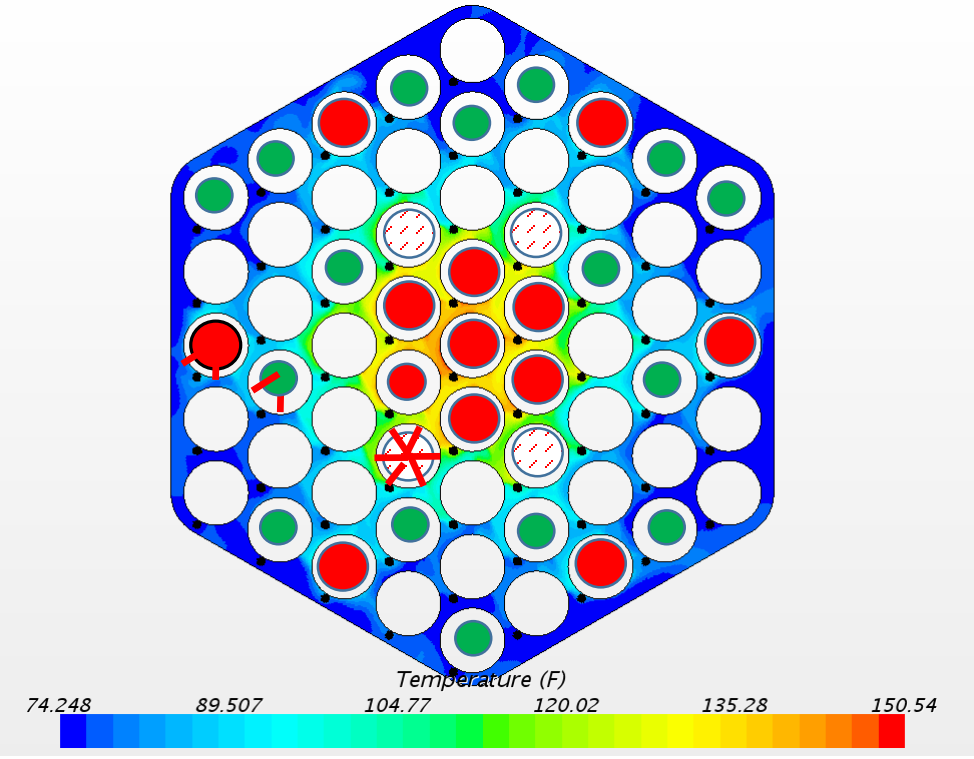


Figure 16. (4+ 5/12) Pitches into Heated Length

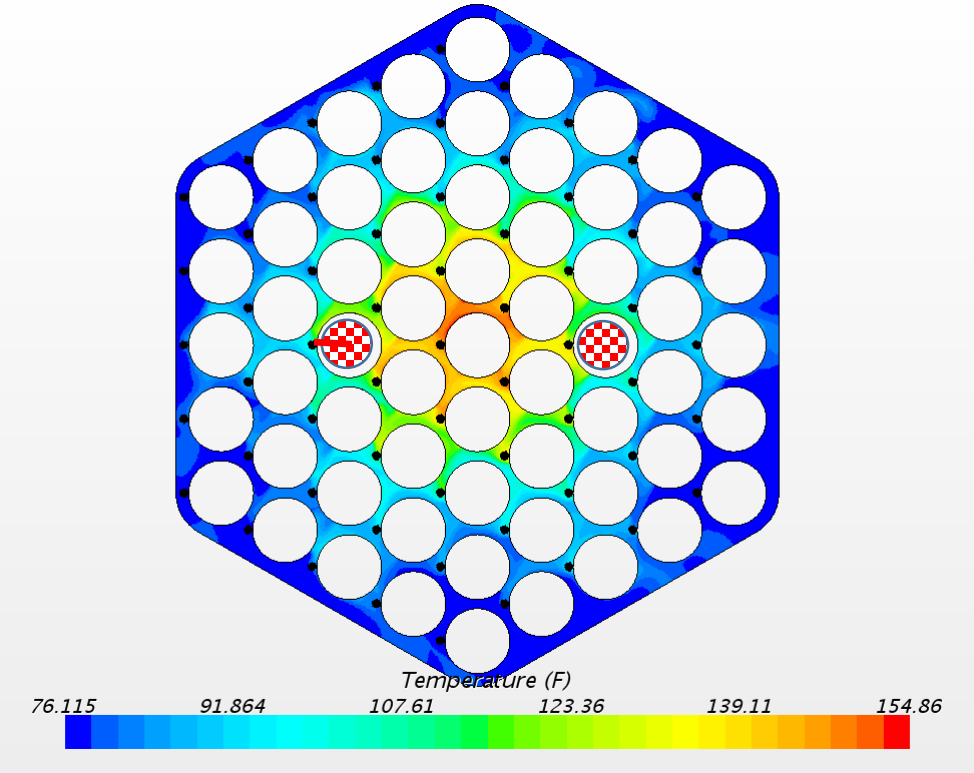


Figure 17. (5 + 3/12) Pitches into Heated Length

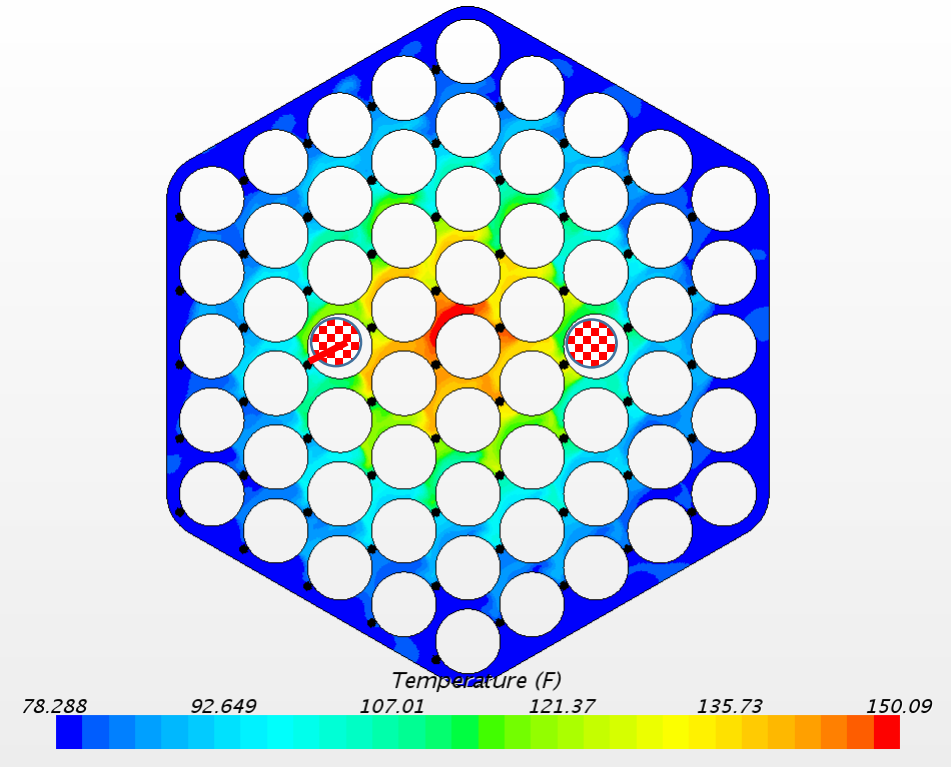


Figure 18. (6 + 4/12) Pitches into Heated Length

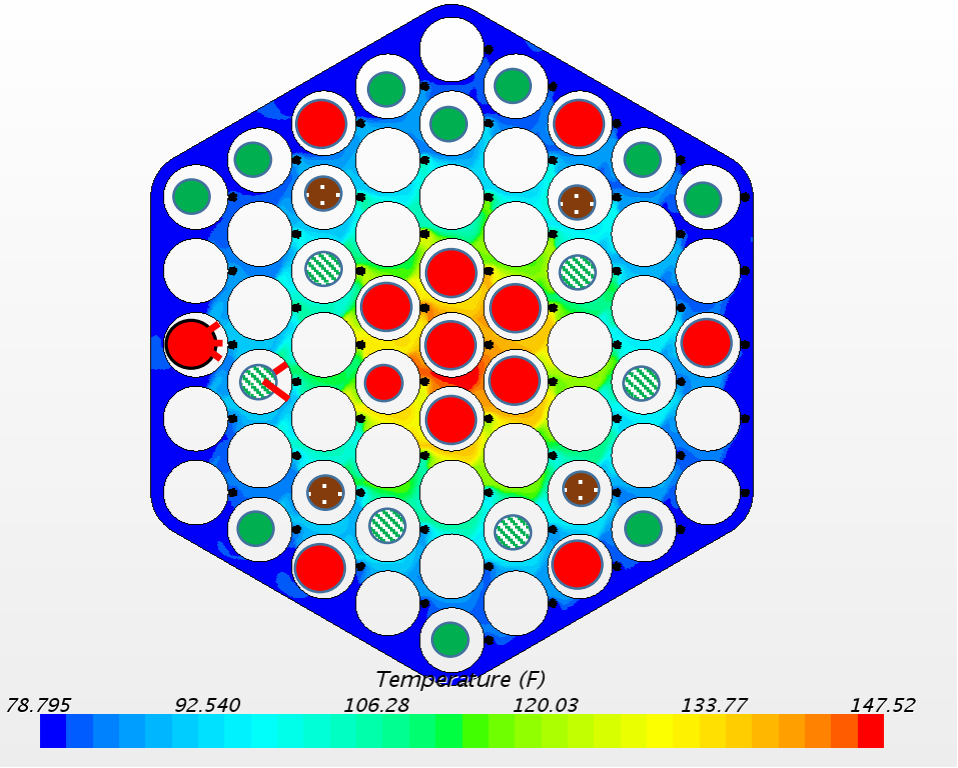


Figure 19. (6 + 9/12) Pitches into Heated Length

11 APPENDIX C

This appendix provides the augmented quality assurance requirements and guidance for implementation of these requirements to this test specification. The following identifies the applicable augmented Quality Assurance Requirements and the measures that should be taken for compliance.

ITS – Augmented Quality Requirements

1. Organization

Measures shall be established for verification of compliance with the requirements of this plan. The normal line organization may verify compliance with the requirements of this plan. A separate or dedicated quality assurance organization is not required.

2. Quality Assurance Program

Quality controls that apply to the work shall be documented. It is expected that the existing body of supplier's procedures or practices will describe the quality controls applied to the subject equipment (or service). A new or separate QA program is not required.

3. Design Control

3.1. Procedures shall describe the process for ensuring that:

- All design requirements are incorporated into the design
- Applicable design inputs are included or correctly translated into design documents
- Deviations from the design inputs are controlled
- Changes to design outputs are identified, controlled, and properly disseminated

3.2. Procedures shall define internal and external interfaces and requirements for coordinating design processes that affect or depend on other disciplines or organizations.

3.3. Design inputs relating to item requirements shall be determined and records maintained. These inputs shall include:

- Functional and performance requirements
- Applicable statutory and regulatory requirements
- Where applicable, information derived from previous similar designs
- Where applicable, information derived from testing or analyses
- Other requirements essential for design and development

3.4. Design outputs shall be in a form suitable for verification against the design inputs and shall be approved prior to release.

3.5. Design outputs shall:

- Meet the input requirements
- Provide appropriate information for purchasing and production
- Contain or reference acceptance criteria
- Specify the characteristics of the item that are essential for its intended performance

3.6. Procedures shall establish when design reviews are performed. Design reviews shall be performed to evaluate the ability of the results of the design to meet requirements, and to identify any problems and propose necessary actions.

Normal supervisory review of the designer's work is an adequate control measure as long as the supervisor is technically qualified to perform that review. However, TP management may require independent review for certain work tasks. Records of the results of the reviews shall be maintained.

3.7. Design verification shall be performed in accordance with procedures to ensure that the design outputs have met the design input requirements. Records of the results of the verification and any necessary actions shall be maintained.

3.8. Design changes shall be identified and records maintained. The changes shall be reviewed, verified and validated, as appropriate, and approved before implementation. The review of design changes shall include evaluation of the effect of the changes on other in-process or completed design. Records of the results of the review of changes and any necessary actions shall be maintained.

4. Procurement Document Control

Applicable design bases and other requirements necessary to assure component performance, including design requirements, shall be included or referenced in documents for procurement of items and services, and deviations therefrom shall be controlled.

5. Instructions, Procedures, and Drawings

Activities affecting quality shall be performed in accordance with documented instructions, procedures, or drawings of a type appropriate to the circumstances, and that include acceptance criteria, where applicable, to determine that the work has been performed correctly. This may include such things as written instructions, plant procedures, cautionary notes on drawings, and special instructions or work orders. Any methodology which provides the appropriate degree of guidance to personnel performing activities important to component functional performance will satisfy this requirement.

6. Document Control

The issuance and change of documents that specify quality requirements or prescribe activities affecting quality shall be controlled to assure that correct documents are employed.

7. Control of Purchased Items and Services

Measure are to be established to ensure that all purchased items and services conform to appropriate procurement documents.

8. Identification and Control of Purchased Items

Measures shall be established, where necessary, to identify purchased items and preserve their investment protection important functional performance capability. Examples of circumstances requiring such control include the storage of environmentally sensitive equipment or material, and the storage of equipment or material that has a limited shelf-life.

9. Control of Special Processes

Measures shall be established to control special processes, including welding, heat treating, and non-destructive testing. Applicable codes, standards, specifications, criteria, and other special requirements may serve as the basis of these controls.

10. Inspection

Inspections shall be performed where necessary to verify conformance of an item or activity to specified requirements, or to verify that activities are being satisfactorily accomplished.

11. Test Control

Measures shall be established, as appropriate, to test items, equipment or material prior to installation to demonstrate conformance with design requirement. Tests shall be performed in accordance with test procedures. Test results shall be recorded and evaluated to ensure that test requirements have been met.

11.1. Procedures shall describe the requirements for software testing. The level of test control shall be commensurate with the determined safety classification of the design work being performed with the software.

11.2. Testing performed directly or by contracted companies shall be performed in accordance with documented and approved requirements. Such requirements will be contained in applicable procedures or work instructions and, for contracted testing, conveyed in applicable procurement documents. Establishment of test requirements shall be determined by the manager that will use the test results in the design or specification. Tests are performed in accordance with test procedures or plans that are prepared by the organization performing the test, or under TP procedures when contracted testing is performed under the TP quality assurance program.

12. Control of Measuring and Test Equipment

Measures shall be established to control, calibrate, and adjust measuring and test equipment at specific intervals.

13. Handling, Storage, and Shipping

Handling, storage, cleaning, packaging, shipping, and preservation of items shall be controlled to prevent damage or loss and to minimize deterioration.

14. Inspection, Test, and Operating Status

Measure shall be established to identify items that have satisfactorily passed required tests and inspections, and to indicate status of inspection, test, and operability as appropriate.

15. Control of Nonconforming Items

Items that do not conform to specified requirements shall be identified and controlled to prevent inadvertent installation or use.

16. Corrective Action

Measure shall be established to ensure that failures, malfunctions, deficiencies, deviations, defective components, and noncompliance are properly identified, reported, and corrected.

17. Records

Records shall be prepared and maintained to furnish evidence that the above requirements for design, procurement, document control, inspection, and test activities have been met.

18. Audits

Audits or periodic reviews shall be conducted and documented to verify compliance with design and procurement documents, instructions, procedures, drawings, and inspection and test activities. Audits which are independent of line management are not required if line management periodically reviews and documents the adequacy of the supplier's processes and takes any necessary corrective action. Line management is responsible for determining whether reviews conducted by line management or audits conducted by an organization independent of line management are appropriate.

APPENDIX C: TWRP-31-RPT-0033, AFAFC HEATED BUNDLE AS-BUILT REPORT



Uncontrolled When Printed

ENGINEERING REPORT

Document Number:	TWRP-31-RPT-0033	**Revision:**	0
Document Title:	AFAFC Heated Bundle As-Built Report		
Issuing Organization:	Design Qualification	**Released Date:**	1/24/2017
		Page Number:	1 of 53

Approval

Title	Name	Signature	Date
Originator, Thermal Hydraulics Test and Analysis Engineer	Brian Jackson	Approved in Agile	1/24/2017
Reviewer, CFD and Thermal-Hydraulic Testing Engineer	Mathieu Martin	Approved in Agile	1/24/2017
Approver, Manager, Thermal Hydraulic Test & Analysis	Mike Steer	Approved in Agile	1/24/2017

Document Quality Level per TWRP-NS-PROC-0002:

Quality Level 1 ☐ Quality Level 2 ☒ Quality Level 3 ☐ N/A ☐

Contains Open Items: Yes ☐ No ☒

Revision History

Revision No.	Effective Date	Affected Section(s)	Description of Change(s)
0	1/24/2017	All	Initial Release

TABLE OF CONTENTS

1 OBJECTIVE 5
2 STERN HEATER ROD AS-BUILT MEASUREMENTS 5
2.1 Heater Dimensional Measurements 5
2.2 Heater Functional Measurements 11
3 NON-HEATED TUBE AS-BUILT MEASUREMENTS 16
3.1 Non-Heated Tube Dimensional As-Built Measurements 17
3.2 Non-Heated Tube Functional Measurements 27
4 NON-DEFORMED DUCT AS-BUILT MEASUREMENTS 29
4.1 Non-Deformed Duct Dimensional Measurements 29
4.2 Non-Deformed Duct Instrumentation Measurements 30
5 DEFORMED DUCT AS-BUILT MEASUREMENTS 32
5.1 Deformed Duct Dimensional Measurements 32
5.2 Deformed Duct Instrumentation Measurements 34
6 AS INSTALLED CONFIGURATION 34
6.1 As-Installed Geometry 34
6.2 As-Installed Instruments 39
7 REFERENCES 46
8 APPENDIX A 47
9 APPENDIX B 48
10 APPENDIX C 51
11 APPENDIX D 52

LIST OF TABLES

Table 1: Heater Rod Diameter Measurements 7
Table 2. Heater Rod Axial Length Measurements 9
Table 3. STERN Heating Element Length Measurements 12
Table 4. As-Measured Heater Power Profile 13
Table 5. Heater Rod Type 13
Table 6. As-Built Standard Heater Rod Thermocouple Axial Positions 14
Table 7. As-Built Azimuthal Heater Rod Thermocouple Axial Positions 14
Table 8. As-Built Axial Heater Rod Thermocouple Axial Positions 15
Table 9. As-Designed Thermocouple Clocking Positions 15
Table 10. Non-Conformance of Heater Rod Thermocouple Clocking Positions 16
Table 11. Non-Heated Tube Types 16
Table 12. Non-Heated Tube Nominal Section OD Measurements 17
Table 13. Non-Heated Tube Necked Section OD Measurements 19
Table 14. Non-Heated Tube Wire Wrap Measurements 22
Table 15. Non-Heated Tube Length Measurements 24
Table 16. Non-Heated Tube Thermocouple Location Measurements 28
Table 17. Non-Heated Tube Pressure Tap Location Measurements 28

Table 18. Non-Deformed Duct External Face Specified Thermocouple Locations 31
Table 19. Deformed Duct Values 33
Table 20. As-Installed Axial Positioning 35
Table 21. Heater Rod Numbering Cross-linking 39
Table 22. Standard Heater Rod Thermocouple As-Built Locations 40
Table 23. Azimuthal Heater Rod Thermocouple As-Built Locations 40
Table 24. Axial Heater Rod Thermocouple As-Built Locations 41
Table 25. Non-Heated Tube As-Built Thermocouple Locations 41
Table 26. Non-Heated Tube As-Built Pressure Tap Locations 42
Table 27. Inner Duct Wall Thermocouple Lateral Positions 42
Table 28. As-Built Non-Deformed Duct Thermocouple Locations 43
Table 29. As-Built Deformed Duct Thermocouple Locations 44
Table 30. As-Built Non-Deformed Duct Pressure Tap Locations 44
Table 31. STERN Heating Element to Final Heater Numbering Reference 48
Table 32. STERN Power Profile Measurements 49

LIST OF FIGURES

Figure 1. Sections of the Heater 6
Figure 2. Lower Transition Collar 10
Figure 3. Upper End Cap 11
Figure 4. As-Installed Non-Heated Tube Thermocouples 27
Figure 5. Non-Deformed Duct Single Axial Section 29
Figure 6. Complete Non-Deformed Duct 30
Figure 7. Non-Deformed Duct External Thermocouple 32
Figure 8. Deformed Duct Visual Representation 33
Figure 9. Duct Lettering View from Top 36
Figure 10. Installed Pin Bundle 37
Figure 11. Heater Rod Position Map 38
Figure 12. As-Built Internal Duct Wall Thermocouples 43
Figure 13. STERN Power Profile Measurements Plot 50
Figure 14. Bundle Axial Configuration 53

1 OBJECTIVE

The objective of this document is to report the as-built measurements of the heated bundle fabricated for the Advanced Fuel Assembly Flow Characterization (AFAFC) heated bundle tests in support of DOE grant DE-NE0008321, Toward a Longer-Life Core: Thermal Hydraulics CFD Simulations and Experimental Investigations of Deformed Fuel Assemblies. This document contains all test section geometry and instrumentation location for the as-built, as-installed bundle to fully define the dimensions of the test section. In addition, it contains information with respect to the thermal profile of the heater rods. The majority of reported values herein were taken on individual bundle components (heaters, tubes, duct, wire) before installation into the loop to ensure consistency with equipment specifications. The final section (Section 6) provides detail of the as-installed configuration. This section is of most use for the modeling analyst as it gives an overall summary of the bundle geometry, configuration and locations of the instruments after installation.

This is a 61 pin bundle, of which 19 are high power heater rods and the rest are non-heated tubes. Two separate ducts were used for two different tests. The same 61 pin bundle was used with each of the separate ducts. The different ducts correspond to a nominal duct representing a prototypical beginning of life duct geometry, and a deformed duct representing a later-in-life duct geometry. Reported measurements contained herein include both Contractor Inspection Report data, and receipt inspection values measured by TerraPower. These are identified accordingly. Details of the test and equipment are provided in the Test Specification [1] and the Functions and Requirements Documents [2, 3, 4, 5], however this report contains all as-built measurements. Measurement values are presented in the unit system that was used during measurement. Due to different measurement types and organizations involved in the fabrication and inspection of these parts, values are presented in both metric and English units. Some derived parameters are given in both units. Final experiment test conditions will be reported in the Experiment Test Reports to be produced following completion of the tests. This information will be contained in the project's Final Scientific Technical Report.

2 STERN HEATER ROD AS-BUILT MEASUREMENTS

22 high powered heater rods (3 extra) were procured for the 19 to be installed in the bundle. Each of the rods was instrumented with internal embedded thermocouples. In the following tables, heater rods with an * are the 3 spare heater rods that were not installed in the bundle during these tests, however, measurements are included for completeness.

2.1 Heater Dimensional Measurements

TerraPower measured heater rod dimensions upon receipt from STERN Laboratories. These included both diameter and length measurements. Diameter measurements were taken with the TerraPower calibrated calipers. Length measurements were taken with a tape measure. Figure 1 gives an overview of the axial configuration of the heater rods. The heaters have an upper end cap, followed by the bulk of the heater rod that is 9.5 mm in diameter and called the nominal diameter section. The upper end cap has a through-hole that is used for the wire wrap attachment. At the bottom of the nominal diameter section, the heater clad transitions to a smaller diameter section. A transition collar is used at this location to which the wire wrap is attached. In the measurements below, the smaller diameter section is called the necked section. This necked region was designed to be 7.6mm in diameter, but was fabricated by swaging down 5/16" tubing. To reach the 7.6mm diameter that was needed for installation into the loop, additional machining was required beyond just the swaging. To minimize work, only the bottom 12" of the necked down region was machined down to the 7.6mm diameter because this is what was needed for installation into the loop. The additional ~8" above the 7.6mm machined portion was left at its swaged down diameter; approximately 0.007" oversized from the 7.6 mm value. This was permissible because this section does not impact the flow in the bundle because it is below the start of the duct. The figure below

shows the sections of the heater. Diameter measurements were taken in the nominal diameter section, and also in the machined length of the necked section. In the heated length, the heater was constructed of a tubular heating element. This element was filled and surrounded with a Magnesium Oxide insulation material. This was all enclosed in a thin tube of Monel k500 sheath, and finally with a thin tube of Monel k500 clad. The thermocouples were embedded between the sheath and the clad. Heater clad and sheath measurements were not taken, but STERN laboratories provided values for these parts.

Lengths measured and reported correspond to the total heater length, and the nominal diameter length. The total heater length goes from the top of the heater to the bottom of the necked section (does not include copper conductor), and the nominal diameter length goes from the top of the heater to the top of the transition collar (includes the upper end cap). These are reported below. Each of the heater rods was engraved with an ID number. This is given in the tables below.

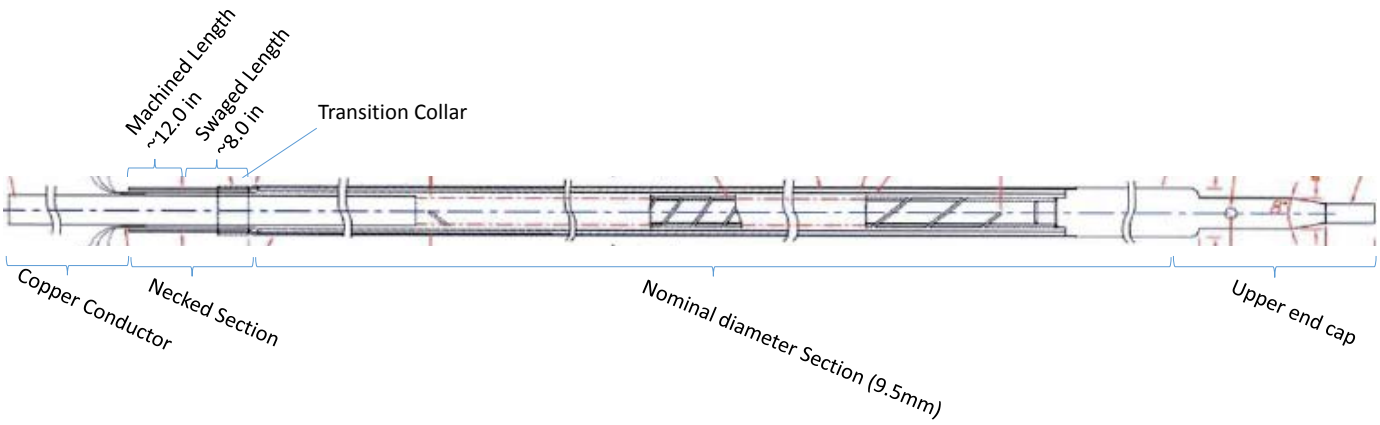


Figure 1. Sections of the Heater

2.1.1 Heater Diameter Measurements

Five outside diameter measurements were taken for each heater rod. 3 were taken along the length of nominal diameter (9.5 mm) and 2 were taken along the machined portion of the necked down smaller diameter section (7.6 mm). Nominal diameter measurements were taken 2 ft above the necked to nominal diameter transition, at the axial center of the nominal diameter section, and 2 ft below the bottom of the upper end cap. Necked down section measurements were taken 2 inches above the bottom of the clad, and 2 inches down into the machined portion.

Table 1: Heater Rod Diameter Measurements

Tube ID	Nominal OD Location #1 (mm)	Nominal OD Location #2 (mm)	Nominal OD Location #3 (mm)	Nominal Average OD (mm)	Necked OD #1 (mm)	Necked OD #2 (mm)	Ave Necked OD (mm)
789-C-1	9.49	9.52	9.52	9.510	7.64	7.60	7.620
789-C-2	9.49	9.50	9.53	9.507	7.60	7.63	7.615
789-C-3	9.48	9.50	9.53	9.503	7.62	7.62	7.620
789-C-4	9.49	9.53	9.53	9.517	7.63	7.63	7.630
789-C-5	9.50	9.55	9.55	9.533	7.63	7.61	7.620
789-C-6	9.49	9.52	9.54	9.517	7.63	7.61	7.620
789-C-7 *	9.50	9.53	9.53	9.520	7.61	7.59	7.600
789-C-8	9.49	9.51	9.51	9.503	7.60	7.62	7.610
789-C-9 *	9.49	9.52	9.52	9.510	7.60	7.61	7.605
789-C-10	9.50	9.50	9.51	9.503	7.59	7.62	7.605
789-C-11	9.49	9.54	9.55	9.527	7.60	7.57	7.585
789-C-12	9.53	9.53	9.52	9.527	7.61	7.63	7.620
789-C-13	9.48	9.53	9.53	9.513	7.59	7.61	7.600
789-C-14	9.49	9.52	9.51	9.507	7.62	7.61	7.615
789-C-15	9.49	9.52	9.53	9.513	7.60	7.57	7.585
789-C-16	9.50	9.53	9.53	9.520	7.58	7.58	7.580
789-C-18	9.49	9.53	9.53	9.517	7.62	7.62	7.620
789-C-19 *	9.48	9.52	9.53	9.510	7.60	7.59	7.595
789-C-20	9.50	9.53	9.54	9.523	7.62	7.61	7.615
789-C-21	9.52	9.52	9.53	9.523	7.59	7.61	7.600
789-C-22	9.49	9.52	9.52	9.510	7.59	7.62	7.605
789-C-23	9.49	9.51	9.51	9.503	7.59	7.59	7.590

Overall Averaged Diameter of Nominal Section	9.514 mm
Range of all Nominal Section Diameter Measurements	9.48 – 9.55 mm
Range of Heater Average Diameter Values	9.503 – 9.533 mm
Overall Averaged Diameter of Necked Section	7.607 mm

* Spare heater rods: not used in these test experiments

The outer layer of the heater is a clad layer, inside of which is a sheath layer. Both these layers were constructed from Monel k500 material. STERN laboratories did provide material properties at specific temperatures (Appendix A). Diameter measurements of the clad and sheath were not measured by TerraPower, but provided by the vendor STERN Laboratories. Clad ID reported as 0.335” in the heated length. Sheath ID reported as 0.267”. References are provided in Appendix A.

2.1.2 Heater Axial Length Measurements

Axial length measurements of total length, and length of the nominal diameter (9.5 mm) section were taken by TerraPower upon receipt (the nominal diameter length includes the upper end cap length). The total length corresponds to the length from the top of the end cap to the bottom of the necked down diameter portion of clad (it does not include the length of the copper conductors extending out the bottom of the clad). Measurement of the nominal diameter section length was from the top of the end cap to the top of the transition of the necked diameter section.

Table 2. Heater Rod Axial Length Measurements

Tube ID	Total length (mm)	Length from diameter transition to top of end cap (mm)
789-C-1	5081.59	4543.43
789-C-2	5081.59	4551.36
789-C-3	5081.59	4548.19
789-C-4	5083.18	4545.01
789-C-5	5081.56	4548.16
789-C-6	5083.18	4549.78
789-C-7 *	5080.00	4546.60
789-C-8	5081.59	4549.78
789-C-9 *	5080.00	4545.01
789-C-10	5078.41	4545.01
789-C-11	5081.56	4548.16
789-C-12	5083.18	4548.16
789-C-13	5081.59	4549.78
789-C-14	5078.41	4545.01
789-C-15	5081.59	4551.36
789-C-16	5080.00	4548.19
789-C-18	5083.18	4551.36
789-C-19 *	5081.59	4543.43
789-C-20	5083.18	4549.78
789-C-21	5080.00	4549.78
789-C-22	5083.18	4549.78
789-C-23	5076.83	4543.43

Overall Average of Total length	5081.22 mm
Range of Heater Total Lengths	5076.83 – 5083.18 mm
Overall Average of Nominal Diameter section	4547.75 mm
Range of Heater Nominal Diameter Lengths	4543.43 – 4551.36 mm

* Spare heater rods: not used in these test experiments

2.1.3 Heater Wire Wrap Measurements

Following fabrication of the wire wrap, visual inspection was performed. This included both ensuring wire wrap direction and also the wire wrap pitch. All heaters had their wire wrap the correct direction (clockwise from bottom to top viewpoint) per the Test Specification. The wire wrap pitch as specified was 11.22". This was verified by placing the wire wrapped heater in a cradle that had marks that identified the as-designed wire wrap pitch lengths for comparison to the as-built dimensions. Wire wrap pitch showed acceptable agreement for all heaters. Measurements of the OD of the wire wrap used on the heater rods was not measured. However, wire wrap diameter measurements were taken for all the wire wrapped non-heated tubes and both heaters and non-heated tubes used the same source wire material for wire wrapping. These measurements were very consistent and provided in Table 14.

2.1.4 End Cap and Transition Pieces

Both the lower transition collar and upper end cap are outside of the duct length of the test bundle, and therefore will most likely not be included in modeling efforts. However, visual inspection of the lower transition collars was performed for receipt acceptance. Inspection of the upper end cap included: visual inspection of the 12 o'clock mark on top end, caliper measurement of the distance from top of end cap to wire wrap attachment through-hole, and visual inspection of the clocking of the through-hole with respect to the 12 o'clock mark. The 12 o'clock mark is used during heater installation in the bundle to ensure all heaters and non-heated tubes are installed rotationally in phase. The location and clocking of the through-hole sets the wire wrap clocking. The lower transition collars and the upper end caps of all heaters were acceptable. Pictures of these components from one heater rod are shown below as an example.



Figure 2. Lower Transition Collar



Figure 3. Upper End Cap

2.2 Heater Functional Measurements

2.2.1 Heating Element

The heater rod consists of an internal cylindrical shaped heating element filled with insulation, then a layer of insulation, Monel k500 steel sheath and Monel k500 outer clad. Therefore, due to the internal location of the heating element, many of the measurements reported herein are from the contractor STERN Laboratories' Inspection Report: position, length, electrical resistance, and power profile. The final position of the heating element in the cladding is identified through use of a magnet to identify the nickel transition pieces that are used at the top and bottom of the element. During receipt inspections, this measurement was verified by TerraPower. However, reported herein are the values measured by STERN Laboratories. Measurements support that the heating element begins 1949.45 mm from the clad bottom.

The following table presents measurements as reported in the STERN Laboratories Inspection Report for heating element length and electrical resistance. As stated in the STERN Technical Specification [6], the electrical resistance is reduced slightly during swaging, and then this is recovered during the initial heat-up. Therefore these values are slightly low with respect to design specifications. However, STERN laboratories also measured resistances of the heating filaments before swaging and these were acceptable per the specification.

Table 3. STERN Heating Element Length Measurements

Tube ID	Heating Element Length (mm)	Electrical Resistance (Ω)
789-C-1	1698.00	1.8020
789-C-2	1700.00	1.8316
789-C-3	1714.00	1.8143
789-C-4	1699.00	1.8216
789-C-5	1700.00	1.8139
789-C-6	1698.00	1.8328
789-C-7 *	1701.00	1.8277
789-C-8	1699.00	1.8279
789-C-9 *	1702.00	1.8148
789-C-10	1702.00	1.8141
789-C-11	1700.00	1.8274
789-C-12	1702.00	1.7985
789-C-13	1700.00	1.8563
789-C-14	1703.00	1.8094
789-C-15	1703.00	1.8495
789-C-16	1710.00	1.8437
789-C-18	1705.00	1.8321
789-C-19 *	1704.00	1.8195
789-C-20	1702.00	1.8054
789-C-21	1705.00	1.8098
789-C-22	1702.00	1.8263
789-C-23	1709.00	1.8020

Average heating element Length	1702.64 mm
Range of heating element lengths	1698 – 1714 mm
Average Resistance	1.8218 Ω
Range of min to max resistance	1.7985 – 1.8563 Ω

* Spare heater rods: not used in these test experiments

Measurements were performed by STERN Labs on the heating elements before installation into the heaters. These included incremental resistances along the length of the heating elements, and power profiles measurements. The specified power profile is a cosine shaped curve with allowable ±5% at any given point. Incremental resistance measurements were taken at 10 axial locations for each heater rod. All heater rod power measurements were acceptable. These measurements are provided in the Appendix B.

The heat flux profile as measured by STERN Labs was averaged for all heater rods and was fit to a curve across the heated length averaged for all heater rods as measured by STERN Labs.

Table 4. As-Measured Heater Power Profile

Parameter	Value	Notes
Heater Power Profile	$f(x) = Ax^4 + Bx^3 + Cx^2 + Dx + E$	Fit 4th order polynomial to STERN average measured values [3]. Where x is the elevation and 0 ≤ x ≤ 1.70264 m A = 4.408017E-1; B = -1.564781E+0; C = 2.536355E-1; D = 1.935061E+0; E = 2.969667E-1

2.2.2 Heater Rod Thermocouples

Each of the heater rods has 8 or 9 internal thermocouples that are embedded between the sheath and the outer clad. The locations of these thermocouples was specified in the Test Specification, and were verified after fabrication through use of a solder iron. Three types of heater rods were used. The heater rods were the same in heater element design, but differed in thermocouple instrumentation specification. Table 5 records STERN heater number and type.

Table 5. Heater Rod Type

Heater Type	Heater Number (STERN Numbering)
Standard Heater	01 – 12, 16, 21, 23
Azimuthal Heater	13, 14, 18, 19, 22
Axial Heater	15, 20

The following table presents the results for these location verification measurements. During measurement it was found that the labeling of some pairs of thermocouples was switched: these have been identified as such in the table below. These measurements were performed by TerraPower following receipt of the heater rods and reported below. The tables have been split by heater rod type, and also by axial and clocking position of the thermocouples. Aside from the labeling errors, and a single rod that needed some physical re-work on the end cap rotation, all measurements for thermocouple measurements were acceptable.

Table 6. As-Built Standard Heater Rod Thermocouple Axial Positions

	Measurement of TC from top of heater rod (color corresponds to wire labeling) (inches)							
STERN Number	Orange	Purple	Black	Green	Yellow	Blue	Gray	Red
1	89.5625	89.5625	89.5625	73.6875	73.6875	47.5	47.5	47.5
2	89.5625	89.5625	89.5625	73.6875	73.6875	47.5	47.5	47.5
3	89.5625	89.5625	89.5625	73.6875	73.6875	47.5	47.5	47.5
4	89.6875	89.6875	89.6875	73.6875	73.6875	47.5625	47.5625	47.5
5 ‡	89.75	89.75	89.75	73.8125	73.8125	47.625	47.625	47.625
6 ‡	89.75	89.75	89.75	73.8125	73.8125	47.75	47.75	47.75
7 *	89.5625	89.625	89.625	73.6875	73.625	47.5	Not Measured	47.5
8	89.5625	89.5625	89.5625	73.6875	73.6875	47.5	47.5	47.5
9 *	89.5625	89.5625	89.5625	73.75	73.75	47.5	47.5	47.5
10	89.625	89.625	89.625	73.6875	73.625	47.5	47.5	47.5625
11 ‡	89.75	89.75	89.75	73.875	73.875	47.625	47.625	47.625
12 ‡	89.75	89.75	89.75	73.8125	73.8125	47.625	47.625	47.625
16	89.625	89.625	89.625	73.6875	73.6875	47.5	47.5625	47.5
21 ‡	89.75	89.75	89.75	73.875	73.875	47.625	47.625	47.625
23	89.625	89.625	89.625	73.625	73.6875	47.5	47.5	47.5625

‡ These heater rods were shipped prior to the balance of the heater rods and these TerraPower measurements were taken on an earlier date.

Table 7. As-Built Azimuthal Heater Rod Thermocouple Axial Positions

	Measurement of TC from top of heater rod (color corresponds to wire labeling) (inches)							
STERN Number	Orange	Purple	Black	Green	Yellow	Blue	Gray	Red
13	89.625	73.75	73.75	73.75	73.75	89.5625	Not Measured	73.75
14	89.5625	73.75	73.6875	73.75	73.6875	89.5625	73.75	73.75
18	89.6875	73.6875	73.8125	73.75	73.625	89.6875	73.8125	73.75
19 *	89.6875	73.75	73.6875	73.75	73.75	89.625	73.75	73.75
22	89.5625	73.75	73.75	73.6875	73.6875	89.5625	73.75	73.75

Table 8. As-Built Axial Heater Rod Thermocouple Axial Positions

	Measurement of TC from top of heater rod (color corresponds to wire labeling color) (inches)								
STERN Number	Orange	Purple	Black	Green	Yellow	Blue	Gray	Red	White
15	89.5625	87.6875	102.625	76.5	64.375	52.1875	Not Measured	114.8125	91.5
20	89.5625	87.75	102.75	76.5	64.375	52.25	42.125	114.875	91.5

Clocking position measurements of the thermocouples were primarily measured as Acceptable or Not, or with additional notes of deviations from the test specification design. The following table presents the as-designed clocking positions for each thermocouple of the three heater types identified with the color of their label which corresponds to the previous tables. Most of the clocking positions of the heater rod thermocouples were acceptable and consistent with the as-designed locations. These clocking positions are from the perspective of looking upward from the bottom of the heater. The 12 o'clock mark is consistent with the mark on the top of the end cap, and as installed is pointing at to the duct corner between duct faces A and F. This results in most of the thermocouples being either directly behind the wire wrap or 30° off of the wire wrap on each side.

Table 9. As-Designed Thermocouple Clocking Positions

	Design of Clocking Position of Thermocouples looking Upward from the Bottom (color corresponds to wire labeling)								
Heater Type	Orange	Purple	Black	Green	Yellow	Blue	Gray	Red	White
Standard	12	1	11	4	6	8	9	10	N/A
Azimuthal	12	1	11	3	5	6	7	9	N/A
Axial	12	1	10	2	3	4	5	9	11

As-built thermocouple clocking positions were consistent with as-designed specifications for most heater rods. The table below presents explanation for the pins with deviations from the as-designed specification. Three of these were not used in the test bundle. Labeling issues are minor in that traceability is provided here. Heater rod #7 was re-worked to bring the clocking rotation in conformance and consistency with the Test Specification.

Table 10. Non-Conformance of Heater Rod Thermocouple Clocking Positions

STERN Number	Non-conformance from as-designed and additional explanation
7 *	In conformance. Upon receipt it was found TC clocking locations were rotated by 30°. Chris Love (IV Labs) re-worked heater to rotate end cap by cutting and re-welding the endcap so TC clocking locations are consistent with design.
9 *	Swapped TC labeling: TC orange and purple are switched; green and yellow are switched; blue and gray switched.
14	TC purple: measurement recorded that it was measured between clocking positions 1 and 2 (as opposed to directly on 1 o'clock). This could also be due to measurement uncertainty of the method.
19 *	Swapped TC labeling: TC green and yellow switched; gray and red switched.

3 NON-HEATED TUBE AS-BUILT MEASUREMENTS

65 non-heated tube were fabricated by Intellectual Ventures Labs. These tubes were divided into 5 separate types that had unique instrumentation fabrication. Of the 65 tubes, 46 were sent to AREVA Fuels for use in the experiment pin bundle. The others were used for fit-up testing of the pin bundle in the fabricated ducts at IV Labs. Below describes the different types of non-heated tubes.

Table 11. Non-Heated Tube Types

Tube Type	Qnty	Description
A	21	Instrumented with 6 thermocouples each embedded into outer wall surface
B	16	Tubes without any instrumentation
B – used for fit-up testing	19	Non-instrumented tubes that were used in fit up testing only. The as-built measurements reported in this section do not differentiate these tubes used for fit-up testing, and those type B used in the final bundle.
C	4	Instrumented with an internal pressure tube and tap for bundle internal pressure measurements. These 4 had the same clocking and height position.
D	4	Instrumented with an internal pressure tube and tap for bundle internal pressure measurements. These 4 had the same clocking and height position which was different from type C tubes.
E	1	Instrumented with 7 outer wall TCs. 6 TCs correspond to locations consistent with Type A tubes, and a 7th near the tube bottom to measure bundle inlet temperatures.

Similar to the heater rods, these tubes consisted of an upper end cap, a larger diameter section for the bulk of the axial length, and a necked down diameter section. Since these were not heated, they did not contained a lower copper conductor. In addition, instead of a transition collar from the larger to smaller diameter sections, a butt weld was performed connecting the raw tubing of these two diameter sections.

One primary difference with respect to the STERN heaters was that a slightly different diameter tube was used for the nominal section length tubing. To accommodate the use of off-the-shelf tubing, 3/8" OD tubing was used. This is slightly different from the 9.5 mm OD sizing of the heater rods, however 3/8" is within the diameter acceptable tolerance range for the heater rods. These tubes were fabricated from SS304. Mill report for the nominal diameter section is provided in Appendix C. Reported herein are the dimensional and functional measurements of the as-built parts.

3.1 Non-Heated Tube Dimensional As-Built Measurements

Fabrication consisted of welding the nominal diameter, necked diameter and upper end cap portions together and then wire wrapping. Measurements reported herein include both measurements taken of the base components before fabrication and after assembly fabrication. Before-fabrication measurements include OD measurements of the tubing material used for the nominal diameter sections. Following fabrication, diameter measurements of the smaller necked diameter section, length measurements and wire wrap pitch measurements were taken.

3.1.1 Non-Heated Tube Diameter Measurements

The non-heated tubes were fabricated from 20 foot long 3/8" OD x 0.065" ID stainless steel tubing sections. Spare tubing was purchased and the 46 tubes that gave the tightest average OD diameter range were selected for use in the final pin bundle. Three outer diameter measurements were taken for each tube: approximately 1 foot from the top, 1 foot from the bottom, and the axial middle of the tube. ID measurements were not taken. Reported here are the measurement values for the 46 tubes used for the non-heated tubes in the pin bundle. These measurements were taken of the raw tubing before non-heated tube fabrication. Measurements were taken with the Terrapower calibrated caliper. Since only the 46 tubes that gave the tightest average OD diameter were used, the tube number below corresponds to the tube number out of the original total set purchased and was used during receipt inspections but was not used further. The individual tubes below were not traced to their final tube type use (ie Type A, Type B, etc) or installation position in the bundle. OD measurements were also taken of the Type B tubes that were only used for fit-up testing to ensure a tight OD diameter range during the fit-up testing. These measurements are not reported as these tubes were not used in the final test bundle. The Table Item Number in the table below is provided for convenience to provide total count.

Table 12. Non-Heated Tube Nominal Section OD Measurements

Table Item Number	Tube Number	Measure 1 (in)	Measure 2 (in)	Measure 3 (in)	Ave (in)	St Dev (in)
1	1	0.3765	0.377	0.3765	0.376667	0.000289
2	3	0.3765	0.377	0.3765	0.376667	0.000289
3	5	0.3775	0.377	0.376	0.376833	0.000764
4	8	0.377	0.3775	0.3765	0.377	0.0005
5	10	0.376	0.377	0.378	0.377	0.001
6	12	0.3765	0.3765	0.378	0.377	0.000866
7	15	0.377	0.3765	0.377	0.376833	0.000289
8	19	0.377	0.377	0.377	0.377	0.0

9	22	0.377	0.377	0.377	0.377	0.0
10	23	0.3775	0.376	0.3765	0.376667	0.000764
11	26	0.377	0.377	0.3765	0.376833	0.000289
12	29	0.377	0.377	0.377	0.377	0.0
13	30	0.377	0.377	0.377	0.377	0.0
14	33	0.377	0.3765	0.377	0.376833	0.000289
15	34	0.377	0.3765	0.3775	0.377	0.0005
16	42	0.3775	0.376	0.377	0.376833	0.000764
17	43	0.377	0.3765	0.377	0.376833	0.000289
18	44	0.377	0.377	0.377	0.377	0.0
19	46	0.376	0.3775	0.377	0.376833	0.000764
20	50	0.377	0.3765	0.377	0.376833	0.000289
21	52	0.377	0.377	0.377	0.377	0.0
22	58	0.377	0.377	0.3765	0.376833	0.000289
23	59	0.3765	0.377	0.377	0.376833	0.000289
24	61	0.377	0.3765	0.3765	0.376667	0.000289
25	64	0.3775	0.377	0.376	0.376833	0.000764
26	65	0.377	0.377	0.376	0.376667	0.000577
27	66	0.377	0.377	0.3765	0.376833	0.000289
28	68	0.3765	0.377	0.377	0.376833	0.000289
29	69	0.376	0.377	0.377	0.376667	0.000577
30	72	0.377	0.377	0.377	0.377	0.0
31	76	0.3765	0.377	0.377	0.376833	0.000289
32	77	0.377	0.3765	0.377	0.376833	0.000289
33	78	0.377	0.377	0.3765	0.376833	0.000289
34	79	0.377	0.376	0.377	0.376667	0.000577
35	80	0.377	0.377	0.376	0.376667	0.000577
36	81	0.3775	0.3765	0.376	0.376667	0.000764
37	86	0.378	0.377	0.376	0.377	0.001
38	87	0.377	0.376	0.377	0.376667	0.000577

39	90	0.377	0.377	0.377	0.377	0.0
40	91	0.377	0.3765	0.377	0.376833	0.000289
41	94	0.377	0.3765	0.3765	0.376667	0.000289
42	96	0.377	0.376	0.377	0.376667	0.000577
43	97	0.377	0.3765	0.377	0.376833	0.000289
44	98	0.3765	0.3765	0.377	0.376667	0.000289
45	99	0.377	0.3765	0.3765	0.376667	0.000289
46	100	0.3765	0.377	0.3775	0.377	0.0005

Overall Average Tube Diameter	0.3768 in
Range of all diameter measurements	0.3760 – 0.3780 in
Range of Non-heated tube average diameter values	0.3767 – 0.3770 in

The smaller diameter tubing measurement was performed after fabrication and wire wrapping. Measurements were taken 2” above the bottom of the section, and 2” below the transition weld between tubes of different diameter. The reported measurements below are reported for all Type B tubes: both those used in the pin bundle, and those only used in fit up testing. Because this part of the tube is outside the duct region, traceability of the Type B tubes in the list below that were used in the bundle and those used for fit-up testing was not kept. Measurements were taken with the TerraPower calibrated caliper. Numbering below was only used during measurement. The Table Item Number in the table below is provided for convenience to provide total count.

Table 13. Non-Heated Tube Necked Section OD Measurements

Table Item Number	Type	Measurement 1 (mm)	Measurement 2 (mm)	Ave Measurement
1	Type A	7.86	7.87	7.865
2	Type A	7.88	7.88	7.88
3	Type A	7.87	7.88	7.875
4	Type A	7.87	7.86	7.865
5	Type A	7.86	7.86	7.86
6	Type A	7.87	7.87	7.87
7	Type A	7.88	7.88	7.88
8	Type A	7.88	7.87	7.875
9	Type A	7.88	7.88	7.88
10	Type A	7.88	7.89	7.885

11	Type A	7.87	7.87	7.87
12	Type A	7.85	7.86	7.855
13	Type A	7.88	7.88	7.88
14	Type A	7.86	7.86	7.86
15	Type A	7.85	7.86	7.855
16	Type A	7.87	7.86	7.865
17	Type A	7.87	7.88	7.875
18	Type A	7.88	7.88	7.88
19	Type A	7.87	7.88	7.875
20	Type A	7.88	7.88	7.88
21	Type A	7.88	7.88	7.88
22	Type E	7.83	7.84	7.835
23	Type B	7.86	7.87	7.865
24	Type B	7.84	7.85	7.845
25	Type B	7.86	7.85	7.855
26	Type B	7.88	7.88	7.88
27	Type B	7.87	7.88	7.875
28	Type B	7.88	7.86	7.87
29	Type B	7.87	7.88	7.875
30	Type B	7.87	7.87	7.87
31	Type B	7.87	7.87	7.87
32	Type B	7.87	7.88	7.875
33	Type B	7.88	7.88	7.88
34	Type B	7.88	7.88	7.88
35	Type B	7.87	7.87	7.87
36	Type B	7.86	7.85	7.855
37	Type B	7.87	7.86	7.865
38	Type B	7.87	7.88	7.875
39	Type B	7.88	7.88	7.88

40	Type B	7.86	7.86	7.86
41	Type B	7.87	7.85	7.86
42	Type B	7.86	7.86	7.86
43	Type B	7.87	7.86	7.865
44	Type B	7.86	7.87	7.865
45	Type B	7.85	7.85	7.85
46	Type B	7.86	7.85	7.855
47	Type B	7.84	7.84	7.84
48	Type B	7.86	7.87	7.865
49	Type B	7.85	7.85	7.85
50	Type B	7.86	7.88	7.87
51	Type B	7.88	7.87	7.875
52	Type B	7.84	7.86	7.85
53	Type B	7.86	7.86	7.86
54	Type B	7.85	7.87	7.86
55	Type B	7.88	7.88	7.88
56	Type B	7.85	7.86	7.855
57	Type B	7.86	7.87	7.865
58	Type C	7.86	7.85	7.855
59	Type C	7.85	7.83	7.84
60	Type C	7.86	7.88	7.87
61	Type C	7.84	7.83	7.835
62	Type D	7.83	7.86	7.845
63	Type D	7.85	7.87	7.86
64	Type D	7.82	7.83	7.825
65	Type D	7.85	7.84	7.845

Overall Average of Smaller Diameter Tubing Diameter	7.8645 mm
Range of All smaller diameter measurements	7.82 – 7.89 mm
Range of Ave Small Diameter Values	7.825 – 7.885 mm

Measurements of the wire wrap diameter were performed following fabrication and wire wrapping. Two measurements were taken for the wire wrap of each rod: 1’ below the upper through hole, and 1’ above the lower weld location. Measurements were taken with the TerraPower calibrated caliper. The Table Item Number in the table below is provided for convenience to provide total count.

Table 14. Non-Heated Tube Wire Wrap Measurements

Table Item Number	Type	Measurement 1 (mm)	Measurement 2 (mm)	Ave Measurement
1	Type A	1.71	1.71	1.71
2	Type A	1.71	1.72	1.715
3	Type A	1.73	1.72	1.725
4	Type A	1.73	1.71	1.72
5	Type A	1.72	1.70	1.71
6	Type A	1.71	1.72	1.715
7	Type A	1.71	1.72	1.715
8	Type A	1.72	1.72	1.72
9	Type A	1.71	1.71	1.71
10	Type A	1.71	1.71	1.71
11	Type A	1.72	1.72	1.72
12	Type A	1.71	1.72	1.715
13	Type A	1.71	1.71	1.71
14	Type A	1.71	1.71	1.71
15	Type A	1.71	1.71	1.71
16	Type A	1.71	1.71	1.71
17	Type A	1.71	1.72	1.715
18	Type A	1.71	1.71	1.71
19	Type A	1.71	1.71	1.71
20	Type A	1.72	1.71	1.715
21	Type A	1.71	1.71	1.71
22	Type E	1.72	1.70	1.71
23	Type B	1.71	1.71	1.71
24	Type B	1.68	1.67	1.675

25	Type B	1.71	1.70	1.705
26	Type B	1.71	1.71	1.71
27	Type B	1.70	1.71	1.705
28	Type B	1.71	1.70	1.705
29	Type B	1.71	1.70	1.705
30	Type B	1.70	1.69	1.695
31	Type B	1.71	1.70	1.705
32	Type B	1.70	1.71	1.705
33	Type B	1.71	1.71	1.71
34	Type B	1.70	1.70	1.70
35	Type B	1.71	1.70	1.705
36	Type B	1.70	1.70	1.70
37	Type B	1.70	1.69	1.695
38	Type B	1.71	1.71	1.71
39	Type B	1.70	1.71	1.705
40	Type B	1.69	1.70	1.695
41	Type B	1.71	1.70	1.705
42	Type B	1.71	1.72	1.715
43	Type B	1.71	1.69	1.70
44	Type B	1.71	1.71	1.71
45	Type B	1.70	1.69	1.695
46	Type B	1.70	1.69	1.695
47	Type B	1.69	1.70	1.695
48	Type B	1.69	1.69	1.69
49	Type B	1.70	1.69	1.695
50	Type B	1.70	1.70	1.70
51	Type B	1.70	1.70	1.70
52	Type B	1.71	1.70	1.705
53	Type B	1.71	1.71	1.71

54	Type B	1.70	1.71	1.705
55	Type B	1.70	1.69	1.695
56	Type B	1.68	1.70	1.69
57	Type B	1.71	1.70	1.705
58	Type C	1.71	1.72	1.715
59	Type C	1.71	1.71	1.71
60	Type C	1.69	1.71	1.70
61	Type C	1.71	1.7	1.705
62	Type D	1.72	1.71	1.715
63	Type D	1.7	1.71	1.705
64	Type D	1.71	1.71	1.71
65	Type D	1.69	1.71	1.70

Overall Average of Wire Wrap Diameter measurements	1.7062 mm
Range of All Wire wrap Diameter Measurements	1.67 – 1.73 mm
Range of Average Wire Wrap diameter values	1.675 – 1.725 mm

3.1.2 Non-Heated Tube Length Measurements

Measurements were taken of the non-heated tube length consisting of total length and the length of the nominal diameter section measurements. The nominal diameter section length goes from the top of the end cap to the top of the transition weld to the smaller diameter tubing. These measurements were performed with a tape measure. These values are given below. Tube numbering in Table 15 below corresponds to the numbering in Table 14. The Table Item Number in the table below is provided for convenience to provide total count.

Table 15. Non-Heated Tube Length Measurements

Table Item Numbering	Type	Total length (in)	Length of Nominal Diameter Section (in)
1	Type A	200	180.25
2	Type A	200	180.25
3	Type A	200	180.25

4	Type A	200	180.25
5	Type A	200	180.25
6	Type A	200	180.25
7	Type A	200	180.25
8	Type A	200	180.25
9	Type A	200	180.25
10	Type A	200	180.25
11	Type A	200	180.25
12	Type A	200	180.25
13	Type A	200	180.25
14	Type A	200	180.25
15	Type A	200	180.25
16	Type A	200	180.25
17	Type A	200	180.25
18	Type A	200	180.25
19	Type A	200	180.25
20	Type A	200	180.25
21	Type A	200	180.25
22	Type E	200	180.25
23	Type B	200	180.25
24	Type B	200	180.25
25	Type B	200	180.375
26	Type B	200	180.375
27	Type B	200	180.25
28	Type B	200	180.25
29	Type B	200	180.375
30	Type B	200	180.375
31	Type B	200	180.25
32	Type B	200	180.25

33	Type B	200	180.25
34	Type B	200	180.375
35	Type B	200	180.25
36	Type B	200	180.25
37	Type B	200	180.25
38	Type B	200	180.25
39	Type B	200	180.25
40	Type B	200	180.25
41	Type B	200	180.25
42	Type B	200	180.25
43	Type B	200	180.375
44	Type B	200	180.25
45	Type B	200	180.25
46	Type B	200	180.25
47	Type B	200	180.25
48	Type B	200	180.25
49	Type B	200	180.25
50	Type B	200	180.25
51	Type B	200	180.25
52	Type B	200	180.25
53	Type B	200	180.375
54	Type B	200	180.25
55	Type B	200	180.25
56	Type B	200	180.25
57	Type B	200	180.25
58	Type C	200	180.125
59	Type C	200	180.5
60	Type C	200	180.25
61	Type C	200	180.25

62	Type D	200	180.5
63	Type D	200	180.375
64	Type D	200	180.25
65	Type D	200	180.25

Overall Average of Total length	200.0 in
Range of Total Length Measurements	200.0 in
Overall Average of Nominal Diameter Section Length	180.2712 in
Range of Nominal Diameter Section lengths	180.125 – 180.5 in

3.1.3 Non-Heated Tube As-Fabricated Wire Wrapping Measurements

Following fabrication, visual inspection was performed of the wire wrapping. This included both to ensure wire wrap direction and also the wire wrap pitch. All non-heated tubes had their wire wrap the correct direction (clockwise from bottom to top viewpoint) per the Test Specification. The wire wrap pitch as specified was 11.22". A verification cradle was used in which the wire wrapped tube was placed into it and the as-designed pitch intervals were identified. Wire wrap pitch showed acceptable agreement for all tubes, except a single Type C tube showed larger wire wrap pitch (less than 1.0" greater than specified) near the lower end of the tube for 3 pitches. However, this section of tubing with this deviation is in the entrance region and therefore is not expected to negatively affect the flow field in the measurement region.

3.2 Non-Heated Tube Functional Measurements

Type A non-heated tubes were instrumented with 6 thermocouples each. These thermocouples were embedded in the outer tube wall to measure the fluid temperature with the leads running downward through the inside of the tube. The figure below is an example of the configuration of the thermocouples in as-fabricated non-heated tubes.



Figure 4. As-Installed Non-Heated Tube Thermocouples

The 6 thermocouples were placed at 3 different axial locations, and at each of the heights the two thermocouples were 60° from each other which corresponds to 30° to each side of the wire wrap. Measurements were taken with a tape measure to ensure consistency of axial location with respect to the Test Specification. Clocking of the thermocouples was checked visually with respect to the end cap. The end cap has an engraved mark that sets the 12 o'clock position. All Type A non-heated tube thermocouples were acceptable and consistent with the Test Specification. The single Type E non-heated tube has the same position configuration for 6 thermocouples like Type A tubes, but also has an additional thermocouple at the bottom. Location of this was consistent with the Test Specification. Below are the values from the Test Specification for which confirmatory measurements were taken. These measurements were taken from the top of the heater rod looking downward (which is different from as-specified in the Test Specification).

Table 16. Non-Heated Tube Thermocouple Location Measurements

Thermocouple Label	Length from top of end cap to TC (in)	TC clocking position looking downward (end cap mark at 12 o'clock)
A1	47.49	4
A2	47.49	2
B1	73.67	8
B2	73.67	6
C1	89.57	1
C2	89.57	11
Type E Extra TC	166.93	6

Type C and Type D non-heated tubes had a single pressure tap of 0.030" each in its outer wall that was connected to a pressure tube that ran down the middle of the tube. Measurements were taken with a tape measure and clocking verified visually using the end cap engraved mark as a reference. All Type C and D non-heated tube pressure tap locations were acceptable and consistent with the Test Specification as provided below.

Table 17. Non-Heated Tube Pressure Tap Location Measurements

Pressure Tap	Length from top of end cap to pressure tap (in)	TC clocking position looking downward (end cap mark at 12 o'clock)
Type C Rod Tap	89.57	9
Type D Rod Tap	47.49	9

Additional detail of the thermocouple locations with respect to the as-installed bundle configuration and positioning is presented in Section 6.2.2.

4 NON-DEFORMED DUCT AS-BUILT MEASUREMENTS

Dimensional and instrumentation as-built measurements were taken of the non-deformed duct.

4.1 Non-Deformed Duct Dimensional Measurements

The duct consists of 4 axial sections where each axial section consists of 2 clam shell sides that are bolted together to form the hexagonal duct. These 4 sections are then bolted together axially to form the duct. The figure below shows a single axial section of the duct showing the two clam-shell sides bolted together. The seam between sides of the clam-shells intersects two of the internal hexagonal duct flow area faces. For each individual clam shell, measurements of the flat-to-flat dimensions were taken at each axial end.



Figure 5. Non-Deformed Duct Single Axial Section

Length measurements for each axial sections were taken following bolting together of the clam-shell sides. Following assembly of the complete duct (all 8 sections), flat-to-flat measurements were taken near each axial end for the flat-to-flat dimensions that span across the clam shell seam. The figure below is a picture of the assembled duct with all 8 sections during pressure testing.



Figure 6. Complete Non-Deformed Duct

Measurements were consistent with the design drawings. For the total duct length measurement, this was consistent with the Test Specification value of 166.5". For the duct inner flat-to-flat dimension measurements: these differed from the value in the Test Specification (Rev 2). In the Test Specification, the flat-to-flat dimension was proportional to the pin pitch, which came from the as-designed non-heated tube diameter. Upon measurement of the raw steel tubing diameters as reported in Table 12, the pin pitch value was updated corresponding to the as-built average non-heated tube diameter. This in turn updated the flat-to-flat dimension. This updated flat-to-flat dimension was used in the design drawings and the as-built measurements were consistent with this value. This flat-to-flat value is 3.622". Similarly, the radius of curvature for the duct corners was adjusted to 0.27" to be consistent with the updated flat-to-flat value.

The inner duct wall surface profile which for the non-deformed duct was a flat surface had a +/- 0.0012 inch tolerance. Following fabrication, the microscopic roughness was measured and found to be between 13- 18 microinch finish measured with a Mahr Pocket Surf profilometer.

4.2 Non-Deformed Duct Instrumentation Measurements

The non-deformed duct had pressure taps and was instrumented with thermocouples. Measurements were taken to confirm conformance with the Test Specification. All pressure taps were consistent as outlined in Table 13 of the Test Specification, except for tap #1. As stated in the Test Specification, the location as outlined may be obstructed by the lower duct flange. Therefore, in the design drawings, tap #1 is specified at an axial location of 40.2 mm from the duct bottom. The as-built location was consistent with this specification in the design drawings. Locations of the pressure taps are provided in tabular form for the final installed duct in Section 6.2.6.

The Test Specification initially defined that 24 thermocouples were specified to be installed along duct face E at the inner surface of the duct to measure the fluid temperature. The thermocouples were installed from outside the duct. Measurements were taken with tape measure to verify the as-installed axial locations of these thermocouples. Lateral positioning was verified by tape measure as well. Of the 24 specified thermocouples, only 22 were installed. The axial locations of the as-installed thermocouples at the inner duct wall surface were consistent with as-designed specifications as presented in Table 19 of the Test Specification. The lateral positions of the 22 installed thermocouples were consistent with the Test Specification. The exception from the Test Specification was at the axial heights of 2409.0 mm and 3074.0 mm (from the bottom of the complete duct), only 5 thermocouples were installed: the corner thermocouple was not installed at these heights. In addition to these thermocouples initially defined in the Test Specification, 2 additional thermocouples were installed near the duct entrance to measure inlet fluid temperature. Locations of internal duct thermocouples are provided in tabular form for the final installed duct in Section 6.2.4.

In addition to the thermocouples installed on the inner face of the non-deformed duct, thermocouples were installed on the outside surface of the duct. The locations of the external face thermocouples was changed following issuance of the Test Specification. All these thermocouples were attached on duct face E and the lateral midpoint between corners at 12 different heights. The following table gives the designed thermocouple locations with respect to the duct entrance. Numbering was only used in measurements.

Table 18. Non-Deformed Duct External Face Specified Thermocouple Locations

Thermocouple Number	Height from duct bottom (mm)	Height from duct bottom (in)
1	1767.5	69.59
2	1886.4	74.27
3	2005.2	78.95
4	2052.5	80.81
5	2171.4	85.49
6	2337.5	92.03
7	2409.0	94.84
8	2456.4	96.71
9	2622.5	103.25
10	2741.4	107.93
11	2907.5	114.47
12	3074.0	121.02

Thermocouple location measurements showed consistency with the table above with a few exceptions. The locations of thermocouples #3, 4, 7 and 12 are at the same locations as internal thermocouples and are therefore obstructed from installation at this point. For these locations the thermocouples were moved 1/8” below the specified location. The figure below gives an example of these thermocouples attached to the outside of the duct.



Figure 7. Non-Deformed Duct External Thermocouple

5 DEFORMED DUCT AS-BUILT MEASUREMENTS

Dimensional and instrumentation as-built measurements were taken of the deformed duct. Similar to the non-deformed duct, this duct was constructed of 8 separate clam-shell pieces that were bolted together both laterally and axially.

5.1 Deformed Duct Dimensional Measurements

Similar to the non-deformed duct, both flat-to-flat and axial measurements were taken. Axially measurements were taken separately for each of the 4 axial sections with a tape measure. All 4 measurements are consistent with the Test Specification value of 41.625” to 1/16” accuracy.

In the non-deformed duct, the inner duct faces are all flat. In the deformed duct, for some axial sections the inner duct faces bow outward creating a larger flow area with respect to the non-deformed duct. It should be noted that no actual deformation is occurring, but instead the instead faces are machined to give an inner face geometry profile that represents a deformed duct. The duct wall thickness was sized to ensure no material deformation occurs in this test duct. The deformation is defined as a curved surface in relation to the flat face design of the non-deformed duct as specified in the Test Specification. The curved surface is an interpolation of two curves that are both cosine in shape: one curve in the axial direction, the other in the lateral direction between duct face corners. This has the effect of enlarging and then returning to nominal the duct flow area. This deformation only occurs for axial duct sections #2 and #3: duct sections #1 and #4 are identical in shape to those of the non-deformed duct. Flat to flat dimensions of the axial duct sections #1 and #4 were measured with a tape measure. These were confirmed to be consistent with the Engineering Drawings and corresponds to a value of 3.622”.

The curves that define the deformation are provided in the Test Specification [1][4]. The curves are useful because they define the additional material that is machined from the inner duct face surface to make the deformed shape in relation to the flat faces of the non-deformed duct. The following illustrates and defines the deformation as used in the CAD model:

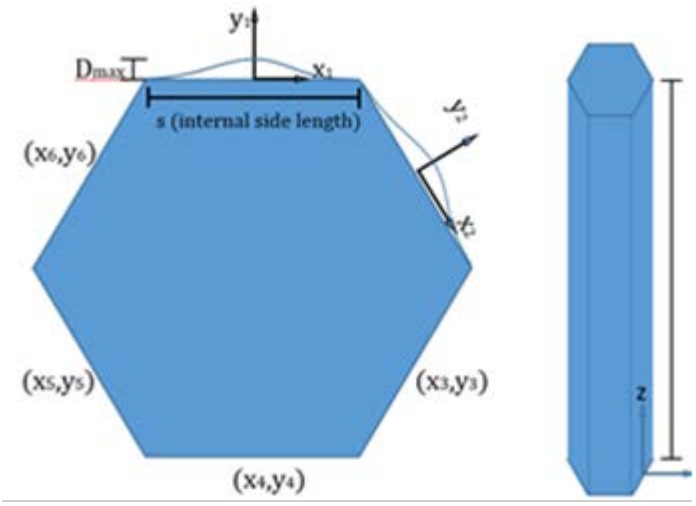


Figure 8. Deformed Duct Visual Representation

Table 19. Deformed Duct Values

Parameter	**Value**	**units**
Axial Curve	$y = D_{max} * \sin(\pi * z/1710)$	
Lateral Curve	$y = D_{max} * \left(\cos\left(\pi * \frac{x}{\left(\frac{s}{2}\right)} \right) + 1 \right)/2$	
x, y, z coordinate directions (with respect to dilation; unique for each duct face)	See image above	
D_{max}	1.08	mm
s (duct side length)	45.09	mm
Total dilation axial length	1710	mm
Beginning of Dilation (Axial Height from duct bottom)	1150.2	mm
End of Dilation (Axial Height from duct bottom)	2860.2	mm

The CAD software interpolates the two equations to produce a surface that defines the relative surface with respect to the non-deformed design. The value of 's' which defines the duct side length across which the lateral deformation occurs corresponds to the length of only the flat surface of the inner hex faces: it does not include the curved corner lengths.

As-built measurements of all of the clam-shell pieces were taken by the IV Laboratories Inspection Department to compare the as-built deformation with the CAD model of the designed deformation. These

measurements were taken with a FARO ScanArm, where a probe was run over the finished duct piece sections. The measurement technique creates a point cloud of thousands of measured points and then compares them to the CAD model. At each location a height difference between the as-built and the CAD model was calculated. For sections #1 and #4, this corresponded to the nominal straight walls of the hexagonal inner faces. For duct sections #2 and #3, this height difference included the axial and lateral shaped deformation curves. The Root Mean Square of all measurements taken for the height difference from the design value was 0.00347” (0.088 mm). This value does not consider any treatment of outlier measurements and is therefore conservative. The accuracy to the design specifications for the radius of curvature was included in this measurement and consistent with the specified value of 0.27”.

Following fabrication, the microscopic roughness was measured and found to be between 13 - 18 microinch finish measured with a Mahr Pocket Surf profilometer.

5.2 Deformed Duct Instrumentation Measurements

Similar to the non-deformed bundle, this bundle was instrumented with pressure taps and internal and external thermocouples. Measurements were taken by TerraPower to confirm the as-built locations of these thermocouples. Pressure tap locations were consistent with the Test Specification. These values corresponding to the as-installed bundle are provided in Section 6.2.7.

Internal duct thermocouples were consistent with the non-deformed duct: axial locations were consistent with the Test Specification. Similar to the non-deformed duct, two of the sets of thermocouples only had 5 thermocouples at the heights of 2409.0 mm and 3074.0 mm from the entrance of the complete duct as they were missing the corner thermocouple. Location values corresponding to the as-installed bundle are provided in Section 6.2.5. 2 additional thermocouples were installed near the duct entrance to measure fluid inlet temperature.

Final locations for the external duct thermocouples were measured by TerraPower. Following issuance of the Test Specification, the locations of the external duct thermocouples was changed. Table 18 provides the axial locations for these thermocouples with respect to the bottom of the duct. Measurements were taken by TerraPower to ensure consistency with the as-designed locations. All measurements were consistent with Table 18 except the locations that were obstructed by the internal duct thermocouple probes. Of these, thermocouples #3, 4, and 7 were installed 1/8” below the specified location and thermocouple 12 was installed 1/8” above the specified location. All thermocouples were installed at the lateral midpoint of duct face E.

6 AS INSTALLED CONFIGURATION

This section describes the installed configuration of the pin bundle and duct in the test loop. This section may have most direct application for the CFD analyst in their numerical model construction and extraction of results at the as-installed instrument locations. Section 6.1 presents the geometry of the as-installed bundle, and then Section 6.2 presents details of the as-installed instrumentation, including locations.

6.1 As-Installed Geometry

6.1.1 Bundle Geometry

As described above, the heaters and the pins are longer length than the duct. For final installation the pins pass through the duct and are attached to the loop both above and below the duct through the use of upper and lower tie plates. The duct also separately attaches to the loop, therefore the pins and the duct are not physically attached to each other.

Appendix D provides a drawing of the axial dimensions of the duct and pins in the loop. For the experiment, the length of the bundle can be considered to correspond to the duct length (166.5”).

The bundle contains an entrance region, a heated region, an additional measurement region and an exit region. Table 20 gives the axial lengths of these components. The sum of the entrance length, heated length, additional measurement length and exit length is consistent with the total duct length. The heated length corresponds to the average heater element length and location provided in Section 2.2.1. The heated axial power profile is provided in Section 2.2.1.

Table 20. As-Installed Axial Positioning

Parameter	Value	Reference in Relation to Duct	Reference in Relation to Heaters
Total Duct Length	166.5 in (4229.1 mm)	N/A	N/A
Entrance Length	45.65 in (1159.55 mm)	0 – 45.65 in (0 – 1159.55 mm)	31.12 – 76.77 in (790.45 – 1950 mm)
Heated Length	67.03 in (1702.64 mm)	45.65 – 112.68 in (1159.55 – 2862.19 mm)	76.77 – 143.80 in (1950.0 – 3652.64 mm)
Additional Measurement Length	22.78 in (578.55 mm)	112.68 – 135.46 in (2862.19 – 3440.74 mm)	143.80 – 166.58 in (3652.64 – 4231.19 mm)
Exit Length	31.04 in (788.36 mm)	135.46 – 166.5 in (3440.74 – 4229.1 mm)	166.58 – 197.62 in (4231.19 – 5019.55 mm)

Consistent with values provided in Sections 4.1 and 5.1, the duct flat to flat dimension is 3.622” with a corner radius of curvature of 0.27 in. Details of the deformed duct deformation shape is provided in Section 5.1. The duct sides are lettered A – F. This lettering is referenced for instrumentation locations and pin clocking specification. The image below shows the duct lettering as pins are inserted from above. As shown, the duct lettering is sequential in the counter-clockwise direction when looking downward at the duct and bundle from above.

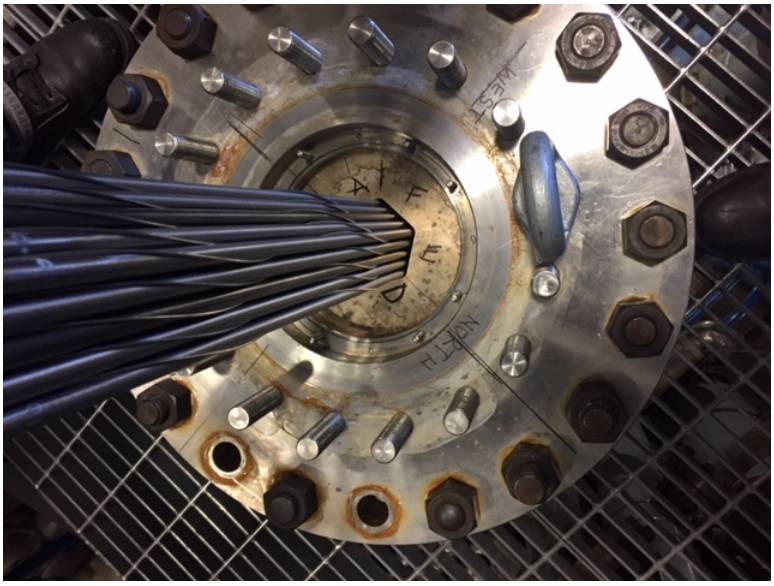


Figure 9. Duct Lettering View from Top

Heater diameters are provided in Table 1, with an average value given. Non-heated pin diameters are provided in Table 12, with an average value given. Wire wrap diameter values are given in Table 14, with an average value given. The wire wrap pitch (axial length for one wire wrap revolution around a pin) is 285.0 mm.

6.1.2 Pin Location Configuration in Bundle

The following picture shows the pin bundle installed with all end cap marks in-phase and pointing in the direction of the corner between duct faces A and F, as specified in the Test Specification. The end cap marks correspond to 12 o'clock with respect to the pin wire wrap and pin instrumentation clocking. Another reference for the pin wire wrap clocking that is more applicable to the numerical simulation analyst is that the wire wrap clocking is at 12 o'clock (pointing in direction of corner of duct faces A and F) 19.55 mm (0.77 in) above the duct entrance and again at 12 o'clock at the beginning of the heated length. The wire wrap rotates clockwise along the flow direction and has a wire wrap pitch length (axial length for one wire wrap revolution around a pin) of 285.0 mm.

Two values represent the pin to pin pitch, the first is the pin pitch as built in the upper tie plate in Figure 10 below. This value is 0.442 in (11.23 mm). This value corresponds to a tightly packed bundle using the original as-designed non-heated pin outer diameter and as-designed wire wrap diameter. As reported in Section 3.1.1, the average as-built non-heated pin diameter (0.3768 in) and average as-built wire wrap diameter (1.7062 mm) results in a tightly packed pin pitch of 0.44397 in (11.2769 mm), which is slightly larger than the as-designed pin pitch value. This value may be more representative of the pin pitch in the bundle. However, due to the long length of the pins and tube and heater flexibility, the pins have the ability to spread out laterally in the bundle during operation given the additional size of the wall subchannel gap.

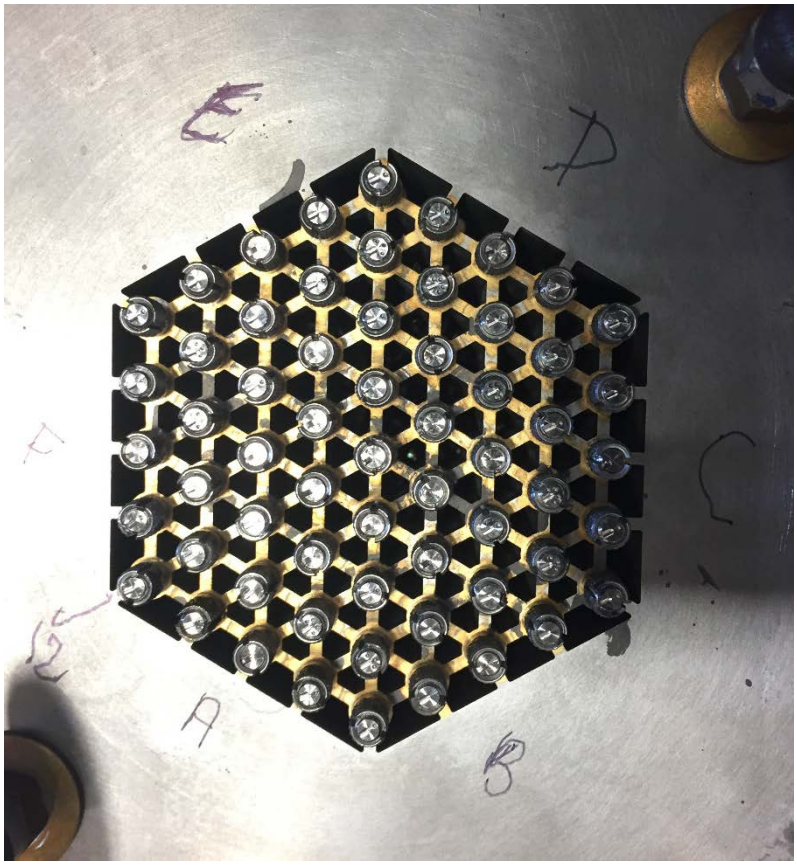


Figure 10. Installed Pin Bundle

As described in the Test Specification, the experiment used 19 heater rods and 42 non-heated tubes in the bundle. Figure 11 below provides the as-installed position configuration for both the non-deformed duct and deformed duct experiments looking upward at the bottom of the bundle. The numbering of the position map does not correspond to the STERN heater rod numbering. Table 21 below provides the cross-labeling between the position map (Figure 11) and STERN heater rod numbers (Table 1, Table 2, Table 3). The heater rod at position 17 failed and therefore is X-ed out in Figure 11. Traceability of specific non-heated tubes from fabrication to final installation location was not kept. However, Figure 11 does present locations for the different types of non-heated tubes.

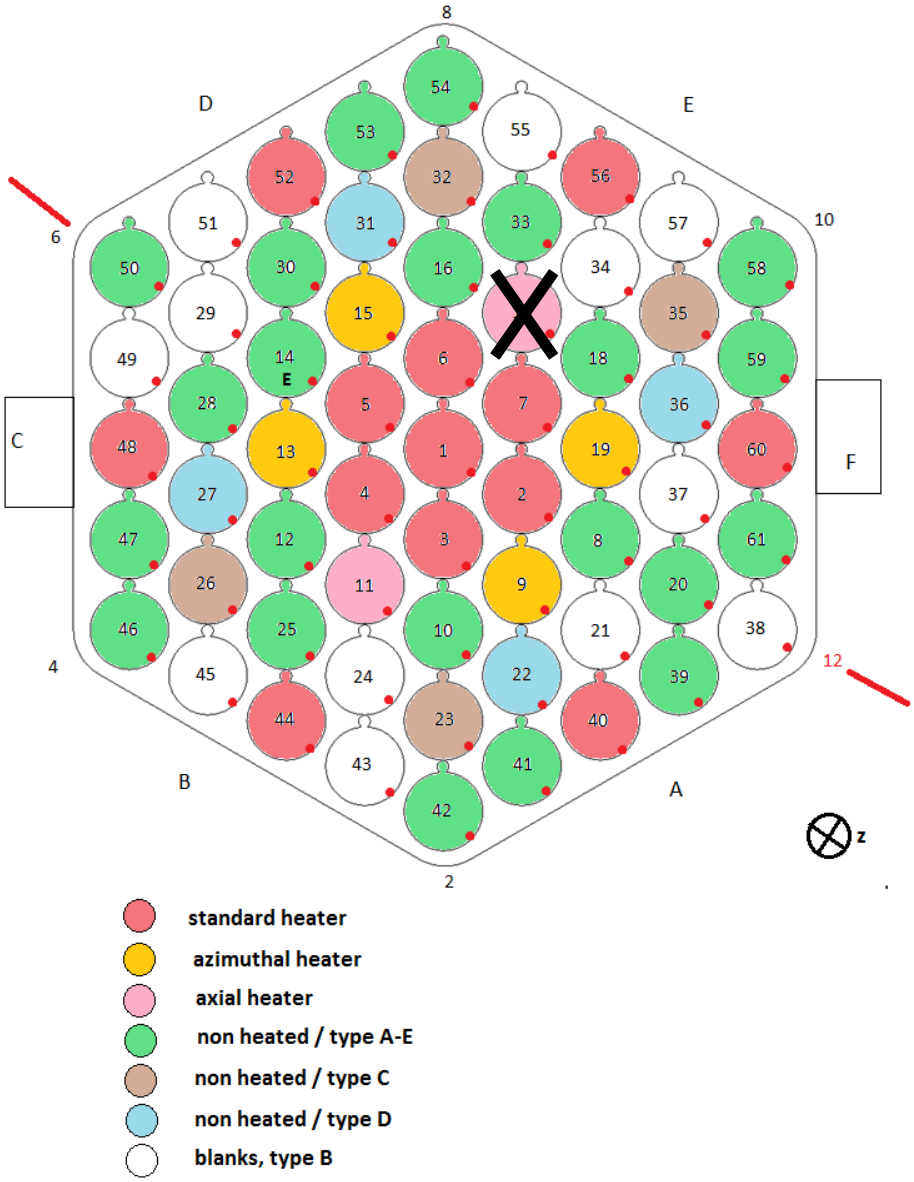


Figure 11. Heater Rod Position Map

Table 21. Heater Rod Numbering Cross-linking

Position Number in Figure 11	STERN Heater Serial Number
1	789-C-16
2	789-C-04
3	789-C-10
4	789-C-05
5	789-C-06
6	789-C-02
7	789-C-23
9	789-C-14
11	789-C-20
13	789-C-13
15	789-C-22
17	789-C-15
19	789-C-18
40	789-C-01
44	789-C-08
48	789-C-12
52	789-C-21
56	789-C-11
60	789-C-03

6.2 As-Installed Instruments

Both the non-deformed and deformed heated bundles were instrumented with thermocouples and pressure taps. All instrumentation in these bundles was attached to the bundle hardware components and therefore fixed in location and is reported in this As-Built Report. Both the non-deformed and deformed bundles used the same pin bundle, therefore pin instrumentation of thermocouples and pressure taps is applicable to both bundles.

6.2.1 Heater Rod Thermocouple Locations

Each heater rod was instrumented with special K-type (+/- 1.1 C uncertainty) thermocouples. The tables below provide the as-built location details for thermocouples for each different heater type. The Test

Specification document [1] provides details of the as-designed locations. This information is similar to that provided in Section 2.2.2, but from the reference of the duct entrance. These table correct for any thermocouple labeling errors reported in Section 2.2.2.

Table 22. Standard Heater Rod Thermocouple As-Built Locations

	Measurement of TC from Duct Entrance (color corresponds to wire labeling) (inches)							
STERN Number	Orange	Purple	Black	Green	Yellow	Blue	Gray	Red
1	79.32	79.32	79.32	95.19	95.19	121.38	121.38	121.38
2	79.32	79.32	79.32	95.19	95.19	121.38	121.38	121.38
3	79.32	79.32	79.32	95.19	95.19	121.38	121.38	121.38
4	79.19	79.19	79.19	95.19	95.19	121.32	121.32	121.38
5	79.13	79.13	79.13	95.07	95.07	121.26	121.26	121.26
6	79.13	79.13	79.13	95.07	95.07	121.13	121.13	121.13
8	79.32	79.32	79.32	95.19	95.19	121.38	121.38	121.38
10	79.26	79.26	79.26	95.19	95.26	121.38	121.38	121.32
11	79.13	79.13	79.13	95.01	95.01	121.26	121.26	121.26
12	79.13	79.13	79.13	95.07	95.07	121.26	121.26	121.26
16	79.26	79.26	79.26	95.19	95.19	121.38	121.32	121.38
21	79.13	79.13	79.13	95.01	95.01	121.26	121.26	121.26
23	79.26	79.26	79.26	95.26	95.19	121.38	121.38	121.32

Table 23. Azimuthal Heater Rod Thermocouple As-Built Locations

	Measurement of TC from Duct Entrance (color corresponds to wire labeling) (inches)							
STERN Number	Orange	Purple	Black	Green	Yellow	Blue	Gray	Red
13	79.26	95.13	95.13	95.13	95.13	79.32	Not measured	95.13
14	79.32	95.13*	95.19	95.13	95.19	79.32	95.13	95.13
18	79.19	95.19	95.07	95.13	95.26	79.19	95.07	95.13
22	79.32	95.13	95.13	95.19	95.19	79.32	95.13	95.13

Table 24. Axial Heater Rod Thermocouple As-Built Locations

	Measurement of TC from Duct Entrance (color corresponds to wire labeling color) (inches)								
STERN Number	Orange	Purple	Black	Green	Yellow	Blue	Gray	Red	White
15	79.32	81.19	66.26	92.38	104.51	116.69	Not measured	54.07	77.38
20	79.32	81.13	66.13	92.38	104.51	116.63	126.76	54.01	77.38

As-built thermocouple clocking is provided in Table 9. Clocking is referenced looking upward from the bottom of the heaters and the 12 o'clock position corresponds to the corner between duct faces A and F. As-built clocking for all thermocouples of all heater rods was consistent with these values except for the purple labeled thermocouple for heater rod 14. This as-built clocking location was measured between 1 and 2 o'clock instead of the specified 1 o'clock.

6.2.2 Non-Heated Tube Thermocouple Locations

22 of the 46 non-heated tubes were instrumented with special K-type (+/- 1.1 C uncertainty) thermocouples. 21 of the 22 thermocouple-instrumented non-heated tubes had thermocouples at the same positions: three axial heights with two thermocouples each. The final thermocouples-instrumented non-heated tube had the six thermocouples consistent in location as the others, and then an additional thermocouple at a lower axial height. This non-heated tube was at pin location #14 in Figure 11. The table below provides location details for thermocouples for the non-heated tubes. This is similar to presented in Section 3.2, but from the reference of the duct entrance, therefore thermocouple clocking is from the perspective of looking upwards from the bottom of the pin, which is opposite from that presented in Table 16.

Table 25. Non-Heated Tube As-Built Thermocouple Locations

Thermocouple Label	Length from Duct Entrance (in)	TC clocking position looking upwards from bottom of pin (12 o'clock at A-F duct corner)
A1	121.39 (3083.31mm)	8
A2	121.39 (3083.31mm)	10
B1	95.21 (2418.33mm)	4
B2	95.21 (2418.33mm)	6
C1	79.31 (2014.47mm)	11
C2	79.31 (2014.47mm)	1
Type E Extra TC	1.95 (49.53mm)	6

6.2.3 Non-Heated Pressure Tapped Tubes

Eight of the non-heated tubes were instrumented with 0.030” pressure taps. Four had pressure taps at a specific axial height, while the other four had pressure taps at a different axial height. Details of axial position and clocking. Positional specification of the as-built locations of these pressure taps is provided in the table below. This is similar to that provided in Section 3.2, but from the reference of the duct entrance, therefore tap clocking is looking upwards from the bottom of the bundle, which is opposite from Table 17. Locations of these pressure-tap instrumented non-heated tubes in the pin bundle is provided in Figure 11.

Table 26. Non-Heated Tube As-Built Pressure Tap Locations

Pressure Tap	Length from Duct Entrance (in)	Tap clocking position looking upwards from bottom (end cap mark at 12 o’clock)
Type C Rod Tap	79.31 (2014.47mm)	3
Type D Rod Tap	121.39 (3083.31mm)	3

6.2.4 Non-Deformed Duct Thermocouple Locations

The as-built non-deformed duct was instrumented with 24 internal duct wall thermocouples. These thermocouples were special K-type (+/- 1.1 C uncertainty) 1/16” thermocouples and positioned at the internal duct wall surface: they did not protrude into the duct flow area, but were mounted from outside the duct flush with the internal duct face. 22 of these were located at four axial heights with each height designed to have six thermocouples, however two heights only had five thermocouples installed, therefore for a total of 22 thermocouples. All six thermocouples were designed to be at the same lateral positions on the inner duct wall. All thermocouples were instrumented on duct face E. Figure 12 and Table 27 below present the lateral positions of these thermocouples. Table 27 uses an X coordinate system for convenience that spans across duct face E from corner to corner. The two heights that only had five thermocouples did not have thermocouples at the corner between duct faces D and E. Two additional thermocouples were installed at a lower height to measure the inlet fluid temperature. These were installed centered on duct faces A and E.

Table 27. Inner Duct Wall Thermocouple Lateral Positions

TC Number	Lateral Inner Duct Wall TC Locations
1	Perpendicular to outer duct surface at corner between duct faces D and E
2	X = +16.878 mm (0.665 in)
3	X = +5.626 mm (0.222 in)
4	Laterally centered on duct face E (X = 0.0 mm)
5	X = -5.626 mm (-0.222 in)
6	X = -16.878 mm (-0.665 in)

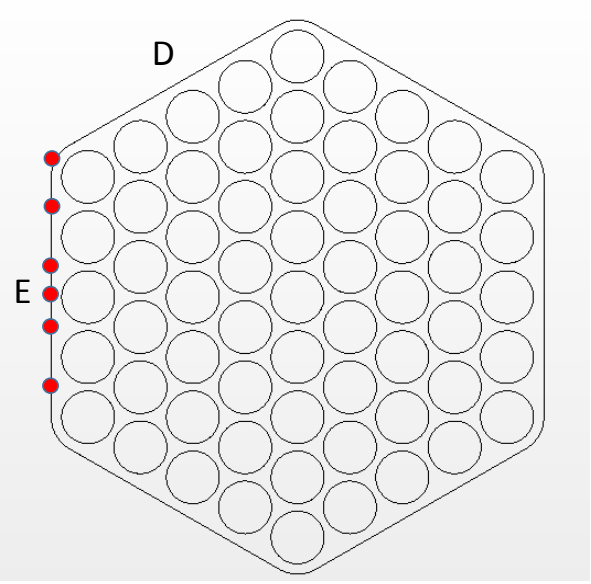


Figure 12. As-Built Internal Duct Wall Thermocouples

The tables below provides the axial locations for these thermocouples in reference to the duct entrance.

Table 28. As-Built Non-Deformed Duct Thermocouple Locations

Height from duct entrance (mm)	Number of TCs/ height
2005.2	6
2052.7	6
2409.0	5
3074.0	5
40.2	2 (Centered on duct faces A and E)

6.2.5 Deformed Duct Thermocouple Locations

Similar to the non-deformed duct, the deformed duct was instrumented with 24 internal duct wall thermocouples. These thermocouples were special K-type (+/- 1.1 C uncertainty) 1/16” thermocouples and positioned at the internal duct wall surface: they did not protrude into the duct flow area, but were mounted from outside the duct flush with the internal duct face. 22 of these were located at four axial heights with each height designed to have six thermocouples, however two heights only had five thermocouples installed, therefore for a total of 22 thermocouples. All six thermocouples were designed to be at the same lateral positions on the inner duct wall. All thermocouples were instrumented on duct face E. Figure 12 and Table 27 present the lateral positions of these thermocouples. The two heights that only had five thermocouples did not have thermocouples at the corner between duct faces D and E. The table below provides the axial locations for these thermocouples in reference to the duct entrance. Two additional thermocouples were installed at a lower height to measure the inlet fluid temperature. These were installed centered on duct faces A and E.

Table 29. As-Built Deformed Duct Thermocouple Locations

Height from duct entrance (mm)	Number of TCs/ height
2005.2	6
2052.7	6
2409.0	5
3074.0	5
40.2	2 (Centered on duct faces A and E)

6.2.6 Non-Deformed Duct Pressure Tap Locations

The non-deformed duct was fabricated with pressure taps at different locations for pressure drop measurements. Pressure taps were installed at different axial heights and different duct faces, however, all pressure taps were centered on the duct face between duct corners. The pressure taps were 1/8" NPT in diameter.

The table below provides the pressure tap locations from the reference of the duct entrance.

Table 30. As-Built Non-Deformed Duct Pressure Tap Locations

Pressure Tap Identifiers	Height from duct bottom (mm)	Duct Face of Pressure Tap (All taps were centered on duct face)
PT #1	40.2	Face B
PT #2	295.2	Face B
PT #3	390.2	Face B
PT #4	485.2	Face B
PT #5	580.2	Face B
PT #6	722.7	Face B
PT #7	865.2	Face B
PT #8	1007.7	Face B
PTs #9 – 12	1150.2	Faces A, B, D, E
PT #13	1292.7	Face B
PT #14	1435.2	Face B
PT #15	1720.2	Face B
PTs #16 – 18	2005.2	Faces A, B, D
PTs #19 - 21	2385.2	Faces A, B, E
PTs #22	2575.2	Faces B
PT #23	2860.2	Face B

PTs #24 – 26	3074.0	Faces A, B, D
PT #27 - 28	3430.2	Faces B, E
PT # 29 - 30	4000.2	Faces B, E

6.2.7 Deformed Duct Pressure Tap Locations

Similar to the non-deformed duct, the deformed duct was fabricated with pressure taps at different locations for pressure drop measurements. Pressure taps were installed at different axial heights and different duct faces, however, all pressure taps were centered on the duct face between duct corners. The pressure taps were 1/8” NPT in diameter. These pressure taps were located at the same positions as the non-deformed duct given in Table 30.

7 REFERENCES

[1] TWRP-31-TSPEC-0011-Rev-2, AFAFC AREVA Heated Bundle Experiment Test Specification, 2016.

[2] TWRP-31-FRD-0001-Rev-2, AFAFC Heated Bundle Heater Rod Specification, 2016

[3] TWRP-31-FRD-0002-Rev-1, AFAFC Non-Heated Tubes Specification, 2016

[4] TWRP-31-FRD-0003-Rev-2, AFAFC Duct Specification, 2016

[5] TWRP-31-FRD-0004-Rev-0, AFAFC Heater and Non-Heated Tube Wire Wrapping Requirements, 2015

[6] SLTS-89-Rev-1, Technical Specification (SLTS) for Design and Manufacture of Heater Rods for TerraPower, STERN Laboratories, 2015

8 APPENDIX A

This sections contains email from STERN Laboratories with values of heated clad ID and sheath ID.

Brian Jackson

From: [redacted]
Sent: Wednesday, November 18, 2015 3:13 AM
To: Tom Reeves
Cc: [redacted] Brian Jackson; Daniel Leonard
Subject: Re: Rod Characterization for Analysis

Tom,

Richard has provided me with the clad and sheath dimensions for the heated and unheated sections, see below. A typical contact resistance that I use which fits the test data reasonably well is 0.012 K.m^2/kW.

Best regards,

Rick

Final dimensions:

- Clad OD (Filament Region): 0.374"
- Clad ID (Filament Region): 0.335"
- Clad OD (Filament Region): 0.299"
- Clad ID (Electrode Region): 0.261"
- Sheath OD: 0.3407"
- Sheath ID: 0.267"

Specific Heat of the Clad (assume average temperature of 320 Deg. C): 490.4 J/(kg*degC)
Specific Heat of the Sheath (assume average temperature of 340 Deg. C): 492.6 J/(kg*degC)

Thermal Conductivity of the Clad (assume average temperature of 320 Deg. C): 25.8 W/(m*degC)
Thermal Conductivity of the Sheath (assume average temperature of 340 Deg. C): 26.3 W/(m*degC)

Density: 8.44 g/ cm^3

The material information was retrieved from the link below:

www.specialmetals.com/documents/**Monel** alloy **K-500**.pdf

9 APPENDIX B

This section contains STERN heating power profile measurements. These measurements were taken on the raw heating element parts, and therefore the heating element numbering does not correspond to the heater number. The following table presents the traceability.

Table 31. STERN Heating Element to Final Heater Numbering Reference

STERN Tube ID	Heating Element Number (tube number in Table 32)
789-C-1	27
789-C-2	1
789-C-3	4
789-C-4	7
789-C-5	10
789-C-6	13
789-C-7 *	15
789-C-8	16
789-C-9 *	18
789-C-10	30
789-C-11	33
789-C-12	36
789-C-13	12
789-C-14	21
789-C-15	34
789-C-16	32
789-C-18	31
789-C-19 *	29
789-C-20	28
789-C-21	26
789-C-22	35
789-C-23	17

Table 32. STERN Power Profile Measurements

Axial Power Profile Verification

Item No.	Tube No. 59622	Axial Location (%)									
		5.0%	15.0%	25.0%	35.0%	45.0%	55.0%	65.0%	75.0%	85.0%	95.0%
1	14	-0.009	-0.016	-0.011	-0.009	-0.004	0.001	-0.008	0.007	0.004	0.015
2	16	-0.008	-0.020	-0.011	-0.021	0.000	-0.002	-0.003	0.022	0.009	0.006
3	36	-0.018	-0.016	-0.016	-0.014	-0.012	-0.003	0.012	0.010	0.011	0.018
4	21	-0.006	-0.013	-0.016	-0.010	-0.007	0.013	0.004	-0.007	0.012	0.002
5	4	-0.009	-0.013	-0.006	-0.013	-0.012	0.010	-0.001	-0.002	0.015	0.002
6	27	-0.007	-0.017	-0.017	-0.004	-0.006	0.010	-0.002	0.000	0.013	0.001
7	18	-0.007	-0.018	-0.016	-0.009	0.008	-0.018	0.006	0.007	0.010	0.009
8	33	-0.008	-0.014	-0.014	-0.012	-0.004	0.001	-0.004	0.012	0.005	0.011
9	10	-0.018	-0.012	-0.016	-0.018	0.003	-0.009	0.007	0.014	0.004	0.015
10	13	-0.009	-0.020	-0.008	-0.012	-0.003	-0.005	0.004	-0.001	0.014	0.011
11	7	-0.015	-0.014	-0.009	-0.016	0.006	-0.006	-0.001	0.013	0.003	0.009
12	15	-0.019	-0.017	-0.018	-0.011	-0.009	0.001	0.008	0.007	0.009	0.019
13	1	-0.011	-0.013	-0.011	-0.005	-0.019	0.008	0.003	-0.004	0.011	0.012
14	30	-0.012	-0.014	-0.013	-0.013	-0.002	-0.005	0.004	0.005	0.011	0.011
15	35	-0.013	-0.021	-0.020	-0.014	0.008	-0.010	0.011	0.007	0.008	0.016
16	26	-0.009	-0.009	-0.014	-0.016	0.003	0.008	-0.005	0.005	0.011	-0.003
17	19	-0.011	-0.007	-0.016	-0.017	-0.015	-0.005	0.010	0.014	0.007	0.012
18	17	-0.013	-0.016	-0.018	-0.007	-0.002	-0.005	0.006	0.011	0.001	0.013
19	3	-0.016	-0.023	-0.015	-0.009	0.002	0.002	-0.003	0.001	0.015	0.017
20	12	-0.017	-0.010	-0.015	-0.010	0.002	-0.014	0.015	0.001	0.008	0.011
21	34	-0.011	-0.019	-0.004	-0.006	-0.009	-0.003	0.007	-0.006	0.010	0.012
22	29	-0.017	-0.014	-0.001	-0.028	-0.012	0.002	0.004	0.011	0.010	0.016
23	31	-0.010	-0.012	-0.011	-0.012	-0.019	0.005	-0.002	0.008	0.010	0.013
24	28	-0.010	-0.008	-0.004	-0.022	-0.002	-0.002	-0.006	0.010	0.010	0.005
25	32	-0.013	-0.014	-0.021	-0.007	-0.016	-0.018	0.021	0.016	0.009	0.013
	Minimum	-0.019	-0.023	-0.021	-0.028	-0.019	-0.018	-0.008	-0.007	0.001	-0.003
	Average	-0.012	-0.015	-0.013	-0.013	-0.005	-0.002	0.003	0.006	0.009	0.011
	Maximum	-0.006	-0.007	-0.001	-0.004	0.008	0.013	0.021	0.022	0.015	0.019

Nominal Axial Power Profile

x (%)	0.0%	5.0%	15.0%	25.0%	35.0%	45.0%	55.0%	65.0%	75.0%	85.0%	95.0%	100%
x (m)	0.000	0.086	0.257	0.428	0.599	0.770	0.941	1.112	1.283	1.454	1.625	1.710
0.05	0.250	0.522	0.849	1.127	1.330	1.436	1.436	1.330	1.127	0.849	0.522	0.350
x	0.300	0.472	0.799	1.077	1.280	1.386	1.386	1.280	1.077	0.799	0.472	0.300
-0.05	0.350	0.422	0.749	1.027	1.230	1.336	1.336	1.230	1.027	0.749	0.422	0.250

Absolute Maximum Deviation from Nominal Axial Power Profile

Range Check	0.019	0.023	0.021	0.028	0.019	0.018	0.021	0.022	0.015	0.019

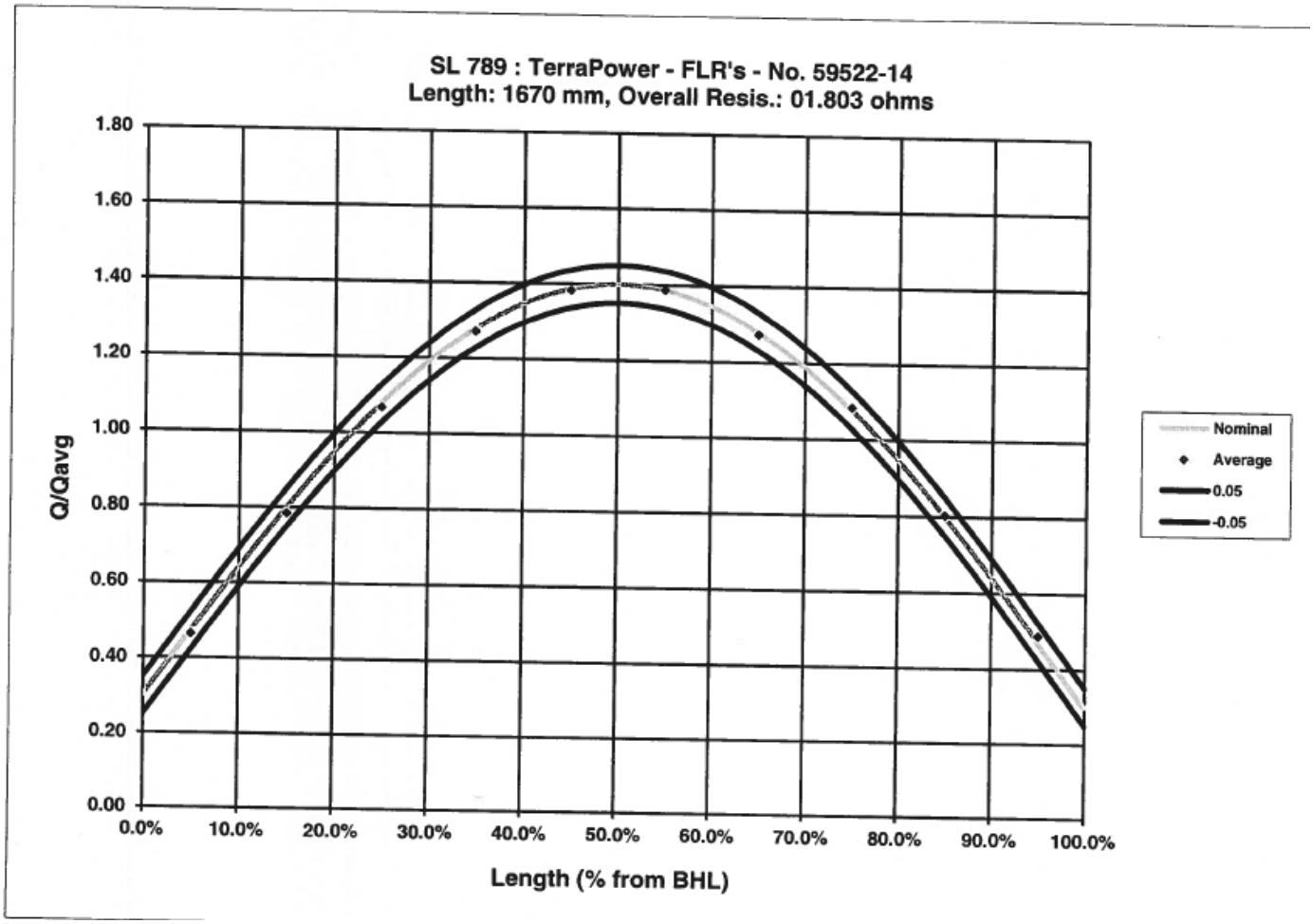


Figure 13. STERN Power Profile Measurements Plot

10 APPENDIX C

Mill report for non-heated tubes.

PUFA™

Producer of Premium Stainless Steel Seamless Tubes

MILL TEST REPORT

Purchaser.: PAC Stainless, LTD.					**Certificate No.:** 15-7-37				
Contract No.: PAC P.O.					**Date of Issue.:** 2015.7.17				
Commodity: Stainless Steel Seamless Tubes			**Specifications:** ASTM A213-14/ASME SA213-13/ASTM A269-14 EAW						
Process: Cold Drawn					**Delivery Condition:** OD Polished to 240 Grit				
Steel Grade	**Heat Number**	**Lot Number**	**Dimensions**						
TP304/TP304L	YX1410-664	5-167	3/8" x 0.065" x 20'						
Chemical Composition by Weight (%)									
Element	**C**	**Mn**	**P**	**S**	**Si**	**Cr**	**Ni**	**Mo**	**Co**
Requirements	≤0.035	≤2.00	≤0.045	≤0.030	≤1.00	18.00-20.00	8.00-12.00	-	-
Ladle Analysis	0.010	0.63	0.028	0.001	0.46	18.33	8.05	-	-
Product Analysis	0.019	0.79	0.033	0.001	0.51	18.52	8.50	-	-
Mechanical Properties									
Test Item	**Elongation (% in 2")**		**Tensile Strength (MPa) Rm**				**Yield Strength (MPa) Rp / 0.2%**		
Requirements	≥35		≥515				≥205		
Test Results	63/64		680/690				240/250		
Test Item	**Reduction of Area Z (%)**	**Hardness**	**Cold Bend Test**	**Flaring Test**	**Flattening Test**		**Flange Test**	**P.M.I. Test**	
Requirements	-	HRB≤80	-	30%	e=0.09		-	-	
Test Results	-	78/80	-	Passed	Passed		-	OK	
Test Item	**Eddy Current Test**	**Air Underwater Pressure Test**	**Ultrasonic Test**	**Intergranular Corrosion Test**	**Macroscopic Inspection**				
Requirements	ASTM E 426	-	-	ASTM A262 E	End Cut	Appearance			
Test Results	Passed	-	-	OK	OK	OK			

ISO 9001:2008 Certified by Intertek 110703068 **PED Certified by SZUTEST 2195-PED-1221604**

Additional Remarks:

(1) All tubes annealed to above 1900 Deg F and water quenched below 800 Deg F in 3 minutes
(2) All tubes tested per ASTM A1016-14
(3) Materials is NACE MR0103-2007 compliant (per Section 2.5)
(4) Materials is NACE MR0175/ISO 15156-2003 compliant (per Section 4.2.1)
(5) In Compliance with EN 10204-3.1
(6) In Compliance with RoHS Stipulation
(7) No weld repair performed
(8) Free from mercury contamination
(9) Free from radioactive contamination
(10) Billets melt and pipes/tubes manufactured in China
(11) All tubes 100% PMI tested
(12) All tubes 100% Eddy Current tested

By:

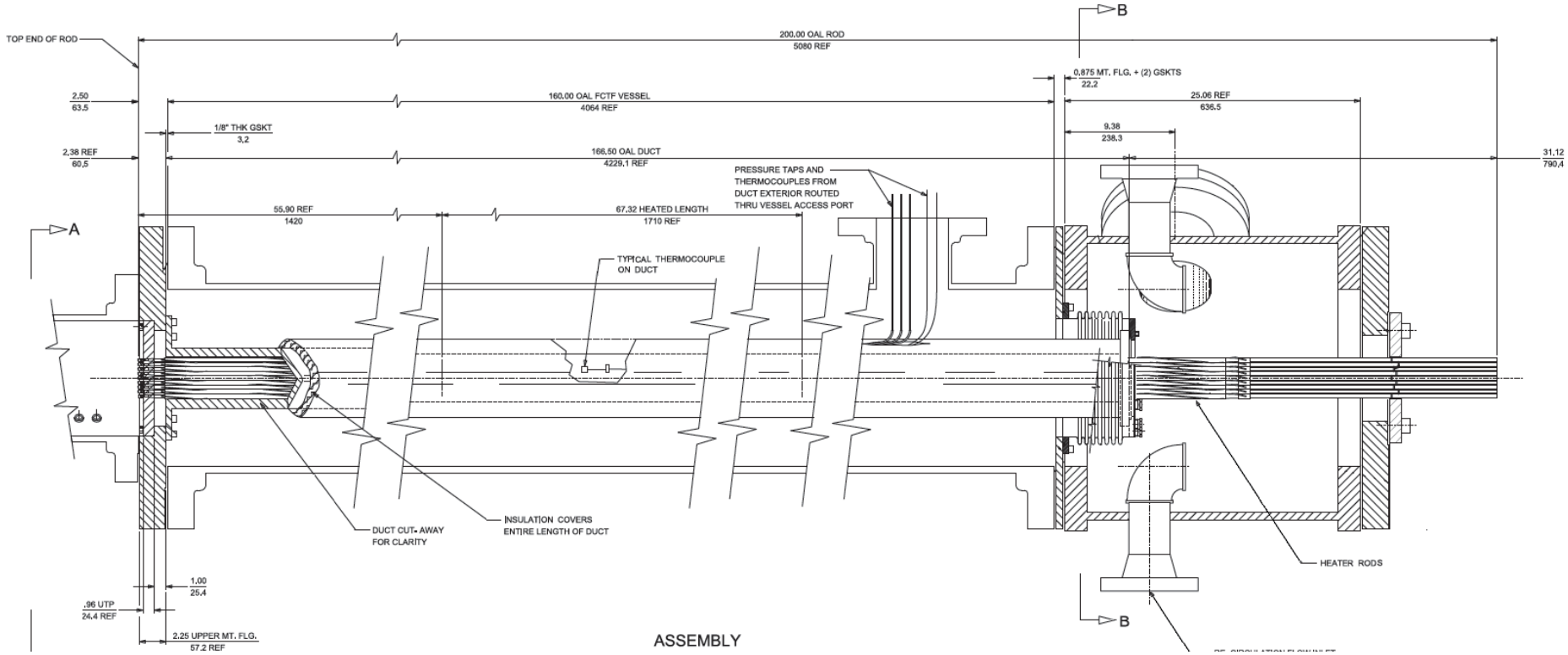
James Shi / Manager
Quality Control Department

We hereby certify that this report is true and correct.

Shanghai Pufa Stainless Steel Pipe Factory

11 APPENDIX D

Axial configuration drawing of duct and pins installed in test facility loop.



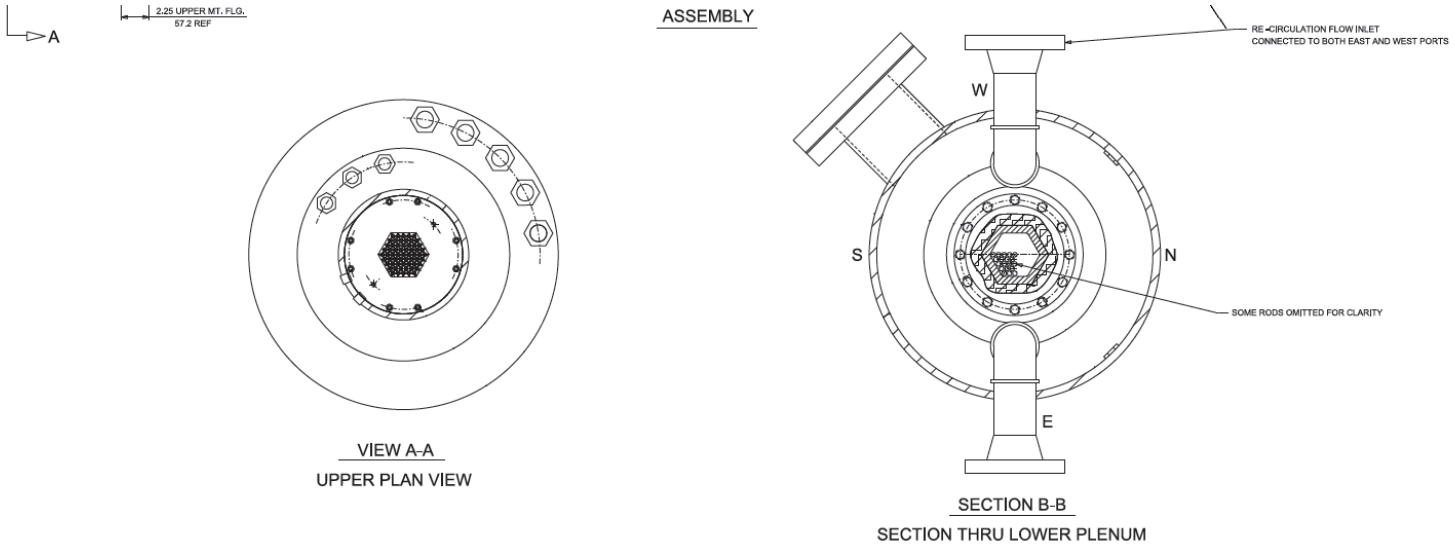


Figure 14. Bundle Axial Configuration

END OF DOCUMENT

APPENDIX D: TWRP-31-RPT-0022, AFAFC RANS PRE-TEST SIMULATION REPORT



Uncontrolled When Printed

ENGINEERING REPORT

Document Number:	TWRP-31-RPT-0022	**Revision:**	0
Document Title:	AFAFC RANS Pre-Test Simulation Report	**Approval Date** *(Final Signature Date)*:	2/6/2017
Issuing Organization:	Design Qualification	**Effective Date** *(for Procedures Only)*:	
		Page:	1 of 78

Approval

Title	Name	Signature	Date
Originator, Computational Fluid Dynamics Post-Doc	Daniel Leonard	Approved in Agile	2/3/2017
Reviewer, Thermal Hydraulics Test and Analysis Engineer	Brian Jackson	Approved in Agile	2/3/2017
Approver, Group Lead, Thermal-Hydraulic Test and Analysis	Mike Steer	Approved in Agile	2/6/2017

Document Quality Level per TWRP-NS-PROC-0002:

Quality Level 1 ☐ Quality Level 2 ☒ Quality Level 3 ☐ N/A ☐

Contains Open Items: Yes ☐ No ☒

Revision History

Revision No.	Effective Date	Affected Section(s)	Description of Change(s)
0	2/6/2017	All	Initial Release, Simulations reviewed by Nate Salpeter

TABLE OF CONTENTS

1 PURPOSE 8
2 SUMMARY 8
3 BACKGROUND 9
4 METHODS AND APPROACH 10
4.1 Momentum Source and Solver Conditions 10
4.2 Geometry and Boundary Conditions 12
4.3 Solution Verification Approach 18
4.4 Model Sensitivity Approach 22
4.5 Method of Manufactured Solutions 24
5 VERIFICATION RESULTS AND DISCUSSION 27
5.1 Code Verification 27
5.2 Round-off, Iterative, and Statistical Sampling Errors 30
5.3 Non-Deformed Bundles 31
5.4 Deformed Bundles 45
5.5 Turbulence Model Sensitivity 48
5.6 Momentum Source Coefficient Sensitivity 52
5.7 Summary and Choices of Meshes, Models, and Conditions 54
6 OFFICIAL PRE-TEST RESULTS 55
6.1 Non-Deformed Isothermal Bundle 55
6.2 Deformed Isothermal Bundle 59
6.3 Non-deformed and Deformed Heated Bundles 63
7 CONCLUSIONS 68
8 REFERENCES 70
9 APPENDICES 70
9.1 Non-deformed Isothermal Bundle Mesh Convergence 70
9.2 Non-deformed Heated Bundle Mesh Convergence 74
9.3 Deformed Isothermal Bundle Mesh Convergence 75
9.4 Deformed Heated Bundle Mesh Convergence 76

LIST OF TABLES

Table 4-1: Geometric values of CFD non-deformed isothermal bundle. 13
Table 4-2: Geometric values of CFD non-deformed heated bundle. 14
Table 4-3: Boundary conditions of the isothermal bundles. 16
Table 4-4: Boundary conditions of the heated bundles. 16
Table 4-5: Cell size ratios of the isothermal/heated bundle meshes and their names. 18
Table 4-6: Cell size ratios and numbers of cells for each mesh of the manufactured solution simulations 26
Table 5-1: Percent differences of bundle pressure drop from Richardson extrapolation value for all meshes. 33
Table 5-2: Percent differences of heated bundle pressure drop from Richardson extrapolation value for all meshes. 42

LIST OF FIGURES

Figure 4-1: Description and illustration of body force components for the momentum source method 11

Figure 4-2: Transverse projection of body force vectors in cell locations of the wire-wrap. Contours of axial velocity are shown for non-momentum source cells. 11
Figure 4-3: Axial cross-sections of (a) the non-deformed isothermal bundle and (b) the non-deformed heated bundle. 13
Figure 4-4: Illustration (not to scale) of the deformed CFD heated bundle, dimensions, and the functional form of the deformation. Note that the heated bundle actually has rounded corners. 15
Figure 4-5: Illustration (not to scale) of the deformed CFD isothermal bundle, dimensions, and the functional form of the deformation. 15
Figure 4-6: Boundary heat flux at the inner diameter of the sheath of the heated pins displaying the axial profile of the heated length. 17
Figure 4-7: Normalized heat flux at the inner diameter of the sheath versus the axial position of the heater. Note that the total heated length is 1.71 m (6P). 18
Figure 4-8: Number of cells versus cell size ratio for non-deformed isothermal and non-deformed heated bundles. 19
Figure 4-9: Transverse cell distribution for (a) Coarsest, (b) Coarse, (c) Medium, (d) Fine, and (e) Finest meshes shown with contours of transverse velocity magnitude [m/s]. 20
Figure 4-10: Number of cells in specific directions versus cell size ratio for the non-deformed isothermal bundle. 21
Figure 4-11: Fine mesh of the non-deformed heated bundle. 21
Figure 4-12: Average, maximum, and minimum $y+$ values for all non-deformed meshes. 23
Figure 4-13: Average, maximum, and minimum $y+$ values for all deformed meshes. 24
Figure 4-14: Constant coefficients for the 2D subsonic steady-state ideal gas Euler equations manufactured solution. Coefficients from [9]. 25
Figure 4-15: Boundary conditions for the 2D subsonic steady-state ideal gas Euler equations MMS simulation. 26
Figure 4-16: Contours of the energy source term determined from the manufactured solution. 26
Figure 5-1: $L2$-norm of the discretization error versus cell size ratio h for each state variable (1st-order numerical schemes. 28
Figure 5-2: Observed Order of Accuracy versus cell size ratio for each state variable (1st-order numerical schemes). 28
Figure 5-3: $L2$-norm of the discretization error versus cell size ratio h for each state variable (2nd-order numerical schemes). 29
Figure 5-4: Observed Order of Accuracy versus cell size ratio for each state variable (2nd-order numerical schemes). 29
Figure 5-5: Root-mean-square of residual versus iteration for each PDE solved in the simulation of the non-deformed heated bundle. 30
Figure 5-6: (a) Temperature probes on the outlet surface of the non-deformed heated bundle simulation (fine mesh) shown with temperature contours on that surface. (b) Temperature versus iteration for the four probes on the outlet surface. 31
Figure 5-7: Non-deformed isothermal bundle pressure drop (based on mass-flow averages at inlet and outlet) versus cell size ratio h for all meshes. The red-filled square at $h = 0$ represents the Richardson extrapolation based on the Coarsest, Coarse, and Medium meshes. 32
Figure 5-8: Pressure drops between Face B pressure probes at various axial heights and at the inlet versus the number of wire pitches into the non-deformed isothermal bundle for all meshes. 33
Figure 5-9: Line probe at 3.25P (wire-wrap at 12 o'clock) from center pin to center of Face A, overlaid on axial slice of velocity magnitude contours. 34
Figure 5-10: Velocity magnitude versus radial position from the center of the duct at 2.416P (wire-wrap at 2 o'clock) for all meshes. 35

Figure 5-11: Velocity magnitude versus radial position from the center of the duct at 3.084P (wire-wrap at 10 o'clock) for all meshes. 36
Figure 5-12: Velocity magnitude versus radial position from center of the duct at 3.25P (wire-wrap at 12 o'clock) for all meshes. 36
Figure 5-13: Contours of magnitude of projected transverse velocities [m/s] of an edge sub-channel at 3.25P (wire-wrap at 12 o'clock) for the (a) Coarsest, (b) Coarse, (c) Medium, (d) Fine, and (e) Finest meshes. 37
Figure 5-14: x-component of velocity (transverse) versus number of wire pitches into the bundle (axially) for all meshes. 38
Figure 5-15: y-component of velocity (transverse) versus number of wire pitches into the bundle (axially) for all meshes. 38
Figure 5-16: Pressure drops between Face B pressure probes at various axial heights and at the inlet versus the number of wire pitches into the non-deformed isothermal bundle for the Fine mesh and a transversely-Fine/axially-Coarsest mesh. 39
Figure 5-17: Velocity magnitude versus radial position from the center of the duct at 2.416P (wire-wrap at 2 o'clock) for the Fine mesh and the transversely-Fine/axially-Coarsest mesh. 40
Figure 5-18: Velocity magnitude versus radial position from the center of the duct at 3.084P (wire-wrap at 10 o'clock) for the Fine mesh and the transversely-Fine/axially-Coarsest mesh. 40
Figure 5-19: Non-deformed heated bundle pressure drop (based on mass-flow averages at inlet and outlet) versus cell size ratio h for all meshes. The red-filled square at $h = 0$ represents the Richardson extrapolation based on the Coarsest, Coarse, and Medium meshes. 41
Figure 5-20: Pressure drops between Face B pressure probes at various axial heights and at the inlet versus the number of wire pitches into the non-deformed heated bundle for all meshes. 42
Figure 5-21: Notation for labeling of pin measurement configuration, row number, and location number. 43
Figure 5-22: Notation and locations of specific pins examined in this report. 43
Figure 5-23: Temperature versus the clocking location of each thermocouple on heated pin STA001 for all meshes. Axial locations are also given for each thermocouple. 44
Figure 5-24: Temperature versus the clock location of each thermocouple on heated pin AZI208 for all meshes. Axial locations are also given for each thermocouple. 45
Figure 5-25: Temperature versus the clock location of each thermocouple on non-heated tube TUB201 for all meshes. Axial locations are also given for each thermocouple. 45
Figure 5-26: Pressure drops between Face B pressure probes at various axial heights and at the inlet versus the number of wire pitches into the deformed isothermal bundle for all meshes. 46
Figure 5-27: Velocity magnitude versus radial position from center of the duct at axial height of maximum duct deformation z = 3.75P (wire-wrap at 6 o'clock) for all meshes of the deformed bundle. 47
Figure 5-28: Pressure drops between Face B pressure probes at various axial heights and at the inlet versus the number of wire pitches into the deformed heated bundle for all meshes. 48
Figure 5-29: Temperature versus the clocking location of each thermocouple on heated pin STA001 for all meshes of the deformed bundle. Axial locations are also given for each thermocouple. 48
Figure 5-30: Non-deformed Isothermal bundle pressure drops for the four turbulence models and the predicted pressure drop from the Cheng-Todreas correlation. 49
Figure 5-31: Non-deformed isothermal pressure drops between Face B pressure probes at various axial heights and at the inlet versus the number of wire pitches into the non-deformed isothermal bundle for the four turbulence models. 50
Figure 5-32: Velocity magnitude versus radial position from the center of the duct at 2.416P (wire-wrap at 2 o'clock) for the four turbulence models. 50
Figure 5-33: Non-deformed heated bundle pressure drops for the four turbulence models and the predicted pressure drop from the Cheng-Todreas correlation. 51

Figure 5-34: Non-deformed heated pressure drops between Face B pressure probes at various axial heights and at the inlet versus the number of wire pitches into the non-deformed heated bundle for the four turbulence models. 52
Figure 5-35: Temperature versus the clocking location of each thermocouple on heated pin STA001 in the non-deformed heated bundle for all four turbulence models. Axial locations are also given for each thermocouple. 52
Figure 5-36: Velocity magnitude versus radial position from center of the duct at axial height of z = 2.75P (wire-wrap at 6 o'clock) for varying MS coefficient in the non-deformed isothermal bundle. 53
Figure 5-37: Temperature versus radial position from center of the duct at axial height of z = 6.42P (wire-wrap at 5 o'clock) for varying MS coefficient in the non-deformed heated bundle. 54
Figure 6-1: Non-deformed isothermal pressure drops between Face B pressure probes at various axial heights and at the inlet versus the number of wire pitches into the bundle. Pressure drops on other Faces shown at z = 2.25P and z = 3.0P. 55
Figure 6-2: Axial cross-section displaying pressure contours [Pa] at z = 2.25P. 56
Figure 6-3: Velocity magnitude versus radial position from the center of the duct at z = 2.25P, z = 2.75P, and z = 3.25P. 57
Figure 6-4: Axial cross-sections at (a) z = 2.25P, (b) z = 2.75P, and (c) z = 3.25P, displaying velocity magnitude [m/s] and the line probe. 57
Figure 6-5: Velocity magnitude versus radial position from the center of the duct at z = 2.584P and z = 3.085P. 58
Figure 6-6: Axial cross-sections at (a) z = 2.584P and (b) z = 3.085P, displaying velocity magnitude [m/s] and the line probe. 58
Figure 6-7: Velocity magnitude versus radial position from the center of the duct at z = 2.417P and z = 2.918P. 59
Figure 6-8: Axial cross-sections at (a) z = 2.417P and (b) z = 3.918P, displaying velocity magnitude [m/s] and the line probe. 59
Figure 6-9: Deformed isothermal pressure drops between Face B pressure probes at various axial heights and at the inlet versus the number of wire pitches into the bundle. Pressure drops on other Faces shown at z = 2.25P and z = 3.75P. 60
Figure 6-10: Velocity magnitude versus radial position from the center of the duct at z = 2.25P, z = 3.25P, z = 4.25P, and z = 5.25P. For each the wire-wrap is at 12 o'clock. 61
Figure 6-11: Velocity magnitude versus radial position from the center of the duct at height of max duct deformation z = 3.75P (wire-wrap = 6 o'clock). 61
Figure 6-12: Velocity magnitude versus radial position from the center of the duct at z = 2.5833P, z = 3.5833P, and z = 4.5833P. For each the wire-wrap is at 4 o'clock. 62
Figure 6-13: Velocity magnitude versus radial position from the center of the duct at z = 2.9167P, z = 3.9167P, and z = 4.9167P. For each the wire-wrap is at 8 o'clock. 62
Figure 6-14: Axial cross-sections of velocity magnitude [m/s] showing (a) non-deformed isothermal velocity vectors, (b) deformed isothermal velocity vectors, (c) non-deformed isothermal contours, and (d) deformed isothermal contours. 63
Figure 6-15: Non-deformed heated pressure drops between Face B pressure probes at various axial heights and at the inlet versus the number of wire pitches into the bundle. Pressure drops on other Faces shown at z = 0P and z = 3P. 64
Figure 6-16: Deformed heated pressure drops between Face B pressure probes at various axial heights and at the inlet versus the number of wire pitches into the bundle. Pressure drops on other Faces shown at z = 0P and z = 3P. 64
Figure 6-17: Temperature versus the clocking location of each thermocouple on heated pins STA001 and STA407 for non-deformed and deformed bundles. Axial locations are also given for each thermocouple. 65

Figure 6-18: Axial cross-section at height of peak heat flux displaying temperature contours [˚C] around the center pin (STA001) and thermocouple clocking locations of 11, 12, and 1. 66
Figure 6-19: Temperature versus the clocking location of each thermocouple on heated pin AXI204 for non-deformed and deformed bundles. Axial locations are also given for each thermocouple. 67
Figure 6-20: Temperature versus the clocking location of each thermocouple on heated pin AZI208 for non-deformed and deformed bundles. Axial locations are also given for each thermocouple. 67
Figure 6-21: Temperature versus the clocking location of each thermocouple on non-heated tubes TUB201 and TUB207 for non-deformed and deformed bundles. Axial locations are also given for each thermocouple. 68
Figure 9-1: Velocity magnitude versus radial position from the center of the duct at 2.25P (wire-wrap at 12 o'clock) for all meshes. 70
Figure 9-2: Velocity magnitude versus radial position from the center of the duct at 2.583P (wire-wrap at 4 o'clock) for all meshes. 71
Figure 9-3: Velocity magnitude versus radial position from the center of the duct at 2.75P (wire-wrap at 6 o'clock) for all meshes. 71
Figure 9-4: Velocity magnitude versus radial position from the center of the duct at 2.917P (wire-wrap at 8 o'clock) for all meshes. 72
Figure 9-5: Contours of magnitude of projected transverse velocities [m/s] of a corner sub-channel at 3.25P (wire-wrap at 12 o'clock) for the (a) Coarsest, (b) Coarse, (c) Medium, (d) Fine, and (e) Finest meshes. 72
Figure 9-6: Contours of magnitude of projected transverse velocities [m/s] of an interior sub-channel at 3.25P (wire-wrap at 12 o'clock) for the (a) Coarsest, (b) Coarse, (c) Medium, (d) Fine, and (e) Finest meshes. 73
Figure 9-7: Temperature versus the clocking location of each thermocouple on heated pin STA407 for all meshes. Axial locations are also given for each thermocouple. 74
Figure 9-8: Temperature versus the clocking location of each thermocouple on heated pin AXI204 for all meshes. Axial locations are also given for each thermocouple. 74
Figure 9-9: Temperature versus the clocking location of each thermocouple on unheated tube TUB207 for all meshes. Axial locations are also given for each thermocouple. 75
Figure 9-10: Deformed isothermal bundle pressure drop (based on mass-flow averages at inlet and outlet) versus cell size ratio h for all meshes. The red-filled square at $h = 0$ represents the Richardson extrapolation based on the Coarsest, Coarse, and Medium meshes. 75
Figure 9-11: Deformed heated bundle pressure drop (based on mass-flow averages at inlet and outlet) versus cell size ratio h for all meshes. The red-filled square at $h = 0$ represents the Richardson extrapolation based on the Coarsest, Coarse, and Medium meshes. 76
Figure 9-12: Temperature versus the clocking location of each thermocouple on heated pin STA407 for all meshes. Axial locations are also given for each thermocouple. 76
Figure 9-13: Temperature versus the clocking location of each thermocouple on heated pin AXI204 for all meshes. Axial locations are also given for each thermocouple. 77
Figure 9-14: Temperature versus the clocking location of each thermocouple on heated pin AZI208 for all meshes. Axial locations are also given for each thermocouple. 77
Figure 9-15: Temperature versus the clocking location of each thermocouple on unheated tube TUB201 for all meshes. Axial locations are also given for each thermocouple. 78
Figure 9-16: Temperature versus the clocking location of each thermocouple on unheated tube TUB207 for all meshes. Axial locations are also given for each thermocouple. 78

1 PURPOSE

The objective of this report is to present quantitative code verification, solution verification, and sensitivity analyses for Reynolds Averaged Navier-Stokes (RANS) Computational Fluid Dynamics (CFD) simulations of isothermal and heated wire wrapped 61-pin bundles (with both beginning-of-life and end-of-life duct geometries). Moreover, these analyses are used to guide the final selection of meshes, models, and model coefficients, for the official blind pre-test results that are included herein. Ultimately, the purpose of this effort is to judge the accuracy of current TerraPower CFD methodologies to predict important flow and heat transfer features in liquid-metal-cooled nuclear fuel assemblies with wire-wrapped fuel pins. This report is part of the Advanced Fuel Assembly Flow Characterization (AFAFC) project which consists of both experiments and numerical simulations, and uses surrogate fluids and electrically heated fuel pins to substitute for the liquid metal coolant and the nuclear heat source.

2 SUMMARY

The results and conclusions of this report are concisely summarized below.

- Round-off error, iterative error, and statistical sampling error were proven to be negligible.
- Five mesh sizes were investigated for each bundle in a systematic mesh refinement study (Coarsest, Coarse, Medium, Fine, and Finest).
- Monotonic mesh convergence was displayed for most variables of interest.
- Results showed little variability when the mesh was refined beyond the Fine mesh.
- Results showed little sensitivity to mesh densities investigated in axial direction.
- Quantitative “exact” solution and discretization error estimates were questionable as the formal asymptotic region of convergence was not achieved.
- Four two-equation RANS turbulence models were tested for sensitivity, and while there was some pressure drop variation amongst the models, they all were within roughly 5-10% of a widely used empirical pressure drop correlation. There were only small temperature and velocity field variations amongst the turbulence models used.
- Coefficient for the momentum source model of wire-wrapping was tested for sensitivity. Some slight variations were visible in the velocity and temperature fields but nothing significant. No variations were visible in the pressure drops.
- Deformed duct wall bundle cases showed similar convergence and model sensitivity behavior to the non-deformed cases.
- Based on the solution verification procedure, the Fine mesh and the Menter k-ω SST turbulence model were chosen for the official pre-test results.
- Official Pre-Test results are presented for the non-deformed and deformed isothermal and heated bundle simulations and results provided corresponding to proposed pressure tap, LDV, PIV, and thermocouple locations of the experiments.
- Deformed duct cases displayed differences in the velocity profiles (decreased velocity magnitudes in the deformed regions) and variations in the temperature samples (increased temperatures in the deformed region), relative to the non-deformed bundles.
- As expected, no hot-spots were observed at the contact points of the wire-wrap and pins. While this physical phenomenon may occur in reality, it was not expected to be seen with the

momentum source approach as it does not currently have the ability to model the correct heat transfer through the wire-wrap.

- The official Pre-Test results will be compared directly to the experimental data and high-fidelity LES data to assess the validity of TerraPower's CFD approach as long as the experiment boundary conditions are consistent with those simulated. If differences in boundary conditions exist, post-test simulations will be run for the experiment benchmark.

- Code verification was conducted with the Method of Manufactured Solutions. Positive results were obtained with first-order numerical schemes but second-order schemes have not yet been verified. Future work will continue to verify second-order schemes.

Future work includes running post-test simulations (using similar methods) with as-built conditions and comparing these to the experiments as well. Further methods, such as using a body-fitted mesh around the wire-wrapping, will be investigated as well. The post-test simulations will be essential to the solution validation procedure and uncertainty quantification of the CFD simulations. The entire V&V process will ultimately provide the level of confidence that can be expected when estimating pressure drops, velocities, and temperatures with TerraPower's CFD methods for flow through a wire-wrapped fuel assembly.

3 BACKGROUND

TerraPower is participating in a cooperative project among industry, the national lab system, and academia to perform Verification and Validation (V&V) of Computational Fluid Dynamics (CFD) methods for predicting the flow and heat transfer within liquid-metal-cooled nuclear fuel assemblies with wire-wrapped fuel pins. This project is referred to as the Advanced Fuel Assembly Flow Characterization (AFAFC) project. It consists of both experimental and numerical components, and uses surrogate fluids and electrically heated fuel pins to substitute for the liquid metal coolant and the nuclear heat source. The experiments include both unheated assemblies to measure the flow velocities with Laser Doppler Velocimetry (LDV) and Particle Image Velocimetry (PIV), as well as heated assemblies to measure the temperatures of the fluid and the simulated fuel pins with thermocouples. Both sets of experiments also measure the pressure at multiple locations in the system. The numerical component of this work involves high-fidelity Large-Eddy Simulation (LES) modeling and industry-standard Reynolds-Averaged Navier-Stokes (RANS) modeling of the experiments. Furthermore, the experiments and simulations will be conducted on two duct geometries: the first is a non-deformed hexagonal duct that has flat internal duct faces that represents a beginning of life geometry. The other is a deformed duct where the internal hexagonal flow area enlarges then decreases along the axial height to represent the changes that occur to the duct geometry from pressure and irradiation effects in the core. The assembly geometries are generic, but preserve characteristic non-dimensional numbers typical of liquid-metal-cooled fast reactor assemblies.

This report describes the methods and results of the industrial, RANS-based CFD code solution verification and then presents the official RANS pre-test results. These simulations are the responsibility of TerraPower. The simulations are performed for the following experiment test geometries:

- Isothermal non-deformed bundle
- Heated non-deformed bundle
- Isothermal deformed bundle
- Heated deformed bundle.

These flows are computed with the test design specifications [1] [2], without the aid of any experimental results. Later, post-test calculations will be performed incorporating the actual test conditions and input from some of the experimental results.

Since this report focuses entirely on TerraPower's component of the AFAFC project (verification and presentation of industry-standard RANS CFD pre-test simulations), the other components of the project are

not discussed much beyond this section. To provide a better understanding of the scope of the entire AFAFC project, the other components of the project are outlined briefly below:

- AREVA Fuels is responsible for the non-deformed and deformed heated bundle experiments with the heated bundle components being provided by TerraPower. This testing will be conducted at the AREVA Richland Fuel Cooling Test Facility (FCTF) water flow loop. The purpose of the heated bundle experiments is to "investigate and measure thermal distribution and pressure drop behavior of heated 61-pin, hexagonally packed fast reactor test assemblies in the fully turbulent regime [1]" to obtain CFD validation data. In each 61-pin bundle, 19 of the pins are electrically heated. The tests, which are designed to provide flow and heat transfer conditions representative of those in typical liquid-metal cooled nuclear fuel assemblies with wire-wrapped fuel pins, have over 350 installed thermocouples and 40 installed pressure taps. More details of the heated bundle experiments can be found in the AFAFC AREVA Heated Bundle Experiment Test Specification [1].

- Texas A&M University (TAMU) is responsible for the non-deformed and deformed isothermal bundle experiments. The purpose of the isothermal experiments is to provide velocity field and velocity point measurements using PIV and LDV, respectively, and pressure drop measurements as well. These isothermal measurements will provide data from bundles which are dynamically and geometrically scaled to the heated bundles, which will be utilized for CFD V&V. The isothermal bundle velocity and pressure data will complement the heated bundle temperature and pressure data. Acrylic ducts, pins, and wires, along with a working fluid that provides a Matched Index of Refraction (MIR), are used to allow for the optical velocity measurements. Further information of the isothermal bundle experiments can be found in the TAMU Fuel Assembly Flow Visualization Test Specification [2].

- Argonne National Lab (ANL) is responsible for the high-fidelity Spectral Element LES modeling of the isothermal and heated bundle experiments, using the Nek5000 code. These high-fidelity simulations will be compared with the experimental results, and also used for benchmarking TerraPower's pre-test and post-test RANS results.

The remaining sections of this report proceed as follows. Section 4 provides the methods used for the RANS simulations presented in this pre-test report. First the momentum source methodology is reviewed and the solver conditions are discussed. Next the geometry and boundary conditions of the simulations are provided, along with the approaches to solution verification and model sensitivity analyses. In Section 5, the code and solution verification results are presented and discussed, focusing largely on mesh refinement, turbulence model sensitivity, and momentum source modelling sensitivity. Based on these results, a particular mesh, a particular turbulence model, and momentum source conditions are chosen for the official pre-test results. These results are presented and discussed in Section 6 and will be used in a blind comparison with the experimental results. Finally, Section 7 will summarize the report and provide information on future work of the AFAFC project.

4 METHODS AND APPROACH

4.1 Momentum Source and Solver Conditions

The CD-Adapco commercial CFD suite Star-CCM+ is used to solve the RANS pre-test simulations of both the isothermal and heated bundles. Star-CCM+ v10.02.010 is utilized for all of the simulations to ensure that differences are not due to software versions. These RANS simulations of helically wire-wrapped fuel assemblies employ meshes of bare pins without the wire-wrap in the bundle. The effect of wire-wrap on the flow is accounted for by introducing a Momentum Source (MS) into the governing fluid equations. The MS, originally developed at ANL, is only applied to cells corresponding to the location of the wire-wrap, and the MS components in each cell are based on the local flow field [3]. This methodology simplifies the geometry and mesh generation and reduces the cell count, while still capturing the effects of the wire-wrap. The MS approach is used for all of the assembly simulations performed in this study.

The MS appears as a body force term in the momentum equation and has three orthogonal components (two in plane with the circular cross-section of the wire and one tangential along the centerline of the wire). The force components are based on lift and drag equations. The two force components in plane with the

circular cross-section of the wire prevent flow from penetrating the wire surface, introducing the bulk swirl observed in wire-wrapped bundles, while the component tangential to the centerline of the wire introduces a frictional force which modifies the pressure drop along the length of the bundle. A friction factor based on a correlation of flow through a tube is required and input by the user to determine the force component tangential to the wire centerline. The body force components are illustrated in Figure 4-1, and the implementation of the momentum source in Star-CCM+ is shown in Figure 4-2.

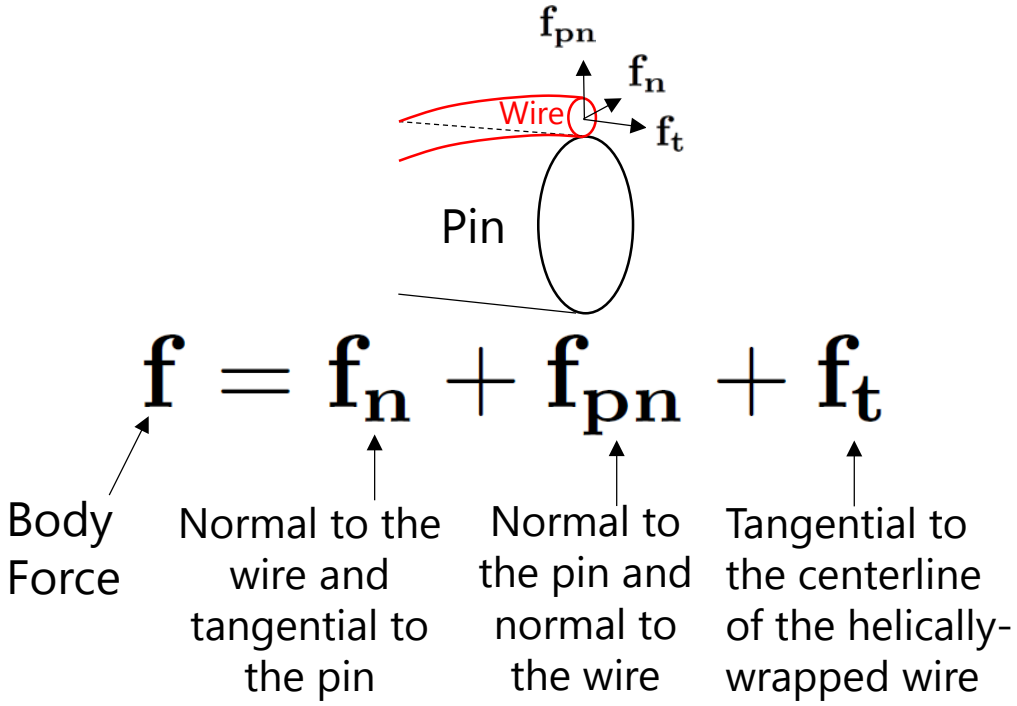


Figure 4-1: Description and illustration of body force components for the momentum source method

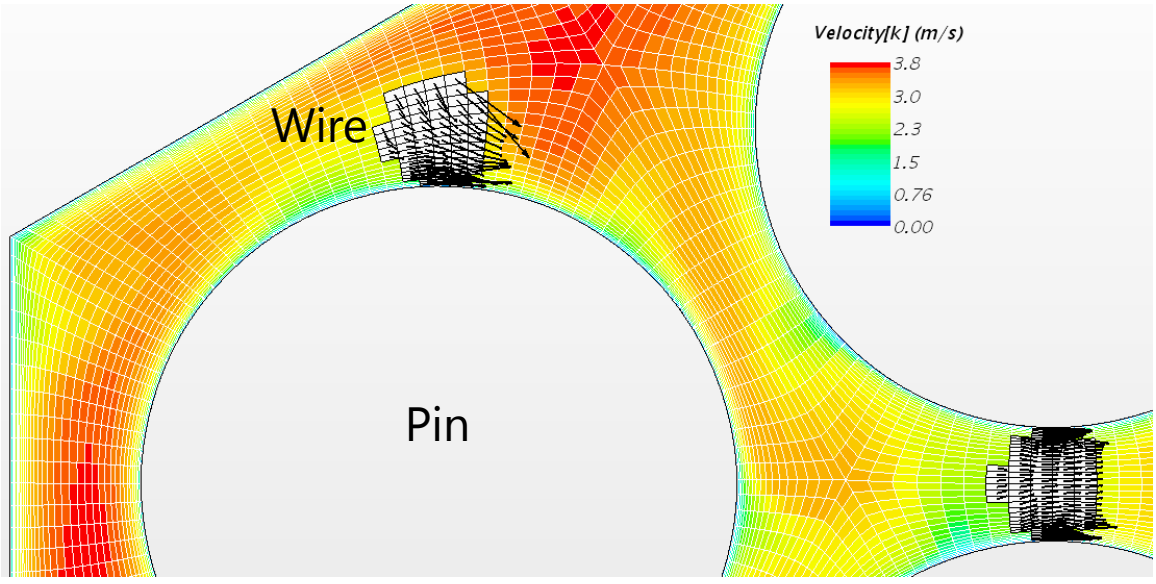


Figure 4-2: Transverse projection of body force vectors in cell locations of the wire-wrap. Contours of axial velocity are shown for non-momentum source cells.

The force components are derived from the governing equations with the following assumptions:

- Steady-state flow (neglect time-dependent term when modeling the body force)
- The body force is the dominant contributor to the change of fluid momentum in the wire normal direction (neglect pressure gradient and viscous effects when modeling the body force)
- Velocity gradients are proportional to cell center velocity in normal directions
- A general form of friction factor is sufficient to model the force tangential to the wire centerline.

The proportionality coefficient of the normal forces is referred to as the MS coefficient and it must take on a value greater than 2.0 to prevent flow through the wire surface [3]. The sensitivity of this coefficient to the simulation results is investigated in Section 5.6. A basic correlation for tube flow is used to determine the friction factor for the force tangential to the wire centerline.

Both isothermal and heated bundle simulations use the following common solver conditions:

- The Segregated Flow solver (pressure-based SIMPLE approach) to solve the RANS equations for steady, three-dimensional, turbulent flow, with gravitational effects.
- The 2nd-order upwind scheme (see [4] for details) for discretization of the convective term, and the Hybrid Gauss-Least Squares approach using Venkatakrishnan limiters to solve for gradients.
- A number of two-equation turbulence models are utilized in a sensitivity study, and each model uses 2nd-order upwind convection schemes. Blended wall-functions are used for all of the turbulence models and it is shown that the average y^+ values are adequate for this type of modeling (Section 4.4.1).
- The discretized linear systems are always solved iteratively with the algebraic multigrid approach using under-relaxation factors to improve convergence behavior.

Simulation conditions which are unique to the isothermal bundles are:

- The working fluid is P-Cymene (to provide a MIR between the acrylic bundle and fluid, for flow-visualization measurements) with constant density of 857.0 kg/m^3 and dynamic viscosity of 8.76e-4 Pa-s, which corresponds to the design conditions of the experiment.

Solver and simulation conditions which are unique to the heated bundles are:

- Segregated Fluid Temperature solver with 2nd-order upwind convection discretization to solve the energy equation for the flow and the conjugate heat transfer in the solid clad and sheath of the heated pins.
- The working fluid is H_2O where the following functions are modeled as polynomial functions of temperature: density, dynamic viscosity, specific heat, and thermal conductivity.
- The default turbulent Prandtl number for H_2O of 0.9 is used. A sensitivity study is not conducted for this value here, but will be in the post-test analysis.
- The clad and sheath of the heated pins have material properties of Monel alloy K-500 (density of 8440 kg/m^3) at average temperatures of 320˚C (thermal conductivity of 25.8 W/m*K) and 340˚C (thermal conductivity of 26.3 W/m*K), respectively. Material properties are provided by STERN labs (the manufacturers of the heated pins).

4.2 Geometry and Boundary Conditions

Geometric details of all four “as-designed” experimental bundle cases were outlined in the test specifications [1] [2]. However, it is not necessary for the CFD studies to incorporate the entire experimental flow loop systems into the simulations. Thus, the geometrical details of the CFD computations were finalized in the AFAFC Benchmark Specification [5]. The geometries of the RANS pre-test simulations, adhering to the as-

designed test specifications and the benchmark specification are presented in this section, along with the boundary conditions of the computations.

4.2.1 Geometries

Scaled geometric similarity is maintained, aside from some details below, between the isothermal and heated bundle cases. This is accomplished by all bundles having the following properties:

- 61-pins
- Hexagonal ducts
- The same proportional wall gaps between the outer row of wires and the duct walls (0.77% of the flat-to-flat length for the non-deformed ducts)
- A similar functional form of the deformed duct walls (see [1] [2]), where the shape of the deformation is determined by a cosine curve.
- A similar pin-pitch-to-pin-diameter ratio (1.189 for the isothermal cases and 1.18 for the heated cases)
- The same wire-pitch-to-pin-diameter ratio (30).

The one noticeable geometric difference between the isothermal and heated bundles is that the corners of the duct walls are sharp for the isothermal bundles, while they have a radius of curvature of 6.84 mm for the heated bundles. The non-deformed geometries of the isothermal and heated bundles are shown in Figure 4-3. For the heated bundle, the 19 heated pins are clearly visible as the solid cladding and solid sheath (both with the material properties of Monel alloy K-500) are modeled. Numerical details of the non-deformed isothermal and heated geometries are given in Table 4-1 and Table 4-2, respectively. Note that for all of the bundles, only the inner duct walls are considered in the CFD geometry, and for all unheated pins (for all bundles), the outer surfaces of the pins mark boundaries of the computational domain (*i.e.* nothing is modeled interior to the outer surface of the unheated pins).

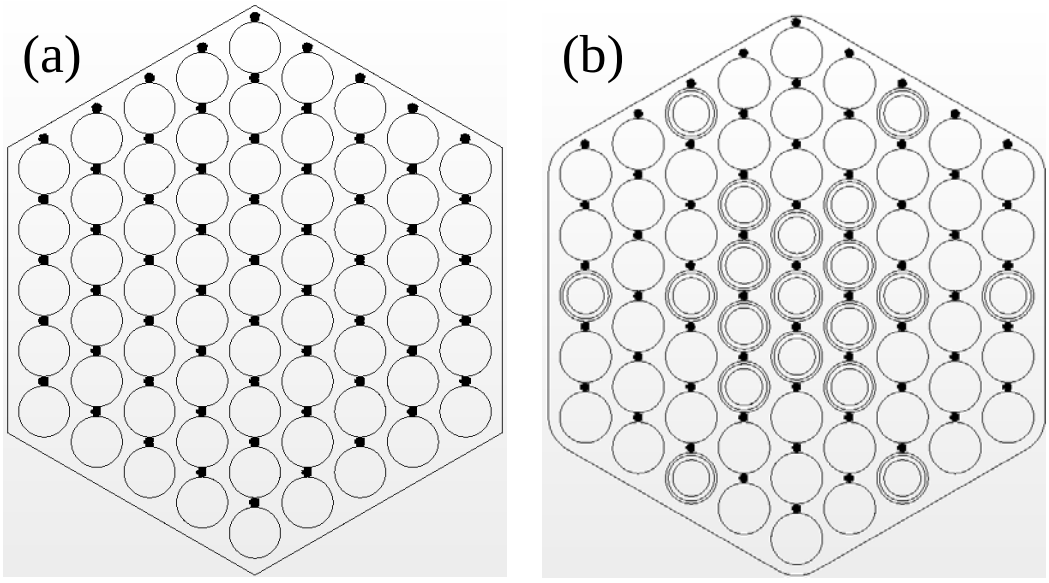


Figure 4-3: Axial cross-sections of (a) the non-deformed isothermal bundle and (b) the non-deformed heated bundle.

Table 4-1: Geometric values of CFD non-deformed isothermal bundle.

Parameter	Value	Units
Wire Wrap Pitch Length	1 (0.476)	P = wire-pitches (m)
Duct Length	3.5 (1.666)	P (m)

Internal Duct Flat-to-Flat	153.8	mm
Duct Wall Gap	0.77% of Duct Flat-to-Flat	-
Wire Wrap OD	3.0	mm
Wire Wrap Direction	Clockwise	In axial direction of flow
Pin Clad OD	15.9	mm

Table 4-2: Geometric values of CFD non-deformed heated bundle.

Parameter	Value	Units
Wire Wrap Pitch Length	1 (0.285)	P = wire-pitches (m)
Duct Length	13 (3.705)	P (m)
Entrance Length	4 (1.14)	P (m)
Heated Length	6 (1.71)	P (m)
Non-Heated Measurement Length	2 (0.57)	P (m)
Exit Length	1 (0.285)	P (m)
Internal Duct Flat-to-Flat	91.64	mm
Duct Wall Gap	0.77% of Duct Flat-to-Flat	-
Duct Corner Radius of Curvature	6.84	mm
Wire Wrap OD	1.73	mm
Wire Wrap Direction	Clockwise	In axial direction of flow
Unheated Tube Clad OD	9.525	mm
Heated Pin Clad OD	9.5	mm
Heated Pin Clad ID	8.509	mm
Heated Pin Sheath OD	8.509	mm
Heated Pin Sheath ID	6.782	mm

The deformed heated bundle has the same geometrical properties as the non-deformed heated bundle except that the inner duct wall bulges outward gradually over a specified axial length to represent the geometry of an end-of-life duct (the bulged duct is a cosine shape in both the axial direction and transversely between each corner of the duct). In the heated bundle, the deformation length occurs over the same length of the bundle which is heated. An illustration of the deformation, its functional form, and other geometrical details of the deformed heated bundle are shown in Figure 4-4. In the isothermal experiment, the deformed bundle not only has a deformed inner duct wall, but is also 2 wire pitches (0.9525 m) longer than the non-deformed case. An illustration of the deformation, its functional form, and other geometrical details of the deformed isothermal bundle are shown in Figure 4-5.

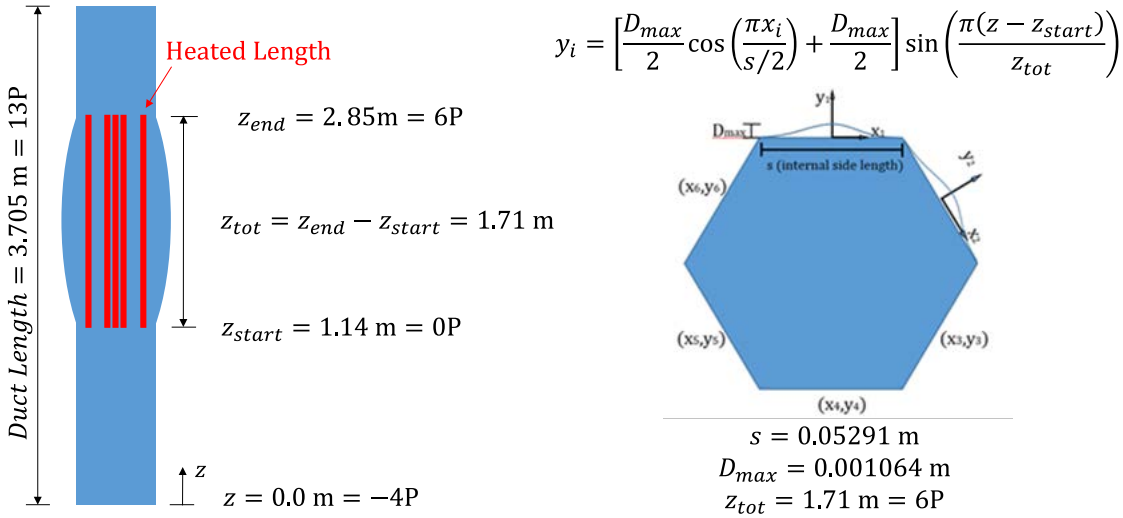


Figure 4-4: Illustration (not to scale) of the deformed CFD heated bundle, dimensions, and the functional form of the deformation. Note that the heated bundle actually has rounded corners.

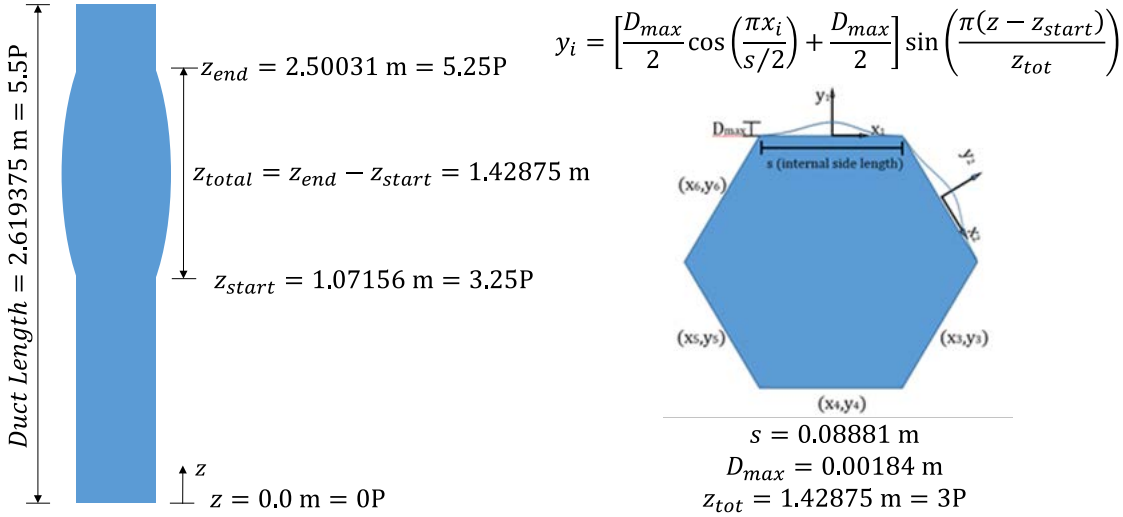


Figure 4-5: Illustration (not to scale) of the deformed CFD isothermal bundle, dimensions, and the functional form of the deformation.

4.2.2 Boundary Conditions

The boundary conditions (BC) of the isothermal and heated bundles are provided in Table 4-3 and Table 4-4, respectively. For all the pre-test cases, a flat inlet velocity profile is assumed as is suggested in the AFAFC Benchmark Specification [5]. The mass flow rates are adjusted to consider the MS: as the MS approach allows for flow through cells where the solid wire would normally be, the mass flow rate must be increased. This allows for the same inlet velocity as would be observed in the experiment, while maintaining the specified Reynolds number when using the geometric flow area and hydraulic diameter of the experiment. The relationship for the CFD mass flow rate $\dot{m}_{CFD}$ relative to the experimental value $\dot{m}_{EXP}$ is

$$\dot{m}_{CFD} = \dot{m}_{EXP}\frac{A_{inCFD}}{A_{inEXP}}$$

where A_{inCFD} and A_{inEXP} are the CFD and experimental flow areas at the inlet to the simulation (note that the CFD flow area is larger due to the inclusion of the wire cross-sectional area).

Table 4-3: Boundary conditions of the isothermal bundles.

Region	Boundary Surface(s)	Star CCM+ Boundary Condition	Values
P-Cymene (Fluid)	Inlet	Mass Flow Inlet	Mass Flow Rate = 19.16 kg/s (Re = 20e3) Pressure extrapolated from adjacent cell
P-Cymene (Fluid)	Outlet	Flow-Split Outlet	Velocity extrapolated from adjacent cell (only 1 outlet surface) Pressure extrapolated from adjacent cell
P-Cymene (Fluid)	Duct/Pins	No-Slip Wall	Velocity = 0 Pressure extrapolated from adjacent cell

Table 4-4: Boundary conditions of the heated bundles.

Region	Boundary Surface(s)	Star-CCM+ Boundary Condition	Specified Values
H_2O (Fluid)	Inlet	Mass Flow Inlet	Mass Flow Rate = 9.88 kg/s (Re = 20e3) Temperature = 32.22˚C Pressure extrapolated from adjacent cell
H_2O (Fluid)	Outlet	Flow-Split Outlet	Velocity extrapolated from adjacent cell (only 1 fluid outlet surface) Pressure extrapolated from adjacent cell Temperature extrapolated from adjacent cell
H_2O (Fluid)	Duct/Un-heated Tubes	No-Slip Wall	Velocity = 0 Pressure extrapolated from adjacent cell Adiabatic
H_2O (Fluid)	Heated Pins	No-Slip Wall/Interface with Outer Clad	Velocity = 0 Pressure extrapolated from adjacent cell No contact resistance for conjugate heat transfer
Clad (Solid)	Outer	Wall/Interface with Heated Pins	No contact resistance for conjugate heat transfer
Clad (Solid)	Inner	Wall/Interface with Outer Sheath	Contact resistance for conjugate heat transfer = 0.012 $K*m^2/kW$ (provided by STERN labs)

Clad (Solid)	Bottom/Top	Wall	Adiabatic
Sheath (Solid)	Outer	Wall/Interface with Inner Clad	Contact resistance for conjugate heat transfer = 0.012 K*m^2/kW (provided by STERN labs)
Sheath (Solid)	Inner	Wall	Heat flux profile described below
Monel Sheath (Solid)	Bottom/Top	Wall	Adiabatic

The fluid temperature at the inlet to the heated bundle is specified to the design specifications [1]. In the post-tests an adjustment to the inlet temperature and flowrate may need to be considered to account for the actual as-tested conditions. The heat flux is specified on the heated length of the inner diameter of the sheath, with the heat flux profile provided in the test specification [1]. This approach to the pre-test simulations was outlined in the benchmark specification [5]. An image of the heat flux source on the inner sheath of the heated pins is shown in Figure 4-6, and a plot of the normalized axial heat flux profile on these pins is shown in Figure 4-7. Each heated pin has a net power of 24 kW, resulting in a total power into the bundle of 456 kW. The benchmark specification also states that the pre-test simulations are to be run with adiabatic duct walls and adiabatic unheated tubes, and these boundaries are set as such. Between the clad and the sheath, a contact resistance is specified, which was provided by STERN labs (the manufacturers of the heated pins). The turbulence inlet conditions are set to a turbulence intensity of 3% (a sensitivity study may be conducted on this value in the future) and the turbulent length scale was calculated at 20% of the estimated turbulent boundary layer height (standard approach for internal flows). More details on the turbulence modeling are provided in Section 4.4.1.

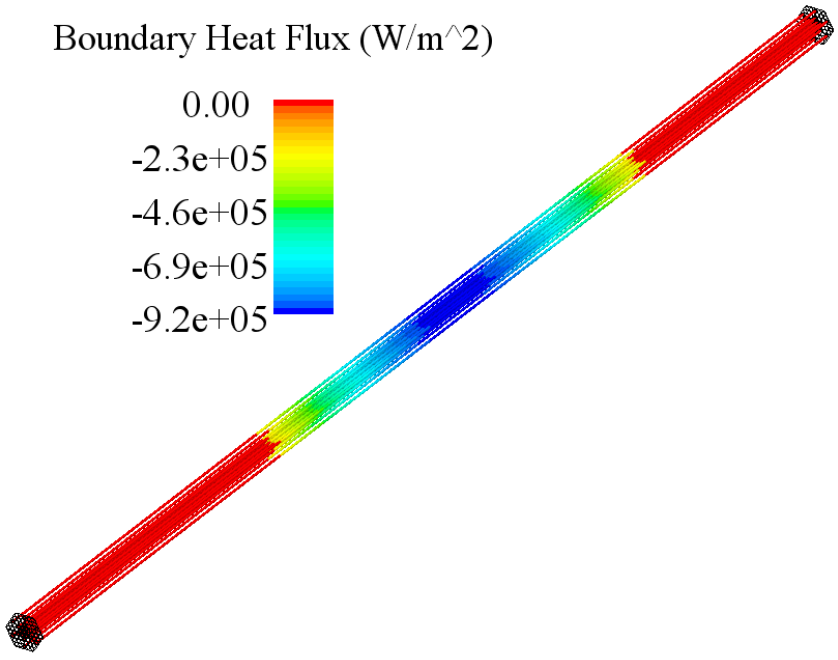


Figure 4-6: Boundary heat flux at the inner diameter of the sheath of the heated pins displaying the axial profile of the heated length.

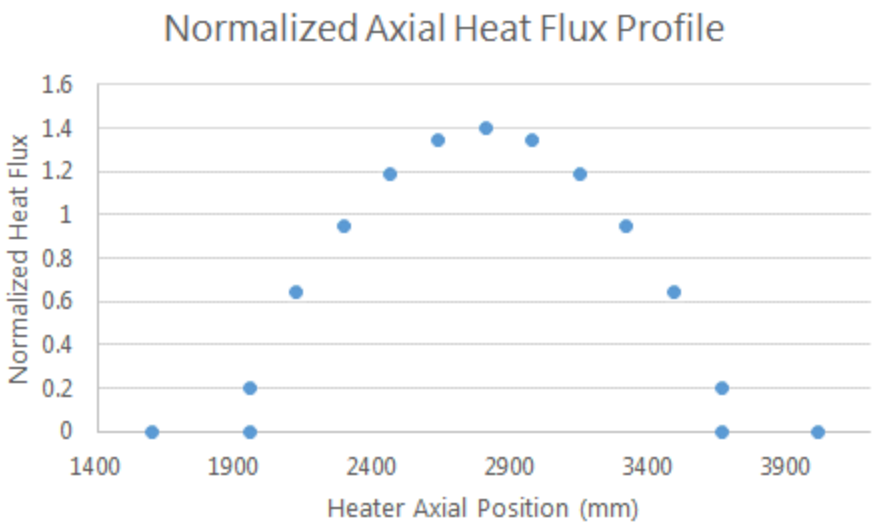


Figure 4-7: Normalized heat flux at the inner diameter of the sheath versus the axial position of the heater. Note that the total heated length is 1.71 m (6P).

4.3 Solution Verification Approach

Solution verification is the process of determining if the results from a numerical simulation of a mathematical model provide an adequate level of accuracy for their intended use [6]. One of the major objectives of this report is to provide confidence in the presented official pre-test results through quantitative solution verification. This primarily requires monitoring variables of interest across various mesh sizes to show numerical convergence to a specific value. A formal analysis is also possible to calculate an "exact" solution (*i.e.* if the mesh cell size approached an infinitesimal value) which can be used to provide the discretization error between the CFD solution and the "exact" solution. In this section, the details of the simulation meshes are provided, along with a description of a process to determine the "exact" solution called Richardson Extrapolation.

4.3.1 Mesh Refinement

As mentioned, the process of running simulations on various meshes is essential to solution verification. To perform a formal solution verification study that allows for Richardson extrapolation and an estimate of the discretization error, a systematic refinement is necessary [6]. That is, the refinement must be uniform in all spatial directions. A systematic mesh refinement is conducted here over a range of five meshes. These meshes are named according to the convention in Table 4-5 where the cell size ratio $h = \Delta x_i / \Delta x_{i,ref}$ where the reference cell sizes are based on the Finest mesh. Figure 4-8 provides the non-deformed isothermal and heated bundles' total cell counts for all mesh refinement levels. The deformed bundles have similar cell size ratios, and while the deformed heated bundle has a similar cell count, the deformed isothermal bundle has more cells because it is two pitches longer than the non-deformed isothermal bundle.

Table 4-5: Cell size ratios of the isothermal/heated bundle meshes and their names.

Isothermal Cell Size Ratio h	Heated Cell Size Ratio h	Mesh Name
1.98	2.0	Coarsest
1.71	1.72	Coarse
1.5	1.5	Medium
1.33	1.33	Fine
1.0	1.0	Finest

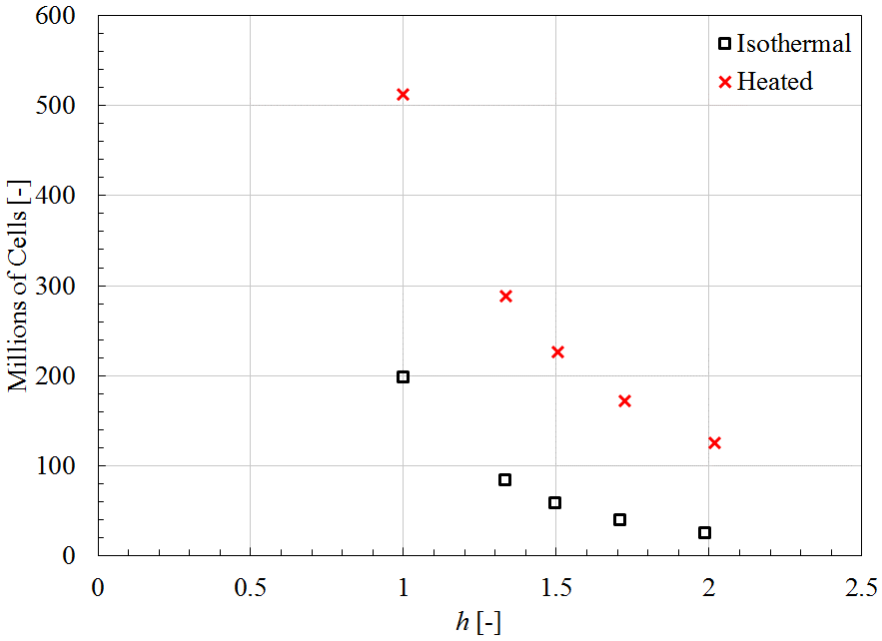


Figure 4-8: Number of cells versus cell size ratio for non-deformed isothermal and non-deformed heated bundles.

The distribution of the transverse cells for each level of mesh refinement of the non-deformed isothermal bundle can be visualized in Figure 4-9. There is a similar distribution of transverse cells for all of the bundles. Note that the shape of the wire wrap varies with mesh, becoming more realistically shaped with refinement. This is due to the surface of the wire not being preserved in the current MS approach, which reduces cell count, and thus improves computational cost (this V&V study will test the validity of this method). The number of cells in each direction of the non-deformed isothermal bundle is also provided in Figure 4-10. In addition to systematic refinement, a proportional coarsening of the axial cell distribution was also investigated and results are presented in Section 5.3.2.

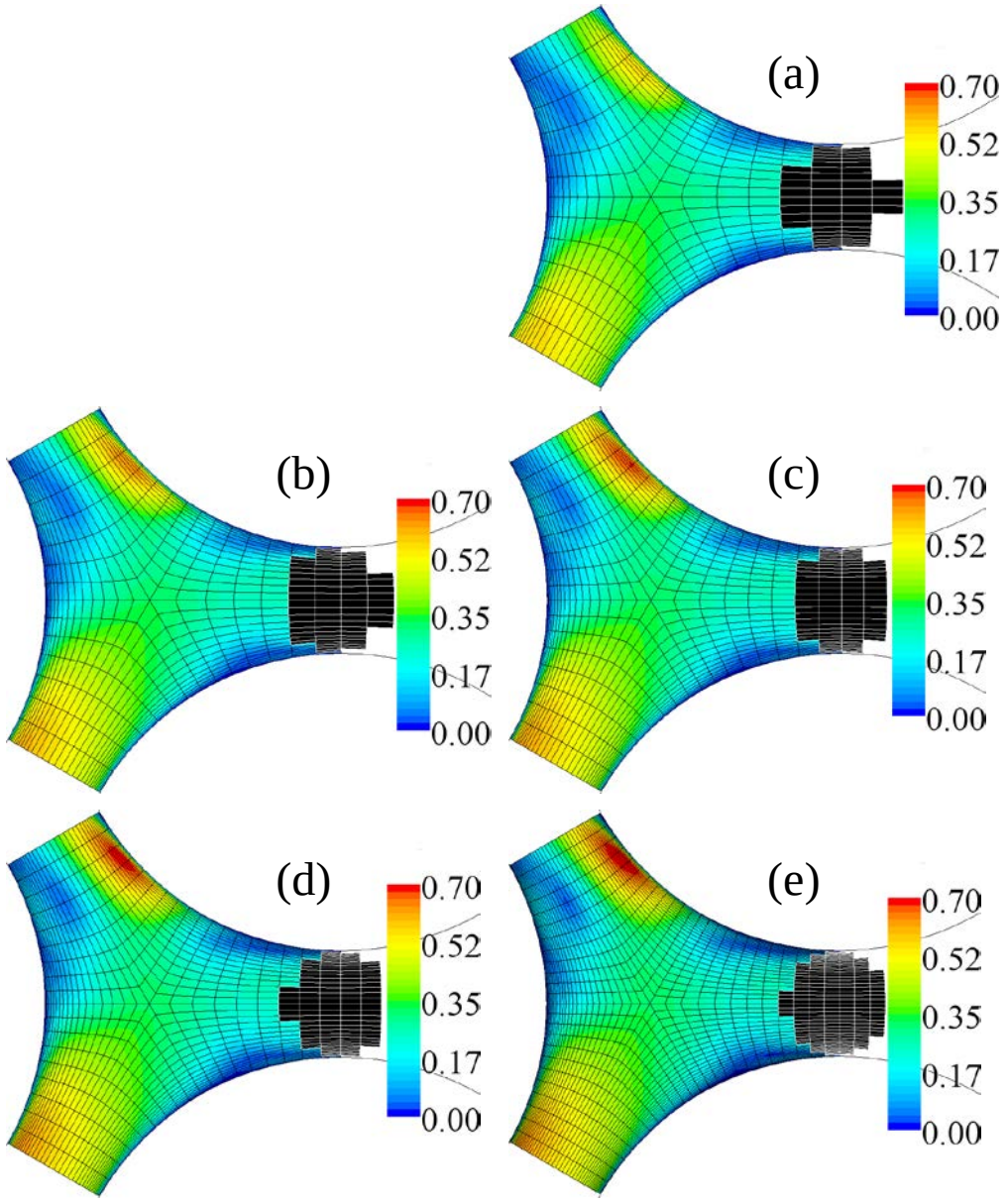


Figure 4-9: Transverse cell distribution for (a) Coarsest, (b) Coarse, (c) Medium, (d) Fine, and (e) Finest meshes shown with contours of transverse velocity magnitude [m/s].

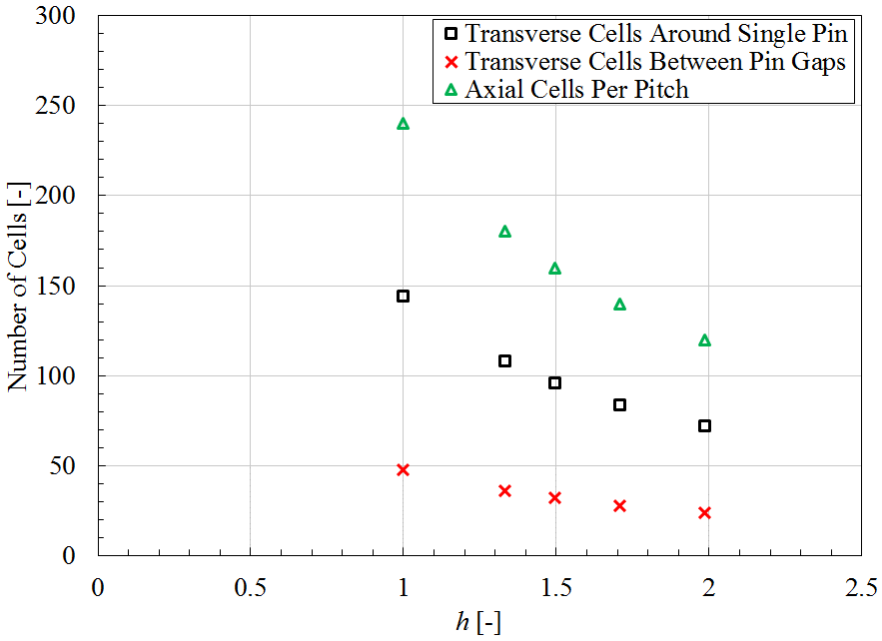


Figure 4-10: Number of cells in specific directions versus cell size ratio for the non-deformed isothermal bundle.

A close-up view of the Fine heated bundle mesh is shown in Figure 4-11. The red curves mark the boundaries between the fluid region, solid cladding, and solid sheath. For all mesh levels, the recommended 4-5 cells [4] across the thickness of the solid regions are present.

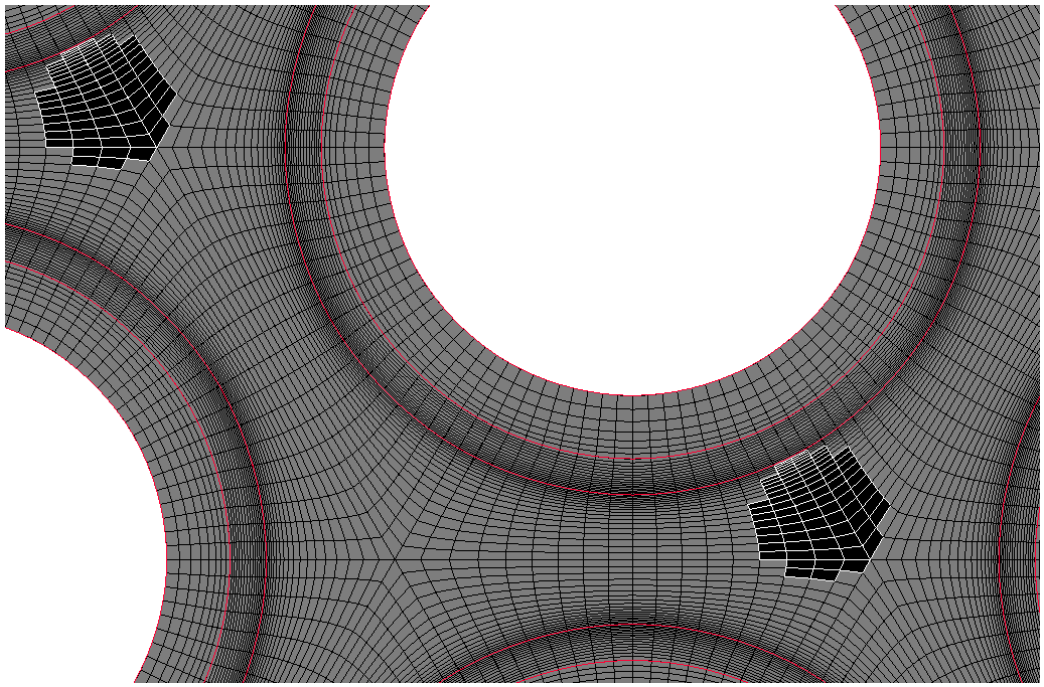


Figure 4-11: Fine mesh of the non-deformed heated bundle.

4.3.2 Richardson Extrapolation

The most common formal approach for estimating an exact solution to the discretized partial differential equation system of a numerical fluid mechanics problem is to perform a Richardson Extrapolation. A Richardson extrapolation is only accurate if the variable of interest has reached the asymptotic region of convergence. Thus, it is necessary to ensure that the Observed Order of Accuracy (OOA) approaches the

Formal Order of Accuracy (FOA). This requires at least three mesh levels that have been systematically refined and a variable of interest which is recommended to be a global (integrated) quantity rather than a local variable [6]. The OOA is the rate at which the variable of interest converges, and the FOA is the order of accuracy of the discretization schemes used for the mathematical model. Once the Richardson extrapolation is used to estimate the exact solution, the discretization error (the difference between the solution to the discretized equations and the exact solution to the mathematical model) can be estimated as well.

Consider three generic levels of systematic mesh refinement (coarse = 1, medium = 2, and fine =3) that have non-constant grid refinement factors $r_{12} = h_2/h_1 \neq r_{23} = h_3/h_2$. The OOA $\hat{p}$ can be determined for a variable of interest f by

$$\hat{p} = \frac{\ln\left[\left(\frac{r_{12}^{\hat{p}} - 1}{r_{23}^{\hat{p}} - 1}\right)\left(\frac{f_3 - f_2}{f_2 - f_1}\right)\right]}{\ln(r_{12})}$$

using a direct substitution iterative procedure. If the OOA approaches the FOA, then an accurate estimate of the exact solution $\bar{f}$ can be determined with a Richardson extrapolation as

$$\bar{f} = \frac{f_1 - f_2}{r_{12}^{\hat{p}} - 1}$$

and from this, the discretization error from the fine mesh $\bar{\varepsilon}_h$ can be calculated with

$$\bar{\varepsilon}_h = f_h - \bar{f}.$$

For complex practical problems, it is often difficult to achieve the asymptotic region of convergence [6]. In this case, the Richardson extrapolation and resulting discretization error estimate are not expected to provide quality exact solution and error estimates. For the results presented in this report, the Richardson extrapolation and discretization error are calculated with these approaches in the appropriate situations.

4.4 Model Sensitivity Approach

To investigate the sensitivity of the simulations to the choice of model and model parameters, a series of simulations are conducted with varying conditions. A number of turbulence models are examined, to study the effect this choice has on the results. Furthermore, to understand how the momentum source coefficient affects the solution variables of interest, the coefficient is given various values. These additional simulations will assist in selecting the simulation models used for the official pre-test results, although a final decision on which model choices should be used cannot be made until the experimental data becomes available. In this section, the model choices are introduced.

4.4.1 Turbulence Modeling

Four two-equation RANS turbulence models are investigated to determine their effect on the solution. These models are the Menter k-ω SST model, the Wilcox Standard k-ω model, the Standard k-ε model, and the Realizable k-ε model. The Standard k-ε model is the most widely used for industrial applications, although it is known to perform poorly under large adverse pressure gradients [7], rotating flows, and flow in non-circular ducts. The Realizable k-ε model is thought to be an improvement over the Standard k-ε model under all the circumstances where the Standard k-ε model performs poorly. The Wilcox Standard k-ω model has been shown to give improved results for boundary layers under adverse pressure gradient when compared with the Standard k-ε model, although it shows high sensitivity to the free-stream specific dissipation rate (and thus the inlet conditions). The Menter k-ω SST model derives the ω transport equation directly from the Standard k-ε model, and has a cross-diffusion term when compared with the Wilcox Standard k-ω model. It uses a blending function which allows for the k-ω model in the near-wall region and the k-ε model in the far-wall region. This allows for the improvement of the Standard k-ε model in the boundary layer under adverse pressure gradients, and also allows the boundary layer to be insensitive to the free-stream specific dissipation rate. The Menter k-ω SST model may be considered as the state-of-

the-art of linear eddy viscosity two-equation RANS turbulence models for industrial applications. As such, it is used in this report for the mesh sensitivity and momentum source sensitivity analyses.

For all of the models, the turbulence inlet conditions are set to 3% turbulence intensity and a turbulent length scale that is 22% of the inlet turbulent boundary layer thickness. These turbulence intensities and length scales are typical for wall-bounded inlet flows with moderate turbulence. At the outlet boundary, the turbulence variables are extrapolated from the interior cells. The wall BCs for turbulent kinetic energy are that the gradient normal to the wall is zero. The wall BCs for the dissipation rate and the specific dissipation rate are determined with the wall conditions specified in [4] for two-layer wall modeling and all-y^+ wall-modeling, respectively. These blended wall-function approaches allow for quality results on meshes with $y^+ < 5$ and $y^+ > 30$ but provide poor results on $5 < y^+ < 30$ [8]. With the prescribed flow conditions and the small gaps between pins, it is difficult to conduct a systematic mesh refinement study with $y^+ > 30$ and not reach the region of $5 < y^+ < 30$ (which would give inaccurate results). Thus, the average y^+ was ensured to be less than 5 for all levels of mesh refinement, for both the non-deformed and deformed meshes. Figure 4-12 and Figure 4-13 show the average, maximum, and minimum y^+ values for all of the non-deformed and deformed meshes.

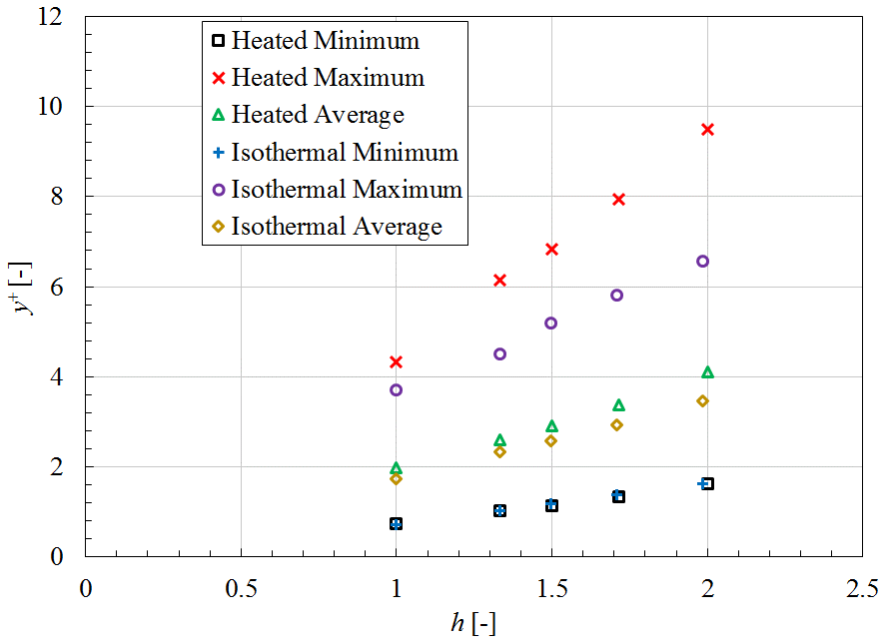


Figure 4-12: Average, maximum, and minimum y^+ values for all non-deformed meshes.

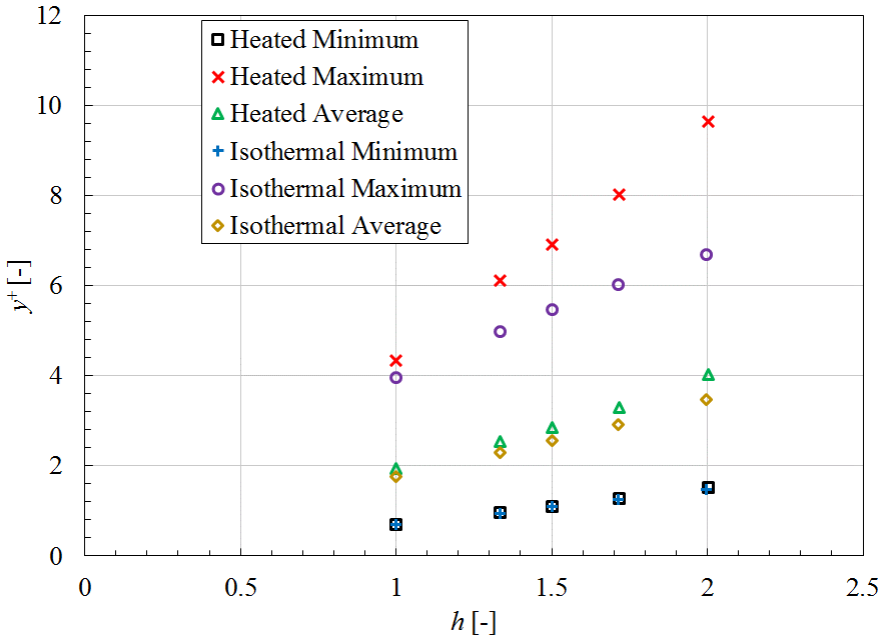


Figure 4-13: Average, maximum, and minimum y^+ values for all deformed meshes.

4.4.2 Momentum Source Coefficient

The normal forces of the momentum source model include a multiplication coefficient. The purpose of the coefficient is to make sure the velocity gradient is large enough to block the flow from entering or leaving the wire in the normal directions. It is mentioned that the MS coefficient should be greater than 2.0 to accomplish this task [3], but the reasoning behind this statement is ambiguous in the literature. Moreover, no maximum value of the coefficient is mentioned. Thus, a sensitivity study of coefficients greater than 2.0 is conducted to determine if the variables of interest show any appreciable variation.

4.5 Method of Manufactured Solutions

The Method of Manufactured Solutions (MMS) is an approach to create exact solutions for complex systems of non-linear Partial Differential Equations (PDE) to allow for formal code verification. It consists of choosing a solution (*a priori*) to the math model, operating the system of PDE onto the solution to obtain an analytical source term, and then inserting the source term into the PDE and numerically solving this new system with the source term. Thus, the numerical solution with the source term included should converge to the chosen exact solution at the rate of the FOA of the system. To verify that the OOA approaches the FOA a mesh refinement study is conducted. The L_2-norm (and sometimes the L_∞-norm) of the discretization error is used as a measure of global error to determine the OOA. If the OOA approaches the FOA then the code is verified to be correct. If it does not, then the code must have an error.

To initialize the development of the MMS to eventually be applied to the full 3D RANS Navier-Stokes equations (with the energy equation and two-equation turbulence models), a simple and well-studied case was chosen to implement in Star-CCM+. The 2D subsonic steady-state ideal gas Euler equations are solved. The governing equations with their respective source terms (generated through the MMS) are:

$$\frac{\partial(\rho u)}{\partial x}+\frac{\partial(\rho v)}{\partial y}=s_m(x,y)$$

$$\frac{\partial(\rho u^2+p)}{\partial x}+\frac{\partial(\rho uv)}{\partial y}=s_x(x,y)$$

$$\frac{\partial(\rho vu)}{\partial x}+\frac{\partial(\rho v^2+p)}{\partial y}=s_y(x,y)$$

$$\frac{\partial(\rho u e_t + p u)}{\partial x} + \frac{\partial(\rho v e_t + p v)}{\partial y} = s_e(x,y)$$

$$p = \rho R T$$

Here, ρ is density, u is the x-component of velocity, v is the y-component of velocity, p is the pressure, R is the ideal gas constant, and T is the temperature. The source terms for the mass, x-momentum, y-momentum, and energy equations are s_m, s_x, s_y, and s_e, respectively. These source terms are generated with the manufactured solution which is chosen as:

$$\rho(x,y) = \rho_0 + \rho_x \sin\left(\frac{a_{\rho x}\pi x}{L}\right) + \rho_y \cos\left(\frac{a_{\rho y}\pi y}{L}\right)$$

$$u(x,y) = u + u_x \sin\left(\frac{a_{ux}\pi x}{L}\right) + u_y \cos\left(\frac{a_{uy}\pi y}{L}\right)$$

$$v(x,y) = v_0 + v_x \cos\left(\frac{a_{vx}\pi x}{L}\right) + v_y \sin\left(\frac{a_{vy}\pi y}{L}\right)$$

$$p(x,y) = p_0 + p_x \cos\left(\frac{a_{px}\pi x}{L}\right) + p_y \sin\left(\frac{a_{py}\pi y}{L}\right)$$

Terms such as ρ_0, ρ_x, ρ_y, $a_{\rho x}$, and $a_{\rho y}$ are constant coefficients. The coefficients in this study are provided in Figure 4-14 and are from [9]. In fact, this initial test problem presented here follows that of [9]. The only differences are the code used and that Star-CCM+ does not allow for the full over-specification of the boundary conditions (as was done in [9]) but requires some boundary variables to be extrapolated from interior cells. The boundary conditions of this study are illustrated in Figure 4-15, and show that the problem is solved on a 2D box. The energy source term generated from the manufactured solution is shown in Figure 4-16. For the mesh refinement study, 5 meshes are used, and their cell size ratio and number of cells are shown in Table 4-6. As is shown in Section 5, this simple case displays potential coding errors for 2nd-order schemes, and the method will not be extended to more complex governing equations until this issue can be resolved. Current work within the Star-CCM+ development team is expected to resolve the issue and allow the method to be extended to equations representative of those used for the pre-test bundle simulations presented in this report.

Equation, ϕ	ϕ_0	ϕ_x	ϕ_y	ϕ_z	$a_{\phi x}$	$a_{\phi y}$	$a_{\phi z}$
ρ (kg/m^3)	1.	0.15	-0.1	0.	1.	0.5	0.
u (m/s)	70.	5.	-7.	0.	1.5	0.6	0.
v (m/s)	90.	-15.	8.5	0.	0.5	2./3.	0.
w (m/s)	0.	0.	0.	0.	0.	0.	0.
p (N/m^2)	$1.\times10^5$	0.2×10^5	0.5×10^5	0.	2.	1.	0.

Figure 4-14: Constant coefficients for the 2D subsonic steady-state ideal gas Euler equations manufactured solution. Coefficients from [9].

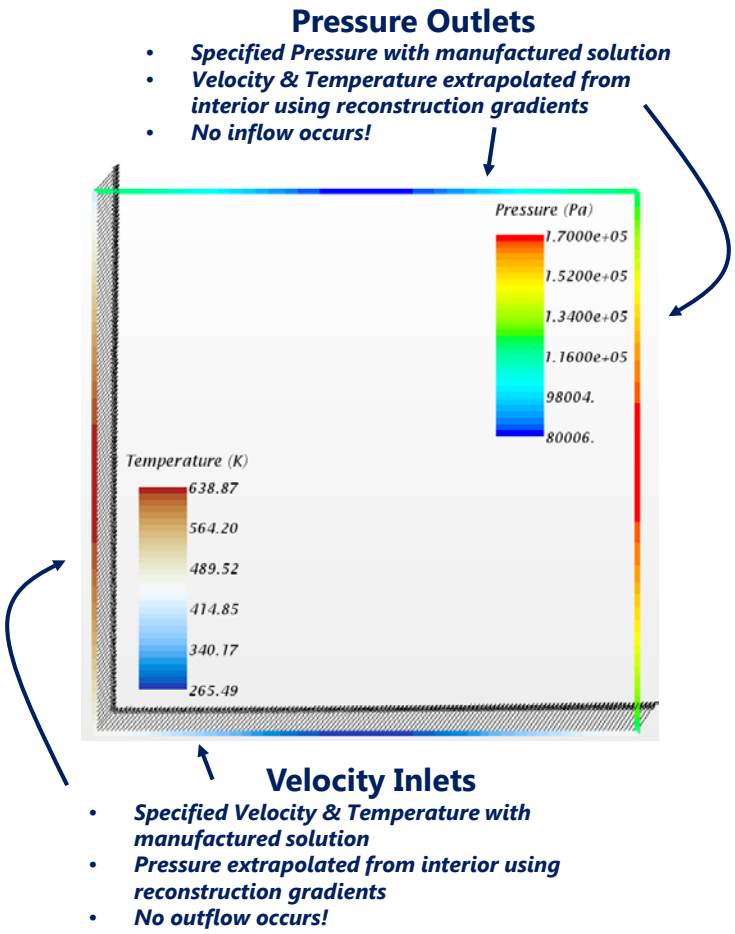


Figure 4-15: Boundary conditions for the 2D subsonic steady-state ideal gas Euler equations MMS simulation.

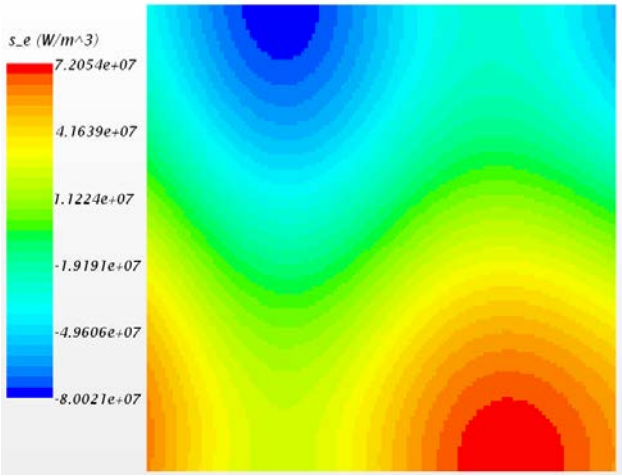


Figure 4-16: Contours of the energy source term determined from the manufactured solution.

Table 4-6: Cell size ratios and numbers of cells for each mesh of the manufactured solution simulations

h	16	8	4	2	1
Cells	8x8	16x6	32x32	64x64	128x128

5 VERIFICATION RESULTS AND DISCUSSION

Code verification is meant to ensure that the code correctly represents the math model [6]. Essentially, when a code is verified, it is claimed to not have coding mistakes in its implementation. There are a number of ways to accomplish this task. Here, one of the more formal and rigorous approaches is adopted. The MMS is used to provide the OOA of a set a simplified governing equations in an attempt to provide confidence in the code. In the future, the method will be extended to the more complex equations used for the pre-test results.

Solution verification is the process of determining if the results from a numerical simulation of a mathematical model provide an adequate level of accuracy for their intended use [6]. This task is accomplished through the verification of input data, verification of post-processing tools, and the estimation of numerical error. In this work, the input data was first verified by the author, and then checked again by the two reviewers of this document, to ensure that it was in accordance with the design specifications [1] [2]. The post-processing of simulation data in this study is minimal, as the raw data from the computations is presented in most instances. For the few cases where the output data is operated upon (*i.e.* spatial integration of variable fields at axial cross-sections, calculation of observed orders of accuracy, and Richardson extrapolation), the tools were verified to be working correctly by the author (through comparisons with integration tools built with field functions and comparisons with hand calculations). Numerical error estimation is perhaps the most significant form of solution verification as it is necessary to build solution confidence in all scientific numerical simulations. An estimation of numerical errors can help determine if a particular simulation sufficiently adheres to the underlying mathematical model, if further action needs to be taken for it to do so, or if those errors must be accounted for as uncertainty. The following sections display analyses to estimate numerical errors (round-off, iterative, statistical sampling, and discretization errors) for the CFD simulations of the heated and isothermal bundles (both non-deformed and deformed).

The following sections present code and solution verification results and discussion. In Section 5.1 the code verification results will be presented and discussed. The remaining material in Section 5 is focused on solution verification, and displays analyses to estimate numerical errors (round-off, iterative, statistical sampling, and discretization errors) for the CFD simulations of the heated and isothermal bundles (both non-deformed and deformed).

5.1 Code Verification

The MMS is used to verify the Star-CCM+ 2D subsonic steady-state ideal gas Euler solver. First, 1st-order numerical schemes are used, and then the verification analysis is conducted with 2nd-order numerical schemes. The L_2-norm of the discretization errors for each of the state variables solved for using 1st-order schemes are shown in Figure 5-1 for each of the mesh refinement levels. It is evident that the rate of convergence of the global discretization error is similar to that of a 1st-order scheme. While this qualitative approach provides some degree verification, calculating the OOA and comparing that to the FOA is the most rigorous approach and is shown in Figure 5-2. It is clear that the OOA converges to the FOA with mesh refinement, and thus, the code is quantitatively verified for these particular code options.

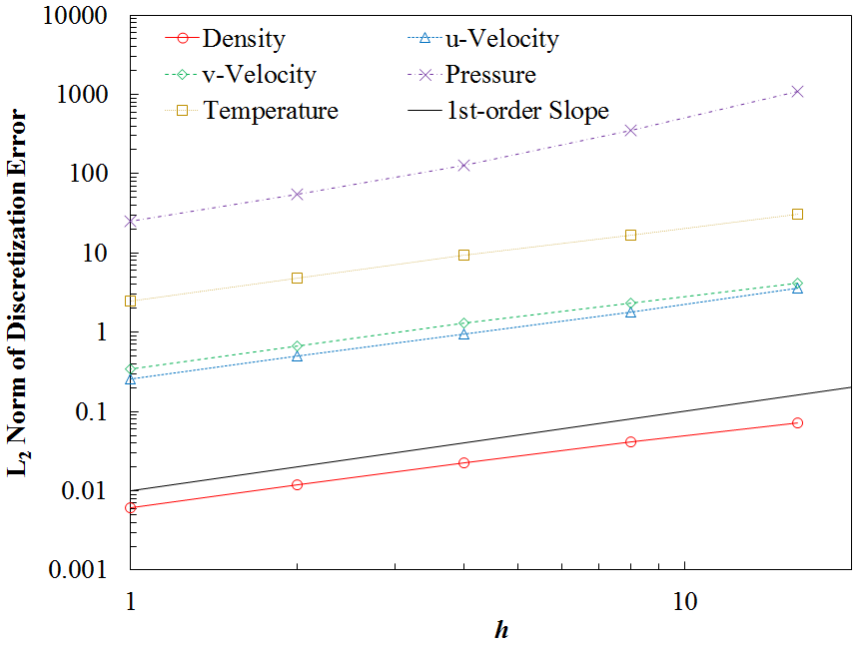


Figure 5-1: L_2-norm of the discretization error versus cell size ratio h for each state variable (1st-order numerical schemes.

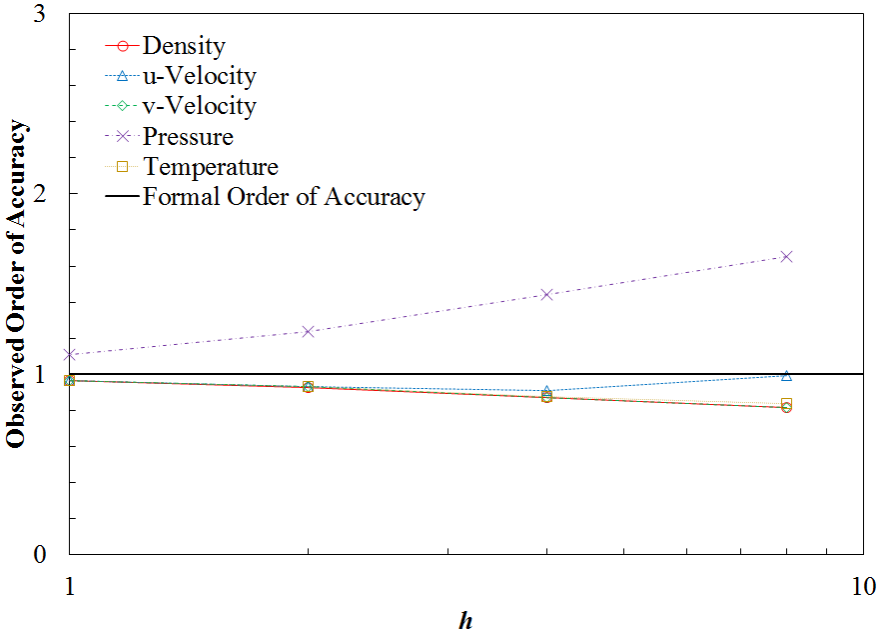


Figure 5-2: Observed Order of Accuracy versus cell size ratio for each state variable (1st-order numerical schemes).

Next, 2nd-order numerical schemes are used and the simulations are repeated. Figure 5-3 and Figure 5-4 show the convergence of the state variables and the OOA of the state variables, respectively. As the mesh is refined, the measure of global discretization error deviates from that of 2nd-order schemes. This is better illustrated with the OOA decreasing well below the FOA with mesh refinement. These results indicate that the 2nd-order schemes for this solver may contain a bug. Initial correspondence with CD-Adapco has brought forth the opinion that the boundary conditions should be investigated further. The problem has been sent to the Star-CCM+ development team with the hope of resolving the issue. Until this issue has been resolved, this component of code verification has been put on hold. However, more

complex manufactured solutions for the Navier-Stokes equations have already been implemented in Star-CCM+. Additionally, implementation of standard two-equation RANS turbulence model manufactured solutions have been investigated, and should be possible to implement in Star-CCM+ in the future. These extensions, and an extension to three-dimensions, allow the verification to be more in tune with the solver options used for the pre-test bundle simulations presented in this report.

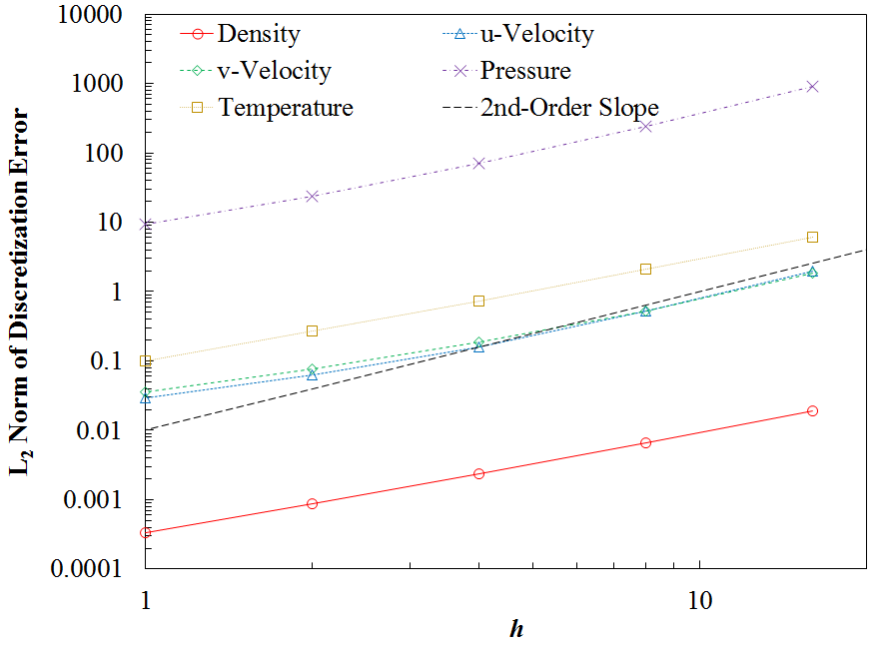


Figure 5-3: L_2-norm of the discretization error versus cell size ratio h for each state variable (2nd-order numerical schemes).

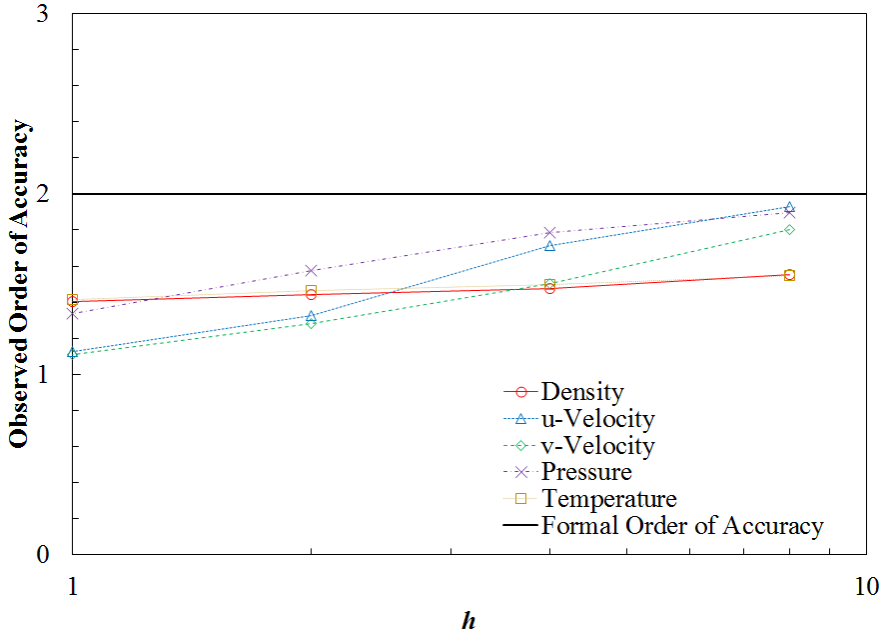


Figure 5-4: Observed Order of Accuracy versus cell size ratio for each state variable (2nd-order numerical schemes).

5.2 Round-off, Iterative, and Statistical Sampling Errors

The round-off, iterative, and statistical sampling errors can be estimated fairly easily (relative to discretization error) for a given CFD simulation. Round-off error occurs due to the finite numbers and operations that are inherent to digital computers. The precision of a simulation allows for a practical estimation of round-off error [6]. Star-CCM+ provides both mixed and double-precision code versions. The double precision version sets all variables of floating point data as double precision, while the mixed precision version only sets coordinate locations, pressure, and displacements as double precision with the remaining variables being single precision. A simulation of the non-deformed isothermal bundle was run to iterative convergence with both versions of the code. The results (not shown) indicate that there is negligible variation between the two versions of the code for this class of simulations, which entails that round-off error is insignificant when the solution is iteratively converged. Therefore, the remaining results presented in this report are obtained with the mixed precision code, due to the fact that the double precision version requires greater computational cost [4] and results in negligible variation from the mixed precision version.

Iterative error, occurring when iterative methods are used for numerical solutions (as is often the case with CFD), is the difference between a current approximate solution and the exact solution to an equation [6]. It can be monitored with the residual of the equation. If the residual approaches machine zero, the iterative error approaches zero as well, and is then a negligible source of error to the overall CFD numerical solution. For all the of the simulations presented in this report, the root-mean-square of the residuals for the discretized partial differential equations display monotonic convergence to machine zero (or very small values). Figure 5-5 shows the iterative convergence of a typical simulation. At iteration 800, a discontinuity appears due to the momentum source being initiated to account for the wire wrap. Otherwise, monotonic convergence is visible until the residuals remain constant for many iterations. All simulations were run until the residuals reached small values and then remained relatively constant for roughly 1000 iterations. Since this approach essentially provides the iterative solution as the number of iterations approaches infinity, the iterative error for these computations is negligible with respect to other sources of error.

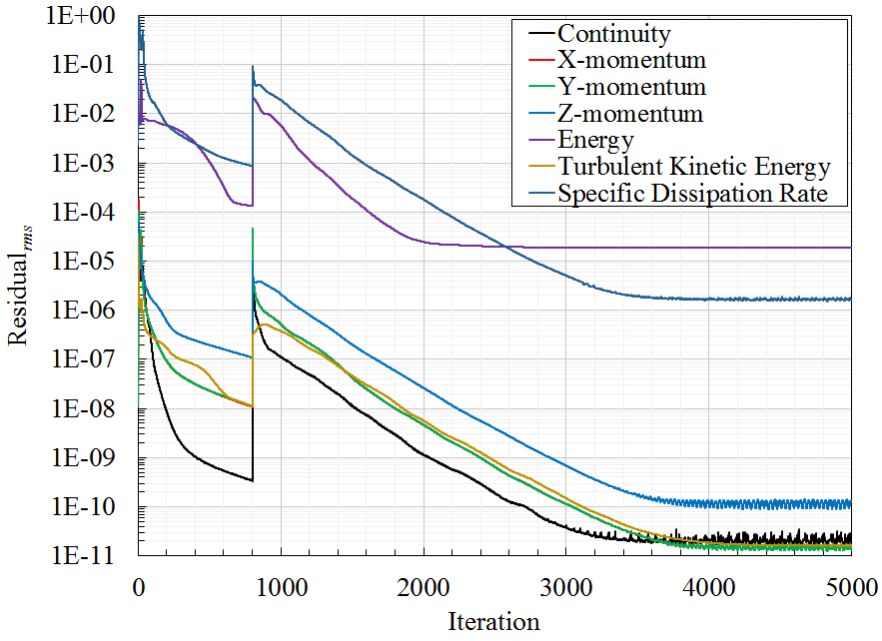


Figure 5-5: Root-mean-square of residual versus iteration for each PDE solved in the simulation of the non-deformed heated bundle.

Statistical sampling errors can occur if variables are fluctuating with respect to iteration and this phenomenon is not accounted for. It is common for the variables of a steady-state CFD solution to oscillate with iteration, even if there is a perceived iterative convergence of the residuals. Thus, it is important to check how the variables behave across a range of iterations. Therefore, variables of interest are monitored for the converged solutions. Figure 5-6 shows an example of this monitoring, with temperature probes at the outlet

of the non-deformed heated bundle and their measured fluctuation across 1000 iterations of a converged solution. Clearly, there is no evident oscillation in the temperature, and this ensures that the statistical sampling error is negligible. This result is similar with other variables and for other simulations as well.

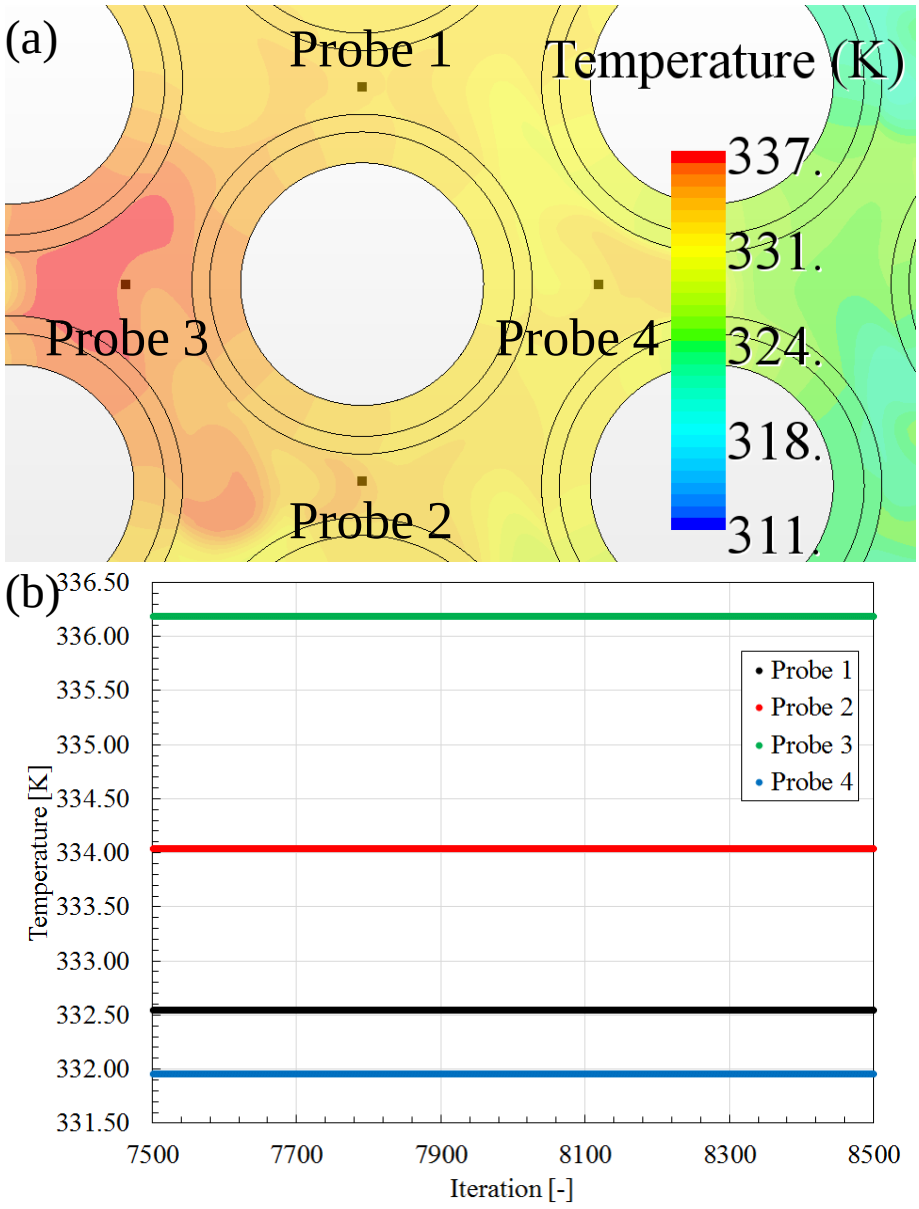


Figure 5-6: (a) Temperature probes on the outlet surface of the non-deformed heated bundle simulation (fine mesh) shown with temperature contours on that surface. (b) Temperature versus iteration for the four probes on the outlet surface.

5.3 Non-Deformed Bundles

In this section, a systematic mesh refinement study is presented for the non-deformed isothermal and non-deformed heated bundles. This exercise is conducted to display mesh convergence of the solutions, build confidence in the pre-test results, and attempt to estimate discretization errors of the pre-test predictions. The isothermal bundle analysis monitors pressure drops and velocity fields as variables of interest, while the heated bundle analysis is focused on pressure drops and temperature fields. An axial-direction mesh sensitivity study is also presented to provide evidence that the fine mesh can be coarsened by a great deal in this direction without any appreciable difference in the results.

5.3.1 Isothermal Bundle

The isothermal bundle experiments focus on velocity field measurements (using PIV and LDV) and pressure measurements (using pressure taps). To display mesh convergence of the simulations, subsets of the proposed results from each measurement technique are shown and discussed. Additionally, mass-flow averages of variables at axial slices of the bundle are presented to provide a more global measure of convergence, rather than for the individual points of the measurement locations.

Figure 5-7 shows that the bundle pressure drop approaches a constant value with a systematic mesh refinement, and this supports mesh convergence. An extrapolated value of the exact solution is also shown as the cell size ratio h approaches 0. The OOA of the Coarsest, Coarse, and Medium meshes is 4.32 and this is inconsistent with the FOA of 2.0. Recall that the OOA must approach the FOA to consider the solution "rigorously" converged, and for the Richardson extrapolation to be a quality estimate of the exact solution. However, these three meshes are used for the Richardson extrapolation because any other combinations of three meshes results in even higher OOA. For instance, the three finest meshes give an OOA of 18.1, and while this will produce a Richardson extrapolation which is very close to the Fine mesh result, the method of Richardson extrapolation is even less applicable here. It is thought that since the results approach a fairly constant value by the Fine mesh (and that value is within 5% less than that of the widely used Cheng-Todreas pressure drop correlation) that the bundle pressure drop can be considered converged by the Fine mesh.

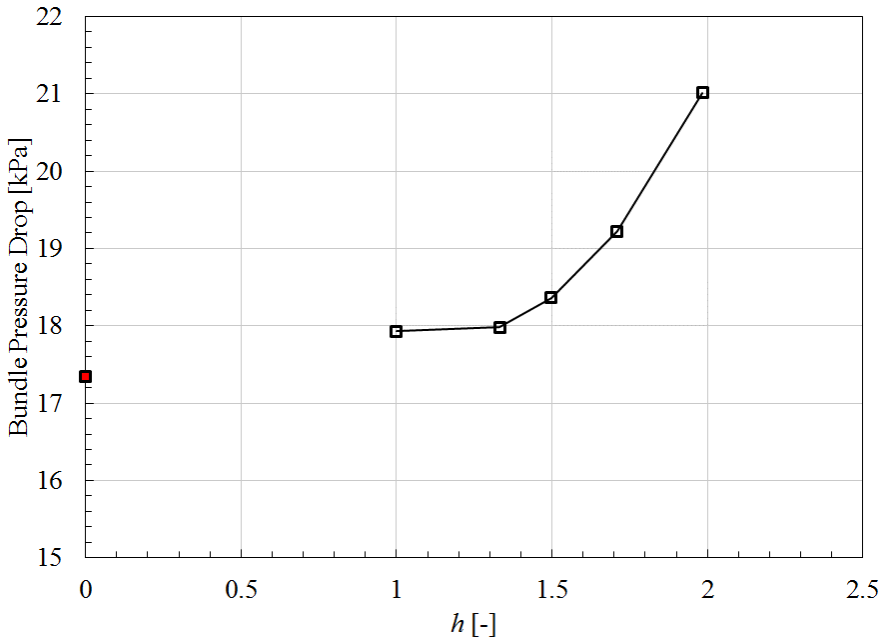


Figure 5-7: Non-deformed isothermal bundle pressure drop (based on mass-flow averages at inlet and outlet) versus cell size ratio h for all meshes. The red-filled square at $h = 0$ represents the Richardson extrapolation based on the Coarsest, Coarse, and Medium meshes.

Table 5-1 provides the percent difference between the bundle pressure drop calculated for each mesh and the Richardson extrapolation value. The value of the discretization error for the Fine mesh ($h = 1.33$) is calculated to be 729 Pa. It should be noted that there is a high degree of difficulty, and it is often impossible, to achieve a successful Richardson extrapolation that gives a quality estimate of the discretization error for a practical CFD problem [6]. In this case, caution should be taken in using this Richardson extrapolation as an exact solution. Still, the presented mesh sensitivity results build confidence that the Fine mesh provides a converged solution for the pressure field.

Table 5-1: Percent differences of bundle pressure drop from Richardson extrapolation value for all meshes.

Cell Size Ratio h	Mesh	Bundle Δp % Error from Richardson extrapolation
1.98	Coarsest	21.8
1.71	Coarse	11.4
1.5	Medium	6.4
1.33	Fine	4.2
1.0	Finest	3.9

Figure 5-8 displays pressure drops based on the difference between a probe at the bundle inlet on Face B and probes located at various axial heights on Face B. Monotonic convergence is seen for each of the axial locations, and similar to the bundle pressure drop, the Finest mesh shows relatively little variation from the Fine mesh. The OOA, Richardson extrapolation, and percent differences between the pressure drops from each mesh and the Richardson extrapolation have similar values to those calculated with the total bundle pressure drop. From this collection of pressure probes on a single duct face, it is also evident that the pressure drop along a single face does not follow a linear trend over the length of the bundle. This occurs due to the transverse pressure gradient that develops due to the wire-wrap, and which rotates in phase with the wire-wrap along the length of the duct [10].

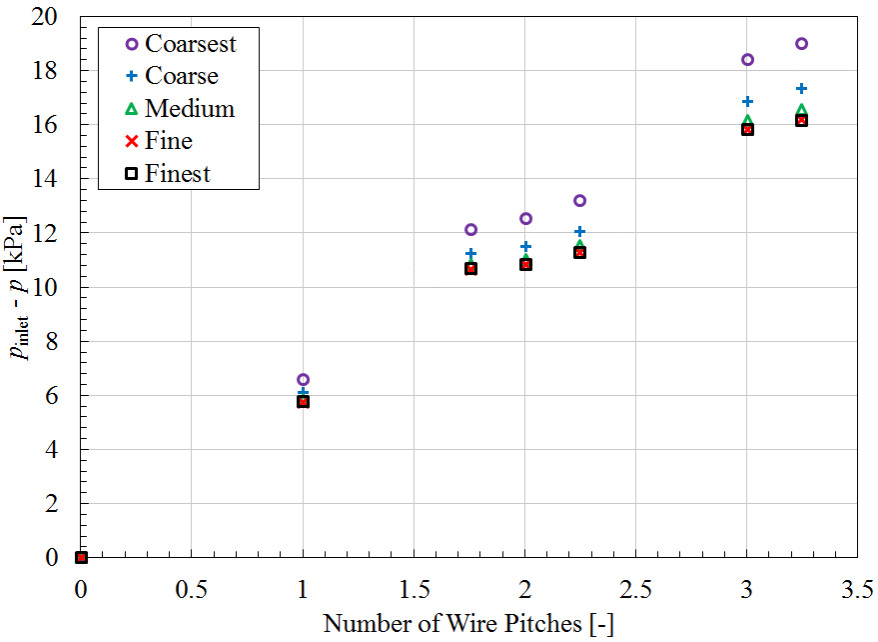


Figure 5-8: Pressure drops between Face B pressure probes at various axial heights and at the inlet versus the number of wire pitches into the non-deformed isothermal bundle for all meshes.

To examine the mesh convergence behavior of the isothermal bundle velocity field, the results from the proposed experiment LDV measurement locations can be sampled. The proposed measurement locations are to have the line probe originating at the outer diameter of the center pin and extending outward to the center of Face A (see Figure 5-9). These LDV Wall Effect line probes are meant to measure the effect of larger flow areas in the wall sub-channels when compared with internal sub-channels [2]. The measurements are proposed to be spaced by one wire radius, and the line probes are proposed to be placed between 2.25P and 3.25P at 0.166P intervals. To test the simulations for convergence and to capture the full flow profile between the pins, these seven line probes are constructed to have a higher density of points than the experiments have. When the actual locations of the experimental LDV points are reported, the pre-test simulation data will be processed at those exact locations for validation with the experiments. Three of the line probe results are presented here to display mesh convergence, while the other four line probes are

shown in Appendix 9.1. Data from other proposed LDV measurement types and locations [2] will be extracted from the pre-test simulations when the actual experimental locations are received. In Figure 5-9 the line probe extends from the center pin to Face A with the wire-wrap oriented at 12 o'clock looking up through the bundle from the inlet. The wire rotates clockwise from this orientation as it moves up through the bundle and the Duct Faces A-F progress in the clockwise direction as well.

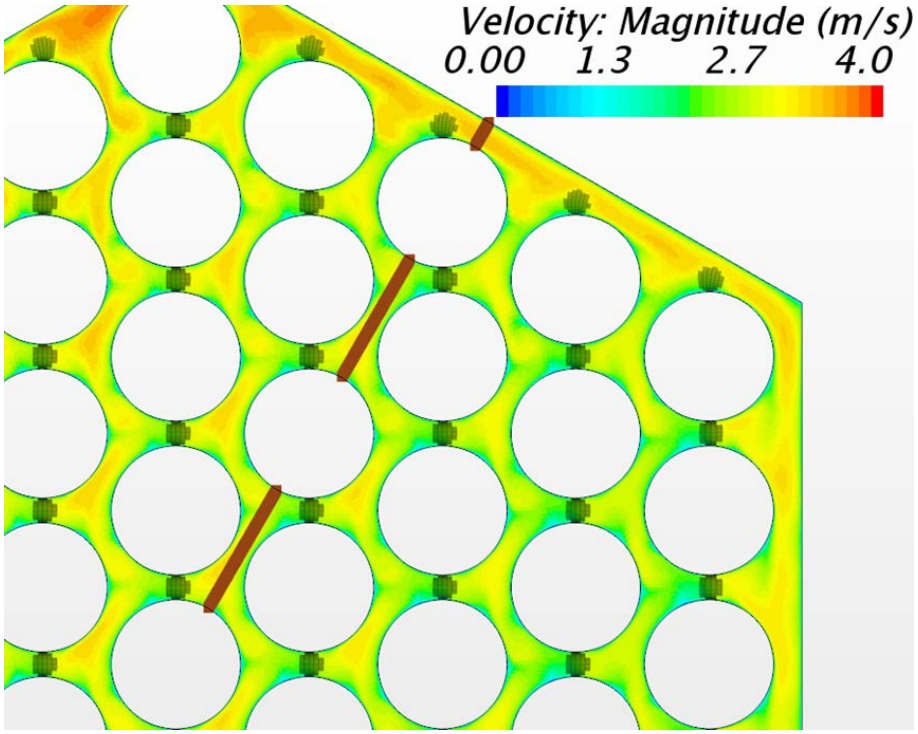


Figure 5-9: Line probe at 3.25P (wire-wrap at 12 o'clock) from center pin to center of Face A, overlaid on axial slice of velocity magnitude contours.

The velocity profiles from the line probe at 2.416P (an axial location where the wire-wrap is at 2 o'clock) are shown in Figure 5-10. The data gaps between the profiles are where the CFD line probe passes through the pins and therefore is outside the fluid domain. As the probe locations approach the pin walls, the velocity approaches zero. It should be noted that there is some level of interpolation to the probe points which varies for each level of mesh refinement since the probe points do not always align with the cell centers. Still, it is clear that the profiles match well for all the meshes as the wall is approached. In the regions farther from the wall, monotonic mesh convergence is visible at most points although at many locations there is very little variation in the results between meshes. At some distinct locations where there are peaks or troughs *(i.e.* radius of 0.048 m) there can be differences of over 11% between the Coarsest and Finest meshes. However, by the Medium and Fine meshes there are hardly any differences between these profiles and that of the Finest mesh at any of the probe locations.

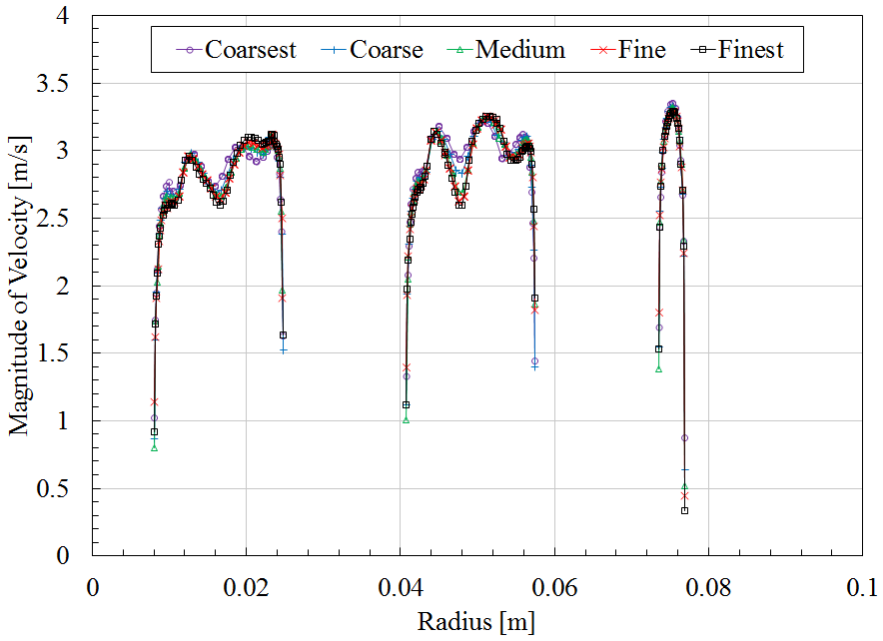


Figure 5-10: Velocity magnitude versus radial position from the center of the duct at 2.416P (wire-wrap at 2 o'clock) for all meshes.

Figure 5-11 displays the velocity profiles at 3.084P (an axial location where the wire-wrap is at 10 o'clock). The small data gaps that occur in the middle of two wider profiles are where the wires are located. Note that the velocity does not approach zero as the probes approach the location of the wires. Recall that the momentum source is used rather than a resolved mesh around the wires, and that the wire locations are made up of cells with fluid flow; therefore a no-slip condition is not imposed as the probe approaches this location. The velocity field within the wire was consciously omitted in these results, as the experiments will not have flow in this region. The local CFD velocity field results should be considered suspect and unreliable in the regions close to the wires. The future validation of the CFD with the experiments will help determine errors of these CFD results in the regions close to the wires. As with the previous line probe presented, the profiles of this line probe show little variation with refinement after the Medium mesh. Figure 5-12, which displays the profiles at 3.25P (wire-wrap at 12 o'clock), shows little variation with refinement for all the meshes. A formal mesh convergence analysis was not conducted on each of the local velocity values. Such analyses are not recommended for local quantities [6], and moreover, at most locations the values vary so little amongst the five meshes that a high degree of solution confidence can be built from the results.

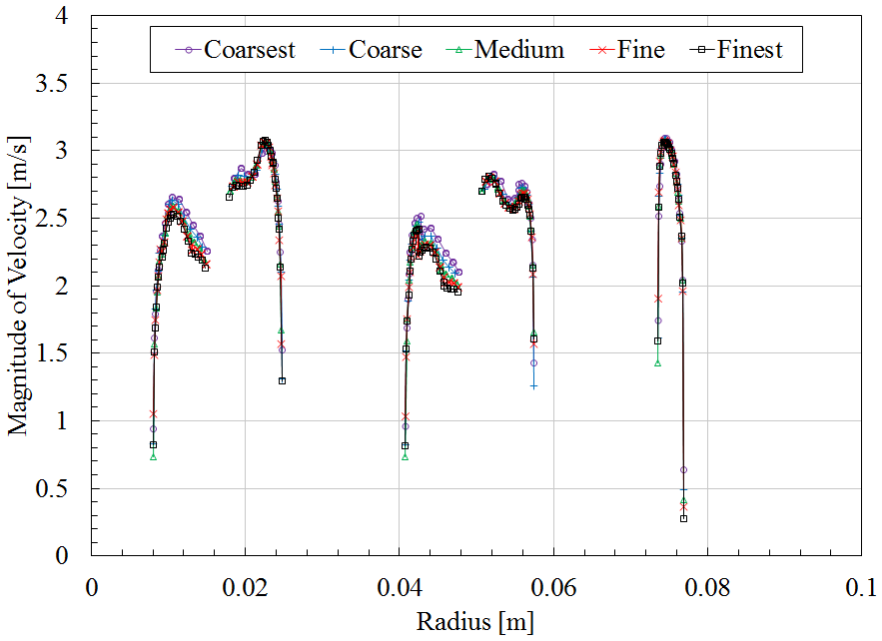


Figure 5-11: Velocity magnitude versus radial position from the center of the duct at 3.084P (wire-wrap at 10 o'clock) for all meshes.

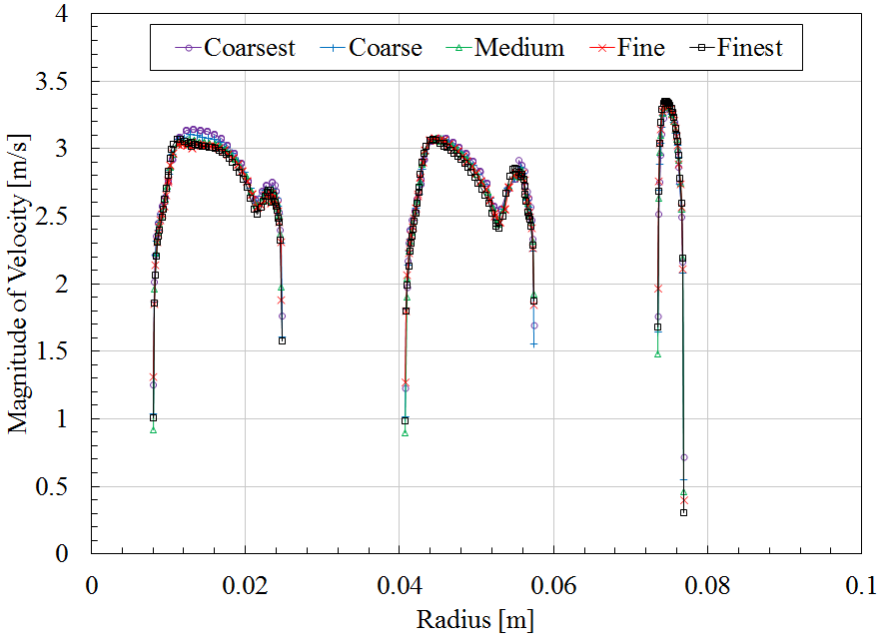


Figure 5-12: Velocity magnitude versus radial position from center of the duct at 3.25P (wire-wrap at 12 o'clock) for all meshes.

The magnitude of velocity is largely dominated by the axial velocity but it is also important to determine the transverse velocities in the bundle. Other proposed experiment measurements for the velocity field use PIV at various locations in the bundle. Individual sub-channel projected transverse velocity measurements were chosen as a representative PIV case to display mesh convergence. The test specification mentions that these particular measurements are to provide insight into the amount of mixing across sub-channels, and insight into the separation of vortices from the trailing edges of the wires [2]. The qualitative mesh convergence of the transverse velocity magnitudes for a proposed edge sub-channel measurement location are shown in Figure 5-13. The field does not vary much over the five meshes except for the intensity of the

higher magnitudes in the vicinity of the wire-wrap. Even these regions display little variation from the Fine mesh results. Overall, these images provide confidence in the solution mesh convergence of this particular region. Similar results from other common PIV regions, such as a corner sub-channel and an internal sub-channel, can be seen in Appendix 9.1. Note that the cross-section of the wire-wrap becomes a more realistic round shape as the mesh is refined. The irregular shapes of the wire for the coarse meshes may prove to be a potential drawback of this particular implementation of the MS approach. The original development of the MS method [3] preserved the surface of the wires regardless of the mesh size, while the current implementation presented here does not.

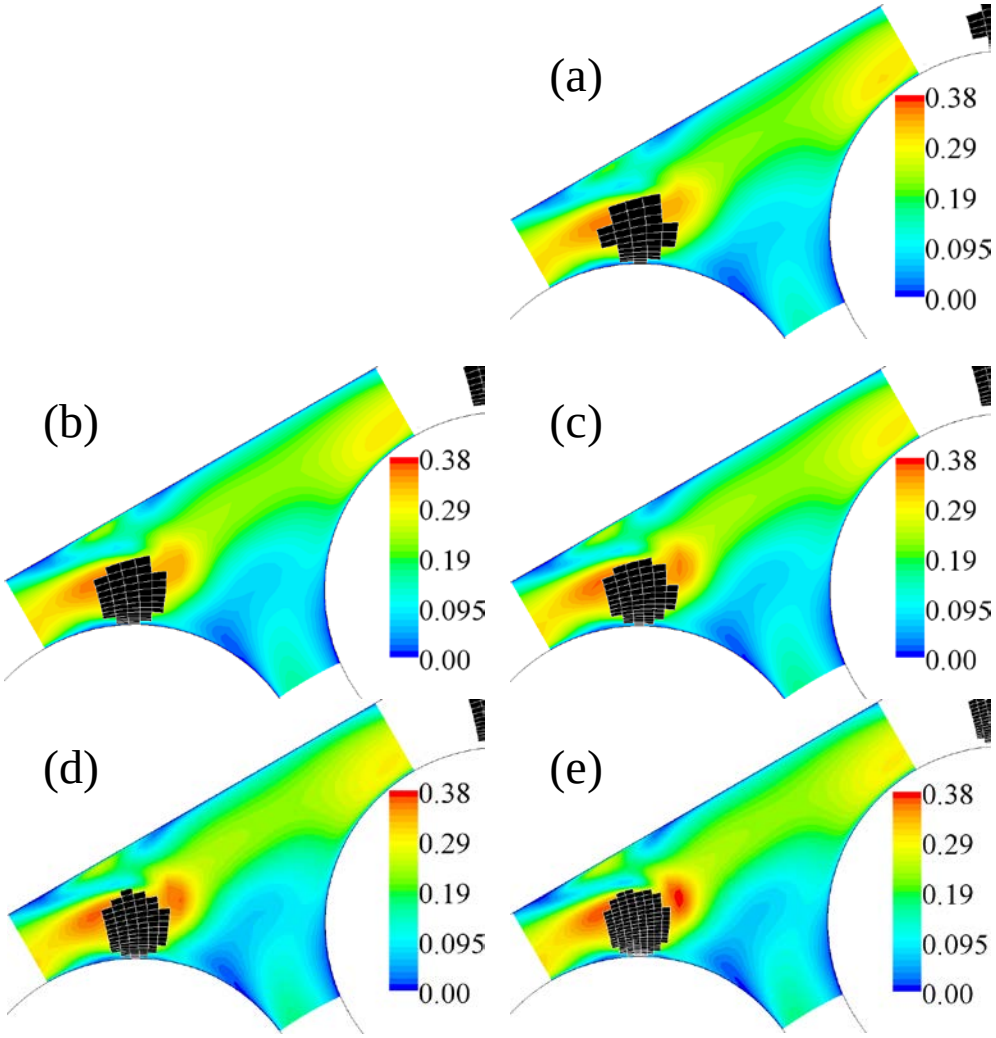


Figure 5-13: Contours of magnitude of projected transverse velocities [m/s] of an edge sub-channel at 3.25P (wire-wrap at 12 o'clock) for the (a) Coarsest, (b) Coarse, (c) Medium, (d) Fine, and (e) Finest meshes.

For a more global picture of the transverse velocity field mesh convergence, mass-flow averages of the x and y components of the velocity were sampled at various axial cross-sections between 2.25P and 3.25P. Figure 5-14 and Figure 5-15 show these results and display suitable mesh independence at most locations by the Medium mesh.

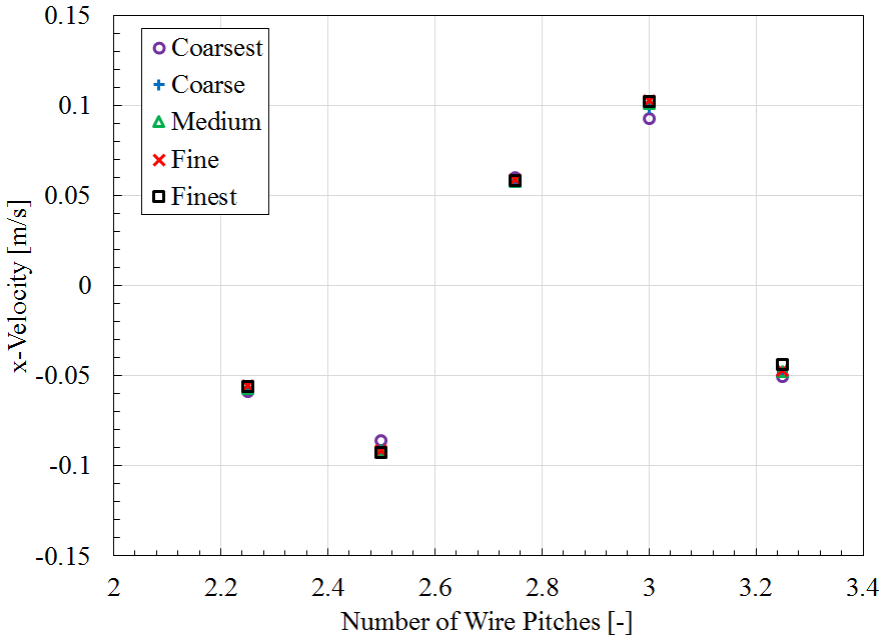


Figure 5-14: x-component of velocity (transverse) versus number of wire pitches into the bundle (axially) for all meshes.

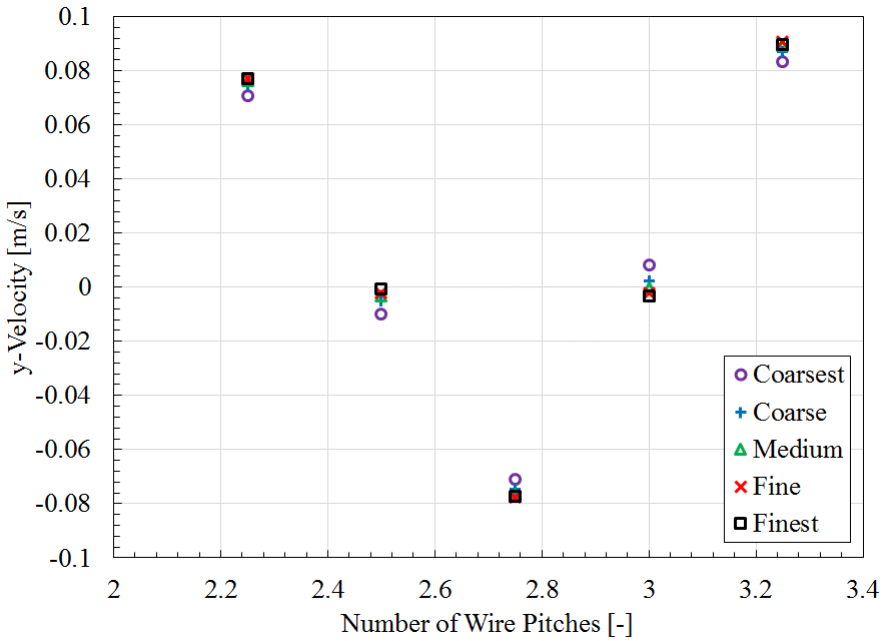


Figure 5-15: y-component of velocity (transverse) versus number of wire pitches into the bundle (axially) for all meshes.

5.3.2 Axial Mesh Sensitivity

An axial-direction mesh sensitivity study is also presented in addition to the systematic mesh refinement described earlier. While a systematic refinement is required for a textbook estimation of the discretization error [6], for the specific variables of interest, it can over predict the necessary level of refinement. Here, the non-deformed isothermal Fine mesh is coarsened in the axial direction such that it has the cell distribution of the Coarsest mesh in that direction while maintaining the cell distribution of the Fine mesh in the transverse directions (radial and azimuthal). The Fine mesh is used as the base case for this study because it was previously shown that the pressure and velocity results show little variation between the Fine

and Finest meshes. Figure 5-16 shows that the pressure drop results between the two meshes have no appreciable differences. Furthermore, Figure 5-17 and Figure 5-18 show that there is no appreciable difference between the meshes for the velocity profiles at proposed line probes. Other proposed velocity measurements give similar results between the two meshes as well. Thus, the solution does not require axial refinement past the Coarsest level to reach the converged solution. This notion can provide a 32% reduction in mesh size (27 million fewer cells) from the Fine mesh and still achieve the same results. The transversely-Fine/axially-Coarsest mesh is also roughly 2 million cells less than the Medium mesh. While the remaining isothermal bundle cases do not take advantage of this possible cell reduction, the heated bundle cases only have refinement in the transverse directions and maintain the Coarsest cell distribution in the axial direction.

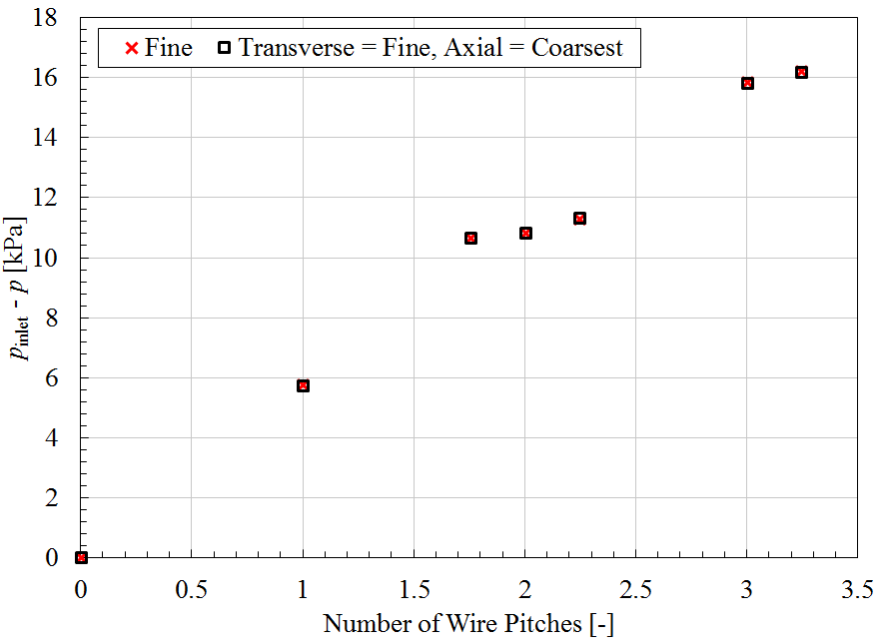


Figure 5-16: Pressure drops between Face B pressure probes at various axial heights and at the inlet versus the number of wire pitches into the non-deformed isothermal bundle for the Fine mesh and a transversely-Fine/axially-Coarsest mesh.

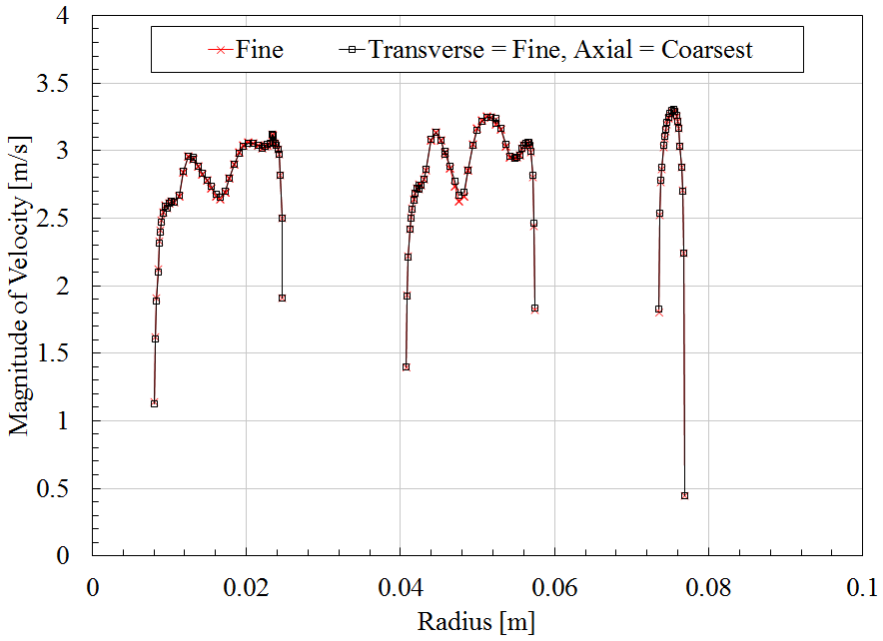


Figure 5-17: Velocity magnitude versus radial position from the center of the duct at 2.416P (wire-wrap at 2 o'clock) for the Fine mesh and the transversely-Fine/axially-Coarsest mesh.

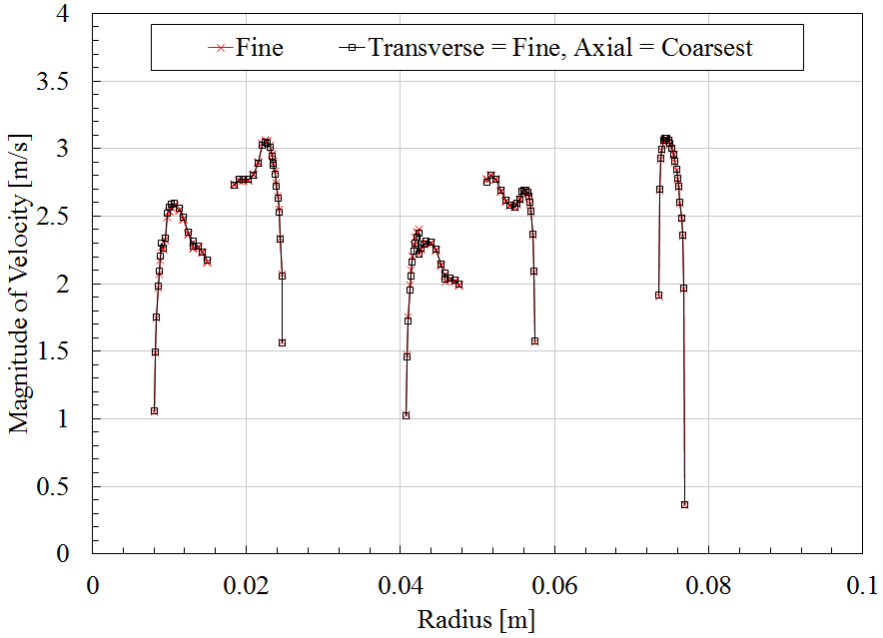


Figure 5-18: Velocity magnitude versus radial position from the center of the duct at 3.084P (wire-wrap at 10 o'clock) for the Fine mesh and the transversely-Fine/axially-Coarsest mesh.

5.3.3 Heated Bundle

The heated bundle experiments focus on temperature measurements (using thermocouples) and pressure measurements (using pressure taps). To display mesh convergence of the simulations, subsets of the results from each proposed measurement technique are shown and discussed. Additionally, the difference between mass-flow averages of pressure at the inlet and outlet of the bundle are presented to provide a more global measure of convergence, rather than for the individual points of the measurement locations. The systematic mesh refinement of the heated bundle mesh only occurs in the two transverse directions (azimuthally around the pins and radially between the pins). This was done to reduce the cell count as the

heated bundle has 13 pitches in the axial direction which is much greater than the 3.5 pitches of the isothermal bundle. Moreover, an argument can be made based on the study in Section 5.3.2, that refining in the axial direction past the Coarsest mesh is unnecessary. For the heated bundle, the cell size ratio h is determined based on the 2D systematic refinement in the transverse directions.

Figure 5-19 shows that the bundle pressure drop monotonically approaches a constant value with a systematic mesh refinement, and this suggests mesh convergence. An extrapolated value of the exact solution, based on the Coarsest, Coarse, and Medium meshes, is also shown as the cell size ratio h approaches 0. The OOA of the Coarsest, Coarse, and Medium meshes is 1.92 and this is consistent with the FOA of 2.0. Recall that the OOA must approach the FOA to consider the solution "rigorously" converged, and for the Richardson extrapolation to be a quality estimate of the exact solution. Even though these results imply that this Richardson extrapolation can be considered a quality estimate of the exact solution, the Fine and Finest mesh results show a trend towards a much higher bundle pressure drop than the Richardson extrapolation. The three finest meshes give an OOA of 6.7, and while this will produce a Richardson extrapolation of 121,800 Pa (within 3% of the Fine mesh), the method of Richardson extrapolation is even less applicable here. As with the non-deformed isothermal bundle, the OOA increases further with refinement. This convergence behavior (with unknown origin at this point, although the MS is a suspected culprit) precludes these mesh convergence results from being accurate estimates of the bundle pressure drop based on Richardson extrapolation. It is thought that since the results approach a fairly constant value by the Fine mesh (and that value is within 7% less than that of the widely used Cheng-Todreas pressure drop correlation) that the bundle pressure drop can be considered adequately converged by the Fine mesh.

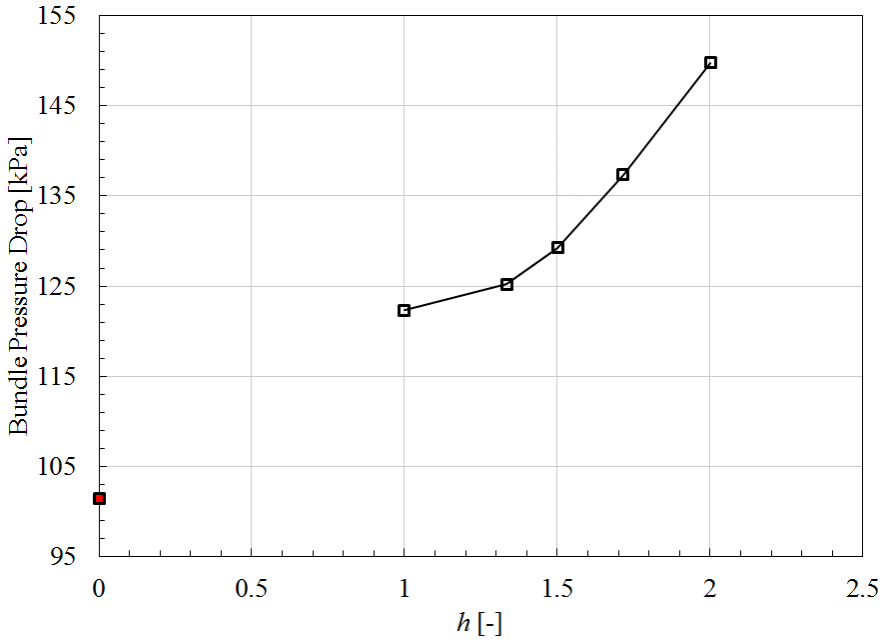


Figure 5-19: Non-deformed heated bundle pressure drop (based on mass-flow averages at inlet and outlet) versus cell size ratio h for all meshes. The red-filled square at $h = 0$ represents the Richardson extrapolation based on the Coarsest, Coarse, and Medium meshes.

Table 5-2 provides the percent difference between the bundle pressure drop calculated for each mesh and the Richardson extrapolation value. The value of the discretization error for the Fine mesh ($h = 1.33$) is calculated to be 27,752 Pa. It should be noted that there is a high degree of difficulty, and it is often impossible, to achieve a successful Richardson extrapolation that gives a quality estimate of the discretization error for a practical CFD problem [6]. In this case, caution should be taken in using this Richardson extrapolation as an exact solution. Still, the presented mesh sensitivity results build confidence that the Fine mesh provides a converged solution for the pressure field.

Table 5-2: Percent differences of heated bundle pressure drop from Richardson extrapolation value for all meshes.

Cell Size Ratio h	Mesh	Bundle Δp % Error from Richardson extrapolation
2.0	Coarsest	47.6
1.72	Coarse	35.4
1.5	Medium	27.4
1.33	Fine	23.4
1.0	Finest	20.6

Figure 5-20 displays pressure drops based on the difference between a probe at the bundle inlet on Face B and probes located at various axial heights on Face B. Monotonic convergence is seen for each of the axial locations, and similar to the bundle pressure drop, the Finest mesh shows relatively little variation from the Fine mesh.

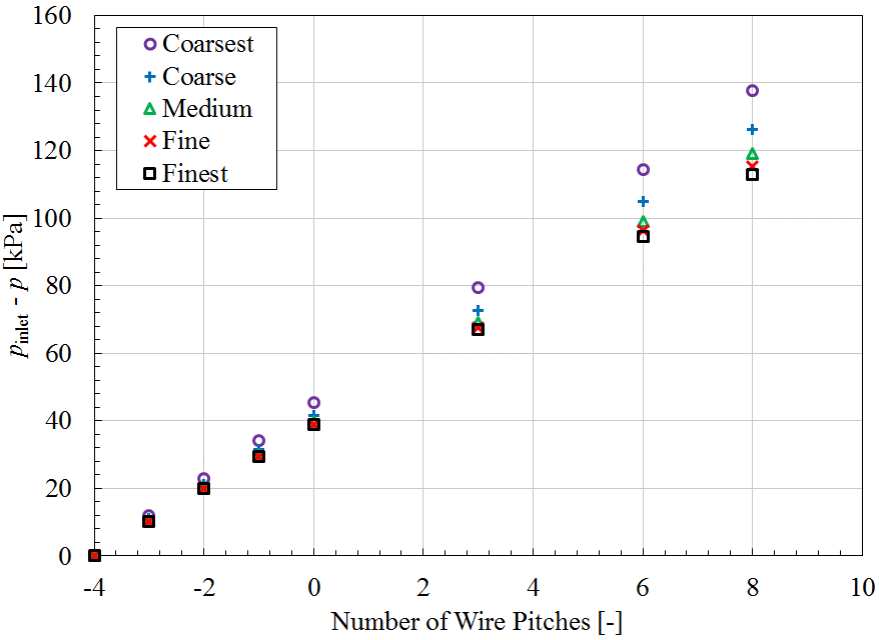


Figure 5-20: Pressure drops between Face B pressure probes at various axial heights and at the inlet versus the number of wire pitches into the non-deformed heated bundle for all meshes.

To examine the mesh convergence behavior of the heated bundle temperature field, the results from the proposed thermocouple measurement locations can be sampled. With such a large number (over 350 [1]) of proposed thermocouple measurement locations on various pins and duct faces, only 22 locations are presented here with an additional 23 provided in Appendix 9.2. These 22 thermocouples are distributed throughout the bundle and on different types of pins. During the validation phase, the other thermocouple results will be extracted from the saved pre-test simulations for comparison. The notation for the pin description and locations are given in Figure 5-21 and Figure 5-22.

STA = Standard Configuration

AXI = Axial Configuration

AZI = Azimuthal Configuration

TUB = Unheated Tube Configuration

STA001 = Standard Configuration Heated Pin in row 0 and location 01.

AZI206 = Azimuthal Configuration Heated Pin in row 2 and location 06.

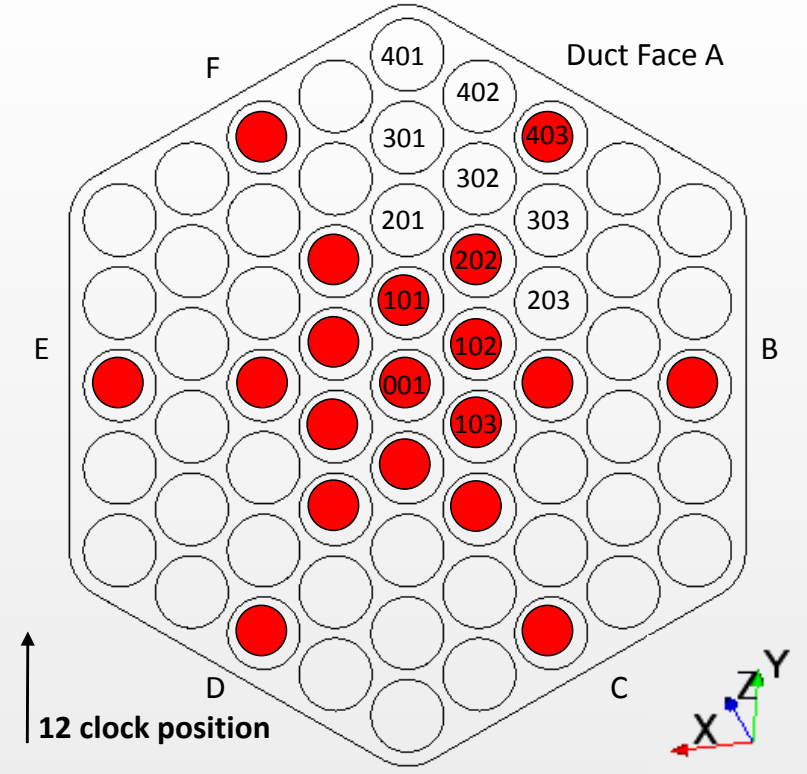


Figure 5-21: Notation for labeling of pin measurement configuration, row number, and location number.

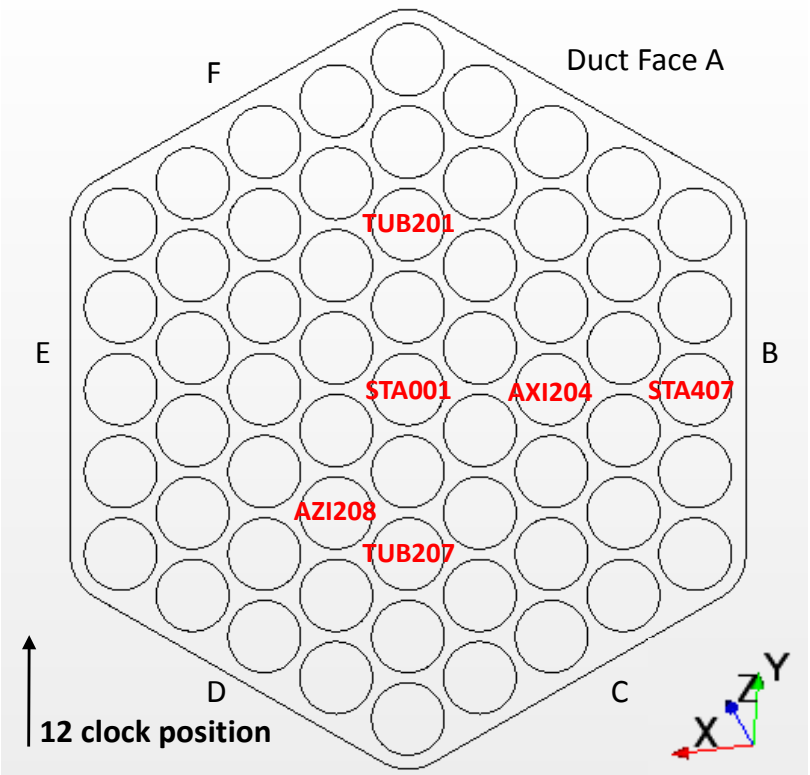


Figure 5-22: Notation and locations of specific pins examined in this report.

Figure 5-23 shows the0 temperatures at the thermocouple locations on the heated pin with Standard configuration at the center of the bundle (abbreviated STA001 where STA = Standard configuration, 0 =

Row 0, and 01 = Pin #01 in that row) for all of the meshes. Recall that the heated region extends between z = 0P and z = 6P, and that the heated pin thermocouples are not placed at the clad-fluid interface, but are imbedded in the pins at the clad-sheath interface. The temperatures of the thermocouples above the heated region show good convergence, as the results do not vary much between meshes. However, for the locations within the heated region, mesh independence is not truly attained, even by the Fine mesh. In the heated region, the values between the Fine and Finest mesh may only differ by roughly 2-4%, but since the values between the Medium and Fine meshes only differ by roughly 1-2%, questions can be raised as to whether the temperature field (in the heated region) is mesh independent or not. Nonetheless, as the temperatures are fairly close to each other for all of the meshes, it is expected that the Fine mesh can provide suitably converged pre-test results.

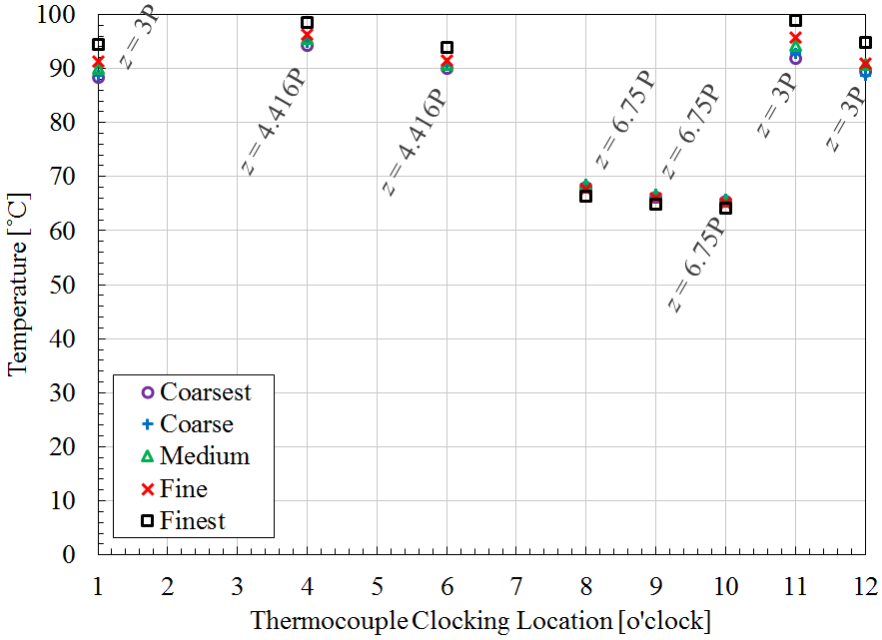


Figure 5-23: Temperature versus the clocking location of each thermocouple on heated pin STA001 for all meshes. Axial locations are also given for each thermocouple.

Figure 5-24 provides the temperatures at the thermocouple locations on the heated pin with Azimuthal configuration in 2nd pin row (abbreviated AZI208 where AZI = Azimuthal configuration, 2 = Row 2, and 08 = Pin #08 in that row) for all the meshes. Note that all the thermocouples are in the heated region (and embedded between the clad and sheath), and thus, all of the results show similar behavior with mesh refinement to those thermocouple readings in the heated region of STA001. That is, while there is monotonic behavior, and the difference between the Finest and Fine mesh results is only 3-4%, the difference between the Fine and Medium mesh results is usually even smaller. Again, since the temperatures are fairly close for all meshes, it is expected that the Fine mesh can provide acceptable results for the pre-tests. The temperatures sampled from the non-heated tube in the 2nd pin row (abbreviated TUB201 where TUB = non-heated Tube configuration, 2 = Row 2, and 01 = Pin #01) are shown in Figure 5-25. As the results show little variation amongst the meshes, it is clear that this region of the temperature field is converged for any of the mesh choices. This is true whether the values are sampled within or outside of the heated region. Recall that TUB201 is unheated and that the thermocouples are on the outer surface of the tube rather than embedded between the clad and the sheath. These differences between TUB201 and the heated pins could be a factor in the increased difficulty to display temperature field convergence within the heated region of the heated pins.

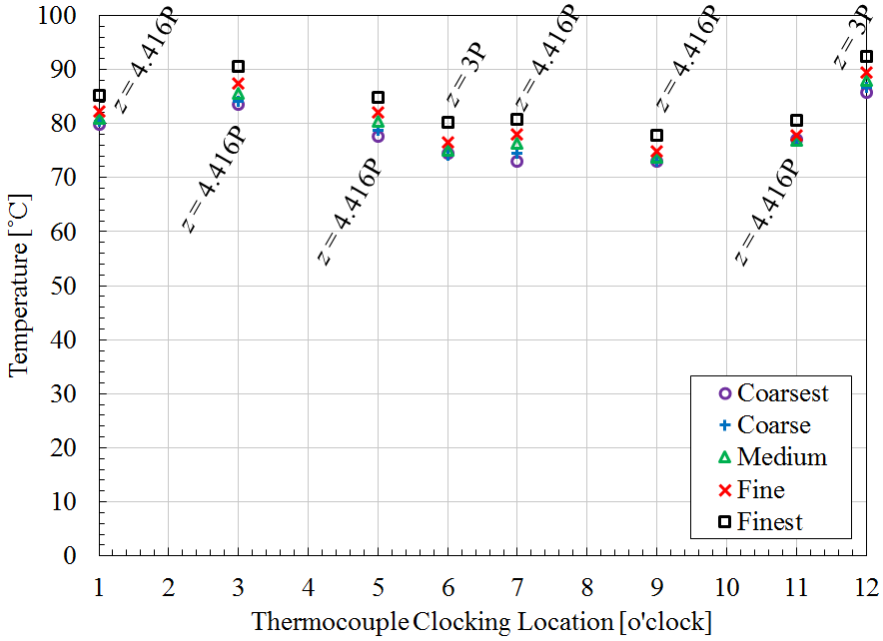


Figure 5-24: Temperature versus the clock location of each thermocouple on heated pin AZI208 for all meshes. Axial locations are also given for each thermocouple.

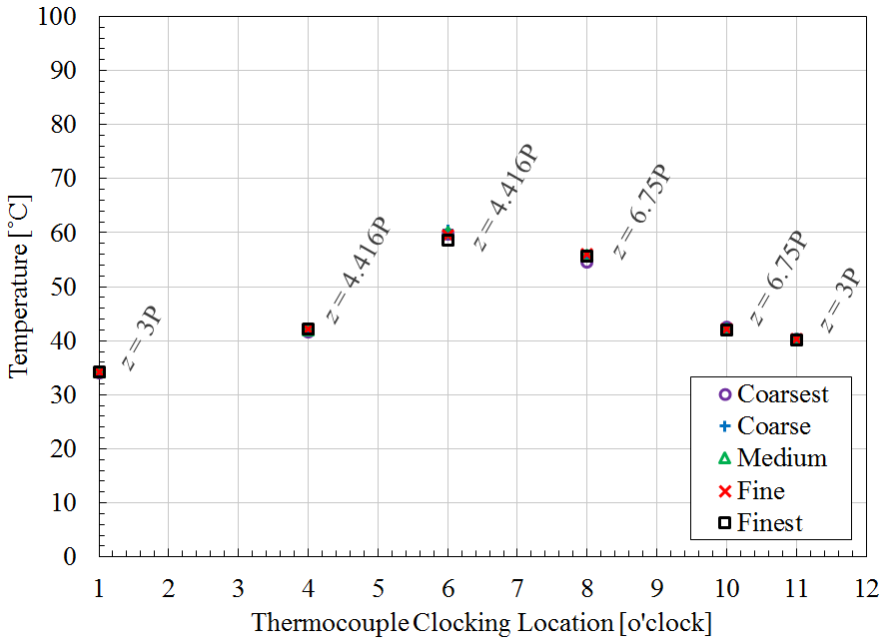


Figure 5-25: Temperature versus the clock location of each thermocouple on non-heated tube TUB201 for all meshes. Axial locations are also given for each thermocouple.

5.4 Deformed Bundles

In this section, a systematic mesh refinement study is presented for the deformed isothermal and deformed heated bundles. This exercise is conducted to display mesh convergence of the solutions and build confidence in the pre-test results. The isothermal bundle analysis monitors pressure drops and velocity fields as variables of interest, while the heated bundle analysis is focused on pressure drops and temperature fields. Since the deformed bundles are only slightly different from the non-deformed bundles, their convergence behavior is similar. Therefore, an abbreviated version of the analysis presented for the

non-deformed cases is presented here for the deformed cases. The remaining details of the mesh convergence analysis are shown in Appendices 9.3 and 9.4.

5.4.1 Isothermal Bundle

Figure 5-26 displays pressure drops based on the difference between a probe at the bundle inlet on Face B and probes located at various axial heights on Face B. Monotonic convergence is seen for each of the axial locations, and the Finest mesh shows relatively little variation from the Fine mesh. Also, note that the deformed isothermal bundle is 5.5 pitches in length which is 2 pitches longer than the non-deformed isothermal bundle. Figure 5-27 shows the velocity profiles from a proposed line probe measurement at an axial height of z = 3.75P. This is at the height of the maximum transverse duct deformation and 1.5P into the 3P long deformation region of the duct. Clearly, the profiles vary little between the various meshes, implying that the simulations have reached a converged solution for this variable of interest.

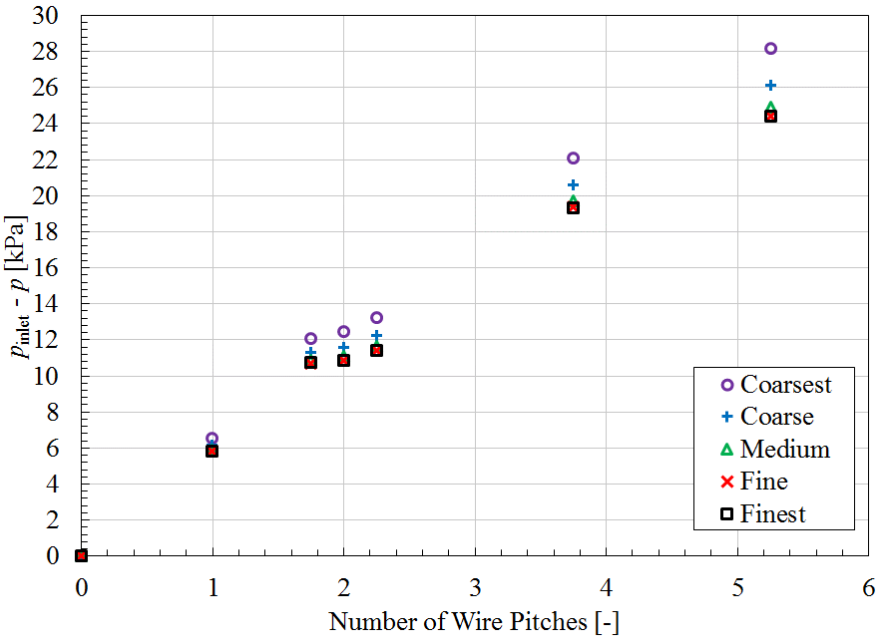


Figure 5-26: Pressure drops between Face B pressure probes at various axial heights and at the inlet versus the number of wire pitches into the deformed isothermal bundle for all meshes.

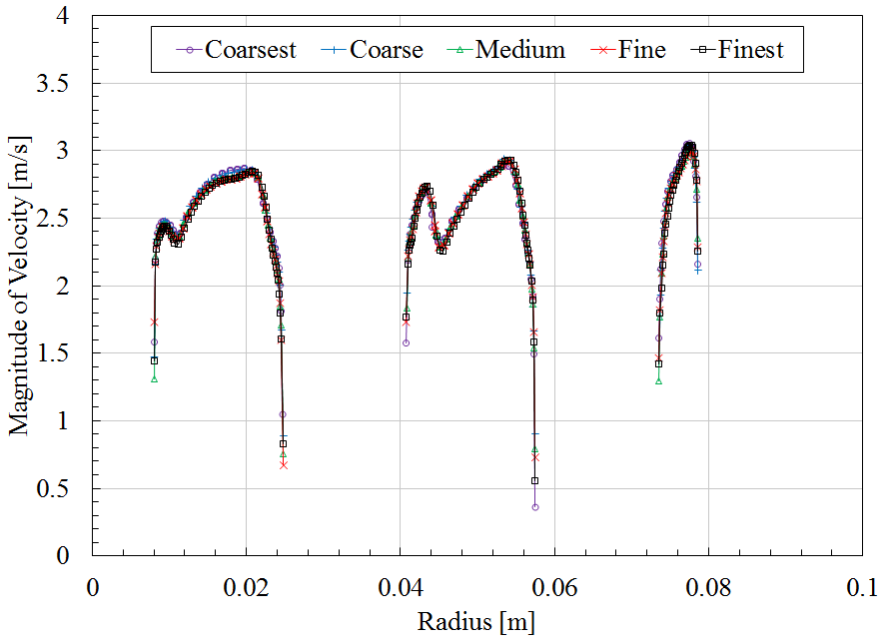


Figure 5-27: Velocity magnitude versus radial position from center of the duct at axial height of maximum duct deformation z = 3.75P (wire-wrap at 6 o'clock) for all meshes of the deformed bundle.

5.4.2 Heated Bundle

Figure 5-28 displays pressure drops based on the difference between a probe at the bundle inlet on Face B and probes located at various axial heights on Face B. Monotonic convergence is seen for each of the axial locations, and the Finest mesh shows relatively little variation from the Fine mesh. Figure 5-29 shows the temperatures at the thermocouple locations on the heated pin with Standard configuration at the center of the bundle (abbreviated STA001 where STA = Standard configuration, 0 = Row 0, and 01 = Pin #01 in that row) for all of the meshes. Mesh convergence behavior is similar to the non-deformed case where the temperatures of the thermocouples above the heated region show good convergence, and for the locations within the heated region, mesh independence is not truly attained (even by the Fine mesh). However, as the temperatures are fairly close to each other for all of the meshes, it is expected that the Fine mesh can provide suitably converged pre-test results.

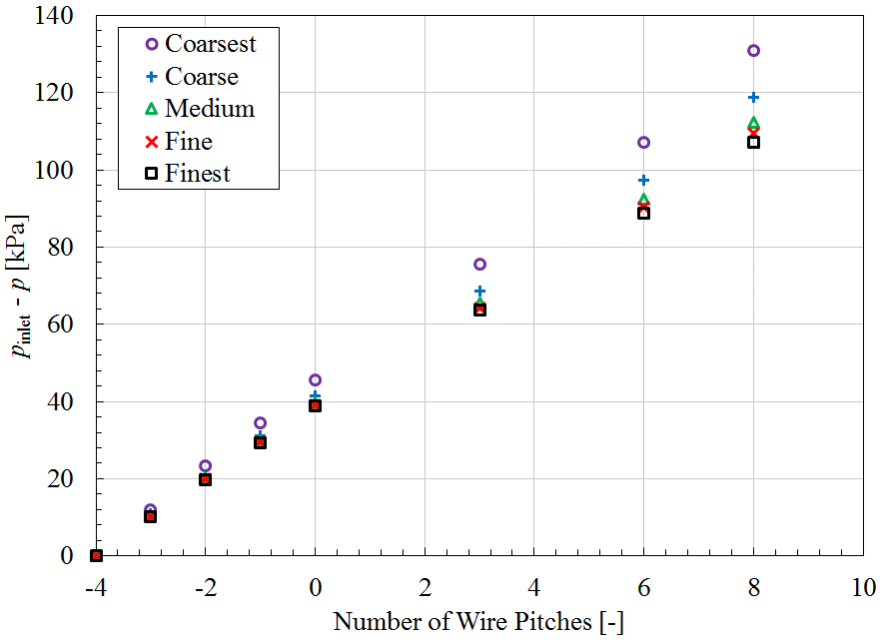


Figure 5-28: Pressure drops between Face B pressure probes at various axial heights and at the inlet versus the number of wire pitches into the deformed heated bundle for all meshes.

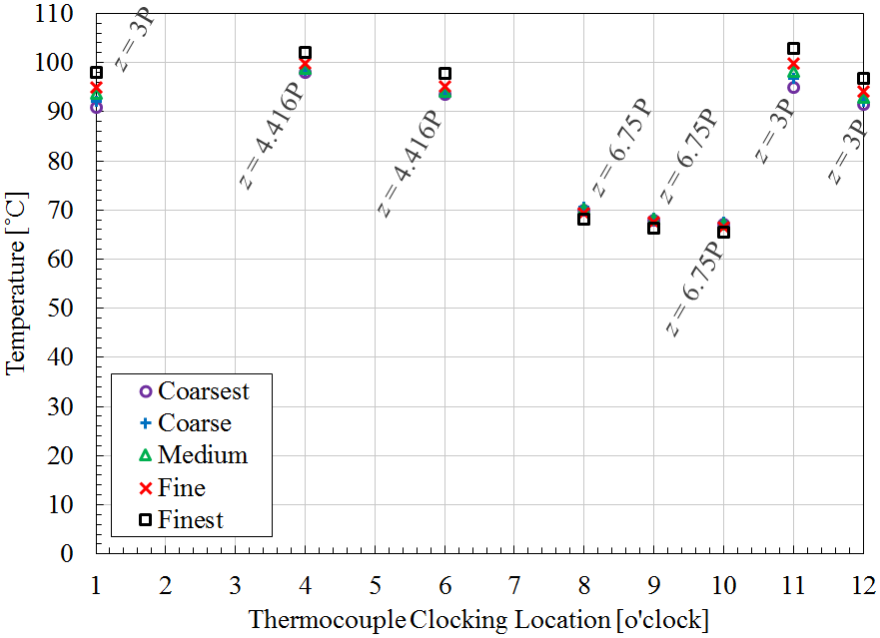


Figure 5-29: Temperature versus the clocking location of each thermocouple on heated pin STA001 for all meshes of the deformed bundle. Axial locations are also given for each thermocouple.

5.5 Turbulence Model Sensitivity

The previously presented mesh convergence studies were conducted with the Menter k-ω SST RANS turbulence model. To understand the sensitivity of the simulations to a chosen turbulence model, three other turbulence models are also tested. These other models are the Wilcox Standard k-ω model, the Standard k-ε model, and the Realizable k-ε model. The Fine mesh is used for the comparison of all of the turbulence models. An additional mesh sensitivity study is not conducted for these three other models, and thus it is assumed that (since these models are RANS models and that the k-ω SST model has the strictest

conditions when it comes to wall cell height) the Fine mesh provides an adequately converged solution for all of the models. Additionally, since the simulations of the deformed bundles vary so little in flow conditions and geometry from the non-deformed bundles, the turbulence model sensitivity studies are only done for the non-deformed isothermal and non-deformed heated bundles.

5.5.1 Isothermal Bundle

The bundle pressure drop (based on mass-flow averages at the inlet and outlet) of the four turbulence models is compared with the Cheng-Todreas 1-D bundle pressure drop correlation in Figure 5-30. The four models give pressure drops within roughly 13% of each other. The Standard and Realizable k-ε models over predict the pressure drop by approximately 9% and 6.5% respectively, relative to the correlation. The Menter k-ω SST and Wilcox Standard k-ω models under predict the pressure drop by roughly 4% and 1% respectively, relative to the correlation. Note that the correlation can have an error of +/- 15%. Figure 5-31 shows the pressure drops along the length of Face B for all of the turbulence models. Similar differences between the models are seen at each location as seen with the bundle pressure drop. Comparisons with the Cheng-Todreas correlation (linear drop across bundle) at different heights is not reasonable here, as these individual probes on the face are subject to the skew of the transverse pressure gradient caused by the wire-wrapping.

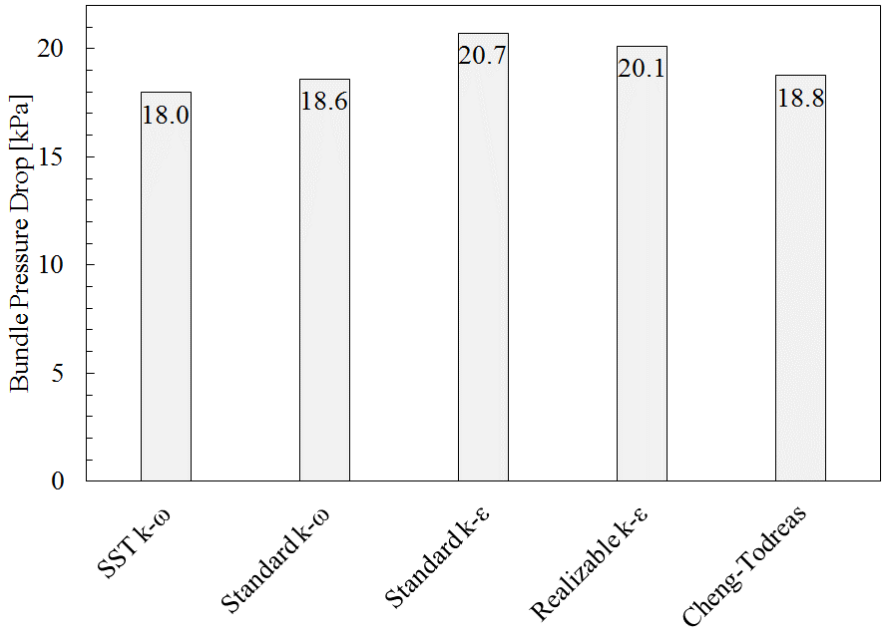


Figure 5-30: Non-deformed Isothermal bundle pressure drops for the four turbulence models and the predicted pressure drop from the Cheng-Todreas correlation.

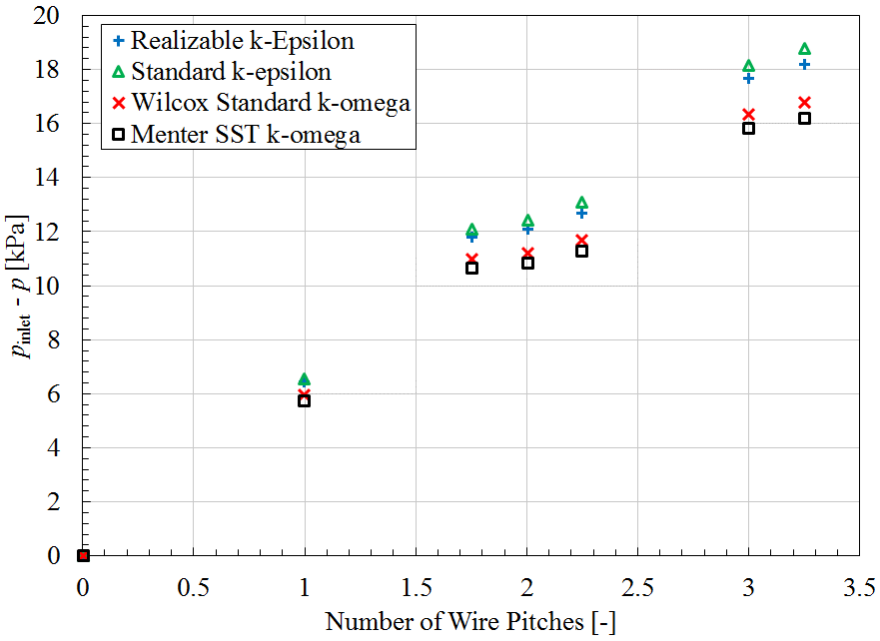


Figure 5-31: Non-deformed isothermal pressure drops between Face B pressure probes at various axial heights and at the inlet versus the number of wire pitches into the non-deformed isothermal bundle for the four turbulence models.

The velocity profiles for each model from the CFD line probe at 2.416P (an axial location where the wire-wrap is at 2 o'clock) are shown in Figure 5-32. There is little difference between the two k-ω models over the entire dataset. Additionally, the Realizable k-ε matches these two models fairly well. However, while the Standard k-ε model matches the other models well in many locations it does not capture many of the peaks and troughs the other models do when sharp gradients occur in the field. At some of these distinct locations, the Standard k-ε model results can vary by roughly 10% from the other models. The other CFD line probes show similar results to the one presented here.

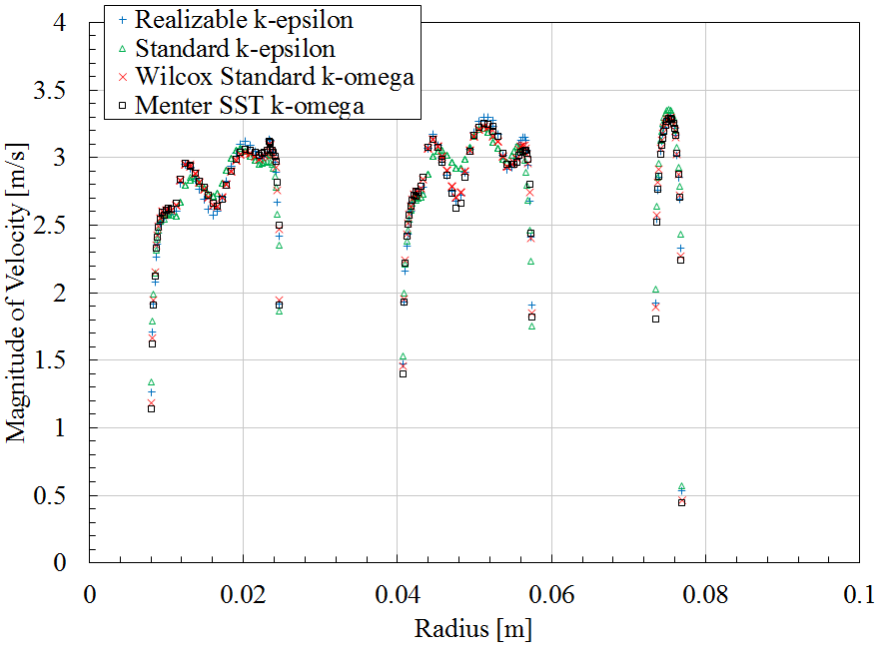


Figure 5-32: Velocity magnitude versus radial position from the center of the duct at 2.416P (wire-wrap at 2 o'clock) for the four turbulence models.

5.5.2 Heated Bundle

The heated bundle pressure drop (based on mass-flow averages at the inlet and outlet) of the four turbulence models is compared with the Cheng-Todreas bundle pressure drop correlation in Figure 5-33. The four models give pressure drops within roughly 12% of each other. The Standard and Realizable k-ε models over predict the pressure drop by approximately 5% and 1% respectively, relative to the correlation. The Menter k-ω SST and Wilcox Standard k-ω models under predict the pressure drop by roughly 7% and 4% respectively, relative to the correlation. Note that the correlation can have an error of +/- 15%. Figure 5-34 shows the pressure drops along the length of Face B for all of the turbulence models. Similar differences between the models are seen at each location as seen with the total bundle pressure drop. An example of the variation in temperatures is given in Figure 5-35 for thermocouple locations on STA001. The temperatures on the pin surfaces are fairly insensitive to the choice of turbulence model. At all locations, a similar temperature is seen with all turbulence models except the Standard k-ε model, which consistently displays slightly lower temperatures.

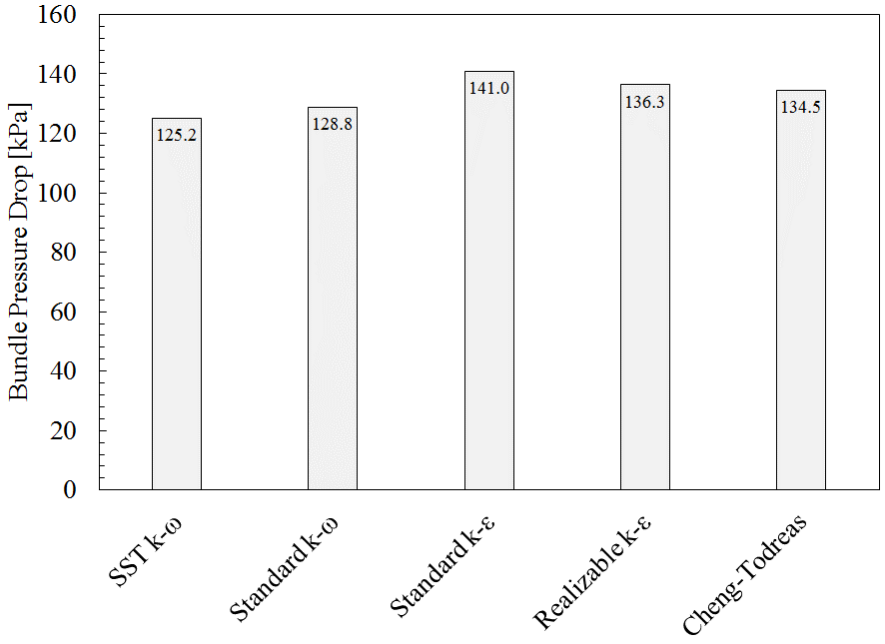


Figure 5-33: Non-deformed heated bundle pressure drops for the four turbulence models and the predicted pressure drop from the Cheng-Todreas correlation.

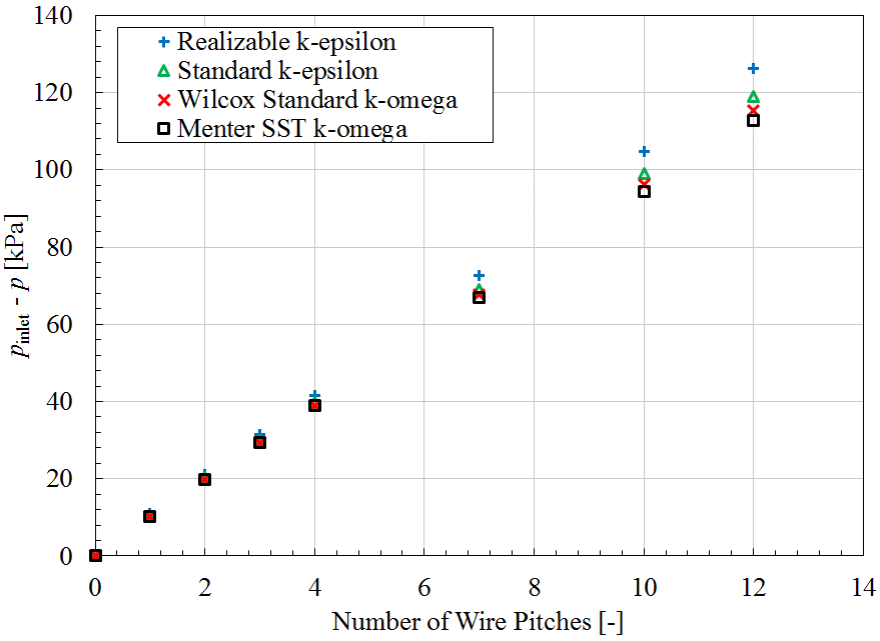


Figure 5-34: Non-deformed heated pressure drops between Face B pressure probes at various axial heights and at the inlet versus the number of wire pitches into the non-deformed heated bundle for the four turbulence models.

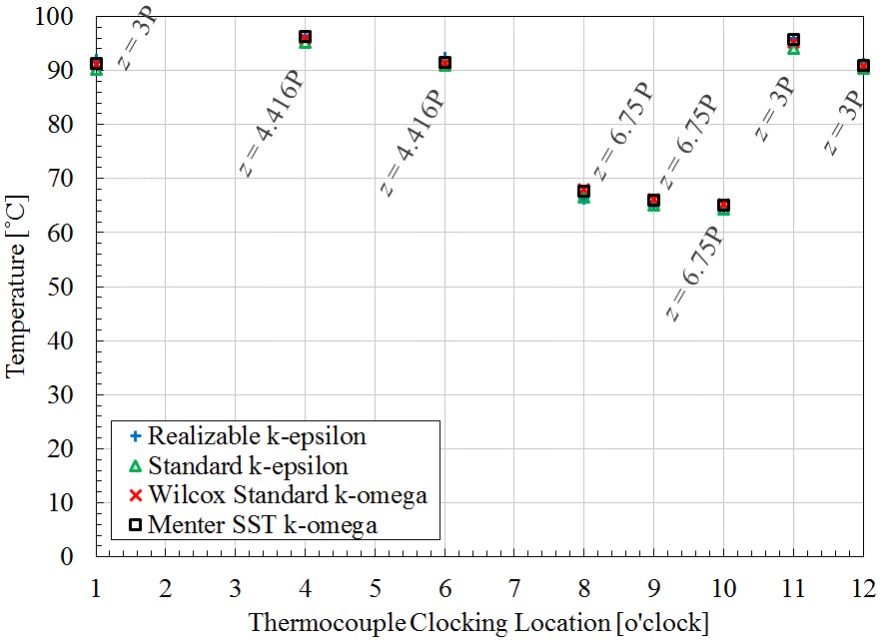


Figure 5-35: Temperature versus the clocking location of each thermocouple on heated pin STA001 in the non-deformed heated bundle for all four turbulence models. Axial locations are also given for each thermocouple.

5.6 Momentum Source Coefficient Sensitivity

The normal forces of the momentum source model include a multiplication coefficient. The purpose of the coefficient is to make sure the velocity gradient is large enough to block the flow from entering or leaving the wire in the normal directions. It is mentioned that the MS coefficient should be greater than 2 to accomplish this task [3], but the reasoning behind this statement is ambiguous in the literature. Moreover, no maximum value of the coefficient is mentioned. Thus, a sensitivity analysis for a range of MS coefficient values above 2.0 are investigated here. The MS coefficient was given values of 3.0, 4.0, 5.0, and 10.0 and

the Fine mesh was used with the Menter k-ω SST turbulence model. The value of the coefficient for the previous cases (mesh and turbulence model sensitivity) was 4.0, and this was based on preliminary testing of the MS methodology at TerraPower [8], but this value has not been validated.

The pressure field showed negligible variation with this range of MS coefficients (results not shown). However, the velocity field did display appreciable differences between the choices of coefficient. Figure 5-36 shows the velocity profiles and it is clear that when the coefficient is raised to 10.0, higher velocity magnitudes are present in the centers of the profiles. Similar behavior is observed in the temperature field. By taking a line probe that is used for velocity sampling and instead sampling the temperature profiles between pins, the effect of varying the momentum source coefficient can be visualized (see Figure 5-37). When the coefficient is raised to 10.0, high temperature is seen in the middle of the inner profile, and a slight temperature increase is seen in the outermost profile as well. As there is no guidance as to which value of the coefficient is more acceptable and accurate, the value of 4.0 that was used in previous studies at TerraPower, will be used for the final pre-test results. The impact of the value of this coefficient will be investigated in the post-test solution validation phase of the project by comparison to the experiment results.

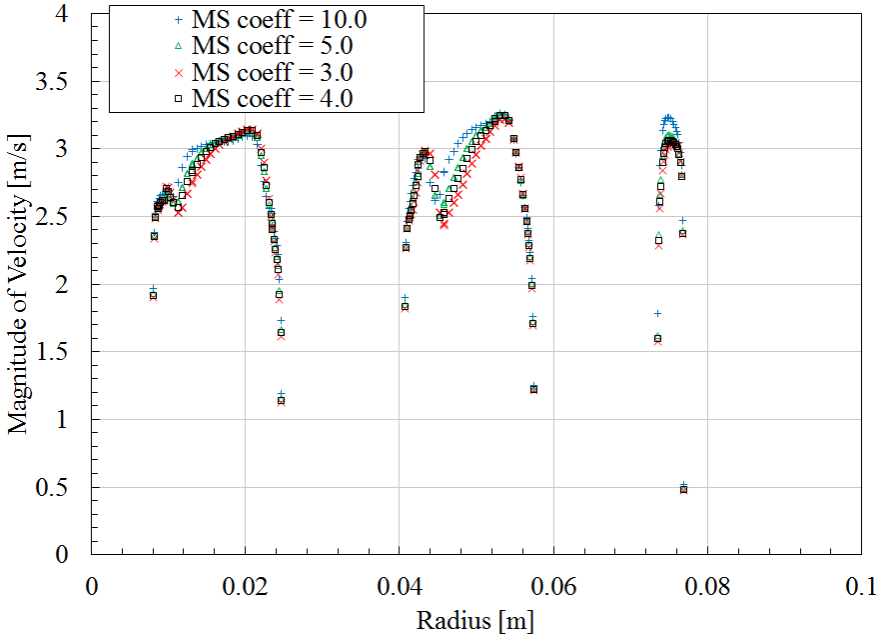


Figure 5-36: Velocity magnitude versus radial position from center of the duct at axial height of z = 2.75P (wire-wrap at 6 o'clock) for varying MS coefficient in the non-deformed isothermal bundle.

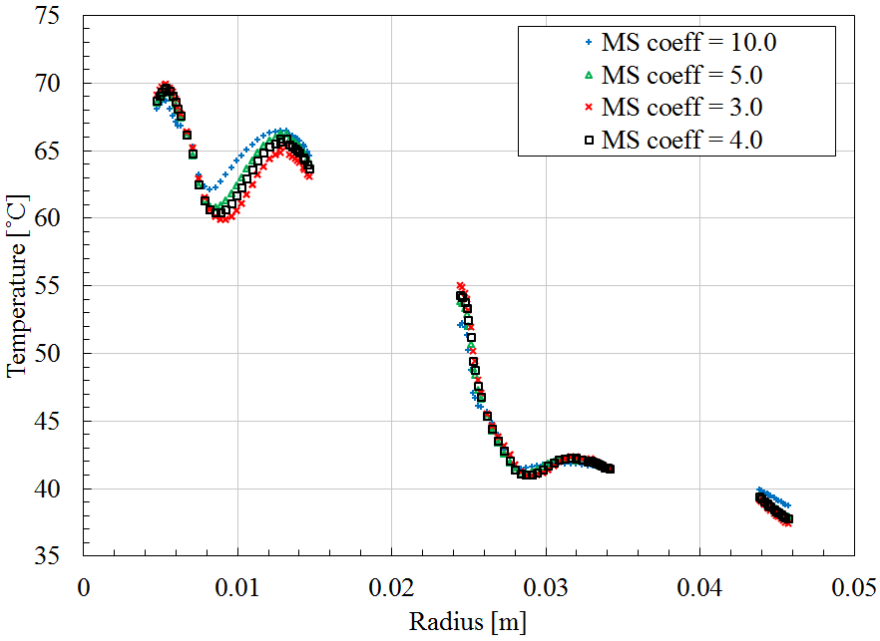


Figure 5-37: Temperature versus radial position from center of the duct at axial height of z = 6.42P (wire-wrap at 5 o'clock) for varying MS coefficient in the non-deformed heated bundle.

5.7 Summary and Choices of Meshes, Models, and Conditions

In this chapter, solution verification was thoroughly accomplished. Round-off, iterative, and statistical sampling error were proven to be negligible by running simulations with multiple precision, displaying iterative convergence, and showing that variables of interest did not fluctuate with iteration after the solution was deemed iteratively converged. Discretization error was investigated with a couple approaches. A mesh refinement study was undertaken to formally calculate the discretization error by means of Richardson extrapolation to find the "exact" solution. However, in many cases the Richardson extrapolation was either not trusted (the OOA was far from the FOA), or was inappropriate for use (local sampling points). Thus, the discretization error was informally analyzed, and shown to be minimal, by proving that the variables of interest (for globally and locally proposed pressure, velocity, and temperature measurements) changed by small percentages if the Fine mesh was used (relative to the Finest mesh). In other words, although there was a non-constant rate of convergence of the variables of interest which precluded them from accurate Richardson extrapolation and formal discretization error estimates, the variables still monotonically converged to distinct values by the Fine mesh and changed little with further refinement. The only exceptions were the local temperatures of the heated pins, within the heated region. These results did not display trends towards convergence that were as convincing as other results, but nonetheless, they still showed little variation with further refinement past the Fine mesh.

Additionally, various RANS turbulence models were investigated to show that the solutions were not sensitive to the model choice. While the velocity and temperature fields did not display much appreciable difference amongst the models, the pressure drops did show a range of results. Even so, that range was not too large and all values were within roughly 5-10% of an experimental correlation. As the Menter k-ω SST model is thought to be the most applicable model for this type of flow (provides advantageous k-ω performance in the boundary layer and reduced boundary layer sensitivity to freestream conditions by using k-ε far from the wall [4]), and was the most tested in the solution verification analysis, it is chosen to provide the official pre-test results in Section 6. With respect to the choice of the Momentum Source Coefficient value, the velocity and temperature fields do display appreciable variation, but only if the MS coefficient is raised by an order of magnitude. Thus, the value of 4.0 that was used in previous analyses (and meets the model criterion of being greater than 2.0) is an acceptable choice for the official pre-test results.

In conclusion, the major result of the solution verification procedure is that the Fine mesh, Menter k-ω SST turbulence model, and momentum source coefficient of 4.0, will provide acceptably converged, and fairly

insensitive results for the official pre-test analysis. Note that, although the isothermal bundle official pre-test results still use the Fine mesh in the axial direction (the heated bundle uses the Coarsest mesh in the axial direction), it was proven that the same results can be obtained using the Fine mesh with the Coarsest mesh cell distribution in the axial direction. Following availability of the experiment results, investigation of the turbulence model and the momentum source coefficient value will be reanalyzed.

6 OFFICIAL PRE-TEST RESULTS

After the solution verification analysis of Section 5, a specific mesh refinement level, turbulence model, and momentum source coefficient were chosen in an effort to obtain the best pre-test results. It was determined that the Fine mesh, the Menter k-ω SST RANS turbulence model, and a momentum source coefficient of 4.0, would provide quality results for both the isothermal and heated bundles. Here, the final results for the pre-test cases (using the mesh refinement level, model and conditions mentioned) are provided and discussed. Not all of the results corresponding to the proposed measurements are reported here. Rather a sampling of pressure, velocity, and temperature results are presented from the simulations. However, the simulations are readily available to easily extract any further data which is deemed necessary.

6.1 Non-Deformed Isothermal Bundle

The results of the non-deformed isothermal bundle duct face pressure drops (where the pressure drops are calculated between a point on Face B at the inlet and points on various duct faces downstream) are shown in Figure 6-1. Pressures were extracted and pressure drops calculated that correspond to locations specified to be instrumented in the experiments. By looking at the pressure drop along Face B, it is clear that the trend of the pressure drop along a face is not linear. While a linear pressure drop can be expected for planar averaged pressure similar to the global bundle correlations of Cheng and Todreas [11], local pressures are affected by a transverse pressure gradient which forms as a result of the wire-wrapping [10]. The transverse pressure gradient is a steady-state feature but it does rotate axially in phase with the wire-wrap. This leads to the non-linear pressure drop trend along a duct face when referenced to the inlet pressure. Figure 6-1 shows the transverse pressure gradient with taps on three other duct faces at z = 2.25P and z = 3.0P, and Figure 6-2 gives the pressure contours showing the gradient at an axial cross-section of z = 2.25P. The bundle pressure drop between inlet and outlet of the non-deformed bundle is 18 kPa, which is roughly 4% less than the estimate of the Cheng-Todreas correlation.

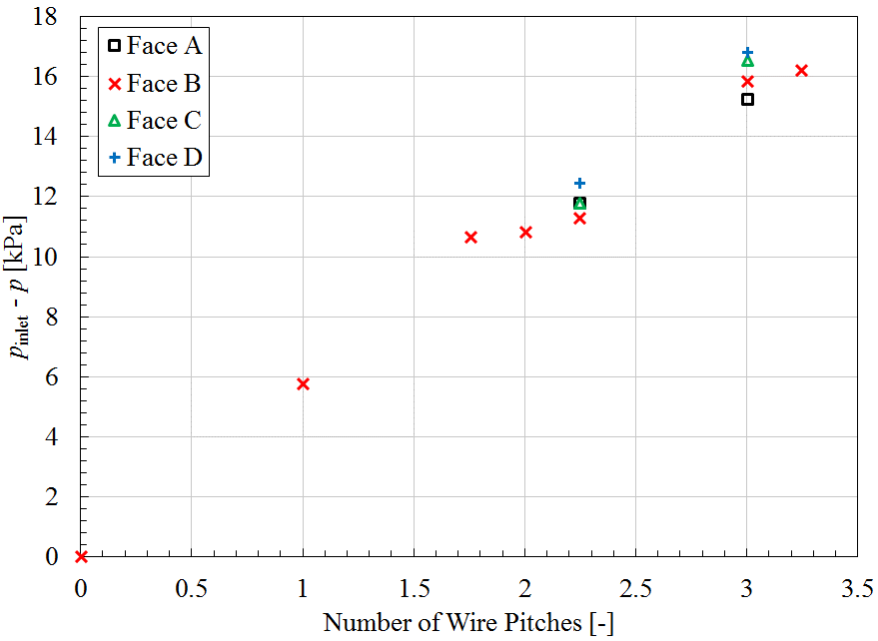


Figure 6-1: Non-deformed isothermal pressure drops between Face B pressure probes at various axial heights and at the inlet versus the number of wire pitches into the bundle. Pressure drops on other Faces shown at z = 2.25P and z = 3.0P.

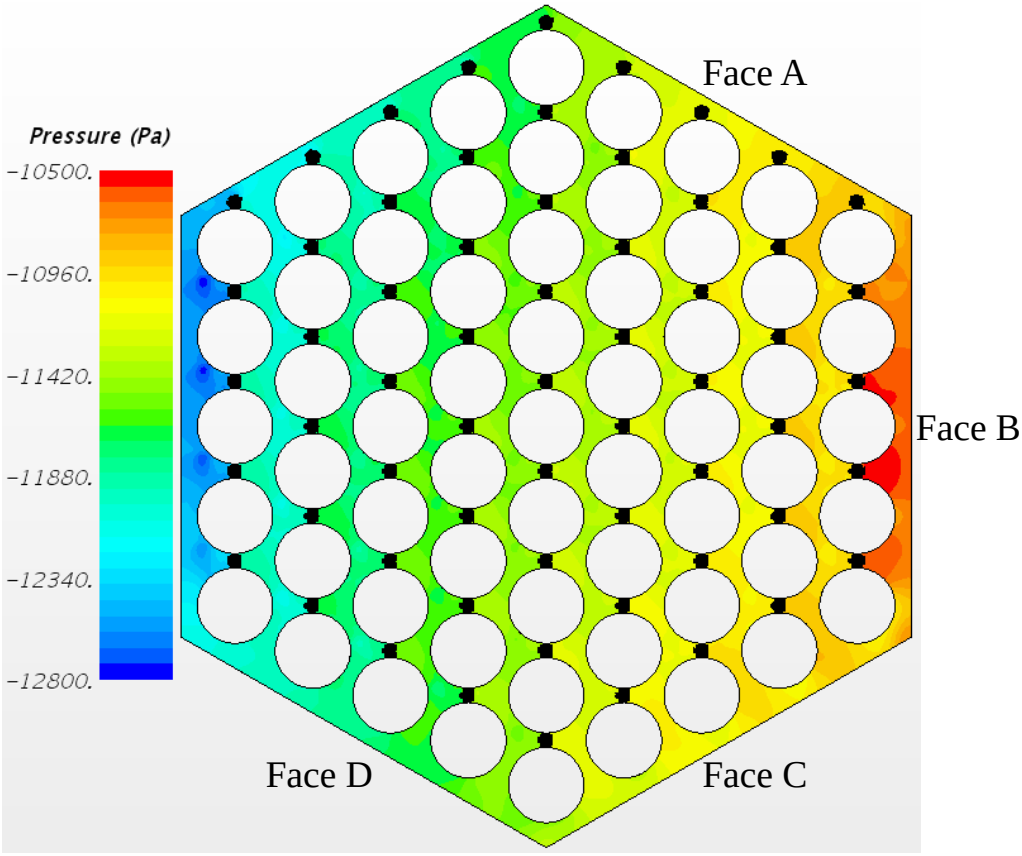


Figure 6-2: Axial cross-section displaying pressure contours [Pa] at z = 2.25P.

Figure 6-3 displays the velocity magnitudes of three axial locations. Recall that the line probes start at the center pin and point outwards to 1 o'clock (towards Face A, shown in Figure 6-4). The line probes shown in Figure 6-3 are for axial locations when the wire-wrap location is at 12 o'clock and 6 o'clock. Note that there are two line probes when the wire-wrap is at 12 o'clock, and these are one wire pitch apart. The results at the higher axial location show a slight reduction of the peaks of each profile, which can be expected due to losses as the flow progresses through the duct. Otherwise, the profiles at these two axial heights show very similar shapes. The velocity field when the wire-wrap is at 6 o'clock shows close to mirrored profiles from the others, except for the outermost profile. This profile exhibits a roughly 9% reduction in peak velocity relative to the outermost profiles when the wire-wrap is at 12 o'clock. The contours of the velocity magnitudes at each of these axial locations can be seen in Figure 6-4.

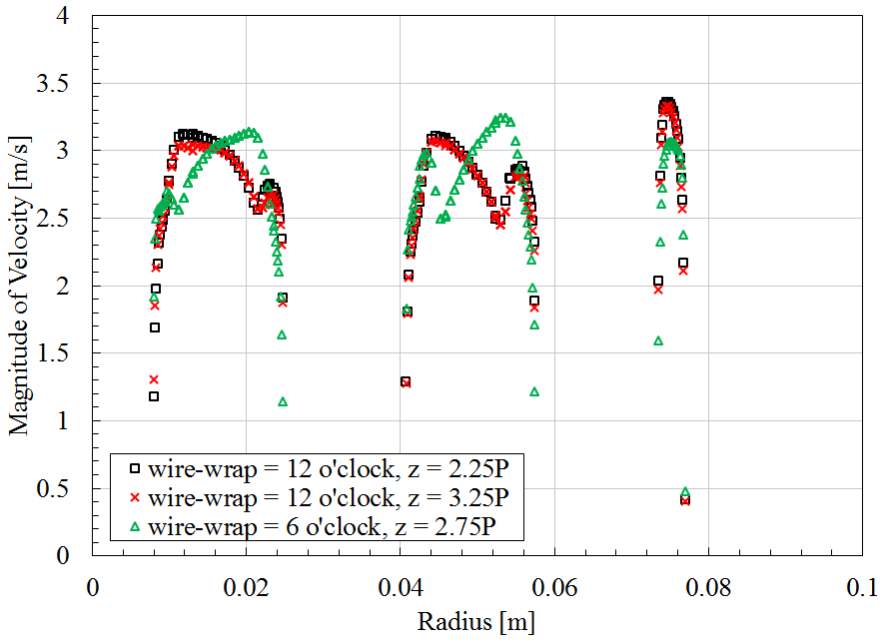


Figure 6-3: Velocity magnitude versus radial position from the center of the duct at z = 2.25P, z = 2.75P, and z = 3.25P.

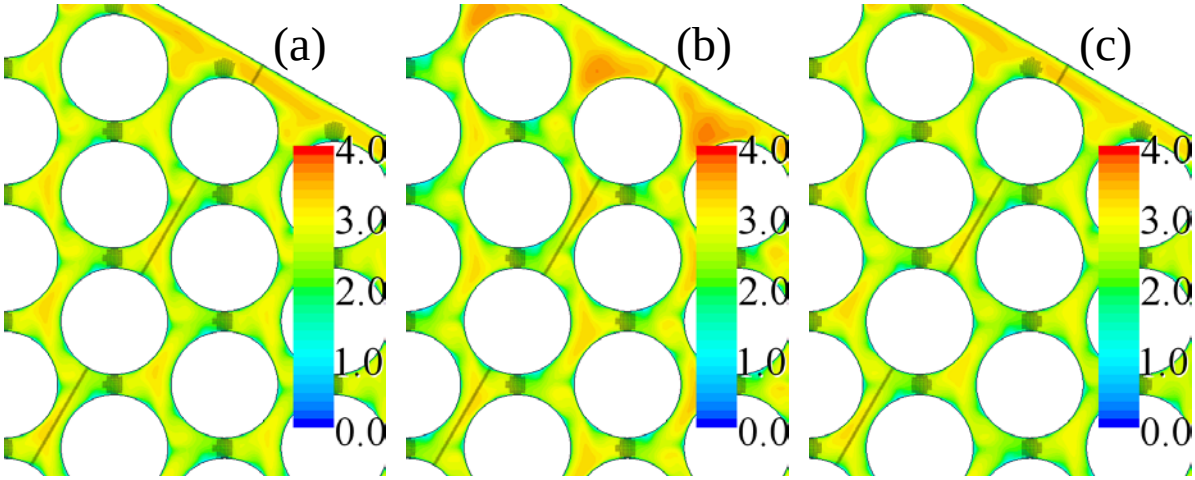


Figure 6-4: Axial cross-sections at (a) z = 2.25P, (b) z = 2.75P, and (c) z = 3.25P, displaying velocity magnitude [m/s] and the line probe.

The velocity profiles of the line probe at axial locations where the wire-wrap is at 4 o'clock and 10 o'clock are shown in Figure 6-5. These line probes pass through the wire-wrap at the inner and middle profiles and therefore there is a gap in the velocity results shown. The inner 10 o'clock profile is close to a mirror of the inner 4 o'clock profile. The middle profiles show mirror-like behavior as well except that the peaks of the 10 o'clock middle profile are not as prominent as those of the 4 o'clock middle profile. When the wire-wrap is at 4 o'clock, the outer profile experiences the highest sampled velocity magnitudes amongst all the line probes, while the outer profile when the wire-wrap is at 10 o'clock shows some of the lowest peak velocities sampled in the outer region amongst all the line probes. This plot shows that the outer channel displays a roughly 20% difference in peak velocity at heights with the wire wrap at different clocking positions. The contours of the velocity magnitudes at each of these axial locations can be seen in Figure 6-6.

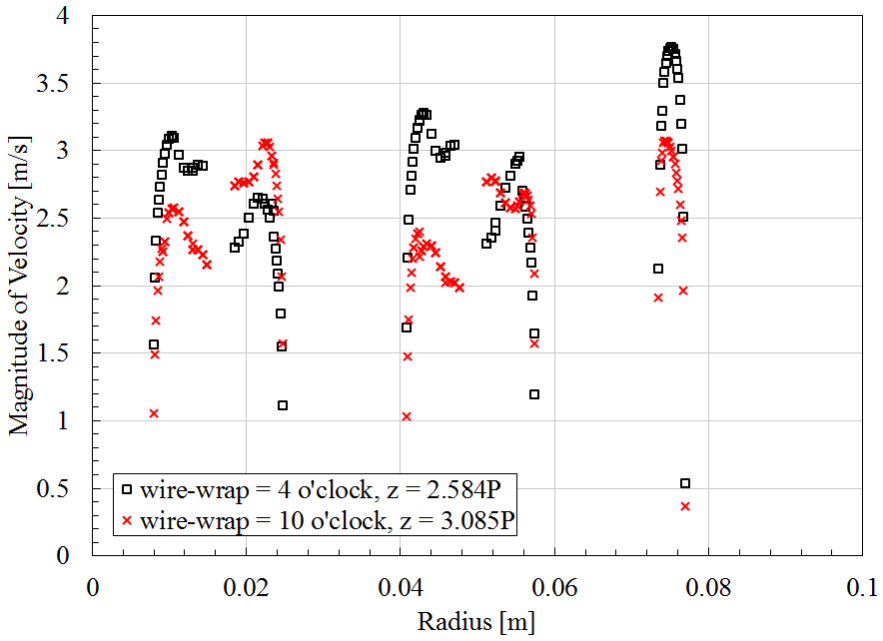


Figure 6-5: Velocity magnitude versus radial position from the center of the duct at z = 2.584P and z = 3.085P.

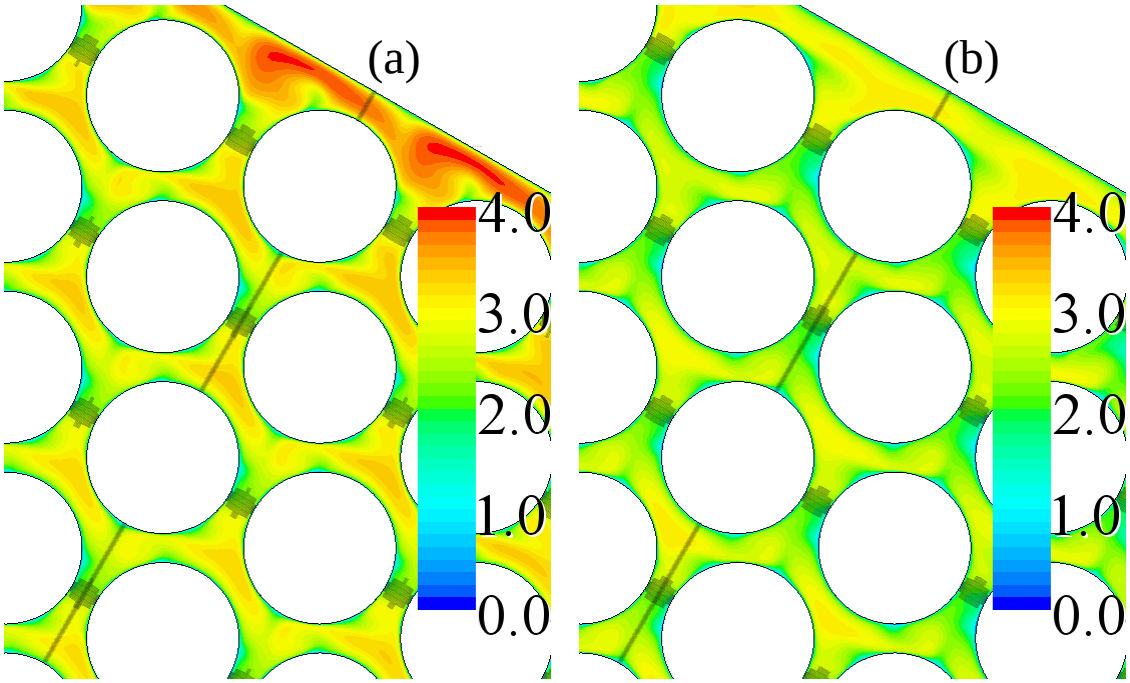


Figure 6-6: Axial cross-sections at (a) z = 2.584P and (b) z = 3.085P, displaying velocity magnitude [m/s] and the line probe.

The profiles sampled with the line probes at axial heights where the wire-wrap is at 2 o'clock and 8 o'clock are shown in Figure 6-7. The inner profiles again display a mirrored shape relative to each other while the middle profile shows a mirrored shape with lower peaks on the profile farther (axially) into the bundle. The outer profiles display similar maximum velocity magnitudes. The contours of the velocity magnitudes at each of these axial locations can be seen in Figure 6-8.

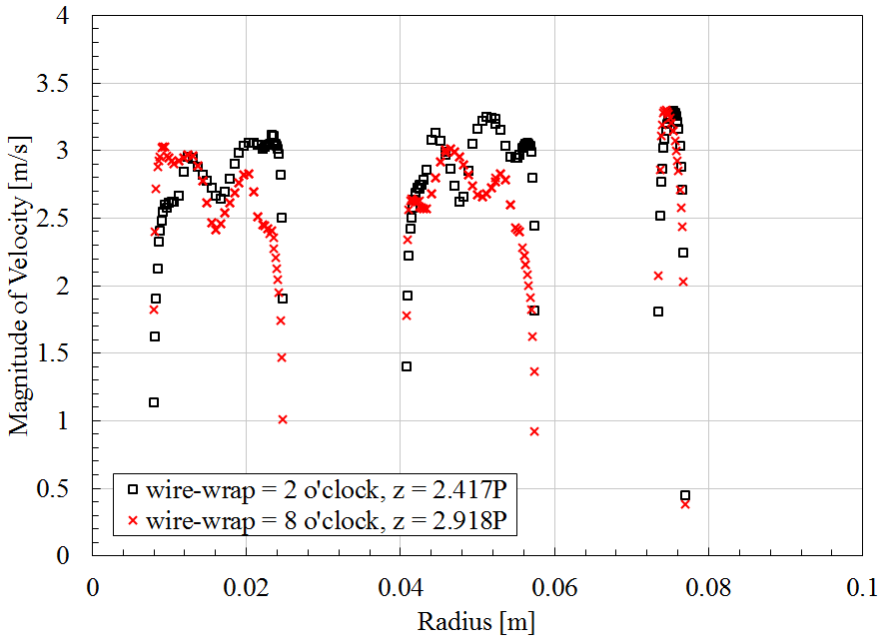


Figure 6-7: Velocity magnitude versus radial position from the center of the duct at z = 2.417P and z = 2.918P.

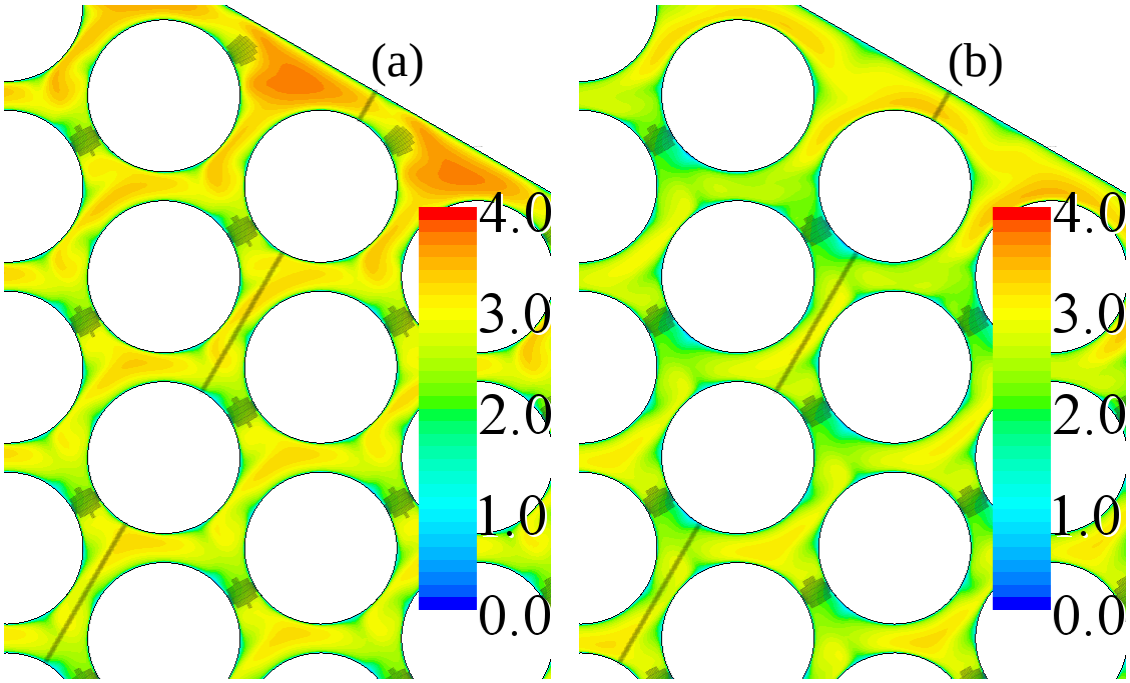


Figure 6-8: Axial cross-sections at (a) z = 2.417P and (b) z = 3.918P, displaying velocity magnitude [m/s] and the line probe.

6.2 Deformed Isothermal Bundle

The results of the deformed isothermal bundle duct face pressure drops are shown in Figure 6-9. The axial pressure drop along the duct length can be seen with probes on Face B, while the effect of the transverse pressure gradient can be seen with probes on three other duct faces at z = 2.25P and z = 3.75P. The bundle pressure drop between inlet and outlet of the deformed bundle is 26.2 kPa, which is roughly 11% less than an estimate based on a non-deformed bundle of the same length (Cheng-Todreas correlation). The fact that the deformed bundle is 11% less than the correlation while the non-deformed bundle is 4% less than the correlation is expected, as the deformation increases the flow area, thus it should decrease the pressure drop relative to the non-deformed bundle.

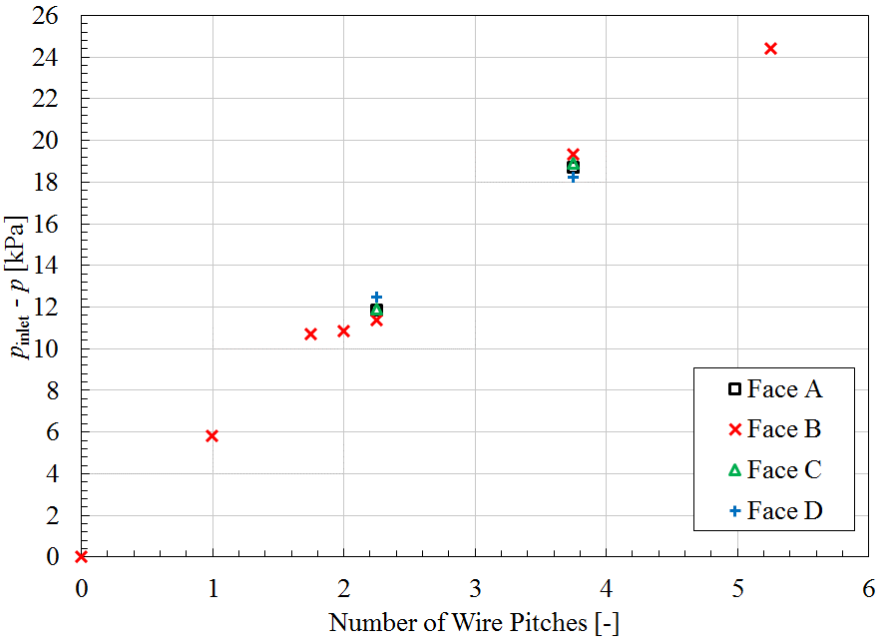


Figure 6-9: Deformed isothermal pressure drops between Face B pressure probes at various axial heights and at the inlet versus the number of wire pitches into the bundle. Pressure drops on other Faces shown at z = 2.25P and z = 3.75P.

Figure 6-10 displays the velocity magnitudes of four axial locations. The line probes shown are for axial locations when the wire-wrap location is at 12 o'clock. The deformed region occurs between z = 2.25P and z = 5.25P (with max deformation at z = 3.75P), and therefore the duct is non-deformed at these two heights. The heights of the other two profiles shown are +/- 0.5 pitches from the height of max deformation. As flow progresses through the deformed region, the profiles can show decreases of up to 16% at some locations of the inner and middle profiles. As the duct becomes non-deformed again, the regions of the inner and middle profiles away from the pin walls do not return close to the magnitudes prior to the deformation, but remain similar to the profiles in the deformed region. Note that near the pin walls, the velocities at the exit of the deformed region are close to those at the entrance to the deformed region. The outer profile decreases slightly and widens as the duct deforms, but as the duct returns to the non-deformed axial height, the outer profile returns to practically match that prior to deformation. Thus, at these wire-wrap locations, the consequences of the duct deformation are more apparent in the velocity field at the centers of the inner/middle profiles, than at the outer edges of the bundle where the duct wall deformation occurs. Figure 6-11 displays the profiles at the height of maximum deformation.

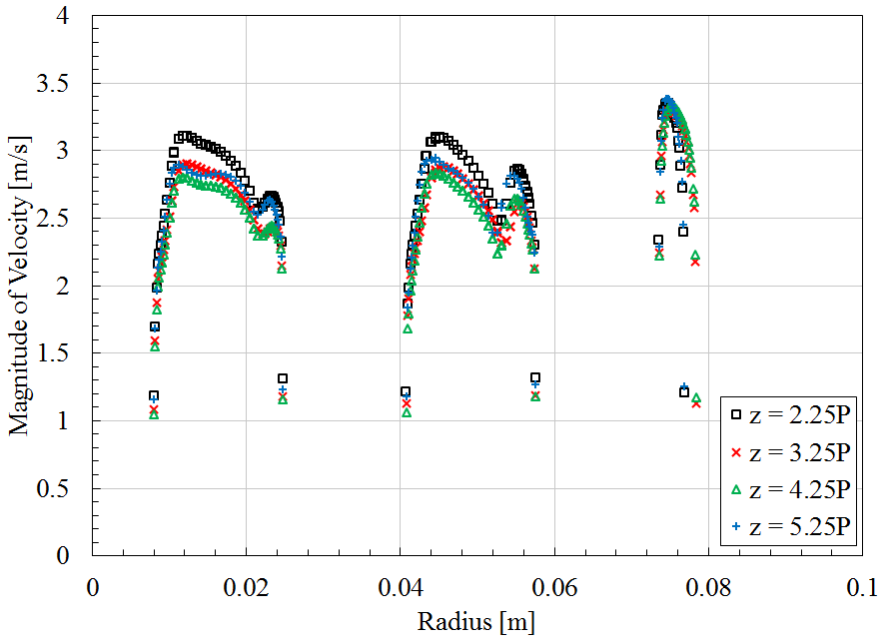


Figure 6-10: Velocity magnitude versus radial position from the center of the duct at z = 2.25P, z = 3.25P, z = 4.25P, and z = 5.25P. For each the wire-wrap is at 12 o'clock.

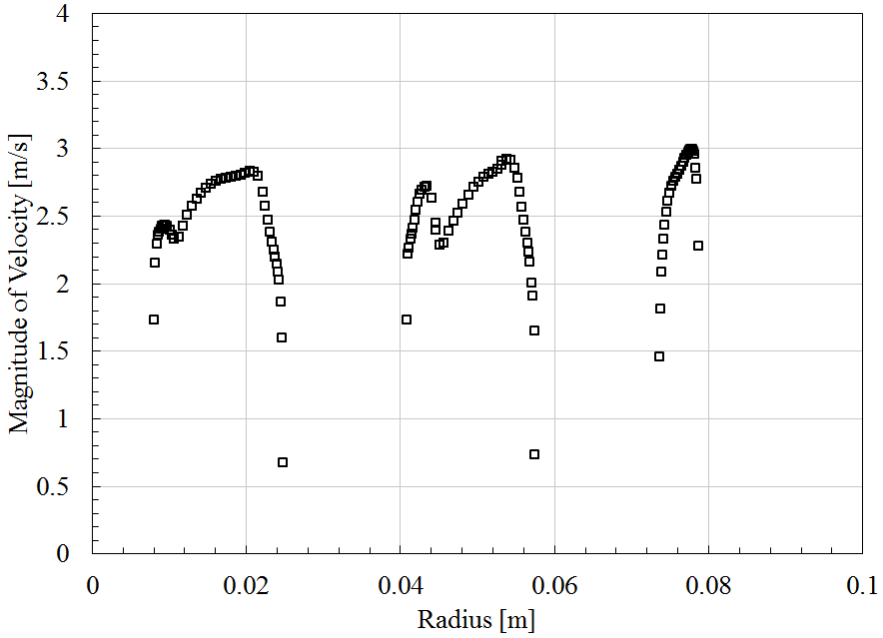


Figure 6-11: Velocity magnitude versus radial position from the center of the duct at height of max duct deformation z = 3.75P (wire-wrap = 6 o'clock).

The profiles of the CFD line probes at 3 axial heights in the deformed region corresponding to wire-wrapping at 4 o'clock are shown in Figure 6-12. Again, the magnitudes decrease as the height of maximum deformation is approached. As the deformation returns to non-deformed, the inner and middle profiles remain close to the profiles near maximum deformation, while the outermost profile returns to similar peak magnitudes seen before the deformation. The profiles of the line probes at 3 axial heights in the deformed region, corresponding to wire-wrapping at 8 o'clock, are shown in Figure 6-13 and also display similar trends across the axial height that were exhibited with the other wire-wrap locations.

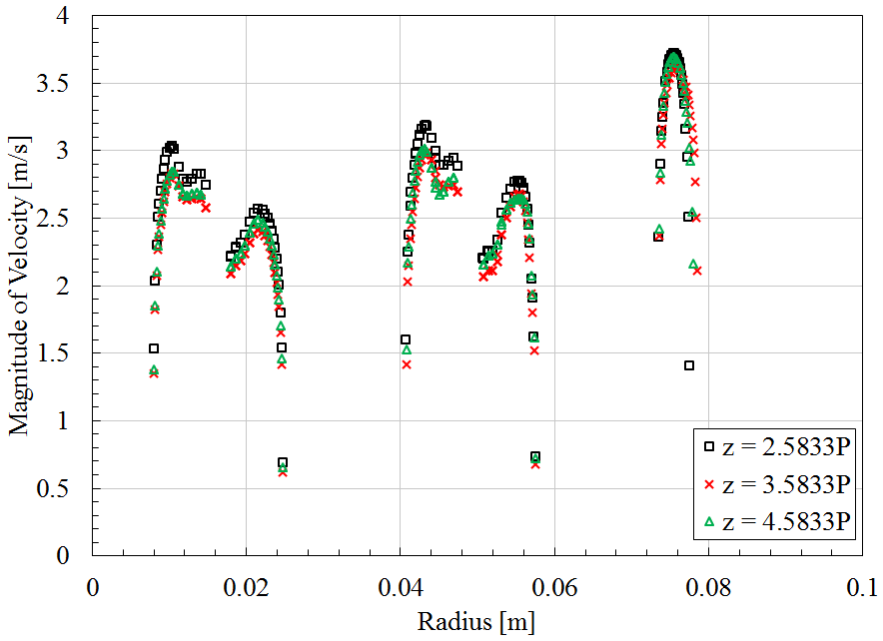


Figure 6-12: Velocity magnitude versus radial position from the center of the duct at z = 2.5833P, z = 3.5833P, and z = 4.5833P. For each the wire-wrap is at 4 o'clock.

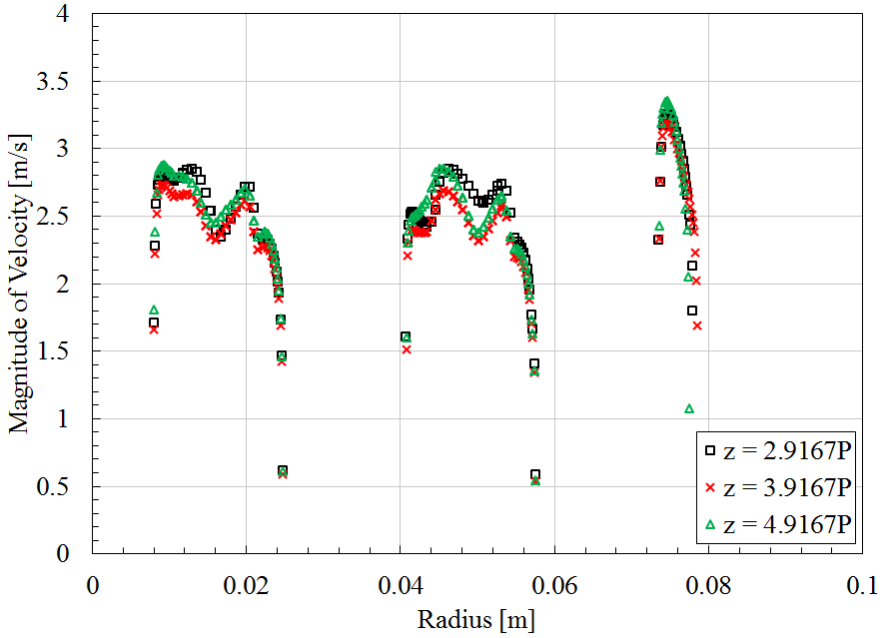


Figure 6-13: Velocity magnitude versus radial position from the center of the duct at z = 2.9167P, z = 3.9167P, and z = 4.9167P. For each the wire-wrap is at 8 o'clock.

A sample of the CFD results corresponding to proposed PIV measurements are presented here for both the non-deformed and deformed bundles. Figure 6-14 shows both the vector field and the magnitudes of the transverse velocity for both bundles at the height of maximum deformation (z = 3.75P). An edge sub-channel near a face center (where the peak deformation occurs at the duct wall of the left side of the deformed images) is displayed to illustrate results from potential PIV measurement locations. Results from other sub-channels and different axial heights are readily available for extraction from the simulations to aid in the solution validation process.

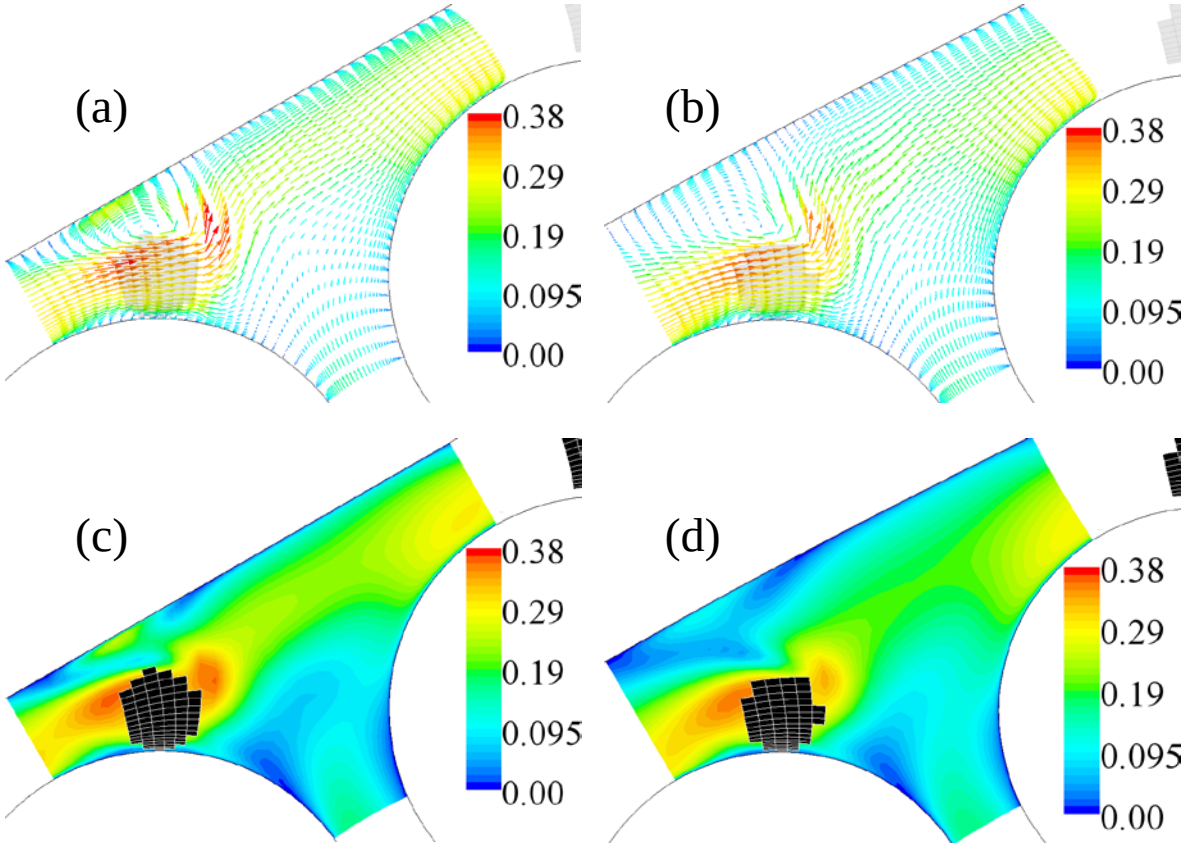


Figure 6-14: Axial cross-sections of velocity magnitude [m/s] showing (a) non-deformed isothermal velocity vectors, (b) deformed isothermal velocity vectors, (c) non-deformed isothermal contours, and (d) deformed isothermal contours.

6.3 Non-deformed and Deformed Heated Bundles

The results of the non-deformed heated bundle duct face pressure drops are shown in Figure 6-15. The axial pressure drop along the duct length can be seen with probes on Face B, while the effect of the transverse pressure gradient can be seen with probes on three other duct faces at z = 0P and z = 3P. Similar results for the deformed bundle can be seen in Figure 6-16. The bundle pressure drop for the non-deformed bundle between the inlet and outlet is 125.2 kPa, which is 7% less than Cheng-Todreas correlation, while that of the deformed bundle is 119.4 kPa which is 11% less than the correlation and roughly 5% less than the non-deformed bundle simulation. The lower pressure drop is expected due to the higher flow area in the region of the deformed duct walls.

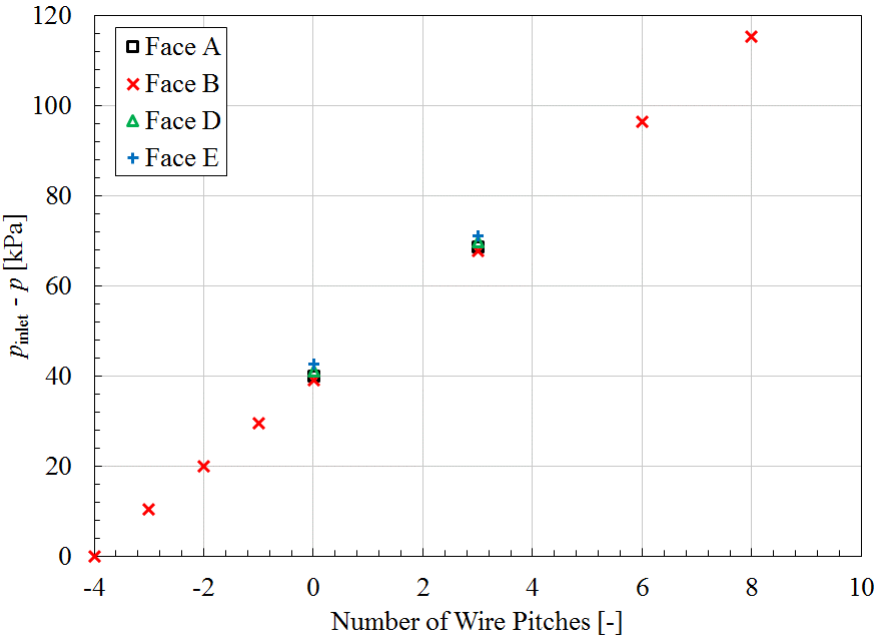


Figure 6-15: Non-deformed heated pressure drops between Face B pressure probes at various axial heights and at the inlet versus the number of wire pitches into the bundle. Pressure drops on other Faces shown at z = 0P and z = 3P.

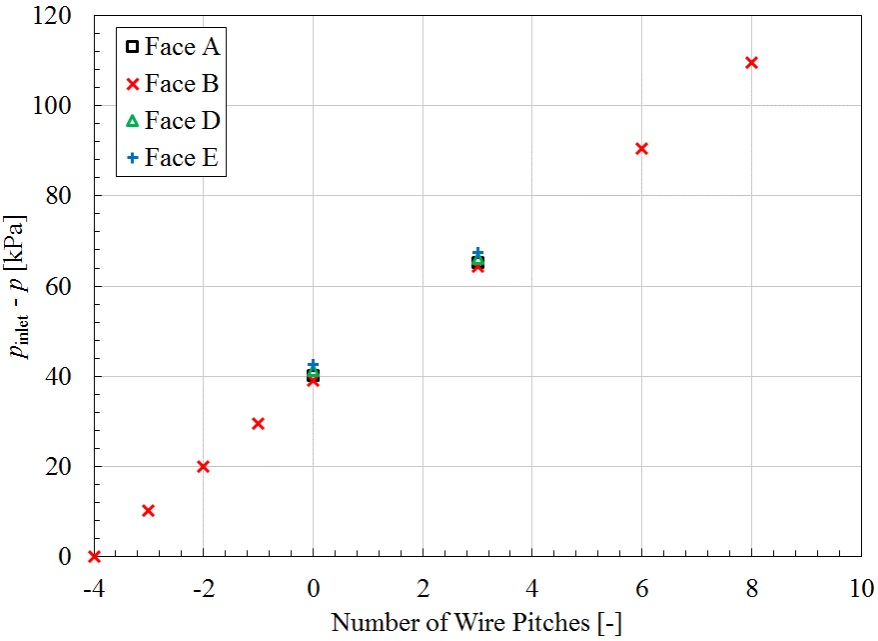


Figure 6-16: Deformed heated pressure drops between Face B pressure probes at various axial heights and at the inlet versus the number of wire pitches into the bundle. Pressure drops on other Faces shown at z = 0P and z = 3P.

Temperatures sampled at the proposed experiment thermocouple locations on two Standard configuration heated pins are shown in Figure 6-17 for both the non-deformed and deformed bundles. One of the rods is at the center of the bundle (STA001) and the other is on the outermost row of the bundle (STA407). The temperatures at the center pin are higher in all instances than the ones extracted at corresponding locations on the outer pin. This is expected as the center pin is surrounded by heated pins while the outer pin is isolated in a region of non-heated tubes and the duct wall. The center pin shows a temperature value greater

between the non-deformed to the deformed bundle of up to 4% (occurring at the axial height of max deformation z = 3P). All other temperatures of the deformed bundle center pin exhibit higher temperatures than the non-deformed bundle center pin, although the difference is greater in the heated region than outside the heated region. Contributing to this is the flow redistribution that occurs where more flow goes through the wall subchannels due to the larger flow area of the wall subchannels in the deformed bundle in comparison to the non-deformed bundle. Since the larger flow area in the deformed region results in lower flow velocities, this behavior is expected. For the outer pin, the behavior is similar in the heated region, but the differences are smaller. Outside the heated region, and even at some points within this region, the differences are negligible. Note that the temperatures behind the wires (12 o'clock and 9 o'clock in figure below) do not display a spike relative to the temperatures on either side of the wire. The most likely reason that this expected hot spot behind the wire does not appear in the results is because the wire is a region of flow in the simulations (due to the MS methodology), and this does not provide an accurate representation of the true heat transfer conditions. The temperature field along with the MS pin cells and the location of thermocouples is shown in Figure 6-18.

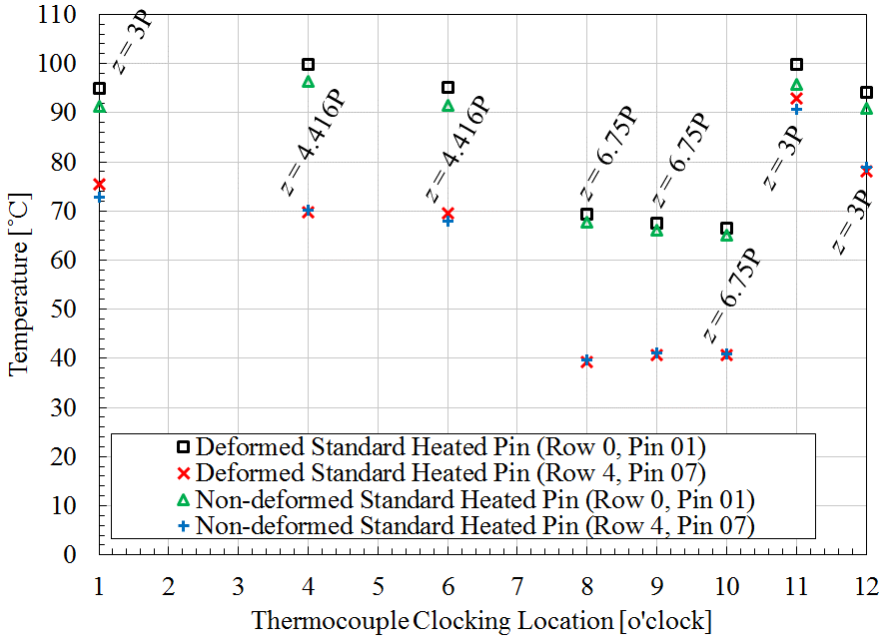


Figure 6-17: Temperature versus the clocking location of each thermocouple on heated pins STA001 and STA407 for non-deformed and deformed bundles. Axial locations are also given for each thermocouple.

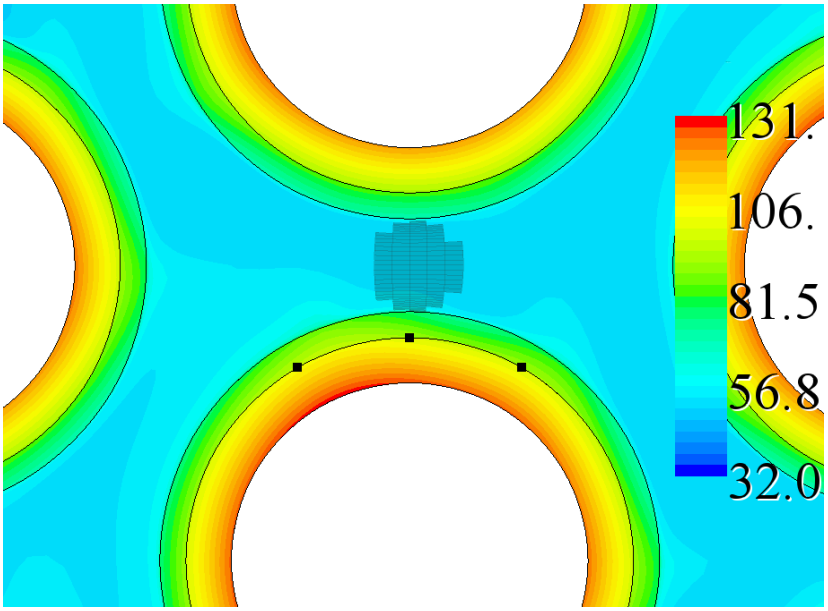


Figure 6-18: Axial cross-section at height of peak heat flux displaying temperature contours [˚C] around the center pin (STA001) and thermocouple clocking locations of 11, 12, and 1.

The Axial configuration heated pin in the second row (AXI204) shows increased temperatures in the heated region of the deformed bundle (relative to the non-deformed bundle). The maximum increase of roughly 4% occurs about +/- 0.5 pitches from the location of max deformation (in other words, at z = 2.833P and z = 3.166P). These results are shown in Figure 6-19. It is also clear that near the start of the heated region (z = 0.75P) and after the heated region, there is negligible difference between the non-deformed and deformed temperatures, while near the end of the heated region (z = 5.25P) there are still appreciable differences between the two. Figure 6-20 displays the temperatures sampled from an Azimuthal heated pin (AZI208) at z = 4.166P. It shows a difference of roughly 16 ˚C (19% difference) between 3 o'clock and 9 o'clock of the deformed case, and slightly less difference for the non-deformed case. Note that the lower temperature side of this pin is adjacent to non-heated tubes, while the higher temperature side is in the vicinity of another heated pin.

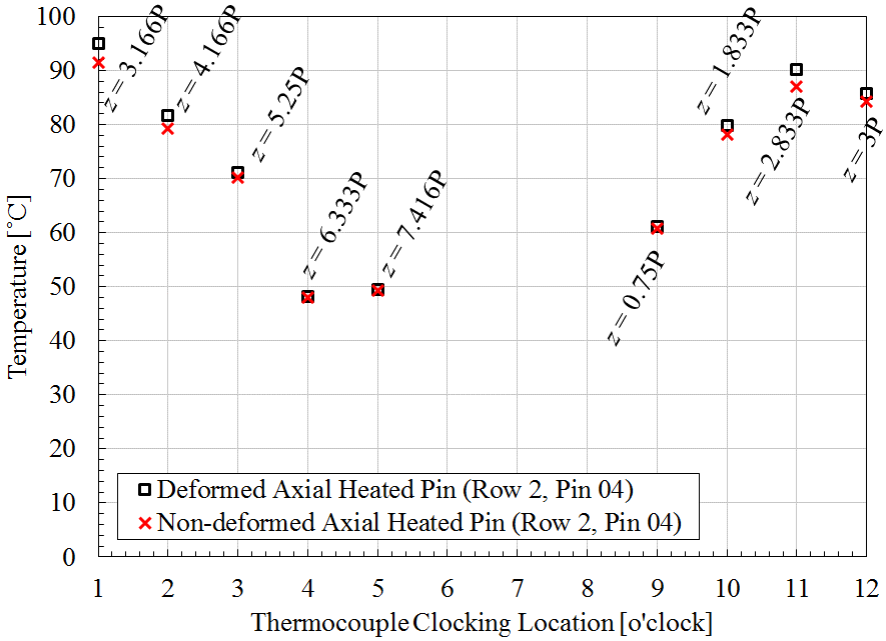


Figure 6-19: Temperature versus the clocking location of each thermocouple on heated pin AXI204 for non-deformed and deformed bundles. Axial locations are also given for each thermocouple.

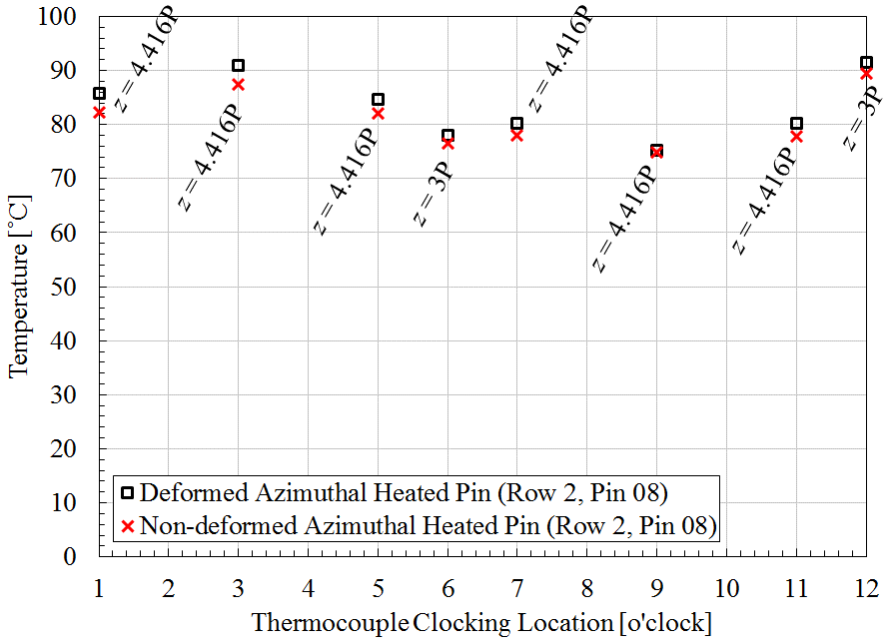


Figure 6-20: Temperature versus the clocking location of each thermocouple on heated pin AZI208 for non-deformed and deformed bundles. Axial locations are also given for each thermocouple.

Figure 6-21 shows the temperatures on two different non-heated tubes for both duct geometries. There is little difference between non-heated tube temperatures of the deformed duct relative to the non-deformed duct. However, the non-heated tubes do display large transverse temperature gradients (roughly 40% for TUB201) across the wire at z = 4.416P. Due to this large gradient across the wire, it seems that the wire-wrap plays a much more important role for the non-heated tubes, than for the heated pins, in creating sharp transverse temperature differences on the rod surfaces.

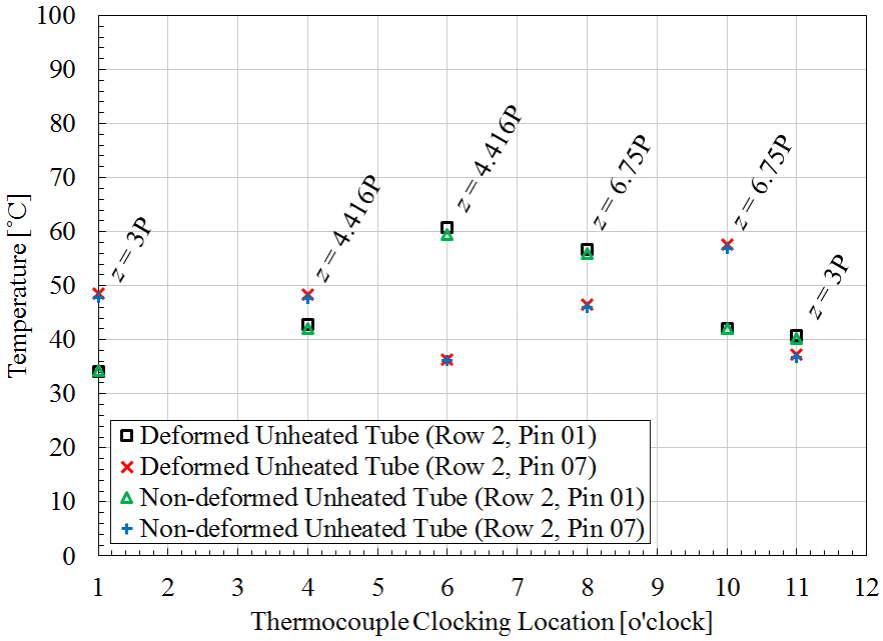


Figure 6-21: Temperature versus the clocking location of each thermocouple on non-heated tubes TUB201 and TUB207 for non-deformed and deformed bundles. Axial locations are also given for each thermocouple.

7 CONCLUSIONS

This report provided solution verification and official pre-test results for non-deformed and deformed ducted isothermal and heated bundle CFD simulations. These simulations were conducted in accordance with test and benchmark specifications [1] [2] [5] provided for the experiments and the computations. CFD simulations, using two-equation RANS turbulence models and momentum sources in place of the wire-wrap, were conducted across a range of mesh sizes in an effort to display mesh convergence for the variables of interest. The round-off error, statistical sampling error, and iterative error were all examined and shown to provide negligible contributions to the overall error of the simulations.

Convergence behavior of the bundle pressure drop implied that the asymptotic region (consistent convergence of the results at an OOA that matches the FOA) was not achieved for this variable, and thus that the presented Richardson extrapolation of the “exact” solutions should be considered with reservation. However, for practical CFD problems, it is often very difficult or impossible to reach an asymptotic region [6], and there can be many factors in the complexity of the simulation and models that cause this. Still, the large number of meshes (five) run for each bundle to complete iterative convergence, and the clear monotonic convergence of the results by the Fine mesh (relative to the Finest mesh), provides a large degree of confidence in the presented solution verification process. The velocity field displayed similar convergence characteristics. Global transverse velocity samples, while not always displaying convergence behavior where the OOA matched the FOA, did display monotonic convergence with little variation by the refinement level of the Fine mesh. The local velocity magnitude samples showed little variation over a range of meshes, and it was concluded that the Fine mesh was adequate to capture it.

The local temperature results varied in their mesh refinement convergence behavior based on the location of the sample. For instance, results on the surfaces on the unheated tubes showed little variation over the range of meshes. Temperature results in the heated pins showed little variation with mesh size when the samples were outside of the heated length of the pin. However, the temperature results in the heated length did show appreciable variation with mesh size. Moreover, these results in the heated pins, and within the heated region, did not always display decent convergence behavior by the Fine mesh, although the variation between the Fine and Finest meshes (and amongst most meshes for that matter) was relatively small.

Although the Fine mesh was still chosen for the official pre-test results, the temperature samples within the heated length of the heated pins could potentially have more error than at other locations in the bundle.

An axial mesh sensitivity study was also conducted on the non-deformed isothermal bundle. This test showed that the Fine mesh could be axially coarsened to have the axial cell distribution of the Coarsest mesh, and still provide the same results as the Fine mesh itself. In other words, the simulation results were not very sensitive to axial cell distribution beyond the Coarsest level. This result was applied to the heated bundle simulations due to the long length of the bundle. This allowed for only transverse refinement in the heated bundle mesh studies, and provided a great reduction in the computational cost of these simulations and in future isothermal bundle simulations as well. The convergence behavior of the deformed duct cases was similar to that of the non-deformed ducts. That is to say, the Fine mesh proved adequate enough to capture the mesh-converged pressure, velocity, and temperature fields for the deformed ducts as well.

Model sensitivity studies of turbulence model, and momentum source coefficient value were conducted on the Fine meshes of the non-deformed isothermal and non-deformed heated bundle cases. The studies examined four common two-equation RANS turbulence models. The velocity and temperature fields displayed little difference amongst the four models. The pressure fields did show differences, but all models provided pressure drop results which were within roughly 5-10% of the Cheng and Todreas correlation for wire wrapped fuel assemblies. A coefficient used in the momentum source modeling (that prevents flow from penetrating the cells that make up the outer surface of the wire) was also tested for sensitivity. Changes to the coefficient did not affect the pressure drop values but did show impact on the velocity and temperature fields, although they were not significant. After the solution verification procedure, the Fine mesh and the Menter k-ω SST turbulence model were chosen for the official pre-test results. Further investigation into these modeling choices will be continued following acquisition of experimental data.

The official pre-test results were presented for all of the cases. They provided results corresponding to the proposed pressure tap, LDV, PIV, and thermocouple experiment locations. Interesting features, such as the alteration of the velocity profiles and the variation in the temperature results due to the duct deformation were discussed. Results also showed that no hot spots were observed at the contact points of the wire-wrap and the pins. These hot spots, which have been discussed in the literature, were not expected to be captured with the momentum source approach. The momentum source has fluid flow in the cells where the wire-wrap should be, and thus, has different heat transfer characteristics than a solid metal wire. The official pre-test results will be compared directly to the experimental data and high-fidelity LES data, when it becomes available, to assess the validity of TerraPower's CFD approach. If there are substantial differences between the pre-test simulations and the as-tested experiments, these comparisons will be of limited value. Post-test simulations will address any changes from the as-designed experiment conditions and the as-tested conditions.

Code verification, using the MMS, was conducted on Star-CCM+ for simplified governing equations. Results with 1st-order numerical schemes provided rigorous proof that the code was implemented correctly. Results with 2nd-order numerical schemes showed that there may be an error in the implementation of the algorithm or boundary conditions. The problem was sent to the Star-CCM+ development team in an attempt to resolve this issue. Manufactured solutions have been implemented for the Navier-Stokes equations and have been further investigated for two-equation RANS turbulence models. These manufactured solutions, which better represent the solvers used for the pre-test simulations, will be tested when the current issues with the simplified governing equations are resolved.

Future work includes running post-test simulations (using similar methods) with as-tested conditions and comparing these to the experiments as well. Further analyses of the sensitivity studies on selection of turbulence model and value of momentum source coefficient will be continued. Other sensitivity studies may also be undertaken, such as inlet flow profile sensitivity, sensitivity of the heat flux into the bundle from the heated pins, and heat loss through the duct walls. Further methods, such as using a body-fitted mesh around the wire-wrapping, will be investigated as well. The post-test simulations, will be essential to the solution validation procedure and uncertainty quantification of the CFD simulations. Additionally, code verification will continue when the current problems have been addressed by the Star-CCM+ development team. The entire V&V process will ultimately provide the level of confidence that can be expected when

estimating pressure drops, velocities, and temperatures with TerraPower's CFD methods for flow through a wire-wrapped fuel assembly.

8 REFERENCES

[1] "TWRP-31-TSPEC-0011-Rev-2, AFAFC AREVA Heated Bundle Experiment Test Specification".

[2] "TWRP-31-TSPEC-0010-Rev-1, TAMU Fuel Assembly Flow Visualization Test Specification".

[3] R. Hu and T. H. Fanning, "Development of a Three-Dimensional Momentum Source Model for Wire-Wrapped Rod Bundles," in *The 14th International Topical Meeting on Nuclear Reactor Thermalhydraulics, NURETH-14*, Toronto, Ontario, Canada, 2011.

[4] CD-Adapco, STAR-CCM+ User Guide.

[5] "TWRP-31-TREP-0004-Rev-0, AFAFC Benchmark Specification".

[6] W. Oberkampf and C. Roy, Verification and Validation in Scientific Computing, New York: Cambridge University Press, 2010.

[7] D. Wilcox, Turbulence Modeling for CFD, Anaheim: DCW Industries, 1998.

[8] "TP1-1.9.31-RPT-0004-Rev-0, CFD Modeling Methods for Fuel Assemblies".

[9] C. Roy, T. Smith and C. Ober, "Verification of a Compressible CFD Code using the Method of Manufactured Solutions," *AIAA Paper,* 2002.

[10] "TWRP-31-RPT-0019, AREVA Proof-of-Fabrication Pressure Drop Results Explanation".

[11] S.-K. Cheng and N. E. Todreas, "Hydrodynamic Models and Correlations for Bare and Wire-Wrapped Hexagonal Rod Bundles - Bundle Friction Factors, Sub-Channel Friction Factors and Mixing Parameters," *Nuclear Engineering and Design,* vol. 92, pp. 227-251, 1986.

9 APPENDICES

9.1 Non-deformed Isothermal Bundle Mesh Convergence

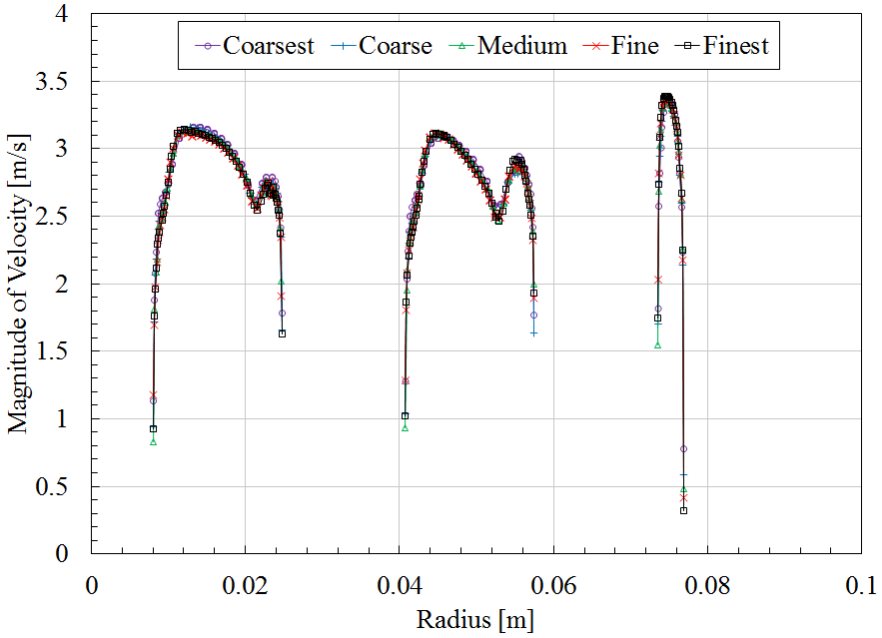


Figure 9-1: Velocity magnitude versus radial position from the center of the duct at 2.25P (wire-wrap at 12 o'clock) for all meshes.

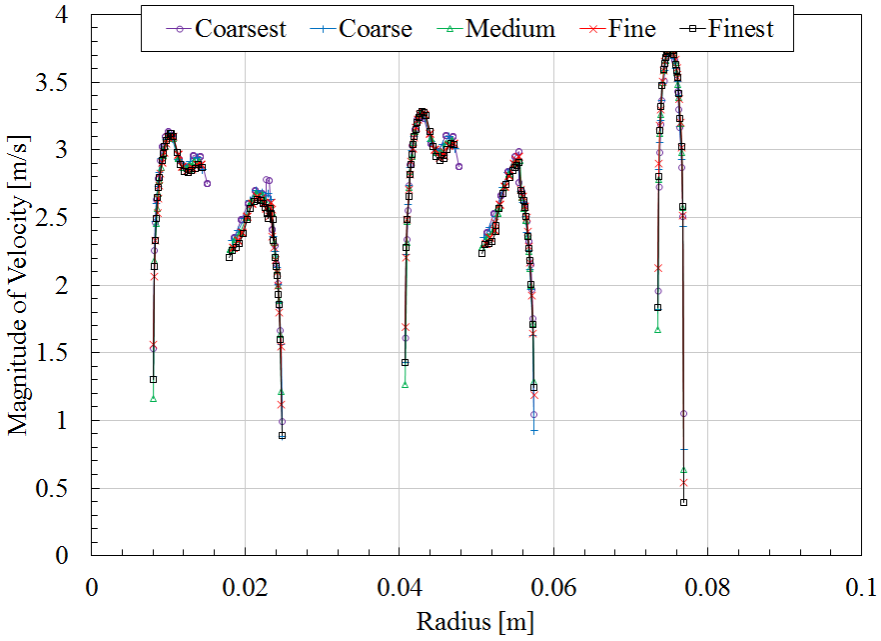


Figure 9-2: Velocity magnitude versus radial position from the center of the duct at 2.583P (wire-wrap at 4 o'clock) for all meshes.

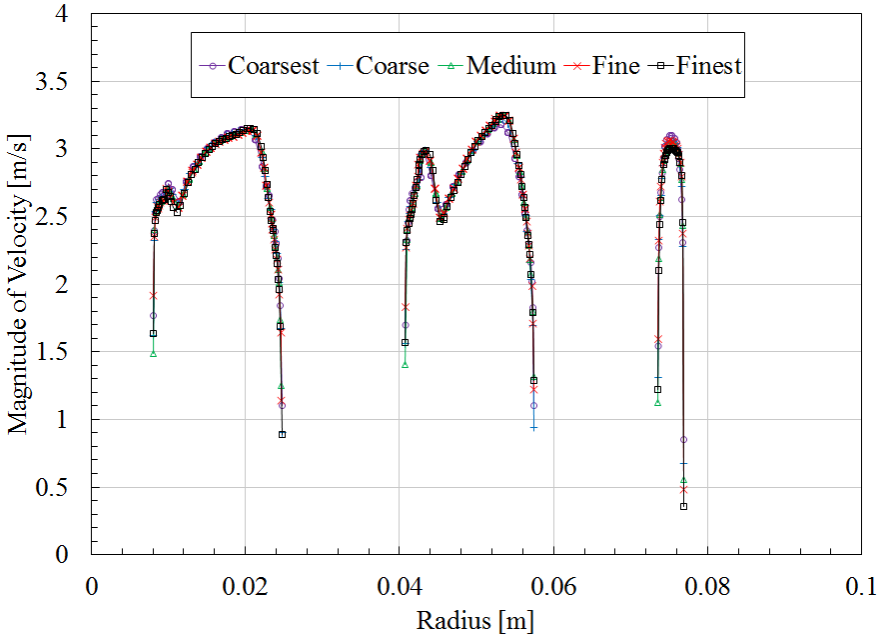


Figure 9-3: Velocity magnitude versus radial position from the center of the duct at 2.75P (wire-wrap at 6 o'clock) for all meshes.

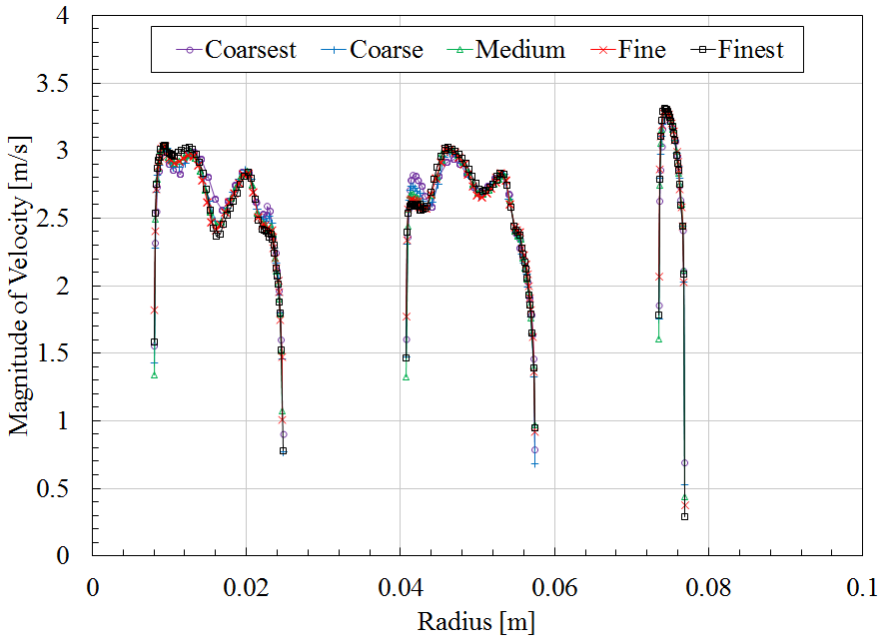


Figure 9-4: Velocity magnitude versus radial position from the center of the duct at 2.917P (wire-wrap at 8 o'clock) for all meshes.

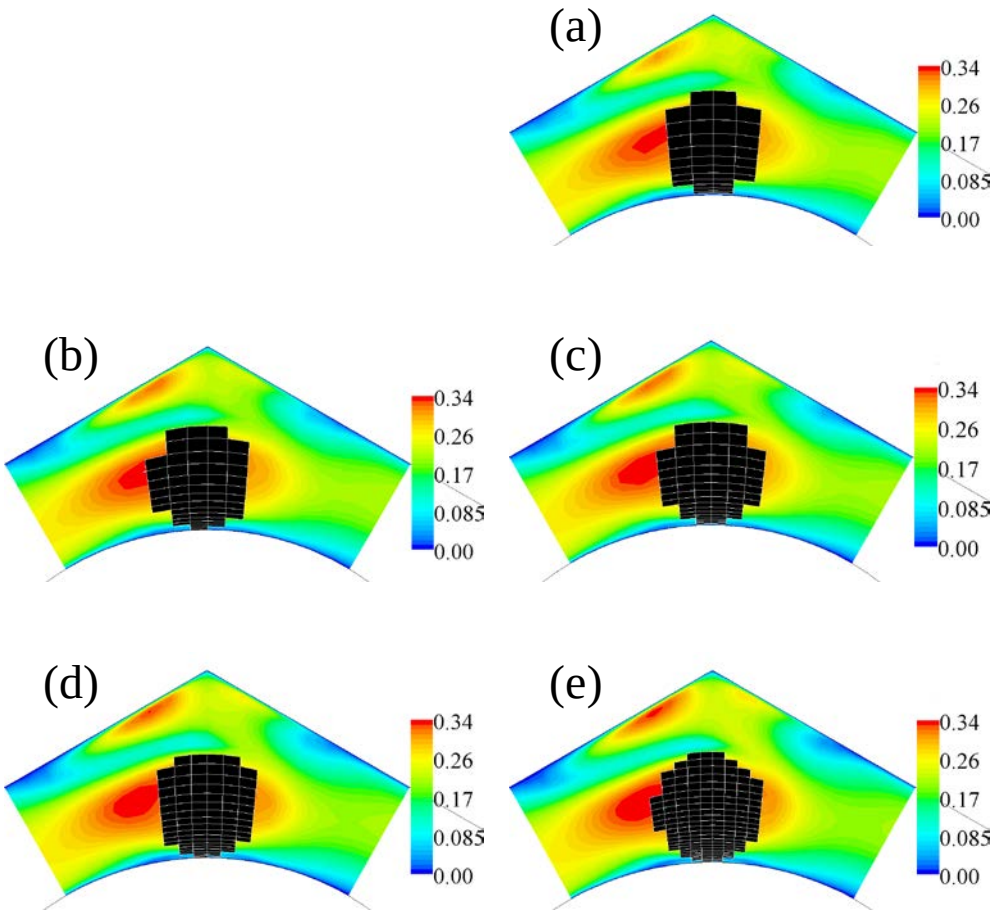


Figure 9-5: Contours of magnitude of projected transverse velocities [m/s] of a corner sub-channel at 3.25P (wire-wrap at 12 o'clock) for the (a) Coarsest, (b) Coarse, (c) Medium, (d) Fine, and (e) Finest meshes.

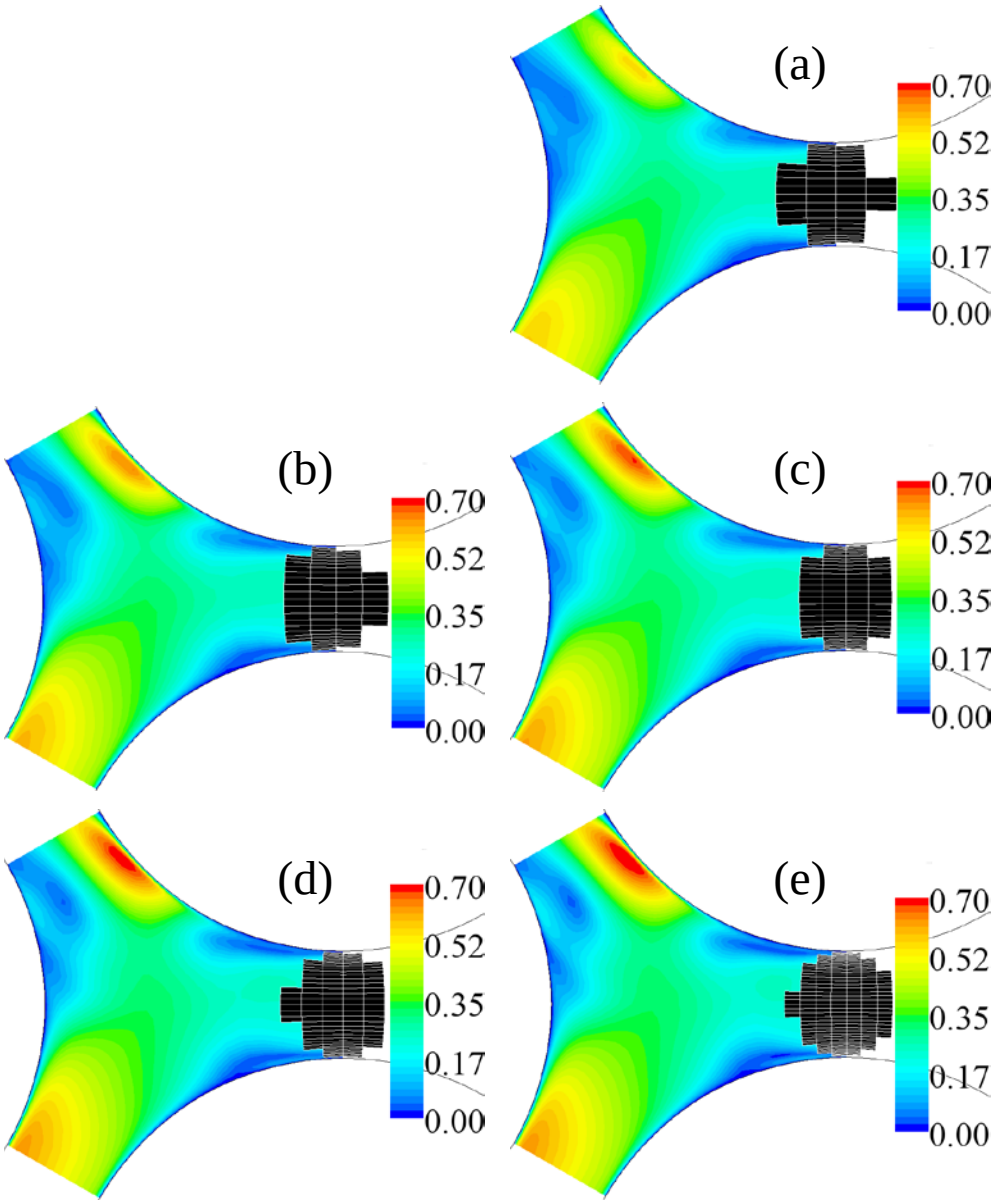


Figure 9-6: Contours of magnitude of projected transverse velocities [m/s] of an interior sub-channel at 3.25P (wire-wrap at 12 o'clock) for the (a) Coarsest, (b) Coarse, (c) Medium, (d) Fine, and (e) Finest meshes.

9.2 Non-deformed Heated Bundle Mesh Convergence

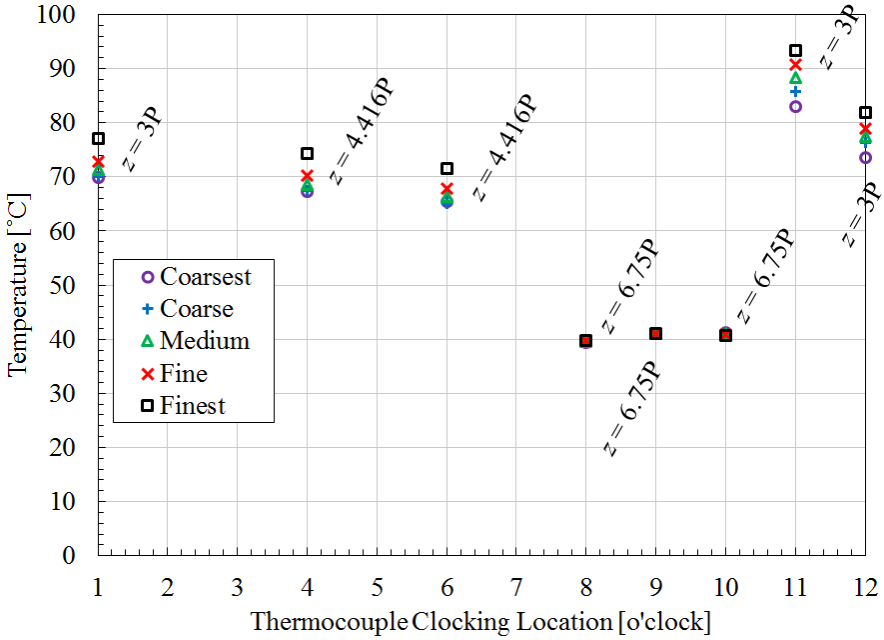


Figure 9-7: Temperature versus the clocking location of each thermocouple on heated pin STA407 for all meshes. Axial locations are also given for each thermocouple.

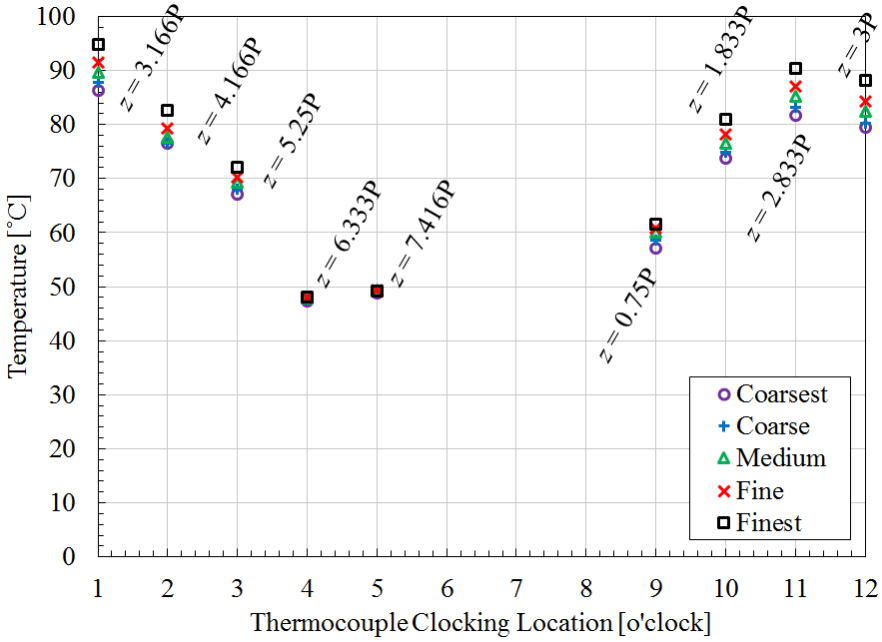


Figure 9-8: Temperature versus the clocking location of each thermocouple on heated pin AXI204 for all meshes. Axial locations are also given for each thermocouple.

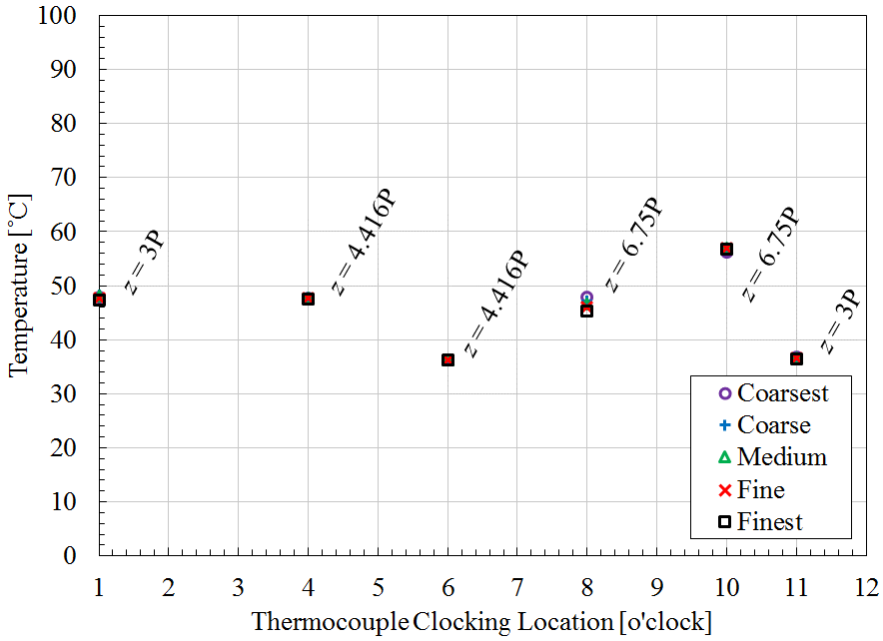


Figure 9-9: Temperature versus the clocking location of each thermocouple on unheated tube TUB207 for all meshes. Axial locations are also given for each thermocouple.

9.3 Deformed Isothermal Bundle Mesh Convergence

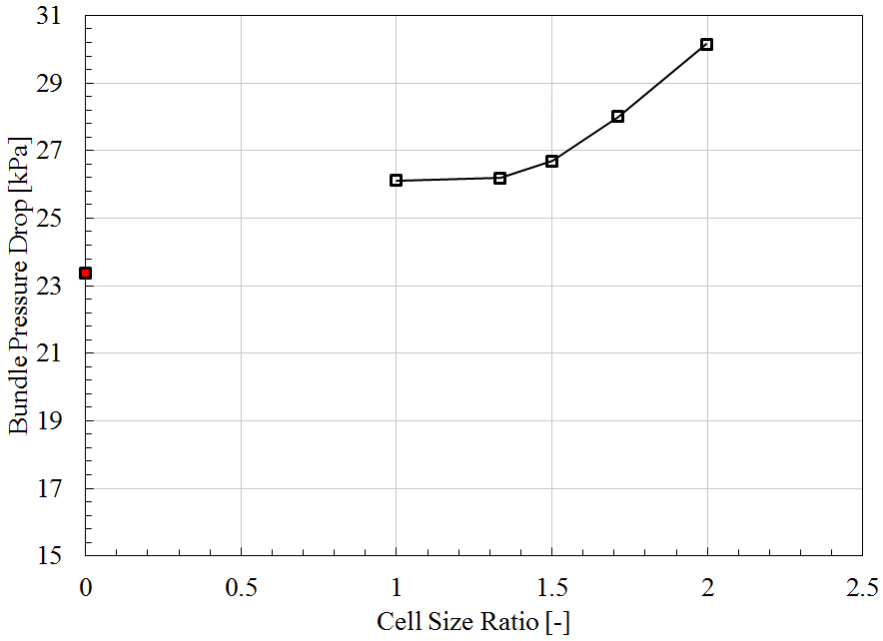


Figure 9-10: Deformed isothermal bundle pressure drop (based on mass-flow averages at inlet and outlet) versus cell size ratio h for all meshes. The red-filled square at $h = 0$ represents the Richardson extrapolation based on the Coarsest, Coarse, and Medium meshes.

9.4 Deformed Heated Bundle Mesh Convergence

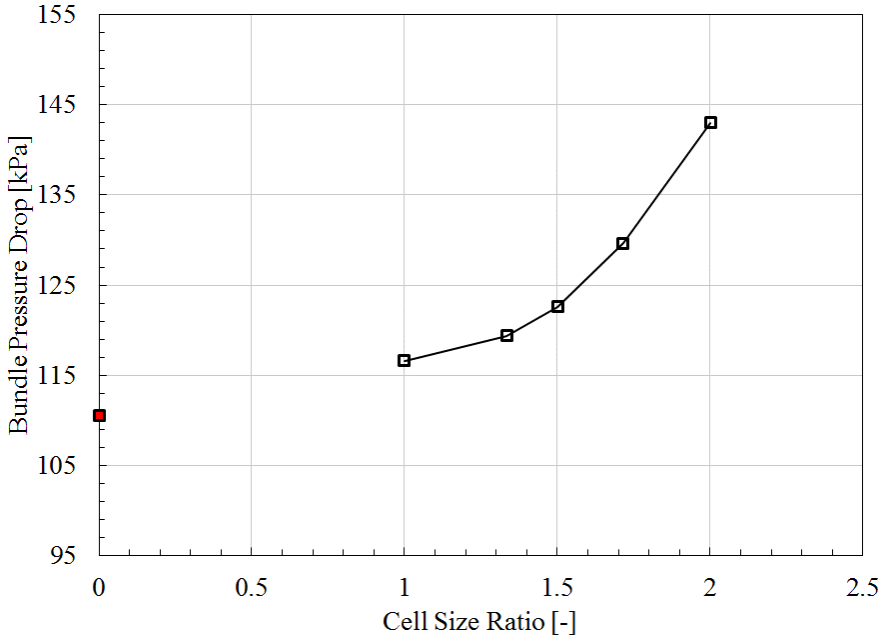


Figure 9-11: Deformed heated bundle pressure drop (based on mass-flow averages at inlet and outlet) versus cell size ratio h for all meshes. The red-filled square at h = 0 represents the Richardson extrapolation based on the Coarsest, Coarse, and Medium meshes.

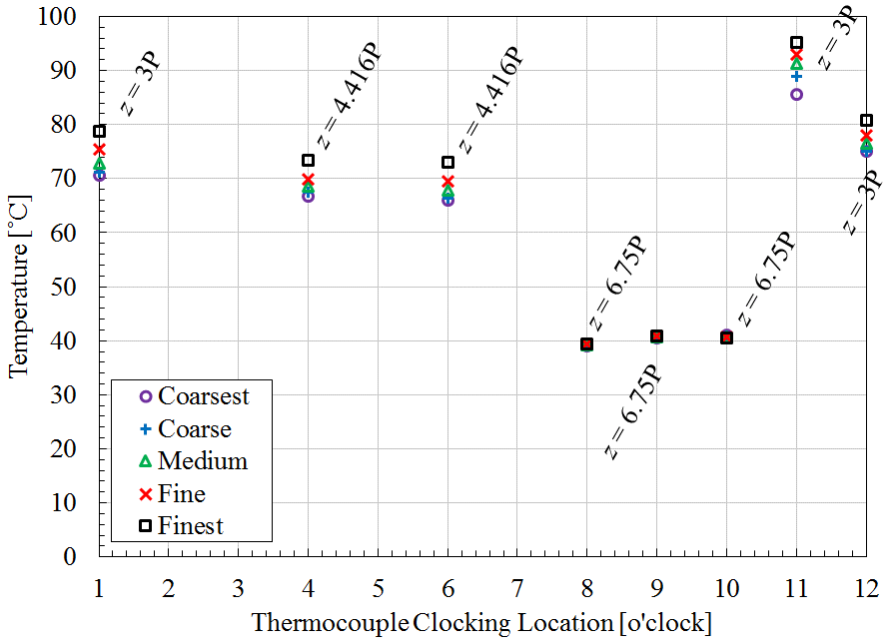


Figure 9-12: Temperature versus the clocking location of each thermocouple on heated pin STA407 for all meshes. Axial locations are also given for each thermocouple.

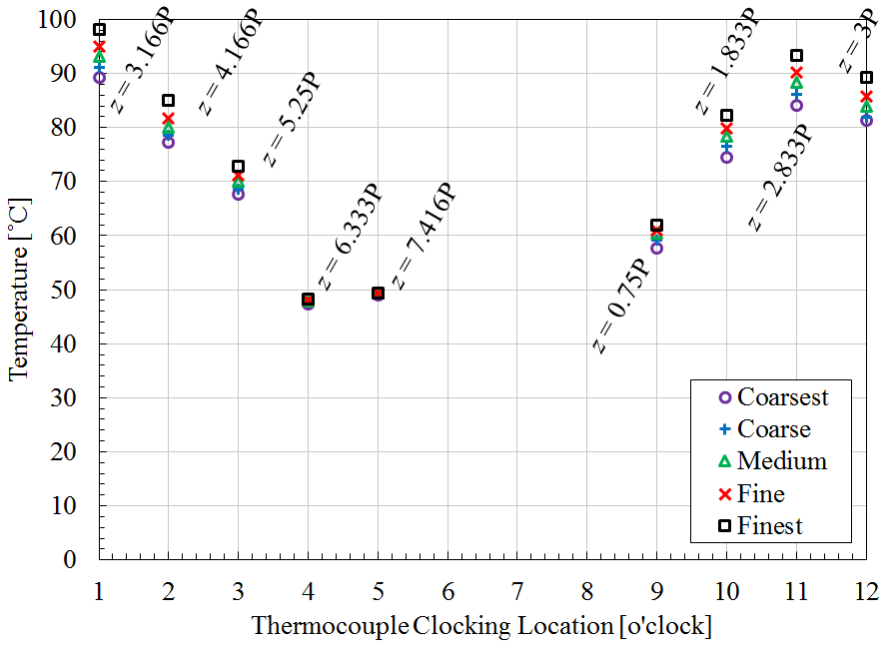


Figure 9-13: Temperature versus the clocking location of each thermocouple on heated pin AXI204 for all meshes. Axial locations are also given for each thermocouple.

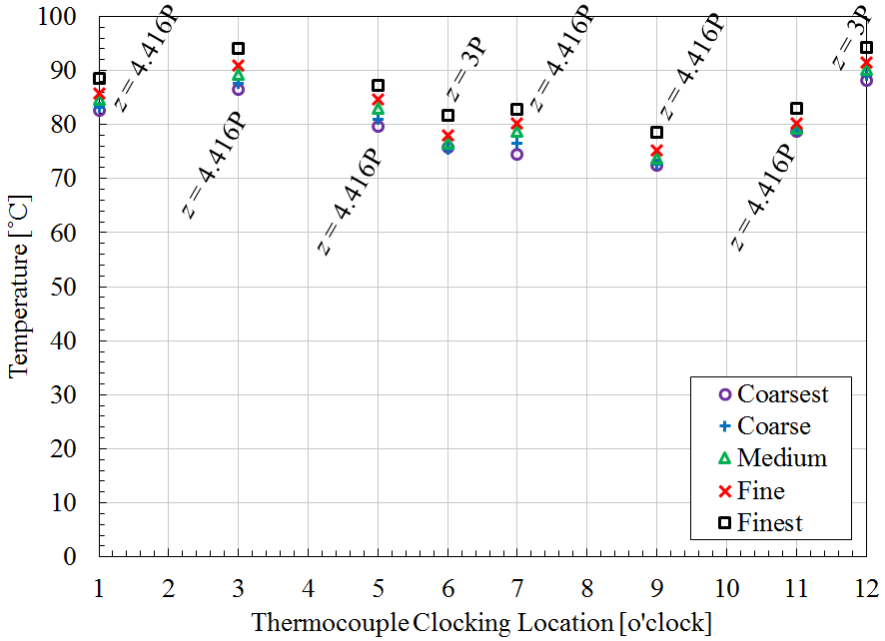


Figure 9-14: Temperature versus the clocking location of each thermocouple on heated pin AZI208 for all meshes. Axial locations are also given for each thermocouple.

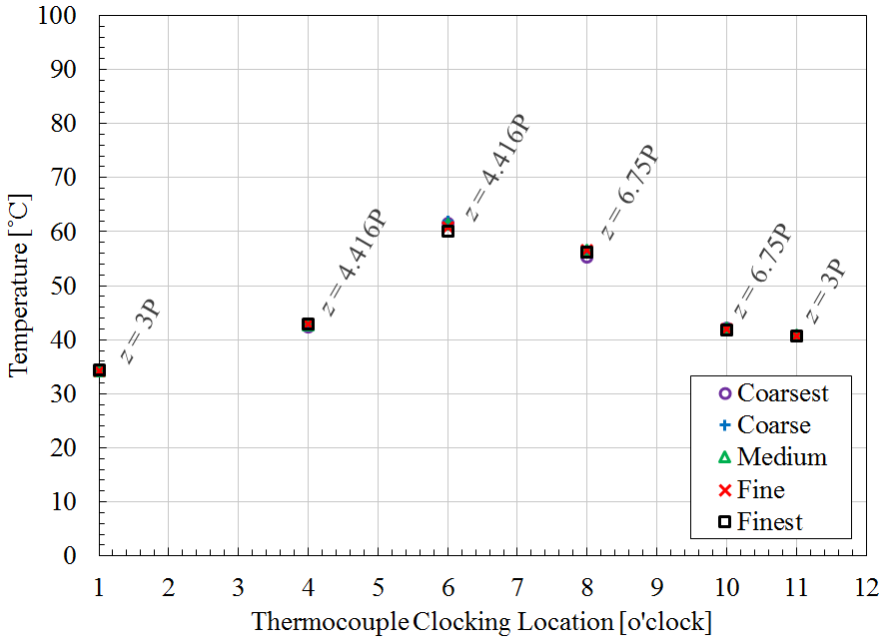


Figure 9-15: Temperature versus the clocking location of each thermocouple on unheated tube TUB201 for all meshes. Axial locations are also given for each thermocouple.

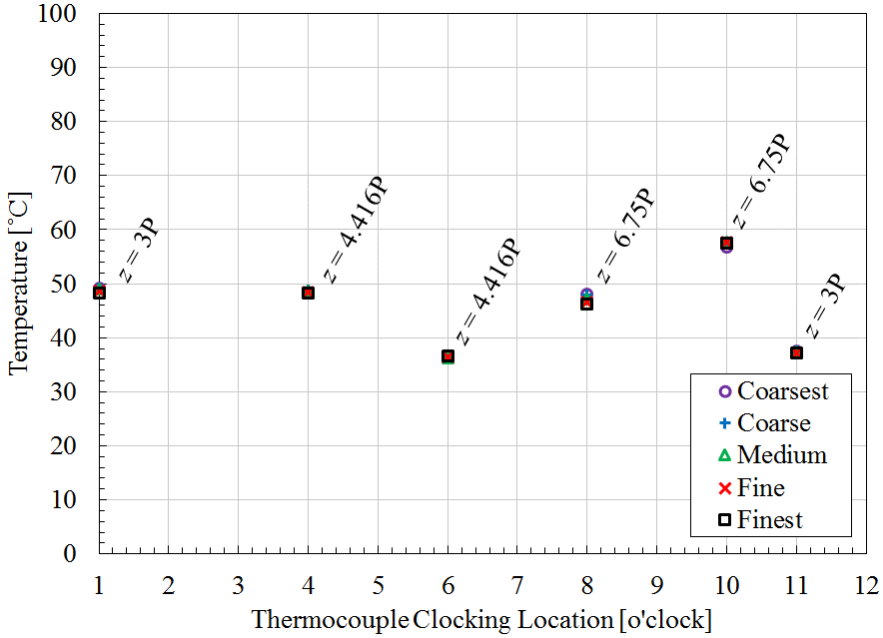


Figure 9-16: Temperature versus the clocking location of each thermocouple on unheated tube TUB207 for all meshes. Axial locations are also given for each thermocouple.

END OF DOCUMENT

APPENDIX E: TWRP-31-RPT-0032, AFAFC POST-TEST SIMULATION DETAILS

ENGINEERING REPORT

Document Number:	TWRP-31-RPT-0032	**Revision:**	0
Document Title:	AFAFC Post-Test Simulation Details	**Approval Date** *(Final Signature Date)***:**	2/6/2017
Issuing Organization:	Design Qualification	**Effective Date** *(for Procedures Only)***:**	
		Pages:	Page 1 of 16

Approval

Title	Name	Signature	Date
Originator, Thermal Hydraulics Test and Analysis Engineer	Brian Jackson	Approved in Agile	2/3/2017
Reviewer, CFD and Thermal-Hydraulic Testing Engineer	Mathieu Martin	Approved in Agile	2/6/2017
Approver, Manager, Thermal Hydraulic Test & Analysis	Mike Steer	Approved in Agile	2/6/2017

Document Quality Level per TWRP-NS-PROC-0002:

Quality Level 1 ☐ Quality Level 2 ☒ Quality Level 3 ☐ N/A ☐

Contains Open Items: Yes ☐ No ☒

Revision History

Revision No.	Effective Date	Affected Section(s)	Description of Change(s)
0	2/6/2017	All	Initial Release

TABLE OF CONTENTS

1 OBJECTIVE 4
2 POST-TEST SIMULATIONS DETAILS 4
2.1 Isothermal Flow Visualization Non-Deformed Bundle Post-Test Simulations 4
2.1.1 Flow Visualization Non-Deformed Bundle Geometry Details 4
2.1.2 Flow Visualization Non-Deformed Bundle As-Tested Conditions 5
2.1.3 Flow Visualization Non-Deformed Bundle CFD Inputs 5
2.2 Isothermal Flow Visualization Deformed Bundle Post-Test Simulations 6
2.3 Heated Non-Deformed Bundle Post-Test Simulations 6
2.3.1 Heated Non-Deformed Bundle Geometry Details 6
2.3.2 Heated Non-Deformed Bundle As-Tested Conditions 7
2.3.3 Heated Non-Deformed Bundle CFD Inputs 9
2.4 Heated Deformed Bundle Post-Test Simulations 10
2.4.1 Heated Deformed Bundle Geometry Details 11
2.4.2 Heated Deformed Bundle As-Tested Conditions 13
2.4.3 Heated Deformed Bundle CFD Inputs 14
3 REFERENCES 16

LIST OF TABLES

Table 1. Isothermal Non-Deformed Post-Test Geometry Details 4
Table 2. Isothermal Non-Deformed Post-Test Boundary Conditions 5
Table 3. Isothermal Non-Deformed CFD Assumptions 5
Table 4. Heated Non-Deformed Bundle Post-Test Geometry Details 6
Table 5. Heated Non-Deformed Post-Test Boundary Conditions 7
Table 6. Heated Non-Deformed Bundle CFD Assumptions 9
Table 7. Heated Deformed Bundle Post Test Geometry Details 11
Table 8. Deformed Duct Values 13
Table 9. Heated Deformed Bundle As-Test Conditions 13
Table 10. Heated Deformed Bundle CFD Assumptions 14

LIST OF FIGURES

Figure 1. Heater Rod Position Map 8
Figure 2. Deformed Duct Visual Representation 12

1 OBJECTIVE

The objective of this document is to record the CFD simulation geometry and boundary conditions used for the numerical analyses of the experiments that are part of the Advanced Fuel Assembly Flow Characterization Project support of DOE Award Number DE-NE0008321. As part of the project, both pre-test and post-test simulations of the experiments are performed. The pre-test simulations include specifications as outlined in the Test Specifications [1][2]. Post-test simulations include as-built and as-tested conditions that may be different from the design conditions. As preparation of the Test Reports is concurrent with the post-test simulations work, this document supplies test as-built and as-tested descriptions that are used by the CFD analysts for the post-test simulations. This document will reference the Test Specifications, As-built reports [3][4] and Test Summary Reports [5] as appropriate.

The details of each experiment are presented in Section 2. For each experiment, 3 tables are presented that correspond to as-built geometry, as-tested conditions, and CFD modeling assumptions that are used as inputs to the CFD simulations. As-built geometry measurements are reported in the units they were measured in. Other systems of units are reported in parentheses.

2 POST-TEST SIMULATIONS DETAILS

2.1 Isothermal Flow Visualization Non-Deformed Bundle Post-Test Simulations

This section contains the geometry and test conditions of the isothermal flow visualization non-deformed bundle experiments to be used in the post-test simulations.

2.1.1 Flow Visualization Non-Deformed Bundle Geometry Details

Presenting details provided in the TAMU Wire-Wrapped As-Built Geometry (Non-Deformed Bundle) [4], the following geometry details represent the as-built geometry and are used in the post-test simulations. The TAMU report provides geometry details of two bundles that were constructed for the project: a preliminary bundle, and a final bundle that corresponds to the tests described in this report. Values presented in Table 1 corresponds to the second bundle fabricated and reported in the TAMU document [4]. Units reported correspond to the units used in reporting and/or measurement. Secondary units are presented in parentheses.

Table 1. Isothermal Non-Deformed Post-Test Geometry Details

Parameter	Value	Reference
Duct Inner Flat-to-flat	6.085 in (0.1546 m) *	Flat-to-flat of the enclosure reported in [4]
Test Section Bundle Length	65.625 in (1.667 m)	[4]
Pin OD	0.6251 in (1.5878E-2 m)	Average values from [4]
Wire OD	3.0 mm (0.11811 in)	Average values from [4]
Pin Pitch	1.8878E-2 m (0.74321 in)	Calculated from Pin + Wire. Reported in [4]
Wire Pitch	0.47625 m (18.75 in)	Appendix of [5]. Wire pitch equals 30 * specified pin diameter
Wire Wrap Direction	Clockwise	[4] In direction of flow (looking upwards)

Wire wrap clocking angle reference	Discussed in CFD Assumptions Table	
Duct Corner Detail	Sharp corners	[4]

* The inner flat to flat was measured at both the entrance and exit of the duct. This value is that average.

2.1.2 **Flow Visualization Non-Deformed Bundle As-Tested Conditions**

Multiple flow visualization tests were performed by Texas A&M University. The different tests corresponded to measurements at different bundle locations. All of these tests had the same target flow conditions (flow rates, fluid temperatures), however there were minor variations from test to test. These values are reported in the corresponding test reports. The operating conditions reported herein correspond to test PCM-11-E [5]. This test corresponds to a specific measurements plane. In this test, 3 separate datasets were taken. For each dataset, a time averaged flowrate and fluid inlet temperature was recorded and reported. Values in the following table are averaged over the 3 datasets of test PCM-11-E and are recommended for use as CFD boundary conditions. Additional specific operating conditions for each dataset are available in the test report and the corresponding test data [5].

Table 2. Isothermal Non-Deformed Post-Test Boundary Conditions

Parameter	**Value**	**Reference**
Fluid	P-cymene	As-tested conditions [5]
Fluid Inlet Temperature	23.73 ^{o}C	Average value from [5]
Fluid Density	854.21 kg/m^3	Average values from [5]
Fluid Viscosity	8.04E-4 Pa-s	Average values from [5]
Inlet Flowrate (Re #)	300.19 GPM (19,357 Re)	Average values from [5]

2.1.3 **Flow Visualization Non-Deformed Bundle CFD Inputs**

The following are CFD assumptions used in the models.

Table 3. Isothermal Non-Deformed CFD Assumptions

Parameter	**Value**	**Notes**
Wire wrap clocking angle reference	90°: pointed at duct face E at bundle entrance	In TAMU As-Built Geometry Report [4], it specifies this value as 89.83^{o}. CFD will use 90°. This results in wire pointing at the corner between faces A and F at a height of P = 2.25 from bundle entrance.
Inlet Flow Profile	Flat	CFD simulation assumption
Inlet Turbulence Intensity	3 %	CFD simulations assumption based on moderate turbulence at inlet
Inlet Turbulent Length Scale	8.7419E-5 m	CFD simulations assumption based on 22% fraction of turbulent boundary layer thickness given by $BL_{thick} = {0.37 * D_h}/{Re_{Dh}^{1/5}}$

2.2 Isothermal Flow Visualization Deformed Bundle Post-Test Simulations

Experiments of the isothermal flow visualization deformed bundle were not performed.

2.3 Heated Non-Deformed Bundle Post-Test Simulations

This section contains the geometry and test conditions of the heated non-deformed bundle experiments to be used in the post-test simulations.

2.3.1 Heated Non-Deformed Bundle Geometry Details

Units reported correspond to the units used in reporting and/or measurement. Secondary units are presented in parentheses.

Table 4. Heated Non-Deformed Bundle Post-Test Geometry Details

Parameter	Value	Reference
Duct Flat-to-Flat distance	3.622 in (0.092 m)	Section 4.1 of [3]
Bundle Total Length	Discussed in CFD Assumptions Table	
Bundle Entrance Length	Discussed in CFD Assumptions Table	
Bundle Heated Length	5.97 wire pitches	Designed to be 6 pitches in length. The as-built heater length was slightly less (see Heater heated length dimension below)
Bundle Additional Measurement Length	2.03 wire pitches	The as built of this section was slightly longer due to the as-built heater length being slightly shorter.
Bundle Exit Length	Discussed in CFD Assumptions Table	
Heater Outer Clad OD	9.514 mm (0.37457 in)	Average heated OD reported in [3]
Heater Clad ID/ Heater Sheath OD	0.335 in (8.509E-3 m)	Reported in [3]. Reference from email from STERN Labs
Heater Sheath ID	0.267 in (6.7818E-3 m)	Reported in [3]. Reference from email from STERN Labs
Heater Clad and Sheath Material	Monel K500	[3]
Heater heated length	1702.64 mm (67.0331 in)	Section 2.2.1 of [3]. *This length is referenced from the beginning of heated length section and corresponds to 5.97 wire pitch length.*
Non-Heated Tube OD	0.3768 in (9.57072E-3 m)	Average non-heated tube OD reported in Section 3.1.1 of [3]
Non-Heated Tube wall thickness	0.065 in (1.651E-3 m)	Steel tubing order. As-built values not measured
Non-Heated Tube Material	SS304	Steel Tubing order [3]
Wire OD	1.7062 mm (0.06717 in)	Average wire wrap OD reported in Section 3.1.1 of [3] for non-heated tubes

Pin Pitch	Discussed in CFD Assumptions Table	
Wire Pitch	11.22 in (0.28499 m)	Section 3.1.3 of [3]
Wire Wrap Direction	CW in flow direction	Section 3.1.3 of [3]
Wire wrap clocking angle reference	Wire points to 12 o'clock 4 pitches below start of heated length	[3]. This results in the wire wrap pointed at the duct faces A – F corner at the start of the heated length and at 19.55 mm above the physical duct entrance. Additional detail for CFD model below.
Duct Corner Detail	Radius of curvature = 0.27 in (6.858E-3 m)	Reported in [3].

2.3.2 **Heated Non-Deformed Bundle As-Tested Conditions**

The as-tested conditions which are to be used for CFD boundary conditions are presented below. These values correspond to test 05. Test data from this test will accompany the final report project.

Table 5. Heated Non-Deformed Post-Test Boundary Conditions

Parameter	**Value**	**Reference**
Fluid	Water	
Fluid Inlet Temperature	32.07 ^{o}C	Test Data from 8/23/2016, average of two temperature measurements at inlet plenum
System Pressure	120.42 psia	Test Data from 8/23/2016: upper plenum measurement
Inlet Flowrate (Re #)	9.53 kg/s (20,296 Re)	Test Data from 8/23/2016. Calculated Reynolds number with as-built geometry
Power Profile	Discussed in CFD Assumptions Table	STERN took power profile measurements at 10 axial positions for each heater rod [3].
Heater Rod Bank 1 Per Heater Power	22.643 kW	Test Data from 8/23/2016
Bank 1 Heaters Positions	1, 3, 6 and 7	Corresponds to numbering in Figure 1
Heater Rod Bank 2 Per Heater Power	22.845 kW	Test Data from 8/23/2016
Bank 2 Heaters Positions	4, 5, 11 and 15	Corresponds to numbering in Figure 1
Heater Rod Bank 3 per Heater Power	22.747 kW	Test Data from 8/23/2016
Bank 3 Heaters Positions	2, 9, 19, 40 and 60	Corresponds to numbering in Figure 1
Heater Rod Bank 4 Per Heater Power	22.801 kW	Test Data from 8/23/2016
Bank 4 Heaters Positions	13, 44, 48, 52 and 56	Corresponds to numbering in Figure 1

Below presents the heater rod installed configuration in the bundle. Different from the Test Specification, only 18 heater rods were used because the heater rod at position #17 (as numbered in Figure 1 below) failed. Below is a picture of the heater rod as-installed positioning from the point of view of the bottom of the duct looking upwards. The rods were ID-ed and the specific position for each heater rod was recorded. However, for the CFD simulations, the heat flux power profile of each rod was modeled as the same.

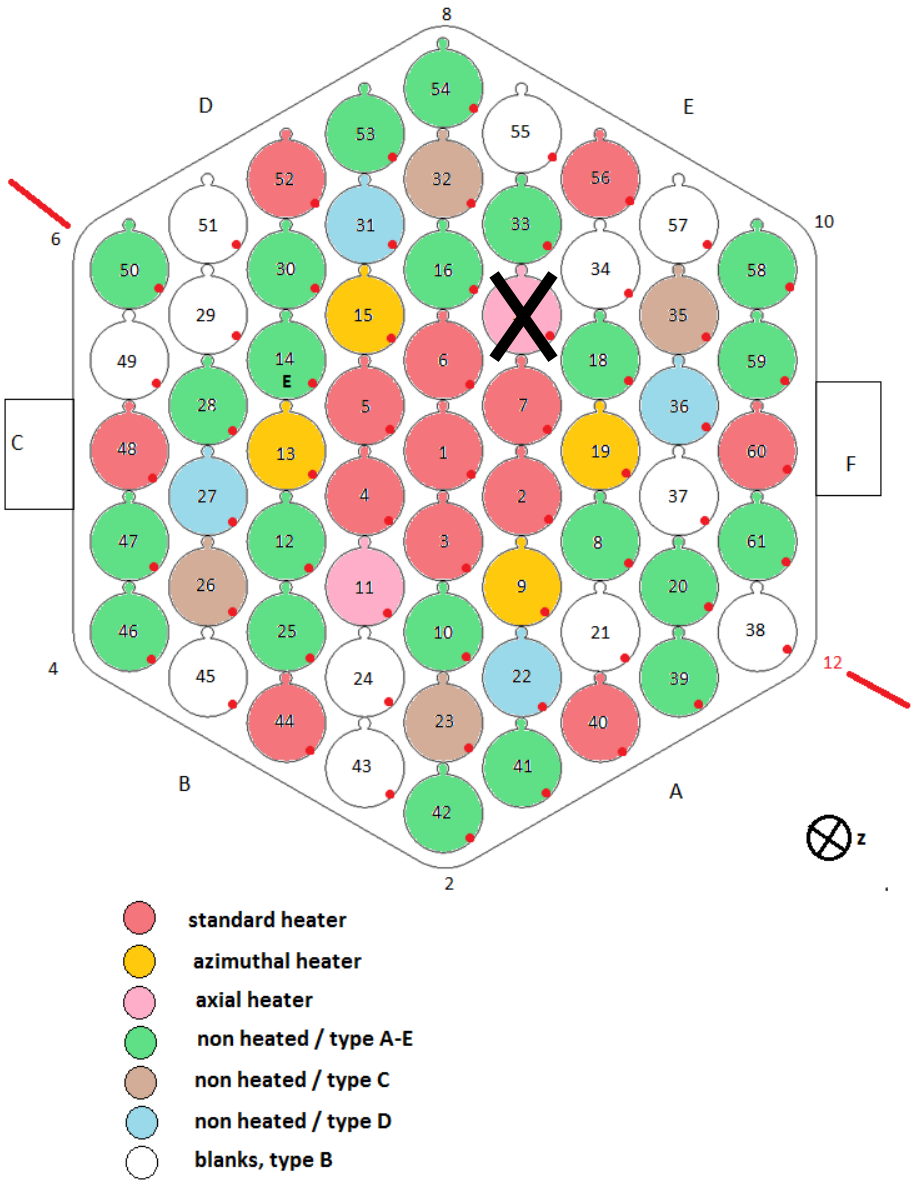


Figure 1. Heater Rod Position Map

The heater rod heated length, and power profile were measured during fabrication for each heater [3]. However, for CFD modeling all heaters used the average heated length and the average heat flux profile

of all heaters. Powers for each rod corresponded to the Heater Rod Bank measurements. Each rod of a given power bank has the same power.

2.3.3 **Heated Non-Deformed Bundle CFD Inputs**

The following are CFD assumptions used in the models.

Table 6. Heated Non-Deformed Bundle CFD Assumptions

Parameter	**Value**	**Notes**
CFD Bundle Total Length (length in wire pitch) *	3.705 m (145.866 in) (13 wire pitches)	CFD modeling choice. Measured values of the duct are from Section 4.1 of [3]. CFD model is shorter than physical duct by approximately 1.8 wire pitch lengths.
CFD Bundle Entrance Length	4 wire pitches	CFD modeling choice. Measured values from duct entrance to start of heated length is 4.07 wire pitches. Neglected initial 0.7 wire pitch length
CFD Bundle Exit Length	1 wire pitch	CFD modeling choice. The actual experiment has 2.8 wire-pitch lengths of exit section
Wire Wrap Clocking Reference	Wire points to 12 o'clock at start of heated length	Corresponds to 12 o'clock wire clocking at start of CFD bundle which begins 4 wire pitches below the start of the heated length
Pin Pitch	11.2769E-3 m (0.44397 in)	CFD Assumption: the AREVA Fuels TerraPower Upper Tie Plate Heated Bundle FCTF Test Drawing no 9240043- Rev000 specifies 11.23 mm. However the value used corresponds to sum of the non-heated tube OD (0.3768") and the wire OD (1.7062 mm) to avoid physical interference overlap which is not realistic.
Water Density Equation	$f(x) = Ax^4 + Bx^3 + Cx^2 + Dx + E$	Polynomial fit from NIST data over 30 – 150 C temperature range at 120 psia. Units: kg/m^3 A = -3.692197E-8; B = 1.760644E-5; C = -5.340272E-3; D = 3.104617E-2; E = 1.001279E+3
Water Viscosity Equation	$f(x) = Ax^4 + Bx^3 + Cx^2 + Dx + E$	Polynomial fit from NIST data over 30 – 150 C temperature range at 120 psia. Units: Pa-s A = 3.877881E-12; B = -1.834899E-9; C = 3.414143E-7; D = -3.166995E-5; E = 1.482958E-3
Water Thermal Conductivity Equation	$f(x) = Ax^4 + Bx^3 + Cx^2 + Dx + E$	Polynomial fit from NIST data over 30 – 150 C temperature range at 120 psia. Units: W/m-K A = -5.036200E-11; B = 4.573771E-8; C = -1.712259E-5; D = 2.573759E-3; E = 5.526839E-1
Water Specific Heat Equation	$f(x) = Ax^4 + Bx^3 + Cx^2 + Dx + E$	Polynomial fit from NIST data over 30 – 150 C temperature range at 120 psia. Units: J/g-K A = 2.396215E-10; B = -5.153426E-8; C = 1.201097E-5; D = -6.621017E-4; E = 4.187765E+0
Monel k500 density	8440 kg/m^3	[6]

Monel k500 Thermal Conductivity Equation	$f(x) = Ax^4 + Bx^3 + Cx^2 + Dx + E$	[6] Polynomial fit from data over 21 – 400 C temperature range. Units W/m-C A = -5.329191E-10; B = 3.995858E-7; C = -8.652170E-5; D = 3.397929E-2; E = 1.652099E+1
Monel k500 Specific Heat Equation	$f(x) = Ax^4 + Bx^3 + Cx^2 + Dx + E$	[6] Polynomial fit from data over 21 – 400 C temperature range. Units: J/kg-C A = 1.108163E-8; B = -8.314960E-6; C = 1.383569E-3; D = 2.937520E-1; E = 4.119959E+2
Thermal Resistance gap between clad and sheath	1.7E-4 (m^2-C)/W	Tuned to match heater rod temperature measurements. Heater rod thermocouples not used for benchmark so does not impact validation. Only needed if two layer heater modeled.
SS304 density	7900 kg/m^3	[7]
SS304 thermal conductivity equation	$f(x) = Ax^2 + Bx + C$	[7] Polynomial fit from data over 26 – 326 C temperature range. Units: W/m-C A = -3.333333E-6; B = 1.751233E-2; C = 1.443220E+1
SS 304 heat capacity equation	$f(x) = Ax^2 + Bx + C$	[7] Polynomial fit from data over 26 – 326 C temperature range. Units: J/kg-C A = -5.666667E-4; B = 4.670967E-1; C = 4.648670E+2
Heater Power Profile	$f(x) = Ax^4 + Bx^3 + Cx^2 + Dx + E$	Fit 4th order polynomial to STERN average measured values [3]. Where x is the elevation and 0 ≤ x ≤ 1.70264 m A = 4.408017E-1; B = -1.564781E+0; C = 2.536355E-1; D = 1.935061E+0; E = 2.969667E-1
Inlet Flow Profile	Flat	CFD simulation assumption
Inlet Turbulence Intensity	3 %	CFD simulations assumption based on moderate turbulence at inlet
Inlet Turbulent Length Scale	5.1E-5 m	CFD simulations assumption based on 22% fraction of turbulent boundary layer thickness given by $BL_{thick} = {0.37 * D_h}/{Re_{Dh}^{1/5}}$

* The complete length of the bundle was not used in TerraPower simulations. These simulations modeled a total bundle length of 3.705 m. This corresponds to 13 wire pitch lengths corresponding to 4 pitches for entrance length, ~6 pitches of the heated length, ~2 pitches of additional measurement length, and 1 pitch of exit length. As described above, the heated length was slightly less than 6 pitches in length.

2.4 Heated Deformed Bundle Post-Test Simulations

The deformed heated bundle tests used the same pin bundle geometry as the non-deformed heated tests, but used a different duct as the wrapper around the pin bundle. This duct was not flat walled on the inner surface, but had a shape to represent duct geometry conditions at a later time in reactor life. Operating

conditions were selected to be consistent with the non-deformed heated bundle tests. All values are reported below.

2.4.1 **Heated Deformed Bundle Geometry Details**

Units reported correspond to the units used in reporting and/or measurement. Secondary units are presented in parentheses.

Table 7. Heated Deformed Bundle Post Test Geometry Details

Parameter	**Value**	**Reference**
Duct Flat-to-Flat distance	3.622 in (0.092 m)	Section 5.1 of [3]
Bundle Total Length	Discussed in CFD Assumptions Table	
Bundle Entrance Length	Discussed in CFD Assumptions Table	
Bundle Heated Length	5.97 wire pitches	Designed to be 6 pitches in length. The as-built heater length was slightly less (see Heater heated length dimension below)
Bundle Additional Measurement Length	2.03 wire pitches	The as built of this section was slightly longer due to the as-built heater length being slightly shorter.
Bundle Exit Length	Discussed in CFD Assumptions Table	
Heater Outer Clad OD	9.514 mm (0.37457 in)	Average heated OD reported in [3]
Heater Clad ID/ Heater Sheath OD	0.335 in (8.509E-3 m)	Email from STERN Labs. In Appendix of [3]
Heater Sheath ID	0.267 in (6.7818E-3 m)	Email from STERN Labs. In Appendix of [3]
Heater Clad and Sheath Material	Monel K500	[3]
Heater heated length	1702.64 mm (67.0331 in)	Section 2.2.1 of [3]. *This length is referenced from the beginning of heated length section and corresponds to 5.97 wire pitch length.*
Non-Heated Tube OD	0.3768 in (9.57072E-3 m)	Average non-heated tube OD reported in [3]
Non-Heated Tube wall thickness	0.065 in (1.651E-3 m)	Steel tubing order. As-built values not measured
Non-Heated Tube Material	SS304	Steel Tubing order [3]
Wire OD	1.7062 mm (0.06717 in)	Average wire wrap OD reported in [3]
Pin Pitch	Discussed in CFD Assumptions Table	

Wire Pitch	11.22 in (0.28499 m)	[3]
Wire Wrap Direction	CW in flow direction	[3]
Wire wrap clocking angle reference	Wire points to 12 o'clock 4 pitches below start of heated length	[3]. This results in the wire wrap pointed at the duct faces A – F corner at the start of the heated length and at 19.55 mm above the physical duct entrance. Additional detail for CFD model below.
Duct Corner Detail	Radius of curvature = 0.27 in (6.858E-3 m)	[3].
Duct Deformation Detail	Axial and transverse cosine shape	Reported in [3]. Additional details below.

The deformed duct had a wall profile that enlarged the inner duct flow area by application of a cosine shape in the axial direction corresponding to the heated length and the lateral for each face between duct corners. The following figure and table from [3] presents this description.

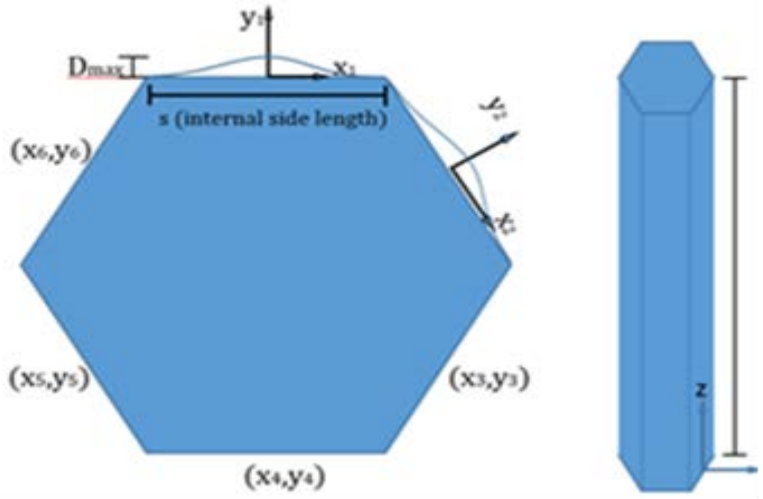


Figure 2. Deformed Duct Visual Representation

Table 8. Deformed Duct Values

Parameter	Value	units
Axial Curve	$y = D_{max} * \sin(\pi * z/1710)$	
Lateral Curve	$y = D_{max} * \left(\cos\left(\pi * \frac{x}{\left(\frac{s}{2}\right)} \right) + 1 \right)/2$	
x, y, z coordinate directions (with respect to dilation; unique for each duct face)	See image above	
D_{max}	1.08	mm
s (duct side length)	45.09	mm
Total dilation axial length	1710	mm
Beginning of Dilation (Axial Height from duct bottom)	1150.2	mm
End of Dilation (Axial Height from duct bottom)	2860.2	mm

2.4.2 **Heated Deformed Bundle As-Tested Conditions**

The as-tested conditions which are to be used for CFD boundary conditions are presented below. This test corresponds to test 19. Test data from this test will accompany the final report project.

Table 9. Heated Deformed Bundle As-Test Conditions

Parameter	Value	Reference
Fluid	Water	
Fluid Inlet Temperature	32.31 ^{o}C	Test Data from 10/05/2016, average of two temperature measurements at inlet plenum
System Pressure	120.29 psia	Test Data from 10/05/2016: upper plenum measurement
Inlet Flowrate (Re #)	9.58 kg/s (20.500 Re)	Test Data from 10/05/2016:
Power Profile	Discussed in CFD Assumptions Table	STERN took power profile measurements at 10 axial positions for each heater rod [3].
Heater Rod Bank 1 Per Heater Power	22.613 kW	Test Data from 10/05/2016
Bank 1 Heaters Positions	1, 3, 6 and 7	Corresponds to numbering in Figure 1
Heater Rod Bank 2 Per Heater Power	22.610 kW	Test Data from 10/05/2016

Bank 2 Heaters Positions	4, 5, 11 and 15	Corresponds to numbering in Figure 1
Heater Rod Bank 3 per Heater Power	22.754 kW	Test Data from 10/05/2016
Bank 3 Heaters Positions	2, 9, 19, 40 and 60	Corresponds to numbering in Figure 1
Heater Rod Bank 4 Per Heater Power	22.663 kW	Test Data from 10/05/2016
Bank 4 Heaters Positions	13, 44, 48, 52 and 56	Corresponds to numbering in Figure 1

Similar to the heated non-deformed test, only 18 heater rods were used. The map corresponds to Figure 1. As described in Section 2.3.2, all heater rods were modeled with the same power profile and all heater rods in each power bank were modeled as the same power output.

2.4.3 **Heated Deformed Bundle CFD Inputs**

The following are CFD assumptions used in the models.

Table 10. Heated Deformed Bundle CFD Assumptions

Parameter	**Value**	**Notes**
CFD Bundle Total Length (length in wire pitch) *	3.705 m (145.866 in) (13 wire pitches)	CFD modeling choice. Measured values of the duct are from Section 4.1 of [3]. CFD model is shorter than physical duct by approximately 1.8 wire pitch lengths.
CFD Bundle Entrance Length	4 wire pitches	CFD modeling choice. Measured values from duct entrance to start of heated length is 4.07 wire pitches. Neglected initial 0.7 wire pitch length
CFD Bundle Exit Length	1 wire pitch	CFD modeling choice. The actual experiment has 2.8 wire-pitch lengths of exit section
Wire Wrap Clocking Reference	Wire points to 12 o'clock at start of heated length	Corresponds to 12 o'clock wire clocking at start of CFD bundle which begins 4 wire pitches below the start of the heated length
Pin Pitch	11.2769E-3 m (0.44397 in)	CFD Assumption: the AREVA Fuels TerraPower Upper Tie Plate Heated Bundle FCTF Test Drawing no 9240043- Rev000 specifies 11.23 mm. However the value used corresponds to sum of the non-heated tube OD (0.3768") and the wire OD (1.7062 mm) to avoid physical interference overlap which is not realistic.
Water Density Equation	$f(x) = Ax^4 + Bx^3 + Cx^2 + Dx + E$	Polynomial fit from NIST data over 30 – 150 C temperature range at 120 psia. Units: kg/m^3 A = -3.692197E-8; B = 1.760644E-5; C = -5.340272E-3; D = 3.104617E-2; E = 1.001279E+3
Water Viscosity Equation	$f(x) = Ax^4 + Bx^3 + Cx^2 + Dx + E$	Polynomial fit from NIST data over 30 – 150 C temperature range at 120 psia. Units: Pa-s A = 3.877881E-12; B = -1.834899E-9; C = 3.414143E-7; D = -3.166995E-5; E = 1.482958E-3

Water Thermal Conductivity Equation	$f(x) = Ax^4 + Bx^3 + Cx^2 + Dx + E$	Polynomial fit from NIST data over 30 – 150 C temperature range at 120 psia. Units: W/m-K A = -5.036200E-11; B = 4.573771E-8; C = -1.712259E-5; D = 2.573759E-3; E = 5.526839E-1
Water Specific Heat Equation	$f(x) = Ax^4 + Bx^3 + Cx^2 + Dx + E$	Polynomial fit from NIST data over 30 – 150 C temperature range at 120 psia. Units: J/g-K A = 2.396215E-10; B = -5.153426E-8; C = 1.201097E-5; D = -6.621017E-4; E = 4.187765E+0
Monel k500 density	8440 kg/m^3	[6]
Monel k500 Thermal Conductivity Equation	$f(x) = Ax^4 + Bx^3 + Cx^2 + Dx + E$	[6] Polynomial fit from data over 21 – 400 C temperature range. Units W/m-C A = -5.329191E-10; B = 3.995858E-7; C = -8.652170E-5; D = 3.397929E-2; E = 1.652099E+1
Monel k500 Specific Heat Equation	$f(x) = Ax^4 + Bx^3 + Cx^2 + Dx + E$	[6] Polynomial fit from data over 21 – 400 C temperature range. Units: J/kg-C A = 1.108163E-8; B = -8.314960E-6; C = 1.383569E-3; D = 2.937520E-1; E = 4.119959E+2
Thermal Resistance gap between clad and sheath	1.7E-4 (m^2-C)/W	Tuned to match heater rod temperature measurements. Heater rod thermocouples not used for benchmark so does not impact validation. Only needed if two layer heater modeled.
SS304 density	7900 kg/m^3	[7]
SS304 thermal conductivity equation	$f(x) = Ax^2 + Bx + C$	[7] Polynomial fit from data over 26 – 326 C temperature range. Units: W/m-C A = -3.333333E-6; B = 1.751233E-2; C = 1.443220E+1
SS 304 heat capacity equation	$f(x) = Ax^2 + Bx + C$	[7] Polynomial fit from data over 26 – 326 C temperature range. Units: J/kg-C A = -5.666667E-4; B = 4.670967E-1; C = 4.648670E+2
Heater Power Profile	$f(x) = Ax^4 + Bx^3 + Cx^2 + Dx + E$	Fit 4th order polynomial to STERN average measured values [3]. Where x is the elevation and 0 ≤ x ≤ 1.70264 m A = 4.408017E-1; B = -1.564781E+0; C = 2.536355E-1; D = 1.935061E+0; E = 2.969667E-1
Inlet Flow Profile	Flat	CFD simulation assumption
Inlet Turbulence Intensity	3 %	CFD simulations assumption based on moderate turbulence at inlet
Inlet Turbulent Length Scale	5.1E-5 m	CFD simulations assumption based on 22% fraction of turbulent boundary layer thickness given by $BL_{thick} = {0.37 * D_h}/{Re_{Dh}^{1/5}}$

3 REFERENCES

[1] TWRP-31-TSPEC-0011-Rev-2, AFAFC AREVA Heated Bundle Experiment Test Specification, 2016.

[2] TWRP-31-TSPEC-0010-Rev-2, TAMU Fuel Assembly Flow Visualization Test Specification, 2016.

[3] TWRP-31-RPT-0033-Rev-0, AFAFC Heated Bundle As-Built Report, 2016.

[4] TAMU-WW-AS-Rev-2, TAMU Wire-Wrapped As-Built Geometry (Non-Deformed Bundle), Project number DE-NE0008321, 2016.

[5] TAMU-WW-TEST-PCM-11-E-Rev-2, TAMU Wire-Wrapped Test Summary of Test PCM-11 at the Exterior Subchannel, 2016.

[6] Online Metal Properties: specialmetals.com. Properties for monel alloy k500.

[7] Incropera, DeWitt, Bergman, Lavine, Fundamentals of Heat and Mass Transfer, 6th ed. John Wiley & Sons, 2007.

END OF DOCUMENT



APPENDIX F: TWRP-31-RPT-0036, AFAFC RANS POST-TEST SIMULATION REPORT



Uncontrolled When Printed

ENGINEERING REPORT

Document Number:	TWRP-31-RPT-0036	**Revision:**	0
Document Title:	AFAFC RANS Post-Test Simulation Report	**Approval Date** *(Final Signature Date)*:	2/26/2017
Issuing Organization:	Design Qualification	**Effective Date** *(for Procedures Only)*:	
		Pages:	Page 1 of 50

Approval

Title	Name	Signature	Date
Originator, Computational Fluid Dynamics Post-Doc	Daniel Leonard	Approved in Agile	2/24/2017
Reviewer, Thermal Hydraulics Test and Analysis Engineer	Brian Jackson	Approved in Agile	2/24/2017
Approver, Group Lead, Thermal-Hydraulic Test and Analysis	Mike Steer	Approved in Agile	2/26/2017

Document Quality Level per TWRP-NS-PROC-0002:

Quality Level 1 ☐ Quality Level 2 ☒ Quality Level 3 ☐ N/A ☐

Contains Open Items: Yes ☐ No ☒

Revision History

Revision No.	Effective Date	Affected Section(s)	Description of Change(s)
0	2/26/2017	All	Initial Release

TABLE OF CONTENTS

1 PURPOSE 7
2 SUMMARY 7
3 BACKGROUND 8
4 METHODS AND APPROACH 9
4.1 Momentum Source and Solver Conditions 10
4.2 Geometry and Boundary Conditions 12
5 CONCLUSIONS OF THE PRE-TEST REPORT 17
5.1 Summary of Pre-Test Conclusions 17
5.2 Post-Test Mesh, Turbulence Model, and Momentum Source Coefficient 18
6 POST-TEST RESULTS & DISCUSSION 19
6.1 Heated Bundles 19
6.2 Isothermal Bundle 42
7 CONCLUSIONS 48
8 REFERENCES 49

LIST OF TABLES

Table 4-1: Geometric values of CFD non-deformed isothermal bundle. 13
Table 4-2: Geometric values of CFD non-deformed heated bundle. 13
Table 4-3: CFD boundary conditions of the isothermal bundle. 14
Table 4-4: CFD boundary conditions of the heated bundles. 15
Table 4-5: Heater power per pin for the set of pins in each power bank, for both the non-deformed and deformed heated bundles 17
Table 5-1: Number of mesh cells, representative of various directions, for each bundle. Also shown is the total number of mesh cells for each bundle. 19
Table 6-1: CFD and experimental pressure drops on Face B, across specified axial segments of the non-deformed heated bundle, along with the percent error between the two methods. 22
Table 6-2: CFD and experimental pressure differences between taps on duct Face B and taps on particular unheated tubes at 3 o'clock, along with the percent error between the two methods. Note that each pressure difference is taken at a certain axial height. Duct faces and tap locations are identified in Figure 6-1 and Figure 6-2 23
Table 6-3: CFD and experimental planar mean temperature differences from inlet and the errors between the two methods. 25
Table 6-4: CFD and experimental pressure drops on Face B, across specified axial segments of the deformed heated bundle, along with the percent error between the two methods. 33
Table 6-5: CFD and experimental pressure differences between taps on duct Face B and taps on particular unheated tubes at 3 o'clock, along with the percent error between the two methods. Note that each pressure difference is taken at a certain axial height. Duct faces and tap locations are identified in Figure 6-14 and Figure 6-15 34
Table 6-6: CFD and experimental planar mean temperature differences from inlet and the errors between the two methods. 36
Table 6-7: CFD and experimental pressure drops on Face F, across specified axial segments of the non-deformed isothermal bundle, along with the percent difference between the two methods. 45
Table 6-8: CFD and experimental pressure differences between taps on duct Face F and taps on other duct faces, along with the percent difference between the two methods. Note that each pressure difference is taken at a certain axial height. 46

Table 6-9: Velocity components (averaged over entire measurement plane E) for the CFD and EXP along with the error between the CFD and EXP..... 48

LIST OF FIGURES

Figure 4-1: Description and illustration of body force components for the momentum source method..... 11

Figure 4-2: Transverse projection of body force vectors in cell locations of the wire-wrap. Contours of axial velocity are shown for non-momentum source cells. 11

Figure 4-3: Axial cross-sections of (a) the non-deformed isothermal bundle and (b) the non-deformed heated bundle. 13

Figure 4-4: Illustration (not to scale) of the deformed CFD heated bundle, dimensions, and the functional form of the deformation. Note that the heated bundle actually has rounded corners. 14

Figure 4-5: Boundary heat flux [W/m^2] at the inner diameter of the sheath of the heated pins displaying the axial profile of the heated length..... 16

Figure 4-6: Illustration of heated bundle displaying which pins belong to each power bank, looking up from the inlet to the bundle. The number within each pin represents which power bank that pin belongs to. ... 17

Figure 5-1: Mesh of the non-deformed heated bundle for the post-test simulations. 19

Figure 6-1: Cross-section of non-deformed heated bundle 3 pitches (3P) above the start of the heated length. Locations of pressure taps (orange dots and rectangles) and heated pins (pins with red dots) are displayed. The pin with the blue “X” is the pin with the failed heater. View is looking upwards from the inlet to the bundle. 20

Figure 6-2: Cross-section of non-deformed heated bundle 6.75 pitches (6.75P) above the start of the heated length. Locations of pressure taps (orange dots and rectangles) and heated pins (pins with red dots) are displayed. The pin with the blue “X” is the pin with the failed heater. View is looking upwards from the inlet to the bundle. 21

Figure 6-3: CFD and experimental pressure drops on Face B, across specified axial segements of the non-deformed heated bundle. The length of a line segment represents the axial length the pressure drop is measured across. 22

Figure 6-4: Cross-sectional plane at axial height of 4.4167P above the start of the heated length where wire-wrap is at 5 o’clock. Heated pins represented by red dots. Pink dots show locations (4 o’clock and 6 o’clock of certain unheated tubes, and on duct Face E) where temperatures were sampled from. Unheated tubes where temperatures are taken from are labeled with numbers 1-22 and wall locations where temperatures are taken from are labeled as w1-w5. 24

Figure 6-5: Cross-sectional plane at axial height of 4.4167P above the start of the heated length where wire-wrap is at 5 o’clock. Scalar contours are the difference between local temperature and the planar mean [˚C] (planar mean is determined by averaging temperatures from sampling locations). Close to the wall of the center heated pin the fluid temperature can reach 42˚C above the planar mean. 25

Figure 6-6: Temperature differences from Plane B mean for 4 o’clock locations on the external surfaces of specified unheated tubes. 26

Figure 6-7: Temperature differences from Plane B mean for 6 o’clock locations on the external surfaces of specified unheated tubes. 26

Figure 6-8: Temperature differences from Plane B mean for duct Face E locations. 27

Figure 6-9: Cross-sectional plane at axial height of 6.75P above the start of the heated length where wire-wrap is at 9 o’clock. Heated pins represented by red dots. Pink dots show locations (8 o’clock and 10 o’clock of certain unheated tubes, and on duct Face E) where temperatures were sampled from. Unheated tubes where temperatures are taken from are labeled with numbers 1-22 and wall locations where temperatures are taken from are labeled as w1-w5. 28

Figure 6-10: Cross-sectional plane at axial height of 6.75P above the start of the heated length where wire-wrap is at 9 o’clock. Scalar contours are the difference between local temperature and the planar mean [˚C] (planar mean is determined by averaging temperatures from sampling locations). 29

Figure 6-11: Temperature differences from Plane C mean for 8 o'clock locations on the external surfaces of specified unheated tubes. 30
Figure 6-12: Temperature differences from Plane C mean for 10 o'clock locations on the external surfaces of specified unheated tubes. 30
Figure 6-13: Temperature differences from Plane C mean for duct Face E locations. 31
Figure 6-14: Cross-section of deformed heated bundle 3 pitches (3P) above the start of the heated length. Locations of pressure taps (orange dots and rectangles) and heated pins (pins with red dots) are displayed. The pin with the blue "X" is the pin with the failed heater. 32
Figure 6-15: Cross-section of non-deformed heated bundle 6.75 pitches (6.75P) above the start of the heated length. Locations of pressure taps (orange dots and rectangles) and heated pins (pins with red dots) are displayed. The pin with the blue "X" is the pin with the failed heater. 32
Figure 6-16: CFD and experimental pressure drops on Face B, across specified axial segements of the deformed heated bundle. The length of a line segment represents the axial length the pressure drop is measured across. 33
Figure 6-17: Cross-sectional plane at axial height of 4.4167P above the start of the heated length where wire-wrap is at 5 o'clock. Heated pins represented by red dots. Pink dots show locations (4 o'clock and 6 o'clock of certain unheated tubes, and on duct Face E) where temperatures were sampled from. Unheated tubes where temperatures are taken from are labeled with numbers 1-22 and wall locations where temperatures are taken from are labeled as w1-w5. 35
Figure 6-18: Cross-sectional plane at axial height of 4.4167P above the start of the heated length where wire-wrap is at 5 o'clock. Scalar contours are the difference between local temperature and the planar mean [˚C] (planar mean is determined by averaging temperatures from sampling locations). Close to the wall of the center heated pin the fluid temperature can reach 42˚C above the planar mean. 36
Figure 6-19: Temperature differences from Plane B mean for 4 o'clock locations on the external surfaces of specified unheated tubes. 37
Figure 6-20: Temperature differences from Plane B mean for 6 o'clock locations on the external surfaces of specified unheated tubes. 37
Figure 6-21: Temperature differences from Plane B mean for duct Face E locations. 38
Figure 6-22: Cross-sectional plane at axial height of 6.75P above the start of the heated length where wire-wrap is at 9 o'clock. Heated pins represented by red dots. Pink dots show locations (8 o'clock and 10 o'clock of certain unheated tubes, and on duct Face E) where temperatures were sampled from. Unheated tubes where temperatures are taken from are labeled with numbers 1-22 and wall locations where temperatures are taken from are labeled as w1-w5. 39
Figure 6-23: Cross-sectional plane at axial height of 6.75P above the start of the heated length where wire-wrap is at 9 o'clock. Scalar contours are the difference between local temperature and the planar mean [˚C] (planar mean is determined by averaging temperatures from sampling locations). 40
Figure 6-24: Temperature differences from Plane C mean for 8 o'clock locations on the external surfaces of specified unheated tubes. 41
Figure 6-25: Temperature differences from Plane C mean for 10 o'clock locations on the external surfaces of specified unheated tubes. 41
Figure 6-26: Temperature differences from Plane C mean for duct Face E locations. 42
Figure 6-27: Drawings of the non-deformed isothermal bundle showing the orientation of the PIV laser sheet for measuring the velocity field. Cross-sectional drawing is a top-down view (looking down from the bundle exit). Drawings courtesy of TAMU [10]. 43
Figure 6-28: Images from the CFD simulations of the (a) CFD data extraction area which aligns with the PIV measurement area, and (b) a cross-sectional view of the bundle displaying the 5 sets of CFD extraction planes which were averaged through the thickness to account for the 1.5 mm thickness of the laser sheet. Contours are of horizontal velocity. 44
Figure 6-29: CFD and experimental pressure drops on Face F, across specified axial segements of the non-deformed isothermal bundle. The length of a line segment represents the axial length the pressure drop is measured across. 45

Figure 6-30: Plane E contour plots of normalized velocity for (a) CFD in x-direciton, (b) CFD in y-direction, (c) EXP in x-direction, (d) EXP in y-direction, (e) Difference between CFD in x-direction and EXP in y-direction, and (e) Difference between CFD in y-direction and EXP in y-direction. CFD velocity values were averaged across a 1.5 mm thickness (z-dir) corresponding to PIV laser-sheet thickness. 47

1 PURPOSE

This report documents numerical simulation scope that is part of the Advanced Fuel Assembly Flow Characterization (AFAFC) project which consists of both experimental and numerical components, and uses surrogate fluids and electrically heated fuel pins to substitute for the liquid metal coolant and the nuclear heat source. The objective of this report is to provide solution validation for Reynolds Averaged Navier-Stokes (RANS) Computational Fluid Dynamics (CFD) simulations of isothermal and heated wire wrapped 61-pin bundle experiments with both beginning-of-life and end-of-life duct geometries. Results from these blind post-test numerical simulations are presented and compared to experimental data in an effort to determine the efficacy of current TerraPower CFD methodologies for predicting important flow and heat transfer features in liquid-metal-cooled nuclear fuel assemblies with wire-wrapped fuel pins. These blind post-test simulations are conducted with “as-built” geometry and “as-tested” conditions from the experiments, but the experimental results are not made available until after the numerical results have been obtained.

2 SUMMARY

The results and conclusions of this report are concisely summarized below.

- Non-deformed isothermal bundle experiment data was not self-consistent. It displayed large differences in axial pressure drops measured on the duct walls for successive uniform lengths corresponding to single wire pitch lengths. While some differences are expected due to developing flow effects, the large differences in the test data are unexpected due to the consistent flow area along the bundle length. Reported herein, the numerical simulation results are compared to the test data, however, the use of the quality of the comparisons must consider the anomalies in the test data.

- Non-deformed isothermal bundle experiment PIV data in the external wall sub-channels showed an average axial velocity that was slower than the flow area averaged bulk bundle velocity. This is unexpected: due to the packing configuration of the pins in the hexagonal duct, the wall subchannels are larger in flow area than the internal bundle subchannels which results in lower flow resistance for flow through the wall subchannels. TerraPower recommends additional detailed critical review of the experiment data before use for CFD validation.

- Non-deformed and deformed heated bundle experiment data was self-consistent and did not display any appreciable anomalies.

- The thermocouples embedded within the heated pins of the heated bundles could not be used for validation analysis as there was large uncertainty in the experiment contact resistance between the sheath and cladding. This uncertainty would not allow for accurate modeling of the

resistance in the CFD simulations. The thermocouples on the external surface of the unheated tubes were not affected by this and were used for the validation analysis.

- Axial pressure drops, calculated from heated bundle simulations, match experiments well.
- Mean CFD temperatures at different axial heights are always within 7% of experimental results.
- The vast majority of local CFD temperatures are within experimental uncertainty.
- CFD results for non-deformed heated and deformed heated bundles show similar error behavior relative to corresponding experimental results.
- Satisfactory qualitative agreement between the isothermal experiments and CFD for normalized velocity components was shown.
- The poor quantitative agreement between CFD mean dimensional velocity components and isothermal bundle experiments may be due to some uncertainty associated with the experiment measurement location (as reported in experiment test reports).
- The bundle Transverse Pressure Gradient (TPG) that rotates (spatially) in phase with the wire-wrapping along the length of the bundle affects pressure drop results along duct faces across axial lengths of non-integer multiples of wire-pitch. The CFD results seem to over-predict the magnitude of this TPG.

Future work consists of analyzing more substantial validation datasets from the experiments, developing alternate metrics for validation of the CFD results, performing more sensitivity analyses of CFD models and conditions, resolving issues with unexpected behavior from the isothermal experiments, and comparing the CFD results to the high-fidelity CFD benchmark results from ANL.

3 BACKGROUND

TerraPower is supporting the DOE cooperative project, “Toward a Longer-Life Core: Thermal Hydraulics CFD Simulations and Experimental Investigation of Deformed Fuel Assemblies, DE-NE0008321, that includes industry, the national lab system, and academia to perform Verification and Validation (V&V) of Computational Fluid Dynamics (CFD) methods for predicting the flow and heat transfer within liquid metal cooled nuclear fuel assemblies with wire-wrapped fuel pins. This project is referred to as the Advanced Fuel Assembly Flow Characterization (AFAFC) project. It consists of both experimental and numerical components, and uses surrogate fluids and electrically heated fuel pins to substitute for the liquid metal coolant and the nuclear heat source. The experiments include both unheated Matched Index of Refraction (MIR) assemblies to measure the flow velocities with Particle Image Velocimetry (PIV) and Particle Tracking Velocimetry (PTV), as well as heated assemblies to measure the temperatures of the fluid and the simulated fuel pins with thermocouples. Both sets of experiments also measure the pressure at multiple locations in the system. The numerical component of this work involves high-fidelity Large-Eddy Simulation (LES) modeling and industry-standard Reynolds-Averaged Navier-Stokes (RANS) modeling of the experiments. Furthermore, the experiments and simulations were conducted on two duct geometries: the first is a non-deformed hexagonal duct that has flat internal duct faces that represents a beginning of life geometry. The other is a deformed duct where the internal hexagonal flow area enlarges then decreases along the axial height to represent the changes that occur to the duct geometry from pressure and irradiation effects in the core. The assembly geometries are generic, but they have dimensions typical of liquid metal cooled fast reactor assemblies.

This report presents the methods and results of the industrial, RANS-based CFD simulations and conducts solution validation by comparing the CFD results with the experimental data. These RANS CFD computations are the responsibility of TerraPower. The simulations performed modeled the following experiments that were executed as part of the project:

- Isothermal non-deformed bundle

- Heated non-deformed bundle
- Heated deformed bundle.

These flows are computed using geometric, flow, and boundary specifications from the AFAFC Post-Test Simulation Details report [1], without the aid of any insight into the experimental results (in a "blind" fashion). The geometric, flow, and boundary specifications for these post-test calculations are the actual test conditions and geometry from the experiments ("as-built" geometry and "as-tested" conditions).

Since this report focuses entirely on TerraPower's scope of the AFAFC project (presentation and validation of industry-standard RANS CFD post-test simulations), the other components of the project are not discussed much beyond this section. To provide a better understanding of the scope of the entire AFAFC project, the other components of the project are outlined briefly below:

- AREVA Fuels is responsible for conducting the non-deformed and deformed heated bundle experiments with the heated bundle components that were loaned to the project by TerraPower. This testing was conducted at the AREVA Richland Fuel Cooling Test Facility (FCTF) water flow loop. The purpose of the heated bundle experiments was to "investigate and measure thermal distribution and pressure drop behavior of heated 61-pin, hexagonally packed fast reactor test assemblies in the fully turbulent regime [2]" to obtain CFD validation data. In each 61-pin bundle, 19 of the pins were designed to be electrically heated. The tests, which were designed to provide flow and heat transfer conditions representative of those in typical liquid-metal cooled nuclear fuel assemblies with wire-wrapped fuel pins, have over 350 installed thermocouples and 40 installed pressure taps in the test assembly. More details of the heated bundle experiments can be found in the AFAFC AREVA Heated Bundle Experiment Test Specification [2] and will be available in corresponding test reports.

- Texas A&M University (TAMU) performed the non-deformed isothermal bundle experiments. The purpose of the isothermal experiments was to provide high resolution velocity field and velocity point measurements using PIV and PTV, respectively, and pressure drop measurements as well. These isothermal measurements provide data from bundles which are dynamically and geometrically scaled to the heated bundles, which will be utilized for CFD V&V. The isothermal bundle velocity and pressure data complement the heated bundle temperature and pressure data. Acrylic ducts, pins, and wires, along with a working fluid that provides a Matched Index of Refraction (MIR), was used to allow for the optical velocity measurements. Further information of the isothermal bundle experiments can be found in the TAMU Fuel Assembly Flow Visualization Test Specification [3] and will be available in corresponding test reports.

- Argonne National Lab (ANL) is responsible for the high-fidelity Spectral Element LES modeling of the isothermal and heated bundle experiments, using the Nek5000 code. These high-fidelity simulations provide a comparison to the experimental results, and also benchmarking of the TerraPower post-test RANS results.

The remaining sections of this report proceed as follows. Section 4 provides the methods used for the RANS simulations. First the momentum source methodology is reviewed and the solver conditions are discussed. Next, the geometry and boundary conditions of the simulations are provided, along with the approaches to solution verification and model sensitivity analyses. In Section 5, the code and solution verification results from the AFAFC RANS Pre-Test Simulation Report [4] are reviewed. The pre-test results provided guidelines for mesh and model specifications for these post-test results. The post-test results are presented and discussed in Section 6, and are used in a blind comparison with the experiment results. Finally, Section 7 summarizes the report and provides information on future work of the AFAFC project.

4 METHODS AND APPROACH

The methods and approach to the post-test simulations followed the methods investigated and identified during the pre-test simulations and were thoroughly covered in the AFAFC RANS Pre-Test Simulation

Report [4]. However, some aspects of that discussion are critical to an understanding of the post-test results, and thus, are included in this report as well. For instance, an understanding of the Momentum Source (MS) methodology for simulating the wire-wrapping is an important limitation to the simulations, and is therefore included in this section. Furthermore, as the pre-test simulations were based on "as-designed" geometry and "as-designed" test conditions while the post-test simulations are based on "as-built" and "as-tested" geometry and test conditions, the differences between the two sets of simulations are presented in this section. Other details of the post-test simulations that were determined from the verification and sensitivity analyses in the pre-test report [4], such as mesh size and turbulence model, are summarized in this section as well.

4.1 Momentum Source and Solver Conditions

The CD-Adapco commercial CFD suite Star-CCM+ is used to solve the RANS post-test simulations of both the isothermal and heated bundles. Star-CCM+ v10.02.010 is utilized for all of the simulations to ensure that differences are not due to software versions. These RANS simulations of helically wire-wrapped fuel assemblies employ meshes of bare pins without the wire-wrap explicitly modeled in the bundle geometry. The effect of wire-wrap on the flow is accounted for by introducing a local Momentum Source (MS) into the governing fluid equations. The MS, originally developed at ANL, is only applied to cells corresponding to the location of the wire-wrap, and the MS components in each cell are based on the local flow field [5]. This methodology simplifies the geometry and mesh generation and reduces the cell count, while still capturing the effects of the wire-wrap. The MS approach is used for all of the assembly simulations performed in this study.

The MS appears as a body force term in the momentum equation and has three orthogonal components (two in plane with the circular cross-section of the wire and one tangential along the centerline of the wire). The force components are based on lift and drag equations. The two force components in plane with the circular cross-section of the wire prevent flow from penetrating the wire surface, introducing the bulk swirl observed in wire-wrapped bundles, while the component tangential to the centerline of the wire introduces a frictional force which modifies the pressure drop along the length of the bundle. A friction factor based on a correlation of flow through a tube is required to determine the component tangential to the wire centerline. The body force components are illustrated in Figure 4-1, and the implementation of the momentum source in Star-CCM+ is shown in Figure 4-2.

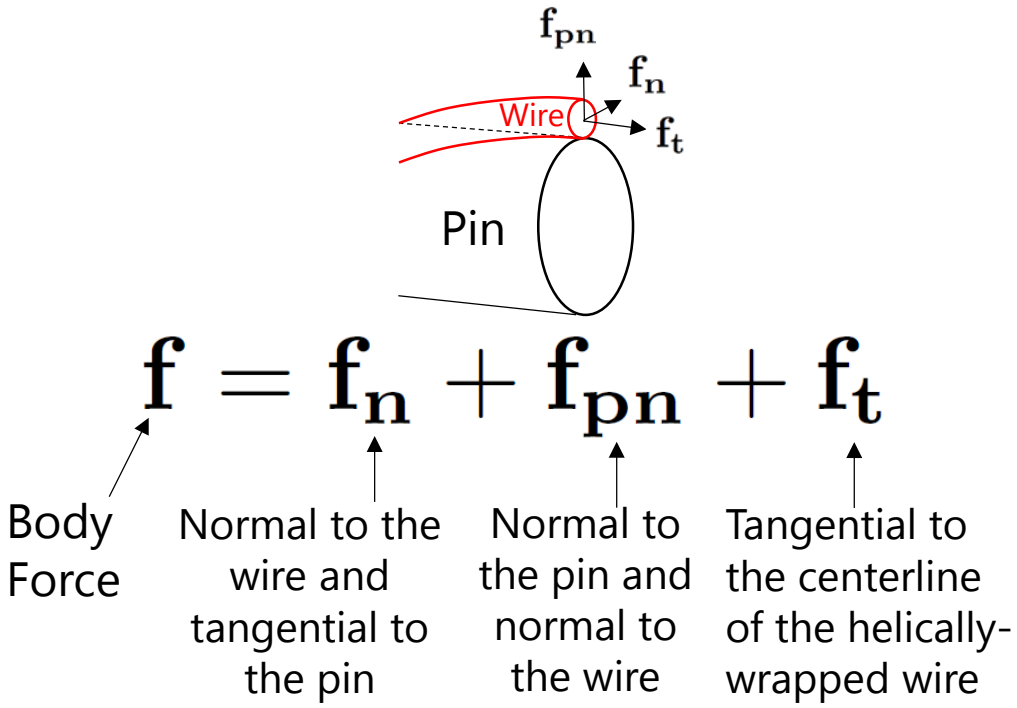


Figure 4-1: Description and illustration of body force components for the momentum source method

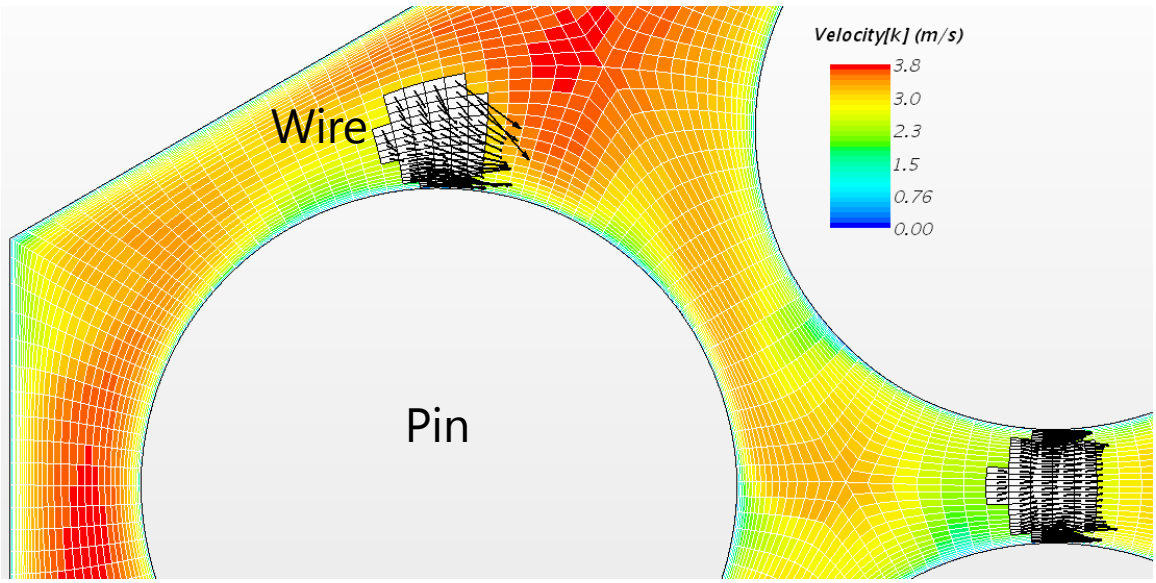


Figure 4-2: Transverse projection of body force vectors in cell locations of the wire-wrap. Contours of axial velocity are shown for non-momentum source cells.

The force components are derived from the governing equations with the following assumptions:

- Steady-state flow (neglect time-dependent term when modeling the body force)
- The body force is the dominant contributor to the change of fluid momentum in the wire normal direction (neglect pressure gradient and viscous effects when modeling the body force)
- Velocity gradients are proportional to cell center velocity in normal directions

- A general form of friction factor is sufficient to model the force tangential to the wire centerline.

The proportionality coefficient of the normal forces is referred to as the MS coefficient and it must take on a value greater than 2.0 to prevent flow through the wire surface [5]. A basic correlation for tube flow is used to determine the friction factor for the force tangential to the wire centerline.

Both the isothermal and heated bundle simulations use similar solver and simulation conditions to those outlined in the pre-test report [4]. Any changes from the pre-test simulation conditions and solvers are listed below:

- The working fluid (P-Cymene) used for the isothermal bundle experiment still has constant density and constant viscosity but the values are now specified in the AFAFC Post-Test Simulation Details report [1] that correspond to the as-tested inlet temperature.
- The cladding of the non-heated tubes is now included in the heated bundle simulations
- The material properties of the non-heated tube cladding, the heated pin cladding, and the heated pin sheath, have material properties which are modeled as polynomial functions of temperature and are specified in the AFAFC Post-Test Simulation Details report [1]. For the pre-test simulations, the solid material properties were not functions of temperature.

4.2 Geometry and Boundary Conditions

Geometric details of all three “as-built” experimental bundle cases were outlined in the AFAFC Post-Test Simulation Details report [1]. The geometries of the RANS post-test simulations, adhering to the “as-built” specifications are presented in this section, along with the boundary conditions of the computations.

4.2.1 Geometries

Scaled geometric similarity is maintained, aside from some details below, between the isothermal and heated bundle cases. This is accomplished by all bundles having the following properties:

- 61-pins
- Hexagonal ducts
- The same proportional wall gaps between the outer row of wires and the duct walls (the inner duct flat-to-flat distance is 0.77% greater than the flat-to-flat length of the tightly packed pin bundle which includes wires)
- A similar functional form of the deformed duct walls (see [2] [3]), where the shape of the deformation is determined by a cosine curve.
- A similar pin pitch to pin diameter ratio, P/D, was used (1.189 for the isothermal cases and 1.18 for the heated cases for the “as-designed” assemblies).
- The same wire pitch to pin diameter ratio (H/D of 30 for the “as-designed” assemblies).

The one noticeable geometric difference between the isothermal and heated bundles is that the corners of the duct walls are sharp for the isothermal bundles, while they have a radius of curvature for the heated bundles (as reported in the AFAFC Post-Test Simulation Details report [1]). The non-deformed geometries of the isothermal and heated bundles are shown in Figure 4-3. For the heated bundle, the 19 heated pins are clearly visible as the solid cladding and solid sheath (both with the material properties of Monel alloy K-500) are modeled. The heated bundle also models the stainless steel unheated tubes. These solid tubes were included after a numerical sensitivity study revealed that temperatures on the tube outer surfaces (where thermocouples are embedded in the experiments) varied in an appreciable manner relative to when the solid tube was not modeled. Numerical details of the non-deformed isothermal and heated post-test geometries are given in Table 4-1 and Table 4-2, respectively, and are also provided in the AFAFC Post-Test Simulation Details report [1]. Note that for all of the bundles, only the inner duct walls are considered in the CFD geometry.

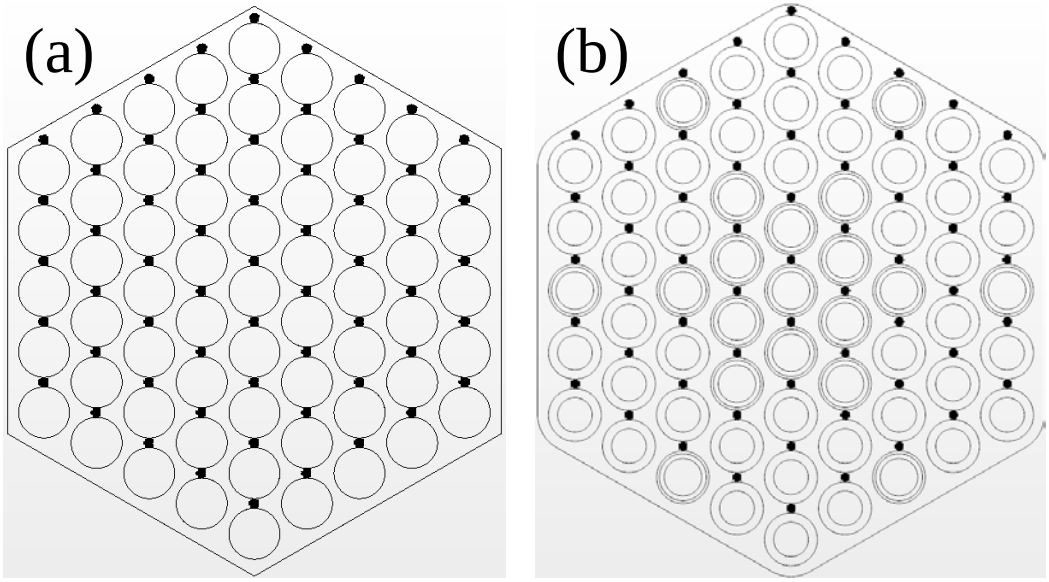


Figure 4-3: Axial cross-sections of (a) the non-deformed isothermal bundle and (b) the non-deformed heated bundle.

Table 4-1: Geometric values of CFD non-deformed isothermal bundle.

Parameter	Value	Units
Wire Wrap Pitch Length	1 (0.47625)	P = wire-pitches (m)
Duct Length	3.5 (1.667)	P (m)
Internal Duct Flat-to-Flat	154.6	mm
Wire Wrap OD	3.0	mm
Wire Wrap Direction	Clockwise	In axial direction of flow
Pin Clad OD	15.878	mm

Table 4-2: Geometric values of CFD non-deformed heated bundle.

Parameter	Value	Units
Wire Wrap Pitch Length	1 (0.285)	P = wire-pitches (m)
Duct Length	13 (3.705)	P (m)
Entrance Length	4 (1.14)	P (m)
Heated Meas. Length	5.97 (1.71)	P (m)
Non-Heated Meas. Length	2.03 (0.57)	P (m)
Exit Length	1 (0.285)	P (m)
Internal Duct Flat-to-Flat	92.0	mm
Duct Corner Radius of Curvature	6.858	mm
Wire Wrap OD	1.7062	mm
Wire Wrap Direction	Clockwise	In axial direction of flow
Unheated Tube Clad OD	9.57072	mm
Unheated Tube Clad ID	6.26872	mm
Heated Pin Clad OD	9.514	mm
Heated Pin Clad ID	8.509	mm
Heated Pin Sheath OD	8.509	mm
Heated Pin Sheath ID	6.7818	mm

It should be noted that the axial length of the CFD heated bundle simulation geometry is shorter (13 wire pitches) than the actual experiment, but that it is sufficient due to the long entrance and exit lengths modeled at a large distance from the instrumented region. The deformed heated bundle has the same geometric

properties as the non-deformed heated bundle except that the inner duct wall bulges outward gradually over a specified axial length to represent the geometry of an end-of-life duct (the bulged duct is a cosine shape in both the axial direction and transversely between each corner of the duct). In the heated bundle, the deformation length occurs along the same length which is heated. An illustration of the deformation, its functional form, and other geometric details of the deformed heated bundle are shown in Figure 4-4.

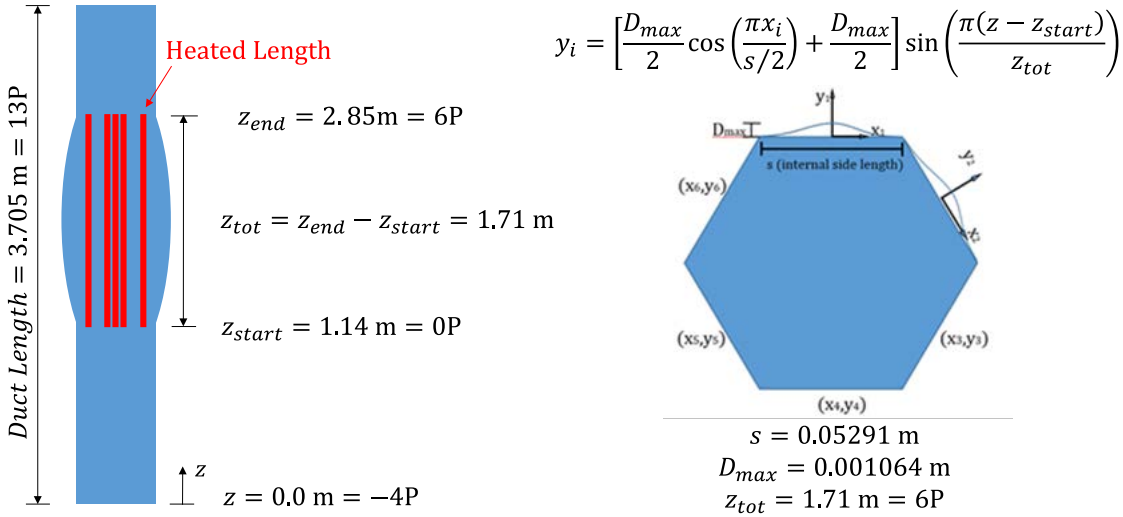


Figure 4-4: Illustration (not to scale) of the deformed CFD heated bundle, dimensions, and the functional form of the deformation. Note that the heated bundle actually has rounded corners.

4.2.2 Boundary Conditions

The boundary conditions (BCs) of the isothermal and heated bundles are provided in Table 4-3 and Table 4-4, respectively. For all of the post-test cases, a flat inlet velocity profile is assumed as is specified in the AFAFC Post-Test Simulation Details report [1]. The mass flow rate BCs are adjusted to account for the difference in flow area due to the use of the MS: as the MS approach allows for flow through cells where the solid wire would normally be, the mass flow rate must be increased. This allows for the same inlet velocity as would be observed in the experiment, while maintaining the specified Reynolds number when using the geometric flow area and hydraulic diameter of the experiment. The relationship for the CFD mass flow rate $\dot{m}_{CFD}$ relative to the experimental value $\dot{m}_{EXP}$ is

$$\dot{m}_{CFD} = \dot{m}_{EXP}\frac{A_{inCFD}}{A_{inEXP}}$$

where A_{inCFD} and A_{inEXP} are the CFD and experimental flow areas at the inlet to the simulation (note that the CFD flow area is larger due to the inclusion of the wire cross-sectional area).

Table 4-3: CFD boundary conditions of the isothermal bundle.

Region	Boundary Surface(s)	Star CCM+ Boundary Condition	Values
P-Cymene (Fluid)	Inlet	Mass Flow Inlet	$\dot{m}_{EXP}$ = 19.16 kg/s (Re = 19357) Pressure extrapolated from adjacent cell
P-Cymene (Fluid)	Outlet	Flow-Split Outlet	Velocity extrapolated from adjacent cell (only 1 outlet surface) Pressure extrapolated from adjacent cell

P-Cymene (Fluid)	Duct/Pins	No-Slip Wall	Velocity = 0 Pressure extrapolated from adjacent cell

Table 4-4: CFD boundary conditions of the heated bundles.

Region	Boundary Surface(s)	Star-CCM+ Boundary Condition	Specified Values
H_2O (Fluid)	Inlet	Mass Flow Inlet	Non-deformed $\dot{m}_{EXP}$ = 9.53 kg/s (Re = 20296) Temperature = 32.29˚C Deformed $\dot{m}_{EXP}$ = 9.58 kg/s (Re = 20500) Deformed Temperature = 32.53˚C Pressure extrapolated from adjacent cell
H_2O (Fluid)	Outlet	Flow-Split Outlet	Velocity extrapolated from adjacent cell (only 1 fluid outlet surface) Pressure extrapolated from adjacent cell Temperature extrapolated from adjacent cell
H_2O (Fluid)	Duct/Heated Pins/Un-heated Tubes/	No-Slip Wall/Interface with Outer Clad/Interface with Outer Unheated Tubes	Velocity = 0 Pressure extrapolated from adjacent cell No contact resistance for conjugate heat transfer
Clad (Solid)	Outer	Wall/Interface with Heated Pins	No contact resistance for conjugate heat transfer
Clad (Solid)	Inner	Wall/Interface with Outer Sheath	Contact resistance for conjugate heat transfer = 1.7E-4 (m^2-C)/W
Clad (Solid)	Bottom/Top	Wall	Adiabatic
Sheath (Solid)	Outer	Wall/Interface with Inner Clad	Contact resistance for conjugate heat transfer = 1.7E-4 (m^2-C)/W
Sheath (Solid)	Inner	Wall	Heat flux profile described below
Sheath (Solid)	Bottom/Top	Wall	Adiabatic

Unheated Tube Cladding (Solid)	Outer	Wall/Interface with Outer Unheated Tubes	No contact resistance for conjugate heat transfer
Unheated Tube Cladding (Solid)	Inner/ Bottom/Top	Wall/Interface with Outer Unheated Tubes	Adiabatic

The fluid temperature at the inlet to the heated bundle was measured in the experiments and is reported in the AFAFC Post-Test Simulation Details report [1]. The heat flux BC is specified on the heated length of the inner diameter of the sheath, with the heat flux profile provided in the AFAFC Post-Test Simulation Details report [1]. An image of the heat flux source on the inner sheath of the heated pins is shown in Figure 4-1. The heater power per pin, for the set of pins in each power bank, is shown in Table 4-5, and the map showing which heated pins belong to which power bank is provided in Figure 4-6. Note that for one of the heated pins, which has a blue "X" in it, the heater failed and was turned off in the experiments. Therefore, in the CFD simulations there is no heat flux from this heated pin. The benchmark specification [6] states that the simulations are to be run with adiabatic duct walls and adiabatic boundaries on the inner surface of the unheated tubes, and these boundaries are set as such. Between the clad and the sheath, a contact resistance is specified, which was estimated based on information from STERN Labs (the manufacturers of the heated pins). The turbulence inlet conditions are set to a turbulence intensity of 3% (a sensitivity study may be conducted on this value in the future) and the turbulent length scale was calculated at 20% of the estimated turbulent boundary layer height (standard approach for internal flows).

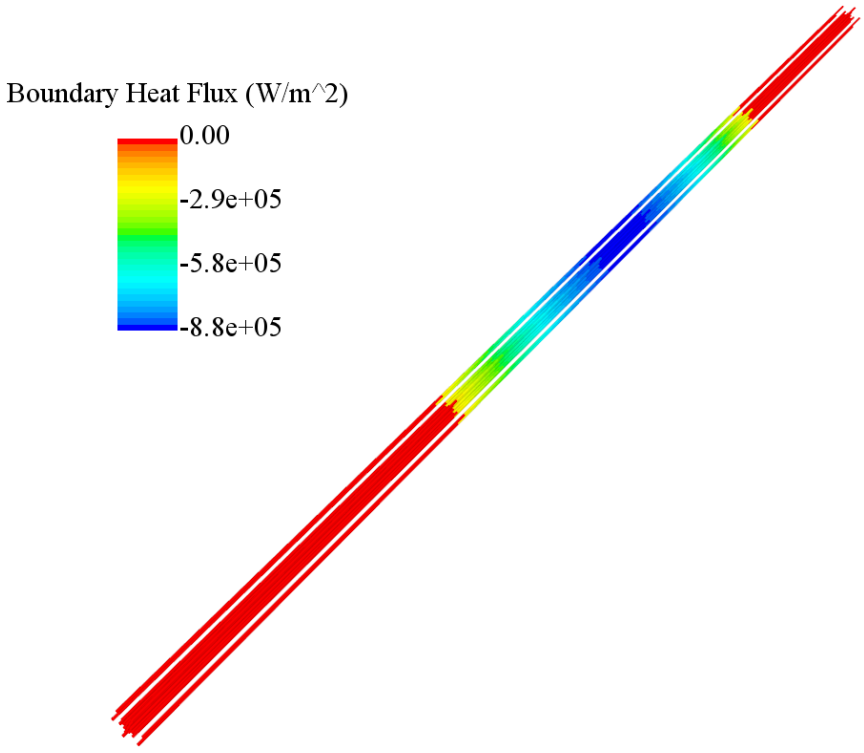


Figure 4-5: Boundary heat flux [W/m^2] at the inner diameter of the sheath of the heated pins displaying the axial profile of the heated length.

Table 4-5: Heater power per pin for the set of pins in each power bank, for both the non-deformed and deformed heated bundles.

Power Bank Number	Non-Deformed Heater Power Per Pin [kW]	Deformed Heater Power Per Pin [kW]
1	22.643	22.613
2	22.845	22.610
3	22.748	22.754
4	22.802	22.663

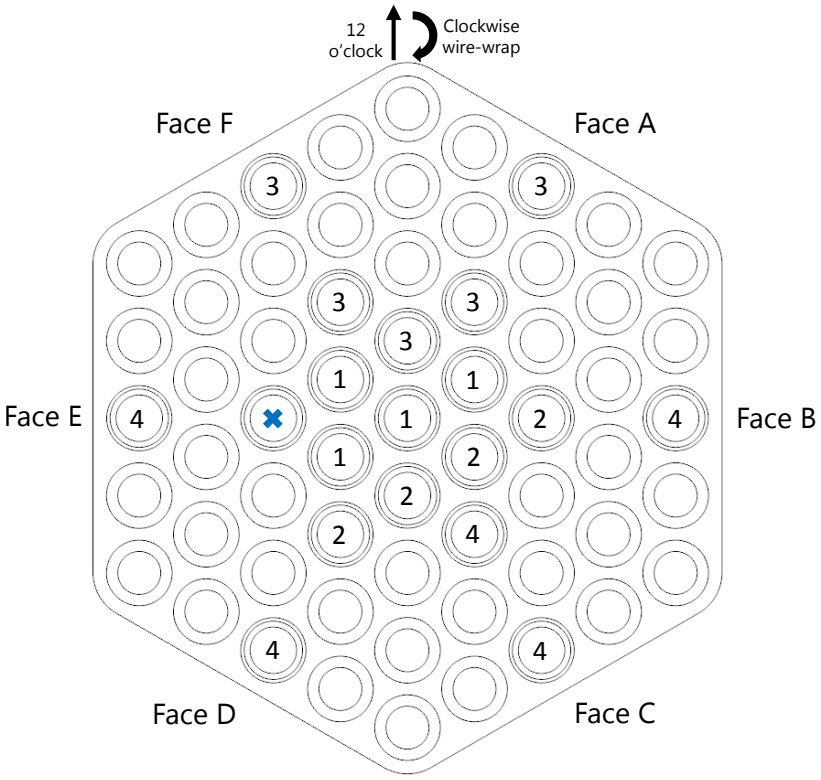


Figure 4-6: Illustration of heated bundle displaying which pins belong to each power bank, looking up from the inlet to the bundle. The number within each pin represents which power bank that pin belongs to.

5 CONCLUSIONS OF THE PRE-TEST REPORT

Code and solution verification are processes for determining if the results from a numerical simulation of a mathematical model provide an adequate level of accuracy for their intended use [7]. The major objective of the pre-test report [4] was to provide confidence in the blind post-test results through quantitative code and solution verification. This section reviews the results of the pre-test report, which are used as guidelines for the blind post-test simulations. The post-test simulation meshes and turbulence model are also discussed.

5.1 Summary of Pre-Test Conclusions

The key conclusions of the pre-test report [4] are concisely summarized below.

- Round-off error, iterative error, and statistical sampling error were proven to be negligible.
- Five fully-structured mesh sizes were investigated for each bundle in a systematic mesh refinement study (Coarsest, Coarse, Medium, Fine, and Finest). Monotonic mesh convergence was displayed for most variables of interest. Results showed little variability when the mesh was refined beyond the Fine mesh.
- Results displayed little sensitivity when Fine mesh was coarsened in the axial direction).
- Four two-equation RANS turbulence models were tested for sensitivity, and while there was some pressure drop variation amongst the models, they all were within roughly 5-10% of the widely used Cheng and Todreas [8] empirical pressure drop correlation. There were only small temperature and velocity field variations amongst the turbulence models used.
- Coefficient for the momentum source model of wire-wrapping was tested for sensitivity. Some slight variations were visible in the velocity and temperature fields but nothing significant. No variations were visible in the pressure drops.

5.2 Post-Test Mesh, Turbulence Model, and Momentum Source Coefficient

Based on the solution verification procedure, the Fine mesh (with the Coarsest spacing in the axial direction) and the Menter k-ω SST turbulence model are chosen for all of the blind post-test simulations presented herein. The Menter k-ω SST model is chosen as it is thought to be the most applicable model for this type of flow (provides advantageous k-ω performance in the boundary layer and reduced boundary layer sensitivity to freestream conditions by using k-ε far from the wall [9]). The post-test wall boundaries employ All-y^+ wall-modeling. The average y^+ is ensured to be less than 5, and thus not within the buffer region where the model can produce erroneous results, for all of the meshes. A momentum source coefficient of 4.0 is chosen for the blind post-test simulations as this value is above 2.0 (recommended by [5]) and results were fairly insensitive to variation of the coefficient.

Table 5-1 provides the number of cells representative of various directions in each post-test bundle along with the total number of cells in each bundle. The total number of cells in the deformed heated bundle is slightly greater than the total in the non-deformed heated bundle because the deformed bundle has a few more cells between the outermost pin row and the duct wall. This is because the gap between the outermost pin row and the duct wall is slightly larger at the deformed locations of the duct. Figure 5-1 displays the

fully-structured post-test mesh in the non-deformed heated bundle showing the fluid region, heated pin cladding, heated pin sheath, and cells where the momentum source is used to represent the wire-wrapping.

Table 5-1: Number of mesh cells, representative of various directions, for each bundle. Also shown is the total number of mesh cells for each bundle.

Bundle	Number of circumferential cells around a pin	Number of cells across fluid gap between pin surfaces	Number of axial cells per wire pitch	Total number of cells in mesh
Non-deformed Heated	108	36	120	337.65E6
Deformed Heated	108	36	120	343.30E6
Non-deformed Isothermal	108	36	120	56.7E6

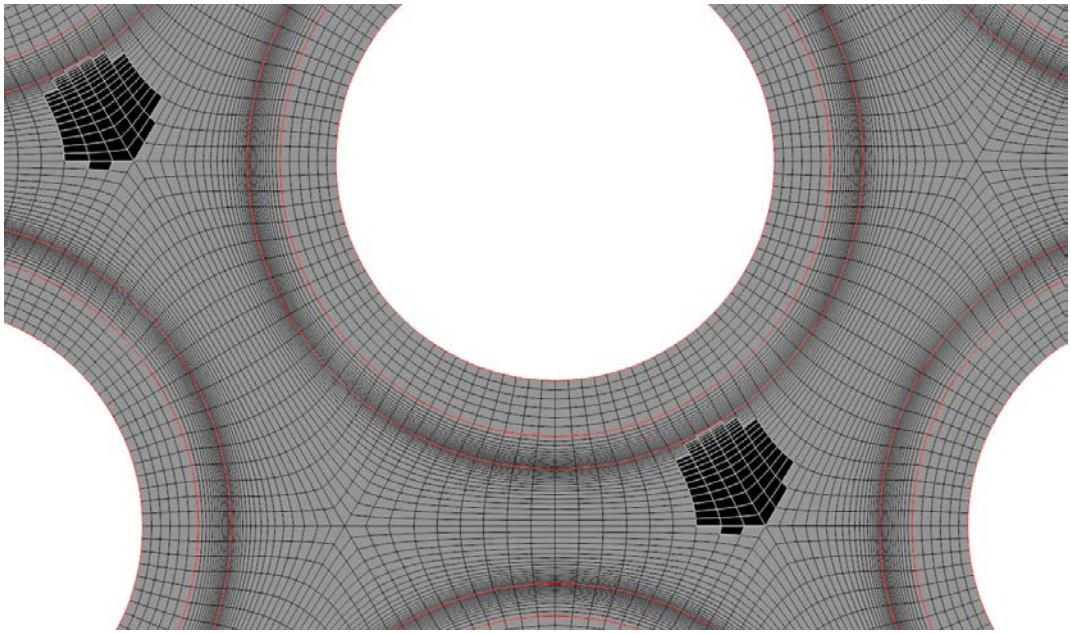


Figure 5-1: Mesh of the non-deformed heated bundle for the post-test simulations.

6 POST-TEST RESULTS & DISCUSSION

The blind post-test CFD results for the non-deformed heated bundle, the deformed heated bundle, and the non-deformed isothermal bundle are presented in this section. The CFD results are compared to limited validation data sets from the experimental results in an attempt to validate the CFD methods and models. The heated bundle cases present pressure drop and temperature results. CFD pressure and temperature values were obtained from the duct and pin walls at locations specified in the experimental results in the Final Scientific Technical Report. CFD velocity measurements were obtained from locations in the fluid which are specified in the experimental data [10].

6.1 Heated Bundles

6.1.1 Non-Deformed Heated Bundle

To determine the pressure drop of the CFD non-deformed heated bundle, pressures were extracted at the midpoints of particular duct wall faces at various axial heights from the start of the heated length of the

bundle. Figure 6-1 shows a cross-section of the bundle 3P above the start of the heated length (the midpoint location of the heated length), where P represents a single wire pitch length. The heated pins, the pressure tap locations on Face B and D, and the pressure tap locations on two unheated tubes are displayed. Figure 6-2 shows a similar image but with the pressure taps at a cross-section 6.75P above the start of the heated length.

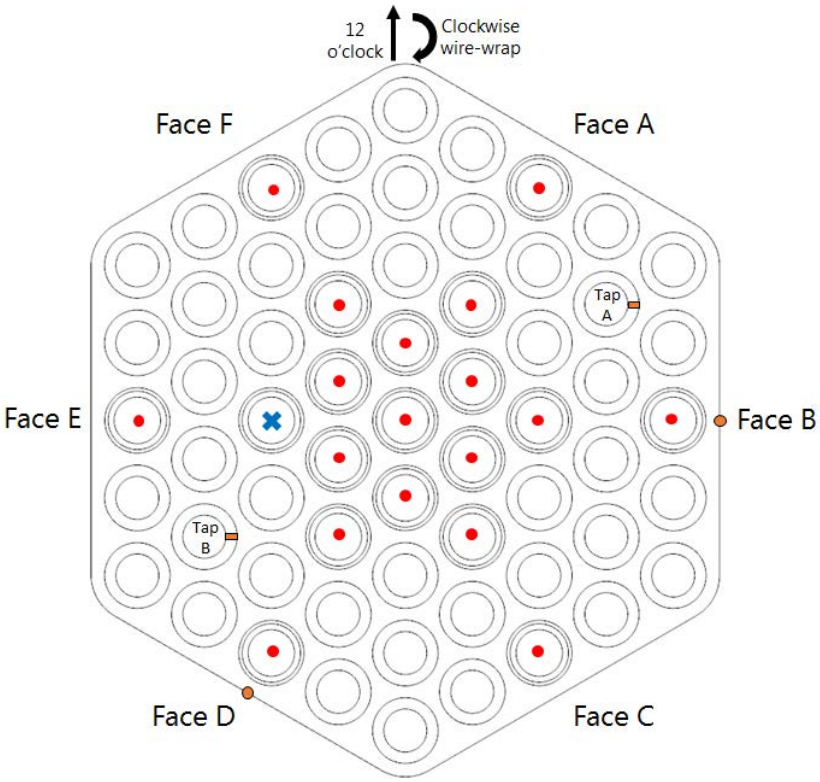


Figure 6-1: Cross-section of non-deformed heated bundle 3 pitches (3P) above the start of the heated length. Locations of pressure taps (orange dots and rectangles) and heated pins (pins with red dots) are displayed. The pin with the blue "X" is the pin with the failed heater. View is looking upwards from the inlet to the bundle.

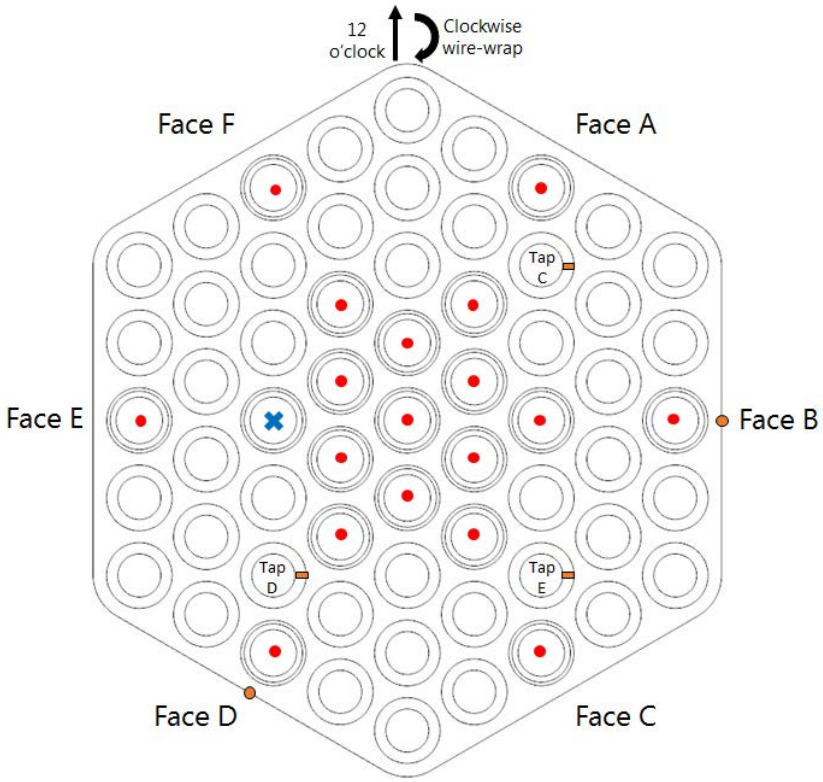


Figure 6-2: Cross-section of non-deformed heated bundle 6.75 pitches (6.75P) above the start of the heated length. Locations of pressure taps (orange dots and rectangles) and heated pins (pins with red dots) are displayed. The pin with the blue "X" is the pin with the failed heater. View is looking upwards from the inlet to the bundle.

The CFD and experimental pressure drops, calculated between different axial locations on duct Face B are provided in Figure 6-3. In this plot, the horizontal length of a line segment represents the axial length of the bundle corresponding to the pressure drop. The value (on the vertical axis) represents the value of the pressure drop itself. From this figure it is clear that the CFD pressure drops compare well to the experiment results. Table 6-1 provides the numeric values of these pressure drops as well as the error of the CFD results relative to the experiment results. It can be seen that the CFD over-predicts the Δp across the first wire pitch into the bundle. This was expected, as the inlet velocity profile for the CFD simulations had a flat distribution while in the experiment the profile would not have been flat and because the CFD did not model the complete entrance length of the physical experiment. Thus, the CFD shows increased losses over this pitch as the profile is adjusted to a more physically realistic profile. For the remainder of the pressure drops over integer multiples of wire pitch, the CFD under-predicts the pressure drop relative to the experiment by no more than 5%.

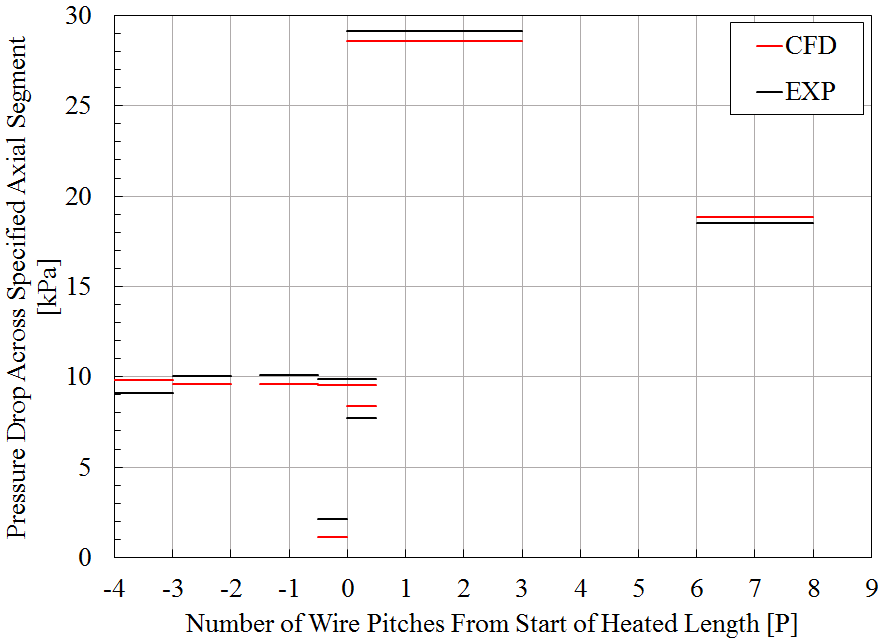


Figure 6-3: CFD and experimental pressure drops on Face B, across specified axial segements of the non-deformed heated bundle. The length of a line segment represents the axial length the pressure drop is measured across.

Table 6-1: CFD and experimental pressure drops on Face B, across specified axial segments of the non-deformed heated bundle, along with the percent error between the two methods.

Axial Segment	Number of Pitches [P]	Δp_{CFD} [Pa]	Δp_{EXP} [Pa]	Error [%]	EXP Accuracy [Pa]
-4P to -3P	1	9820.5	9103.2	7.9	+/- 78
-3P to -2P	1	9599.5	10048.5	-4.5	-
-1.5P to -0.5P	1	9611.2	10114.7	-5.0	-
-0.5P to 0P	0.5	1141.9	2146.7	-46.8	-
0P to 0.5P	0.5	8390.2	7711.9	8.8	-
-0.5P to 0.5P	1	9532.1	9858.5	-3.3	-
0P to 3P	3	28590.0	29146.7	-1.9	+/- 194
6P to 8P	2	18861.0	18529.0	1.79	+/- 770
0P to 3P (Face D)	3	28592.3	28379.8	0.7	+/- 194

The CFD and experiment results show that more error is present over successive half wire pitch lengths than for pressure drops over integer multiples of wire pitch. They also show a non-linear pressure drop along the duct face as the drop is much lower over the first half-pitch than the second half-pitch. This is due to a Transverse Pressure Gradient (TPG) that forms due to the wire-wrapping. This TPG, spatially rotates in phase with the wire-wrapping along the axial length of the bundle. Thus, a difference from a correlation

predicted linear pressure drop is present in the pressure drop along the axial length of a single duct face for non-integer multiples of wire pitch. It is evident that the CFD results show more error over the 2 half-pitches than for the same full wire pitch. There is no conclusive evidence to why this is at this point, but it is possible that the CFD is not predicting the TPG as well as it predicts the axial pressure drop, resulting in more error across non-integer multiples of wire pitch. In fact, the CFD seems to be over-predicting the magnitude of the TPG.

Table 6-2 provides pressure differences between pressure taps on duct Face B and on taps on the outer surface of particular unheated tubes. This is done at two different axial heights. It is clear that much more error occurs in these values than for the axial pressure drops along the duct face. A possible reason for this could be that the CFD is having an issue predicting the characteristics of the TPG correctly. Since the pressure taps for which differences are taken between are at the same axial height, there should be no effect from the axial pressure gradient in these results.

Table 6-2: CFD and experimental pressure differences between taps on duct Face B and taps on particular unheated tubes at 3 o'clock, along with the percent error between the two methods. Note that each pressure difference is taken at a certain axial height. Duct faces and tap locations are identified in Figure 6-1 and Figure 6-2.

Number of Wire Pitches from Start of Heated Length	Sampled between Duct Face _ /Tap _ at 3 o'clock	Δp_{CFD} [Pa]	Δp_{EXP} [Pa]	Error [%]
3P	B/A	-749.2	830.3	-190.2
3P	B/B	553.0	1973.4	-72.0
6.75P	B/C	461.1	743.0	-38.0
6.75P	B/D	994.6	86.2	1054.0
6.75P	B/E	2450.0	1736.5	41.1

CFD temperature results are extracted from locations on the outer surface of specific unheated tubes, and on duct Face E, at two different axial heights. The first plane, known as Plane B, is shown in Figure 6-4 and is at an axial height 4.4167P above the start of the heated length. Therefore, this plane is within the heated length of the bundle since the heated length is 6 wire pitches in length. At this plane, the wire-wrapping is at 5 o'clock, as seen in Figure 6-4. CFD temperature values are extracted on specified unheated tubes in Figure 6-4 on either side of the wire at 4 o'clock and 6 o'clock, and on Face E at five different locations that corresponds to thermocouple locations in the experiment. The unheated tubes from which temperature values are extracted, are numbered in Figure 6-4. Figure 6-5 plots temperature values of the difference between the local temperature and the CFD planar mean temperature for Plane B, where the planar mean is determined from an average of the local temperatures at the specified extraction points. This image can be used to inspect the temperature gradients in the plane and how they correspond to the local temperatures at the specified data extraction locations on the outer surfaces of the unheated tubes.

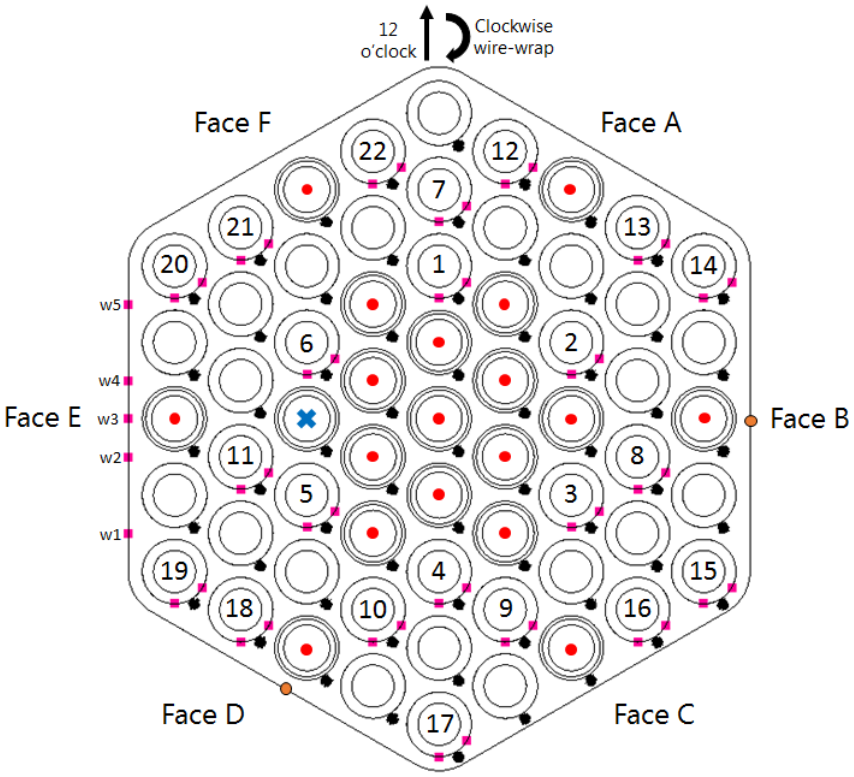


Figure 6-4: Cross-sectional plane at axial height of 4.4167P above the start of the heated length where wire-wrap is at 5 o'clock. Heated pins represented by red dots. Pink dots show locations (4 o'clock and 6 o'clock of certain unheated tubes, and on duct Face E) where temperatures were sampled from. Unheated tubes where temperatures are taken from are labeled with numbers 1-22 and wall locations where temperatures are taken from are labeled as w1-w5.

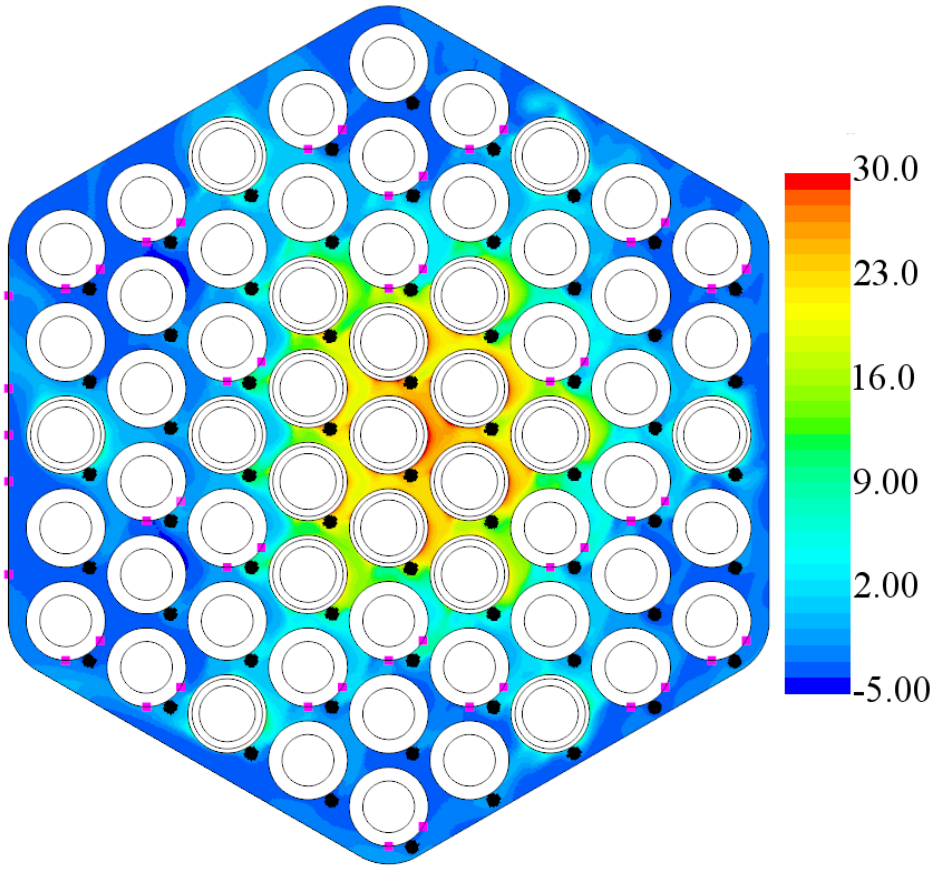


Figure 6-5: Cross-sectional plane at axial height of 4.4167P above the start of the heated length where wire-wrap is at 5 o'clock. Scalar contours are the difference between local temperature and the planar mean [˚C] (planar mean is determined by averaging temperatures from sampling locations). Close to the wall of the center heated pin the fluid temperature can reach 42˚C above the planar mean.

The temperature rise from the average bundle inlet temperature to Plane B (and Plane C which is 6.75P above the start of the heated length and shown in Figure 6-9) is presented in Table 6-3 for the CFD and experiment. Note that the CFD values for the mean temperatures correspond to an average of the extracted locations that is the same as the experiment thermocouple locations. Both planes show little error between the CFD and experiment average temperature results.

Table 6-3: CFD and experimental planar mean temperature differences from inlet and the errors between the two methods.

Plane	Number of Wire Pitches from Start of Heated Length	CFD Planar Mean Temp. – CFD Inlet Temp. [˚C]	EXP Planar Mean Temp. – EXP Inlet Temp. [˚C]	Error [%]
B	4.4167P	5.95	5.62	5.8
C	6.75P	8.88	8.65	2.6

Figure 6-6 displays the comparison of CFD temperature results to experiment temperature data for the 4 o'clock positions of specified unheated tubes at Plane B. The value is the temperature difference from the planar mean from all of the thermocouples in Plane B. Error bars for the experiments are shown and are +/- 2˚C to correspond to the individual thermocouple uncertainty of +/- 1˚C as provided in the experimental results of the Final Scientific Technical Report. It is evident that all but one of the CFD temperatures lie

within the experimental results error bars. Figure 6-7 shows the comparison for the 6 o'clock temperatures. Here, four CFD temperatures lie outside of the error bars of the experiment results. Note that at both the 4 o'clock and 6 o'clock positions, higher temperatures are observed in the tubes closer to the interior of the bundle, as this is where the bulk of the heated pins are located. The temperature differences on the duct wall are shown in Figure 6-8 and only one CFD value is outside of the experiment error bars.

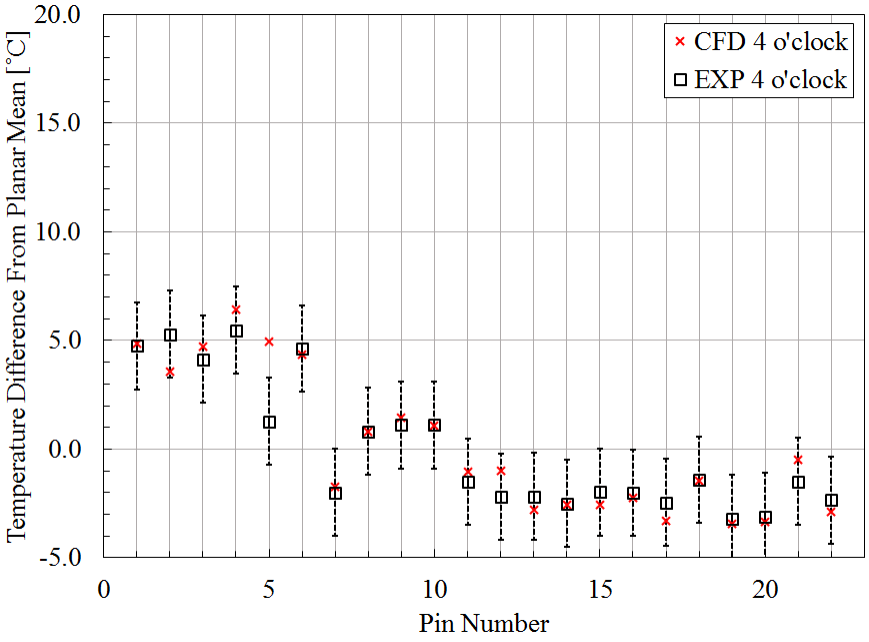


Figure 6-6: Temperature differences from Plane B mean for 4 o'clock locations on the external surfaces of specified unheated tubes.

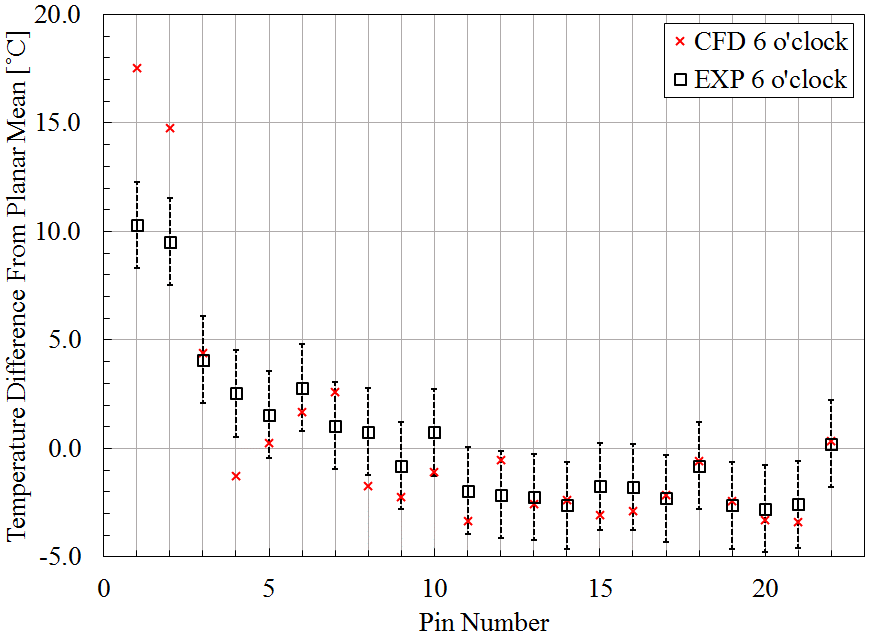


Figure 6-7: Temperature differences from Plane B mean for 6 o'clock locations on the external surfaces of specified unheated tubes.

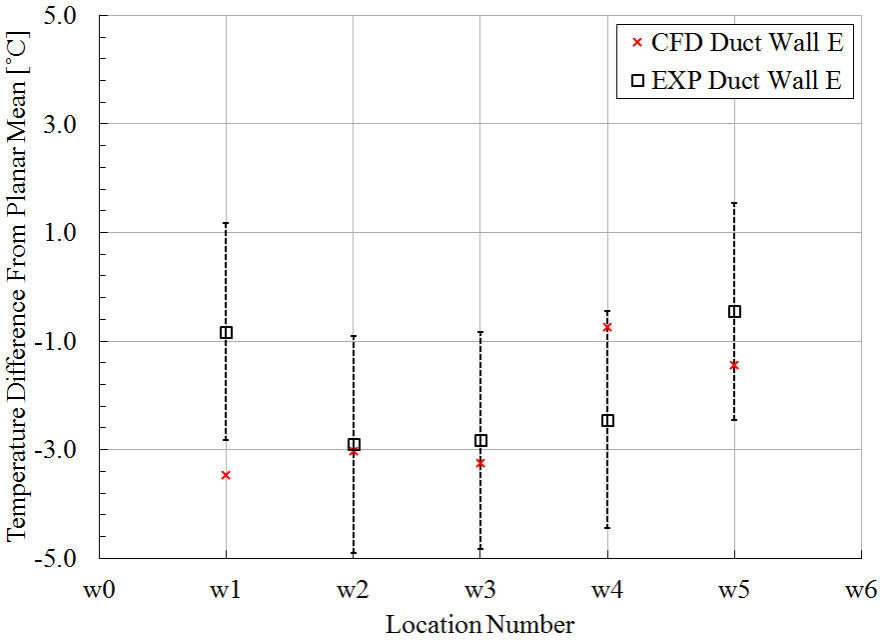


Figure 6-8: Temperature differences from Plane B mean for duct Face E locations.

The second plane, known as Plane C, is shown in Figure 6-9 and is at an axial height 6.75P above the start of the heated length. Therefore, this plane is outside of the heated length of the bundle. At this plane, the wire-wrapping is at 9 o'clock, as seen in Figure 6-9. Temperature values are extracted on specified unheated tubes in Figure 6-9 on either side of the wire at 8 o'clock and 10 o'clock, and on Face E at five different locations. The unheated tubes from which temperature values are taken, are numbered in Figure 6-9. Figure 6-10 shows the difference between the local temperature and the planar mean temperature for Plane C. This image can be used to inspect the temperature gradients in the plane and how they correspond to the local temperatures at the specified data extraction locations on the outer surfaces of the unheated tubes.

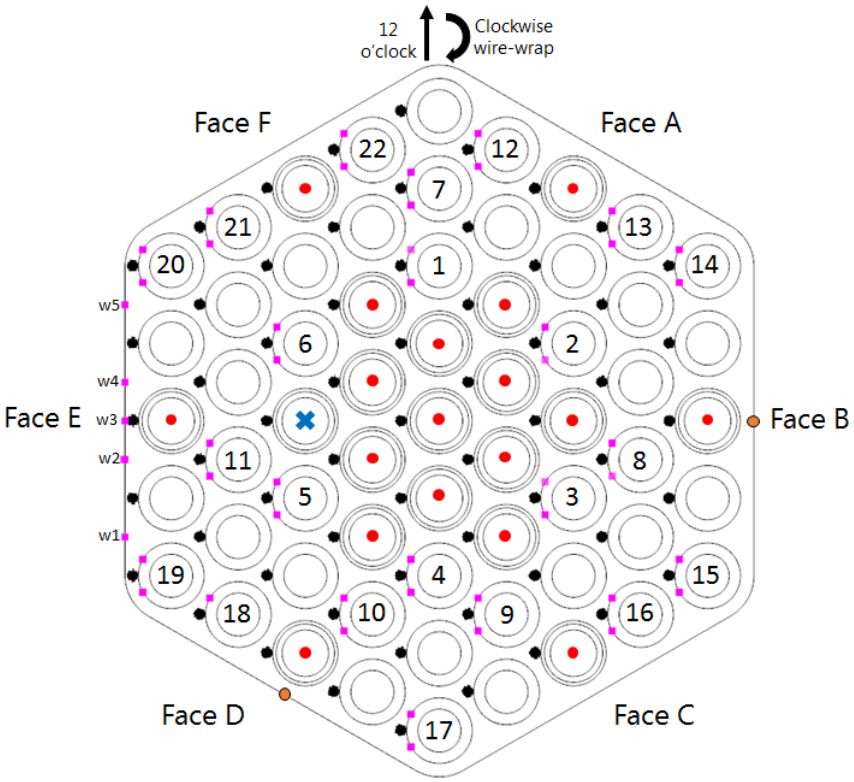


Figure 6-9: Cross-sectional plane at axial height of 6.75P above the start of the heated length where wire-wrap is at 9 o'clock. Heated pins represented by red dots. Pink dots show locations (8 o'clock and 10 o'clock of certain unheated tubes, and on duct Face E) where temperatures were sampled from. Unheated tubes where temperatures are taken from are labeled with numbers 1-22 and wall locations where temperatures are taken from are labeled as w1-w5.

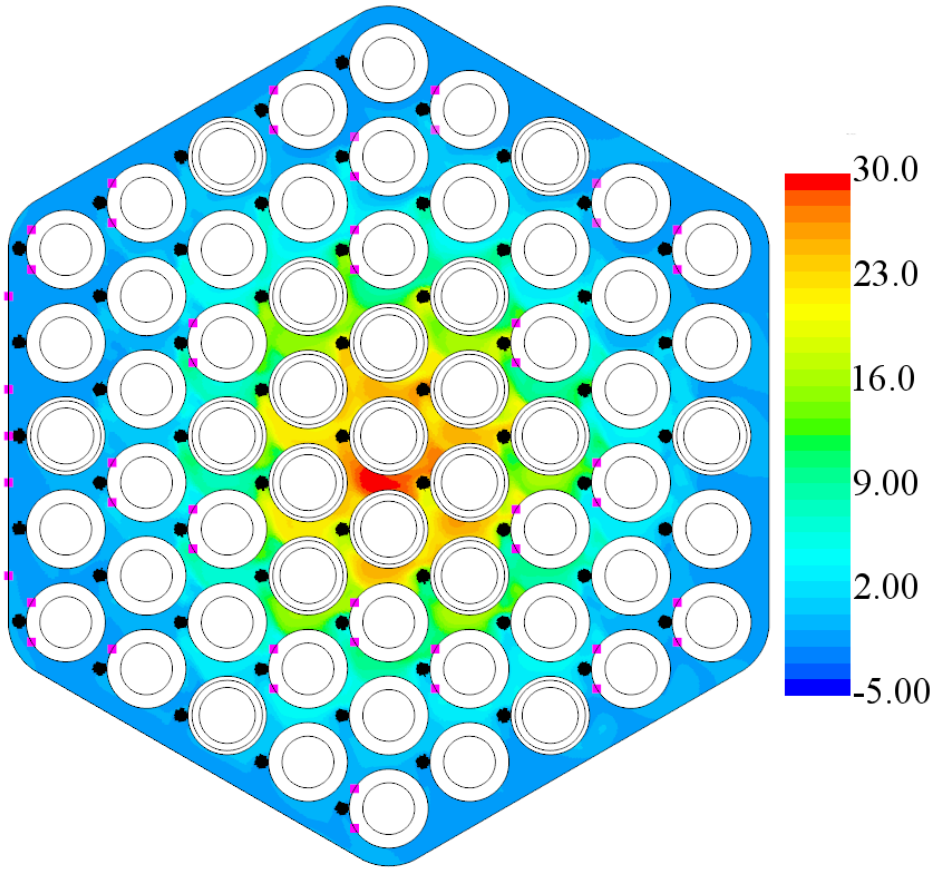


Figure 6-10: Cross-sectional plane at axial height of 6.75P above the start of the heated length where wire-wrap is at 9 o'clock. Scalar contours are the difference between local temperature and the planar mean [˚C] (planar mean is determined by averaging temperatures from sampling locations).

Figure 6-11 displays the comparison of CFD temperature results to experiment temperature results for the 8 o'clock positions of specified unheated tubes at Plane C. The value is the temperature difference from the planar mean from all of the thermocouples in Plane C. Error bars for the experiments are shown and are +/- 2˚C as provided by the experimental results in the Final Scientific Technical Report. Note that only 2 of the CFD temperatures (out of 22) lie outside of the error bars of the experimental results. Figure 6-12 shows the comparison for the 10 o'clock temperatures. Here, 7 CFD temperatures lie outside of the error bars of the experimental results and most of these occur in the higher temperature region closer to the interior of the bundle. Note that even though the CFD temperatures of some of the interior tubes (tubes 1-4) are outside of the experiment bounds, they still follow the same trend as the experiment data for those tubes. The temperatures on the duct wall are shown in Figure 6-13 and all of the CFD values are within the experiment error bars.

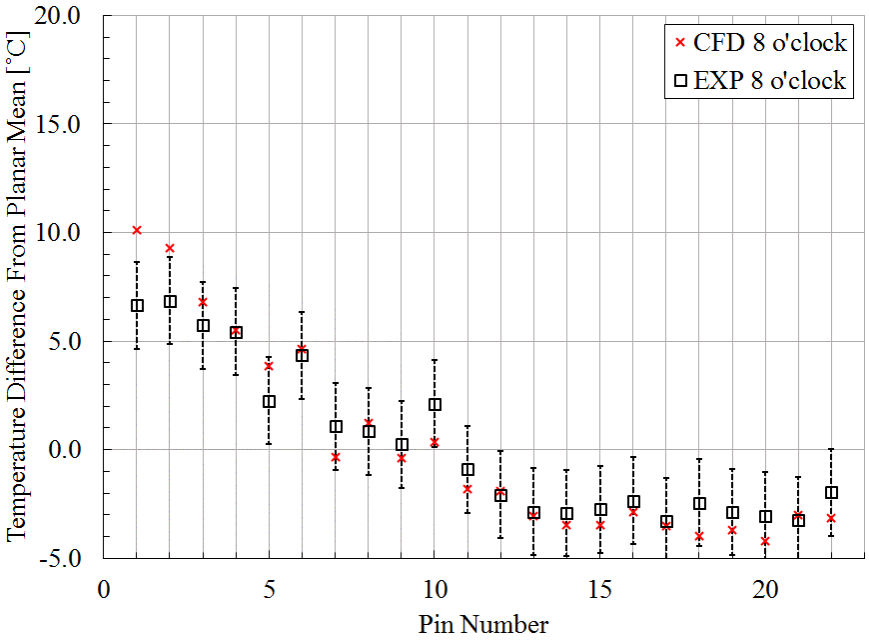


Figure 6-11: Temperature differences from Plane C mean for 8 o'clock locations on the external surfaces of specified unheated tubes.

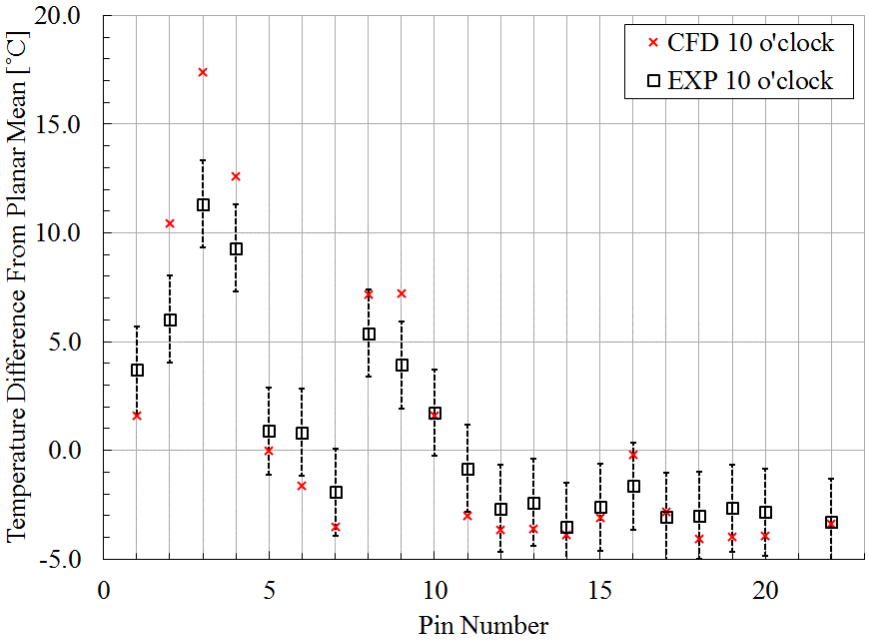


Figure 6-12: Temperature differences from Plane C mean for 10 o'clock locations on the external surfaces of specified unheated tubes.

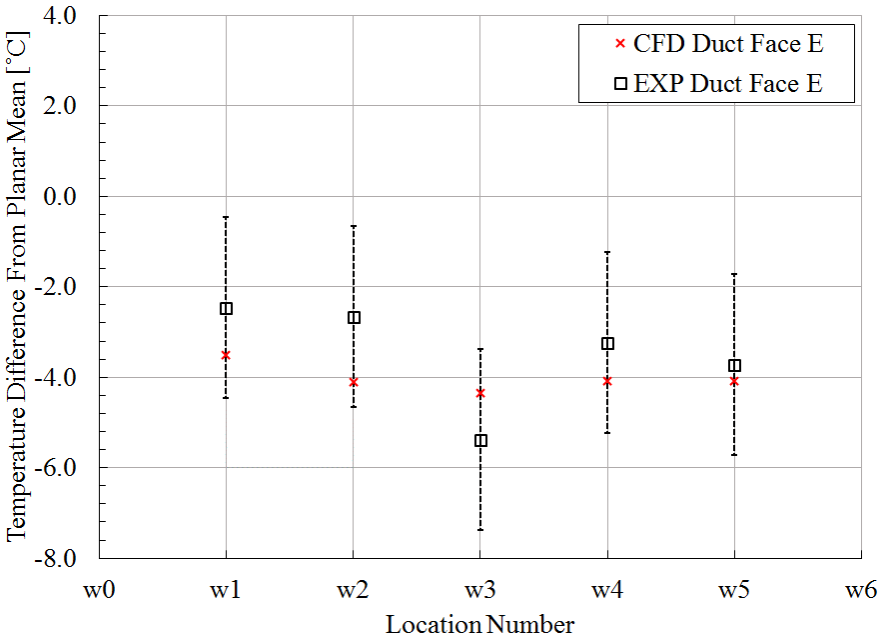


Figure 6-13: Temperature differences from Plane C mean for duct Face E locations.

6.1.2 Deformed Heated Bundle

To determine the pressure drop of the CFD deformed heated bundle, pressures were extracted at the midpoints of particular duct wall faces at various axial heights from the start of the heated length of the bundle. Figure 6-14 shows a cross-section of the bundle 3P above the start of the heated length (the midpoint location of the heated length), where P represents a single wire pitch length. The heated pins, the pressure tap locations on Face B and D, and the pressure tap locations on two unheated tubes are displayed. Figure 6-15 shows a similar image but with the pressure taps at a cross-section 6.75P above the start of the heated length. This plane is above the heated length, and therefore also above the deformed region.

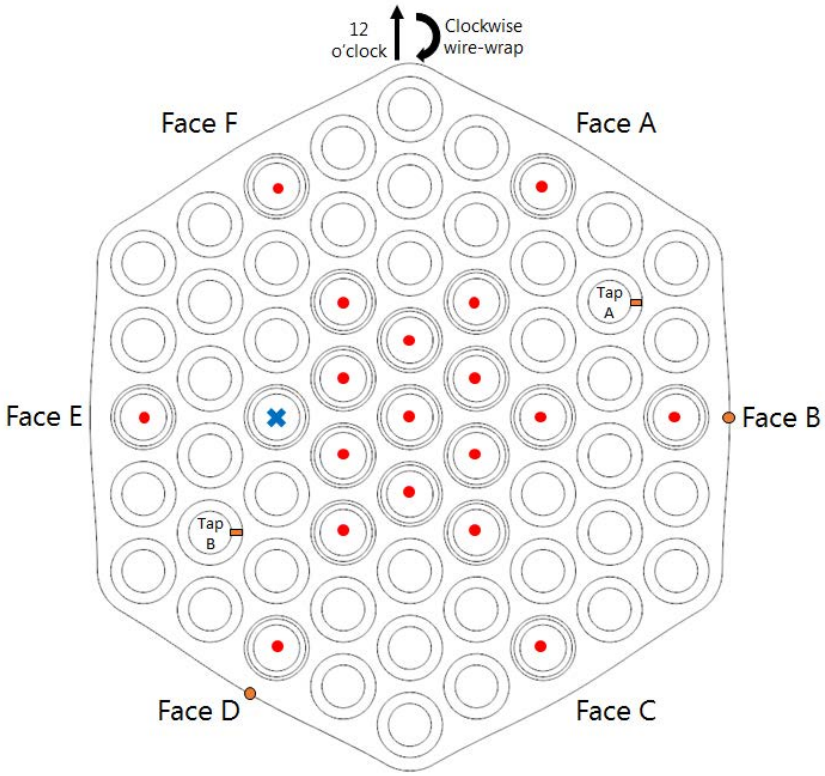


Figure 6-14: Cross-section of deformed heated bundle 3 pitches (3P) above the start of the heated length. Locations of pressure taps (orange dots and rectangles) and heated pins (pins with red dots) are displayed. The pin with the blue "X" is the pin with the failed heater.

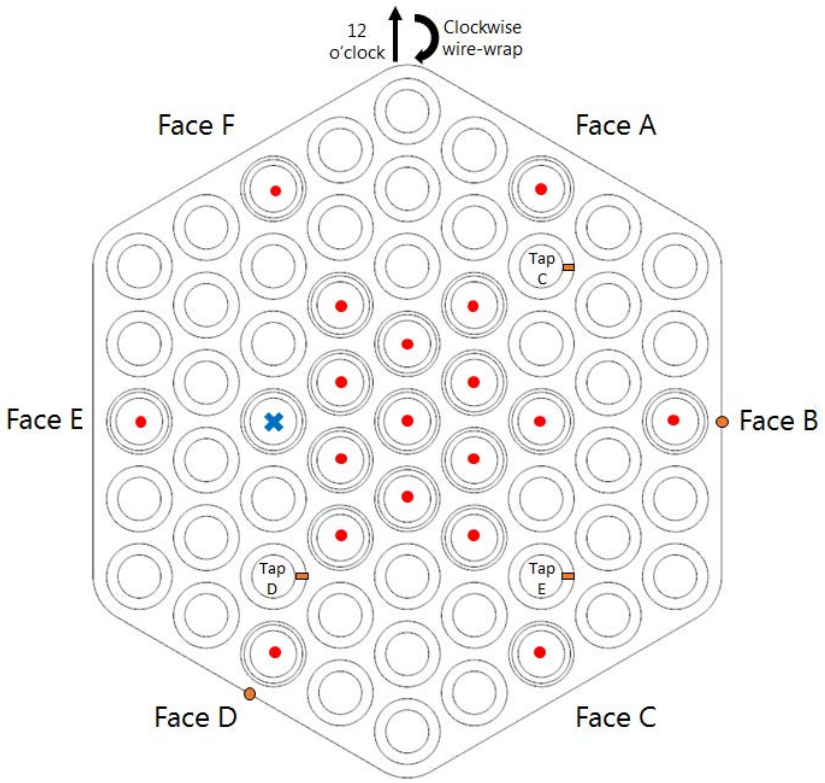


Figure 6-15: Cross-section of non-deformed heated bundle 6.75 pitches (6.75P) above the start of the heated length. Locations of pressure taps (orange dots and rectangles) and heated pins (pins with red dots) are displayed. The pin with the blue "X" is the pin with the failed heater.

The CFD and experiment pressure drops, calculated between different axial locations on duct Face B are provided in Figure 6-16. In this plot, the horizontal length of a line segment represents the axial length of the bundle for which the pressure drop was determined across. The value (on the vertical axis) represents the value of the pressure drop itself. From this figure it is clear that the CFD pressure drops compare well to the experimental results. Table 6-4 provides the numeric values of these pressure drops as well as the error of the CFD results relative to the experiment results. It can be seen that the CFD over-predicts the Δp across the first wire pitch into the bundle. This was expected, as the inlet velocity profile for the CFD simulations had a flat distribution while in the experiment the profile would not have been flat. Thus, the CFD shows increased losses over this pitch as the profile is adjusted to a more physically realistic profile. For most of the other pressure drops over integer multiples of wire pitch, the CFD usually predicts the pressure drop relative to the experiment within 2%. It is interesting to note that just downstream of the deformed region (6P to 8P), the pressure drop is over-predicted by the CFD by roughly 9%.

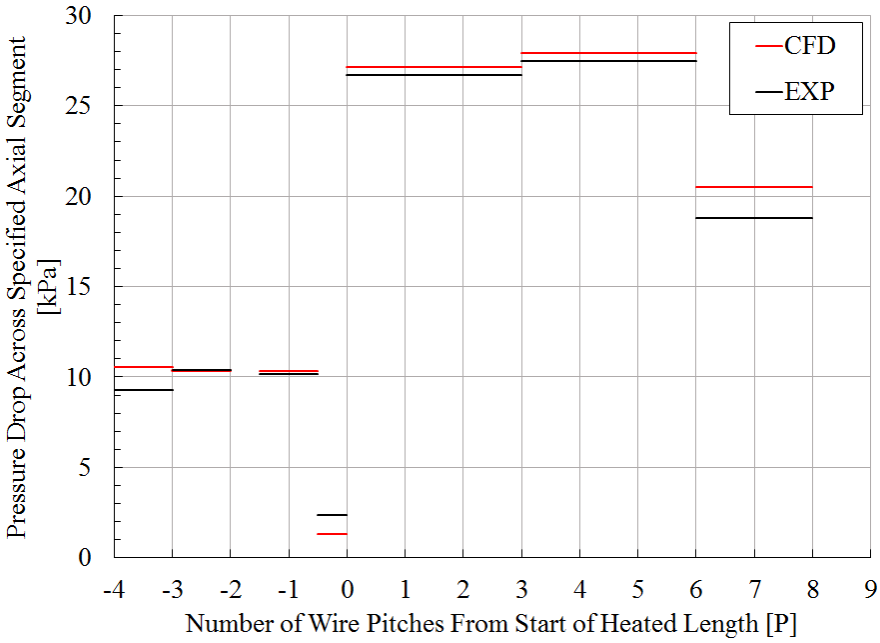


Figure 6-16: CFD and experimental pressure drops on Face B, across specified axial segements of the deformed heated bundle. The length of a line segment represents the axial length the pressure drop is measured across.

Table 6-4: CFD and experimental pressure drops on Face B, across specified axial segments of the deformed heated bundle, along with the percent error between the two methods.

Axial Segment	Number of Pitches [P]	Δp_{CFD} [Pa]	Δp_{EXP} [Pa]	Error [%]	EXP Accuracy [Pa]
-4P to -3P	1	10531.6	9267.0	13.6	+/- 78
-3P to -2P	1	10370.8	10379.6	-0.1	-
-1.5P to -0.5P	1	10310.6	10174.7	1.3	-
-0.5P to 0P	0.5	1293.6	2349.1	-44.9	-
0P to 3P	3	27174.3	26700.5	1.8	+/- 194
3P to 6P	3	27934.8	27453.8	1.8	-

6P to 8P	2	20489.8	18820.2	8.9	+/- 770
0P to 3P (Face D)	3	26936.7	26482.5	1.7	+/- 194

The CFD and experimental results over a half wire pitch interval shows more error is present than in pressure drops over integer multiples of wire pitch. This is similar to the non-deformed bundle. Again, there is no conclusive evidence to why this is, but the CFD seems to be over-predicting the magnitude of the TPG, resulting in more error of pressure drop comparisons across non-integer multiples of wire pitch than across integer multiples of wire pitch.

Table 6-5 provides pressure differences between pressure taps on duct Face B and on taps on the outer surface of particular unheated tubes. This is done at two different axial heights. It is clear that much more error occurs in these values than for the axial pressure drops along the duct face. A possible reason for this could be that the CFD is having an issue predicting the characteristics of the TPG correctly. Since the pressure taps for which differences are taken between are at the same axial height, there should be no effect from the axial pressure drop in these results.

Table 6-5: CFD and experimental pressure differences between taps on duct Face B and taps on particular unheated tubes at 3 o'clock, along with the percent error between the two methods. Note that each pressure difference is taken at a certain axial height. Duct faces and tap locations are identified in Figure 6-14 and Figure 6-15.

Number of Wire Pitches from Start of Heated Length	Sampled between Duct Face _ /Tap _ @ 3 o'clock	Δp_{CFD} [Pa]	Δp_{EXP} [Pa]	Error [%]
3P	B/A	972.2	352.3	176.0
3P	B/B	2363.6	-	-
6.75P	B/C	-818.2	-	-
6.75P	B/D	600.6	2123.5	-71.7
6.75P	B/E	475.7	1029.7	-53.8

Temperature results are taken from locations on the outer surface of specific unheated tubes, and on duct Face E, across planes at two different axial heights. The first plane, known as Plane B, is shown in Figure 6-17 and is at an axial height 4.4167P above the start of the heated length. Therefore, this plane is within the heated length of the bundle since the heated length is 6 wire pitches in length. At this plane, the wire-wrapping is at 9 o'clock, as seen in Figure 6-17. Temperature values are taken on specified unheated tubes in Figure 6-17, on either side of the wire, at 8 o'clock and 10 o'clock, and on Face E at five different locations. The unheated tubes from which temperature values are taken, are numbered in Figure 6-17.

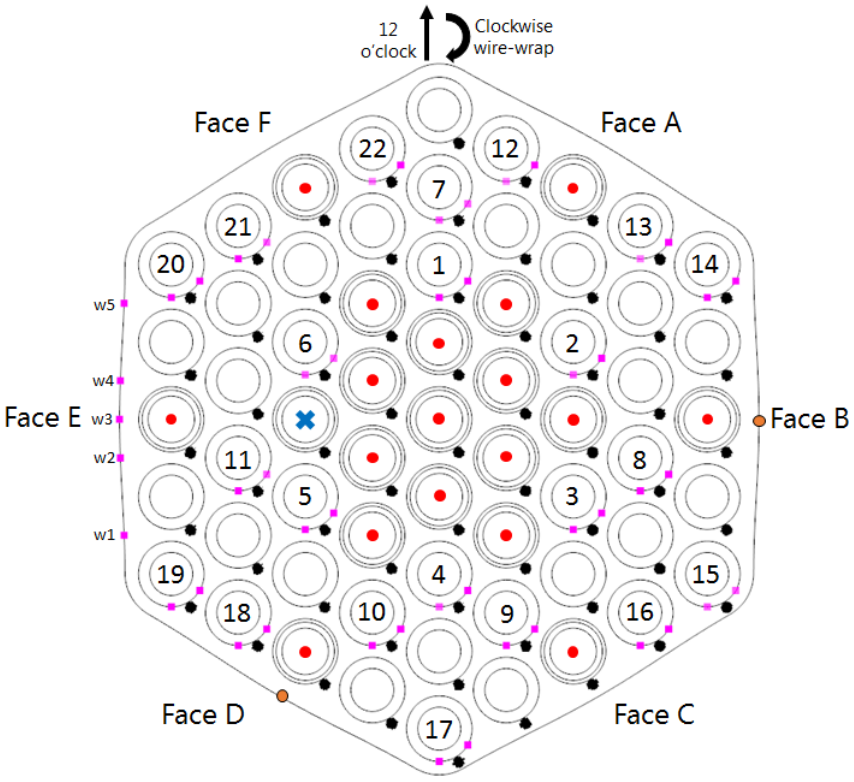


Figure 6-17: Cross-sectional plane at axial height of 4.4167P above the start of the heated length where wire-wrap is at 5 o'clock. Heated pins represented by red dots. Pink dots show locations (4 o'clock and 6 o'clock of certain unheated tubes, and on duct Face E) where temperatures were sampled from. Unheated tubes where temperatures are taken from are labeled with numbers 1-22 and wall locations where temperatures are taken from are labeled as w1-w5.

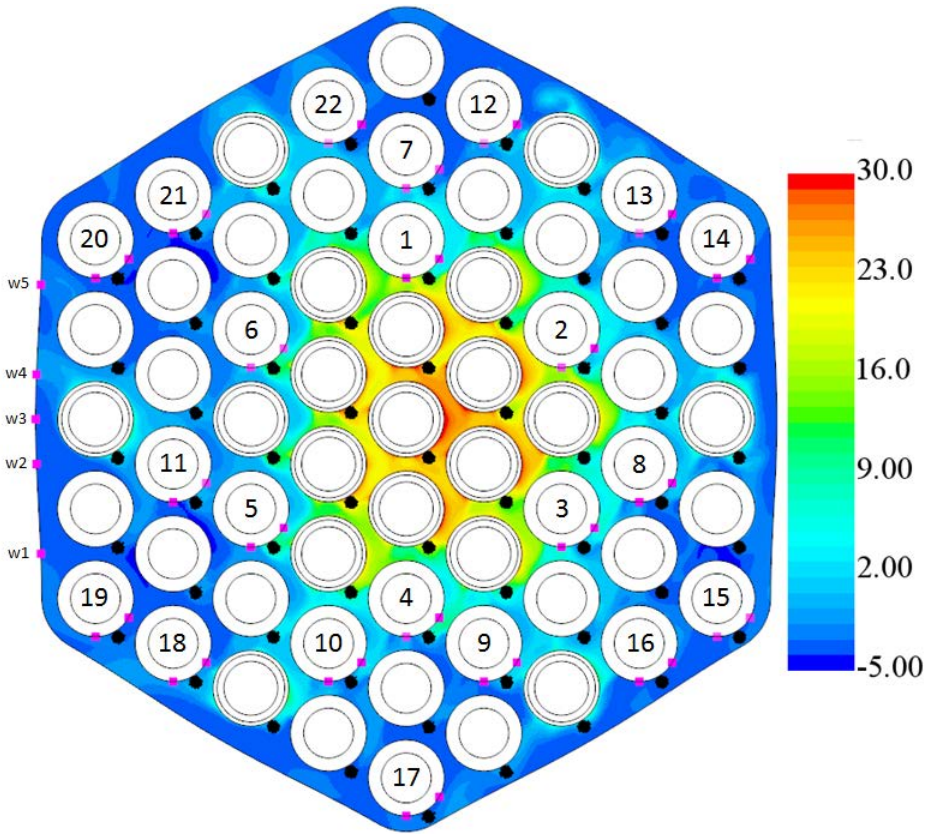


Figure 6-18: Cross-sectional plane at axial height of 4.4167P above the start of the heated length where wire-wrap is at 5 o'clock. Scalar contours are the difference between local temperature and the planar mean [˚C] (planar mean is determined by averaging temperatures from sampling locations). Close to the wall of the center heated pin the fluid temperature can reach 42˚C above the planar mean.

The temperature rise of the planar mean temperatures, relative to the bundle inlet temperature, from Plane B (and Plane C which is 6.75P above the start of the heated length and shown in Figure 6-22) can be seen in Table 6-6. Note that the CFD values for the mean temperatures are taken at the same locations as the experiment thermocouple locations. Both planes show little error between the CFD and experiment average temperature values. Figure 6-18 shows the difference between the local temperature and the planar mean temperature for Plane B. This image can be used to inspect the temperature gradients in the plane and how they correspond to the results extracted at specific locations on the outer surfaces of the unheated tubes.

Table 6-6: CFD and experimental planar mean temperature differences from inlet and the errors between the two methods.

Plane	Number of Wire Pitches from Start of Heated Length	CFD Planar Mean Temp. – CFD Inlet Temp. [˚C]	EXP Planar Mean Temp. – EXP Inlet Temp. [˚C]	Error [%]
B	4.4167P	6.09	5.70	6.93
C	6.75P	8.64	8.50	1.68

Figure 6-19 displays the comparison of CFD temperature results to experimental temperature results for the 4 o'clock positions of specified unheated tubes at Plane B. The value is the temperature difference from the planar mean from all of the thermocouples in Plane B. Error bars for the experiments are shown and are

+/- 2˚C as provided by the experimental results in the Final Scientific Technical Report. It is evident that all but one of the CFD temperatures lie within the experimental results error bars. Figure 6-20 shows the comparison for the 6 o'clock temperatures. Here, only 4 CFD temperatures lie outside of the error bars of the experimental results. Note that at both the 4 o'clock and 6 o'clock positions, higher temperatures are observed in the tubes closer to the interior of the bundle, as this is where the bulk of the heated pins are located. The temperatures on the duct wall are shown in Figure 6-21 and no CFD values are outside of the experimental error bars.

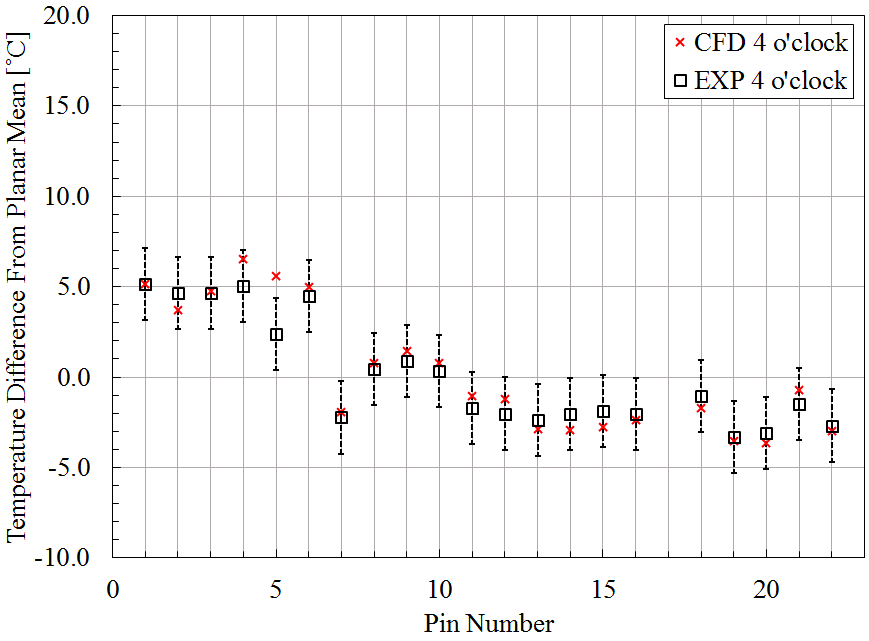


Figure 6-19: Temperature differences from Plane B mean for 4 o'clock locations on the external surfaces of specified unheated tubes.

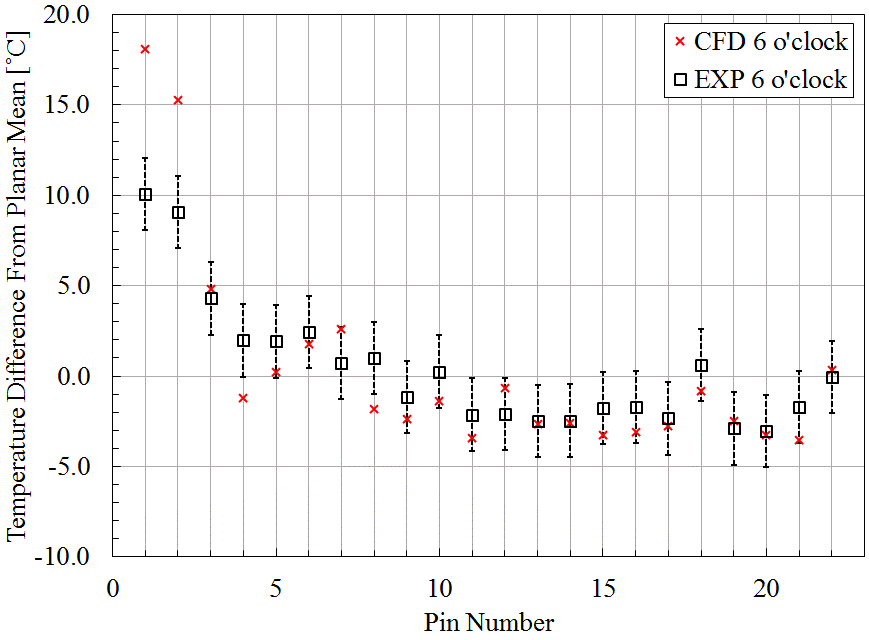


Figure 6-20: Temperature differences from Plane B mean for 6 o'clock locations on the external surfaces of specified unheated tubes.

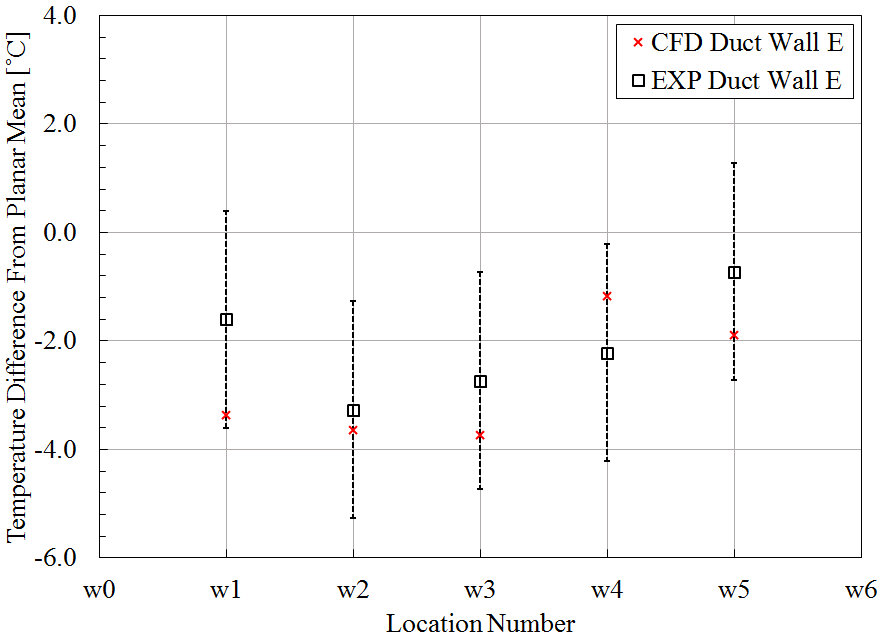


Figure 6-21: Temperature differences from Plane B mean for duct Face E locations.

The second plane, known as Plane C, is shown in Figure 6-22 and is at an axial height 6.75P above the start of the heated length. Therefore, this plane is outside of the heated length of the bundle. At this plane, the wire-wrapping is at 9 o'clock, as seen in Figure 6-22. Temperature values are taken on specified unheated tubes in Figure 6-22 on either side of the wire at 8 o'clock and 10 o'clock, and on Face E at five different locations. The unheated tubes from which temperature values are taken, are also numbered here. Figure 6-23 shows the difference between the local temperature and the planar mean temperature for Plane C. This image can be used to inspect the temperature gradients in the plane and how they correspond to the results extracted at specific locations on the outer surfaces of the unheated tubes.

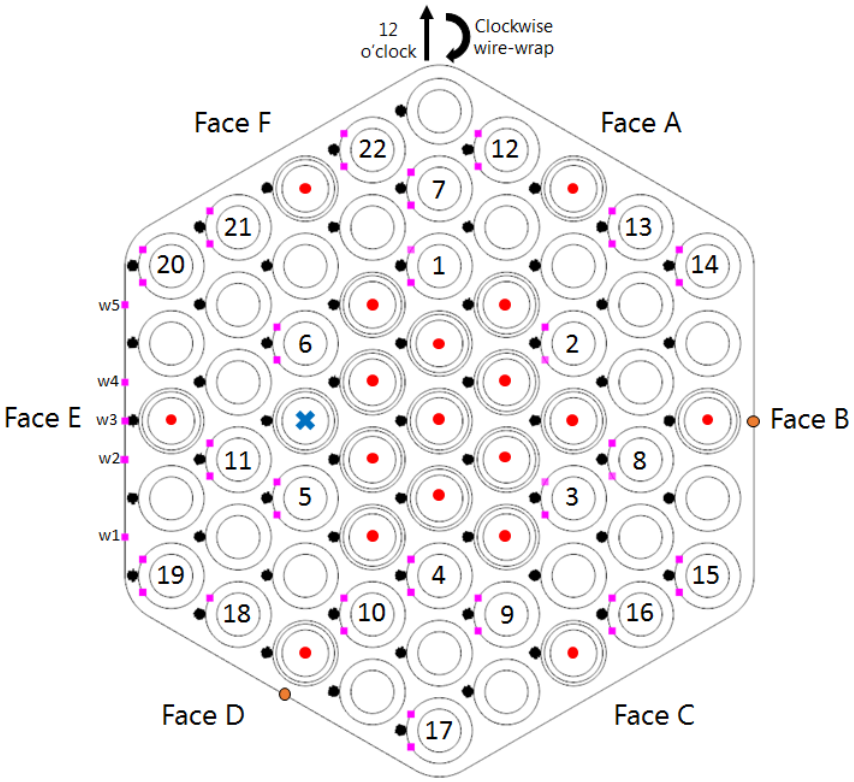


Figure 6-22: Cross-sectional plane at axial height of 6.75P above the start of the heated length where wire-wrap is at 9 o'clock. Heated pins represented by red dots. Pink dots show locations (8 o'clock and 10 o'clock of certain unheated tubes, and on duct Face E) where temperatures were sampled from. Unheated tubes where temperatures are taken from are labeled with numbers 1-22 and wall locations where temperatures are taken from are labeled as w1-w5.

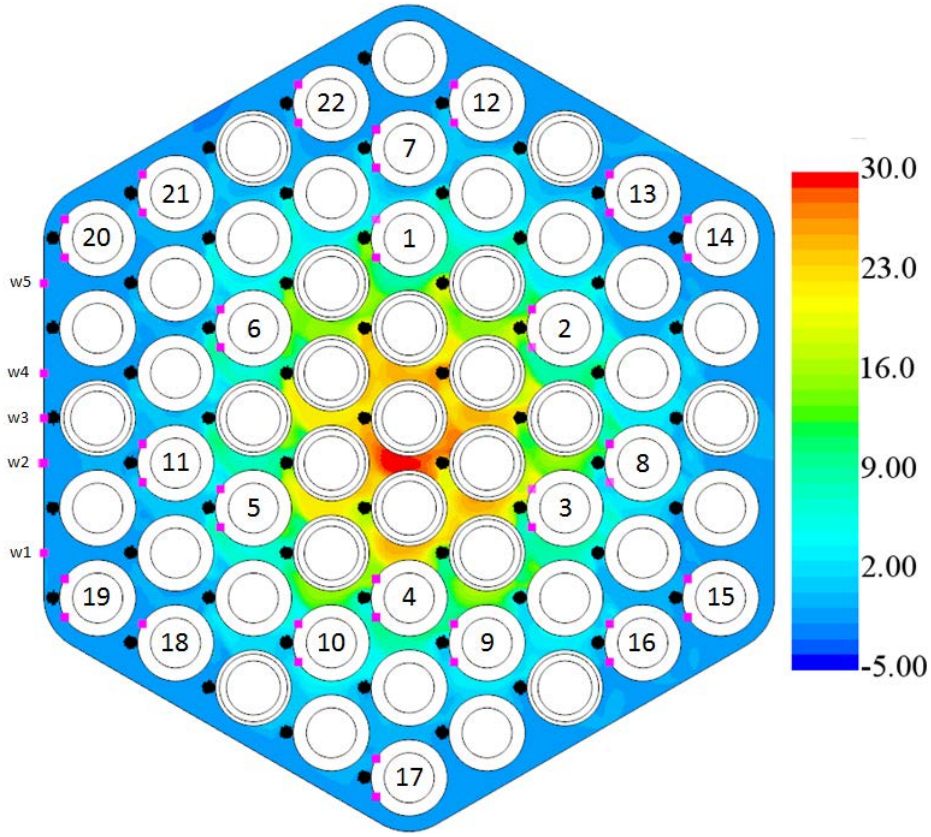


Figure 6-23: Cross-sectional plane at axial height of 6.75P above the start of the heated length where wire-wrap is at 9 o'clock. Scalar contours are the difference between local temperature and the planar mean [˚C] (planar mean is determined by averaging temperatures from sampling locations).

Figure 6-24 displays the comparison of CFD temperature results to experimental temperature results for the 8 o'clock positions of specified unheated tubes at Plane C. The value is the temperature difference from the planar mean from all of the thermocouples in Plane C, where the CFD planar mean corresponds to the average temperature of the extracted temperatures and the experiment planar mean is from the experiment thermocouple measurements. Error bars for the experiments are shown and are +/- 2˚C as provided by the experiment results in the Final Scientific Technical Report. Note that only two of the CFD temperatures (out of 22) lie outside of the error bars of the experimental results. Figure 6-25 shows the comparison for the 10 o'clock temperatures. Here, seven CFD temperatures lie outside of the error bars of the experiment results and most of these occur in the higher temperature region closer to the interior of the bundle. Note that even though the CFD temperatures of some of the interior tubes (tubes 1-4) are outside of the experiment bounds, they still follow the same trend as the experimental results for those tubes. The temperatures on the duct wall are shown in Figure 6-26 and all of the CFD values are within the experiment error bars.

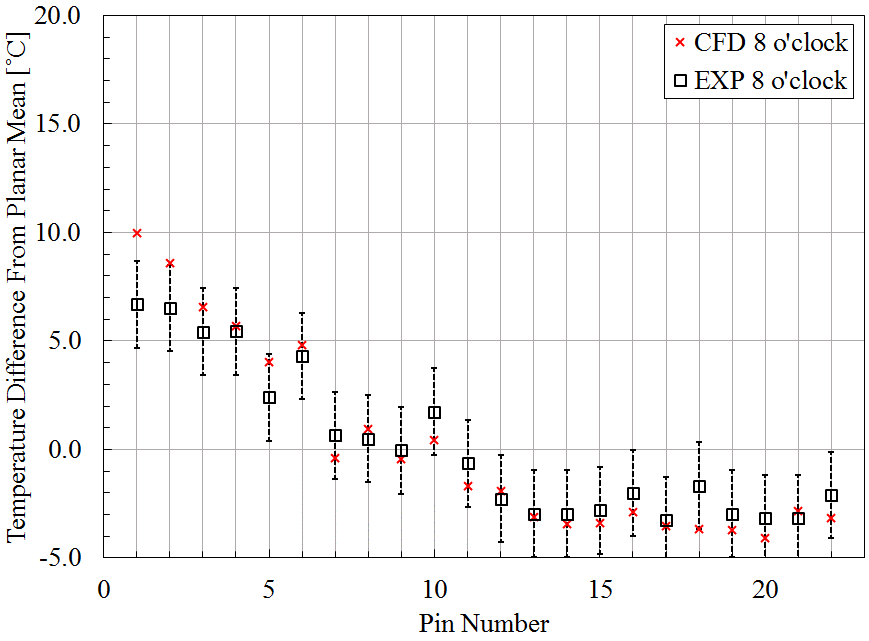


Figure 6-24: Temperature differences from Plane C mean for 8 o'clock locations on the external surfaces of specified unheated tubes.

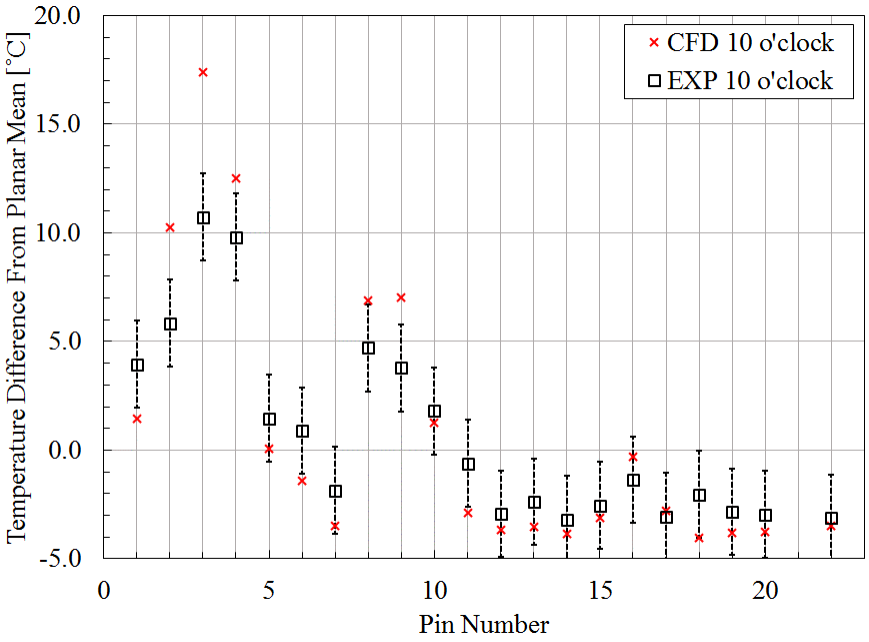


Figure 6-25: Temperature differences from Plane C mean for 10 o'clock locations on the external surfaces of specified unheated tubes.

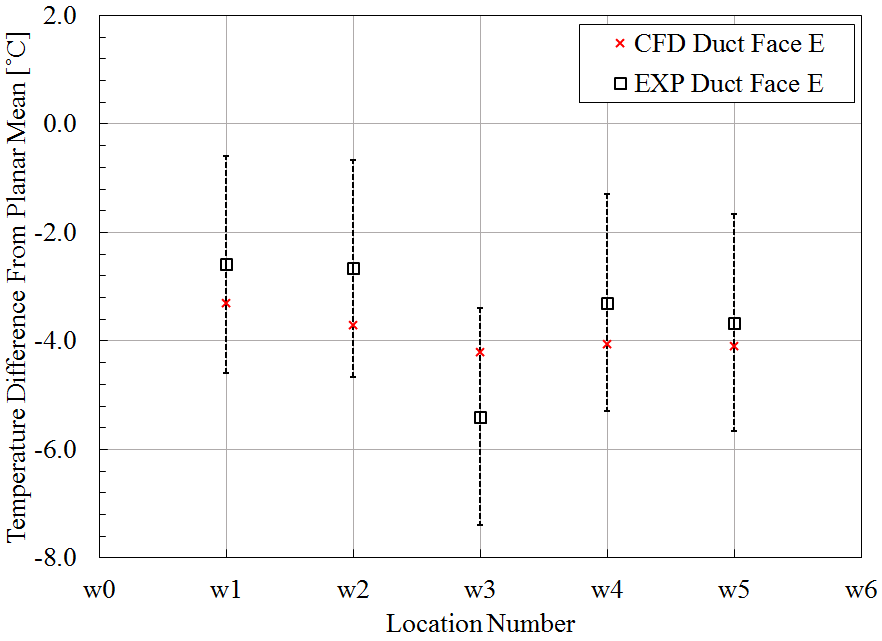


Figure 6-26: Temperature differences from Plane C mean for duct Face E locations.

6.2 Isothermal Bundle

Before considering the following validation of TerraPower's CFD simulations to the experiment data provided by TAMU, it should be noted that the non-deformed isothermal bundle experiment data was not self-consistent. It displayed anomalies in pressure drops measured on the duct walls, and in the average axial velocity (relative to the bulk velocity) for the PIV plane between the outermost pin row and a duct wall. Due to this, the provided experiment data and comparisons provided in this section are of limited use for CFD validation. It is recommended that a critical review of the experiment data is needed before decisive conclusions are drawn from the following analysis with the CFD simulations.

A limited validation dataset from the non-deformed isothermal bundle experiment are presented and compared with the CFD results in this section. The pressure drops are presented in a manner similar to those of the heated bundles. However, velocity results are presented as well for the isothermal bundle. PIV was used to obtain time-averaged velocity data across particular optical planes in the bundle. In this report, the results are from Plane E (see [10]) which is parallel to duct Face F and between the outer row of pins and the duct wall. This plane (which actually consists of two optical measurement planes stacked vertically) is roughly 0.24P in axial length, and begins 2.476P into the bundle. Figure 6-27 shows the position of Plane

E in the bundle. The measurement region has a grid of 114x178 points where velocity measurements were taken.

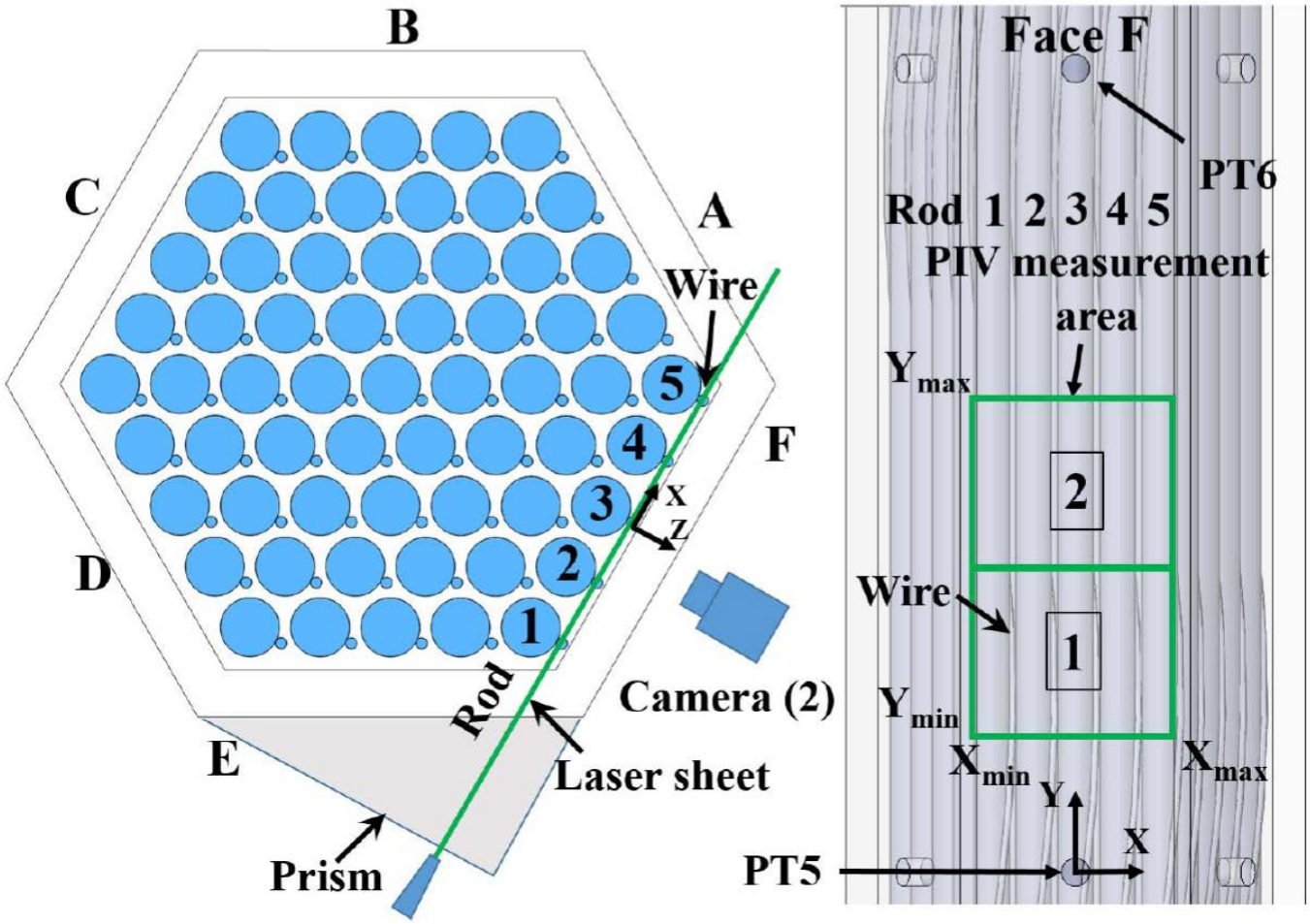


Figure 6-27: Drawings of the non-deformed isothermal bundle showing the orientation of the PIV laser sheet for measuring the velocity field. Cross-sectional drawing is a top-down view (looking down from the bundle exit). Drawings courtesy of TAMU [10].

As is seen in Figure 6-28, Plane E is not intersected by any wires as they are wrapping around the other side of the pin in this region at this height. The measurement plane, which is defined by a laser sheet, has a thickness. This thickness is specified to be 1.5 mm [10] +/- 0.5 mm with 0.5 mm location uncertainty perpendicular from the duct face. CFD velocity results were extracted at 5 different depths of the plane for each point in the plane, and were averaged over the thickness. This entailed 5 different sets of points across the thickness of the plane that were averaged for the CFD solution. Figure 6-28 also shows the thickness of the measurement plane. Note that the locations of the Plane E CFD grid points (corresponding to the experimental data [10]) do not occur at cell centers in the CFD simulations, and thus, the velocities are interpolated to the Plane E grid points for the CFD results.

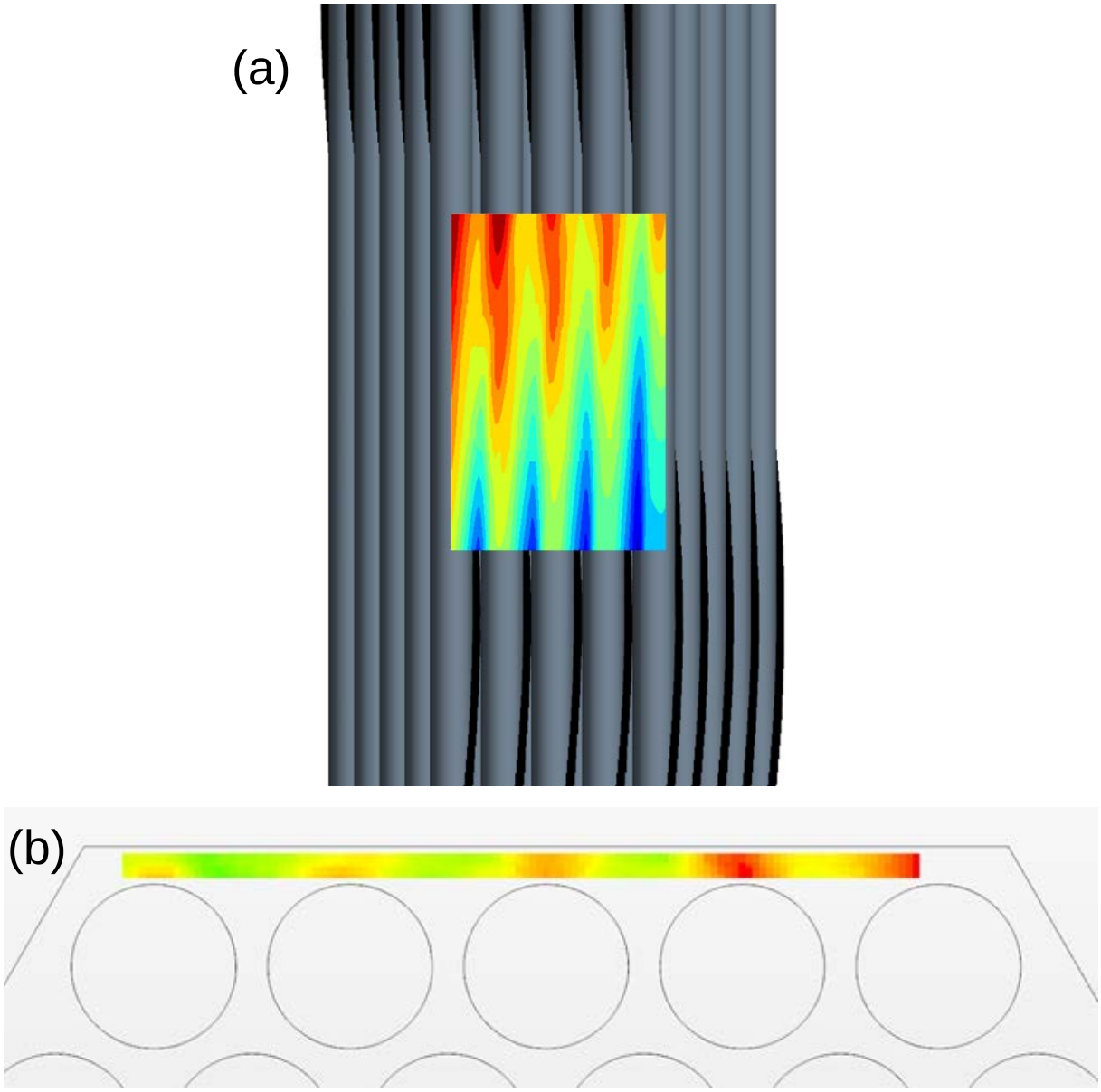


Figure 6-28: Images from the CFD simulations of the (a) CFD data extraction area which aligns with the PIV measurement area, and (b) a cross-sectional view of the bundle displaying the 5 sets of CFD extraction planes which were averaged through the thickness to account for the 1.5 mm thickness of the laser sheet. Contours are of horizontal velocity.

To determine the pressure drop of the CFD non-deformed heated bundle, pressures were extracted at the midpoints of particular duct wall faces at various axial heights from the start of the heated length of the bundle which is consistent with the experiment pressure measurements.

6.2.1 Non-Deformed Isothermal Bundle Comparisons

To determine the pressure drop of the CFD isothermal bundle (non-deformed), pressures were extracted at the midpoints of particular duct wall faces at various axial heights from the start of the bundle which corresponded to the experiment measurements. For the experiments, pressure measurements (not differential pressures) were taken at the tap locations, and these values were then used to calculate pressure drops between various taps. Note that this approach can introduce additional error to the experiments relative to direct measurements of pressure drop between two pressure taps. The CFD and experiment pressure drops, calculated between different axial locations on duct Face F are provided in Figure 6-29. In this plot, the horizontal length of a line segment represents the axial length of the bundle that correspond to

the pressure drop. The value (on the vertical axis) represents the value of the pressure drop itself. Table 6-7 provides the numeric values of these pressure drops as well as the difference between the CFD results relative to the experiment results. These comparisons showed large differences between the CFD and the isothermal experiments. These large differences were not seen for the comparisons between the CFD and the heated bundle experiments. As shown in the table below, some of the experiment measurements were unexpected: there is very large variation in the pressure drop measurements across sequential single pitch lengths which is unexpected due to the constant flow area along the bundle. For the pressure drops across a single wire-pitch the CFD predicts consistent values. That is to say that these two pressure drops across a single pitch have roughly the same value. However, for unknown reasons, these corresponding pressure drops for the experiments are different from each other, with the pressure drop from 1P to 2P being much lower than that between 2P and 3P. This results in a rather large difference from the CFD results for the drop between 1P and 2P. For the remainder of the pressure drops over non-integer multiples of wire pitch , the CFD can display differences up to 63% relative to the experiments.

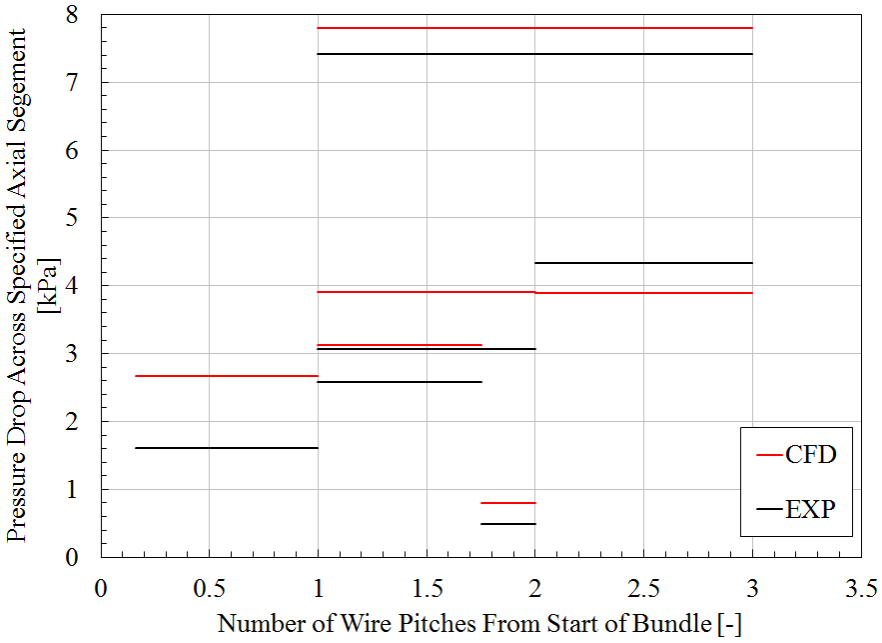


Figure 6-29: CFD and experimental pressure drops on Face F, across specified axial segements of the non-deformed isothermal bundle. The length of a line segment represents the axial length the pressure drop is measured across.

Table 6-7: CFD and experimental pressure drops on Face F, across specified axial segments of the non-deformed isothermal bundle, along with the percent difference between the two methods.

Axial Segment	Number of Pitches [P]	Δp_{CFD} [Pa]	Δp_{EXP} [Pa]	Difference [%]
0.16P to 1P	0.84	2663.3	1614.1	65.0
1P to 1.75P	0.75	3121.1	2588.8	20.6
1.75P to 2P	0.25	791.3	484.9	63.2
2P to 3P	1	3886.6	4343.2	-10.5
1P to 3P	2	7798.9	7416.8	5.2
1P to 2P	1	3912.3	3073.6	27.3

Table 6-8 provides pressure differences between pressure taps on duct Face F and on taps on other duct faces at the same axial height. This can provide a measurement of the TPG. It is clear that much more difference occurs in these values than for the axial pressure drops along the duct face. This is partly due to the very low pressure values of this measurement and simulation. Another possible reason for this could be that the CFD is having an issue predicting the characteristics of the TPG correctly as in the heated bundle cases comparison. Since the pressure taps for which differences are taken between are at the same axial height, there should be no effect from the axial pressure drop in these results. Another possible source of the difference is because the measured pressure were small compared to the pressure transducer range.

Table 6-8: CFD and experimental pressure differences between taps on duct Face F and taps on other duct faces, along with the percent difference between the two methods. Note that each pressure difference is taken at a certain axial height.

Number of Wire Pitches from Start of Bundle	Sampled between Duct Face _ /Duct Face _	Δp_{CFD} [Pa]	Δp_{EXP} [Pa]	Error [%]
2.25P	F/E	416.0	-296.3	240.4
2.25P	F/D	-157.6	8.8	1896.8
2.25P	F/A	-641.2	353.0	281.6
3P	F/E	556.4	-381.1	246.0
3P	F/D	1140.1	-733.5	255.4
3P	F/A	-103.9	-90.7	-14.5

The CFD results for the normalized horizontal and normalized vertical (axial) velocities are compared with the corresponding normalized experimental PIV results in Figure 6-30. As described above, these CFD results were averaged across a specified depth in the CFD geometry that corresponded to the experiment laser plane thickness. Each velocity component is normalized by the maximum of that particular component in the plane. The normalized results are effective for comparing the gradients between the experiment and simulation. Qualitatively, both components of the normalized velocity compare well between the two. The horizontal velocity component displays distinct features that arise from the flow swirling around the pins due to the wire-wrapping. Lower horizontal velocity is seen in regions which are aligned with the gaps between the pins. In those regions, reverse flow, or flow in the direction opposite to the bulk swirl (the bulk swirl is in the direction of the wire-wrapping), is visible. Higher horizontal velocity is visible in regions which are aligned with the pins themselves. The vertical velocity component displays higher values in regions which are aligned with the pins as well. However, the higher vertical velocities occur at the lower region of the domain whereas the higher horizontal velocities are seen at the higher region of the domain.

While the normalized velocity components of the CFD and PIV compare favorably from a qualitative standpoint, a closer look can show that a quantitative comparison do not match as well between the two. For a more quantitative look, the difference is taken between normalized components of each method and shown in Figure 6-30 (e) and (f). In this figure, the lighter colors are closer to zero (zero implies that the CFD and PIV velocity component matches exactly at that point) and the darker colors are further away from zero. It is clear that the CFD and PIV normalized velocity components differ from each other in certain locations more than others, and these locations are commonly where larger gradients occur in the velocity field.

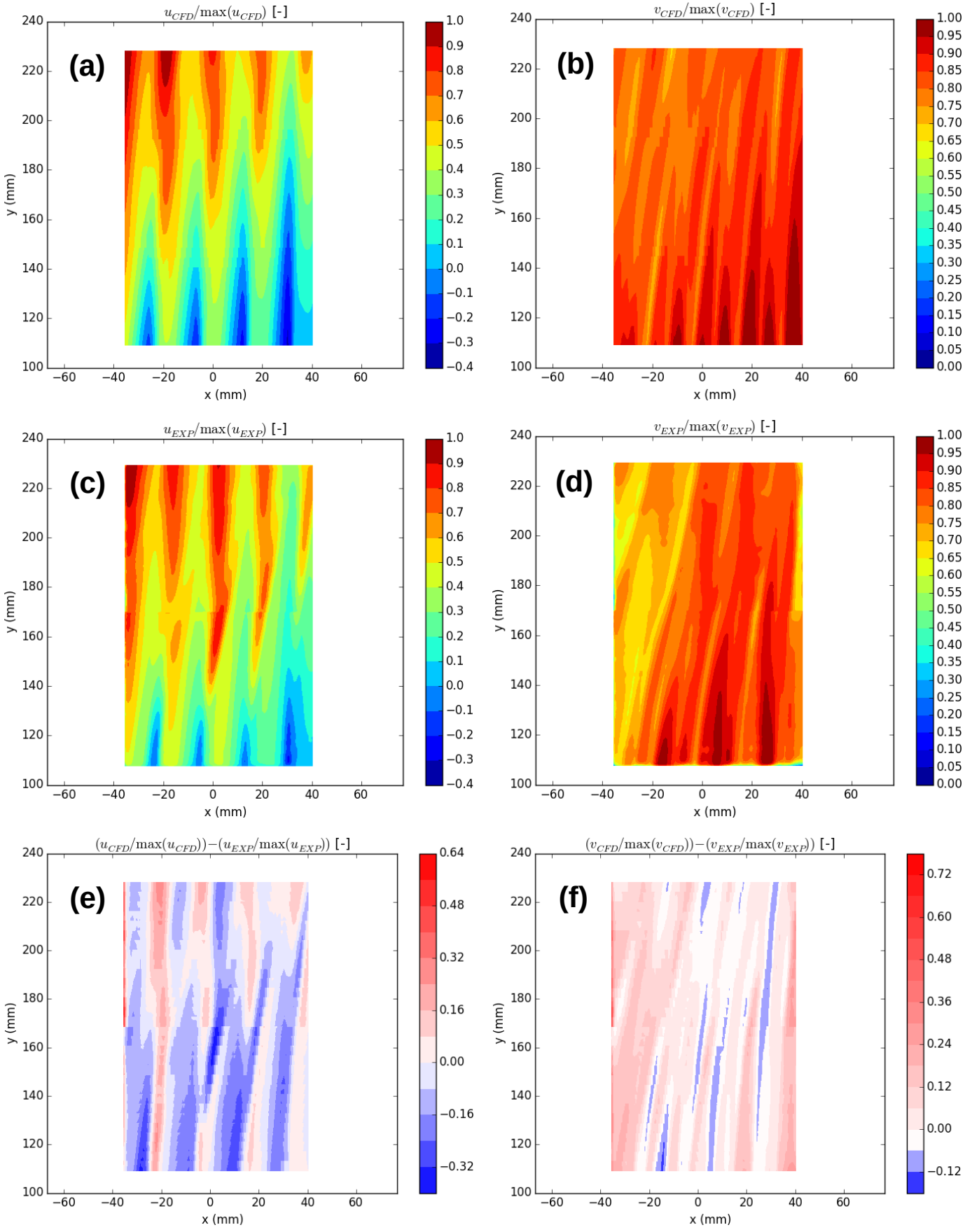


Figure 6-30: Plane E contour plots of normalized velocity for (a) CFD in x-direciton, (b) CFD in y-direction, (c) EXP in x-direction, (d) EXP in y-direction, (e) Difference between CFD in x-direction

and EXP in y-direction, and (e) Difference between CFD in y-direction and EXP in y-direction. CFD velocity values were averaged across a 1.5 mm thickness (z-dir) corresponding to PIV laser-sheet thickness.

Additional quantitative comparisons are presented below. Although the normalized velocity components show adequate qualitative agreement, there is an important caveat to be considered when analyzing the normalized values. That is, while the normalization is effective in demonstrating differences between the spatial distribution and normalized magnitude of each velocity component, it can disguise the differences in the true magnitude of the velocity component. Table 6-9 shows the averages of the Plane E velocity components for both CFD and the experiments. For comparison, the flow area averaged axial velocity corresponding to the reported experiment flowrate, and consistent with the simulation was 2.36 m/s. Typically, in these bundle flows, higher area averaged velocities are seen in the wall subchannels and lower velocities are seen in the internal subchannels. This is due to the difference in flow resistance between internal subchannels and near the wall. This trend for the wall subchannel axial velocity in comparison to the flow area averaged bundle velocity is also impacted by the pin distribution in the bundle, as well as proximity near the duct wall. Very near the duct wall the axial velocities decrease due to wall effects. From this analysis, it is evident that the averaged horizontal and vertical velocities have significant differences between the CFD and experiment. Note that the Particle Image Velocimetry (PIV) uncertainty in the mean vertical (axial) velocity for this measurement plane was reported to be +/- 3% [10]. As stated above, the PIV laser sheet was reported to have a 1.5 mm thickness with +/- 0.5 mm uncertainty in the thickness, and an additional 0.5 mm location uncertainty in the direction perpendicular to the duct face.

Table 6-9: Velocity components (averaged over entire measurement plane E) for the CFD and EXP along with the error between the CFD and EXP.

	CFD Plane E Average Velocity [m/s]	PIV Plane E Average Velocity [m/s]	Difference [%]	EXP Accuracy [%]
Horizontal (x-direction)	0.26	0.37	-30.8	-
Vertical (y-direction)	2.74	2.17	26.1	+/- 3

7 CONCLUSIONS

This report provided solution validation for the non-deformed duct isothermal bundle, the non-deformed duct heated bundle, and the deformed duct heated bundle CFD simulations. The simulations used geometric properties and boundary conditions corresponding to the test conditions as reported in the AFAFC Post-Test Simulation Details report [1]. Based on the AFAFC RANS Pre-Test Simulation Report [4], a two-equation RANS turbulence model was chosen for the post-test simulations along with parameters for the momentum sources which were used in place of the wire-wrap. The AFAFC RANS Pre-Test Simulation Report [4] also helped guide the choice of mesh resolution that would provide an acceptably converged solution for the post-test simulations.

The heated bundle simulations (non-deformed and deformed) both provided acceptable axial pressure drop results along the duct faces which matched well with the experiments. For lengths corresponding to integer multiples of wire-pitch length, the pressure drops on the duct faces were generally within 5% of the experimental values. For lengths corresponding to non-integer multiples of wire-pitch, the CFD pressure drops showed more error relative to the experiments. This is due to an over-prediction of the magnitude of a Transverse Pressure Gradient that forms across the bundle and rotates in phase with the wire-wrapping as it passes along the axial length of the bundle. This poor prediction would only affect the non-integer multiples of wire-pitch. Thus, the simulations seem to predict the axial pressure drop well, but may be having some difficulty capturing the Transverse Pressure Gradient.

Temperatures from the heated bundle CFD solutions were compared with the experiments at thermocouple locations on the non-heated tube outer surfaces and on the duct walls. Temperatures averaged over thermocouple locations at each of two axial planes, the mean CFD temperatures never exceeded 7% error

relative to the experiments. The vast majority of the local normalized CFD temperatures were within the error bars of the experiment temperature measurements. Of the few local CFD temperatures which were outside of the error bars, most of these were at locations of high temperature gradients, and therefore are subject to thermocouple location sensitivity.

The non-deformed isothermal bundle simulations pressure drops showed poor agreement with the experiments. Integer multiples of wire-pitch displayed a range of difference from 5% to 27% between the CFD and experiment. However, experiment results showed inconsistent pressure drops between consecutive measurements across single wire-pitches. This was unexpected due to the constant flow area throughout the bundle. For the pressure drops corresponding to the same locations, the simulations displayed consistent pressure drops across those single wire-pitches. In this case, the unexpected behavior was present in the experiment, while the simulations behaved as expected. As with the heated bundles, pressure drops for non-integer multiples of wire-pitch resulted in more difference than with integer multiples of wire-pitch, and this is thought to be due to the incorrect simulation of the Transverse Pressure Gradient.

The velocities of the non-deformed isothermal bundle were also compared between simulation and experiment. CFD velocities were extracted at grid points corresponding to the PIV measurements and averaged across a specified thickness corresponding to the laser sheet thickness. The measurement plane was in a region parallel to a duct face and between the duct face and the outer most row of pins. Results showed good qualitative agreement between the experiment and simulation for normalized velocity components. However, for the non-normalized velocity components, there were large discrepancies in mean flow in the plane between experiment and simulation. Both the mean CFD horizontal and vertical velocities in the plane were close to 30% different from the experiments. The experiment reported a mean axial velocity in the measurement plane that was less than the flow area averaged axial velocity corresponding to the reported bundle flowrate. This was unexpected due to the typical higher axial velocities that are seen in the wall subchannel due to lower flow resistance. This behavior can be impacted by pin distribution in the bundle, as well as measurement plane location: velocity measurements closer to the wall are smaller due to wall effects. The CFD results were consistent with this expected effect of higher velocities in the wall subchannels, but the experiment displayed a mean velocity on the measurement plane of less than the flow area averaged velocity. Due to the issues with the isothermal bundle experiment pressure drops and mean axial velocity measurements, it is recommended that the isothermal experiment data not be used for CFD validation until further critical review and satisfactory acceptance of the test data is performed.

Blind post-test RANS CFD simulations were conducted based on as-built and as-designed conditions, and were compared with the corresponding experiments. In most cases, the results adequately validated TerraPower's CFD methodology for predicting pressure drops and local temperature measurements. Local velocity results compared well, in a qualitative sense, with the experiments. However, there are still open questions pertaining to the isothermal experimental results. Future work consists of analyzing more substantial validation datasets from the experiments, developing alternate metrics for validation of the CFD results, performing more sensitivity analyses of CFD models and conditions, resolving issues with unexpected behavior from the isothermal experiments, and comparing the CFD results to the high-fidelity CFD benchmark results from ANL.

8 REFERENCES

[1] "TWRP-31-RPT-0032-Rev-0, AFAFC Post-Test Simulation Details," 2017.

[2] "TWRP-31-TSPEC-0011-Rev-2, AFAFC AREVA Heated Bundle Experiment Test Specification".

[3] "TWRP-31-TSPEC-0010-Rev-1, TAMU Fuel Assembly Flow Visualization Test Specification".

[4] "TWRP-31-RPT-0022-Rev-0, AFAFC RANS Pre-Test Simulation Report," 2017.

[5] R. Hu and T. H. Fanning, "Development of a Three-Dimensional Momentum Source Model for Wire-Wrapped Rod Bundles," in *The 14th International Topical Meeting on Nuclear Reactor Thermalhydraulics, NURETH-14*, Toronto, Ontario, Canada, 2011.

[6] "TWRP-31-TREP-0004-Rev-0, AFAFC Benchmark Specification".

[7] W. Oberkampf and C. Roy, Verification and Validation in Scientific Computing, New York: Cambridge University Press, 2010.

[8] S.-K. Cheng and N. E. Todreas, "Hydrodynamic Models and Correlations for Bare and Wire-Wrapped Hexagonal Rod Bundles - Bundle Friction Factors, Sub-Channel Friction Factors and Mixing Parameters," *Nuclear Engineering and Design,* vol. 92, pp. 227-251, 1986.

[9] CD-Adapco, STAR-CCM+ User Guide.

[10] "TAMU-WW-TEST-PCM-11-E Rev.2.0, TAMU Wire-Wrapped Test Summary of Test PCM-11 at the Exterior Subchannel," 2016.

END OF DOCUMENT

APPENDIX G: TWRP-31-TSPEC-0010, TAMU FUEL ASSEMBLY FLOW VISUALIZATION TEST SPECIFICATION

Thermal Hydraulic CFD Simulations and Experimental Investigation of Deformed Fuel Assemblies

U.S. Department of Energy
DE-NE0008321
DUNS # 789479578

Document Title:	TAMU Fuel Assembly Flow Visualization Test Specification
Document Number:	TWRP-31-TSPEC-0010
Prepared By:	TerraPower
Date:	04/14/16
Revision:	2

Name	Title / Company	Signatory Role	Signature	Date
Mike Steer	Technical Rep. / TerraPower	Approver		4/14/2016
Rodolfo Vaghetto	Technical Rep. / Texas A&M University	Approver		04/15/2016
Elia Merzari	Technical Rep. / Argonne National Lab	Approver		4/21/2016
Tom Galioto	Project Manager/ AREVA Fuels	Recipient		4.19.16
Anthony Chang	Project Manager/ AFS	Recipient		4/18/2016
Brian Mays	Principal Investigator / AFS	Recipient		4/18/2016

Record of Revisions*			Revision: 1
Item #	**Description of Change**	**Effected Pages / Sections**	**Change Initiator**
1	Larger diameter pins	pg. 5	Brian Jackson
2	Wire wrap method	pg. 5	Brian Jackson
3	Flowrate	pgs. 5, 20	Brian Jackson
4	Updated originator from Nate Salpeter to Brian Jackson	Title Block	Brian Jackson

* Revision 1 was an internal TerraPower revision that was not approved by all project partners.

Record of Revisions			Revision: 2
Item #	**Description of Change**	**Effected Pages / Sections**	**Change Initiator**
1	Addition that TAMU QA Guidelines Document will be followed to meet Augmented Quality.	Section 2, 3, and Appendix.	Brian Jackson



Uncontrolled When Printed

TEST SPECIFICATION

Document Number:	TWRP-31-TSPEC-0010	**Revision:**	2
Document Title:	TAMU Fuel Assembly Flow Visualization Test Specification	**Approval Date** *(Final Signature Date)*:	4/14/2016
Issuing Organization:	Core Design	**Effective Date** *(for Procedures Only)*:	
		Pages:	Page 1 of 25

Approval

Title	Name	Signature	Date
Originator, Thermal Hydraulics Test and Analysis Engineer	Brian Jackson	Approved in Agile	4/13/2016
Reviewer, Reactor Systems Thermal and Fluids Analyst Consultant	Nate Salpeter	Approved in Agile	4/13/2016
Reviewer, Manager, Thermal Hydraulic Test & Analysis	Mike Steer	Approved in Agile	4/14/2016
Approver, Manager, Design Qualification	Rob Corbin	Approved in Agile	4/14/2016

Document Safety Classification per TWRP-NS-PROC-0002 ('N/A' for Procedures / policies / manuals / guides): Safety-Related ☐ Non-Safety Related ☐ Augmented Quality ☒ N/A ☐

QA Criterion (Select 'N/A' for documents other than procedures/policies/manuals/guides): N/A

Revision History

Revision No.	Effective Date	Affected Section(s)	Description of Change(s)
0	6/19/2015		Initial Release
1	12/21/2015		Larger diameter pins, wire wrap method, and associated dimensional and flowrate changes. Updated Originator from Nate Salpeter to Brian Jackson
2	4/14/2016	2, 3	Reference to the TAMU Wire-Wrapped QA Guidelines

TABLE OF CONTENTS

1 TEST OBJECTIVE 4
1.1 Test Scope 4
1.2 Non-Deformed Assembly Test 5
1.3 Deformed Test Assembly 18
2 REPORTING 22
3 REFERENCES 22
4 APPENDIX 22

LIST OF TABLES

Table 1: Fuel Assembly Dimensions for Non-Deformed Duct and Pin Configuration 6
Table 2: Fuel Assembly Dimensions for Non-Deformed Duct and Pin Configuration 7
Table 3: Pressure Tap Locations for non-deformed configuration 17
Table 4: Preliminary LDV Measurement Locations for non-deformed test configuration – Actual locations and quantity to be determined based on shakedown 17
Table 5: Preliminary PIV Measurement Locations for non-deformed test configuration– Actual locations and quantity to be determined based on shakedown 18
Table 6. Dilated Duct Values 18
Table 7: Conservative Predicted Flow Conditions for TAMU facility for long duct configuration. 20
Table 8: Pressure Tap Locations for deformed configuration 21
Table 9: Preliminary LDV Measurement Locations for deformed test configuration – Actual locations and quantity to be determined based on shakedown 21
Table 10: Preliminary PIV Measurement Locations for deformed test configuration – Actual locations and quantity to be determined based on shakedown 22

LIST OF FIGURES

Figure 1: Laminar to turbulent flow transition map (from Ref. [1]) for wire wrapped hex pack rod bundles.. 6
Figure 2: Wire wrap direction is specified as clockwise when looking upwards from below the bundle (downstream flow direction) 8
Figure 3: Mock Fuel Assembly Schematic showing inlet plenum boundary condition characterization measurements at P=-0.5P where P=0 is the bottom of the wire wrapped pins. 10
Figure 1-4: Mock Fuel Assembly Schematic showing development LDV measurements in outer subchannel from P=0.25 to P=3.25 at axial intervals of dZ=P/3. 11
Figure 5: Mock Fuel Assembly Schematic showing placement of LDV measurement volumes with respect to wire position in outer subchannel from P=0.25 to P=3.25 at axial intervals of dZ=P/3. 11
Figure 6: Mock Fuel Assembly Schematic showing placement of LDV measurements for wall effect measurements (black points) and LDV grid for PIV verification (blue points) 13
Figure 7: Mock Fuel Assembly Schematic showing stepped vertical measurement window approach (right). External and internal sub-channel PIV measurement planes (vertical orientation) are indicated by red lines. 14
Figure 8: High and low risk vertical PIV measurement locations 15
Figure 9: Mock Fuel Assembly Schematic showing horizontal PIV measurement regions to be measured at heights specified in Table 5. 16
Figure 10: Deformed duct definition for the TAMU deformed assembly flow test 19

1 TEST OBJECTIVE

The purpose of this test is to investigate and measure flow and pressure drop behavior of two configurations (non-deformed and deformed) of a mock 61-pin fuel assembly in the fully turbulent flow regime for purposes of generating CFD validation grade data. This test will provide valuable isothermal velocity and pressure data to complement the non-isothermal temperature and pressure measurements to be performed at AREVA. The test will follow Augmented Quality as given in the Appendix.

1.1 Test Scope

To support verification and validation (V&V) of computational fluid dynamics (CFD) calculations, high quality characterization of flow in the same flow regime as those encountered in wire wrapped fuel assemblies prototypic of liquid metal fast reactors is needed. Measurements of velocity fields are to be made with Particle Image Velocimetry (PIV), point velocity measurements with Laser Doppler Velocimetry (LDV), and with basic flow visualization of mixing between inner and outer sub-channels. In addition, pressure drop measurements locations are defined in this test specification. The measurement locations for the LDV and PIV measurements as well as flow visualization are recommendations based on early scoping of flow behavior and are only defined as preliminary measurement locations. As the shakedown test is carried out by TAMU and pre-test predictions by TerraPower and Argonne National Laboratory are developed, the additional information may be used to inform and update measurement locations on the basis of measurement capabilities, accuracy, and flow physics. These updated and prioritized measurement locations will be defined during the shakedown test in a measurement specification document. It should be noted the number of locations indicated here is not indicative of the final number of measurements pending prioritization of measurements in the measurement specification.

To facilitate the visual access needed to make measurements using the aforementioned techniques, application of the Matched Index of Refraction (MIR) approach is to be applied by using acrylic test sections with acrylic mock fuel pins and the test fluid P-Cymene. The pressure drop across the components of the fuel assembly will be measured for the range of Reynolds numbers as specified in this document. Because the flow testing will use P-Cymene as a working fluid, the testing will be scaled to match Reynolds numbers associated with those tested in the heated 61 pin assembly tested at the AREVA Richland, WA facility. The pressure taps are installed such that data can be obtained to measure hydraulic losses across identified sections of the test assembly.

The following functional requirements of the hydraulic flow loop shall apply:

1. Be flowrate controlled
2. Have temperature monitors to ensure steady temperature during testing and report operating temperatures
3. Measure flowrate in the test loop
4. Measure pressure and temperature upstream of the test section
5. Measure pressure and temperature downstream of the test section
6. Contain a mechanism (e.g. pressure relief valve to the dump tank) to ensure the test section is protected from damage due to over-pressurization.
7. Contain a data acquisition system with appropriate QA qualification such that reliable and repeatable measurements are ensured.
8. Provide a test section that has sufficient entry length prior to measurement locations to ensure a fully developed flow.

9. Provide a test section that has sufficient length after last measurement location to ensure downstream features have minimal effect on upstream flow measurements

10. Provide visual access using the matched index of refraction (MIR) technique to perform flow visualization and laser based diagnostic measurements specified in this test specification.

1.2 Non-Deformed Assembly Test

The non-deformed test assembly is designed to provide CFD validation pertaining to beginning of life fuel assembly geometries prior to duct and fuel pin dilation. The test needs to provide sufficient development length (2.25 pitches) and exit length (0.25 pitches), as well as adequate axial length for fully developed measurements between axial locations P=2.25 and P=3.25. At P=0, the clocking position of the wire should be such that at the axial height of P=2.25, the wire clocking shall be such that it is pointed towards the corner of the bundle between duct faces A and F (Figure 2). The wire wrap direction is clockwise when viewing the test assembly from below looking up as shown in Figure 2. The experimental fuel assembly design has a fuel pin diameter (D) of 5/8” and a wire wrap diameter of 3mm. The acrylic wire will be wrapped around the acrylic pin. The resulting effective pitch-to-diameter ratio (P/D) is specified to be 1.189. The components and fabrication tolerances shall be reported. The test assembly dimensions for the non-deformed case are detailed in table 1.

The Reynolds number to be tested is 20,000 and is specified to maintain conditions below the maximum allowable pressure (20psig) designated for of test section materials. The corresponding bundle pressure drop is estimated to be approximately 4.8 psig, or 32,777kPa, based on Cheng and Todreas correlations for the geometry, Reynolds number, and test fluid specified in table 1. This includes hydrostatic pressure effects. At this Reynolds number, flow is within the fully turbulent regime as indicated in Figure 1. Table 2 details the predicted flow conditions. For the non-deformed assembly test, the duct inner flat to flat length corresponds to the length across a tightly packed bundle plus an additional 0.77% length for the wall gap. Tightly packed means that the pin pitch is the sum of the pin and wire diameters. This wall gap spacing is equivalent to 25% of a wire diameter along each wall perimeter between the outer row of wires and the duct wall. Fabrication method of the duct and bundle may necessitate adjustment to this value from the design drawings and therefore should be verified during the fabrication process of the pins to ensure sufficient clearance is included in the manufactured duct such that assembly is possible without excessive amounts of clearance. As-built dimensions will be reported for use in post-test simulations. As part of the assembly, a thin stainless steel wire with sufficiently thin diameter such that minimal flow disruption is observed may be used to compact the pins and wires. These wires are intended to be used during experiment operation. In doing so, additional vibration resistance is achieved as is tighter control over P/D values throughout the assembly.

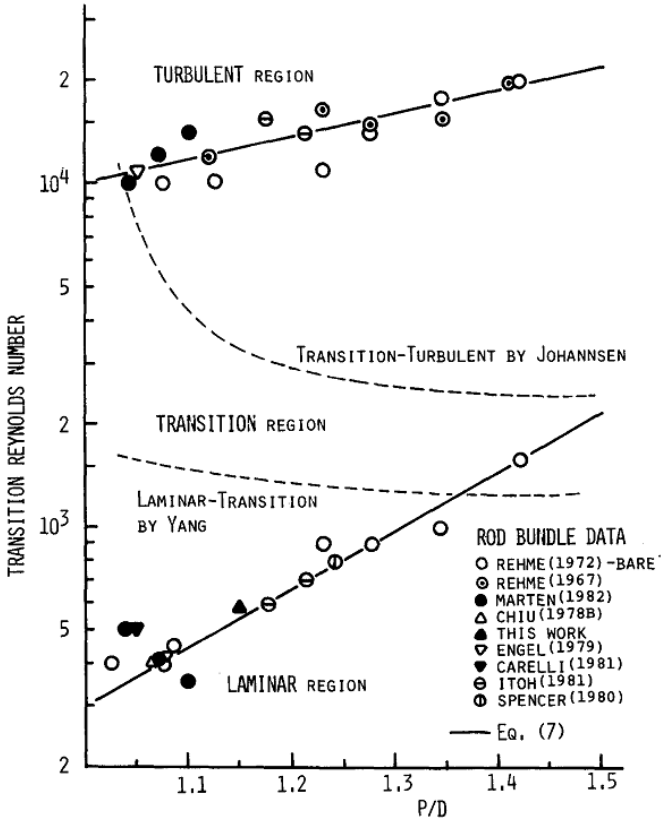


Figure 1: Laminar to turbulent flow transition map (from Ref. [1]) for wire wrapped hex pack rod bundles

Table 1: Fuel Assembly Dimensions for Non-Deformed Duct and Pin Configuration

		(m)	(in)
Inner Duct Side Length	L	0.0888	3.496
Pin Diameter	Pd	0.0159	0.625
Wire Diameter	Wd	0.0030	0.118
P/D	(Pd+Wd)/Pd	1.1890	(dimensionless)
Gap between pins and wires	g	0.0000	0
Inner Duct Flat to Flat (includes 0.77% clearance)	Ftfc	0.1538	6.056
Duct Inner Corner to Corner	Ctc	0.1776	6.993
Flow Area	Af	0.007986 m^2	12.378 in^2
Total Wetted Perimeter	Pt	4.1500	163.386
Hydraulic Diameter	Dh	0.0077	0.303

Table 2: Fuel Assembly Dimensions for Non-Deformed Duct and Pin Configuration

	Value	Unit	Alternate Units
Viscosity	0.000876	Pa-s	
Density	857	kg/m^3	
Flow area	0.007986	m^2	
Length	1.667	m	
Fluid	Pcymene		
Reynolds	20000		
Operating Temperature	25	C	
mdot (kg/s)	18.18	kg/s	
q (watts)	n/a		
vel m/s	2.66	m/s	
Volumetric Flow Rate (gpm)	336.19	gpm	
DP (Pa)	18,763	Pa	2.72PSI
Friction Factor (Cheng & Todreas)	0.0287		
Cbt	0.170		
H/D	30		
P/D (submerged w/o gap)	1.189		
# of pitches	3.5		
Pitch Length	0.476	m	
Hydrostatic head within bundle	14,013.7	Pa	2.03PSI
Total Pressure at bottom of bundle (15% margin)	37,693	Pa	5.47PSI

Pressure taps will be used to measure pressure drop. Local velocity measurements will be taken using Laser Doppler Velocimetry (LDV) and Particle Image Velocimetry (PIV). This document specifies the locations for these measurements. Due to the symmetry of the test section, a geometry basis is used to specify measurement locations. This is shown in Figure 2. Wire wrap position is specified as clock position looking from the bottom of the bundle upwards, in the direction of flow. From this direction, the wire is wrapped clockwise around the pins. The duct faces are labeled A – F. The faces are ordered also in a clockwise direction from the perspective of the bottom of the bundle looking upwards. Due to the challenge of use of an acrylic test section, some of the locations may need to be updated pending feedback during the instrumentation shakedown phase.

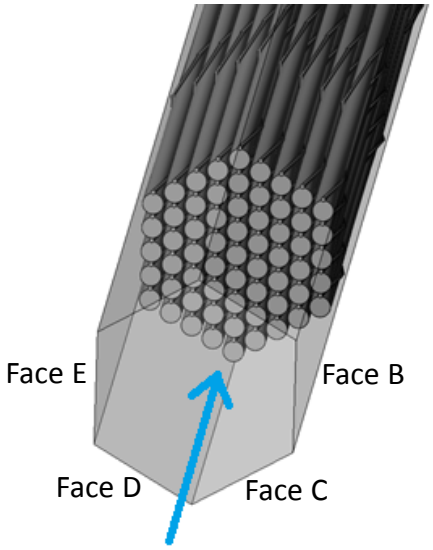


Figure 2: Wire wrap direction is specified as clockwise when looking upwards from below the bundle (downstream flow direction)

The suggested axial locations of the pressure taps in the fuel pin bundle are provided to capture the following effects:

- Axially developing flow in the fuel bundle. To capture the flow development in the pin bundle, the 2.0 wire wrap pitches after entry into the duct is spanned by four axial pressure taps along duct face B. These pressure taps correspond to taps 1b through 4b.
- Flow asymmetry will exist due to the wire wrap, and four pressure taps with 60° azimuthal offsets (i.e. located on four adjacent fuel assembly duct faces: faces A - D) are to be installed following conclusion of flow visualization experiments. These pressure taps correspond to taps 5 (a-d) and are at a height of P=2.25.
- To measure how flow asymmetry changes with respect to wire wrap clocking, four pressure taps with 60° azimuthal offsets (i.e. located on four adjacent fuel assembly duct faces: faces A - D) are to be installed following conclusion of flow visualization experiments. These pressure taps correspond to taps 6 (a-d) and are at a height of P=3.0.
- An additional pressure tap (7b) will be used at P = 3.25 on duct face B.

  <u>Azimuthal Locations</u>

  - Risk –The measurement accuracy of the existing TAMU pressure transducer hardware may not be of sufficient accuracy for a relevant measurement of pressure gradient in the horizontal direction at this flow condition.
  - Basis – Pre-test CFD predictions may indicate lower than expected pressure differentials across the bundle. These values will be assessed following these CFD simulations.

- Mitigation – Reduce the number of azimuthal locations to only opposite faces or use differential pressure transducers with higher sensitivity (depending on their accessibility to TAMU laboratory) for measuring azimuthal pressure differences. Measurements may be omitted altogether if the pressure gradient is below the measuring range of the available instrumentation.

Axial Locations

- Risk – Some of the specified locations along the bundle may not be guaranteed due to interference with other components of the test section.
- Basis – Location PT#1a may be too close to the test section inlet flange based on the expected tap size. Location PT#4a is adjacent to the flow measurement section and may interfere with the visualization instrumentation. Locations PT#6a-6d may be too close to the test section outlet flange based on the expected tap size.
- Mitigation – Location PT#1a tap size can be minimized or location may be moved upward to allow required clearance to the flange. Location PT#4a may be included only after completion of the flow measurements, moved downward or completely removed. Locations PT#6a-6d tap size can be minimized or location may be moved downward to allow required clearance to the flange or completely removed.

- Pressure Taps upstream and downstream of assembly.

  There are 13 pressure taps that will be augmented by a pressure tap upstream of the test section and downstream of the test section, for a total of 15 pressure taps. For the flow asymmetry tests, inlet pressure taps may be reduced to an essential subset (e.g. inlet and P=2.25 taps) to guarantee repeatable data based on previous pressure measurements at these locations while allowing re-positioning the previous inlet taps to obtain the asymmetric measurements. Instrumentation location detail is provided in Table 3. The taps may be connected via a manifold as the tests do not necessitate simultaneous measurements so long as all taps are acquired within the same testing sequence. Pre-test and post-test flow verification data for temperature and flow should be provided to ensure conditions remain constant throughout pressure tap sequencing.

  - Risk – Operability of the manifolds and valves during the test sequence may be difficult and may affect the pressure measurements.
  - Basis – Due larger number of pressure taps measurements than the available pressure transducers, valves need to be installed to allow multiple connections.
  - Mitigation – This issue will be investigated during shakedown. The total number of pressure measurement locations may be reduced based on the timings and procedures identified during shakedown.

  The suggested locations of Laser Doppler Velocimetry measurements in the fuel pin bundle are provided to capture the effects listed below. The exact measurement locations and number are to be defined during shakedown tests and during pre-test CFD predictions within an updated measurement specification document to be issued at a later date. The following locations are only defined as preliminary measurement locations and it should be noted the number of locations indicated here are not indicative of the final number of measurements pending prioritization of measurements in the measurement specification.

- Inlet velocity profile prior to the bundle to quantify flow asymmetry. Flow straightening prior to entry into the mock test assembly helps provide a controlled flow that has limited entry effects. One example of inlet flow characterization (may take several forms) is to assume measurement locations are at an axial position P= -0.5 and are from flat to flat as indicated by green points in figure 3. These measurements may be taken from flat to flat with increments such that 10 measurements may be made across the bundle. Average velocity and RMS values are to be reported. Lower bundle attachment strategy and plenum geometries are to be engineered by TAMU, and measurement locations may be updated pending design.

- Example axially developing flow measurements in the fuel bundle using LDV. To capture the flow development in the pin bundle, three wire wrap pitches shortly after entry into the duct is spanned by LDV measurements beginning with P=0.25 and ending at P=3.25 in wall subchannels on duct face A. The sub-channels and positioning of the LDV points are indicated on Figure 4 by red markers. Figure 5 illustrates measurement volume locations with respect to wire wrap azimuthal position to avoid LDV measurements placed within the acrylic wire. Average velocity and RMS values are to be reported. Lower bundle attachment hardware is to be engineered by TAMU, and measurement locations may be updated upon hardware design completion. The decision on total number of points or increased number of sub-channels to be measured will depend on allowable contact time of the acrylic test section and pins with the P-Cymene which is known to degrade the surface characteristics over time.

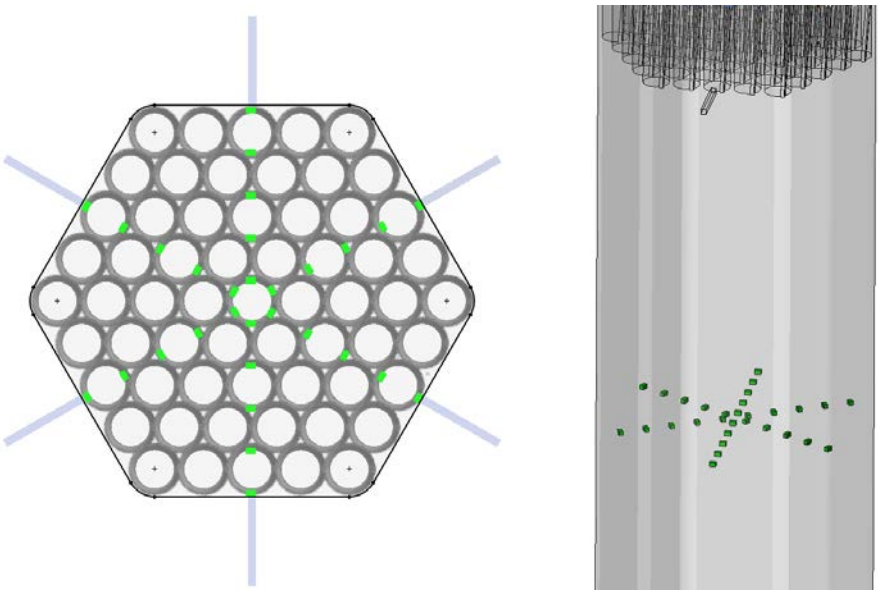


Figure 3: Mock Fuel Assembly Schematic showing inlet plenum boundary condition characterization measurements at P=-0.5P where P=0 is the bottom of the wire wrapped pins.

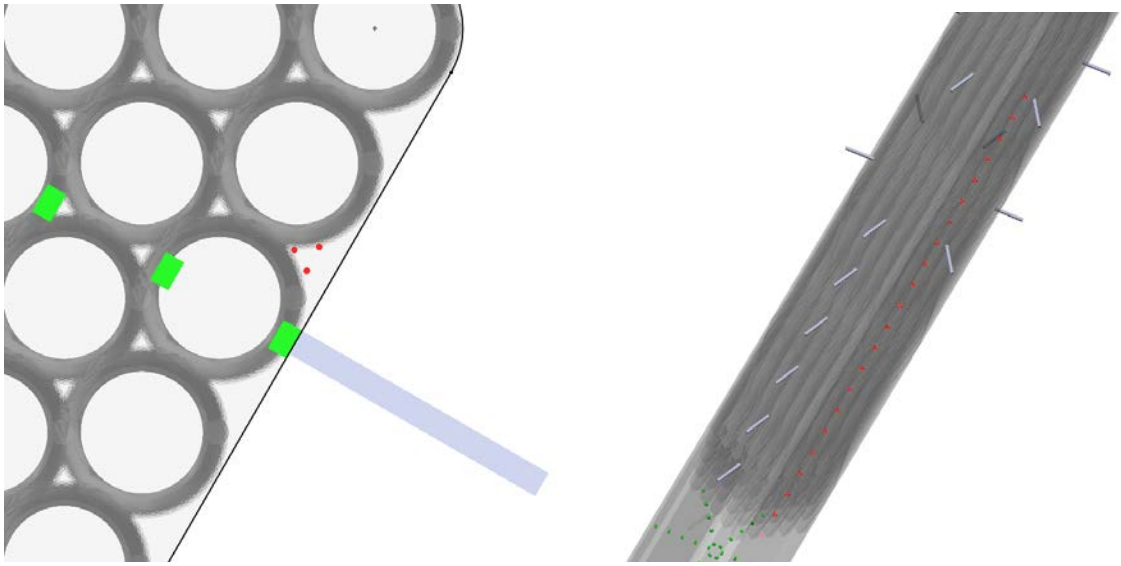


Figure 1-4: Mock Fuel Assembly Schematic showing development LDV measurements in outer subchannel from P=0.25 to P=3.25 at axial intervals of dZ=P/3.

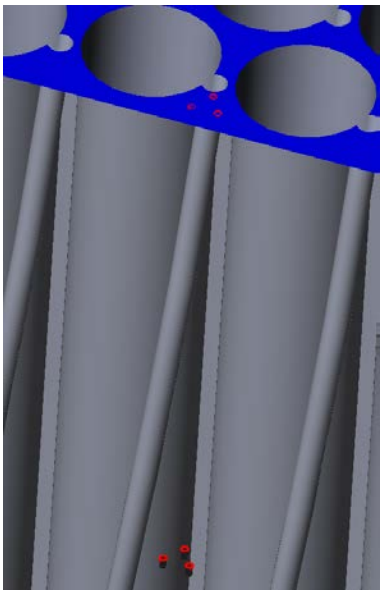


Figure 5: Mock Fuel Assembly Schematic showing placement of LDV measurement volumes with respect to wire position in outer subchannel from P=0.25 to P=3.25 at axial intervals of dZ=P/3.

- Wall effects for external and internal sub-channels
    - The effect of larger flow areas in the sub-channels neighboring the wall (excluding the corner sub-channels) has been shown to result in preferential flow behavior within the outer 2-3 rows of sub-channels and therefore lower localized bundle temperatures in comparison to the internal sub-channels. The measurements recommended would be taken between planes 2.25 and 3.25 at 0.166P intervals along the line indicated in Figure 6 at the various axial heights. These measurements would provide insight to the axial flow distribution with respect to wire pitch in relation to the sub-channel. The spacing of measurements along the line probes should be half the diameter of the wire wrap diameter. The decision on total number of points or increased number of sub-channels to be measured will depend on allowable contact time of the acrylic test section and pins with the P-Cymene which is known to degrade the surface characteristics over time.
- Verification LDV measurements for particle image velocimetry (PIV) measurements
    - Obtaining redundant measurements with alternate measurement techniques will be done on specific sub-channels in order to verify accuracy of PIV measurements that are to be done on a larger set of sub-channels. Measurements in the horizontal plane shall be taken from above the bundle and the axial position of measurements is dependent on outlet plenum design, LDV standoff distance, and PIV standoff distance for making reliable and accurate measurements. An example of a measurement grid within an external subchannel is indicated in figure 6. Measurements from the side of the bundle to provide axial flow should be provided pending instrumentation capabilities (two LDV heads). The decision on total number of points or increased number of sub-channels to be measured is to be decided subsequent to final shakedown of facility.

<u>Overall Measurement Uncertainty</u>

- Risk – Measurement uncertainty may be high.
- Basis – Measurement volume size of LDV fringe pattern is expected to be the same order of magnitude of the flow gaps in the bundle.
- Mitigation – Uncertainty needs to be evaluated during shakedown. Measurement locations may be moved to minimize uncertainty.

<u>Subchannel Accessibility</u>

- Risk – Internal Subchannels may not be accessible.
- Basis – Laser beams need to pass through multiple pin rows with no gaps.
- Mitigation – Accessibility and error estimation need to be investigated during shakedown. Internal subchannels may not be covered by LDV measurements. Alternate measurements approaches will be investigated to obtain data.

<u>Required Measurement Time</u>

- Risk – Duration of point measurements may be large.
- Basis – Duration depends on particle concentration, flow velocity, and location.

- Mitigation – Duration will be investigated during shakedown. Depending on the evaluation, number of allowed measurements per test run may be reduced.

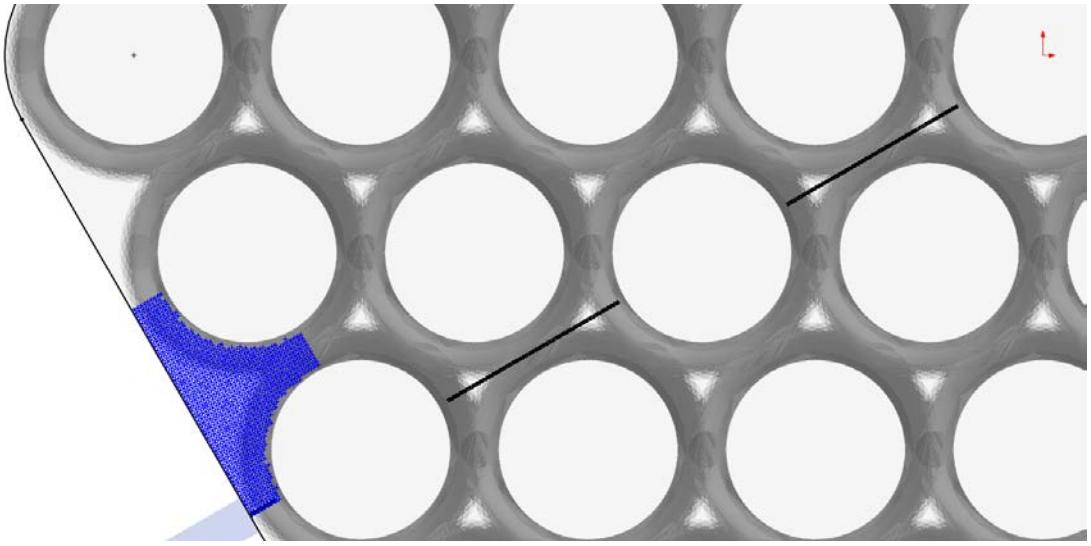


Figure 6: Mock Fuel Assembly Schematic showing placement of LDV measurements for wall effect measurements (black points) and LDV grid for PIV verification (blue points)

Particle image velocimetry (PIV) is to be used to provide 2 dimensional flow fields within the mock fuel assembly. The exact measurement locations and number are to be defined during shakedown tests and during pre-test CFD predictions within an updated measurement specification document to be issued at a later date. The following locations are only defined as preliminary measurement locations and it should be noted the number of locations indicated here are not indicative of the final number of measurements pending prioritization of measurements in the measurement specification.

The preliminary locations of Particle Image Velocimetry (PIV) measurements in the fuel bundle are provided to capture the following effects:

- Bulk swirl phenomena in the outer sub-channels.
  - Wire-wrapped fuel assemblies result in a helical velocity profile around the outer faces of the hexagonal duct as the in phase wires sweep past the adjacent duct face as shown in Figure 7. The resulting helix introduces a bulk swirl in assembly that results in transverse flow/pressure gradients at a given axial height. To capture the external sub-channel behavior for different wire clocking relative to the neighboring duct face, the outer sub-channel velocities should be measured in vertical plane sections over one pitch length beginning at axial location P=2.25 and ending at P=3.25. Measurement field of view should be consistent with those recommended by TAMU for accurate data acquisition.

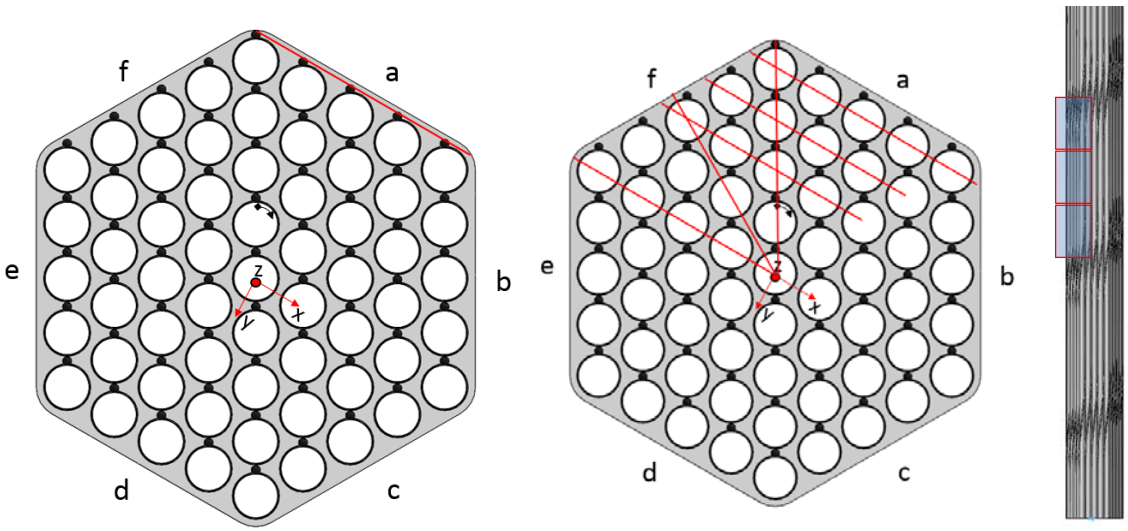


Figure 7: Mock Fuel Assembly Schematic showing stepped vertical measurement window approach (right). External and internal sub-channel PIV measurement planes (vertical orientation) are indicated by red lines.

- Individual sub-channel projected horizontal velocities
    - In addition to providing insight into the amount of mixing across sub-channels, this measurement type provides insight into separation of vortices from the trailing edge of the wire wrap. The sub-channels of interest are indicated in Figure 9 and are at axial locations indicated in Table 5. These measurements are to be performed at the sub-channel level in order to obtain data with sufficient accuracy and detail for CFD validation. As these measurements will need to be made from above, the axial locations have been suggested to ensure there are no adverse effects from the outlet plenum on the measurement planes.

The risk in performing the PIV measurements was identified in specific locations of the test section as shown in Figure 8.

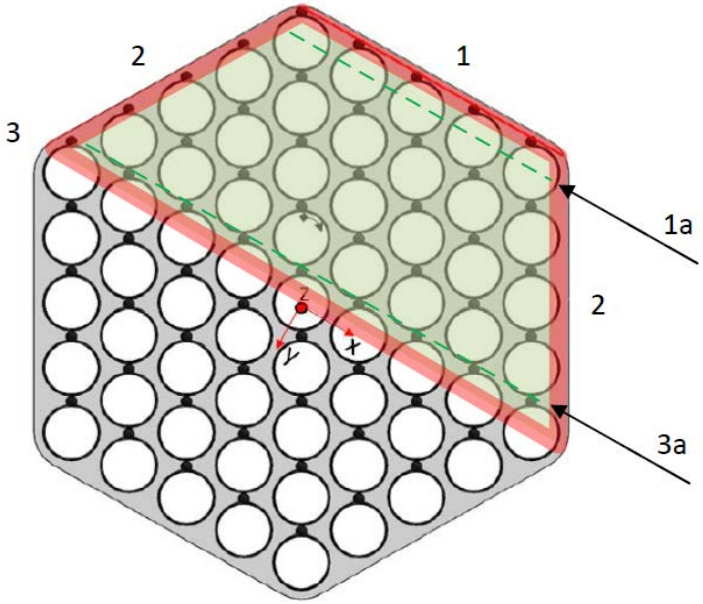


Figure 8: High and low risk vertical PIV measurement locations.

Vertical Plane Measurements – Near Wall (1)

- Risk – Planes parallel to the enclosure faces and near the enclosure faces cannot be accessed with the laser sheet.
- Basis – Light disturbance due to the enclosure edges
- Mitigation – Move the measuring plan far from the enclosure's corners (see plane 1a)

Vertical Plane Measurements – Near Wall (2)

- Risk – Planes that cut through the enclosure faces and are in the vicinity of the enclosure are difficult to access.
- Basis – Standard laser/camera setups may not be applied to these locations/angles
- Mitigation – New techniques may be investigated during shakedown to access these areas with different camera/laser configurations OR measurement locations may be removed.

Vertical Plane Measurements – Center Row Centerline (3)

- Risk – Planes passing through the pin center row centerline are difficult to access with the laser sheet.
- Basis – Light disturbance due to the enclosure edges
- Mitigation – Location can be moved in the sub-channel adjacent to the centerline (along line 3a).

Horizontal Plane Measurements

- Risk – Horizontal measurement plane at 0.25P from the end of the bundle is too far from camera for accurate measurement. Other accessibility issues need to be considered.
- Basis – Based on optimal camera settings, measurement area size, and standard horizontal and vertical velocity ranges, the maximum allowed focal distance may be lower than the geometrical distance between the measurement plane and the top of the upper plenum.
- Mitigation – Optimize (minimize) the axial length of the upper plenum. Use available telecentric lenses or consider procuring lenses to achieve longer working distance.

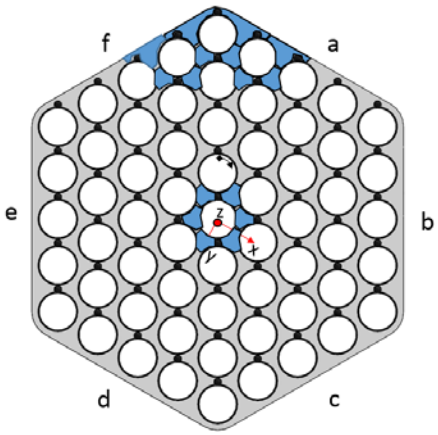


Figure 9: Mock Fuel Assembly Schematic showing horizontal PIV measurement regions to be measured at heights specified in Table 5.

Axial flow measurements to serve as redundant verification measurements between the PIV and LDV measurements should be taken in locations identified in the measurement specification document.

The following flow visualization experiments are suggested for visualizing mixing phenomena within the mock test assembly. These measurements would be complimentary and are considered secondary to the detailed PIV and LDV measurements unless flow visualization measurements are deemed essential to establish PIV and LDV measurement locations. Non-staining dyes shall be used to avoid staining of the test assembly.

Microbubble or non-staining dye injection along the outer sub-channel using a pressure tap location as the point of injection. Vertical (from the side) and horizontal (from above) images at different axial heights would provide valuable insight into mixing between interior and exterior sub-channels.

Microbubble or non-staining dye injection from an interior injection location within the fuel assembly would provide valuable insight into mixing between interior and exterior sub-channels. One possible approach might be the use of a hypodermic tube to translate the injection point from a pressure tap location into the bundle.

Table 3: Pressure Tap Locations for non-deformed configuration

Pressure Tap Identifier(s)	Axial Location
PT #0 (Installed during facility construction)	Inlet plenum PT following flow straightener prior to position P=0. Tap location TBD in development of facility P&ID.
PTs #1b-4b (Installed during facility construction)	PT along duct face B at locations P=0 (or within 1 rod diameter if space limited by flange), P=1, P=1.75, and P=2.0
PTs #5a-5d (following all flow visualization tests)	PTs at axial position P=2.25 along duct faces A through D giving a total of 4 pressure tap locations at this axial height for pressure asymmetry measurements.
PTs #6a-6d (following all flow visualization tests)	PTs at axial position P=3.0 along duct faces A through D giving a total of 4 pressure tap locations at this axial height for pressure asymmetry measurements.
PT #7b (following all flow visualization tests)	PT at axial position P = 3.25 centered on duct face B.
PT #8 (Installed during facility construction)	PT located after outlet plenum following flow 'collection' into common outlet. Tap location TBD in development of facility P&ID.

Table 4: Preliminary LDV Measurement Locations for non-deformed test configuration – Actual locations and quantity to be determined based on shakedown

LDV Measurement Identifier(s)	Location
LDV IP #0-N	Inlet Plenum profile characterization at P= -0.5m from flat to flat in each of the three directions orthogonal to the duct walls
LDV OSP #0 – N	Outer subchannel measurement of development length between heights P=0.25 and P=3.25 with axial spacing of P/3 on duct face A.
LDV LP #1 - N	Wall Effect Line probes at axial heights P=2.25 through P=3.25 with 0.167P increments along the line indicated in Figure 4. Line Probe measurement spacing should be 1/2 of one wire diameter. If there are major differences between P=2.25 and P=3.25, proceed to measure in the same axial increments along the same line to the outlet.
LDV GS 1 - N	Grid sweeps in one external subchannel, one corner subchannel, and one internal subchannel. One grid sweep should be done with an LDV scan capturing axial velocity and one horizontal component. Another set of grid sweeps should be done from above to capture horizontal velocity components in order to verify PIV measurements indicated by PIV HP #1-X in table 3.

Table 5: Preliminary PIV Measurement Locations for non-deformed test configuration– Actual locations and quantity to be determined based on shakedown

PIV Measurement Identifier(s)	Location
PIV VP OSC #1 – N	Outer sub-channel in vertical planes direction at P=2.25 through P=3.25
PIV VP ISC #1 – N	Inner sub-channel in vertical planes direction at P=2.25 through P=3.25
PIV HP # 1- N	Horizontal sub-channel measured from above bundle. Measurement planes should be captured at P=3.25 and sub-channel locations that correspond to different wire clocking angles relative to the parent pin.

1.3 Deformed Test Assembly

The deformed test assembly test is designed to provide CFD validation pertaining to later in life fuel assembly geometries following duct dilation. To provide sufficient development length (2.25 pitches) and exit length (0.25 pitches), as well as adequate axial length for duct expansion and duct contraction characteristic of duct deformation, the test section needs to be at minimum 5.5 wire pitch lengths, where the deformation will occur over 3 wire pitch lengths after the development length. Similar to the non-deformed bundle, at P=0, the clocking position of the wire should be such that at the axial height of P=2.25, the wire clocking shall be such that it is pointed towards the corner between duct faces A and F. Table 7 indicates pressure predictions for a 5.5 pitch length bundle with a non-deformed duct geometry to provide a conservative estimate for ensuring duct pressure limits are maintained. The expected pressure loss with bypass flow in the external subchannels will be less than this conservative value.

The duct deformation is to be over the ranges of P=2.25 to P=5.25 and the peak displacement from the nominal non-deformed geometry is defined as indicated in figure 10. Peak deformation of 1.84 mm is located midway along the axial span over which the deformation is defined (P=3.75) and at the center of each face of the duct. Peak flow area increase is approximately 6.1% at the axial height corresponding to maximum duct deformation. Functional forms of deformation are provided to simplify geometry definition. Final CAD geometry will be provided by TerraPower to TAMU for manufacturing.

Table 6. Dilated Duct Values

Parameter	Value	units
Dilation of inner duct surface in functional form *	$y = \left[\frac{D_{max}}{2} * cos\left(\frac{x * \pi}{s/2}\right) + \frac{D_{max}}{2}\right] * sin\left(\frac{(z) * \pi}{z_{tot}}\right)$	
x, y, z coordinate directions (with respect to dilation; unique for each duct face)	See image below	
D_{max}	1.84	mm
s (duct side length)	88.81	mm
Total dilation length (z_{tot})	1428.8	mm
Beginning of Dilation	P = 2.25 (Z = 0 in equation above)	

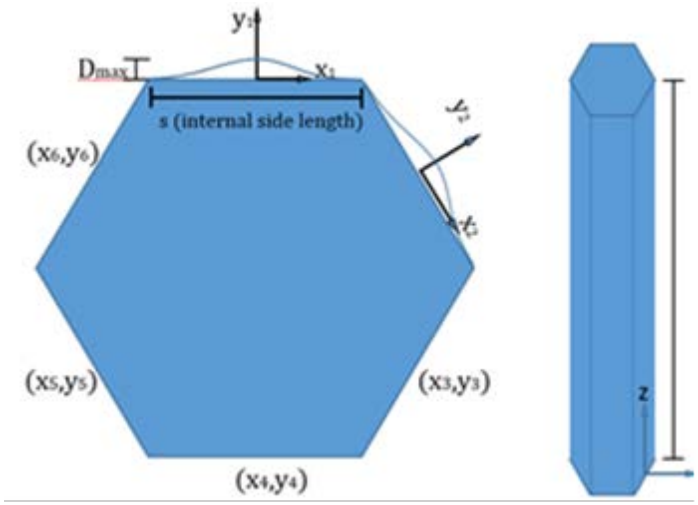


Figure 10: Deformed duct definition for the TAMU deformed assembly flow test

Deformed Duct Dimensions

- Risk – Duct deformation features (y = f(x, z) from Figure 10) may not be achievable.
- Basis – Selected materials and construction techniques limitations may not allow the desired shape.
- Mitigation – Final dimensions and shape may be changed based on the inputs from the manufacturer. Alternative construction techniques may be investigated.

As in the case of the non-deformed fuel assembly, the pins shall be bound together with ultra-thin stainless steel wire to control P/D as well as provide increased resistance to flow induced vibration. For this test, pressure measurements taken at the locations corresponding to those indicated in table 7. The suggested LDV (table 8) and PIV (table 9) measurements within the bypass region are to be designed to capture the influence of the change in cross sectional area of the outer subchannel and the subsequent excursion of flow from the interior subchannels to the outer regions. Additionally, LDV and PIV measurements should capture the impact of the reduction in flow area in the outer subchannels as the duct walls contract back towards the fuel pins. The exact measurement locations and number are to be defined during shakedown tests and during pre-test CFD predictions within an updated measurement specification document to be issued after shakedown testing. The following locations are only defined as preliminary measurement locations and it should be noted the number of locations indicated here are not indicative of the final number of measurements pending prioritization of measurements in the measurement specification. The same risks and mitigation approaches exist for the deformed bundle as in the non-deformed bundles.

Table 7: Conservative Predicted Flow Conditions for TAMU facility for long duct configuration.

	Value	Unit	Alternate Units	
Viscosity	0.000876	Pa-s		
Density	857	kg/m3		
Non-deformed Flow area	0.00799	m2		
Length	2.619	m		
Fluid	Pcymene			
Reynolds	20000			
Operating Temperature	25	C		
mdot (kg/s)	18.18	kg/s		
q (watts)	n/a			
vel m/s	2.66	m/s		
Volumetric Flow Rate (gpm)	336.19	gpm		
DP (Pa)	29,484.6	Pa	4.276	PSI
Friction Factor (Cheng & Todreas)	0.0287			
Cbt	0.170			
H/D	30			
P/D	1.189			
# of pitches	5.5			
Pitch Length	0.476	m		
Hydrostatic head within bundle	22,021.5	Pa	3.194	PSI
Total Pressure at bottom of bundle (15% margin)	59,232.0	Pa	8.59	PSI

Table 8: Pressure Tap Locations for deformed configuration

Pressure Tap Identifier(s)	Axial Location
PT #D0 (Installed During Construction)	Inlet plenum PT following flow straightener prior to position P=0. Tap location TBD in development of facility P&ID.
PTs #D1b-D4b (Installed During Construction)	PT along duct face B at locations P=0 (or within 1 rod diameter if space limited by the flange), P=1, P=1.75, and P=2.0
PTs #D5a-D5d (following all flow visualization tests)	PTs at axial position P=2.25 along duct faces A to D giving a total of 4 pressure tap locations at this axial height for pressure asymmetry measurements.
PTs #D6a-D6d (following all flow visualization tests)	PTs at axial position P=3.75 along duct faces A to D giving a total of 4 pressure tap locations at this axial height for pressure asymmetry measurements.
PT #D7b (following all flow visualization tests)	PT at height P=5.25 centered on duct face B.
PT #D8 (Installed During Construction)	PT located after outlet plenum following flow 'collection' into common outlet. Tap location TBD in development of facility P&ID.

Table 9: Preliminary LDV Measurement Locations for deformed test configuration – Actual locations and quantity to be determined based on shakedown

LDV Measurement Identifier(s)	Location
LDV IP #D0-DN	Inlet Plenum profile characterization at P= -0.5m from flat to flat in each of the three directions orthogonal to the duct walls
LDV OSP #D1– DN	Outer subchannel measurement of development length between heights P=2.25 and P=5.25 with axial spacing of P/3, in addition to measurements at the maximum dilation plane of P = 3.75.
LDV LP #D1 – DN	Wall Effect Line probes at axial heights between P=2.25 and P=5.25 with axial spacing equivalent to P/3, in addition to measurements at the maximum dilation plane of P = 3.75 and line probe measurements taken along the line indicated in figure 6. Line Probe measurement spacing should be 1/2 of one wire diameter.
LDV GS D1 and DN	Grid sweeps in one external subchannel, one corner subchannel, and one internal subchannel. One grid sweep should be done with an LDV scan capturing axial velocity and one horizontal component. Another set of grid sweeps should be done from above to capture horizontal velocity components in order to verify PIV measurements indicated by PIV HP #1-X in table 8.

Table 10: Preliminary PIV Measurement Locations for deformed test configuration – Actual locations and quantity to be determined based on shakedown

PIV Measurement Identifier(s)	Location
PIV VP OSC #1 – N	Outer sub-channel in vertical planes direction at P=2.25 through P=5.25
PIV VP ISC #1 – N	Inner sub-channel in vertical planes direction at P=2.25 through P=5.25
PIV HP # 1- N	Horizontal sub-channel measured from above bundle. Measurement planes should be captured at P=3(flow excursion), P=3.75 (maximum bypass), and P=4.5(flow re-introduction). These measurements might be taken at location and sub-channel locations that correspond to different wire clocking angles relative to the parent pin.

2 REPORTING

Acceptance criteria include demonstration of stable instrumentation signals (i.e., no data drift) with quantified variability for all dP, flow and temperature measurements. Any duplicate measurements (e.g. flowrate) shall be documented and provided. Data should be provided in metric (MKS) units. Formatting of final data package are to be established as part of the measurement specification document.

Laboratory best practices and procedures for quality assurance will be followed in this experiment program and follow Augmented Quality Requirements as given in the Appendix, which is met by adherence to the TAMU Wire-Wrapped QA Guidelines [2]. This includes using calibrated measurement equipment; providing and following written procedures for test execution; inspection, measurement and documentation of test geometry, test conditions, measurements and uncertainties; reviews to verify that activities are being satisfactorily accomplished; and following methods to take corrective action as needed with respect to procedures, documentation or nonconforming items.

3 REFERENCES

[1] Cheng, S and Todreas, N.E. “Hydrodynamic Models and Correlations for Bare and Wire-Wrapped Hexagonal Rod Bundles – Bundle Friction Factors, Subchannel Friction Factors and Mixing Parameters”, Nuclear Engineering and Design 92 (1986)

[2] TAMU Wire-Wrapped QA Guidelines, Document TAMU-WW-QA Revision 0, Project # DE-NE0008321, Optical Diagnostic Flow and Thermal Science Laboratory at Texas A&M University, 2016.

4 APPENDIX

This appendix provides the augmented quality assurance requirements and guidance for implementation of these requirements to this test specification. The following identifies the applicable augmented Quality Assurance Requirements and the measures that should be taken for compliance. Testing for this Test Specification will be performed in accordance to the TAMU Wire-Wrapped QA Guidelines to meet these requirements.

ITS – Augmented Quality Requirements

1. Organization

Measures shall be established for verification of compliance with the requirements of this plan. The normal line organization may verify compliance with the requirements of this plan. A separate or dedicated quality assurance organization is not required.

2. Quality Assurance Program

Quality controls that apply to the work shall be documented. It is expected that the existing body of supplier's procedures or practices will describe the quality controls applied to the subject equipment (or service). A new or separate QA program is not required.

3. Design Control

3.1. Procedures shall describe the process for ensuring that:

- All design requirements are incorporated into the design
- Applicable design inputs are included or correctly translated into design documents
- Deviations from the design inputs are controlled
- Changes to design outputs are identified, controlled, and properly disseminated

3.2. Procedures shall define internal and external interfaces and requirements for coordinating design processes that affect or depend on other disciplines or organizations.

3.3. Design inputs relating to item requirements shall be determined and records maintained. These inputs shall include:

- Functional and performance requirements
- Applicable statutory and regulatory requirements
- Where applicable, information derived from previous similar designs
- Where applicable, information derived from testing or analyses
- Other requirements essential for design and development

3.4. Design outputs shall be in a form suitable for verification against the design inputs and shall be approved prior to release.

3.5. Design outputs shall:

- Meet the input requirements
- Provide appropriate information for purchasing and production
- Contain or reference acceptance criteria
- Specify the characteristics of the item that are essential for its intended performance

3.6. Procedures shall establish when design reviews are performed. Design reviews shall be performed to evaluate the ability of the results of the design to meet requirements, and to identify any problems and propose necessary actions.

Normal supervisory review of the designer's work is an adequate control measure as long as the supervisor is technically qualified to perform that review. However, TP management may require independent review for certain work tasks. Records of the results of the reviews shall be maintained.

3.7. Design verification shall be performed in accordance with procedures to ensure that the design outputs have met the design input requirements. Records of the results of the verification and any necessary actions shall be maintained.

3.8. Design changes shall be identified and records maintained. The changes shall be reviewed, verified and validated, as appropriate, and approved before implementation. The review of

design changes shall include evaluation of the effect of the changes on other in-process or completed design. Records of the results of the review of changes and any necessary actions shall be maintained.

4. Procurement Document Control

Applicable design bases and other requirements necessary to assure component performance, including design requirements, shall be included or referenced in documents for procurement of items and services, and deviations therefrom shall be controlled.

5. Instructions, Procedures, and Drawings

Activities affecting quality shall be performed in accordance with documented instructions, procedures, or drawings of a type appropriate to the circumstances, and that include acceptance criteria, where applicable, to determine that the work has been performed correctly. This may include such things as written instructions, plant procedures, cautionary notes on drawings, and special instructions or work orders. Any methodology which provides the appropriate degree of guidance to personnel performing activities important to component functional performance will satisfy this requirement.

6. Document Control

The issuance and change of documents that specify quality requirements or prescribe activities affecting quality shall be controlled to assure that correct documents are employed.

7. Control of Purchased Items and Services

Measure are to be established to ensure that all purchased items and services conform to appropriate procurement documents.

8. Identification and Control of Purchased Items

Measures shall be established, where necessary, to identify purchased items and preserve their investment protection important functional performance capability. Examples of circumstances requiring such control include the storage of environmentally sensitive equipment or material, and the storage of equipment or material that has a limited shelf-life.

9. Control of Special Processes

Measures shall be established to control special processes, including welding, heat treating, and non-destructive testing. Applicable codes, standards, specifications, criteria, and other special requirements may serve as the basis of these controls.

10. Inspection

Inspections shall be performed where necessary to verify conformance of an item or activity to specified requirements, or to verify that activities are being satisfactorily accomplished.

11. Test Control

Measures shall be established, as appropriate, to test items, equipment or material prior to installation to demonstrate conformance with design requirement. Tests shall be performed in accordance with test procedures. Test results shall be recorded and evaluated to ensure that test requirements have been met.

11.1. Procedures shall describe the requirements for software testing. The level of test control shall be commensurate with the determined safety classification of the design work being performed with the software.

11.2. Testing performed directly or by contracted companies shall be performed in accordance with documented and approved requirements. Such requirements will be contained in applicable procedures or work instructions and, for contracted testing, conveyed in applicable procurement documents. Establishment of test requirements shall be determined by the manager that will use the test results in the design or specification. Tests are performed in accordance with test procedures or plans that are prepared by the organization performing the test, or under TP procedures when contracted testing is performed under the TP quality assurance program.

12. Control of Measuring and Test Equipment

Measures shall be established to control, calibrate, and adjust measuring and test equipment at specific intervals.

13. Handling, Storage, and Shipping

Handling, storage, cleaning, packaging, shipping, and preservation of items shall be controlled to prevent damage or loss and to minimize deterioration.

14. Inspection, Test, and Operating Status

Measure shall be established to identify items that have satisfactorily passed required tests and inspections, and to indicate status of inspection, test, and operability as appropriate.

15. Control of Nonconforming Items

Items that do not conform to specified requirements shall be identified and controlled to prevent inadvertent installation or use.

16. Corrective Action

Measure shall be established to ensure that failures, malfunctions, deficiencies, deviations, defective components, and noncompliance are properly identified, reported, and corrected.

17. Records

Records shall be prepared and maintained to furnish evidence that the above requirements for design, procurement, document control, inspection, and test activities have been met.

18. Audits

Audits or periodic reviews shall be conducted and documented to verify compliance with design and procurement documents, instructions, procedures, drawings, and inspection and test activities. Audits which are independent of line management are not required if line management periodically reviews and documents the adequacy of the supplier's processes and takes any necessary corrective action. Line management is responsible for determining whether reviews conducted by line management or audits conducted by an organization independent of line management are appropriate.

APPENDIX H: TWRP-31-TREP-0004, AFAFC BENCHMARK SPECIFICATION

Thermal Hydraulic CFD Simulations and Experimental Investigation of Deformed Fuel Assemblies

U.S. Department of Energy
DE-NE0008321
DUNS # 789479578

Document Title:	AFAFC Benchmark Specification
Document Number:	TWRP-31-TREP-0004
Prepared By:	TerraPower
Date:	2/22/2016
Revision:	0

Name	Title / Company	Signatory Role	Signature	Date
Brian Jackson	Technical Rep. / TerraPower	Preparer		2/22/16
Tom Galioto	Project Manager / AREVA Fuels	Approver		5.2.16
Elia Merzari	Technical Rep. / Argonne National Lab	Approver	See Below	
Rodolfo Vaghetto	Technical Rep. / Texas A&M University	Recipient		05/16/16
Anthony Chang	Project Manager/ AFS	Recipient		3/15/16
Brian Mays	Principal Investigator / AFS	Recipient		2/24/16

Thermal Hydraulic CFD Simulations and Experimental Investigation of Deformed Fuel Assemblies

U.S. Department of Energy
DE-NE0008321
DUNS # 789479578

Document Title:	AFAFC Benchmark Specification
Document Number:	TWRP-31-TREP-0004
Prepared By:	TerraPower
Date:	2/22/2016
Revision:	0

Name	Title / Company	Signatory Role	Signature	Date
Brian Jackson	Technical Rep. / TerraPower	Preparer		2/22/16
Tom Galioto	Project Manager / AREVA Fuels	Approver		
Elia Merzari	Technical Rep. / Argonne National Lab	Approver		3/18/16
Rodolfo Vaghetto	Technical Rep. / Texas A&M University	Recipient		
Anthony Chang	Project Manager/ AFS	Recipient		3/15/16
Brian Mays	Principal Investigator / AFS	Recipient		2/24/16

Record of Revisions			Revision: 0
Item #	**Description of Change**	**Effected Pages / Sections**	**Change Initiator**

ENGINEERING REPORT

Document Number:	TWRP-31-TREP-0004	**Revision:**	0
Document Title:	AFAFC Benchmark Specification	**Approval Date** *(Final Signature Date)***:**	2/22/2016
Issuing Organization:	Core Design	**Effective Date** *(for Procedures Only)***:**	
		Pages:	Page 1 of 16

Approval

Title	Name	Signature	Date
Originator, Thermal Hydraulics Test and Analysis Engineer	Brian Jackson	Approved in Agile	2/17/2016
Reviewer, Computational Fluids Dynamics Post Doc	Daniel Leonard	See attached	2/22/2016
Reviewer, Manager, Thermal Hydraulic Test & Analysis	Mike Steer	Approved in Agile	2/18/2016
Approver, Manager, Design Qualification	Rob Corbin	Approved in Agile	2/22/2016

Document Safety Classification per TWRP-NS-PROC-0002 ('N/A' for Procedures / policies / manuals / guides): Safety-Related ☐ Non-Safety Related ☒ Augmented Quality ☐ N/A ☐

QA Criterion (Select 'N/A' for documents other than procedures/policies/manuals/guides): N/A

TerraPower

ENGINEERING REPORT

Document Number:	TWRP-31-TREP-0004	**Revision:**	0
Document Title:	AFAFC Benchmark Specification	**Approval Date** *(Final Signature Date)*:	
Issuing Organization:	Core Design	**Effective Date** *(for Procedures Only)*:	
		Pages:	Page 1 of 16

Approval

Title	Name	Signature	Date
Originator, Thermal Hydraulics Test and Analysis Engineer	Brian Jackson		
Reviewer, Computational Fluids Dynamics Post Doc	Daniel Leonard		2/22/16
Reviewer, Manager, Thermal Hydraulic Test & Analysis	Mike Steer		
Approver, Manager, Design Qualification	Rob Corbin		

Document Safety Classification per TWRP-NS-PROC-0002 ('N/A' for Procedures / policies / manuals / guides): Safety-Related ☐ Non-Safety Related ☒ Augmented Quality ☐ N/A ☐

QA Criterion (Select 'N/A' for documents other than procedures/policies/manuals/guides): N/A

Revision History

Revision No.	Effective Date	Affected Section(s)	Description of Change(s)
0	2/22/2016		Initial release

TABLE OF CONTENTS

1 OBJECTIVE AND PURPOSE 4
1.1 Summary 4
2 INTRODUCTION AND BACKGROUND 5
3 EXPERIMENT GEOMETRY AND TEST CONDITION 6
3.1 Experiment Geometry 6
3.2 Operating Conditions 6
4 BENCHMARK MEASUREMENTS 7
4.1 Heated Bundle Measurements 7
4.2 Flow Visualization Measurements 9
5 MODELING METHODOLOGY 11
5.1 Computational Domain Geometry 11
5.2 Boundary Conditions 12
5.3 Wire Wrap Modeling Approximations 13
5.4 Transient Modeling Methods 13
5.5 Results Extraction 13
6 MODELING ASSUMPTIONS 14
7 CFD BENCHMARKING METHODS 14
7.1 StarCCM+ Verification 14
7.2 Nek5000 Verification 14
7.3 Validation Comparisons 14
7.4 Simulation Validation 15
8 REFERENCES 16

LIST OF TABLES

Table 1-1. Document Summary of V&V Project 4
Table 4-1. Heated Bundle Instrumentation 8

1 OBJECTIVE AND PURPOSE

The purpose of this benchmark specification document is to provide a description of the verification and validation (V&V) plan to be implemented for the Advanced Fuel Assembly Flow Characterization (AFAFC) Department of Energy (DOE) grant 1163 titled "Toward a Longer-Life Core: Thermal Hydraulic Computational Fluid Dynamics (CFD) Simulations and Experimental Investigation of Deformed Fuel Assemblies" such that the work scope is fully defined to ensure success of this V&V project, and that the data produced is complete to be used as an available validation dataset for future validation efforts. This document provides the basis for description of the experiments, numerical simulation methods, reporting requirements, and benchmarking methods: this information is contained herein, or in referenced project documents (listed below). The project includes two experimental programs to be performed at AREVA Fuels and Texas A&M University, and two numerical modeling programs to be performed at TerraPower and Argonne National Laboratory (ANL).

1.1 Summary

Fundamental to a successful verification and validation effort is appropriate documentation. Proper documentation of the experiment component of the project allows measured results to be used as a validation dataset for later studies. The following table lists the documents that will be produced and the information that these documents will contain that is needed for a successful V&V project. The final project report will contain a summary of all critical information used for the V&V tasks of the project, as well as complete information needed to use the datasets in later V&V efforts.

Table 1-1. Document Summary of V&V Project

Item	Document	V&V Related Information Contained in Document
1	Benchmark Specification	Description of benchmark measurements, CFD methodologies
2	Heated Bundle Test Specification [1]	Bundle geometry design, operating conditions, and measurement types and locations
3	Flow Visualization Test Specification [2]	Bundle geometry design and operating conditions
4	Heated Bundle Geometry Design Drawings [3]	Engineering design drawings of bundle components
5	Flow Visualization Design Drawings [4]	Engineering design drawings of bundle components
6	Heated Bundle As-Built Geometry	As built drawings of bundle components
7	Flow Visualization Bundle As-Built Geometry	As built drawings of bundle components
8	Flow Visualization Measurement Specification Document	Measurement types and locations following measurement shakedown phase
9	Heated Bundle Test Procedure	Operating and measurement procedures
10	Flow Visualization Test Procedure	Operating and measurement procedures
11	Heated Bundle Test Report	As tested conditions and measurement results. May reference data files with measurements.
12	Flow Visualization Test Report	As tested conditions and measurement results. May reference data files with measurements.
13	LES Nek5000 Pre-Test Simulation Report	Experiment as-designed geometries, simulations boundary conditions, methods and results. May reference result data files.
14	LES Nek5000 Post-Test Simulation Report	Experiment as-tested geometries, simulation boundary conditions, methods and results. May reference result data files.
15	RANS StarCCM+ Pre-Test Simulation Report	Experiment as-designed geometries, simulation boundary conditions, methods and results. May reference result data files.

Item	Document	V&V Related Information Contained in Document
16	RANS StarCCM+ Post-Test Simulation Report	Experiment as-tested geometries, simulation boundary conditions, methods and results. May reference result data files.
17	Final Project Report	Will contain or reference all information describing the verification and validation performed under the project, and information needed to use datasets in later V&V efforts.

2 INTRODUCTION AND BACKGROUND

The DOE grant 1163 is a CFD verification and validation study that consists of both experimental and simulation work scopes to study fluid and heat transfer in a generic fast reactor wire wrapped fuel assembly at both nominal geometry conditions and with a deformed duct geometry. The test geometry is a 61 helically wire wrapped pin bundle to be run at turbulent flow conditions using simulant fluids in lieu of sodium. The project includes two experiment programs and two numerical simulation programs modeling the experiments:

1. Heated bundle, temperature and pressure drop measurement experiments to be performed at AREVA Fuels in Richland, Washington [1]

2. Isothermal matched index of refraction (MIR) experiments measuring local velocities and pressure drops to be performed at Texas A&M University [2].

3. 2-equation RANS industry standard CFD pre-test and post-test simulations performed at TerraPower with the StarCCM+ CFD software.

4. Spectral Element Large Eddy Simulations pre-test and post-test simulations performed by Argonne National Laboratory with the Nek5000 code.

The bundle size dimensions including duct, pin diameter and wire diameter are different for the two experimental programs due to the unique flow loops and measurement methods to be employed. However, for comparisons of the physical flow phenomena in the experiments, the two experiments will test at the same Reynolds number, and the pin pitch to pin diameter ratio (P/D) geometry is within 0.7%. Due to the duct fabrication methods for the two experiments, the hexagonal duct corners are different in the two experiments. The heated bundle uses rounded corners, more prototypic of generic fast reactor fuel assemblies, while the MIR bundle uses a sharp corner geometry.

The heated bundle experiment design uses heater rods for 19 of the 61 pins. The other pins will be non-heated tubes. The heaters and non-heated tubes of the bundle are fabricated with more than 250 total thermocouples to provide point measurements for use in CFD validation. Thermocouples in the heater rods measure internal clad temperatures, while the non-heated tube thermocouples measure fluid water temperature at the tube external surface. Pressure transducers will also be used to measure pressure drop across various pin bundle lengths. The pins are configured in a hexagonal packing arrangement and contained in a hexagonal duct. The pin bundle length consisting of both pins and the duct is approximately 14 wire pitches in length, with a heated length of 6 wire pitch lengths. The deformed duct has cosine shaped dilation of the inner walls bowing outward in the axial direction and the lateral directions between duct corners. The dilation is symmetric for all duct faces. The dilation occurs over the 6 wire pitch heated length with a maximum dilation occurring at the axial mid-height of the heated length. This enlarges the flow area in this region with respect to the nominal duct geometry case.

The isothermal matched index of refraction experiments will be run at Texas A&M University. The pins, wires and duct walls in the measurement region will be constructed of acrylic and the loop will use p-cymene as the working fluid thus matching the index of refraction between fluid and solid components. Internal bundle velocities will be measured using laser Doppler velocimetry (LDV) and Particle Image Velocimetry (PIV). The total length of these bundles are 3.5 wire pitch lengths for the

nominal geometry, and 5.5 wire pitch lengths for the deformed bundle. Pressure transducers will also be used to measure bundle pressure drops.

Simulations of the experiment cases will be run at TerraPower and Argonne National Laboratory (ANL). Simulations at TerraPower will use StarCCM+ to run industry standard 2-equation RANS models. These simulations do not explicitly model the wire wrap geometry, but instead use simplifying methods to model the wire wrap that decrease the meshing requirements of the computational domain. ANL will model the experiments using the Nek5000 spectral element Large Eddy Simulation code. Both pre-test and post-test simulations will be conducted by TerraPower and ANL. The pre-test simulations will be conducted with the as-designed geometric and operational parameters. If needed, post-test simulations will be conducted with as-built and as-tested conditions if they are found to differ appreciably from the as-designed dimensions and conditions. Both the pre-test and post-test simulations will be conducted blind with respect to the experiment data. For each of the pre- and post-test simulations, each simulation program will run cases of the 4 tests:

(1) Heated bundle nominal geometry experiment

(2) Heated bundle deformed duct experiment

(3) MIR nominal geometry experiment

(4) MIR deformed duct experiment

There are some potential numerical sensitivity studies that may be performed following availability of the test data.

3 EXPERIMENT GEOMETRY AND TEST CONDITION

This chapter summarizes the geometric designs of the experiments and operational set points at which the validation data will be collected. Full descriptions of this information is not contained herein, but in the test specification documents.

3.1 Experiment Geometry

Test specifications for each of the experimental programs were produced that contain the geometry and operational set points of the experiments [1], [2]. From the design information in the test specifications, engineering drawings are produced for the bundle components (pins, duct walls, etc.) [3], [4] which are used for fabrication of the test sections. The test specification fully defines the fluid domain bundle geometry consisting of pins, wires and internal duct wall boundaries. However, the engineering drawings provide additional information such as wall thicknesses, wire attachment design detail, and upstream and downstream flow geometry. These as-designed geometries are used in the pre-test simulations.

During fabrication and acceptance of experiment test sections and loop hardware, as-built measurements of the components and test sections will be obtained and released through as-built experiment test section reports, or as part of an as-built released drawings package. These updated as-built dimensions will be documented and used in the post-test simulations, as necessary.

3.2 Operating Conditions

The design operating conditions for the experiment programs are provided in the Test Specification documents [1], [2]. Operating conditions correspond to a turbulent Reynolds number of 20,000. Pre-test simulations will use the design inlet flowrate and fluid temperature for both experiments, and the design heater power for the heated bundle case, including heater position configuration, heated length, and heat flux profile.

During operation of the tests, the boundary conditions will be measured and documented in the Test Reports. Post-test simulations of the heated bundle will include the as-tested operating conditions including inlet flowrate, inlet fluid temperature and measured heat flux detail. As part

of the MIR bundle experiments, the inlet velocity distribution will be characterized with laser based velocity measurements, and therefore will be included as boundary condition inputs for the post-test simulations of this experiment.

Both experiments are designed to be thermally insulated from the environment. In the heated bundle case, temperature measurements will be taken on the outside of the duct to ensure this assumption, or as needed, to provide input and inclusion in post-test simulations.

4 BENCHMARK MEASUREMENTS

This section describes the measurements that will be taken to be used for the CFD benchmarking. This includes the as-built measurements, boundary conditions, CFD benchmarking measurement instruments, CFD benchmarking measurement locations, and CFD benchmarking measurement types. Each experiment test program is presented individually in this section.

4.1 Heated Bundle Measurements

The CFD benchmarking measurements in the heated bundle include point temperature measurements and pressure drops. Boundary conditions consist of the geometry of the test assembly, inlet flow conditions, outlet conditions, pin power detail, and duct outer wall thermal conditions.

4.1.1 Heated Bundle As-Built Measurements

The following lists the as-built geometry detail of the heated bundle that will be measured and documented in the as-built reporting and Test Report.

1. Duct geometry. This includes duct length, inner and outer flat-to-flats measured for the 3 flat-to-flat pairs at different axial positions, duct skewness, and deformed geometry deformation.

2. Heater diameters. The heater fabricator of the 19 heater rods will report pin diameters of all heaters taken at different axial heights and at different azimuthal rotation positions.

3. Non-heated tubes. Similar to the heater rods, the non-heated tubes will be measured for outer diameter.

4. Wire wrap. The wire wrap has an associated tolerance from the manufacturer. Measurements of the outer diameter will be taken along different lengths of the wire and at different azimuthal rotation positions.

5. Wire wrap positioning. The as-built wire wrap positioning will be measured and reported. Following testing, verification will be performed to ensure wire wrap positioning was maintained from pre-test conditions. This includes wire wrap clocking position at wire termination positions and associated axial heights, and the wire pitch lengths.

6. Pin clocking position in duct. The wire wrap of all pins rotates around the pins in phase. Measurements will be taken to record wire wrap upper termination clocking.

7. The inlet plenum and outlet plenum geometry will be recorded. It is not expected that this flow geometry will affect the bundle flow phenomena, however measurements of the geometry detail will be recorded and available. It is expected the need of their use will be evident after the pre-test simulations.

8. Pin location configuration. Each heater and non-heated tube will have a unique ID number. Their location in the assembly will be recorded. This is necessary

because different heater and non-heated tubes use different thermocouple positions.

9. Pin assembly configuration. Thermocouples are fixed in position to measure fluid temperature in the wall subchannels. Therefore the pin assembly rotation configuration in the duct will be recorded.

10. Pin assembly vertical position. The vertical position of each heater and non-heated tube will be verified and recorded. Given the internal heating element, and thermocouples in these parts, vertical positioning with respect to the duct is needed.

4.1.2 Heated Bundle Instrumentation Locations

The bundle is instrumented with thermocouples and pressure transducers for use as CFD benchmarking data. The table below presents the instrument count for the heated bundle to be used for CFD comparison. It is possible that some of the instruments may provide unreliable data from the experiments. The large number of instruments ensures that sufficient experiment data will still be available for CFD validation. The bundle is instrumented with heater rod thermocouples, non-heated tube thermocouples, and internal duct wall thermocouples for CFD validation. In addition, thermocouples will be used to measure outer duct wall temperatures and inlet fluid temperatures to confirm flow loop boundary conditions. The bundle is instrumented with 30 pressure taps along the duct walls to measure axial pressure drop. In addition to the 30 duct wall pressure taps, pressure measurements will be taken at 8 internal bundle locations through use of non-heated tubes.

Table 4-1. Heated Bundle Instrumentation

Parameter	**Quantity**
Heater Rod Thermocouples	154
Non-Heated Tube Thermocouples	132
Internal Duct Wall Thermocouples	24
Duct Wall Pressure Taps	30
Internal Pressure Taps	8

Specific instrument location specification is provided in the Test Specification [1]. The following lists the instrument location detail to be recorded. Since most of the thermocouples are internal to the heaters and non-heated tubes, most of these measurements will be taken on the individual components before installation in the assembly or during acceptance of the externally contracted parts.

1. Heater rod thermocouples. STERN Labs will verify thermocouple positions following fabrication.

2. Non-heated tube thermocouples. TerraPower with its associated contractor will specify, then measure and record as-built positions. Each tube has a unique ID number, and the tube will have a marking to provide an azimuthal reference position.

3. Duct pressure tap. TerraPower with its associate contractor will specify, then measure and record as-built positions

4. Duct internal thermocouples. Thermocouples will measure the fluid temperature in specific wall subchannels by being run through the duct wall from the outside. TerraPower and its associated contractor will specify, then measure and record as-built positions.

5. Duct outer thermocouples. Thermocouples will measure the outer duct wall temperature to quantify duct heat loss. AREVA Fuels will measure and record the as-installed locations of these thermocouples.

6. System measurements. System measurements include loop fluid temperature, pressure and flowrate. AREVA Fuels will record where these measurements are taken.

4.1.3 Heated Bundle Measurement Outputs

Time averaged measurements will be produced from the heated bundle experiments. Procedures for data collection will be described in the Test Procedures documents. Methods will be effected to ensure instrument calibration, steady state operation, and sufficient data acquisition time for uncertainty reduction. This data will be documented in the test report. Due to the large amount of numerical data from the tests, accompanying .csv or excel files will be produced and time stamped as the test data package for storage to be publicly available. The following lists the measurements from the heated bundle tests.

1. Thermocouple measurements. For each thermocouple, time averaged values with associated uncertainties, rms fluctuations with associated uncertainties, measurement time, and sampling rates, shall be recorded and reported. The measurements will be reported in degrees Celsius.

2. Pressure drop measurements. For each pressure tap pair, time averaged values with associated uncertainties, rms fluctuations with associated uncertainties, measurement time, and sampling rates shall be recorded and reported. The measurements will be reported in Pascals.

3. System measurements. System measurements of temperature, pressure and flowrate shall include time averaged values and associated uncertainties, rms fluctuations with associated uncertainties, measurement times and sampling rates.

4.2 Flow Visualization Measurements

Laser based measurements will be used in the flow visualization bundle experiments to measure point velocities. In addition, pressure drops across different axial sections of the bundle will be measured. Boundary conditions consist of the geometry of the test assembly, inlet flow conditions, and outlet conditions.

4.2.1 Flow Visualization As-Built Measurements

The following shall be reported following the bundle fabrication and loop installation.

1. Duct Geometry. This includes duct length, inner and outer flat-to-flats measured for the 3 flat-to-flat pairs at different axial positions, duct skewness, and deformed geometry deformation.

2. Pin diameters. Pin outer diameters will be measured at different axial heights and different azimuthal rotation positions.

3. Wire wrap. The acrylic wire wrap has an associated tolerance from the manufacturer. Measurements of the outer diameter will be taken along different lengths of the wire and at different azimuthal rotation positions.

4. Wire wrap positioning. The as-built wire wrap positioning will be measured and reported. This includes wire wrap clocking position at wire termination positions and associated axial heights. Wire pitch and wire pitch consistency will be measured and recorded. Wire wrap movement during tests will be also reported.

5. Pin assembly position in duct. The wire wrap of all pins rotates around the pins in phase. Measurements will be taken to record wire wrap clocking position in the duct and pin position with respect to the duct. Pressure measurements will be taken by tapping the duct wall, therefore pin assembly positioning in the duct is necessary.

6. The inlet plenum and outlet plenum will be recorded. It is not expected that this flow geometry will affect the bundle flow phenomena, however measurements of the geometry detail will be recorded and available. It is expected the need of their use will be evident after the pre-test simulations.

7. Pin assembly vertical position. The vertical position of the pin assembly in the duct will be measured.

4.2.2 Flow Visualization Bundle Measurement Locations

The laser based measurement techniques of Particle Image Velocimetry (PIV) and Laser Doppler Velocimetry (LDV) will be used to measure local velocities in the flow visualization bundle. Internal bundle velocities are able to be captured through the use of the matched index of refraction method. Due to the challenges with these types of measurements, the specific locations and measurement acquisition times will be finalized during the measurement shakedown phase of the MIR bundle test program. Factors that affect these measurements include seeding density, acquisition times, local fluctuations, surface reflections and others. Therefore, listed here are the types of measurements that will be acquired from this bundle. Further detail of the planned locations and descriptions of the types of measurements is provided in the test specification [2]. A measurement specification document will be produced following the instrumentation shakedown which will define updated and prioritized measurement locations.

Pressure Measurements

1. Pressure drop measurements to capture flow development.

2. Multiple pressure measurements at specific axial planes to capture the pressure field asymmetry due to wire wrap.

3. Axial pressure drop across various lengths of the bundle.

Laser Doppler Velocimetry Measurements

1. Inlet velocity profile to quantify flow profile at the inlet.

2. Wall subchannel measurements at intervals in the axial direction.

3. Inner subchannel measurements at intervals in the axial direction.

4. Cross bundle measurements from the wall subchannels into the bundle to measure internal subchannel velocities as well.

5. High resolution point measurements for specific subchannels and heights for use in PIV validation

Particle Image Velocimetry Measurements

1. Vertical plane outer subchannel measurements to capture the expected bulk swirl.

2. Vertical plane measurements from the wall into internal subchannels.

3. Horizontal plane subchannel measurements for wall and internal subchannels.

4.2.3 Flow Visualization Bundle Measurement Outputs

The following data will be presented in the test report. In addition, due to the large amount of numerical data from the tests, accompanying .csv or excel files will be produced and time stamped to be publicly available.

1. Measurement location detail. Locations of the laser based measurements taken, and the pressure tap locations will follow the reference position convention presented in the Test Specification document [2].

2. LDV measurements. For each LDV measurement set, time averaged values of velocity components as well as fluctuating components should be reported with associated uncertainties. Measurement time and sampling rates shall be reported as well. Sufficient documentation should be provided to back-up uncertainty values, calibration, and measurement location confidence either for individual measurements or for a given measurement set that shares similarity. Measurement values will be reported in metric units.

3. PIV measurements. For each PIV measurement plane, time averaged values of velocity components as well as fluctuating components should be reported with associated uncertainties, in addition to measurement time and sampling rates. Sufficient documentation should be provided to back-up uncertainty values, calibration, and measurement location confidence either for individual measurements or for a given measurement set that shares similarity. Measurement values will be reported in metric units

4. Pressure drop measurements. For each pressure tap pair, time averaged values with associated uncertainties, rms fluctuations with associated uncertainties, measurement time, and sampling rates shall be recorded and reported. The measurements will be reported in Pascals.

5. System measurements. System measurements of temperature, pressure and flowrate shall include time averaged values and associated uncertainties, rms fluctuations with associated uncertainties, measurement times and sampling rates.

5 MODELING METHODOLOGY

Simulations will be performed using 2-equation turbulent modeling with the industry code STARCCM+ and also with the spectral element Large Eddy Simulation code NEK5000.

5.1 Computational Domain Geometry

The CFD simulations will maintain consistency with the experiment dimensions of pin diameter, wire diameter, wire pitch, duct inner flat-to-flat, duct corner geometry detail, and pin packing geometry. The length of the bundle is different for the two experiment programs. The lengths for each of the experiment designs were chosen while considering entrance effects to ensure that the flow profiles were fully developed once the flow reached the region of measurement. Both experiments use an inlet plenum to reduce inlet bundle flow skewness that may form from the flow loop designs.

The heated bundle experiment has a long entrance length of approximately 4 wire pitch lengths, followed by a measurement region 8 wire pitches in length, and finally an exit length of approximately 2.5 wire pitch lengths. This long entrance length, and overall length of the bundle was due in part to compatibility requirements between the bundle and already constructed flow loop. Given this long entrance length, combined with the effect of the wire wrap normalization, the flow is expected to be fully developed before the measurement region. The geometry of the CFD model to be used in the 2-equation CFD simulations will include the full entrance length of 4 wire pitch lengths, the 8 wire pitch length of the measurement region, and a single wire wrap length at the exit. Due to the much higher computational requirements

for the LES simulations, a model with the complete length of the heated bundle experiment is not possible. Methods to capture the physical behavior of fluid and thermal fields in the LES are being explored. It is expected this will include periodic boundary conditions and mapping outlet thermal boundary fields as inlet conditions in models representing downstream sections of the bundle.

The MIR bundle experiments have a total length of 3.5 wire pitch lengths for the nominal geometry case, and 5.5 wire pitch lengths for the deformed bundle case. The CFD simulations will model this entire length. Both experiments have 2.25 wire pitch lengths of entrance region before the measurements for flow development. As stated above, during operation of the experiments, the inlet velocity field in the entrance region will be characterized, which will be used in post-test simulations.

The heated bundle uses 19 heaters which are instrumented on the inner clad surface with thermocouples. The heaters have an inner sheath that is directly in contact with the clad. The sheath contains the heating element. To use these thermocouple measurements for use in the CFD validation, the CFD models will include the outer clad and at a minimum, a partial thickness of the sheath for the heater rods. The other non-heated tubes can be modeled in the CFD simulation as wall boundaries at the non-heated tube-fluid interface. The wall thickness of the duct will not be modeled in the pre-test CFD simulations. Instead the boundary of the computational domain will extend to the fluid boundary inside the duct in the lateral directions. However, the as-built duct wall thickness will be reported for potential use in the post-test simulations if the measurements quantifying heat loss indicate the need.

In the model of the MIR bundle, no solid components will be modeled. The model will only consist of the fluid domain in the bundle.

5.2 Boundary Conditions

Inlet Flow: For the heated bundle simulations, mass flow rates and temperatures corresponding to the design set points and the measured flow rates and temperature, with a flat velocity profile will be used for the pre-test simulations. Time averaged measured values of flowrate and temperature will be used for the post-test simulations. Simulations for the MIR bundle will use corresponding design flowrates, flat velocity profile and temperatures for the pre-test simulations. For the post-test simulations, experimental data from the velocity profile characterization measurements may be used to update the inlet velocity profile.

Heater Powers: Design values of per rod heater power, heated length specification and heat flux is provided in the heated bundle test specification [1]. For use in CFD boundary conditions, the per rod power will be converted to a heat flux value that accounts for the heated length, and the surface area of the inner rod boundary at which the heat flux is specified. Heat flux profiles will be characterized following heater fabrication. These profiles, with measured heater rod bank powers will be available for use in the post-test simulations.

Duct Wall Thermal Conditions: Models for both experimental programs will use adiabatic duct wall boundary conditions for pre-test simulations. The heated bundle duct will be insulated to minimize heat loss. Thermocouples on the outer surface of the duct, along with total fluid temperature rise through the duct will provide an estimate of heat loss in the experiments that may be used in post-test simulations as needed, in addition to potential sensitivity studies quantifying this effect. The MIR bundle will be operated near room temperature, and therefore in the CFD simulations adiabatic wall boundary conditions will also be used.

Non-Heated Tubes, Pins and Wires: Adiabatic thermal boundary conditions will be used for the non-heated tubes in the heated bundle experiments, and for all acrylic pins in the MIR bundle experiment. The wire wrap surfaces will also be modeled as adiabatic.

5.3 Wire Wrap Modeling Approximations

The line contact between the wire wrap and the pins creates meshing challenges for CFD. Different methods will be used for the different CFD simulation efforts.

5.3.1 StarCCM+ Simulation Wire Wrap Modeling Method

The CFD simulations to be run at TerraPower with an industry standard CFD code, will use two potential methods to minimize meshing requirements. The first is a momentum source method for modeling the wire wrap [5]. In this method, the boundaries of the wire wrap surface are not explicitly meshed, but instead the mesh represents a bare pin bundle. At the physical positions of the wire wrap, lift and drag momentum sources are calculated and applied to the CFD partial differential equations for the mesh volumes associated with the wire locations. With proper choice of the momentum source, the effect on the fluid is the same as if the wire geometry was resolved as part of the mesh. A second method uses the mesh morphing capability in StarCCM+ to form the wires from an initial bare pin bundle. Verification and validation of these methods is one purpose of this study.

5.3.2 Nek5000 Simulation Wire Wrap Modeling Method

The Nek5000 simulations resolve the geometry of the wire wrap. Due to the tightly packed design of the bundle, this creates a line contact as the wire wraps around the pin, and also creates a point contact between the wire and neighboring pins every wire pitch length. These simulations use a fillet at the line contact between the wire and its pin. This fillet can have an effect on the heat transfer at this location, therefore sensitivity studies are being performed to inform the fillet geometry to be used. At the point of contact between the wire and the neighboring pin, the wire is flattened such that a small fluid gap, which is therefore meshed, remains between the wire and the neighboring pin.

5.4 Transient Modeling Methods

The Nek5000 simulations are Large Eddy Simulations, and therefore use transient simulation methods. Time averaged measurements from the experiments will be used as boundary conditions with appropriate synthetic turbulence conditions. In addition, unsteady-RANS methods with steady boundary conditions will be used for some simulations to be run with the StarCCM+ code.

5.5 Results Extraction

Results will be extracted from the CFD simulations that correspond to the experiment measurements to be used in the validation benchmarking. This includes measurement types, measurement locations, and where applicable, measurement acquisition methods (time series, standard deviation calculation, etc.).

StarCCM+ will run steady state simulations for both the pre-test and post-test cases. Following convergence of these models, the results files will be saved. Results will be extracted at locations as specified in the Test Specifications, and in the case of the Flow Visualization Bundle, in the Measurement Specification Document. The pre-test simulations will be completed before the experiment test cases. Therefore, in the case of the flow visualization bundle where the measurement locations will not be finalized until shakedown, results extraction of the numerical simulation will wait until measurement locations have been finalized.

Similarly, Nek5000 simulations will record the time history of the calculation fields and the results will be extracted for the measurement locations. Similar time averaging as used in the in the experiments will be applied to the Nek5000 simulations. The locations are to be extracted per the test specifications [1], [2], measurement specification document, test procedures and final test reports.

6 MODELING ASSUMPTIONS

The following modeling assumptions are employed in the CFD simulations. However, both of these assumptions will be investigated through numerical sensitivity studies and post simulation results extraction.

1. Sufficient entrance length in the heated bundle and flow visualization simulations to capture experiment entrance effects. The experiments have been designed to minimize these effects. Investigation of simulation results will quantify this modeling assumption and support feedback for additional sensitivity studies, or the need for an addition of upstream components in the simulation model.

2. Geometry modification of the wire wrap in the Nek5000 simulations has a minimal effect on the flow field and temperature distribution. Currently planned sensitivity studies are investigating the impact of these geometry modifications.

7 CFD BENCHMARKING METHODS

7.1 StarCCM+ Verification

Rigorous methods will be employed for the verification of the StarCCM+ simulations. This includes both code verification and solution verification. Code verification will use the method of manufactured solutions and includes convergence tests, and order-of-accuracy tests for the different models to be used in the simulations of the experiments. The method of manufactured solutions is used to produce an artificial exact solution for application of the code verification methods [6]. Solution verification of the StarCCM+ simulations of the experiment tests includes confirmation of mesh independence, Richardson extrapolation for uncertainty estimates, and simulation convergence through use of monitors and residuals.

7.2 Nek5000 Verification

Nek5000 is an open-source CFD code designed specifically for DNS and LES simulations of transitional and turbulent flows in complex domains. It is based on the spectral element method, which is a high-order weighted residual technique that combines the geometric flexibility of finite elements with the rapid convergence and tensor-product efficiencies of global spectral methods. Temporal discretization is based on a high-order splitting that is 3rd-order accurate in time and reduces the coupled velocity-pressure Stokes problem to four independent Helmholtz and one elliptic solve per timestep: one for each velocity component and one for the pressure. A particularly important benefit of Nek5000 are its scalable iterative and coarse-grid solvers that are central to parallel efficiency including algebraic multigrid (AMG). The verification and validation procedure will follow closely the earlier work that has been performed for a range of complex flow geometries [7] including OECD/NEA Vatenfall T-junction [8] and MATiS rod-bundle benchmark experiments [9] and 19 pin wire-wrap bundles [10].

7.3 Validation Comparisons

Results will be extracted from the NEK5000 and StarCCM+ numerical simulations for comparison to the experiment measurements. In addition to direct comparisons to the experiment measurements, code-to-code comparison can include many other types of quantities: area integrated values, minimum and maximum values, and derived quantities. The following list is not a comprehensive or final list, but types of comparisons to be made. Location and specific parameters are not yet finalized.

1. Time and area averaged specific internal, wall and corner subchannel temperatures

2. Maximum and minimum pin surface temperatures, including temperature peaking near wire-wrap contact locations

3. Pressure drop in developing flow length section

4. Fully developed pressure drop results
5. Transverse pressure gradient at specific axial planes in the bundle
6. Subchannel area averaged bulk swirl (transverse) velocities
7. Subchannel flow splits
8. Velocity distribution near the wire-wrap.

7.4 Simulation Validation

The experiment data will be used for the numerical simulation validation. The experiments will measure time series for each respective instrument and provide an average and standard deviation value. The average value will be compared to the steady state numerical simulation results for validation. Measurements extracted from the heated bundle tests for comparison include the following.

1. Heater rod internal clad temperature measurements
2. Non-heated tube surface fluid temperature measurements
3. Internal duct wall surface fluid temperature measurements
4. Pressure drop measurements for developing flow, fully developed flow
5. Pressure gradient skew at bundle axial planes

Local velocities, measured with PIV and LDV, in addition to bundle pressure drops will be measured in the flow visualization experiment for CFD validation. As stated above, the measurements to be measured in the flow visualization bundle will be finalized during shakedown testing, and documented in the Measurement Specification Document.

8 REFERENCES

1. TWRP-31-TSPEC-011, AFAFC AREVA Heated Bundle Experiment Test Specification, 2015.
2. TWRP-31-TSPEC-0010, TAMU Fuel Assembly Fuel Visualization Test Specification, 2015.
3. Heated Bundle Hardware Design Drawings Package.
4. MIR Bundle Hardware Design Drawings Package.
5. Hu, R., Fanning, T.H., “Progress Report on Development of Intermediate Fidelity Fuel Assembly Analysis Methods,” Argonne National Laboratory, ANL-NE-11/35. September 2011.
6. Oberkampf, W.L., Roy, C.J., Verification and Validation in Scientific Computing, Cambridge University Press, 2010.
7. Merzari, E., et al., “Large-Scale Simulation of Nuclear Reactors: Issues and Perspectives,” 16th International Topical Meeting on Nuclear Reactor Thermalhydraulics (NURETH-16). August 30-September 4, Chicago, IL, 2015.
8. Obabko, A. V., et al., Large eddy simulation of thermo-hydraulic mixing in a T-junction, in Nuclear Reactor Thermal Hydraulics and Other Applications, ed. D. Guill, InTech, 2012.
9. Obabko, A. V., et al., “Verification and Validation of Nek5000 for T-Junction, Matis, SIBERIA, and Max Experiments,” 16th International Topical Meeting on Nuclear Reactor Thermalhydraulics (NURETH-16). August 30-September 4, Chicago, IL, 2015.
10. Doolaard, H. J., et al., “CFD Benchmark for a Heavy Liquid Metal Fuel Assembly,” 16th International Topical Meeting on Nuclear Reactor Thermalhydraulics (NURETH-16). August 30-September 4, Chicago, IL, 2015.

TEXAS A&M UNIVERSITY PROJECT DOCUMENTS

APPENDIX I: TAMU-WW-QA, TAMU WIRE-WRAPPED QA GUIDELINES

TECHNICAL DOCUMENT COVER PAGE

Document No:	TAMU-WW-QA	Revision: 0	Page 1 of 5
Doc Title:	TAMU Wire-Wrapped QA Guidelines		
Projects No:	DE-NE0008321		
Project Name:	Toward a Longer Life Core: Thermal-Hydraulic CFD Simulations and Experimental Investigation of Deformed Fuel Assemblies		

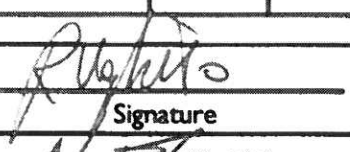
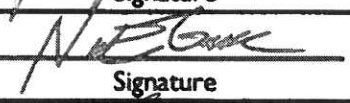
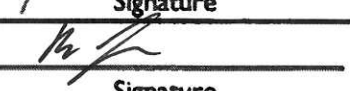
Document Purpose/Summary:

This document describes the generic QA guidelines followed by Texas A&M University

Total Page Count: 5 pages.

TECHNICAL DOCUMENT COVER PAGE

Document No:	TAMU-WW-QA	Revision:	0	Page 2 of 5

TAMU Prepared By:	Rodolfo Vaghetto Printed/Typed Name	 Signature	04/06/2016 Date
TAMU Reviewed By:	Nolan Goth Printed/Typed Name	 Signature	04/06/2016 Date
Approved By:	Brian Jackson Printed/Typed Name	 Signature	04/13/2016 Date

REVISION HISTORY LOG

Document Number: TAMU-WW-QA Revision: 0

Document Title: TAMU Wire-Wrapped QA Guidelines

REVISION	DATE	DESCRIPTION
Rev.0	04/06/2016	Final release

1.0 GUIDELINES

While 10 CFR 50 Appendix B and ASME NQA-1 will not be applied to this project, Texas A&M University (TAMU) performs this work under the current revision of the Texas Experiment Engineering Station (TEES) guidelines for laboratory best practices and research conduct. These guidelines are attached to the project contract.

In addition, TAMU also follows specific Quality Assurance (QA) guidelines when conducting the experimental activity under the same contract. These guidelines are listed below.

Documentation
Documentation produced during the period of performance is be stored and maintained throughout the project. This documentation consists of:

1) Generic test procedures describing generic guidelines followed when performing the tests. This include:
    a. Water tests procedures: fill, startup, run, shutdown, and drain
    b. P-cymene tests procedures: fill, startup, run, shutdown, and drain

    The procedures include generic guidelines on how to use the DAQ, the labview setup, and how we verify the measurement system setup (pressure, flow rate, and temperature)
2) Instrumentation/Hardware list, (including part number and description) for each component of the experimental facility listed below:
    a. Pump
    b. Flow meter
    c. Pressure transducers
    d. DAQ
    e. Laser and cameras
3) Material List, including the chemicals and other materials used when performing the experiments.
4) Calibration records and/or other factory certification.
5) The Project Safety Analysis (PSA) report.
6) Material safety datasheets (when required).
7) Final engineering drawings
8) Training records including the required TEES training list, and the review of test scope (deliverables and schedule), QA guidelines, test procedures implemented and issues log.

Work will be performed by personnel listed in the training records documentation which contains the list of TEES mandatory training.

The documentation listed above (items 1 to 8) will have a cover sheet including document number and title, a signature sheet, and revision history, similarly to the documents produced by TAMU as part of the deliverables listed in the project contract.

Laboratory Best Practices on MIR-based Measurement Techniques.
MIR-based measurement techniques (PIV and LDV) will be performed only by highly qualified personnel using the available instrumentation of the laboratory. Although written procedures for the use of these systems are not prepared for this project, the personnel will conduct the measurements following the laboratory best practices. A description of the pre-test verification and calibration of the instrumentation in use, and the post-processing software analysis will be included in the test report.

Walk Down

Formal audits for this project are not planned. TAMU will allow one walk-down in lieu of QA audits. It is of AREVA responsibility to notify TAMU at least two (2) weeks prior their arrival for performing the observation/walk down. The documentation listed above (items 1 to 8) will be available during the walk down.

APPENDIX J: TAMU-WW-AS, TAMU WIRE-WRAPPED AS-BUILT GEOMETRY (NON-DEFORMED BUNDLE)

TECHNICAL DOCUMENT COVER PAGE

Document No:	TAMU-WW-AS	Revision: 2	Page 1 of 21
Doc Title:	TAMU Wire-Wrapped As-Built Geometry (Non-Deformed Bundle)		
Projects No:	DE-NE0008321		
Project Name:	Toward a Longer Life Core: Thermal-Hydraulic CFD Simulations and Experimental Investigation of Deformed Fuel Assemblies		

Document Purpose/Summary:

This document describes the "as-built" dimensions of the critical geometrical parameters of the test section of the isothermal non-deformed experimental bundle.

Total Page Count: 21 pages.

TECHNICAL DOCUMENT COVER PAGE

Document No:	TAMU-WW-AS	Revision: 2	Page 2 of 21

TAMU Prepared By:	Nolan Goth		11/02/16
	Printed/Typed Name	Signature	Date
TAMU Reviewed By:	Rodolfo Vaghetto		11/2/16
	Printed/Typed Name	Signature	Date
Approved By:			
	Printed/Typed Name	Signature	Date

REVISION HISTORY LOG

Document Number: TAMU-WW-AS Revision: 2

Document Title: TAMU Wire-Wrapped As-Built Geometry (Non-Deformed Bundle)

REVISION	DATE	DESCRIPTION
Draft	11/04/2015	Initial draft for review.
Draft 2	12/11/2015	Comments from TerraPower Incorporated
Rev.0	01/25/2016	Rev.0 released
Rev.1	10/21/2016	Updated rod and wire characterization for second non-deformed bundle. Added sections for wire-clocking angle, wire-clocking direction, flow inlet/outlet axial locations, and total rod length.
Rev.2	11/02/2016	Included additional geometrical information based on TerraPower request

Table of Contents

1.0 Introduction and Scope 6
2.0 Test Section As-Built Geometry 6
2.1 Axial Coordinate System 6
2.2 Test Section Enclosure 8
2.3 Total Rod Length 9
2.4 Wire-Clocking Angle 9
2.5 Wire-Wrap Direction 11
2.6 Flow Inlet and Outlet Ports 11
2.7 First Non-Deformed Bundle 11
2.7.1 Rods 11
2.7.2 Wire Spacers 13
2.7.3 Fabrication Process 15
2.8 Second Non-Deformed Bundle 16
2.8.1 Rods 16
2.8.2 Wire Spacer 17
2.8.3 Fabrication Process 19
3.0 Pressure transducer Final Location 20
4.0 References 21

Acronyms and Definitions

Acronym	Definition
TAMU	The Texas A&M University
CFD	computational fluid dynamics
FTF	flat-to-flat

1.0 INTRODUCTION AND SCOPE

To support the validation of computation fluid dynamics (CFD) calculations, high quality characterization of flow in the same flow regime as those encountered in wire wrapped fuel assemblies prototypic of liquid metal fast reactors is needed. TAMU performs experimental tests focusing on investigating and measuring flow and pressure drop behavior of two geometries (non-deformed and deformed) of a mock 61-rod hexagonal fuel assembly for purposes of generating CFD validation grade data.

This document defines the as-built geometry of the experimental non-deformed test section that will be used gather data from the experimental tests. The dimensions and manufacturing tolerances are provided in this document. Engineering drawings of the test section are also attached to this document.

2.0 TEST SECTION AS-BUILT GEOMETRY

The dimensions reported in this section represent the as-built configuration of the non-deformed geometry. The components of the test section included are:

- The acrylic test section enclosure (Section 2.0)
- The first non-deformed bundle (Section 2.7)
- The second non-deformed bundle (Section 2.8)

2.1 Axial Coordinate System

This section defines the relationship between the two notations used to denote various axial positions. The first notation is described in TWRP-31-TSPEC-00100 Rev. 1 [1], where various axial positions are denoted by the pitch number (I.E. visualization region between P = 2.25 and P = 3.25). The second notation is the z-axis, which measures the vertical height in inches. The origin of the z-axis (z = 0) is equivalent to a pitch number of zero (P = 0). This origin is at the interface between the upper flange of the lower plenum and lower flange of the test section. Figure 1 displays a side view of the test section denoting major axial positions using the second notation method.

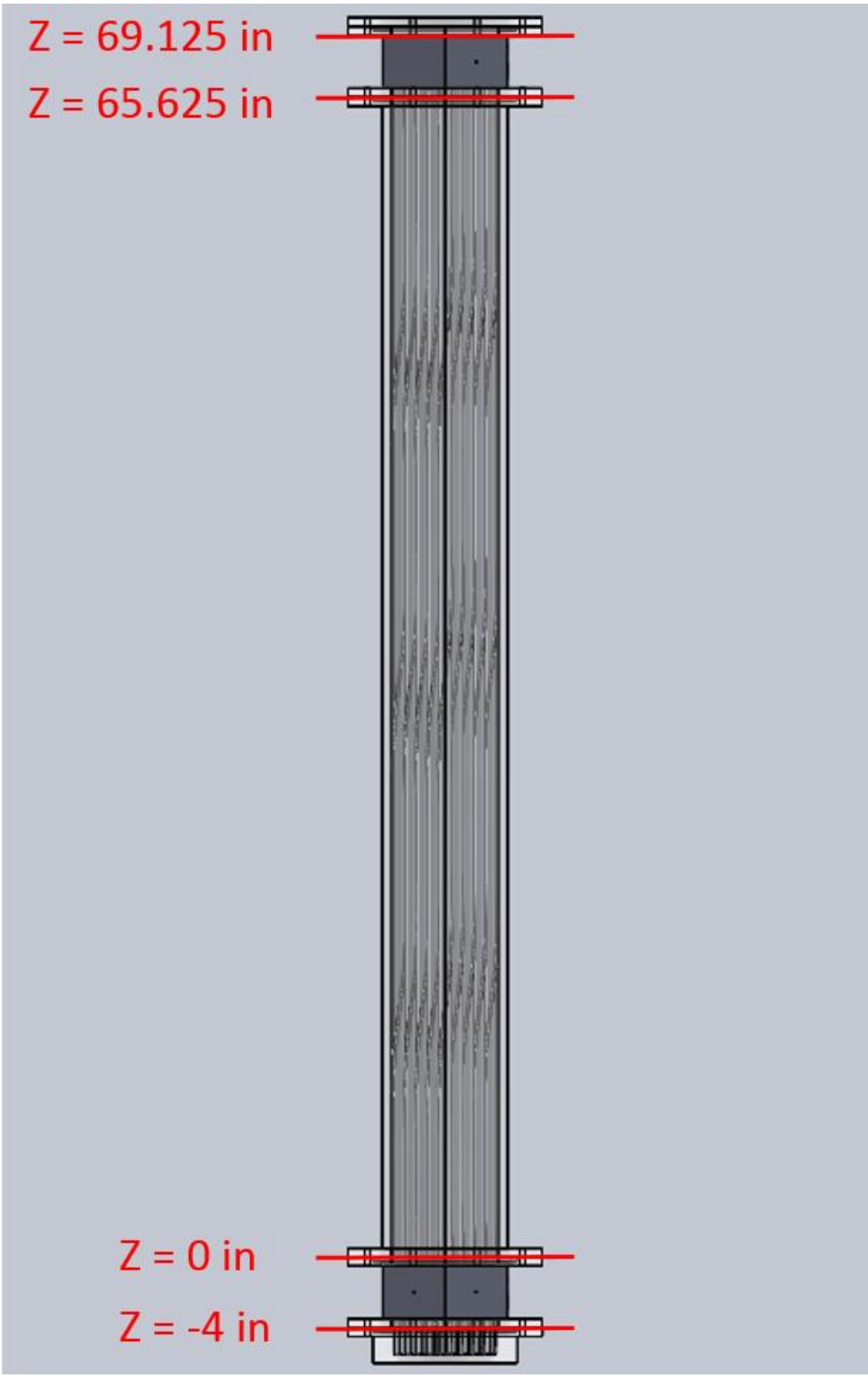


Figure 1. Side-view of the test section with major axial positions

2.2 Test Section Enclosure

The hexagonal test section enclosure was designed following the specifications provided in TWRP-31-TSPEC-0010 Rev. 1 [1]. Table 2.2.1 displays the inner flat-to-flat (FTF) distance of the sides of the enclosure for the test specification and design values.

Table 2.2.1 – Specified and designed inner FTF of the test section enclosure (units of inches)

Test Spec FTF (in)	Design FTF (in)
6.070	6.056

The FTF measurements below are of (1) the outer FTF of the hexagonal guide plate used to manually fabricate the enclosure, and of (2) the inner FTF of the entrance and exit of the test section enclosure. Table 2.2.2 displays the three outer FTF distances of the hexagonal guide plate.[1] These measurements were taken at the midpoint between corners.

Table 2.2.2 - As-built inner FTF distances of the hexagonal guide plate (units of inches)

Measurement #	FTF 1 (in)	FTF 2 (in)	FTF 3 (in)	FTF Average (in)
1	6.065	6.061	6.063	-
2	6.063	6.063	6.063	-
3	6.064	6.062	6.065	-
Average	6.064	6.062	6.064	6.063
Std. Dev.	0.000816	0.000816	0.000943	0.000859

Using the same caliper, the inner FTF of the entrance and exit of the test section enclosure were also measured. Measurements were repeated at different locations along each face. Due to the higher difficultly in performing these measurements on the inner FTF of the enclosure, the standard deviation of the measurement was significantly higher than the standard deviation of the measurements taken on the guide plate.

Average FTF (Test Section Entrance) = 6.082 in with a standard deviation of 0.03175 in

Average FTF (Test Section Exit) = 6.088 in with a standard deviation of 0.02758 in

[1] Three measurements of the FTF distance were taken for each of the three two-side sets. The measurements were performed using a caliper (Starrett No.180, accuracy 0.001")

2.3 Total Rod Length

The total rod length exposed to the working fluid is 73.125 inches. This accounts for the following sections:

- Lower plenum rod length = 4 inches
- Test section rod length = 65.625 inches
- Upper plenum rod length = 3.5 inches

The length of the section within the upper plenum is less than the one within lower plenum by 0.5 inches due to the presence of the upper guide plate (thickness = 0.5 inches) utilized to maintain the triangular lattice.

2.4 Wire-Clocking Angle

The wire-clocking angle at the bottom of the rod was chosen such that the wire would be positioned in the corner of the hexagonal enclosure formed by Face F and A. The following images are top-view cross-sections of the fuel bundle. The wire-clocking angles are relative to the corner of the hexagonal enclosure Faces C and D. The starting wire-clocking angle was chosen such that the angle would be 180° at an axial location of z = 42.1875 inches (P=2.25), as defined in [1]. Figure 2 displays the hexagonal enclosure face labeling scheme.

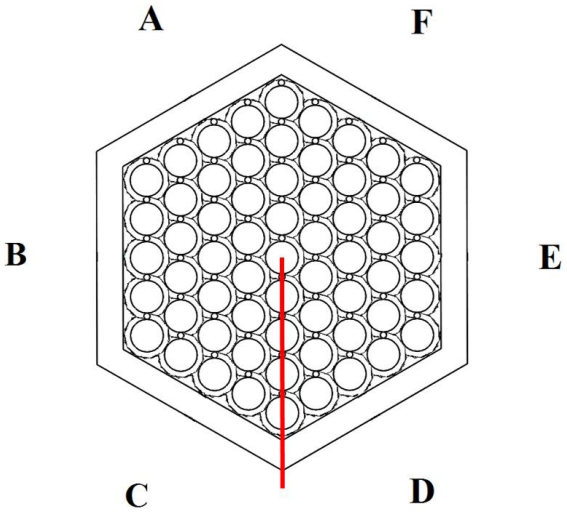


Figure 2. Face labeling scheme showing a wire-clocking angle of 180°

Figure 3 displays the starting wire-clocking angle when it emerges from the lower plate and begins its helical sweep. The axial location is z = -4 inches (P = -0.213). The angle is 13.19° from a line that passes through the corners formed by Faces C and D.

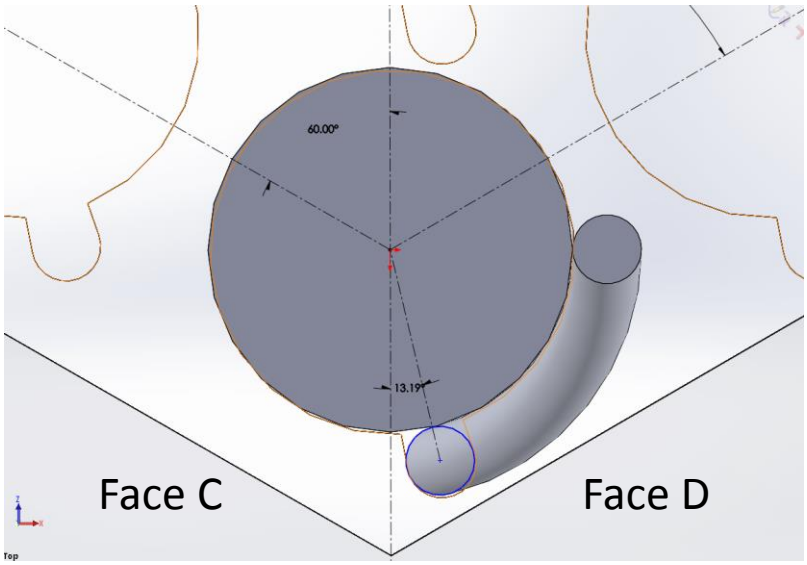


Figure 3. Wire-clocking angle at z = -4 inches (P= -0.213)

Figure 4 displays the wire-clocking angle at an axial location of z = 0 inches (P=0). The angle is 89.83° from a line that passes through the corners formed by Faces C and D.

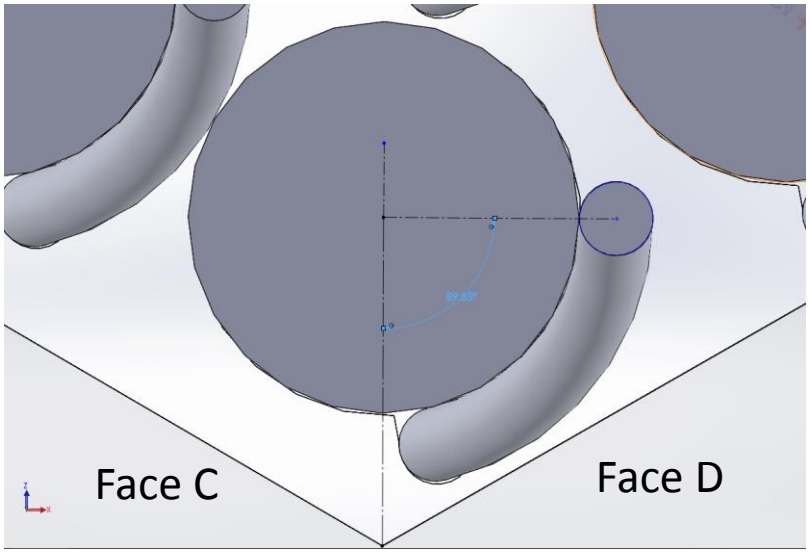


Figure 4. Wire-clocking angle at z = 0 inches (P=0)

2.5 Wire-Wrap Direction

The direction of the wire wrap follows the requirement reported in the test specs [1]. The wire is wrapped clockwise around the rod in the direction of the flow (looking from the bottom of the assembly).

2.6 Flow Inlet and Outlet Ports

The flow inlet/outlet ports were located on Faces B and E. The ports were circular in shape with a inner diameter of 2 inches. The inlet ports had a centerline axial location of z = -2 inches. The outlet ports had a centerline axial location of z = 67.625 inches.

2.7 First Non-Deformed Bundle

2.7.1 Rods

Cast acrylic rods were produced by PolyOne. The target rod diameter was specified in the TWRP-31-TSPEC-0010 Rev. 1 [1]. The selected diameter and casting tolerance was 0.625 in ± 0.010 in. In-house characterization consisted of measuring each rod diameter in three different axial locations. This was performed using a Mitutoyo digital caliper with an accuracy of ±0.001 in. Axial locations 1, 2, and 3 were defined to be distances from the bottom of the rod. These distances were approximately 4 in, 37 in, and 70 in. A total of 94 rods were characterized using this process. The average of the three axial location measurements was calculated for all 94 rods. The final 61 rods that were closest to the mean value were then selected. Table 2.7.1.1 shows the dimensions of the final 61 rods selected with the method described. The average rod diameter was 0.6267 inches with a standard deviation of 0.0006 inches.

Table 2.7.1.1 – First Bundle Fuel Rod Characterization (diameter in inches) [2]

Rod #	Location 1	Location 2	Location 3	Average	Std. Dev.
1	0.6255	0.6260	0.6285	0.6267	0.0013
2	0.6265	0.6250	0.6265	0.6260	0.0007
4	0.6260	0.6260	0.6280	0.6267	0.0009
7	0.6260	0.6270	0.6270	0.6267	0.0005
9	0.6275	0.6270	0.6275	0.6273	0.0002
10	0.6270	0.6265	0.6270	0.6268	0.0002
11	0.6270	0.6270	0.6280	0.6273	0.0005

[2] The rod # label is with respect to the total number of rods investigated and may not be sequential

12	0.6265	0.6260	0.6280	0.6268	0.0008
13	0.6275	0.6275	0.6270	0.6273	0.0002
16	0.6260	0.6265	0.6275	0.6267	0.0006
18	0.6255	0.6260	0.6275	0.6263	0.0008
19	0.6265	0.6270	0.6260	0.6265	0.0004
20	0.6275	0.6275	0.6270	0.6273	0.0002
21	0.6270	0.6270	0.6275	0.6272	0.0002
22	0.6255	0.6260	0.6260	0.6258	0.0002
23	0.6275	0.6280	0.6275	0.6277	0.0002
24	0.6250	0.6255	0.6265	0.6257	0.0006
26	0.6270	0.6280	0.6290	0.6280	0.0008
28	0.6270	0.6260	0.6270	0.6267	0.0005
31	0.6260	0.6255	0.6275	0.6263	0.0008
32	0.6255	0.6260	0.6275	0.6263	0.0008
33	0.6265	0.6265	0.6270	0.6267	0.0002
34	0.6270	0.6265	0.6275	0.6270	0.0004
35	0.6255	0.6260	0.6270	0.6262	0.0006
36	0.6270	0.6270	0.6265	0.6268	0.0002
37	0.6275	0.6280	0.6275	0.6277	0.0002
38	0.6270	0.6270	0.6270	0.6270	0.0000
39	0.6250	0.6250	0.6265	0.6255	0.0007
41	0.6250	0.6255	0.6260	0.6255	0.0004
42	0.6255	0.6250	0.6265	0.6257	0.0006
44	0.6255	0.6265	0.6255	0.6258	0.0005
46	0.6260	0.6260	0.6270	0.6263	0.0005
47	0.6270	0.6265	0.6265	0.6267	0.0002
48	0.6260	0.6255	0.6255	0.6257	0.0002
49	0.6260	0.6280	0.6275	0.6272	0.0008
50	0.6270	0.6265	0.6285	0.6273	0.0008
53	0.6265	0.6265	0.6280	0.6270	0.0007
54	0.6280	0.6265	0.6270	0.6272	0.0006
55	0.6270	0.6265	0.6270	0.6268	0.0002
56	0.6255	0.6265	0.6275	0.6265	0.0008
57	0.6270	0.6270	0.6270	0.6270	0.0000
58	0.6255	0.6250	0.6285	0.6263	0.0015
59	0.6265	0.6255	0.6255	0.6258	0.0005
60	0.6260	0.6265	0.6265	0.6263	0.0002
61	0.6285	0.6275	0.6285	0.6282	0.0005

62	0.6265	0.6265	0.6275	0.6268	0.0005
63	0.6275	0.6275	0.6280	0.6277	0.0002
65	0.6270	0.6265	0.6265	0.6267	0.0002
66	0.6265	0.6260	0.6260	0.6262	0.0002
67	0.6255	0.6250	0.6250	0.6252	0.0002
69	0.6255	0.6255	0.6260	0.6257	0.0002
70	0.6270	0.6270	0.6270	0.6270	0.0000
71	0.6260	0.6265	0.6270	0.6265	0.0004
72	0.6270	0.6255	0.6275	0.6267	0.0008
75	0.6265	0.6275	0.6270	0.6270	0.0004
76	0.6270	0.6265	0.6255	0.6263	0.0006
81	0.6270	0.6265	0.6275	0.6270	0.0004
40	0.6260	0.6255	0.6265	0.6260	0.0004
84	0.6275	0.6265	0.6285	0.6275	0.0008
89	0.6255	0.6260	0.6275	0.6263	0.0008
92	0.6265	0.6260	0.6280	0.6268	0.0008

2.7.2 Wire Spacers

Extruded acrylic wire spacers were procured from Wuxi YanYang International Trading Co., Ltd. The target wire spacer diameter was specified in the TWRP-31-TSPEC-0010 Rev. 1 [1]. The selected diameter and extrusion tolerance was 0.003 m ± 0.00015 m. In-house characterization consisted of measuring each wire spacer diameter in three different axial locations. This was performed using the same Mitutoyo caliper used for the rod characterization. Axial locations 1, 2, and 3 were defined to be distances from the bottom of the wire spacer. These distances were 4 in, 37 in, and 70 in. A total of 73 wire spacers were characterized using this process. The average of the three axial location measurements was calculated for all 73 wire spacers. The final 61 wire spacers that were closest to the mean value were then selected. Table 2.7.2.1 shows the dimensions of the final 61 wire spacers selected with the method described. The average wire diameter was 0.00297 m with a standard deviation of 0.00003 m.

Table 2.7.2.1 - Wire Spacer Characterization (diameter in m) [3]

Wire #	Location 1	Location 2	Location 3	Average	Std. Dev.
1	0.00298	0.00296	0.00302	0.00299	0.00002

[3] The wire # label is with respect to the total number of wires investigated and may not be sequential

2	0.00301	0.00296	0.00295	0.00297	0.00003
4	0.00294	0.00291	0.00297	0.00294	0.00002
5	0.00299	0.00298	0.00295	0.00297	0.00002
8	0.00293	0.00296	0.00295	0.00295	0.00001
9	0.00299	0.00297	0.00298	0.00298	0.00001
10	0.00303	0.00304	0.00301	0.00303	0.00001
11	0.00298	0.00298	0.00301	0.00299	0.00001
12	0.00302	0.00297	0.00296	0.00298	0.00003
14	0.00303	0.00294	0.00300	0.00299	0.00004
15	0.00298	0.00295	0.00303	0.00299	0.00003
18	0.00304	0.00302	0.00299	0.00302	0.00002
19	0.00301	0.00300	0.00303	0.00301	0.00001
21	0.00297	0.00302	0.00296	0.00298	0.00003
22	0.00295	0.00300	0.00298	0.00298	0.00002
23	0.00303	0.00302	0.00296	0.00300	0.00003
24	0.00301	0.00299	0.00298	0.00299	0.00001
25	0.00297	0.00301	0.00303	0.00300	0.00002
26	0.00294	0.00299	0.00298	0.00297	0.00002
27	0.00298	0.00301	0.00299	0.00299	0.00001
28	0.00294	0.00294	0.00293	0.00294	0.00000
29	0.00295	0.00296	0.00297	0.00296	0.00001
30	0.00300	0.00295	0.00303	0.00299	0.00003
31	0.00297	0.00292	0.00295	0.00295	0.00002
33	0.00295	0.00297	0.00303	0.00298	0.00003
34	0.00298	0.00298	0.00300	0.00299	0.00001
35	0.00300	0.00299	0.00296	0.00298	0.00002
36	0.00300	0.00296	0.00294	0.00297	0.00002
37	0.00294	0.00297	0.00296	0.00296	0.00001
38	0.00296	0.00301	0.00303	0.00300	0.00003
39	0.00295	0.00296	0.00298	0.00296	0.00001
41	0.00296	0.00293	0.00297	0.00295	0.00002
42	0.00297	0.00295	0.00294	0.00295	0.00001
43	0.00302	0.00297	0.00298	0.00299	0.00002
44	0.00298	0.00305	0.00299	0.00301	0.00003
45	0.00297	0.00296	0.00300	0.00298	0.00002
46	0.00293	0.00294	0.00295	0.00294	0.00001
47	0.00298	0.00296	0.00291	0.00295	0.00003
48	0.00302	0.00299	0.00303	0.00301	0.00002

49	0.00300	0.00297	0.00299	0.00299	0.00001
50	0.00294	0.00300	0.00294	0.00296	0.00003
51	0.00297	0.00296	0.00294	0.00296	0.00001
52	0.00297	0.00294	0.00296	0.00296	0.00001
53	0.00298	0.00293	0.00295	0.00295	0.00002
54	0.00296	0.00294	0.00293	0.00294	0.00001
55	0.00292	0.00295	0.00300	0.00296	0.00003
56	0.00296	0.00296	0.00290	0.00294	0.00003
57	0.00298	0.00300	0.00300	0.00299	0.00001
58	0.00298	0.00291	0.00292	0.00294	0.00003
59	0.00296	0.00296	0.00295	0.00296	0.00000
60	0.00294	0.00293	0.00294	0.00294	0.00000
62	0.00298	0.00296	0.00295	0.00296	0.00001
63	0.00297	0.00294	0.00293	0.00295	0.00002
64	0.00302	0.00298	0.00296	0.00299	0.00002
65	0.00299	0.00301	0.00298	0.00299	0.00001
66	0.00290	0.00298	0.00293	0.00294	0.00003
68	0.00297	0.00294	0.00299	0.00297	0.00002
69	0.00295	0.00296	0.00297	0.00296	0.00001
71	0.00297	0.00295	0.00296	0.00296	0.00001
72	0.00296	0.00300	0.00296	0.00297	0.00002
73	0.00297	0.00299	0.00296	0.00297	0.00001

2.7.3 Fabrication Process

A low viscosity version of ethyl-2-cyanoacrylate was the adhesive used in the fabrication process. The wire was first adhered to the lower 1.5 inches of the rod. For this lower attachment section, the axis of the rod and wire were set parallel with assistance from an aluminum guide block containing milled rod/wire holes. The wire was then helically wrapped around the rod and adhered to the upper 0.5 inches of the rod. Before attaching the wire to the top, tension was applied to the wire to remove slack and mate the rod and wire surfaces. A 3D printed guide block was utilized to set the appropriate wire-clocking angle at the top of the rod.

2.8 Second Non-Deformed Bundle

2.8.1 Rods

Cast acrylic rods were procured from Boedeker. The target rod diameter was identical to the first bundle, as defined in Section 2.7.1. The same In-house characterization process was repeated for 58 new rods. Table 2.8.1.1 shows the dimensions of the 58 new rods. A portion of the 58 new rods, along with several salvaged rods from the first non-deformed bundle, were selected to be used in the second non-deformed bundle. The average rod diameter was 0.6251 inches with a standard deviation of 0.0014 inches.

Table 2.8.1.1 – Second Bundle Fuel Rod Characterization (diameter in inches)

Rod #	Location 1	Location 2	Location 3	Average	Std. Dev.
1	0.6245	0.6265	0.6250	0.6253	0.0008
2	0.6255	0.6250	0.6245	0.6250	0.0004
3	0.6260	0.6260	0.6260	0.6260	0.0000
4	0.6255	0.6255	0.6255	0.6255	0.0000
5	0.6250	0.6250	0.6275	0.6258	0.0012
6	0.6255	0.6255	0.6255	0.6255	0.0000
7	0.6255	0.6255	0.6255	0.6255	0.0000
8	0.6255	0.6255	0.6255	0.6255	0.0000
9	0.6280	0.6240	0.6220	0.6247	0.0025
10	0.6260	0.6260	0.6245	0.6255	0.0007
11	0.6225	0.6240	0.6220	0.6228	0.0008
12	0.6240	0.6265	0.6230	0.6245	0.0015
13	0.6260	0.6450	0.6300	0.6337	0.0082
14	0.6290	0.6255	0.6255	0.6267	0.0016
15	0.6260	0.6250	0.6250	0.6253	0.0005
16	0.6235	0.6235	0.6210	0.6227	0.0012
17	0.6225	0.6260	0.6235	0.6240	0.0015
18	0.6230	0.6235	0.6235	0.6233	0.0002
19	0.6250	0.6230	0.6270	0.6250	0.0016
20	0.6300	0.6270	0.6270	0.6280	0.0014
21	0.6350	0.6230	0.6250	0.6277	0.0052
22	0.6280	0.6300	0.6260	0.6280	0.0016
23	0.6245	0.6245	0.6305	0.6265	0.0028
24	0.6245	0.6250	0.6245	0.6247	0.0002
25	0.6245	0.6240	0.6270	0.6252	0.0013
26	0.6240	0.6255	0.6230	0.6242	0.0010

27	0.6270	0.6235	0.6235	0.6247	0.0016
28	0.6295	0.6250	0.6250	0.6265	0.0021
29	0.6280	0.6260	0.6240	0.6260	0.0016
30	0.6250	0.6240	0.6240	0.6243	0.0005
31	0.6240	0.6240	0.6245	0.6242	0.0002
32	0.6315	0.6250	0.6270	0.6278	0.0027
33	0.6245	0.6245	0.6210	0.6233	0.0016
34	0.6245	0.6225	0.6230	0.6233	0.0008
35	0.6235	0.6225	0.6220	0.6227	0.0006
36	0.6245	0.6265	0.6250	0.6253	0.0008
37	0.6275	0.6240	0.6250	0.6255	0.0015
38	0.6225	0.6235	0.6200	0.6220	0.0015
39	0.6260	0.6235	0.6230	0.6242	0.0013
40	0.6340	0.6240	0.6245	0.6275	0.0046
41	0.6250	0.6230	0.6235	0.6238	0.0008
42	0.6230	0.6250	0.6250	0.6243	0.0009
43	0.6255	0.6245	0.6225	0.6242	0.0012
44	0.6250	0.6230	0.6250	0.6243	0.0009
45	0.6245	0.6245	0.6230	0.6240	0.0007
46	0.6255	0.6220	0.6250	0.6242	0.0015
47	0.6250	0.6245	0.6245	0.6247	0.0002
48	0.6230	0.6250	0.6250	0.6243	0.0009
49	0.6260	0.6245	0.6230	0.6245	0.0012
50	0.6250	0.6200	0.6250	0.6233	0.0024
51	0.6240	0.6240	0.6220	0.6233	0.0009
52	0.6240	0.6250	0.6250	0.6247	0.0005
53	0.6250	0.6250	0.6250	0.6250	0.0000
54	0.6250	0.6255	0.6250	0.6252	0.0002
55	0.6245	0.6250	0.6250	0.6248	0.0002
56	0.6250	0.6240	0.6245	0.6245	0.0004
57	0.6245	0.6250	0.6260	0.6252	0.0006
58	0.6250	0.6250	0.6250	0.6250	0.0000

2.8.2 Wire Spacer

Extruded acrylic wire spacers were procured from Wuxi YanYang International Trading Co., Ltd. The target wire spacer diameter was identical to the first bundle, as defined in Section 2.7.2. The same In-house characterization process was repeated for 200 new wire spacers. The final 61 wire spacers that were closest to the mean value were then selected. Table 2.8.2.1 shows the dimensions of the selected

61 wire spacers used in the second non-deformed bundle. The average wire spacer diameter was 0.00300 m with a standard deviation of 0.00003 m.

Table 2.8.2.1 – Second Bundle Wire Spacer Characterization (diameter in m)[4]

Wire #	Location 1	Location 2	Location 3	Average	Std. Dev.
6	0.00297	0.00299	0.00290	0.00295	0.00004
7	0.00300	0.00301	0.00300	0.00300	0.00000
8	0.00294	0.00293	0.00291	0.00293	0.00001
9	0.00300	0.00300	0.00300	0.00300	0.00000
13	0.00299	0.00298	0.00297	0.00298	0.00001
14	0.00299	0.00295	0.00302	0.00299	0.00003
15	0.00290	0.00295	0.00300	0.00295	0.00004
16	0.00300	0.00300	0.00300	0.00300	0.00000
17	0.00303	0.00300	0.00300	0.00301	0.00001
18	0.00297	0.00300	0.00295	0.00297	0.00002
19	0.00300	0.00302	0.00290	0.00297	0.00005
20	0.00296	0.00290	0.00296	0.00294	0.00003
21	0.00290	0.00293	0.00300	0.00294	0.00004
23	0.00300	0.00305	0.00301	0.00302	0.00002
24	0.00302	0.00303	0.00305	0.00303	0.00001
25	0.00301	0.00301	0.00301	0.00301	0.00000
26	0.00304	0.00301	0.00300	0.00302	0.00002
27	0.00295	0.00300	0.00300	0.00298	0.00002
28	0.00304	0.00302	0.00301	0.00302	0.00001
29	0.00301	0.00301	0.00301	0.00301	0.00000
30	0.00300	0.00300	0.00301	0.00300	0.00000
31	0.00300	0.00309	0.00305	0.00305	0.00004
32	0.00297	0.00302	0.00302	0.00300	0.00002
33	0.00295	0.00300	0.00303	0.00299	0.00003
34	0.00300	0.00301	0.00300	0.00300	0.00000
35	0.00301	0.00304	0.00300	0.00302	0.00002
36	0.00301	0.00300	0.00300	0.00300	0.00000
37	0.00306	0.00300	0.00305	0.00304	0.00003
38	0.00300	0.00301	0.00300	0.00300	0.00000

[4] The wire # label is with respect to the total number of wires investigated and may not be sequential

39	0.00301	0.00299	0.00301	0.00300	0.00001
40	0.00305	0.00300	0.00309	0.00305	0.00004
41	0.00305	0.00304	0.00302	0.00304	0.00001
42	0.00301	0.00301	0.00305	0.00302	0.00002
43	0.00303	0.00288	0.00306	0.00299	0.00008
44	0.00305	0.00302	0.00307	0.00305	0.00002
45	0.00303	0.00308	0.00301	0.00304	0.00003
48	0.00303	0.00303	0.00301	0.00302	0.00001
49	0.00305	0.00304	0.00301	0.00303	0.00002
51	0.00302	0.00301	0.00300	0.00301	0.00001
52	0.00305	0.00301	0.00303	0.00303	0.00002
53	0.00300	0.00303	0.00297	0.00300	0.00002
55	0.00306	0.00303	0.00307	0.00305	0.00002
60	0.00305	0.00285	0.00303	0.00298	0.00009
61	0.00296	0.00297	0.00293	0.00295	0.00002
65	0.00302	0.00298	0.00303	0.00301	0.00002
70	0.00296	0.00299	0.00300	0.00298	0.00002
72	0.00298	0.00294	0.00297	0.00296	0.00002
74	0.00302	0.00301	0.00300	0.00301	0.00001
75	0.00304	0.00295	0.00302	0.00300	0.00004
78	0.00297	0.00299	0.00293	0.00296	0.00002
82	0.00301	0.00305	0.00303	0.00303	0.00002
83	0.00292	0.00291	0.00293	0.00292	0.00001
88	0.00301	0.00303	0.00300	0.00301	0.00001
89	0.00302	0.00301	0.00301	0.00301	0.00000
91	0.00300	0.00304	0.00296	0.00300	0.00003
92	0.00301	0.00294	0.00297	0.00297	0.00003
93	0.00303	0.00304	0.00301	0.00303	0.00001
94	0.00300	0.00300	0.00305	0.00302	0.00002
96	0.00300	0.00298	0.00302	0.00300	0.00002
97	0.00300	0.00305	0.00303	0.00303	0.00002
99	0.00300	0.00301	0.00295	0.00299	0.00003

2.8.3 Fabrication Process

The fabrication process defined in Section 2.7.3 was repeated for the second non-deformed bundle. A series of additional steps was then performed to fully adhere the wire along the entire length of the rod. After attaching the wire to the rod bottom/top, the wire was tacked at eight different axial locations. After curing, inspection was performed on the wire position at the eight tacked locations and at midpoints

between the tacked located. After passing this inspection, the wire was then fully adhered to the rod by applying adhesive to both sides of the wire along its entire length.

3.0 PRESSURE TRANSDUCER FINAL LOCATION

Holes were drilled and tapped into the acrylic hexagonal test section enclosure to accommodate pressure transducer hardware. Table 3.1 lists the final locations of the holes that will accommodate the pressure transducers. Measurements have been performed using a straight-edged ruler with a 0.0625 in accuracy. Holes are located at the midpoint of the width of each face, corresponding to 2.0625 ± 0.0625 in from the external corners of the hexagonal enclosure.

Table 3.1 – Final axial location of all pressure taps

Pressure Tap ID	Final Axial Location (z-coordinate) (in)[5],[6]	Final Axial Location (pitch number)
PT #0	-2.0000	-0.11
PT #1f	3.0000	0.16
PT #2f	18.7500	1.00
PT #3f	32.8125	1.75
PT #4f	37.5000	2.00
PT #5d	42.1875	2.25
PT #5e	42.1875	2.25
PT #5f	42.1875	2.25
PT #5a	42.1875	2.25
PT #6d	56.2500	3.00
PT #6e	56.2500	3.00
PT #6f	56.2500	3.00
PT #6a	56.2500	3.00
PT #7f	60.9375	3.25
PT #8	67.6250	3.61

[5] The axial uncertainty of all pressure transducer final locations is ± 0.0625 in.

[6] The axial position z = 0.0 reference is located at the interface between the upper flange of the lower plenum and the lower flange of the test section.

4.0 REFERENCES

1. TWRP-31-TSPEC-0010 Rev. 1, TAMU Fuel Assembly Flow Visualization Test Specification

APPENDIX K: TAMU-WW-TEST-PCM-11-E, TAMU WIRE-WRAPPED TEST SUMMARY OF TEST PCM-11 AT THE EXTERIOR SUBCHANNEL

TECHNICAL DOCUMENT COVER PAGE

Document No:	TAMU-WW-TEST-PCM-11-E	Revision: Rev.2.0	Page 1 of 22
Doc Title:	TAMU Wire-Wrapped Test Summary of Test PCM-11 at the Exterior Subchannel		
Projects No:	DE-NE0008321		
Project Name:	Toward a Longer Life Core: Thermal-Hydraulic CFD Simulations and Experimental Investigation of Deformed Fuel Assemblies		

Document Purpose/Summary: This document summarizes the conditions of the experimental test PCM-11-E, and provides instructions for reading the associated pressure and velocity data produced by the experimental test.

Total Page Count: 22 pages.

TECHNICAL DOCUMENT COVER PAGE

Document No:	TAMU-WW-TEST-PCM-11-E	Revision: Rev.2.0	Page 2 of 22

TAMU Prepared By:	Nolan Goth		12/13/16
	Printed/Typed Name	Signature	Date
	Philip Jones		12/13/16
	Printed/Typed Name	Signature	Date
TAMU Reviewed By:	Thien Nguyen		12/13/16
	Printed/Typed Name	Signature	Date
	Rodolfo Vaghetto		12/13/16
	Printed/Typed Name	Signature	Date
Approved By:			
	Printed/Typed Name	Signature	Date

REVISION HISTORY LOG

Document Number: TAMU-WW-TEST-PCM-11-E Revision: Rev.2.0

Document Title: TAMU Wire-Wrapped Test Summary of Test PCM-11 at the Exterior Subchannel

REVISION	DATE	DESCRIPTION
Draft	10/04/16	Initial draft for review.
Rev.1	11/02/2016	Comments from TerraPower incorporated
Rev.1.1	11/21/2016	Included discussion on PIV error estimation and calibration (Appendix III)
Rev.2.0	12/12/2016	Changed reference coordinate system (Section 2.3) and updated file naming (Section 3.1)

Table of Contents

1.0 Introduction and Scope 6
2.0 Test Description 6
2.1 Experimental Setup 6
2.1.1 Data Acquisition Hardware 7
2.1.2 Temperature Hardware 8
2.1.3 Flow Rate Hardware 8
2.1.4 Pressure Hardware 8
2.1.5 Imaging Hardware 8
2.2 Pressure Measurement Location 9
2.3 Velocity Measurement Location 9
2.3.1 Laser Alignment 10
2.4 Boundary Conditions 11
2.4.1 Temperature 11
2.4.2 Pump 11
2.4.3 Volumetric Flow Rate 11
2.4.4 Reynolds Number 12
3.0 Data Sets 13
3.1 List of Electronic Attachments 13
3.2 Volumetric Flow Rate Data 14
3.3 Pressure Data 15
3.4 Velocity (PIV) Data: Instantaneous, Mean, rms, and Reynolds stress. 15
4.0 References 17
Appendix I: Turbine Flow Meter Calibration for p-Cymene 18
Appendix II: Bundle Geometry Calculation 20
Appendix III: notes on piv system calibration and error estimation 22

Acronyms and Definitions

Acronym	Definition
TAMU	The Texas A&M University
CAD	computer-aided-design
CFD	computational fluid dynamics
DP	differential pressure
FS	full scale
FTF	flat-to-flat
GPM	gallon per minute
PIV	particle image velocimetry
RMS	root-mean-square
RTD	resistance thermometer detector
VFD	variable frequency drive

1.0 INTRODUCTION AND SCOPE

This test summary provides information about the experimental setup, boundary conditions, and data sets for the experimental test PCM-11 performed on June 27, 2016. The experimental setup describes the data acquisition, temperature, flow rate, pressure, and imaging hardware utilized to collect data. The boundary conditions are the fluid temperature, centrifugal pump rotational frequency, and volumetric flow rate during the experimental test. The data sets contain the instantaneous and time-averaged flow rate, pressure (axial and azimuthal), and velocity measurements, along with the particle image velocimetry (PIV) statistical analysis.

2.0 TEST DESCRIPTION

An isothermal experimental flow test was conducted utilizing the 61-pin Hexagonal Wire-Wrapped Flow Facility. The test was performed to generate high spatial and temporal resolution data sets of the velocity in a vertical plane and wall pressures through the fuel bundle. The working fluid in the experimental test was p-Cymene. The bundle utilized in this test was the Second Non-Deformed Bundle, with geometric parameters defined in [1]. The measurement process was repeated three times, generating three sets of data. Each set contains time-synchronized PIV and gauge pressure measurements, along with a unique set differential pressure measurements that were not time-synchronized. Both of the PIV and gauge pressure measurements can be averaged over all three sets. The differential pressure measurements in each set correspond to a unique lineup as described in Section 3.3. The measurement length and frequency of each set is provided in section 3.0.

2.1 Experimental Setup

The experimental facility contains two loops. Figure 1 displays a computer-aided design (CAD) model of the experimental facility. The primary loop performs the experimental function. The primary loop includes the following components:

- The hexagonal test section containing the 61-pin wire-wrapped experimental fuel bundle
- The primary tank is used as storage between experiments and as an inline surge volume. The primary pump and associated variable frequency drive (VFD) to control the flow rate in the test section
- An inline turbine flow meter
- A resistance temperature detector (RTD)
- Nine pressure transducers and two differential pressure transducers

The secondary loop performs volume control, temperature control, and filtration. The secondary loop contains the following components:

- The secondary tank
- The secondary pump and associated VFD

- A heat exchanger supplied with chilled water to control the primary loop temperature
- A filtration system

The test section can be divided into three distinct sections can be identified in the test bundle:

- The lower (inlet) plenum located at the bottom of the bundle
- The central section (test section) where the flow measurements will be conducted
- The upper (outlet) plenum located at the top of the bundle.

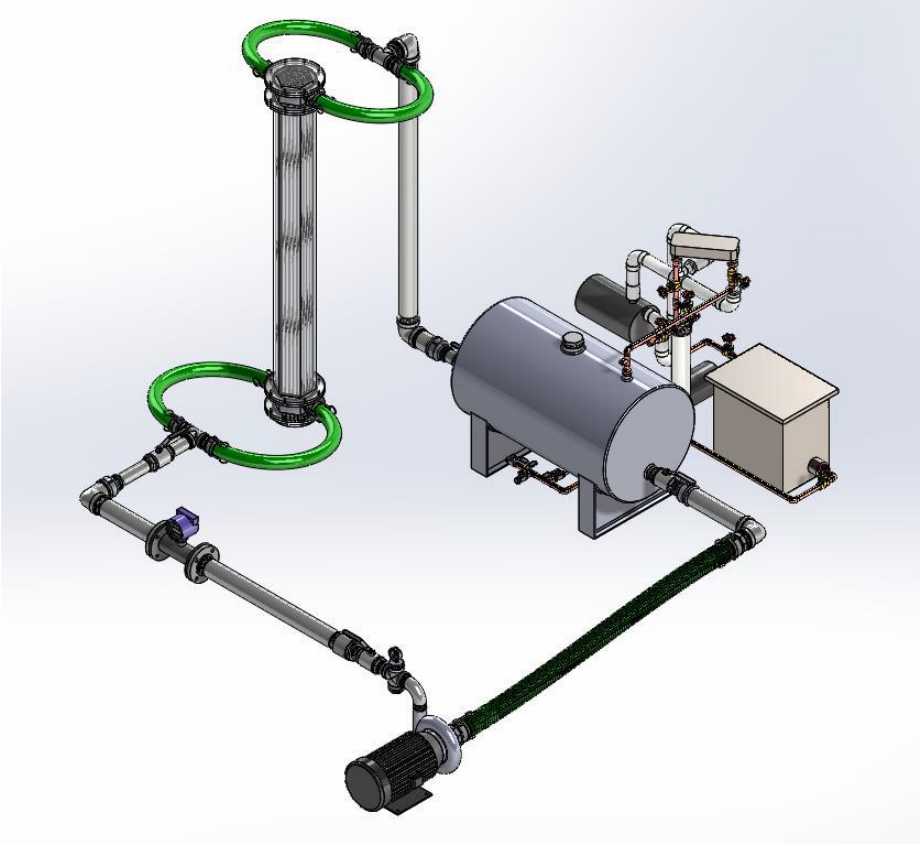


Figure 1. CAD rendering of the experimental facility

2.1.1 Data Acquisition Hardware

The data acquisition hardware consisted of equipment manufactured by National Instruments. The chassis used was a 4-slot model SCXI-1000. The input cards were 32-channel analog input modules, with model numbers of SCXI-1100 and SCXI-1102.

2.1.2 Temperature Hardware

An RDF Corporation resistance temperature device (RTD) was utilized to measure the temperature of the p-Cymene during the experiment. The accuracy of the device is ±0.3˚C at 0˚C with an operating range of -196 ˚C to 480˚C.

2.1.3 Flow Rate Hardware

A Sponsler in-line precision turbine flowmeter was utilized to measure the volumetric flow rate of the working fluid. The Sponsler flowmeter used was a SP3-MB-PHL-D-4X. The uncertainty of the flowmeter analog output is 0.025% of full scale at 20 °C. The full scale reading is 600 gallons per minute (GPM). A Sponsler IT400 totalizer recorded the analog output from the flowmeter with a digital uncertainty of ±1 GPM.

2.1.4 Pressure Hardware

High accuracy pressure transducers were utilized to measure the wall pressure on Face F at various axial locations. Specifications can be found in Table 1.

Table 1. Pressure hardware used in the experimental test

Position In Facility	Model Number	Device Description	Accuracy
0F	PX309-030G5V	30 psi Gauge Pressure	< 4% FS
1F	PX309-030G5V	30 psi Gauge Pressure	< 4% FS
2F	PX419-030G5V	30 psi Gauge Pressure	< 0.1% FS
3F	PX419-030G5V	30 psi Gauge Pressure	< 0.1% FS
4F	PX419-030G5V	30 psi Gauge Pressure	< 0.1% FS
5F	MMG015V5P1D0T4A6CEPS	15 psi Gauge Pressure	<0.1% F.S
6F	PX419-030G5V	30 psi Gauge Pressure	< 0.1% FS
7F	MMG015V5P1D0T4A6CEPS	15 psi Gauge Pressure	<0.1% F.S
8A	PX309-015G5V	15 psi Gauge Pressure	< 1% FS
5 D/E/F/A	P55D-4-N-20-S-5-A	5 inch H_2O Differential Pressure	< 4.28% FS
6 D/E/F/A	MMDWB10WBIV5P2D0T2A2CE	10 inch H_2O Differential Pressure	< 0.1% FS

2.1.5 Imaging Hardware

The PIV system consisted of a 10 W continuous laser at a wavelength of 527 nm and two digital CMOS Phantom M310 cameras. The laser beam was adjusted by beam combination optics to form a 1.5 mm thick laser sheet for the PIV measurements. The laser position was adjusted with three motorized linear

translation stages. The high-speed Phantom M310 cameras have a full resolution of 1280 x 800 pixels, a pixel size of 20 x 20 μm^2 and 12-bit depth image capturing. Seeding particles were silver-coated hollow glass spheres with a mean diameter of 16 µm and a density of 1.6 g cm^{-3}.

2.2 Pressure Measurement Location

The locations of the pressure measurements are defined in [1].

2.3 Velocity Measurement Location

The location of velocity measurements was in the set of exterior subchannels near the wall of Face F, Figure 2. The vertical laser sheet used to illuminate particles for the PIV measurements is represented by the green line (a) (data will be on the plane x-y). The PIV measurement window for each camera is represented by the green rectangles (b). An X-Y coordinate system was assigned to represent horizontal and vertical directions in the laser sheet. The origin of the X-Y coordinate system is shown in Figure 2. The origin is selected as follow:

- x = 0 at the midpoint of face F (inner side)
- y = 0 at centerline of PT#5 (corresponding to the axial location of 2.25 pitches, as defined in [1, 2])
- z = 0 at face F (inner side)

The positive direction of each axis is also shown in Figure 2.

The minimum and maximum X-Y coordinates of the visualization region are X_{min} = -35.50 mm, X_{max} = 40.35 mm, Y_{min} = 107.70 mm, and Y_{max} = 229.18 mm. The x-y plane is located at a z = -1.88 mm.

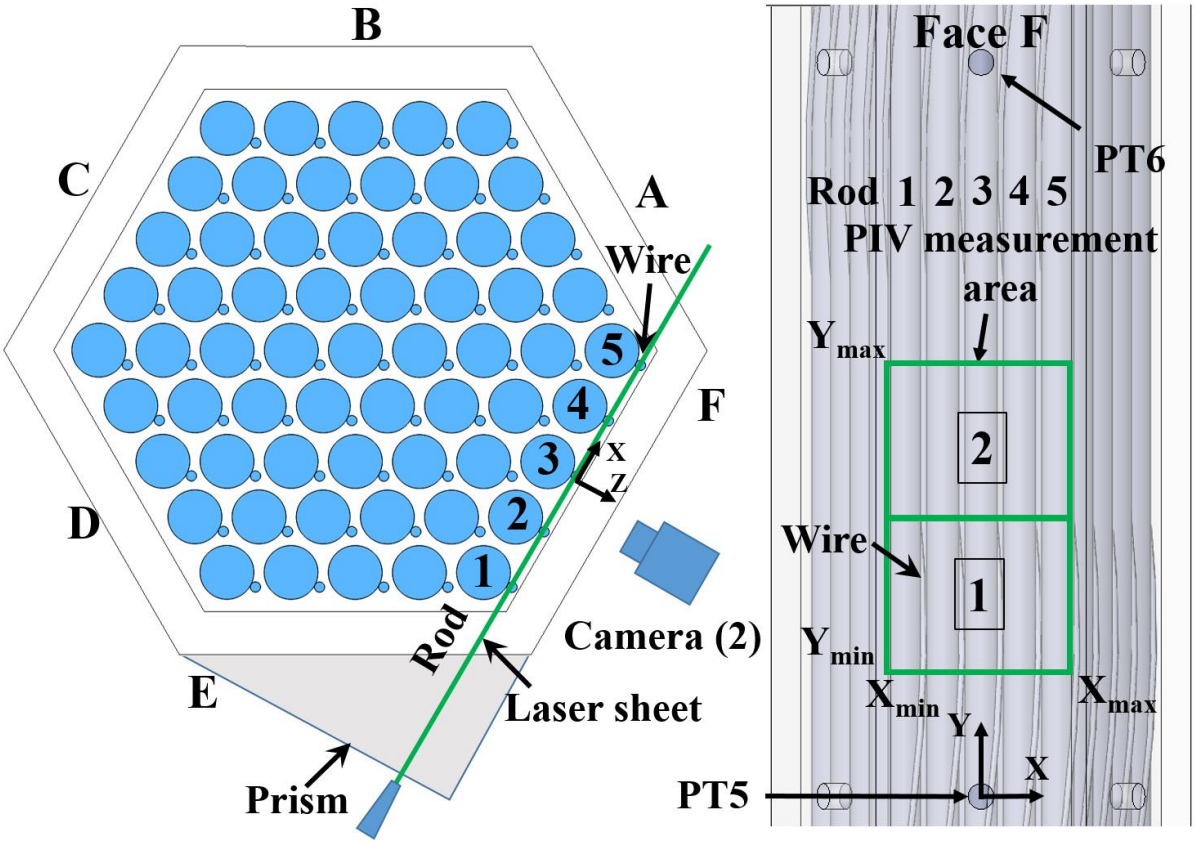


Figure 2. (a) Top view of the fuel bundle denoting the laser and camera positions. (b) Side view of the PIV measurement windows for Camera 1 and 2.

2.3.1 Laser Alignment

A three-dimensional traversing system was utilized to perform fine spatial adjustments of the laser sheet within the test section. The laser alignment process started by adjusting the base of the laser until the laser sheet was parallel with the inner surface of the wall forming Face F. A parallel orientation was confirmed by visual inspection. The relative intensity of the laser sheet in the two corners of Face F was monitored until equal. Next, the laser sheet was laterally traversed until it intersected the exterior row of rods. Again, by visual inspection, the laser sheet was confirmed to simultaneous intersect each rod in

the plane parallel to face F. The laser sheet had a thickness of 1.5 mm ±0.5mm[1]. The distance of the laser sheet from the tangent to the exterior rods was 1.88 mm ±0.5mm[2].

2.4 Boundary Conditions

This section describes the environmental conditions that existed during the experimental test. The quantities of interest were the fluid temperature, the pump frequency, the volumetric flow rate, and the Reynolds number.

2.4.1 Temperature

The temperature was monitored near the pump outlet using a resistance thermometer detector (RTD). The RTD had an uncertainty of ± 0.3 °C. Table 2 contains the temperature of the working fluid measured at the beginning of each data set.

Table 2. Working fluid temperature measured at the beginning of each run

	Fluid Temp (°C)
Set 1	23.3 ± 0.3
Set 2	23.7 ± 0.3
Set 3	24.2 ± 0.3

2.4.2 Pump

The centrifugal pump driving the working fluid was operated at a frequency of 51.5 Hz for all three data sets. The frequency was controlled by a variable frequency drive (VFD)

2.4.3 Volumetric Flow Rate

The average volumetric flow rate for the three sets recorded by the flowmeter for each data set is presented in Table 3. This average is the arithmetic average of the data points recorded during each set. More information is provided in Appendix I.

[1] The thickness of the laser sheet was estimated by measuring the thickness of the projected laser sheet on a flat surface using a ruler of 0.5 mm precision.
[2] Error in the laser sheet location is based on the precision of the ruler used to identify the laser sheet position on the traversing system

Table 3. Averaged volumetric flow rate of each run

	Flow Rate (gal min^{-1})
Set 1	300.06 ± 1.3
Set 2	300.15 ± 1.3
Set 3	300.37 ± 1.3

2.4.4 Reynolds Number

The bundle-averaged Reynolds number for each set was calculated and shown in Table 4. The bundle-averaged Reynolds number was calculated based on the bulk velocity, along with the as-built bundle hydraulic diameter. The pin diameter, wire diameter, and flat-to-flat dimensions used in the hydraulic diameter calculation are the average values from the 61-rod, 61-wire, and 3 enclosure FTF characterizations provided in [1]. The bulk velocity was defined by the averaged volumetric flow rate. Appendix II shows the equations used to calculate the as-built flow area, hydraulic diameter, and wetted perimeter.

The bundle averaged Re number was calculated from Equation 1. Temperature-dependent density and viscosity values of the fluid were linearly interpolated based on the measured temperature of each set, Section 2.4.1 [3]. These values are presented in Table 4.

$$Re = \frac{\rho U_m D_H}{\mu} \tag{1}$$

Table 4. Bundle-averaged Reynolds number

	Fluid Temperature (°C)	Density ($kg\ m^{-3}$)	Bulk Velocity ($m\ s^{-1}$)	Hydraulic Diameter (m)	Dynamic Viscosity (Pa sec)	Reynolds Number
Set 1	23.3	854.58	2.358	7.728 E-3	8.094 E-4	19,239
Set 2	23.7	854.18	2.359	7.728 E-3	8.040 E-4	19,362
Set 3	24.2	853.86	2.360	7.728 E-3	7.999 E-4	19,471

3.0 DATA SETS

This section provides information on the contents of the data files and instruction on how to read them. Three data sets were generated for this experimental test. Each set contains associated flow rate, pressure, and velocity files. Further description of each subset is provided in Sections 3.2, 3.3, and 3.4, respectively. A list of electronic attachments is included in Section 3.1

Table 5 defines the measurement duration and sampling frequency of each measurement in the following data sets.

Table 5. Measurement duration and sampling frequency for each data set

	PIV		Gauge Pressure		Differential Pressure	
	Measurement Duration (sec)	Sampling Frequency (Hz)	Measurement Duration (sec)	Sampling Frequency (Hz)	Measurement Duration (sec)	Sampling Frequency (Hz)
Set1 F-E	~ 3	2800	5.36	2800	9.90	1000
Set2 F-D	~ 3	2800	5.99	2800	10	1000
Set3 F-A	~ 3	2800	4.67	2800	10	1000

3.1 List of Electronic Attachments

The following files are submitted as electronic attachments. The files are archived into a .zip file named REV2-TAMU-WW-TEST-PCM-11-E-DATA.zip. The file is uploaded into the TerraPower ftp server under the folder *DOE Grant 1163/TAMU/PCM-11-E.*

The file contains the following data (time stamp is reported next to the file name).

Volumetric Flow Rate Data

REV2-TAMU-WW-TEST-PCM-11-E-FLOWRATE-SET1.csv 12/12/2016 10:05AM

REV2-TAMU-WW-TEST-PCM-11-E-FLOWRATE-SET2.csv 12/12/2016 10:06AM

REV2-TAMU-WW-TEST-PCM-11-E-FLOWRATE-SET3.csv 12/12/2016 10:07AM

REV2-TAMU-WW-TEST-PCM-11-E-FLOWRATE-AVERAGE.csv 12/12/2016 10:04AM

Pressure Data

REV2-TAMU-WW-TEST-PCM-11-E-PRESSURE-SET1-F-E.csv 11/21/2016 2:15PM

REV2-TAMU-WW-TEST-PCM-11-E-PRESSURE-SET2-F-D.csv 11/21/2016 2:16PM

REV2-TAMU-WW-TEST-PCM-11-E-PRESSURE-SET3-F-A.csv 11/21/2016 2:14PM

REV2-TAMU-WW-TEST-PCM-11-E-PRESSURE-AVERAGE.csv 12/12/2016 9:44AM

Velocity (PIV) Data

REV2-TAMU-WW-TEST-PCM-11-E_Inst_Vel-SET1.zip (all files with time stamp 12/07/2016 5:16PM to 10:39PM)

REV2-TAMU-WW-TEST-PCM-11-E_Vel_Stats_Mean-SET1.dat 12/11/2016 2:59PM

REV2-TAMU-WW-TEST-PCM-11-E_Vel_Stats_RMS-SET1.dat 12/11/2016 2:59PM

REV2-TAMU-WW-TEST-PCM-11-E_Vel_Stats_UV-SET1.dat 12/11/2016 2:59PM

REV2-TAMU-WW-TEST-PCM-11-E_Inst_Vel-SET2.zip (all files with time stamp 12/07/2016 5:17PM to 10:42PM)

REV2-TAMU-WW-TEST-PCM-11-E_Vel_Stats_Mean-SET2.dat 12/11/2016 3:46PM

REV2-TAMU-WW-TEST-PCM-11-E_Vel_Stats_RMS-SET2.dat 12/11/2016 3:46PM

REV2-TAMU-WW-TEST-PCM-11-E_Vel_Stats_UV-SET2.dat 12/11/2016 3:46PM

REV2-TAMU-WW-TEST-PCM-11-E_Inst_Vel-SET3.zip (all files with time stamp 12/07/2016 5:18PM to 10:44PM)

REV2-TAMU-WW-TEST-PCM-11-E_Vel_Stats_Mean-SET3.dat 12/11/2016 3:49PM

REV2-TAMU-WW-TEST-PCM-11-E_Vel_Stats_RMS-SET3.dat 12/11/2016 3:49PM

REV2-TAMU-WW-TEST-PCM-11-E_Vel_Stats_UV-SET3.dat 12/11/2016 3:49PM

REV2-TAMU-WW-TEST-PCM-11-E_Vel_Stats_Mean-combined.dat 12/11/2016 4:00PM

REV2-TAMU-WW-TEST-PCM-11-E_Vel_Stats_RMS-combined.dat 12/11/2016 4:00PM

REV2-TAMU-WW-TEST-PCM-11-E_Vel_Stats_UV-combined.dat 12/11/2016 4:00PM

3.2 Volumetric Flow Rate Data

Three files are provided containing the instantaneous volumetric flow rate for each set:

REV2-TAMU-WW-TEST-PCM-11-E-FLOWRATE-SET1.csv

REV2-TAMU-WW-TEST-PCM-11-E-FLOWRATE-SET2.csv

REV2-TAMU-WW-TEST-PCM-11-E-FLOWRATE-SET3.csv

A summary file is included, which contains the arithmetic average, standard deviation, and k-factor conversion for each set.

REV2-TAMU-WW-TEST-PCM-11-E-FLOWRATE-AVERAGE.xlsx

The summary file contains the calculation to convert the raw flow meter output (working fluid = water) into the actual flow rate (working fluid = p-Cymene). More information on data conversion is provided in Appendix II.

3.3 Pressure Data

Three files are provided containing the instantaneous pressures for each set:

REV2-TAMU-WW-TEST-PCM-11-E-PRESSURE-SET1-F-E.csv

REV2-TAMU-WW-TEST-PCM-11-E-PRESSURE-SET2-F-D.csv

REV2-TAMU-WW-TEST-PCM-11-E-PRESSURE-SET3-F-A.csv

Each file contains a unique pair of letters at the end of the filename. This corresponds to the two faces being measured by the azimuthal differential pressure (DP) transducers. Set 1 contains the DP data between faces F and E. Set 2 contains the DP data between faces F and D. Set 3 contains the DP data between faces F and A.

The pressure data from PT0 – PT8 were recorded during the same time interval as the velocity measurements using an electronic pulse to trigger the start of the data acquisition. The DP data was recorded immediately after recording the data from PT0 – PT8.

The signal output from the DP transducers was factory calibrated in inches of water. The provided files contain the raw DP data in inches of water, along with a column containing the conversion into psi using the following conversion factors from [4] in Equation 3.

$$Pressure\ (inch\ water) = \left[\frac{2.4884\times10^{2}\ Pa}{1\ inch\ water\ at\ 60\ ^{\circ}\mathrm{F}}\right]\left[\frac{1\ psi}{6.894757\times10^{3}\ Pa}\right] \quad (3)$$

A summary file is included, which contains the arithmetic average and standard deviation for each set.

REV2-TAMU-WW-TEST-PCM-11-E-PRESSURE-AVERAGE.xlsx

NOTE: PT5, PT7, and PT8 were off-scale for this test, as the maximum reading of these transducers is 15 psig.

3.4 Velocity (PIV) Data: Instantaneous, Mean, rms, and Reynolds stress.

The velocity data provided represents a two dimensional array, but is presented in a one dimensional vector. The vector field consists of 114 point on x-direction, and 178 points on y-direction. Notes on calibration and error estimation are provided in Appendix III.

All data are stored in .dat format. These files contain multiple columns without headers.

Each set is identified in the file name (SET1, SETE2, SET3). File naming is consistent within the sets. As an example, contain for SET1 is described below:

REV2-TAMU-WW-TEST-PCM-11-E_Inst_Vel-SET1.zip:

This file contains 8308 .dat files of the instantaneous velocity. The structure of each file is described in Table 5.

Table 6. Instantaneous Velocity .dat File Structure

Column #	1	2	3	4	5	6
Parameter	X	Y	Z	u	v	w
Unit	mm	mm	mm	m/s	m/s	m/s

REV2-TAMU-WW-TEST-PCM-11-E_Vel_Stats_Mean-SET1.dat:

This file contains the time-averaged velocity for set 1. The structure of the file is shown in Table 6.

Table 7. Mean Velocity .dat File Structure

Column #	1	2	3	4	5	6
Parameter	X	Y	Z	u	v	w
Unit	mm	mm	mm	m/s	m/s	m/s

REV2-TAMU-WW-TEST-PCM-11-E_Vel_Stats_RMS-SET1.dat:

This file contains the root mean square (rms) fluctuating velocity. The file structure is described in Table 7.

Table 8. rms File Structure

Column #	1	2	3	4	5	6
Parameter	X	Y	Z	u'_rms	v'_rms	w'_rms
Unit	mm	mm	mm	m/s	m/s	m/s

REV2-TAMU-WW-TEST-PCM-11-E_Vel_Stats_UV-SET1.dat

This file contains the Reynold Stress $\overline{u'v'}$. The file structure is described in Table 8.

Table 9. Reynolds Stress File Structure

Column #	1	2	3	4
Parameter	X	Y	Z	$\overline{u'v'}$
Unit	mm	mm	mm	$m^2\ s^{-2}$

NOTE: in all .dat files, z is constant and equal to the laser sheet location (1.88 mm). The velocity component along the z-direction and all related parameters are 0.

The .dat files marked as "combined" contain the same information and structure of the files described above for set 1. However, the statistical values are computed based on the total number of instantaneous velocities (3 x 8308 = 24924).

4.0 REFERENCES

1. TAMU-WW-AS Rev.1, TAMU Wire-Wrapped As-Built Geometry (Non-Deformed Bundle)
2. TWRP-31-TSPEC-0010 Rev. 1 , TAMU Fuel Assembly Flow Visualization Test Specification,
3. P-Cymene Chemical Information Sheet. Cameo Chemicals, Database of Hazard Materials, June 1999.
4. Appendix B.9 Factors for units listed by kind of quantity or field of science, NIST Guide, https://www.nist.gov/pml/nist-guide-si-appendix-b9-factors-units-listed-kind-quantity-or-field-science
5. S.-K. CHENG and N. E. TODREAS, "Hydrodynamic Models and Correlations for Bare and Wire-Wrapped Hexagonal Rod Bundles — Bundle Friction Factors, Subchannel Friction Factors and Mixing Parameters," Nucl. Eng. Des., 92, , 227–251 (1986).

APPENDIX I: TURBINE FLOW METER CALIBRATION FOR P-CYMENE

Since the flow meter was originally calibrated with water as the working fluid, the data presented in the output file is the flow rate of the fluid if it was water. Because the working fluid, p-Cymene, has a different density and viscosity than water, it was required to generate a new calibration of the turbine flow meter with p-Cymene as the working fluid.

This was achieved using an Omega FPT-6130 high accuracy pitot tube with an Omega high accuracy differential pressure transducer. The Omega FPT-6130 high accuracy Pitot tube had an accuracy of < 1% of the volumetric flow rate. Three different Omega differential pressure transducers were utilized, because the range of DP measured by each transducer is small relative to the total span of DP required to fully calibrate the turbine flow meter. Each Omega differential pressure transducer had the following maximum pressure reading, associated accuracy, and flow meter frequency range in which each differential pressure transducer was used, Table 109.

Table 10. Differential pressure transducers utilized in the p-Cymene k-factor calibration

Differential Pressure Transducer	Maximum Pressure (psi)	Accuracy (% Full Scale)	Flow Meter Frequency Range (Hz)
Omega MMDWB10WBIV5P2D0T2A2CE	0.36	< 0.1% FS	0-100
Omega MMDWB001BIV5P2D0T2A2CE	1.0	< 0.1% FS	100-160
Omega MMDWB005BIV5P2D0T2A3CE	5.0	< 0.1% FS	160-300

The rate meter determined the volumetric flow rate by multiplying the turbine rotational frequency by a multiplication factor, the factory calibrated k-factor. A new p-Cymene k-factor was calculated from the pitot flow, turbine meter output, and the factory k-factor. Presented in Figure 3 is a plot of the p-Cymene k-factor as a function of turbine flow meter frequency. The factory calibrated k-factor for water was 43.2411. The p-Cymene volumetric flow rate is calculated by Equation 4.

$$Flow\ Rate_{pcy} = Indicated\ Flow\ Rate\left(\frac{k_{H2O}}{k_{pcy}}\right) \quad (4)$$

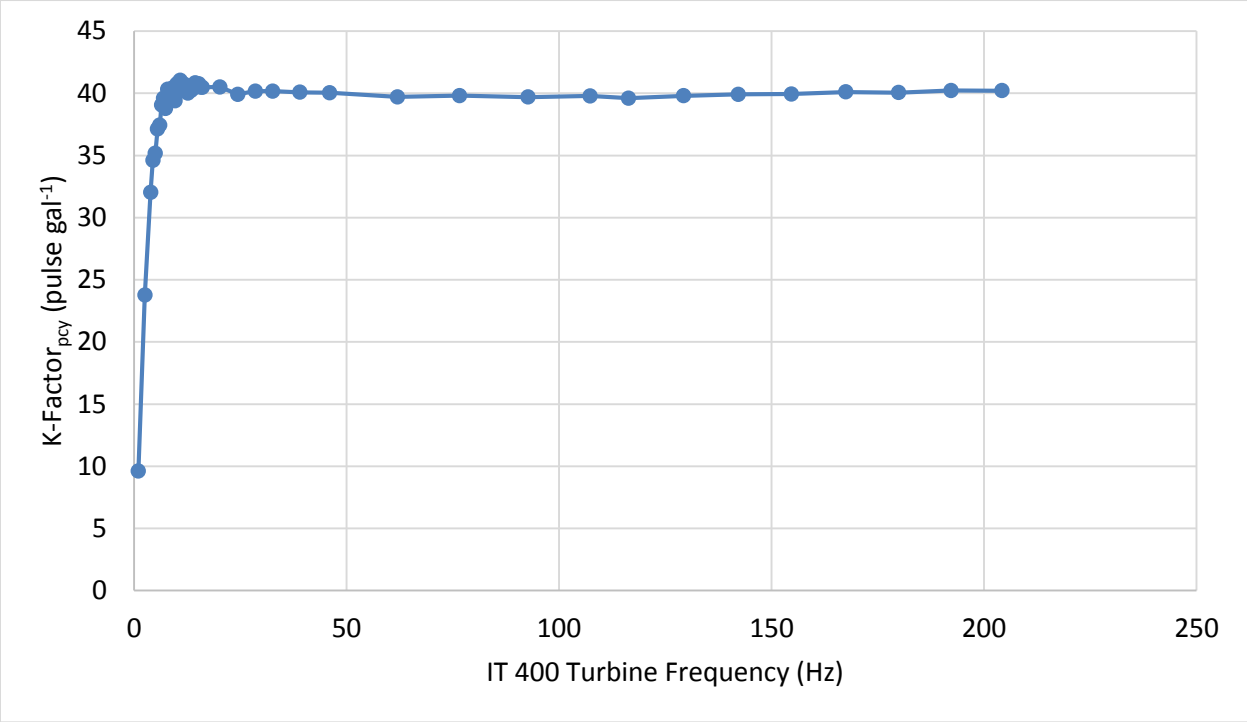


Figure 3. p-Cymene k-factor plotted versus the turbine flow meter rotational frequency

APPENDIX II: BUNDLE GEOMETRY CALCULATION

From [5], the following expressions describe the variables used in the bundle geometry calculation. The subscripts one, two, and three correspond to the interior, wall, and corner sub channels respectively. P is the rod pitch, D is the pin diameter, D_{wire} is the wire spacer diameter, D_h is the hydraulic diameter, W is the edge pitch, N_i is the number of each sub channel, and H is the wire spacer lead or axial distance required for the spacer to complete one revolution around the pin. D, D_{wire}, and $W$are from the rod, wire and flat-to-flat characterization performed in [1]. The cosine term takes into account the elliptical projected area of the wire due to it not being parallel to the flow.

Parameter	Value	Unit
N_1	96	n/a
N_2	24	n/a
N_3	6	n/a
P	1.8878 E-2	m
D	1.5880 E-2	m
D_{wire}	3.0000 E-3	m
W	1.9548 E-2	m
$FTF_{enclosure}$	1.5400 E-1	m
FTF_{bundle}	1.5266 E-1	m
A_1	5.1747 E-5	m^2
A_2	1.1661 E-4	m^2
A_3	4.3637 E-5	m^2
A_{Bundle}	8.0281 E-3	m^2
$P_{wet,1}$	2.9688 E-2	m
$P_{wet,2}$	4.8564 E-2	m
$P_{wet,3}$	2.3302 E-2	m
$P_{wet,bundle}$	4.1554	m
H	4.7625 E-1	m

$$W = D + G_{wall}$$

$$G_{wall} = FTF_{enclosure} - FTF_{bundle}$$

$$FTF_{bundle} = \frac{8P\sqrt{3}}{2} + D + 2D_{wire}$$

$$A_1 = \left(\frac{\sqrt{3}}{4}\right)P^2 - \frac{\pi D^2}{8} - \frac{\pi D_{wire}^2}{8\cos(\theta)}$$

$$A_2 = \left(W - \frac{D}{2}\right)P - \frac{\pi D^2}{8} - \frac{\pi D_{wire}^2}{8\cos(\theta)}$$

$$A_3 = \frac{\left(W - \frac{D}{2}\right)^2}{\sqrt{3}} - \frac{\pi D^2}{24} - \frac{\pi D_{wire}^2}{24\cos(\theta)}$$

$$A_{Bundle} = N_1 A_1 + N_2 A_2 + N_3 A_3$$

$$P_{wet,1} = \frac{\pi D}{2} + \frac{\pi D_{wire}}{2\cos(\theta)}$$

$$P_{wet,2} = P + \frac{\pi D}{2} + \frac{\pi D_{wire}}{2\cos(\theta)}$$

$$P_{wet,3} = \frac{\pi D}{6} + \frac{2\left(W - \frac{D}{2}\right)}{\sqrt{3}} + \frac{\pi D_{wire}}{6\cos(\theta)}$$

$$P_{wet,Bundle} = N_1 P_{wet,1} + N_2 P_{wet,2} + N_3 P_{wet,3}$$

$$D_h = \frac{4\,A_{Bundle}}{P_{wet,Bundle}}$$

$$\cos(\theta) = \frac{H}{\sqrt{H^2 + \left(\pi(D + D_w)\right)^2}}$$

APPENDIX III: NOTES ON PIV SYSTEM CALIBRATION AND ERROR ESTIMATION

The system was calibrated using LaVision ® calibration plates. The methodology adopted followed the guidelines published and described in [A-III-1].

The software used for the PIV imaging post-processing is the PRANA code developed by Virginia Tech. Performance and uncertainty of the PRANA RPC algorithm have been previously accessed (A-III-2, A-III-3, A-III-4, and A-III-5).

The analysis described in this report analysis was limited to estimate the overall uncertainty in the PIV velocity measurements. This was estimated to be approximately 0.1 pixels which yields to an uncertainty of less than 3% of the mean axial velocity.

[A-III-1]. Wieneke, B. "Stereo-PIV using self-calibration on particle images". Experiments in Fluids (2005) 39: 267–280 DOI 10.1007/s00348-005-0962-z

[A-III-2]. Timmins, B. H., Wilson, B. W., Smith, B. L. and Vlachos, P. P. ,"A method for automatic estimation of instantaneous local uncertainty in particle image velocimetry measurements". Experiments in Fluids 53(4): 1133–1147.

[A-III-3]. Wilson, B. M. and Smith, B. L., "Uncertainty on PIV mean and Fluctuating velocity due to Bias and Random Errors", Measurement Science and Technology 24(3): 035302.

[A-III-4]. Charonko, J. J. and Vlachos, P. P.,"Estimation of Uncertainty Bounds for Individual Particle Image Velocimetry Measurements from Cross-Correlation Peak Ratio". Measurement Science and Technology 24(6): 065301.

[A-III-5]. Boomsma, A., Bhattacharya, S., Troolin, D., Pothos, S. and Vlachos, P., "A Comparative Experimental Evaluation of Uncertainty Estimation Methods for Two-Component PIV". Measurement Science and Technology 27(9): 094006.

APPENDIX L: TAMU-WW-TEST-PCM-16-C2, TAMU WIRE-WRAPPED TEST SUMMARY OF TEST PCM-16-C2 (CENTER PLANE - 30° OFFSET)

TECHNICAL DOCUMENT COVER PAGE

Document No:	TAMU-WW-TEST-PCM-16-C2	Revision: Rev.1	Page 1 of 21
Doc Title:	TAMU Wire-Wrapped Test Summary of Test PCM-16-C2 (Center plane - 30° offset)		
Projects No:	DE-NE0008321		
Project Name:	Toward a Longer Life Core: Thermal-Hydraulic CFD Simulations and Experimental Investigation of Deformed Fuel Assemblies		

Document Purpose/Summary: This document summarizes the conditions of the experimental test PCM-16-C2, and provides instructions for reading the associated flowrate and velocity data produced by the experimental test.

Total Page Count: 21 pages.

TECHNICAL DOCUMENT COVER PAGE

Document No:	TAMU-WW-TEST-PCM-16-C2	Revision: Rev.1	Page 2 of 21

TAMU Prepared By:	Nolan Goth		12/15/16
	Printed/Typed Name	Signature	Date
	Philip Jones		12/15/16
	Printed/Typed Name	Signature	Date
TAMU Reviewed By:	Thien Nguyen		12/12/16
	Printed/Typed Name	Signature	Date
	Rodolfo Vaghetto		12/15/16
	Printed/Typed Name	Signature	Date
Approved By:			
	Printed/Typed Name	Signature	Date

REVISION HISTORY LOG

Document Number: TAMU-WW-TEST-PCM-16-C2 Revision: Rev.1

Document Title: TAMU Wire-Wrapped Test Summary of Test PCM-16-C2 (Center plane - 30° offset)

REVISION	DATE	DESCRIPTION
Rev.0	11/23/16	First Release.
Rev.1	12/14/16	Changed reference coordinate system (Section 2.2) and updated file naming (Section 3.1)

Table of Contents

1.0 Introduction and Scope 6
2.0 Test Description 6
2.1 Experimental Setup 6
2.1.1 Data Acquisition Hardware 7
2.1.2 Temperature Hardware 7
2.1.3 Flow Rate Hardware 8
2.1.4 Imaging Hardware 8
2.2 Velocity Measurement Location 8
2.2.1 Laser Alignment 10
2.3 Boundary Conditions 10
2.3.1 Temperature 10
2.3.2 Pump 10
2.3.3 Volumetric Flow Rate 11
2.3.4 Reynolds Number 11
3.0 Data Sets 12
3.1 List of Electronic Attachments 12
3.2 Volumetric Flow Rate Data 14
3.3 Velocity (PIV) Data: Instantaneous, Mean, rms, and Reynolds stress. 14
4.0 References 16
Appendix I: Turbine Flow Meter Calibration for p-Cymene 17
Appendix II: Bundle Geometry Calculation 19
Appendix III: Notes on PIV System Calibration and Error Estimation 21

Acronyms and Definitions

Acronym	Definition
TAMU	The Texas A&M University
CAD	computer-aided-design
CFD	computational fluid dynamics
DP	differential pressure
FS	full scale
FTF	flat-to-flat
GPM	gallon per minute
PIV	particle image velocimetry
RMS	root-mean-square
RTD	resistance thermometer detector
VFD	variable frequency drive

1.0 INTRODUCTION AND SCOPE

This test summary provides information about the experimental setup, boundary conditions, and data sets for the experimental test PCM-16-C2 performed on August 04, 2016. The experimental setup describes the data acquisition, temperature, flow rate, and imaging hardware utilized to collect data. The boundary conditions are the fluid temperature, centrifugal pump rotational frequency, and volumetric flow rate during the experimental test. The data sets contain the instantaneous and time-averaged flow rate, instantaneous velocity measurements, along with the particle image velocimetry (PIV) statistical analysis.

2.0 TEST DESCRIPTION

An isothermal experimental flow test was conducted utilizing the 61-pin Hexagonal Wire-Wrapped Flow Facility. The test was performed to generate high spatial and temporal resolution data sets of the velocity in a vertical plane. Pressure measurements were not recorded during this test. The working fluid in the experimental test was p-Cymene. The bundle utilized in this test was the Second Non-Deformed Bundle, with geometric parameters defined in [1]. The measurement process was repeated three times, generating three sets of flowrate and velocity data.

2.1 Experimental Setup

The experimental facility contains two loops. Figure 1 displays a computer-aided design (CAD) model of the experimental facility. The primary loop performs the experimental function. The primary loop includes the following components:

- The hexagonal test section containing the 61-pin wire-wrapped experimental fuel bundle
- The primary tank is used as storage between experiments and as an inline surge volume. The primary pump and associated variable frequency drive (VFD) to control the flow rate in the test section
- An inline turbine flow meter
- A resistance temperature detector (RTD)
- Nine pressure transducers and two differential pressure transducers

The secondary loop performs volume control, temperature control, and filtration. The secondary loop contains the following components:

- The secondary tank
- The secondary pump and associated VFD
- A heat exchanger supplied with chilled water to control the primary loop temperature
- A filtration system

The test section can be divided into three distinct sections can be identified in the test bundle:

- The lower (inlet) plenum located at the bottom of the bundle
- The central section (test section) where the flow measurements will be conducted
- The upper (outlet) plenum located at the top of the bundle.

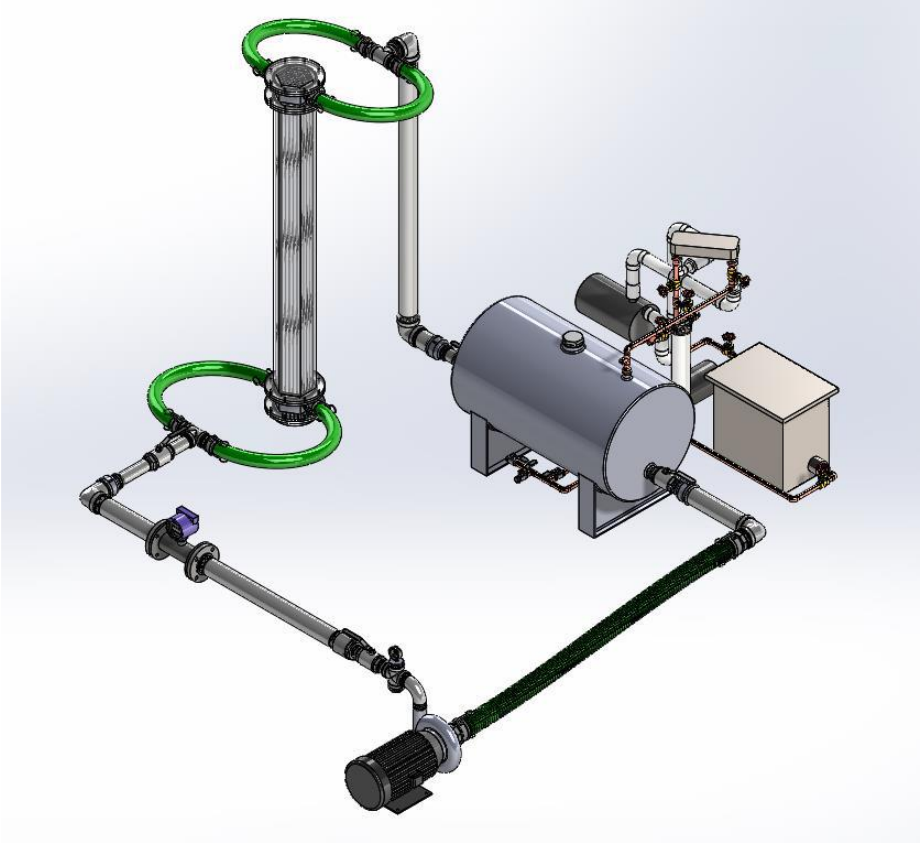


Figure 1. CAD rendering of the experimental facility

2.1.1 Data Acquisition Hardware

The data acquisition hardware consisted of equipment manufactured by National Instruments. The chassis used was a 4-slot model SCXI-1000. The input cards were 32-channel analog input modules, with model numbers of SCXI-1100 and SCXI-1102.

2.1.2 Temperature Hardware

An RDF Corporation resistance temperature device (RTD) was utilized to measure the temperature of the p-Cymene during the experiment. The accuracy of the device is ±0.3˚C at 0˚C with an operating range of -196 ˚C to 480˚C.

2.1.3 Flow Rate Hardware

A Sponsler in-line precision turbine flowmeter was utilized to measure the volumetric flow rate of the working fluid. The Sponsler flowmeter used was a SP3-MB-PHL-D-4X. The uncertainty of the flowmeter analog output is 0.025% of full scale at 20 °C. The full scale reading is 600 gallons per minute (GPM). A Sponsler IT400 totalizer recorded the analog output from the flowmeter with a digital uncertainty of ±1 GPM.

2.1.4 Imaging Hardware

The PIV system consisted of a 10 W continuous laser at a wavelength of 527 nm and two digital CMOS Phantom M310 cameras. The laser beam was adjusted by beam combination optics to form a 1.5 mm thick laser sheet for the PIV measurements. The laser position was adjusted with three motorized linear translation stages. The high-speed Phantom M310 cameras have a full resolution of 1280 x 800 pixels, a pixel size of 20 x 20 μm^2 and 12-bit depth image capturing. Seeding particles were silver-coated hollow glass spheres with a mean diameter of 16 µm and a density of 1.6 g cm^{-3}.

2.2 Velocity Measurement Location

The location of velocity measurements was in the set of interior subchannels denoted in Figure 2. The vertical laser sheet used to illuminate particles for the PIV measurements is represented by the green line (a). The figure also shows the location of the prism used during the experiment. A closeup of the subchannels of interest (SC1 and SC2) can be seen in (c). The PIV measurement window for each camera is represented by the green rectangles (b). In (b), pins are dark grey and the subchannels are light grey. The wires of neighboring pins cross into SC1 and SC2 at various axial locations. These wires are visible as dark grey sweeps across the subchannels. An Y-Z coordinate system was assigned to represent horizontal and vertical directions in the laser sheet. The origin of the Y-Z coordinate system is shown in Figure 2. The origin is selected as follow:

- x = 0 at the midpoint of face A (inner side)
- y = 0 at centerline of PT#5 (corresponding to the axial location of 2.25 pitches, as defined in [1, 2])
- z = 0 at face A (inner side)

The positive direction of each axis is also shown in Figure 2.

The minimum and maximum Y-Z coordinates of the visualization region are listed below:

Subchannel 1 (SC1)

Y_{min} = 28.0 mm, Y_{max} = 154.4 mm

Z_{min} = -69.0 mm, and Z_{max} = -53.2 mm.

Subchannel 2 (SC2)

Y_{min} = 28.0 mm, Y_{max} = 154.4 mm

Z_{min} = -36.3 mm, and Z_{max} = -20.5 mm.

The y-z plane is located at a x = 0 mm.

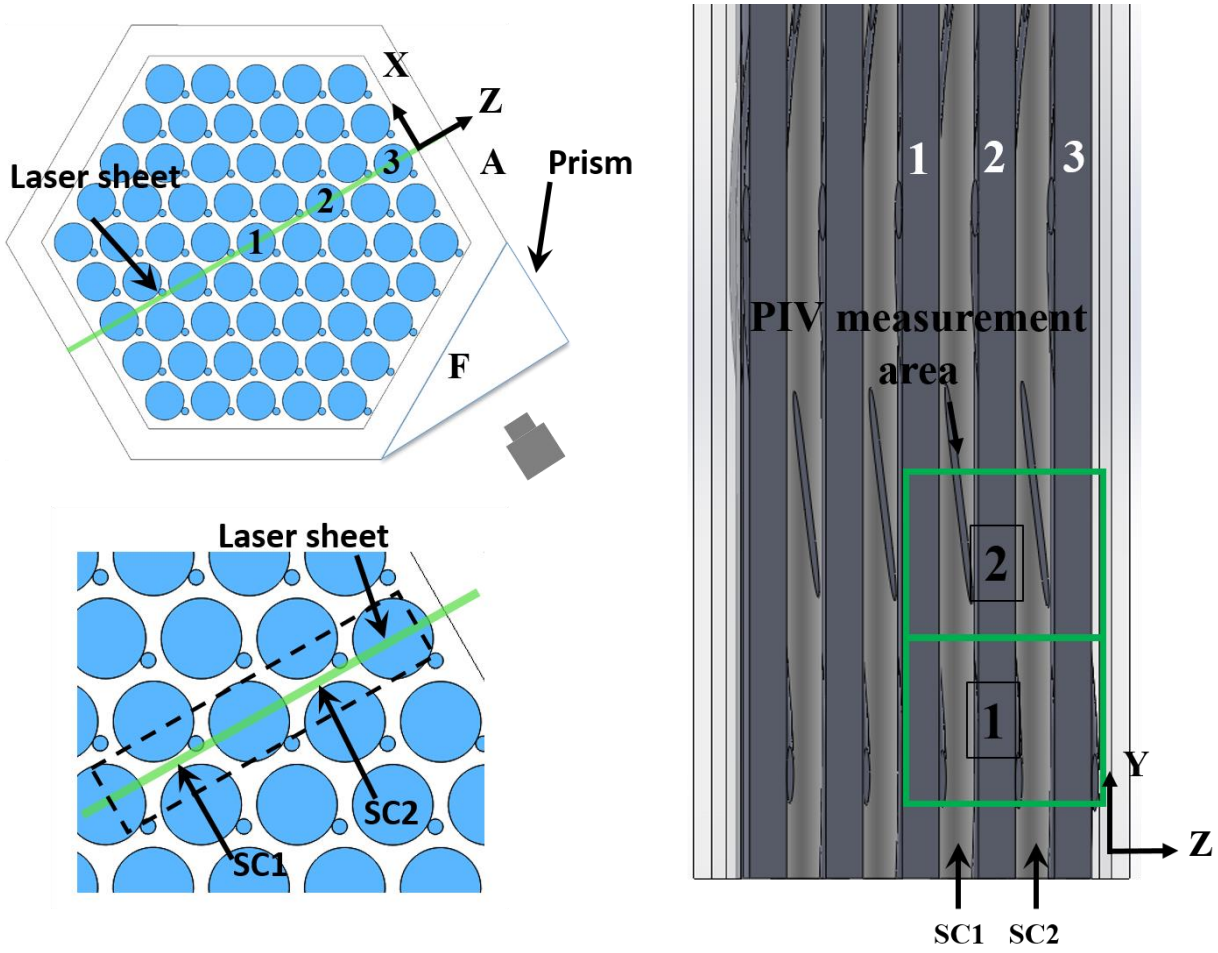


Figure 2. (a) Top view of the fuel bundle denoting the laser and camera positions. (b) Side view of the PIV measurement windows for Camera 1 and 2. (c) Top view close-up of SC1 and SC2.

2.2.1 Laser Alignment

A three-dimensional traversing system was utilized to perform fine spatial adjustments of the laser sheet within the test section. The laser alignment process started by placing the laser perpendicular Face D and Face A (opposite sides of the hexagonal enclosure). The laser sheet was then moved laterally until the laser sheet intersected the horizontal midpoints of Face D and Face A simultaneously. The midpoints of Face D and Face A were located using two rulers with 0.03125 inch markings. The laser sheet had a thickness of 1.5 mm ±0.5mm[1].

2.3 Boundary Conditions

This section describes the environmental conditions that existed during the experimental test. The quantities of interest were the fluid temperature, the pump frequency, the volumetric flow rate, and the Reynolds number.

2.3.1 Temperature

The temperature was monitored near the pump outlet using a resistance thermometer detector (RTD). The RTD had an uncertainty of ± 0.3 °C. Table 1 contains the temperature of the working fluid measured at the beginning of each data set.

Table 1. Working fluid temperature measured at the beginning of each run

	Fluid Temp (°C)
Set 1	19.8 ± 0.3
Set 2	20.0 ± 0.3
Set 3	20.3 ± 0.3

2.3.2 Pump

The centrifugal pump driving the working fluid was operated at a frequency of 51.5 Hz for all three data sets. The frequency was controlled by a variable frequency drive (VFD)

[1] The thickness of the laser sheet was estimated by measuring the thickness of the projected laser sheet on a flat surface using a ruler of 0.5 mm precision.

2.3.3 Volumetric Flow Rate

The average volumetric flow rate for the three sets recorded by the flowmeter for each data set is presented in Table 2. This average is the arithmetic average of the data points recorded during each set. More information is provided in Appendix I.

Table 2. Averaged volumetric flow rate of each run

	Flow Rate (gal min^{-1})
Set 1	301.96 ±1.3
Set 2	302.09 ±1.3
Set 3	301.81 ±1.3

2.3.4 Reynolds Number

The bundle-averaged Reynolds number for each set was calculated and shown in Table 3. The bundle-averaged Reynolds number was calculated based on the bulk velocity, along with the as-built bundle hydraulic diameter. The pin diameter, wire diameter, and flat-to-flat dimensions used in the hydraulic diameter calculation are the average values from the 61-rod, 61-wire, and 3 enclosure FTF characterizations provided in [1]. The bulk velocity was defined by the averaged volumetric flow rate. Appendix II shows the equations used to calculate the as-built flow area, hydraulic diameter, and wetted perimeter.

The bundle averaged Re number was calculated from Equation 1. Temperature-dependent density and viscosity values of the fluid were linearly interpolated based on the measured temperature of each set, Section 2.3.1 [3]. These values are presented in Table 3.

$$Re = \frac{\rho U_m D_H}{\mu} \tag{1}$$

Table 3. Bundle-averaged Reynolds number

	Fluid Temperature (°C)	Density (kg m^{-3})	Bulk Velocity (m s^{-1})	Hydraulic Diameter (m)	Dynamic Viscosity (Pa sec)	Reynolds Number
Set 1	19.8	857.41	2.373	7.728 E-3	8.472 E-4	18,558
Set 2	20.0	857.24	2.374	7.728 E-3	8.450 E-4	18,610
Set 3	20.3	857.00	2.372	7.728 E-3	8.405 E-4	18,688

3.0 DATA SETS

This section provides information on the contents of the data files and instruction on how to read them. Three data sets were generated for this experimental test. Each set contains associated flow rate and velocity files. Further description of each subset is provided in Sections 3.2 and 3.3. A list of electronic attachments is included in Section 3.1

Table 4 defines the measurement duration and sampling frequency of each measurement in the following data sets.

Table 4. Measurement duration and sampling frequency for each data set

	PIV	
	Measurement Duration (sec)	Sampling Frequency (Hz)
Set 1	~ 3	2800
Set 2	~ 3	2800
Set 3	~ 3	2800

3.1 List of Electronic Attachments

The following files are submitted as electronic attachments. The files are archived into a .zip file named REV1-TAMU-WW-TEST-PCM-16-C2-DATA.zip. The file is uploaded into the TerraPower ftp server under the folder *DOE Grant 1163/TAMU/PCM-16-C2.*

The file contains the following data (time stamp is reported next to the file name).

Volumetric Flow Rate Data

REV1-TAMU-WW-TEST-PCM-16-C2-FLOWRATE-SET1.csv 10/21/2016 1:19PM

REV1-TAMU-WW-TEST-PCM-16-C2-FLOWRATE-SET2.csv 10/21/2016 1:19PM

REV1-TAMU-WW-TEST-PCM-16-C2-FLOWRATE-SET3.csv 10/21/2016 1:19PM

REV1-TAMU-WW-TEST-PCM-16-C2-FLOWRATE-AVERAGE.xlsx 10/21/2016 1:19PM

Velocity (PIV) Data – Subchannel 1

REV1-TAMU-WW-TEST-PCM-16-C2_SUB1_Inst_Vel-SET1.zip 12/14/2016 6:57PM

REV1-TAMU-WW-TEST-PCM-16-C2_SUB1_Vel_Stats_Mean-SET1.dat 12/14/2016 11:46AM

REV1-TAMU-WW-TEST-PCM-16-C2_SUB1_Vel_Stats_RMS-SET1.dat 12/14/2016 11:46AM

REV1-TAMU-WW-TEST-PCM-16-C2_SUB1_Vel_Stats_VW-SET1.dat 12/14/2016 11:46AM

REV1-TAMU-WW-TEST-PCM-16-C2_SUB1_Inst_Vel-SET2.zip 12/14/2016 8:34PM
REV1-TAMU-WW-TEST-PCM-16-C2_SUB1_Vel_Stats_Mean-SET2.dat 12/14/2016 11:50AM
REV1-TAMU-WW-TEST-PCM-16-C2_SUB1_Vel_Stats_RMS-SET2.dat 12/14/2016 11:50AM
REV1-TAMU-WW-TEST-PCM-16-C2_SUB1_Vel_Stats_VW-SET2.dat 12/14/2016 11:50AM
REV1-TAMU-WW-TEST-PCM-16-C2_SUB1_Inst_Vel-SET3.zip 12/14/2016 8:35PM
REV1-TAMU-WW-TEST-PCM-16-C2_SUB1_Vel_Stats_Mean-SET3.dat 12/14/2016 11:50AM
REV1-TAMU-WW-TEST-PCM-16-C2_SUB1_Vel_Stats_RMS-SET3.dat 12/14/2016 11:50AM
REV1-TAMU-WW-TEST-PCM-16-C2_SUB1_Vel_Stats_VW-SET3.dat 12/14/2016 11:50AM
REV1-TAMU-WW-TEST-PCM-16-C2_SUB1_Vel_Stats_Mean-combined.dat 12/14/2016 12:07PM
REV1-TAMU-WW-TEST-PCM-16-C2_SUB1_Vel_Stats_RMS-combined.dat 12/14/2016 12:07PM
REV1-TAMU-WW-TEST-PCM-16-C2_SUB1_Vel_Stats_VW-combined.dat 12/14/2016 12:07PM

Velocity (PIV) Data – Subchannel 2

REV1-TAMU-WW-TEST-PCM-16-C2_SUB2_Inst_Vel-SET1.zip 12/14/2016 8:35PM
REV1-TAMU-WW-TEST-PCM-16-C2_SUB2_Vel_Stats_Mean-SET1.dat 12/14/2016 11:53AM
REV1-TAMU-WW-TEST-PCM-16-C2_SUB2_Vel_Stats_RMS-SET1.dat 12/14/2016 11:53AM
REV1-TAMU-WW-TEST-PCM-16-C2_SUB2_Vel_Stats_VW-SET1.dat 12/14/2016 11:53AM
REV1-TAMU-WW-TEST-PCM-16-C2_SUB2_Inst_Vel-SET2.zip 12/14/2016 8:36PM
REV1-TAMU-WW-TEST-PCM-16-C2_SUB2_Vel_Stats_Mean-SET2.dat 12/14/2016 11:56AM
REV1-TAMU-WW-TEST-PCM-16-C2_SUB2_Vel_Stats_RMS-SET2.dat 12/14/2016 11:56AM
REV1-TAMU-WW-TEST-PCM-16-C2_SUB2_Vel_Stats_VW-SET2.dat 12/14/2016 11:56AM
REV1-TAMU-WW-TEST-PCM-16-C2_SUB2_Inst_Vel-SET3.zip 12/14/2016 7:59PM
REV1-TAMU-WW-TEST-PCM-16-C2_SUB2_Vel_Stats_Mean-SET3.dat 12/14/2016 11:57AM
REV1-TAMU-WW-TEST-PCM-16-C2_SUB2_Vel_Stats_RMS-SET3.dat 12/14/2016 11:57AM
REV1-TAMU-WW-TEST-PCM-16-C2_SUB2_Vel_Stats_VW-SET3.dat 12/14/2016 11:57AM
REV1-TAMU-WW-TEST-PCM-16-C2_SUB2_Vel_Stats_Mean-combined.dat 12/14/2016 12:11PM
REV1-TAMU-WW-TEST-PCM-16-C2_SUB2_Vel_Stats_RMS-combined.dat 12/14/2016 12:11PM
REV1-TAMU-WW-TEST-PCM-16-C2_SUB2_Vel_Stats_VW-combined.dat 12/14/2016 12:11PM

3.2 Volumetric Flow Rate Data

Three files are provided containing the instantaneous volumetric flow rate for each set:

REV1-TAMU-WW-TEST-PCM-16-C2-FLOWRATE-SET1.csv

REV1-TAMU-WW-TEST-PCM-16-C2-FLOWRATE-SET2.csv

REV1-TAMU-WW-TEST-PCM-16-C2-FLOWRATE-SET3.csv

A summary file is included, which contains the arithmetic average, standard deviation, and k-factor conversion for each set.

REV1-TAMU-WW-TEST-PCM-16-C2-FLOWRATE-AVERAGE.xlsx

The summary file contains the calculation to convert the raw flow meter output (working fluid = water) into the actual flow rate (working fluid = p-Cymene). More information on data conversion is provided in Appendix I.

3.3 Velocity (PIV) Data: Instantaneous, Mean, rms, and Reynolds stress.

The velocity data provided represents a two dimensional array, but is presented in a one dimensional vector. For each subchannel, the vector field consists of 23 point in the x-direction, and 177 points in the y-direction. Notes on calibration and error estimation are provided in Appendix III.

All data are stored in .dat format. These files contain multiple columns without headers.

Each set is identified in the file name (SET1, SETE2, SET3). File naming is consistent within the sets. As an example, content for SET1 of subchannel 1 is described below:

REV1-TAMU-WW-TEST-PCM-16-C2_SUB1_Inst_Vel-SET1.zip:

This file contains 8309 .dat files of the instantaneous velocity. The structure of each file is described in Table 5

Table 5. Instantaneous Velocity .dat File Structure

Column #	1	2	3	4	5	6
Parameter	X	Y	Z	u	v	w
Unit	mm	mm	mm	m/s	m/s	m/s

REV1-TAMU-WW-TEST-PCM-16-C2_SUB1_Vel_Stats_Mean-SET1.dat:

This file contains the time-averaged velocity for set 1. The structure of the file is shown in Table 6.

Table 6. Mean Velocity .dat File Structure

Column #	1	2	3	4	5	6
Parameter	X	Y	Z	u	v	w
Unit	mm	mm	mm	m/s	m/s	m/s

REV1-TAMU-WW-TEST-PCM-16-C2_SUB1_Vel_Stats_RMS-SET1.dat:

This file contains the root mean square (rms) fluctuating velocity. The file structure is described in Table 7.

Table 7. rms File Structure

Column #	1	2	3	4	5	6
Parameter	X	Y	Z	u'_rms	v'_rms	w'_rms
Unit	mm	mm	mm	m/s	m/s	m/s

REV1-TAMU-WW-TEST-PCM-16-C2_SUB1_Vel_Stats_VW-SET1.dat

This file contains the Reynolds Stress $\overline{u'v'}$. The file structure is described in Table 8.

Table 8. Reynolds Stress File Structure

Column #	1	2	3	4
Parameter	X	Y	Z	$\overline{u'v'}$
Unit	mm	mm	mm	$m^2\ s^{-2}$

NOTE: in all .dat files, z is constant and set to zero. The velocity component along the z-direction and all related parameters are 0.

The .dat files marked as "combined" contain the same information and structure of the files described above for set 1. However, the statistical values are computed based on the total number of instantaneous velocities (3 x 8309 = 24927).

4.0 REFERENCES

1. TAMU-WW-AS Rev.1, TAMU Wire-Wrapped As-Built Geometry (Non-Deformed Bundle)
2. TWRP-31-TSPEC-0010 Rev. 1 , TAMU Fuel Assembly Flow Visualization Test Specification,
3. P-Cymene Chemical Information Sheet. Cameo Chemicals, Database of Hazard Materials, June 1999.
4. Appendix B.9 Factors for units listed by kind of quantity or field of science, NIST Guide, https://www.nist.gov/pml/nist-guide-si-appendix-b9-factors-units-listed-kind-quantity-or-field-science
5. S.-K. CHENG and N. E. TODREAS, "Hydrodynamic Models and Correlations for Bare and Wire-Wrapped Hexagonal Rod Bundles — Bundle Friction Factors, Subchannel Friction Factors and Mixing Parameters," Nucl. Eng. Des., 92, 227–251 (1986).

APPENDIX I: TURBINE FLOW METER CALIBRATION FOR P-CYMENE

Since the flow meter was originally calibrated with water as the working fluid, the data presented in the output file is the flow rate of the fluid if it was water. Because the working fluid, p-Cymene, has a different density and viscosity than water, it was required to generate a new calibration of the turbine flow meter with p-Cymene as the working fluid.

This was achieved using an Omega FPT-6130 high accuracy pitot tube with an Omega high accuracy differential pressure transducer. The Omega FPT-6130 high accuracy Pitot tube had an accuracy of < 1% of the volumetric flow rate. Three different Omega differential pressure transducers were utilized, because the range of DP measured by each transducer is small relative to the total span of DP required to fully calibrate the turbine flow meter. Each Omega differential pressure transducer had the following maximum pressure reading, associated accuracy, and flow meter frequency range in which each differential pressure transducer was used, Table 99.

Table 9. Differential pressure transducers utilized in the p-Cymene k-factor calibration

Differential Pressure Transducer	Maximum Pressure (psi)	Accuracy (% Full Scale)	Flow Meter Frequency Range (Hz)
Omega MMDWB10WBIV5P2D0T2A2CE	0.36	< 0.1% FS	0-100
Omega MMDWB001BIV5P2D0T2A2CE	1.0	< 0.1% FS	100-160
Omega MMDWB005BIV5P2D0T2A3CE	5.0	< 0.1% FS	160-300

The rate meter determined the volumetric flow rate by multiplying the turbine rotational frequency by a multiplication factor, the factory calibrated k-factor. A new p-Cymene k-factor was calculated from the pitot flow, turbine meter output, and the factory k-factor. Presented in Figure 3 is a plot of the p-Cymene k-factor as a function of turbine flow meter frequency. The factory calibrated k-factor for water was 43.2411. The p-Cymene volumetric flow rate is calculated by Equation 4.

$$Flow\ Rate_{pcy} = Indicated\ Flow\ Rate\left(\frac{k_{H2O}}{k_{pcy}}\right) \quad (4)$$

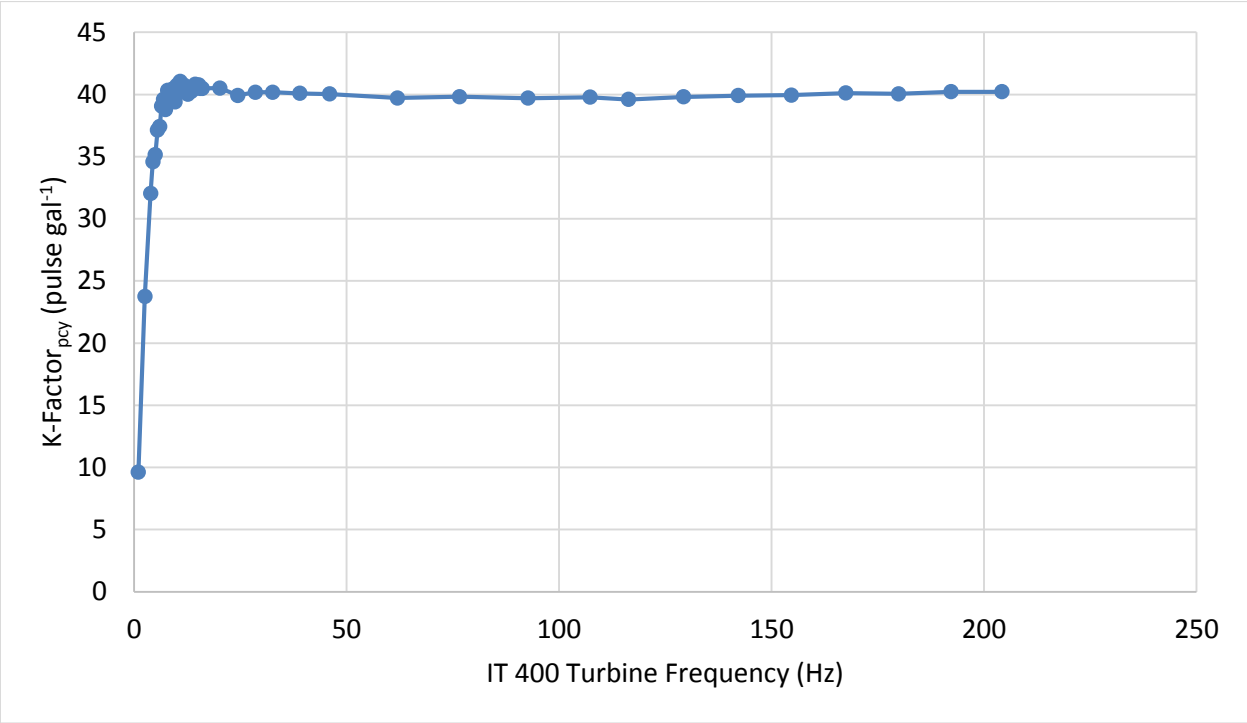


Figure 3. p-Cymene k-factor plotted versus the turbine flow meter rotational frequency

APPENDIX II: BUNDLE GEOMETRY CALCULATION

From [5], the following expressions describe the variables used in the bundle geometry calculation. The subscripts one, two, and three correspond to the interior, wall, and corner sub channels respectively. P is the rod pitch, D is the pin diameter, D_{wire} is the wire spacer diameter, D_h is the hydraulic diameter, W is the edge pitch, N_i is the number of each sub channel, and H is the wire spacer lead or axial distance required for the spacer to complete one revolution around the pin. D, D_{wire}, and $W$are from the rod, wire and flat-to-flat characterization performed in [1]. The cosine term takes into account the elliptical projected area of the wire due to it not being parallel to the flow.

Parameter	Value	Unit
N_1	96	n/a
N_2	24	n/a
N_3	6	n/a
P	1.8878 E-2	m
D	1.5880 E-2	m
D_{wire}	3.0000 E-3	m
W	1.9548 E-2	m
$FTF_{enclosure}$	1.5400 E-1	m
FTF_{bundle}	1.5266 E-1	m
A_1	5.1747 E-5	m^2
A_2	1.1661 E-4	m^2
A_3	4.3637 E-5	m^2
A_{Bundle}	8.0281 E-3	m^2
$P_{wet,1}$	2.9688 E-2	m
$P_{wet,2}$	4.8564 E-2	m
$P_{wet,3}$	2.3302 E-2	m
$P_{wet,bundle}$	4.1554	m
H	4.7625 E-1	m

$$W = D + G_{wall}$$

$$G_{wall} = FTF_{enclosure} - FTF_{bundle}$$

$$FTF_{bundle} = \frac{8P\sqrt{3}}{2} + D + 2D_{wire}$$

$$A_1 = \left(\frac{\sqrt{3}}{4}\right)P^2 - \frac{\pi D^2}{8} - \frac{\pi D_{wire}^2}{8\cos(\theta)}$$

$$A_2 = \left(W - \frac{D}{2}\right)P - \frac{\pi D^2}{8} - \frac{\pi D_{wire}^2}{8\cos(\theta)}$$

$$A_3 = \frac{\left(W - \frac{D}{2}\right)^2}{\sqrt{3}} - \frac{\pi D^2}{24} - \frac{\pi D_{wire}^2}{24\cos(\theta)}$$

$$A_{Bundle} = N_1 A_1 + N_2 A_2 + N_3 A_3$$

$$P_{wet,1} = \frac{\pi D}{2} + \frac{\pi D_{wire}}{2\cos(\theta)}$$

$$P_{wet,2} = P + \frac{\pi D}{2} + \frac{\pi D_{wire}}{2\cos(\theta)}$$

$$P_{wet,3} = \frac{\pi D}{6} + \frac{2\left(W - \frac{D}{2}\right)}{\sqrt{3}} + \frac{\pi D_{wire}}{6\cos(\theta)}$$

$$P_{wet,Bundle} = N_1 P_{wet,1} + N_2 P_{wet,2} + N_3 P_{wet,3}$$

$$D_h = \frac{4\,A_{Bundle}}{P_{wet,Bundle}}$$

$$\cos(\theta) = \frac{H}{\sqrt{H^2 + \left(\pi(D + D_w)\right)^2}}$$

APPENDIX III: NOTES ON PIV SYSTEM CALIBRATION AND ERROR ESTIMATION

The system was calibrated using LaVision ® calibration plates. The methodology adopted followed the guidelines published and described in [A-III-1].

The software used for the PIV imaging post-processing is the PRANA code developed by Virginia Tech. Performance and uncertainty of the PRANA RPC algorithm have been previously accessed (A-III-2, A-III-3, A-III-4, and A-III-5).

The analysis described in this report analysis was limited to estimate the overall uncertainty in the PIV velocity measurements. This was estimated to be approximately 0.1 pixels which yields to an uncertainty of less than 3% of the mean axial velocity.

[A-III-1]. Wieneke, B. "Stereo-PIV using self-calibration on particle images". Experiments in Fluids (2005) 39: 267–280 DOI 10.1007/s00348-005-0962-z

[A-III-2]. Timmins, B. H., Wilson, B. W., Smith, B. L. and Vlachos, P. P. ,"A method for automatic estimation of instantaneous local uncertainty in particle image velocimetry measurements". Experiments in Fluids 53(4): 1133–1147.

[A-III-3]. Wilson, B. M. and Smith, B. L., "Uncertainty on PIV mean and Fluctuating velocity due to Bias and Random Errors", Measurement Science and Technology 24(3): 035302.

[A-III-4]. Charonko, J. J. and Vlachos, P. P.,"Estimation of Uncertainty Bounds for Individual Particle Image Velocimetry Measurements from Cross-Correlation Peak Ratio". Measurement Science and Technology 24(6): 065301.

[A-III-5]. Boomsma, A., Bhattacharya, S., Troolin, D., Pothos, S. and Vlachos, P., "A Comparative Experimental Evaluation of Uncertainty Estimation Methods for Two-Component PIV". Measurement Science and Technology 27(9): 094006.

APPENDIX M: TAMU-WW-TEST-PCM-14-INT1, TAMU WIRE-WRAPPED TEST SUMMARY OF TEST PCM-14-INT1 AT INTERIOR SUBCHANNEL ONE

TECHNICAL DOCUMENT COVER PAGE

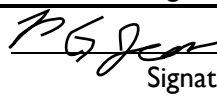
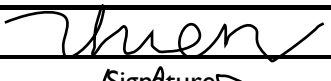
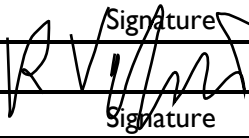
Document No:	TAMU-WW-TEST-PCM-14-INT1	Revision: Rev.0	Page 1 of 19
Doc Title:	TAMU Wire-Wrapped Test Summary of Test PCM-14-INT1 at Interior Subchannel One		
Projects No:	DE-NE0008321		
Project Name:	Toward a Longer Life Core: Thermal-Hydraulic CFD Simulations and Experimental Investigation of Deformed Fuel Assemblies		

Document Purpose/Summary: This document summarizes the conditions of the experimental test PCM-14-INT1, and provides instructions for reading the associated flowrate and velocity data produced by the experimental test.

Total Page Count: 19 pages.

TECHNICAL DOCUMENT COVER PAGE

Document No:	TAMU-WW-TEST-PCM-14-INT1	Revision: Rev.0	Page 2 of 19

TAMU Prepared By:	Nolan Goth		12/20/16
	Printed/Typed Name	Signature	Date
	Philip Jones		12/20/16
	Printed/Typed Name	Signature	Date
TAMU Reviewed By:	Thien Nguyen		12/20/16
	Printed/Typed Name	Signature	Date
	Rodolfo Vaghetto		12/20/16
	Printed/Typed Name	Signature	Date
Approved By:			
	Printed/Typed Name	Signature	Date

REVISION HISTORY LOG

Document Number: TAMU-WW-TEST-PCM-14-INT1 Revision: Rev.0

Document Title: TAMU Wire-Wrapped Test Summary of Test PCM-14-INT1 at Interior Subchannel One

REVISION	DATE	DESCRIPTION
Rev.0	12/19/2016	First release

Table of Contents

1.0 Introduction and Scope 6
2.0 Test Description 6
2.1 Experimental Setup 6
2.1.1 Data Acquisition Hardware 7
2.1.2 Temperature Hardware 7
2.1.3 Flow Rate Hardware 8
2.1.4 Imaging Hardware 8
2.2 Velocity Measurement Location 8
2.2.1 Laser Alignment 10
2.3 Boundary Conditions 10
2.3.1 Temperature 10
2.3.2 Pump 10
2.3.3 Volumetric Flow Rate 11
2.3.4 Reynolds Number 11
3.0 Data Sets 12
3.1 List of Electronic Attachments 12
3.2 Volumetric Flow Rate Data 13
3.3 Velocity (PTV) Data: Mean, rms, and Reynolds stress. 13
4.0 References 15
Appendix I: Turbine Flow Meter Calibration for p-Cymene 16
Appendix II: Bundle Geometry Calculation 18

Acronyms and Definitions

Acronym	Definition
TAMU	The Texas A&M University
CAD	computer-aided-design
CFD	computational fluid dynamics
DP	differential pressure
FS	full scale
FTF	flat-to-flat
GPM	gallon per minute
PTV	particle tracking velocimetry
RMS	root-mean-square
RTD	resistance thermometer detector
VFD	variable frequency drive

1.0 INTRODUCTION AND SCOPE

This test summary provides information about the experimental setup, boundary conditions, and data sets for the experimental test PCM-14-INT1 performed on August 2nd, 2016. The experimental setup describes the data acquisition, temperature, flow rate, and imaging hardware utilized to collect data. The boundary conditions are the fluid temperature, centrifugal pump rotational frequency, and volumetric flow rate during the experimental test. The data sets contain the instantaneous and time-averaged flow rate, instantaneous velocity measurements, along with the particle tracking velocimetry (PTV) statistical analysis.

2.0 TEST DESCRIPTION

An isothermal experimental flow test was conducted utilizing the 61-pin Hexagonal Wire-Wrapped Flow Facility. The test was performed to generate high spatial and temporal resolution data sets of the velocity in a vertical plane. Pressure measurements were not recorded during this test. The working fluid in the experimental test was p-Cymene. The bundle utilized in this test was the Second Non-Deformed Bundle, with geometric parameters defined in [1]. The measurement process was repeated three times, generating three sets of flowrate and velocity data. The PTV measurements can be averaged over all three sets. The measurement length and frequency of each set is provided in section 3.0.

2.1 Experimental Setup

The experimental facility contains two loops. Figure 1 displays a computer-aided design (CAD) model of the experimental facility. The primary loop performs the experimental function. The primary loop includes the following components:

- The hexagonal test section containing the 61-pin wire-wrapped experimental fuel bundle
- The primary tank is used as storage between experiments and as an inline surge volume. The primary pump and associated variable frequency drive (VFD) to control the flow rate in the test section
- An inline turbine flow meter
- A resistance temperature detector (RTD)
- Nine pressure transducers and two differential pressure transducers

The secondary loop performs volume control, temperature control, and filtration. The secondary loop contains the following components:

- The secondary tank
- The secondary pump and associated VFD
- A heat exchanger supplied with chilled water to control the primary loop temperature
- A filtration system

The test section can be divided into three distinct sections can be identified in the test bundle:

- The lower (inlet) plenum located at the bottom of the bundle
- The central section (test section) where the flow measurements will be conducted
- The upper (outlet) plenum located at the top of the bundle.

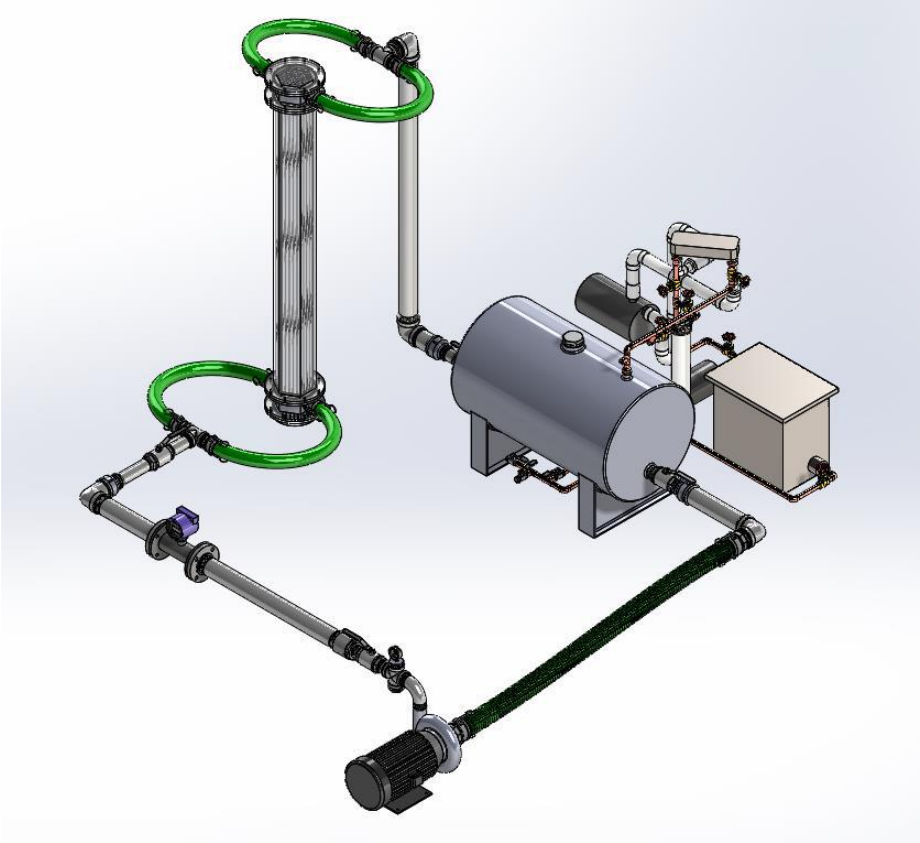


Figure 1. CAD rendering of the experimental facility

2.1.1 Data Acquisition Hardware

The data acquisition hardware consisted of equipment manufactured by National Instruments. The chassis used was a 4-slot model SCXI-1000. The input cards were 32-channel analog input modules, with model numbers of SCXI-1100 and SCXI-1102.

2.1.2 Temperature Hardware

An RDF Corporation resistance temperature device (RTD) was utilized to measure the temperature of the p-Cymene during the experiment. The accuracy of the device is ±0.3˚C at 0˚C with an operating range of -196 ˚C to 480˚C.

2.1.3 Flow Rate Hardware

A Sponsler in-line precision turbine flowmeter was utilized to measure the volumetric flow rate of the working fluid. The Sponsler flowmeter used was a SP3-MB-PHL-D-4X. The uncertainty of the flowmeter analog output is 0.025% of full scale at 20 °C. The full scale reading is 600 gallons per minute (GPM). A Sponsler IT400 totalizer recorded the analog output from the flowmeter with a digital uncertainty of ±1 GPM.

2.1.4 Imaging Hardware

The PTV system consisted of a 10 W continuous laser at a wavelength of 527 nm and two digital CMOS Phantom M310 cameras. The laser beam was adjusted by beam combination optics to form a 1.5 mm thick laser sheet for the PTV measurements. The laser position was adjusted with three motorized linear translation stages. The high-speed Phantom M310 cameras have a full resolution of 1280 x 800 pixels, a pixel size of 20 x 20 μm^2 and 12-bit depth image capturing. Seeding particles were silver-coated hollow glass spheres with a mean diameter of 16 µm and a density of 1.6 g cm^{-3}.

2.2 Velocity Measurement Location

The location of velocity measurements was in the set of interior subchannels formed by the row of pins nearest to Face F, Figure 2. The vertical laser sheet used to illuminate particles for the PTV measurements is represented by the green line (a). The PTV measurement window for each camera is represented by the green rectangles (b). An X-Y coordinate system was assigned to represent horizontal and vertical directions in the laser sheet. The coordinate system is identical to the coordinate system used in [6]. The origin of the coordinate system is shown in Figure 2. The origin is selected as follow:

- x = 0 at the midpoint of face F (inner side)
- y = 0 at centerline of PT#5 (corresponding to the axial location of 2.25 pitches, as defined in [1, 2])
- z = 0 at face F (inner side)

Subchannel 1 (SC1)

X_{min} = -29.7 mm, and X_{max} = -26.7 mm.

Y_{min} = 25.7 mm, Y_{max} = 156.5 mm

Subchannel 2 (SC2)

X_{min} = -10.8 mm, and X_{max} = -7.8 mm.

Y_{min} = 25.7 mm, Y_{max} = 156.5 mm

Subchannel 3 (SC3)

X_{min} = 8.0 mm, and X_{max} = 11.0 mm.

Y_{min} = 25.7 mm, Y_{max} = 156.5 mm

Subchannel 4 (SC4)

X_{min} = 26.9 mm, and X_{max} = 29.9 mm.

Y_{min} = 25.7 mm, Y_{max} = 156.5 mm

The x-y plane is located at a z = -11.69 mm.

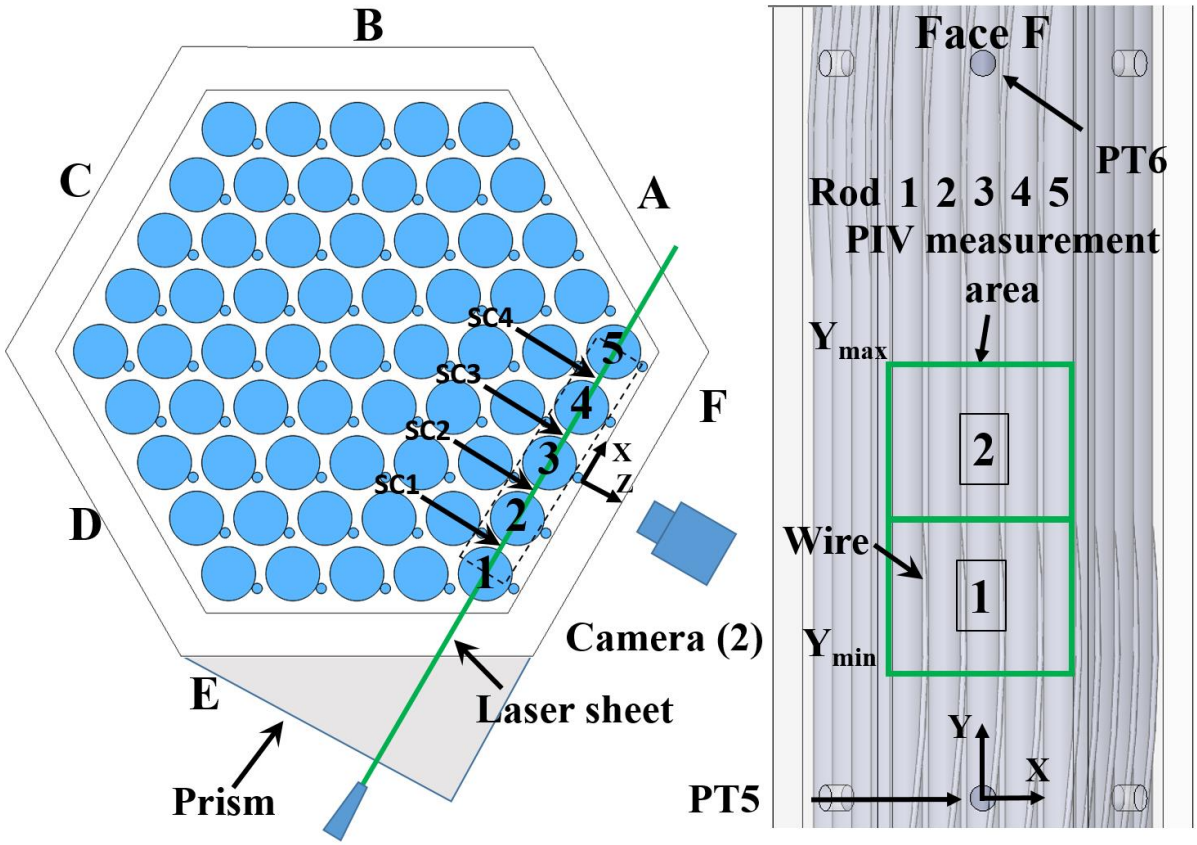


Figure 2. (a) Top view of the fuel bundle denoting the laser and camera positions. (b) Side view of the PTV measurement windows for Camera 1 and 2.

2.2.1 Laser Alignment

A three-dimensional traversing system was utilized to perform fine spatial adjustments of the laser sheet within the test section. The laser alignment process started by adjusting the base of the laser until the laser sheet was parallel with the inner surface of the wall forming Face F. A parallel orientation was confirmed by visual inspection. The relative intensity of the laser sheet in the two corners of Face F was monitored until equal. Next, the laser sheet was laterally traversed until it intersected the exterior row of rods. Again, by visual inspection, the laser sheet was confirmed to simultaneous intersect each rod in the plane parallel to face F. Finally, the laser sheet was traversed until equally bisecting rods of the first row. The laser sheet had a thickness of 1.5 mm ±0.5mm[1].

2.3 Boundary Conditions

This section describes the environmental conditions that existed during the experimental test. The quantities of interest were the fluid temperature, the pump frequency, the volumetric flow rate, and the Reynolds number.

2.3.1 Temperature

The temperature was monitored near the pump outlet using a resistance thermometer detector (RTD). The RTD had an uncertainty of ± 0.3 °C. Table 1 contains the temperature of the working fluid measured at the beginning of each data set.

Table 1. Working fluid temperature measured at the beginning of each run

	Fluid Temp (°C)
Set 1	22.0 ± 0.3
Set 2	22.4 ± 0.3
Set 3	22.5 ± 0.3

2.3.2 Pump

The centrifugal pump driving the working fluid was operated at a frequency of 51.5 Hz for all three data sets. The frequency was controlled by a variable frequency drive (VFD)

[1] The thickness of the laser sheet was estimated by measuring the thickness of the projected laser sheet on a flat surface using a ruler of 0.5 mm precision.

2.3.3 Volumetric Flow Rate

The average volumetric flow rate for the three sets recorded by the flowmeter for each data set is presented in Table 2. This average is the arithmetic average of the data points recorded during each set. More information is provided in Appendix I.

Table 2. Averaged volumetric flow rate of each run

	Flow Rate (gal min^{-1})
Set 1	301.32 ± 1.3
Set 2	301.07 ± 1.3
Set 3	301.08 ± 1.3

2.3.4 Reynolds Number

The bundle-averaged Reynolds number for each set was calculated and shown in Table 4. The bundle-averaged Reynolds number was calculated based on the bulk velocity, along with the as-built bundle hydraulic diameter. The pin diameter, wire diameter, and flat-to-flat dimensions used in the hydraulic diameter calculation are the average values from the 61-rod, 61-wire, and 3 enclosure FTF characterizations provided in [1]. The bulk velocity was defined by the averaged volumetric flow rate. Appendix II shows the equations used to calculate the as-built flow area, hydraulic diameter, and wetted perimeter.

The bundle averaged Re number was calculated from Equation 1. Temperature-dependent density and viscosity values of the fluid were linearly interpolated based on the measured temperature of each set, Section 2.3.1 [3]. These values are presented in Table 3.

$$Re = \frac{\rho U_m D_H}{\mu} \tag{1}$$

Table 3. Bundle-averaged Reynolds number

	Fluid Temperature (°C)	Density ($kg\ m^{-3}$)	Bulk Velocity ($m\ s^{-1}$)	Hydraulic Diameter (m)	Dynamic Viscosity (Pa sec)	Reynolds Number
Set 1	22.0	855.63	2.368	7.728 E-3	8.234 E-4	19,014
Set 2	22.4	855.31	2.366	7.728 E-3	8.191 E-4	19,091
Set 3	22.5	855.22	2.366	7.728 E-3	8.175 E-4	19,127

3.0 DATA SETS

This section provides information on the contents of the data files and instruction on how to read them. Three data sets were generated for this experimental test. Each set contains associated flow rate and velocity files. Further description of each subset is provided in Sections 3.2 and 3.3. A list of electronic attachments is included in Section 3.1

Table 4 defines the measurement duration and sampling frequency of each measurement in the following data sets.

Table 4. Measurement duration and sampling frequency for each data set

	PTV	
	Measurement Duration (sec)	Sampling Frequency (Hz)
Set 1	~ 3	2800
Set 2	~ 3	2800
Set 3	~ 3	2800

3.1 List of Electronic Attachments

The following files are submitted as electronic attachments. The files are archived into a .zip file named REV0-TAMU-WW-TEST-PCM-14-INT1-DATA.zip. The file is uploaded into the TerraPower ftp server under the folder *DOE Grant 1163/TAMU/PCM-14-INT1*.

Volumetric Flow Rate Data

REV0-TAMU-WW-TEST-PCM-14-INT1-FLOWRATE-SET1.csv 11/22/2016 2:54PM

REV0-TAMU-WW-TEST-PCM-14-INT1-FLOWRATE-SET2.csv 11/22/2016 2:54PM

REV0-TAMU-WW-TEST-PCM-14-INT1-FLOWRATE-SET3.csv 11/22/2016 2:54PM

REV0-TAMU-WW-TEST-PCM-14-INT1-FLOWRATE-AVERAGE.csv 11/22/2016 2:54PM

Velocity (PTV) Data

REV0-TAMU-WW-TEST-PCM-16-C2_SUB1_Vel_Stats-Combined.dat 12/15/2016 3:53PM

REV0-TAMU-WW-TEST-PCM-16-C2_SUB1_Vel_Stats-SET1.dat 12/15/2016 2:24PM

REV0-TAMU-WW-TEST-PCM-16-C2_SUB1_Vel_Stats-SET2.dat 12/15/2016 2:32PM

REV0-TAMU-WW-TEST-PCM-16-C2_SUB1_Vel_Stats-SET3.dat 12/15/2016 1:16PM

REV0-TAMU-WW-TEST-PCM-16-C2_SUB2_Vel_Stats-Combined.dat 12/15/2016 3:59PM

REV0-TAMU-WW-TEST-PCM-16-C2_SUB2_Vel_Stats-SET1.dat 12/15/2016 2:29PM

REV0-TAMU-WW-TEST-PCM-16-C2_SUB2_Vel_Stats-SET2.dat 12/15/2016 2:58PM

REV0-TAMU-WW-TEST-PCM-16-C2_SUB2_Vel_Stats-SET3.dat 12/15/2016 3:03PM

REV0-TAMU-WW-TEST-PCM-16-C2_SUB3_Vel_Stats-Combined.dat 12/15/2016 4:15PM

REV0-TAMU-WW-TEST-PCM-16-C2_SUB3_Vel_Stats-SET1.dat 12/15/2016 3:03PM

REV0-TAMU-WW-TEST-PCM-16-C2_SUB3_Vel_Stats-SET2.dat 12/15/2016 3:11PM

REV0-TAMU-WW-TEST-PCM-16-C2_SUB3_Vel_Stats-SET3.dat 12/15/2016 3:19PM

REV0-TAMU-WW-TEST-PCM-16-C2_SUB4_Vel_Stats-Combined.dat 12/15/2016 4:15PM

REV0-TAMU-WW-TEST-PCM-16-C2_SUB4_Vel_Stats-SET1.dat 12/15/2016 3:20PM

REV0-TAMU-WW-TEST-PCM-16-C2_SUB4_Vel_Stats-SET2.dat 12/15/2016 3:47PM

REV0-TAMU-WW-TEST-PCM-16-C2_SUB4_Vel_Stats-SET3.dat 12/15/2016 3:51PM

3.2 Volumetric Flow Rate Data

Three files are provided containing the instantaneous volumetric flow rate for each set:

REV0-TAMU-WW-TEST-PCM-14-INT1-FLOWRATE-SET1.csv

REV0-TAMU-WW-TEST-PCM-14-INT1-FLOWRATE-SET2.csv

REV0-TAMU-WW-TEST-PCM-14-INT1-FLOWRATE-SET3.csv

A summary file is included, which contains the arithmetic average, standard deviation, and k-factor conversion for each set.

REV0-TAMU-WW-TEST-PCM-14-INT1-FLOWRATE-AVERAGE.xlsx

The summary file contains the calculation to convert the raw flow meter output (working fluid = water) into the actual flow rate (working fluid = p-Cymene). More information on data conversion is provided in Appendix II.

3.3 Velocity (PTV) Data: Mean, rms, and Reynolds stress.

The velocity data provided represents a two dimensional array, but is presented in a one dimensional vector. The vector field consists of 16 point on x-direction, and 328 points on y-direction. Notes on calibration and error estimation are provided in Appendix III.

All data are stored in .dat format. These files contain multiple columns without headers.

Each set is identified in the file name (SET1, SETE2, SET3). File naming is consistent within the sets. As an example, content for SET1 is described below:

REV0-TAMU-WW-TEST-PCM-16-C2_SUB1_Vel_Stats-SET1.dat:

This file contains all velocity statistics for set 1 on sub-channel 1. The structure of the file is shown in Table 5.

Table 5. Velocity Statistics .dat File Structure

Column #	1	2	3	4	5	6	7	8	9	10
Parameter	X	Y	Z	u	v	w	u_rms	v_rms	w_rms	uv
Unit	mm	mm	mm	m/s	m/s	m/s	m/s	m/s	m/s	m^2/s^2

NOTE: in all .dat files, z is constant and equal to the laser sheet location (-11.69 mm). The velocity component along the z-direction and all related parameters are 0.

The .dat files marked as "combined" contain the same information and structure of the files described above for set 1. However, the statistical values are computed based on the total number of instantaneous velocities (3 x 8308 = 24924).

4.0 REFERENCES

1. TAMU-WW-AS Rev.1, TAMU Wire-Wrapped As-Built Geometry (Non-Deformed Bundle)
2. TWRP-31-TSPEC-0010 Rev. 1 , TAMU Fuel Assembly Flow Visualization Test Specification,
3. P-Cymene Chemical Information Sheet. Cameo Chemicals, Database of Hazard Materials, June 1999.
4. Appendix B.9 Factors for units listed by kind of quantity or field of science, NIST Guide, https://www.nist.gov/pml/nist-guide-si-appendix-b9-factors-units-listed-kind-quantity-or-field-science
5. S.-K. CHENG and N. E. TODREAS, "Hydrodynamic Models and Correlations for Bare and Wire-Wrapped Hexagonal Rod Bundles — Bundle Friction Factors, Subchannel Friction Factors and Mixing Parameters," Nucl. Eng. Des., 92, , 227–251 (1986).
6. TAMU-WW-TEST-PCM-11-E-rev2.0, TAMU Wire-Wrapped Test Summary of Test PCM-11 at the Exterior Subchannel.

APPENDIX I: TURBINE FLOW METER CALIBRATION FOR P-CYMENE

Since the flow meter was originally calibrated with water as the working fluid, the data presented in the output file is the flow rate of the fluid if it was water. Because the working fluid, p-Cymene, has a different density and viscosity than water, it was required to generate a new calibration of the turbine flow meter with p-Cymene as the working fluid.

This was achieved using an Omega FPT-6130 high accuracy pitot tube with an Omega high accuracy differential pressure transducer. The Omega FPT-6130 high accuracy Pitot tube had an accuracy of < 1% of the volumetric flow rate. Three different Omega differential pressure transducers were utilized, because the range of DP measured by each transducer is small relative to the total span of DP required to fully calibrate the turbine flow meter. Each Omega differential pressure transducer had the following maximum pressure reading, associated accuracy, and flow meter frequency range in which each differential pressure transducer was used, Table 69.

Table 6. Differential pressure transducers utilized in the p-Cymene k-factor calibration

Differential Pressure Transducer	Maximum Pressure (psi)	Accuracy (% Full Scale)	Flow Meter Frequency Range (Hz)
Omega MMDWB10WBIV5P2D0T2A2CE	0.36	< 0.1% FS	0-100
Omega MMDWB001BIV5P2D0T2A2CE	1.0	< 0.1% FS	100-160
Omega MMDWB005BIV5P2D0T2A3CE	5.0	< 0.1% FS	160-300

The rate meter determined the volumetric flow rate by multiplying the turbine rotational frequency by a multiplication factor, the factory calibrated k-factor. A new p-Cymene k-factor was calculated from the pitot flow, turbine meter output, and the factory k-factor. Presented in Figure 3 is a plot of the p-Cymene k-factor as a function of turbine flow meter frequency. The factory calibrated k-factor for water was 43.2411. The p-Cymene volumetric flow rate is calculated by Equation 4.

$$Flow\ Rate_{pcy} = Indicated\ Flow\ Rate\left(\frac{k_{H2O}}{k_{pcy}}\right) \quad (4)$$

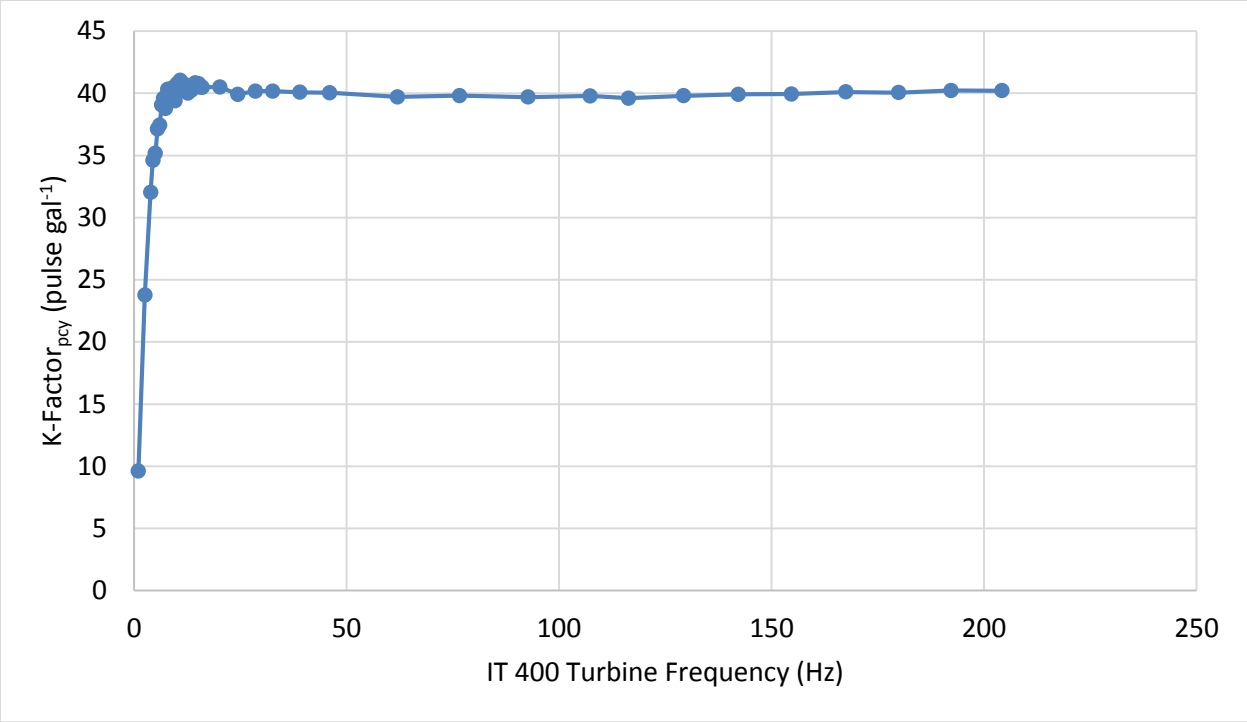


Figure 3. p-Cymene k-factor plotted versus the turbine flow meter rotational frequency

APPENDIX II: BUNDLE GEOMETRY CALCULATION

From [5], the following expressions describe the variables used in the bundle geometry calculation. The subscripts one, two, and three correspond to the interior, wall, and corner sub channels respectively. P is the rod pitch, D is the pin diameter, D_{wire} is the wire spacer diameter, D_h is the hydraulic diameter, W is the edge pitch, N_i is the number of each sub channel, and H is the wire spacer lead or axial distance required for the spacer to complete one revolution around the pin. D, D_{wire}, and $W$are from the rod, wire and flat-to-flat characterization performed in [1]. The cosine term takes into account the elliptical projected area of the wire due to it not being parallel to the flow.

Parameter	Value	Unit
N_1	96	n/a
N_2	24	n/a
N_3	6	n/a
P	1.8878 E-2	m
D	1.5880 E-2	m
D_{wire}	3.0000 E-3	m
W	1.9548 E-2	m
$FTF_{enclosure}$	1.5400 E-1	m
FTF_{bundle}	1.5266 E-1	m
A_1	5.1747 E-5	m^2
A_2	1.1661 E-4	m^2
A_3	4.3637 E-5	m^2
A_{Bundle}	8.0281 E-3	m^2
$P_{wet,1}$	2.9688 E-2	m
$P_{wet,2}$	4.8564 E-2	m
$P_{wet,3}$	2.3302 E-2	m
$P_{wet,bundle}$	4.1554	m
H	4.7625 E-1	m

$$W = D + G_{wall}$$

$$G_{wall} = FTF_{enclosure} - FTF_{bundle}$$

$$FTF_{bundle} = \frac{8P\sqrt{3}}{2} + D + 2D_{wire}$$

$$A_1 = \left(\frac{\sqrt{3}}{4}\right)P^2 - \frac{\pi D^2}{8} - \frac{\pi D_{wire}^2}{8\cos(\theta)}$$

$$A_2 = \left(W - \frac{D}{2}\right)P - \frac{\pi D^2}{8} - \frac{\pi D_{wire}^2}{8\cos(\theta)}$$

$$A_3 = \frac{\left(W - \frac{D}{2}\right)^2}{\sqrt{3}} - \frac{\pi D^2}{24} - \frac{\pi D_{wire}^2}{24\cos(\theta)}$$

$$A_{Bundle} = N_1 A_1 + N_2 A_2 + N_3 A_3$$

$$P_{wet,1} = \frac{\pi D}{2} + \frac{\pi D_{wire}}{2\cos(\theta)}$$

$$P_{wet,2} = P + \frac{\pi D}{2} + \frac{\pi D_{wire}}{2\cos(\theta)}$$

$$P_{wet,3} = \frac{\pi D}{6} + \frac{2\left(W - \frac{D}{2}\right)}{\sqrt{3}} + \frac{\pi D_{wire}}{6\cos(\theta)}$$

$$P_{wet,Bundle} = N_1 P_{wet,1} + N_2 P_{wet,2} + N_3 P_{wet,3}$$

$$D_h = \frac{4\,A_{Bundle}}{P_{wet,Bundle}}$$

$$\cos(\theta) = \frac{H}{\sqrt{H^2 + \left(\pi(D + D_w)\right)^2}}$$

PROJECT CONFERENCE DOCUMENTS

APPENDIX N: PROJECT CONFERENCE PAPERS AND PRESENTATIONS

Experimental Data Sets for CFD Calculations of Flow and Heat Transfer in Deformed Fuel Assemblies

Brian E. Mays,* R. Brian Jackson,† Tom Reeves,† Nate Salpeter‡

*AREVA Federal Services LLC, 3315 Old Forest Road, Lynchburg, VA 24501
†TerraPower LLC, 330 120th Ave NE, Suite 100, Bellevue, WA 98005
‡AER Consulting, P.O. Box 219, Half Moon Bay, CA 94019
brian.mays@areva.com, brjackson@terrapower.com, treeves@terrapower.com, nate@aeratio.com

INTRODUCTION

Liquid-metal fast-breeder reactors (LMFBRs) have traditionally used fuel assemblies consisting of a hexagonal array of pins enclosed in a hexagonally shaped duct. Each fuel pin is surrounded by a wire that is wrapped in a helical configuration and is used to separate the pins sufficiently to allow sodium coolant to flow through the assembly. The helical wire wrap also promotes mixing of the coolant.

Experience with these assemblies has shown that they begin to deform with time during normal operation leading to significant changes in the core thermal-hydraulics. For example, deformations of assemblies in the Experimental Breeder Reactor-2 and the Fast Flux Test Facility lead to pin overheating resulting from pin-to-duct and pin-to-pin contact [1].

This problem is well known and was investigated extensively in the 1970s and early 1980s [2–6]. This was a period, however, before the development of modern Computational Fluid Dynamics (CFD) computer codes. Therefore, the experiments performed at the time did not record their results in sufficient detail to be useful for compiling validation datasets for CFD codes. Most of the experiments focused on bulk measurements, such as pressure drop across the bundle. When the effects of deformation of the fuel assembly were investigated, the studies performed to quantify these effects considered only bare pins without the wire wrap [1].

With the resurgence of interest in LMFBRs in recent years, particularly in designs that leverage long-life performance of the fuel [7, 8], the need has arisen for high-resolution, transient, full-field measurements of the fluid velocity and temperature and an accurate description of the test conditions, including a precise description of the geometry, that are suitable for the validation and benchmarking of CFD codes to predict the thermal-hydraulic behavior of flow in wire-wrapped fuel bundles.

This paper describes a project to produce a validation-quality set of data that can be used to benchmark CFD codes for modeling flow and thermal performance in wire-wrapped fuel assemblies of the kind used by LMFBR designs. In addition, this effort investigates the changes to the flow and other phenomena that occur in the deformed geometries that occur later in a fuel assembly's life.

This work is being performed by a team of four organizations. The experimental work is being performed by AREVA and Texas A&M University. The computational work, both to support the experiments and to perform blind benchmark calculations, is being performed by TerraPower, LLC, and Argonne National Lab (ANL).

The experiments use a geometry that consists of a complete assembly of 61 wire-wrapped pins that is surrounded by a hexagonal duct. This configuration was considered the minimum size necessary to adequately capture the important results of interests, such as the thermal gradients across the assembly and the velocity field effects into the assembly resulting from the surrounding duct. These types of effects cannot be captured by a geometry consisting of only a small group of fuel pins.

EXPERIMENTS

This project consists of four benchmark-quality experiments: two experiments to measure the velocity field throughout the wire-wrapped bundle and two experiments to provide information about the heat transfer and thermal mixing in the fluid flowing through the assembly. All four experiments also measure the pressure field at multiple locations in the test section of the flow loop, which provides essential information about the flow, such as the pressure drop across the simulated fuel bundle.

Table I presents several of the key parameters of the two sets of experiments. Because of the constraints imposed by the measurement techniques used for the tests and by the fabrication of the test components, the dimensions of the two sets of experiments are not identical. Nevertheless, certain key non-dimensional parameters, such as the pitch-to-diameter ratio (P/D), are consistent in all of the experiments.

Isothermal Flow Experiments

The first set of experiments, performed by Texas A&M University, uses optical techniques to generate high-precision, high-fidelity measurements of the flow field within the bundle. The experimental setup consists of a flow loop with a measurement region constructed from an optically transparent acrylic material [9]. The simulated assembly—consisting of the 61 mock wire-wrapped fuel pins and the surrounding hexagonal duct, both constructed of the same acrylic material—is located within this region. No thermal phenom-

TABLE I. Key parameters for the two sets of experiments.

Parameter	Isothermal Experiments	Heated Experiments
Pin material	Acrylic	Metal
Working fluid	*p*-Cymene	Water
Pin OD (mm)	15.88	9.5
Wire OD (mm)	3.0	1.73
Pitch-to-diameter ratio (P/D)	1.189	1.182
Bundle length (wire pitches)	14.8	3.5

ena are explored in these tests; the entire loop remains at a controlled, uniform (ambient) temperature.

A Matched Index of Refraction (MIR) approach is used for the velocity measurements. Therefore, *p*-cymene is used as the test fluid flowing through the loop, because it is optically compatible with the acrylic material used for the test section. The velocity fields are measured using two techniques, Particle Image Velocimetry (PIV) [10] and Laser Doppler Velocimetry (LDV), with the latter being used to provide point measurements of the flow at specific locations within the assembly. In addition to the velocity measurements, taps along the measurement region of the flow loop provide pressure drop information [11].

Heated Bundle Experiments

In the second set of experiments, the simulated bundle contains electrical heaters to study the heat transfer to the test fluid as it flows through the assembly. This set of experiments is being performed at AREVA's Fuel Cooling Test Facility (FCTF) [12]. This test loop is located at AREVA's Richland, Washington, facility and was originally used for testing light water reactor fuel assemblies. It has been refurbished and modified to perform these experiments. The test fluid used in this loop is water.

The simulated assembly for this test is metallic and consists of a hexagonal duct and 61 wire-wrapped pins, 19 of which contain heaters. The locations of the heated pins are shown in Figure 1. One heated pin is located along the center of each of the six duct sides; the remaining heaters are concentrated in the center of the bundle. The heaters are divided into six banks, each with its own independent power supply, allowing the operators to control the power across the bundle to produce phenomenologically interesting peaking patterns and temperature gradients.

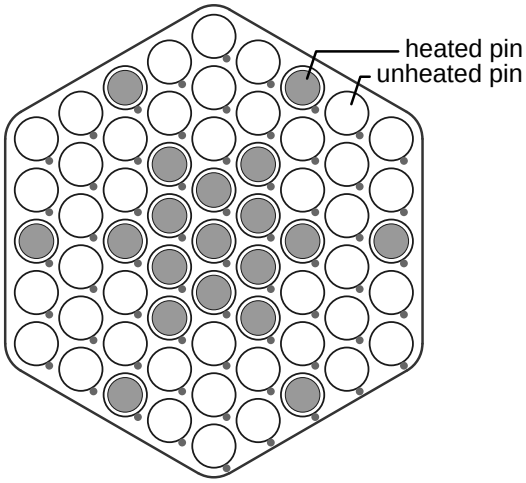


Fig. 1. Locations of the heated pins in the bundle.

The test section is divided into regions, which are diagrammed in Figure 2. The bottom of the section consists of the entrance region, which is four wire pitches long (i.e., four complete turns of the helical wire wraps surrounding the pins), where the flow is allowed to develop so as to eliminate entrance effects from the presence of the duct. Measurements are taken over the next eight wire pitches. This region is followed by an exit region at the top of the test section (not shown in Figure 2) to eliminate any effects from the top of the duct. The first six wire pitches of the measurement region are heated. The axial heat flux of the electrical heaters has a cosine shape, shown in Figure 2, which is representative of typical axial core power peaking.

Over 350 thermocouples are used provide temperature measurements throughout the test section. All 19 heated pins contain thermocouples located along the inside of the wire-wrapped tube to measure the internal cladding surface temperature. Most of the heaters have eight thermocouples positioned at three elevations in the measurement region. Of the remaining heaters, four have six thermocouples evenly spaced around the circumference of the pin to measure the azimuthal temperature distribution, and two have thermocouples located at nine locations along the length the pin to capture the axial temperature distribution.

Of the remaining (unheated) pins, 22 contain six thermocouples each, which are located on the outside of the metallic tube to measure the temperature of the fluid at the surface,

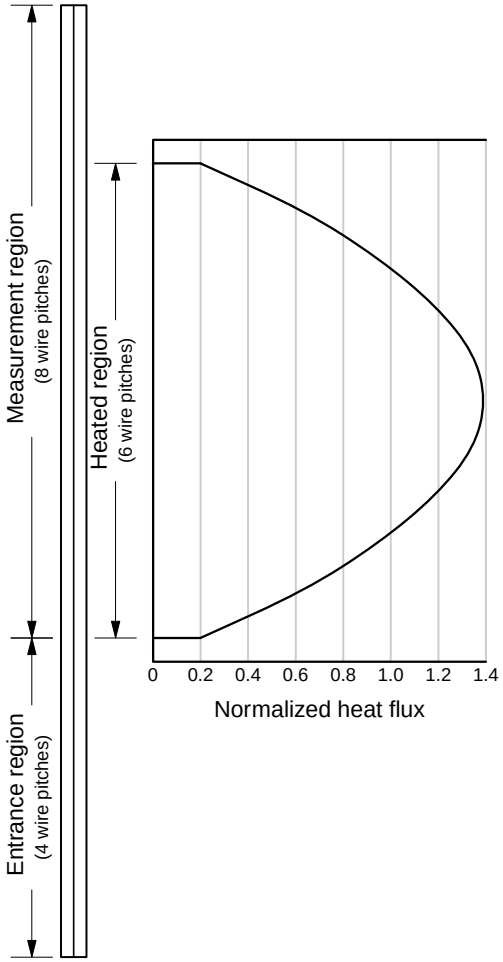


Fig. 2. The regions of the heated test assembly and heat flux supplied by the electrical heaters.

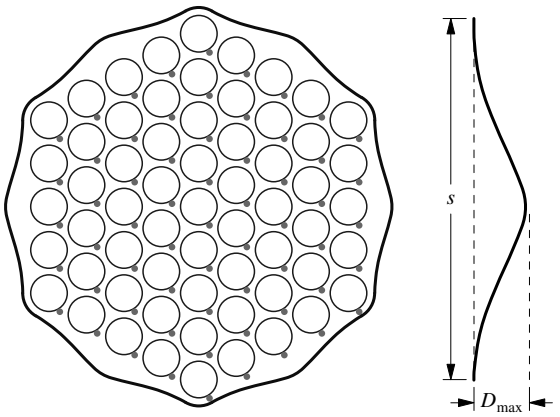


Fig. 3. Deformation of the hexagonal duct used to simulate later-in-life conditions of a fuel assembly. The amount of deformation is exaggerated to illustrate the shape of the duct.

and four contain taps to measure the internal bundle pressure. Additional thermocouples and pressure taps are located along the duct walls, with temperature measurements being made both on the inside surfaces and on the outside surfaces of the duct.

The Deformed Geometry

Both the experiments measuring the isothermal flow and the experiments with a heated bundle are performed in two geometrical configurations. The first is the as-designed geometry representative of a fuel assembly at beginning of life, such as the configuration diagrammed in Figure 1. The other series of tests use a geometry in which the sides of the hexagonal duct are altered to simulate the effect of potential deformations that could occur later in the life of a fuel assembly. For these tests, all six sides are deformed outward according to a cosine-like shape that is parameterized by the length of the side s and the maximum amount of outward deformation D_{max}, as shown in Figure 3.

NUMERICAL SIMULATIONS

This project differs from previous experimental work in this area in that the issues that are important for accurately modeling the system with CFD not only have been considered but also have been instrumental in guiding the design of the experiments. Two teams of CFD modelers—one at Terrapower, the other at ANL—have provided key input for the design of the experiments. Scoping calculations with CFD tools were used to determine the locations of the heaters, the sensors, and other factors to maximize the usefulness of the data to be collected for CFD validation purposes. This collaboration of modeling and experimentation continued during the construction and shakedown phases of the experiments to optimize the tests according to the most recent test data.

In addition to helping design and implement the experiments, CFD simulations are performed as part of this project to provide an example of blind benchmark calculations. As the tests began, both modeling groups performed pre-test calculations of the flow through the bundles. As the tests were performed and the data about the actual conditions of the test became available, the benchmark calculations were run again to incorporate this new information and evaluate its effect on the results.

The Reynolds-Averaged Navier-Stokes Approach

The modeling team at Terrapower is using an industry-standard, commercially available CFD code to perform the benchmark calculations, similar to the tools that are expected to be employed by a reactor vendor to design, optimize, and analyze an advanced LMFBR. This code uses the Reynolds-Averaged Navier-Stokes (RANS) approach to model the turbulence in the flow.

Because of the limitations of this approach, particularly in small geometries, some specialized techniques are being used to model important phenomena, such as the Momentum Source Method [13], which is used to model the effects of the wire wrap instead of explicitly representing the wire in the CFD mesh. Verification of the solution generated by this methodology has been performed via an iterative and mesh convergence analysis combined with sensitivity studies [14]. Validation of this approach will be provided by comparison of the numerical solutions to the results of the four experiments.

The Large Eddy Simulation Approach

The other modeling team, at ANL, is using an advanced CFD tool that has been developed as part of the Department of Energy's Nuclear Energy Advanced Modeling and Simulation (NEAMS) program. This code, Nek5000 [15], is based on the spectral element method [16] and is capable of performing high-fidelity Large-Eddy Simulation (LES) modeling of turbulence in complex flows. In contrast to the RANS modeling being performed by Terrapower, the wire wraps around the pins are explicitly represented in the computational mesh. The initial results of simulations performed by this code are encouraging [17].

CONCLUSIONS

Through a combination of high-fidelity data from precisely defined experiments and modern CFD simulations performed in concert, this project will provide valuable insight into the many complex flow phenomena that occur in wire-wrapped bundles, such as vortex shedding, cross flow, and bypass flow, which affect the thermal performance of LMFBR fuel assemblies. This combined effort will result in greater insight into the local flow behavior and a better understanding of the shortcomings, limitations, and uncertainties associated with current modeling practices.

The final set of experimental data and numerical simulation results will be made available upon completion of this project as an open-source data set that can be used to improve, validate, and benchmark CFD codes and modeling methods.

ACKNOWLEDGMENTS

This work was performed to support Department of Energy Award number DE-NE0008321.

REFERENCES

1. E. U. KAHN, "LMFBR In-Core Thermal-Hydraulics: The State of the Art and U.S. Research and Development Needs," Tech. Rep. PNL-3337, Pacific Northwest Laboratory (1980).
2. M. H. FONTANA et al., "Temperature Distribution in a 19-Rod Simulated LMFBR Fuel Assembly in a Hexagonal Duct," Tech. Rep. ORNL-TM-4113, Oak Ridge National Laboratory (1973).
3. Y. B. CHEN, K. IP, and N. E. TODREAS, "Velocity Measurements in Edge Subchannels of Wire Wrapped LMFBR Fuel Assemblies," AEC Research and Development Report COO-2245-11TR, Department of Nuclear Engineering, Massachusetts Institute of Technology (1974).
4. C. L. WHEELER, D. S. ROWE, and J. D. SMITH, "An Experimental Study of Axial and Cross Flow Velocity in a 7-Pin Wire Wrapped Bundle," Tech. Rep. BNWL-1804, Pacific Northwest Laboratory (1974).
5. T. OHTAKE, S. URUWASHI, and K. TAKAHASHI, "Velocity Measurements in the Subchannel of the Wire-Spaced Subassembly," *Nucl. Technol.*, **30**, *3*, 333–349 (1976).
6. R. ROIDT, M. CARELLI, and R. MARKLEY, "Experimental Investigations of the Hydraulic Field in Wire-Wrapped LMFBR Core Assemblies," *Nucl. Eng. Des.*, **62**, *1–3*, 295–321 (1980).
7. P. HEJZLAR et al., "Terrapower, LLC Traveling Wave Reactor Development Program Overview," *Nucl. Eng. Technol.*, **45**, *6*, 731–744 (2013).
8. M. HACKETT et al., "HT9 Strain Modeling for Fuel Pin Deformation," in *Proc. ICONE22*, Prague, Czech Republic, July 7–11, 2014, ASME International (2014).
9. R. VAGHETTO et al., "Flow Field and Pressure Measurements in a 61-Pin Wire-Wrapped Bundle," *Trans. Am. Nucl. Soc.*, **115** (2016).
10. N. GOTH et al., "Particle Image Velocimetry Measurements in a Wire-Wrapped 61-Pin Hexagonal Fuel Bundle," *Trans. Am. Nucl. Soc.*, **115** (2016).
11. N. GOTH et al., "Pressure Measurements in a Wire-Wrapped 61-Pin Hexagonal Fuel Bundle," *Trans. Am. Nucl. Soc.*, **115** (2016).
12. M. MARTIN, K. DUGGAN, and T. GALIOTO, "Heated Bundle Test in AREVA NP's Fuel Cooling Test Facility," *Trans. Am. Nucl. Soc.*, **115** (2016).
13. R. HU and T. H. FANNING, "A Momentum Source Model for Wire-Wrapped Rod Bundles—Concept, Validation, and Application," *Nucl. Eng. Des.*, **262**, 371–389 (2013).
14. D. J. LEONARD et al., "CFD Verification and Validation of Wire-Wrapped Pin Assemblies," *Trans. Am. Nucl. Soc.*, **115** (2016).
15. P. FISCHER et al., "Petascale Algorithms for Reactor Hydrodynamics," *Journal of Physics: Conference Series*, **125**, 012076 (2008).
16. Y. MADAY, A. T. PATERA, and E. M. RØNQUIST, "An Operator-Integration-Factor Splitting Method for Time-Dependent Problems: Application to Incompressible Fluid Flow," *J. Sci. Comp.*, **5**, *4*, 263–292 (1990).
17. A. V. OBABKO, E. MERZARI, and P. F. FISCHER, "Nek5000 Large-Eddy Simulations for Thermal-Hydraulics of Deformed Wire-Wrap Fuel Assembles," *Trans. Am. Nucl. Soc.*, **115** (2016).

Flow Field and Pressure Measurements in a 61-Pin Wire-Wrapped Bundle

R. Vaghetto, N. Goth, M. Childs, P. Jones, S. Lee, D.T. Nguyen, Y.A. Hassan

Texas A&M Nuclear Engineering: 3133 TAMU, College Station, TX, 77843
r.vaghetto@tamu.edu, negcm7@tamu.edu, masonchilds@tamu.edu, pgjones87@tamu.edu, sayalee@tamu.edu, thien.duy.ng@tamu.edu, y-hassan@tamu.edu

INTRODUCTION

Texas A&M University is conducting isothermal flow tests in a wire-wrapped, 61-pin hexagonal fuel bundle to support the research on advanced nuclear fuel development sponsored by the Department of Energy (DOE). The purpose of these tests is to produce high spatial- and temporal-resolution measurements of the flow and pressure measurements at different locations of the test bundle. The data resulting from these tests will be used to benchmark numerical simulations of the experiments using both industry-standard Reynolds-averaged Navier-Stokes (RANS) based Computation Fluid Dynamics (CFD) methods [1] and a highly resolved Large Eddy Simulation (LES) computer code [2].

DESCRIPTION OF THE FACILITY

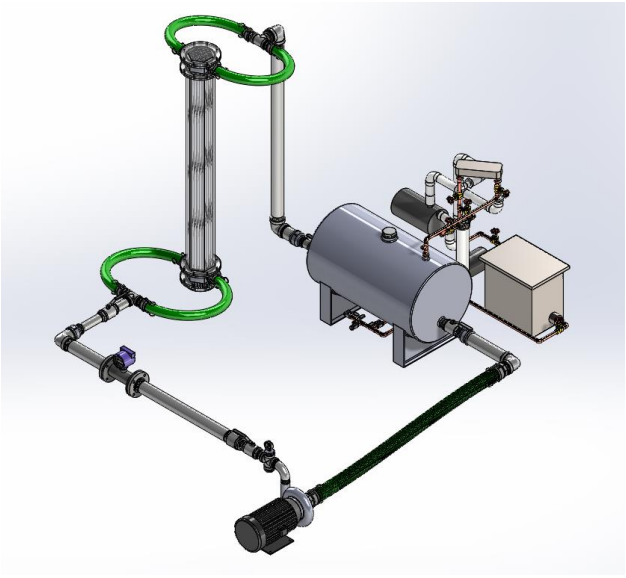


Fig. 1. Perspective Diagram of the Experimental Facility

The experimental facility consists of two loops, a primary loop and a secondary loop. The primary loop, which provides the flow for the experiments, includes the following components:

- The primary tank, used to store the working fluid between experiments, and as an inline surge volume.
- The primary pump and associated variable frequency drive (VFD), which controls the flow rate in the test section
- An inline turbine flow meter
- A resistance temperature detector (RTD)
- Nine pressure transducers
- The hexagonal test section containing the 61-pin bundle

The secondary loop performs volume control, temperature control, and filtration. It contains the following components:

- The secondary tank
- The secondary pump and associated VFD
- A heat exchanger supplied with chilled water to control the primary loop temperature

A filtration system.

All pumps, tanks, and piping are made of stainless steel. Chemical-resistant flexible hoses are used to connect the test section inlets and outlets to the primary loop. The hoses are used to minimize vibrations in the test section.

The test section can be divided into three distinct sections can be identified in the test bundle:

- The lower (inlet) plenum located at the bottom of the bundle
- The central section (test section) where the flow measurements will be conducted
- The upper (outlet) plenum located at the top of the bundle.

The test section contains a hexagonally shaped fuel bundle consisting of 61 helically wrapped pins arranged in a triangular lattice. The pins are attached to a bottom plate that is connected to the lower plenum. The flow enters the lower plenum and exits the upper plenum symmetrically from the sides of each plenum. The central section containing the bundle is 3.5 wire pitches long to allow for flow development and to minimize exit effects, while providing sufficient space for velocity measurements over one full wire pitch.

The pins, wires, and hexagonal duct enclosure are made of transparent acrylic to allow for flow visualization and measurements using laser diagnostic velocity measurement techniques such as Particle Image Velocimetry (PIV) and Laser Doppler Velocimetry (LDV).

The facility is also equipped with a set of nine pressure transducers to measure the pressure at multiple axial and azimuthal locations. The locations of these pressure transducers are indicated in Fig. 2.

The pressure transducer installed at the lower plenum, labeled PT#0, is used to monitor the maximum pressure of the test section. The total pressure drop across the test section is given by the difference between the pressure measurements at PT#0 (entrance tap) and PT#8 (exit tap). Seven of the pressure transducers (labeled PT#1 to PT#7) are installed along a single face of the hexagonal duct to record the pressure at multiple axial locations in the test section. These taps capture the pressure of the axially developing flow in the test section.

Additional pressure taps have been installed on four adjacent hexagonal duct faces at two axial locations in the fully developed region to measure the azimuthal pressure gradient at these elevations. These taps are used to quantify the flow asymmetry that results from the helical wire surrounding the pins. Comparing the pressure measurements at the two axial locations captures how the flow asymmetry changes with the orientation of the helically wrapped wire.

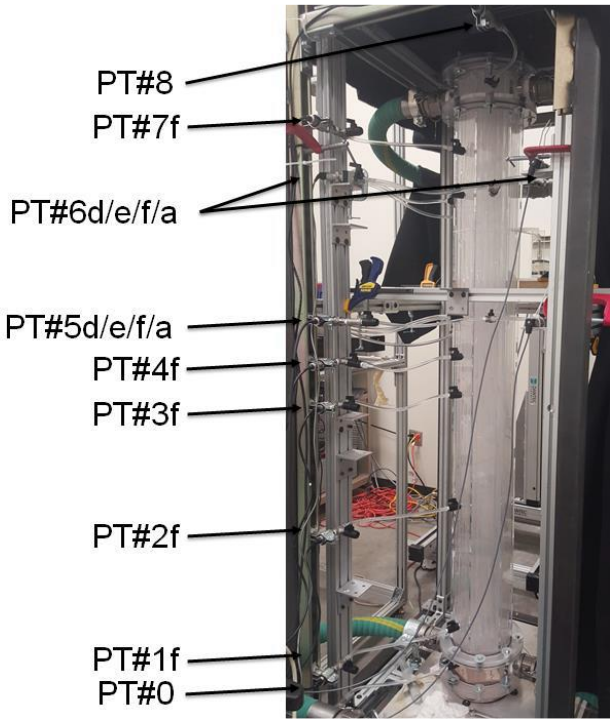


Fig. 2. Pressure tap locations in the hexagonal duct

EXPERIMENTAL ACTIVITY

The experimental activity conducted as part of this project provides the velocity and pressure data necessary to characterize of the flow inside hexagonal fuel bundles of helically wrapped pins. The data resulting from these experiments will support benchmarking of both RANS-based and highly resolved LES turbulence models for computational fluid dynamics analysis. Further validation and extension of existing correlations for pressure drop calculations is also possible with this data set.

The full three-dimensional velocity field in the edge, corner, and interior sub-channels of the fuel bundle can be quantified using the matched-index-of-refraction technique. The flow loop is able to accommodate a variety of working fluids, including water and p-cymene. Water is used to measure the pressure distribution in flows spanning a wide range of Reynolds numbers including laminar, transition, and turbulent regimes. The pressure data will be compared with the pressure drop correlations available in the literature [3], and if these correlations do not agree with the data, they will be used to generate new correlations.

p-cymene is used for matched-index-of-refraction, laser-based techniques, such as PIV and LDV. These techniques are capable of producing high-resolution velocity measurements in edge, corner, and interior sub-channels. Table I provides the locations of the velocity field measurements as the distance between the wall of the hexagonal duct and the plane along which optical measurements are taken. These planes are shown in Fig. 3 along with the regions of interest. Figure 3 also shows an additional measurement plane, labeled Plane 6, which is not parallel to the other five planes.

Table I. Location of the Velocity Measurements

Plane	Name	Position (mm)
1	Exterior 1	1.88
2	Interior 1	11.69
3	Interior 2	28.04
4	Interior 3	44.37
5	Interior 4	76.50

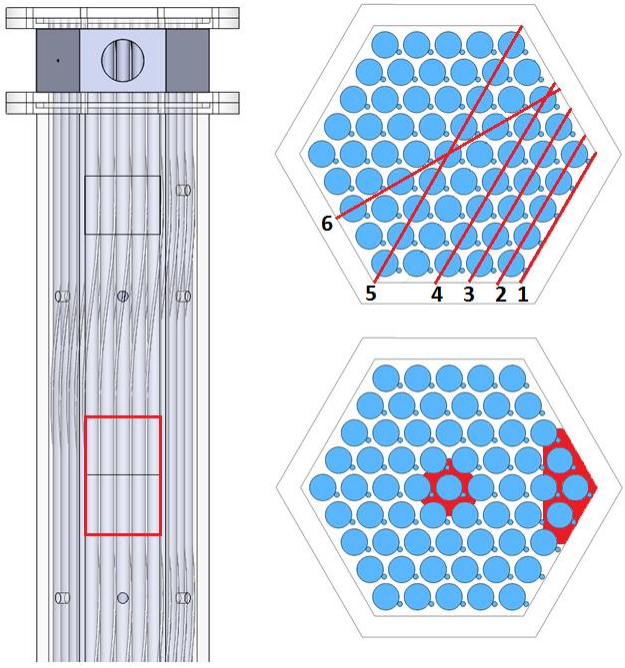


Fig. 3. Vertical and horizontal laser diagnostic velocity measurement locations

An example of the time-averaged velocity field is presented in Fig. 4 for water flowing with a Reynolds number of 11,000. This velocity field was captured using PIV at the location labeled in Table I as Exterior 1.

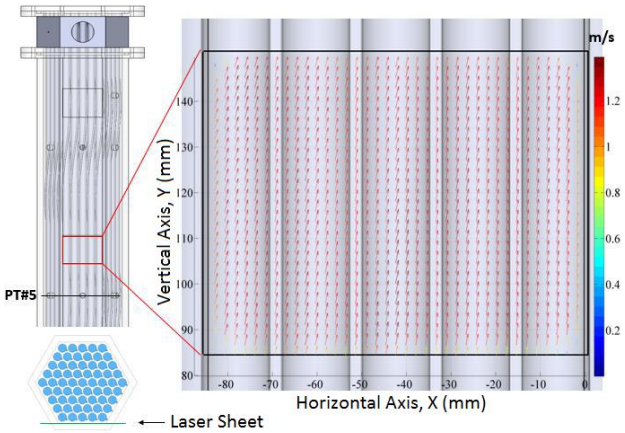


Fig. 4. PIV time-averaged velocity field for the Exterior 1 location

Figure 5 shows the instantaneous vector displacements of p-cymene fluid at the interior sub-channel 3, which were measured using the technique of particle tracking velocimetry (PTV).

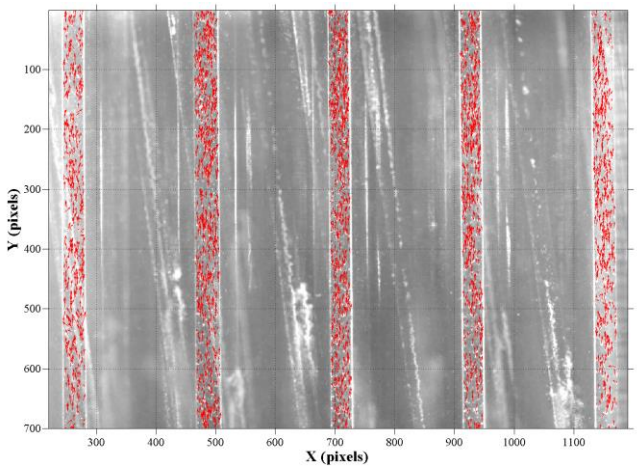


Fig. 5. PTV Instantaneous Vectors Displacement (Interior Subchannel)

CONCLUSIONS

An experimental facility has been designed and constructed to conduct isothermal flow experiments on a hexagonal fuel bundle of 61 wire-wrapped pins. These experiments will produce high-resolution flow measurements and pressure data that will be suitable for validation and benchmarking of modern CFD codes.

NOMENCLATURE

CFD = computational fluid dynamics
DOE = Department of Energy
LES = large-eddy simulation
LDV = laser Doppler velocimetry
PIV = particle image velocimetry
PTV = particle tracking velocimetry
RANS = Reynolds-averaged Navier-Stokes
VFD = variable frequency drive

ACKNOWLEDGMENTS

This work was performed for the Department of Energy under contract DE-NE0008321. The authors would like to mention the collaboration of the other participants of the project for the continuous technical interaction, and in particular Nate Salpeter and Brian Jackson (TerraPower) for the test specifications provided.

REFERENCES

1. D. J. LEONARD et al., "CFD Verification and Validation of Wire-Wrapped Pin Assemblies," Trans. Am. Nucl. Soc., 115 (2016).
2. A. V. OBABKO, E. MERZARI, and P. F. FISCHER, "Nek5000 Large-Eddy Simulations for Thermal-Hydraulics of Deformed Wire-Wrap Fuel Assembles," Trans. Am. Nucl. Soc., 115 (2016).
3. S.-K. CHENG and N. E. TODREAS, "Hydrodynamic Models and Correlations for Bare and Wire-Wrapped Hexagonal Rod Bundles - Bundle Friction Factors, Subchannel Friction Factors and Mixing Parameters," Nucl. Eng. Des., 92, 2, 227-251 (1986).

Particle Image Velocimetry Measurements in a Wire-Wrapped 61-Pin Hexagonal Fuel Bundle

N. Goth, M. Childs, P. Jones, S. Lee, D.T. Nguyen, R. Vaghetto, Y.A. Hassan

Texas A&M Nuclear Engineering: 3133 TAMU, College Station, TX, 77843
negcm7@tamu.edu, masonchilds@tamu.edu, pgjones87@tamu.edu, sayalee@tamu.edu, thien.duy.ng@tamu.edu, r.vaghetto@tamu.edu, y-hassan@tamu.edu

INTRODUCTION

Liquid metal fast reactor fuel assemblies using sodium as a coolant typically utilize a tightly packed triangular lattice of fuel pins enclosed in a hexagonal duct. The fuel pins are typically wrapped with a helical wire spacer. The primary function of the wire spacers is to maintain a gap between neighboring fuel pins. They also mitigate vortex-induced vibration and enhance sub-channel mixing to increase convective heat transfer.

Many experiments have been performed to study thermal-hydraulic characteristics, primarily pressure drops, of the wire-wrapped fuel bundles. Novendstern [1] developed a semi-empirical model to predict pressure losses in a hexagonal array of wire-wrapped pins in the turbulent flow regime. Rehme [2] proposed pressure drop correlations for a wide range of geometrical parameters, such as pitch-to-diameter ratio P/D from 1.125 to 1.417, lead-to-wire diameter ratio H / d_m from 6 to 45, and number of pins n from 7 to 61. Cheng and Todreas [3] introduced their hydrodynamic models for subchannel friction factors and mixing parameters in a 37-pin fuel bundle, which covered the laminar, transition and turbulent flow regimes.

Computational fluid dynamics (CFD) offers an opportunity to validate the above correlations and investigate the flow characteristics in the subchannels. Several numerical studies of the wire-wrapped fuel bundles have been performed and most of them are Reynolds-Averaged Navier-Stokes (RANS) based simulations with various turbulence models. Ahmad and Kim [4] performed RANS simulations of 7- and 19-pin bundles using the k-omega SST turbulent model, while Gajapathy et al. [5] performed RANS simulations on 7-pin bundles using the k-epsilons model. Recently, Fischer et al. [6] carried out large-eddy simulation (LES) calculations on wire-wrapped fuel bundles to obtain higher-resolution numerical of subchannel behavior.

The geometrical complexity of the hexagonal wire-wrapped fuel bundle has limited experimental activities to pressure drop measurements. A database of pressure drops and flow-field measurements in a 61-pin wire-wrapped hexagonal fuel bundle is not available to benchmark the existing correlations and validate the CFD calculations.

Texas A&M University is conducting isothermal flow experiments in a wire-wrapped 61-pin hexagonal fuel bundle to support the research on advanced nuclear fuel development sponsored by the Department of Energy (DOE). The purpose of these tests is to perform high spatial and temporal resolution measurements of the flow and pressure

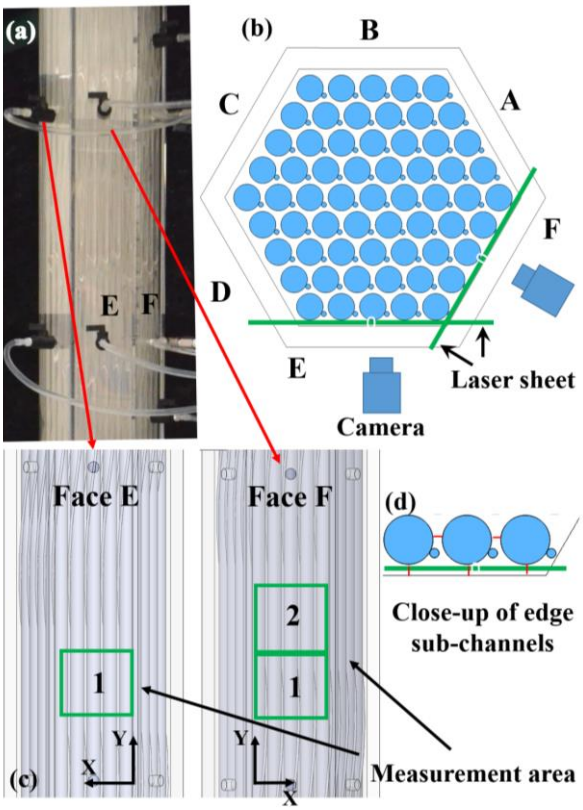


Fig. 1. 61-pin fuel bundle and PIV experimental setup.

measurements at different locations in the fuel bundle. The experimental facility employs matched-index-of-refraction (MIR) techniques and laser diagnostic velocity measurement techniques such as particle image velocimetry (PIV) and laser Doppler velocimetry (LDV). The result of this experimental activity will be an experimental database of pressure and flowfield measurements that will be suitable for validating CFD computer codes.

FACILITY DESCRIPTION

An experimental facility containing a mock 61-pin hexagonal fuel bundle with helically wrapped wire spacers has been constructed to conduct isothermal flow tests. The experimental fuel bundle is organized in a triangular lattice. The pins, wires, and hexagonal duct enclosure are made of transparent poly (methyl methacrylate) to allow access for optical laser measurements. The experimental facility is designed to work with water or p-cymene as the working

fluid. P-cymene has nearly the same refractive index (RI) as acrylic (n = 1.49) at room temperature and can be used as part of a MIR technique for flow visualizations and measurements in the edge, corner and interior subchannels. In this paper, PIV measurements are presented for both water and p-cymene in four edge subchannels near the wall. This region is designated by the green laser sheet in Fig. 1(b). The Reynolds number in this set of flow fields varied from 4,000 to 11,000 based on the bulk axial velocity, V_0, and hydraulic diameter of the test section.

The experimental facility contains two loops. The primary loop performs the experimental function. The primary loop includes the following components:

- The primary tank is used as fluid storage between experiments and as an inline surge volume.
- The primary pump and associated variable frequency drive (VFD), which control the flow rate in the test section
- An inline turbine flow meter
- A resistance temperature detector (RTD)
- Nine pressure transducers
- The hexagonal test section containing the 61-pin bundle

The secondary loop performs volume control, temperature control, and filtration. The secondary loop contains the following components:

- The secondary tank
- The secondary pump and associated VFD
- A heat exchanger supplied with chilled water to control the primary loop temperature

PIV EXPERIMENTAL SETUP

Figure 1(a) shows the acrylic hexagonal enclosure and 61-pin fuel bundle equipped with axial and azimuthal pressure transducers. Fig. 1(b) and 1(c) show the PIV experimental setup and measurement areas located between the enclosure inner wall and outer pins. Note that the origin of the coordinate system used for the measurements for face ***E*** of the duct, is at the bottom right corner of the visualization area as shown in Fig. 1(c). The velocity components corresponding to the *x*, *y* and *z* directions are *U*, *V* and *W* for the time-averaged velocity and *u*', *v*' and *w*' for the fluctuations about the time-averaged velocity, respectively.

The PIV measurements in water (denoted as PIV-H2O) were performed in region 1 on face ***E*** by using a 10 W continuous laser at the wavelength of 527 nm and a high-speed Memrecam GX-3 camera. The PIV measurements in water used fluorescent particles (UVPMS-BO Cospheric) that have a mean diameter of 50 μm, a density of 1.0 g cm^{-3} and an emission wavelength of 600 nm.

The PIV measurements in p-cymene (denoted as PIV-PCY) were performed in regions 1 and 2 on face ***F*** using the same laser and two digital CMOS Phantom M310 cameras. The seeding particles were silver-coated hollow glass spheres with a mean diameter and density of 16 μm and 1.6 g cm^{-3}.

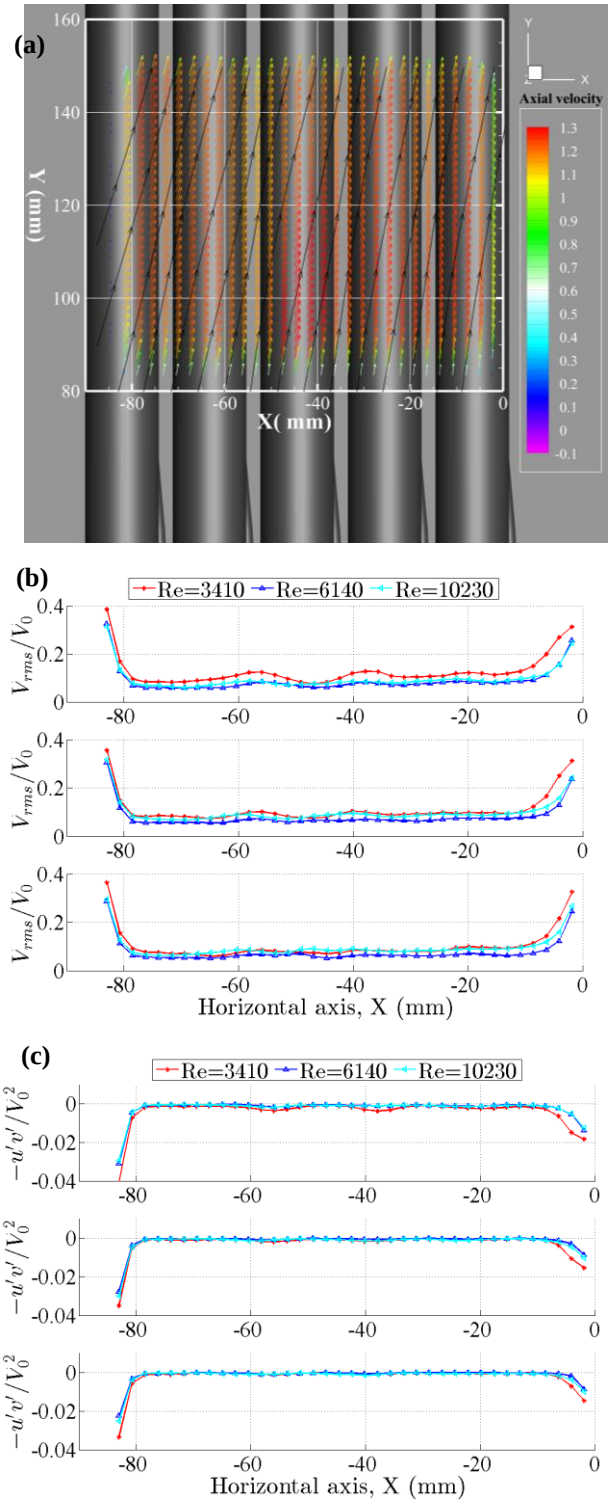


Fig. 2. Results from PIV measurements (PIV-H2O) on face E. (a) The ensemble-averaged velocity vector for Re=10230. The color contour shows the axial velocity component. Profiles of (b) V_{rms} and (c) $-u'v'$ are shown for y = 100, 120 and 140 mm. These profiles have been normalized by the bulk axial velocity, V_0.

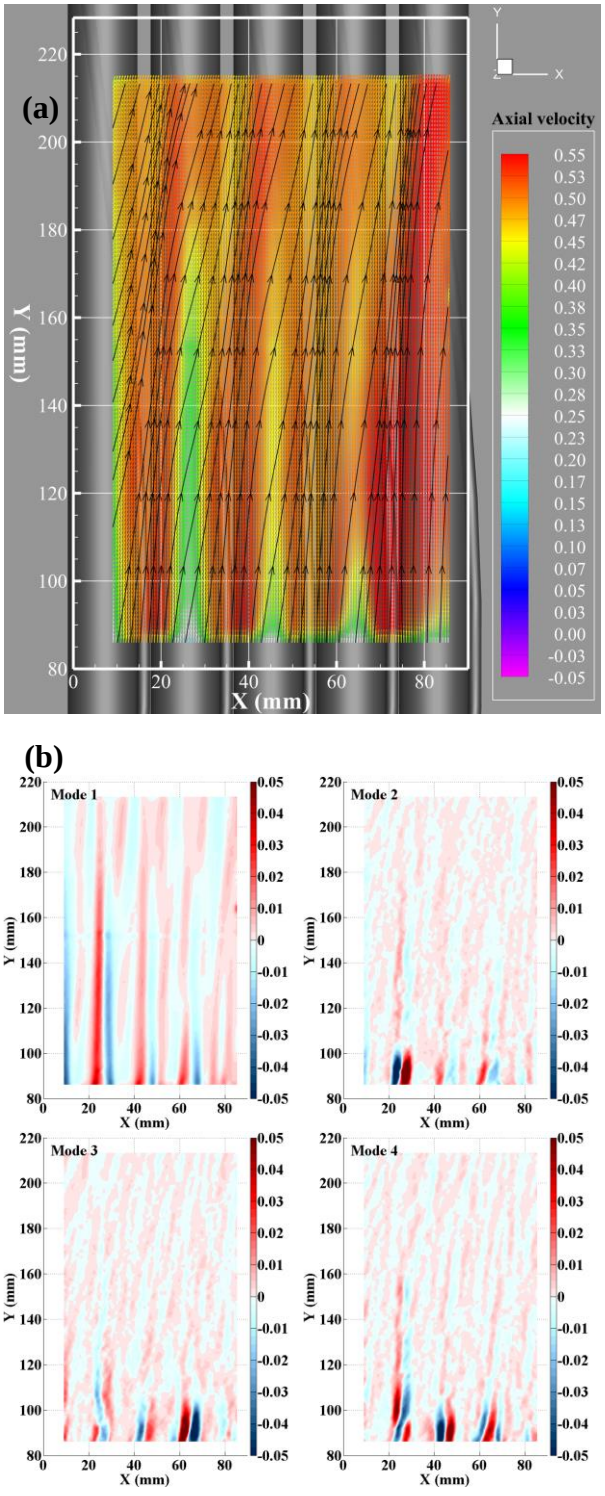


Fig. 3: Results from PIV measurements with p-cymene on face F. (a) The ensemble-averaged velocity vector for Re=3500. The color contour shows the axial velocity component. (b) The first four POD modes, obtained from POD analysis of the PIV vorticity fields.

The silver coating yielded a strong light intensity in the PIV-PCY images. The laser beam was adjusted by beam combination optics to form a 1.5-mm-thick laser sheet. To illuminate the vertical plane highlighted in Fig. 1(b), the laser sheet was guided through a triangular prism (not shown), which was attached on the outer enclosure wall. For all experiments, the laser position was adjusted with three motorized linear translation stages.

All PIV images were captured at 12-bit color depth. Sequences of 3087 images (for Memrecam GX-3) and 8310 images (for Phantom M310) in a single-frame mode were recorded during each experimental run with a sampling rate ranging from 400 Hz to 1600 Hz depending on the Reynolds number of the flow. The raw PIV images for each Reynolds number were collected four times to increase the sample size and ensure the dataset would statistically represent the flow characteristics. The applied PIV processing algorithms were advanced multi-pass, multi-grid PIV processing algorithms. These are based on robust phase correlations that have been implemented for the PRANA codes by Virginia Tech [7,8]. For the PIV-H2O tests, the first PIV processing pass started with an interrogation window of 128 × 128 pixels and the final pass ended with a window of 32 × 32 pixels. For the PIV-PCY tests, the initial and final interrogation windows were 64 × 64 pixels and 16 × 16 pixels. Velocity vectors were calculated from the correlation map with a Gaussian peak fit for sub-pixel accuracy [9]. Inside each pass, statistical validations were performed to identify and replace erroneous vectors. A median filter [10] was applied and standard deviations of the neighboring vectors were used to filter out spurious vectors.

RESULTS

Figure 2 shows the ensemble averaged velocity vector fields and turbulent profiles obtained from the PIV-H2O tests for the Reynolds numbers of 3410, 6140 and 10230. It can be seen that the flow patterns follow the direction of the helical wire spacer in a clockwise rotational direction although the wire spacers are not present in the measurement area. As can be seen in Fig. 1(d), the sides of each edge subchannel have the smallest flow area where points on the pin surface are closest to the enclosure inner wall. The flow area gradually increases when the points move toward the center of each edge subchannel. Because of this, the flow accelerates and then decelerates correspondingly as it passes through the gaps of the edge-subchannels. Profiles of the root-mean-square (r.m.s) axial fluctuating velocity V_{rms} and Reynolds stress $u'v'$ also show local peaks when the flow decelerates.

Figure 3 presents the ensemble-averaged velocity vectors from the PIV-PCY tests on face ***F*** for flow with a Reynolds number of 3500. In this case, the measurement area is larger as it is the combined view from two cameras covering adjacent regions. The vertical stripes of smaller

velocities are caused by particle deposition on some of the pins.

Proper orthogonal decomposition (POD) analysis [11,12] was applied to the vorticity fields calculated from the PIV velocity snapshots to reveal the coherent structures of the near-wall region. In Fig. 3(b), the first four POD modes are illustrated. Mode 1 shows a flow pattern with elongated structures that is similar to the mean flow while the other low-order POD modes reveal smaller and shorter scale structures. It should be emphasized that the current PIV experimental setup measured velocity vector fields in the vertical planes. The POD modes extracted from the corresponding vorticity snapshots revealed the projections of the vortex tubes as they move through the vertical laser plane. Further investigations and comparisons to CFD calculations are essential to validate the findings.

CONCLUSIONS

The mock 61-pin hexagonal fuel bundle with helically wrapped wire spacers has been successfully constructed and operated with water and p-cymene, which matches the refractive index of acrylic. PIV measurements have been performed between the pins and hexagonal enclosure on two different enclosure faces for the range of Reynolds number between 4,000 and 11,000. The mean velocity and Reynolds stresses were computed from the PIV vector fields. Further investigations will be carried out at various interior subchannel locations. The experimental data collected from these tests will be used to benchmark CFD calculations of the experimental configurations using both RANS [13] and LES [14] methods for turbulence modeling.

NOMENCLATURE

CFD = computational fluid dynamics
DOE = Department of Energy
LDV = laser Doppler velocimetry
LES = large-eddy simulation
MIR = matched-index-of-refraction
PIV-H2O = PIV measurements with water as the fluid
PIV-PCY = PIV measurements with p-cymene as the fluid
POD = proper orthogonal decomposition
RANS = Reynolds-Averaged Navier-Stokes
RI = refractive index
RTD = resistance temperature detector
VFD = variable frequency drive

ACKNOWLEDGEMENTS

This work was performed for the Department of Energy under contract DE-NE000832.

REFERENCES

1. E. NOVENDSTERN, “Turbulent Flow Pressure Drop Model for Fuel Rod Assemblies Utilizing a Helical Wire-Wrap Spacer System,” *Nucl. Eng. Des.*, **22**, *1*, 28–42 (1972).
2. K. REHME, “Pressure Drop Correlations for Fuel Element Spacers,” *Nucl. Technol.*, **17**, 15–23 (1973).
3. S.-K. CHENG and N. E. TODREAS, “Hydrodynamic Models and Correlations for Bare and Wire-Wrapped Hexagonal Rod Bundles — Bundle Friction Factors, Subchannel Friction Factors and Mixing Parameters,” *Nucl. Eng. Des.*, **92**, *2*, 227–251 (1986).
4. I. AHMAD and K.-Y. KIM, “Flow and Convective Heat Transfer Analysis Using RANS for a Wire-Wrapped Fuel Assembly,” *J. Mech. Sci. Technol.*, **20**, *9*, 1514–1524 (2006).
5. R. GAJAPATHY et al., “CFD Investigation of Effect of Helical Wire-Wrap Parameters on the Thermal Hydraulic Performance of 217 Fuel Pin Bundle,” *Ann. Nucl. Energy*, **77**, 498–513 (2015).
6. P. FISCHER, J. LOTTES, and A. SIEGEL, “Large Eddy Simulation of Wire-Wrapped Fuel Pins I: Hydrodynamics in a Periodic Array,” in *Proc. M&C + SNA*, Monterey, California, April 15–19, 2007, American Nuclear Society (2007).
7. A. ECKSTEIN and P. P. VLACHOS, “Digital Particle Image Velocimetry (DPIV) Robust Phase Correlation,” *Meas. Sci. Technol.*, **20**, *5*, 055401 (2009).
8. A. ECKSTEIN and P. P. VLACHOS, “Assessment of Advanced Windowing Techniques for Digital Particle Image Velocimetry (DPIV),” *Meas. Sci. Technol.*, **20**, *7*, 075402 (2009).
9. M. RAFFEL et al., *Particle Image Velocimetry: A Practical Guide*, Springer-Verlag (2007).
10. J. WESTERWEEL, “Efficient Detection of Spurious Vectors in Particle Image Velocimetry Data,” *Exp. Fluids*, **16**, *3–4* (1994).
11. G. BERKOOZ, P. HOLMES, and J. L. LUMLEY, “The Proper Orthogonal Decomposition in the Analysis of Turbulent Flows,” *Annu. Rev. Fluid Mech.*, **25**, *1*, 539–575 (1993).
12. L. SIROVICH and M. KIRBY, “Low-Dimensional Procedure for the Characterization of Human Faces,” *J. Opt. Soc. Am. A*, **4**, *3*, 519 (1987).
13. D. J. LEONARD et al., “CFD Verification and Validation of Wire-Wrapped Pin Assemblies,” *Trans. Am. Nucl. Soc.*, **115** (2016).
14. A. V. OBABKO, E. MERZARI, and P. F. FISCHER, “Nek5000 Large-Eddy Simulations for Thermal-Hydraulics of Deformed Wire-Wrap Fuel Assembles,” *Trans. Am. Nucl. Soc.*, **115** (2016).

Pressure Measurements in a Wire-Wrapped 61-Pin Hexagonal Fuel Bundle

N. Goth, P. Jones, M. Childs, S. Lee, D.T. Nguyen, R. Vaghetto, Y.A. Hassan

Texas A&M Nuclear Engineering: 3133 TAMU, College Station, TX, 77843
negcm7@tamu.edu, pgjones87@tamu.edu, masonchilds@tamu.edu, sayalee@tamu.edu, thien.duy.ng@tamu.edu, r.vaghetto@tamu.edu, y-hassan@tamu.edu

INTRODUCTION

Texas A&M University is conducting isothermal experiments in a wire-wrapped 61-pin hexagonal fuel bundle to support the research on advanced nuclear fuel development sponsored by the Department of Energy (DOE). The purpose of these experiments is to produce high spatial and temporal resolution measurements of the flow and pressure measurements at different locations of the test bundle. The experimental data will be used to benchmark numerical simulations of the experiments using both industry-standard Reynolds-averaged Navier-Stokes (RANS) based computational fluid dynamics (CFD) methods [1] and highly resolved large eddy simulations (LES) [2].

FACILITY DESCRIPTION

The experimental fuel bundle is consists of 61 wire-wrapped pins arranged in a triangular lattice. The pins, wires, and hexagonal duct enclosure are made of transparent to allow for flow visualization measurements using laser diagnostic velocity measurement techniques.

The 61-pin hexagonal fuel bundle is tightly packed with only the wire spacer enforcing the triangular lattice along the length of the bundle. The length of the duct inner flat-to-flat (FTF) is equivalent to the fuel bundle FTF plus an extra 0.77%. Primary dimensions are identified in Fig. 1.

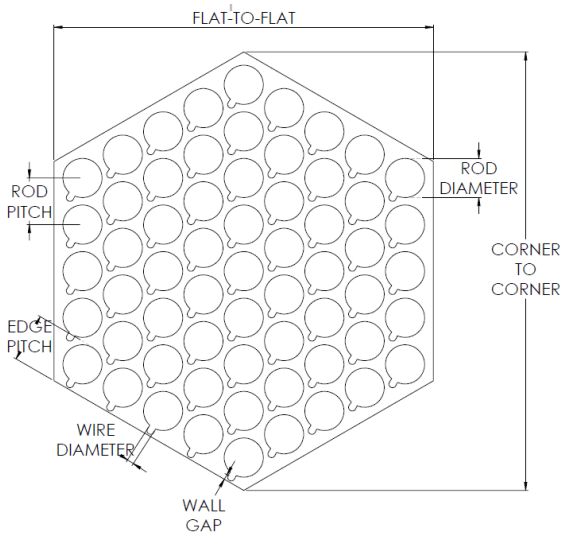


Fig. 1. 61-pin hexagonal fuel bundle configuration

The facility is equipped with pressure transducers to measure the pressure at various axial and azimuthal locations along the duct walls. Fig. 2 shows the location of the pressure taps (PT).

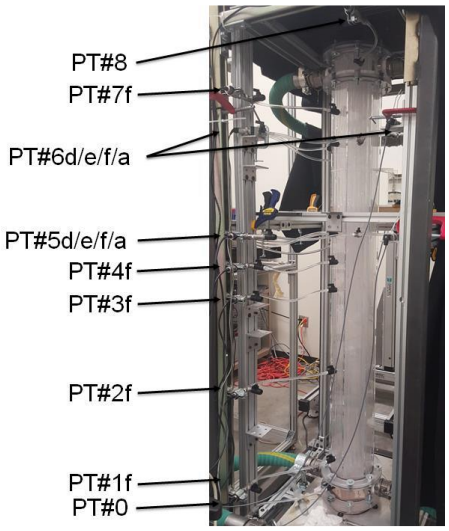


Fig. 2. Pressure tap locations in the hexagonal duct

Nine of the pressure taps measure the pressure drop across the wire-wrapped fuel bundle. PT#0 is installed at the lower inlet plenum to monitor the maximum pressure of the test section. The total pressure drop through the entire test section is measured by the difference in pressure measured by PT#0 (inlet tap) and PT#8 (outlet tap). Pressure transducers PT#1-7 are installed on the same face of the hexagonal duct to record the pressure at seven axial locations along the test section. These taps capture the axially developing flow in the fuel bundle.

At two axial locations in the fully developed region, pressure taps are installed on four adjacent hexagonal faces of the duct to measure the azimuthal pressure gradient. Each set of these taps captures the flow asymmetry that exists due to the helically wrapped wire spacer. The two sets at two axial locations capture how the flow asymmetry changes as the orientation of the helically wrapped wire spacer changes.

The pressure transducer hardware installed in the experimental facility is summarized in Table I. The accuracy of each transducer is relative to its full scale (FS) reading. The two sets of transducers labeled PT #5_d/e/f/a and PT #6_d/e/f/a are the differential pressure transducers described

above. These sets are located on four adjacent faces of the hexagonal enclosure.

Table I. Pressure Transducer Hardware Summary

PT #	Axial Location (Wire Pitch)	Full Scale (Pa)	Accuracy (% Full Scale)
0	Inlet	206843	< 4.0
1	0.16	206843	< 4.0
2	1.00	206843	< 0.1
3	1.75	206843	< 0.1
4	2.00	206843	< 0.1
5	2.25	103421	< 0.1
5_d/e/f/a	2.25	1244	< 4.3
6	3.00	206843	< 0.1
6_d/e/f/a	3.00	2488	< 0.1
7	3.25	103421	< 0.1
8	Exit	103421	< 1.0

The facility is equipped with a secondary loop to provide temperature control of the primary fluid. A resistance temperature detector (RTD) is used to measure the primary fluid temperature. The primary fluid was maintained between 294.5 K and 295.5 K.

EXPERIMENTAL PROCEDURE

All experimental runs were performed at constant operating temperatures and flow rates. The temperature was controlled using the secondary loop chilled water heat exchanger. The flow rate was controlled using a variable frequency drive (VFD) to maintain a constant speed of the primary centrifugal pump.

Before each experimental run, a specific procedure was conducted to prepare the facility. The preparation consisted of filling the primary loop with deionized water up to the elevation of the highest pressure transducer, PT#8. A vent valve remained open to atmosphere to allow air to exit the facility. The first verification of the instrumentation was performed with a static volume of water. The pressure readings of each transducer was compared to the expected hydrostatic head at each elevation.

After confirming that readings were within the acceptable range of the reference values, fluid was added to the facility to complete the filling process. Gradually, the primary pump speed was increased to 0.00757 $m^3 s^{-1}$ with the use of the VFD. This flow rate was maintained for approximately 5 minutes to remove any remaining air from the primary loop. A final verification of the pressure readings was performed at 0.00315 $m^3 s^{-1}$ to confirm repeatability from previous runs.

Pressure data was recorded at each flow rate for a period of 10 seconds. The measurement was repeated three times for each flow rate. Table II describes the range of operating parameters for the pressure measurements.

Table II. Experimental Run Parameter Range

Parameter	Value
Min Flow Rate	0.00315 $m^3 s^{-1}$ (Re ≈ 3200)
Max Flow Rate	0.00945 $m^3 s^{-1}$ (Re ≈ 9500)
Flow Rate Step Size	0.000631 $m^3 s^{-1}$
Fluid Temperature	295 K
Data Collection Duration	10 s
Sample Rate	1000 Hz
Number of Repetitions	3

RESULTS

This experimental activity has produced a set of friction factors for the range of Reynolds numbers from 3200 to 9500 where deionized water was the fluid. According to Cheng and Todreas [3], this data set contains measurements in the transition and transition-turbulent regimes. An evaluation of existing wire-wrapped fuel bundle friction factor correlations was performed by Chen et al. [4], who noted that, "an intermittency factor was introduced for correlating behavior in the transition regime". Further validation and extension of existing correlations for pressure drop calculations is also possible with this experimental data set.

The detailed Cheng-Todreas (CTD) correlation was chosen to compare with the experimentally determined friction factor, because of its highest Agreement Index and Credit Score as presented by Chen et al. [4]. The application range of the CTD correlation is presented in Table III. N_r stands for the number of pins in the bundle. The 61-pin hexagonal fuel bundle used in this experiment meets the applicability requirements.

Table III. CTD Application Range [4]

N_r	P/D	H/D	Re range	Uncertainty
19-217	1.0- 1.42	4.0 - 52.0	50 - 10^6	± 14%

The pressure drop across PT#5 and PT#7 was selected to calculate the friction factor. These pressure transducers are located in the fully developed region of the fuel bundle and span one full wire spacer pitch. Exit effects are negligible due to the 0.25 wire pitch length that exists in the test section before the exit plenum is reached.

The gauge pressure was determined at each location by averaging the transducer output over the 10 second periods of all three trials. The hydrostatic head was subtracted from the gauge pressure at each flow rate. Therefore, the frictional pressure drop through the fuel bundle is represented by the pressure difference between PT#5 and PT#7. The friction factor was calculated from Equation 1.

$$f = \Delta P \left(\frac{H_d}{L}\right)\left(\frac{2}{\rho V^2}\right) \quad (1)$$

Figure 3 compares the CTD correlation to the experimental data set for Reynolds numbers ranging from 3200 to 9500. The CTD correlation has varying uncertainties

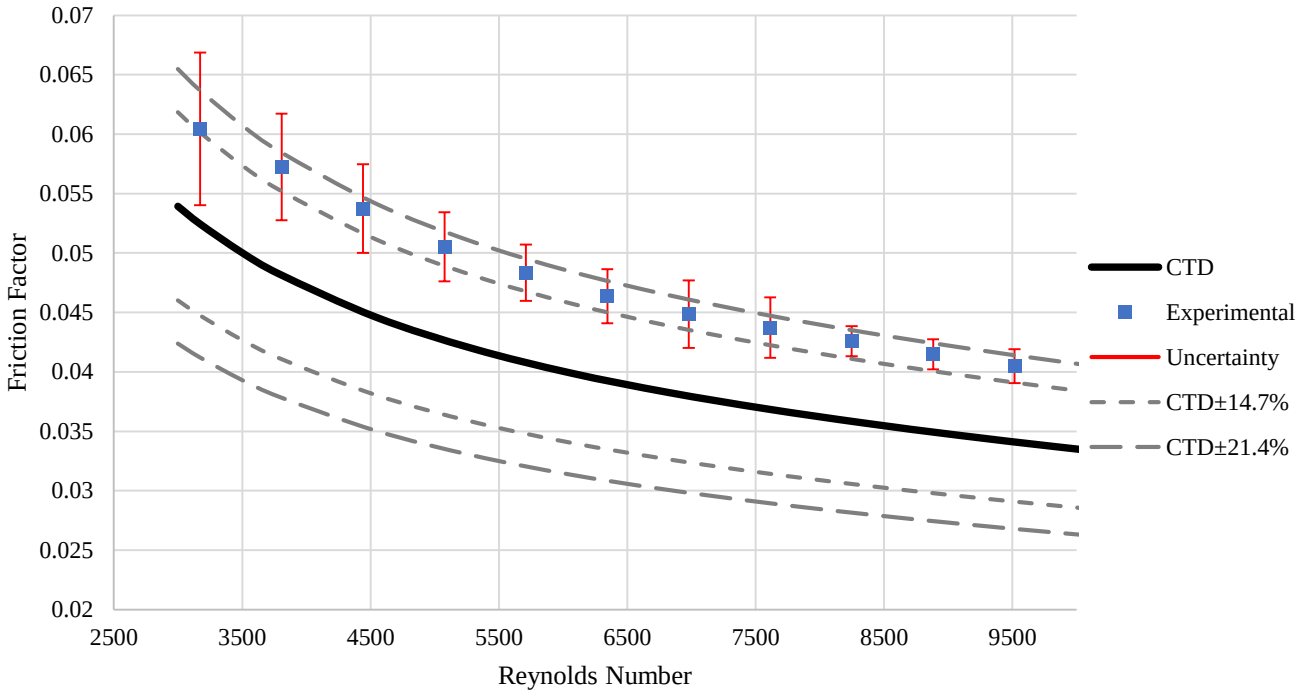


Fig. 3. Comparison of the friction factor determined from the CTD correlation and the experimental data set for Reynolds numbers from 3200 to 9500. CTD uncertainties for turburlent and transition (14.7%), along with laminar (21.4%) flow are included.

based on the flow regime. The uncertainties (at 90% confidence) provided by Chen et al. [4] are ±14.7% for the turbulent and transition regimes and ±21.4% for the laminar regime. These uncertainties are represented by dashed lines in Fig. 3.

The uncertainty of the experimental friction factor is also presented. This uncertainty is the result of the accuracy of the pressure transducers and variation of the three repeated measurements. The uncertainty in the pressure measurement from the hydrostatic head is represented by Equation 2. The uncertainty in the pressure measurements for each flow rate including multiple measurements is represented by Equation 3. The uncertainty was propagated throughout the post-processing of subtracting the hydrostatic head from the pressure measurements. For each flow rate, this uncertainty is represented by Equation 4.

$$\sigma_{0GPM} = \sqrt{\text{PTAccuracy}^2} \tag{2}$$

$$\sigma_{xGPM} = \sqrt{\text{PTAccuracy}^2 + \sigma_{Means}^2} \tag{3}$$

$$\sigma_{xGPM-NoFlow} = \sqrt{\sigma_{0GPM}^2 + \sigma_{xGPM}^2} \tag{4}$$

The uncertainties of the experimental data set is represented by Equation 5 and shown as vertical error bars in Fig. 3.

$$\sigma_{5-7} = \sqrt{\sigma_{xGPM-NoFlow,PT5}^2 + \sigma_{xGPM-NoFlow,PT7}^2} \tag{5}$$

Uncertainty in the Reynolds number was not included in these uncertainty estimates because the fluid temperature was controlled to within ±1 K, and density and viscosity are well defined for water at 295 K. A quality inline turbine flow meter and centrifugal pump with VFD were used to achieve the desired flow rate for each experimental measurement. However, the uncertainty in the flow velocity has not been included at this time.

CONCLUSION

A series of tests were conducted to study the pressure drop in a wire-wrapped 61-pin hexagonal fuel bundle for flows over a range of Reynolds numbers in the transition and transition-turbulent flow regimes. Experimental results were compared to the CTD correlation and found in good agreement with correlation predictions. In particular, the experimental friction factor was toward the upper region of the CTD error bounds. The analysis of the experimental data suggest that that the experimental friction factor trends

towards the turbulent upper error bound for higher Reynolds numbers.

NOMENCLATURE

CFD = computational fluid dynamics
CTD = detailed Cheng and Todreas correlation
DOE = Department of Energy
FS = full scale
FTF = flat-to-flat
LES = large-eddy simulation
N_r = number of pins in the hexagonal fuel bundle
PT = pressure tap
RANS = Reynolds-averaged Navier-Stokes
Re = Reynolds number
VFD = variable frequency drive

ACKNOWLEDGEMENTS

This work was performed for the Department of Energy under contract DE-NE000832.

REFERENCES

1. D. J. LEONARD et al., "CFD Verification and Validation of Wire-Wrapped Pin Assemblies," *Trans. Am. Nucl. Soc.*, **115** (2016).

2. A. V. OBABKO, E. MERZARI, and P. F. FISCHER, "Nek5000 Large-Eddy Simulations for Thermal-Hydraulics of Deformed Wire-Wrap Fuel Assembles," *Trans. Am. Nucl. Soc.*, **115** (2016).

3. S.-K. CHENG and N. E. TODREAS, "Hydrodynamic Models and Correlations for Bare and Wire-Wrapped Hexagonal Rod Bundles — Bundle Friction Factors, Subchannel Friction Factors and Mixing Parameters," *Nucl. Eng. Des.*, **92**, , 227–251 (1986).

4. S. CHEN, N. TODREAS, and N. NGUYEN, "Evaluation of Existing Correlations for the Prediction of Pressure Drop in Wire-Wrapped Hexagonal Array Pin Bundles," *Nucl. Eng. Des.*, **267**, 109–131 (2014).

Heated Bundle Test in AREVA NP's Fuel Cooling Test Facility

Mathieu Martin, Kelly Duggan, Tom Galioto

AREVA NP Inc, 2101 Horn Rapids Road, Richland, WA, 99352
Mathieu.martin@areva.com, Kelly.Duggan@areva.com, Tom.Galioto@areva.com

INTRODUCTION

As part the Department of Energy (DOE) initiative for advanced nuclear fuel development, AREVA NP is performing a series of flow and thermal mixing tests on a simulated, internally heated bundle of wire-wrapped fuel pins of the type commonly used in liquid-metal fast-breeder reactors at its Fuel Cooling Test Facility (FCTF) in Richland, Washington. The FCTF is part of the Product Development Test Facility (PDTF), which is a dedicated facility for advanced thermal-hydraulic testing of nuclear fuel assemblies. Initially developed to perform post Loss Of Coolant Accident (LOCA) testing, i.e., spray and reflood tests, this test facility has been adapted to accommodate the unique requirements of the heated bundle tests described here.

The purpose of this test is to investigate and measure thermal distribution and pressure drop behavior for two configurations (non-deformed and deformed duct) of heated 61-pin, hexagonally packed fast reactor test assembly in a fully turbulent regime for generating Computational Fluid Dynamics (CFD) validation grade data. This test is performed in conjunction with high fidelity flow field measurement experiments [1] and high fidelity CFD [2,3] to provide a comprehensive understanding of the flow inside such a design.

The present paper focuses on the heated bundle test performed at AREVA NP. First, the test loop is described and then an overview of the test activities is presented.

FCTF DESCRIPTION

The Test Loop

A simplified schematic of the FCTF is presented in Fig. 1. The system is composed of two loops, a primary side and secondary side. The primary side includes the test assembly where measurements are taken. The secondary side provides heat transfer to the cooling tower, which serves as the ultimate heat sink.

The FCTF includes several pressure vessels. The primary pressure vessel contains the test assembly consisting of a simulated fuel element with electrically heated rods. The pressure vessel can accommodate prototypic sizes of fuel mockups, including the 61-pin bundle used by the present test campaign.

The power supplied to groups of heaters inside the rods can be controlled independently, which allows the tests to simulate a wide variety of radial power distributions. Thermocouples measure the temperature on the inside of the cladding of the rods with heaters. The vessel surrounding the test section contains ports to accommodate the wires used for the instrumentation.

An AC power supply, composed of several channels controlled by Silicon Control Rectifiers (SCR), allows the electric power to be gradually applied to the heaters. Since each SCR is controlled independently, the power supplied to groups of rods can be adjusted by the operator to produce various radial peaking patterns. Over one megawatt of total electric power is available to be supplied to the heaters.

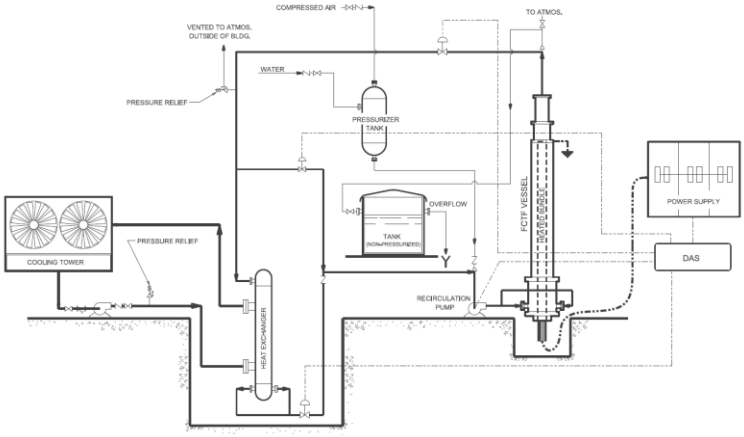


Fig. 1. Simplified Schematic of the FCTF.

The primary loop contains the following components:

- The test section
- A recirculation pump with a Variable Frequency Drive (VFD) to provide control over the flow
- Several pneumatic valves, which allow for even greater flow control
- Flow measurement instrumentation, with built-in redundancies
- Two heat exchangers to cool the system

To control the inlet temperature in the test section, a bypass was added to the primary loop to allow "hot" water to be directly injected into the lower plenum without being cooled. This allows a superior level of temperature control and avoids having to adjust the secondary cooling loop. A Proportional Integral Derivative (PID) control loop is used to set and control the specified temperature. A

pressurization system was also added on the primary side to apply pressure in the test loop using compressed air.

The secondary loop is functionally simpler than the primary loop. It includes the shell side of the heat exchangers, a recirculation pump controlled by VFD, and an open air-cooled cooling tower. A Data Acquisition System (DAS) is used to record all of the instrumentation channels and to control all the systems. Due to the large amount of thermal and mechanical energy present in the system during operation, a Programmable Logic Controller (PLC) is used to control the loop and guarantees safe operation for personnel and test hardware.

Instrumentation

The test loop contains two vortex flow meters, upstream and downstream the test section, pressure transducers and a series of thermocouples across the piping to monitor the system. The electric power supplied to the heaters is measured independently for each SCR.

The tests being performed require a large amount of data to be recorded. Over 350 thermocouples are present in the system. About 160 of those thermocouples are located inside the heater rods. Many of the others are located on the external surfaces of the unheated rods to monitor wall temperatures as well as water temperature. Multiple pressure taps are installed in various locations across the test section to capture the hydraulic behavior.

Along with the system instruments, the DAS monitors all channels scanned by the PLC to ensure safe operation as defined in the programmed logic. The PLC reacts to any unwanted event (high temperature, sudden loss of primary or secondary flow, etc.) and can take appropriate actions (e.g., shut down power) without operator intervention.

TEST ACTIVITY

Test Section Description

The test section is a 61-pin bundle arranged in a hexagonal pattern. Each pin is wire-wrapped as shown in Fig. 2.

The 61-pin bundle is enclosed in a hexagonal duct and located in the main vessel of the primary loop. During this test campaign, two ducts are used, one representing beginning of life (BOL) conditions and another more representative of later-in-life (LIL) conditions. The LIL duct has faces that are deformed from their original, as-designed shape to account for the effects of creep and other thermomechanical phenomena that occur with time during an assembly's operational lifetime. Characterizing the impact that these deformations have on the thermal behavior of the fuel assembly is a key part of this test.



Fig. 2. The test section.

Operation of the loop proceeds as follows. First, the primary system is pressurized to avoid boiling along the surface of the pins when the power is applied. As the power is gradually applied to the heaters concurrently during startup, the system is monitored for any unwanted excursion. Once the target power is achieved, steady flow through the loop is maintained until thermal equilibrium and a steady-state flow are verified by the instrumentation. At this point, the data collection commences until a sufficient amount of data for statistical evaluation has been gathered.

Test Specifications

Two ducts are being tested with identical boundary conditions to evaluate potential impact of the LIL versus BOL geometries on the thermal behavior of the wire-wrapped bundle. For these tests, the flow rate is adjusted to produce a flow with a Reynolds number of 20,000 inside the bundle. The inlet temperature is 32°C, and the total power applied to the heaters is 456 kW with a cosine axial shape. The pressure of the loop is regulated to maintain a pressure of 1 MPa at the exit of the test section.

CFD was used extensively to determine the boundary conditions of the test to achieve the goals of the experiments while meeting safety requirements. Figure 3 shows an example of one of these CFD simulations illustrating the temperature distribution in the fluid and in the cladding of the heated pins of the bundle in the middle of the heated length where the heater power is largest. CFD calculations such as this one also were used to optimize the thermal gradients across the bundle of pins to maximize the usefulness of the measurements for benchmarking purposes.

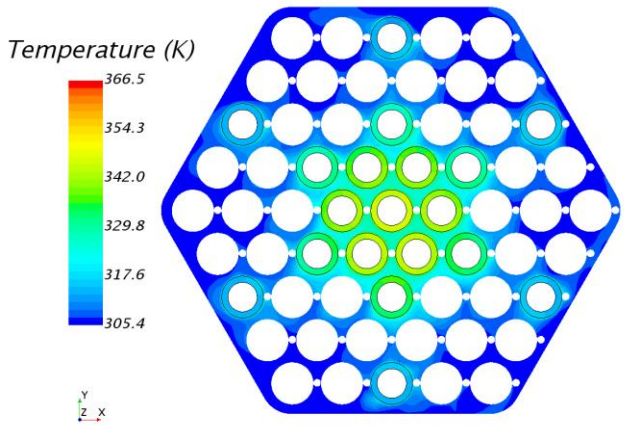


Fig. 3. Temperature profile at the peak of the cosine power shape

CONCLUSION

As part of the DOE advanced fuel research project, AREVA NP is conducting advanced thermal-hydraulic testing to characterize the thermal-hydraulic behavior of a bundle of wire-wrapped fuel pins. The testing at AREVA's Fuel Cooling Test Facility uses an electrically heated bundle to study the heat transfer and thermal mixing of fluid as it passes through the simulated fuel assembly. The data collected during this test will be compared to other similar experiments [1] and CFD calculations [2,3] as part of a benchmarking effort.

ACKNOWLEDGMENTS

This work was performed for the Department of Energy under contract DE-NE0008321.

REFERENCES

1. R. VAGHETTO et al., "Flow Field and Pressure Measurements in a 61-Pin Wire-Wrapped Bundle," *Trans. Am. Nucl. Soc.*, **115** (2016).

2. D. J. LEONARD et al., "CFD Verification and Validation of Wire-Wrapped Pin Assemblies," *Trans. Am. Nucl. Soc.*, **115** (2016).

3. A. V. OBABKO, E. MERZARI, and P. F. FISCHER, "Nek5000 Large-Eddy Simulations for Thermal-Hydraulics of Deformed Wire-Wrap Fuel Assembles," *Trans. Am. Nucl. Soc.*, **115** (2016).

CFD Verification and Validation of Wire-Wrapped Pin Assemblies

Daniel J. Leonard[a], R. Brian Jackson[a], K. Michael Steer[a], Tom Reeves[a], Nate Salpeter[b]

[a] *TerraPower LLC.: 330 120th Ave NE Suite 100, Bellevue, WA, 98005, c-dleonard@terrapower.com*
[b] *AER Consulting: P.O. Box 219, Half Moon Bay, CA 94019, nate@aeratio.com*

INTRODUCTION

TerraPower is participating in a cooperative project among industry, the national lab system, and academia to perform Verification and Validation (V&V) of Computational Fluid Dynamics (CFD) methods for predicting the flow and heat transfer within liquid-metal-cooled nuclear fuel assemblies with wire-wrapped fuel pins. This project, consisting of both experimental and numerical components, uses surrogate fluids and electrically heated fuel pins to substitute for the liquid metal coolant and the nuclear heat source. The experiments include both unheated assemblies to measure the flow velocities with Laser Doppler Velocimetry (LDV) and Particle Image Velocimetry (PIV), as well as heated assemblies to measure the temperatures of the fluid and the simulated fuel pins with thermocouples. Both sets of experiments also measure the pressure at multiple locations in the system. The numerical component of this work involves high-fidelity Large-Eddy Simulation (LES) modeling and industry-standard Reynolds-Averaged Navier-Stokes (RANS) modeling of the experiments. Furthermore, the experiments and simulations will be conducted on two duct geometries: the first is a non-deformed hexagonal duct that has flat internal duct faces that represents a beginning of life geometry. The other is a deformed duct where the internal hexagonal flow area enlarges then decreases along the axial height to represent the changes that occur to the duct geometry from pressure and irradiation effects in the core.

This paper describes the methods and results of the industrial, RANS-based CFD code verification, solution verification, and solution validation. The V&V simulations are being performed for the following experiment test geometries:

- Isothermal non-deformed bundle
- Heated non-deformed bundle
- Isothermal deformed bundle
- Heated deformed bundle.

These flows have been computed at first with the pre-test design specifications, without the aid of any experimental results. Later, post-test calculations will be performed incorporating the actual test conditions and input from some of the experimental results.

These RANS simulations of helically wire-wrapped fuel assemblies employ meshes of bare pins without the wire-wrap in the bundle. The effect of wire-wrap on the flow is accounted for by introducing a momentum source into the governing fluid equations. The momentum source is only applied to cells corresponding to the location of the wire-wrap, and its components in each cell are based on the local flow field [1]. This methodology simplifies the geometry and mesh generation and reduces the cell count, while still capturing the effects of the wire-wrap. The momentum source approach is used for all of the assembly simulations performed in this study.

VERIFICATION AND VALIDATION METHODS

The purpose of the Advanced Fuel Assembly Flow Characterization (AFAFC) project is to provide experimental data of wire-wrapped bundles specifically for CFD V&V. As V&V and uncertainty quantification are critical to determining the reliability of CFD simulations, it is

essential to have the required experimental data for both beginning-of-life and later-in-life assembly configurations to examine the validity of the numerical effort. Additionally, it is important to verify both the CFD code and the CFD solution as part of the overall V&V process. The procedures and processes employed for code/solution verification and solution validation are explained in this section.

Code Verification

Code verification is conducted on a commercial CFD code (Star-CCM+) with the Method of Manufactured Solutions (MMS). This approach attempts to verify the code by proving that the Observed Order of Accuracy (OOA) converges to the Formal Order of Accuracy (FOA) with mesh refinement. While the code verification simulations do not represent the realistic nuclear fuel assembly geometry, nor are they required to, the simulation parameters are chosen to be consistent with those of the actual validation simulations. Therefore, if the code is verified to be correct for those particular parameters, then it is verified to be correct for more complex geometries as well, so long as the same parameters apply.

The MMS procedure is conducted for two sets of simulation parameters which correspond to the isothermal and heated bundle experiments. This method allows for the construction of an exact solution for complex partial differential equations, which can be compared to the numerical solution to obtain the discretization error and the OOA. The general process of the MMS (as described by reference [2]) is as follows:

1. Establish the mathematical model: $L(u) = 0$
2. Choose the solution: $\hat{u}$
3. Operate the mathematical model onto the manufactured solution to obtain an analytical source term: $s = L(\hat{u})$
4. Insert the source term into mathematical model and numerically solve for this new expression: $L(u) = s$

The L_n-norms of the discretization error of the dependent variables are used to obtain a global measure of the OOA and its converged value with mesh refinement.

Solution Verification

Solution verification is conducted through iterative and mesh convergence analyses of the variables of interest. Additionally, various turbulence models, mesh spacing in particular directions, and momentum source modeling coefficient values are investigated to assess their sensitivity.

The results of the solution verification and sensitivity analyses are used to finalize modeling methods for the set of pre-test simulations. The set includes a single simulation (with a particular mesh resolution, turbulence model, and momentum source coefficient) for each of the proposed experimental tests (non-deformed isothermal, deformed isothermal, non-deformed heated, and deformed heated). Since these pre-test results are finalized before the experiments are conducted, they are blind to the experimental results, and the selection of the simulation results is based entirely on the solution verification and model sensitivity analyses.

Solution Validation

During the post-test phase of the project, the experimental results will be analyzed and compared with the pre-test results. However, the actual experiments may not be built exactly to the design specifications. These inconsistencies between the as-designed and the as-built experiment can result in differences between the pre-test CFD simulation results (which are based on the as-designed experiment) and the actual experimental results. Therefore, a series of post-test simulations of the actual conditions of the test will be conducted to determine the efficacy of the CFD approach with more consistency.

RESULTS

Code Verification

Figure 1 displays the results of the MMS analysis of the Star-CCM+ code with the 2D steady-state, subsonic ideal-gas Euler equations discretized with first-order FOA. As the mesh is refined, the dependent OOA of the dependent variables is shown to converge to the FOA of the numerical schemes. Thus, the code is verified for these particular code parameters. This approach is currently being applied to more complex governing equations representative of the experiments (higher FOA, 3D, and incorporating turbulence models).

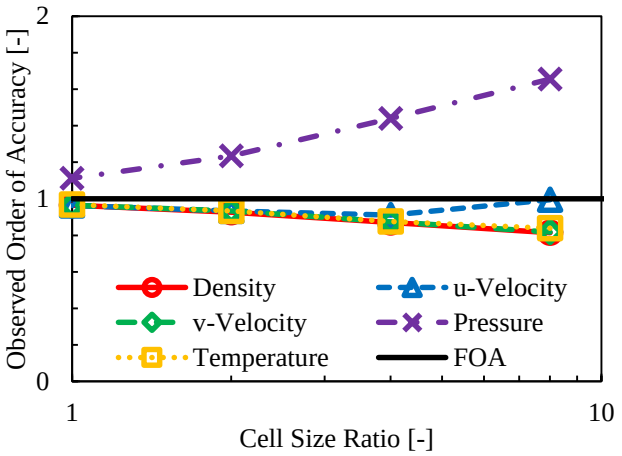


Fig. 1. The OOA converges to the FOA with mesh refinement using the Star-CCM+ commercial code.

Solution Verification

The temperature profile on the duct walls of the non-deformed heated bundle is shown in Fig. 2. The higher temperature streaks are a result of flow features which arise from the heated pin distribution and the helical wire-wrapping of the pins. The pressure drop across the non-deformed isothermal bundle is shown in Fig. 3 for all levels of a systematic mesh refinement along with a Richardson extrapolated value (at $h = 0$). The extrapolated pressure drop is not assumed to be a quality estimate of the exact value because the OOA of 4.32 is inconsistent with the FOA of 2.0. However, the mesh refinement study does display convergence of the pressure drop relatively close to this extrapolated value by the "Fine" mesh ($h = 1.33$). It is shown that the "Fine" mesh predicts the pressure drop to within 4.23% of the extrapolated value (see Table 1) while the next level of refinement results in a relatively small variation.

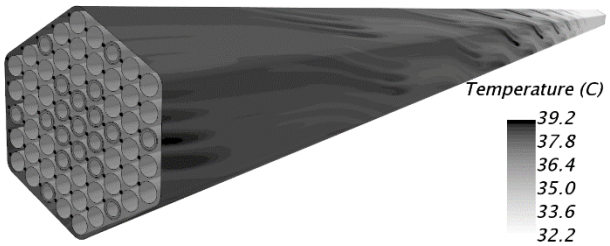


Fig. 2. Thermal profile on the non-deformed heated bundle duct.

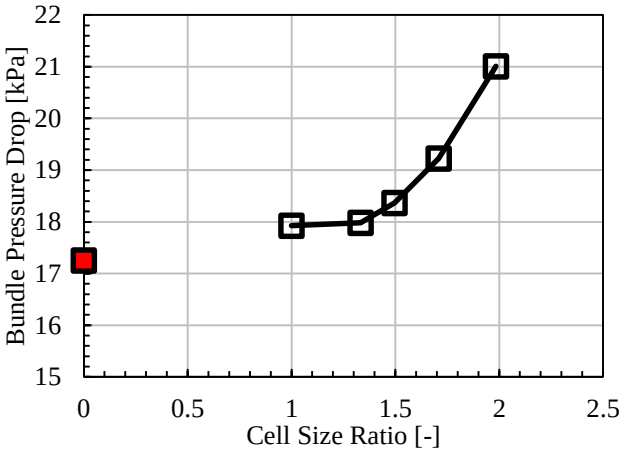


Fig. 3. Net pressure drop of the non-deformed isothermal bundle versus cell size ratio along with Richardson extrapolation based on the three coarsest meshes.

Table 1. Percent difference from the Richardson extrapolation (RE) of the non-deformed isothermal bundle pressure drop for several mesh resolutions.

Cell Size Ratio h	Pressure Drop % Difference from RE
2.0	21.8
1.5	6.44
1.33	4.23

Figure 4 displays a line of potential LDV locations for which the magnitude of the velocity in the non-deformed isothermal simulation is sampled, as well as a plot of the sampled velocity profiles calculated using five mesh resolutions. Little variation is seen in the velocity profile with mesh refinement, choice of turbulence model (not shown), and choice of momentum source coefficient (also not shown). These results suggest that even the coarser meshes are fairly sufficient for capturing the velocity profile at this particular axial location even though the finer meshes may be necessary to accurately compute the bundle pressure drop.

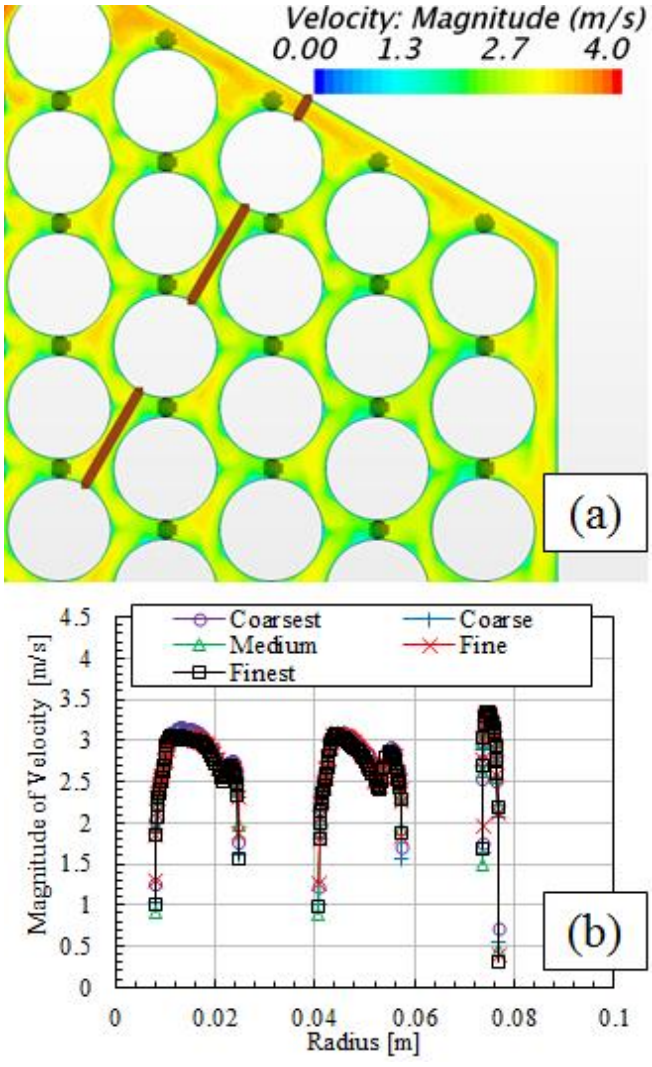


Fig. 4. (a) A transverse cross-section of the non-deformed isothermal bundle showing velocity magnitude contours and a line of potential locations for LDV measurements. (b) The velocity magnitude at each potential LDV point versus the distance from the center of the bundle.

Solution Validation

Pre-Test

After analyzing all of the pre-test mesh and model sensitivity studies, a single CFD simulation was selected (based on the pre-test analyses) as a final pre-test simulation for each of the four configurations (non-deformed heated, non-deformed isothermal, deformed heated, and deformed isothermal). The results from these blind simulations will be compared to the experimental results as they become available.

Post-Test

As the pre-test simulations are based on the as-designed experimental operational conditions and geometry, a second set of simulations will be conducted following the completion of the experiments. These post-tests will use the as-built geometry and as-tested conditions. The results from these computations will again be validated by comparing them to the experimental results.

NOMENCLATURE

h = cell size ratio
L = differential operator
s = analytical source term
u = dependent variable
$\hat{u}$ = analytical form of the manufactured solution
AFAFC = Advanced Fuel Assembly Flow Characterization
CFD = Computational Fluid Dynamics
FOA = Formal Order of Accuracy
LDV = Laser Doppler Velocimetry
LES = Large-Eddy Simulation
MMS = Method of Manufactured Solutions
OOA = Observed Order of Accuracy
PIV = Particle Image Velocimetry

RANS = Reynolds-Averaged Navier-Stokes
RE = Richardson Extrapolation
V&V = Verification and Validation

ACKNOWLEDGEMENTS

This material is provided to support the Department of Energy [National Nuclear Security Administration] Award Number [DE-NE0008321].

Disclaimer: "Neither the United States Government nor any agency thereof, nor any of their employees, makes any warranty, express or implied, or assumes any legal liability or responsibility for the accuracy, completeness, or usefulness of any information, apparatus, product, or process disclosed, or represents that its use would not infringe privately owned rights. Reference herein to any specific commercial product, process, or service by trade name, trademark, manufacturer, or otherwise does not necessarily constitute or imply its endorsement, recommendation, or favoring by the United States Government or any agency thereof. The views and opinions of authors expressed herein do not necessarily state or reflect those of the United States Government or any agency thereof."

REFERENCES

1. R. HU and T. H. FANNING, "A Momentum Source Model for Wire-Wrapped Rod Bundles—Concept, Validation, and Application," *Nucl. Eng. Des.*, **262**, 371–389 (2013).

2. W. L. OBERKAMPF and C. J. ROY, *Verification and Validation in Scientific Computing*, Cambridge University Press (2010).

Nek5000 Large-Eddy Simulations for Thermal-Hydraulics of Deformed Wire-Wrap Fuel Assemblies

Aleksandr V. Obabko, Elia Merzari, Paul F. Fischer[†]

Argonne National Laboratory, Argonne, IL
[†]*University of Illinois at Urbana-Champaign, Urbana, IL*
obabko@mcs.anl.gov

INTRODUCTION

The prediction of thermal performance in wire wrapped assemblies is vital to evaluate overall reactor performance and safety and thus to make a viable carbon-free energy production technology. Recent interest in advanced fuel cycles and reactor fuel recycling has led to renewed interest in the development of liquid-metal-cooled fast reactors over the past 15 years in the United States [1]. Several private companies have expressed continued interest in this technology, with a particular focus on longer life cores. The prediction of thermal performance in fuel assemblies is vital to evaluate overall reactor performance and safety, and it is particularly important as the assembly ages. In fact, the effect of pin and duct deformation driven by thermal expansion and radiation damage is increasingly important as reactor designs look toward longer assembly lifetimes.

The fuel pins in each fuel assembly of a sodium-cooled fast reactor are separated by wire wrap spacers, which are simply wires that are helically wrapped around the pin along the pin axis. While designs vary significantly, a single assembly typically contains 61 to 271 pins in a hexagonal array, with 3 to 5 turns of the wire wrap along the length of each pin. In addition to spacing the pins, the wire wrap promotes thermal mixing of the coolant between channels in the pin array to reduce peak fuel temperatures.

Thermal-hydraulic analysis of wire-wrapped rod bundle flows is challenging for several reasons. The flow is fully turbulent, with a Reynolds number based on the hydraulic diameter, $Re_h = UD_h/\nu$ (i.e. the per channel Re), in the range from 15,000 to 150,000. The wire wrap introduces additional turbulence and establishes a bulk rotation of the fluid within the assembly. Because it creates multiple contact points and lines, the wire wrap makes the geometry and, consequently, the computational mesh relatively complex compared to, e.g., bare bundles. Moreover, with more than 400 subchannels and $L/D_h \approx 360$ (based on 217 pins), the geometry of a single assembly is quite large.

Since there are several hundred assemblies in the reactor, most thermal-hydraulics analysis to date has been based on very coarse lumped parameter models. More recently, high performance workstations have enabled the use of subchannel models in which a few hundred degrees of freedom per channel are used to represent mass, momentum, and energy balances at axial positions along the channel, and where inter-channel mixing is modeled using experimentally determined correlations. Since subchannel models require far less memory and execute relatively quickly compared to computational fluid dynamics (CFD) methods, they will likely continue to play an important role in reactor-scale analysis for the foreseeable future. However, they require a lot of physical models as a result of the space averaging and closing the equation systems especially in order to evaluate thermal-hydraulic performance of a given assembly in the presence of large deformations such as those encountered later-in-life. In the latter regime, which is the focus of this project, the methodology of subchannel analysis cannot easily account for the complex flow patterns that may be introduced as a consequence of changes in the geometry of the fuel assembly and thus requires the physical modeling input from theory, experiments, and validated CFD DNS (direct numerical simulation) or LES (large-eddy simulation) results.

Several efforts to apply CFD to wire-wrapped geometries have already been reported. In particular a set of preliminary LES, in which the governing equations are solved with minimal closure modeling was performed with multiple pin counts [2] of a single-wire-wrap without heat transfer. These calculations, reaching as many as two billion degrees of freedom (dof) for a 217-pin bundle carried out with Nek5000, were the first high-fidelity simulations performed in this type of geometry. Recently, as a first step toward conjugate heat transfer problem, 19-pin calculations [3] have been performed and compared to lower-fidelity, but faster-turn-around, Reynolds averaged Navier-Stokes (RANS) modeling. However, the 61-pin configuration presents an optimal platform to study the thermal-hydraulics behavior of the wire-wrapped assemblies due to a reasonable compromise of the geometry size and simulation complexity versus hydrodynamics trends of increasing pin count.

As such, a well-characterized validation program has been defined for the thermal-hydraulic CFD modeling of 61-pin hexagonal packed fuel assemblies with helically wire-wrapped pins for both non-deformed beginning-of-life geometries and deformed later-in-life geometries typical of sodium-cooled fast reactors. The motivation for this work is the need to validate CFD codes to accurately model the flow and thermal performance of wire-wrapped fuel assemblies, particularly the deformed later-in-life bundles. The effect of pin and duct deformation is increasingly important as reactor designs look toward longer assembly lifetimes. As a part of a larger collaborative project with TerraPower, Texas A&M University (TAMU), and AREVA, this validation work consists of CFD simulations of four con-current experiments. Pre-test numerical simulations corresponding to each of the experiments has been conducted and are planned to be followed by post-test simulations that will incorporate test information as it becomes available to account for any as-built differences in geometry of test section and its specifications including the differences in boundary conditions of the actual tests. This paper focuses on Nek5000 LES results for the isothermal/TAMU undeformed configuration as a first step toward and initial conditions for the deformed isothermal/TAMU and/or conjugate heat trans-

fer/AREVA cases.

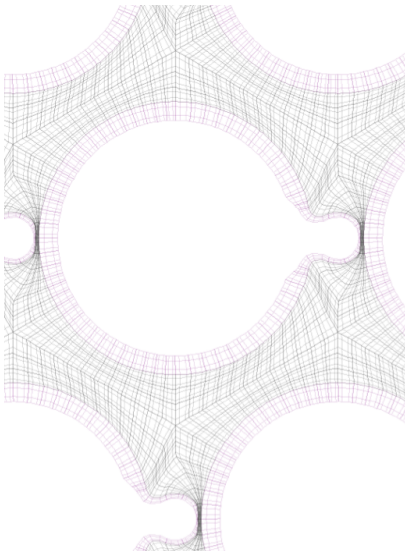


Fig. 1. A portion of LES fluid mesh surrounded by a cladding layer of elements for conjugate-heat-transfer cases.

COMPUTATIONAL APPROACH

In this LES study we have used Nek5000 code for 61-pin wire-wrapped bundles.

The open-source Nek5000 community code features a stabilized formulation that makes it appropriate for direct numerical simulation (DNS) and large eddy simulation (LES) of turbulent flows. Spatial discretization is based on the spectral element method (SEM), which is a high-order, weighted residual technique that combines the geometric flexibility of the finite-element method (FEM) with the tensor-product efficiency of spectral methods [4]. In the SEM, the solution is approximated by tensor product polynomials of degree N on each of E elements, giving rise to $n \approx EN^3$ unknown basis coefficients for each field (velocity, pressure, temperature, etc.). Typical values of N are $7 \ldots 15$, which imply roughly a thousand fold decrease in the number of elements compared with that of an FEM mesh having the same number of degrees of freedom (dof).

Nek5000 employs high-order semi-implicit time stepping schemes that decouple the Navier-Stokes equations into independent advection, diffusion, and pressure projection substeps. The principal computational bottleneck in simulating unsteady incompressible and low-Mach number flows is the elliptic problem governing the pressure, which must be computed implicitly at each time step. The SEM-based Poisson system is solved with preconditioned conjugate gradients or generalized minimum residual (GMRES) method. Preconditioning is based on variational multigrid using local overlapping Schwarz methods for element-based smoothing at resolution N and $N = 3$, coupled with a global coarse grid problem based on linear elements, which is solved in parallel by using algebraic multigrid. In order to efficiently use the IBM Blue Gene/Q (BGQ) system, architecture-tuned computational and communication kernels are implemented. Using the Message Passing Interface (MPI) programming model, Nek5000 has been recently shown to scale up to over 1 million ranks of various machines.

RESULTS

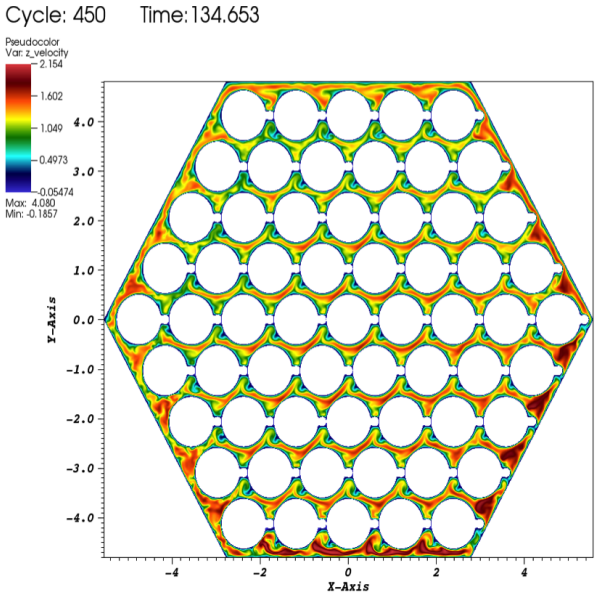


Fig. 2. Transverse cross-section of the instantaneous axial velocity near the onset of the transition from laminar to turbulent flow at $Re = 3,000$.

As a first step in this con-current experiment and simulation validation study, we focused on undeformed isothermal/TAMU configuration. All results reported here have $E = 1.6$ million elements of a polynomial degree $N = 5$, i.e. about $EN^3 \approx 200$ million degrees of freedom, scaled up to 65,536 MPI ranks of Myra BGQ supercomputer at Argonne Leadership Computational Facility (ALCF).

Figure 1 shows a single pin region of computational spectral-element mesh of fluid domain with an extra layer of cladding elements to solve for the conjugate heat transfer cases of AREVA validation tests. Note that only the fluid elements are used for the isothermal computations of TAMU tests.

Figure 2 shows a transverse cross-section of the instantaneous axial velocity near the onset of the transition from laminar to turbulent flow at $Re = 3,000$. As expected, the highest axial velocity regions occurs near the wall channels.

Figure 3 shows the instantaneous axial velocity along four cross-sections at $Re = 10,000$ that illustrates the three-dimensional aspects of the flow in this wire-wrap-induced geometry. Figure 4 shows a transverse cross-section of the time-averaged axial velocity at $Re = 10,000$. Figure 5 shows the profile of time averaged axial velocity (solid) at Re=15,000. In order to illustrative sensitivity to time-averaging interval we have also included an average over approximately the last quarter (dash) and last half (dash-dot) of the time averaging

interval. We are currently checking the mesh sensitivity for this case and the preliminary results indicate little dependence on polynomial order.

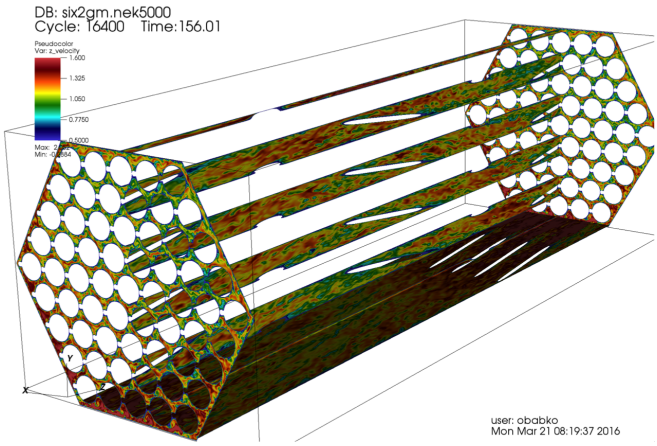


Fig. 3. Four cross-sections of instantaneous axial velocity at $Re = 10,000$.

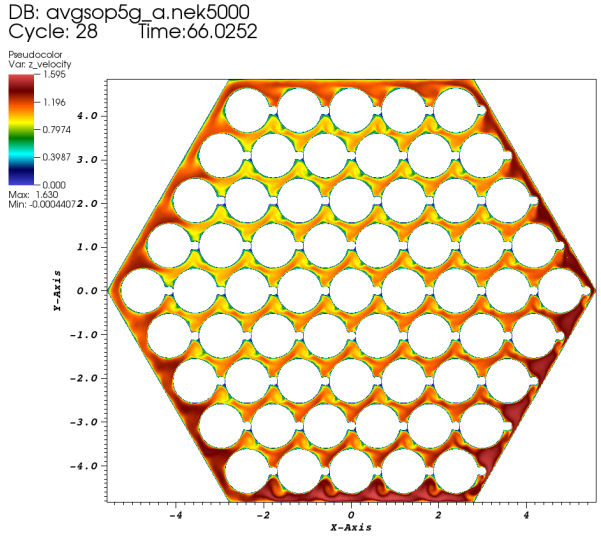


Fig. 4. Transverse cross-section of the instantaneous axial velocity at $Re = 15,000$.

CONCLUSIONS

As a part of a larger collaborative validation project with TerraPower, Texas A&M University, and AREVA, we have presented LES results for undeformed single wire-wrap 61-pin geometry. Pre-test Nek5000 isothermal simulations are carried away in the range of Reynolds numbers from $Re = 3,000$ to $15,000$ and will be soon compared to the con-current experiment data. The undeformed conjugate-heat-transfer and deformed simulations are under way.

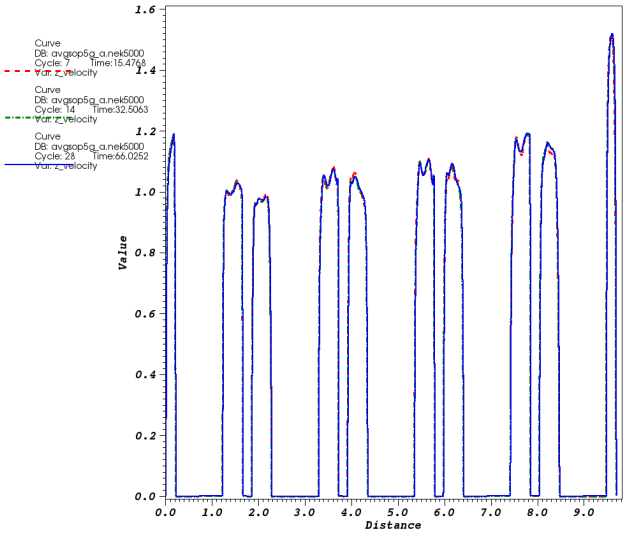


Fig. 5. Profile of the axial velocity at $Re = 15,000$ averaged over the full (dashed), last half (dash-dot) and quarter time interval (solid).

ACKNOWLEDGMENTS

We gratefully acknowledge the comments made by anonymous referees and the help of reservation crew of Argonne Leadership Computing Facility (ALCF).

This work was performed for the Department of Energy under contract DE-NE0008321. It has been also supported in part by Nuclear Energy (NE) Advanced Modeling and Simulation (NEAMS) Program of Department of Energy (DOE) and in part by the U.S. DOE Office of Science and Advanced Scientific Computing Research, under Contract DE-AC02-06CH11357. The use of resources of the ALCF, which is a DOE Office of Science User Facility supported under Contract DE-AC02-06CH1135 has been provided as a part of Argonne Leadership Computational Challenge (ALCC) allocation.

This paper was prepared as an account of work sponsored by an agency of the United States Government. Neither the United States Government nor any agency thereof, nor UChicago Argonne, LLC, nor any of their employees or officers, makes any warranty, express or implied, or assumes any legal liability or responsibility for the accuracy, completeness, or usefulness of any information, apparatus, product, or process disclosed, or represents that its use would not infringe privately owned rights. Reference herein to any specific commercial product, process, or service by trade name, trademark, manufacturer, or otherwise, does not necessarily constitute or imply its endorsement, recommendation, or favoring by the United States Government or any agency thereof. The views and opinions of document authors expressed herein do not necessarily state or reflect those of the United States Government or any agency thereof, Argonne National Laboratory, or UChicago Argonne, LLC.

REFERENCES

1. E. U. KHAN, "LMFBR In-Core Thermal-Hydraulics: The State of the Art and U.S. Research and Development Needs," Tech. Rep. PNL-3337, Battelle Pacific Northwest Laboratory (1980).
2. P. F. FISCHER, J. LOTTES, A. SIEGEL, and P. PALMIOTTI, "Large Eddy Simulation Of Wire-Wrapped Fuel Pins I: Hydrodynamics in a Periodic Array," in "Joint International Topical Meeting on Mathematics & Computation and Supercomputing in Nuclear Applications (M&C + SNA 2007)," Monterey, CA (April 2007), American Nuclear Society.
3. H. DOOLAARD, A. SHAMS, F. ROELOFS, K. V. TICHELEN, S. KEIJERS, J. D. RIDDER, J. DEGROOTE, J. VIERENDEELS, I. D. PIAZZA, E. MERZARI, A. OBABKO, and P. FISCHER, "CFD BENCHMARK FOR A HEAVY LIQUID METAL FUEL ASSEMBLY," *NURETH-16 Paper*, **22944** (2015).
4. M. DEVILLE, P. FISCHER, and E. MUND, *High-Order Methods for Incompressible Fluid Flow*, Cambridge University Press, Cambridge (2002).


AREVA

Toward a Longer-Life Core

Experimental Data Sets for CFD Calculations of Flow and Heat Transfer in Deformed Fuel Assemblies

Brian Mays, AREVA
Brian Jackson, TerraPower
Tom Reeves, TerraPower
Nate Salpeter, AER Consulting

ANS Winter Meeting – November 8, 2016

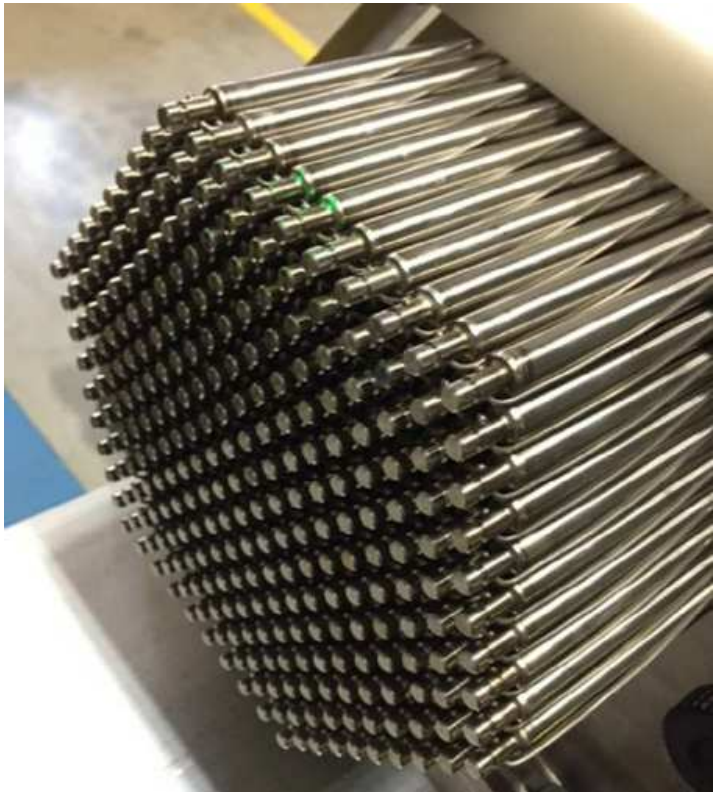
AREVA

Background

Geometry

Liquid-metal-cooled fast-breeder reactor (LMFBR) fuel assemblies

- **Hexagonally packed geometry**

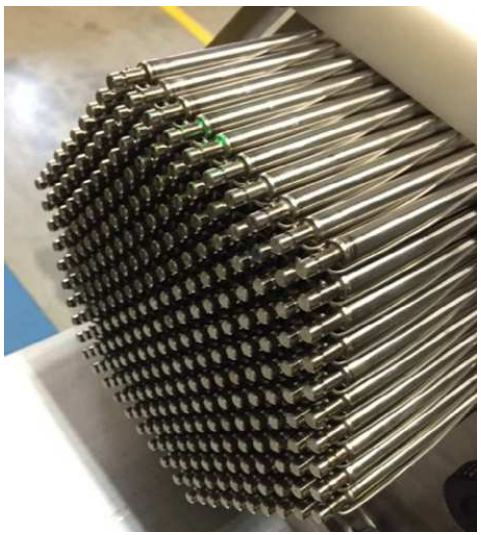


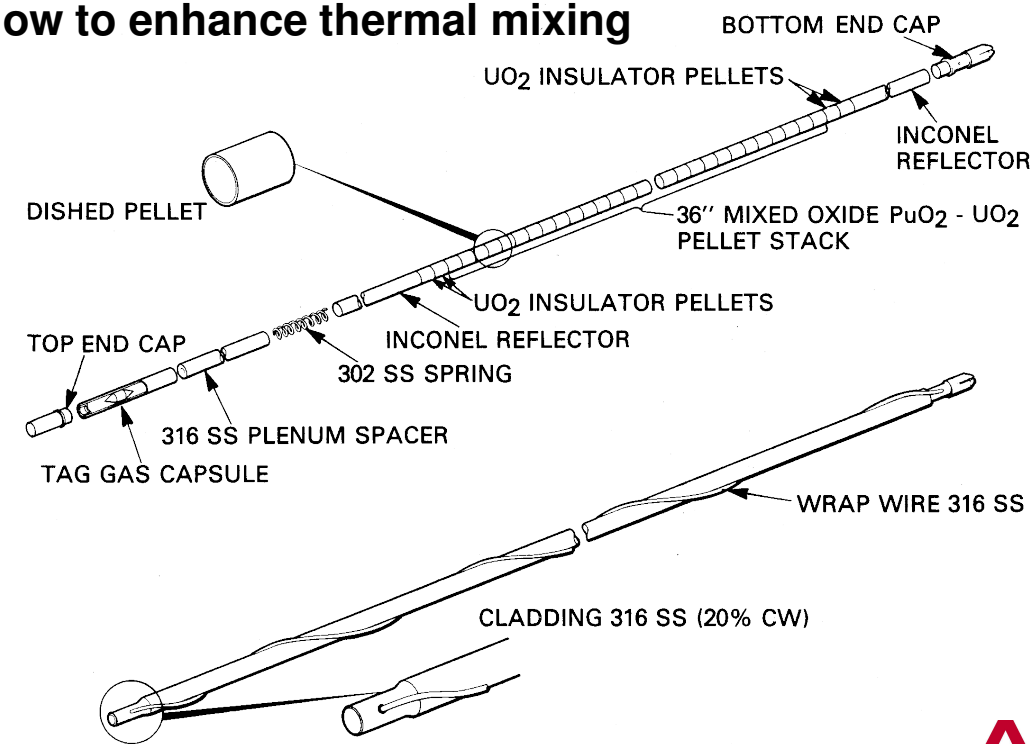
Background

Geometry

Liquid-metal-cooled fast-breeder reactor (LMFBR) fuel assemblies

- **Hexagonally packed geometry**
- **Helically wire-wrapped pins**
  - **Provides spacing between pins (eliminates spacers)**
  - **Imparts rotation on the flow to enhance thermal mixing**



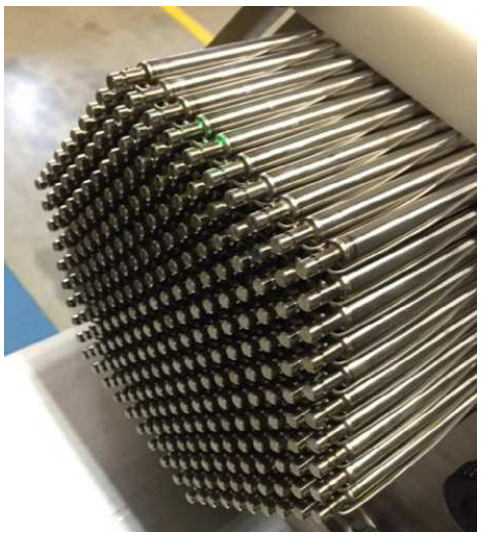


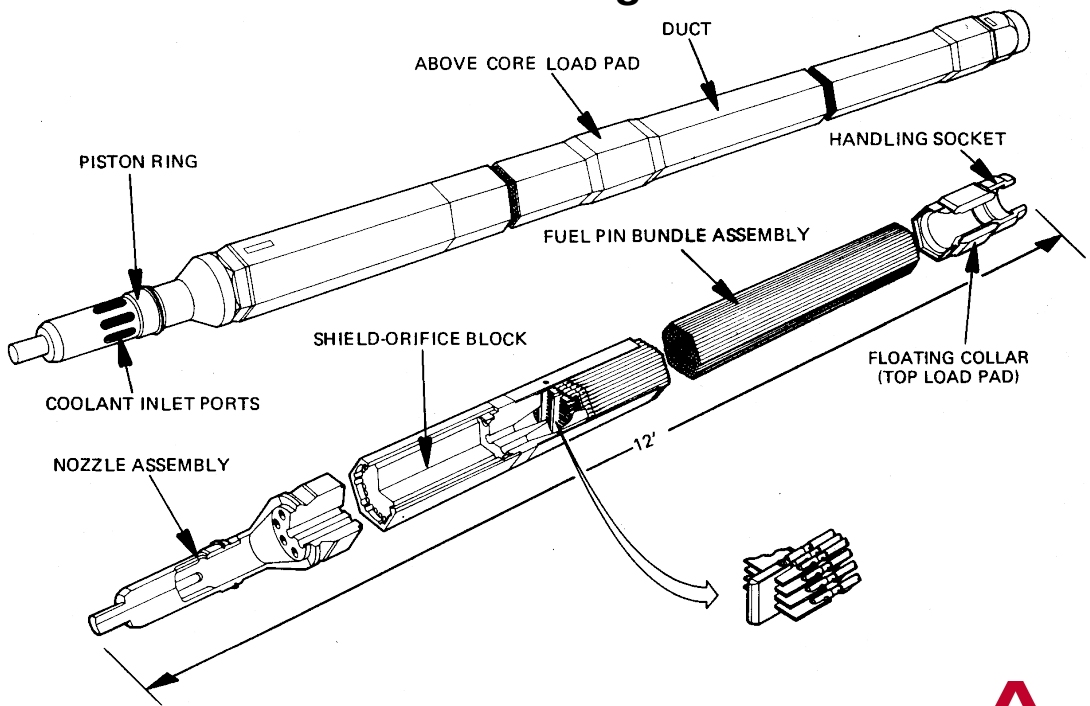
Background

Geometry

Liquid-metal-cooled fast-breeder reactor (LMFBR) fuel assemblies

- **Hexagonally packed geometry**
- **Helically wire-wrapped pins**
  - **Provides spacing between pins (eliminates spacers)**
  - **Imparts rotation on the flow to enhance thermal mixing**
- **Hexagonal duct**





Background

Deformation

- **Experience has demonstrated that changes in the geometry occur in the assemblies during operation from**
  - **Pressure gradients**
  - **Thermal creep**
  - **Irradiation effects**
- **Over time the fuel pins and the surrounding ducts swell and deform**

Background

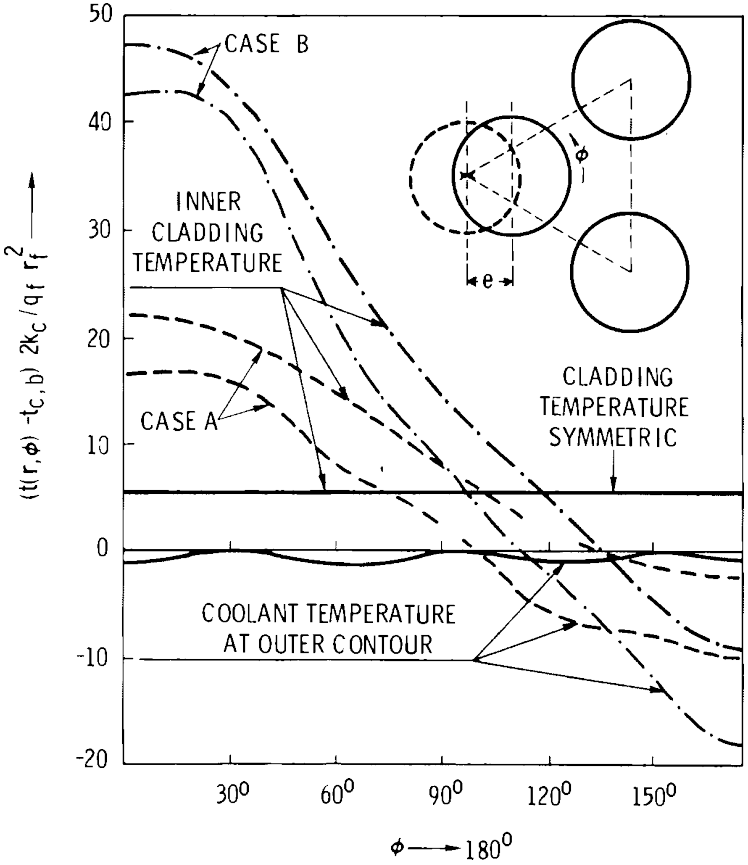
Deformation

- Experience has demonstrated that changes in the geometry occur in the assemblies during operation from
  - Pressure gradients
  - Thermal creep
  - Irradiation effects
- Over time the fuel pins and the surrounding ducts swell and deform
- Local thermal and flow characteristics affect fuel performance
  - EBR-II and FFTF experienced local overheating due to pin-to-duct or pin-to-pin contact, which limited assembly lifetimes
  - Deformations of the assembly geometry affect the flow resistance, changing the flow distribution and pressure drop across the core
  - Flow through the core determines the thermal mixing and the potential for thermal striping on downstream components

Background

Analysis

- **Studies of the effects of assembly deformation considered only dislocated bare pins without the wire wrap**

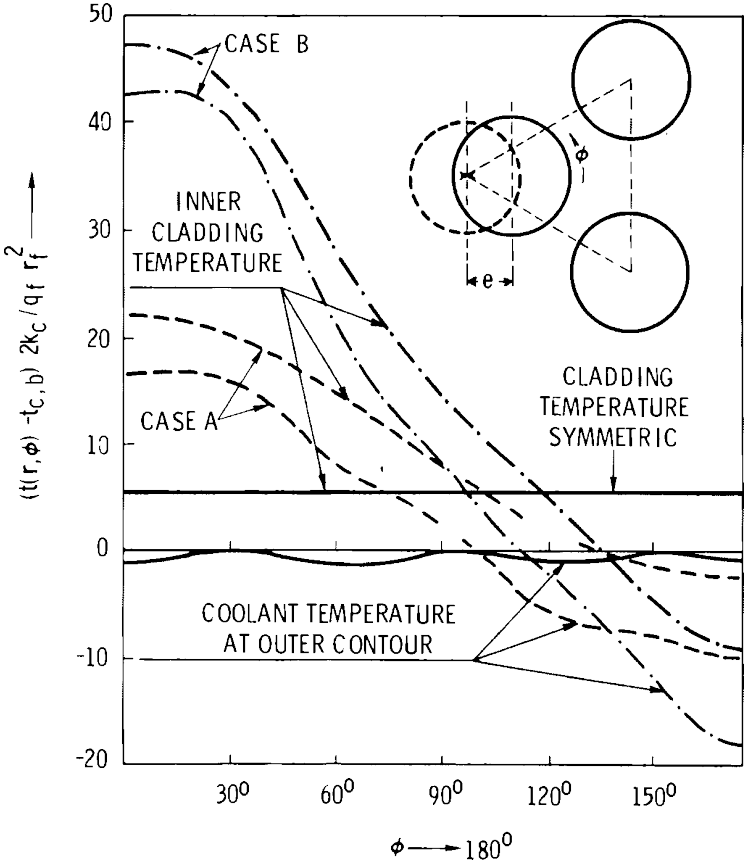


Johannsen and Wolf, *Nucl. Eng. Des.* 15:29 (1971).

Background

Analysis

- **Studies of the effects of assembly deformation considered only dislocated bare pins without the wire wrap**
- **Computational Fluid Dynamics (CFD) is uniquely suited to capture these effects**
  - **System and sub-channel codes do not provide sufficient thermal and flow field resolution to quantify these effects**
  - **CFD models and methodologies need to be validated**



Johannsen and Wolf, *Nucl. Eng. Des.* 15:29 (1971).

Validation Data

- **Existing data from experiments have limitations**
  - **Legacy experiments were not conducted for CFD validation**
  - **Often use only bulk measurements, such as pressure drop**
  - **Poor resolution**
  - **Incomplete reporting of test geometry and operating conditions**
  - **Inconsistent or incomplete description of measurement locations**
- **Previous experiments focused only on nominal geometries**

Validation Data

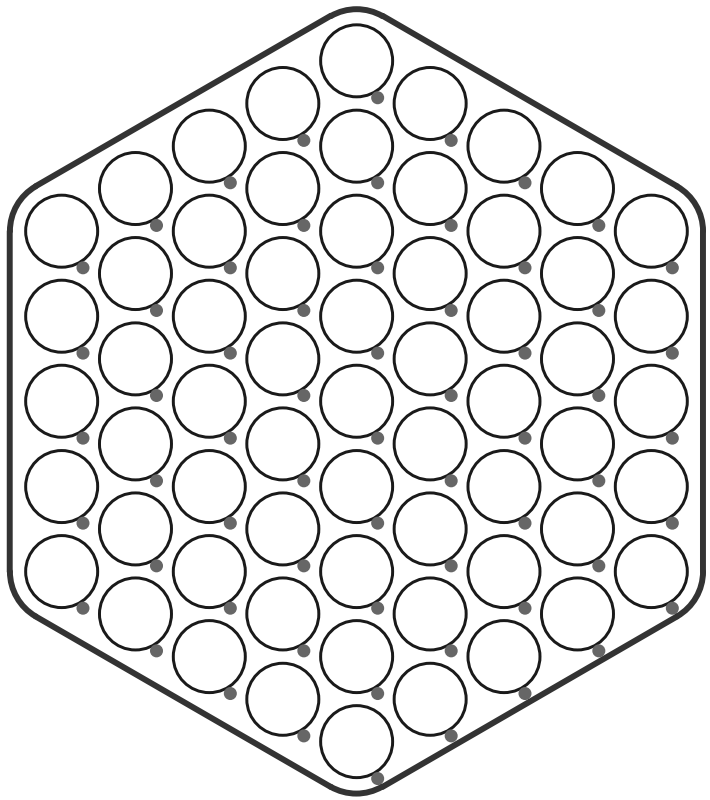
- **Existing data from experiments have limitations**
  - **Legacy experiments were not conducted for CFD validation**
  - **Often use only bulk measurements, such as pressure drop**
  - **Poor resolution**
  - **Incomplete reporting of test geometry and operating conditions**
  - **Inconsistent or incomplete description of measurement locations**
- **Previous experiments focused only on nominal geometries**
- **CFD validation-grade data**
  - **High-resolution velocity and temperature measurements**
  - **Accurate descriptions of the geometry and test conditions**
    - Full description of geometries
    - Details of pumps, flowmeters, pressure transducers, etc.
    - Calibration documentation
  - **Sufficient control and monitoring to get realistic boundary conditions**
    - Mass flow rates, pressure, velocity, and temperature measurements
  - **Uncertainty quantification of all datasets**

Objective

- **This project will fill this gap by producing detailed experimental data sets for wire-wrapped fuel assemblies**

Objective

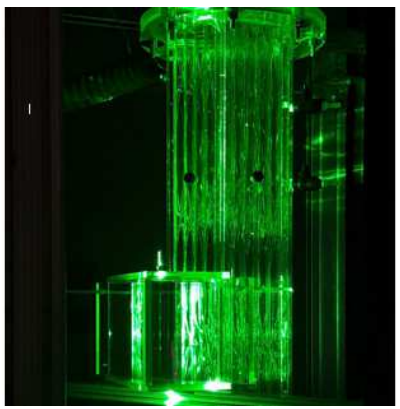
- **This project will fill this gap by producing detailed experimental data sets for wire-wrapped fuel assemblies**
- **Geometry: 61-pin bundle**
  - **Minimizes wall effects**
  - **Limits computational requirements**



Objective

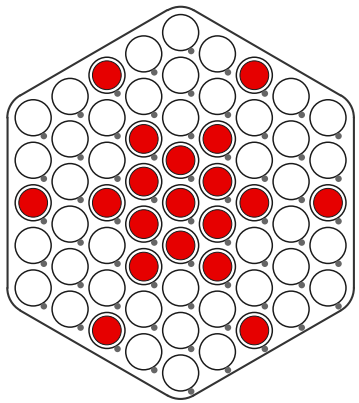
- **This project will fill this gap by producing detailed experimental data sets for wire-wrapped fuel assemblies**
- **Geometry: 61-pin bundle**
  - **Minimizes wall effects**
  - **Limits computational requirements**
- **Two kinds of tests:**

Isothermal



High-fidelity, full-field flow measurements

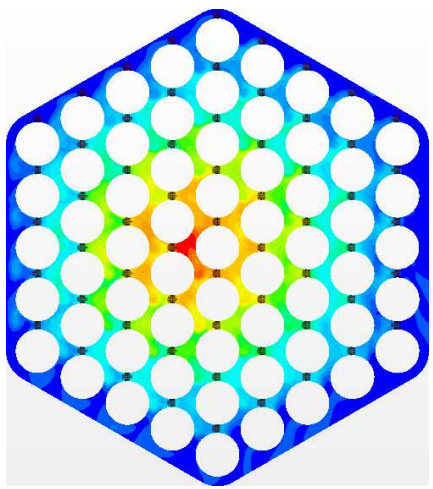
Heated



Temperature and pressure measurements

Objective

- This project will fill this gap by producing detailed experimental data sets for wire-wrapped fuel assemblies
- Geometry: 61-pin bundle
  - Minimizes wall effects
  - Limits computational requirements
- Two kinds of tests:
  - Isothermal – High-fidelity, full-field flow measurements
  - Heated – Temperature and pressure measurements
- Numerical benchmark calculations



Objective

- This project will fill this gap by producing detailed experimental data sets for wire-wrapped fuel assemblies
- Geometry: 61-pin bundle
  - Minimizes wall effects
  - Limits computational requirements
- Two kinds of tests:
  - Isothermal – High-fidelity, full-field flow measurements
  - Heated – Temperature and pressure measurements
- Numerical benchmark calculations
- This is a comprehensive validation study to
  - Improve understanding of uncertainties
  - Increase the reliability of predictive methods for modeling flow and thermal performance in LMFBR assemblies

The Team


TEXAS A&M
UNIVERSITY


TerraPower


AREVA


Argonne
NATIONAL LABORATORY

The Team

Testing

TEXAS A&M UNIVERSITY

AREVA

Simulation

TerraPower™

Argonne NATIONAL LABORATORY

The Team

	Testing	Simulation
Isothermal Flow	TEXAS A&M UNIVERSITY	TerraPower
Heated Bundle	AREVA	Argonne NATIONAL LABORATORY

The Team

	Testing	Simulation
Isothermal Flow	TEXAS A&M UNIVERSITY	TerraPower — Industry Standard (RANS)
Heated Bundle	AREVA	Argonne NATIONAL LABORATORY — High Performance (LES)

The Tests

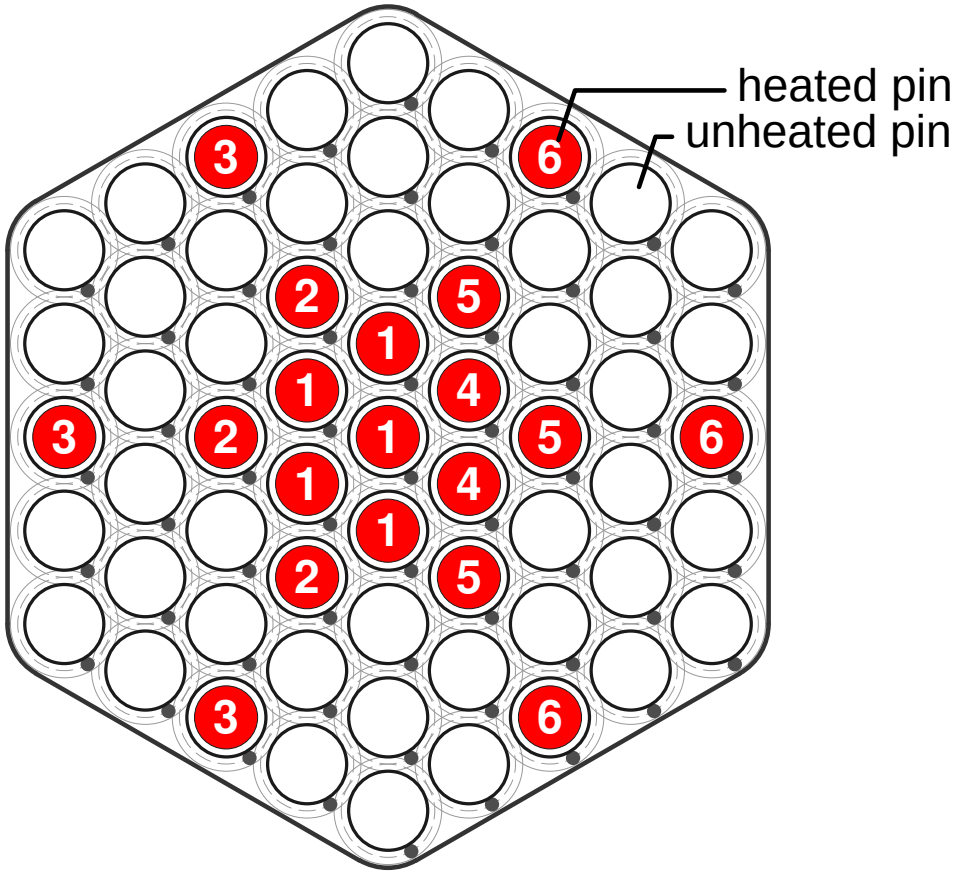
Parameter	Isothermal Experiments	Heated Experiments
Pin material	Acrylic	Metal
Working fluid	*p*-Cymene	Water
Pin OD (mm)	15.88	9.5
Wire OD (mm)	3.0	1.73
Pitch-to-diameter ratio (P/D)	1.189	1.182
Bundle length (wire pitches)	3.5	14.8

The Tests

Parameter	Isothermal Experiments		Heated Experiments
Pin material	Acrylic		Metal
Working fluid	*p*-Cymene		Water
Pin OD (mm)	15.88		9.5
Wire OD (mm)	3.0		1.73
Pitch-to-diameter ratio (P/D)	1.189	$\Longleftrightarrow$	1.182
Bundle length (wire pitches)	3.5		14.8

Heated Bundle Tests

Bundle

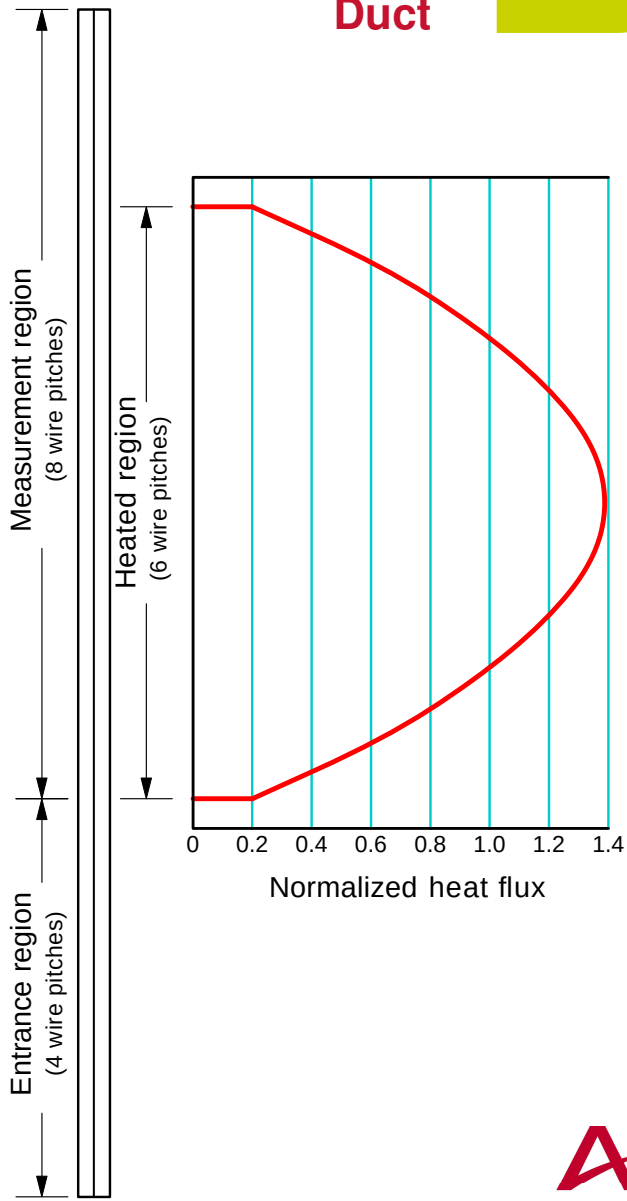


- **Geometry**
  - **19 heated rods**
    - Arranged in 6 banks
    - 30 kW per rod
    - 570 kW total input power
  - **42 non-heated tubes**
- **Test conditions**
  - **Inlet temperature: 90 °F**
  - **System pressure: 150 psia**

Heated Bundle Tests

Duct

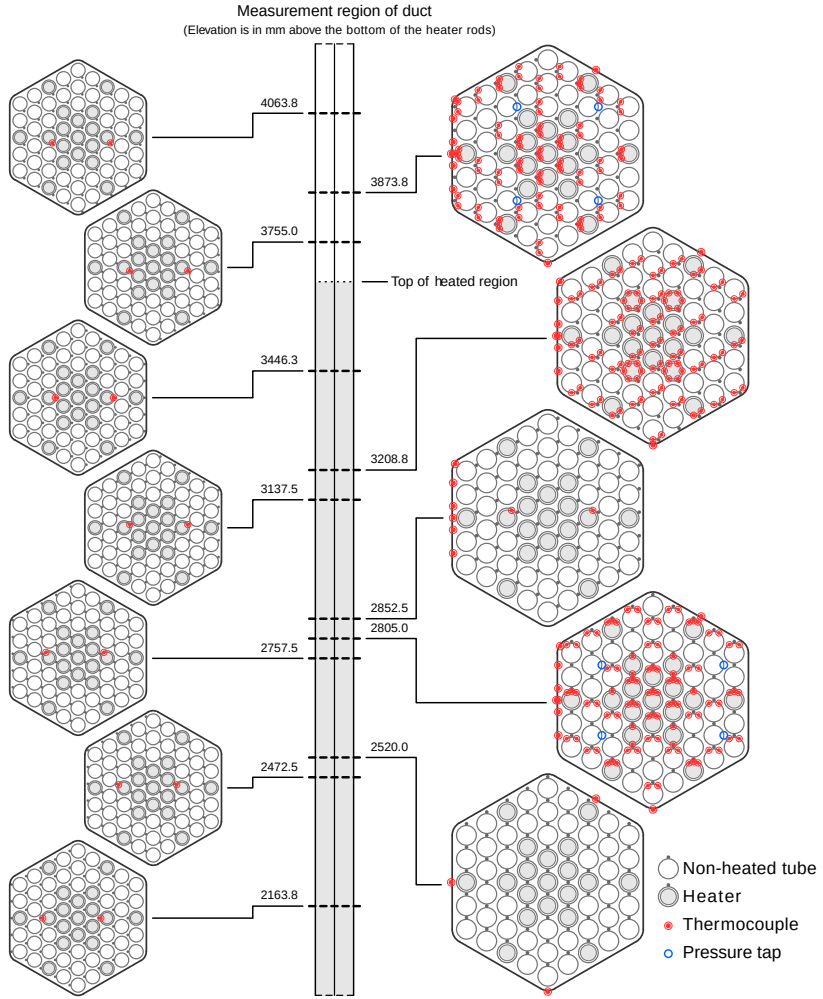
- 4.3 m duct length (14.8 wire pitches)
- Entrance region – 4 wire wraps
- Measurement region – 8 wire wraps
  - Includes a heated region – 6 wire wraps
  - Cosine-shaped axial heat flux
- Exit region at top (not shown)



Heated Bundle Tests

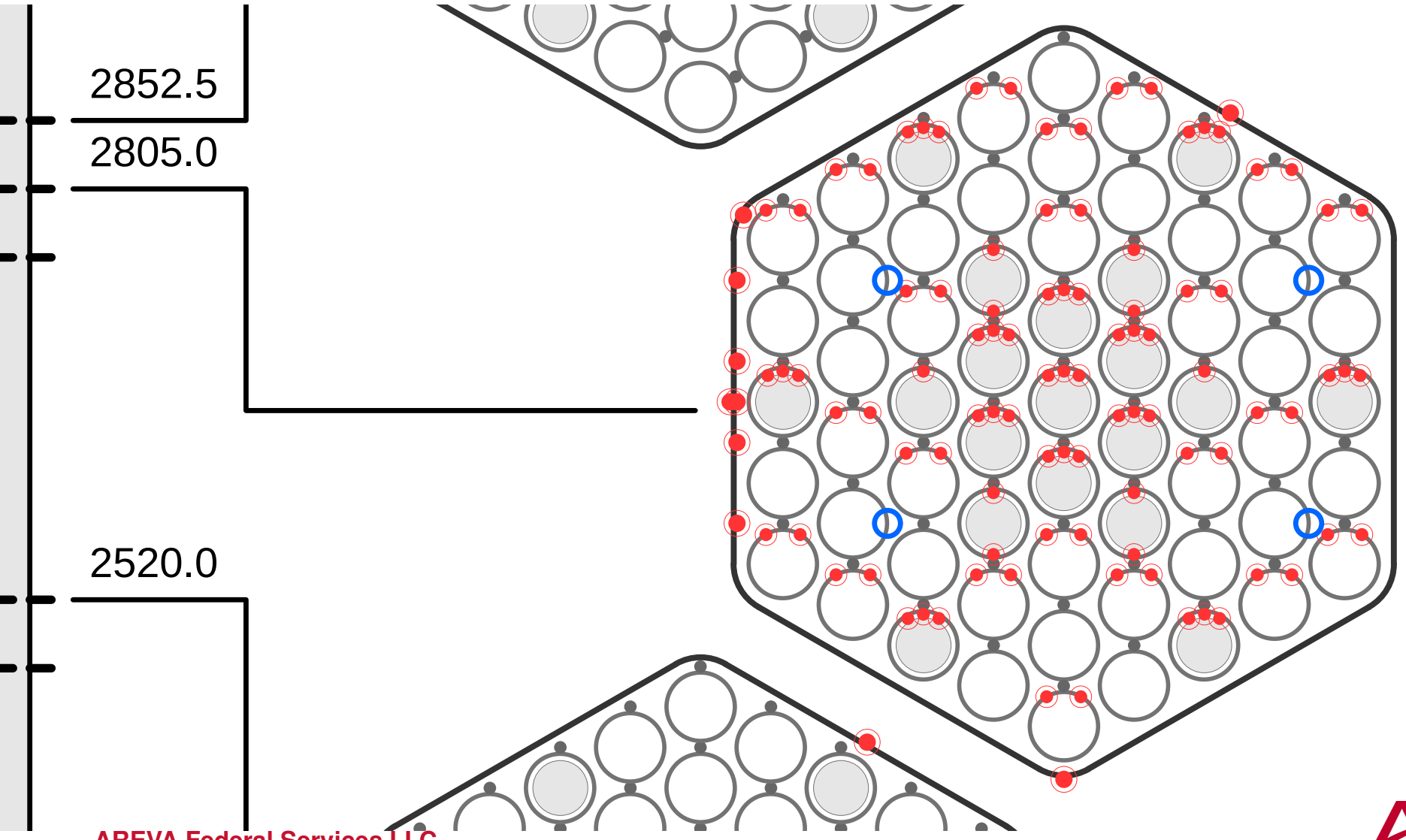
Measurements

- Over 350 thermocouples
  - 2 heaters have 9 thermocouples along their length
  - 4 heaters have 6 thermocouples along their circumference (8 total)
  - Remaining heaters have 8 thermocouples at 3 elevations
  - 22 of the 42 non-heated tubes have 6 thermocouples each
  - 24 thermocouples on the duct
- 38 pressure taps
  - 30 duct wall taps capture axial and azimuthal pressure
  - 8 taps in non-heated tubes
- Locations selected from preliminary CFD calculations



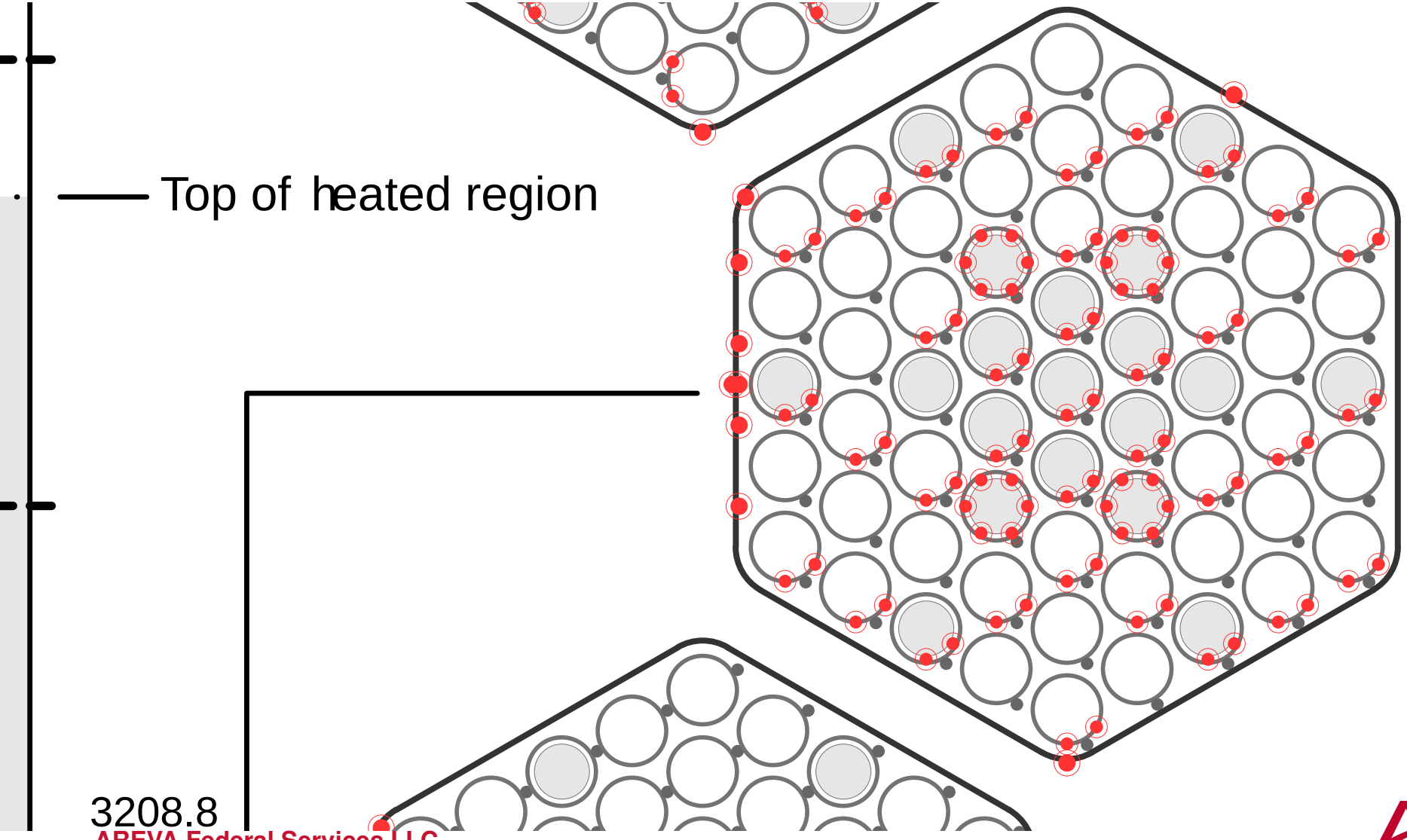
Heated Bundle Tests

Measurements – Middle of Heated Region



Heated Bundle Tests

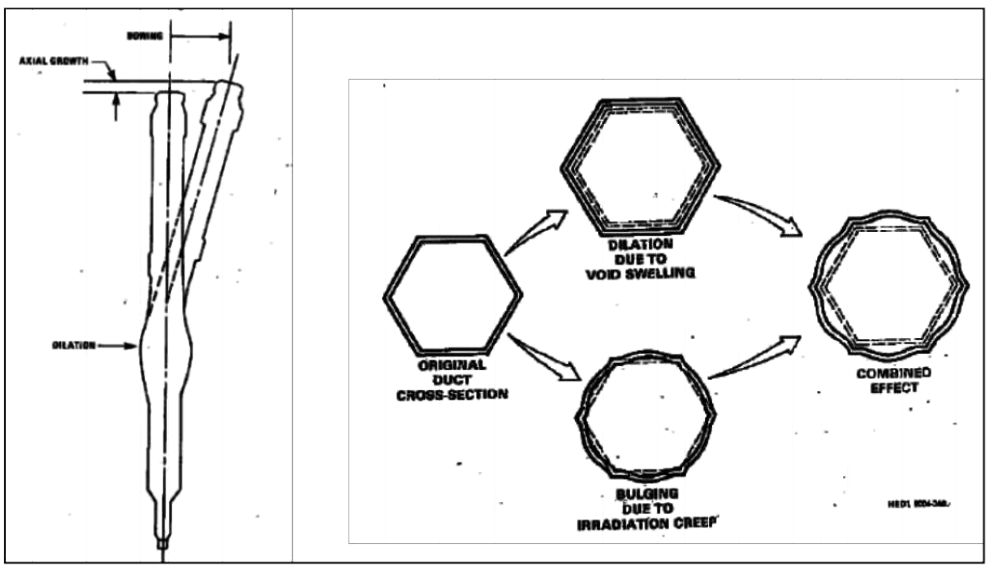
Measurements – Upper Heated Region

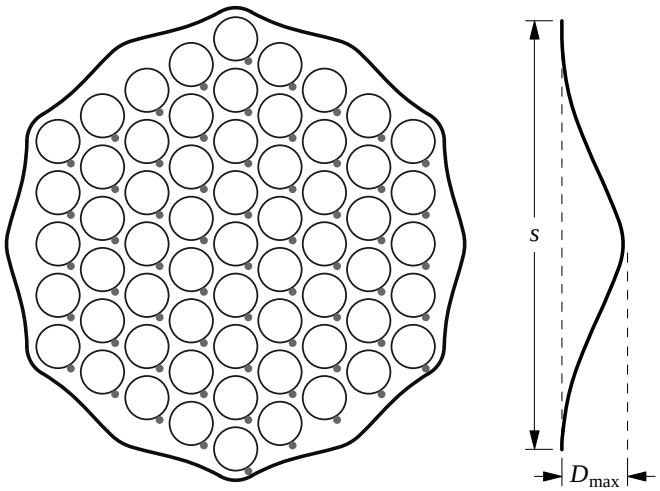


Heated Bundle Tests

Deformed Geometry

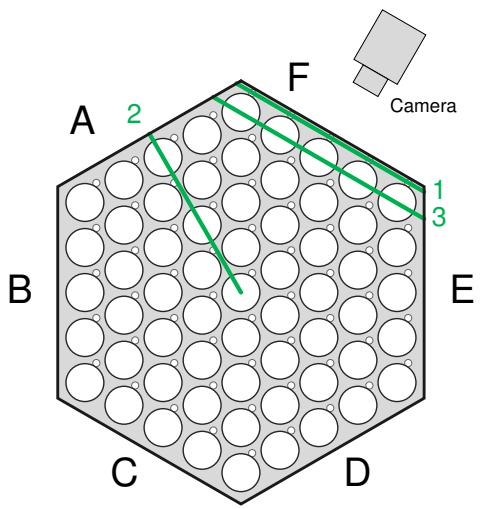
- **Two test geometries**
  - **Non-deformed duct: Represents a bundle at beginning of life**
  - **Deformed duct: Inner face dilation represents a bundle at later in life**

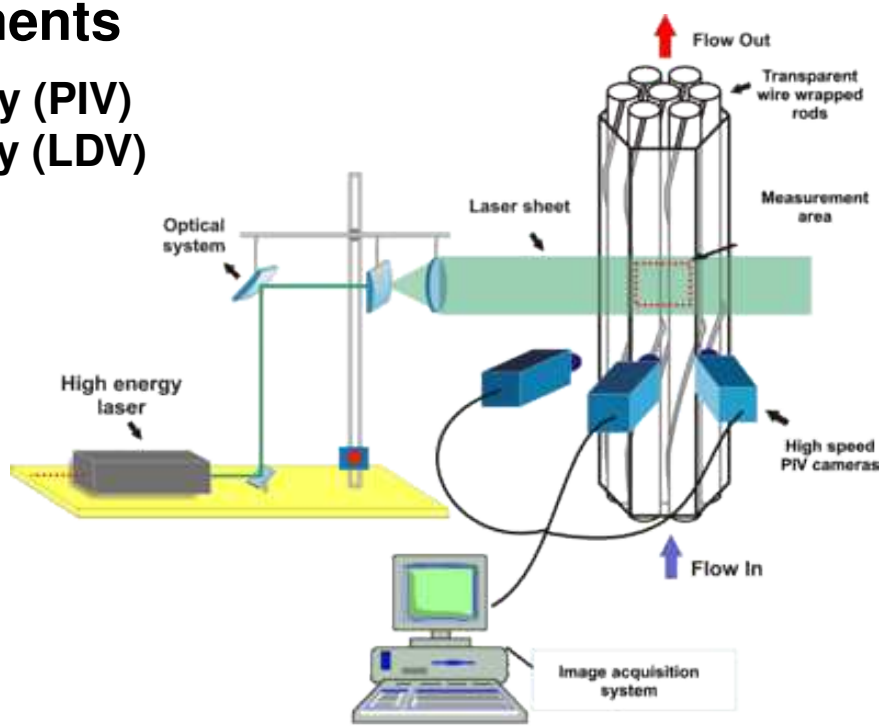




Flow Visualization Test

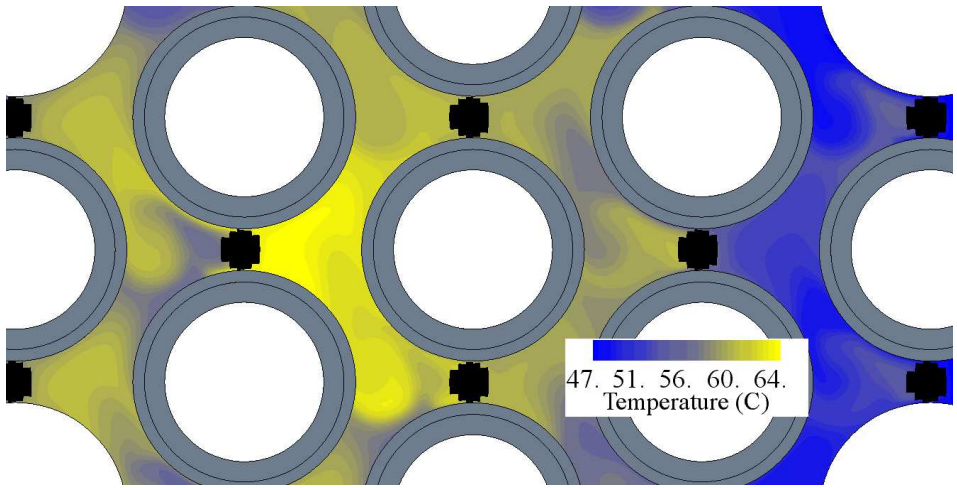
- **15 pressure taps along duct walls and in inlet/outlet plenums**
  - **9 axial locations to capture pressure drop**
  - **At 2 axial locations, 4 taps along adjacent sides capture pressure differences in the azimuthal direction**
- **Local velocity measurements**
  - **Particle Image Velocimetry (PIV)**
  - **Laser Doppler Velocimetry (LDV)**





Numerical Simulations

- **Numerical simulations are performed as part of the project**
  - **Scoping calculations to design the tests**
  - **Pre-test blind benchmark calculations using test specifications**
  - **Post-test calculations using as-built geometries and actual test conditions**
- **Two types of CFD calculations**
  - **Industry-standard CFD code using the RANS approach**
  - **Nek5000 CFD code using the LES approach**



Conclusions

- **This project is providing valuable insight in the many complex flow phenomena that affect the thermal performance of LMFBR wire-wrapped fuel assemblies through**
  - **High-fidelity data from experiments**
  - **Modern CFD simulations performed in concert**
- **This will lead to a better understanding of the shortcomings, limitations, and uncertainties associated with current CFD modeling practices**
- **The final set of experimental data and numerical simulation results will be made available as an open-source data set that can be used to improve, validate, and benchmark CFD codes and modeling methods**

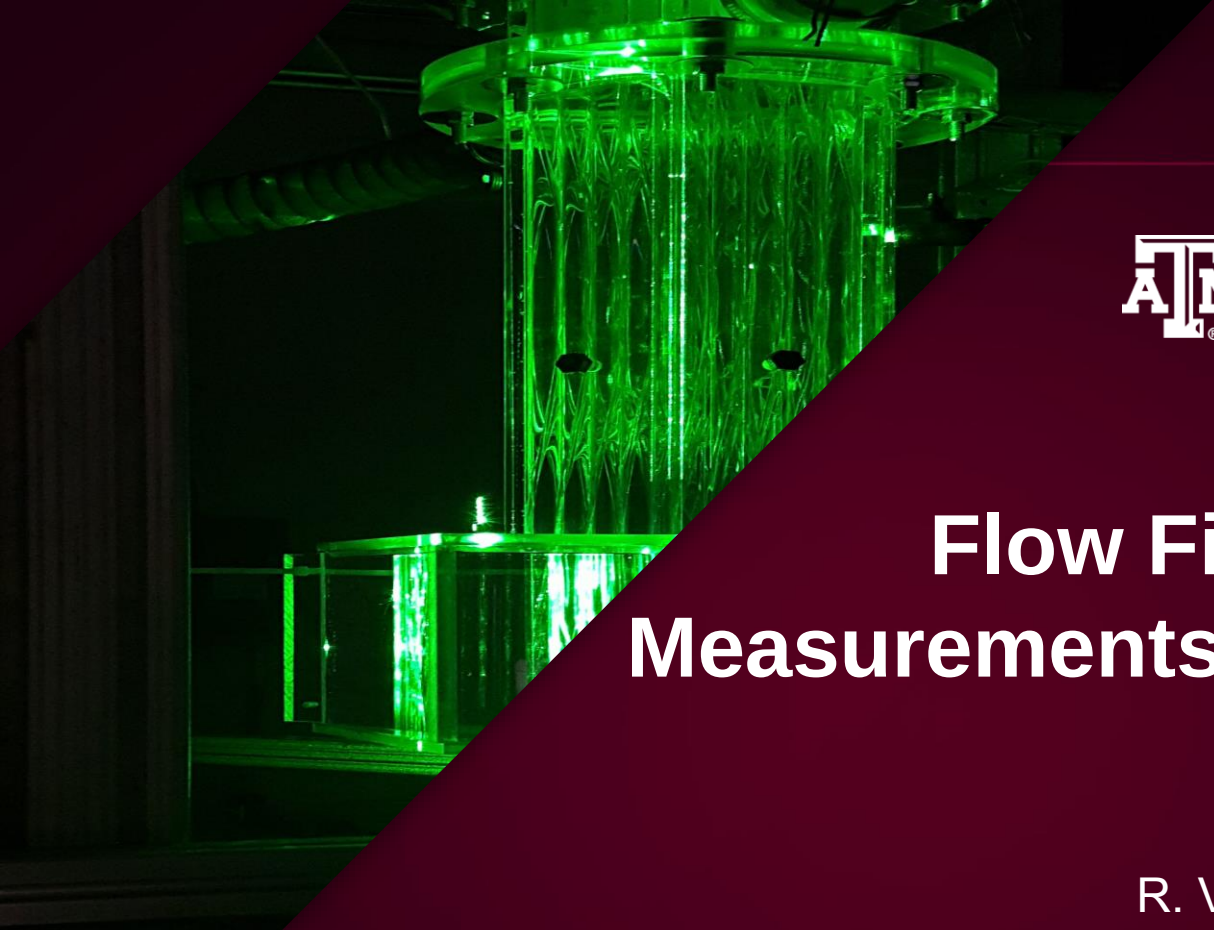
Acknowledgments

This material is based upon work supported by the Department of Energy under Award Number DE-NE0008321.

Disclaimer: "This report was prepared as an account of work sponsored by an agency of the United States Government. Neither the United States Government nor any agency thereof, nor any of their employees, makes any warranty, express or implied, or assumes any legal liability or responsibility for the accuracy, completeness, or usefulness of any information, apparatus, product, or process disclosed, or represents that its use would not infringe privately owned rights. Reference herein to any specific commercial product, process, or service by trade name, trademark, manufacturer, or otherwise does not necessarily constitute or imply its endorsement, recommendation, or favoring by the United States Government or any agency thereof. The views and opinions of authors expressed herein do not necessarily state or reflect those of the United States Government or any agency thereof."

Questions?


AREVA



NUCLEAR ENGINEERING
TEXAS A&M UNIVERSITY

Flow Field and Pressure Measurements in a 61-Pin Wire-Wrapped Bundle

R. Vaghetto
M. Childs
N. Goth
S. Lee
P. Jones
D. T. Nguyen
Y. Hassan

2016 ANS Winter Meeting
Las Vegas, NV, November 6-10, 2016

Participants

AREVA

TerraPower

DEPARTMENT OF ENERGY · UNITED STATES OF AMERICA ·

THE TEXAS A&M UNIVERSITY SYSTEM 1876

Argonne NATIONAL LABORATORY

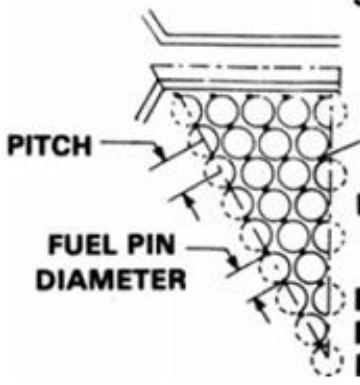
Overview

- Introduction
- Project Objectives
- Facility Overview
- Experimental Capabilities:
  - Velocity measurements
  - Pressure measurements
- Conclusions

Sodium Fast Reactor

- Triangular Lattice
- Helically wrapped wire spacer
- Tightly packed

Typical Parameters	
Thermal Output (MW_{th})	40 - 4000
Coolant Type	Liquid Na
Core Outlet (ºC)	550
Avg. Linear Power (kW/m)	25
Avg. Power Density (kW/l)	1050
Pin Diameter (mm)	6.5
Number pins/bundle	91 - 271



SUBASSEMBLY PIN ROW	PINS PER ROW	TOTAL PINS
1	1	1
2	6	7
3	12	19
4	18	37
5	24	61
6	30	91
7	36	127
8	42	169
9	48	217
10	54	271

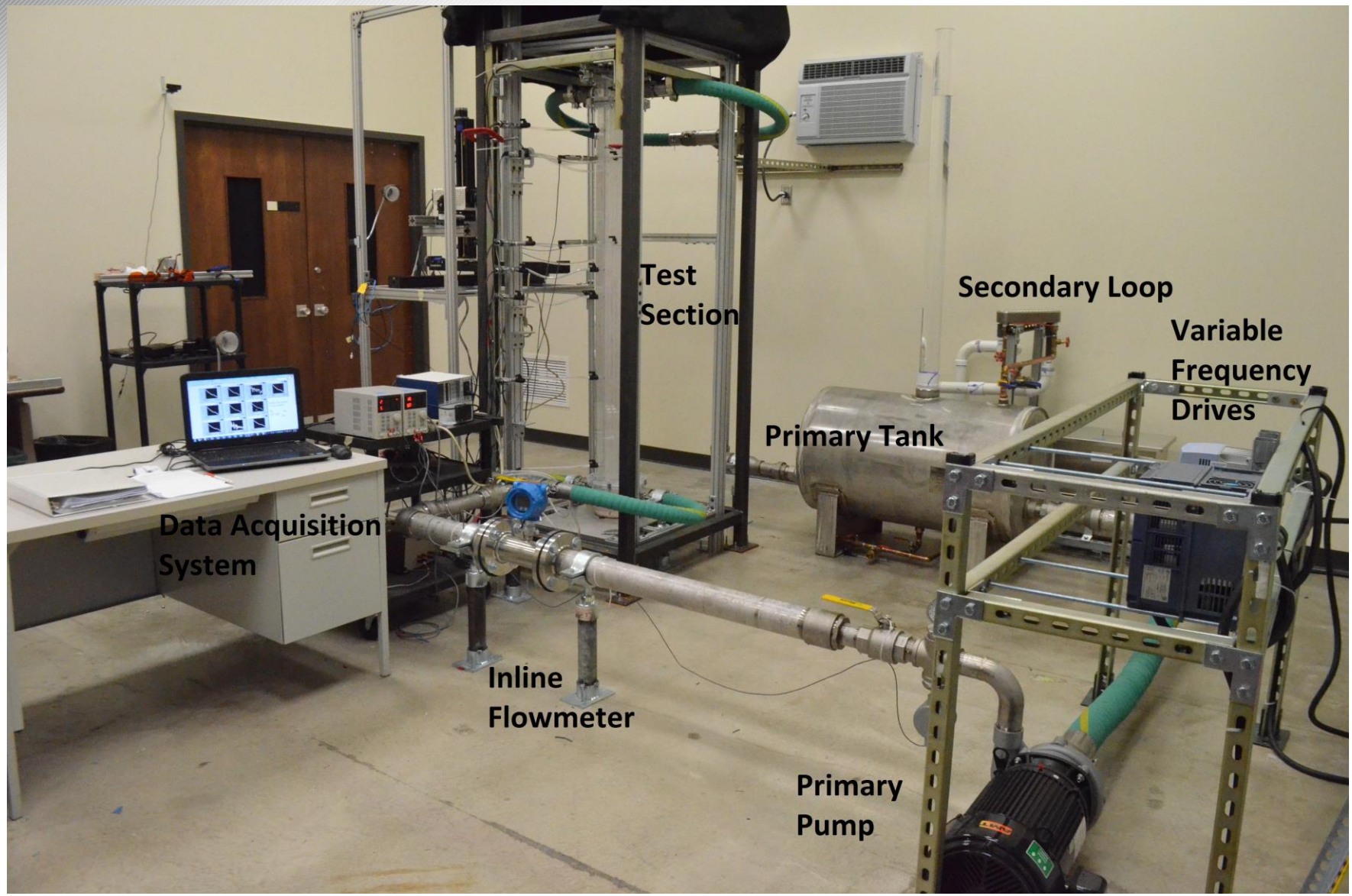
Data Needs

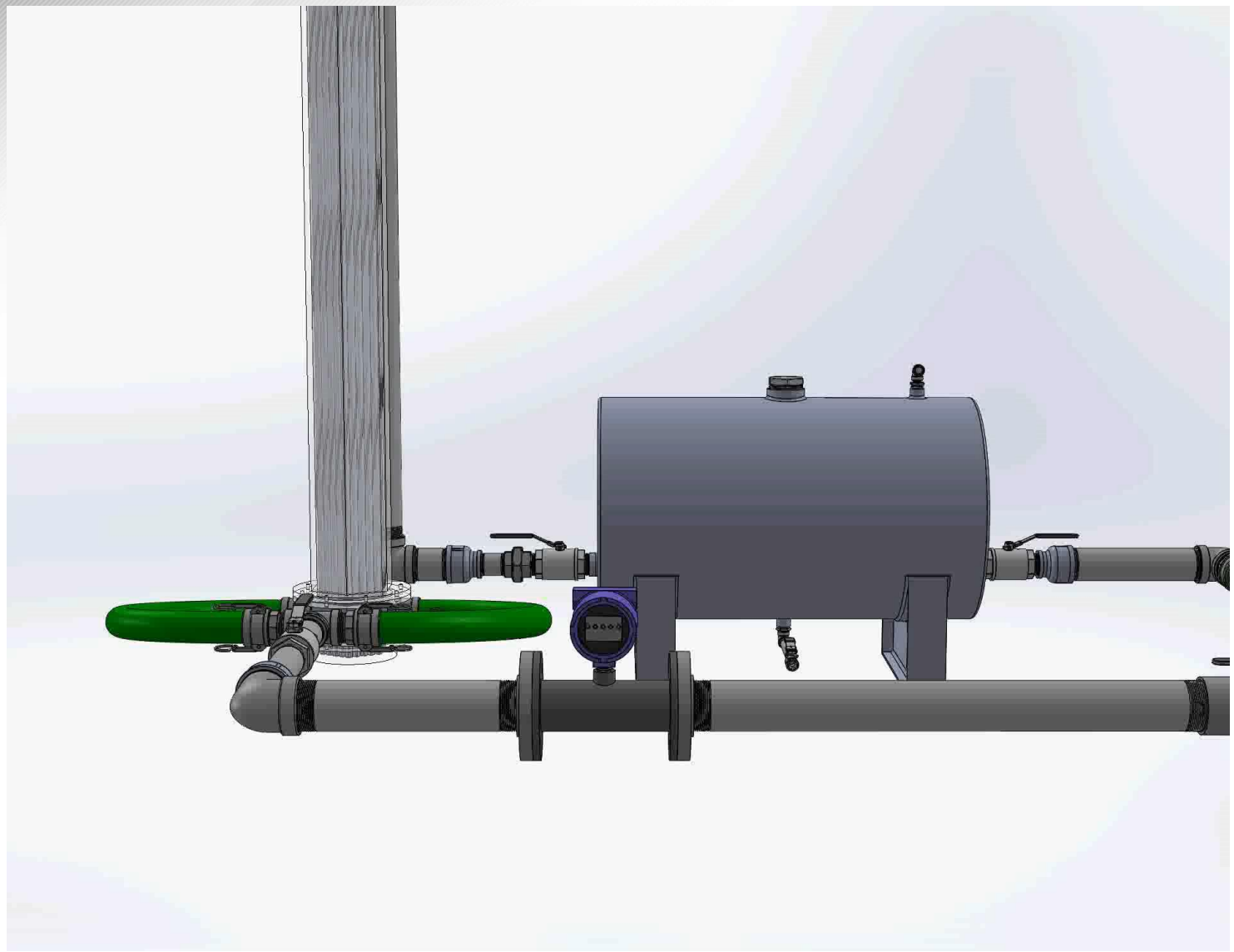
- Recent US upsurge in SFR research
- DOE and Industry interested in performing RANS and LES-based simulations
- Historical data sets may not ideal for validation
  - Lack of:
    - High Spatial resolution data
    - High Temporal resolution data
    - Non-intrusive interior subchannel measurement technique
    - Sufficiently “large” bundle

Project Objectives

- Design and Construct a 61-pin Wire Wrapped Bundle to perform isothermal Matched Index of Refraction (MIR) Flow Tests
- Produce High Spatial and Temporal Resolution Measurements of the Velocity Field at Locations of Interest
- Complement the Data with Axial and Azimuthal Pressure Measurements
- Provide Experimental Data for Validation of Industry-standard RANS-based CFD Codes and Highly Resolved LES approaches.

Facility Overview



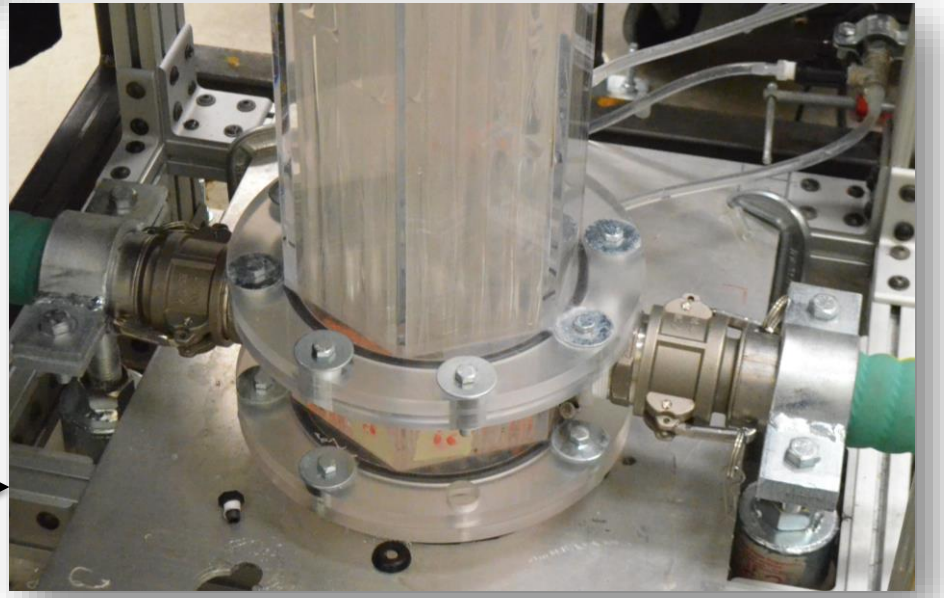


Facility Overview



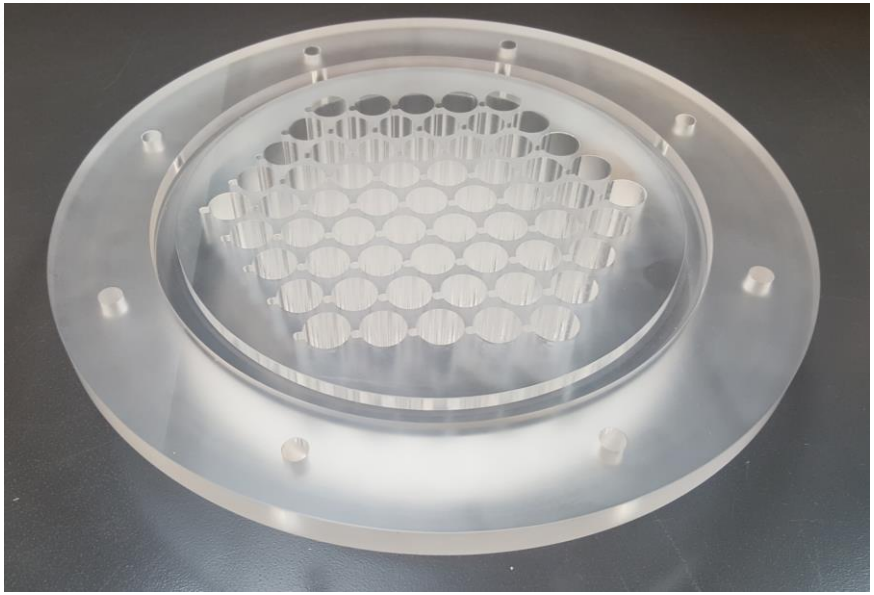
Upper Plenum
- Attachment
- Radial Flow Exit

Lower Plenum
- Attachment
- Radial Flow Inlet



Facility Overview





- Mechanical, Chemical, and Optical Pre-Tests
- In-house Fabrication
- QA Inspection

Facility Overview

Main Features

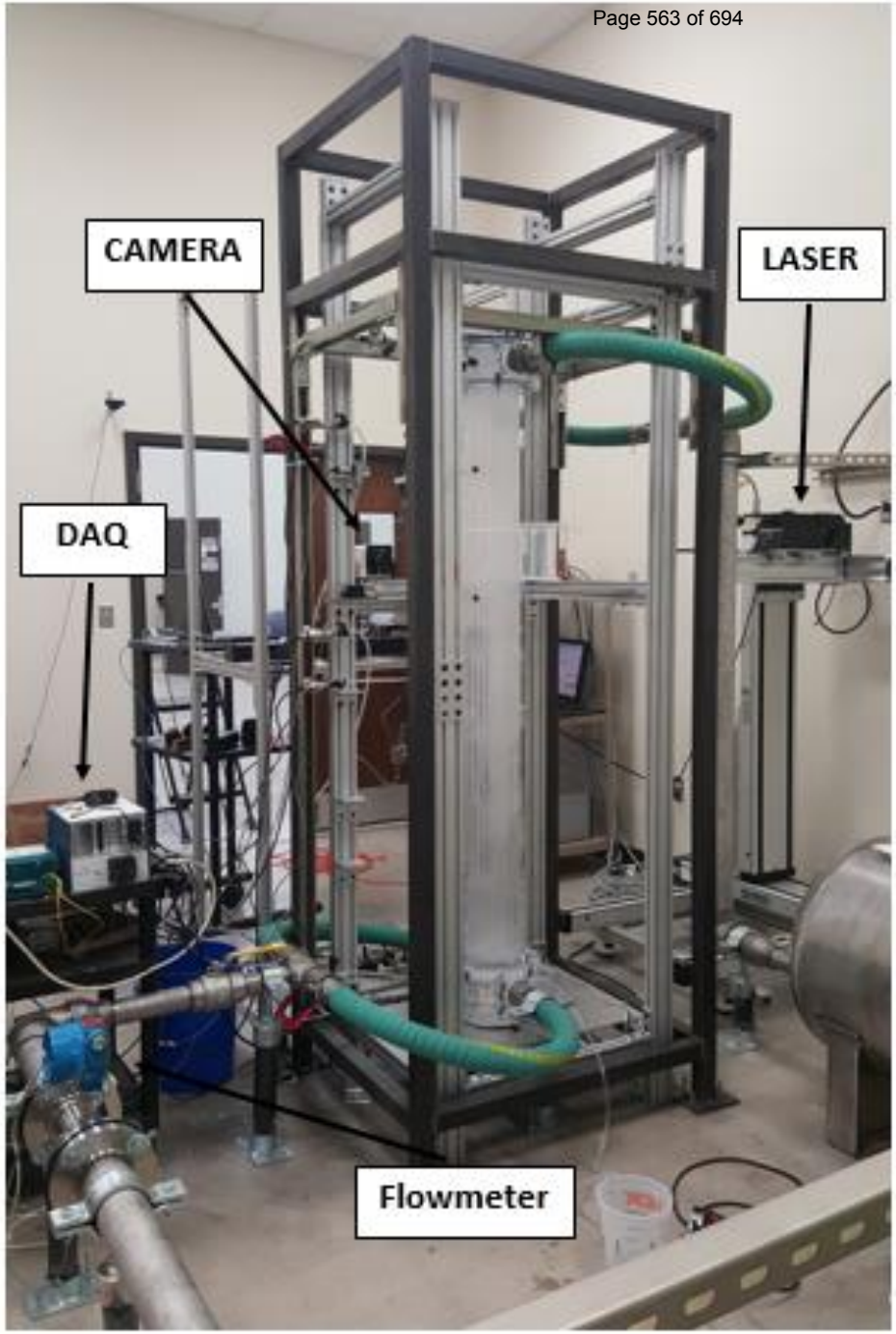
- 61 helically wrapped acrylic pins
- Hexagonal acrylic test section
- Laminar, transition, and turbulent regimes

Instrumentation

- 9 axial pressure transducers
- 6 Azimuthal DP locations
- Additional DP measurements
- Flow rate control
- Temperature control

Measurement Techniques

- Particle Image Velocimetry (PIV)
- Stereoscopic PIV
- Laser Doppler Velocimetry(LDV)



Capabilities: Velocity Measurements

MIR Technique

Fuel Pins: Acrylic

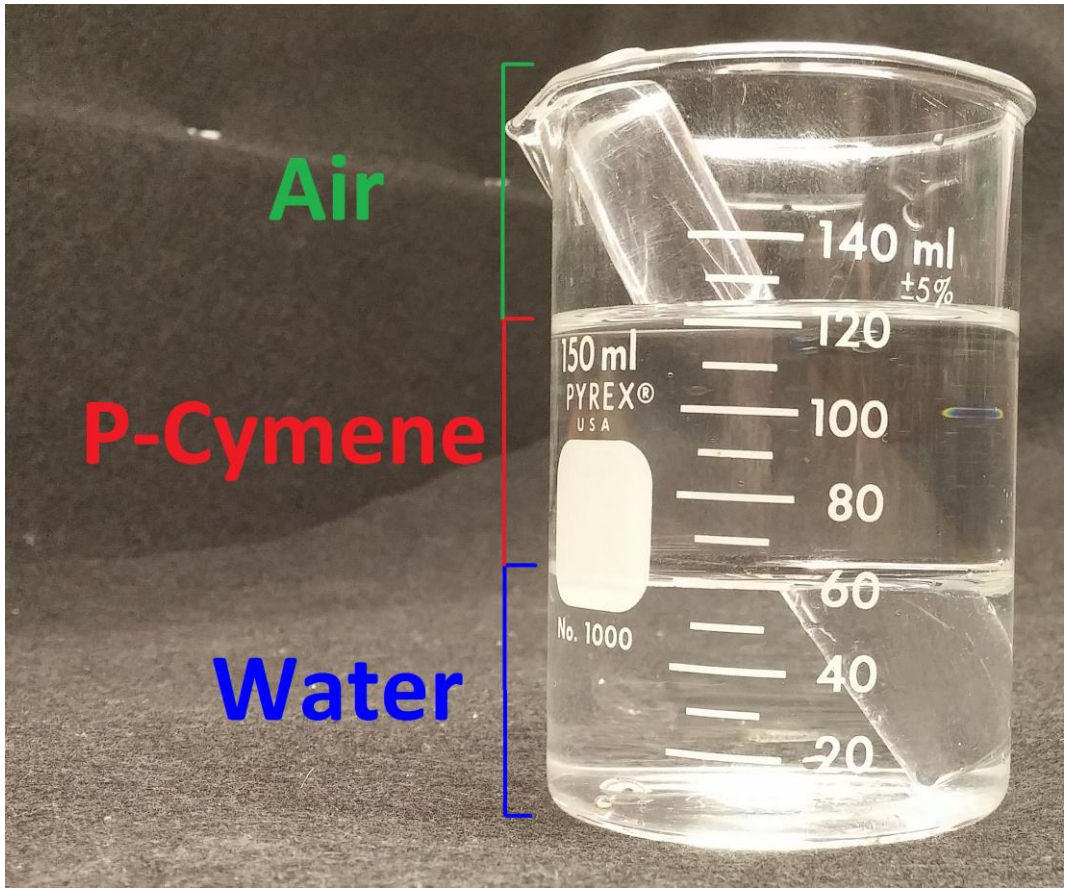
Enclosure: Acrylic

Working Fluid: p-cymene

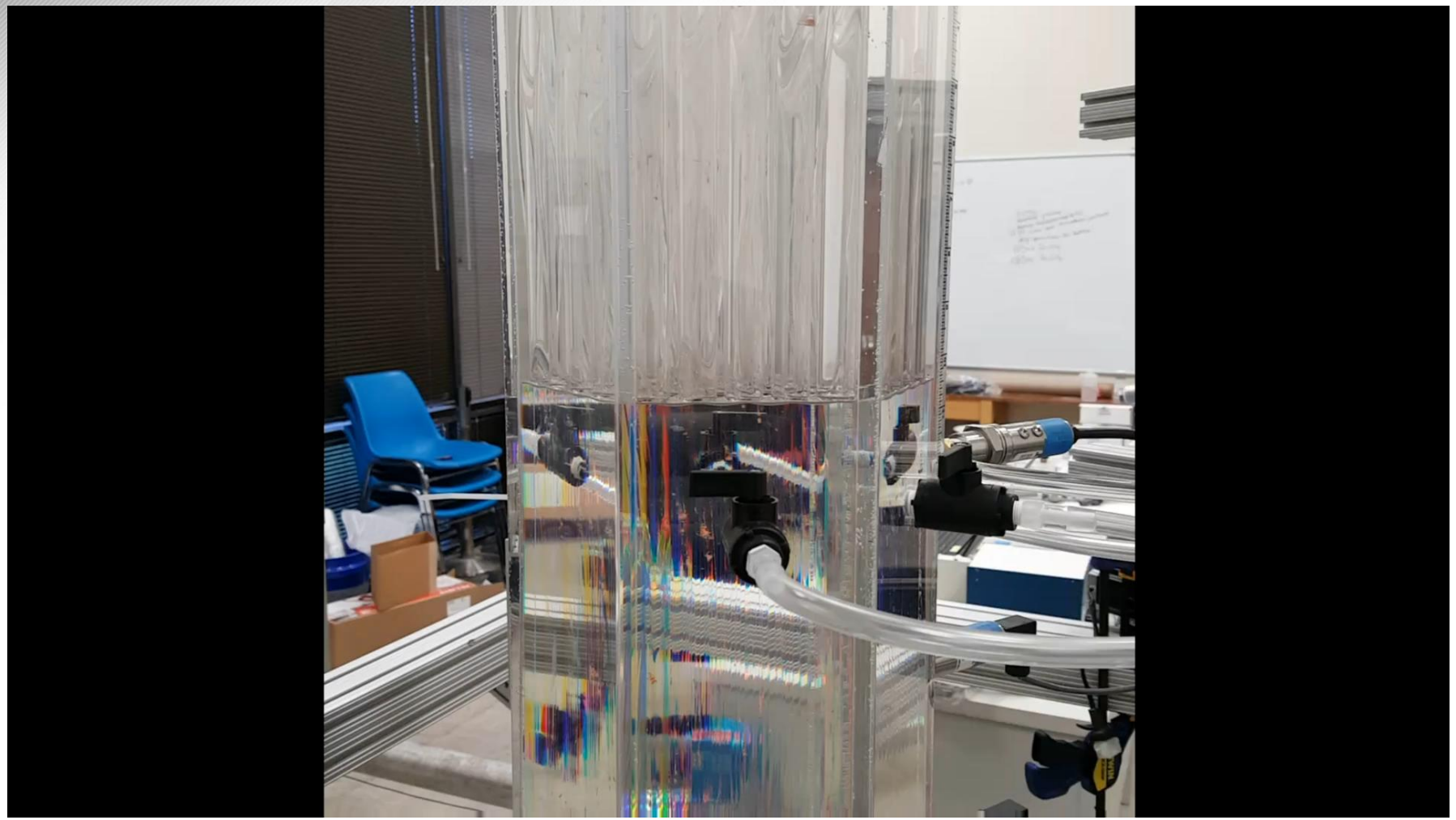
Non-intrusive optical measurements

Particle Image Velocimetry

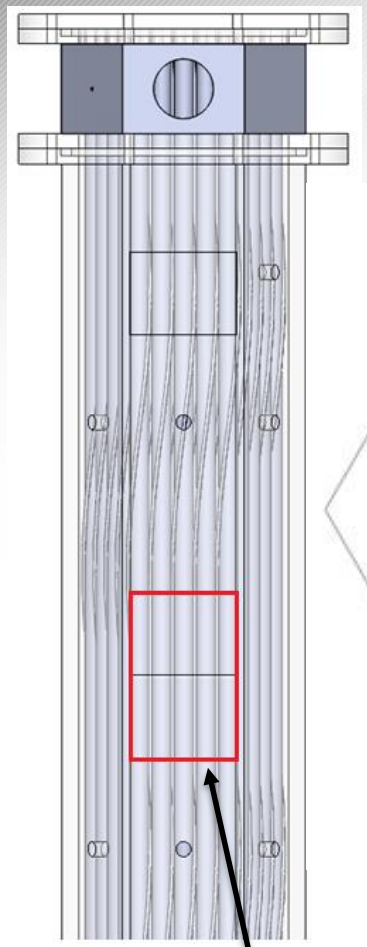
Laser Doppler Velocimetry

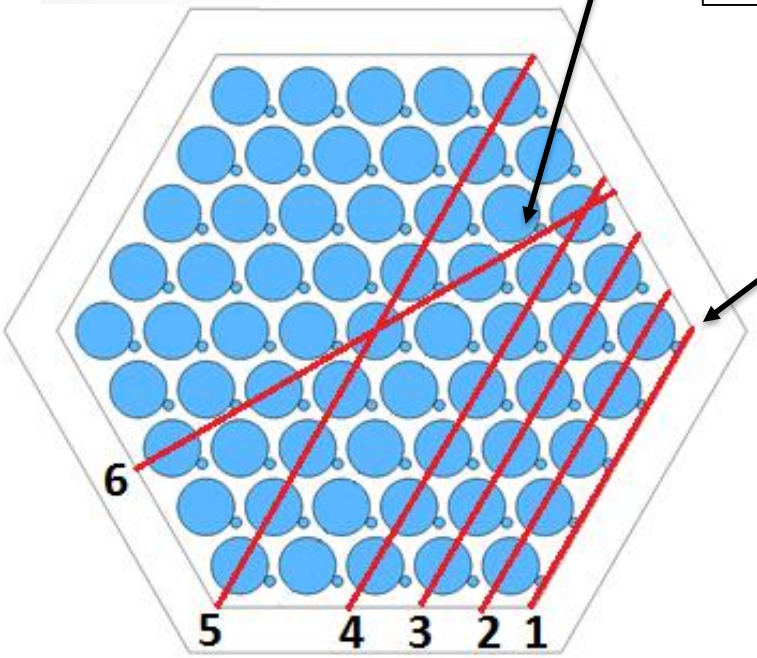


Capabilities: Velocity Measurements



PIV Measurements





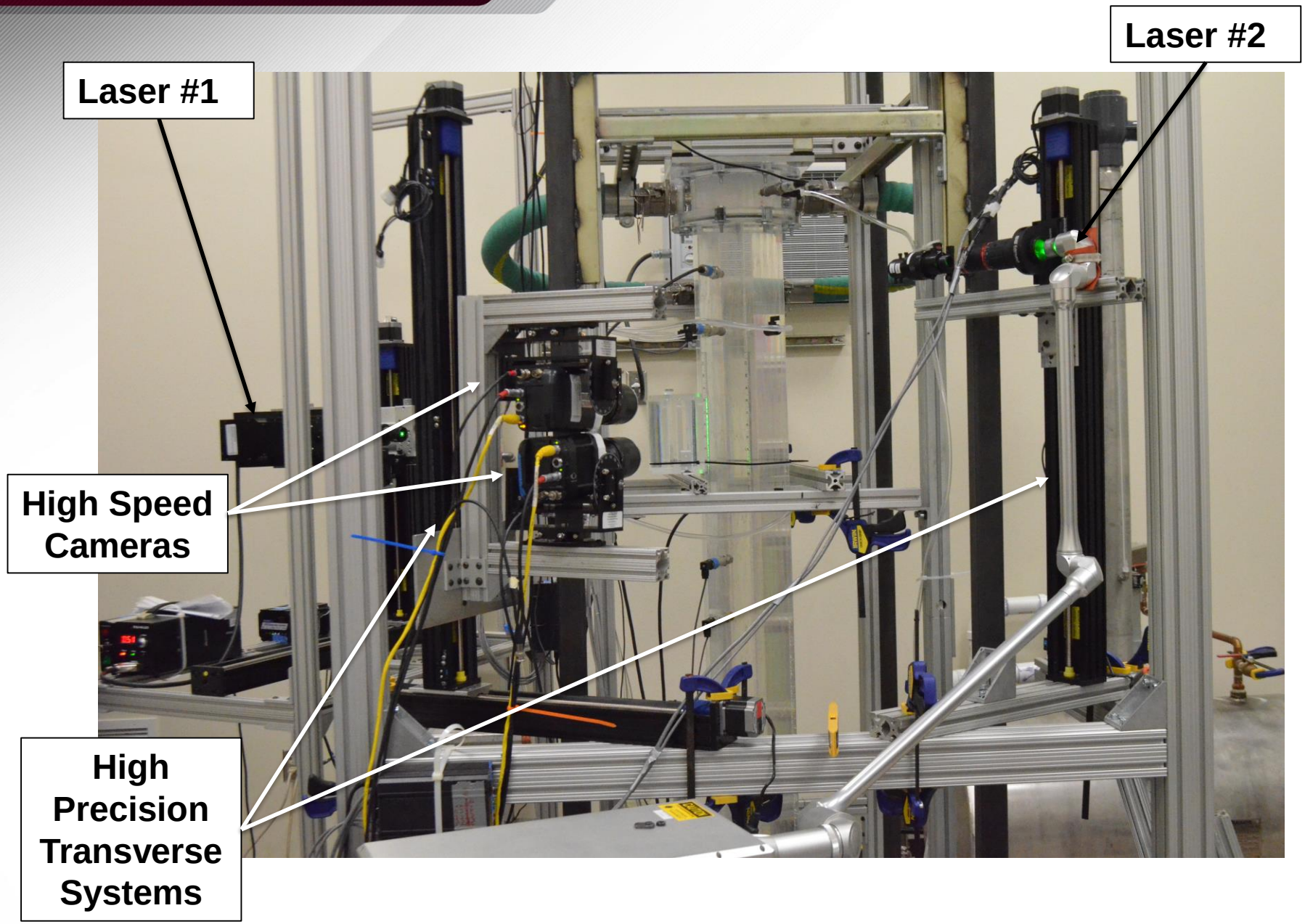
(6) Interior subchannels (30°)

(1) Exterior (near-wall) subchannels

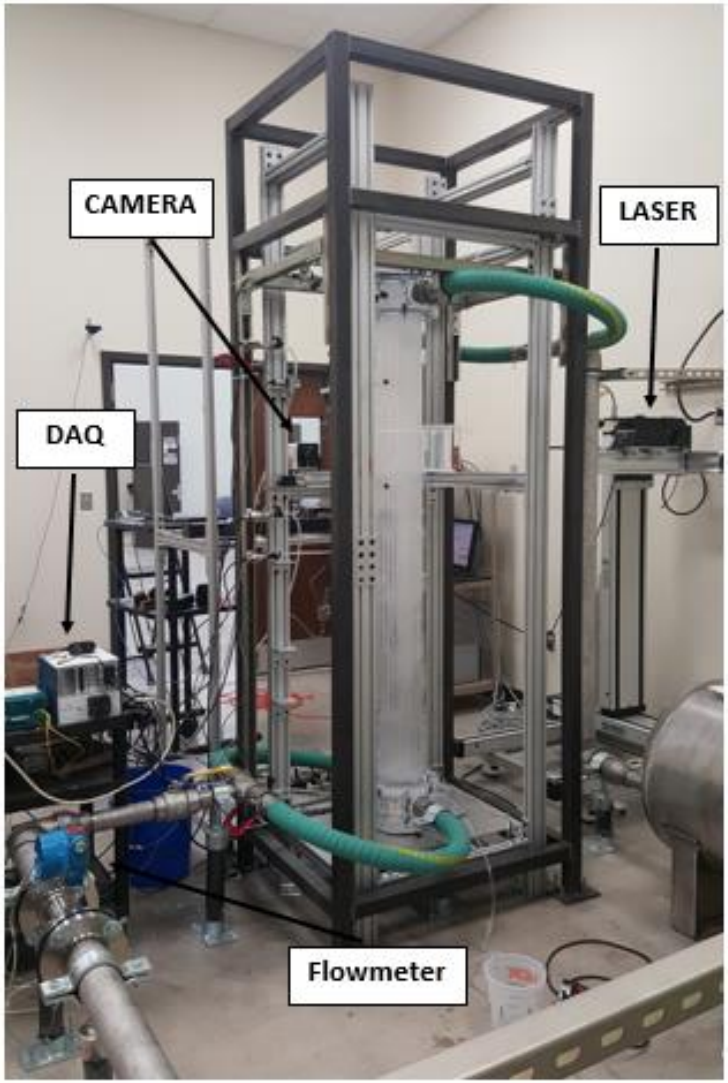
2 x Axial Locations

(2-5) Interior subchannels (parallel to wall)

PIV Setup


Laser #2
Laser #1
High Speed Cameras
High Precision Transverse Systems

Capabilities: Pressure Measurements



9 Axial Pressure Transducers



Azimuthal dP
2 sets of Differential Pressure Transducers

Axial dP

Experiments Conducted

Pressure Measurements

- Laminar, Laminar-to-Transition, Transition-to-turbulent, and turbulent regimes
- Experimental Friction factor compared with existing correlations (CTD)

Velocity Measurements

- Interior and Exterior Subchannels Investigated
- Synchronized Pressure and Velocity Measurements
- 2 Axial Locations
- Transition and Turbulent Regimes (Re ~ 4000 – 20000)

Conclusions

- Design and Construction Completed
- Experimental Capabilities Met

- Pressure Data within a Wide Range of Re, Produced and Compared with CTD Correlation
- Velocity Data Generated

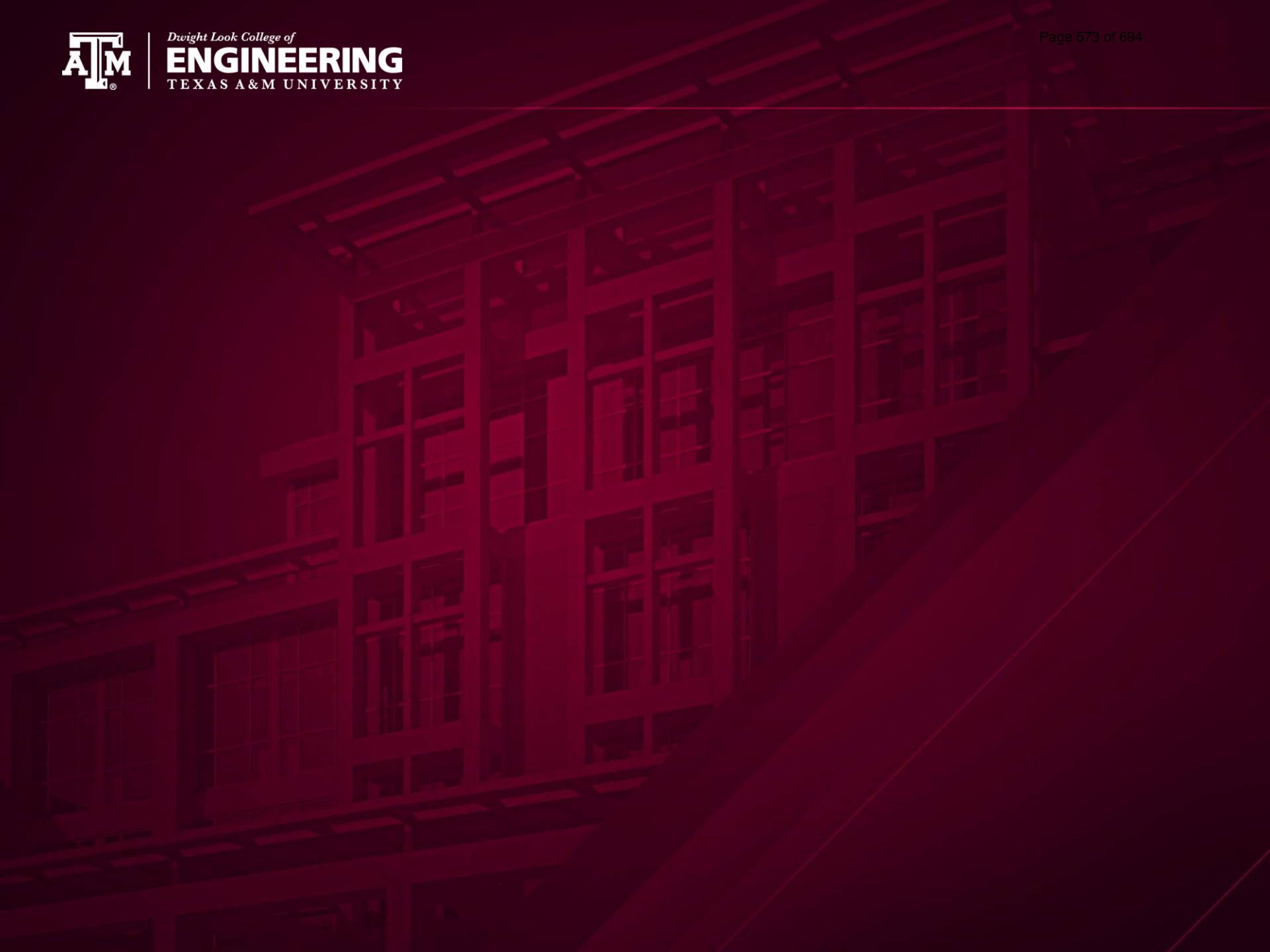
DOE Acknowledgement

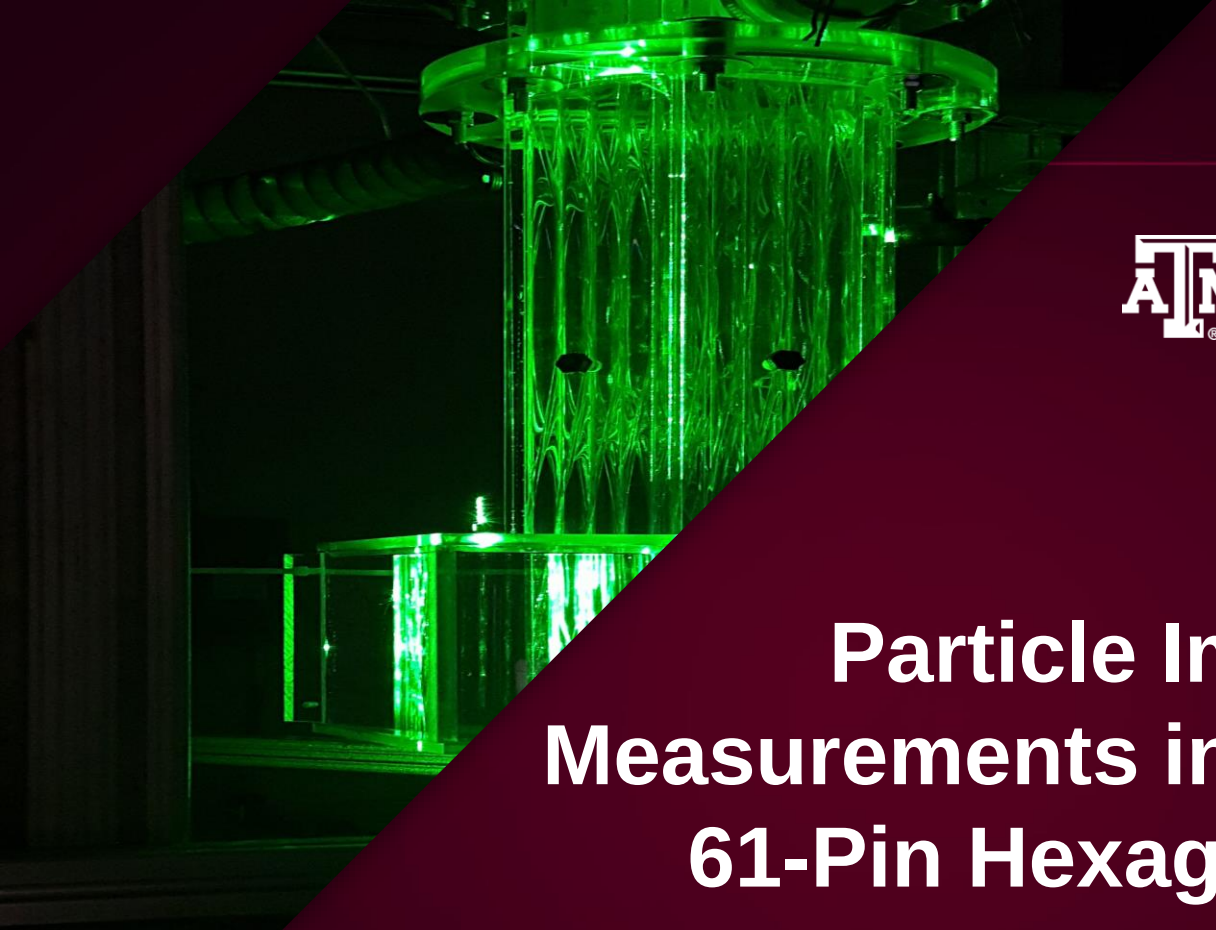
- This material is based upon work supported by the Department of Energy under Award Number DE-NE0008321.

- “This report was prepared as an account of work sponsored by an agency of the United States Government. Neither the United States Government nor any agency thereof, nor any of their employees, makes any warranty, express or implied, or assumes any legal liability or responsibility for the accuracy, completeness, or usefulness of any information, apparatus, product, or process disclosed, or represents that its use would not infringe privately owned rights. Reference herein to any specific commercial product, process, or service by trade name, trademark, manufacturer, or otherwise does not necessarily constitute or imply its endorsement, recommendation, or favoring by the United States Government or any agency thereof. The views and opinions of authors expressed herein do not necessarily state or reflect those of the United States Government or any agency thereof.”

Questions







NUCLEAR ENGINEERING
TEXAS A&M UNIVERSITY

Particle Image Velocimetry Measurements in a Wire-Wrapped 61-Pin Hexagonal Fuel Bundle

***N. Goth**
M. Childs
P. Jones
S. Lee
D. T. Nguyen
R. Vaghetto
Y. Hassan

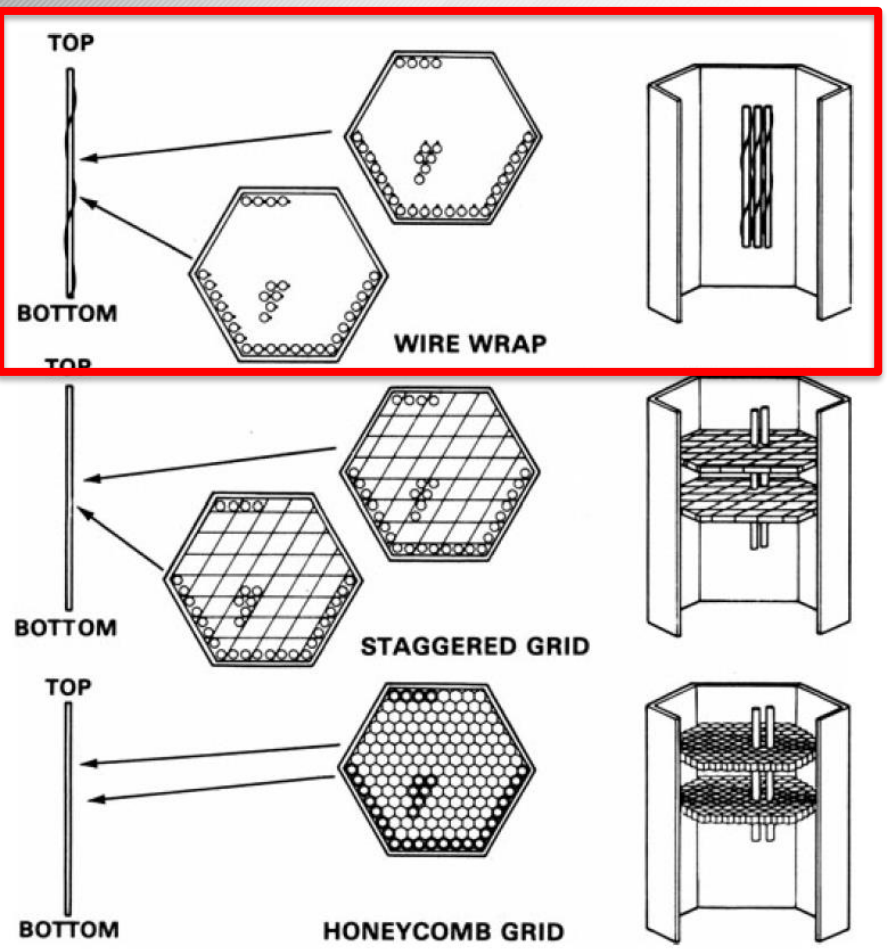
2016 ANS Winter Meeting
Las Vegas, NV, November 6-10, 2016

*Presenter

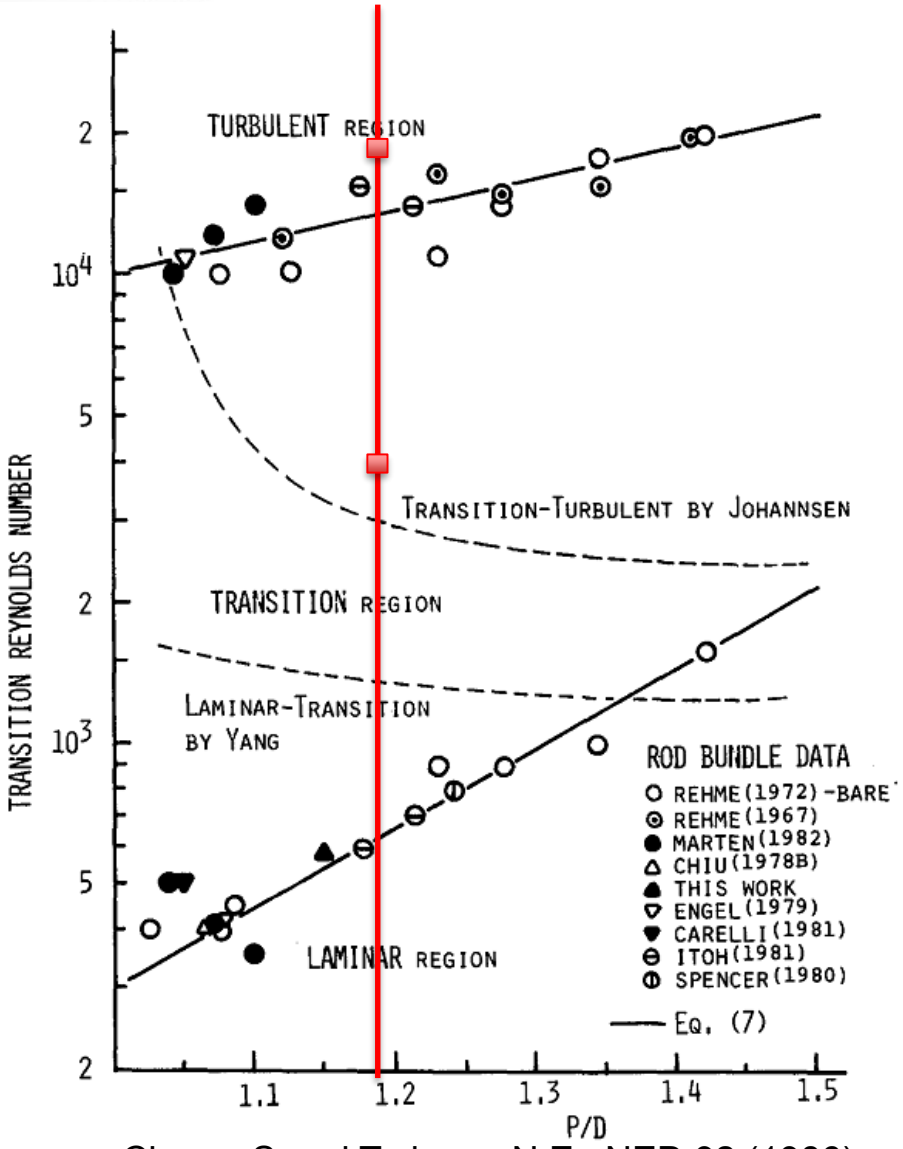
Presentation Overview

- Background on particle image velocimetry
- Shakedown testing with H_2O
  - Exterior Plane (near-wall)
- PIV results with p-Cymene
  - Exterior plane (near-wall)
    - Re = 4,000 and 19,000
  - Center plane (interior subchannels)
    - Re = 19,000
- Future work

Geometry and Flow Regimes



Waltar, A., Todd, D., and Tsvetkov, P.

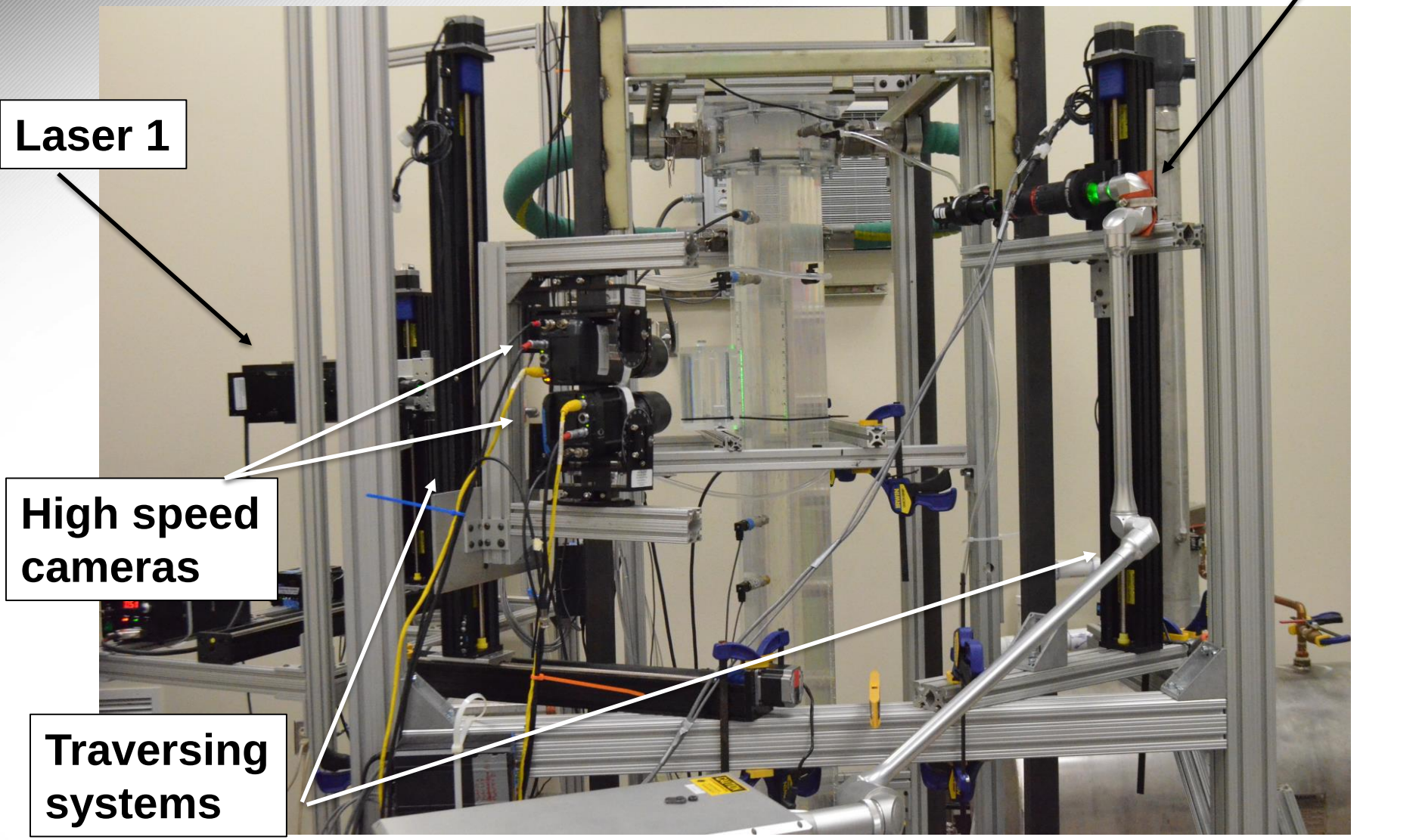


Cheng, S and Todreas, N.E., NED 92 (1986)

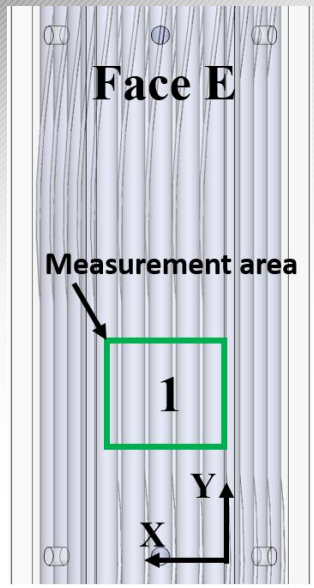
Particle Image Velocimetry

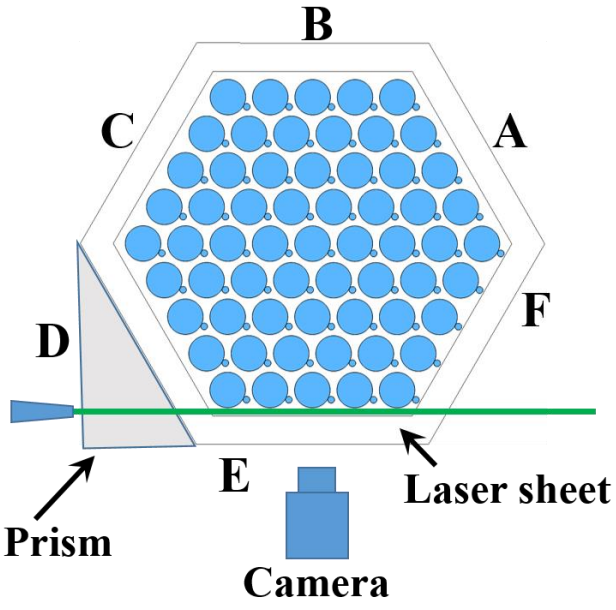
- PIV is laser-based measurement technique
  - Instantaneous velocity
  - Tracer particles
    - Optimum density, diameter and reflectivity
  - Photon source
    - Collimated, monochromatic source (laser, x-ray generator, etc)
  - Photon detector
    - Digital camera
  - Synchronizer
- Advantages
  - Non-intrusive
  - 2D and 3D vector fields
  - High spatial and temporal resolution

PIV Setup

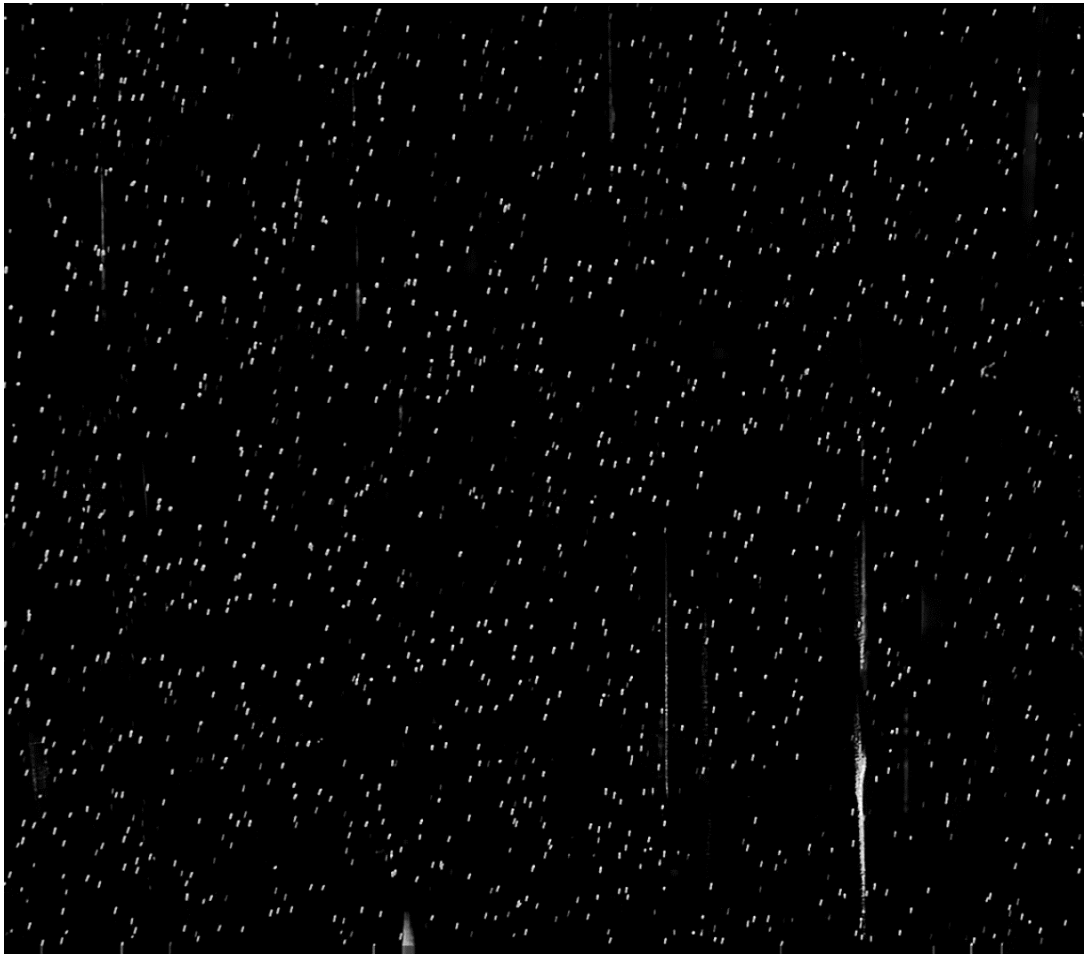


Shakedowns With Water





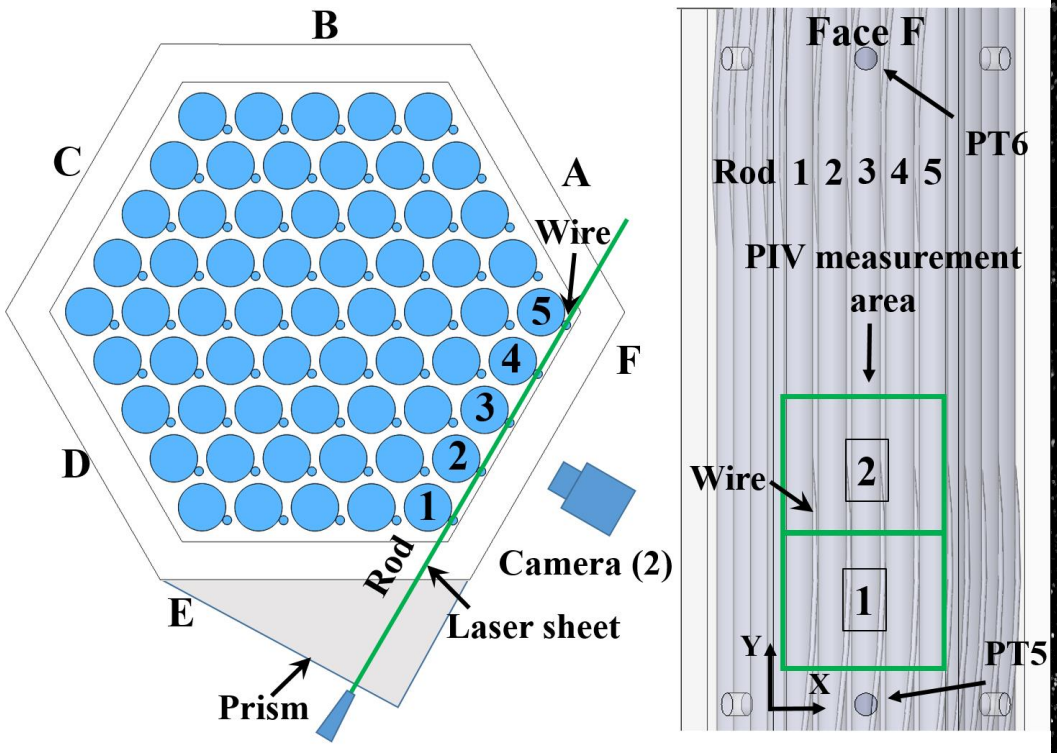
- Exterior plane on Face E near the wall
- Reynolds number of 3,500 – 10,000



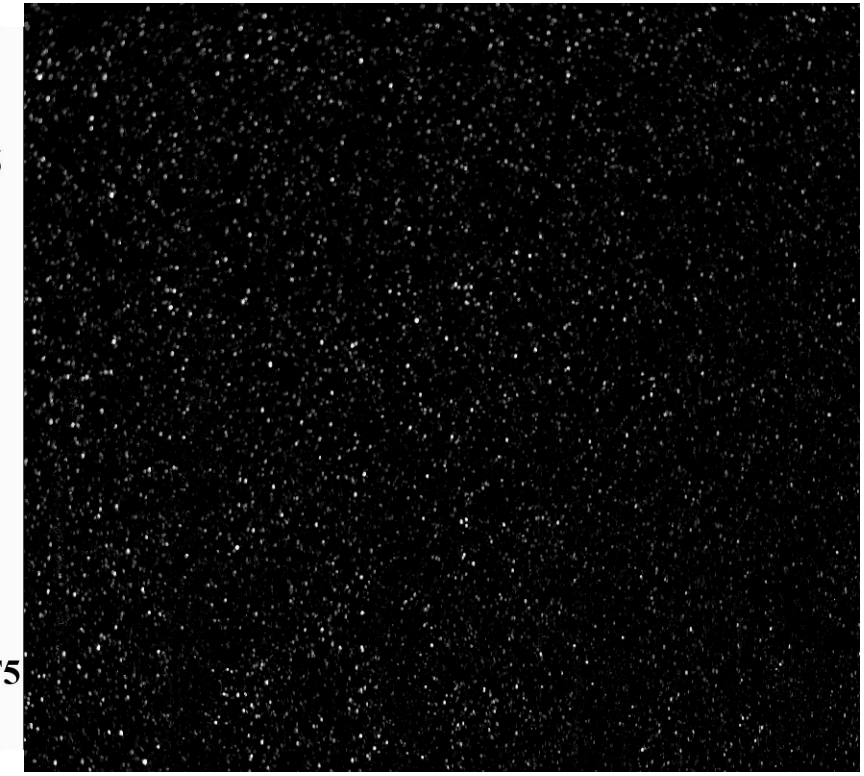


Exterior plane setup
Fluid = p-Cymene

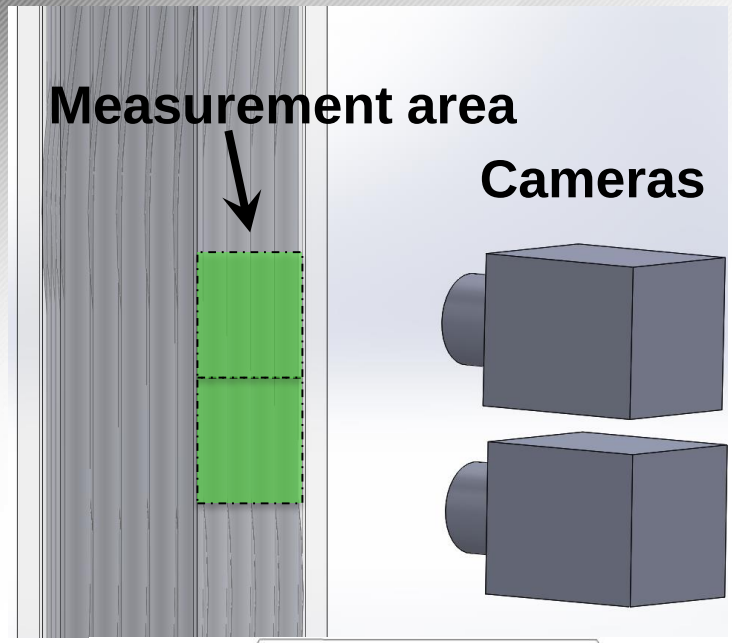
Imaging Hardware Setup

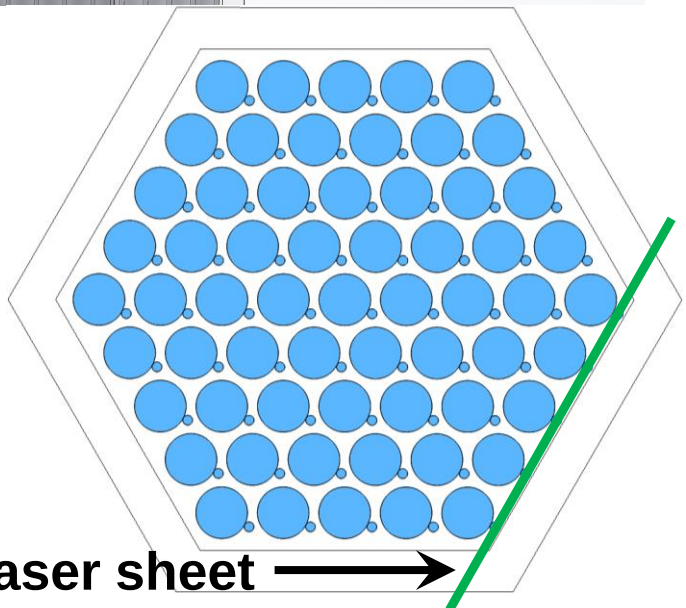


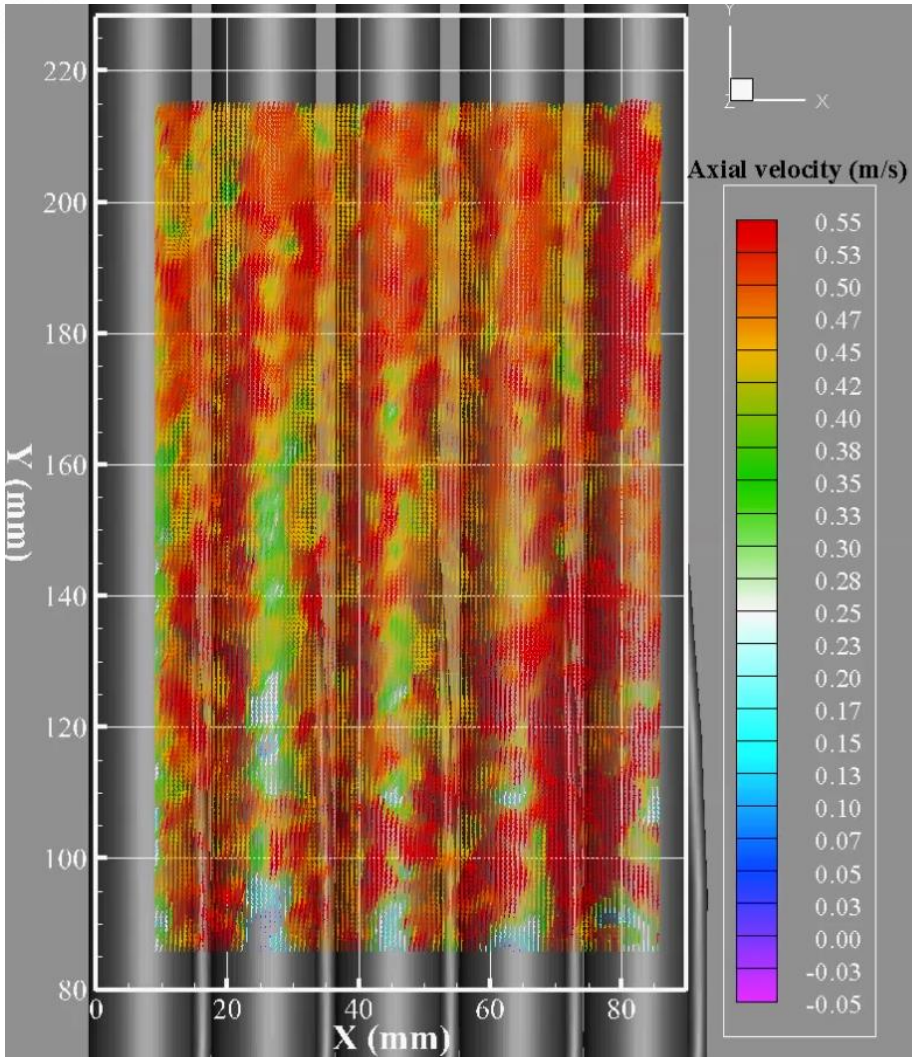
Qualitative video at 25 fps



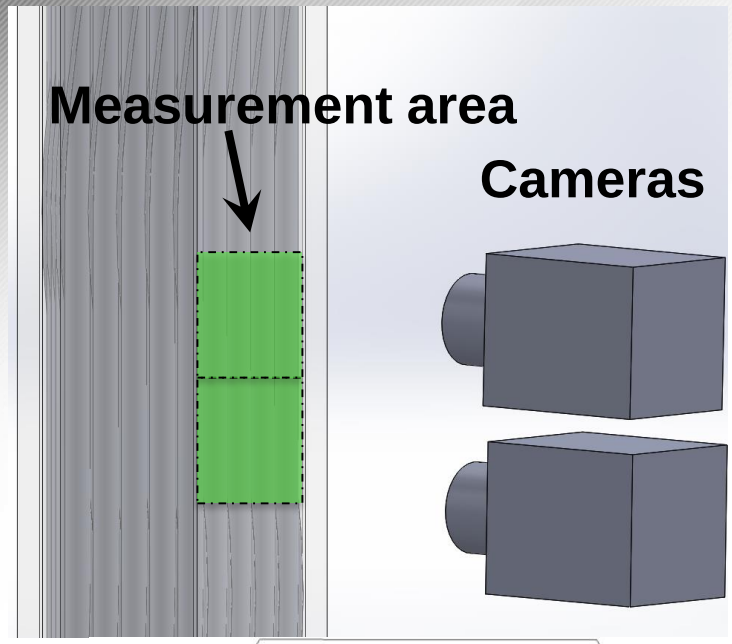
Instantaneous Velocity
Re = 4,000
Fluid = p-Cymene

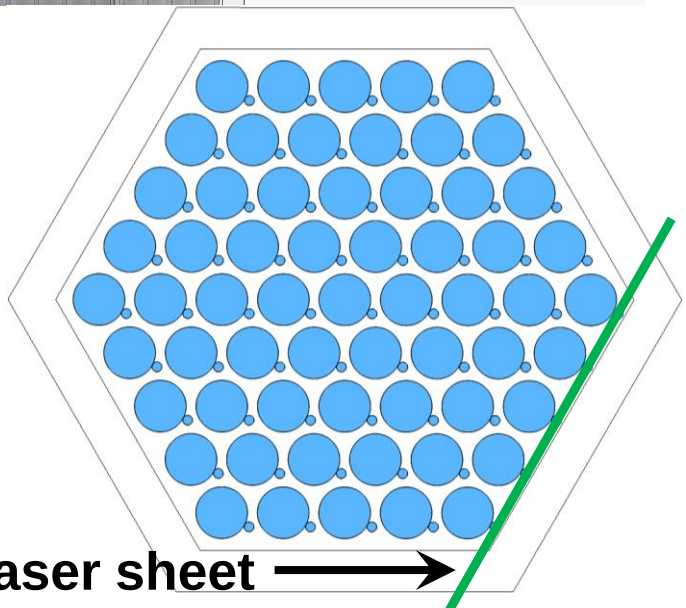


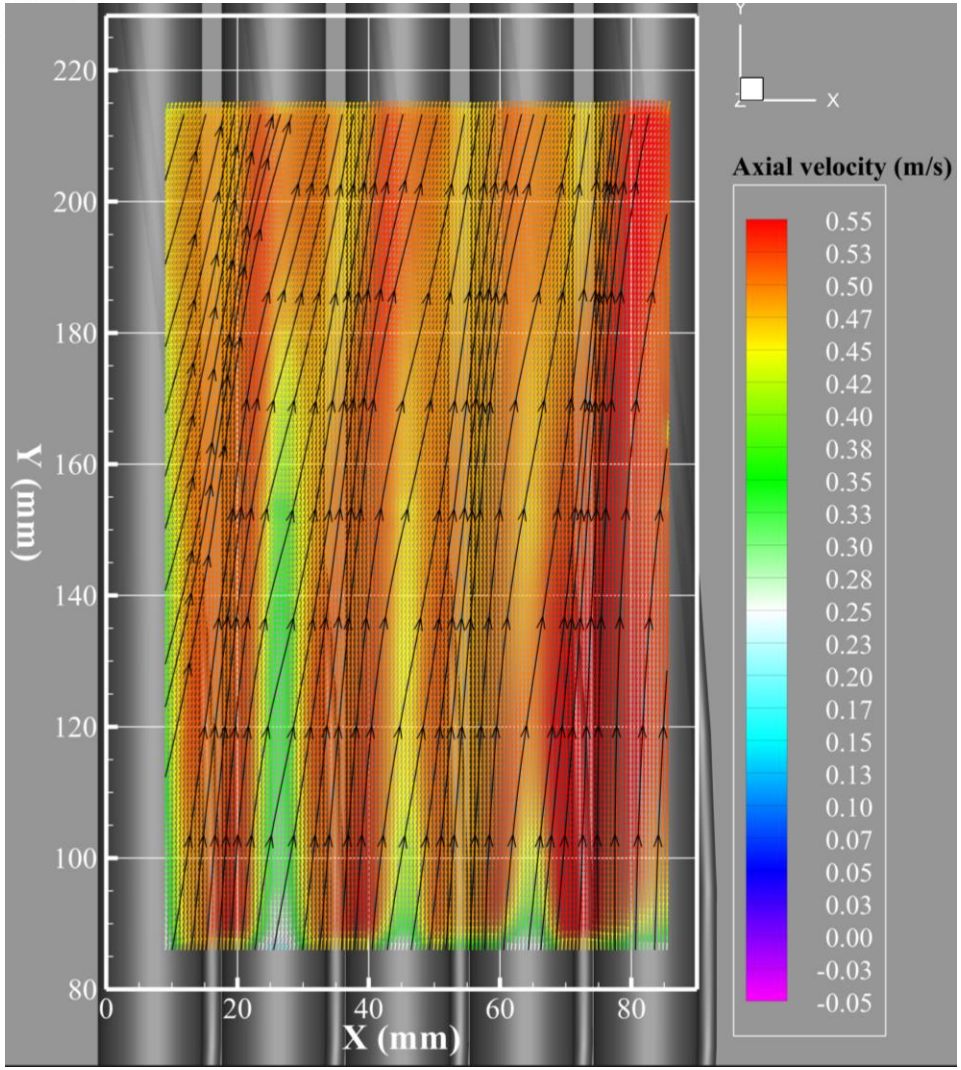




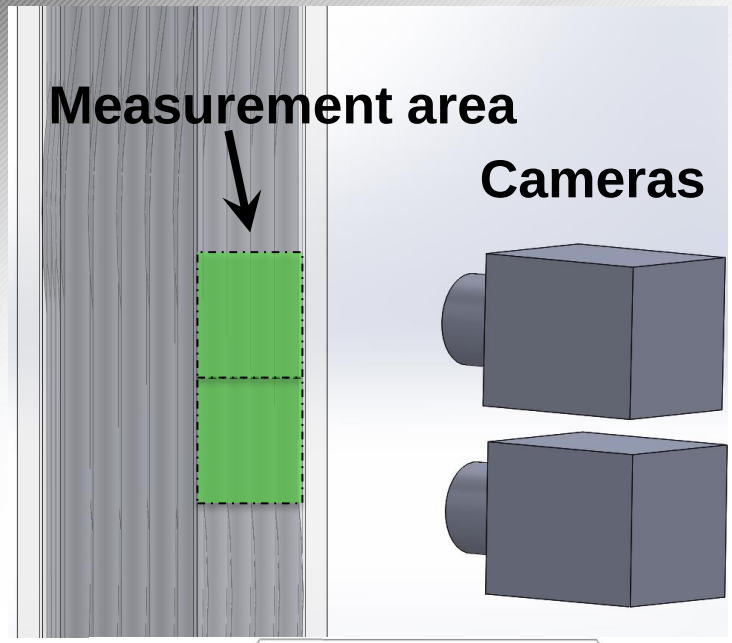
Ensemble-averaged Velocity
Re = 4,000
Fluid = p-Cymene

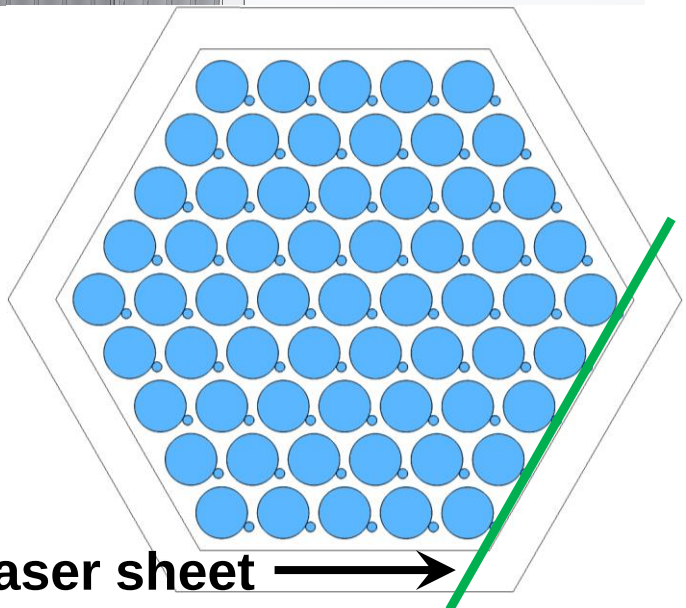


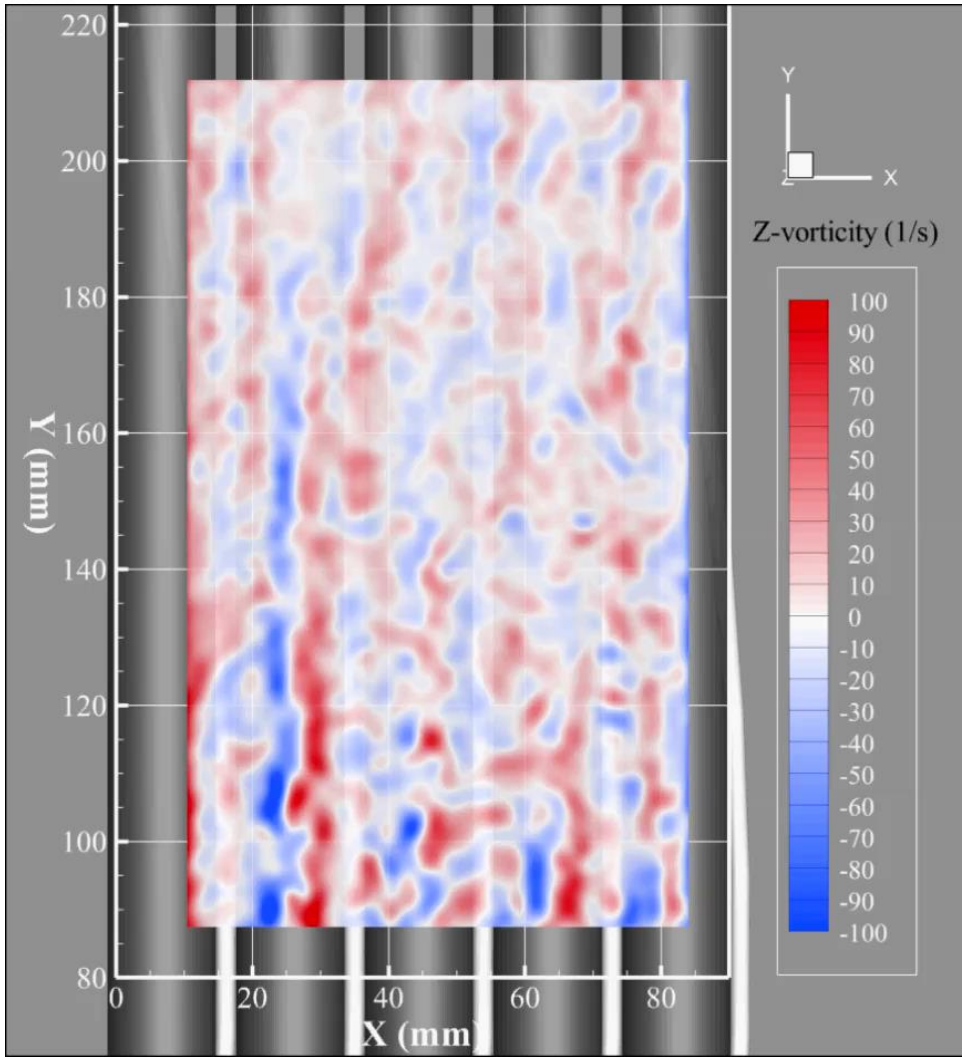




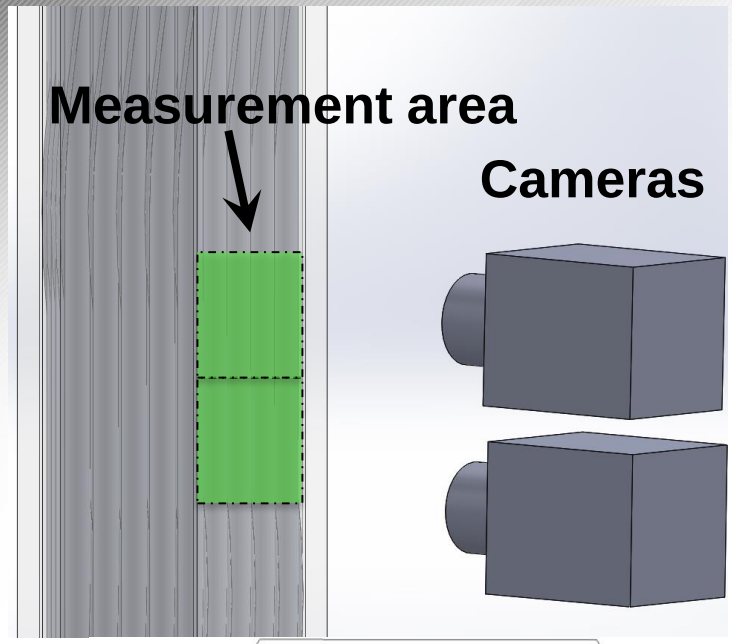
Instantaneous Vorticity
Re = 4,000
Fluid = p-Cymene

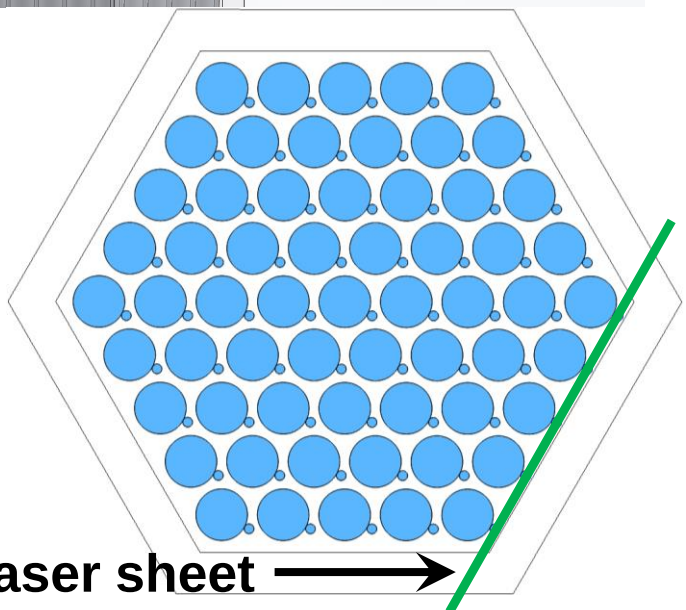


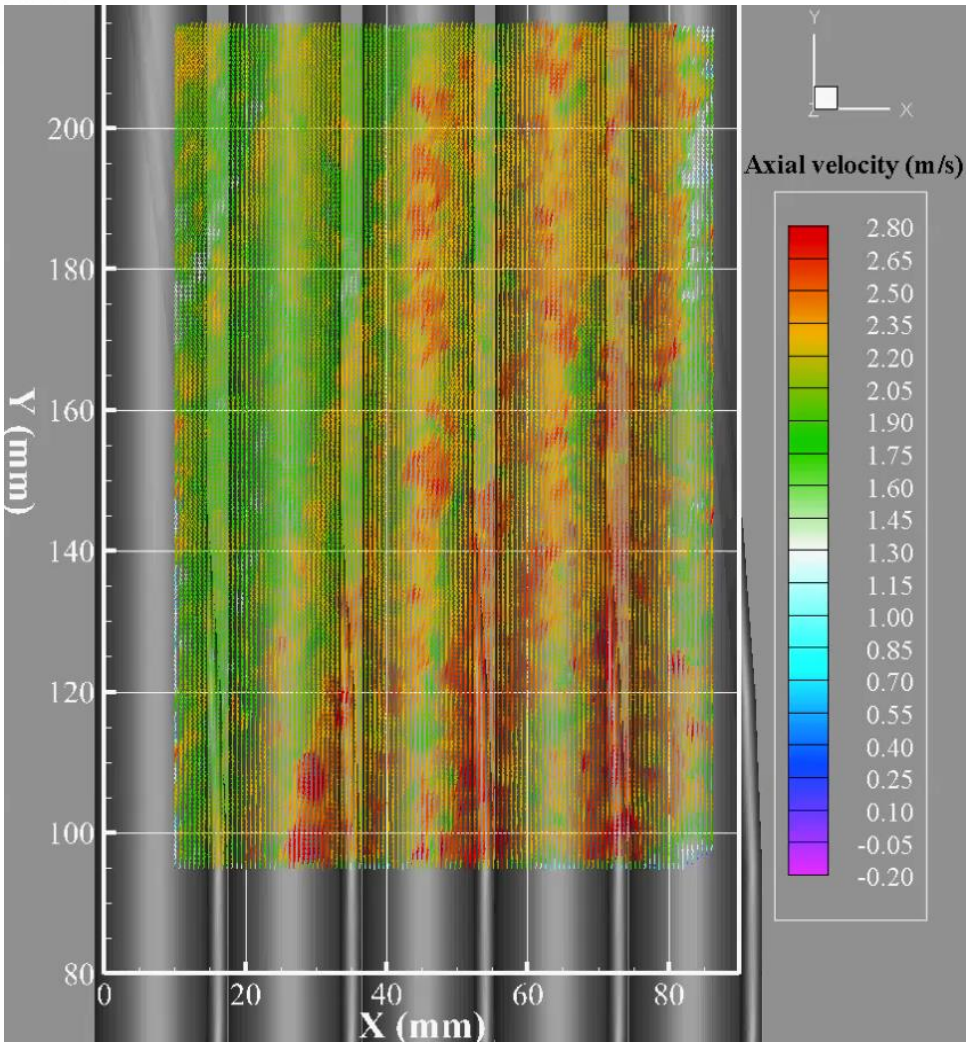




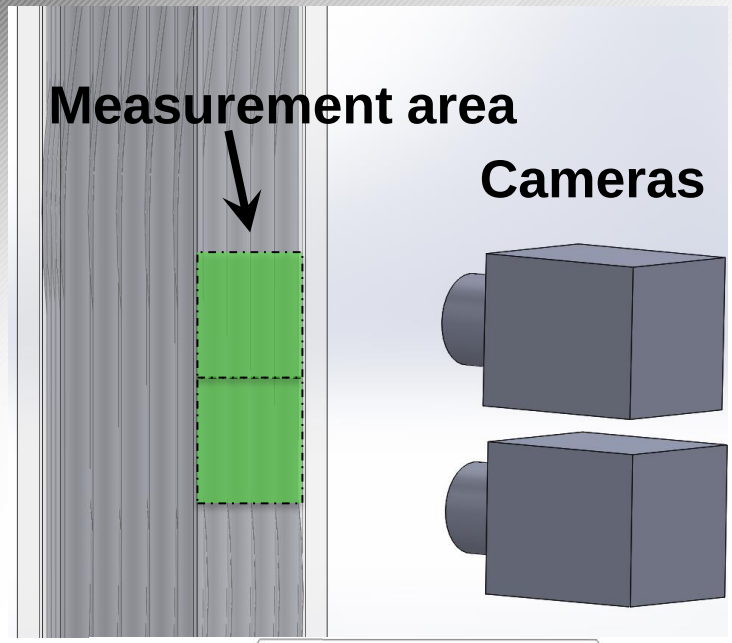
Instantaneous Velocity
Re = 19,000
Fluid = p-Cymene

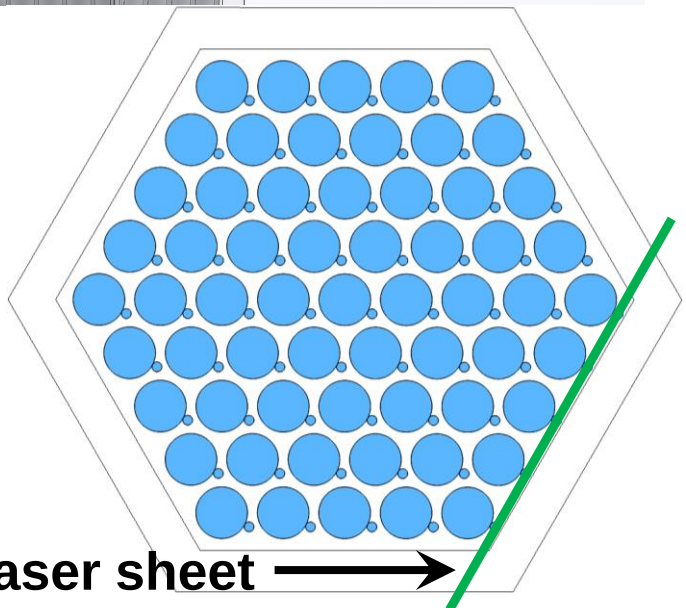


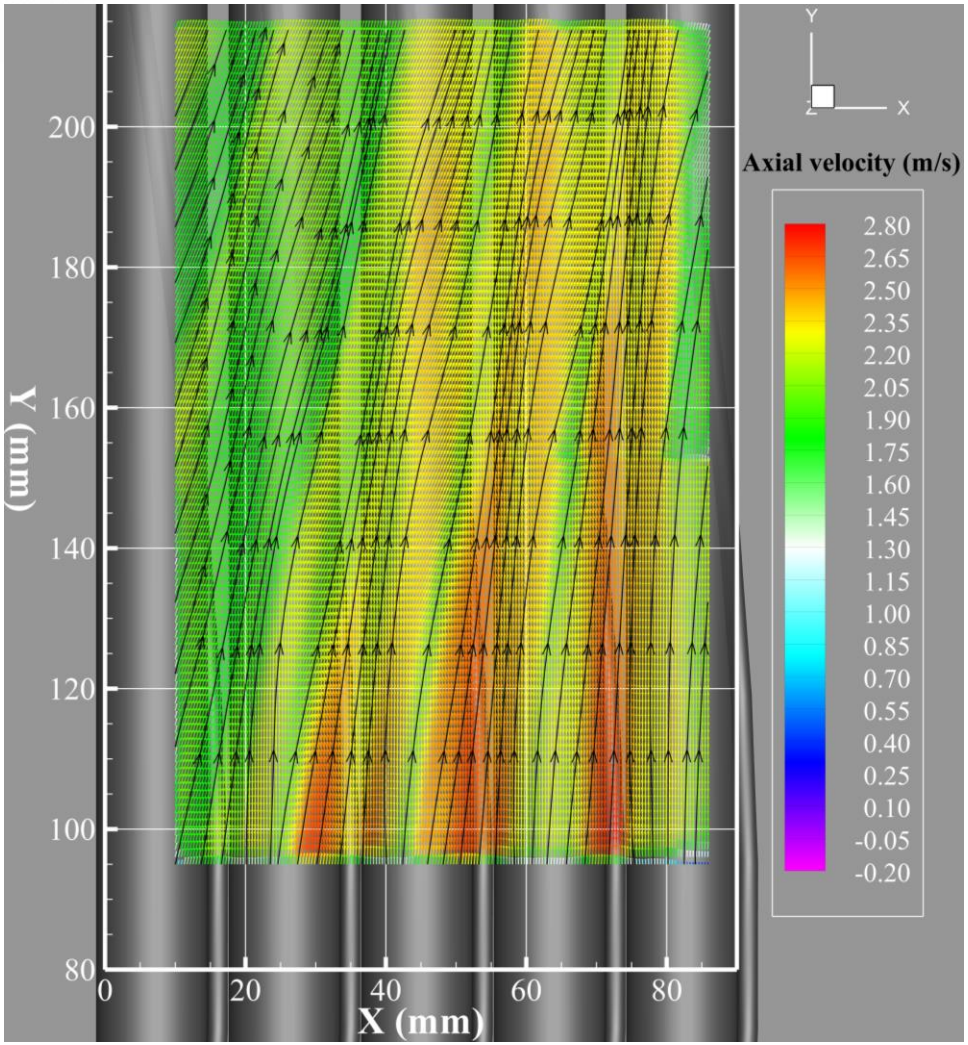




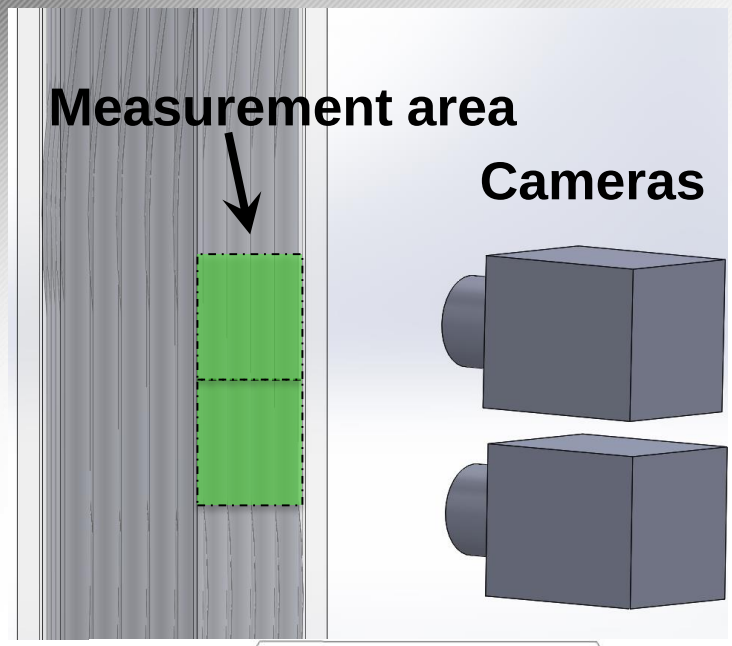
Ensemble-averaged Velocity
Re = 19,000
Fluid = p-Cymene

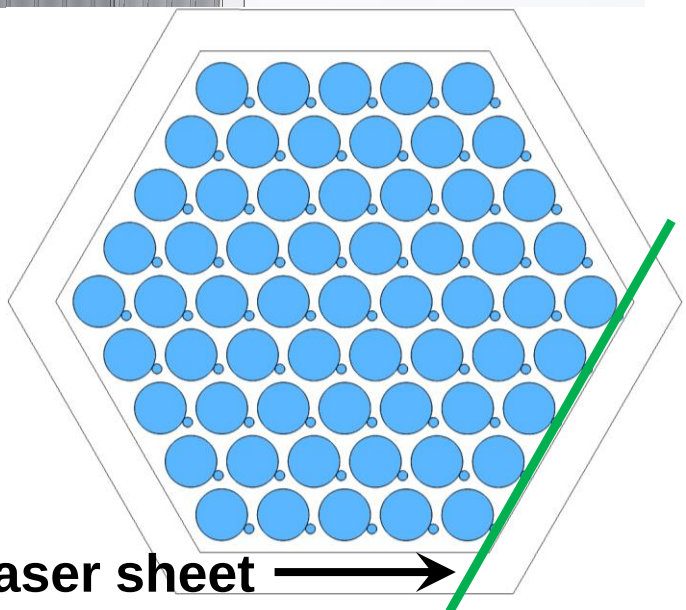


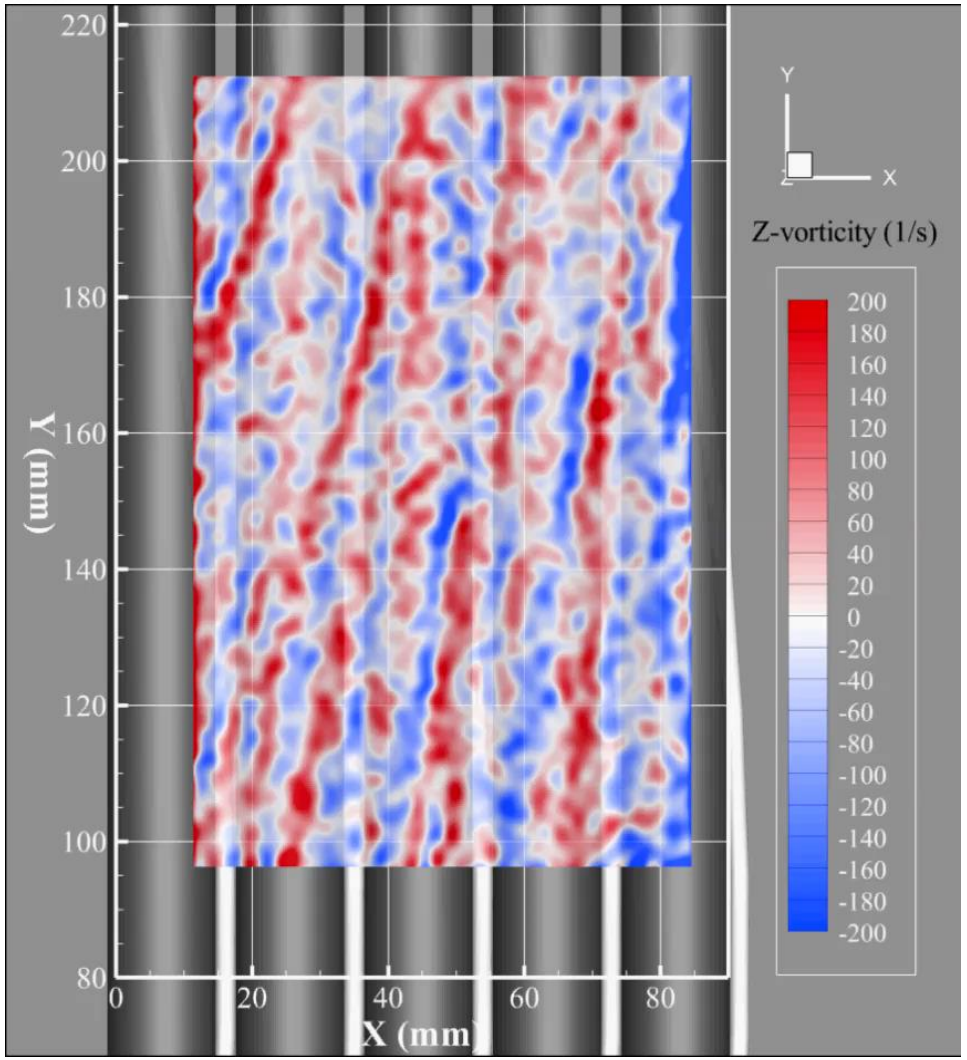




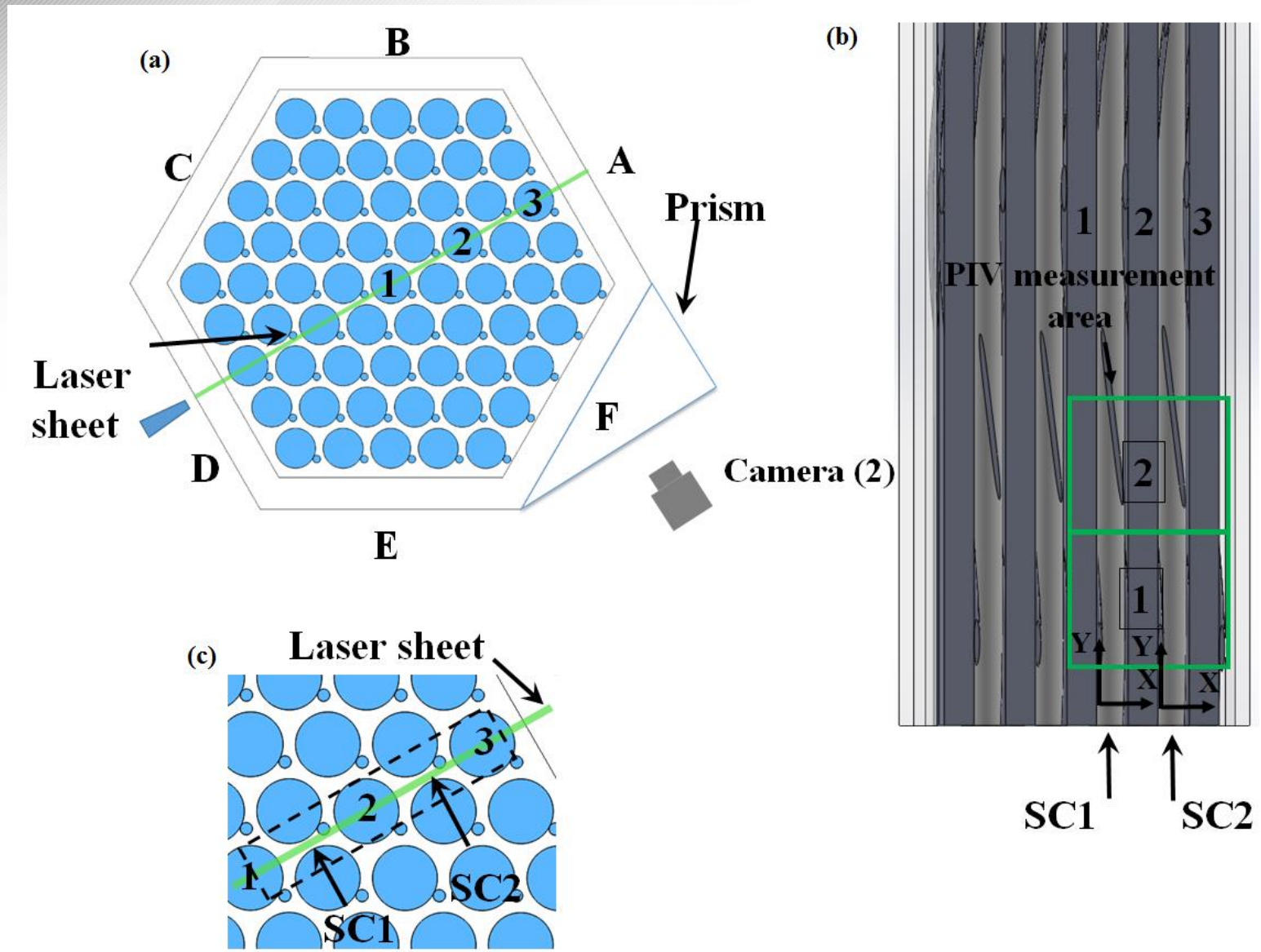
Instantaneous Vorticity
Re = 19,000
Fluid = p-Cymene





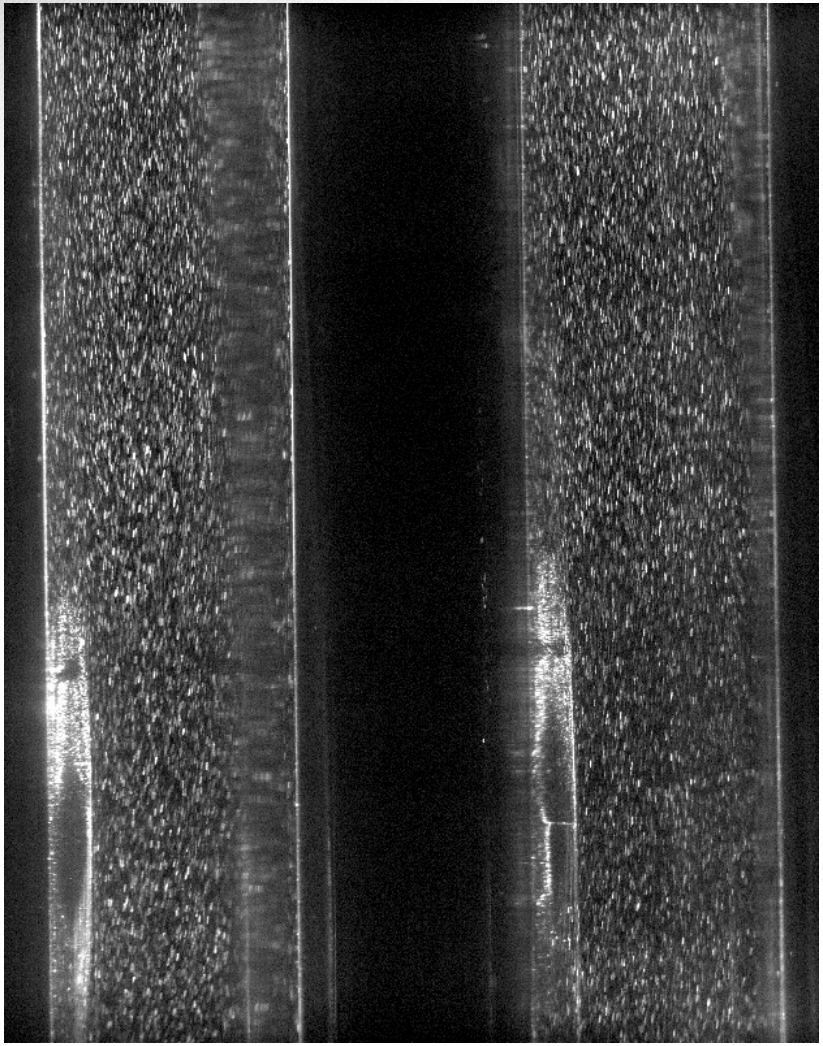


Interior plane setup

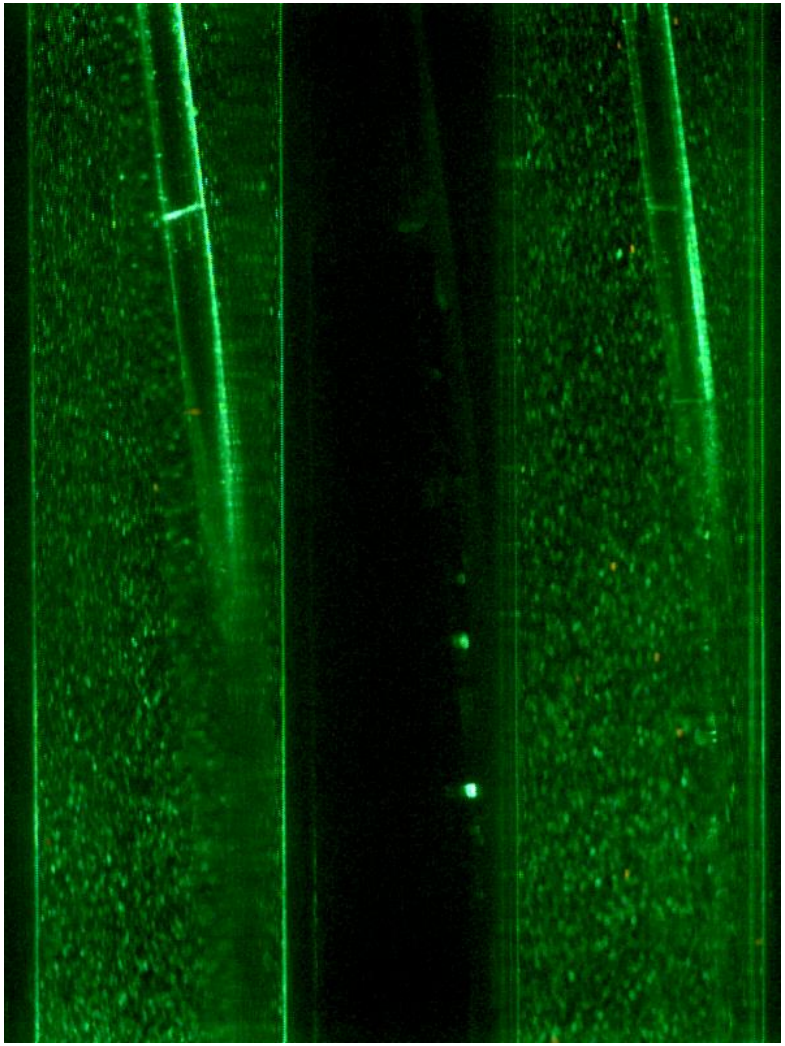


Center plane Qualitative raw videos

Camera 1 (Bottom)



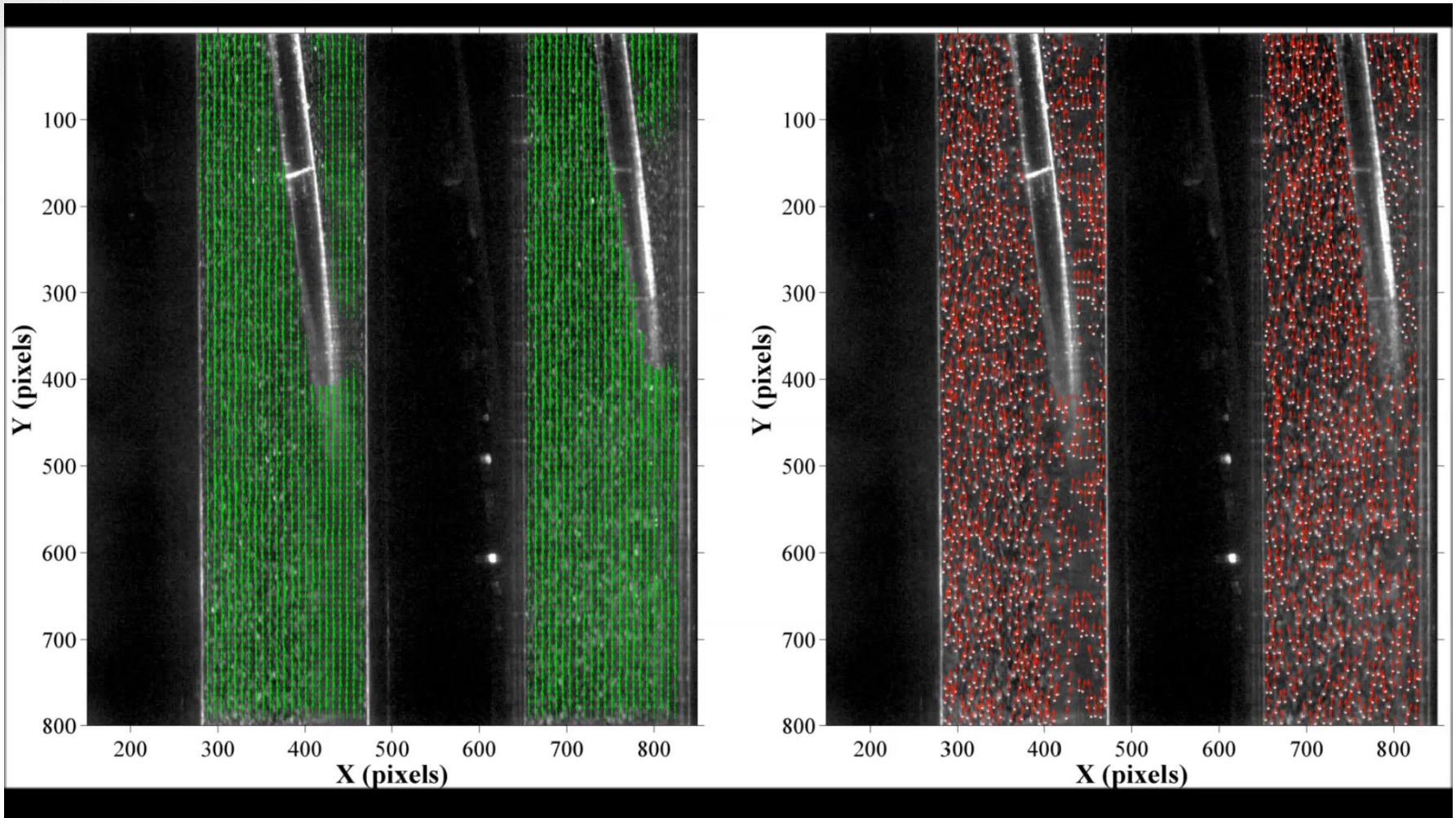
Camera 2 (Top)



Center plane
Re = 19,000
Fluid = p-Cymene

Camera 2 (top)
PIV

Camera 2 (top)
PTV



Summary

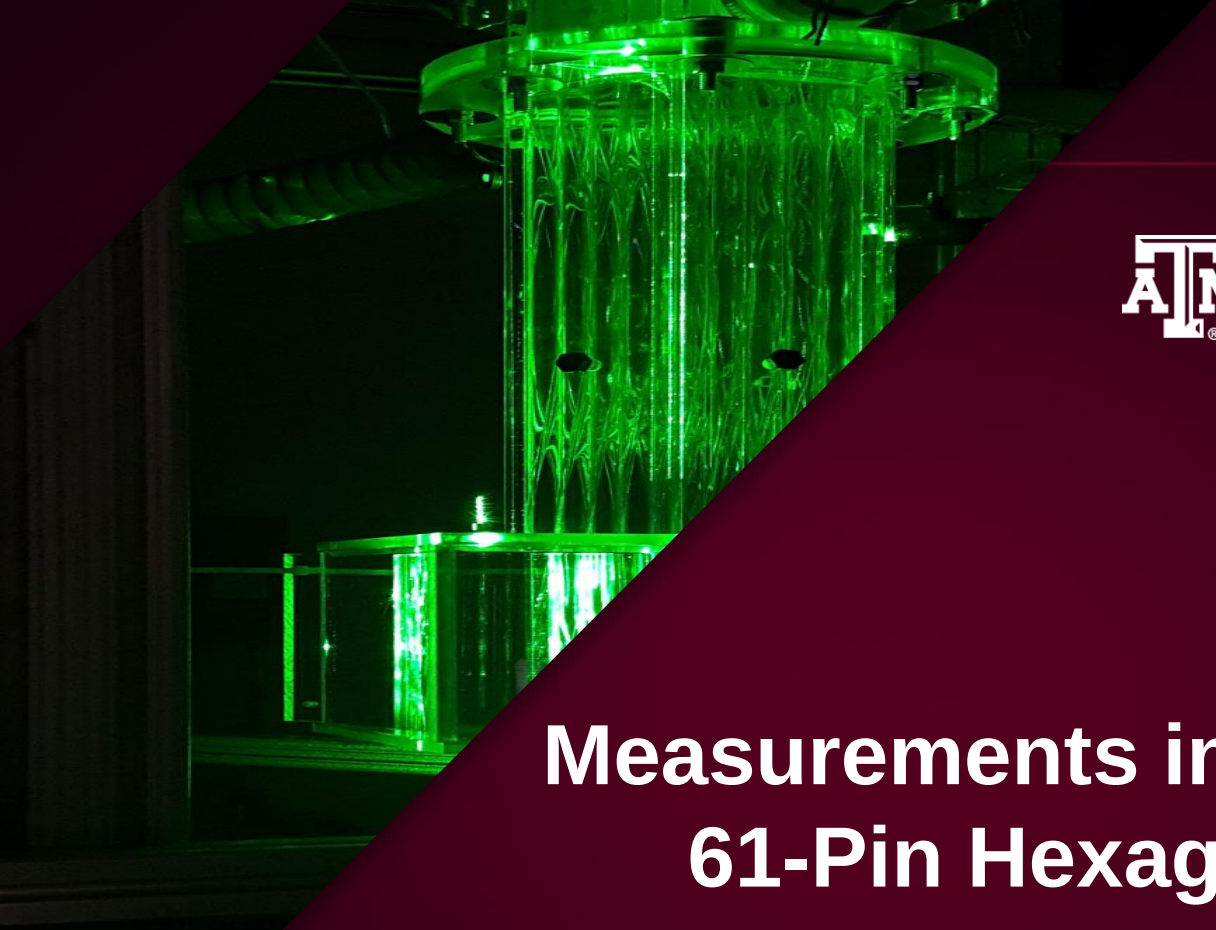
- Performed shakedown tests with H_2O
- Switched the working fluid to p-Cymene to achieve MIR conditions.
- Generated experimental data sets at exterior and interior subchannels for various Reynolds numbers.
- Experimental data sets will be used for validation of simulation results on SFR fuel bundles

DOE Acknowledgement

- This material is based upon work supported by the Department of Energy under Award Number DE-NE0008321.

- “This report was prepared as an account of work sponsored by an agency of the United States Government. Neither the United States Government nor any agency thereof, nor any of their employees, makes any warranty, express or implied, or assumes any legal liability or responsibility for the accuracy, completeness, or usefulness of any information, apparatus, product, or process disclosed, or represents that its use would not infringe privately owned rights. Reference herein to any specific commercial product, process, or service by trade name, trademark, manufacturer, or otherwise does not necessarily constitute or imply its endorsement, recommendation, or favoring by the United States Government or any agency thereof. The views and opinions of authors expressed herein do not necessarily state or reflect those of the United States Government or any agency thereof.”

Questions



NUCLEAR ENGINEERING
TEXAS A&M UNIVERSITY

Pressure Measurements in a Wire-Wrapped 61-Pin Hexagonal Fuel Bundle

N. Goth
M. Childs
*P. Jones
S. Lee
D. T. Nguyen
R. Vaghetto
Y. Hassan

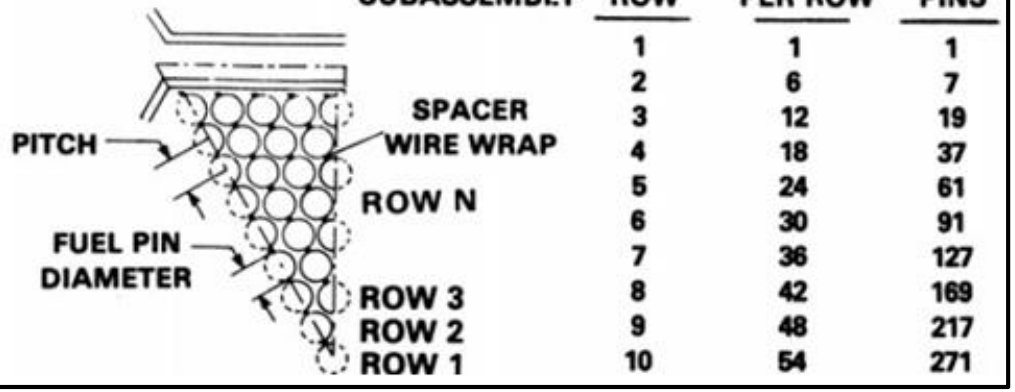
2016 ANS Winter Meeting
Las Vegas, NV, November 6-10, 2016

* Presenter

Presentation Overview

- Introduction
- Hardware overview
- Procedure
- Re and Friction Factor calculations
- Results
- Future work

Introduction



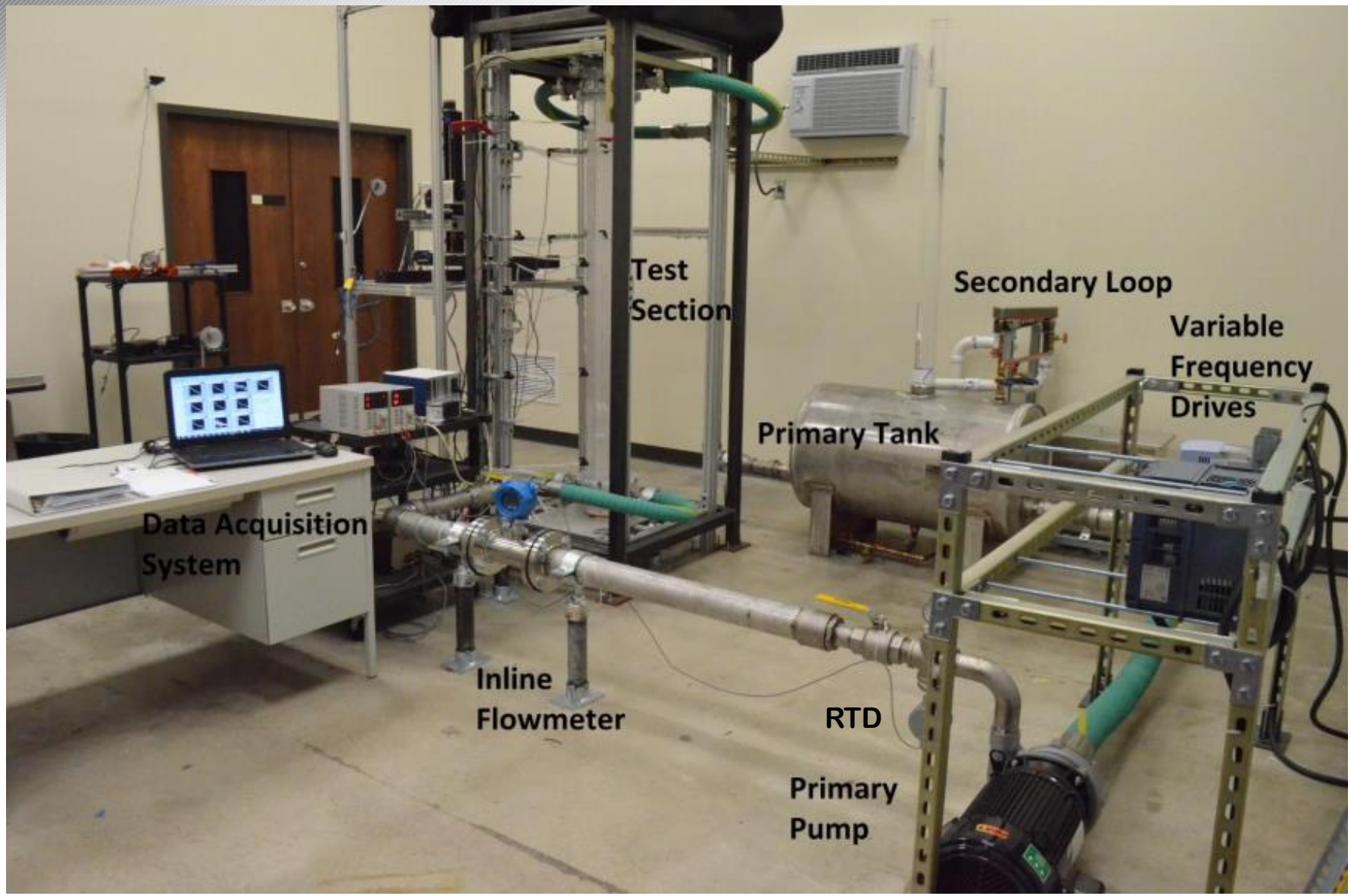
PIN ROW	PINS PER ROW	TOTAL PINS
1	1	1
2	6	7
3	12	19
4	18	37
5	24	61
6	30	91
7	36	127
8	42	169
9	48	217
10	54	271

Experiments
- Isothermal
- MIR flow visualization
- Pressure measurements
  - Laminar, transition, and turbulent regimes

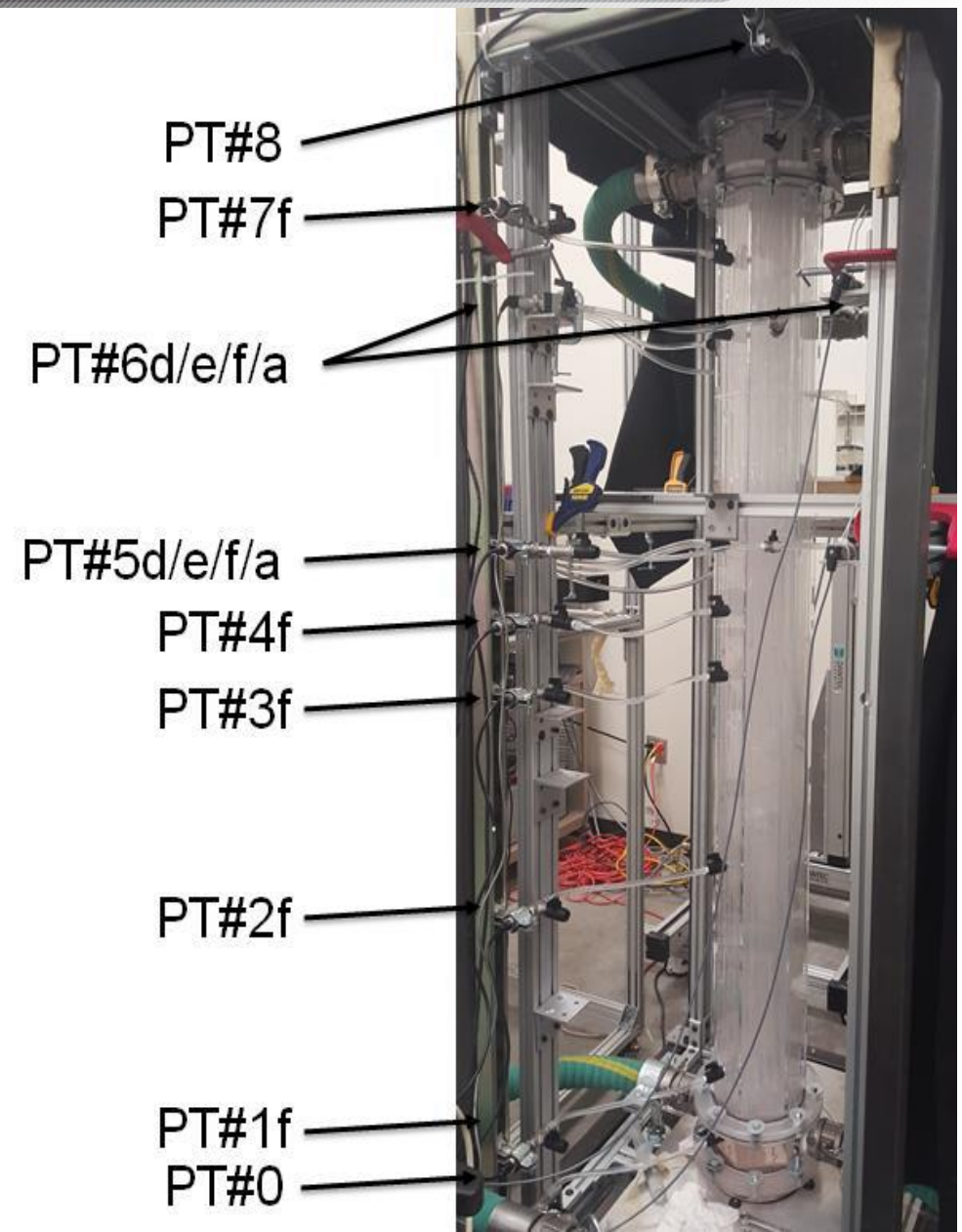
Main Features
- Triangular lattice
- 61 helically wrapped acrylic pins
- Hexagonal acrylic test section

Supplement existing pressure data sets

Hardware Overview



Hardware Overview



9 Axial gauge pressure transducers

- Points of interest, PT2, PT4, PT5, PT6, PT7

3 High accuracy differential transducers

- Azimuthally at PT5 and PT6
- Between PT5f and PT7f

PT#	Pitch	Max(PSI)	Accuracy
2	1.00	30	<0.1% FS
4	2.00	30	<0.1% FS
5	2.25	15	<0.1% FS
6	3.00	30	<0.1% FS
7	3.25	15	<0.1% FS

DP between PT5f and PT7f
10 inches Water, <0.1% FS

Benchmark

- Multiple correlations exist
- CTD Chosen
  - Utilizes sub channel analysis method
  - Interior, Edge, and Corner
  - Valid over a characteristic length H, distance for wire to complete a revolution
- Pressure drop analyzed from
  - PT2-PT4
  - PT4-PT6
  - PT2-PT6
  - PT5-PT7

Correlation	N Pins	P/D	H/D	Regime
CTD	19-217	1.0-1.42	4.0-52.0	L, tr, T
Rehme	7-217	1.06-1.42	8.0-50.0	tr, T
Baxi & Dalle Donne	19-217	1.06-1.42	8.0-96.0	L, tr, T
Our Bundle	**61**	**1.189**	**29.92**	**L, tr, T**

Test Conditions

Parameter	Value
Re Min	250
Re Max	19000
Temperature	22 ± 1.5°C
Sample Rate	1000 Hz
Duration	10 s
Repetitions	3
Working Fluid	P-Cymene

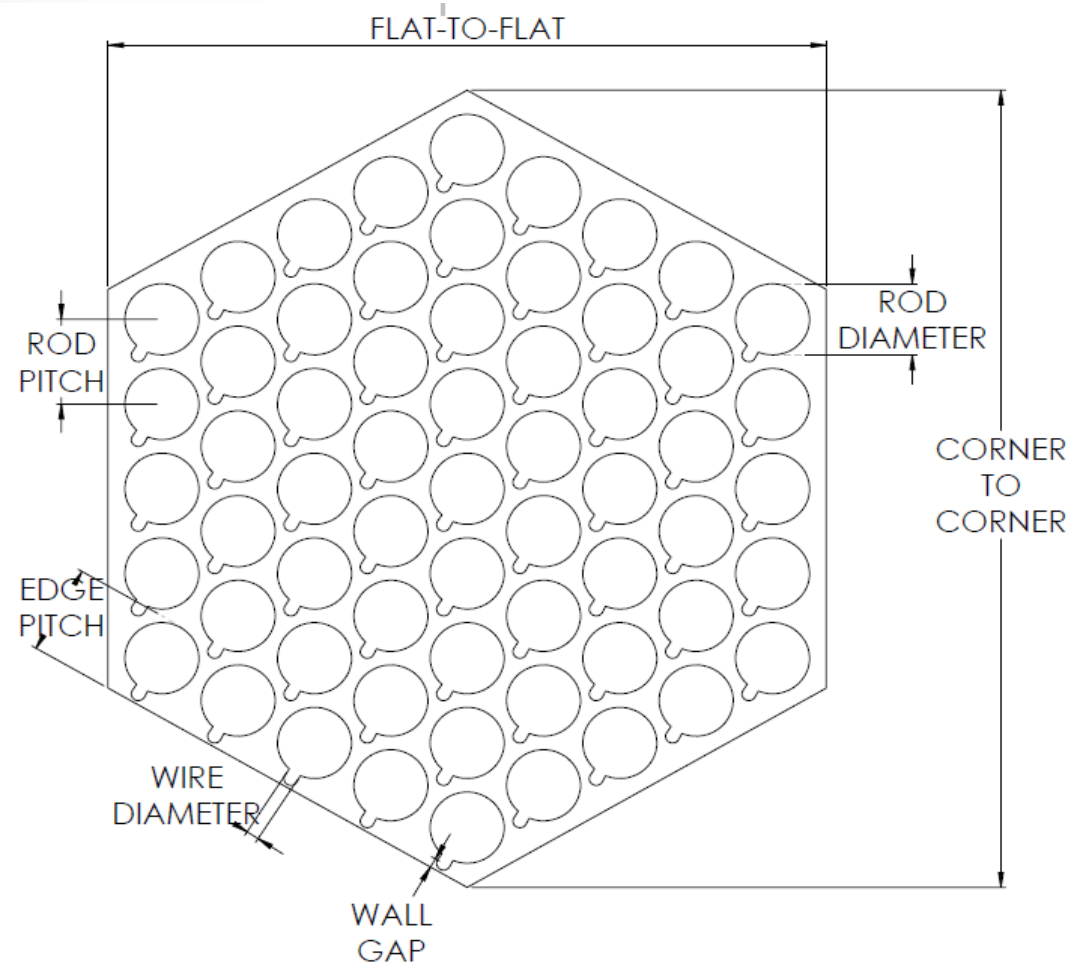
- The VFD driven pump was used to maintain a constant flow rate
- Temperature was maintained using heat exchanger and logged via RTD

Re Estimation

$$Re = \frac{\rho V D_H}{\mu}$$

$$D_H = \frac{4A}{P_{wet}}$$

- Fluid velocity determined from Q and Flow Area
- Flow area and H_D calculated as presented in CTD
  - Sub Channel values are calculated, then summed.
- ρ and μ determined by interpolating fluid properties table based on fluid temperature.



Re Uncertainty

Uncertainty in volumetric flow rate quantified based on uncertainty in turbine meter and associated calibration.

Uncertainty in fluid temperature was not taken into account. Available thermodynamic tables are coarse and not well defined.

$$\sigma_Q = \sqrt{\sigma_{Calibration}^2 + \sigma_{Flow\ Meter}^2}$$

$$\sigma_V = \frac{\sigma_Q}{A_{Bundle}}$$

$$\sigma_{Re} = \frac{\sigma_V D_H}{\nu}$$

Friction Factor

$$f = \Delta P \left(\frac{H_d}{L}\right)\left(\frac{2}{\rho V^2}\right)$$

- ΔP - change in pressure between 5f and 7f
- H_d - hydraulic diameter
- L - length of flow, one spacer pitch
- V - velocity determined from turbine meter
- ρ - determined from temperature dependent thermal properties



Friction Factor Uncertainty

$$\sigma_{0GPM} = \sqrt{PTAccuracy^2}$$

$$\sigma_{xGPM} = \sqrt{PTAccuracy^2 + \sigma_{Means}^2}$$

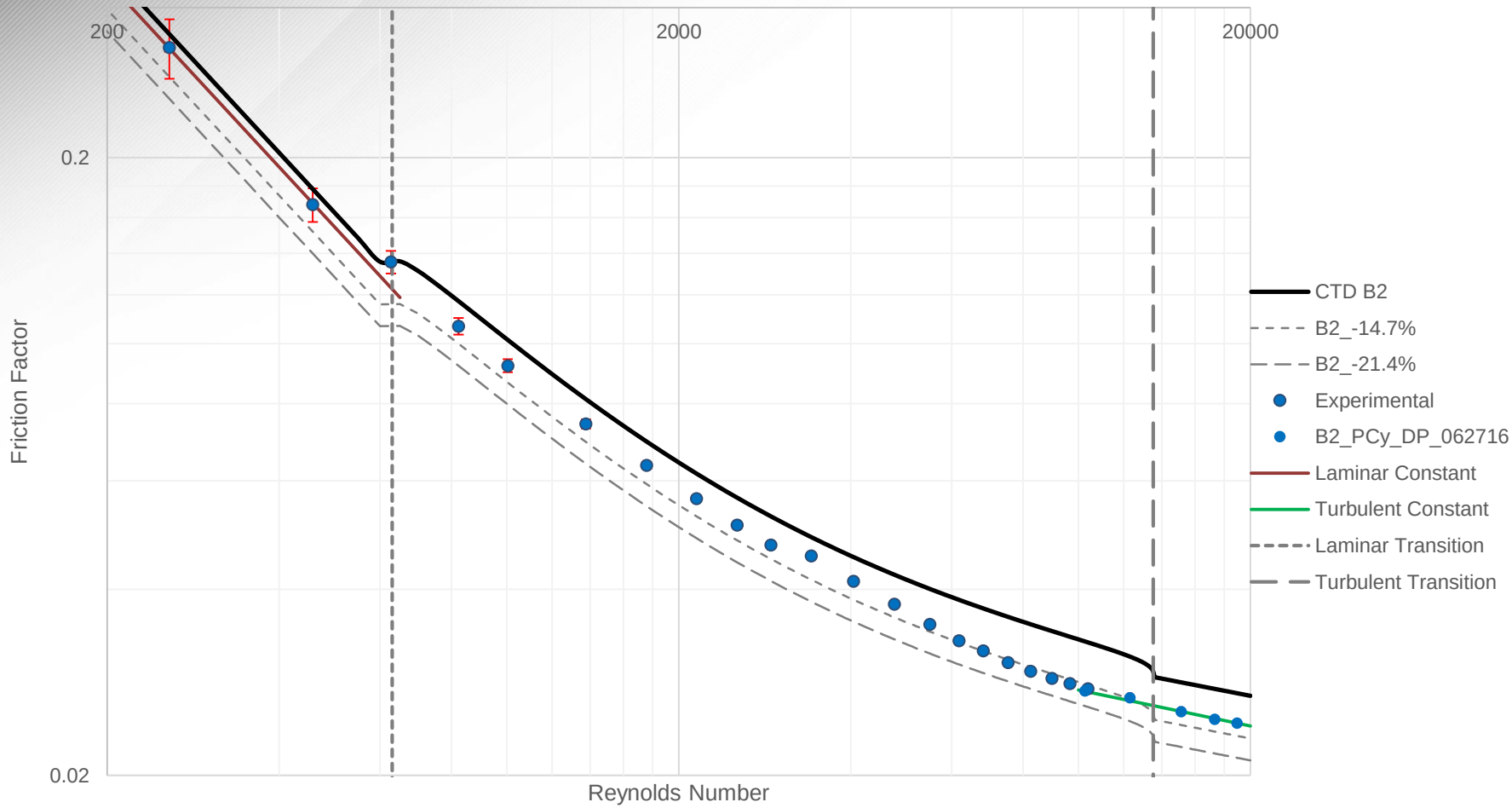
$$\sigma_{xGPM-NoFlow} = \sqrt{\sigma_{0GPM}^2 + \sigma_{xGPM}^2}$$

$$\sigma_f = f\sqrt{\left(\frac{\sigma_{\Delta P}}{\Delta P}\right)^2 + \left(\frac{\sigma_V}{V}\right)^2}$$

Uncertainty in friction factor is comprised of

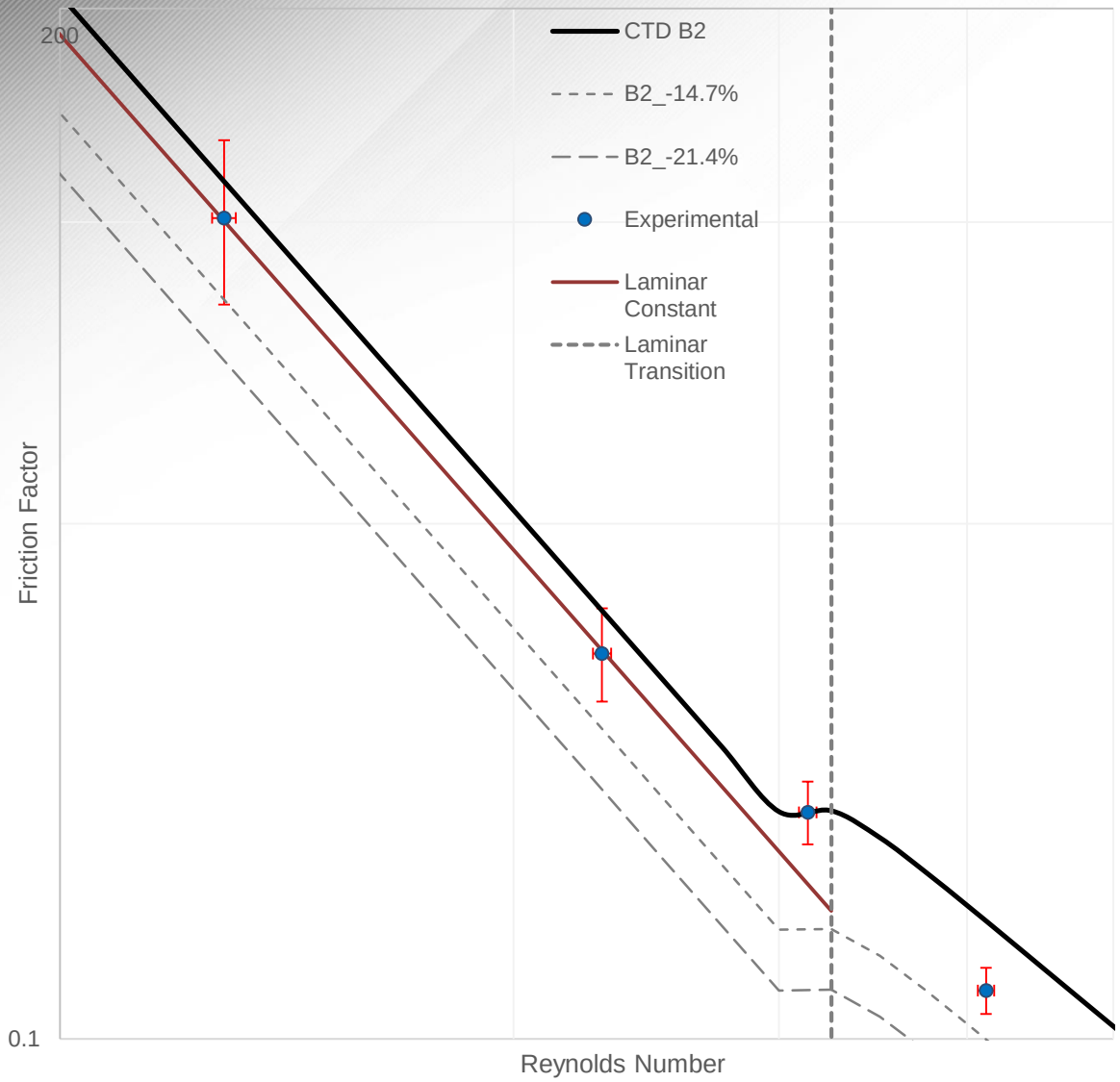
- Pressure transducer accuracy
- Repeated measurements
- Uncertainty in fluid velocity.

P-Cy Results



Re 250-19000

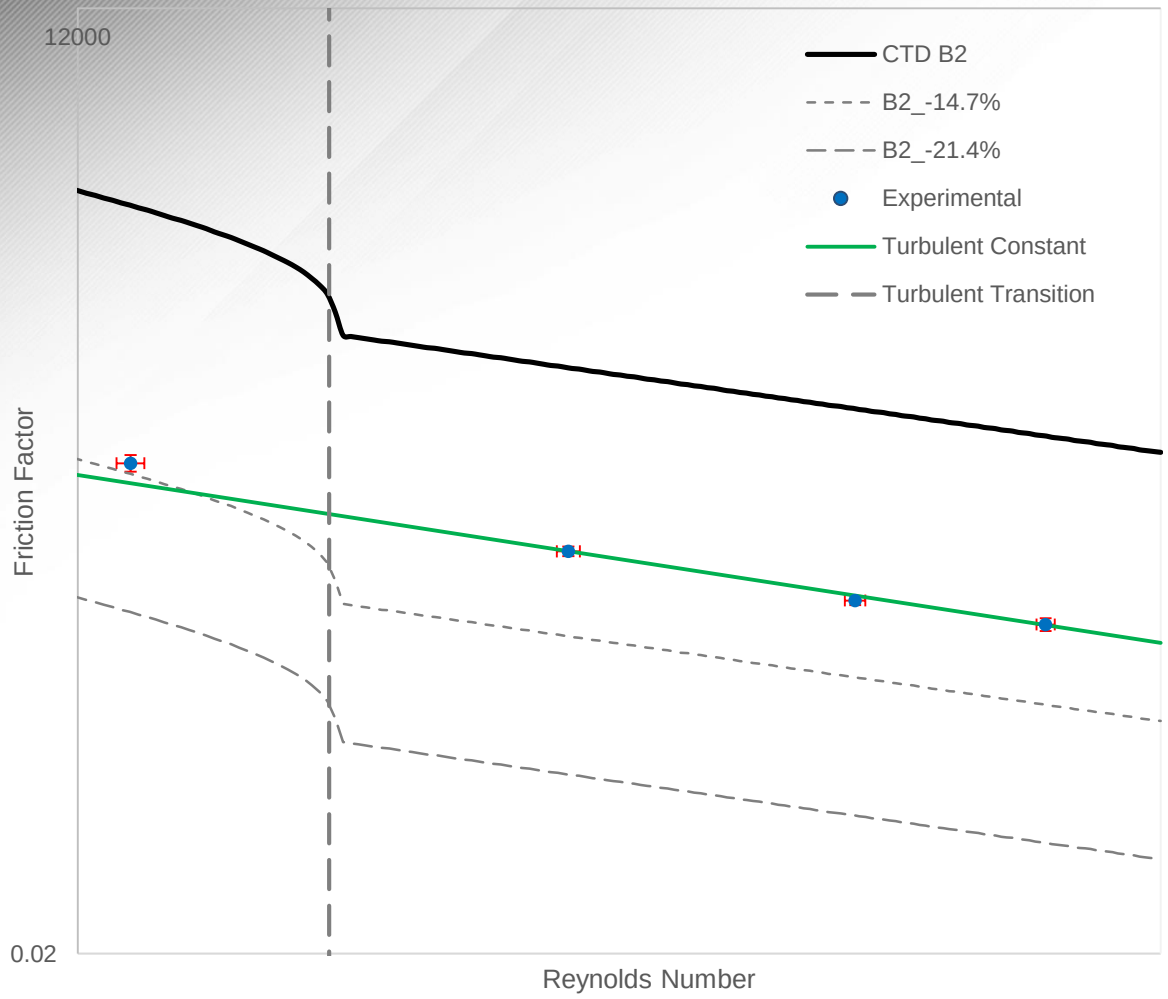
P-Cy Results



$$f = \frac{77.21}{Re}$$

Calculated laminar constant of 77.21 compared to CTD prediction of 81.26

P-Cy Results

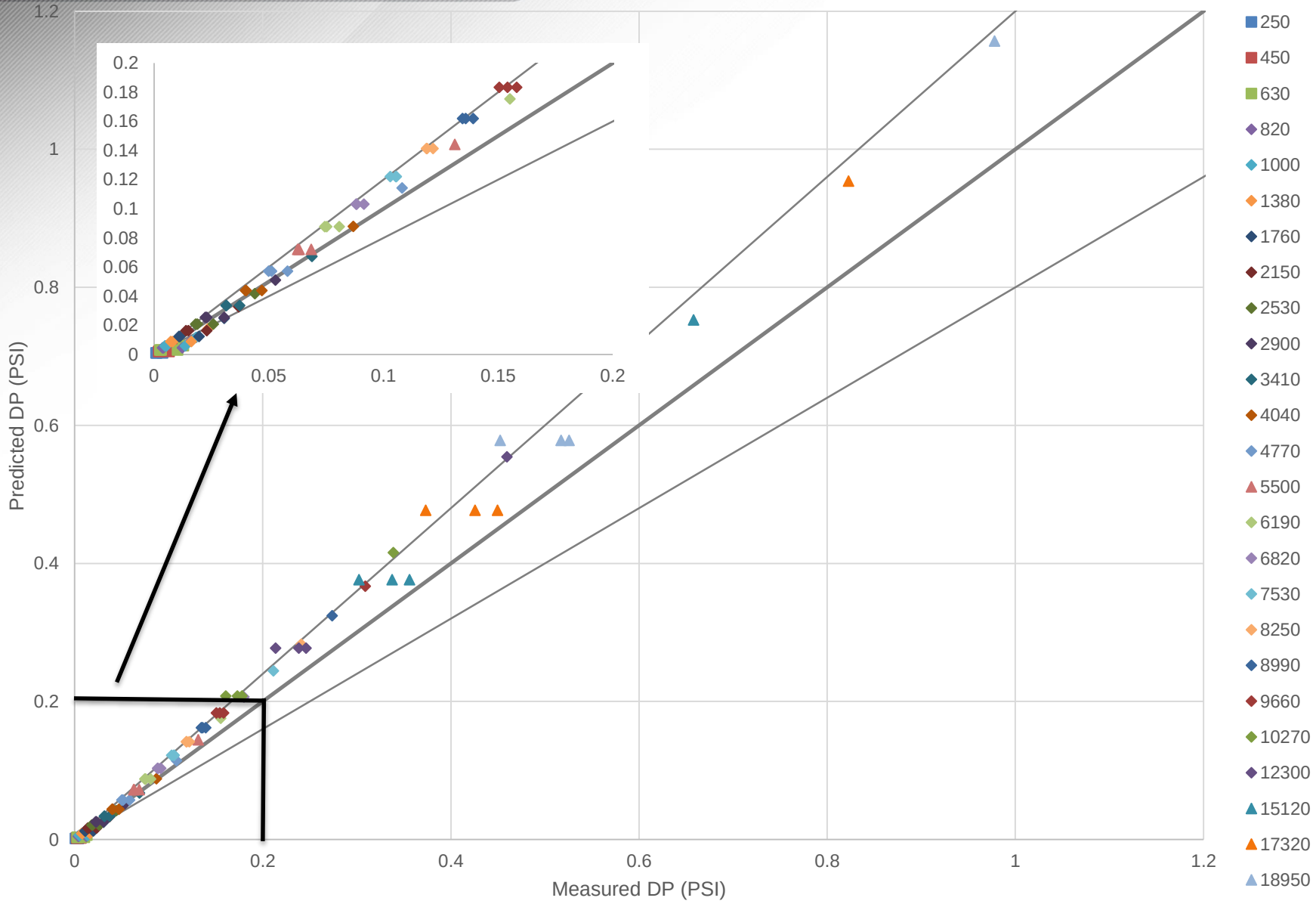


$$f = \frac{0.165}{Re^{0.195}}$$

Calculated turbulent constant of 0.165 compared to CTD prediction of 0.16

CTD assumes value of 0.18 for exponent of Re

P-Cy Results


Predicted DP (PSI)
Measured DP (PSI)
0
0.2
0.4
0.6
0.8
1
1.2
0.02
0.04
0.06
0.08
0.1
0.12
0.14
0.16
0.18
0.05
0.15
250
450
630
820
1000
1380
1760
2150
2530
2900
3410
4040
4770
5500
6190
6820
7530
8250
8990
9660
10270
12300
15120
17320
18950

Summary

- Generated experimental data set for simulation validation of SFR fuel bundle
- Experimental friction factor compared to CTD correlation
  - Values from high accuracy DP transducer found to be in good agreement

DOE Acknowledgement

- This material is based upon work supported by the Department of Energy under Award Number DE-NE0008321.

- “This report was prepared as an account of work sponsored by an agency of the United States Government. Neither the United States Government nor any agency thereof, nor any of their employees, makes any warranty, express or implied, or assumes any legal liability or responsibility for the accuracy, completeness, or usefulness of any information, apparatus, product, or process disclosed, or represents that its use would not infringe privately owned rights. Reference herein to any specific commercial product, process, or service by trade name, trademark, manufacturer, or otherwise does not necessarily constitute or imply its endorsement, recommendation, or favoring by the United States Government or any agency thereof. The views and opinions of authors expressed herein do not necessarily state or reflect those of the United States Government or any agency thereof.”

Questions


AREVA

Heated Bundle Test in the Fuel Cooling Test Facility (FCTF)

Kelly Duggan
Test Engineer, Richland WA

ANS Winter Conference November 8th 2016

AREVA

Outline

- FCTF
  - Test loop Modifications
- Test and hardware specifications
- Test loop operations
- Test loop setup
- Test results

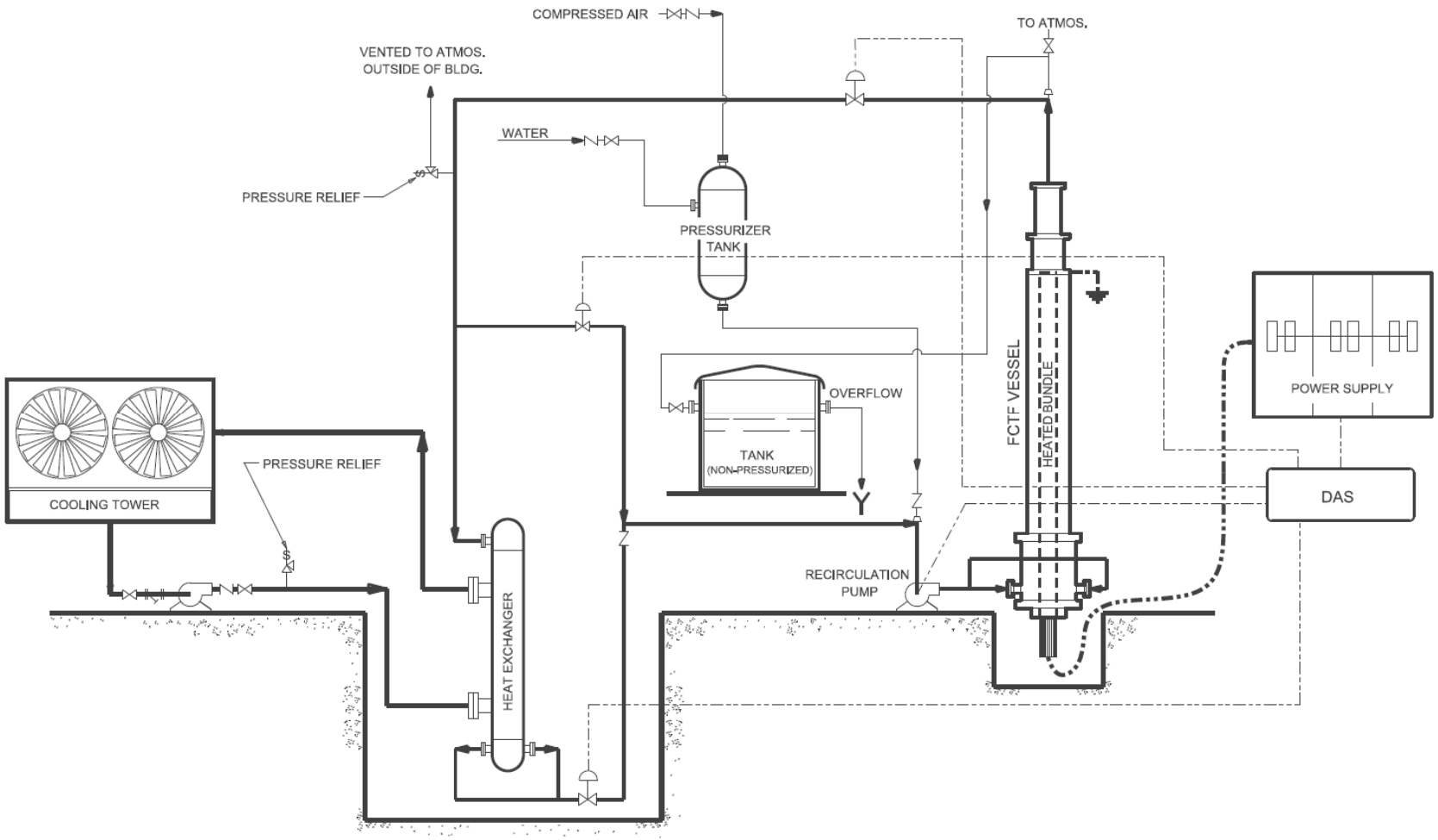
Property of AREVA NP - © AREVA NP
All rights reserved, see liability notice

Heated Bundle Test in the FCTF

- **Fuel Cooling Test Facility (FCTF)**
  - **Designed to simulate post-LOCA conditions**
    - Spray heat transfer for BWR bundles
    - Reflood testing for PWR bundles
- **Available hardware**
  - **High power supply (~600 KW available electric power)**
  - **Multiple pressure vessels**
  - **High capacity heat exchangers and cooling tower to remove heat**
- **Unique set up to provide experienced engineering services**
- **Objective of the test:**
  - ***"Measure thermal distribution and pressure drop with two different ducts under steady state conditions and provide data for CFD validation"***

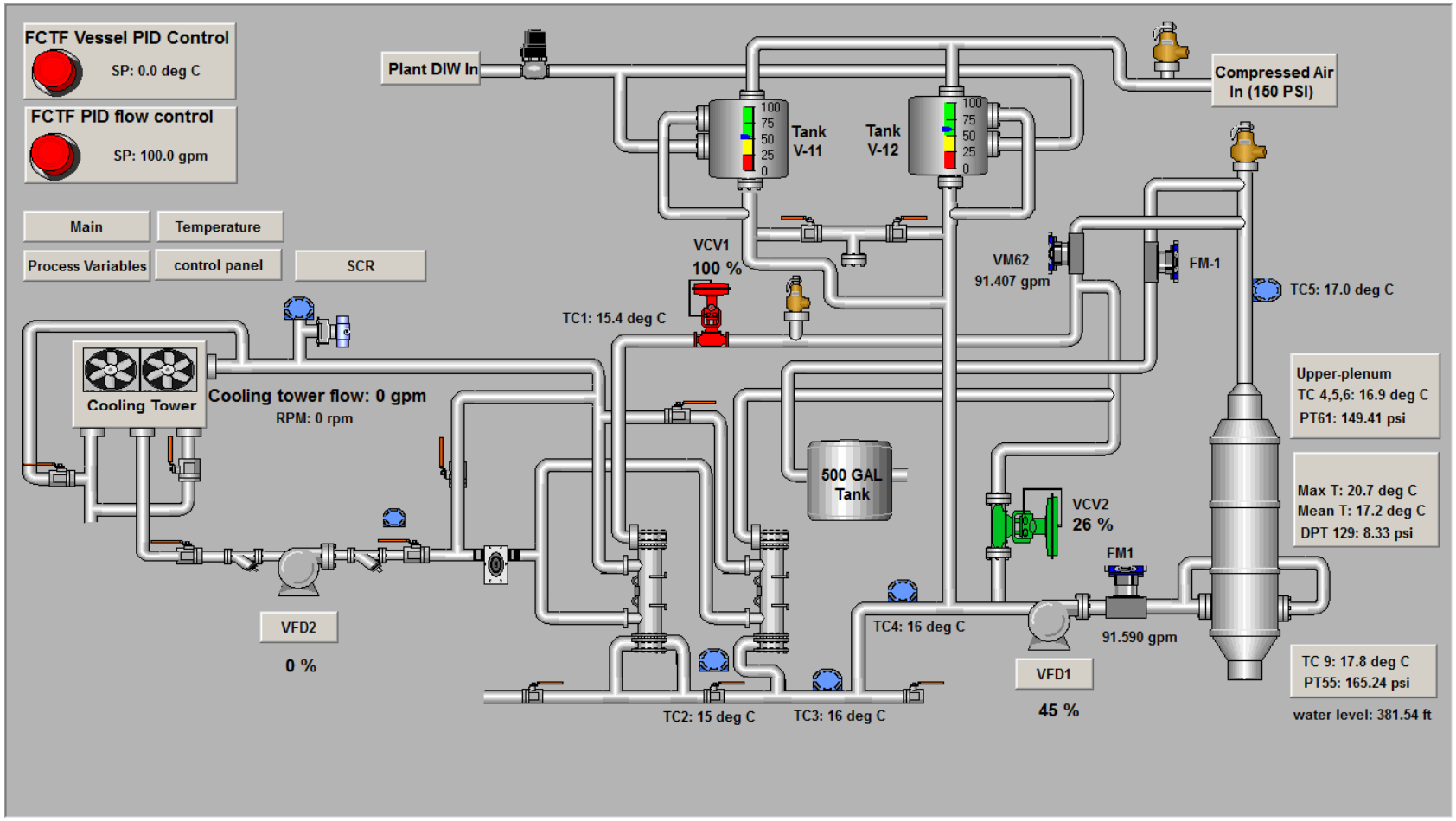
Property of AREVA NP - © AREVA NP
All rights reserved, see liability notice

FCTF Piping Schematic



Property of AREVA NP - © AREVA NP
All rights reserved, see liability notice

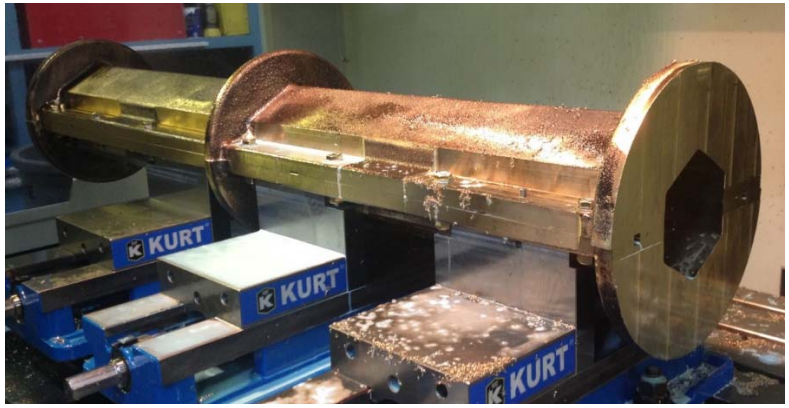
FCTF Data Acquisition Modifications

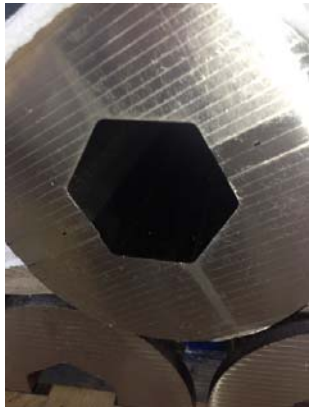


Property of AREVA NP - © AREVA NP
All rights reserved, see liability notice

Heated Bundle Fabrication (provided by TerraPower)

- **Ducts are constructed from bronze clamshell axial sections**
  - **Duct instrumentation includes thermocouples at inner wall/fluid interface and pressure taps on duct face walls**
  - **Beginning of Life non deformed duct**
  - **End Of Life deformed internal faces to simulate EOL conditions**







Property of AREVA NP - © AREVA NP
All rights reserved, see liability notice

Heated Bundle Fabrication

- **TerraPower supplying heated bundle test section equipment**
- **Bundles are 61 wire wrapped pin design**
  - **19 STERN heater rods**
    - 30 kW STERN heaters with 1.7 m cosine power profile heated length
    - Thermocouples embedded in heater wall at axial and azimuthal positions
    - Status: Heating element assembly complete. Thermocouple installation underway
  - **42 Non-heated pins**
    - Fabricated from stock stainless steel tubing
    - Contain thermocouples and pressure taps for internal bundle pressure measurements
    - Status: Machined endcaps complete. Installation of pressure tubes underway



Mock-up heater section for wire wrap attachment



Mock-up cross section below heating filament

Property of AREVA NP - © AREVA NP
All rights reserved, see liability notice

Heated Bundle Assembly



Property of AREVA NP - © AREVA NP
All rights reserved, see liability notice

Test Loop Assembly



Duct with instrumentation and wrapped in insulation

Property of AREVA NP - © AREVA NP
All rights reserved, see liability notice

Test Loop Assembly



Lower duct into main loop pipe

Property of AREVA NP - © AREVA NP
All rights reserved, see liability notice

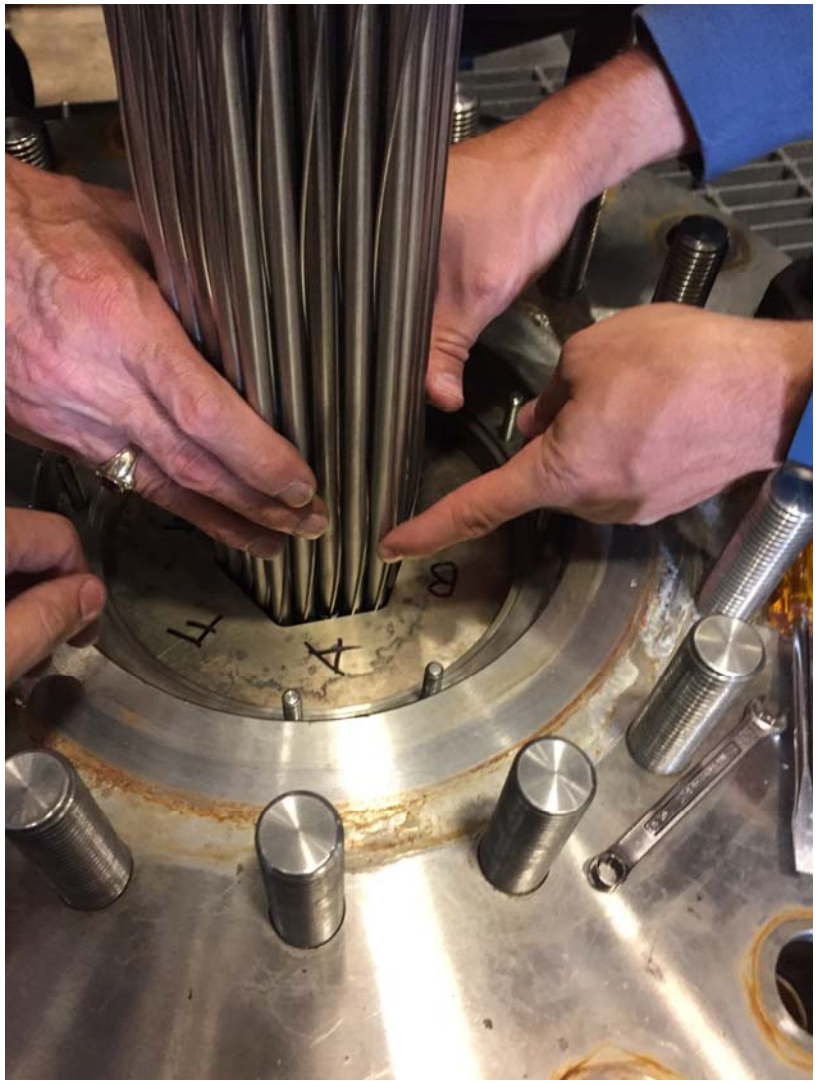
Test Loop Assembly



Loop assembly with duct installed

Property of AREVA NP - © AREVA NP
All rights reserved, see liability notice

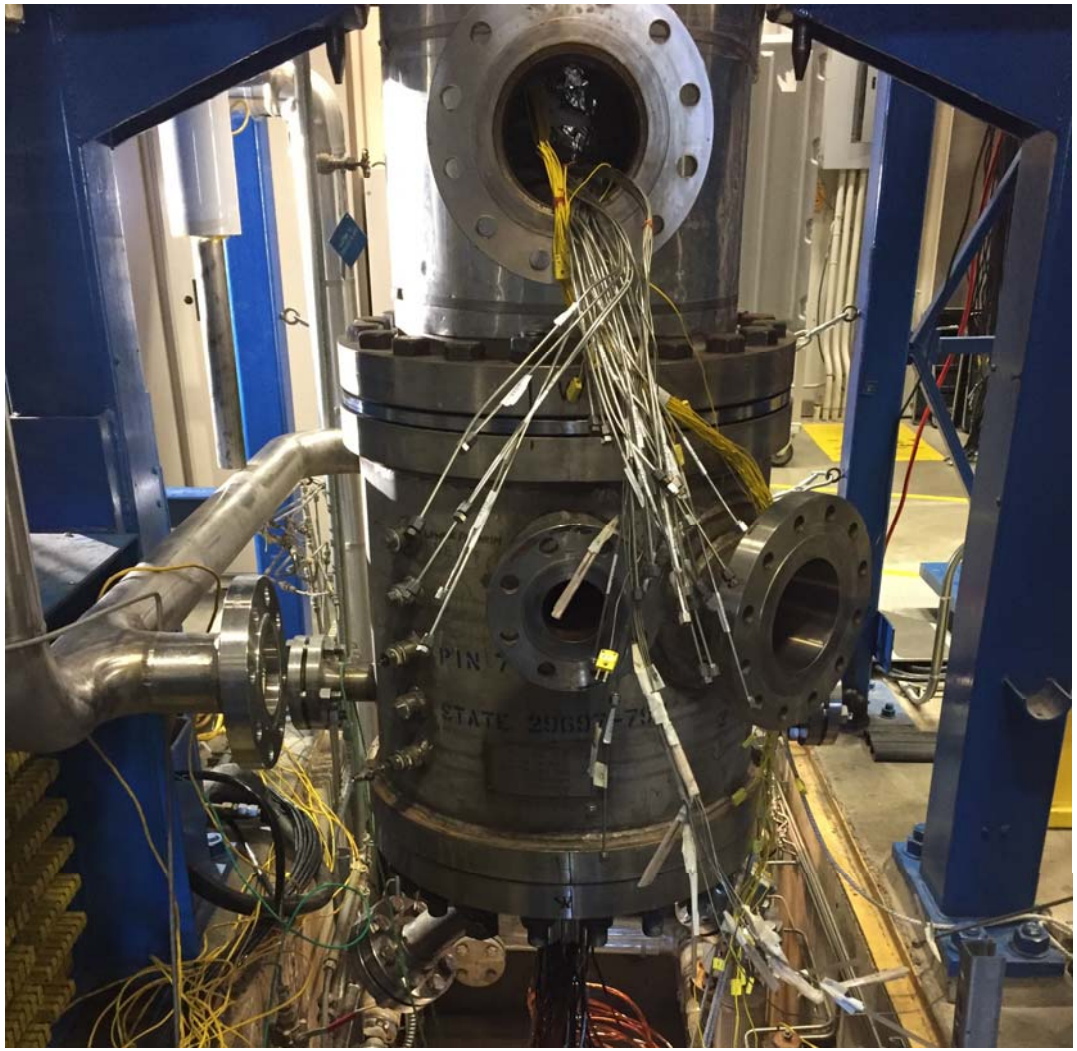
Test Loop Assembly



Lowering the test bundle into duct

Property of AREVA NP - © AREVA NP
All rights reserved, see liability notice

Test Loop Assembly



Loop assembled: Ready for instrumentation hookup

Property of AREVA NP - © AREVA NP
All rights reserved, see liability notice

Measurement Requirements

- 40 pressure taps
  - 30 on the duct, axial and azimuthal distribution
  - 10 in the non-heated tubes to measure pressure inside the bundle
- ~360 thermocouples
  - 152 thermocouples in the cladding of heater rods
  - Non-heated tubes
  - Duct inner surface
  - Duct outside surface to evaluate losses
- Control and report flow and inlet temperature through the test section

Property of AREVA NP - © AREVA NP
All rights reserved, see liability notice

Test specifications

- **Specifications defined by TerraPower with other participant collaboration for consistency and comparisons with flow field**
- **Set points description**
  - **Inlet temperature controlled to steady state before test initiated**

Re	Mass flow [kg/s]	Q rod [W]	Q bundle total [W]	Average EOHL Temp [K]	Max Wall Temp (CFD) [K]	Max Fluid out (CFD) [K]	Pressure Drop across bundle [Pa]
15000	7.03	18000	342000	317.	385.	365.	57306
20000	9.37	24000	456000	317.	394.	367.	83616
25000	11.72	30000	570000	317.	398.	365.	115341

Property of AREVA NP - © AREVA NP
All rights reserved, see liability notice

Test Measurements and Uncertainties

- **Mass flow measurements with two vortex flow meters**
  - 0 to 250 gpm +/- 2.5 gpm
- **30 Differential Pressure measurements**
  - Instrument Range
    - 0 to 12,400 Pa +/- 40Pa
    - 0 to 174,000 Pa +/- 540 Pa
- **Two Mass flow measurements with two vortex flow meters**
- **~20 Type K Thermocouples**
  - 0 to 200 ºC +/- 2 ºC
- **~350 Type K Thermocouples in the heated and non heated pins**
  - +/- 1.3 ºC

Property of AREVA NP - © AREVA NP
All rights reserved, see liability notice

Test Measurement Challenges

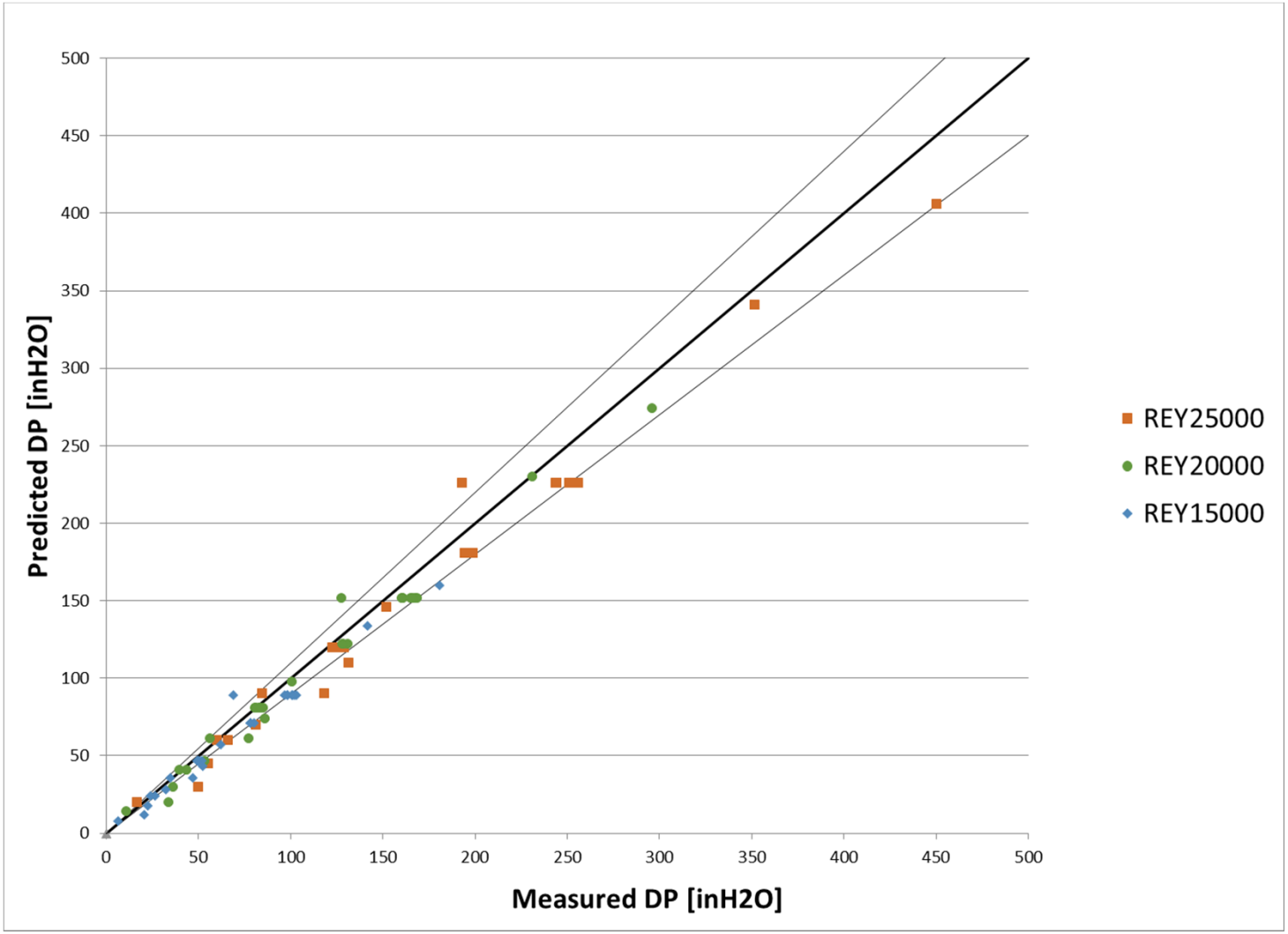
- The Thermocouples in heated pins measuring heater temperatures. Not useful for water temperature

- Pressure tap instrumented pins connected with 1/16” tubing. Intermittent measurements due to difficulty overcoming capillary effect.

Property of AREVA NP - © AREVA NP
All rights reserved, see liability notice

Test Results Pressure Drop Comparison

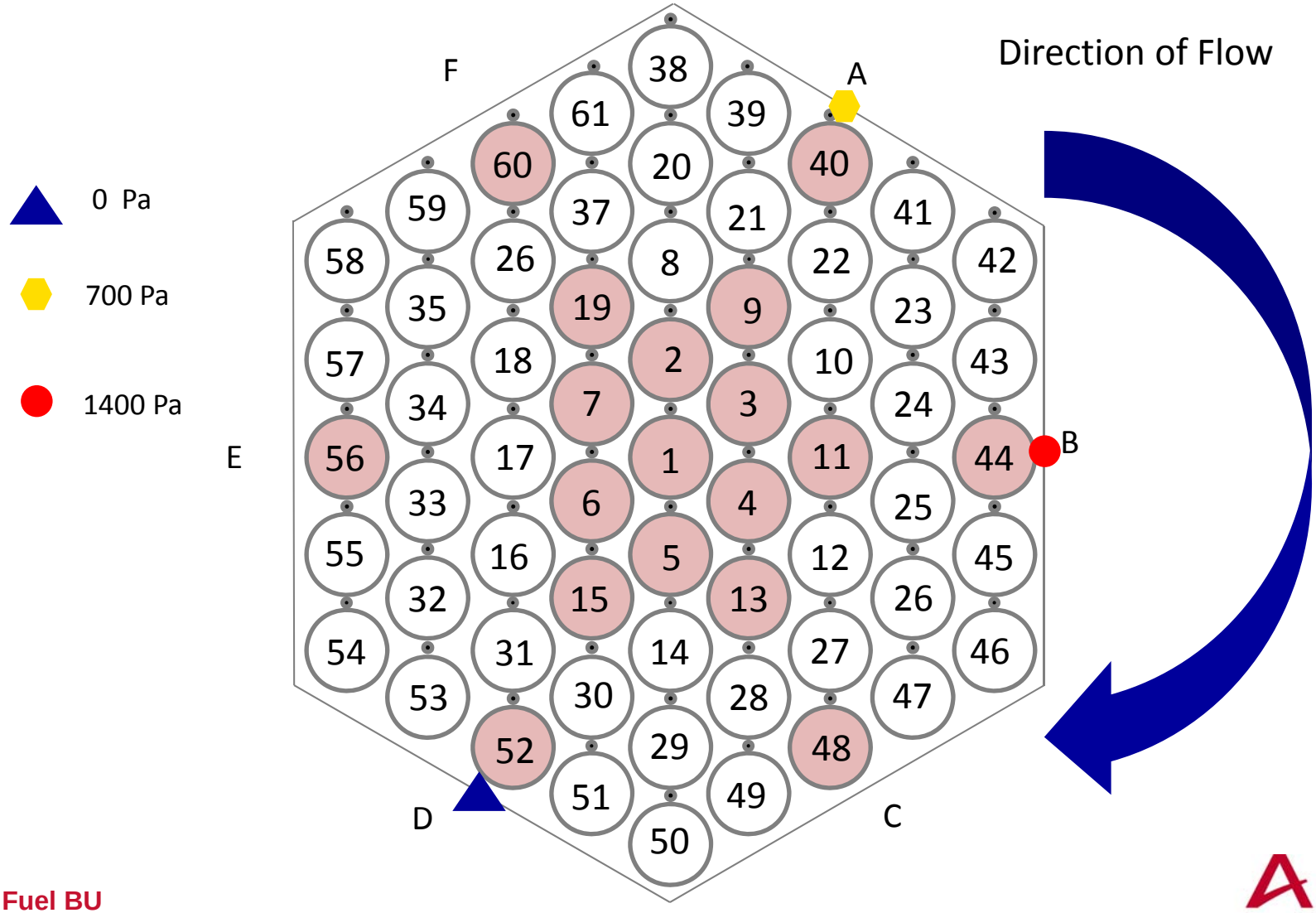
Predictions based on data published by Nuclear Engineering and Design: "Evaluation of existing correlations for predictions of pressure drop in wire-wrapped hexagonal array pin bundles", 2013



Property of AREVA NP - © AREVA NP
All rights reserved, see liability notice

Test Results Pressure Wave:

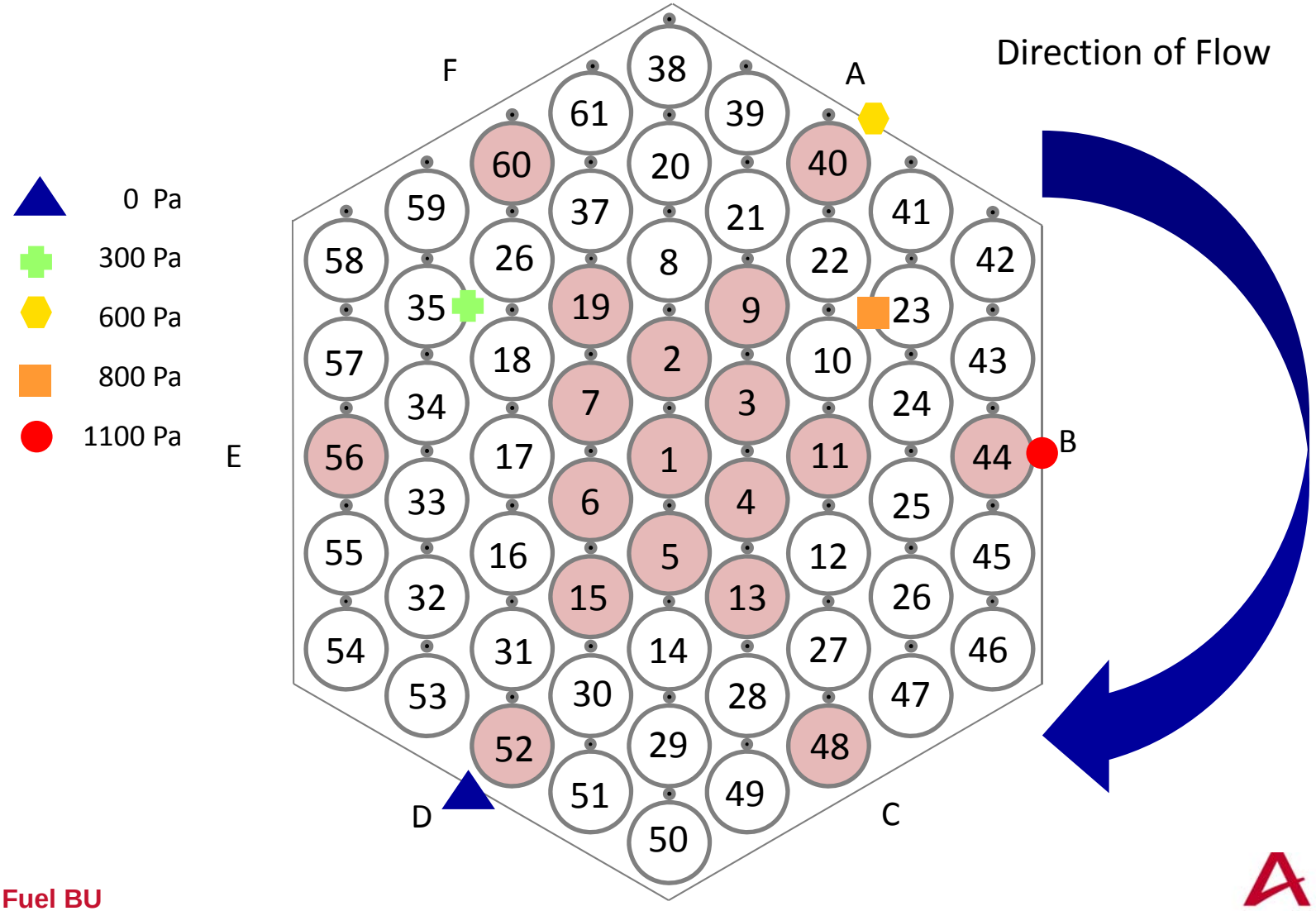
Deformed Duct, Rey=20,000, No Power, Begin Heated Length



Property of AREVA NP - © AREVA NP
All rights reserved, see liability notice

Test Results Pressure Wave:

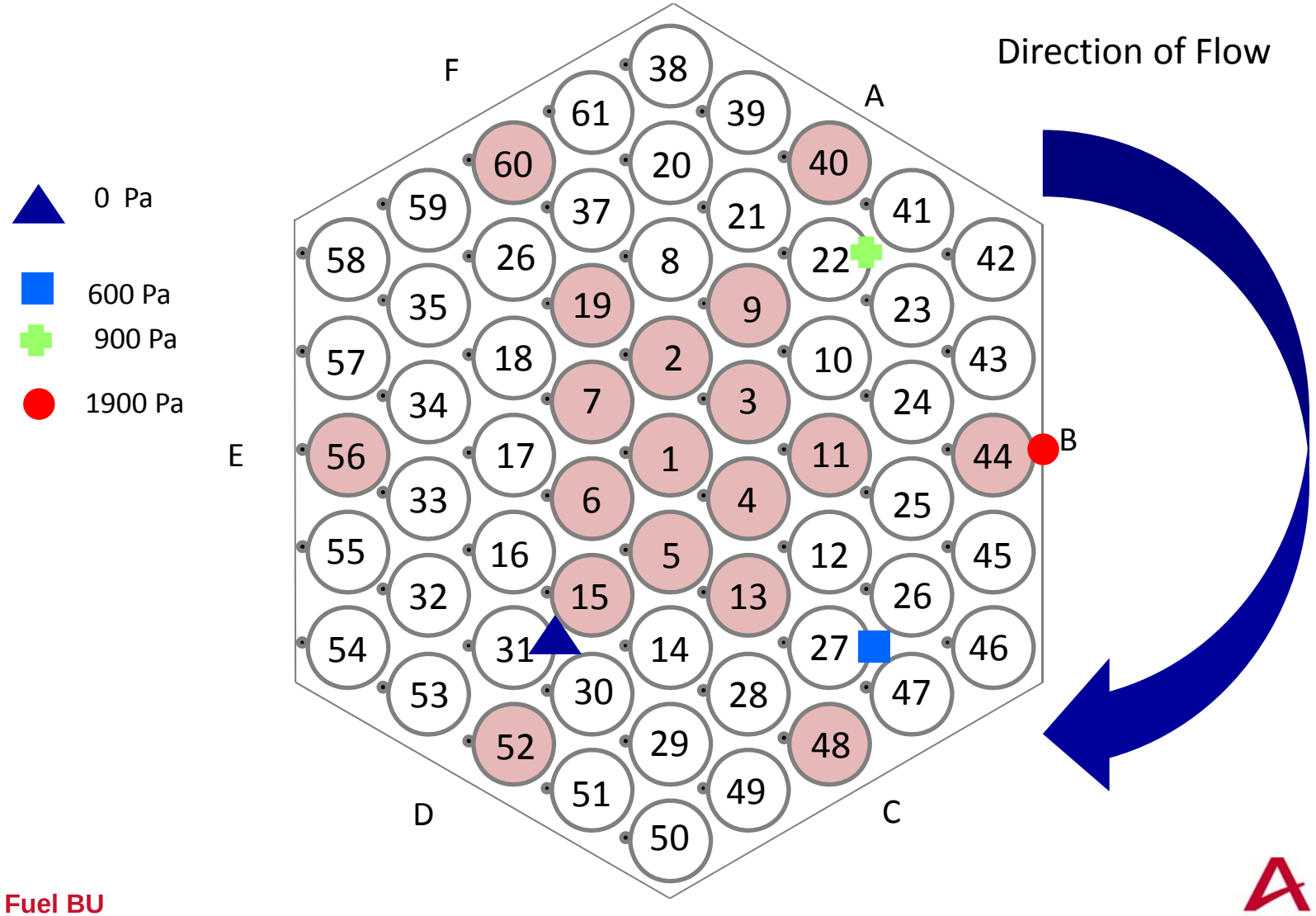
Deformed Duct, Rey=20,000, No Power, 3 Pitched into Heated Length



Property of AREVA NP - © AREVA NP
All rights reserved, see liability notice

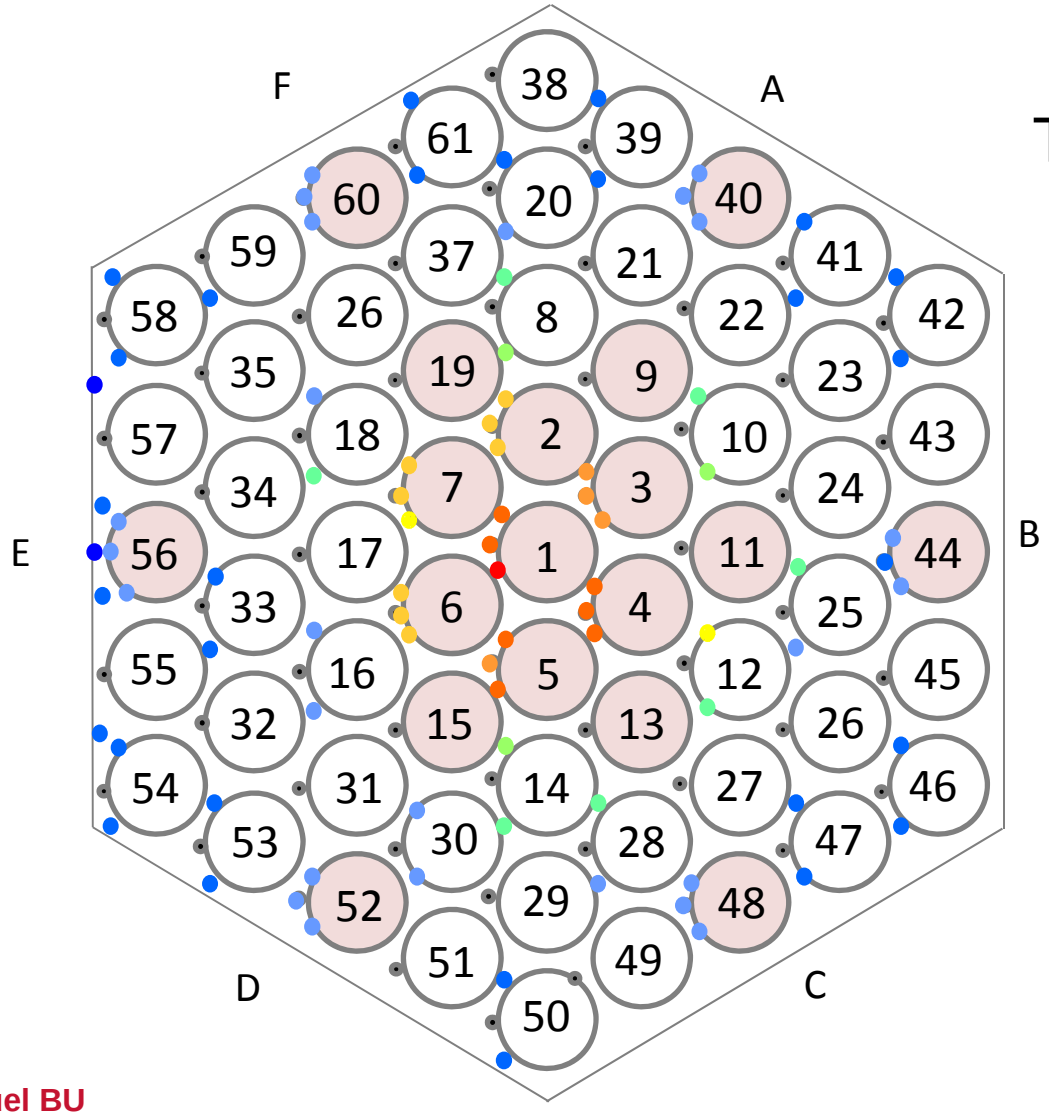
Test Results Pressure Wave:

Non-Deformed Duct, Rey=20,000, No Power, 0.75 Pitches above Heaters



Property of AREVA NP - © AREVA NP
All rights reserved, see liability notice

Test Results Non-Deformed Duct 0.75 above Heated Length



Temperature (C)

- 38-39
- 40-42
- 43-45
- 46-49
- 50-53
- 54-57
- 58-60
- 61-63
- 64-66
- 67

Property of AREVA NP - © AREVA NP
All rights reserved, see liability notice

END OF PRESTATION

Property of AREVA NP - © AREVA NP
All rights reserved, see liability notice

CFD Verification and Validation of Wire-Wrapped Pin Assemblies

Daniel Leonard

Brian Jackson

Michael Steer

Tom Reeves

Nate Salpeter (*AER Consulting*)

ANS Winter Meeting and Nuclear Technology Expo

November 6-10, 2016

Las Vegas, NV

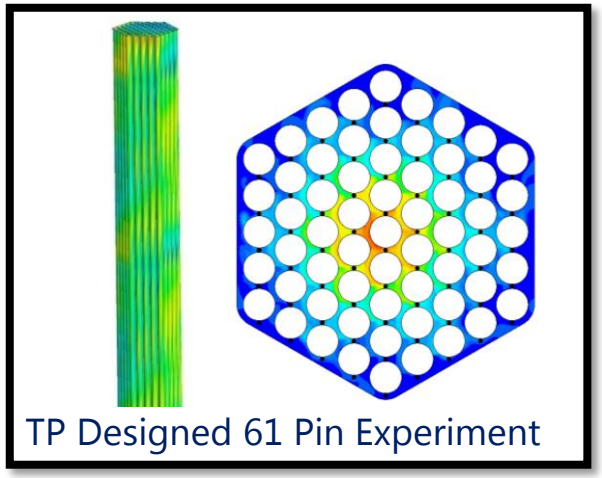
Copyright© 2016 TerraPower, LLC. All Rights Reserved.

Advanced Fuel Assembly Flow Characterization

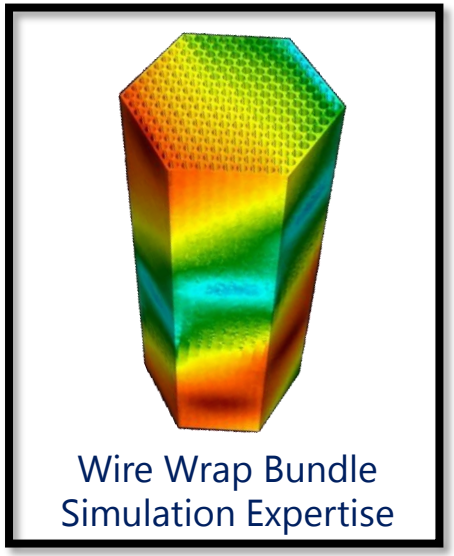
- DOE grant project consisting of experiments and numerical simulations of wire-wrapped bundles (non-deformed & deformed) for verification and validation of CFD tools

TerraPower

- Technical Lead
- Experiment Design
- **Industrial-Level Steady-State RANS Verification & Validation Simulations**



TP Designed 61 Pin Experiment



Wire Wrap Bundle Simulation Expertise

Argonne NATIONAL LABORATORY

- High Resolution (LES) Validation Simulations to be used as numerical 'experiment'

AREVA

- Programmatic Lead
- Heated Bundle Experiments in Water
- Pressure & Temperature Measurements



Heated Bundle Test Expertise



Flow Visualization Expertise

TEXAS A&M UNIVERSITY®

- Isothermal Bundle Experiments in P-Cymene
- Pressure & Laser Based Velocity Measurements

Copyright© 2016 TerraPower, LLC. All Rights Reserved.

Outline

- Objective
  - Industrial-Level Steady-State RANS Verification & Validation Simulations of non-deformed/deformed isothermal and heated bundles
- Code verification
- Solution verification & sensitivity studies (blind pre-test results)
- Solution validation (blind post-test results)
- Summary & future work

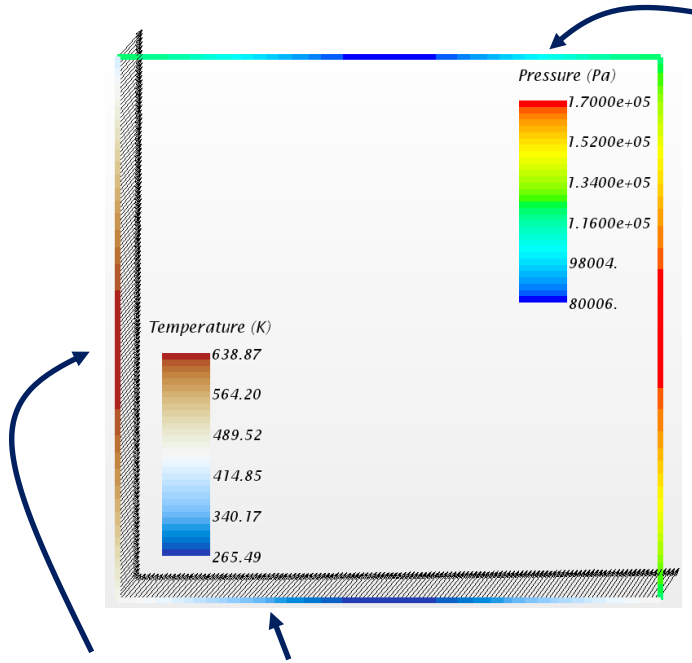
Copyright© 2016 TerraPower, LLC. All Rights Reserved.

Code Verification (Method of Manufactured Solutions)

Simple Case: 2D Subsonic Steady Ideal Gas Euler

Verification of a Compressible CFD Code using the Method of Manufactured Solutions, Roy et al. AIAA 2002

h	16	8	4	2	1
Cells	8x8	16x16	32x32	64x64	128x128



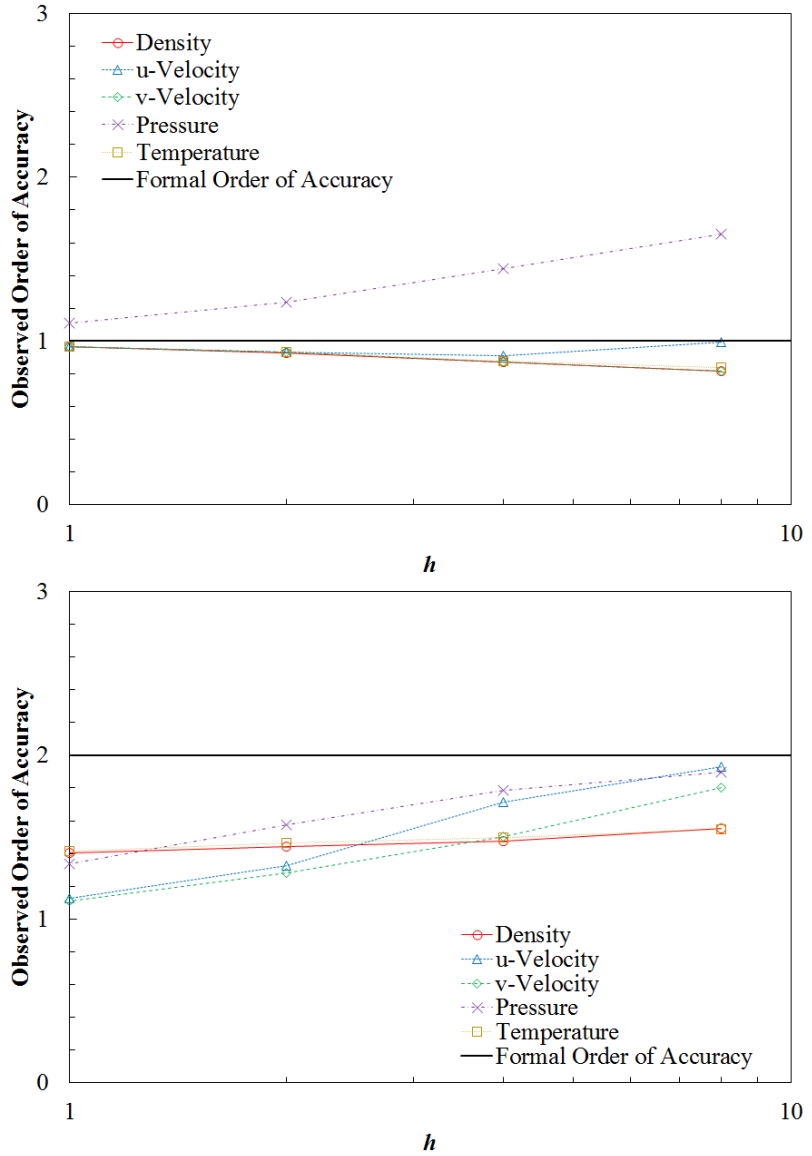
Pressure Outlets

- ***Specified Pressure with manufactured solution***
- ***Velocity & Temperature extrapolated from interior***

Velocity Inlets

- ***Specified Velocity & Temperature with manufactured solution***
- ***Pressure extrapolated from interior***

Note: Roy et al (2002) use over-specified boundaries which can't be done by a Star-CCM+ user



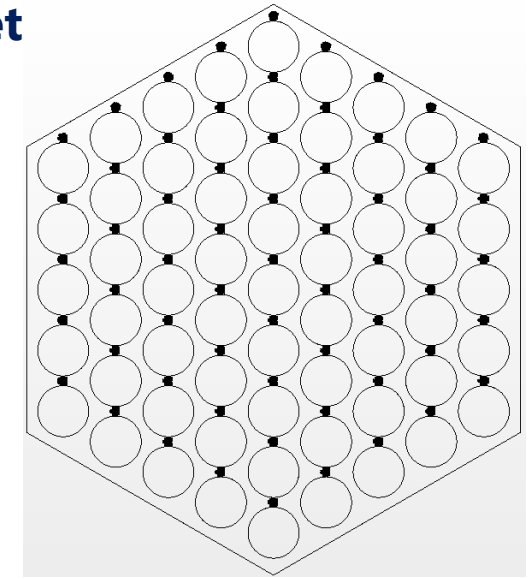
Copyright© 2016 TerraPower, LLC. All Rights Reserved.

TerraPower

Pre-Test Geometry

Isothermal Bundle
consistent with TAMU experiment design

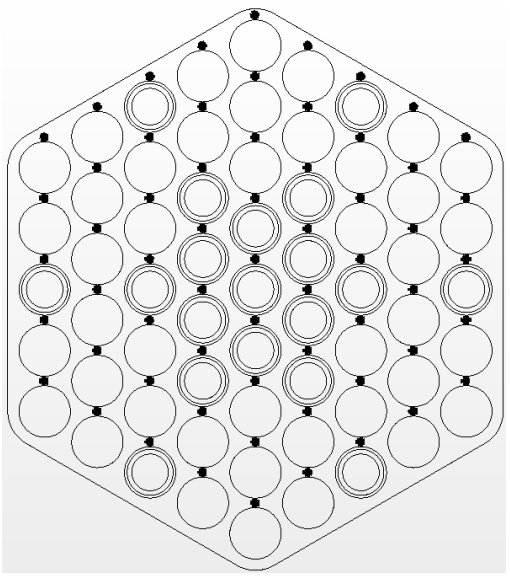
Outlet



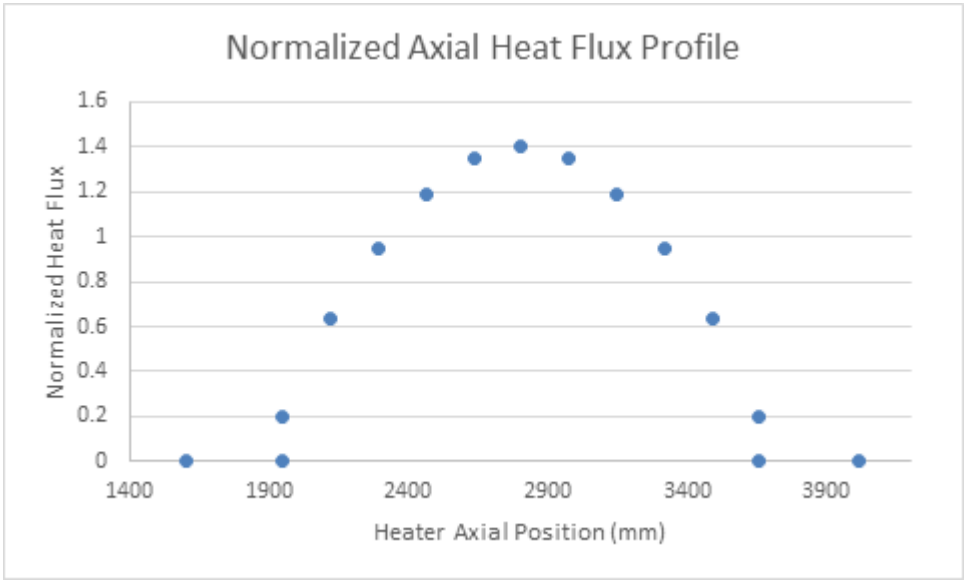
Inlet

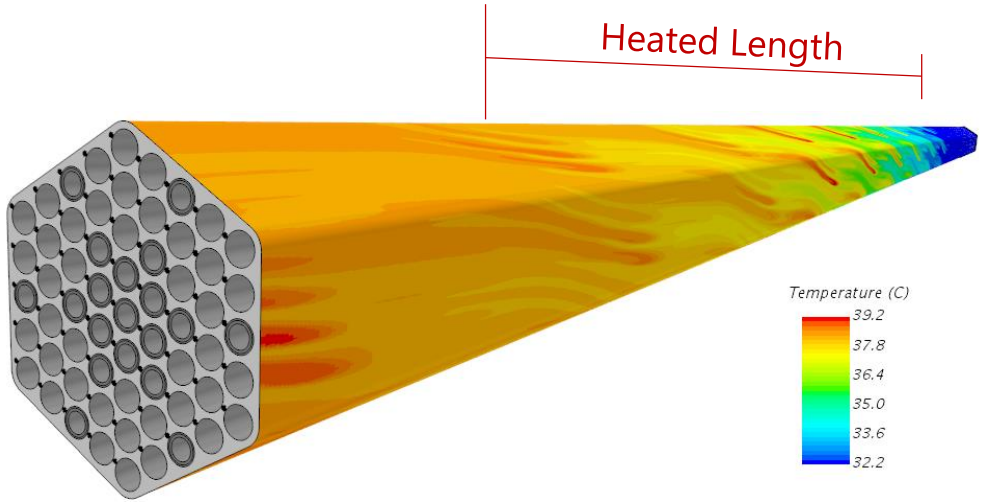
Duct Wall Gap = 0.77% of flat-to-flat
3.5 wire pitches
P-Cymene
Re = 20,000
P/D = 1.189

Heated Bundle
consistent with AREVA experiment design



Duct Wall Gap = 0.77% of flat-to-flat
13 wire pitches
6 heated pitches
19 heated pins (24 kW per pin)
Water
Re = 20,000
P/D = 1.18



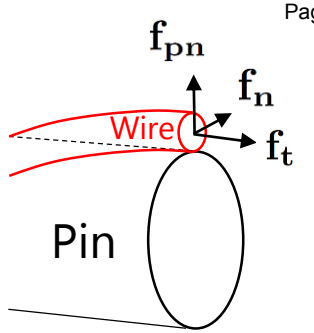


Copyright© 2016 TerraPower, LLC. All Rights Reserved.

TerraPower

Wire Wrap Modeling Approach

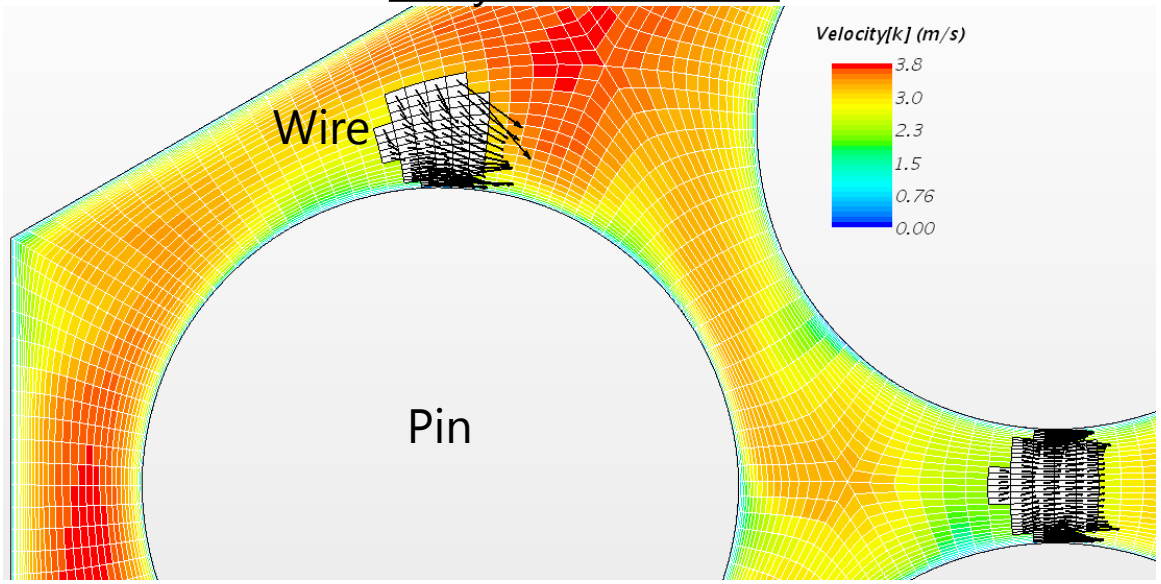
- Momentum Source to represent wire-wrapping
  - Applies body force per unit volume to the fluid momentum equation at cell locations of the wire wrap in place of a body-fitted mesh around the solid wire
  - Originally developed at Argonne National Lab [Hu & Fanning, 2011]
  - Forces are dictated by models based on the local velocity field



$$\mathbf{f} = \mathbf{f_n} + \mathbf{f_{pn}} + \mathbf{f_t}$$

Body Force

Body force vectors



- Momentum source is ideal for initial scoping studies of wire-wrap fuel assemblies
  - 20x speed-up relative to explicit wire resolved approach
  - Avoids complications of body-fitted meshing of wires
  - Quick turn-around time for design modifications

Copyright© 2016 TerraPower, LLC. All Rights Reserved.

TerraPower

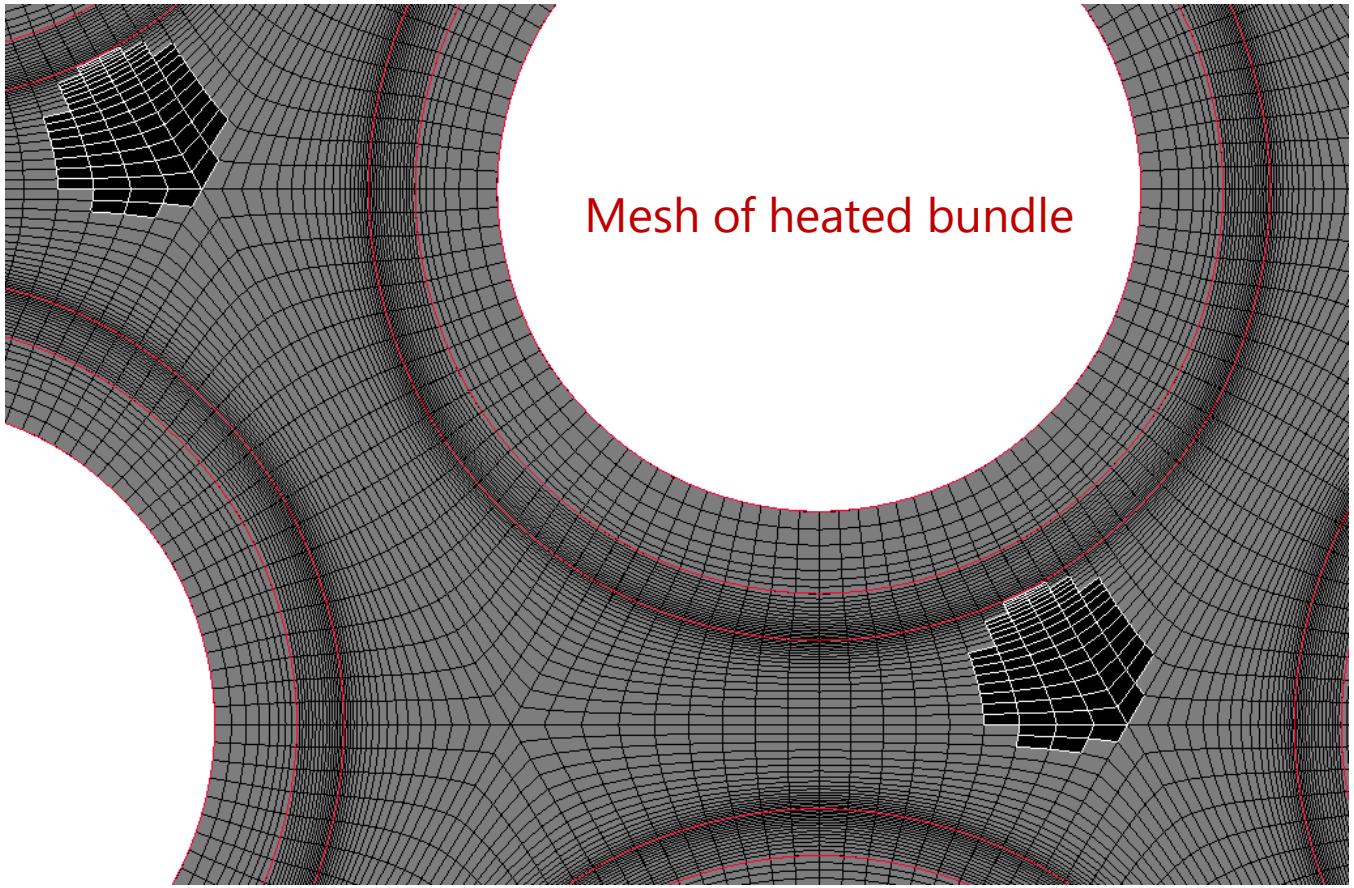
Pre-Test Solution Verification

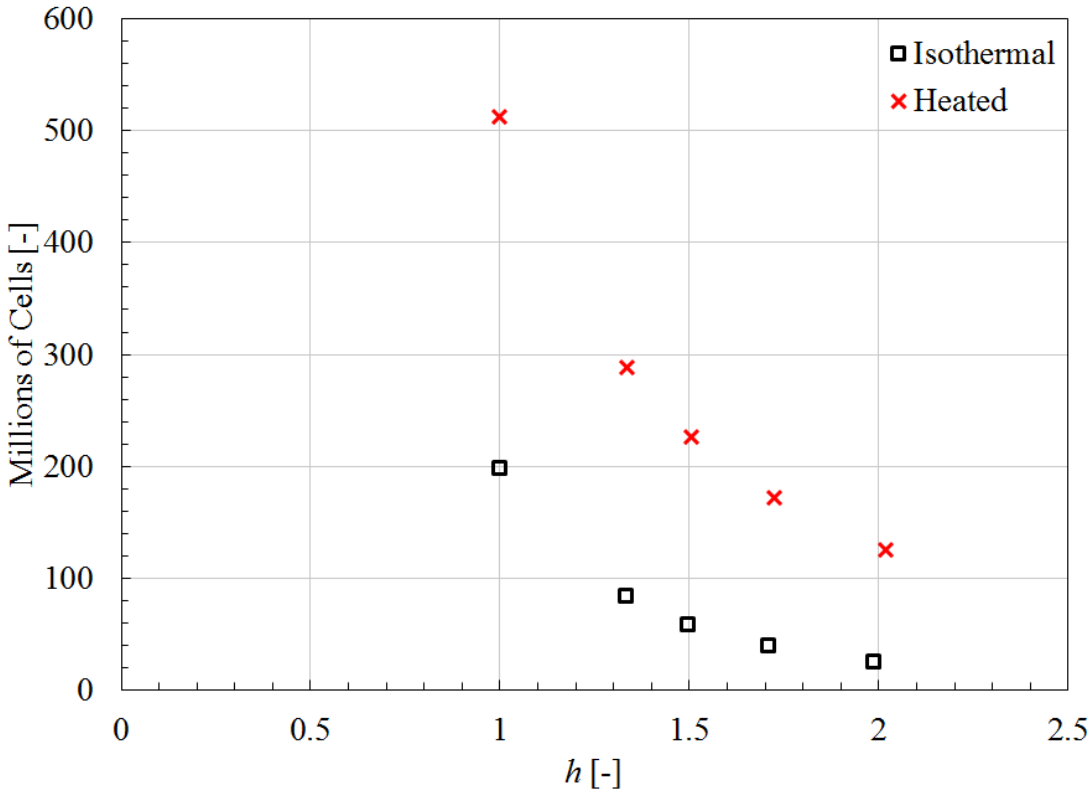
- Round-off, iterative, and statistical sampling errors estimated
  - Negligible Error
  - Had no appreciable effect on solution
- Conduct systematic mesh refinement and analyze variables of interest to determine if asymptotic range reached
- Perform Richardson extrapolation to formally estimate discretization error (not shown here)

Copyright© 2016 TerraPower, LLC. All Rights Reserved.

Pre-Test Meshes

- Fully structured meshes created with GridPro and systematically refined
- All-y^+ wall functions are used
- Average y^+ values less than 5.0 for all meshes

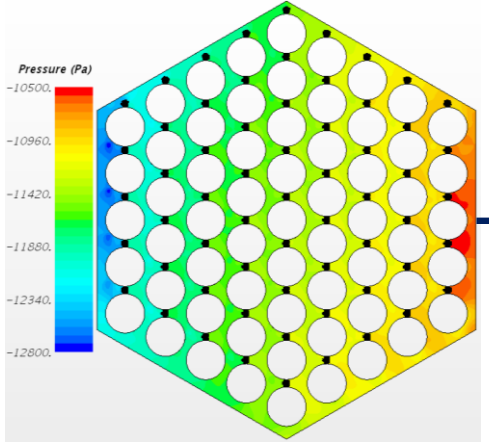




Copyright© 2016 TerraPower, LLC. All Rights Reserved.

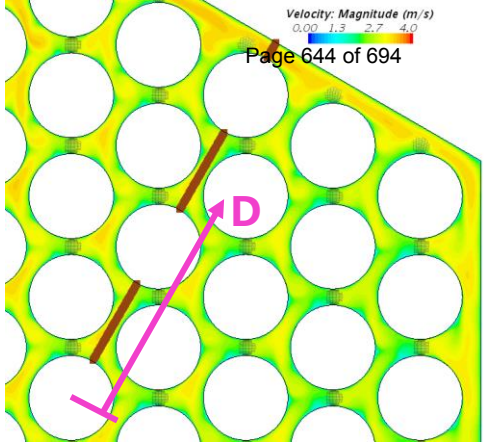
TerraPower

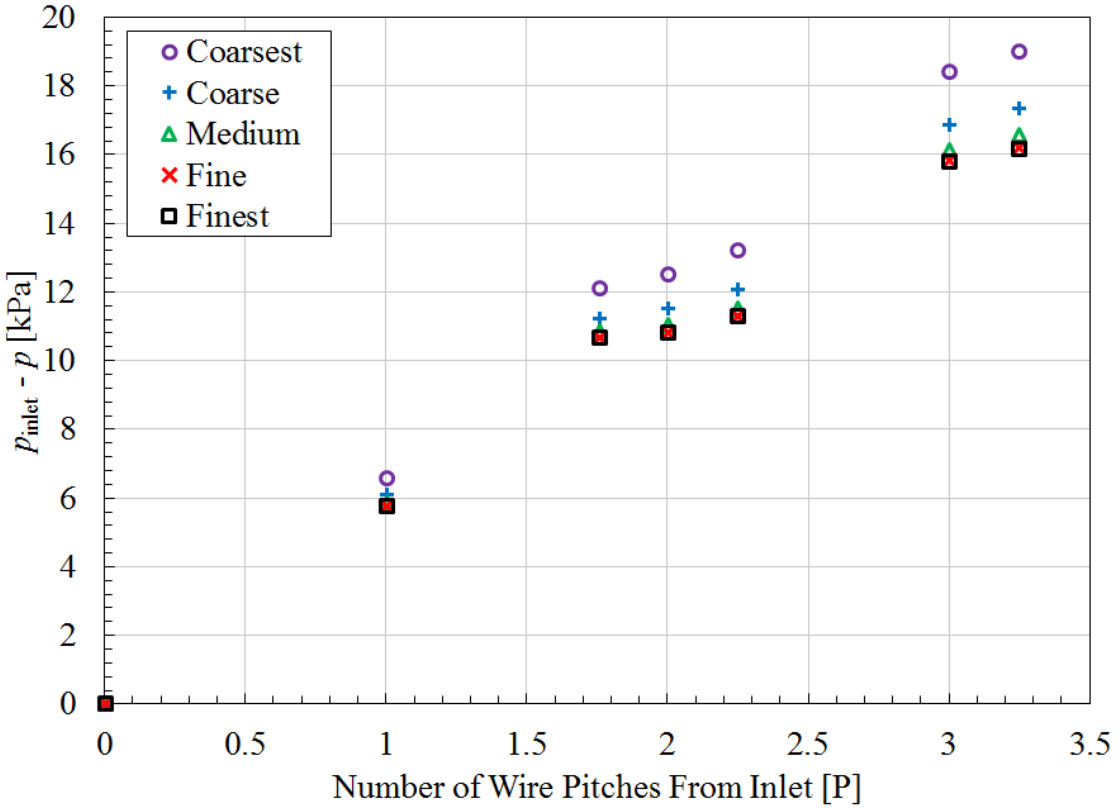
Isothermal Bundle Mesh Sensitivity



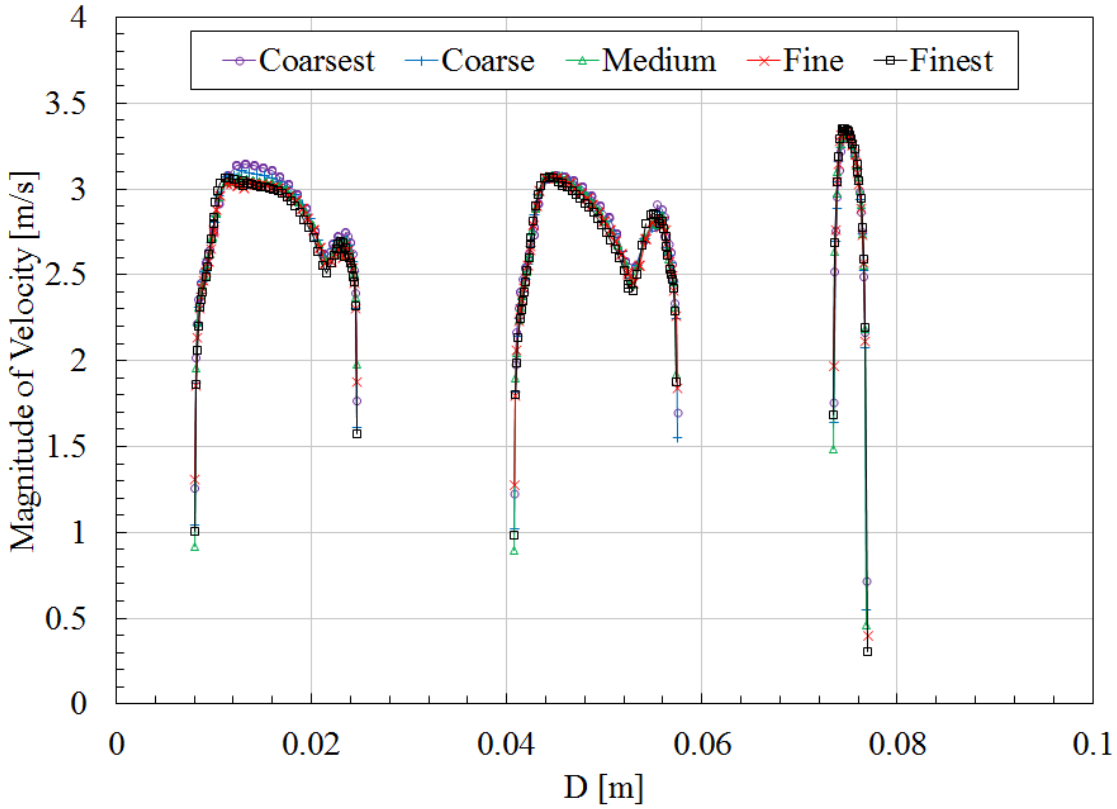
Pressure Tap
(Face B)

Notice the transverse pressure gradient





Duct Face B pressure drops show convergence by Fine mesh



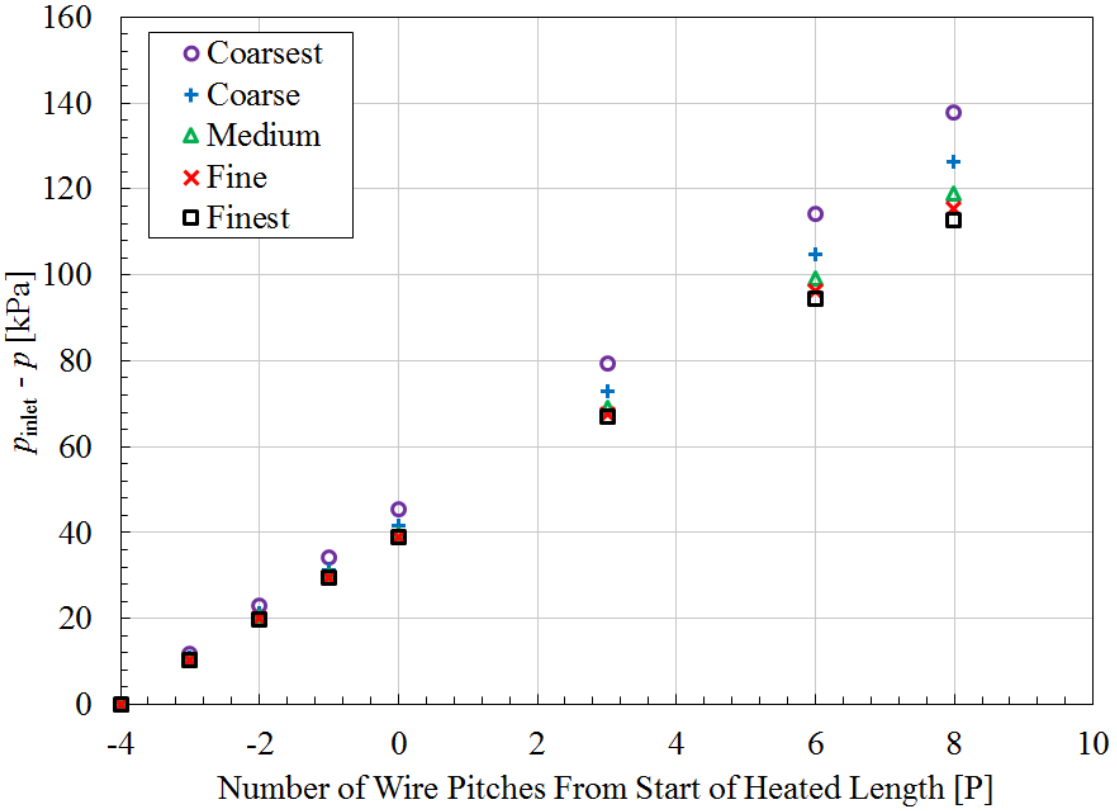
Velocity magnitude profiles show little variation with mesh size

Copyright© 2016 TerraPower, LLC. All Rights Reserved.

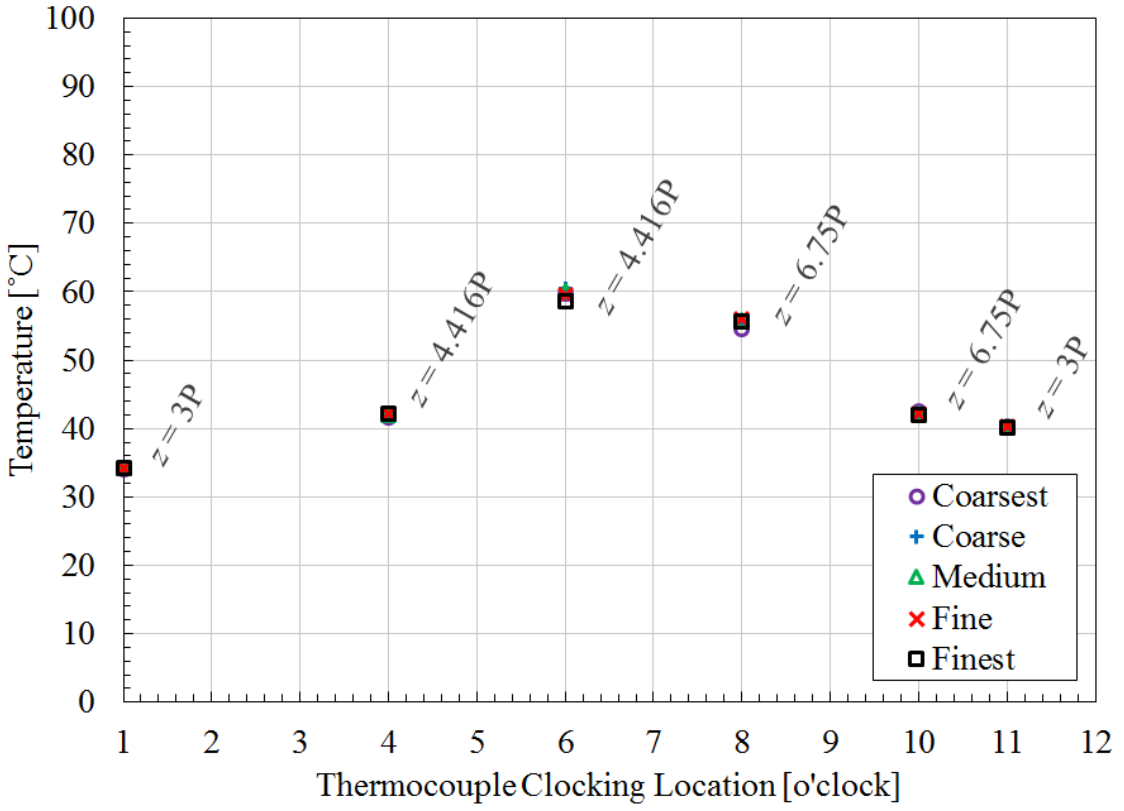
TerraPower

Heated Bundle Mesh Sensitivity

Sampled on duct wall (Face B)



Sampled on outer surface of unheated tube



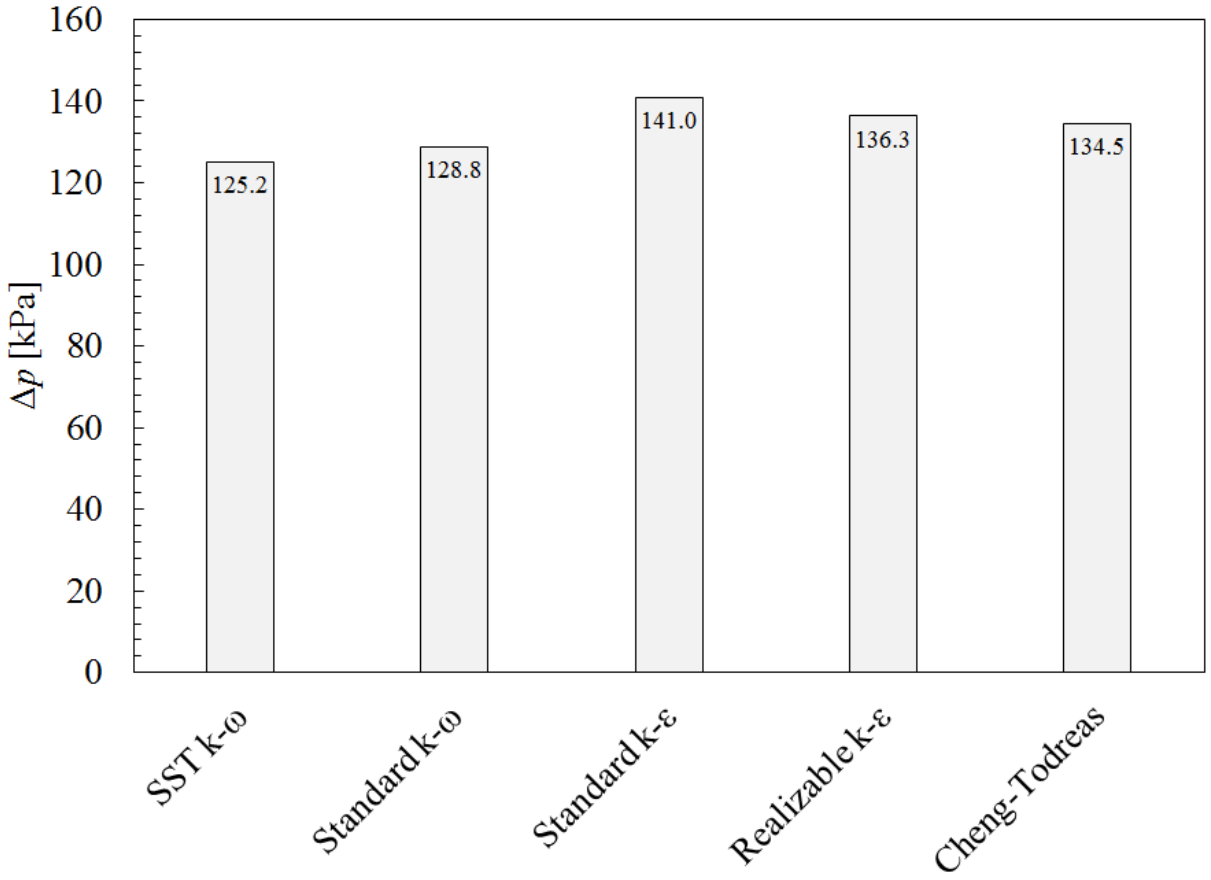
Duct Face B pressure drops show convergence by Fine mesh

Temperatures on unheated tubes show little variation with mesh size

Copyright© 2016 TerraPower, LLC. All Rights Reserved.

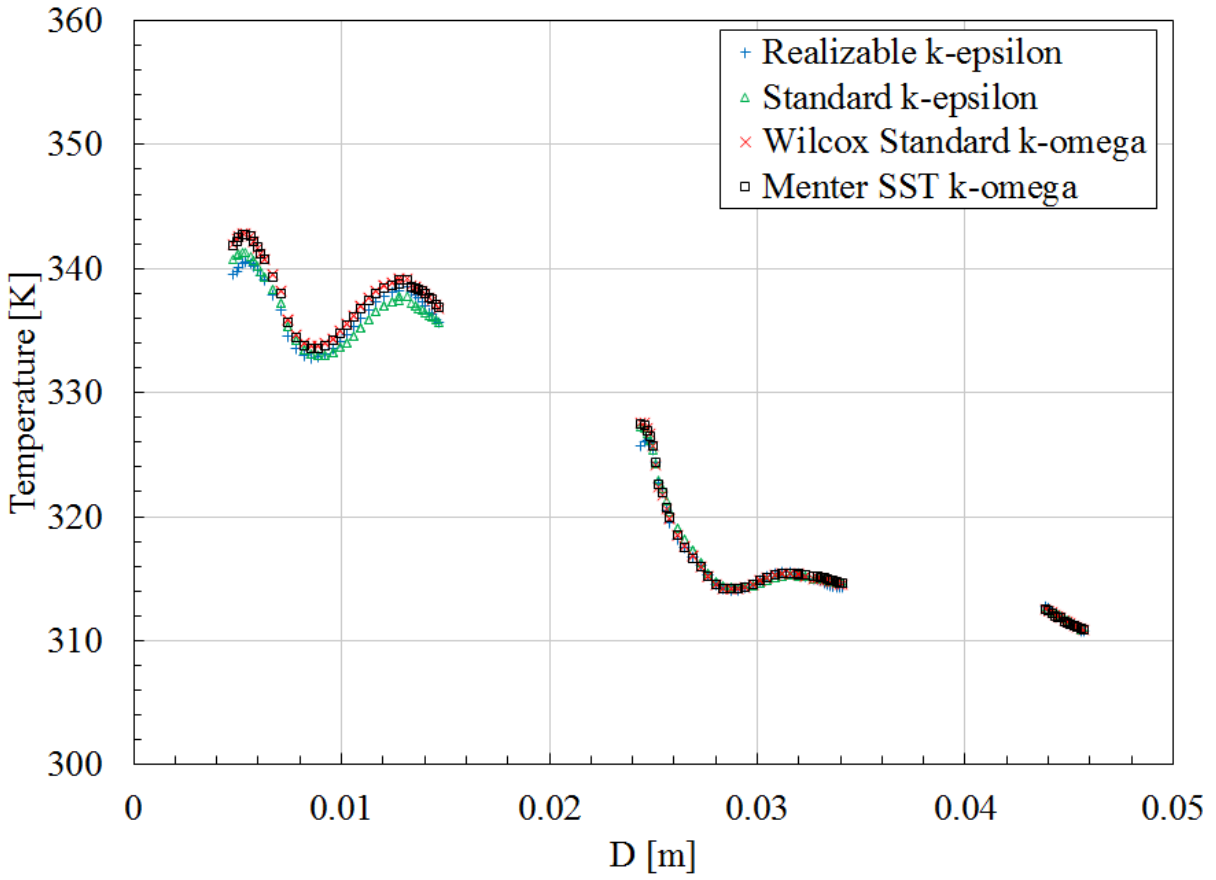
TerraPower

Heated Turbulence Model Sensitivity (Fine Mesh)



All turbulence models predict bundle Δ*p* within ~7% of well-known bundle Δ*p* correlation

Isothermal bundle pressures show similar sensitivity to choice of turbulence model



Temperature profiles show slight variation with choice of turbulence model

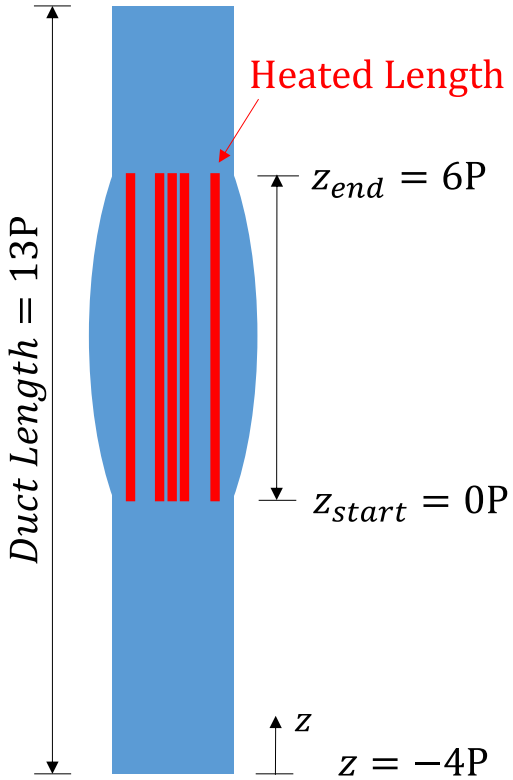
Isothermal bundle velocity field shows little sensitivity to choice of turbulence model

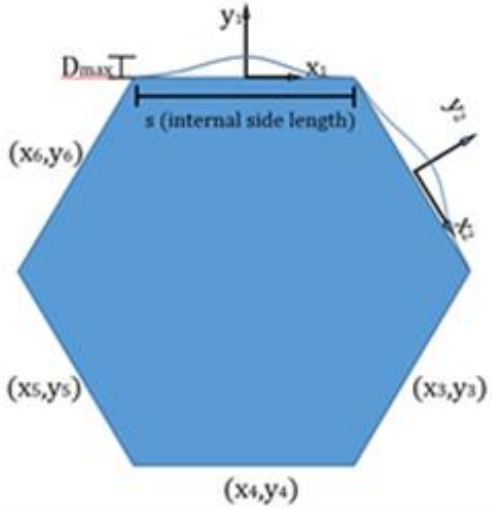
Copyright© 2016 TerraPower, LLC. All Rights Reserved.

TerraPower

Deformed Cases

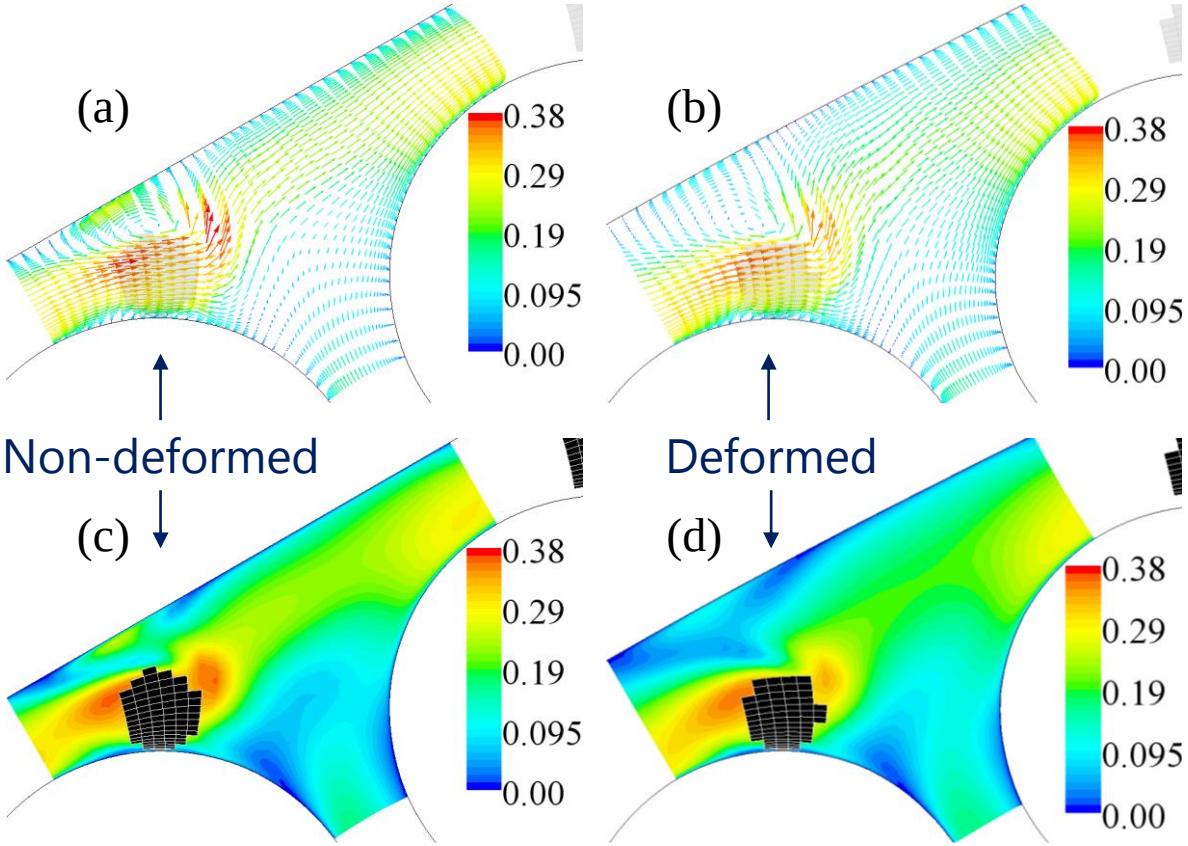
- Deformed pre-test solution verification conducted as well for isothermal and heated bundles





D_{max} = 1.064 mm

Exaggerated illustration of deformed heated bundle



Transverse velocity [m/s] for isothermal bundles

Copyright© 2016 TerraPower, LLC. All Rights Reserved.

TerraPower

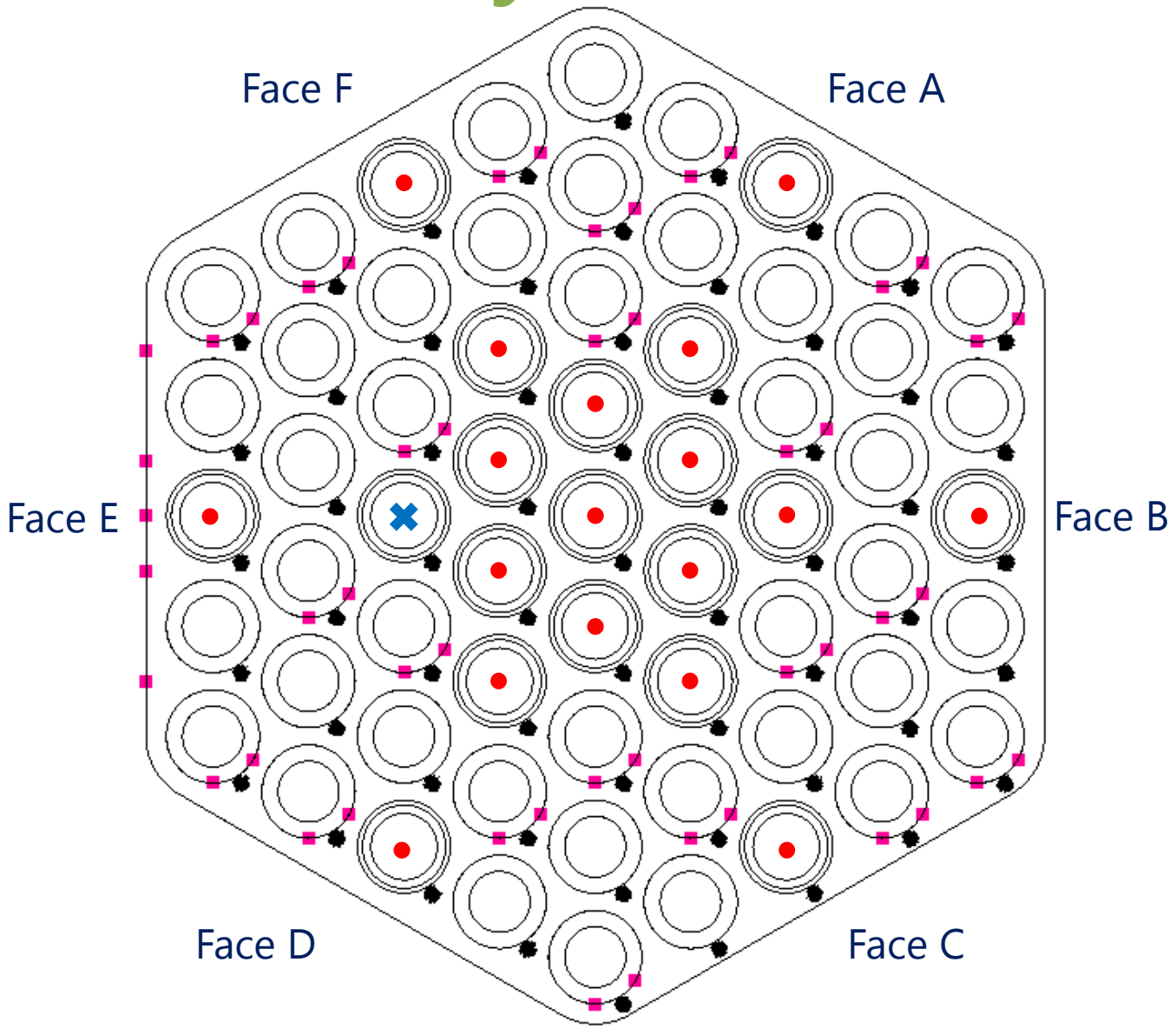
Non-Deformed Post-Test Simulations & Validation

- Post-test simulations use As-Built geometry and As-Tested boundary conditions
  - Very slight changes to geometry between as-built and as-designed
  - Important changes to boundary conditions for heated bundle
- "Fine" meshes and k-ω SST turbulence model chosen for blind post-test simulations
  - k-ω SST chosen because it combines advantages from both k-ω and k-ε
- Non-deformed heated bundle CFD/EXP results presented today
- Non-deformed isothermal bundle CFD results complete and in process of comparing to EXP (not presented today)

Copyright© 2016 TerraPower, LLC. All Rights Reserved.

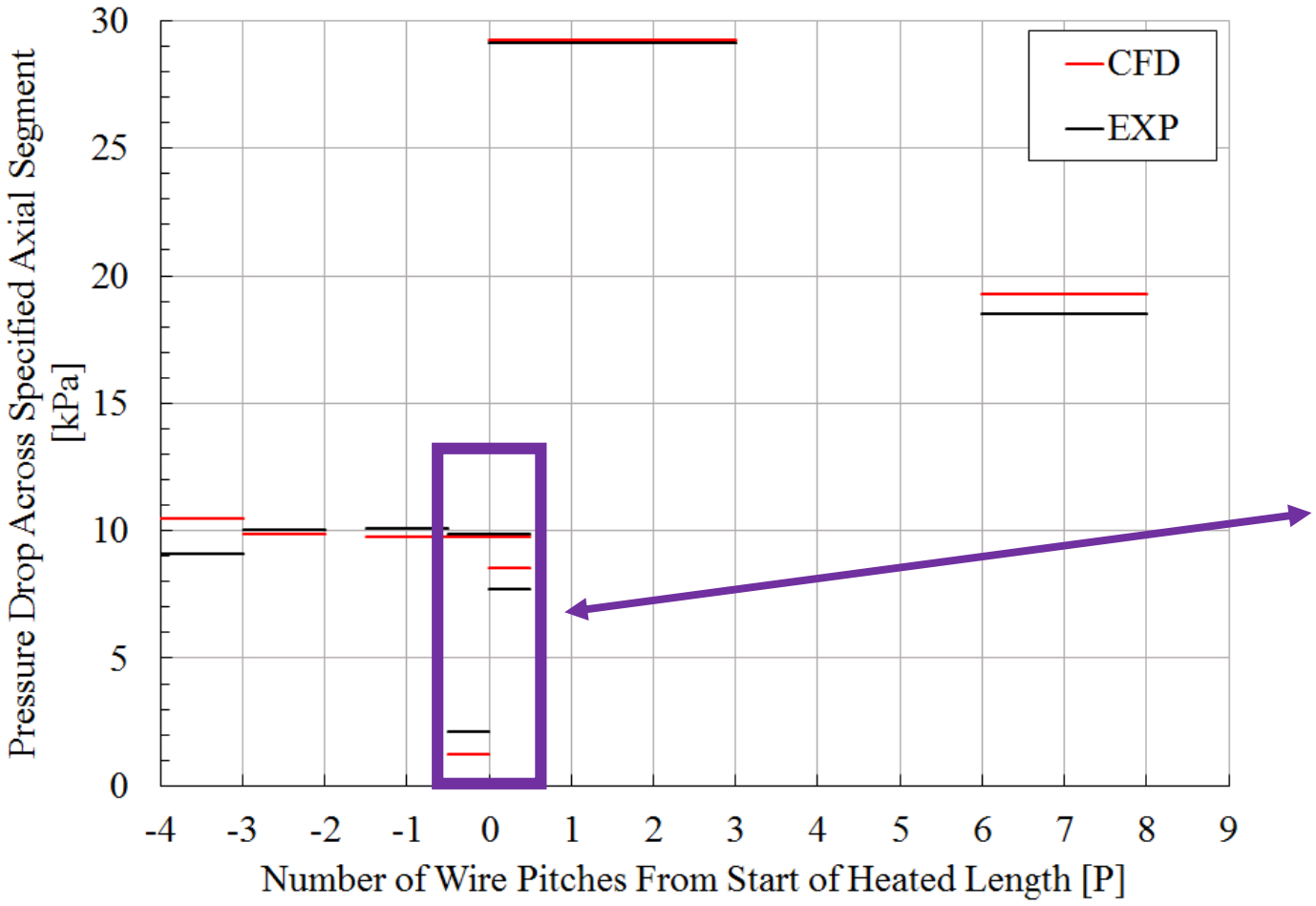
Post-Test Heated Bundle Boundary Conditions

- Heater element in one heated pin failed and was turned off
  - No heat flux from this pin in CFD
- Reynolds number and temperature matched to EXP at CFD inlet
- Unheated tube cladding added to CFD simulation
  - CFD sensitivity studies showed appreciable affect on results



Copyright© 2016 TerraPower, LLC. All Rights Reserved.

Post-Test Heated Bundle Face B Pressure Drops Along Various Axial Segments



Axial Segment	# Pitches [P]	Δp_{CFD} [kPa]	Δp_{EXP} [kPa]	Error [%]
-4P to -3P	1	10.50	9.10	15.3
-3P to -2P	1	9.87	10.05	-1.8
-1.5P to -0.5P	1	9.78	10.12	-3.3
-0.5P to 0P	0.5	1.23	2.15	-42.7
0P to 0.5P	0.5	8.52	7.71	10.5
-0.5P to 0.5P	1	9.75	9.86	-1.1
0P to 3P	3	29.27	29.15	0.4
6P to 8P	2	19.30	18.53	4.1
0P to 3P (Face D)	3	29.20	28.38	2.9

CFD Δp matches well with EXP across integer multiples of wire pitch. CFD under-predicts Δp for 1st half of wire pitch and over-predicts for 2nd half. Expected CFD over-prediction across entry pitch.

Copyright© 2016 TerraPower, LLC. All Rights Reserved.

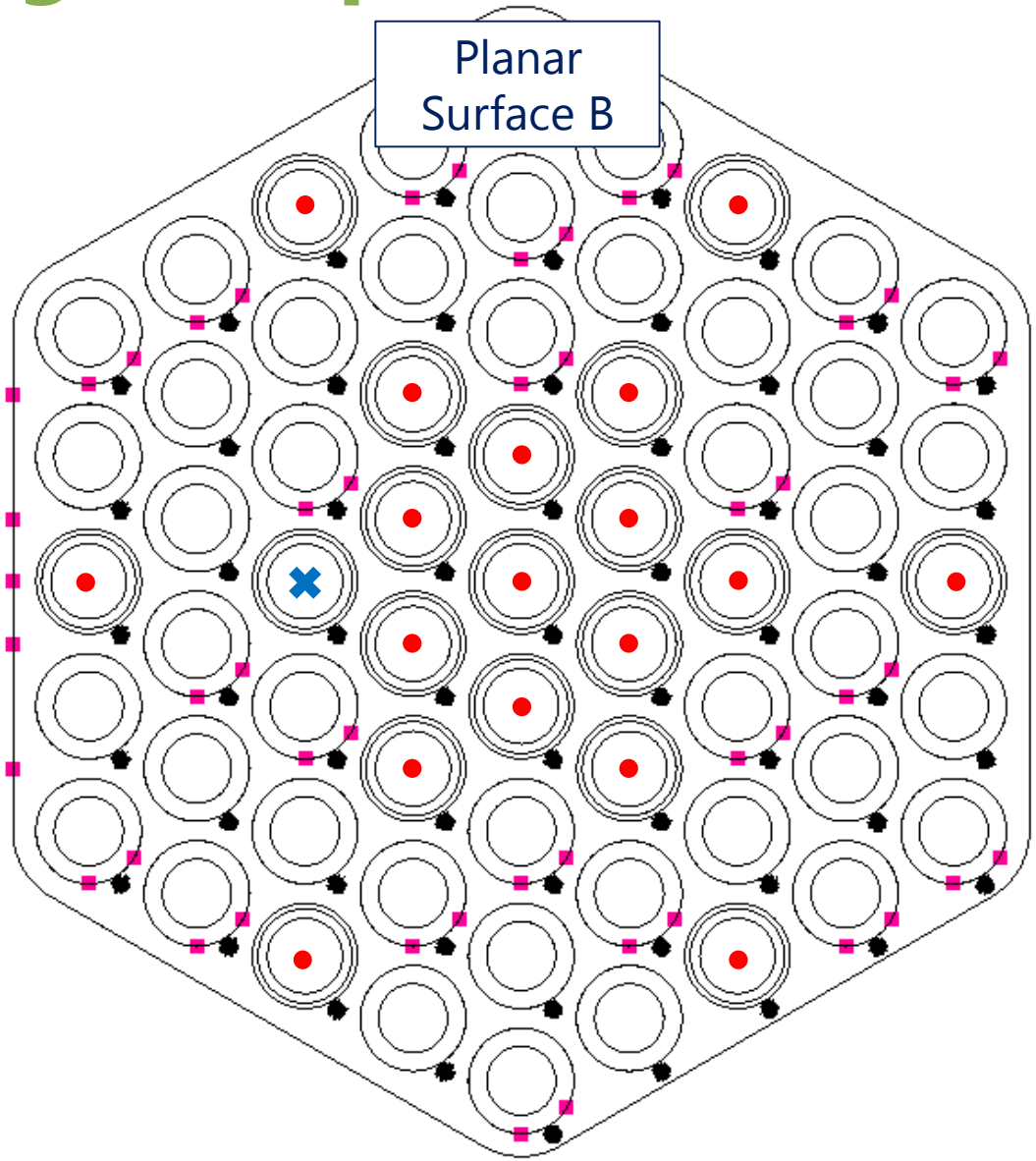
TerraPower

Post-Test Planar Average Temperature

Averages of 49 thermocouple readings (CFD sampling locations in the simulations) distributed throughout each planar surface

Planar Surface	CFD $T_{planarMean} - T_{in}$ [˚C]	EXP $T_{planarMean} - T_{in}$ [˚C]	Error [%]
B (8.417 P)	5.67	5.62	0.94
C (10.75 P)	8.58	8.65	-0.79

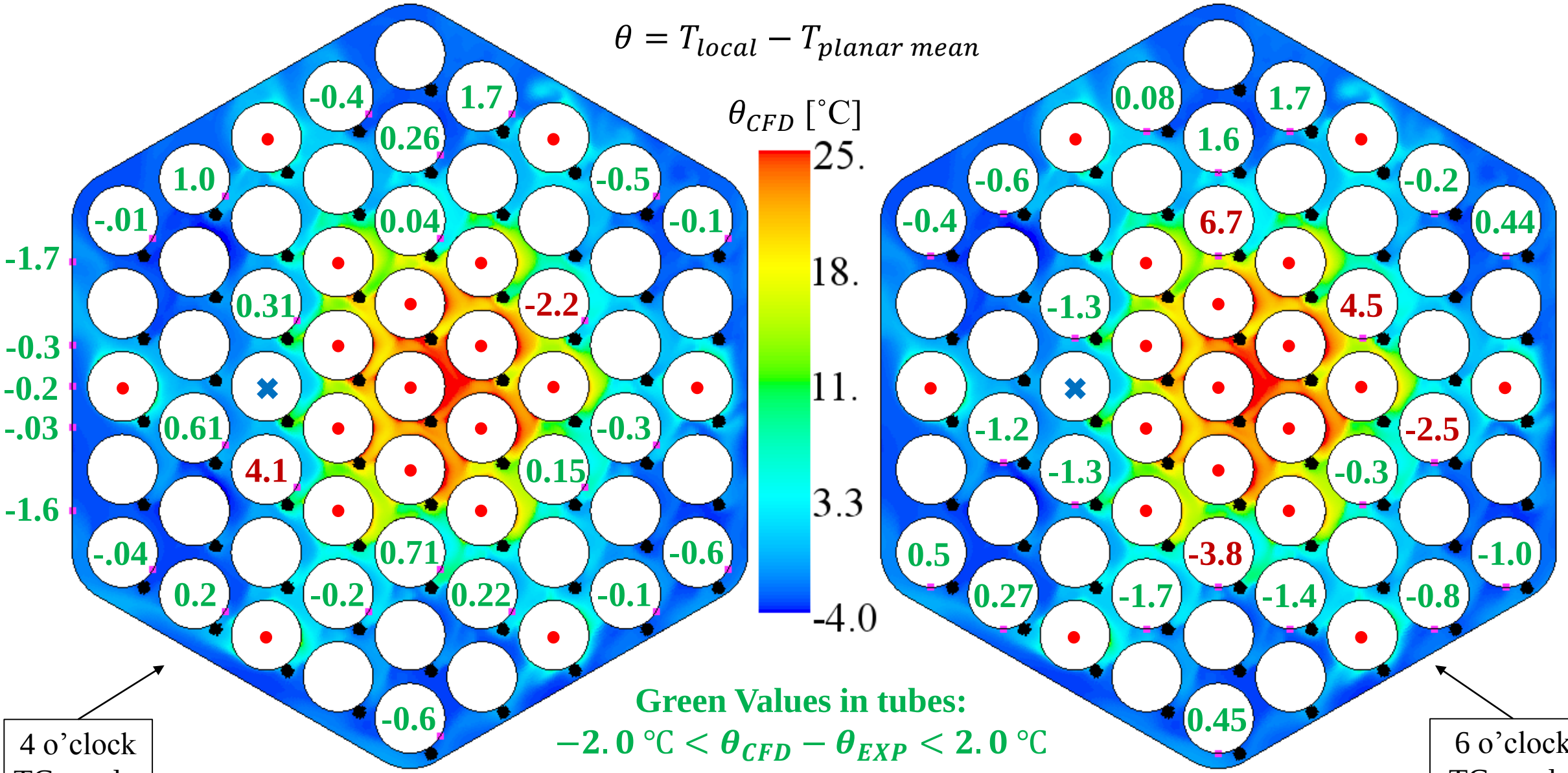
CFD planar averages based on local samples at two axial heights (one within the heated length and the other above it) show excellent agreement with EXP



Copyright© 2016 TerraPower, LLC. All Rights Reserved.

Post-Test Local Temperatures 8.417 Pitches Into Bundle

$$\theta = T_{local} - T_{planar\ mean}$$



4 o'clock TC results

6 o'clock TC results

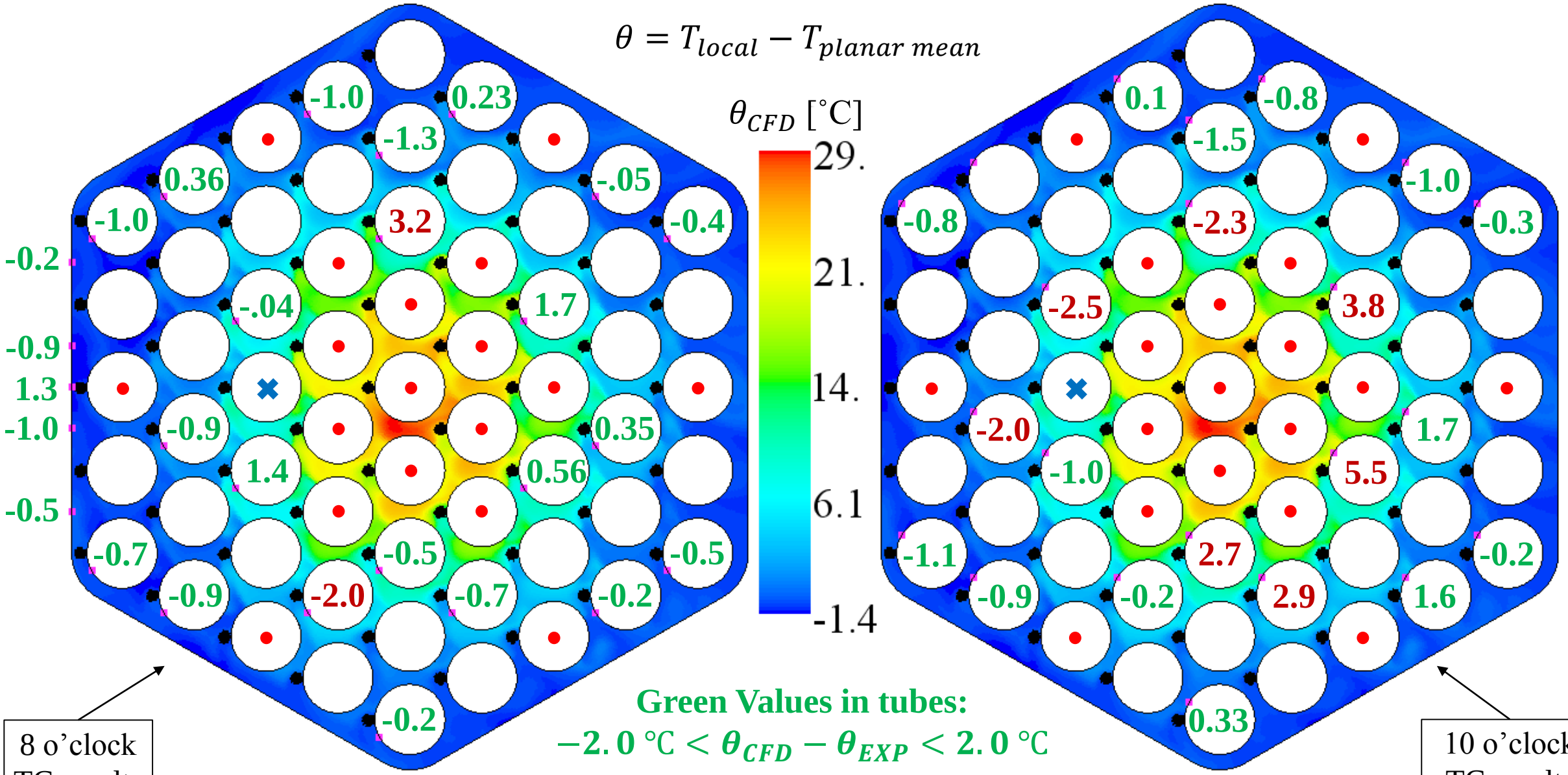
Green Values in tubes:

$$-2.0\ ^{\circ}\mathrm{C} < \theta_{CFD} - \theta_{EXP} < 2.0\ ^{\circ}\mathrm{C}$$

Red Values in tubes: $-2.0^{\circ}\mathrm{C} > \theta_{CFD} - \theta_{EXP} > 2.0^{\circ}\mathrm{C}$

Copyright© 2016 TerraPower, LLC. All Rights Reserved.

Post-Test Local Temperatures 10.75 Pitches Into Bundle



8 o'clock TC results

10 o'clock TC results

Green Values in tubes:
$-2.0\ ℃ < \theta_{CFD} - \theta_{EXP} < 2.0\ ℃$

Red Values in tubes: $-2.0℃ > \theta_{CFD} - \theta_{EXP} > 2.0℃$

Copyright© 2016 TerraPower, LLC. All Rights Reserved.

Summary & Future Work

- Code verification underway with MMS
- Extensive solution verification performed on pre-test bundles with momentum source wire model
- Post-Test simulations conducted on non-deformed heated and isothermal bundles
- Initial validation analysis of heated bundle shows decent agreement with experiments

- Future Work
  - Post-test non-deformed isothermal simulation complete and ready for validation with experiments
  - Post-test deformed cases will be run and compared to experiments
  - Compare results with ANL high-fidelity simulations
  - Run wire-resolved RANS simulations and compare to momentum source and experiments

Copyright© 2016 TerraPower, LLC. All Rights Reserved.

Acknowledgements

- AREVA
- Argonne National Lab
- Texas A&M University
- Department of Energy

This material is provided to support the Department of Energy [National Nuclear Security Administration] Award Number [DE-NE0008321]

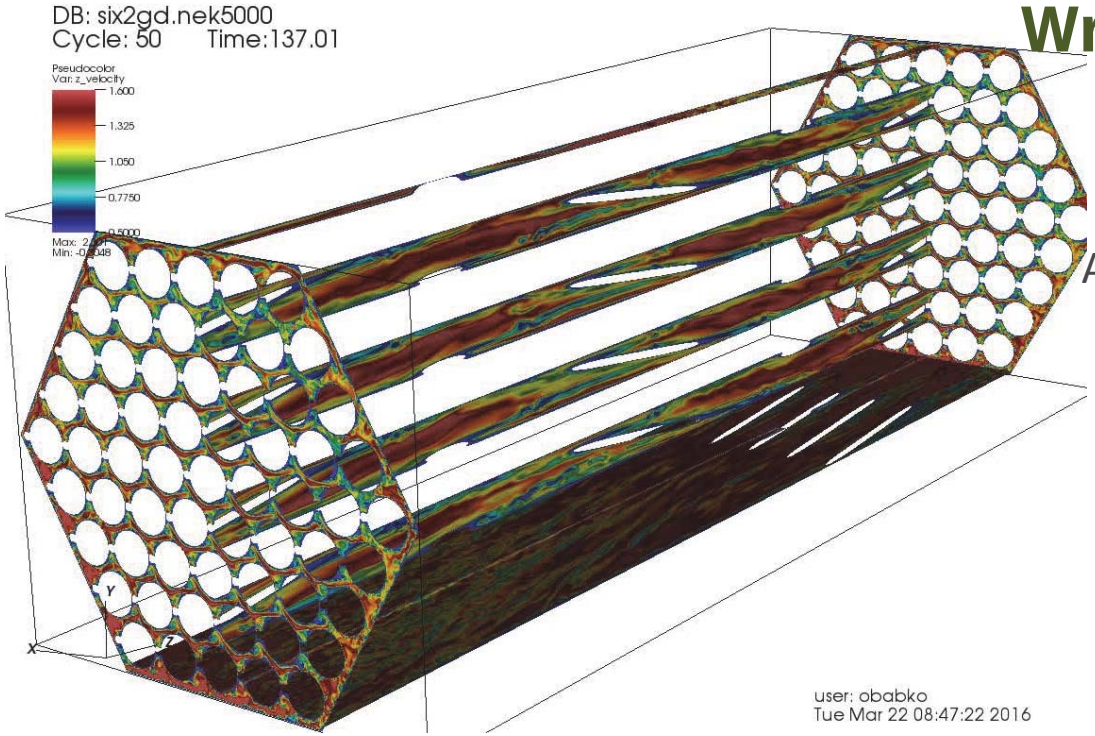
Disclaimer

"Neither the United States Government nor any agency thereof, nor any of their employees, makes any warranty, express or implied, or assumes any legal liability or responsibility for the accuracy, completeness, or usefulness of any information, apparatus, product, or process disclosed, or represents that its use would not infringe privately owned rights. Reference herein to any specific commercial product, process, or service by trade name, trademark, manufacturer, or otherwise does not necessarily constitute or imply its endorsement, recommendation, or favoring by the United States Government or any agency thereof. The views and opinions of authors expressed herein do not necessarily state or reflect those of the United States Government or any agency thereof."

Copyright© 2016 TerraPower, LLC. All Rights Reserved.

Argonne NATIONAL LABORATORY

Nek5000 Large-Eddy Simulations for Thermal-Hydraulics of Deformed Wire-Wrap Fuel Assembles



Aleksandr Obabko, E. Merzari, P.F. Fischer[1]

Argonne National Laboratory, Argonne, IL

obabko@mcs.anl.gov

2016 ANS Winter Meeting & Expo

November 5-10, 2016

Las Vegas, NV

[1] also University of Illinois at Urbana-Champaign (UIUC)

We acknowledge the use of DOE INCITE and ALCC programs. This work was performed for the Department of Energy under contract DE-NE0008321 and is partially provided by US DOE NE Advanced Reactor Technology (ART) and Nuclear Energy Advanced Modeling and Simulation (NEAMS) programs and by DOE Office of Science's Applied Math Program.

U.S. DEPARTMENT OF ENERGY

TH Advanced Modeling

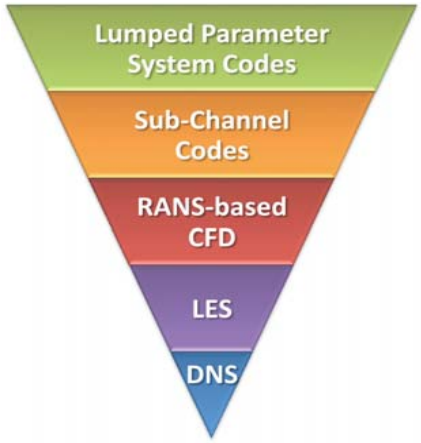
Advanced modeling means getting the RIGHT answer. This requires to capture a range of scales (``eddies'') and to be "as close to 1st principles as possible" (and practical).

SHARP Multiscale/multi-resolution simulation hierarchy:

Increased Costs

1. Lumped-parameter systems codes
2. Subchannel models
3. **RANS (Reynolds-averaged Navier-Stokes)**
4. **LES (large eddy simulation) of turbulence**
5. **DNS (direct numerical simulation) of turbulence**

Increased Modeling



TH module Nek5000 (3,4,5) is highly scalable and efficient spectral element code (from desktop to 1M cores) leveraging full range of DOE's computing resources

Nek5000: Open-Source General Geometry Spectral-Element Code

- Spectral Element Discretization: High accuracy at low cost
  - Also: even when it looks like there is no boundary layer, there actually is (beauty of the Gauss-Lobatto points).
  - Highly respected code in Fluid Dynamics Community.

- Tailored to LES and DNS of turbulent heat transfer, but also supports
  - Low-Mach combustion, MHD, conjugate heat transfer, moving meshes
  - New features in progress: **RANS**, compressible flow (GE), LBM

- Chief Architect: Paul Fischer.
  Scaling: 1999 Gordon Bell Prize; recently run with > 10^6 MPI processes.
  - 2016 R&D 100 Award

- Local Polynomial Nodal Basis:

$$u(x,y)|_{\Omega^e} = \sum_{i=0}^{N}\sum_{j=0}^{N} u_{ij}^e\, h_i(r)\, h_j(s)$$

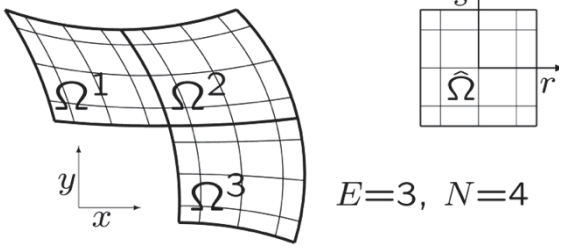
$$h_i(r) \in \mathcal{P}_N(r), \qquad h_i(\xi_j) = \delta_{ij}$$

- x_j = Gauss-Lobatto-Legendre quadrature points:

  - stability (*not* uniformly distributed points)
  - allows pointwise quadrature (for *most* operators…)
  - easy to implement BCs and C^0 continuity



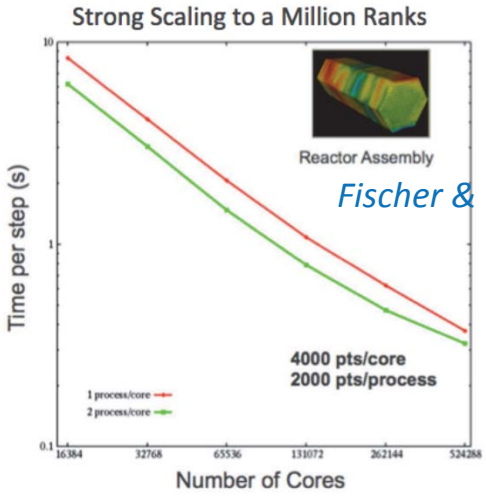
2D basis function, N=10



$E=3,\ N=4$

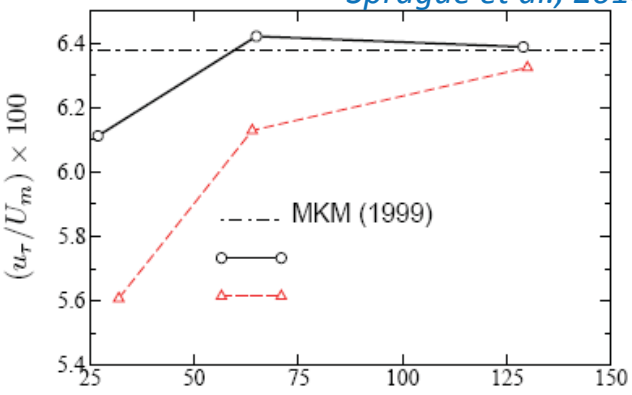
Why SEM code Nek5000?

- Scalability (2k…10k grid points per MPI rank)
  - On track for exascale (1 T dof)
    - Scales beyond 1 M MPI ranks on BG/Q
    - Preliminary good scaling on Intel's A0 Xeon Phi Knight Landing
- Efficiency:
  - Exceptional pressure solvers, state-of-the-art preconditioners.
  - Compilers under a minute -- only MPI dependency
  - High order/SEM (spectral-element based method) => Exponential convergence (for continuous solutions) => mir dof (and time) per accuracy
    - Dispersion errors accumulate linearly with time integration (1.e-2 convergence after 1e5 timesteps requites 1.e-7 per timestep)
    - Great transport properties even for marginally resolved flows
- Flexibility and Easy Extension
  - RANS, two-phase, coupling to neutronics &/or structural mech.
- Verification & Validation (V&V)



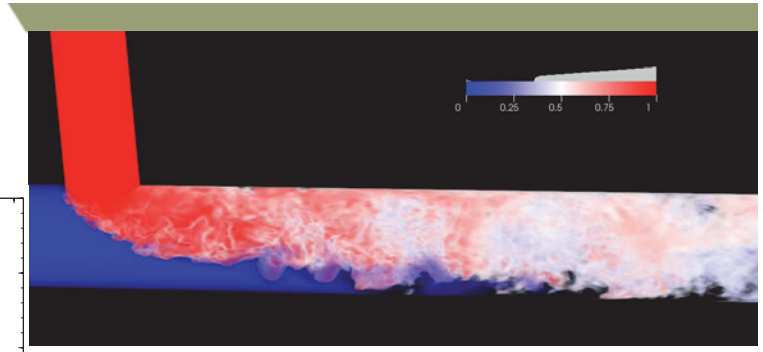
Fischer & Parker 2014

Sprague et al., 2010



n_y: *# of points in wall-normal direction*

III. Thermal Hydraulics (TH) V&V: MATiS & T-junction

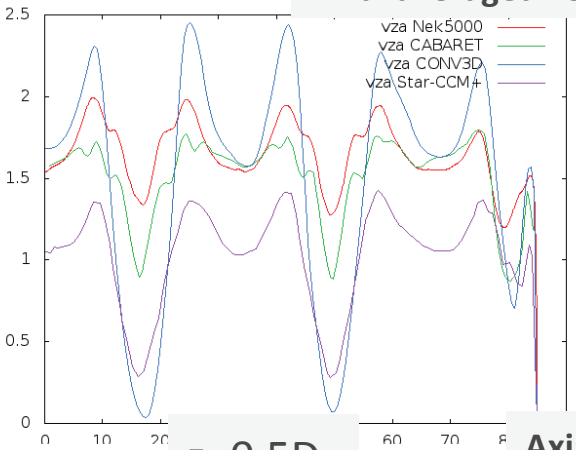


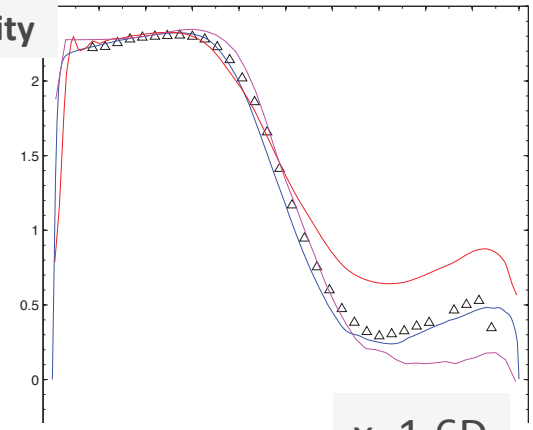
Nek5000 T-junction LES axial velocity

E=62k N=7 (21M dofs)

Re=4*10^4

Axial averaged velocity

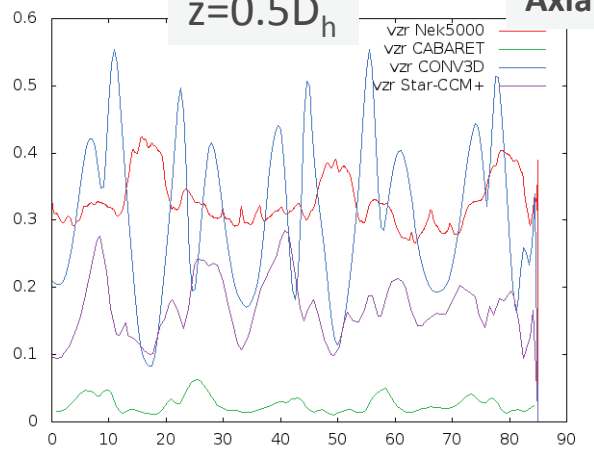


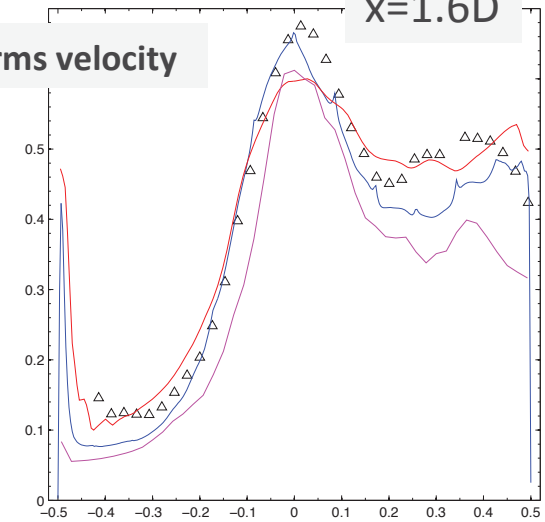


x=1.6D

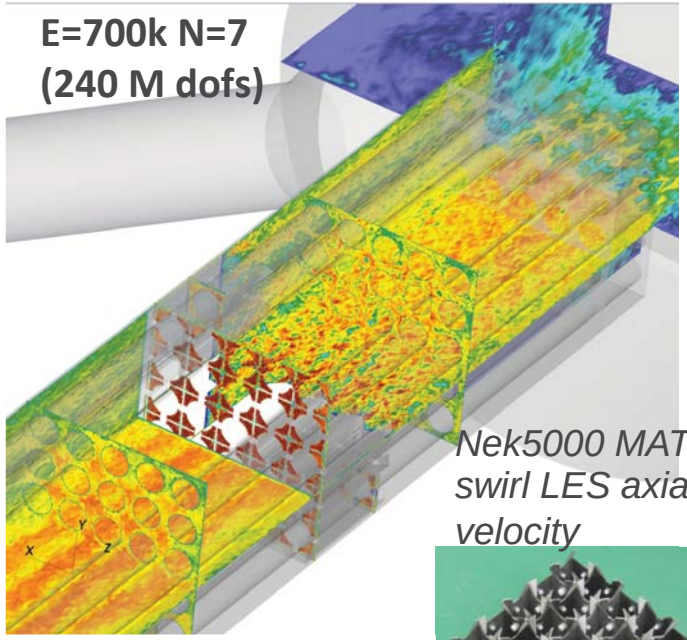
z=0.5D$_h$

Axial rms velocity

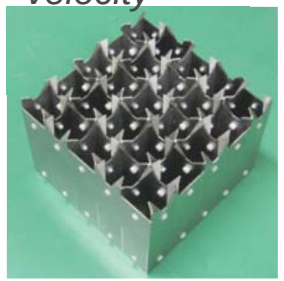




E=700k N=7 (240 M dofs)



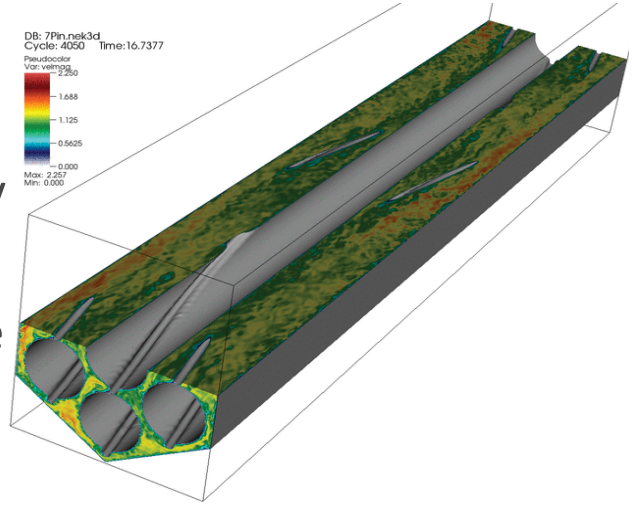
Nek5000 MATIS swirl LES axial velocity

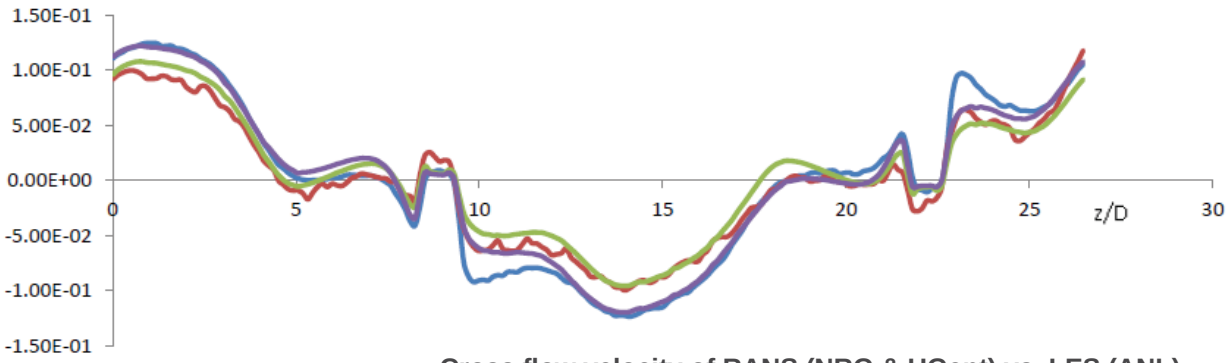


- OECD/NEA 2012 MATiS-H KAERI and 2010 Vattenfall T-junction benchmarks
  - High scores in blind benchmark comparisons – follow-up with IBRAE's CABARET & Conv3D
  - LES simulations were used to guide lower-fidelity but faster-turn-around uRANS simulations (Tomboulides)
  - Stresses an importance of **concurrent** experiment & simulation campaigns

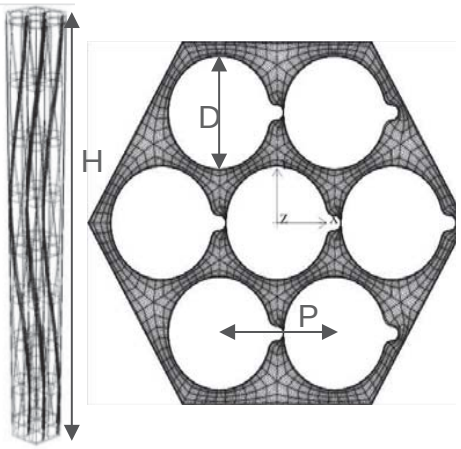
Wire-wrap V&V: LMFR 7-pin INERI Fuel Assemblies
Benchmark (E. Merzari et al., 2016)

- Blind 7-pin wire-wrap hydro benchmark
  - Reference LES of 7-pin wire wrapped fuel assembly (ANL)
  - Axial and cross-flow velocity for various turbulence models
    - NRG 1: Cubic k-ε
    - NRG 2 & UGent: SST k-ω
  - Differences pragmatic vs. high fidelity data: ~5%

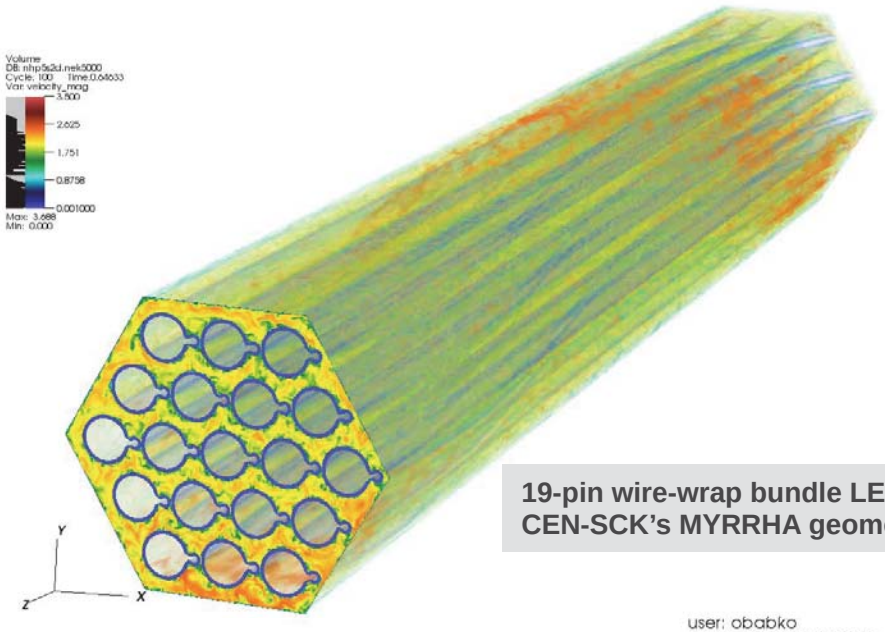




Cross flow velocity of RANS (NRG & UGent) vs. LES (ANL)



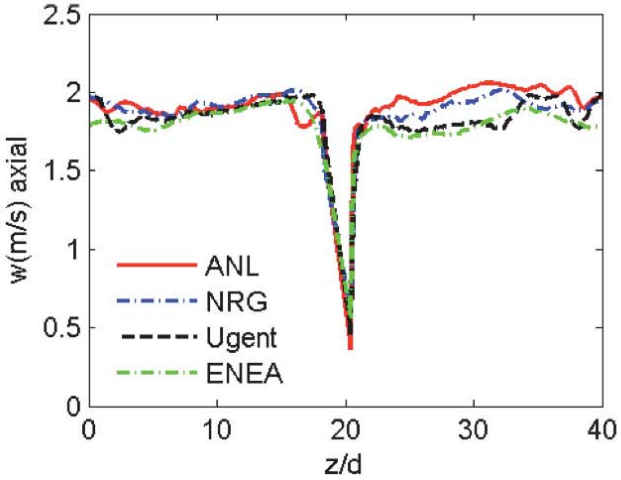
V&V-II : INERI MYRRHA

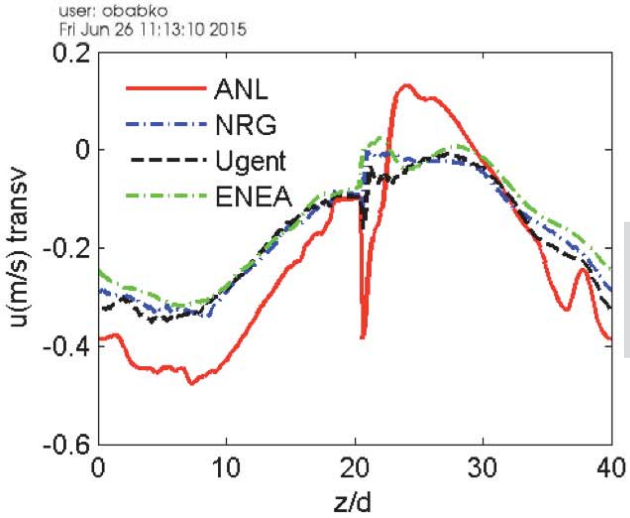


19-pin wire-wrap bundle LES axial velocity in CEN-SCK's MYRRHA geometry

E=838080, N=5 (dof=105M)

- LES of 19-pin wire-wrap of MYRRHA fuel bundle
- Comparison to URANS models from NRG, Ghent, ENEA
  - importance of concurrent experiment & simulations

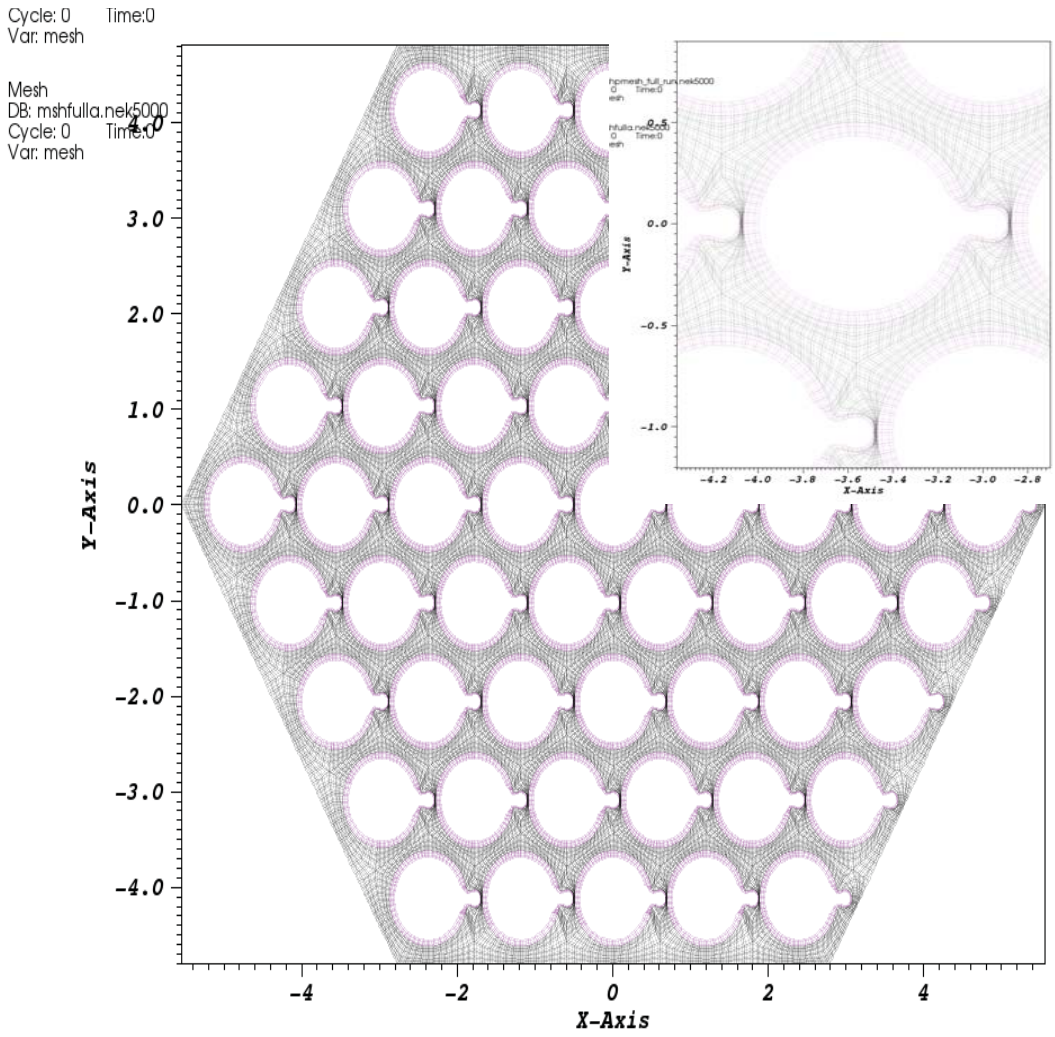




Doolaard et al., NURETH-16, 12944 (2015)

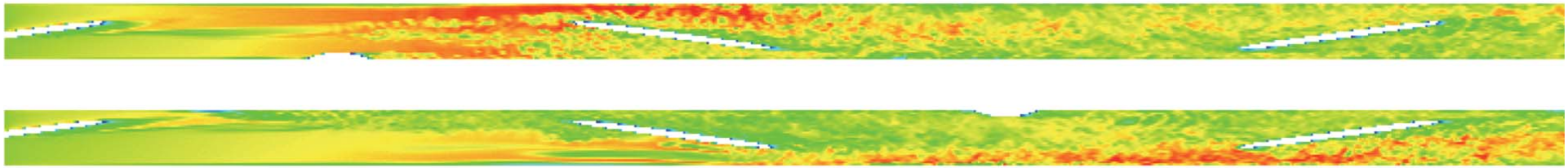
Concurrent V&V: TerraPower, AREVA, TAMU

Conjugate heat transfer mesh (E=2.3M)



- Benchmark: "Modeling and simulation for longer life cores: Thermal Hydraulic simulations and experimental investigation for liquid metal cooled fast reactor fuel assemblies"
  - Isothermal/TAMU bundle for detailed velocity comparison
    - A single wire-wrap 61-pin
  - Conjugate heat transfer / AREVA bundle for detailed velocity comparison
    - Effects of deformation

Boundary Conditions

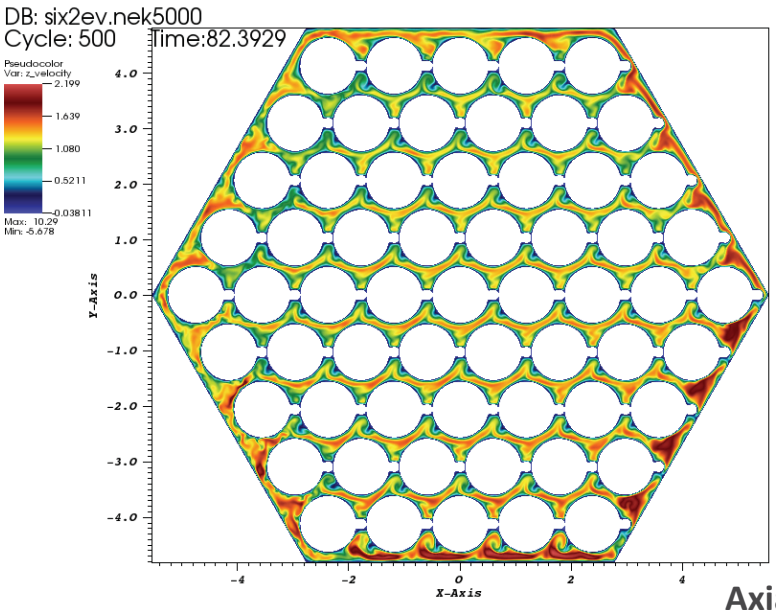


Axial velocity for 3 wire-wraps (Fischer 2007)

- Start w/ LES of hydro/isothermal/non-deformed (TAMU) case
  - Fast and efficient
    - One wire-wrap pitch with axially periodic BC
      - Smaller meshes => faster turn-around
  - Cross-verified against DNS (Pantano & Fischer)

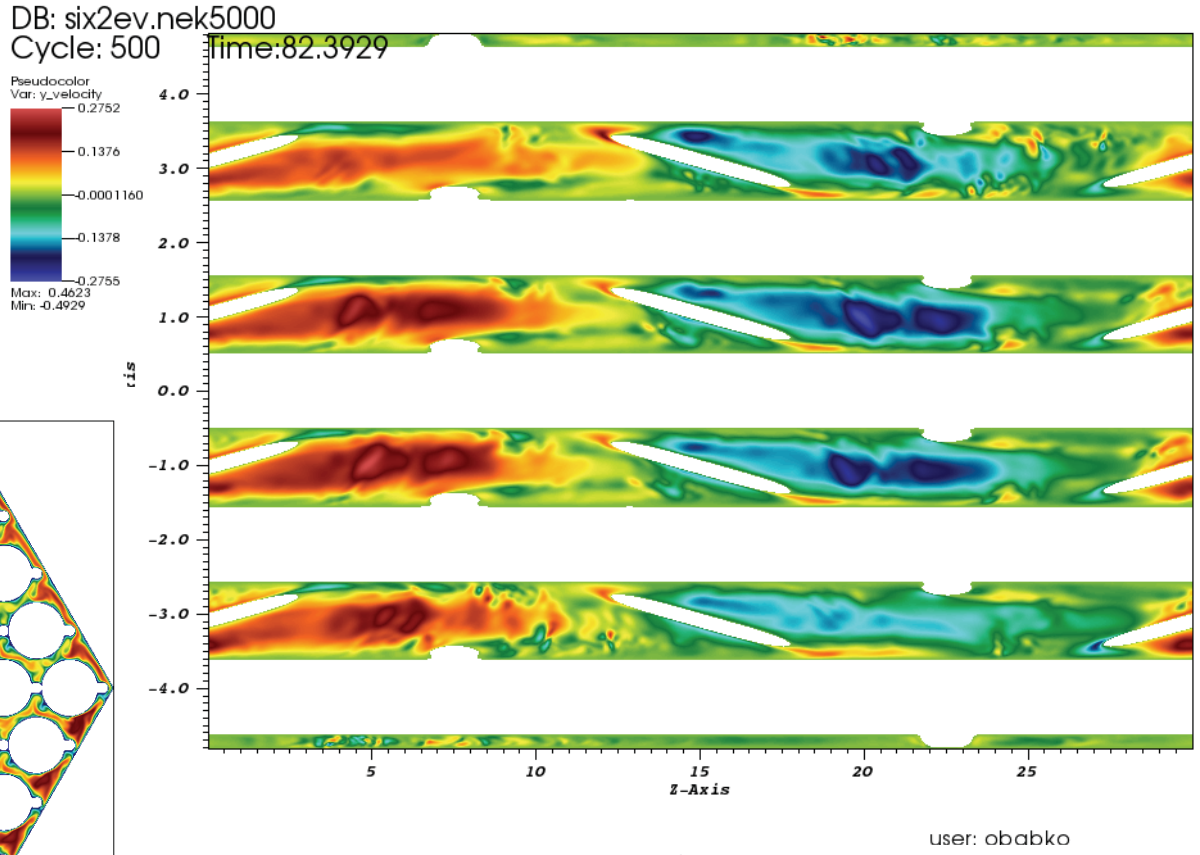
Isothermal/TAMU Case

- Onset of transition
  - Single wire-wrap w/ periodic conditions
  - Re=3e3
  - E=1.6 M, N=5 (200 M dof)
  - Spectral damping



Axial velocity

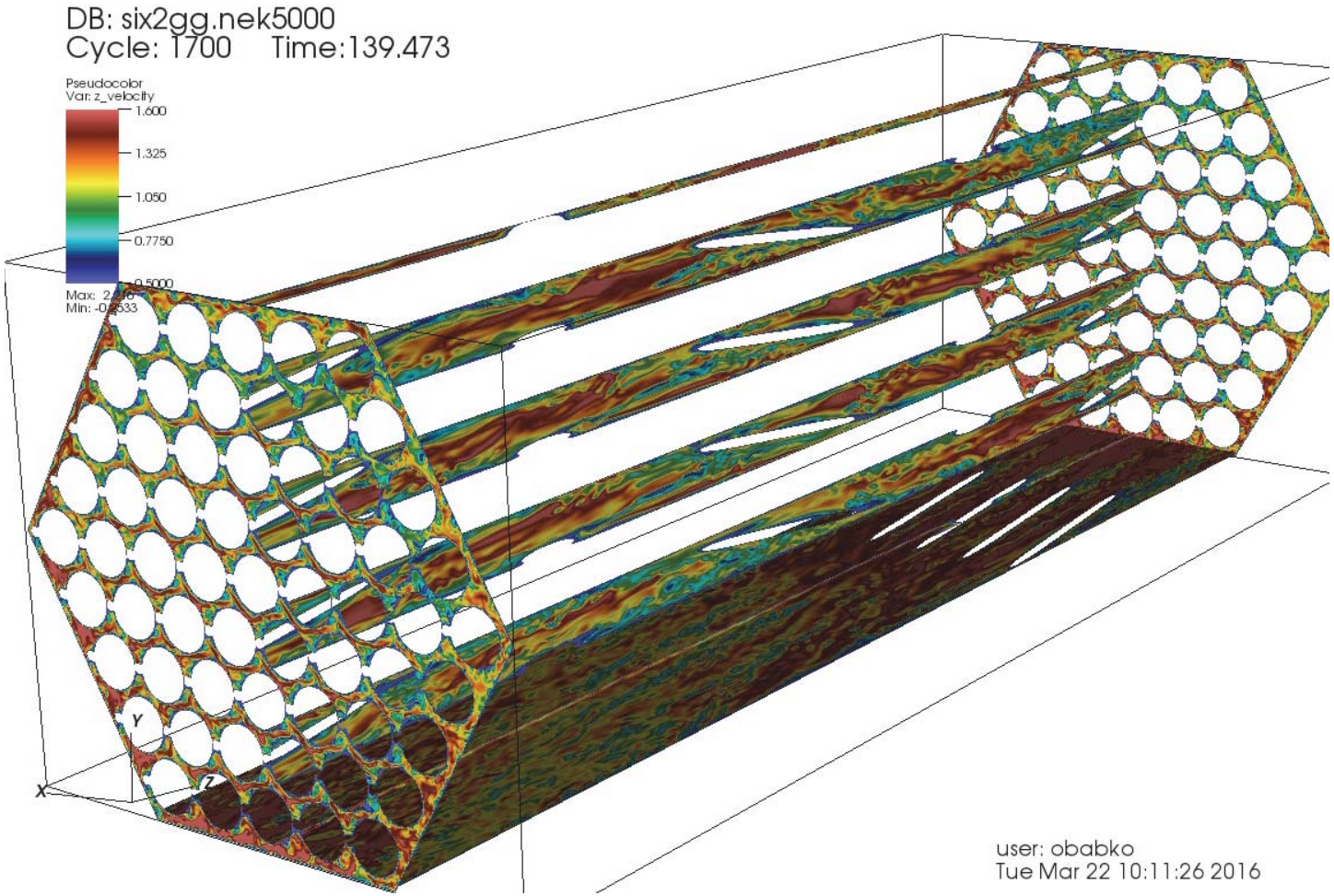
user: obabko



Spanwise velocity

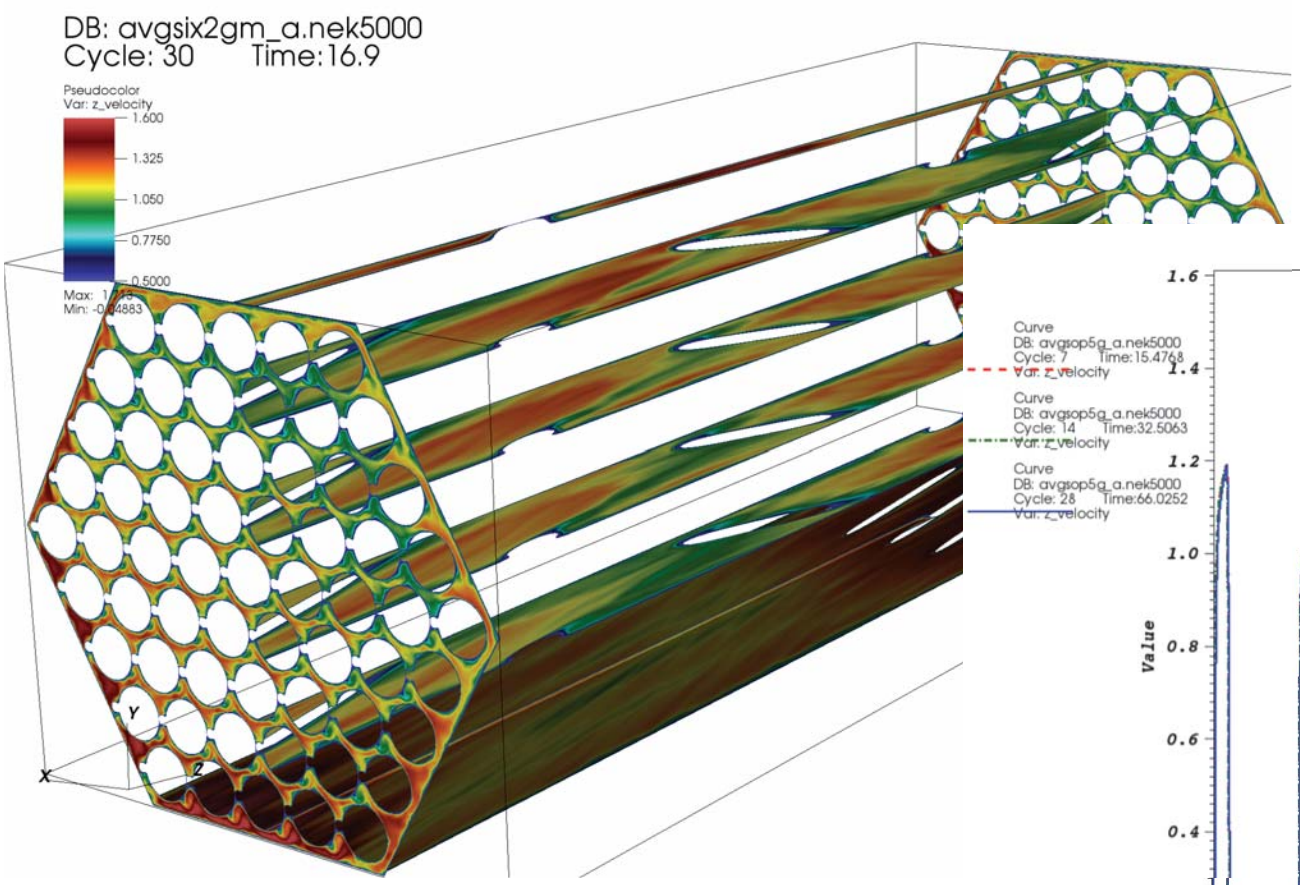
user: obabko

Unsteady Axial velocity at Re=1e4

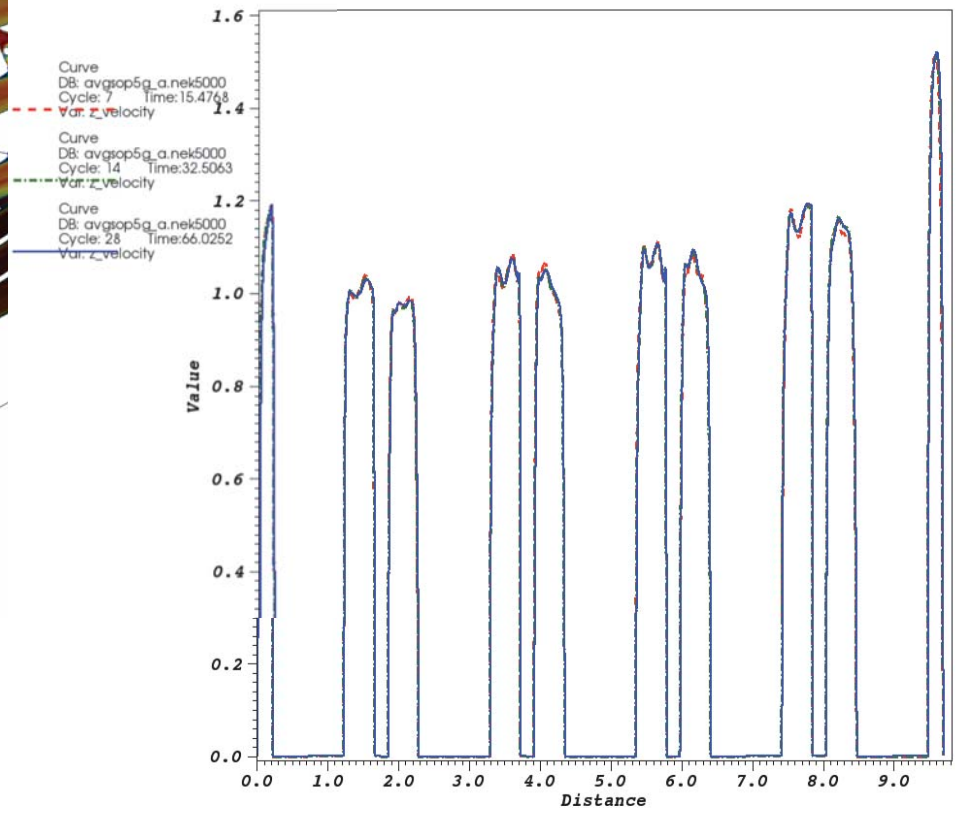


- Done: TAMU's Re=3e3, 1e4, 1.5e4
- Ongoing: TAMU's Re=2e4 & AREVA's cases
  - WireHexMesher

Re=1e4 (Time-Average)



Axial velocity

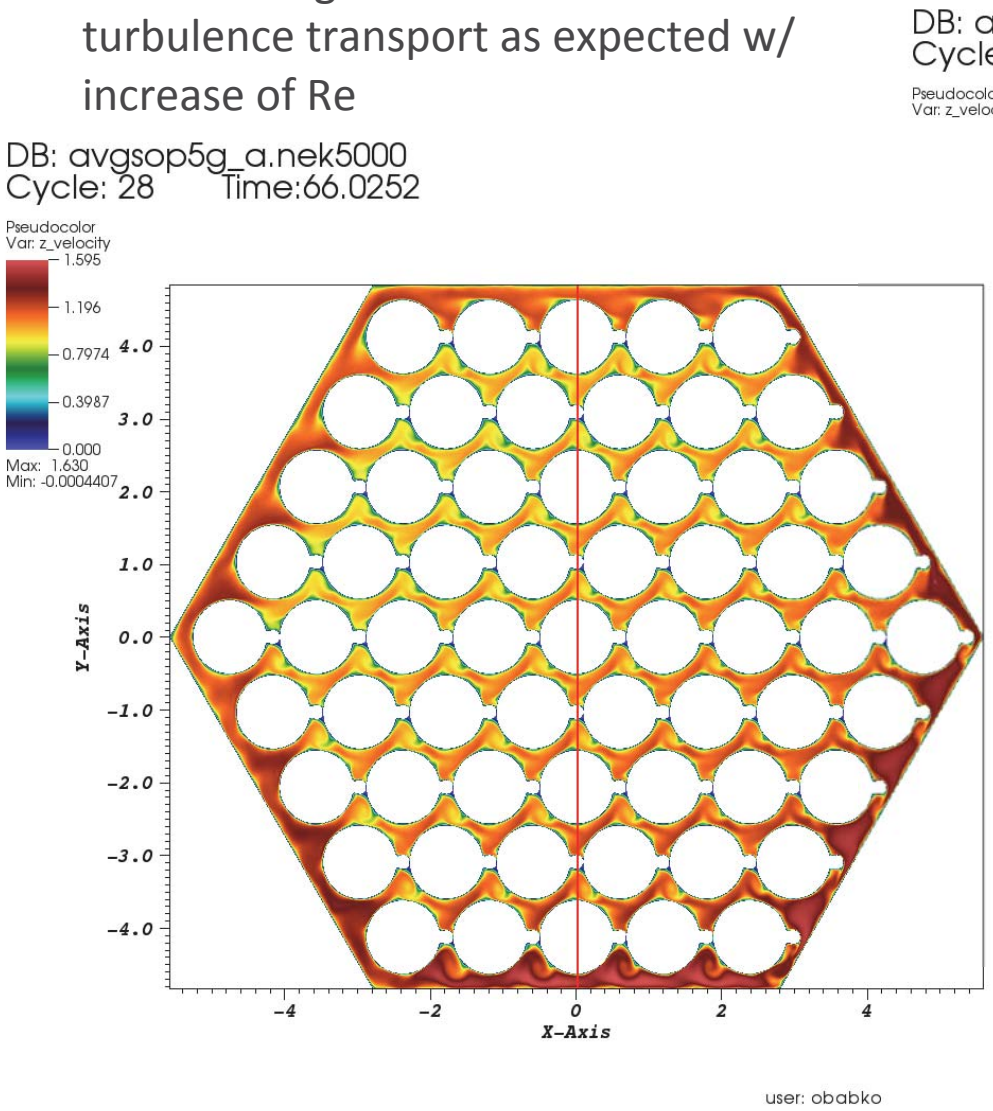


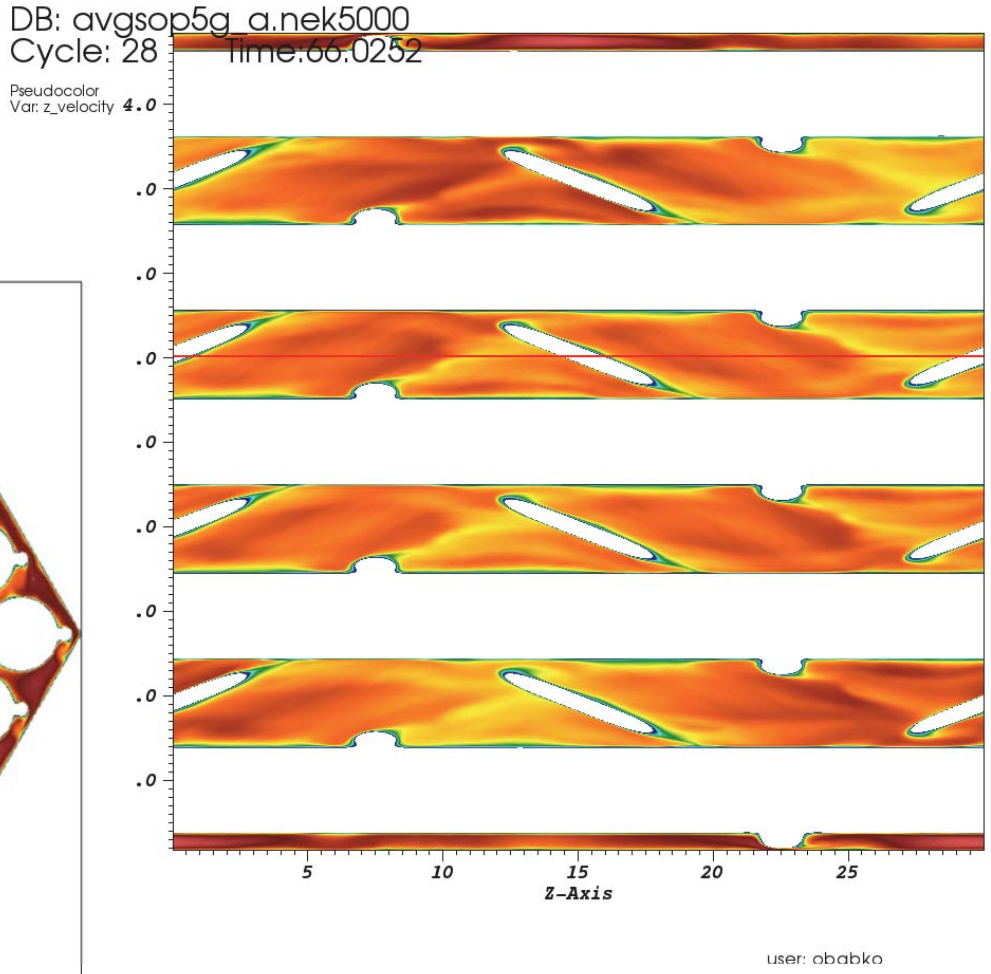
Sensitivity to the time-average interval

user: obabko
Thu Sep 15 17:19:18 2016

Re=15e3 (Time-Averaged)

- More homogenized due to increased turbulence transport as expected w/ increase of Re

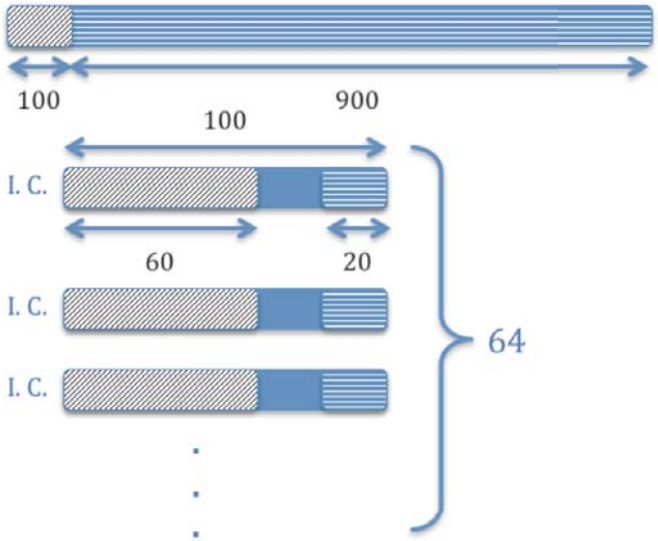


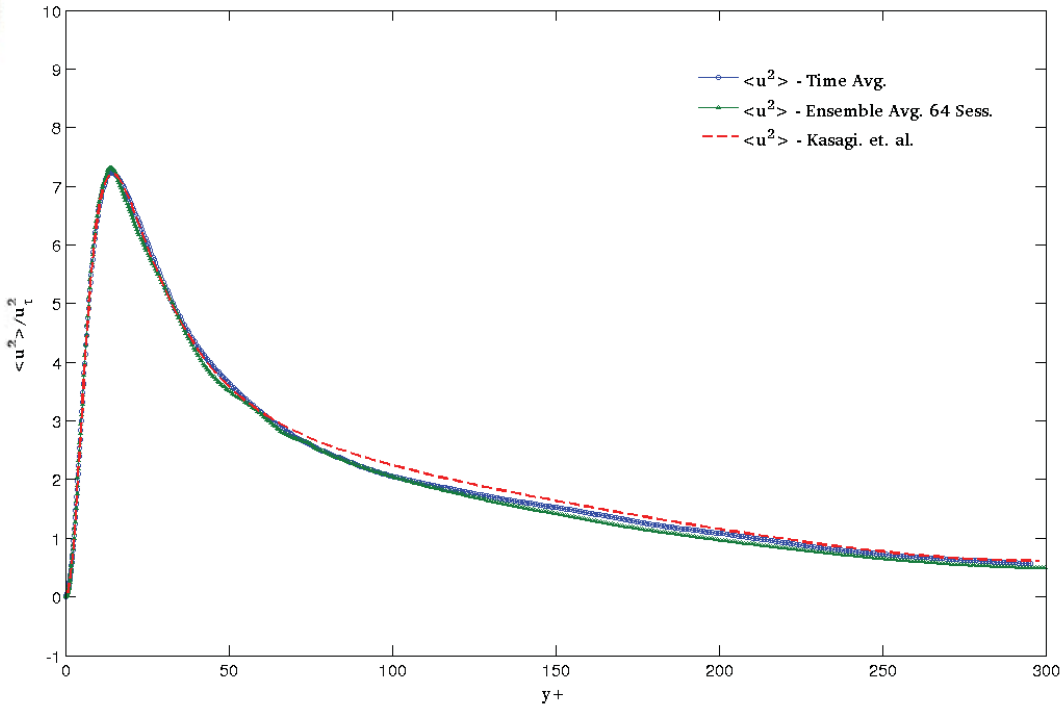


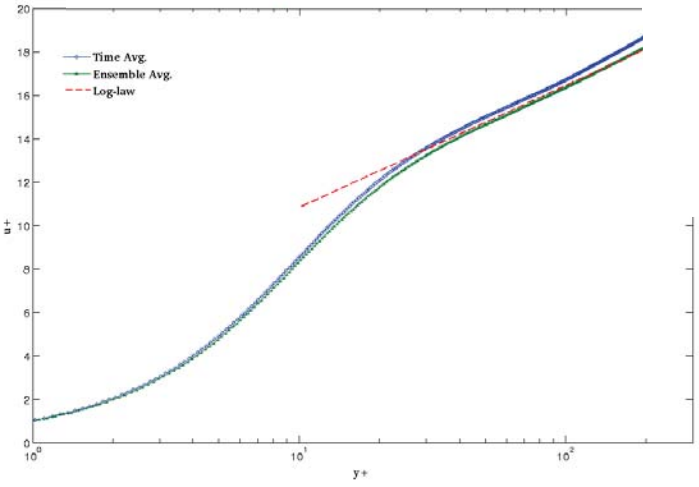
Axial velocity

Nek5000 Ensemble-Average Speed-up

Makarashvili et al. (2016a,b)

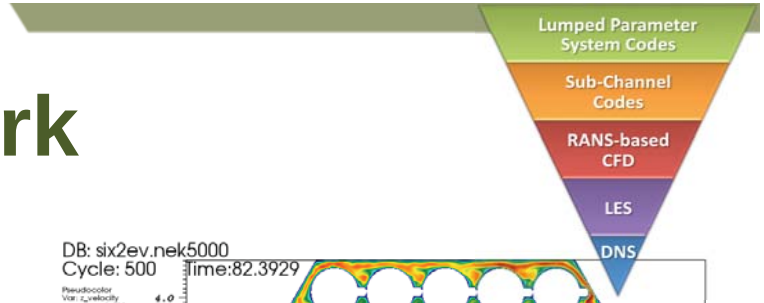




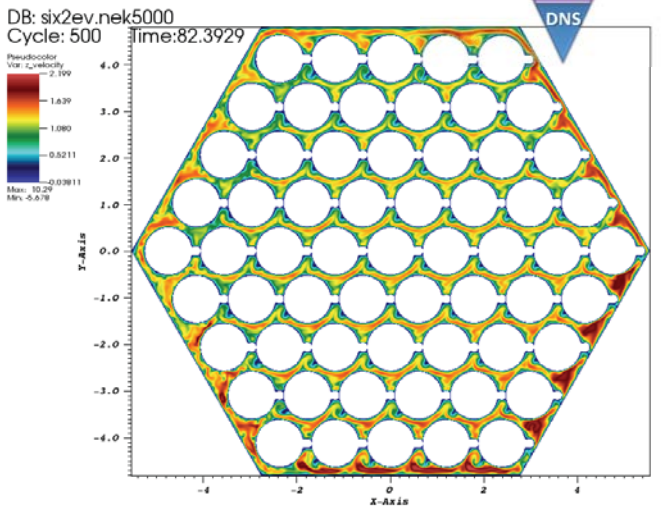


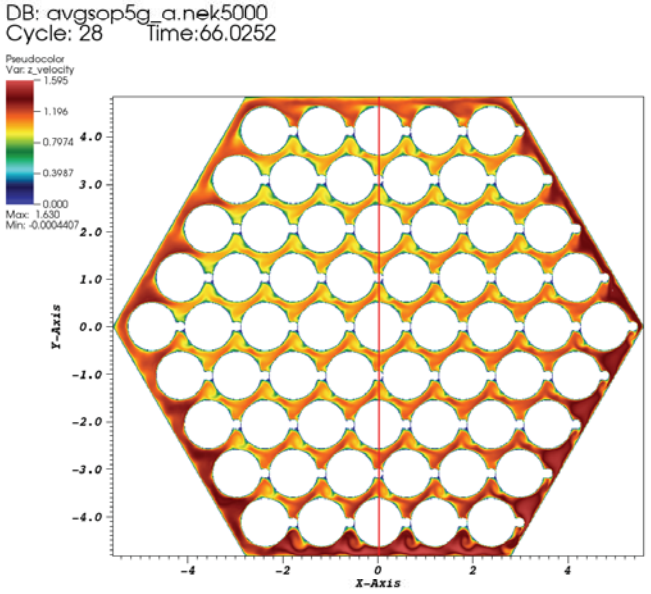
- Up to 64x speed-up demonstrated for turbulent channel flow
- Ongoing tests for more complex cases (T-junction, 61-pin)

Conclusions & Future Work



- Adopted Nek5000 use for thermal-hydraulics
  - Hierarchical approach is both predictive & practical
    - LES, RANS, DNS -- from desktop to 1M processes
    - Validation-driven development:
      - T-junction, Matis, MYRRHA benchmarks
    - Use of LES as a reference to inform uRANS modeling for faster-turn-around
    - Ensemble-averaging speed-up
- 61-pin wire-wrap bundle con-current benchmark
  - Isothermal/TAMU case for detailed velocity comparison
    - Range of Re=3.e3…2e4
    - Preliminary comparison with TAMU
  - Conjugate heat transfer/AREVA setup is ongoing







Disclaimers and Acknowledgments

- This work was performed for the Department of Energy under contract DE-NE0008321. It has been also supported in part by Nuclear Energy (NE) Advanced Modeling and Simulation (NEAMS) Program of Department of Energy (DOE) and in part by the U.S. DOE Office of Science and Advanced Scientific Computing Research, under Contract DE-AC02-06CH11357. The use of resources of the ALCF, which is a DOE Office of Science User Facility supported under Contract DE-AC02-06CH1135 has been provided as a part of Argonne Leadership Computational Challenge (ALCC) allocation.

- This presentation was prepared as an account of work sponsored by an agency of the United States Government. Neither the United States Government nor any agency thereof, nor UChicago Argonne, LLC, nor any of their employees or officers, makes any warranty, express or implied, or assumes any legal liability or responsibility for the accuracy, completeness, or usefulness of any information, apparatus, product, or process disclosed, or represents that its use would not infringe privately owned rights. Reference herein to any specific commercial product, process, or service by trade name, trademark, manufacturer, or otherwise, does not necessarily constitute or imply its endorsement, recommendation, or favoring by the United States Government or any agency thereof. The views and opinions of document authors expressed herein do not necessarily state or reflect those of the United States Government or any agency thereof, Argonne National Laboratory, or UChicago Argonne, LLC
- S

TerraPower

Verification and Model Sensitivity Analyses for Computational Fluid Dynamics Simulations of Wire-Wrapped Nuclear Fuel Assemblies

Daniel Leonard, Ph.D.

Brian Jackson, Ph.D.

Michael Steer



ASME Verification and Validation Symposium

May 18-20

Las Vegas, NV

Copyright© 2016 TerraPower, LLC. All Rights Reserved.

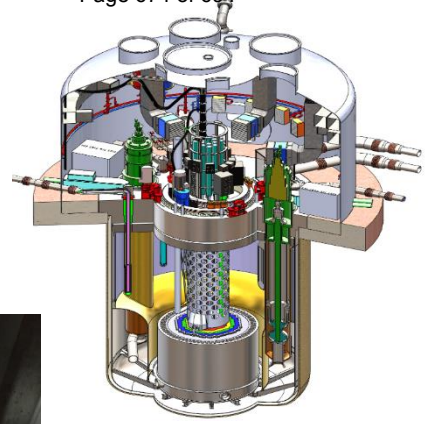
Outline

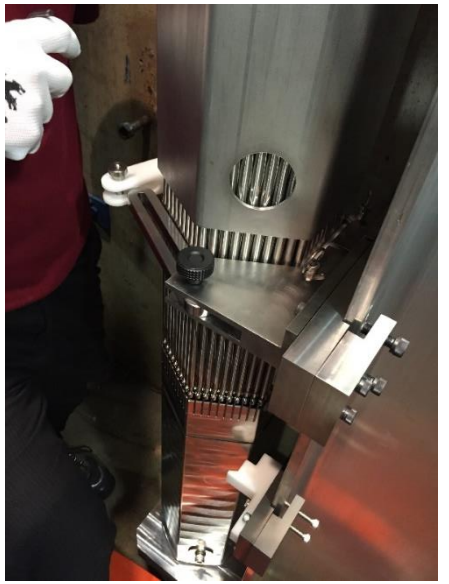
- TerraPower & Advanced Fuel Assembly Flow Characterization Project description
- Code verification
  - Approach (Method of Manufactured Solutions)
  - Order of accuracy results
- Solution verification
  - Geometry, approach, & meshes
  - Mesh refinement results
- Sensitivity studies
  - Turbulence models
  - Momentum source coefficient
- Summary & future work

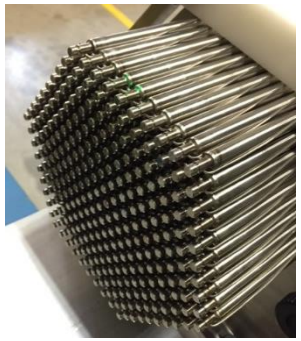
Copyright© 2016 TerraPower, LLC. All Rights Reserved.

TerraPower

- TerraPower was started by Bill Gates, Nathan Myhrvold, & others after invention session in 2006. Privately funded.
- Goal: Investigate advanced fission reactors for world-scale energy production
- Key requirements included high fuel utilization, low barriers to exportation, enhanced safety, and improved cost
- Traveling Wave Reactor was chosen
  - "Breed-and-burn" concept enables fast reactor without reprocessing
  - Has been discussed in literature since at least 1958
- Sodium Fast Reactors utilize ducted fuel assemblies with helically wire-wrapped fuel pins
  - Pressure difference, thermal creep, and irradiation cause ducts and pins to deform over time
  - Prediction of thermal and flow performance vital to overall reactor performance and safety









Mock-up of simulated wire-wrapped fuel pin

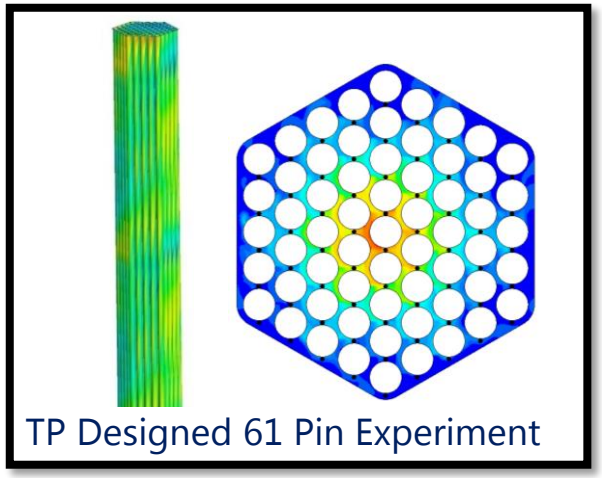
Copyright© 2016 TerraPower, LLC. All Rights Reserved.

Advanced Fuel Assembly Flow Characterization

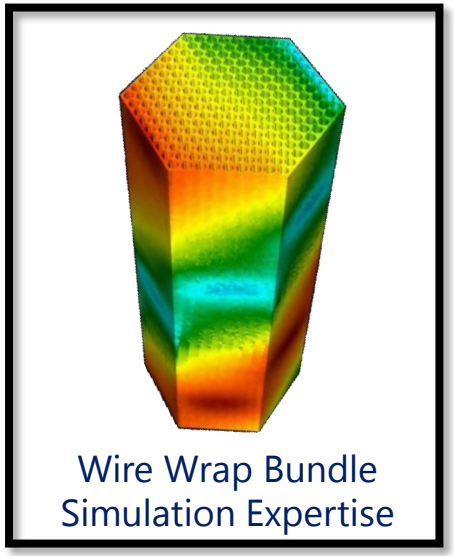
- DOE grant project consisting of experiments and numerical simulations of wire-wrapped bundles (non-deformed & deformed) for verification and validation of CFD tools

TerraPower

- Technical Lead
- Experiment Design
- **Industrial-Level (RANS) Verification & Validation Simulations**



TP Designed 61 Pin Experiment



Wire Wrap Bundle Simulation Expertise

Argonne NATIONAL LABORATORY

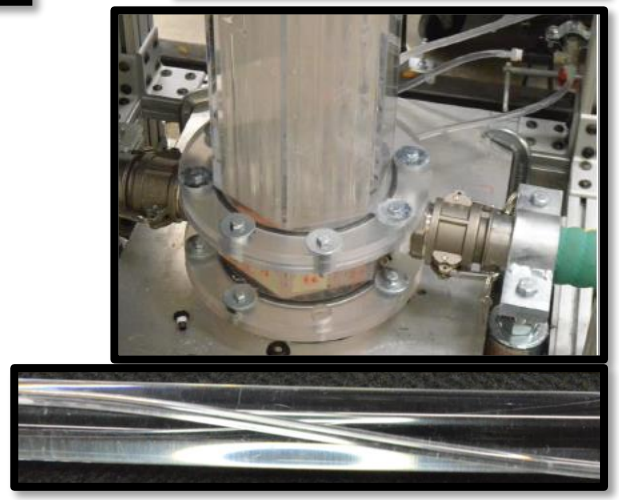
- High Resolution (LES) Validation Simulations

AREVA

- Programmatic Lead
- Heated Bundle Experiments in Water
- Pressure & Temperature Measurements



Heated Bundle Test Expertise



Flow Visualization Expertise

TEXAS A&M UNIVERSITY®

- Isothermal Bundle Experiments in P-Cymene
- Pressure & Laser Based Velocity Measurements

Copyright© 2016 TerraPower, LLC. All Rights Reserved.

Industry-Level V&V Simulations of Wire-Wrapped Bundles

- Previous wire-wrapped experiments were not designed with CFD V&V in mind & none take later-in-life geometric deformations into account
- Code Verification (Method of Manufactured Solutions)
- Pre-Test medium-fidelity RANS simulations
  - Simulations with designed geometries (momentum source used in place of wire-wrapping)
  - Solution verification simulations
  - Model sensitivity simulations
  - Compare blind simulations with experimental results when they become available
- Post-Test RANS simulations
  - Simulations with as-built geometry and measurement locations
  - Validation with experiments
  - Choice of optimal approach/models

Copyright© 2016 TerraPower, LLC. All Rights Reserved.

Code Verification

1. Verify Star-CCM+ commercial code for TerraPower's core design efforts
2. Start with simple equations & build physics & models until consistent with core design CFD modeling
3. Use Method of Manufactured Solutions (MMS) to obtain exact solutions

Establish math model $\mathcal{L}(u) = 0$

Choose the solution *a priori* $\hat{u}$

Operate PDE onto solution to obtain analytical source term $s = \mathcal{L}(\hat{u})$

Insert source term into PDE (the new PDE now has the chosen exact solution) $\mathcal{L}(u) = s$

4. Conduct Order of Accuracy studies for most rigorous code verification

$$\varepsilon_h = u_h - \tilde{u}$$

Discretization Error — **Discrete Solution** — **Exact Solution**

$$\|\varepsilon_h\|_2 = \left(\frac{1}{\Omega}\int_\Omega |\varepsilon_h|^2 d\omega\right)^{1/2}$$

L_2 Norm (global error)

$$\hat{p} = \frac{\ln\left(\frac{\|\varepsilon_{rh}\|}{\|\varepsilon_h\|}\right)}{\ln(r)}$$

Observed Order of Accuracy

Cell Size Ratio

$$r \equiv \frac{h_{\text{coarse}}}{h_{\text{fine}}}$$

Grid Refinement Factor

5. Troubleshoot if Observed Order of Accuracy (OOA) does not match Formal Order of Accuracy (FOA)

Copyright© 2016 TerraPower, LLC. All Rights Reserved.

Governing Equations

Manufactured Solution

- **Analytic functions w/ smooth derivatives**
- **No need to be physically realistic**

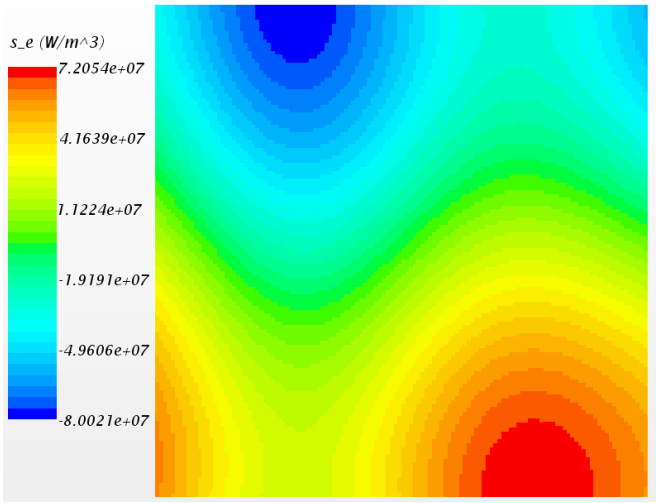
$$\rho(x,y) = \rho_0 + \rho_x \sin\left(\frac{a_{\rho x}\pi x}{L}\right) + \rho_y \cos\left(\frac{a_{\rho y}\pi y}{L}\right)$$

$$u(x,y) = u_0 + u_x \sin\left(\frac{a_{ux}\pi x}{L}\right) + u_y \cos\left(\frac{a_{uy}\pi y}{L}\right)$$

$$v(x,y) = v_0 + v_x \cos\left(\frac{a_{vx}\pi x}{L}\right) + v_y \sin\left(\frac{a_{vy}\pi y}{L}\right)$$

$$p(x,y) = p_0 + p_x \cos\left(\frac{a_{px}\pi x}{L}\right) + p_y \sin\left(\frac{a_{py}\pi y}{L}\right)$$

Analytical source term s_e for energy equation



2D Subsonic Steady Ideal-Gas Euler Equations

$$\frac{\partial(\rho u)}{\partial x} + \frac{\partial(\rho v)}{\partial y} = s_m(x,y)$$

$$\frac{\partial(\rho u^2 + p)}{\partial x} + \frac{\partial(\rho uv)}{\partial y} = s_x(x,y)$$

$$\frac{\partial(\rho vu)}{\partial x} + \frac{\partial(\rho v^2 + p)}{\partial y} = s_y(x,y)$$

$$\frac{\partial(\rho u e_t + pu)}{\partial x} + \frac{\partial(\rho v e_t + pv)}{\partial y} = s_e(x,y)$$

$$p = \rho RT$$

Equation, ϕ	ϕ_0	ϕ_x	ϕ_y	ϕ_z	$a_{\phi x}$	$a_{\phi y}$	$a_{\phi z}$
ρ (kg/m^3)	1.	0.15	-0.1	0.	1.	0.5	0.
u (m/s)	70.	5.	-7.	0.	1.5	0.6	0.
v (m/s)	90.	-15.	8.5	0.	0.5	2./3.	0.
w (m/s)	0.	0.	0.	0.	0.	0.	0.
p (N/m^2)	$1.\times10^5$	0.2×10^5	0.5×10^5	0.	2.	1.	0.

***Verification of a Compressible CFD Code using the Method of Manufactured Solutions*, Roy et al. AIAA 2002**
Table A.2 – Constants for 2D Euler Subsonic Manufactured Solution

Copyright© 2016 TerraPower, LLC. All Rights Reserved.

TerraPower

Solver & Boundary Conditions

- Segregated Flow w/ default expert properties
- Segregated Fluid Temperature w/ default expert properties
- Gradients - Hybrid Gauss-LSQ, Venkatakrishnan limiters, default expert properties
- Two Dimensional, Steady, Inviscid, Ideal Gas
- Mass, energy, and momentum sources determined with manufactured solutions

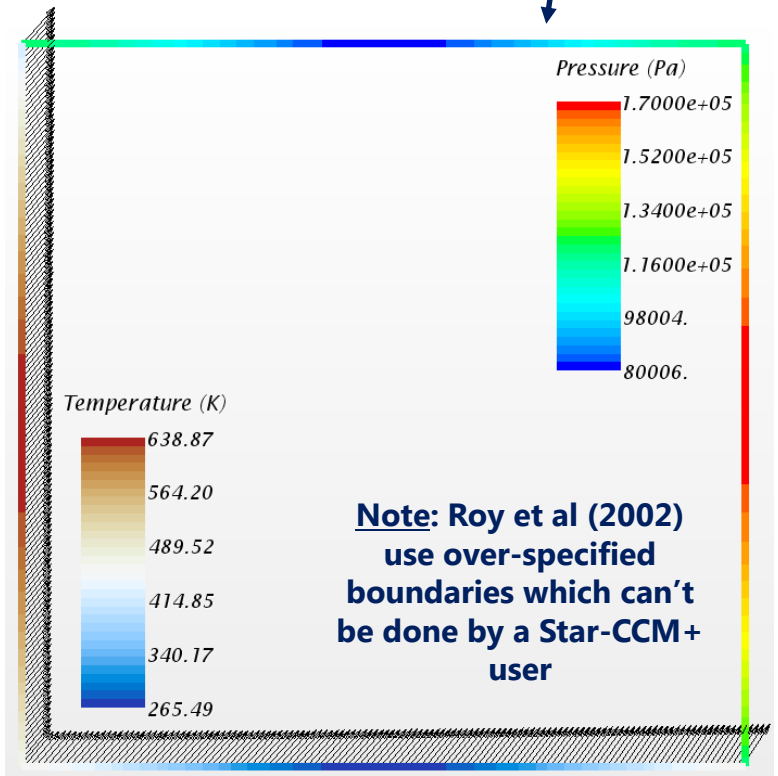
Mesh created with Star-CCM+ 2D mesher of LxL box (L = 1m)

Refinement levels:

h	16	8	4	2	1
Cells	8x8	16x16	32x32	64x64	128x128

Pressure Outlets

- ***Specified Pressure with manufactured solution***
- ***Velocity & Temperature extrapolated from interior using reconstruction gradients***
- ***No inflow occurs!***



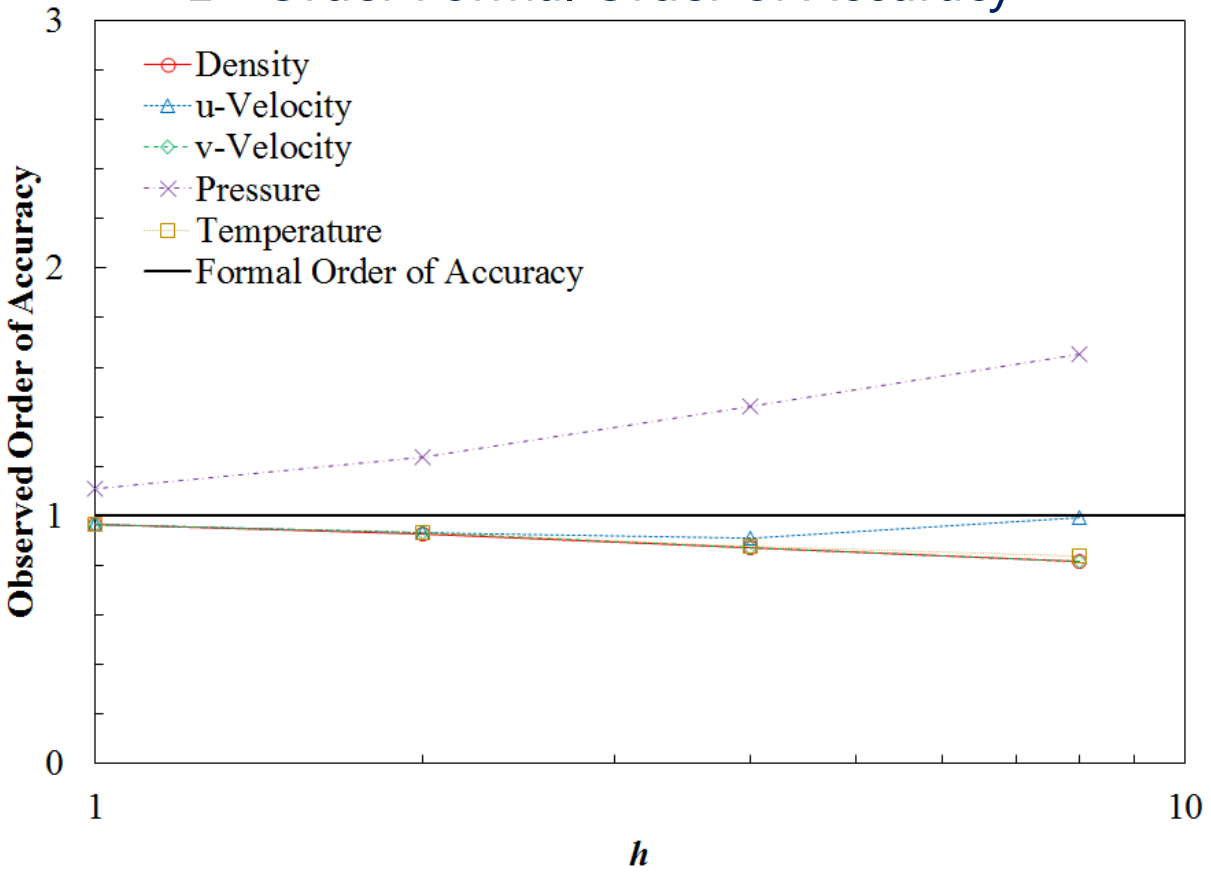
Velocity Inlets

- ***Specified Velocity & Temperature with manufactured solution***
- ***Pressure extrapolated from interior using reconstruction gradients***
- ***No outflow occurs!***

Copyright© 2016 TerraPower, LLC. All Rights Reserved.

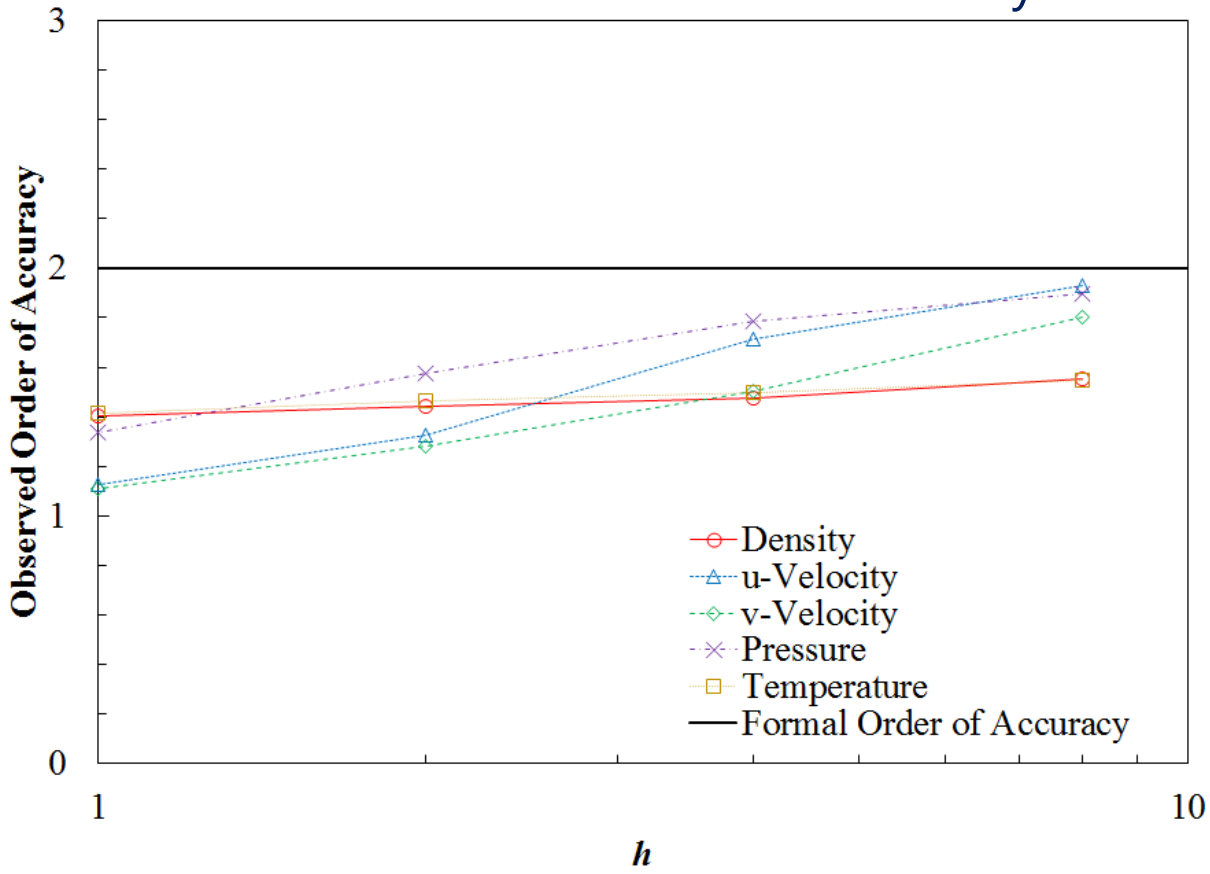
Results

1st-Order Formal Order of Accuracy



Observed Order of Accuracy approaches Formal Order of Accuracy with refinement

2nd-Order Formal Order of Accuracy



Observed Order of Accuracy drops well below Formal Order of Accuracy with refinement

Copyright© 2016 TerraPower, LLC. All Rights Reserved.

TerraPower

Current & Future Code Verification Work

- Working with CD-Adapco to resolve issue with 2nd-Order
  - Development team is checking simulation with over-specified BCs
- Have expanded MMS to Navier-Stokes equations
- Currently working on implementing RANS with two-equation turbulence models
- Future Work
  - Apply to 3D
  - Expand method to include all models required for core validation simulations

Copyright© 2016 TerraPower, LLC. All Rights Reserved.

Solution Verification

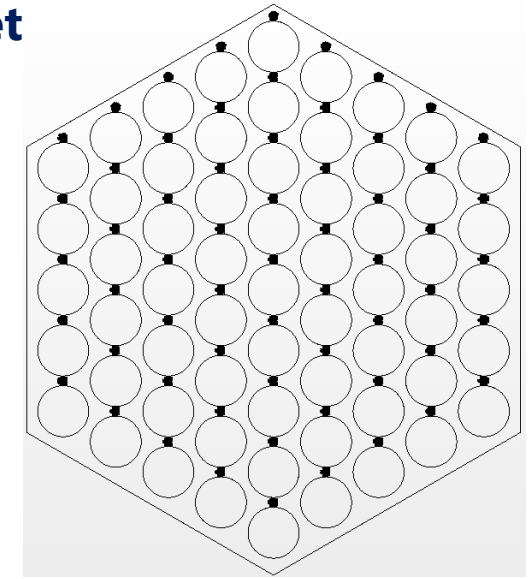
- Round-Off Error investigated by testing simulation with both mixed and double precision
  - Results show no appreciable variation
- Iterative Error minimized by converging residuals to machine zero for all simulations
- Statistical Sampling Error not an issue
  - Variables of interest show no appreciable variation with iterations after solution is converged
- Conduct systematic mesh refinement and analyze variables of interest to determine if asymptotic range has been reached
- Perform Richardson Extrapolation to estimate discretization error

Copyright© 2016 TerraPower, LLC. All Rights Reserved.

Geometry

Isothermal

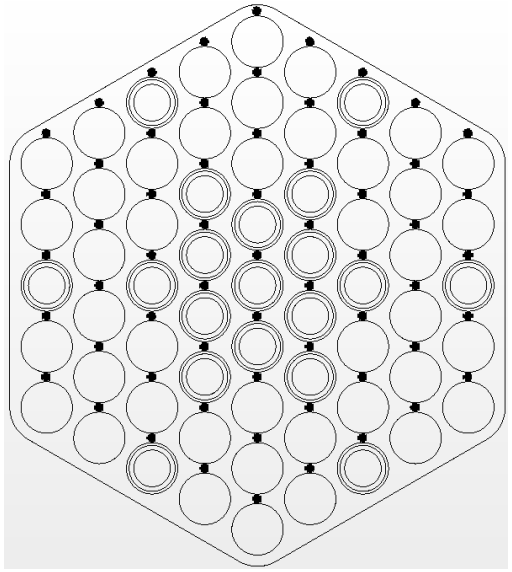
Outlet



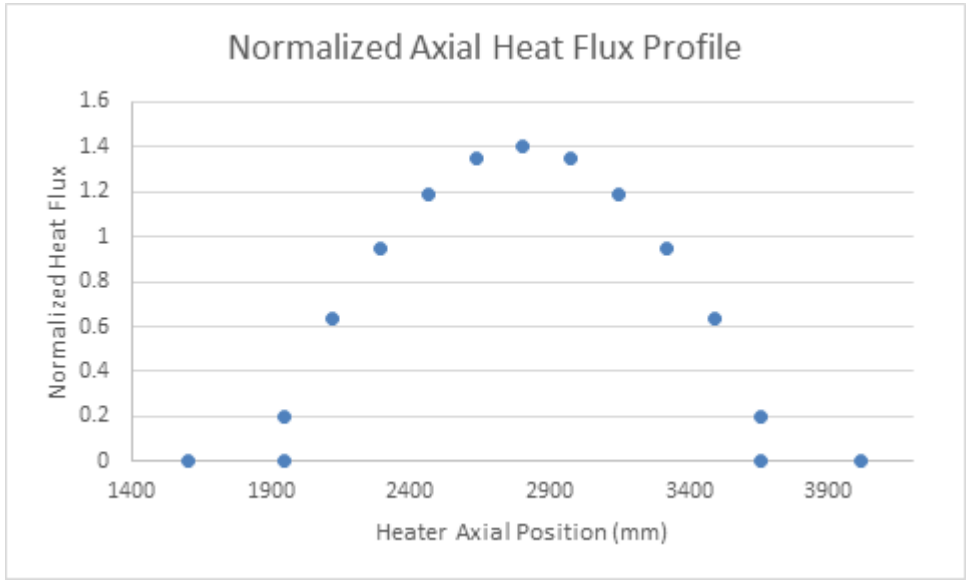
Inlet

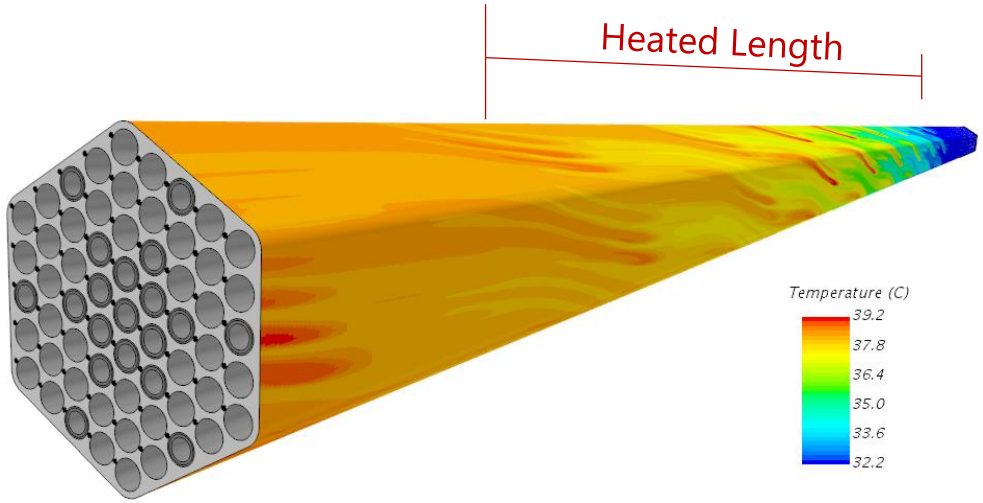
Pin Diameter = 15.9 mm
Wire Diameter = 3 mm
Duct Length = 1667 mm
Duct Wall Gap = 0.77% of flat-to-flat
3.5 wire pitches
P-Cymene
Re = 20,000
P/D = 1.189

Heated



Pin Diameter = 9.5 mm
Wire Diameter = 1.73 mm
Duct Length = 3705 mm
Duct Wall Gap = 0.77% of flat-to-flat
13 wire pitches
6 heated pitches
19 heated pins (24 kW per pin)
Water
Re = 20,000
P/D = 1.18



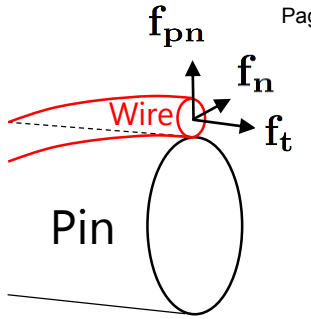


Copyright© 2016 TerraPower, LLC. All Rights Reserved.

TerraPower

Approach

- Momentum Source to represent wire-wrapping
  - Applies body force per unit volume to the fluid momentum equation at cell locations of the wire wrap in place of a body-fitted mesh around the solid wire
  - Originally developed at Argonne National Lab [Hu & Fanning, 2011]
  - Forces are dictated by models based on the local velocity field
  - For the normal forces a multiplication coefficient is present to prevent flow through the wire surface. It's value is included in the sensitivity study



$$\mathbf{f} = \mathbf{f_n} + \mathbf{f_{pn}} + \mathbf{f_t}$$

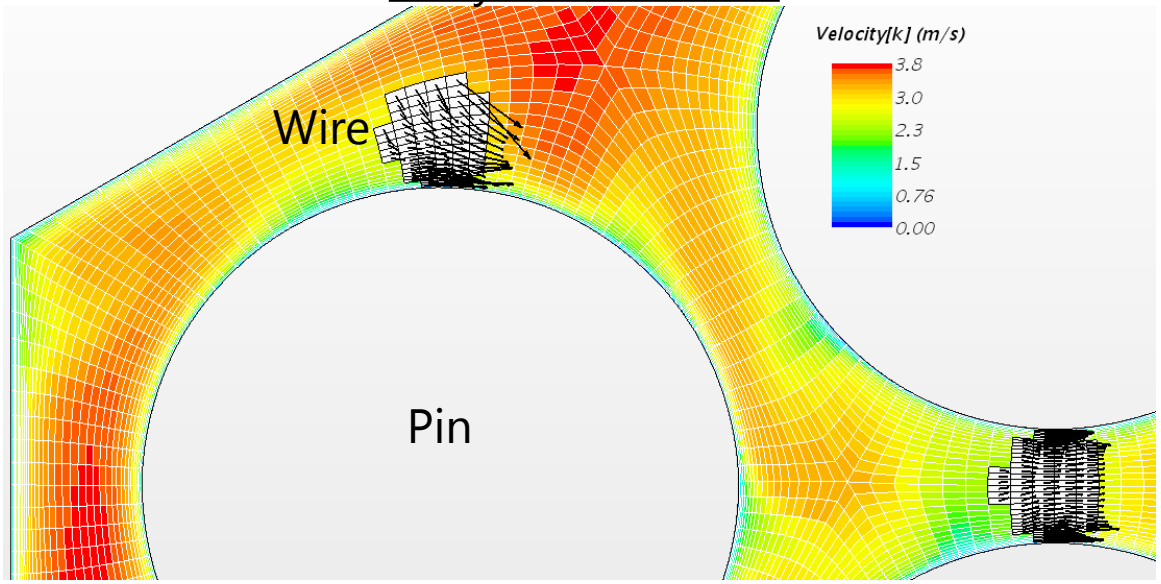
Body Force

Normal to the wire and tangential to the pin

Normal to the pin and normal to the wire

Tangential to the centerline of the helically-wrapped wire

Body force vectors



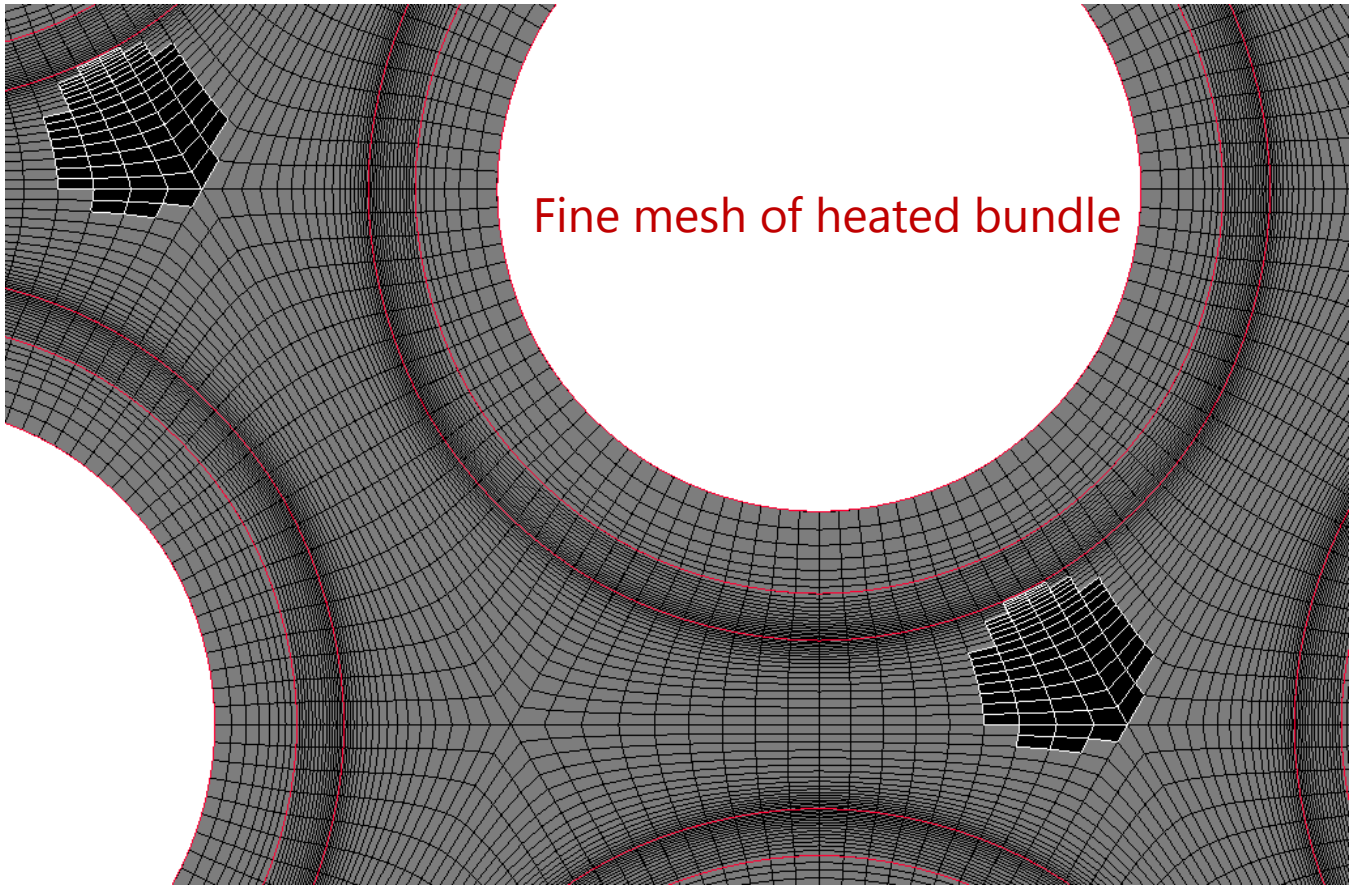
- Momentum source is ideal for initial scoping studies of wire-wrap fuel assemblies
  - Medium fidelity approach reduces computational cost
  - Avoids complications due to body fitted meshing of wires
  - Quick turn-around time for design modifications

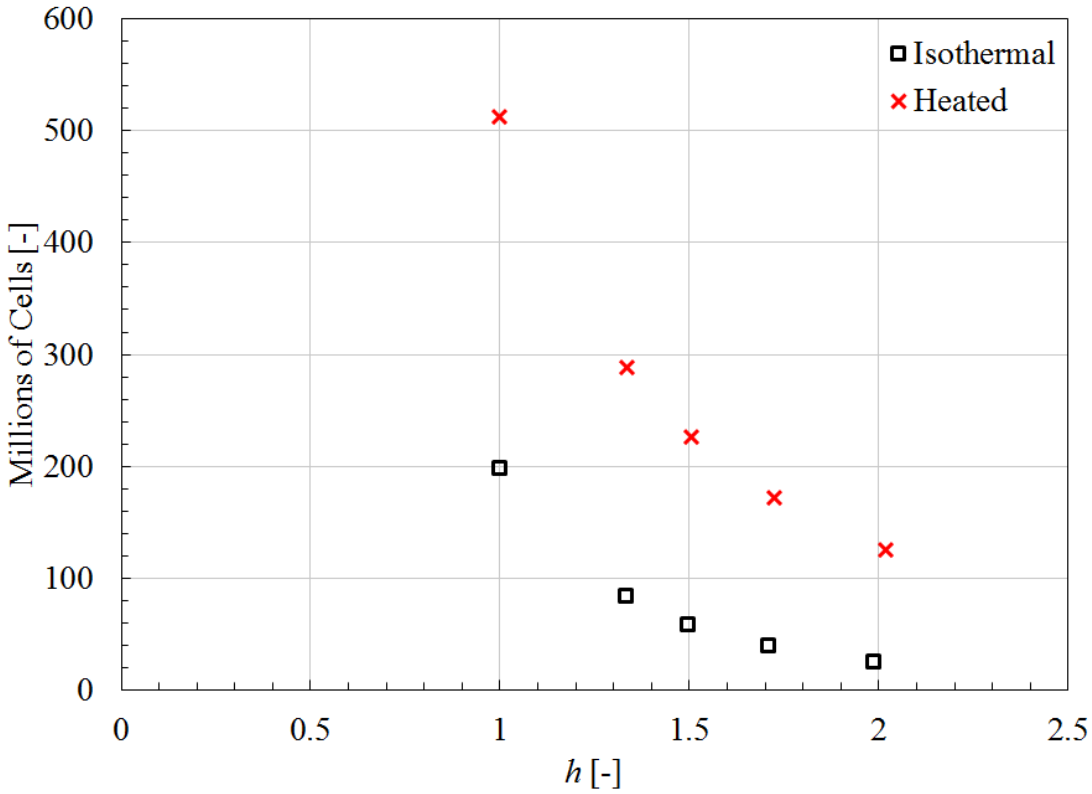
Copyright© 2016 TerraPower, LLC. All Rights Reserved.

TerraPower

Meshes

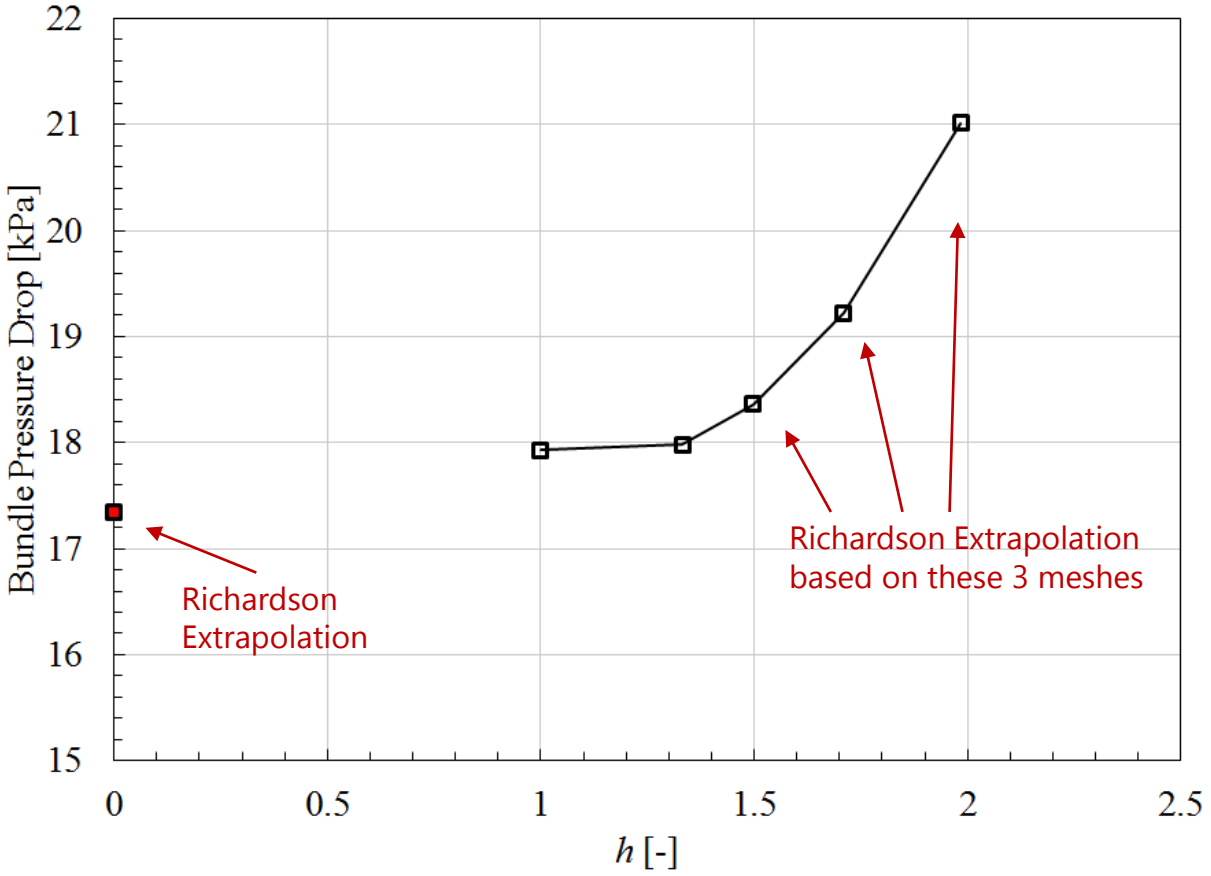
- Fully structured meshes created with GridPro and systematically refined
- Using All-y^+ wall functions
- Average y^+ values less than 5.0 for all meshes





Copyright© 2016 TerraPower, LLC. All Rights Reserved.

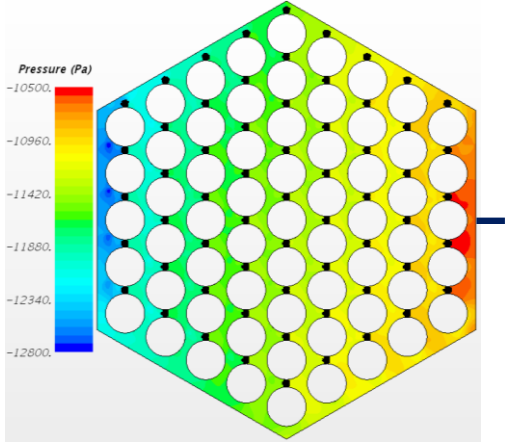
Isothermal Mesh Sensitivity

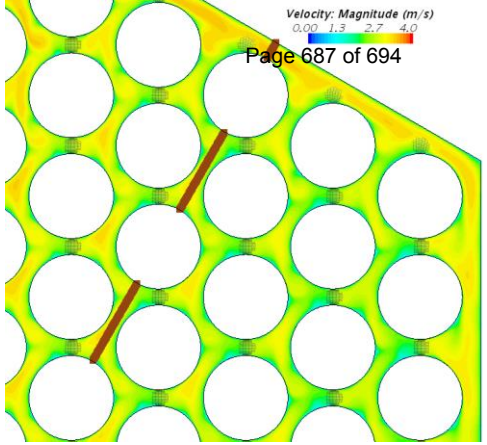


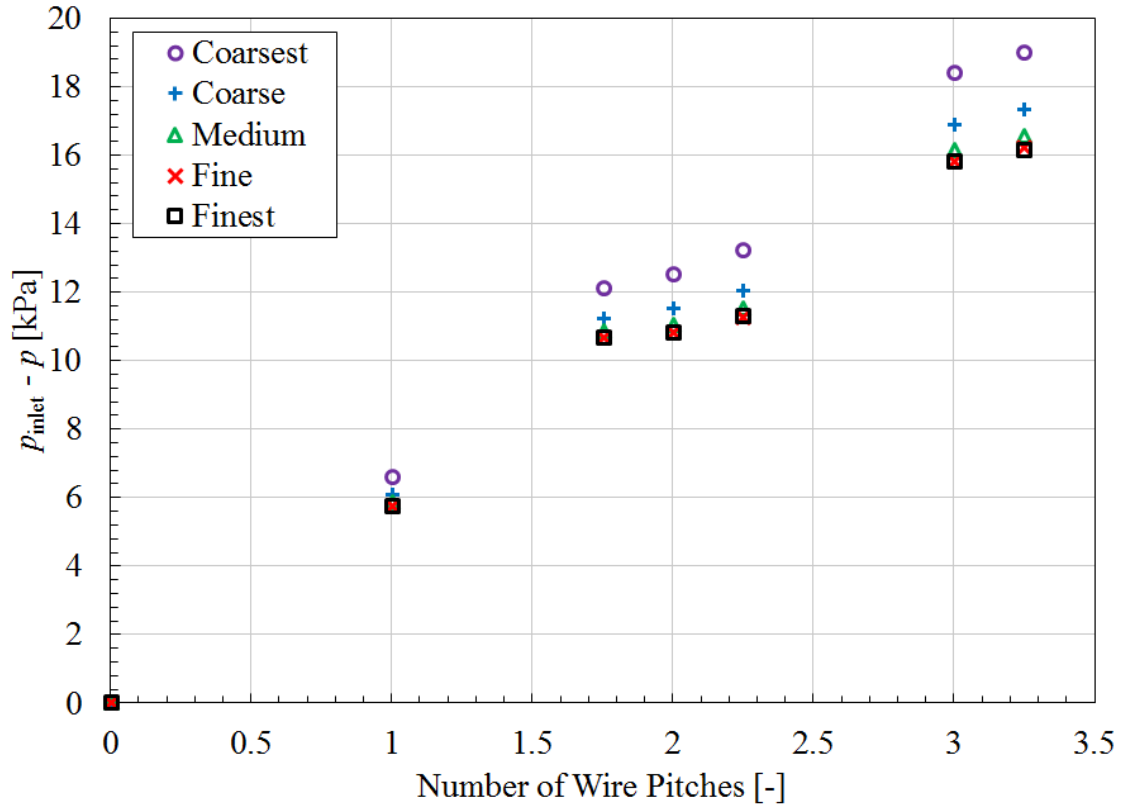
Observed Order of Accuracy	% Error between h=1.98 and RE	% Error between h=1.5 and RE	% Error between h=1.33 and RE	DE Estimate using h=1.33 Mesh [Pa]
4.32	21	6	3.7	642.5

Copyright© 2016 TerraPower, LLC. All Rights Reserved.

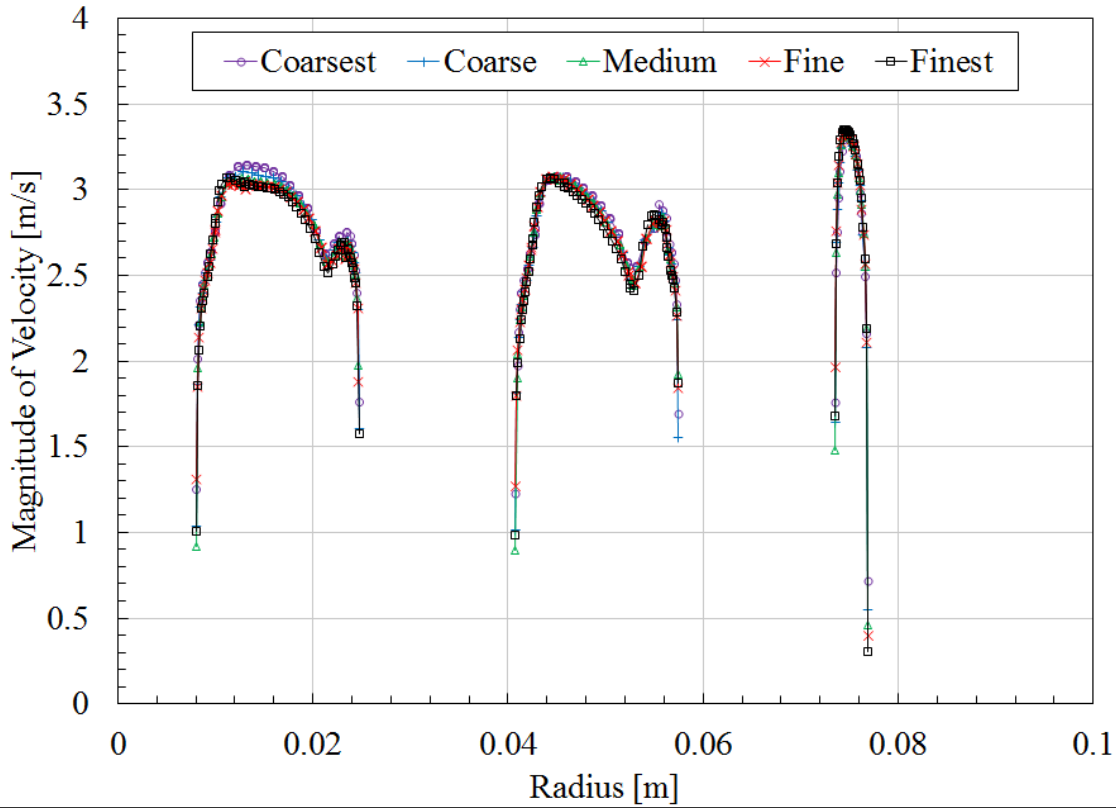
Isothermal Mesh Sensitivity







Wall probe Δp show similar convergence to bundle Δp

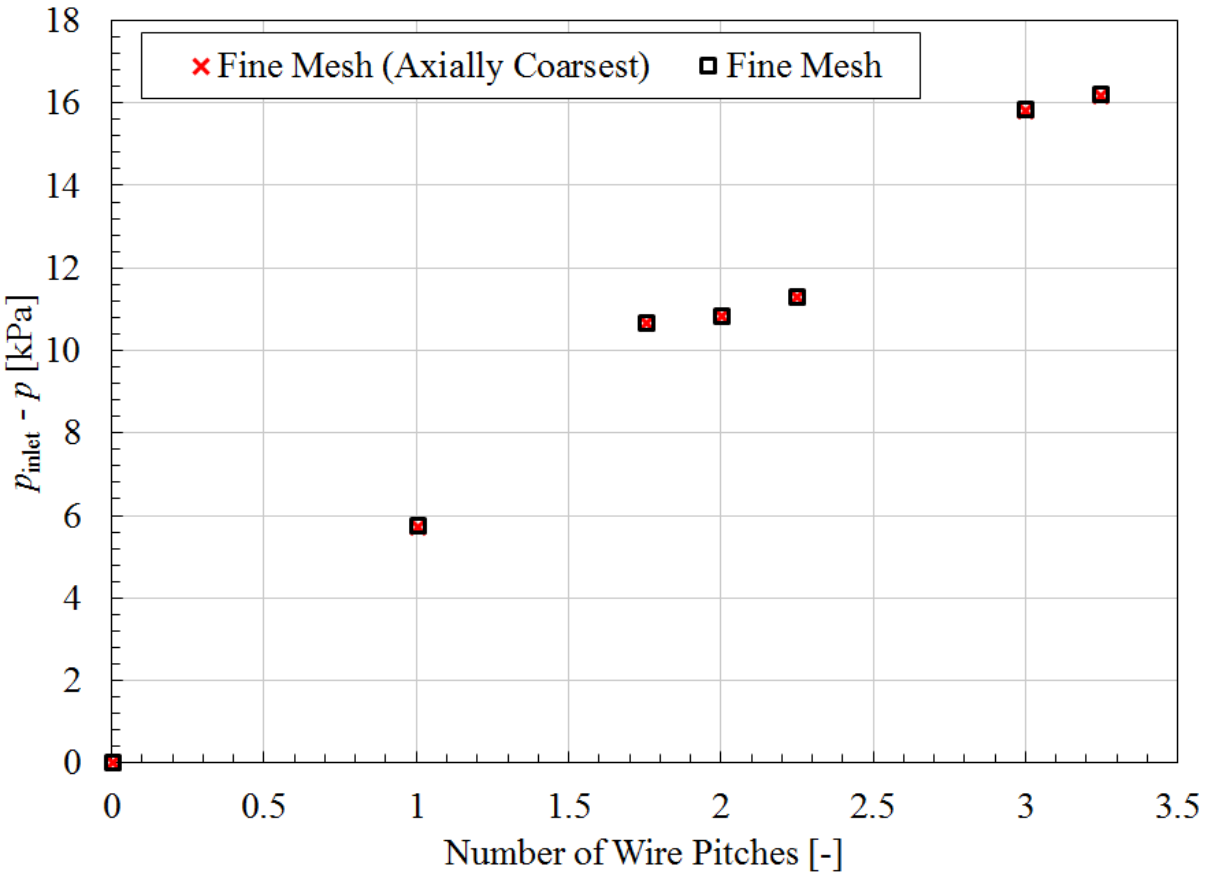


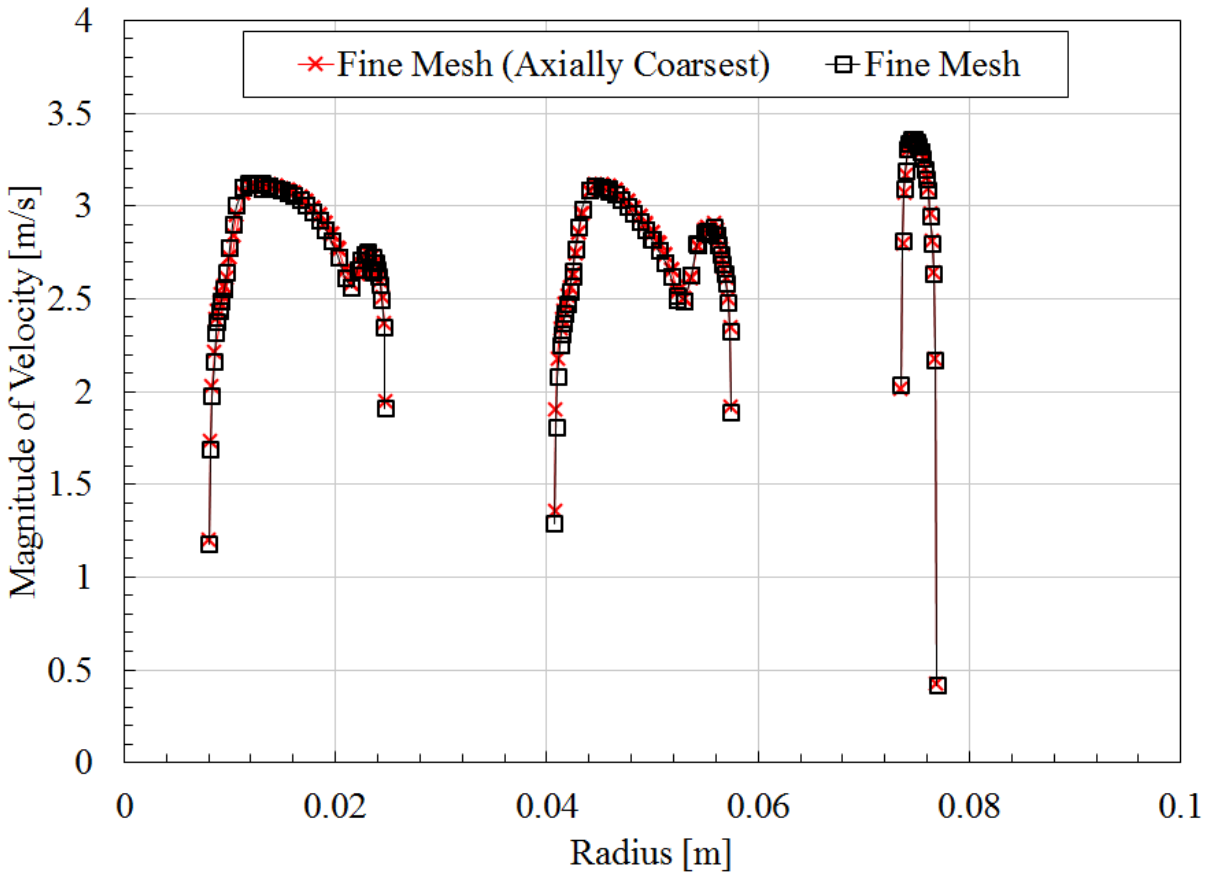
Velocity magnitude profiles show little variation with mesh size

Copyright© 2016 TerraPower, LLC. All Rights Reserved.

TerraPower

Axially Coarsening the Fine Mesh



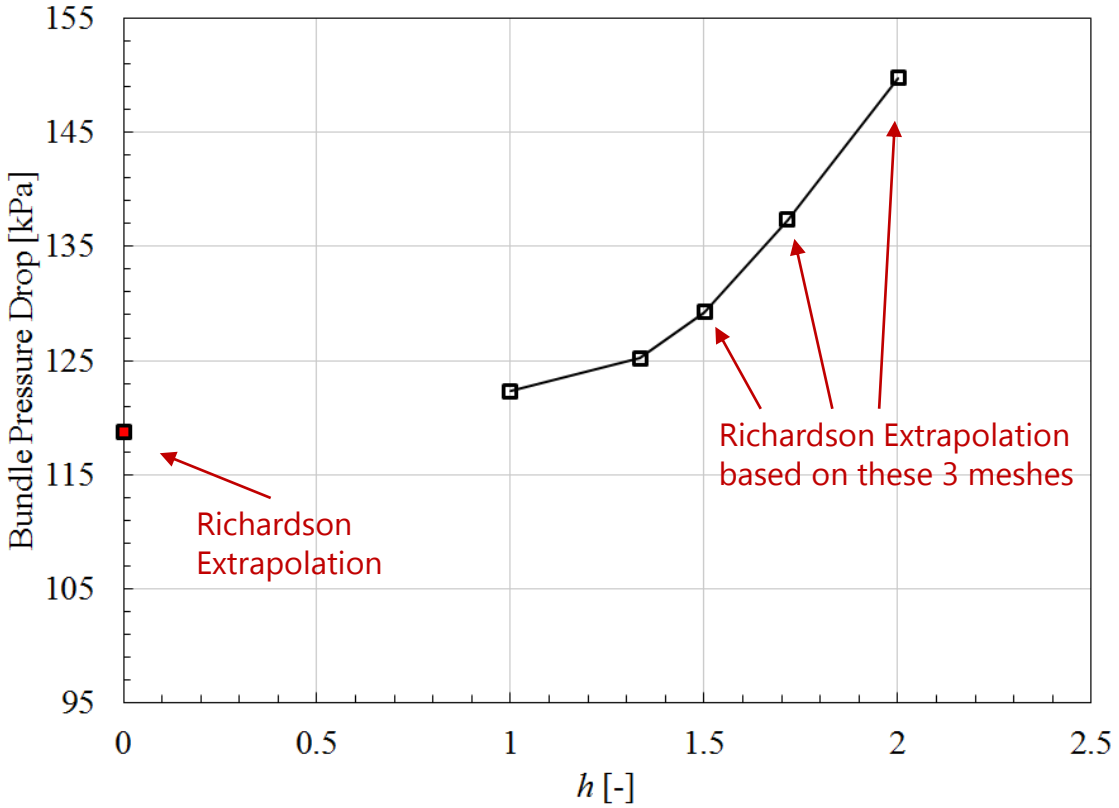


Axially coarsening fine mesh to number of axial cells in the coarsest mesh gives same results
Cell reduction of 27 million cells (32 % reduction)

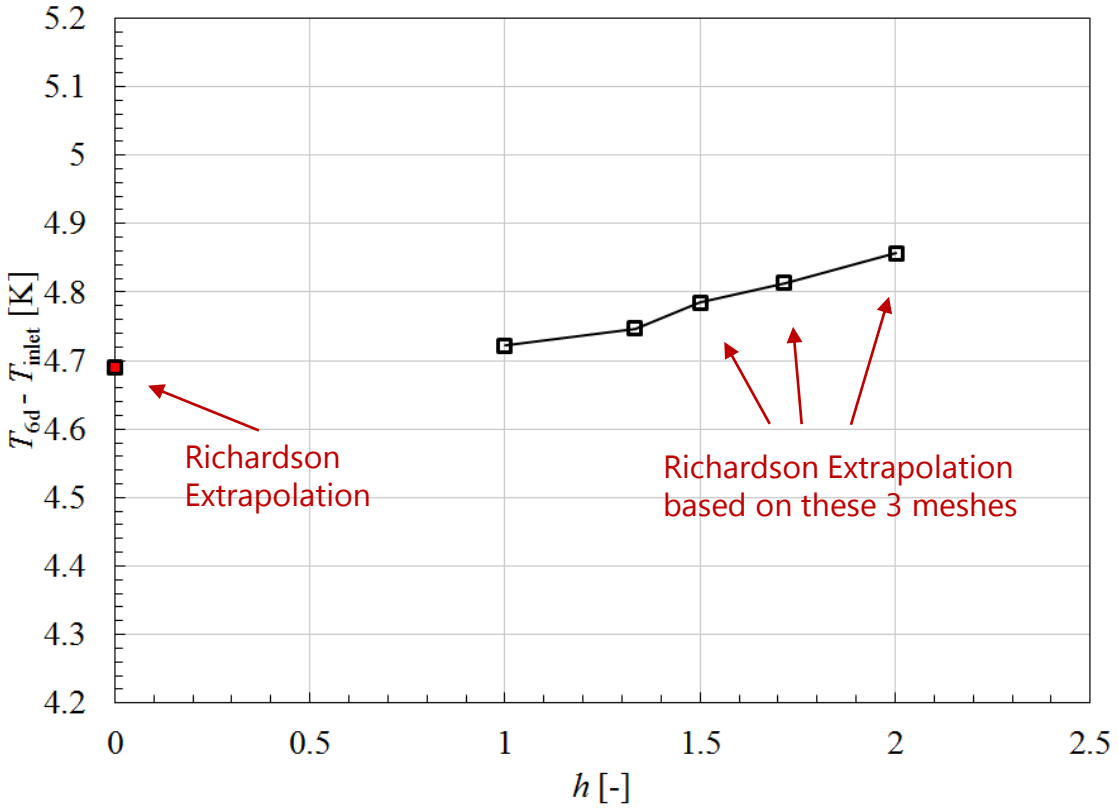
Copyright© 2016 TerraPower, LLC. All Rights Reserved.

TerraPower

Heated Mesh Sensitivity



Observed Order of Accuracy	% Error between h=2.0 and RE	% Error between h=1.5 and RE	% Error between h=1.33 and RE	DE Estimate using h=1.33 Mesh [Pa]
1.92	26.16	8.86	5.46	6485

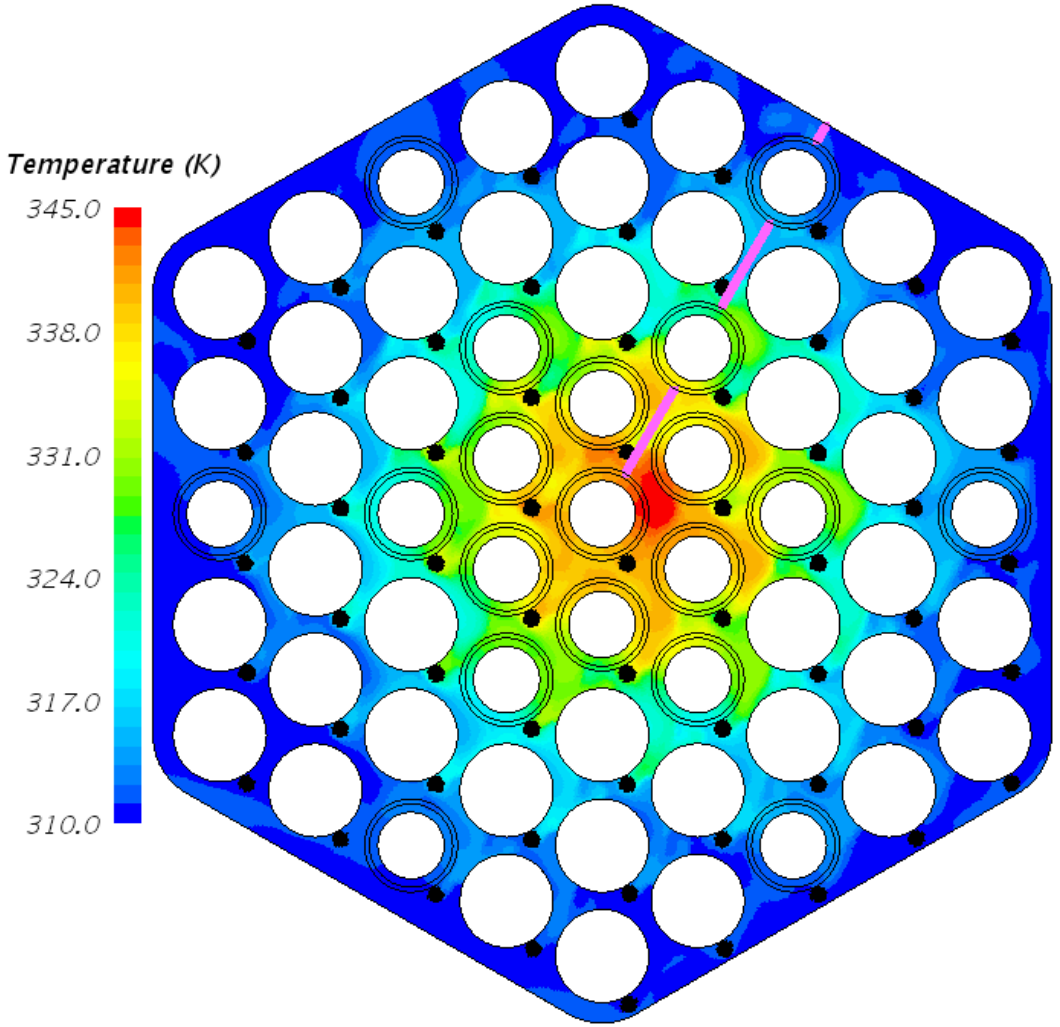


Observed Order of Accuracy	% Error between h=1.98 and RE	% Error between h=1.5 and RE	% Error between h=1.33 and RE	DE Estimate using h=1.33 Mesh [K]
2.05	3.56	2.03	1.21	0.057

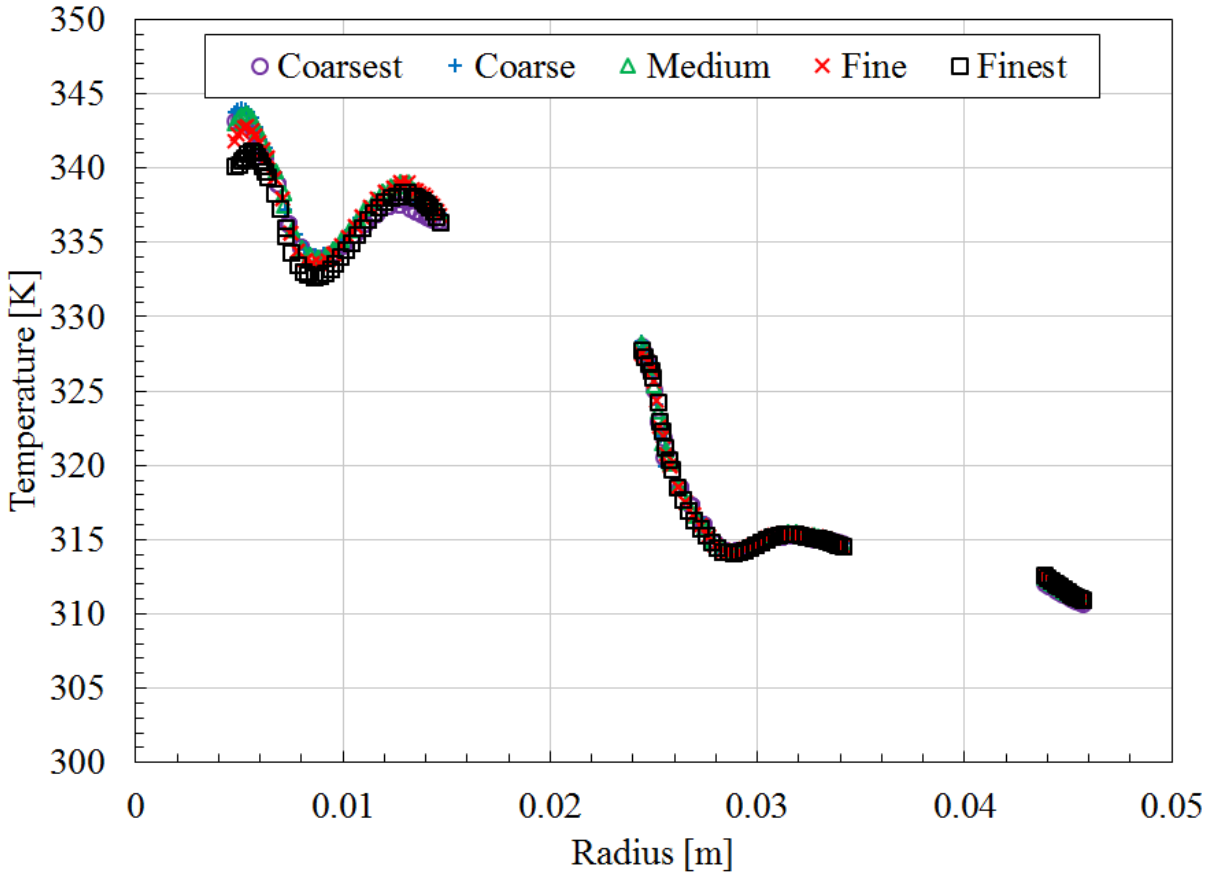
Copyright© 2016 TerraPower, LLC. All Rights Reserved.

TerraPower

Heated Mesh Sensitivity



Probe points just above heated region

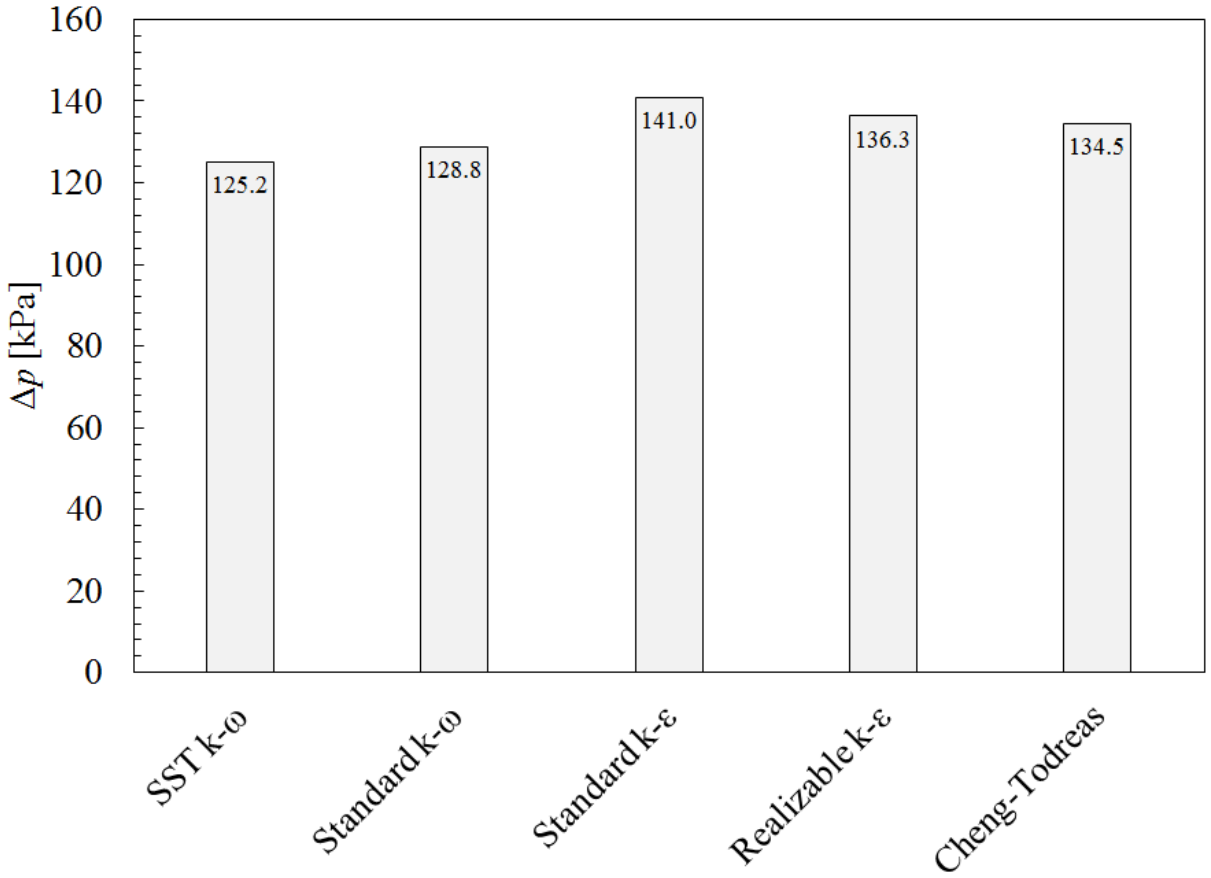


Temperature profiles show little sensitivity to mesh refinement

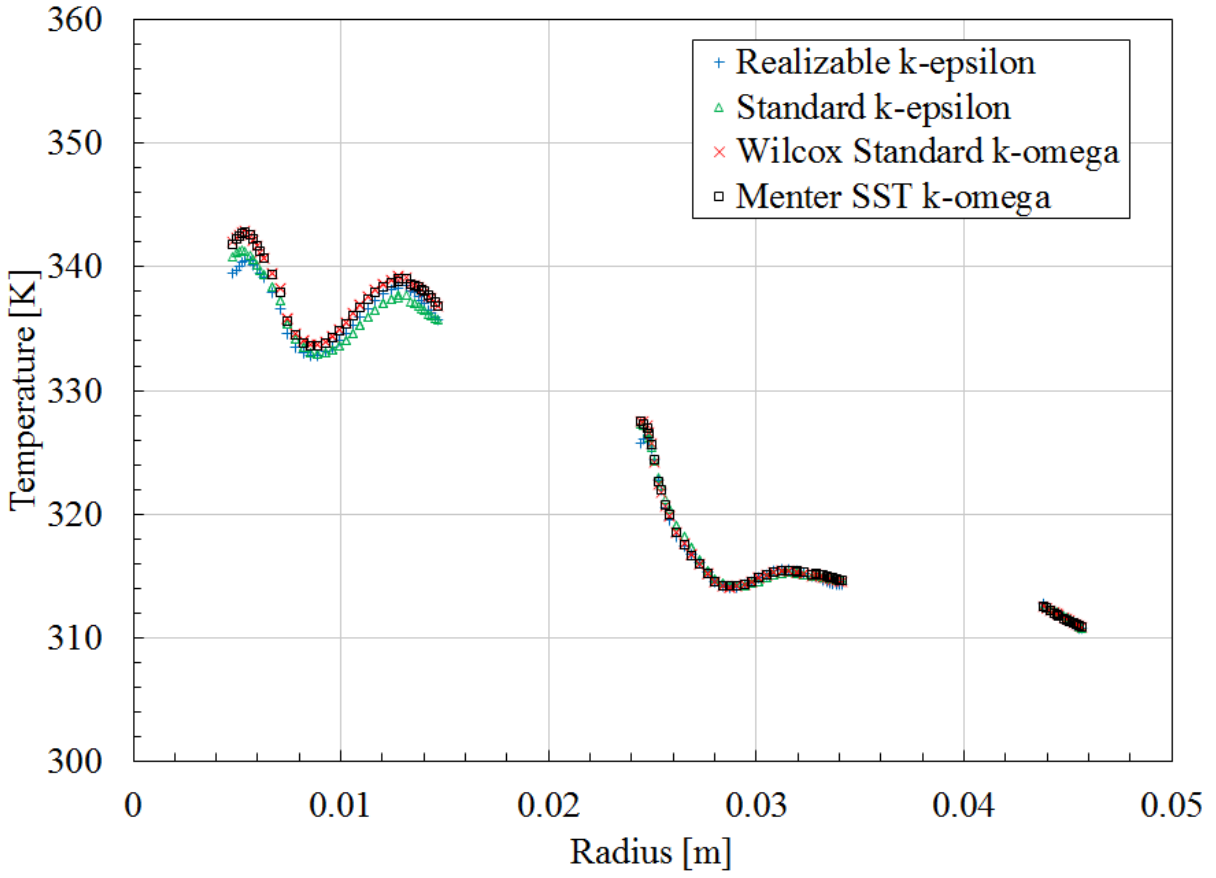
Copyright© 2016 TerraPower, LLC. All Rights Reserved.

TerraPower

Heated Turbulence Model Sensitivity (Fine Mesh)



All turbulence models predict Δ*p* within ~7% of well-known bundle Δ*p* correlation



Temperature profiles show slight variation with choice of turbulence model

Isothermal bundle pressures show similar sensitivity to choice of turbulence model

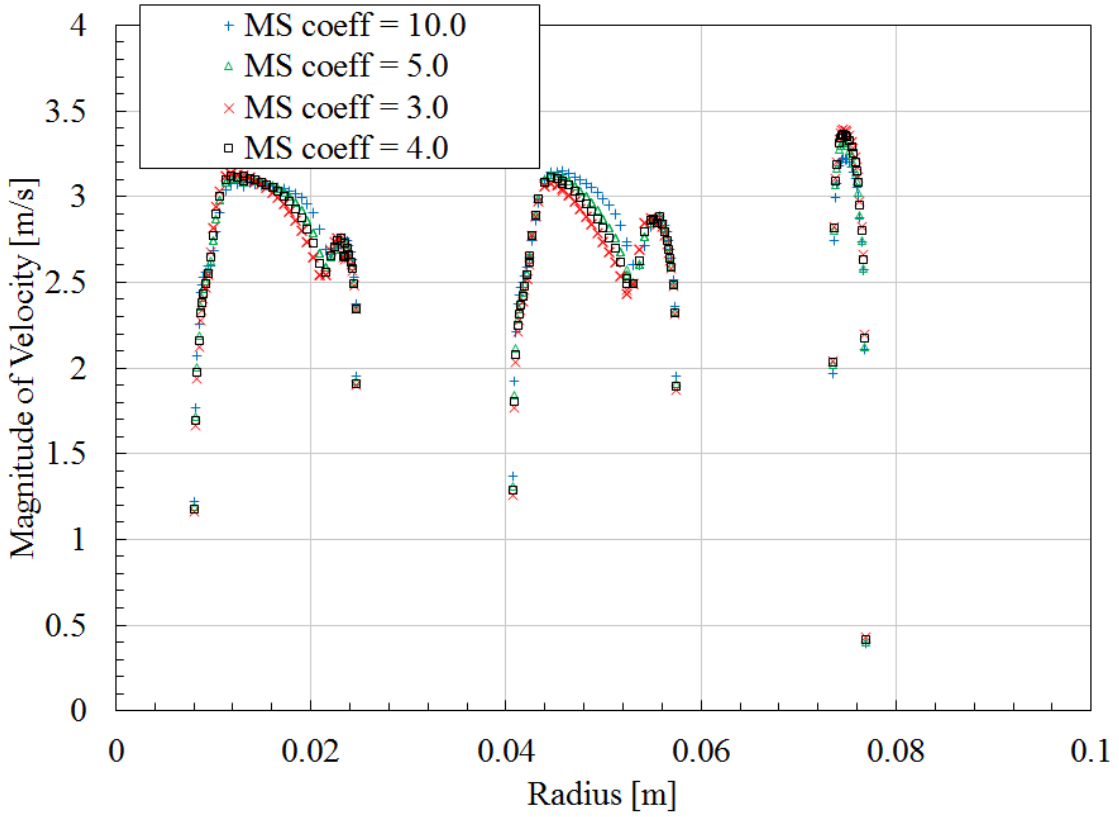
Isothermal bundle velocity field shows little sensitivity to choice of turbulence model

Copyright© 2016 TerraPower, LLC. All Rights Reserved.

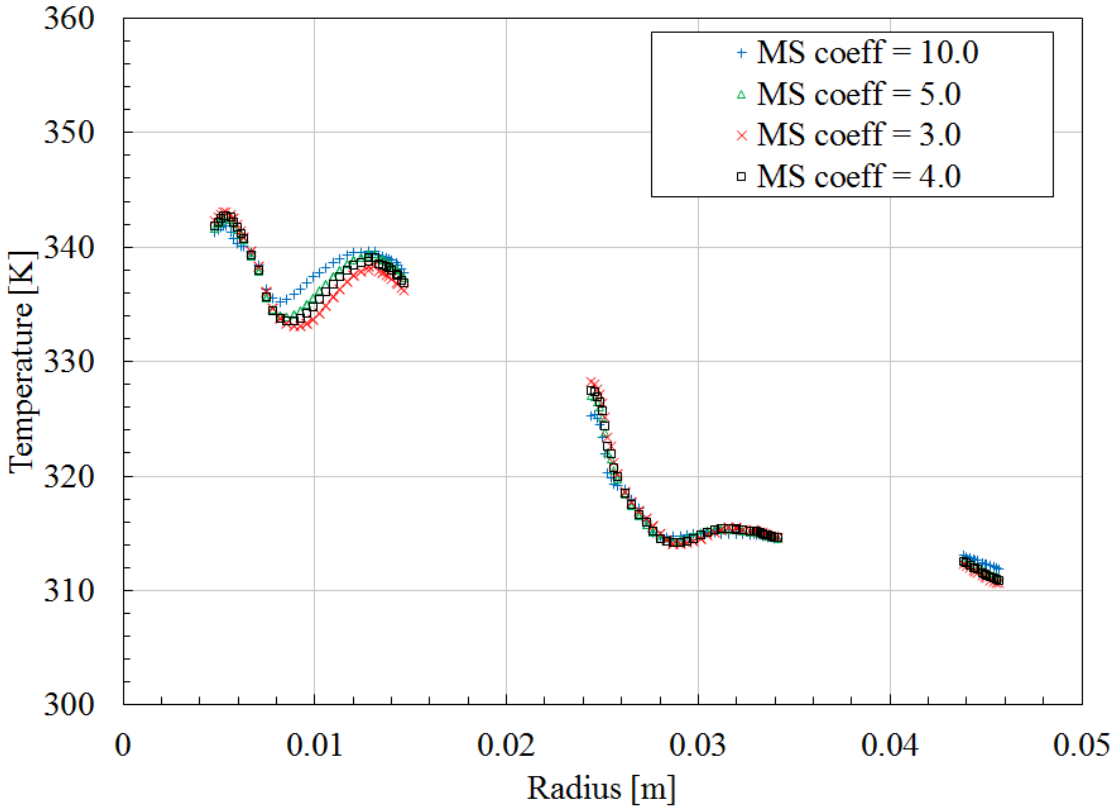
TerraPower

Momentum Source Coefficient Sensitivity (Fine Mesh)

- No appreciable change in pressure values due to varying momentum source coefficient
- Slight variations in velocity and temperature profiles with coefficient value



Isothermal Bundle



Heated Bundle

Copyright© 2016 TerraPower, LLC. All Rights Reserved.

TerraPower

Summary & Future Work

- Summary
  - Method of Manufactured Solutions code verification approach implemented into Star-CCM+
  - Results show convergence and may have uncovered an issue with 2nd-order schemes
  - Solution verification of non-deformed isothermal and heated bundles completed and discretization error estimated from converged solutions
  - Turbulence model sensitivity tests show little variation in velocity and temperature fields; pressure drop results are close to accepted correlation
  - Temperature & velocity fields show some sensitivity to value of momentum source coefficient

- Future Work
  - Expand on code verification & work with CD-Adapco to fix issues
  - Simulate deformed bundle geometries for pre-tests
  - Use verification and sensitivity studies to determine pre-test blind results
  - Perform solution validation and further post-test simulations after test results become available

Copyright© 2016 TerraPower, LLC. All Rights Reserved.

Acknowledgements

- TerraPower
- AREVA
- Argonne National Lab
- Texas A&M University
- Department of Energy

This material is provided to support the Department of Energy [National Nuclear Security Administration] Award Number [DE-NE0008321]

Disclaimer

"Neither the United States Government nor any agency thereof, nor any of their employees, makes any warranty, express or implied, or assumes any legal liability or responsibility for the accuracy, completeness, or usefulness of any information, apparatus, product, or process disclosed, or represents that its use would not infringe privately owned rights. Reference herein to any specific commercial product, process, or service by trade name, trademark, manufacturer, or otherwise does not necessarily constitute or imply its endorsement, recommendation, or favoring by the United States Government or any agency thereof. The views and opinions of authors expressed herein do not necessarily state or reflect those of the United States Government or any agency thereof."